

# IFMBE Proceedings

Katashev · Dekhtyar · Spigulis (Eds.)

Volume 20

NBC – 14th Nordic-Baltic Conference  
on Biomedical Engineering  
and Medical Physics

16–20 June 2008, Riga  
Latvia



**Series Editors: R. Magjarevic and J. H. Nagel**

The International Federation for Medical and Biological Engineering, IFMBE, is a federation of national and transnational organizations representing internationally the interests of medical and biological engineering and sciences. The IFMBE is a non-profit organization fostering the creation, dissemination and application of medical and biological engineering knowledge and the management of technology for improved health and quality of life. Its activities include participation in the formulation of public policy and the dissemination of information through publications and forums. Within the field of medical, clinical, and biological engineering, IFMBE's aims are to encourage research and the application of knowledge, and to disseminate information and promote collaboration. The objectives of the IFMBE are scientific, technological, literary, and educational.

The IFMBE is a WHO accredited NGO covering the full range of biomedical and clinical engineering, healthcare, healthcare technology and management. It is representing through its 58 member societies some 120.000 professionals involved in the various issues of improved health and health care delivery.

IFMBE Officers

President: Makoto Kikuchi, Vice-President: Herbert Voigt, Former-President: Joachim H. Nagel

Treasurer: Shankar M. Krishnan, Secretary-General: Ratko Magjarevic

<http://www.ifmbe.org>

### ***Previous Editions:***

**IFMBE Proceedings NBC 2008 “14th Nordic-Baltic Conference on Biomedical Engineering and Medical Physics”,**  
Vol. 20, 2008, Riga, Latvia, CD

**IFMBE Proceedings APCMBE 2008 “7th Asian-Pacific Conference on Medical and Biological Engineering”,**  
Vol. 19, 2008, Beijing, China, CD

**IFMBE Proceedings CLAIB 2007 “IV Latin American Congress on Biomedical Engineering 2007, Bioengineering Solution for Latin America Health”,** Vol. 18, 2007, Margarita Island, Venezuela, CD

**IFMBE Proceedings ICEBI 2007 “13th International Conference on Electrical Bioimpedance and the 8th Conference on Electrical Impedance Tomography”,** Vol. 17, 2007, Graz, Austria, CD

**IFMBE Proceedings MEDICON 2007 “11th Mediterranean Conference on Medical and Biological Engineering and Computing 2007”,** Vol. 16, 2007, Ljubljana, Slovenia, CD

**IFMBE Proceedings BIOMED 2006 “Kuala Lumpur International Conference on Biomedical Engineering”,**  
Vol. 15, 2004, Kuala Lumpur, Malaysia, CD

**IFMBE Proceedings WC 2006 “World Congress on Medical Physics and Biomedical Engineering”,**  
Vol. 14, 2006, Seoul, Korea, DVD

**IFMBE Proceedings BSN 2007 “4th International Workshop on Wearable and Implantable Body Sensor Networks”,**  
Vol. 13, 2006, Aachen, Germany

**IFMBE Proceedings ICBMEC 2005 “The 12th International Conference on Biomedical Engineering”,**  
Vol. 12, 2005, Singapore, CD

**IFMBE Proceedings EMBEC'05 “3rd European Medical & Biological Engineering Conference, IFMBE European Conference on Biomedical Engineering”,** Vol. 11, 2005, Prague, Czech Republic, CD

**IFMBE Proceedings ICCE 2005 “The 7th International Conference on Cellular Engineering”,**  
Vol. 10, 2005, Seoul, Korea, CD

**IFMBE Proceedings NBC 2005 “13th Nordic Baltic Conference on Biomedical Engineering and Medical Physics”,**  
Vol. 9, 2005, Umeå, Sweden

**IFMBE Proceedings APCMBE 2005 “6th Asian-Pacific Conference on Medical and Biological Engineering”,**  
Vol. 8, 2005, Tsukuba, Japan, CD

**IFMBE Proceedings BIOMED 2004 “Kuala Lumpur International Conference on Biomedical Engineering”,**  
Vol. 7, 2004, Kuala Lumpur, Malaysia

**IFMBE Proceedings MEDICON and HEALTH TELEMATICS 2004 “X Mediterranean Conference on Medical and Biological Engineering”,** Vol. 6, 2004, Ischia, Italy, CD

**IFMBE Proceedings 3rd Latin – American Congress on Biomedical Engineering “III CLAEB 2004”,**  
Vol. 5, 2004, Joao Pessoa, Brazil, CD

**IFMBE Proceedings WC2003 “World Congress on Medical Physics and Biomedical Engineering”,**  
Vol. 4, 2003, Sydney, Australia, CD

**IFMBE Proceedings EMBEC'02 “2nd European Medical and Biological Engineering Conference”,**  
Vol. 3, Parts 1 & 2, 2002, H. Hutten and P. Kroesl (Eds.), Vienna, Austria

IFMBE Proceedings Vol. 20

Alexei Katashev · Yuri Dekhtyar · Janis Spigulis (Eds.)

---

# 14th Nordic-Baltic Conference on Biomedical Engineering and Medical Physics

NBC 2008

16–20 June 2008

Riga, Latvia

## Editors

Alexei Katashev  
Riga Technical University  
Inst. of Biomedical Engineering  
and Nanotechnologies  
Kalku street 1  
Riga, LV-1658  
Latvia  
katashev@latnev.lv

Janis Spigulis  
University of Latvia  
Inst. of Atomic Physics  
and Spectroscopy  
Raina blvd. 19  
Riga, LV-1586  
Latvia  
Janis.Spigulis@lu.lv

Yuri Dekhtyar  
Riga Technical University  
Inst. of Biomedical Engineering  
and Nanotechnologies  
Kalku street 1  
Riga, LV-1658  
Latvia  
dekhtyar@latnet.lv

ISSN 1680-0737

ISBN-13 978-3-540-69366-6

e-ISBN-13 978-3-540-69367-3

DOI 10.1007/978-3-540-69367-3

Library of Congress Control Number: 2008928714

© International Federation of Medical and Biological Engineering 2008

This work is subject to copyright. All rights are reserved, whether the whole or part of the material is concerned, specifically the rights of translation, reprinting, reuse of illustrations, recitation, broadcasting, reproduction on microfilm or in any other way, and storage in data banks. Duplication of this publication or parts thereof is permitted only under the provisions of the German Copyright Law of September 9, 1965, in its current version, and permissions for use must always be obtained from Springer. Violations are liable to prosecution under the German Copyright Law.

The use of general descriptive names, registered names, trademarks, etc. in this publication does not imply, even in the absence of a specific statement, that such names are exempt from the relevant protective laws and regulations and therefore free for general use.

The IFMBE Proceedings is an Official Publication of the International Federation for Medical and Biological Engineering (IFMBE)

*Typesetting:* Data supplied by the authors

*Production:* le-tex publishing services oHG, Leipzig

*Cover design:* deblik, Berlin

Printed on acid-free paper

9 8 7 6 5 4 3 2 1

springer.com

## About IFMBE

The International Federation for Medical and Biological Engineering (IFMBE) was established in 1959 to provide medical and biological engineering with a vehicle for international collaboration in research and practice of the profession. The Federation has a long history of encouraging and promoting international cooperation and collaboration in the use of science and engineering for improving health and quality of life.

The IFMBE is an organization with membership of national and transnational societies and an International Academy. At present there are 52 national members and 5 transnational members representing a total membership in excess of 120 000 worldwide. An observer category is provided to groups or organizations considering formal affiliation. Personal membership is possible for individuals living in countries without a member society. The International Academy includes individuals who have been recognized by the IFMBE for their outstanding contributions to biomedical engineering.

### *Objectives*

The objectives of the International Federation for Medical and Biological Engineering are scientific, technological, literary, and educational. Within the field of medical, clinical and biological engineering its aims are to encourage research and the application of knowledge, and to disseminate information and promote collaboration.

In pursuit of these aims the Federation engages in the following activities: sponsorship of national and international meetings, publication of official journals, cooperation with other societies and organizations, appointment of commissions on special problems, awarding of prizes and distinctions, establishment of professional standards and ethics within the field, as well as other activities which in the opinion of the General Assembly or the Administrative Council would further the cause of medical, clinical or biological engineering. It promotes the formation of regional, national, international or specialized societies, groups or boards, the coordination of bibliographic or informational services and the improvement of standards in terminology, equipment, methods and safety practices, and the delivery of health care.

The Federation works to promote improved communication and understanding in the world community of engineering, medicine and biology.

### *Activities*

Publications of IFMBE include: the journal *Medical and Biological Engineering and Computing*, the electronic magazine *IFMBE News*, and the Book Series on Biomedical Engineering. In cooperation with its international and regional conferences, IFMBE also publishes the IFMBE Proceedings Series. All publications of the IFMBE are published by Springer Verlag. The Federation has two divisions: Clinical Engineering and Health Care Technology Assessment.

Every three years the IFMBE holds a World Congress on Medical Physics and Biomedical Engineering, organized in cooperation with the IOMP and the IUPESM. In addition, annual, milestone and regional conferences are organized in different regions of the world, such as Asia Pacific, Europe, the Nordic-Baltic and Mediterranean regions, Africa and Latin America.

The administrative council of the IFMBE meets once a year and is the steering body for the IFMBE: The council is subject to the rulings of the General Assembly, which meets every three years.

Information on the activities of the IFMBE can be found on the web site at: <http://www.ifmbe.org>.

# Foreword

It is our great pleasure to welcome you at the 14th Nordic-Baltic Conference on Biomedical Engineering and Medical Physics – NBC-2008. The Conference is held every third year in one of the Nordic-Baltic countries under the auspices of the International Federation for Medical and Biological Engineering and traditionally brings together scientists not only from the Nordic-Baltic region, but from the entire world.

Modern Biomedical engineering is dynamic, boosting field of science, benefiting from its intrinsic interdisciplinary nature. That is why the Conference brings together scientists from medicine, chemistry, physics, engineers and computer scientists as well as people from education and business to enjoy the meeting under the motto “*Cooperation for health*”.

Gratitude should be expressed to the members of the International Scientific Committee of the Conference. With the invaluable help from the International Advisory Committee they composed the Program of the Conference, ensuring its scientific quality and relevance to the up-to-date needs. Special thanks to the Local Organizing Committee and to our sponsors, that made Conference happen.

For the first time NBC comes to Riga – the capital city of Latvia, the city of crossroads, rich in its scientific and cultural traditions. During all its 800 year history, Riga connected people from North and South, East and West. By hosting NBC-2008, Riga made one further step on this way. In June, you will enjoy green parks and alleys of the city and feel charming spirit of close Baltic Midsummer.

We are sure you will enjoy NBC-2008 both scientifically and socially, and we do our best to make NBC-2008 an outstanding event.

We are looking forward to meeting you in Riga.

**Associated Professor Alexei Katashev**  
*President of the Latvian Medical  
Engineering and Physics Society,  
Co-Chairman*

**Professor Yuri Dekhtyar**  
*Riga Technical University  
Co-Chairman*

**Professor Janis Spigulis**  
*University of Latvia  
Co-Chairman*

## Conference details

### Name

14<sup>th</sup> Nordic–Baltic Conference  
on Biomedical Engineering  
and Medical Physics

### Short name

NBC-2008

### Venue

Riga, Latvia  
June 16–20, 2008

### Organized by

Latvian Medical Engineering  
and Physics Society

Riga Technical University

<http://www.rtu.lv>

University of Latvia

<http://www.ul.lv>

### In co-operation with

IFMBE – International Federation for  
Medical and Biological Engineering  
<http://www.ifmbe.org>

### Proceedings editors

Yuri Dekhtyar  
Alexei Katashev  
Janis Spigulis

### International Scientific Committee

Yuri Dekhtyar (Co-chairman, Latvia)  
Alexei Katashev (Co-chairman, Latvia)  
Janis Spigulis (Co-chairman, Latvia)  
Peter Eskil Andersen (Denmark)  
Liga Berzina-Cimdina (Latvia)  
Hans-Joachim Hein (Germany)  
Thordur Helgason (Iceland)  
Alexander Khmelev (Russia)  
Arunas Lukosevicius (Lithuania)  
Jaakko Malmivuo (Finland)  
Zigurd Markovic (Latvia)  
Kalju Meigas (Estonia)  
Mamoun Muhammed (Sweden)  
Maria Vatshaug Ottermo (Norway)  
Olli Tolkki (Finland)  
Marta Wasilevska-Radwanska (Poland)

### International Advisory Committee

Piotr Augustyniak (Poland)  
Marcis Auzins (Latvia)  
Anke Bernstein (Germany)  
Leif Bjerkan, (Norway)  
Stelios Christofides (Cyprus)  
Trygve Eftestøl, (Norway)  
Ole Jakob Elle (Norway)  
Ivo Fridolin (Estonia)  
Toril Hernes (Norway)  
Jorun Helbostad, (Norway)  
Hiie Hinrikus (Estonia)  
Timo Jamsa (Finland)  
Arturas Janusauskas (Lithuania)  
Ivars Knets (Latvia)  
Valery Kostylev (Russia)  
Valentina Krilova (Latvia)  
Vitalijs Lakevics (Latvia)  
Thomas Langø (Norway)  
Juris Lauznis (Latvia)  
Cornelius Lewis (United Kingdom)  
Ratko Magjarevic (Croatia)  
Jeva Markovica (Latvia)  
Boris Narkevich (Russia)  
Ake Oberg (Sweden)  
Juris Pelss (Latvia)  
Sergei Popov (Latvia)  
John Georg Seland (Norway)  
Kristine Salma (Latvia)  
Mei Sen (Norway)  
Slavik Tabakov (United Kingdom)  
Ryszard Tadeusiewicz (Poland)  
Pentti Tengvall (Sweden)  
Erkki Vauramo (Finland)  
Jerzy Walecki (Poland)

### Local Organizing Committee

Aldis Balodis  
Veronika Fedotova  
Raimonds Jaks  
Ilona Kuzmina  
Andis Lagzdinsh  
Maksim Shneider  
Fyodor Tyulkin  
Vineta Zemite

### Sponsored by

**SIEMENS**

<http://www.siemens.com>

**Grindex**

<http://www.grindex.lv>

**ARBOR**  
MEDICAL  
KORPORACIJA

<http://www.arbor.lv>

**PHILIPS**

<http://www.philips.com/>

**AB**  
TECHNOLOGY  
CORPORATION

<http://www.abtechnology.lv/>

International Federation for Medical and Biological Engineering  
**IFMBE**

<http://www.ifmbe.org>

**Latvian Council of Science**

<http://www.lzp.lv/>

### Information support

**biomat.net**  
the biomaterials network

<http://www.biomat.net>



# Content

## Invited papers

**Building and Implementing an eHealth Strategy: is there a Good Recipe for Baltic Countries?** ..... 1  
*A. Lukosevicius*

**Biomedical Engineering Program on the Internet for Worldwide Use**..... 5  
*J.A. Malmivuo, J.J. Nousiainen and A. Kybartaitė*

## Biomaterials and Tissue Engineering

**The Modification of Titanium Dioxide MOCVD Coating in TiAlNb after Immersion in Artificial Saliva**..... 8  
*E. Aldea, M.M. Dicu, A. Gleizes and I. Demetrescu*

**Osteogenesis on Surface Selective Laser Sintered Bioresorbable Scaffolds** ..... 12  
*V.N. Bagratashvili, E.N. Antonov, S.M. Howdle, J.M. Kanczler, S. Mirmalek-Sani, V.K. Popov, R.O. Oreffo, C. Upton*

**Investigation of the Bone Cartilage Interface by CLSM**..... 16  
*J. Bossert, T. Keller*

**Improving Titanium Biocompatibility Manipulating Surface Porosity** ..... 19  
*D. Ionita and D. Iordachescu*

**Electrically Charged Hydroxyapatite Enhances Immobilization and Proliferation of Osteoblasts**..... 23  
*Yu. Dekhtyar, N. Polyaka and R. Sammons*

**Titanium Dioxide MOCVD Coating on CoCr Alloy and its Properties in Compare with Phosphate Coatings** ..... 26  
*M.M. Dicu, A. Gleizes and I. Demetrescu*

**Plasma Polymer Coating of Titanium for Improved Bone Implants** ..... 30  
*B. Finke, K. Schroeder, F. Luethen, J.B. Nebe, J. Rychly, K. Liefeth, R. Bader, U. Walschus, S. Lucke, M. Schlosser, H.-G. Neumann, A. Ohl, K.-D. Weltmann*

**Silk-Based Scaffold for Ligament Tissue Engineering** ..... 34  
*H. Liu, H. Fan, E.J.W. Wong, S. Lok Toh, J.C.H. Goh*

**Influence of Hydrogenated Calcium Phosphate Surface on Potential of Stromal Stem Cells in Situ** ..... 38  
*A.V. Karlov, I.A. Khlusov, Y. Dekhtyar, N. Polyaka*

**The Influence of Cultivation Conditions on the Proliferation and Differentiation of Rat Bone Marrow Multipotent Mesenchymal Stromal Cells** ..... 41  
*G. Krievina, N. Bezborodovs, G. Makarenkova, S. Nikulsins, Z. Krumina, D. Babarikins*

**Human Blood Cells Affected by Hydroxyapatite Coated Titanium**..... 45  
*A. Leice, Y. Dekhtyar, N. Britzina, L. Arabere and V. Arhipovich*

**Development of Biomorphic SiC Ceramics for Biomaterial Purposes**..... 48  
*J. Loes, L. Berzina-Cimdina and A. Zhurinsh*

**Release of Quaternary Ammonium Antimicrobial Compounds from Acrylic Bone Cement**..... 52  
*J.W. Nicholson, M. Mathey and V. Surana*

**The Evaluation of Quality and Selection of TiNi Shape Memory Alloy for Medical Purpose**..... 56  
*E.G. Novikova, S.A. Atroshenko*

**Ions Release from Ti Implant Alloys in Simulated Bioliquids**..... 60  
*M. Prodana, M. Caposi, D. Iordachescu*

<b>Stress-Strain State of System “Bone-Implant” Analyzed by FEM and its Comparison with Experimental Results .....</b>	<b>64</b>
<i>L. Rupeks, V. Filipenkova, I. Knets, J. Laizans, V. Vitins</i>	
<b>Fourier Transform Infrared Spectra of Technologically Modified Calcium Phosphates .....</b>	<b>68</b>
<i>K. Salma, N. Borodajenko, A. Plata, L. Berzina-Cimdina, A. Stunda</i>	
<b>Reactogenicity of Synthetic Hydroxyapatite (HAp) Ceramic Materials Implanted in Rabbits Jaws .....</b>	<b>72</b>
<i>I. Salma, M. Pilmane, J. Vetra, L. Berzina-Cimdina, G. Salms, A. Skagers</i>	
<b>Biomechanical Properties of Two Synthetic Biomaterials for Ventricular Septal Defect Closure in Infancy .....</b>	<b>76</b>
<i>L. Smits, I. Ozolanta, V. Ozolins, A. Lacis, V. Kasyanov</i>	
<b>Development of Poly(vinyl alcohol) Based Systems for Wound Dressings .....</b>	<b>80</b>
<i>J. Stasko, M. Kalnins, A. Dzene and V. Tupureina</i>	
<b>Apatite-based Biomaterials Synthesized in Saline Melts.....</b>	<b>83</b>
<i>S.O. Tarasenko, V.F. Zinchenko</i>	
<b>Degradation of Bone Material in Time .....</b>	<b>87</b>
<i>Yu. Dekhtyar, V. Zemite and H.J. Hein</i>	
 <b>Biomechanics, Artificial Organs, Implants and Rehabilitation</b>	
<b>Real-Time EEG Parameterization for Shunt Decision Supporting System During Carotid Endarterectomy .....</b>	<b>91</b>
<i>A. Accardo, M. Cusenza and F. Monti</i>	
<b>Automatic Quantification of Handwriting Characteristics Before and After Rehabilitation.....</b>	<b>95</b>
<i>A. Accardo and I. Perrone</i>	
<b>Reciprocating Orthotics Complex (ROC) for Children Suffering from Cerebral Paralysis and Spinal Diseases .....</b>	<b>99</b>
<i>E. Dukendjiev</i>	
<b>Muscle Movement and Electrodes Motion Artifact during Vibration Treatment.....</b>	<b>103</b>
<i>A. Fratini, P. Bifulco, M. Cesarelli, M. Romano, G. Pasquariello, A. La Gatta and G. Gargiulo</i>	
<b>Mandible and Temporomandibular Disc Movements on Physiological Subjects with Use of MRI.....</b>	<b>107</b>
<i>M. Fricova, J. Krystufek, Z. Horak, V. Peterova and S. Konvickova</i>	
<b>Choice and Impact of a Non-Newtonian Blood Model for Wall Shear Stress Profiling of Coronary Arteries .....</b>	<b>111</b>
<i>L. Goubergrits, E. Wellnhofer and U. Kertzscher</i>	
<b>Validation of Individual Calibration Procedure in Prediction of One Repetition Maximum in Bench Press.....</b>	<b>115</b>
<i>M. Hannula and A. Hirvikoski</i>	
<b>Prediction of One Repetition Maximum in Dumbbell Concentration Curl and Shoulder Press .....</b>	<b>119</b>
<i>M. Hannula, A. Hirvikoski, M. Isorinne and J. Jauhiainen</i>	
<b>Feature Selection for Bayesian Evaluation of Trauma Death Risk.....</b>	<b>123</b>
<i>L. Jakaite and V. Schetinin</i>	
<b>Objective Evaluation of Stroke Patients’ Movement.....</b>	<b>127</b>
<i>Á. Jobbágy, P. Simon, G. Fazekas, P. Harcos, Z. Grosz</i>	
<b>Applying Consumer Technologies to Assistive Device Design .....</b>	<b>131</b>
<i>K. Kaneswaran and K. Arshak</i>	
<b>Finite Element Analysis of Honeycomb-Core Foam on Shock-Absorbing Capability against Childhood Head Injury .....</b>	<b>135</b>
<i>C.Y. Lin, L.T. Chang, T.J. Huang, K.H. Tsai, C.S. Li and G.L. Chang</i>	

<b>Results of Reciprocal Orthosis System with Kinematic Interdependence used in Children with Children Cerebral Paralysis and Spinal Patients.....</b>	<b>139</b>
<i>V. Mihnovich, E. Dukendjiev</i>	
<b>Colorimetric Plantographic Diagnostics of Foot Pathology on the Footprint in Static and Dynamics.....</b>	<b>141</b>
<i>T. Ogurtsova, E. Dukendjiev</i>	
<b>Biomechanical Properties of Glutaraldehyde Treated Human Pericardium.....</b>	<b>143</b>
<i>V. Ozolins, I. Ozolanta, L. Smits, A. Lacis, V. Kasyanov</i>	
<b>Eye Kinematics of Athletes in Non-Familiar Sports Situations.....</b>	<b>146</b>
<i>R. Paeglis, A. Spunde, A. Klavinsh, L. Vilkausha and I. Lacis</i>	
<b>Feasibility Experiment of Gait Training System Using Real-time Visual Feedback of Knee Joint Angle .....</b>	<b>150</b>
<i>J. Park, J. Ku, S. Cho, D.Y. Kim, I.Y. Kim and S.I. Kim</i>	
<b>Investigation of Biomechanical Properties of Different Elements of Human Mitral Valve.....</b>	<b>154</b>
<i>J. Pavars, P. Stradins, R. Lacis, I. Ozolanta, V. Kasyanov</i>	
<b>Development of Research for Machining of Implants with Novel Materials for Bone Surgery .....</b>	<b>156</b>
<i>O.A. Rozenberg, S.V. Sokhan' and V.V. Voznyy</i>	
<b>The Artificial Larynx: A Review of Current Technology and a Proposal for Future Development.....</b>	<b>160</b>
<i>M.J. Russell, D.M. Rubin, B. Wigdorowitz and T. Marwala</i>	
<b>Power Density Spectra of the Velocity Waveforms in Artificial Heart Valves .....</b>	<b>164</b>
<i>A.A. Sakhaeimanesh</i>	
<b>Development of a Generic Assistive Platform to Aid Patients with Motor Disabilities.....</b>	<b>168</b>
<i>F. Senatore, D.M. Rubin and G.J. Gibbon</i>	
<b>Usability Evaluation of Three Unilateral – Propelled Wheelchairs for Hemiplegic Patients .....</b>	<b>172</b>
<i>K.H. Tsai, C.Y. Yeh, H.C. Lo, L.T. Chang, J.S. Lee, C.T. Lee</i>	
<b>The Effect of Gait Speed on Pre- and Postoperative Analysis of Gait Parameters after Total Knee Arthroplasty.....</b>	<b>175</b>
<i>R. Ullmann, M. Hildebrand and S. Leuchte</i>	
 <b>Biomedical Instrumentation and Measurements, Biosensors and Transducers</b>	
<b>Quantitative Analysis of the Activation Strategies during Freezing in Parkinson's Patients.....</b>	<b>179</b>
<i>A. Accardo, S. Mezzarobba, M. Millevoi and F. Monti</i>	
<b>Precise Positioning of Electrodes at Transesophageal Atrial Stimulation Using Multichannel Transesophageal Pacemaker and Lead .....</b>	<b>183</b>
<i>A. Anier, J. Kaik and K. Meigas</i>	
<b>Automated multi-parametric label free 24 channel real-time screening system.....</b>	<b>186</b>
<i>B. Becker, V. Lob, N. Janzen, D. Grundl, F. Ilchmann and B. Wolf</i>	
<b>Decentralized Multi-channel Digitizing of Bioimpedance Signals.....</b>	<b>190</b>
<i>I. Bilinskis, Y. Artyukh and M. Min</i>	
<b>Design and Implementation of Textile Sensors for Biotelemetry Applications.....</b>	<b>194</b>
<i>M. Cerny, L. Martinak, M. Penhaker and M. Rosulek</i>	
<b>The Suitability of Silver Yarn Electrodes for Mobile EKG Monitoring.....</b>	<b>198</b>
<i>A. Comert, M. Honkala, M. Puurtinen and M. Perhonen</i>	
<b>Drawback of ICA Procedure on EEG: Polarity Indeterminacy at Local Optimization .....</b>	<b>202</b>
<i>F. Cong, I. Kalyakin, T. Ristaniemi and H. Lyytinen</i>	

<b>Empirical Mode Decomposition on Mismatch Negativity.....</b>	<b>206</b>
<i>F. Cong, X. Xu, T. Ristaniemi and H. Lyytinen</i>	
<b>Measurement and Control of Ultra-Low Liquid Flowrates for Drug Delivery Application.....</b>	<b>210</b>
<i>C. Damiani, S. Klein, D. Wuttig and B. Nestler</i>	
<b>Hardware Embedded System on a Chip for the Normal ECG Recognition .....</b>	<b>213</b>
<i>A.C. Dimopoulos, C. Pavlatos, G. Papakonstantinou</i>	
<b>Slit-lamp Based Ocular Fluorometry Scanning.....</b>	<b>217</b>
<i>J.P. Domingues, M. Alberto, C. Correia, J. Cunha-Vaz</i>	
<b>Epicardial Acceleration Signal Measured Using a Single Chip 3-axis Accelerometer .....</b>	<b>221</b>
<i>L.A. Fleischer, P.S. Halvorsen, L. Hoff, E. Fosse and O.J. Elle</i>	
<b>Novel Conducting Polymer Composite pH Sensors for Medical Applications.....</b>	<b>225</b>
<i>E.I. Gill, A. Arshak, K. Arshak and O. Korostynska</i>	
<b>Future Trends in Robotic Neurosurgery .....</b>	<b>229</b>
<i>T. Haidegger, L. Kovacs, G. Fordos, Z. Benyo and P. Kazantzides</i>	
<b>Development and Evaluation of One Arm Electrode Based ECG Measurement System .....</b>	<b>234</b>
<i>M. Hannula, H. Hinkula and J. Jauhainen</i>	
<b>Diagnosing Acute Liver Graft Rejection: Experimental Application of an Implantable Telemetric Impedance Device in Native and Transplanted Porcine Livers .....</b>	<b>238</b>
<i>J.H. Harms, A. Schneider, M. Tautenhahn, J. Henke and R. Busch</i>	
<b>Augmentation Index in Different Severity Coronary Heart Disease Patients.....</b>	<b>242</b>
<i>I. Hlimonenko, K. Meigas, M. Viigimaa and K. Temitski</i>	
<b>Photoplethysmographic Measurements and Analysis.....</b>	<b>245</b>
<i>M.J. Huotari, V. Lantto</i>	
<b>Noninvasive Measurement of the Pressure Gradient between the Radial and Finger Arteries .....</b>	<b>248</b>
<i>K. Jagomägi, R. Raamat, J. Talts and U. Ragun</i>	
<b>A Multicenter Study of Removed Uric Acid Estimated by Ultra Violet Absorbance in the Spent Dialysate.....</b>	<b>252</b>
<i>J. Jerotskaja, F. Uhlin and I. Fridolin</i>	
<b>Comparison of Tibial Nerve Somatosensory Evoked Potential Signal-to-Noise Ratios During Anaesthesia .....</b>	<b>257</b>
<i>A.S. Joutsen, P. Puumala, L-P. Lyytikäinen, O. Pajulo, A. Etelämäki, J. Jurva, V. Jäntti and H. Eskola</i>	
<b>Phase Coupling in EEG Burst Suppression during Propofol Anesthesia .....</b>	<b>260</b>
<i>F.E. Kapucu, T. Lipping, V. Jäntti and A.-M. Huotari</i>	
<b>Rhythmic Fluctuations in Intracellular Mg<sup>2+</sup> in Spontaneously Beating Cultured Cardiac Myocytes .....</b>	<b>264</b>
<i>K. Kawahara, R. Sato, D. Matsuyama and S. Iwabuchi</i>	
<b>Importance of Nonlinear Signal Processing in Biomedicine.....</b>	<b>268</b>
<i>W. Klonowski</i>	
<b>An Intelligent Method for Identifying Cardiac Cycles from Tracheal Sounds during Sleep .....</b>	<b>270</b>
<i>A. Kulkas, E. Huupponen and S.-L. Himanen</i>	
<b>Ultrasonic Non-invasive Investigation of Arterial Elasticity .....</b>	<b>274</b>
<i>I. Kupciunas, A. Kopustinskas</i>	
<b>EEG-fMRI Ballistocardiogram Removal: A New Non-linear Dynamic Time Warping Approach .....</b>	<b>278</b>
<i>A.J.L. Kustra, J.M. Fernandes and J.P.S. Cunha</i>	
<b>Local Filtered QRS Duration during Sodium-channel Blockade in Brugada Syndrome Patients.....</b>	<b>282</b>
<i>A.C. Linnenbank, P.G. Postema, M.G. Hoogendijk, P.F.H.M. van Dessel, H.L. Tan and J.M.T. de Bakker</i>	

<b>Development of Flexible Thin Film Microelectrode Arrays for Neural Recordings .....</b>	<b>286</b>
<i>S. Myllymaa, K. Myllymaa, H. Korhonen, K. Djupsund, H. Tanila and R. Lappalainen</i>	
<b>Prediction of Epileptic Seizures for On-Demand Vagus Nerve Stimulation .....</b>	<b>290</b>
<i>K.R. Nielsen, C. Sevcencu, A. Rasmussen and J.J. Struijk</i>	
<b>Apparatus for Short-Wave Inductothermy “Magnetotherm” .....</b>	<b>294</b>
<i>N.A. Nikolov, V.E. Orel, I.I. Smolanka, N.N. Dzyatkovskaya, A.V. Romanov, Yu.I. Mel’nik, M.Yu. Klimanov and V.O. Chernish</i>	
<b>What Conclusions does Rapid Image Classification by Eye Movements Provide for Machine Vision?.....</b>	<b>299</b>
<i>R. Paeglis, A. Kotelnikovs, A. Podniece and I. Lacis</i>	
<b>Analysis of Foveation Sequences in Congenital Nystagmus.....</b>	<b>303</b>
<i>G. Pasquariello, P. Bifulco, M. Cesarelli, M. Romano, A. Fratini</i>	
<b>Numerical Models of Skin Conductivity Changes during Electroporation.....</b>	<b>307</b>
<i>N. Pavšelj and D. Miklavčič</i>	
<b>An Experimental Study of PPG Probe Efficiency Coefficient Determination on Human Body.....</b>	<b>311</b>
<i>K. Pilt, K. Meigas, M. Rosmann, J. Lass and J. Kaik</i>	
<b>Non-linear Assessment of Heart Rate Variability in Ovo-lactovegetarians, Vegans and Omnivores during Oral Glucose Tolerance Test.....</b>	<b>315</b>
<i>T. Princi, I. Fabbro, D. Peterec, M. Fonda, L. Cattin and A. Accardo</i>	
<b>Photoplethysmography Analysis of Artery Properties in Patients with Cardiovascular Diseases .....</b>	<b>319</b>
<i>U. Rubins, A. Grabovskis, J. Grube and I. Kukulis</i>	
<b>Dialysis Adequacy On-line Monitoring Using DiaSens Optical Sensor: Technique and Clinical Application.....</b>	<b>323</b>
<i>A. Scherbakov, I. Fridolin</i>	
<b>Effects of ROI Size on Correlation between ROISR and SNR.....</b>	<b>327</b>
<i>L. Sinkkila, J. Vaisanen, O. Vaisanen and J. Hyttinen</i>	
<b>Effect of Microwave Radiation on EEG Coherence .....</b>	<b>331</b>
<i>A. Suhhova, M. Bachmann, K. Aadamsoo, Ü. Vöhma, J. Lass and H. Hinrikus</i>	
<b>Stress Stages and Changes on EEG by low-level Physical (EMF) and Chemical Stressors .....</b>	<b>335</b>
<i>V. Tuulik, J. Lass and M. Bachmann</i>	
<b>Body Surface Potential Mapping for Noninvasive Ischemia Detection .....</b>	<b>339</b>
<i>M. Tysler, P. Kneppo, V. Rosik, S. Karas, E. Heblakova and J. Muzik</i>	
<b>Effect of Lead Orientation on Bipolar ECG Measurement .....</b>	<b>343</b>
<i>J. Vaisanen, M. Puurtinen and J. Hyttinen</i>	
<b>On the Mechanism of Low Frequency Bioelectromagnetism .....</b>	<b>347</b>
<i>J. Valdmanis, A. Cipijs</i>	
<b>The Effect of Electrode Size on Cortical EEG Sensitivity Distributions.....</b>	<b>350</b>
<i>K. Wendel and J. Malmivuo</i>	
<b>Measurement of Dissolved Oxygen with Lab-on-Chip Systems .....</b>	<b>353</b>
<i>J. Wiest, M. Brischwein, H. Grothe and B. Wolf</i>	
 <b>Biomedical Optics and Lasers</b>	
<b>Effects of Optical Radiation on the Healing of Bone Defect in Rabbits.....</b>	<b>357</b>
<i>Yu. Dehktyar, A. Katashev, J. Katasheva and I. Ozolanta</i>	

<b>Transmyocardial Laser Revascularization in Patients with Diffuse Coronary Artery Disease .....</b>	<b>361</b>
<i>E. Freilibs, R. Lacis and U. Strazdins</i>	
<b>Evaluation of a Fiber-Optic Based Pulsed Laser System for Fluorescence Spectroscopy .....</b>	<b>363</b>
<i>N. Haj-Hosseini, S. Andersson-Engels and K. Wårdell</i>	
<b>Effect of Light Scattering Simulation in the Eye on Different Color Stimuli Perception.....</b>	<b>367</b>
<i>G. Ikaunieks and M. Ozolinsh</i>	
<b>Diffuse Reflectance Spectroscopy During Experimental Radio Frequency Ablation.....</b>	<b>371</b>
<i>J.D. Johansson, A. Zerbinati and K. Wårdell</i>	
<b>Closed-Feedback Control of Laser Soldering of Rat Skin Using Diode Laser .....</b>	<b>375</b>
<i>M.E. Khosroshahi, M.S. Nourbakhsh, S. Saremi and F. Tabatabaee</i>	
<b>Characterization of Input-Output Relations in Single Neurons using Spatiotemporal Photo-stimulation .....</b>	<b>378</b>
<i>M. Krumin and S. Shoham</i>	
<b>Sensor for Measurement of Wear in Total Hip Arthroplasty.....</b>	<b>380</b>
<i>D. Mandat, M. Hrabovsky, V. Havranek, M. Pochmon, T. Rössler, J. Gallo</i>	
<b>Effects of Static and Dynamic Modes on Laser Tissue Soldering: An In-vitro Study .....</b>	<b>383</b>
<i>M.S. Nourbakhsh, M.E. Khosroshahi, S. Saremi and F. Tabatabaee</i>	
<b>Photoplethysmography Device for Detection of Changes in the Vasomotor Parameters of Small Laboratory Animals .....</b>	<b>386</b>
<i>J. Paturskis, V. Veliks, M. Ozols, I. Svikis, R. Erts, J. Spigulis</i>	
<b>Potentialities of Wear Measurement in Total Knee Arthroplasty.....</b>	<b>390</b>
<i>M. Pochmon, T. Rössler, J. Gallo, M. Hrabovský, D. Mandát and V. Havránek</i>	
<b>Optical Non-contact In-vitro Measurement of Total Hip Arthroplasty Wear .....</b>	<b>393</b>
<i>T. Rössler, J. Gallo, M. Hrabovský, D. Mandát, M. Pochmon and V. Havránek</i>	
<b>Spectroscopic Studies on Binding of Cationic Pheophorbide-a Derivative to Model Polynucleotides.....</b>	<b>397</b>
<i>O.A. Ryazanova, I.M. Voloshin, I.Ya. Dubey, L.V. Dubey and V.N. Zozulya</i>	
 <b>Healthcare Management, Education and Training</b>	
<b>ICT and Knowledge Management for the ISO 9001:2000 Standards Compliance of I.R.C.C.S. “Burlo Garofolo” Maternal-children Hospital.....</b>	<b>401</b>
<i>M. Bava, E. Danielli, A. Orsini, D. Tarticchio, L. Vecchi Brumatti, R. Zangrando, F. Zennaro and A. Accardo</i>	
<b>Biotelemetry .....</b>	<b>405</b>
<i>M. Cerny, M. Penhaker</i>	
<b>Five Year Biomedical Engineering Curriculum – Experiences and Results from the First Eight Years .....</b>	<b>409</b>
<i>K. Dremstrup and P. Elberg</i>	
<b>Medical GRID and E-Learning in the Virtual Hospital.....</b>	<b>413</b>
<i>G. Graschew, T.A. Roelofs, S. Rakowsky, P.M. Schlag</i>	
<b>Luebeck’s International BME Master’s Program - Aim and Experiences .....</b>	<b>417</b>
<i>S. Klein, T.M. Buzug and B. Nestler</i>	
<b>Developing Media Rich Virtual Learning Material for Biomedical Engineering Education .....</b>	<b>421</b>
<i>A. Kybartaitė, J. Malmivuo and J. Nousiainen</i>	
<b>Development of the Biomedical Electronics Course for e-Learning .....</b>	<b>425</b>
<i>T. Parve, R. Gordon and M. Min</i>	

<b>Cataract Surgery Simulator for Medical Education &amp; Finite Element/3D Human Eye Model</b> .....	429
<i>J.F. Perez, R. Barea, L. Boquete, M.A. Hidalgo, M. Dapena, G. Vilar, I. Dapena</i>	
<b>COMSOL Multiphysics in Undergraduate Education of Electromagnetic Field Biological Interactions</b> .....	433
<i>P. Togni, M. Cifra and T. Dřížďal</i>	
<b>Actual State of Medical Physics and Biomedical Engineering Education in Poland</b> .....	437
<i>M. Wasilewska-Radwanska and T. Palko</i>	
<b>The Practice for Medical Physics and Engineering Students</b> .....	439
<i>A. Balodis, V. Zemite</i>	

## Information Technology to Health

<b>Scientific Research, Telemedicine and Health Services: the “Burlo Garofolo” Hospital Web Portal</b> .....	442
<i>M. Bava, A. Zambon, L. Vecchi Brumatti, R. Zangrando, A. Accardo and G. Tamburlini</i>	
<b>A Neuro-Fuzzy Approach to the Classification of Fetal Cardiotocograms</b> .....	446
<i>R. Czabanski, M. Jezewski, J. Wrobel, K. Horoba and J. Jezewski</i>	
<b>Visions in Modeling of Cardiac Arrhythmogenic Diseases and their Therapies</b> .....	450
<i>O. Dössel, G. Seemann, D. Farina, D.U.J. Keller, R. Miri, F.M. Weber, D.L. Weiss</i>	
<b>Home Health Monitoring</b> .....	454
<i>Á. Jobbágy, P. Csordás, A. Mersich, R. Magjarević, I. Lacković, J. Mihel</i>	
<b>Time Domain Signal Processing of Tibial Nerve Somatosensory Evoked Potentials During Anesthesia</b> .....	458
<i>A.S. Joutsen, V. Jäntti and H. Eskola</i>	
<b>Modelling Interrupter Measurements of Respiratory Resistance</b> .....	461
<i>J. Talts, J. Kivastik</i>	
<b>Coupling Axis-Length Profiles with Bezier Splines in Finite Element Head Models</b> .....	465
<i>K. Wendel, M. Osadebey and J. Malmivuo</i>	
<b>Analysis of Bioelectrical Uterine Activity for Detection of Threatening Premature Labour</b> .....	469
<i>J. Zietek, K. Horoba, J. Jezewski, A. Matonia, J. Sikora and T. Kupka</i>	

## Medical Imaging, Telemedicine and E-Health

<b>Comparison of DT-CWT Based Rotation Variant and Invariant Methods on Tissue Characterization</b> .....	473
<i>D.B. Aydogan, M. Hannula, T. Arola, P. Dastidar and J. Hyttinen</i>	
<b>CdZnTe Pixel Detectors for Medical Imaging</b> .....	477
<i>A.A. Bulycheva, I.E. Tsirkunova and V.V. Gostilo</i>	
<b>The Analysis of Craniofacial Morphology in Posteroanterior View</b> .....	481
<i>K.-S. Cheng, C.-H. Ou, Y.-T. Chen, J.-K. Liu and C.-L. Kuo</i>	
<b>VAMP – A Vision Based Sensor Network for Health Care Hygiene</b> .....	485
<i>P. Curran, J. Buckley, B. O’Flynn, X. Li, J. Zhou, G. Lacey and S.C. O’Mathuna</i>	
<b>An Augmented Reality Application for Minimally Invasive Surgery</b> .....	489
<i>L.T. De Paolis, M. Pulimeno and G. Aloisio</i>	
<b>Methods for Counting Cells Supported by Digital Image Processing</b> .....	493
<i>D. Dill, A. Scholz, M. Gül and B. Wolf</i>	
<b>Two Aspects of Calibrating a 3D Ultrasonic Computed–Tomography System</b> .....	497
<i>A. Filipik, J. Jan, I. Peterlík, D. Hemzal, R. Jiřík</i>	

<b>A Combined Bayesian Approach to Classifying Venous Flow during Contrast-Agent Injection using Doppler Ultrasound.....</b>	<b>501</b>
<i>M. Forfang, L. Hoff, N. Bérard-Andersen, G.F. Olsen and K. Brabrand</i>	
<b>Optimization of fMRI Processing Parameters for Simultaneous Acquisition of EEG/fMRI in Focal Epilepsy .....</b>	<b>505</b>
<i>M. Forjaz Secca, H.M. Fernandes, J.R. Cabral and A. Leal</i>	
<b>Telemetric Personal Health Monitoring Systems for Asthma and Chronic Obstructive Pulmonary Disease .....</b>	<b>509</b>
<i>M. Guel, A. Scholz, D. Dill and B. Wolf</i>	
<b>Clinical Relevance of Preoperative CT- based Computer Aided 3D- Planning in Hepatobiliary, Pancreatic Surgery and Living Donor Liver Transplantation .....</b>	<b>512</b>
<i>J. Harms, H.-M. Tautenhahn, H. Bourquain, T.H. Kahn, H.-O. Peitgen, J. Fangmann, S. Jonas</i>	
<b>Assessing the Effects of Apneusis on Brain Functional Magnetic Resonance Imaging with Symbolic Dynamics .....</b>	<b>516</b>
<i>A.F.C. Infantosi, F.C. Jandre and C. Elefteriadis</i>	
<b>Breast Ultrasound Segmentation Using Morphologic Operators and a Gaussian Function Constraint .....</b>	<b>520</b>
<i>A.F.C. Infantosi, L.M.S. Luz, W.C.A. Pereira and A.V. Alvarenga</i>	
<b>Image Analysis of DNA Repair and Apoptosis in Tumor Cells with Differing Sensitivity to DNA Damage.....</b>	<b>524</b>
<i>A. Ivanov, M. Ivanova, J. Erenpreisa, S.V. Gloushen, T. Freivalds and M.S. Cragg</i>	
<b>Parameterization of the Optic Nerve Disk in Eye Fundus Images .....</b>	<b>528</b>
<i>D. Jegelevicius, D. Buteikiene, V. Barzdziukas and A. Paunksnis</i>	
<b>3D Medical Image Visualization and Volume Estimation of Pathology Zones .....</b>	<b>532</b>
<i>K. Krechetova, A. Glaz and A. Platkajis</i>	
<b>Biomedical Image Processing Based on Regression Models .....</b>	<b>536</b>
<i>A. Lorencs, I. Mednieks and J. Sinica-Sinavskis</i>	
<b>Analysis of Outliers Effects in Voxel-Based Morphometry by means of Virtual Phantoms.....</b>	<b>540</b>
<i>F. Nocchi, T. Franchin, E. Genovese, D. Longo, G. Fariello and V. Cannatà</i>	
<b>Stroke Monitor as a Device Improving Diagnostic Value of Computed Tomography in Hyperacute Stroke.....</b>	<b>544</b>
<i>A. Przelaskowski, J. Walecki, K. Sklinda and G. Ostrek</i>	
<b>Morphological and Brainstem Physiology Assessment of Patients with Congenital Craniocervical Anomalies .....</b>	<b>548</b>
<i>C.M. Rimkus, A.V. Faria, V.A. Zanardi, V.M.F. Lima, A. Cliquet Jr.</i>	
 <b>Medical Physics</b>	
<b>Quality of the Computed Radiography Image Acquired with Decreased Doses .....</b>	<b>552</b>
<i>L. Bumbure, Y. Dehtyar, R. Falkan, U. Jasper</i>	
<b>Evaluation of Acceptance Criteria for IMRT Plan Verification Based on Results of Film Dosimetry.....</b>	<b>556</b>
<i>K. Chelminski, W. Bulski, P. Kaminski, M. Kania, J. Rostkowska, A. Walewska and M. Zalewska</i>	
<b>Sensitivity of the Brain to Microwave Radiation .....</b>	<b>558</b>
<i>H. Hinrikus, M. Bachmann and J. Lass</i>	
<b>The Impact of the Anomalous Magnetic Field of the Earth on Demographic Indices (using Latvia as an example) .....</b>	<b>562</b>
<i>L. Kartunova, V. Vetrennikov</i>	
<b>Development of the Positron Emission Tomography Center: Medical and Physical Aspects .....</b>	<b>566</b>
<i>A.V. Khmelev, S.E. Evdonin, V.A. Kostylev, S.V. Shiryayev, B.I. Dolgushin</i>	
<b>Modulated Microwave Effects on Visual Event-related Potentials during Oddball Task .....</b>	<b>570</b>
<i>K. Kruusing and J. Lass</i>	



<b>Evaluation of the Independent Dose Calculation Algorithm .....</b>	<b>574</b>
<i>J. Laurikaitienė, M. Laurikaitis, D. Adlienė, G.A. Adlys, S. Raila, F. Nordström, S. Bäck and S. Mattsson</i>	
<b>Dosimetric Properties of Detectors for Quality Control of Intensity Modulated Radiotherapy .....</b>	<b>578</b>
<i>S. Plaude, S. Popov, A. Miller and Y. Dekhtyar</i>	
<b>Considering Dose Rate in Routine X-ray Examination by Thermoluminescent Dosimetry (TLD) in Radiology units of Mazandaran Hospitals .....</b>	<b>582</b>
<i>S.A. Rahimi</i>	
<b>Cost-Effectiveness of the Positron Emission Tomography with [18F]-fluorodeoxyglucose for the Staging and Management of Lung Cancer in Russia .....</b>	<b>586</b>
<i>A.V. Khmelev, S.V. Shiryayev, B.I. Dolgushin, I.D. Gotsadze, I.P. Aslanidi, O.V. Mukhortova, S.E. Evdonin</i>	
<b>Design of an Ultra-Near-Field System for Planar Coded Aperture Nuclear Medicine Imaging .....</b>	<b>590</b>
<i>D.M. Starfield, D.M. Rubin and T. Marwala</i>	
 <b>Micro- and Nanoobjects, Nanostructured Systems, Biophysics</b>	
<b>Semiconductors and Biomedical Structures for Nanobiometric Applications .....</b>	<b>594</b>
<i>B.H. Bairamov, V.V. Toporov, F.B. Bayramov, M. Vasudev, M. Dutta, M.A. Stroschio, and G. Irmer</i>	
<b>Microcells Development and Endocytosis Ability Morphological and Quantitative Characterization in HeLa Cancer Cells .....</b>	<b>598</b>
<i>D. Bema, T. Freivalds, I. Buikis and L. Harju</i>	
<b>Atomic Force Microscopy Study of Yeast Cells Influenced by High Voltage Electrical Discharge .....</b>	<b>602</b>
<i>D. Borovikova, S. Cifansky, Y. Dekhtyar, V. Fedotova, V. Jakushevich, A. Katashev, A. Patmalnieks, A. Rapoport</i>	
<b>Dependence of DNA Electrotransfer into Cells In vitro on Cell Electroporation and DNA Electrophoresis .....</b>	<b>606</b>
<i>K. Čepurnienė, S. Šatkauskas</i>	
<b>Measurement of Temperature Synchronized Yeast Cells kHz Electrical Oscillations.....</b>	<b>610</b>
<i>M. Cifra, J. Pokorný, F. Jelínek, J. Hašek and J. Šimša</i>	
<b>Self – Assembled System: Semiconductor and Virus Like Particles .....</b>	<b>614</b>
<i>Yu. Dekhtyar, A. Kachanovska, G. Mežinskis, A. Patmalnieks, P. Pumpens, R. Renhofa</i>	
<b>Quantum Chemical Simulation of Cytochrome P450 Catalyzed Oxidation and Carcinogenic potency of Benzene Derivatives .....</b>	<b>616</b>
<i>P.N. D'yachkov, N.V. Kharchevnikova, Z.I. Zholdakova, N. Fjodorova, M. Novich and M. Vrachko</i>	
<b>Evaluation of Highly-Water Soluble Drug Physical State in Biodegradable Microcapsules .....</b>	<b>619</b>
<i>D. Loca, O. Pugovics and L. Berzina-Cimdina</i>	
<b>Time-dependent Model of Induced Transmembrane Voltage and Electroporation on Clusters of Cells.....</b>	<b>623</b>
<i>G. Pucihar, T. Kotnik and D. Miklavcic</i>	
<b>Mg<sup>2+</sup> and Ni<sup>2+</sup> ion Effects on Phase Transitions in AU and A2U under Conditions Close to Physiological Ones.....</b>	<b>628</b>
<i>V.A. Sorokin, E.L.Usenko and V.A. Valeev</i>	
<b>Studies of Mechanical Treatment on Surface Charge of Bioactive Composites .....</b>	<b>632</b>
<i>S. Szarska, E. Szmidt, A. Wójcik</i>	
<b>Author Index.....</b>	<b>637</b>
<b>Subject Index .....</b>	<b>643</b>

# Building and Implementing an eHealth Strategy: is there a Good Recipe for Baltic Countries?

A. Lukosevicius

Kaunas University of Technology/Biomedical Engineering Institute, Kaunas, Lithuania

**Abstract** — eHealth is concerned as a sum of technological means for registration, storage, processing and management of health related information. Since Baltic countries are looking for an optimal directions for eHealth development, presentation is discussing harmonization with eHealth developments in the world and EU - main directives: WHO strategy “eHealth for health care delivery” and an action plan for e European eHealth area (2004), standardization efforts, countries – leaders, success stories, lessons learnt and possible examples to follow. Also problems of Baltic countries - commonalities (similar political, social and health care legacy, diversified local health IT systems, demands caused by ageing, social and economic transitions, free market of health services) and specifics. (Legislative and management principles and environment, intensity, targets and priorities of national pilot eHealth projects) are analysed. Facing eHealth development challenges the choice of appropriate strategy and implementation management becomes crucial. It was analyzed Baltic eHealth activities, including Lithuanian experience – recently accepted eHealth strategy and implementation plan (2007-2015). Alternatives of implementation concepts and standard based integration seeking to create a standard-based and citizen-centred architecture are discussed, action priorities by importance and by time sequence are analysed. Analysis leads to conclusion, that the effective Baltic way towards European eHealth area requires avoiding parallelism, sharing experience, providing of pilot cross-boarder trials between Baltic and Nordic countries, defining the role and contribution of biomedical engineering and medical physics.

**Keywords** — eHealth, Baltic countries, strategic planning, interoperability, collaboration

## I. INTRODUCTION

Importance of eHealth as a sum of technological means for registration, storage, processing and management of health related information is rapidly increasing. “eHealth” becomes an inclusive term integrating medical informatics, telemedicine and biomedical engineering, i.e. all methodical and instrumental tools for health information acquisition, management and applications in clinical practice, research and administration. Important feature of eHealth is it’s scale reaching far beyond hospital environment or communication doctor-to-patient or doctor-to-doctor (such point to point communication is usually called telemedicine).

EHealth is a new paradigm creating an integral environment for health services for all users. Clients here are connected to eHealth system, which is at least of region or national (in future – international) scale. Taking into account the complex character of healthcare (high costs, and the need for quality, patient safety, adequate organization and delivery, cross-border care, reimbursement, and liability), eHealth provides one of the most important solutions to address the cost and quality of healthcare. Therefore recently (from the year 2000) a pace of eHealth developments has dramatically risen in majority of countries. World Health Organization (WHO) has approved a strategy “eHealth for health care delivery” (2004) and announced the eHealth as a main instrument of health care improvement over the world, including developing countries [1]. European Union (EU) also issued an important political document “Health—Making Healthcare Better for European Citizens: An Action Plan for a European e-Health Area” [2] which emphasis the need of common EU effort and standard based integration and interoperability [3]. An Action Plan declares that in 2009 European Commission will define standard requirements for eHealth services, legal and security environment in member countries. EHealth conference in Berlin (2007) accepted a Berlin Declaration [4] which outlines six specific actions, including collaboration, setting common roadmap, standardization, certification and accreditation of eHealth systems, involvement of research and industry.

Baltic countries are facing an eHealth development challenges which originate from the specific national needs of the health care from one side and also the need to create common eHealth area in Europe – from the other side. Since national eHealth activities and projects takes the first steps it’s highly important to choose a right strategic direction and implementation concepts.

## II. CHALLENGES OF BALTIC STATES

### A. Facing global eHealth problems

Global health problems – ageing of population, rising of health service and medication costs, environmental risks, rising demands and expectations of citizens, consumptional attitude towards health services [5] – become a challenge

also for Baltic countries. Countries are trying to solve those problems *inter alia* by development of eHealth systems. On this way countries are facing both problems caused by global changes [6] and also by specific environment of countries still under social and economical transition [7].

One of the main problems Baltic countries are facing in eHealth development is instability of eHealth standards [8]. Urgent need to manage effectively health information forces policy makers to take immediate development decisions, neither in conditions when standards are not fully accepted and stable nor in global nor in national scales. Pragmatic decisions still are taken locally and problems with integration of not compatible solutions are significant (for example integration currently takes about 20% of hospital IT spending).

Rising demands of health service consumers and relatively easy migration of citizens (especially within EU) causes first signs of “health tourism” – when people start moving across countries looking for high quality cost-effective health services. This challenge forces national health systems to be economically competitive from one side and also professionally compatible (taking into consideration international quality and information interchange standards) from another. EHealth instruments are potentially effective to cope with both of the above challenges. Therefore progressively thinking health officials are especially eager to implement immediately eHealth solutions into clinical and managerial practice. (EU recommends member states to spend for eHealth no less than 2,5 % of total annual health expenditures, i.e. to make significant strategic investments).

The situation causes a collision of global challenges and needs of eHealth implementations from one side and limited global experience of large scale eHealth developments from another. There is a lack of internationally recognized leading experts of eHealth standards, system developers capable to lead national scale eHealth projects. Even big companies and vendors are taking first steps in this way.

### *B. Specifically Baltic challenges*

In the context of eHealth development Baltic countries have a lot of commonalities typical for all of them: similar political, social and health care legacy, diversified and underdeveloped local health IT systems, demands caused by social and economic transition, health reforms, privatization and emerging free market of health services.

Although Baltic countries are rapidly reaching the development level of EU average, some social and economic processes are still in transition. Rapid economic growth and democratization is accompanied by rather unequal social

services, especially in rural areas, significant differences remain in quality and accessibility of health services across country. Health systems and especially IT solutions are underfinanced to compare with western countries. Allocations for eHealth are less than 1% of all health service expenditures (to be compared with EU recommendation – 2, 5%). Since eHealth is a quite new paradigm – not only a new technologies but a new way of thinking and working, there is a lack of deep understanding of the essence and possibilities of eHealth among political decision makers and in some extent among health specialists and managers. Health systems are experiencing the rising costs of services, medicine, equipment, also lack of specialists due to emigration of doctors, therefore attention of decision makers are directed towards this kind problems. This bias sometimes hampers investment, development of necessary legislative environment, and consequently – implementation of eHealth systems – important tools for all health care problems.

Starting position of Baltic states on the way of eHealth developments is rather favorite: penetration of internet and wireless communications is sufficient and rapidly increasing; broadband telecommunication networks - well developed; number and qualification of general profile IT specialists is high; health reforms in particular countries create a good motivation for eHealth implementations. In contrast with developed Western countries – Baltic countries have no heavy heritage of well functioning local old information systems. This creates a chance to start with modern concepts and advanced solutions without painful destroying of existing systems.

EHealth developments in Estonia [8, 9] Latvia [10, 11] Lithuania [12, 13] – in fact at the moment have no principal differences. However differences could arise due to different development strategies and implementation management. This could cause future problems of integration eHealth systems into common area, according to EU initiatives.

## III. LEADERS TO FOLLOW AND ROLE OF THE STRATEGY

### *A. eHealth lessons worldwide*

The landscape of eHealth developments around the world is presented in [6], by permanently working Global observatory for eHealth [14]. In Europe respectively eHealth monitoring is provided by EHTEL organization [15] and EK portal [16]. Activity analysis shows that in fact there is no completed and implemented interoperable national scale eHealth system anywhere. However there are lot of projects

and organizations supported by big investments and having ambitious long term plans. Among leaders could be mentioned Canada with well established planning and implementation management [17], UK with heavy investments and governmental control [18], Australia with effective administration [19], and USA with pragmatic approach and realistic Enterprise Architecture planning [20].

In Europe Nordic countries are leaders - Denmark with heterogeneous and “bottom-up” built eHealth system; Sweden and Norway with effective telemedicine pilots and practical implementations, Finland with advanced technologies. Big European countries like Germany, France and Spain have difficulties with national scale eHealth system development because of highly diversified systems and complicated legislation. For example Germany as a federal state implements a patient health cards (mainly for insurance purposes) first and Electronic Health Record (EHR) is planned for quite far future.

Although countries are using different eHealth development concepts, implementation methods as well as different level of financial support of activities some common lessons could be extracted: 1) success is highly dependent on management and legislative environment created; 2) proper strategic planning and implementation roadmap is essential; 3) in the beginning physician acceptance is limited and additional time is needed to manage electronic records; 4) investments to eHealth give the high revenue in terms of economy, social and health factors; 5) lack of unanimously accepted standards and problems with information security hamper development.

### B. Role of the strategy

In order to define the own way of eHealth development in the context of the great variety of concepts and approaches countries necessarily are developing particular eHealth strategies. 85 % of countries over the world plan to have eHealth strategies or other similar documents by 2008 [1, 6]. eHealth strategies differ by the level of abstraction and detalization, relation with implementation and by other features: from global WHO and EU strategies [1, 2] to particular strategies of countries and regions, dependent on strategic planning traditions, legislation, awareness and competences. But the importance of strategies in all cases lies in harmonization of efforts, setting goals and terms to achieve them and pointing to the benefits to all users from citizens to ministry level management.

Here possibly valuable Lithuanian experience could be mentioned – recently country approved national eHealth strategy (2007-2015) and implementation plan [12, 13].

### C. Problems of implementation

Implementation planning is inseparable part of the strategy. Strategic plan of implementation should be not a list of actions to be taken, but rather set of goals to be reached, together with concrete measurable implementation indicators, benchmarks and terms. The way how strategic goals could be reached could be partly an object of initiatives coming “bottom up” from local socialists, researchers, vendors and users.

The main development problems arise at the phase of implementation. There is a lack of highly experienced local companies and vendors to run a big national scale projects in Baltic States. eHealth paradigm is quite new and financial support of the development was till now very limited. Big companies like HP, Siemens are using their existing products and offer purchases rather than support a creation of an advanced “bottom up” grown products which are expected.

Management and organizational difficulties also are evident: eHealth projects are typically national – the key is integration in the scale of country. There is a lack of adequate competences and managerial resources to plan lead and supervise such complicated projects. Difficulties are increased by the great variety of partners, their motivations, needs, qualifications.

Although problem of standards could be concerned as global (there are no ultimate world wide accepted standards) locally this makes long term implementation planning problematic. Legislative environment also is not suitable yet and its development lags behind other actions.

## IV. CHOICE OF THE BEST WAY TOWARDS EHEALTH AREA

On the way from the strategy to implementation and evaluation of results lot of important decisions should be taken. Every decision is stipulated by the country specifics but in every stage a choice of best solution is a challenge.

In rapidly changing landscape of eHealth developments and standards two main trends are noticeable: systematic and pragmatic.

*Systematic* concept is provided by expert driven standard development organizations such as CEN TC251, OpenEHR initiative. It is based on thorough definitions of goals and aims, with emphasis to semantics, are patient – centered, oriented to continuity of care of individuals.

From the other side – *pragmatic* concept is driven mainly by vendors and users – (.g. IHE, HL7, EA) and is oriented to communication, exchange of documents provided by isolated health profiles (users), takes the diverse situation in health information as a starting point for simple communication with gradual extension of transactions towards

service oriented architectures, business process management and finally towards semantic interoperability.

In fact two above concepts have positive and negative sides and countries are deciding their best way, usually being a combination of both concepts. Countries usually are profiling existing pre-standards instead of inventing new standards. Industry and vendors are driving pragmatic standard developments process (IHE, HL7), since consultant's-driven standard development originations (CORBA, CEN) are rather not so effective (because of long term fundamental research, negotiations and limited responsiveness to the current and rather urgent needs of market) [21].

Since health system needs for information management are quite urgent, a pragmatic way proposed for example by IHE [22] has been widely taken (70 vendors successfully passed the XDS validation testing at the recent Europe connectathon)

Good recipe in setting of strategic priorities and implementation planning (if there is a good recipe at all) could be probably oriented towards:

- 1) Integrated national wide and standard based system;
- 2) Patient centered and EHR based architecture of the system;
- 3) System ensuring health service continuity across institutions and in time (life-long), oriented towards early prediction and prophylactics;
- 4) Proper combination of systematic and pragmatic concepts;
- 5) Proper combination of top-down (standards, strategy) and bottom-up (implementation alternatives, local initiatives and motivation) concepts;
- 6) Special attention towards security and legislation;
- 7) From the very beginning care about integration and interoperability in semantic, information and technological levels;
- 8) Involvement of all users and actors, agile mode of software engineering.

## V. CONCLUSION

The Baltic way towards European eHealth area requires coordination of strategies, merging efforts of countries with similar situations, avoiding parallelism, sharing experiences. Pilot cross-boarder integration and collaboration trials between Baltic and Nordic countries are essentially important. Biomedical engineering and medical physics here must contribute here by development of new methods and technologies of sensors; computer based diagnostic, information processing and decision support tools.

## ACKNOWLEDGMENT

Work was supported by Lithuanian Ministry of Health and High technology project "IT Sveikata" financed by Lithuanian State Research Fund.

## REFERENCES

1. WHO eHealth for health care delivery at [http://www.who.int/eh/en/eHealth\\_HCD.pdf](http://www.who.int/eh/en/eHealth_HCD.pdf)
2. Health—Making Healthcare Better for European Citizens: at [www.europa.eu.int/information\\_society/qualif/health/index\\_en.htm](http://www.europa.eu.int/information_society/qualif/health/index_en.htm)
3. eHealth interoperability in EU: draft recommendations at [http://ec.europa.eu/information\\_society/newsroom/cf/itemdetail.cfm?item\\_id=3540](http://ec.europa.eu/information_society/newsroom/cf/itemdetail.cfm?item_id=3540)
4. eHealth Conference 2007 Declaration (Berlin, 17 April 2007) at [http://ec.europa.eu/information\\_society/activities/health/docs/events/ehealth2007/eh\\_declaration20070417\\_en.pdf](http://ec.europa.eu/information_society/activities/health/docs/events/ehealth2007/eh_declaration20070417_en.pdf)
5. The future of medicine and the health care in the third millenium at <http://www.globalchange.com/medicine.htm>
6. WHO - eHealth tools and services: needs of the member states at [http://www.who.int/kms/initiatives/tools\\_and\\_services\\_final.pdf](http://www.who.int/kms/initiatives/tools_and_services_final.pdf)
7. eHealth ERA report 2007: eHealth priorities and strategies in European countries at [http://ec.europa.eu/information\\_society/activities/health/docs/policy/ehealth-era-full-report.pdf](http://ec.europa.eu/information_society/activities/health/docs/policy/ehealth-era-full-report.pdf)
8. Facts sheet of Estonia. Strategies and priorities of EU countries at <http://www.ehealthera.org/database/documents/factsheets/Estonia.pdf>
9. eHealth in Estonia at <http://www.ehealthconference-2006.org/pdf/REBANE.pdf> (Estonia)
10. eHealth in Latvia at [http://www.euser.eu.org/eUSER\\_eHealth-CountryBrief.asp?CaseID=2233&CaseTitleID=1074&MenuID=118](http://www.euser.eu.org/eUSER_eHealth-CountryBrief.asp?CaseID=2233&CaseTitleID=1074&MenuID=118)
11. eHealth strategy and implementation in Latvia at [http://www.ehealthera.org/database/documents/ERA\\_Reports/eH-ERA\\_Latvia\\_report\\_April%202007.pdf](http://www.ehealthera.org/database/documents/ERA_Reports/eH-ERA_Latvia_report_April%202007.pdf)
12. Lithuanian eHealth strategy approved at <http://www.epractice.eu/document/3693>
13. Lithuanian eHealth strategy and related documents at [http://www.sam.lt/lt/main/sveikatos\\_apsauga/el\\_sveikata](http://www.sam.lt/lt/main/sveikatos_apsauga/el_sveikata)
14. WHO Global Observatory for eHealth at <http://www.who.int/kms/initiatives/ehealth/en/>
15. European Health Telematics Association EHTEL at <http://www.ehtel.org/SHWebClass.asp?WCI=ShowCat&CatId=1>
16. eHealth: better health care for Europe at [http://ec.europa.eu/information\\_society/activities/health/index\\_en.htm](http://ec.europa.eu/information_society/activities/health/index_en.htm)
17. Canada Health Infoway at <http://www.infoway-inforoute.ca/>
18. UK eHealth association at <http://www.ukeha.co.uk/about.asp>
19. Australia HealthConnect Implementation Strategy at <http://www.health.gov.au/internet/hconnect/publishing.nsf>
20. Enterprise Architecture approach in eHealth at <http://www.hhs.gov/ocio/ea/architecture/index.html> (The HHS Enterprise Architecture)
21. eHealth standards – eHealth directory at [http://www.ehealthdirectory.eu/Terminologies\\_and\\_Classifications/Standards/](http://www.ehealthdirectory.eu/Terminologies_and_Classifications/Standards/)
22. Integrating the healthcare enterprise IHE at <http://www.ihe.net/>

Author: Arunas Lukosevicius  
 Institute: Biomedical Eng. Institute, Kaunas Univ. of Technology.  
 Street: Studentu str. 65  
 City: Kaunas, LT-51369eeee  
 Country: Lithuania  
 Email: arunas.lukosevicius@ktu.lt

# Biomedical Engineering Program on the Internet for Worldwide Use

J.A. Malmivuo, J.J. Nousiainen and A. Kybartaitė

Ragnar Granit Institute, Tampere University of Technology, Tampere, Finland

**Abstract** — Biomedical Engineering, which is a multi-disciplinary and fast developing field of science, covers a large number of sub-specialties. Therefore, for any university, especially for the smaller ones, it is difficult to produce and update high quality teaching material in all aspects of the field. Creating a curriculum on the Internet helps universities and students worldwide in obtaining educational material in this field.

**Keywords** — Biomedical engineering, Internet education, [www.evicab.eu](http://www.evicab.eu)

## I. INTRODUCTION

Internet is more and more used as a platform for educational material and student administration. The use of internet makes the geographical distances to disappear.

Biomedical Engineering is needed all around the world and globalization encourages the students to mobility between universities. It is important that education in Biomedical Engineering is harmonized to facilitate the mobility. The BIOMEDEA project facilitates this within the study programs in European universities.

All this gives strong reasons to develop an education program on the Internet.

This is the basis for the project: European Virtual Campus for Biomedical Engineering – EVICAB. It was funded by the European Commission Education and Training for 2006-2007.

EVICAB offers high-quality courses prepared by the best international teachers. The courses include lecture videos and associated lecture slides. The courses are also associated with additional teaching material like full textbooks, exercises, laboratory exercises etc.

All courses offered by EVICAB are recognized by at least one university in the European Union. Thus it is easy for any other university in the EU to include EVICAB courses to their curriculum.

Because the teaching material in EVICAB is available free of charge and because it can be used via Internet form anywhere in the world, the BME program provided by the EVICAB is available for worldwide use.

EVICAB uses the Wiki-idea but is more strongly controlled by an Administrative Board. This ensures that the teaching material provided by the experts is of high quality and cannot be changed by anyone else than the author. In

addition to the primary teaching material, the courses have windows with free access. These are used for providing additional teaching material by the users of EVICAB. In addition to helping the students, this Wiki material may be utilized by the course author for improving the course.

The teaching material for EVICAB is provided by the best experts free of charge. The benefit from this for the teacher is that his/her reputation as an expert will be strengthened worldwide and this will support his/her career as pedagogue and scientist.

Associated to the EVICAB education there is also developed a method for Internet examinations. This will further strengthen the worldwide use of EVICAB because the geographical location of the students and the teachers does not play any role anymore.

[www.evicab.eu](http://www.evicab.eu)

## II. EVICAB PROJECT

The objective of the project is to develop, build up and evaluate sustainable, dynamical solutions for virtual mobility and e-learning that, according to the Bologna process,

(i) Mutually support the harmonization of the European higher education programs,

(ii) Improve the quality of and comparability between the programs, and

(iii) Advance the post-graduate studies, qualification and certification. These practices will be developed, piloted and evaluated in the field of biomedical engineering and medical physics.

Important goal is that these approaches and mechanisms for virtual e-learning can be extended and transferred from this project also to other disciplines to promote virtual student and teacher mobility and credit transfer between European universities.

## III. EVICAB CONSORTIUM

EVICAB is coordinated by the Ragnar Granit Institute of Tampere University of Technology. Professor Jaakko Malmivuo serves as Director of the project and Assistant Professor Juha Nousiainen as coordinator. The other partners are:

- Mediamasteri Group Ltd, Tampere, Finland
  - Department of Biomedical Engineering, Linköping University, Linköping, Sweden
  - Biomedical Engineering Center, Tallinn University of Technology, Tallinn, Estonia
  - Institute of Biomedical Engineering, Kaunas University of Technology, Kaunas, Lithuania.
  - Department of Biomedical Engineering, Brno University of Technology, Brno, Czech Republic.
- EVICAB welcomes interested institutes to join as associate partners. We hope that the associate partners active participate in producing teaching material to EVICAB.

#### IV. IDEA OF EVICAB

The fundamental idea of the EVICAB is that it offers an open platform for Biomedical Engineering curriculum on the Internet. The openness means the open access to and free right to use the resources of the EVICAB, and an open possibility for all experts in the field to contribute to the development of the content of the virtual curriculum.

Teachers, who are experienced and recognized experts in their field, are encouraged to submit full e-courses, course modules and other teaching material to EVICAB. The material may include many different formats like video lectures, PowerPoint slides, pdf-files, Word files etc.

EVICAB is not a university. The course and student administrations continue in the universities as usual: The teacher, responsible of the course/study program, may select from the EVICAB courses for the BME curriculum of the university. The students study the course either as ordinary lecturing course with the EVICAB material supporting the lectures or the course may be partially or solely studied from EVICAB. The students, or anyone even outside the university, may study EVICAB courses to add their competence in Biomedical Engineering. Thus EVICAB is important also for the persons in the working life to improving their professional competence.

The EVICAB has an Administrative Board which administers the EVICAB curriculum. The board accepts courses of sufficient scientific, pedagogical and technical quality. The board may also invite experts to provide course material to the EVICAB. Courses which apparently are of low quality, either out of date, lower quality than competing courses and not appreciated by the users of the EVICAB will be deleted. Active feedback from the users of EVICAB, both teachers and students, is essential. All this will be realized by utilizing a dynamical quality assurance system.

#### V. IMPACT OF EVICAB ON E-LEARNING

In its completed form, EVICAB will have strong impact on all main levels of the education process:

For students it will provide virtual mobility as a complementary, preparatory, or even substitutive option for physical mobility. The increased number on e-courses for distance learning will give higher variety of qualified studies and degrees.

Teachers will substantially benefit from the open resources, teaching materials and e-courses available through the EVICAB. The support provided for design and development, as well as the good practices and high-quality e-courses will motivate and spur the teachers in the e-course development.

EVICAB will contribute to the harmonization process of BME curricula in Europe in co-operation with BIOMEDEA and will improve the quality of the curricula. Finally, the solutions and models developed for building the virtual BME curriculum can be applied to other disciplines.

#### VI. INTERNET EXAMINATION

Another successful innovation and application in our e-learning activities has been the Internet examination.

In the Internet examination the students make the exam in a computer class. This may be performed simultaneously in several universities. Therefore the students do not need to travel to the location there the course was given.

The students open the Moodle program at the time of the examination and find the examination questions from there. We usually allow the students to use all the material available on the Internet. This requires that instead of asking "What is ..." the examination questions shall be formulated so that they indicate that the student has understood the topic and is able to apply this information. The only thing which is not allowed is communication with another person via e-mail etc. during the examination.

#### VII. MOBILE COURSE MATERIAL

One of the key issues in the EVICAB is to reach the students anywhere and anytime. The learning process should not be dependent on the location of the student. Internet based material supports this idea and hence all the educational resources are provided in the EVICAB platform in the Internet. Not only is the Internet used for media for

learning process but also portable devices such as iPod and mobile phones can be used. In EVICAB project different media are supported. Students may choose the best media for his or her current lifestyle; busy student may, for instance, watch the lecture videos in a bus on the way to or from university.

### VIII. WHY TO PROVIDE COURSES TO EVICAB?

EVICAB is an important teaching and learning method only if it is available free of charge and worldwide. As a consequence, the learning material should be provided free of charge.

Why experienced and competent teachers should provide such material without charge and without receiving royalties? Acceptance of a course by EVICAB will be a certificate for quality. Worldwide distribution to all university students will give exceptional publicity for the author and his/her university. All this will facilitate the sales of traditional teaching material produced by the course author. This will also attract international students from other countries all over the world to apply to the home university of the material author. We already have experience which has proven these issues to be realistic.

The Internet has dramatically changed the distribution of information. Distribution is worldwide, real time and free of delivery costs. The technology also supports wide variety of attractive presentation modalities. All this ensures wide audience and publicity for the material on the Internet. For instance, the Wikipedia dictionary serves as a successful example of this new era of information delivery. On the basis of this publicity it is possible to create markets also for

traditional printed educational material. In addition the EVICAB will provide the platform for all courses free of charge. Pedagogical evaluation and technical support for course design are also provided in request. This will ensure the high quality and up to date virtual learning environment.

### IX. CONCLUSION

In future, the teaching and learning will mainly be based on Internet. The ideas and the technology of EVICAB are not limited only for application on Biomedical Engineering but it may be applied to all fields and levels of education. EVICAB will be the forerunner and show the way to more efficient and high quality education

### ACKNOWLEDGMENT

This work has been supported by the European Commission Education and Training, Ministry of Education in Finland, Academy of Finland and the Ragnar Granit Foundation.

The address of the corresponding author:

Author: Jaakko Malmivuo, Prof.  
Institute: Ragnar Granit Institute  
Tampere University of Technology  
Street: Korkeakoulunkatu 6  
City: 33720 Tampere  
Country: Finland  
Email: jaakko.malmivuo@tut.fi



# The Modification of Titanium Dioxide MOCVD Coating in TiAlNb after Immersion in Artificial Saliva

E. Aldea<sup>1</sup>, M.M. Dicu<sup>1</sup>, A. Gleizes<sup>2</sup> and I. Demetrescu<sup>1</sup>

<sup>1</sup>University Polytechnica Bucharest/General Chemistry Department, Bucharest, Romania

<sup>2</sup>Centre Interuniversitaire de Recherche et d'Ingénierie des Matériaux UMR-CNRS 5085, ENSIACET/INPT, Toulouse, France

**Abstract** — The paper aim is to observed the modification of passive coating obtained on TiAlNb with a Metal-Organic Chemical Vapor Deposition (MOCVD) [1, 2] procedure after immersion in artificial saliva (Fusayama) with calcium content. Two temperatures [T] (400°C and 500°C), two pressures [p] (1 and 20 torr) and variable molecular fraction [χ] from 76 to 5000 were used in MOCVD coating procedures. The X-ray spectrum confirms the dense and uniform deposition of TiO<sub>2</sub> film on TiAlNb alloy surface. The results of analyses used in the present paper contribute of the extended research in the biomaterial domain.

**Keywords** — TiAlNb alloy, MOCVD, artificial saliva, Scanning Electronic Microscopy, contact angle, infrared technique.

## I. INTRODUCTION

Implants are one of the great success stories of modern medicine. It is important to characterize the implant surface and to consider the interfacial phenomenon that occur between surface, biological molecules and cells since implant surfaces with different properties result in different responses at the cellular and consequently at the tissue level around the implant [3-6]. After was demonstrated that the titanium and titanium alloys are excellent implant biomaterial, now the research try to improve the performance of this biomaterials working to the process for the modification of the surface topography and biochemistry for a very good adhesion of the human cell and a better biocompatibility with the body. The use of titanium and his alloys for biomedical applications has increased dramatically in this century, being extensively [7-10] the choice in dentistry dental implants, dental crowns and partial denture frameworks. As titanium, TiAlNb alloy readily passivates to form a protective oxide layer, which accounts for its high corrosion resistance. This protection capacity of the oxide depends on the obtaining procedure and environment [11], taking into account that in bioliquids various processes as adsorption and ions release are taken place.

## II. MATERIALS AND METHODS

### A. Materials

The biomaterial used in this research is a cylindrical form of TiAlNb alloy made from Bucharest Romania IMNR Institute with the following composition (Table 1):

Table 1 Composition of the implant biomaterial [%]

Al	Nb	Fe	C	O	N	H	Ti
5.88	6.65	0.03	0.10	0.20	0.07	0.02	87.05

This cylindrical form was divided in many pastille samples with 2 mm thickness and 1 cm<sup>2</sup> diameter and that represent the expose work sample.

The biometallic sample surface preparation involves: abrasion, chemically polished in 20% HNO<sub>3</sub> + 3% HF from 10 minutes, degreased in boiling benzene from 5 minutes and thoroughly rinsed with tap and distilled water.

The simulated bioliquid was Fusayama artificial saliva with important calcium content [12] as following (Table 2):

Table 2 Composition of the simulated Fusayama saliva

Substance	g/L
NaCl	0.400
KCl	0.900
CaCl <sub>2</sub> ·2H <sub>2</sub> O	0.795
NaH <sub>2</sub> PO <sub>4</sub>	0.690
Urea	1.000

### B. Methods

To improve the biocompatibility resistance of the TiAlNb alloy on the surface samples the TiO<sub>2</sub> was deposition using the Metal-Organic Chemical Vapor Deposition method (MOCVD) [13, 14] at the Toulouse France Institute. In this technique it is mark the precursor (the vapor of a metal-organic complex = [Ti{OCH(CH<sub>3</sub>)<sub>2</sub>}<sub>4</sub>] titanium isopropyl oxide (TTIP)) to reactor with a heated surface which represent the substrate and in this case the solid reaction deposits and forms a thin film on the substrate surface. Pressure was regulated

with a Baratron gauge connected via a pressure controller to a butterfly valve above a vacuum pump. 99.9992% pure N<sub>2</sub> (Air Products) was fed through two lines equipped with MKS mass flow rate controllers, one to sweep away the precursor, the other to dilute it. The deposition temperature was measured with a thermocouple K plugged into the reaction zone.

The used techniques for surface characterization were Scanning Electronic Microscopy (SEM) – [LEO-435 and FEI/Phillips XL30 ESEM with EDAX module], porosimetry and roughness – [interferometer optic Metro-ProTM Zygo New View 100] measurements.

The immersion test was performed in artificial saliva with calcium content. The modification of passive layer was evaluated with Contact Angle (CA) – [DIGIDROP Contact Angle Meter (BGX Scientific Instruments)] and structural infrared (FT-IR) [Perkin Elmer, Spectrum 100] analysis.

### III. RESULTS AND DISCUSSION

The modification of titanium dioxide MOCVD coating on TiAlNb alloy after immersion in Fusayama artificial saliva was observed and analyzed in comparison with the initial cases of TiAlNb/TiO<sub>2</sub> alloy.

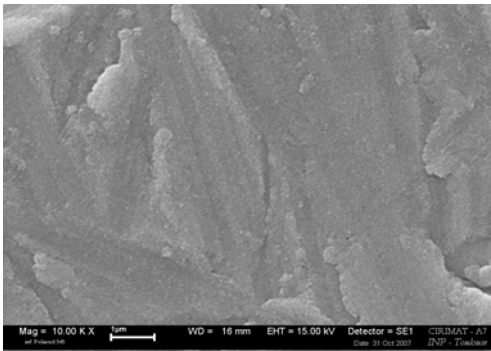


Fig. 1 ESEM image of TiAlNb/TiO<sub>2</sub> – T 500/p 20/χ76

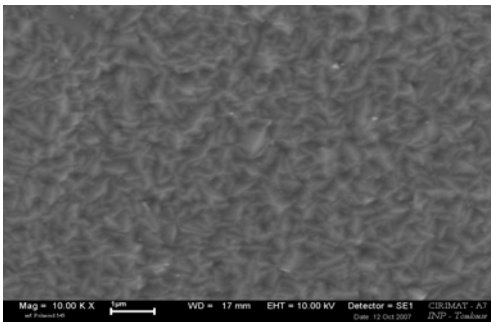


Fig. 2 ESEM image of TiAlNb/TiO<sub>2</sub> – T 400/p 1/χ5000

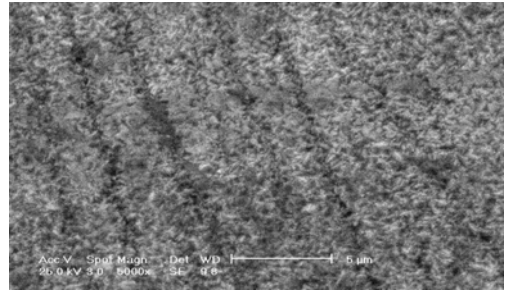


Fig. 3 ESEM image of TiAlNb/TiO<sub>2</sub> – T 400/p 1/χ5000 after immersion one month in artificial saliva

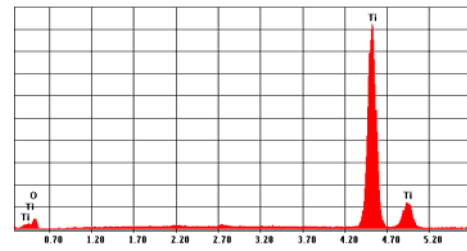


Fig. 4 Spectrum for emission in X-ray from TiAlNb/TiO<sub>2</sub> – T 400/p 1/χ5000

The passive titanium layer is a mixture of oxides with composition and morphology depending on the experimental MOCVD deposition conditions.

One of the biometallic alloy surface characterization was the ESEM method which present the modification on the surface. Figures 1 ÷ 3 present a dens and uniform coating of film TiO<sub>2</sub> on the TiAlNb surface before and after immersion for one month in artificial medium (Fusayama).

The ESEM image is completed by X-ray spectrum which confirms the good deposition of thin films TiO<sub>2</sub> using MOCVD technique (Figure 4).

The surface porosity and roughness values for the TiAlNb/TiO<sub>2</sub> alloy are presented in Table 3 and Figure 5.

Depending on deposition condition, the roughness varies from micro to nano scale as can be seen in the following table. Regarding porosity, this parameter is not a function of deposition condition in this case.

The good wettability of the treated biomaterial surfaces is an interesting aspect in order to obtain chemical interaction with the physiological fluids surfaces and also to avoid cell growth and protein adsorption. It was demonstrate that for a

Table 3 Characterization of surface porosity and roughness

Titanium alloy	Porosity [%]	R <sub>a</sub> [μm]
TiAlNb/TiO <sub>2</sub> – T 400/p 1/χ5000	90	0.066
TiAlNb/TiO <sub>2</sub> – T 500/p 20/χ76	90	0.160

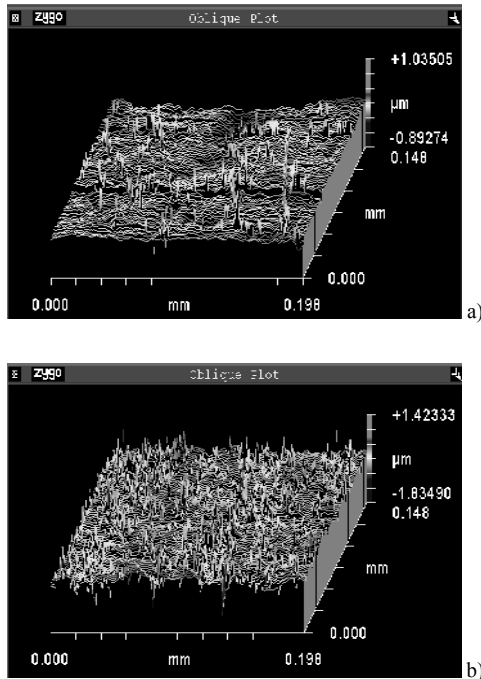


Fig. 5 Roughness 3D images of samples TiAlNb/TiO<sub>2</sub> a) T<sub>d</sub>=400°C (χ = 5000 ppm), b) T<sub>d</sub>=500°C (χ =76 ppm)

successful osteointegration is better to have a lower contact angle value [15, 16].

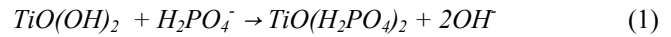
The quality of titanium dioxide deposition on TiAlNb alloy showed the influence on the wettability of the surfaces. Distilled water put on coated samples with TiO<sub>2</sub> formed a regular drop, with a hydrophilic character (Table 4). After immersion of the same samples for one month in artificial medium (Fusayama), the TiAlNb samples covered / uncovered with TiO<sub>2</sub> are a little bit easily wetted.

FT-IR analysis, in the absorbance mode, shows the presence of phosphate and hydroxyl groups formed after immersion of the sample in Fusayama saliva.

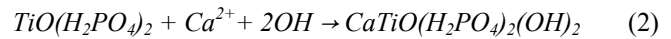
After immersion of TiAlNb/TiO<sub>2</sub> alloy – T 400/p 1/χ 5000 sample in artificial saliva, the phosphate bonded appears at 1083 cm<sup>-1</sup> in the IR spectrum, probably due to the presence of (H<sub>2</sub>PO<sub>4</sub>)<sup>-</sup> on Fusayama composition. The νOH band obtained

is supposed to be involved in the formation of the species like Ti(OH)<sub>2</sub> or hydroxo-complexes such as TiO(OH)<sub>2</sub>.

The H<sub>2</sub>PO<sub>4</sub><sup>-</sup> ion existent in the composition of Fusayama solution is adsorbed on the titanium surface oxide (1):



It is known from literature [17] that phosphate ions are preferentially taken up in the surface film during repassivation and calcium ions are adsorbed on the surface, according to the reaction (2):



The titanium alloy implant biocompatibility increases if the calcium phosphate will form, and that is a very important biointerface process, which helps osteointegration.

#### IV. CONCLUSIONS

The microscopy images present a dens and uniform MOCVD coating TiO<sub>2</sub> film on the TiAlNb surface before and after immersion for one month in artificial saliva (Fusayama). The MOCVD deposition condition determinate a change of the roughness values (from micro to nano), but not also in this case for the porosity value.

For all studied samples before and after immersion in artificial saliva the contact angle determination indicated a hydrophilic character. A decrease in contact angle value is associated with MOCVD deposition condition. Immersion in Fusayama does not change significantly the balance hydrophilic-hydrophobic.

FT-IR analysis, in the absorbance mode, shows the presence of phosphate and hydroxyl groups formed after immersion of the TiAlNb/TiO<sub>2</sub> alloy in Fusayama saliva.

#### ACKNOWLEDGMENT

The authors thank to Prof. Dr. Dionezie Bojin from University Politehnica Bucharest – Materials Science and Engineering Faculty, for his support and precious help regarding ESEM microscopy analysis.

#### REFERENCES

1. Monoy A, Brevet A, Imhoff L, Domenichini B, Lesniewska E, Peterlé PM, Marco de Lucas MC, Bourgeois S (2006) Thin Solid Films 515:687-690
2. Brevet A, Peterlé PM, Imhoff L, Marco de Lucas MC, Bourgeois S (2005) Journal of Crystal Growth 275:e1263-e1268
3. Li SJ, Zhang YW, Sun BB, Hao YL, Yang R (2008) Materials Science and Engineering: A 480:101-108

Table 4 The contact angle values for studied sample

Titanium alloy	Contact angle [°]
TiAlNb	78
TiAlNb/TiO <sub>2</sub> – T 400/p 1/χ 5000	70
TiAlNb/TiO <sub>2</sub> – T 500/p 20/χ 76	68
TiAlNb – Fusayama	78
TiAlNb/TiO <sub>2</sub> – T 400/p 1/χ 5000 – Fusayama	72
TiAlNb/TiO <sub>2</sub> – T 500/p 20/χ 76 – Fusayama	69

4. Xu LJ, Chen YY, Liu ZhG, Kong FT (2008) *Journal of Alloys and Compounds* 453:320-324
5. Boehlert CJ, Cowen CJ, Quast JP, Akahori T, Niinomi M (2008) *Materials Science and Engineering: C* 28:323-330
6. Milošev I, Kosec T, Strehblow HH (2008) *Electrochimica Acta* 53:3547-3558
7. Habibovic P, Li J, Van der Valk CM, Meijer G, Layrolle P, Van Blitterswijk CA, de Groot K (2005) *Biomaterials* 26:23-36
8. Schuler M, Trentin D, Textor M, Tosatti SGP (2006) *Nanomedicine* 1:449-463
9. Elias KL, Daehn GS, Brantley WA, McGlumphy EA (2007) *The Journal of Prosthetic Dentistry* 97:357-365
10. Zaveri N, Mahapatra M, Deceuster A, Peng Y, Li L, Zhou A (2008) *Electrochimica Acta* 53:5022-5032
11. Sovar MM, Aldea E, Mitran V, Miculescu F, Demetrescu I (2008) *Key Engineering Materials* 361-363:1131-1134
12. Aldea E, Grecu I, Demetrescu I (2005) *UPB Sci. Bull Series B* 67:27-33
13. Maekawa T, Kurosaki K, Tanaka T, Yamanaka S (2008) *Surface and Coatings Technology* 202:3067-3071
14. Battiston GA, Gerbasi R, Tiziani A, Figueras A, Garcia G (2000) *Mater. Sci. Forum* 352:151.
15. Oshida Y (2001) Titanium material implants. US Patent No. 6183255
16. Ionita D, Aldea E, Stanciu G, Demetrescu I (2008) *Key Engineering Materials* 361-363:733-736
17. Hanawa T, Asami K, Asaoka K (1998) *J. Biomed Materials Res* 40:530-538

Author: Elena Aldea  
Institute: University Polytechnica Bucharest  
Street: Polizu, No. 1  
City: Bucharest  
Country: Romania  
Email: Aldea\_E@Yahoo.Ca

# Osteogenesis on Surface Selective Laser Sintered Bioresorbable Scaffolds

V.N. Bagratashvili<sup>1</sup>, E.N. Antonov<sup>1</sup>, S.M. Howdle<sup>3</sup>, J.M. Kanczler<sup>2</sup>, S. Mirmalek-Sani<sup>2</sup>, V.K. Popov<sup>1</sup>, R.O. Oreffo<sup>2</sup>, C. Upton<sup>3</sup>

<sup>1</sup> Institute of Laser and Information Technologies RAS, Troitsk, Moscow Region, Russia

<sup>2</sup> Bone & Joint Research Group, University of Southampton, Southampton,

<sup>3</sup> School of Chemistry, University of Nottingham, University Park Nottingham, UK

**Abstract** — In this study we have used a novel surface selective laser sintering (SSLS) technique to develop CAD/CAM designed scaffolds for bone tissue engineering. SSLS polylactic acid scaffolds were evaluated *in vitro* and *in vivo* as templates for human fetal femur-derived cell and adult human bone marrow stromal cell osteogenesis. Both cell types were cultured successfully on SSLS scaffolds with an increase in expression of alkaline phosphatase activity. Cell in-growth and Alcian blue/Sirius red positive staining of matrix deposition were observed on SSLS scaffolds *in vitro* in basal medium and osteogenic culture conditions. Similar results were observed *in vivo* with type I collagen expressed by cells on the scaffolds. In the critical sized femur segmental defect, SSLS scaffolds seeded with the cells enhanced significantly bone tissue regeneration.

**Keywords** — Tissue engineering, laser sintering, scaffolds.

## I. INTRODUCTION

Recent tissue engineering advances based upon porous polymer scaffolds, which act as a delivery vehicle for cells, have led to the possibility of successful repair and restoration of function in damaged or diseased tissues [1]. This involves seeding highly porous biodegradable scaffolds with donor cells and/or growth factors, culturing and then implanting the scaffolds to induce direct growth of a new tissue. The manufacturing of such scaffolds still presents both materials and technical problems. These scaffolds must be biocompatible to minimise adverse inflammatory reactions, augment cellular in-growth and fit anatomically within the bone defect. The imperfection of current techniques (e.g. mold casting, injection molding, foaming, particulate leaching, etc.) has encouraged the development and use of a Rapid Prototyping (RP) approach for reliable fabrication of scaffolds with controlled architecture satisfying a range of requirements related to their strength and toughness, osteoinductivity and osteoconductivity, controlled rate of biodegradation and inflammatory response [2].

We previously reported the development of a new RP method - Surface Selective Laser Sintering (SSLS) [3] enabling precise fabrication of scaffolds even from

thermosensitive biodegradable polymers such as polylactic acid (PLA). In SSLS we can fuse the polymer particles, which do not absorb near infrared ( $\lambda \sim 1.0\mu\text{m}$ ) laser radiation, by controlled melting of the particle surface only (Fig.1). This is achieved by homogeneously distributing a small amount ( $\leq 0.1$  wt.%) of carbon black (CB) nanoparticles over the PLA surface. Carbon absorbs laser energy allowing localized melting and fusion of the PLA particle surface. This controlled melting prevents significant overheating of their internal domains [4]. We have demonstrated that this sintering process does not damage the polymer chemical structure. Moreover, the most of the activity of the enzymes incorporated into individual PLA particles can be retained following SSLS processing [3].

In this study we have used our SSLS poly-(D,L)-lactic acid scaffolds for their *in vitro* and *in vivo* evaluation as templates for human fetal femur-derived cell (HFFDC) and adult human bone marrow stromal cell (HBMSC) osteogenesis.

## II. MATERIALS AND METHODS

Poly (D,L)-lactic acid ( $M_w=108\text{kDa}$ , polydispersity =1.4) was purchased from Alkermes (Boston, MA, USA) and was ground to a fine powder (mean particle diameter of around  $100\mu\text{m}$ ) using a pestle and mortar. A small amount (ca. 0.1wt.%) of furnace carbon black (CB) with surface area  $\approx 100\text{m}^2/\text{g}$  was added to this powder by thorough mixing covering all of the PLA particles.

PLA scaffolds with desired architecture (Fig.1) were fabricated using an experimental prototype of SSLS machine designed and produced by ILIT RAS. It based on continuous wave fibre laser "LS-1.06" (IRE-Polus Ltd, Moscow, Russia) emitting at  $\lambda=1.06\mu\text{m}$  with a maximum power of 10W.

Laser beam was delivered to the powder bed using a silica fiber, magnifying objective, focusing lens and X-Y computer controlled scanner resulting in ca.  $125\mu\text{m}$  diameter laser spot onto the polymer particles. Only CB particles absorb radiation at this wavelength allowing specific surface melting and powder fusion. Laser power

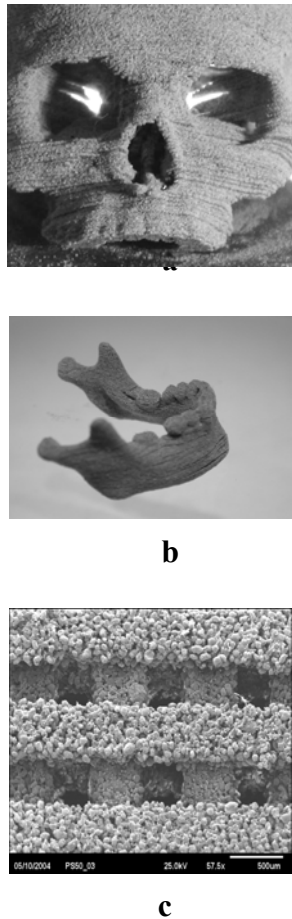


Figure 1. SSLS skull and mandibular biomodels based on NMR data (a, b) and PLA scaffold (c).

density on the focal plane used for reliable sintering of PLA/CB particles at the scan velocity 6 mm/s was  $I_t \approx 1.2 \pm 0.2 \times 10^4 \text{ W/cm}^2$ .

Fetal Calf Serum (FCS) was purchased from Invitrogen, Scotland.  $\alpha$ -MEM, dexamethasone and alkaline phosphatase kits and all other tissue culture reagents were purchased from Sigma-Aldrich, (UK) unless stated. Adult human bone marrow samples were obtained from hematological normal patients undergoing routine elective hip replacement surgery. Cultures were maintained in basal medium ( $\alpha$ -MEM containing 10% FCS) at 37°C in humidified air with 5% CO<sub>2</sub>. Human fetal femurs were obtained following termination of pregnancy according to guidelines issued by the Polkinghorne Report. Femurs were dissected and plated into T25 flasks in 2ml basal medium. Cells were cultured for 7 days from explants before passage and scaffolds seeding.

SSLS scaffolds were individually seeded with HFFDC and adult HBMSC, and cultured for 7 and 28 days. 10  $\mu\text{g/ml}$  Cell Tracker Green™ CMFDA and 5  $\mu\text{g/ml}$  Ethidium Homodimer-1 (CTG/EH-1) (Molecular Probes, Leiden, NL) have been used to label viable and necrotic cells respectively. Prior to fixation, cells were bathed in  $\alpha$ -MEM containing CTG/EH-1 at 37°C for 1 hour. Samples were washed with  $\alpha$ -MEM, and then rinsed in PBS before fixing in 70% ethanol. Samples were visualised on Carl Zeiss Axiovert 200 microscope with software package to capture fluorescently labeled cells. Following culture of cells on SSLS samples, scaffolds were washed in PBS before 1 hour fixation in 3% glutaraldehyde/4% paraformaldehyde in PBS (pH=7.4). After rinses in PBS, scaffolds were dehydrated through 10 min washes in ethanol and transferred to hexamethyldisilazane (Agar Scientific Ltd, UK) for two 10 min washes then excess was allowed to evaporate. Scaffolds were then analysed at FEI Quanta 200 scanning electron microscope with FEI imaging software.

For *in vivo* studies female MF-1 nu/nu immunodeficient mice were purchased from Harlan (Loughborough, UK). The animals were anaesthetised with fentanyl-fluanisone (Hypnorm) (Janssen-Cilag Ltd) and midazolam (Hypnovel) (Roche Ltd) in sterile water at a ratio of 1:1 and a dose of 10ml/kg intraperitoneally. HFFDC seeded and unseeded SSLS scaffolds were cultured in osteogenic medium ( $\alpha$ -MEM/10% FCS with 100  $\mu\text{M}$  ascorbate and 10nM dexamethasone) for 24 hours prior to subcutaneous implantation into mice. Control cultures of fetal cell-seeded SSLS scaffolds were maintained *in vitro* in basal conditions. After 28 days mice were killed and parallel cell cultures stopped. Samples were explanted for histological analysis.

### III. RESULTS AND DISCUSSION

Following seeding onto the SSLS scaffolds, extensive cell adhesion was observed within 24 hours. In extended culture over a period of 7 days, adult HBMSC and HFFDC were observed adhered and viable (Fig.2) HFFDC were observed to cover the scaffold completely forming a sheet of cells in contrast to the adult HBMSC populations. Both types of cells grown on the SSLS scaffolds expressed high activity of alkaline phosphatase.

SEM analysis of HFFDC ability to differentiate in basal and osteogenic culture conditions has showed a progressive proliferation of cells over the scaffolds with complete coverage occurring after 7 days in culture. No significant differences were observed between cells grown in basal and osteogenic medium. Positive staining for Alcian blue and Sirius red staining indicative of proteoglycans and fibrous collagens respectively of HFFDC grown on SSLS scaffolds

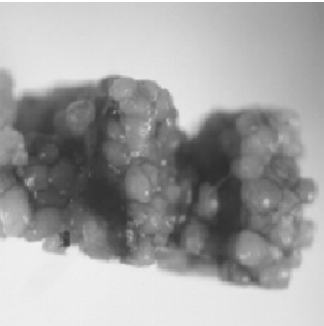
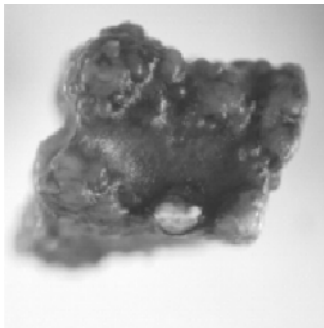
**a****b****c**

Figure 2. *In vitro* cell growth on SSSL scaffolds. (a) Bare SSSL-PLA scaffold, (b) HBMSC seeded and (c) HFFDC seeded scaffolds expressed high activity of alkaline phosphatase. Magnific. 100X.

was observed after 28 days in culture. Cells grown in basal and osteogenic culture medium showed good growth and penetration within the SSSL scaffold assessed by histological examination

To evaluate the ability of these scaffolds to provide a platform for differentiation and mineralisation *in vivo*, basal and osteogenic stimulated HFFDC were seeded onto SSSL scaffolds and subcutaneously implanted into nude mice for 4 weeks. PLA alone was served as negative control. Angiogenesis evidenced by blood vessel growth developed in and around SSSL scaffold (Fig.3).

SSSL scaffolds promoted cell adhesion, proliferation and differentiation with extensive evidence of new bone matrix

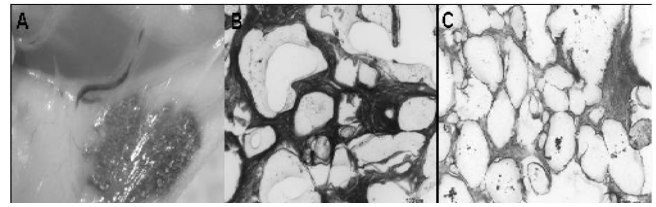


Figure 3. A - Blood vessel growth developed in and around the SSSL scaffold. B - Alcian Blue/Sirius red staining of matrix deposition by HFFDC after 28 days. C - Immunocytochemistry of HFFDC growth on SSSL scaffolds at day 28 *in vivo*, demonstrating type I collagen. Bars = 100  $\mu$ m.

deposition as detected by Alcian blue/Sirius red staining for cartilage and bone. Furthermore, evidence of type I collagen staining was also observed with enhanced expression occurring in osteogenic induced HFFDC seeded SSSL scaffolds.

New bone formation was also examined in a clinically relevant mouse segmental femur defect. Radiological and histological analyses were conducted at 4 weeks post surgery to compare the healing of the implanted SSSL scaffold with and without the addition of HBMSC and HFFDC. There was no detectable repair of the resected bone region over the 4 weeks period in the control group in the absence of a SSSL scaffold. Substantial bone formation and bridging of the defect gap occurred in the groups that contained SSSL scaffolds with enhanced mineralization present in the SSSL scaffold seeded with adult HBMSC group.

#### IV. CONCLUSION

Our studies demonstrate that HBMSC and particularly HFFDC, can grow and survive on SSSL PLA scaffolds and provide a template for osteogenic differentiation *in vivo*. These scaffold implants containing bone marrow derived cells seeded onto them, proved successful in the reparation of a critical sized bone defect. Modifications in the structure of these scaffolds may improve the strength of these scaffolds to match up or surpass the gold standard of bone allograft. Addition of small concentrations of factors such as hydroxyapatite to the PLA/CB mixture would provide the strength to the defect area to allow not only bone growth and repair, but critically, bone remodeling. In fabricating SSSL-PLA scaffolds we have the ability to create structures that can fit anatomically into a bone defect providing the right size, strength and porosity for osteogenesis and the development of a vascular supply for the important nutrient and gaseous exchange needed for tissue regeneration. Moreover, this mild processing route opens up the possibility of incorporating bioactive species such as growth

factors and enzymes which, when released can stimulate and enhance the regeneration of bone with the potential therein for enhanced skeletal regeneration.

#### ACKNOWLEDGEMENTS

We are grateful to the orthopaedics surgeons at the Southampton General Hospital for their aid in facilitating the human bone marrow samples, and to Neil Hanley and David Wilson, University of Southampton for the fetal femur samples. We are grateful to various funding sources, in particular the Wellcome Trust, Royal Society (UK) and Russian Foundation of Basic Research. We thank also the BBSRC and EPSRC. SMH is a Royal Society – Wolfson Research Merit Award Holder.

#### REFERENCES

[1] Hutmacher D.W., (2000) "Scaffolds in tissue engineering bone and cartilage", *Biomaterials*, V. 21, pp.2529-2543.

- [2] Sachlos E. and Czernuszka J.T., (2003) "Making tissue engineering scaffolds work. Review on the application of solid freeform fabrication technology to the production of tissue engineering scaffolds", *European Cells and Materials*, V. 5, pp.29-40.
- [3] Antonov E.N., Bagratashvili V.N., Howdle S.M., Konovalov A.N., Popov V.K., Shakesheff K.M. and Whitaker M.J., (2005) "Three-dimensional bioactive and biodegradable scaffolds fabricated by surface-selective laser sintering", *Advanced Materials*, V. 17, No. 3, 327-330.
- [4] Antonov E.N., Bagratashvili V.N., Howdle S.M., Konovalov A.N., Popov V.K. and Panchenko V.Ya., (2006) "Fabrication of polymer scaffolds for tissue engineering using surface selective laser sintering", *Laser Physics*, V. 16, No. 5, pp.774-787.

Address of the corresponding author:

Author: Victor Bagratashvili  
Institute: Institute of Laser and Information Technologies RAS  
Street: Pionerskaya 2  
City: 142190 Troitsk, Moscow Region  
Country: Russia  
Email: bagrat@laser.ru



# Investigation of the Bone Cartilage Interface by CLSM

J. Bossert<sup>1</sup>, T. Keller<sup>1</sup>

<sup>1</sup> Institute of Materials Science and Technology/Friedrich-Schiller-University Jena, Germany

**Abstract** — A common problem for implants is the stress and the strain at the interface of implant and tissue. The reason for are different mechanical properties of biomaterial and tissue. This mechanical incompatibility might lead to the loosening of the implant. There are several strategies dealing with improving the interface of biomaterial and implants. Here we present data of the architecture of a natural interface that might serve to develop advanced surfaces for solid implants.

From partially decalcified human tali the cartilage could be peeled off. Both, the cartilage and the bone were investigated by Confocal Laser Scanning Microscopy (CLSM). The images give an impression of the roughness and structure of the interface. The resulting three dimensional pictures were quantified by the help of quantitative image analyse software. The quantitative analyse gives information about the real interface area, which is higher than the planar geometrical area, the ratio of bone and cartilage of the transition zone, and about the morphological structure of the interface.

Quantitative data on the amount and structure of the graded interface can be used to model the mechanical properties of the interface and finally might help to create a micro design of the implant surface ideal for osteointegration and optimal load transfer.

**Keywords** — bone, cartilage, interface, CLSM

## I. INTRODUCTION

A well known phenomena for hard tissue implants is the so called stress shielding. This is caused by different mechanical properties of the implant and the remaining tissue, which leads to the effect that the implant is bearing the load whereas the bone starts to resorb. Titanium is usually equipped with a porous surface when used as uncemented implant. The graded interface allows the bone to grow into the pores and results in a tight anchoring of the implant within the bone, be it for hip, knee, ankle, vertebrae or teeth [1, 2]. Although the healing of the bone into the implants interface is promoted in his way stress shielding still may occur. So none of the most long term problems are wear particles that may migrate to the interface. These wear particles cause tissue reactions that compromise the proper function of the interface [3, 4]. Combinations of materials having different mechanical properties however are present in the human body. The combination of cartilage and bone is such a combination of quite different materials. The analyse of the structure of this interface might lead to a better

understanding of the modalities that stabilize the natural interface. The data may serve to develop advanced surfaces for solid implants.

A number of investigations were made to explore the interface of bone, calcified and non calcified cartilage [5-14]. Modern microscopes now give access to a different way and more detailed analyse of these interfaces [15].

## II. MATERIALS AND METHODS

Human tali were prepared for confocal microscopy investigation as described in [15]. The samples were investigated by CLSM (Zeiss Meta) and data evaluation was made using quantitative image analyses (Leica Quantimed).

For CLSM magnifications of 10x and 20x were found to be most appropriated to reveal the structures. Software of CLSM was used to make correction for non planar surfaces. If the samples were placed directly under the CLSM drying during imaging occurred, resulting in deformed surface structures. Therefore the samples were kept in distilled water and immersion objective were used.

## III. RESULTS

Confocal Laser Scanning Microscopy (CLSM) is based on an optical microscope, however using additionally a defined wavelength of a laser. The confocal princip simply spoken gives a signal to the detector only if the light reflected from the sample is exactly in the focus plane. Moving the sample up and down the three dimensional surface of a sample can be detected and virtually reconstructed in the limitations of an optical microscope. Additionally to "normal" light microscopy the noise coming from laser light and scattering from the sample has to be taken into account. Therefore filter algorithms have to be applied which in this case make it difficult to distinguish in a rather rough structured surface fine details form noise. From the virtually reconstructed 3D surface roughness parameters well known from conventional profilometers can be determined. The advantage is that the measuring principle is in a non contact mode and that lines for determination of roughness parameters can be drawn at any position of the image. Furthermore the real surface can be determined - meaning not only the base area of the scanned field but also the three dimensional

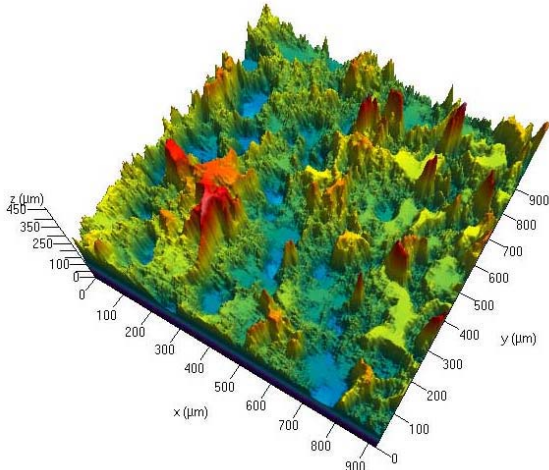


Fig. 1 CLSM – picture of cartilage surface

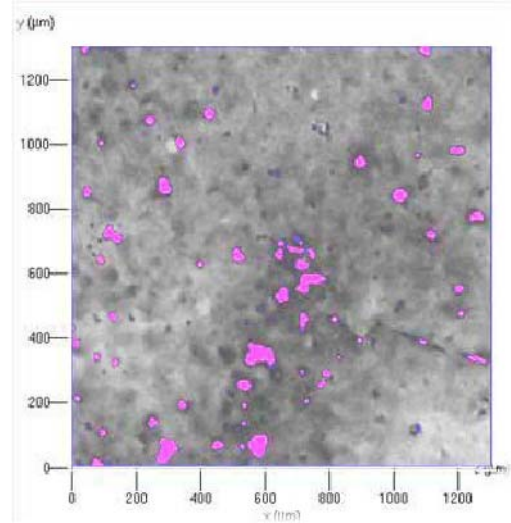


Fig. 3 CLSM – cartilage surface, grey value, filled at high level 125 μm

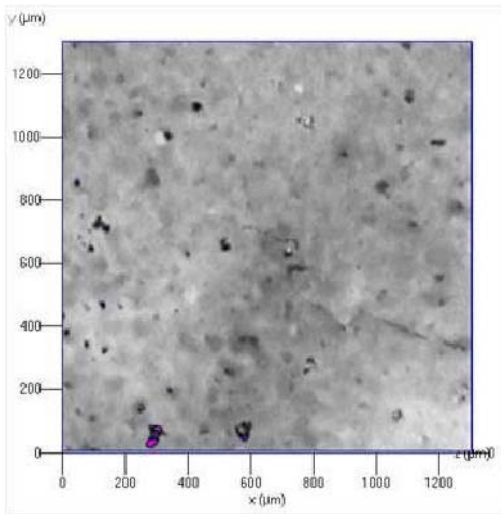


Fig. 2 CLSM – cartilage surface, grey value

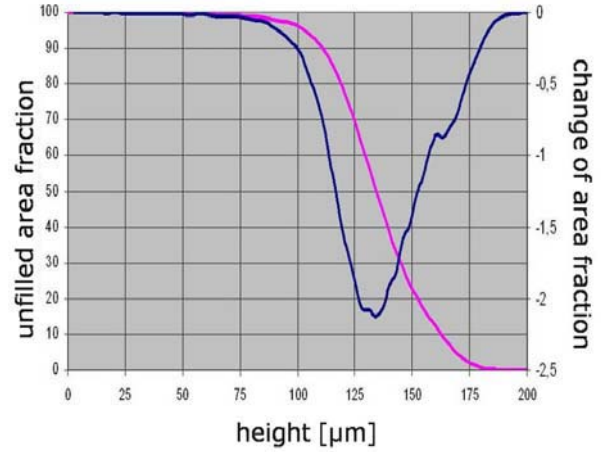


Fig. 4 Remaining unfiled area fraction and change of area fraction depending on height of interface

area and selected areas within. The visible result is a 3-dimensional picture that can be virtually placed in any perspective (Fig. 1).

The height information is represented by the color. It can clearly be seen that the structure of the surface basically is non regular. However some structures like pikes or basins are present. Usual parameters like surface roughness are not applicable to give more detailed information about the surface structure.

An interesting feature is the “filling” of the picture. In this operation a cross-section is made at a desired z-level. Regions higher than this level remain, z-values of lower areas are set to the z-value of the cross section. The principle is that the picture is transferred into a grey image, where

every grey value represents a certain height. Figure 2 and 3 show this effect. Fig. 2 is the original surface and 3 the figure filled at a z-level of 125 μm.

This filling operation now can be used to visualise structures or patterns and gives access to quantification, using conventional image analyse software. For example the area fraction of the unfiled area with respect to the base area can be determined depending on the z-level as shown in Fig. 3. Although the CSLM picture gives height information varying from 0 to 200 μm it seems that most of the the interface ranges from a height level 75 to 180 μm.

So in this example the real interface between bone and cartilage is about 100 μm instead of 200 μm as it might be assumed from the original image. The reason is that it is

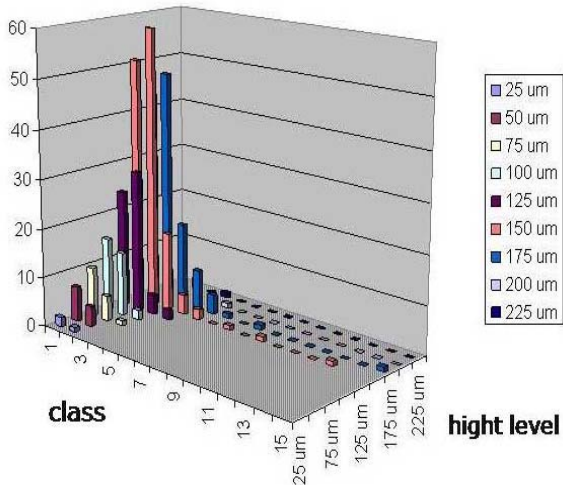


Fig. 5 classification of the filled structures. Number of “islands” with equivalent circle diameter depending on fill level.

quite difficult to find in the microscope the base-line because of the transparency of the cartilage. The deviation of the fill level shows, that the reduction of cartilage at the interface goes smoothly and almost symmetrically.

This kind of evaluation gives an idea of the gradient of the interface, however no information about the structure. By quantitative image analyzing procedures the islands in Figure 3 can be classified depending on their morphological characteristics, such as area or maximum length or equivalent circle diameter. Figure 5 shows the result.

Fig. 5 shows the distribution of islands at fill levels between 25 and 225 $\mu\text{m}$ . The equivalent diameters of the detected islands are classified in 15 groups ranging from a diameter less 0 to 20 $\mu\text{m}$  up to 280-300  $\mu\text{m}$ . After a fill level of 25 $\mu\text{m}$  only a few islands between 0 and 20 and 20 and 40 $\mu\text{m}$  are detected. This means the first structures of the bone are peaks with this diameter. The higher the fill level the greater the spectrum of detected islands are. This means at a fill level of 150 $\mu\text{m}$  for example, that two regions exist where the bone structure has already a diameter of 260 $\mu\text{m}$ , probably grown from the original smaller regions. However still many small regions with a diameter less than 20 $\mu\text{m}$  are detectable. They either are just the first contacts of bone to the cartilage or they belong to long small columns. At a fill level of more than 200  $\mu\text{m}$  only few small structures remain, mostly the whole are consists of bone.

The presented results however show only the evaluation of a single spot. Since the surface of the samples is not planar it is difficult to calculate mean values from different pictures. This makes it even difficult to evaluate one picture because only in some cases there is a linear decrease of height in one picture allowing to make a tilt correction.

## IV. CONCLUSION

CLSM combined with the preparation technique of cartilage-bone interface gives a new method to visualize and characterize the interface between two natural materials with quite different mechanical properties. In order to find a model describing the interface or calculate mechanical properties at the interface more data have to be evaluated and methods have to be developed how these data can be brought together.

## REFERENCES

1. A. Sachse, A. Wagner, M. Keller, O. Wagner, W.D. Wetzel, F. Layher, P. Hortschansky, M. Pietraszczyk, B. Wiederanders, H.J. Hempel, J. Bossert, J. Horn, K. Schmuck, J. Mollenhauer, *Bone* 2005, 37(5), 699.
2. A. Wagner, A. Sachse, M. Keller, M. Aurich, W.D. Wetzel, P. Hortschansky, K. Schmuck, M. Lohmann, B. Reime, J. Metge, F. Arfelli, R. Menk, L. Rigon, C. Muehleman, A. Bravin, P. Coan, J. Mollenhauer, *Phys. Med. Biol.* 2006, 511313
3. C.H. Geerdink, B. Grimm, R. Ramakrishnan, J. Rondhuis, A.J. Verburg, A.J. Tonino, *Acta Orthop.* 2006, 77(5), 719.
4. J.J. Jacobs, N.J. Hallab, R.M. Urban, M.A. Wimmer, *J Bone Joint Surg Am.* 2006, 88 Suppl 2:99.
5. K. Keinan-Adamsky, H. Shinar, G. Navon, *J Orthop Res* 2005, 23, 109.
6. P.L. Mente, J.L. Lewis, *J. Orthop. Res.* 1994, 12, 637.
7. R.J. Minns, F.S. Steven, *J. Anat.* 1977, 123 (2), 437.
8. C. Muehleman, S. Majumdar, A. Sema Issever, F. Arfelli, R.H. Menk, L. Rigon, G. Heitner, B. Reime, J. Metge, A. Wagner, K.E. Kuettner, J. Mollenhauer, *Osteoarthritis Cartilage*, 2004, 12, 97.
9. I. Zizak, P. Roschger, O. Paris, B.M. Misof, A. Berzlanovich, S. Bernstorff, H. Amenitsch, K. Klaushofer Characteristics of mineral particles in the human bone/cartilage interface. *J Struct Biol* 2003, 141, 208.
10. J. Mollenhauer, M. Aurich, C. Muehleman, G. Khelashvilli, T.C. Irving, *Connect Tissue Res* 2003, 44:201.
11. T.R. Oegema Jr., R.J. Carpenter, F. Hofmeister, R.C. Thompson Jr., *Microsc Res Tech.* 1997, 37(4), 324.
12. Z. Schwartz, K. Kieswetter, D.D. Dean, B.D. Boyan, *J Periodontal Res.* 1997, 32(1 Pt 2), 166.
13. Y. Wang, H.W. Wei, T.C. Yu, C.K. Cheng, *Biomed Mater Eng.* 2007, 17(4):241-7.
14. D.D. Anderson, T.D. Brown, E.L. Radin, *Clin. Orthop. Relat. Res.* 1993, 286:298.
15. J.A. Mollenhauer, C. Burkardt, W. Nisch, J. Bossert, J. Hempel, K.D. Jandt, C. Muehleman, *Advanced Engineering Materials* 12-2007, 1097-1103

Author: Jörg Bossert  
 Institute: Institute of Material Science and Technology  
 Street: Lödbergraben 32  
 City: Jena  
 Country: Germany  
 Email: P5jobo@uni-jena.de

# Improving Titanium Biocompatibility Manipulating Surface Porosity

D. Ionita<sup>1</sup> and D. Iordachescu<sup>2</sup>

<sup>1</sup> University Polytechnica Bucharest, General Chemistry Department, Bucharest, Romania

<sup>2</sup> University of Bucharest Romania

**Abstract** — In the present paper the electrochemical behavior of titanium with two surface treatments as alkali-treated (A) and acid-etched (B) in Afnor artificial saliva and in a mixture containing Afnor saliva and hydrogen peroxide was studied using open-potential circuit, polarization and electrochemical impedance spectroscopy measurements.

Various treatments have been applied to increase the roughness and to manipulate surface porosity of implants and improve their integration in the tissues. The addition of H<sub>2</sub>O<sub>2</sub> created on the surface an inner layer more defective and outer layer thicker and porous. The human osteoblast adhesion was influenced by surface roughness and the porosity.

**Keywords** — titanium, surface treatment, cell adhesion, biocompatibility, porosity, roughness.

## I. INTRODUCTION

Metallic materials are being increasingly used in medical applications as implants to restore lost functions or replace organs functioning below acceptable levels.

Many of titanium's properties including a good biocompatibility make it suitable as a material for implants and prostheses, and in the last decade various surface procedures were tested in order to enhance stability and biocompatibility of surface protective natural layer [1].

However, many difficulties remain to be solved. Many in vitro studies have been performed to better understand the mechanisms underlying cell-material interaction. It is now well understood that surface morphology influences the response of cells [2] and particularly their adhesion, which is one of the most critical initial events occurring during the interactions of cells with implants and has further influence on the proliferation and differentiation of bone cells before bone tissue formation.

The surface roughness of titanium substrates is known to have a considerable effect on osteoblastic cell attachment as well as on cell adhesion, proliferation and differentiation [3].

## II. EXPERIMENTAL PART

Commercially pure titanium was used as substrates, with composition (wt %) of Ti > 95%. Titanium plates, 10×10 mm size, were metallographic grinded until 1000 # using SiC

emery paper and cleaned with acetone followed by deionised water. Each specimen was dried at room temperature. Two process conditions were used to obtain two different roughness amplitudes:

A)- alkali-treatment - plates were soaked in 5 mL of 0.5 M NaOH aqueous solutions at 60°C for 24 h, then washed with distilled water and dried at 40°C for 24 h. After alkali treatment, the plates were heated to 220°C.

B)- acid-etching - samples were etched in a 1HF + 4 NHO<sub>3</sub> + 5 H<sub>2</sub>O solution for 10 min, cleaned in deionised distilled for 5 min, and aged in distilled boiling water for 20 min.

Electrochemical measurements were made at 37°C using an electrochemical cell containing Afnor artificial saliva as electrolyte. The composition of artificial saliva was: 0.26g/L Na<sub>2</sub>HPO<sub>4</sub>, 6.70 g/L NaCl, 0.33 g/L KSCN, 0.20g/L KH<sub>2</sub>PO<sub>4</sub>, 1.2g/L KCl, 1.5g/L NaHCO<sub>3</sub>, and the working electrode was Ti. In this artificial saliva was added 1M H<sub>2</sub>O<sub>2</sub>. The potential was measured against saturated calomel electrode. All electrochemical measurements were carried out on a Voltalab 40 equipment. The electrochemical measurements were carried out by monitoring the open-circuit potential (OCP), then recording the polarization resistance (R<sub>p</sub>) by applying ±10mV versus OCP followed by measuring the electrochemical impedance (EIS) in the frequency range from 30KHz to 10mHz with an applied sinusoidal potential of 10 mV.

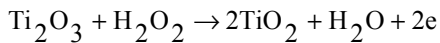
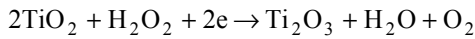
Surface morphology was characterized with scanning electron microscopy (SEM) and atomic force microscopy (AFM). The superficial film formed on the biomaterial surface was evaluated involved also roughness and porosity. Contact angle measurements were carried out in order to evaluate the wettability of the surface-modified alloy as resulting from every treatment.

To reveal the biocompatibility of Ti with both treatments it was compared the behavior of G292 osteoblasts grown on Ti discs or on plastic tissue culture dishes, a widely used material specifically treated by the manufacturer to enhance cell growth. The cells were grown in DMEM (Dulbecco's Modified Eagle Medium) supplemented with 10% FBS (Fetal Bovine Serum) and antibiotics 100 U/ml penicillin and 100 µg/ml streptomycin at 37°C in atmosphere with 5% CO<sub>2</sub>. The analysis was performed over a period of 24 h. The cell morphology and the adherence to the Ti6Al7Nb surface were analyzed by fluorescence microscopy

III. RESULTS AND DISCUSSION

The corrosion potential of samples was monitored for 7 days. At first the potential of two samples trends towards to more negative values. However after a certain time, depends of different surface treatments samples, becoming more electropositive with the immersion time. At the end of 3 days of experiment the corrosion potential of samples was stabilized in both cases: with /without H<sub>2</sub>O<sub>2</sub>. The corrosion potential of Ti sample pronounced decline in the artificial saliva without H<sub>2</sub>O<sub>2</sub> compared with that with H<sub>2</sub>O<sub>2</sub>. Such data are in perfect agreement with of Pan et al [4].

This fact it was attributed to an enhanced oxide film with growth rate accorded to the Pan theory [5] which relates the oxide thickness to the potential difference across the film. Because H<sub>2</sub>O<sub>2</sub> is a strong oxidizer when Ti is brought into contact with H<sub>2</sub>O<sub>2</sub> the process can be illustrated by the following equations:



The mean of corrosion potential of all samples after 7 days of immersion are listed in Table 1.

The effect of surface treatments and the content of H<sub>2</sub>O<sub>2</sub> on potentiodynamic polarization of Ti are shown in Figure 1, and the electrochemical parameters are listed in Table 2.

The corrosion potentials remained very similar as the all condition (around -400mV). There were small anodic current peaks. After the cathodes section, the anodic current densities were very stable up to a quite high potential (>1600 mV/SCE).

Corrosion of the metal occurs with the dissolution of titanium and formation of titanium oxide film on the metal surface. As a result, the film becomes more defective, probably porous and exhibits a relatively low corrosion

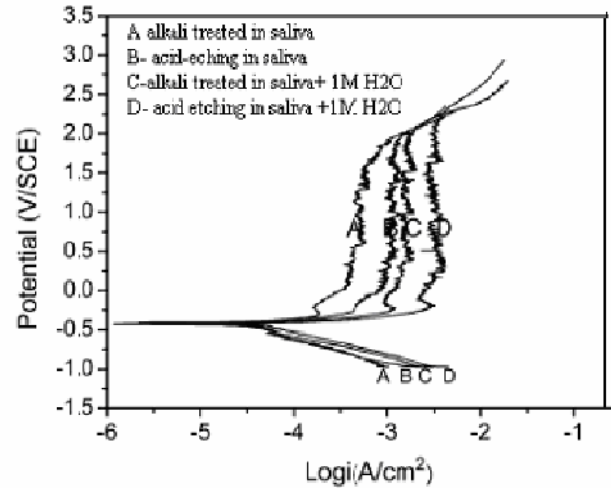


Fig. 1 Polarization curves for Ti in artificial saliva with/without H<sub>2</sub>O<sub>2</sub>

resistance, which provides an explanation for unexpected high rate of in vivo titanium release and oxide/oxidation rate increase when in saliva is added H<sub>2</sub>O<sub>2</sub>

The values of polarization resistance R<sub>p</sub> of the electrodes estimated from linear polarization measurements are recorded in Table 2.

Table 1. Corrosion potential value of Ti after 7 days of immersion

solution	E <sub>cor</sub> (mV vs SCE)	
	Ti (A)	Ti (B)
Afnor saliva	-450	-465
Afnor saliva+H <sub>2</sub> O <sub>2</sub>	-342	-388

Table 2. Corrosion parameters of Ti estimated from polarization measurements

system	E <sub>cor</sub> (mv)	I <sub>cor</sub> (μA/cm <sup>2</sup> )	R <sub>p</sub> (kΩcm <sup>2</sup> )
A in artificial saliva	-430	9.6	277.12
B in artificial saliva	-442	16.2	390.5
A in artificial saliva+H <sub>2</sub> O <sub>2</sub>	-418	16	297.8
B A in artificial saliva+H <sub>2</sub> O <sub>2</sub>	-436	21.5	473.8

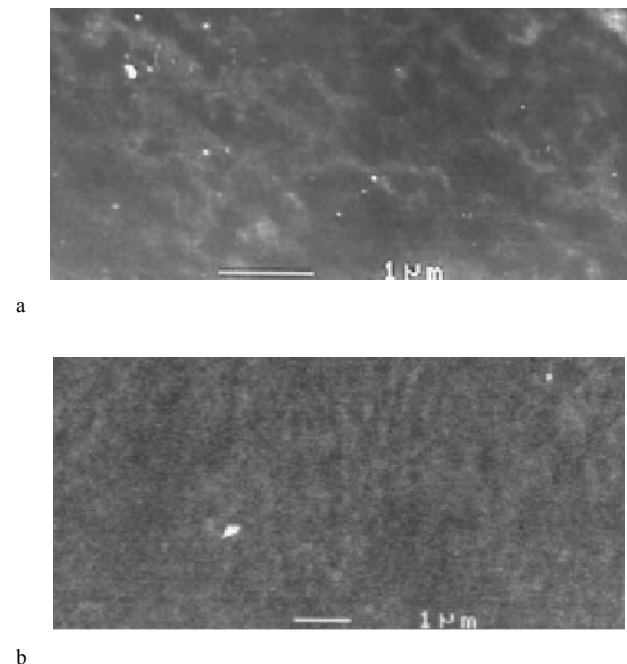


Fig. 2 SEM aspects of titanium alkali treated disks incubated during 7 days. (a) Pure artificial saliva; b) artificial saliva +H<sub>2</sub>O<sub>2</sub>

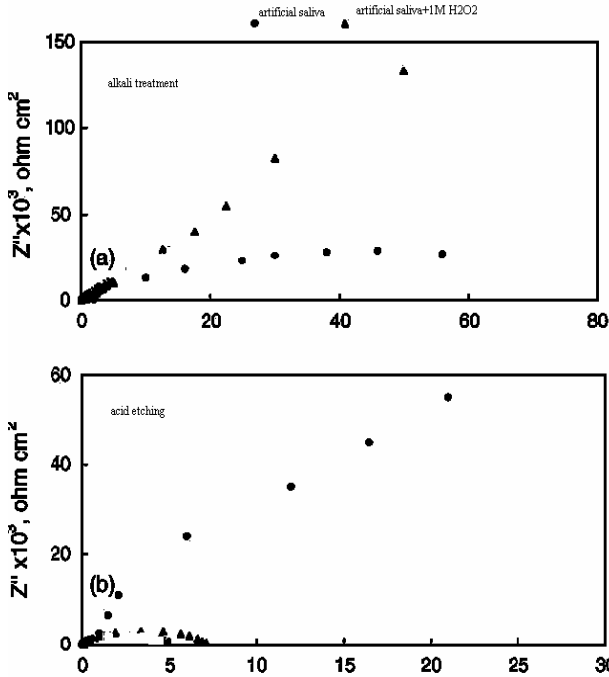


Fig. 3 Nyquist plots for Ti in artificial saliva a) alkali treated, b) acid etching

The value of polarization resistance, and the current density for Ti electrode increases when H<sub>2</sub>O<sub>2</sub> is added in artificial Afnor saliva.

The higher current density in the presence of H<sub>2</sub>O<sub>2</sub> can be attribute of the porous layer [6]. This supposition is sustained by the SEM analysis. On the other hand, the porous layer is expected to facilitate the incorporation of mineral ions and the attachment of cell.

The SEM micrograph analysis (fig.2) revealed that the specimen in artificial saliva with H<sub>2</sub>O<sub>2</sub> display a much rougher morphology than in artificial saliva without H<sub>2</sub>O<sub>2</sub>.

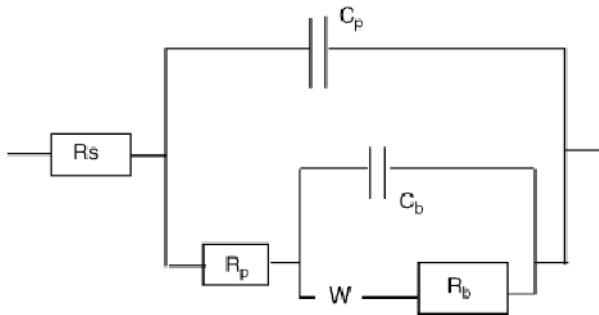


Fig. 4 Equivalent circuit used for impedance data fitting, where R<sub>s</sub> is the resistance of solution, C<sub>b</sub>-the inner layer capacitance, C<sub>p</sub>- the outer layer capacitance, R<sub>b</sub>- inner layer resistance; R<sub>p</sub> outer layer resistance

Table 3. Surface parameters

samples	Porosity (%)	R <sub>a</sub> (μm)
A in saliva	12.8	28.4
B in saliva	6.9	12.5
C in saliva+ H <sub>2</sub> O <sub>2</sub>	30.5	59.4
D in saliva +H <sub>2</sub> O <sub>2</sub>	28.5	38.6

The presence of H<sub>2</sub>O<sub>2</sub> in artificial saliva could have some effects on the properties of the passive film formed on the Ti; this can be observed from EIS measurements.

The Nyquist plot of Ti alkali treated and Ti acid etching in artificial saliva in presented in Figure 3.

The EIS measurement show that H<sub>2</sub>O<sub>2</sub> addition causes some changes in Ti oxide film properties. This spectra indicates the passive film on Ti exhibits a two-layer structure: a dense inner layer and a porous layer. The EIS spectra can be interpreted in terms of two-layer model of the oxide film (Fig. 4)

The specific interaction between the titanium and the H<sub>2</sub>O<sub>2</sub> may account for the growth of the oxide layer and the biocompatibility of the implant.

Surface topography and roughness are considered to be very important for osteointegration. Surface roughness in particular seems to have a direct effect on osteoblast attachment and subsequent proliferation and differentiation [7]. Osteoblast-like cells adhere more readily to rough surfaces.

The porosity of the surface was evaluated after 7 day of immersion using Image J program and the and roughness (R<sub>a</sub>) values were obtained by AFM technique. These surface parameters are presented in the Table 3

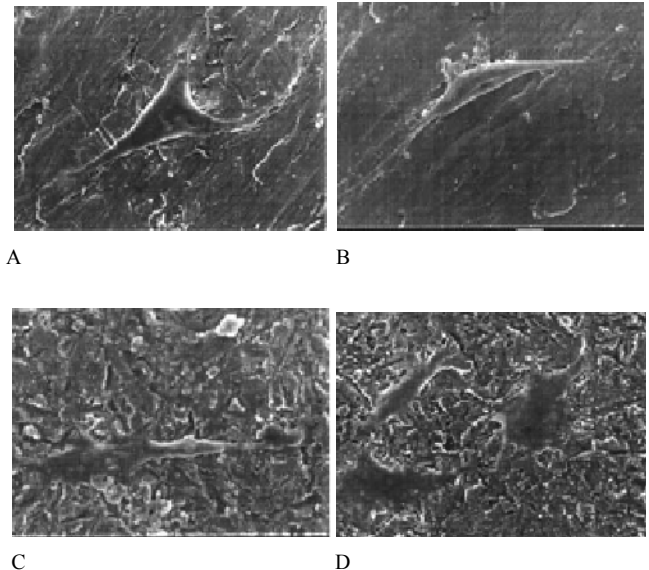


Fig. 5 Cell morphology as a function of treatment surface

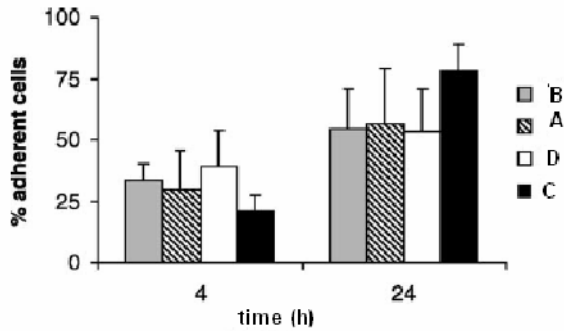


Fig. 6 Cell attachment expressed as percentage of the adherent cells after 4 and 24 h in culture on Ti

The alkali treatment of titanium created a porous and hydrated titanium oxide layer. The contact angle of alkali treatment surface significantly decreased ( $29^{\circ}$ ) compared to that of the acid-etched ( $102^{\circ}$ ). The added of the  $H_2O_2$  decreased the contact angle in the both cases ( $18^{\circ}$  for alkali treated and  $76^{\circ}$  for acid etched).

Osteoblast-like cells were used for *in vitro* tests. Fig. 5 shows that cell morphology was not affected by surface morphology. In the absence of  $H_2O_2$  (A and B) cells were relatively sparse presenting an elongated morphology. Cells cultured on titanium immersed in artificial saliva with  $H_2O_2$  present a spread and flatted morphology, and no particular orientation of cells was observed.

Cell attachment was a time-dependent event. Data are presented in Figure 6

The present results showed that different treatments produced different topographies of Ti surface and, consequently, different surface appearance. Despite these differences, the  $R_a$ , a factor known to influence cell response, was not significantly affected by the methods of Ti surface preparation.

#### IV. CONCLUSION

Under the experimental conditions of this study, the following conclusions can be drawn:

1. The alkali treatment of titanium created a porous and hydrated titanium oxide layer. The contact angle of alkali treatment surface significantly decreased compared to that of the acid-etched .
2. The presence of hydrogen peroxide leads to decreased corrosion resistance of Ti and its alloys and an enhanced dissolution/oxidation rate.
3. Depending on the two-layer model of the oxide film on titanium,  $H_2O_2$  results a more defective inner layer and a thicker and more porous outer layer.
4. Attachment of osteoblast cell increased on rougher and more porous surfaces.

#### REFERENCES

1. Wataha JC. Biocompatibility of dental casting alloys: a review. *J Prosthet Dent* 2000;83:223–34.
2. Sauberlich S, Klee D, Richter EJ, Hocker H, Spiekermann H. Cell culture tests for assessing the tolerance of soft tissue to variously modified titanium surfaces. *Clin Oral Implants Res* 1999;10(5): 379–93.
3. Schwartz J , Avaltroni M. J . Danahy M; P, Silverman B. M, Hanson Eric L. , Schwarzbauer J. E., Midwood K S, Gawalt E. S., Cell attachment and spreading on metal implant materials, *Materials Science and Engineering C* 23 (2003) 395–400
4. Pan J, Liao H, Leygraf C, Thierry D, Li J. Variation of oxide films on titanium induced by osteoblast-like cell culture and the influence of an  $H_2O_2$  pre-treatment. *Journal of Biomedical Materials Research*. 1998; 40(2):244-256.
5. Pan J, Thierry D, Leygraf C. Electrochemical impedance spectroscopy study of the passive oxide film on titanium for implant application. *Electrochimica Acta*. 1996; 41(7/8):1143-1153
6. Assis SL, Wolyne S, Costa I. Corrosion characterization of titanium alloys by electrochemical techniques. *Electrochimica Acta*. 2006; 51(8/9):1815-1819
7. Jo-Young Suh, Bong-Cheol Jang, Xiaolong Zhu, Joo L. Ong and Kyohan Kim, Effect of hydrothermally treated anodic oxide films on osteoblast attachment and proliferation, *Biomaterials*, 2003, 24 (2), 347-355

Author: Daniela Ionita  
 Institute: Politehnica University of Bucharest  
 Street: Polizu no1  
 City: Bucharest  
 Country: Romania  
 Email: md\_ionita@yahoo.com

# Electrically Charged Hydroxyapatite Enhances Immobilization and Proliferation of Osteoblasts

Yu. Dekhtyar<sup>1</sup>, N. Polyaka<sup>1</sup> and R. Sammons<sup>2</sup>

<sup>1</sup> Riga Technical University, Institute of Biomedical Engineering and Nanotechnologies, 1 Kalku str, Riga, Latvia

<sup>2</sup> University of Birmingham, School of Dentistry, St Chad's Queensway, Birmingham B4 6NN, United Kingdom

**Abstract** — Hydroxyapatite (HAP) is in use to fabricate implants in dentistry and orthopaedy. To functionalise a surface of the HAP that has a direct contact to the human cells a surface electrical charge deposition is employed. The current technologies can not provide uniformity of the charge for contrarily situated surfaces.

To overcome such the disadvantage a HAP hydrogenation technology has been reached. As the result the surface charge has been engineered.

The charge was estimated owing to measurements of the photoelectron emission work function. The later was increased to ~ 0.2 eV.

The negatively charged HAP surface in contrast with the uncharged one attached 10 times more osteoblastic cells and increased their proliferation capacity in 1.6 time

**Keywords** — implant, hydroxyapatite, electrical charge, immobilisation, proliferation.

## I. INTRODUCTION

Hydroxyapatite (HAP) is in use to fabricate implants in dentistry and orthopaedy. An external surface of HAP having a direct contact with a human cells provides a great impact to bone or tooth tissue formation [1]. To functionalise the HAP surface different modification technologies are in use, electrical charge deposition being one on them [1, 2, 3].

The technologies that are currently in use [2,3] supply the electrical charge to HAP specimens because of their polarization in an electrical field [2] or due to provision of charged particles radiation [3]. In both cases the opposite surfaces of the HAP based implant are acquiring the unlike (in sign) charges. This provides an inadequate influence to osteoinduction of the bone tissue. The cells, induced by one side of the charged implant surface could be uninduced by an other contrary charged side of the implant. This restricts implementation of the above technologies for medicine.

The article is targeted to reach the technology that supplies the entire HAP based implant surface with the uniformed charge.

## II. METHODS AND MATERIALS

HAP has the hydrogen connected to the oxygen:  $\text{Ca}_5(\text{PO}_4)_3\text{OH}$ . A disposition of the hydrogen in respect to the oxygen has an influence on the HAP surface charge. It was demonstrated the HAP surface electrical charge strongly depends on a density of the protons [5] coupled to the oxygen. Shift of the hydrogen gives an opportunity to affect the charge. For instance external highly pressured hydrogen gas could induce proton disposition at the HAP surface layer. This could be provided because of a pressure induced diffusion/migration [6] of the protons. As the result, the HAP surface will be influenced.

The HAP ceramic specimens that had a diameter 5 mm and thickness 1 mm were supplied from the EC project PERCERAMICS. The porosity of the specimens was equal to zero and their surface morphology had a relief  $\leq 0.5 \mu\text{m}$ .

The specimens were processed by a 6 MPa of the hydrogen gas during 1 hour.

An alteration of the surface charge was estimated because of the photoelectron emission electron work function ( $\phi$ ) measurement. The value of  $\phi$  characterizes an energy that is necessary to supply to an electron to escape it from the solid. During emission electron is influences by an electrical field of the surface charge, that contributes to  $\phi$ .

To measure  $\phi$  photoelectron emission current (I) of the electrons from HAP was induced by ultraviolet photons in a range 3-6 eV. The value of  $\phi$  was identified because of the dependence of I to the photon energy. Particularly, the energy of the photons, when I=0 was assumed as  $\phi$ .

The measurements were provided in vacuum conditions ( $10^{-1}$  Pa) applying a hand made spectrometer [7].

The specimens were tested before and after hydrogenation. The resulted increment of  $\phi$  became as the value of the altered surface charge.

A microbiological test was provided with hydrogenated specimens to verify charge influence on osteoblast cells attachment and proliferation.

The attachment of the cells was explored by the following way.

SAOS-2 human osteoblasts (ATCC Cat No. HTB-85<sup>TM</sup>; LGC Standards, Teddington, UK) were cultured in



McCoy's 5a medium (Gibco, Paisley, UK) containing 10% foetal calf serum (Sigma, UK), 2.5% Hepes (Gibco, Paisley, UK) and 1% Penicillin/Streptomycin (Gibco, Paisley, UK) until confluent, harvested using trypsin-EDTA (Gibco, Paisley, UK) and resuspended in the same medium at a concentration of  $1 \times 10^5$  cells/ml. The cells were allowed to recover from the enzyme for 1h at 37° C and 1 ml of suspension was then added to each specimen in separate wells of a 24-well plate at 37° C in an incubator containing 5% CO<sub>2</sub>, for 30min [8].

Experiments were terminated by removal of the cell suspension and washing three times in phosphate buffered saline to remove non-attached cells. Attached cells were then fixed for 1 h in 2.5% glutaraldehyde in 0.1 M sodium cacodylate buffer, pH 7.3, dehydrated in alcohol and hexamethyldisilazane and further gold-sputter coated for scanning electron microscopy (SEM) using a Jeol Jv3500 microscope at an accelerating voltage of 15kV, working distance 13mm. Images of five non-overlapping fields of view were captured using the SemAfore 4.0 programme (JEOL/Skandinaviska, Sweden) at a magnification of 150x (image area = approximately 800 x 600 μm). The individual cells were counted in each image and the average number of cells was determined.

To test proliferation of the cells, the HAP samples were sterilised in 70% ethanol for 15 min and then dried in air for 10 min. Test samples in 24 well plates were covered with 1 ml of a suspension of SAOS-2 cells, prepared as above, at a density of  $5 \times 10^4$  cells/ml. The cells were allowed to proliferate for 7 days. Culture medium was then removed and the samples were washed in PBS, fixed and prepared for SEM as above. As the cells were not confluent and individual cells could be identified, the cells were counted in 5 separate images at 150x magnification, as described above. Average cell number was estimated.

In both microbiological tests the observed specimens were statistically selected on a base of the Smirnov criteria (significance level 0.05).

### III. RESULTS AND DISCUSSION

The hydrogenation of the HAP ceramic specimens increased their  $\phi$ . This means that the electrical charge became more negative in contrast with the non processed specimens.

The cells were demonstrated attaching capability to the specimen surface (Fig.1).

The number of the attached cells correlated to the increment of  $\phi$  (Fig. 2). The correlation coefficient was equal to 0.67 that is acceptable at the 0.05 level of significance.

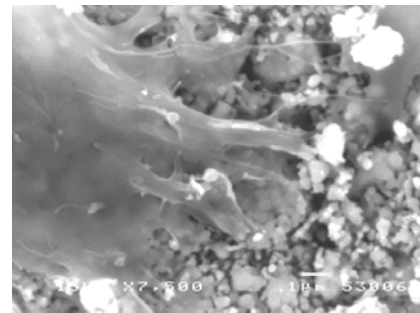
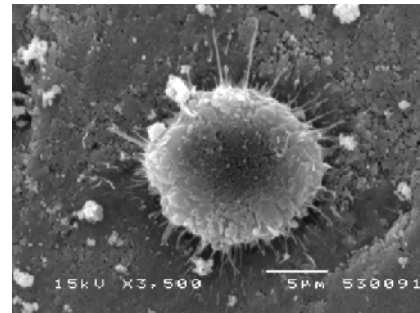


Fig. 1. The osteoblast cell attached to the HAP specimen.

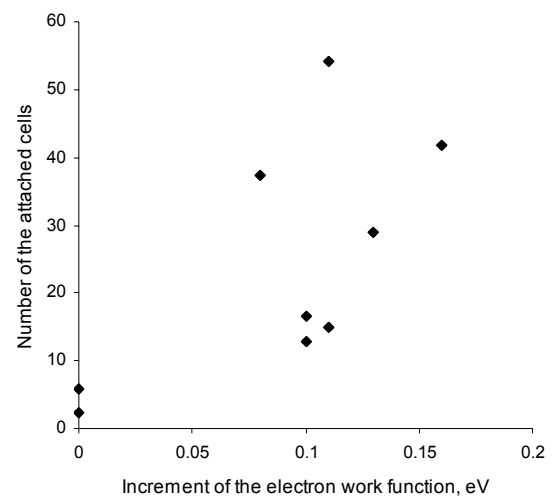


Fig. 2. Correlation of the number of the attached cells to the increment of  $\phi$ .

The number of the attached cells increased 10 times, when the increment of  $\phi$  succeeded +0.18 eV.

The result evidences that the osteoblast cells are more successfully attaching to the surface that electrical charge is shifted to the negative value.

The shift of the charge to the negative value enhanced proliferation of the cells (Fig. 3).

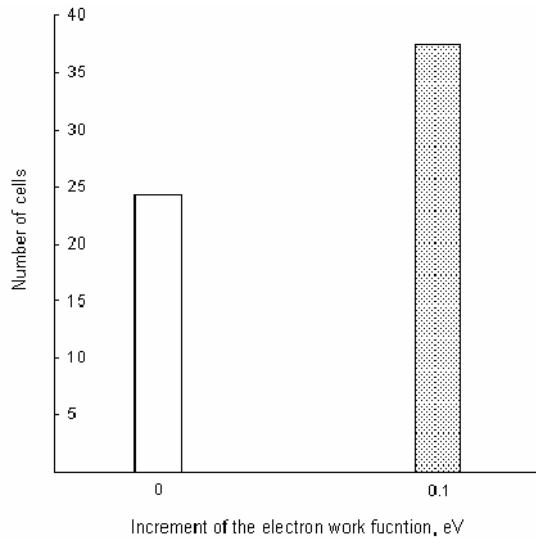


Fig. 3. Influence of the electron work function on proliferation of the cells.

Proliferation increased in 1.6 time when the value of  $\phi$  increased to +0.1 eV.

The achieved results demonstrate that deposition on the surface of negative charge enhances both attaching and proliferation capacity by the osteoblastic cells.

#### IV. CONCLUSIONS

The reached hydrogenation technology increases the negative charge of the HAP surface. This promotes attaching and proliferation of the osteoblasts.

The hydrogenation technology could be employed for the controlled engineering of the HAP surface charge to enhance osteoinduction. There are already the experimental results in favor of this [4].

#### ACKNOWLEDGMENT

The authors are deeply indebted to the:

- EC project PERCERAMICS NMP3-CT-2003-504937 for the HAP specimens delivering;
- OlainFram company for the autoclave provision for hydrogenation.

#### REFERENCES

1. Ratner B., Hoffman A., Schoen F., et al. (1996) Biomaterial science. London.
2. Ito S., Shinomiya K., Nakamura S., Kobayashi T., Nakamura M./ Yamashita K. (2006) Effect of electrical polarization of hydroxyapatite ceramics on new bone formation. Journal of the Japanese Bio-Electrical Research Society, 20: 23-27
3. Aronov D., Molotskii M., Rosenman G. (2007) Charge-induced wettability modification. Applied Phys. Lett. 90: 104104-1-104104-1
4. Karlov A., Khlusov I., Dekhtyar Yu., Polyaka N. Influence of hydrogenated calciumphosphate surface on potential on stromal stem cells in situ. The Abstracts of the present Conference.
5. Bystrov V., Bystrova N., Dekhtyar Yu./, Filippov S., Karlov A., Katashev A., Meissner C., Paramonova E., Patmalnieks A., Polyaka N., Sapronova A. (2006) Size depended electrical properties of hydroxyapatite nanoparticles IFMBE proc. 14.:3149-3150
6. Geguzin Ya. E. Diffusion zone.(1979). Moscow (In Russian).
7. Akmene R.J., Balodis A.J., Dekhtyar Yu.D., Markelova G.N., Matvejevs J.V., Rozenfelds L.B., Sagalovijs G.L., Smirnovs J.S., Tolkačovs A.A., Upmiņš A.I.(1993) Exoelectron emission spectrometre complete set of surface local investigation. Poverhnost, Fizika, Himija, Mehanika (Russian Journal), 8:125.-128.
8. Lumbikanonda, N, & Sammons, R.L. (2001) Bone cell Attachment to Dental Implants of Different Surface characteristics. International Journal of Oral and Maxillofacial Implants. 16: 627-636.

Address of the corresponding author:

Author: Yuri Dekhtyar  
 Institute: Riga Technical University  
 Street: 1 Kalku  
 City: Riga  
 Country: Latvia  
 Email: dekhtyar@latnet.lv

# Titanium Dioxide MOCVD Coating on CoCr Alloy and its Properties in Compare with Phosphate Coatings

M.M. Dicu<sup>1</sup>, A. Gleizes<sup>2</sup> and I. Demetrescu<sup>1</sup>

<sup>1</sup> University Polytechnica Bucharest/General Chemistry Department, Bucharest, Romania

<sup>2</sup> Centre Interuniversitaire de Recherche et d'Ingénierie des Matériaux UMR-CNRS 5085, ENSIACET/INPT, Toulouse, France

**Abstract** — Titanium oxide thin films were processed by MOCVD method. The films were deposited on CoCr alloy substrat using a low pressure reactor. Two temperatures (400<sup>0</sup>C and 500<sup>0</sup>C), 2 pressures (1 and 20 torr) and variable molecular fraction of the precursor it is from 76 to 5000 were used in MOCVD coating procedures. The surfaces were characterized using electronic scanning microscopy (SEM), X-rays analysis (XRD), contact angle and roughness measurements. The corrosion test was cyclic voltametry and was performed in artificial saliva as testing solution.

**Keywords** — CoCr alloy, TiO<sub>2</sub>, MOCVD, phosphate deposition, surface analysis, electrochemical stability

## I. INTRODUCTION

CoCr alloys were introduced since 1930 as biomaterials [1], but due to wear, corrosion and ions release in biofluids, after a while was not in use any more and more expensive implant metallic materials were proposed. Nevertheless, at the end of the last century many coating procedures were developed having important results in reducing ions release, and coated CoCr alloy became again an interesting choice for implant materials. Various techniques of coating have been considered to improve the corrosion resistance and biocompatibility of metallic implants, including plasma spray, physical and chemical vapour deposition, sol gel coating, etc [2]. This paper is focused on the development and testing the behaviour of titania MOCVD deposition on new alloys based on CoCr, and this coating was compared with a bioactive electrochemical phosphate deposition and with an uncoated reference (natural passive) CoCr sample. The technique of Chemical Vapour Deposition (MOCVD) is one the various industrial processes to deposit a thin film on a substrate. The procedure, consisting using of metallo-organic compound as a precursor, results in relatively low deposition temperatures and generally nature-friendly processes [3]. The MOCVD technique has been recently applied to the growth of titanium dioxide coatings [4], which successfully passed several biological tests both in vitro [5,6] and in vivo [7].

The electrochemical process still remain an attractive one because: the implants with much unregulated shapes could

be covered. It is a very fast method, which needs low temperature and low costs [8].

## II. EXPERIMENTAL PART

The chemical composition of the alloy is: Co 61.93%; Cr 27.45%; Mo 6.19%; Fe 1.46%; O 0.54%. This alloy is type ASTM F 75 but nickel free [9]. The artificial saliva was a home made solution with following composition: NaCl 0.600 g/L; KCl 0.720 g/L; CaCl<sub>2</sub>·6H<sub>2</sub>O 0.330 g/L; KH<sub>2</sub>PO<sub>4</sub> 0.680 g/L; Na<sub>2</sub>HPO<sub>4</sub>·12H<sub>2</sub>O 0.856 g/L; KSCN 0.060 g/L; KHCO<sub>3</sub> 1.500 g/L.

The CoCr specimens were mechanically ground, degreased in benzene for 5 minutes, prolonged rinsed with distilled water and dried in hot air.

*Deposition of thin films by MOCVD technique.* Metal-Organic Chemical Vapor Deposition (MOCVD) consists in marking the vapour of a metal-organic complex (the precursor) to reactor with a heated surface (the substrat) so that the solid reaction deposits and progressively forms a thin film on the substrate surface. The precursor was titanium isopropyl oxide [Ti{OCH(CH<sub>3</sub>)<sub>2</sub>}<sub>4</sub>] (TTIP), a liquid at room temperature. Pressure was regulated with a Baratron gauge connected via a pressure controller to a butterfly valve above a vacuum pump. 99.9992% pure N<sub>2</sub> (Air Products) was fed through two lines equipped with MKS mass flow rate controllers, one to sweep away the precursor, the other to dilute it. The deposition temperature was measured with a thermocouple K plugged into the reaction zone.

*Electrochemical deposition.* The electrolyte contains: 2.304 g CaCl<sub>2</sub>·6H<sub>2</sub>O and 0.83 g NH<sub>4</sub>H<sub>2</sub>PO<sub>4</sub> in 250 ml distilled water. The deposition equipment was a potentiostat, the cathode being CoCr sample and the anode a graphite electrode. The electrochemical deposition was performed at 3.5 V tension, temperature of 60<sup>0</sup>C, for 30 minutes. This one was selected having a ratio Ca/P close to 1.67, the one existing in the natural bone.

*Characterization of the samples:*

*Scanning electron microscopy (SEM).* Observation of films surface topography was carried out with a LEO-435

scanning electron microscope, operating at 15 kV and a sonde current intensity of 99 pA. The working distance has varied between 10 and 20 mm.

*X-ray diffraction (XRD).* X-ray diffraction measurements using a vertical diffractometer (Seiffert XRD 3000TT Bragg -Brentano). The used radiation was  $\text{CuK}\alpha_1$ , and in the diffracted fascicle was a graphite monochromator. The patterns were recorded using the  $\theta - \theta$  mode, analyzed with the Analyze program and compared with the corresponding JCPDS files.

*Contact angle measurement.* Water contact angle were measured using a DIGIDROP Contact Angle Meter (BGX Scientific Instruments) at room temperature. The contact angle was measured immediately after drop deposition, with a digital camera, using the program Windrop. For each specimen, the measurement was performed at two different places of the surface by lying 10  $\mu\text{L}$  of distilled water and the temperature  $25^\circ\text{C} \pm 1^\circ\text{C}$ .

*Roughness.* Surface roughness of the specimens was measured with a interferometer optic MetroProTM Zygo New View 100. Arithmetical mean roughness ( $R_a$ ) was taken on two different points of each specimen.

*Cyclic voltammetry.* Cyclic curves were registered with a Voltalab 40 equipment, in artificial saliva as testing solution. The electrode potential was cycled between  $-800\text{ mV}$  and  $+1200\text{ mV}$ , at a scan rate of  $2\text{ mV/s}$ . Platinum and  $\text{Ag/AgCl}$  electrodes served as an auxiliary electrode and a reference electrode respectively. The data statistical treatment was performed with a Medcalc program for biomedical application.

### III. RESULTS AND DISCUSSION

*Scanning electron microscopy (SEM).* The surface morphology of titania MOCVD and electrochemical phosphate depositions was identified with a LEO-435 scanning electron microscope.

The SEM microstructures of the calcium phosphate samples deposited at 3.5 V tension, temperature of  $60^\circ\text{C}$ , for 30 minutes are shown in Figure 1.

For the electrochemically deposited layer at the tension of 3.5V the surface is homogenous, presenting a granular structure and occupies perfectly the surface of the substratum.

The films deposited by MOCVD at different temperatures ( $400^\circ\text{C}$  and  $500^\circ\text{C}$ ), pressures (1 and 20 torr) and variable molecular fraction from 76 to 5000 have been investigated by SEM. Depending on these experimental conditions the deposit morphology varies from compact - uniaxial grain (Figure 2) to porous - columnar growth (Figure 3).

The low growth rate, due to either low molar fraction or low temperature, produced a fine-grained equiaxed struc-

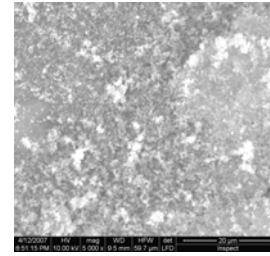


Fig. 1 SEM image of the electrochemically deposited Ca/P on CoCr alloy :  $T=60^\circ\text{C}$ , 30 min,  $3.5\text{ V/cm}^2$

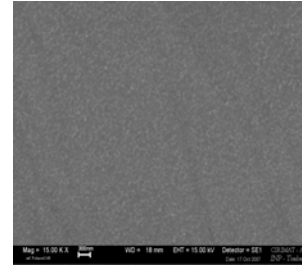


Fig. 2 SEM image of titania MOCVD on CoCr alloy:  $T_d=500^\circ\text{C}$ ,  $P=20\text{ Torr}$ ,  $\chi=76\text{ ppm}$

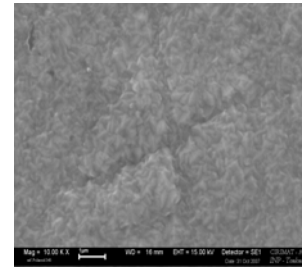


Fig. 3 SEM image of titania MOCVD on CoCr alloy:  $T_d=400^\circ\text{C}$ ,  $P=1\text{ Torr}$ ,  $\chi=5000\text{ ppm}$

ture. Moderate growth rates produced columnar microstructure with segmentation along grain boundaries. High growth rates produced fully dense, highly oriented columnar microstructure.

*Roughness.* In case of the  $\text{TiO}_2$  MOCVD depositions are observed that the surface roughness values are strongly dependent on deposition conditions as can be seen from figures 4 and Table 1.

These results are in accordance with the values found for commercially available implant components. Wennerberg

Table 1 Characterization of surface roughness

CoCr alloy	$R_a$ [ $\mu\text{m}$ ]
CoCr/ $\text{TiO}_2$ - T 500/P 20/ $\chi$ 76	0.068
CoCr/ $\text{TiO}_2$ - T 400/P 1/ $\chi$ 5000	0.117

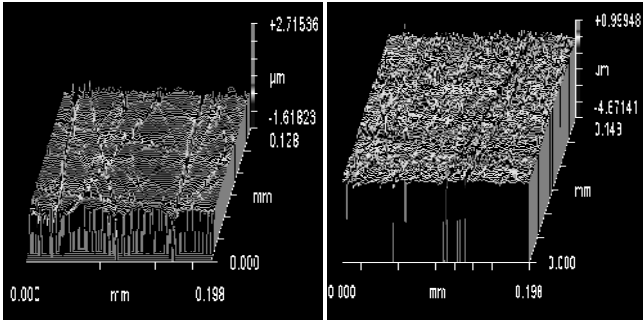


Fig. 4 Roughness 3D images of samples  $T_d=500^{\circ}\text{C}$  ( $\chi=76$  ppm) and  $T_d=400^{\circ}\text{C}$  ( $\chi=5000$  ppm)

and al. [10] suggested that the roughness can be described as smooth for abutments, minimally rough for roughness from 0.5 to 1  $\mu\text{m}$ , intermediately rough for 1 to 2  $\mu\text{m}$ , and rough for 2 to 3  $\mu\text{m}$ . Roughness has been shown to be a key feature for the quality of cell growth.

*X-ray diffraction (XRD).* In the Figure 5 is presented the possible phases that could exist in the electrochemically deposited layer [11]. One can observe a mixture of phases formed from  $\text{Ca}_5(\text{PO}_4)_3(\text{OH})$ ,  $\text{Ca}_9\text{HPO}_4(\text{PO}_4)_5\text{OH}$  and  $\text{Ca}_3(\text{PO}_4)_2 \cdot x \text{H}_2\text{O}$ . The peak from  $26^{\circ}$  indicates the fact that the film growth after the direction of the substrate and that has a monocrystalline behavior. We observed that the diffraction peaks are very broad and the intensities are low. These can be explained by very small crystallite size and high strain in thin films.

Figure 6 presents the XRD patterns for samples prepared at different molar fractions and temperatures. Three phases

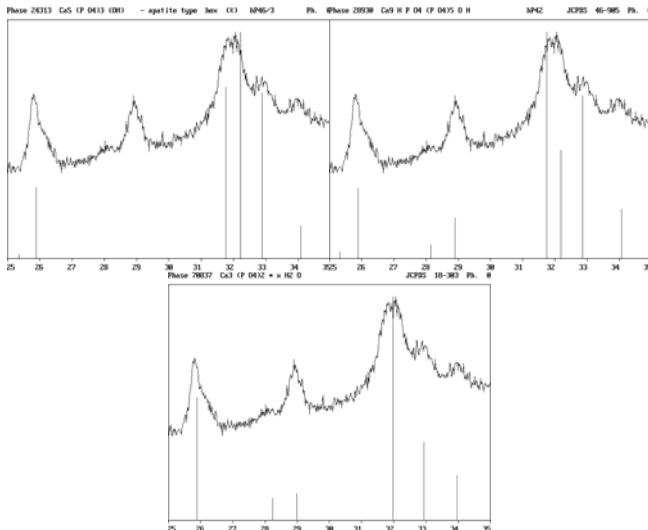


Fig. 5 XRD patterns of the electrochemically deposited phase at  $3.5\text{V}/\text{cm}^2$ ,  $T=60^{\circ}\text{C}$ , 30 min

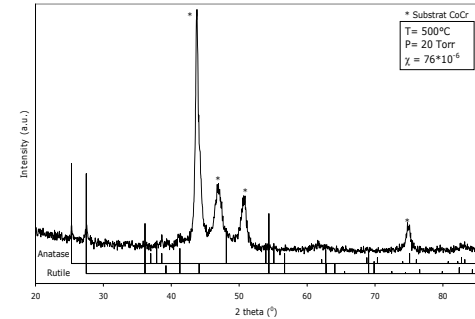
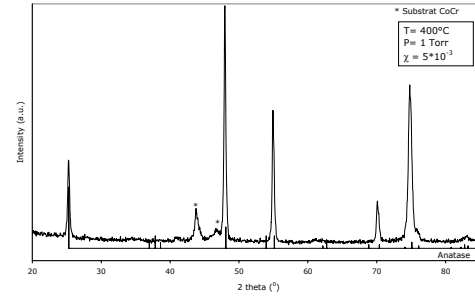


Fig. 6 XRD patterns of  $\text{TiO}_2$  thin films deposited on CoCr alloy substrates

show up: the CoCr substrate and two allotropic forms of  $\text{TiO}_2$ , namely anatase and rutile. The oxide grown at  $400^{\circ}\text{C}$  temperature and 5000 ppm molar fraction is anatase pure. At  $500^{\circ}\text{C}$  temperature and 76 ppm molar fraction the coating is a mixture of anatase and rutile.

*Wettability.* Contact angle measurements were performed for electrochemical phosphate deposition and titania MOCVD deposition in order to evaluate the presence of surface hydroxyl groups on CoCr alloy. As hydroxyl presence is required for biomolecule immobilization the contact angle values could be direct related to cell adherence. In both of the deposition the hydrophilic character was realized by contact angle of water drop on treated CoCr alloy surface. The hydrophilic character of  $\text{TiO}_2$  exposed to UV light is very well documented in the literature [12].

Measured contact angle for the two series of experiences are presented in Table 2.

Table 2 The values water contact angle for studied samples

Sample	Contact angle ( $^{\circ}$ )
CoCr untr.	93
CoCr elech.tr.	44
T400/5000	57
T500/76	86

**Cyclic voltammetry.** Cyclic curves were registered in artificial saliva solution. Figure 7 shows typical potentiodynamic curves for each electrochemical deposition surface, two samples with TiO<sub>2</sub> deposited by MOCVD and untreated samples. The values obtained from cyclic voltammetry for corrosion potential (E<sub>corr</sub>), current density (i<sub>corr</sub>), corrosion rate (v<sub>corr</sub>) and for the passive domain could be seen in the Table 3.

Making a comparison between the samples with TiO<sub>2</sub> films obtained by the MOCVD technique, the electrochemically treated sample and untreated sample, it can be observe an increase of passive domain at 1626 mV for the film grown by the MOCVD at 400<sup>o</sup>C ( $\chi = 5000$  ppm). This phenomenon could be explained by a poor interaction between the alloy and the environment. Table 3 shows that the films of TiO<sub>2</sub> have a current density in the passive potential range that is lower than that of the untreated sample which have a thinner, natural oxide layer.

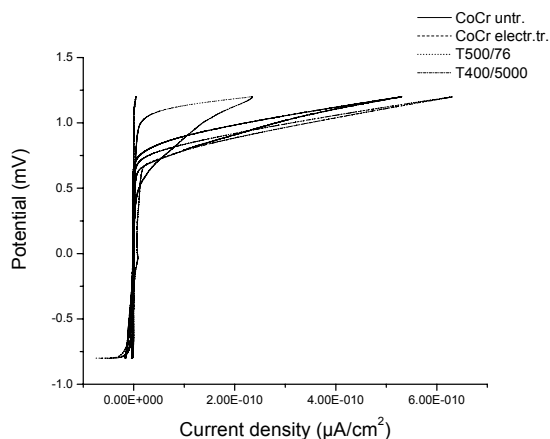


Fig. 7 Cyclic polarization curves for samples CoCr alloy untreated and treated

Table 3 Electrochemical parameters of CoCr alloy untreated and treated

Sample	E <sub>corr</sub> (mV/SCE)	i <sub>corr</sub> (µA/cm <sup>2</sup> )	v <sub>corr</sub> (mm/an)	Passive domain
CoCr untr.	-353	0.65	0.0066	1187
CoCr EC tr.	-291	1.69	0.0171	1254
T500/76	174	0.60	0.0061	1619
T400/5000	1006	0.28	0.0028	1626

#### IV. CONCLUSIONS

The results obtained by XRD indicate that the films consist anatase at 400<sup>o</sup>C and a mixture of anatase and rutile at 500<sup>o</sup>C.

For the electrochemically deposited the surface is homogenous presenting a granular structure and occupies perfectly the surface of the substratum. Depending on the MOCVD experimental conditions the deposit morphology varies from compact - uniaxial grain to porous - columnar growth.

Regarding the corrosion behaviour, the electrochemical data from polarization studies show that all three types CoCr samples, (the natural passive, the bioactive phosphated and the MOCVD coated one), present good stability in studied solution, the corrosion rate corresponding to stable range. The current density and corrosion rate decrease for the TiO<sub>2</sub> films obtained by the MOCVD technique.

#### REFERENCES

1. Sedel L, Cabanela M.E, Surgery H, Dunitz M Ltd (1998) Londra 335:24-26.
2. Jinno T, Kirk S.K, Morito S, Goldberg V.M (2004) J. Arthroplasty 19:102-109.
3. Choy K.L (2003) Progress in Materials Science 48:57
4. Battiston G.A, Gerbasi R, Tiziani A, Figueras A and Garcia G (2000) Mater. Sci. Forum 352:151
5. Casaletto M. P, Ingo G. M, Kaciulis S, Mattogno G, Pandolfi L and Scavia G (2001) Appl. Surf. Sci. 172:167
6. Giavaresi G, Giardino R, Ambrosio L, Battiston G, Gerbasi R, Fini M, Rimondini L and Toricelli P (2003) Int. J. Artif. Organs 26:774
7. Giavaresi G, Ambrosio L, Battiston G. A, Casellato U, Gerbasi R, Fini M, Nicoli Aldini N, Martini L, Rimondini L and Giardino R (2004) Biomaterials 25: 5583
8. Wang S-H, Shih W-J, Wang L.L, Min H.H (2005), J. Eur. Ceram. Soc., 25: 3287-3292
9. Yaszemski M.J, Trantolo D.J, Lewandrowski K.U, Hasirci V, Altobelli D.E, Wise D.L (2003) Biomater. Orthop. Marcel Dekker Inc New York, pp. 72.
10. Wennerberg A, Albrektsson T, Andersson B, Krol J.J (1995) Clin Oral Implants Res 6 : 24
11. Sovar M, Ducu C, Abrudeanu M, Demetrescu I, (2007), The International Conference on Structural Analysis of Advance Materials (ICSAM 2007), CD, TOPIC 1, Biomaterials, No.3, Patras, Grecia.
12. Wang R, Sakai N, Fujishima A, Watanabe T, Hashimoto K (1999) J. Phys. Chem. B 103:2188.

Author: Maria Magdalena Dicu  
 Institute: University Polytechnica Bucharest  
 Street: Polizu, No. 1  
 City: Bucharest  
 Country: Romania  
 Email: ela\_magda@yahoo.com

# Plasma Polymer Coating of Titanium for Improved Bone Implants

B. Finke<sup>1</sup>, K. Schroeder<sup>1</sup>, F. Luethen<sup>2</sup>, J.B. Nebe<sup>2</sup>, J. Rychly<sup>2</sup>, K. Liefeth<sup>3</sup>, R. Bader<sup>4</sup>, U. Walschus<sup>5</sup>, S. Lucke<sup>5</sup>, M. Schlosser<sup>5</sup>, H.-G. Neumann<sup>6</sup>, A. Ohl<sup>1</sup>, K.-D. Weltmann<sup>1</sup>

<sup>1</sup> Leibniz Institute for Plasma Science and Technology (INP), Greifswald, Germany

<sup>2</sup> Department of Internal Medicine, University of Rostock, Rostock, Germany

<sup>3</sup> Institute for Bioprocessing & Analytical Measurement Techniques, Heiligenstadt, Germany

<sup>4</sup> Department of Orthopaedics, University of Rostock, Rostock, Germany

<sup>5</sup> Medical Biochemistry & Molecular Biology, University of Greifswald, Greifswald, Germany

<sup>6</sup> DOT GmbH, Rostock, Germany

**Abstract** — Gas-discharge plasma processes could be very valuable for the modification of titanium surfaces to improve implant performance. Surface properties determine cellular acceptance, a crucial factor of implant healing. There already exists fundamental knowledge about the influence of physicochemical surface properties like roughness, titanium dioxide modifications, cleanness, and (mainly ceramic) coatings on cell behavior *in vitro* and *in vivo*. In this process, the cell adhesion and spreading via integrins was recognised to be a prerequisite for the occupancy of an orthopaedic implant surface. But recent findings indicate an additional adhesion mechanism. Hyaluronan seems to play a key role in the very first encounter with the substrate. Based on this adhesion mechanism of osteoblasts with their negatively charged hyaluronan coat, a new surface functionalization strategy was developed utilizing a positively charged metal surface. For this purpose, titanium was coated with a microwave plasma polymer made from allylamine (PPAAm) to boost the initial adhesion processes. The process development was accompanied by physicochemical surface analysis like XPS, FTIR, contact angle, SEM, and AFM. A very thin, adherent, cross-linked, pinhole- and additive-free PPAAm layer could be deposited, which is resistant to hydrolysis and delamination and equipped with a high density of positively charged amino groups. This titanium surface functionalization was found to be advantageous concerning osteoblastic focal adhesion formation and, in consequence in differentiated cell functions *in vitro*. Intramuscular implantation of test samples in rats revealed a reduced inflammation reaction compared to uncoated titanium *in vivo*.

This gas-discharge plasma-based PPAAm surface modification process could be an alternative to improve the biocompatibility of titanium implants.

**Keywords** — Gas-discharge plasma, plasma polymer, surface modification, cell culture, animal experiments

## I. INTRODUCTION

While hip, knee, and dental implants made from titanium are known for their good clinical performance, improved surface properties could result in better implant healing. In this regard, the rapid cellular acceptance of the implant

surface is the crucial factor for the ingrowth in the bone. This is especially valid for titanium implants which have to bear considerable mechanical strain. Thus, the physicochemical properties of the implant surface like roughness, purity or a thin coating, affect the cellular response *in vitro* and *in vivo*. Coatings which exhibit similarities to the extracellular matrix (ECM) are in widespread use. Typically, immobilized proteins and peptides are used for the improvement of the interface. Cell fixation to surfaces is basically mediated via integrins to an extracellular matrix and has an important influence on many cell functions. But actually, the matrix substance hyaluronan (HA) [1, 2] seems to take a key role in initial interface reactions. A new surface functionalization strategy was developed based on a positively charged implant surface to interact with the negative charge of hyaluronan which is due to the carboxyl group of the glucuronic acid [3, 4]. An amino groups carrying surface would present the desired properties, because these groups are protonated in aqueous solutions at physiological pH values and therefore generate positive charges. Titanium surfaces, however, are negatively charged [5]. While other materials like polymers can be easily equipped with amino groups by ammonia plasma treatment [6], titanium surfaces require an interface layer based on a functionalized siloxane or hydrocarbon polymer [7]. In this regard, plasma polymers might be advantageous since they in parallel fulfil further requirements which are specific for biological environments.

For this purpose, titanium was coated with a microwave plasma polymer made from allylamine (PPAAm) to accelerate the initial adhesion of osteoblasts. A very thin, adherent, cross-linked, pinhole- and additive-free PPAAm layer could be deposited, which is resistant to hydrolysis and delamination and equipped with a sufficient density of positively charged amino groups. This titanium surface functionalization was found to be advantageous concerning both material tests and osteoblastic focal adhesion formation [8] and, in consequence in differentiated cell functions *in vitro*. Furthermore intramuscular implantation of PPAAm coated

test samples in rats revealed a reduced inflammation reaction compared to uncoated titanium *in vivo* [9].

## II. MATERIALS AND METHODS

### A. Materials – Thin film preparation

Polished titanium discs (1-3 cm diameter and  $5 \times 5 \times 1 \text{ mm}^3$ , respectively) with a small roughness ( $R_a = 0.19 \mu\text{m}$ ) were used for plasma treatment, physico-chemical analysis, *in vitro* and *in vivo* investigations. They were decontaminated and activated by a continuous wave (cw) oxygen-plasma (500 W, 50 Pa, 100 sccm  $\text{O}_2$  / 25 sccm Ar) and immediately coated with an about 50-100 nm thin layer of plasma polymerized allylamine (PPAAm). Films were prepared by pulsed low pressure micro wave discharge plasmas (2.45 GHz, 500 W, 50 Pa) (plasma reactor V55G, PlasmaFinish, Germany) [4]. Useful surface properties - an optimal  $\text{NH}_2/\text{C}$  density and simultaneously a well-adherent layer in aqueous environment could be obtained by means of optimization of the duty cycle DC. DC is the ratio of plasma  $t_{\text{on}}$  divided by the overall pulse duration  $t_{\text{on}} + t_{\text{off}}$ . Different plasma on times 5 ms, 10 ms, 100 ms, 300 ms and cw were used. The effective treatment duration of all characterized processes was 144 s.

### B. Methods – Thin film analysis

**XPS:** The elemental chemical surface composition and chemical binding properties of the surfaces were determined by XPS (AXIS ULTRA spectrometer, Kratos, UK) using the monochromatic Al  $K_{\alpha}$  line at 1486 eV (150 W), implemented charge neutralization and a pass energy of 80 eV for estimating the chemical elemental composition or 10 eV for highly resolved C1s and N1s peaks [4]. Amino groups were reacted with 4-trifluoromethylbenzaldehyde (TFBA) at 40° C for 2 h in a saturated gas phase.

**FT-IR:** The PPAAm films were also investigated by the diamond ATR-unit of an FT-IR spectrometer (Spectrum One, Perkin-Elmer, Germany). In this case, Au-sputtered on small polystyrene or polyetheretherketone wafers were used as a basis for PPAAm films to improve sensitivity.

**Thin film thickness:** The thickness of the deposited plasma polymer film was determined by two independent methods in parallel. The mass difference due to coating was compared to a trench prepared on a wafer and measured with a surface profiler Dektak3ST<sup>®</sup> (Veeco, USA). These two methods showed consistent results (about 20 % error).

**Film stability:** To explore the film stability, the samples were sonicated in an ultrasonic bath (Elma, Germany) in ultra pure water for 10 minutes. XPS analysis were performed to investigate the change of the surface composition.

**Water contact angle:** Water contact angles were measured by the sessile drop method using the contact angle meter Digidrop (GBX Instrumentation Scientifique, France). The determination of the angle between the solid surface and the tangent of the drop were performed by computer control.

**Surface charges:** Existing surface charges can be estimated using the zeta-potential by determining the streaming potential in dependence of the pressure with the Electrokinetic Analyzer (A. Paar, Germany). Subsequently the zeta-potential was calculated according to the method of Fairbrother and Mastin [10]. The measurements were performed in 0.001 M KCl solution at pH 6. Poly (diallyldimethyl ammonium chloride) (PolyDadMac) was used as positively charged reference surface.

### C. Methods – Material tests

The mechanical properties and the adhesive strength of the prepared PPAAm surface on Ti were checked by different material tests.

The scratch test was used as qualitative test method after DIN EN ISO 1518 using a tungsten carbide sphere of 1 mm diameter to scratch the surface at different contact loads. Chipping off and delaminating of the thin film coat are the failure criteria analyzed by light microscopy.

Furthermore a quantitative standard adhesive test according to DIN EN 582 was used. The adhesive strength of the coating was evaluated by measuring the pull-off force of two cylinders (25 mm in diameter) attached together with special glue (Klebbi, Sulzer Ltd, Switzerland), one coated and the other grit-blasted.

Wear resistance was investigated in a special testing machine [3]. PPAAm coated cylindrical Ti6AlV4 samples (diameter 12 mm) were moved in cyclic motions ( $10^6$  cycles) in PU-foam (10 pcf, Sawbones, Sweden). The relative motion was set to 500  $\mu\text{m}$  at 5 Hz and a contact pressure of about 2 MPa. The generated wear was gravimetrically identified and surface and wear debris determined by SEM and EDX-analysis.

### D. Methods – In vitro and in vivo investigations

**In vitro cell culture:** Human osteoblasts (MG63 cells) were cultured under serum-free conditions to avoid masking of the amino-functionalized Ti surfaces with adsorbed proteins [11]. Adhesion and cell cycle phases were investigated by flow cytometry by using the equipment FACS Calibur (BD Biosciences, Germany). Spreading and actin cytoskeleton were visualized by confocal microscopy.

**In vivo investigations:** The *in vivo* biocompatibility of the PPAAm-coated titanium compared to pure titanium was



studied after i.m. implantation in male LEWIS rats (age ca. 100 days). The tissue reaction was analysed after 7, 14 and 56 days for each explanted sample by haemalaun-eosin staining of frozen sections and scoring by two independent investigators (rating 0 - no reaction to 3 - severe reaction).

### III. RESULTS AND DISCUSSION

#### A. Physicochemical layer properties

The challenge of plasma polymer deposition for the improvement of cell adhesion is to obtain both very thin in aqueous environments stable films (closed monolayer) and a well defined chemical surface composition.

**XPS:** The effective deposition duration was set to 144 s to ensure a sufficient layer thickness for XPS analysis (>10 nm) otherwise TiO<sub>2</sub> could interfere. The XPS element ratio of the monomer (N/C 33.3 %) was kept by a pulsed plasma with 100 ms plasma on time. Simultaneously, this time range seems to be optimal regarding the N/C ratio, the relatively small oxygen uptake after sonication (Fig. 1) and the NH<sub>2</sub>/C ratio of 2-3 %. This amino group density is relatively low compared to 18 % a value maximum reported for a special RF-plasma [12]. Water contact angles were found in the range of about 50 °.

**FT-IR:** FT-IR studies [8] confirmed a high retention of the structural properties of the monomer allylamine H<sub>2</sub>C=CH-CH<sub>2</sub>-NH<sub>2</sub>. Basic features of the monomer structure as the stretching vibrations of the aliphatic C-H groups,  $\nu$ -CH<sub>2,3</sub> at 2980-2880 cm<sup>-1</sup> and deformation vibrations of amines,  $\delta$ -NH at 1650-1510 cm<sup>-1</sup> are still dominant. Also  $\nu$ -NH stretching vibrations between 3380-3200 cm<sup>-1</sup> are

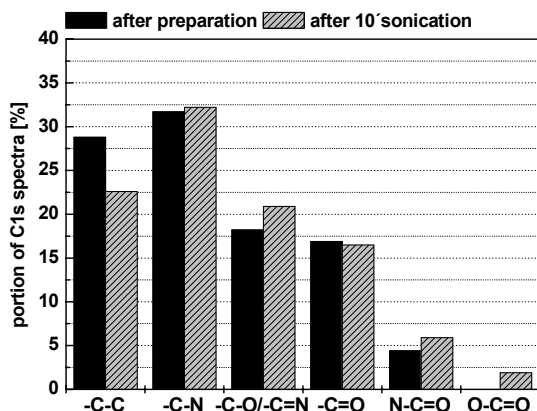


Fig. 1 Comparison of the C1s binding fractions after preparation and following 10 minutes sonication in water.

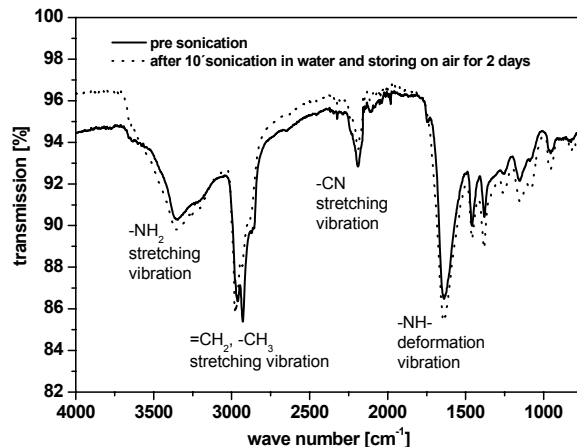


Fig. 2 Comparison of the FT-IR spectra pre and after 10' sonication in water and following storing on air.

clearly visible. But typical plasma effects are also observable as e.g. significantly broadened, disappearing or arising bands. Amino groups were partially transformed into amide, imine or nitrile functional groups by the plasma process. An indication for that is the new band between 2300-2200 cm<sup>-1</sup> associated with stretching vibrations of nitrile groups,  $\nu$ -CN. The PPAAm surface is very stable and does not essentially change after 10' sonication and storing on air (Fig. 2).

**Zeta-potential:** Zeta potential measurements showed the positive charge of the PPAAm surface in aqueous media [4] at pH 6. In comparison with the positive standard substrate PolyDadMac (poly (diallyldimethylammonium chloride), +28.5 mV) and the negatively charged titanium (-3.4 mV) PPAAm represents a positive charge of +7.7 mV. The weak negative surface potential of the pure titanium corresponds to the results found for untreated titanium by Roessler [5].

#### B. Mechanical layer properties

The scratch test show mechanically stable PPAAm films. No chipping off or disruptions could be observed. The adhesive strength was of more than 75 MPa and exceed for this reason the minimum required adhesive strength for medical coatings of 22 Pa (ASTM 1147-F). The PPAAm coated and the uncoated Ti6AlV4 samples revealed similar wear debris of the PU-foam. SEM and EDX-analysis showed no removal of the PPAAm coating after each abrasive wear test.

#### C. In vitro and in vivo properties

The amino-functionalized titanium surface PPAAm is definitely advantageous compared to a pure, polished tita-

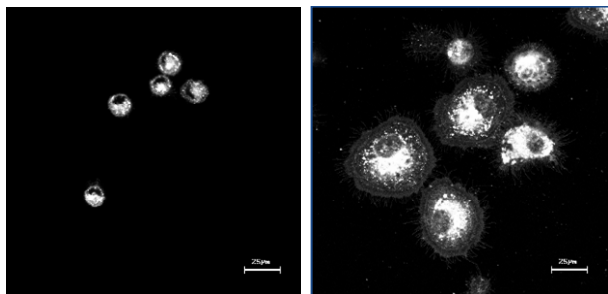


Fig. 3 Spreading of MG-63 cells after 30 min left – on polished Ti, right – on PPAAm.

mium surface concerning the initial cellular effects, i.e. adhesion and spreading. It seems that osteoblasts in the initial phase of contact solely need the charged surface because of their pericellular hyaluronan matrix [8]. Furthermore, cultivation of cells under serum-free conditions resulted in a six-fold higher cell area on functionalized PPAAm compared to pure polished titanium after 30 min (Fig. 3). The spreading process is significantly accelerated.

*In vivo* investigations show a relatively strong tissue reaction (score 2.1) after 7 days in comparison with untreated control samples (score 0.7). In the further course of the study, the inflammatory response decreased for the PPAAm samples and was lower than for the uncoated controls after day 56 (PPAAm: 1.1; control samples: 1.5).

In summary, the PPAAm layer seems to have no long-term negative influence on the *in vivo* performance compared to uncoated titanium.

#### IV. CONCLUSIONS

Very thin (<50 nm thick), adherent, cross-linked, pinhole and additive free PPAAm layers could be deposited by microwave low pressure plasmas. The surfaces were equipped with a relatively high density of positively charged amino groups. Such thin films were resistant to hydrolysis and delamination. Cell culture investigations and implantation studies in rats demonstrated beneficial effects *in vitro* and an *in vivo* performance comparable to controls.

#### ACKNOWLEDGMENT

BF, FL, UW and SL were financially supported by the program TEAM of Mecklenburg-Vorpommern in Germany (UR 0402210). We appreciate technical support of A. Peters and A. Fritsche of the University of Rostock and U. Kellner, G. Friedrichs and M. Polak from the INP Greifswald.

#### REFERENCES

- Zimmermann E, Geiger B, Addadi L (2002) Initial stages of cell-matrix adhesion can be mediated and modulated by cell-surface hyaluronan. *Biophys J* 82:1848-1857
- Cohen M, Klein E, Geiger B, Addadi L (2003) Organization and adhesive properties of the hyaluronan pericellular coat of chondrocytes and epithelial cells. *Biophys J* 85:1996-2005
- Lüthen F, Lange R, Becker P, Rychly J, Beck U, Nebe B (2005) The influence of surface roughness of titanium on  $\beta$ 1- and  $\beta$ 3-integrin adhesion. *Biomaterials* 26:2423-2440
- Nebe B, Lüthen F, Finke B, Bergemann C, Schröder K, Rychly J, Liefeth K, Ohl A (2007) Improved initial osteoblast's functions on amino-functionalized titanium surfaces. *Biomol Eng* 24:447-454
- Roessler S, Zimmermann R, Scharnweber D, Werner C, Worch H (2002) Characterization of oxide layers on TiAl6V4 and titanium by streaming potential and streaming current measurements. *Coll & Surfaces B: Biointerfaces* 26:387-395
- Meyer-Plath A A, Schröder K, Finke B, Ohl A (2003) Current trends in biomaterial surface functionalization - nitrogen-containing plasma assisted processes with enhanced selectivity. *Vacuum* 71:391-406
- Klee D, Böing J, Höcker H (2004) Surface modification of titanium to improve interface compatibility. *Mat-wiss u Werkstofftech* 35:186-191
- Finke B, Luethen F, Schroeder K, Mueller PD, Bergemann C, Frant M, Ohl A, Nebe BJ (2007) The effect of positively charged plasma polymerization on initial osteoblastic focal adhesion on titanium surfaces. *Biomaterials* 28:4521-4534
- Schröder K, Finke B, Lüthen F, Nebe JB, Rychly J, Liefeth K, Bader R, Walschus U, Lucke S, Schlosser M, Ohl A (2007) Plasmachemische Funktionalisierung von Titanoberflächen, Proc. 3. Thüringer Grenz- und Oberflächentage (ThGOT) Erfurt, Germany 2007, ISBN 978-3-00-021859-0, S.285-290
- Fairbrother H, Mastin J (1924) Studies in electro-endosmosis. *J Chem Soc* 75:2318
- Nebe B, Luethen F, Lange R, Beck U (2007) Cellular activity and biomaterial's surface topography. *Mater Sci Forum* 539-543:517-522
- Friedrich J, Kühn G, Mix R, Fritz A, Schönhals A (2003) Polymer surface modification with monofunctional groups of variable types and densities. *J Adh Sci Technol* 17:1591-1617

Author: Karsten Schroeder  
 Institute: Leibniz Institute for Plasma Science and Technology (INP)  
 Street: Felix-Hausdorff-Str. 2  
 City: D-17489 Greifswald  
 Country: Germany  
 Email: schroeder@inp-greifswald.de

# Silk-Based Scaffold for Ligament Tissue Engineering

H. Liu<sup>1</sup>, H. Fan<sup>1</sup>, E.J.W. Wong<sup>1</sup>, S. Lok Toh<sup>2,3</sup>, J.C.H. Goh<sup>1,2</sup>

<sup>1</sup>Department of Orthopedic Surgery, National University of Singapore, Singapore

<sup>2</sup>Division of Bioengineering, National University of Singapore, Singapore

<sup>3</sup>Department of Mechanical Engineering, National University of Singapore, Singapore

**Abstract** — In recent years, silk has been increasingly studied as the scaffold for ligament tissue engineering due to the biocompatibility, slow degradability, and remarkable mechanical properties. Braided silk scaffold modified with short polypeptide also significantly increases collagen synthesis on it. To increase cell attachment and tissue infiltration, the braided scaffold can be incorporated with silk-gelatin microsponges. A novel silk cable-reinforced gelatin/silk fibroin hybrid scaffold was fabricated, which, apart from providing proper mechanical strength and enlarged surface area, also supported the proliferation and differentiation of MSCs on it. The knitted silk mesh is another important silk-based scaffold for its excellent mechanical properties and good nutrients transport. To prevent cells from leaking out of scaffold after seeding, freeze-dried silk microsponges were incorporated into the macropores of knitted scaffold. *In vitro* culture demonstrated that MSCs on scaffolds proliferated vigorously and produced abundant collagen. The transcription levels of ligament-specific genes (collagen I, collagen III, and tenascin-C) also increased significantly with time. The comparison of MSCs and fibroblasts as cell sources for ligament tissue engineering demonstrated that MSC was the most suitable candidate for its vigorous proliferation and ECM production. The MSCs/knitted scaffolds were implanted into rabbits to regenerate ACL *in vivo*. After 24 weeks, histology observation showed that MSCs were distributed throughout the regenerated ligament and exhibited fibroblast morphology. The key ligament ECM components including collagen I, collagen III, and tenascin-C were produced prominently. Furthermore, direct ligament-bone insertion with typical four zones (bone, mineralized fibrocartilage, fibrocartilage, ligament) was reconstructed, which resembled the native structures of ACL-bone insertion. The tensile strength of regenerated ligament also met the mechanical requirements of daily activities. In conclusion, the results imply that silk scaffold has great potentials in future clinical applications.

**Keywords** — Mesenchymal stem cells, silk scaffold, ligament, tissue engineering

## I. INTRODUCTION

As a naturally occurring fibrous protein, silk has unique mechanical properties in fiber form, excellent biocompatibility, cell-controlled degradability, and versatile processability [1]. Braided silk fiber matrix has already been investigated as a possible scaffold material for ligament

tissue engineering. However, braided or embroidered fabrics often encounter problems of nutrient transmission, poor cell seeding, infiltration and matrix production [2]. These scaffolds performed well for a short period after implantation, while the long-term results have been poor. These composite structures were limited by poor tissue integration, poor abrasion, and fatigue failure. Unlike braided fabrics, knitted scaffolds have been shown to possess good internal communicating spaces and favor deposition of collagenous connective tissue matrix, which is crucial for ligament reconstruction. However, knitted scaffold required gel systems, such as fibrin or collagen gel, for cell seeding and was found to be unsuitable for ligament reconstruction in the knee joint, because the cell-gel composite dissociated from the scaffold during motion [3]. Gel systems are also likely to encounter nutrient transmission problems, and cells seeded in a three-dimensional (3D) gel are observed to proliferate more near the surface than in the center of the gel [4]. In order to bypass the problems of cell seeding on knitted scaffolds, we developed a combined silk scaffold with microporous silk sponges being introduced into the openings of a knitted silk scaffold to form a hybrid mesh and a silk cable-reinforced gelatin/silk fibroin hybrid scaffold.

We hypothesized that our novel silk scaffolds could be suitable for *in vitro* ligament tissue engineering using adult human bone marrow-derived mesenchymal stem cells (hMSCs) due to the differences in structure, mechanical properties and biocompatibility when compared with other synthetic biodegradable polymer scaffolds. Therefore, adult hMSCs were seeded on the combined silk scaffold and cultured for 2 weeks. Cell morphology, proliferation, differentiation, and glycosaminoglycan synthesized, were investigated and were compared with responses of cells seeded on the knitted silk scaffold using fibrin gel. The differentiation toward ligament lineage of hMSCs cultured on the scaffolds was assessed by real-time reverse transcriptase-polymerase chain reaction (RT-PCR) for ligament-related extracellular matrix (ECM) markers (e.g., collagen I and III, tenascin-C), immunohistochemistry, and western blot. Moreover, the mechanical properties of cell-scaffold constructs after two weeks in culture were assessed by tensile tests.

## II. MATERIALS AND METHODS

### A. Scaffold fabrication and observation

Raw *Bombyx mori* silk fibers (local name: “Nang Lai” silk fibers) were used in this study. The knitted scaffolds of  $30 \times 60$  mm dimension were fabricated using raw silk fibers with 40 needles on a knitting machine (Silver-reed SK270, Suzhou, China).

The combined silk scaffold was prepared by forming microporous silk sponges in the openings of a knitted silk scaffold. A knitted sericin-free silk scaffold was immersed in the silk solution and frozen at  $-20^{\circ}\text{C}$  for 12 h. After that, it was freeze-dried for 24 h to allow the formation of microporous silk sponges which fill up the openings of the knitted scaffold. The scaffolds obtained were contacted with a 90/10 (v/v) methanol/water solution for 10 min to induce an amorphous to silk II conformational change in the microporous sponges to prevent resolubilization in the cell culture medium.

Four sericin-free silk fibers were braided in one bundle and 2 bundles were braided in one cable. Twelve parallel cables were fixed across a customized polypropylene cylinder mold (diameter: 6mm; length: 6cm). 7ml of 7.0 wt % gelatin solution (Sigma Co. St. Louis) and 13ml of 2.6wt% SF solution were mixed with 4ml of 1.0 wt% 1-ethyl-3-(3-dimethylaminopropyl)- carbodiimide (EDAC) (Sigma Co., St. Louis). The mixture was then poured into cylinder mold for cross-linking. The cross-linked hydrogel was kept in  $-80^{\circ}\text{C}$  for 1 h before lyophilization. The freeze-dried scaffold was immersed in methanol for 30 min to induce  $\beta$ -sheet structural transition and washed several times to remove the residual carbodiimide and methanol. Then the gelatin/silk fibroin hybrid scaffold was lyophilized again for 72 h.

Finally, the scaffolds were dried overnight in a fume hood and then were observed by a phase contrast microscopy (Olympus DP70, Japan). Their morphology was observed by a scanning electron microscopy (SEM, JEOL JSM-5600LV, Japan) operated at a voltage of 3 kV.

### B. Cell seeding and culture on scaffolds

After the scaffolds were cut into small pieces and sterilized by autoclave, hMSCs were seeded at a density of  $2.5 \times 10^5$  cells/scaffold onto each of the scaffolds placing in the wells of a non-treated 6-well culture plate (NUNC, Denmark). The silk scaffolds were seeded by simple pipetting of 200  $\mu\text{L}$  of cell medium suspension onto the scaffolds. Cellular morphology characterization of hMSC-seeded combined silk scaffolds was accomplished using SEM (JEOL JSM-5600LV, Japan) on day 1, 7 and 14.

### C. RT-PCR

Total RNA was extracted from the MSCs ( $0.5 \times 10^6$ ) on scaffold at 1 week and 2 weeks using an RNeasy Mini Kit (Qiagen, Valencia, CA). The RNA extracted from MSCs ( $0.5 \times 10^6$ ) cultured on plate was used as control. The RNA concentration was determined by NnanoDrop (NanoDrop Technologies, Wilmington, DE) and 200 ng RNA was used to synthesize cDNA with Iscript cDNA synthesis kit (Bio-rad laboratories, Hercules, CA). Quantitative real-time PCR reactions was carried out and monitored with a Stratagene Mx3000P system. QuantiTect SYBR Green PCR kit (Qiagen, Valencia, CA) was used to quantify the transcription level of ligament specific markers including collagen I, collagen III, and tenascin-C. Undifferentiated MSCs were used as reference sample and all results were normalized to the transcription level of housekeeping gene (GAPDH). Data were analyzed by Stratagene MxPro QPCR software.

### D. Western-Blot

The expression of ligament specific proteins including collagen I, collagen III, and tenascin-C were examined by western blot analysis. Proteins were extracted from MSCs/scaffold ( $n=4$ ) at 1 week and 2 weeks using pepsin (200 $\mu\text{g}/\text{mL}$  in 0.08M acetic acid; Sigma) for 72 h at  $4^{\circ}\text{C}$ . The pepsin was subsequently inactivated with 1M NaOH. The extract was concentrated using a Nanosep 30 centrifugal filter (30,000 Mw cutoff, Pall Life Sciences, US). Then the samples were separated by electrophoresis in NuPAGE Novex Tris-Acetate Mini gels (Invitrogen, US) and electrophoretically transferred to a supported nitrocellulose membrane (Biorad laboratories, Hercules, CA). The membranes were tested using western blot kit (Invitrogen, US) according to the instructions of vendor. The signal was detected using VersaDoc Imaging System (Biorad laboratories, Hercules, CA).

### E. In vivo study

Forty-eight New Zealand White rabbits (12 weeks old, 2.5–3.0kg) were divided into TEL group (MSCs/scaffold implantation;  $n=24$ ) and control group (scaffold implantation;  $n=24$ ). Then  $3.0 \times 10^6$  autologous MSCs (passage 3) were loaded on each scaffold and cultured in vitro over 8 h for cell adhesion before implantation. The lateral parapatellar arthrotomy was used to expose the right knee joint of rabbit. After the native ACL was excised, the tibial and femoral bone tunnels were created with a 2.0mm diameter drill-bit. The scaffolds with or without MSCs were carefully rolled up along their short axis to produce a tightly wound shaft with 60mm in length and 2.0mm in diameter. The

shaft was passed through the tunnel and both ends were fixed by sutures tied over screws in femur and tibia. All rabbits were allowed to move freely after surgery without plaster immobilization.

III. RESULTS

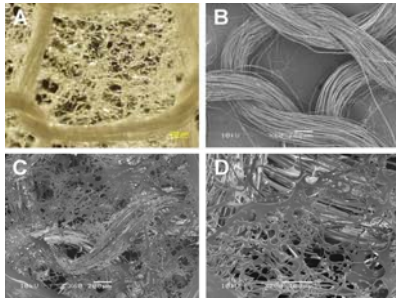


Fig. 1. Phase contrast (A) and SEM (B-D) images of the knitted (B) and combined (A, C, D) silk scaffolds showing web-like microporous silk sponges formed in the openings of the knitted silk scaffold. (A-C) Scale bars = 200 μm; (D) scale bars = 100 μm.



Fig. 2. Observation of the gelatin/silk fibroin hybrid scaffold. (A) gross observation of scaffold; (B) cross section of scaffold; (C) porous structure observed by SEM (×100); (D) Magnified view of the white rectangle frame from (C), demonstrating the hybrid G/SF microsponge around the silk cables (SEM ×150), note: the arrows point to the silk cable and micropores.

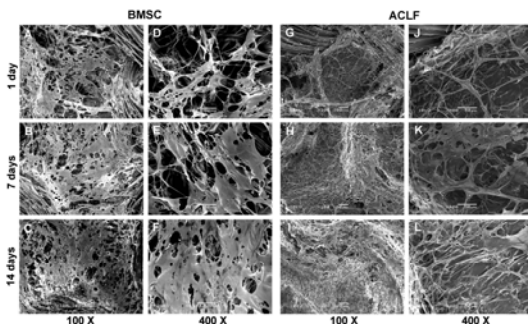


Fig. 3. SEM photomicrographs showing adherence, proliferation, and cell sheet formation by BMSCs (A-F) and ACLFs (G-L) cultured on the combined silk scaffolds for 1, 7, and 14 days. (A-C, G-I) Scale bars = 100 μm; (D-F, J-L) scale bars = 50 μm.

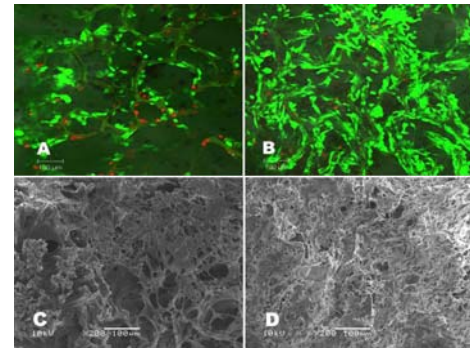


Fig. 4. Viability and distribution of MSCs on gelatin/silk fibroin hybrid scaffold. (A) MSCs on scaffold evaluated by confocal microscope at 1 week (FDA/PI staining; green: live cells; red: dead cells); (B) MSCs on scaffold evaluated by confocal microscope at 2 weeks (FDA/PI staining); (C) MSCs on scaffold observed by SEM (×200) at 1 week; (D) MSCs on scaffold observed by SEM at 2 weeks (×200)

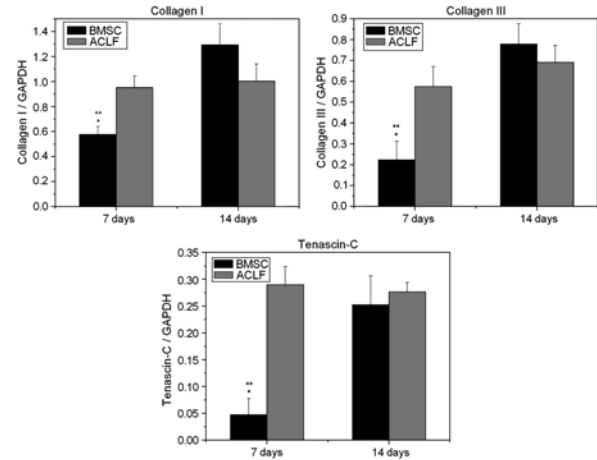


Fig. 5. Expression of ligament-related ECM genes by BMSCs and ACLFs cultured on the combined silk scaffolds for 7 and 14 days. Levels, quantified using real-time RT-PCR, are normalized to the housekeeping gene, GAPDH. \* Significant difference between two groups at each time point ( $p < 0.05$ ) and \*\* Significant difference of one group between two time points ( $p < 0.05$ )

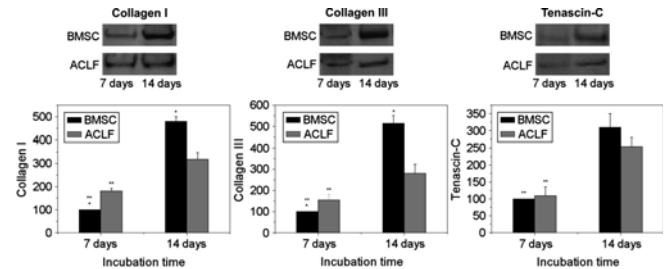


Fig. 6. Western blot analysis of ligament-related ECM proteins by BMSCs and ACLFs cultured on the combined silk scaffolds for 7 and 14 days. Data are shown as means ± standard deviation from 3 samples.

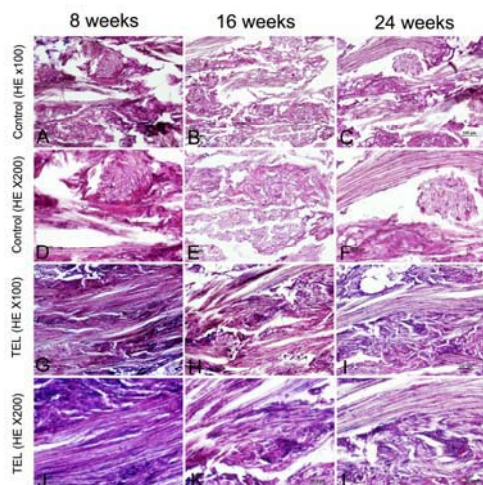


Fig. 7. Histological observation of regenerated ligaments in control group (A~F) and TEL group (G~L) by HE staining at 8, 16, and 24 weeks post-operatively.

#### IV. DISCUSSIONS

Ligaments consist of approximately 75% of collagens (90% is type I and 10% is type III) and less than 1% of elastin, proteoglycans, and glycoproteins. Fibroblasts represent 20% of tissue volume, whereas the extracellular matrix makes up 80%. The complex anatomy of the human ligaments is dependent on the interaction, orientation, and relationships between molecules (such as matrix proteins) and cells. MSCs when grown on the scaffolds retain the expression of these proteins that exert important functions in ligaments. In particular, we observed that MSCs cultured on the combined silk scaffold not only start to organize their morphology but also modulate the expression of some important matrix regulatory proteins of the ligaments. The key matrix components of the constructs include type I and type III collagen which are the major matrix components of the natural ligament and tenascin-C, one of the early marker for embryonic ligament. These components hinted the differentiation of MSC cultured on the scaffolds. In the present study, the transcript levels of these ligament-related ECM gene markers on the combined silk scaffolds were significantly upregulated ( $p < 0.05$ ) (Fig. 5). Protein levels and localization were determined by western blots and immunohistochemical staining, and the results revealed that the deposition of the ECM rich in type I and type III collagen, and tenascin-C on the combined silk scaffolds (Fig. 6). Cellular response is highly related to the 3D geometry of the scaffolds, on which hMSCs recognized that their environment is completely different with that within the fibroin gel and so they attached on the combined silk scaffolds with

suitable morphology and upregulated the genes to compensate for the new environment. It is reasonable to suggest that the unique 3D geometry stimulates and sends signals that may trigger cell-surface receptors and adhesion sites that regulate the genes responsible for the synthesis and secretion of the key ligament ECM components.

After 24 weeks, histology observation showed that MSCs were distributed throughout the regenerated ligament and exhibited fibroblast morphology. The key ligament ECM components including collagen I, collagen III, and tenascin-C were produced prominently. Furthermore, direct ligament-bone insertion with typical four zones (bone, mineralized fibrocartilage, fibrocartilage, ligament) was reconstructed, which resembled the native structures of ACL-bone insertion.

#### V. CONCLUSIONS

Therefore, these data suggest the suitability of the novel silk scaffolds used along with MSCs for the development of a tissue-engineered ligament.

#### ACKNOWLEDGMENT

This research was supported by a grant from the Biomedical Research Council, Singapore.

#### REFERENCES

1. Jin HJ, Kaplan DL. Mechanism of silk processing in insects and spiders. *Nature* 2003;424:1057-1061
2. Karamuk E, Mayer J, Düring M, Wagner B, Bischoff B, Ferrario R, Billia M, Seidl R, Panizzon R, Wintermantel E. Embroidery technology for medical textiles. *Medical Textiles, Proceedings of the 2nd International Conference*, Bolton, 1999
3. Ouyang HW, Toh Siew Lok, Goh JCH, Tay TE, Moe K. Assembly of bone marrow stromal cell sheets with knitted poly(L-Lactide) scaffold for engineering ligament analogs. *J Biomed Mater Res Part B: Appl Biomater* 2005;75B:264-271
4. Patrick CW, Mikos AG, McIntire LV. *Frontiers in Tissue Engineering*. New York: Pergamon; 1998. p. 412-442

Author: James C.H. Goh  
 Institute: Department of Orthopaedic Surgery, National University of Singapore  
 Street: 27 Medical Drive  
 City: Singapore  
 Country: Singapore  
 Email: dosgohj@nus.edu.sg

# Influence of Hydrogenated Calcium Phosphate Surface on Potential of Stromal Stem Cells in Situ

A.V. Karlov<sup>1</sup>, I.A. Khlusov<sup>1</sup>, Y. Dekhtyar<sup>2</sup>, N. Polyaka<sup>2</sup>

<sup>1</sup>Tomsk Branch of FSE «Russian Ilizarov Scientific Centre «Restorative Traumatology and Orthopaedics», Tomsk, Russia

<sup>2</sup>Biomedical Engineering & Nanotechnologies Institute, Riga Technical University, Riga, Latvia

**Abstract** — We have applied novel technique for enhancing bone tissue formation on micro- and nanostructured calcium phosphate (CP) coatings. CP surfaces with “primitive” physical-chemical composition, which is not corresponding to last one in bone, have an active effect on functional properties of mesenchymal stromal cell pull (MSCP). The studied micro-CP coatings, characterized by marked roughness of surface had an osteoinductive potential up to 100 %. Relief of CP coatings from HAP nanoparticles (30-50 nm) does not practically differ from ones designed by use of HAP microparticles. Roughness of all CP nanocoatings had average Ra=5.13-6.43 μm and Rz=18.71-24.16 μm that was corresponded to CP microcoatings one. Probability of bone plate formation on CP nanostructured coatings was only 12.5 %. Hydrogenation of the CP surface layer increased its negative charge that was evaluated by means of photoelectron work function ( $\phi$ ) measurement. An increment of  $\phi$  at the values of ~0.1-1 eV was supplied. This had an effect on the directions of MSCP differentiation. For example, connective tissue growth was improved. For all this, probability of following ossification with growth of membrane reticulated bone was 20 %. Vice versa, decrease of  $\phi$  led to primary formation of bone from bone marrow MSCP. Technique of intracellular RNA staining detected the actively synthesized osteoblasts and bone marrow stromal cells. The above evidences that hydrogenation of CP coatings could in situ effect MSCP differentiation in fibroblasts or osteoblasts associated with stromal cells of hemopoietic inducing microenvironment.

**Keywords** — implants, bone marrow, ectopic osteogenesis, mice

## I. INTRODUCTION

Osteogenous properties of hydroxylapatite and tribasic calcium phosphate, which are the base of mineral bone matrix, are obviously proved per ectopic osteogenesis phenomenon, when bone tissue is generated on the surface of calcium phosphate (CP) materials. M.R. Urist [1] was one of the first scientists, who described this phenomenon in 1965.

Multipotential mesenchymal stromal cells are able to differentiate in osteocytes, chondrocytes, fibrocytes, adipocytes, neurocytes, myocytes and stromal cells, which can maintain a hemopoiesis. However, the choice of differentia-

tion line under the conditions of multicellular systems is still unclear.

Different specimens of CP materials have different ability for osteogenesis depending on their physical-chemical properties (crystallinity and porosity degree, solubility, surface roughness etc.). A key combination of their structure, thickness and dissolution rate for realization of osteogenous potential of mesenchymal stromal cell pull (MSCP) is not found till now.

In this connection, the complex value of physical-chemical parameters of CP material surface in regulation of stromal precursor's differentiation was both of theoretical and practical interest.

## II. TECHNIQUES

62 BALB/c male mice were used in experiment. One implant (diameter of 12 mm, thickness of 1 mm) with applied syngeneic marrow column (average marrow area is 7.5 mm<sup>2</sup>), taken from femur under aseptic conditions, was introduced subcutaneous into each animal (49 animals) under ether-anesthesia. Bone marrow was cultivated for the adhesion on the substrate for 45 min in culture medium, containing 95 % of RPMI-1640 and 5% of embryonic bovine serum. The marrow was a source of MSCP and growth factors. No generation of tissue plates under separate subcutaneous introduction of scaffolds or marrow fragments was noted in mice. The implants were released in 45 days. Standard methods of light thin slices microscopy were used for histological analysis of tissue plates.

Titanium discs were used as substrates. Artificial biocompatible (bioinert or calcium phosphate) surfaces were formed on discs by use of hydroxylapatite (HAP) micro- (70 μm) and nanoparticles (30-50 nm) by the means of anode-spark (microarc) oxidation or schlicker method.

The surface layer of the samples has been saturated with hydrogen at high pressure. Hydrogenation of the CP surface layer increased its negative charge that was evaluated by means of photoelectron work function ( $\phi$ ) measurement. An increment of  $\phi$  at the values of ~0.1-1 eV was supplied.

Surface morphology of biocompatible coatings, their element and phase compositions were determined by scan-

ning electronic microscopy (SEM), micro X-ray spectroscopic analysis (MRS), X-ray diffraction (XRD) and atomic-force microscopy (AFM) methods. The coating thickness and roughness were also measured. Statistical analysis was carried out by Mann-Whitney U-test (Pu). Correlation analysis was carried out according to Spearman rank correlation coefficient (r).

### III. RESULTS

Physical-chemical testing allowed to assign the following groups of biocompatible surfaces conventionally: 1) metal-ceramic (MC); 2) calcium-phosphate dense (CPD) X-ray amorphous and CPD crystal coatings may be determined as smooth, calcium-deficient (atomic calcium/ phosphorus ratio is less than 1.67), thin, finely-porous (pore diameter is less than 50  $\mu\text{m}$ ); 3) calcium-phosphate loose (CPL) X-ray amorphous and CPL crystal was noted as rough, calcium-deficient, thick (thickness is more than 50  $\mu\text{m}$ ), finely-porous (pore's diameter is less than 50  $\mu\text{m}$ ); 3) calcium-phosphate glass ceramic (CPG) had nonstoichiometric ( $\text{Ca/P} > 1.67$ ), thick, macroporous surface (diameter is about 200  $\mu\text{m}$ ).

Tissue reaction showed that there were no signs of inflammation in any observation group in 45 days after subcutaneous implantation of studied discs with syngeneic marrow. It is necessary to make a note of implant biocompatibility, causing only the weak encapsulation, which indicates insignificant reaction of subcutaneous tissue on implant's introduction. Marrow sites of different size, adipose tissue, loose shapeless connective tissue with ossification elements, bone tissue were revealed on different artificial surfaces. Presence of osteoblasts indicated an active bone tissue formation (fig. 1).

Thus, biological test showed that CP surfaces with "primitive" physical-chemical composition, which was not corresponding to last one in bone, had an active effect on MSC differentiation functional properties. The 4 of 6 CP coatings, characterized by marked surface roughness or macroporosity had an osteoinductive potential. CPL and CPG artificial surfaces had maximum probability (100%) of osteogenesis induction. CPL crystal coatings realized osteogenous potential to a lesser degree (67%). In this connection, the attempt to clarify statistically the most important question was made: what surface properties are governing for initiation of MSC adhesion, migration and osteogenous differentiation, leading to metaplasia of marrow and connective tissue into a mature bone. Correlation analysis allowed revealing of differential value of physical and chemical parameters of artificial surface for the regulation of stromal cell pool differentiation in situ. Marrow cell adhesion is the initial stage, predetermining their conduction on artificial surface (the

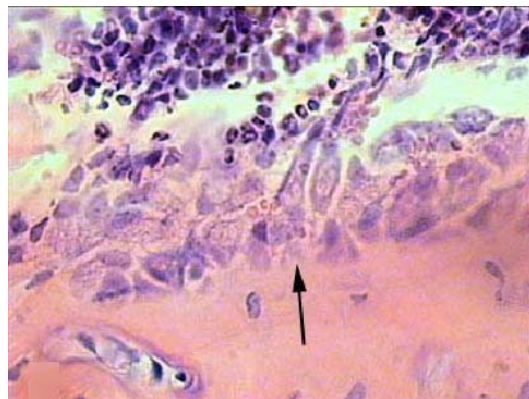


Fig. 1 Osteoblasts immersion in bone matrix on calcium-phosphate surface. Hematoxylin - eosin stain. Magnification 400

area of tissue plate). Histogenesis success depends on surface roughness.

The optimal surface roughness is 4-5 class according to Russian standard ( $R_z=10-40 \mu\text{m}$ ) that allows a differentiating of progenitor stromal cells into connective and adipose tissue under the conditions of specific microenvironment. Focuses of active hemopoiesis (fig.1) also implies an additional MSC differentiation into stromal cells, formatting a hemopoiesis inductive microenvironment. Adhesion and movement of stromal cell (including osteogenous precursors) is necessary, but insufficient condition for their differentiation into bone tissue. Induction of stromal precursor's osteogenous potential (osteoinduction) is determined by ratio of calcium and phosphorus atoms in coating. Presence of hydroxylapatite (atomic ratio  $\text{Ca/P}=1.67$ ) is not the obligate requirement for osteogenesis. In offered experimental system MSC differentiation in osteogenous tissue is blocked only at  $\text{Ca/P} < 0.5$ . Ectopic osteogenesis courses successfully on "thick" surfaces. Minimal CP layer thickness must be 50-80  $\mu\text{m}$ .

In case of formation of CP coatings on titanic substrates from nanosized (30-50 nm) HAP particles, relief does not practically differ from the relief by use of HAP microparticles (fig.2). Roughness of all CP nanocoatings had average  $R_a=5.13-6.43 \mu\text{m}$  and  $R_z=18.71-24.16 \mu\text{m}$  that was corresponded to CP microcoatings one. Probability of bone plate formation on CP nanostructured coatings was only 12.5 %. Hydrogenation of the CP surface layer increased its negative charge that was evaluated by means of photoelectron work function ( $\phi$ ) measurement. This had an effect on the directions of MSC differentiation. For example, connective tissue growth was improved. For all this, probability of following ossification with growth of membrane reticulated bone was 20 %. Vice versa, decrease of  $\phi$  led to primary formation of bone from bone marrow MSC. Technique of



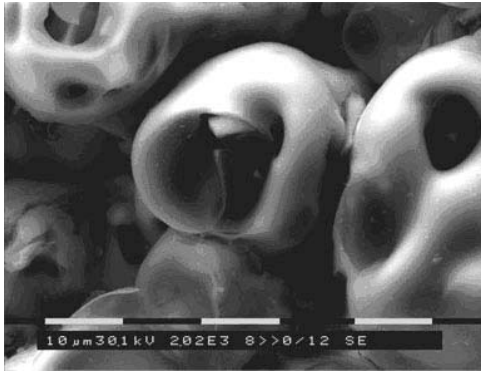


Fig. 2 SEM of calcium phosphate coatings designed by microarc oxidation from HAP nanoparticles

intracellular RNA staining detected the actively synthesized osteoblasts and bone marrow stromal cells.

#### IV. CONCLUSIONS

Stem and committed cells pool is a heterogeneous population, which is under the control of distant and local regulatory mechanisms. Structure-functional units (microregions), including special cells, stromal elements, microcirculation vessels and terminal nerve endings are educed in every tis-

sue. Research shows that not only organic, but also well defined physical and chemical parameters belong to the stromal cell microenvironment. Their local or system changes may have an influence on stromal functional activity. Hydrogenation of CP coatings could in situ effect MSCP differentiation in fibroblasts or osteoblasts associated with stromal cells of hemopoietic inducing microenvironment.

#### ACKNOWLEDGMENT

The project is particular supported by Russian Foundation of Basic Research (RFBR) grant # 08-04-99012.

#### REFERENCES

1. Urist M.R. (1965). Bone: formation by autoinduction. *Science* 150: 893

Author: A.V. Karlov

Institute: Tomsk Branch of FSE «Russian Ilizarov Scientific Centre  
«Restorative Traumatology and Orthopaedics»

Street:

City: Tomsk

Country: Russia

Email: longstreet@yandex.ru

# The Influence of Cultivation Conditions on the Proliferation and Differentiation of Rat Bone Marrow Multipotent Mesenchymal Stromal Cells

G. Krievina<sup>1</sup>, N. Bezborodovs<sup>2</sup>, G. Makarenkova<sup>1</sup>, S. Nikulsins<sup>3</sup>, Z. Krumina<sup>4</sup>, D. Babarikins<sup>4</sup>

<sup>1</sup>University of Latvia, Riga, Latvia

<sup>2</sup>Rigas Stradins University, Riga, Latvia

<sup>3</sup>University Children's Hospital, Latvia

<sup>4</sup>Medical Consulting Service Ltd., Riga, Latvia

**Abstract** — Rat bone marrow multipotent mesenchymal stromal cells (rBM MMSCs) demonstrate a potential to differentiate down the mesodermal pathway but under appropriate experimental condition differentiation into non-mesodermal lineages may occur. Knowing this fact it seems interesting whether prolonged cultivation and preservation affects BM MMSC morphology, differentiation ability into multiple lineages and proliferation capacity. Therefore this study was aimed to investigate the effects of long-term cultivation and cryopreservation on the morphology, proliferation and differentiation potential of rat bone marrow-derived MMSCs *in vitro*.

The effects of long term cultivation and cryopreservation were evaluated by the phenotype and morphology of the cell population. Findings show that the 60<sup>th</sup> passage cells had a smaller, more flattened and spindle-shaped morphology than the 4<sup>th</sup> passage cells before and after cryopreservation. We have also found that the 60<sup>th</sup> passage cells were more proliferative than rBM MMSCs in early passages but the ability to differentiate was more effective in the 4<sup>th</sup> passage cells before cryopreservation. rBM MMSCs from pre- and post- cryopreservation had similar colony formation potential and cellular morphology but disparity in differentiation potential was observed.

The results of the present study provide evidence that rBM MMSCs could be cryopreserved without noticeable loss of viability and proliferative capacity but the differentiation capability may be affected.

**Keywords** — Bone marrow multipotent mesenchymal stromal cells, cryopreservation, long-term culture, transdifferentiation

## I. INTRODUCTION

BM MMSCs are nonhematopoietic multipotent stem-like cells that adhere to culture dishes, have extensive capacities for self-renewal, and are able to proliferate [1] and differentiate into cells of mesenchymal origin such as bone, cartilage, muscle and fat [2,3]. In addition, transdifferentiation of BM MMSCs into cells with neurospecific antigens [4,5,6] has been reported, suggesting that BM MMSCs may be capable of overcoming germ layer commitment.

It has been observed that, rodent BM MMSCs appear to go through a crisis after about 5 - 6 passages [7]. At this point, most of the cells die but a few survive, acquire an enhanced growth rate and give rise to a continuous cell line. The long-term cultivation of rat BM MMSCs may fail due to factors, such as genotypic drift, transformation, phenotypic instability, viral or microbial contamination or incubator failure. The failure of cultivation will result in absence of BM MMSCs for experimental and clinical use. Therefore, it is necessary to preserve BM MMSCs as cell seeds.

The aim of the present research is to compare morphological, phenotypical and functional (ability to differentiate into adipogenic, osteogenic and neurogenic pathways) characteristics of rat BM MMSCs in cultures obtained from different donors and to determine whether these characteristics change during long-term cultivation and after cryopreservation.

## II. MATERIALS AND METHODS

Rat BM MMSCs were harvested, after sacrifice of 130-150 g male Wistar-Kyoto rats, from femurs and tibias, by inserting a 21-gauge needle into the shaft of the bone and flushing it with 10 ml of complete DME medium (Sigma) containing 10% fetal bovine serum (FBS) (Sigma), 2mM L-glutamine (Sigma), 100U/ml penicillin (Sigma) and 100µg/ml streptomycin (Sigma). The recovered cells were then mechanically dissociated and plated in 75cm<sup>2</sup> tissue culture flasks. After 24h, the nonadherent cells were removed by replacing the medium. When the cells grew to 70% confluence, they were harvested with 0.25% trypsin/1mM EDTA (Sigma) for 7 min at 37°C, replated (1:3 dilutions), cultured again to next confluence, and harvested. Rat BM MMSCs used in these studies were passaged from 4 times to 60 times *in vitro*.

Harvested rat BM MMSCs at passage 4 (pre- and post-cryopreservation) and at passage 60 of long-term culture were trypsinized, stained with anti-CD45-FITC (Becton Dickinson) and anti-CD90-PE (Becton Dickinson) and analyzed by flow cytometry (EpicXL, Beckman Coulter).

Rat BM MMSCs at passage 3 of pre-cryopreservation were harvested and centrifuged at  $150\times g$  for 5 min. Pellet was resuspended with DMEM containing 30% FBS and 7% DMSO (Sigma) in a concentration of  $1\times 10^6$  cells/ml, then loaded into a cryopreserving ampoule at 1.5 ml aliquots. Aliquots were cooled to  $-80\text{ }^\circ\text{C}$  at a rate of  $1\text{ }^\circ\text{C}/\text{min}$ , and finally, frozen in a liquid  $\text{N}_2$ -freezer at  $-196\text{ }^\circ\text{C}$ .

After 12 months storage, the frozen vials were thawed in a constant-temperature heating bath at  $37\text{ }^\circ\text{C}$  by shaking lightly. After 1 or 2 min, cells were resuspended in complete medium and centrifuged at  $150\times g$  for 5 min. Then cells were cultured at a concentration of  $2\times 10^4$  cells/ $\text{cm}^2$  to recover 4<sup>th</sup> passage cells.

Osteogenic and adipogenic differentiations of rat BM MMSCs were induced according to a published protocol with some modifications [8]. To achieve osteogenic and adipogenic differentiation, 60<sup>th</sup> passage cells, 4<sup>th</sup> passage pre- and post-cryopreserved cells were seeded at density  $1\times 10^4$  cells/ $\text{cm}^2$  and maintained in growth medium for 3 days. Then medium was replaced to osteogenic or adipogenic differentiation medium for 3 weeks. Osteogenic differentiation was evaluated using Alizarine Red (Sigma) staining. Adipogenesis was assayed by staining of intracellular lipid droplets with Oil Red O (Sigma) as previously described [9].

Sub-confluent cultures of rat BM MMSCs were maintained in DMEM supplemented with 10% FBS. 24 h prior to neuronal induction, culture medium was replaced with pre-induction medium consisting of DMEM/F12 (Sigma), 10% FBS and 10 ng/ml bFGF (Sigma). To initiate neuronal differentiation, the pre-induction medium was removed, and substituted with neuronal induction medium composed of DMEM/F12, 10% FBS, 1 mM DBcAMP (Sigma) and 0.5 mM IBMX for 48h.

Cells in culture dishes were fixed with 4% buffered paraformaldehyde solution (PFA) at room temperature for 10 min. They were then permeabilized in 1% Triton X-100 at room temperature for 10 min and non-specific binding was blocked by a 30 min treatment in HIV scan buffer. The cells were incubated with primary antibodies 2h at room temperature. Mouse- origin primary antisera for nestin, vimentin, NF-M and GFAP, as well as FITC or R-PE (Becton Dickinson) conjugated secondary antisera were used. Optimal dilutions were established for all primary and secondary antibodies.

Incubating with DAPI counterstained all cells. Cultures were examined using a fluorescence microscope (Leica) equipped with phase-contrast, appropriate fluorescence filters, and imaged using Leica digital camera

60<sup>th</sup> passage cell and post-cryopreserved 4<sup>th</sup> passage cell metaphases were prepared from ice-cold methanol: glacial acetic acid (3:1)- fixed cells. Ten micro liters of cell suspen-

sion in fixative were dropped onto the pre-chilled slide from a height of 30 cm. After the slides dried, chromosome spread was stained with Giemsa for 3 min and the chromosome number was counted under the microscope. At least 20 metaphase cells were analyzed from each rat BM MMSCs culture.

### III. RESULTS

Cultured pre- and post-cryopreserved 4<sup>th</sup> passage cells demonstrated a fibroblast-like morphology, producing characteristic parallel assays of cells (three dominant cell types were observed: spindle-shaped, large-irregular shaped and small-round cells). Some cells had granular cytoplasm. On the other hand, the 60<sup>th</sup> passage cells demonstrated only spindle-shaped morphology, were smaller than the 4<sup>th</sup> passage cells before and after cryopreservation and had small number of processes. Nuclei with clearly identified nucleoli and homogeneous cytoplasm were seen in 60<sup>th</sup> passage cells (these cells frequently were multinuclear), moreover, these cells lost the contact inhibition growth property, while both 4<sup>th</sup> passage cultures cells could overlap each other.

60<sup>th</sup> passage cells were highly proliferative and their doubling time was 9-10h in the logarithmic phase (mitotic cells were frequently seen throughout the culture) (Fig.1). The 60<sup>th</sup> passage cells, in contrast to pre- and post-cryopreserved 4<sup>th</sup> passage cells, continued to divide even if the serum concentration in cultivation medium was decreased from 10 to 1%.

FC analysis for size and structure demonstrated that all cell cultures contained three subpopulations of cells: 1)

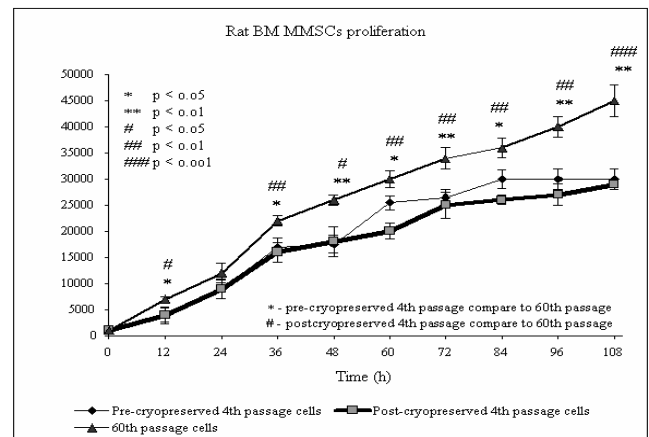


Fig. 1 Proliferation dynamics of 60<sup>th</sup>, pre- and post-cryopreserved 4<sup>th</sup> passage rat BM MMSCs. The groups were analyzed by a paired t-test and it was found that the long-term cultures proliferating activity significantly increased in comparison with both 4<sup>th</sup> passage cultures ( $p < 0.05$ ,  $p < 0.01$  and  $p < 0.001$ ). Data represent means  $\pm$  SD (standard deviation).

large and probably mature cells, 2) medium sized cells and 3) small granular cells (Fig.2).

The immunophenotyping by CD45 and CD90 surface markers showed that  $\geq 97\%$  of the rat BM MMSCs (pre- and post-cryopreserved groups) expressed CD90 and the labeling increased to 100% in the 60<sup>th</sup> passage cells. However, haematopoietic marker CD45 expression was negative ( $\leq 0.7\%$  positive) in all cell cultures (Fig.3)

Incubation of pre-cryopreserved 4<sup>th</sup> passage cells in adipogenic medium resulted in development of several clusters of adipoblasts (more than 40% of all cells adopting the adipoblast morphology) containing intracellular lipid vacuoles, which stained positive (red) with Oil Red O. In contrast both post-cryopreserved and long-term cultures displayed a negative staining for cytoplasmic lipid droplets with Oil red O.

In both pre- and post-cryopreserved 4<sup>th</sup> passage cultures, cells proliferated and reached almost complete confluence at day 5. In pre-cryopreserved culture, nodular cell aggregates

became evident at day 10 of culture and increased up to 21 days. Aggregates were characterized with deposits of amorphous material. In post-cryopreserved culture similar cellular aggregates were observed, but they were smaller and lacked calcium deposition. In contrast 60<sup>th</sup> passage culture lacked boths -cellular aggregates and calcium deposition.

When rat BM MMSCs of all passages were exposed to DbcAMP/IBMX neural induction medium within few hours, the majority of the cells rounded up, and acquired refractile cell bodies and long branching processes. 4<sup>th</sup> passage cells in contrast to 60<sup>th</sup> passage cells, made contacts with undifferentiated rat BM MMSCs. In all cultures some of the cells partially lost contact with the plastic and others completely detached, whereas a limited fraction (20.91% $\pm$ 1.23%) of rat BM MMSCs appeared to be unaffected by treatment. Moreover, in all cultures there was an extensive reduction in cellular proliferation rate and evidence of cell death were obvious.

We evaluated the expression of "neural" proteins by non-induced rat BM MMSCs, and found that, in all three cultures, nearly 100% and 10% of BM MMSCs were positive for the intermediate filament protein nestin and vimentin respectively. We could not detect any expression of NF-M in either untreated or DbcAMP/IBMX- treated pre-and post-cryopreserved and long-term cultured rat BM MMSCs. After 48h of incubation with neural induction medium, the 4<sup>th</sup> passage pre-cryopreserved cells exhibited a much stronger labeling for GFAP than 4<sup>th</sup> passage post-cryopreserved cells, furthermore 60<sup>th</sup> passage cells were negative for this marker.

Preliminary karyotyping analyses showed that rat BM MMSCs in pre- and post-cryopreserved cultures have normal diploid (2n) karyotypes, but 76% cells had abnormal (4n) karyotypes after long-term cultivation.

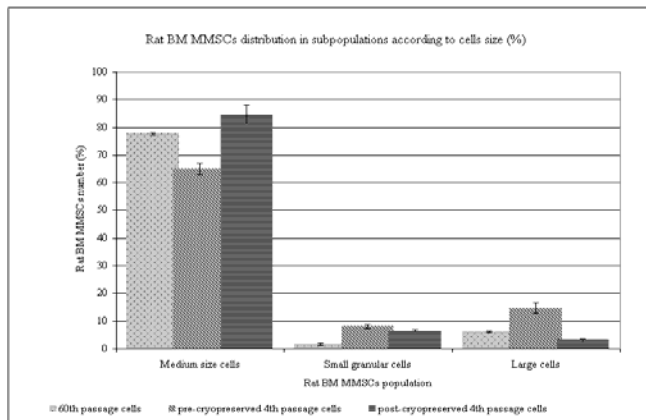


Fig. 2 Rat BM MMSC subpopulations. The SDs are demonstrated on the top of each bar.

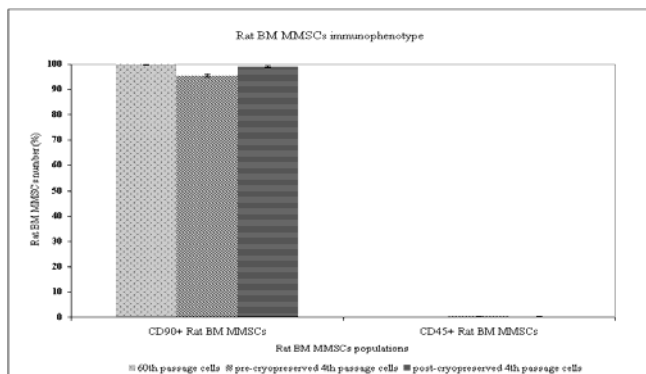


Fig. 3 Expression of CD90 and CD45 markers in pre- and post-cryopreserved 4<sup>th</sup> and 60<sup>th</sup> passage cultures.

#### IV. DISCUSSION

The present study demonstrates the plasticity reduction of rat BM MMSCs by cryopreservation and prolonged cultivation. The exact effects of cryopreservation and long-term cultivation on cell proliferation and differentiation have not been clearly established. Contradictions may occur due to the differences between the cell types and species used. The data in this study demonstrated that, after long-term cultivation and cryopreservation the population of rat BM MMSCs lost its stem cell potential.

Some authors demonstrate that CD90 marker expression declines during long-term cultivation [7,10]. In contrast, our preliminary characterization confirms that rat BM MMSCs, isolated from different animals and cultivated under different conditions, primarily all express CD90 with little or no

lymphohematopoietic cell marker (CD45) expression. On the other hand, we observed different morphological characteristics and different capacity to differentiate after long-term cultivation, pre- and post-cryopreservation. Anokhina et al. [7] hypothesize those morphological differences between BM MMSCs cultures may be due to the method of isolation. A study by Javazon et al. [12] demonstrated that on early passages (pre- and post-cryopreserved) subcultures were characterized by morphological heterogeneity, which declined during long-term cultivation. It is possible that after isolation the ratio of BM MMSCs subpopulations in primary cultures is different and, therefore on late passages, different cell types become predominant [7]. Thus, in 60<sup>th</sup> passage subculture there is a sole dominant cell type – spindle-shaped (3 different sizes). 60<sup>th</sup> passage in contrast to both 4<sup>th</sup> passage cell cultures have lower serum requirement, higher saturation density, shorter population doubling time and growth in confluent monolayer of homologous cells is observed. According to other author observations [1,12,13], these findings suggest, that 60<sup>th</sup> passage cells probably undergo transformation. Moreover karyotype analysis of rat BM MMSC samples showing the tetraploid chromosome content of most of long-term culture cells also suggests that the transformation and maybe even cells immortalization occur.

Numerous studies have shown that BM MMSCs of a mesoderm origin could differentiate into neurons of an ectodermal origin both in vitro and in vivo. Therefore, the ability to differentiate into neurons is an important trait to classify BM MMSCs. Attempts were made to differentiate rat BM MMSCs toward a neuronal fate with phosphodiesterase inhibitor IBMX and cAMP analogue DBcAMP. Both agents can elevate intracellular cAMP levels [10]. We observed similar morphological changes in all 3 cultures, but only fraction of the 4<sup>th</sup> passage pre-cryopreserved cells showed an increased expression of GFAP. Taken together with the observation that a high percentage of apoptotic cells is present in the all cultures exposed to the DBcAMP/IBMX neural induction protocol, the change in cell morphology could be an artifact or a cytotoxic effect of DBcAMP and/or IBMX. Cox et al. [14] also found that IBMX and DBcAMP can induce prostate tumor cells to assume characteristics of neuronal cells. We can therefore hypothesize that morphological changes that occur in post-cryopreserved 4<sup>th</sup> and long term 60<sup>th</sup> passage cultures are only cell shrinkage rather than a process of neuronal differentiation.

## V. CONCLUSION

In summary, our results demonstrate that BM MMSCs in all three cultures have similar immunophenotype and almost the same number of cells expressing the CD90 marker. After long-term in vitro culture and cryopreservation the population of BM MMSCs lost their stem cell potential. We speculate that rat BM MMSCs during long-term in vitro expansion can immortalize and transform spontaneously.

## REFERENCES

1. Dominici M, Blanc K Le, et al. (2006) Minimal criteria for defining multipotent mesenchymal stromal cells. The International Society for Cellular Therapy position statement. *Cytotherapy* 8:315-317
2. Freidenstein A J (1995) Marrow stromal fibroblasts. *Clasif Tissue Int* 56:517
3. Gregory C A, Gunn W G, Reyes E et al. (2005) How wnt signaling affects bone repair by mesenchymal stem cells from the bone marrow. *Ann N Y Acad Sci* 1049:97-106
4. Black I B, Woodbury D (2001) Adult rat and human bone marrow stromal stem cells differentiate into neurons. *Blood Cells, Mol Dis* 27:632-636
5. Deng W, Obrocka M, Fischer I, Prockop D J (2001) In vitro differentiation of human marrow stromal cells into early progenitors of neural cells by conditions that increase intracellular cyclic AMP. *Biochem Biophys Res Commun* 282:148-152
6. Tao H, Rao R, (2005) Cytokine-induced stable neuronal differentiation of human bone marrow mesenchymal stem cells in a serum/feeder cell-free condition. *Develop Growth Differ* 47:423-433
7. Anokhina E B, Buravkova L B (2007) Heterogeneity of stromal cell precursors Isolated from rat bone marrow. *CTB* 1:1-7
8. Freshney R I, Stacey G N, Auerbach J M (2007) *Culture of Human Stem Cells*. Wiley, New Jersey
9. Sottile V, Halleux C, et al. (2002) Stem Cell characteristics of human trabecular bone-derived cells. *Bone* 30:699-704
10. Moore K D, Dillon-Carter O, et al. (1996) In vitro properties of a newly established medulloblastoma cell line, MCD-1. *Mol Chem Neuropathol* 29:107-126
11. Lim J Y, Jeun S S, et al. (2006) Multiple stem cell traits of expanded rat bone marrow stromal cells. *Exp Neurol* 199: 416-426
12. Javazon E H, Colter C D, et al. (2001) Rat marrow stromal cells are more sensitive to plating density and expand more rapidly from single-cell-derived colonies than human stromal cells. *Stem Cells* 19:219-225
13. Rubio D, Castro J G, et al. (2005) Spontaneous Human adult stem cell transformation. *Cancer Res* 65:3035-3039
14. Cox M E, Deeble P D, et al. (1999) Acquisition of neuroendocrine characteristics by prostate tumor cells is reversible: Implications for prostate cancer progression. *Cancer Res* 59:3821-3830

Author: Gita Krievina  
 Institute: University of Latvia, Department of Biology  
 Street: Kronvalda bulvaris 4, LV-1010  
 City: Riga  
 Country: Latvia  
 Email: gita.krievina@gmail.com

# Human Blood Cells Affected by Hydroxyapatite Coated Titanium

A. Leice<sup>1</sup>, Y. Dekhtyar<sup>2</sup>, N. Britzina<sup>3</sup>, L. Arabere<sup>4</sup> and V. Arhipovich<sup>1</sup>

<sup>1</sup>Pauls Stradins Health and Social Care College, Jurmala, Latvia

<sup>2</sup>Riga Technical University, Riga, Latvia

<sup>3</sup>Latvian Institute of Cardiology, Riga, Latvia

<sup>4</sup>SIA "BaltInfoLab" laboratory, Riga, Latvia

**Abstract** — The paper demonstrates an influence of the Titanium coated with hydroxyapatite on human blood cells.

**Keywords** — red- white- blood, cells, platelets, titanium plate, hydroxyapatite

## I. INTRODUCTION

To improve biocompatibility of Titanium (Ti) implants they are often coated with hydroxyapatite (HAP) layers. To reach this novel advanced approaches are delivered by modern technologies. Therefore, both physical- chemical and biological interactions of the HAP coated Ti implants with blood cells pay a great attention [1, 2, 3, etc.].

The pulsed laser deposition (PLD) is a comparatively new technology that has a capability to control thickness and quality of HAP coating. However the influence of PLD HAP coated Ti implants on blood cells volume and aggregation, that is important for provision of biocompatibility, is not still reflected by literature.

The paper is directed to reveal the changes in blood samples.

## II. MATERIALS AND METHODS

The specimens (Ti:HAP) prepared from Ti 2 mm thick plates (1x2 cm<sup>2</sup>) cut off the Ti (grade A) tape and further deposited with HAP layer (thickness 1 μm) by means of the PLD technology were supplied from the EC project PERCERAMICS.

Directly before the experiment the Ti:HAP plates were carefully washed in acetone, ethanol and finally dried in air consequently.

Venous blood specimens from 70 volunteers were collected in Vacutainer K2-EDTA tubes (Becton-Dickinson) with EDTA.

The blood specimens were tested by means of ABX Micros OT automated hematology analyzer, delivering a standard package of blood characteristics including counts of red (RBC), platelets (PLT) and white (WBC) blood cells, values of mean platelet volume (MPV), mean cell volume

(MCV), mean cell hemoglobin (MCH), content of hemoglobin (HGB) and hematocrit (HCT).

The experiment had been performed at room temperature.

The initial test of the collected specimens from each volunteer was provided first. Each initially tested specimen was divided into two portions: "reference" (RP) and "experiment" (EP).

The Ti:HAP were positioned within the EP, however the RP were kept Ti:HAP free. Both EP and RP were tested simultaneously four times during one hour.

The corresponding blood parameters for RP and EP were differed. To analyze the differences of consequential test results from initial or prior characteristic values, as well as differences between RP and EP blood values of corresponding test, the pair-sample *t* statistic was used, keeping the significance level at  $p < 0,05$ .

## III. RESULTS

The mean values of the blood parameters at the initial test and provided in Table 1 evidence that blood specimens had normal hematological profiles.

### A. The Erythrocyte and their characteristic changes in time

The results demonstrated in Fig.1,2 express differences (DIF) between the data acquired at the second, third, fourth or fifth test and the initial one

Table 1 Initial test results of the blood parameters

Parameter	Mean value	n	Standard deviation
RBC [ $10^{12}/l$ ]	4.54	70	0,56
HGB [g/l]	13,30	70	2,32
HCT [%]	39,53	70	5,99
MCV [ $\mu m^3$ ]	86,93	70	8,53
MCH [pg]	29,22	70	3,67
MCHC [g/dl]	33,49	70	1,84
RDW [%]	14,03	70	2,15
PLT [ $10^9/l$ ]	288,8	70	91,27
PCT [%]	0,242	70	0,065
MPV [ $\mu m^3$ ]	8,54	70	0,942
PDW [%]	12,94	70	1,75
WBC [ $10^9/l$ ]	7,10	70	2,204

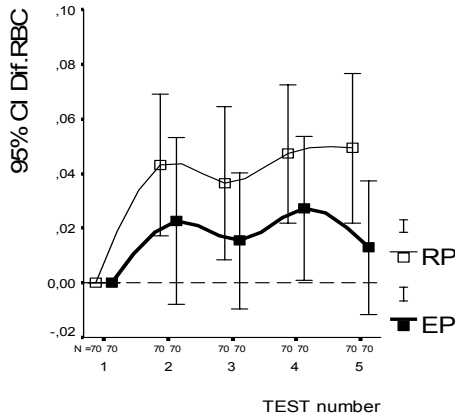


Fig.1 The RBC counts differences from initial value from test to test.

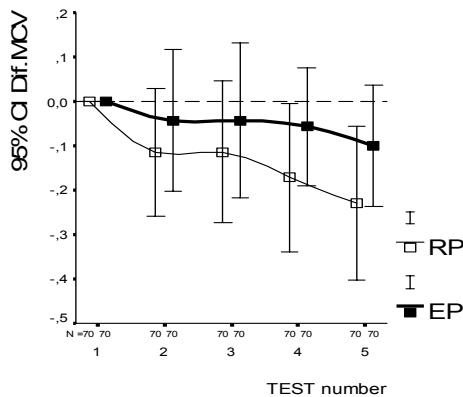


Fig.2 The MCV values differences from initial value from test to test.

The RBC counts trended to increase in time both in RP and EP blood and had accompanied by consequent decreasing of MCV values. This nevertheless is more expressed in RP blood than in EP with Ti:HAP positioned in it. The trend appeared to be significantly different if compare with the values of all 4 tests together by pair-sample t-test ( $p < 0.0005$  for RBC counts,  $p < 0.019$  for MCV values).

*B. The platelet and their characteristic changes in time*

Comparison each RP blood test results to previous tests results evidenced the platelets count was relatively constant over the time. The same was stated for PCT values of RP blood, because this parameter is a function of PLT numbers. Both parameters increased in EP blood. Statistics to compare EP and RP platelet is demonstrated by Table 2.

Fig. 3 that expresses differences (DIF) between the data acquired at the second, third, fourth or fifth test and the initial one demonstrates MPV values “from test to test” augmenta-

Table 2 The differences of the platelet parameters and t-test results

Time of the test (corresponds to)	Parameter	Mean difference	t	Sign. level
10 min	PLT.RP - PLT.EP	-10,37	-2,36	,000
	PCT.RP - PCT.EP	-0,106	-2,38	,000
	MPV.RP - MPV.EP	,051	,71	,473
	PDW.RP - PDW.EP	-,152	-,08	,326
20 min	PLT.RP - PLT.EP	-5,27	-5,35	,006
	PCT.RP - PCT.EP	-0,042	-4,2	,027
	MPV.RP - MPV.EP	,019	-1,38	,507
40 min	PLT.RP - PLT.EP	-8,01	-2,83	,001
	PCT.RP - PCT.EP	-0,075	-2,27	,038
	MPV.RP - MPV.EP	,006	,67	,903
60 min	PLT.RP - PLT.EP	-3,87	-3,50	,067
	PCT.RP - PCT.EP	-0,013	-2,12	,699
	MPV.RP - MPV.EP	,061	-,12	,241
	PDW.RP - PDW.EP	,201	-,63	,097

tion. The result was similar in both compared blood portions (Table 2).

*C. 2.3. The Leucocytes counts changes in time*

Counts of WBC were stable in time for both blood portions. There were not any differences neither between the tests in each blood portion, or in all tests together.

IV. DISCUSSION

The changes in platelet mean volume and partly in red blood cell count are considered as the process of ageing of blood sample stored at room temperature for 48 hours. Alteration of the blood parameters begins from the first hour of blood sample storage. Pair-samples t-test statistic reveals the result is significant. Increase in RBC counts and decrease of mean erythrocyte volume indicates instability of the cells over time. This process in the EP blood samples is delayed.

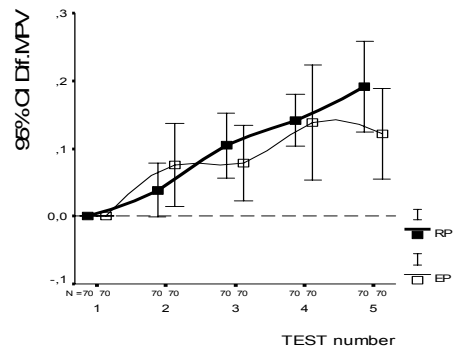


Fig.3. MPV value changes from test to test in EP and RP blood.

PLT counts, as well as PCT values were higher in EP blood if compared to RP blood in all tests. It suggests the PLT protection from aggregation that was resulted by blood contact with Ti:HAP. Progressive increase of MPV indicates swellings of PLT are equal in both blood portions. This was confirmed by *t*-test, supposing, that platelet activation was not influenced by blood exposition with Ti:HAP.

#### V. CONCLUSION

1. The Ti coated with HAP has an influence on the human blood cells.
2. The platelets are perhaps protected from aggregation and erythrocytes became more stable because of the Ti:HAP influence.
3. The developed procedure could be in use to test biomaterials influence on blood cells

#### ACKNOWLEDGMENT:

The authors are indebted to the EC project NMP3-CT-2003-504937 "PERCERAMICS" for the Ti:HAP provision.

#### REFERENCES:

1. S. Deb, J. Giri, S. Dasgupta, D. Datta and D. Bahadur. Synthesis and characterization of biocompatible hydroxyapatite coated ferrite. Bull. Mater. Sci., Vol. 26, No. 7, December 2003, pp. 655–660.
2. K. Vijayanand, Deepak K. Pattanayak, T. R. Rama Mohan, R. Banerjee. Interpreting Blood-Biomaterial Interactions from Surface Free Energy and Work of Adhesion. Trends Biomater. Artif. Organs, Vol 18 (2), January 2005. pp.73-83.
3. Furusono T, Yasuda S, Kimura T, Kyotani S, Tanaka J, Kishida A. Nano-scaled hydroxylapatite/polymer composite IV. Fabrication and cell adhesion properties of a three – dimensional scaffold made of composite material with a silk fibron substrate to develop a percutaneous device. In: Inc. J Biomed Mater Res. 57:366-373.
4. Sandra Lejniece „Klīniskā hematoloģija” 2005g, 297
5. S.A.Vogelaar, D.Posthurma, D.Boomsma, C.Kluft Blood sample stability at room temperature for counting red and white blood cells and platelets. Vascular Pharmacology 39 (2002) 123-125.
6. Lippi U, Schinella M, Modena N, Nicoli M, 1987. Unpredikteble effects of K<sub>3</sub>EDTA on mean platelet volume. Am .J. Clin.Pathol.87, 391-393.
7. Martin J.F., Bath P.M., Burr M.L., 1991 Influence of platelet size on outcome after myocardial infarction. Lancet 338, 1409-1411.

Author: Alevtina Leice  
 Institute: Pauls Stradins Health and Social Care College  
 Street: Lidonu 22-38  
 City: Riga LV-1055  
 Country: LATVIA  
 Email: alevtina.leice@inbox.lv



# Development of Biomorphic SiC Ceramics for Biomaterial Purposes

J. Locs<sup>1</sup>, L. Berzina-Cimdina<sup>1</sup> and A. Zhurinsh<sup>2</sup>

<sup>1</sup> Riga Technical University, Riga Biomaterials Innovation and Development Centre, Pulka street 3/3, LV 1007, Riga, Latvia

<sup>2</sup> Latvian State Institute of Wood Chemistry, Dzerbenes street 27, LV 1006, Riga, Latvia

**Abstract** — Microstructure of several wooden breeds was investigated and discussed as perspective biomorphic SiC ceramics precursor for biomaterial purposes. Pine tree (*Pinus silvestris*) with shaped sample dimensions of 20 x 20 x 5 mm (axial) was selected as raw material. SiO<sub>2</sub> sol-gel solution was prepared using ethanol, tetraethoxysilane, distilled water and hydrochloric acid. Samples were impregnated under vacuum and pressure conditions. Impregnation and drying procedures were repeated several times, to increase SiO<sub>2</sub> amount introduced in the samples. SEM microphotographs of samples were taken and are demonstrating the localization of SiO<sub>2</sub> in wood.

Impregnated samples were processed using high temperature and inert atmosphere and porous biomorphic SiC ceramics were obtained. Microstructure, crystalline phase composition and chemical functional groups of biomorphic SiC ceramics were investigated.

**Keywords** — wood, SiC, biomorphic, biomaterial.

## I. INTRODUCTION

Silicon-based ceramic materials are either currently being used or under active consideration for use in a wide variety of applications in different industries. These materials have high strength, good oxidation and corrosion resistance, high thermal conductivity and good thermal shock resistance [1]. Silicon carbide is a commonly used ceramic material with attractive properties such as high strength, stiffness, good wear and corrosion resistance, etc., some of which are characteristic of typical covalently bonded materials. A number of manufacturing approaches have been used to fabricate these materials including hot pressing/hot isostatic pressing, sintering, reaction bonding/reaction forming, polymer pyrolysis, and chemical vapor deposition. There has been a great deal of interest in utilizing biomimetic approaches to fabricate a wide variety of silicon-based materials [2].

Up to now, several technologies have been developed for obtaining porous silicon carbide (SiC) ceramic materials from wood precursors and some of them are as follows: reactive Si vapor infiltration and reactive infiltration with Si-containing melts. Impregnation with silicon dioxide (SiO<sub>2</sub>) nanoparticles containing sol, with metal organic precursors and with sol-gel derived SiO<sub>2</sub> sol solution also has been used to derive SiC ceramic materials [3-13]. As a result of carbothermal reactions, single-phase SiC ceramics with a relatively high porosity is commonly obtained.

Recently, biomorphic SiC coated with bioactive glass has been proposed as an alternative to titanium and titanium alloy devices due to its low density, bio-inertness, interconnected porosity and improved mechanical properties [14]. Also a study of deposition of hydroxyapatite thin films on biomorphic SiC is done in past years [15].

In this paper microstructure of several wooden breeds was investigated and discussed as prospective biomorphic SiC ceramics. To obtain biomorphic ceramics pine tree was used. Such biomorphic SiC ceramics in future can become important base for biomaterial purposes.

## II. EXPERIMENTAL PROCEDURE

### A. Materials and methods

For microstructure investigations of different wooden breeds, following softwood: spruce and pine trees and hardwood: apple, alder, aspen, birch, elm, maple, lime, ash, oak, plum and mahogany trees were used. Also woody evergreen plant: bamboo was investigated. Samples were pyrolysed in oxygen free atmosphere at 500 °C for easier sample preparation for structure investigations with scanning electron microscope (SEM).

Biomorphic SiC ceramics were obtained from pine tree wood shaped in dimensions of 20 x 20 x 5 mm (axial) and dried at 105 °C for 24 h. SiO<sub>2</sub> sol was prepared using TEOS - tetraethyl orthosilicate (Aldrich, Ref.: 131903), distilled water, 36% hydrochloric acid and ethanol at a suitable molar ratio to obtain the concentration of SiO<sub>2</sub> sol equal to ≈ 15 % by weight.

Wood samples were placed in a self-made impregnation vessel, evacuated for 5 min up to a 520 mbar vacuum, then showered with SiO<sub>2</sub> sol and delayed for 5 min before the pressure increasing in the vessel up to the atmospheric pressure. Further samples and SiO<sub>2</sub> sol were moved to a custom-made hydraulic isostatic press with the following pressure increase up to 30 MPa with a 5 min hold time. After high-pressure treatment, the samples were placed in a drying oven increasing temperature up to 105 °C with the hold time 24 h at the maximum temperature. Impregnation cycles were repeated three times to achieve sufficient SiO<sub>2</sub> content for SiC ceramics preparation. Pyrolysis of the samples was performed in an oxygen free atmosphere at 500 °C with the rate 120 °C/h to

form a  $\text{SiO}_2/\text{C}_B$  (biocarbon) composite. Further sample processing was performed in a modified high-temperature furnace in an Ar atmosphere for 1600 °C with the rate 300 °C/h. The temperature was raised up to the desired and hold for 4 h to conduct the carbothermal reaction between  $\text{SiO}_2$  and  $\text{C}_B$ , resulting in the formation of  $\beta\text{-SiC}$ .

For crystalline phase identification X-ray diffraction was measured on a powder X-ray diffractometer (PANalytical X'Pert Pro) using Cu radiation produced at 40 kV and 30 mA.

The microstructure of the samples was investigated using a scanning electron microscope (Tescan Mira/LMU).

Fourier transformation infrared spectrometer (Varian Scimitar 800) in the wave number range of 4000-400  $\text{cm}^{-1}$  was used for sample investigations in transmission mode in dry air atmosphere using KBr pellet technology.

### III. RESULTS AND DISCUSSION

#### A. Microstructure investigations

Softwoods such as pine and spruce are generally needle-leaved evergreen trees, whereas hardwoods such as oak and alder are typically broadleaf, deciduous trees. Softwoods and hardwoods differ not only in terms of the types of trees from which they are derived, but they also differ in terms of their component cells. Both softwoods and hardwoods are formed of variety complex micro structural elements described in detail by R.Rowell [16]. The most important difference between the two general kinds of wood is that hardwoods have a characteristic type of cells called vessels whereas softwoods mostly are formed of tracheids (Fig.1).

For not impregnated samples dimension decrease of about 26 % in radial and axial and 31 % in tangential dimension occurred during pyrolysis wherewith dimensions of the pores are respectively smaller. Pore diameters for pyrolysed hardwood samples (Fig. 1b-l) vary in range from 5 – 250  $\mu\text{m}$ . Ash and oak trees have several large pores in diameter around 250  $\mu\text{m}$  while pores in other hardwood derived samples are not bigger than 150  $\mu\text{m}$ . Wall thicknesses of all samples vary from 2 – 20  $\mu\text{m}$  depending of the location.

Softwoods (Fig. 1m,l) consists of more homogenous pores in diameter ranges from 10 – 50  $\mu\text{m}$  and late wood derived pores are round shaped with a thinner cell wall than the rectangular early wood ones.

Obtained sample microstructure from woody evergreen plant bamboo is completely different, having pores of 5 – 200  $\mu\text{m}$  in diameter where pore walls are 2 – 10  $\mu\text{m}$  thick.

Depending of raw material used porous SiC ceramics with different microstructure could be obtained. In present paper pine tree was used as raw material.

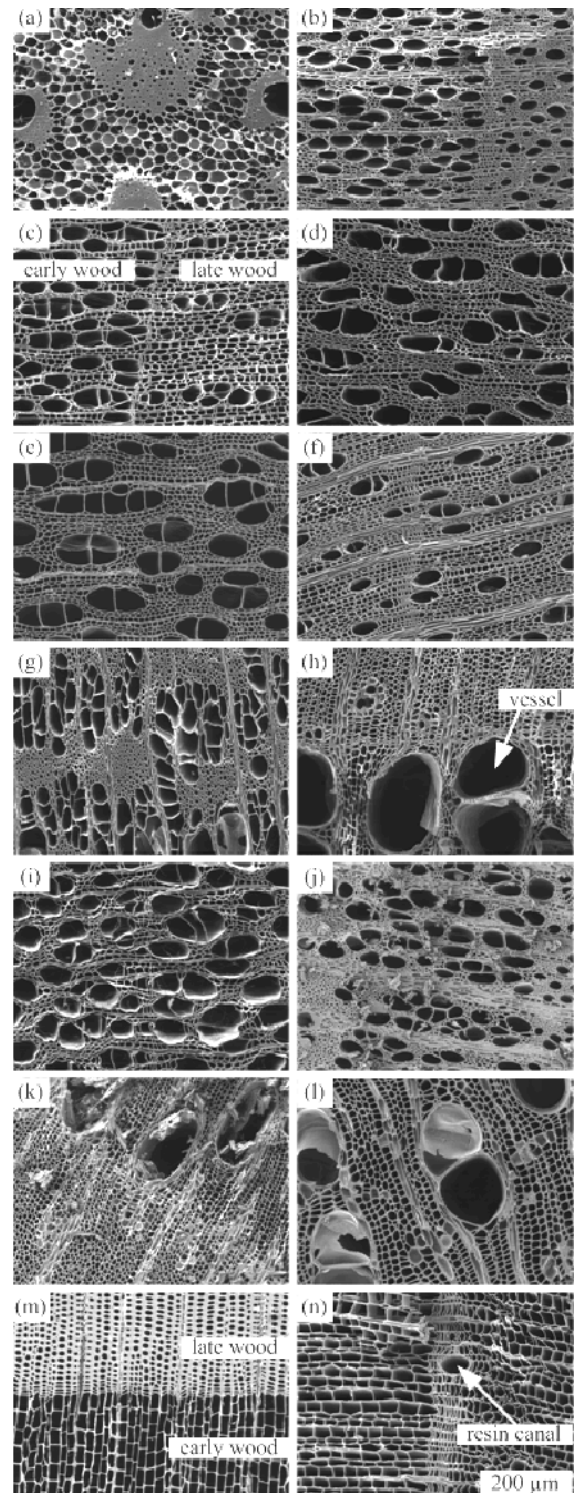


Fig. 1 SEM micrographs of different wooden breeds: woody evergreen plant – (a) bamboo, hardwoods – (b) apple, (c) alder, (d) aspen, (e) birch, (f) maple, (g) elm, (h) ash, (i) lime, (j) plum, (k) oak and (l) mahogany tree and softwoods – (m) spruce and (n) pine tree, pyrolysed at 500°C

### B. SEM, XRD and FT-IR analysis of obtained SiC ceramics

**SEM analysis:** After pine wood is impregnated with  $\text{SiO}_2$  sol subsequent gelling and drying occurs and a  $\text{SiO}_2$  gel/wood composite is formed. After pyrolysis of the  $\text{SiO}_2$  gel/wood composite a  $\text{SiO}_2/\text{C}_B$  composite is formed. SEM micrographs of  $\text{SiO}_2/\text{C}_B$  composite and the porous SiC ceramics obtained at  $1600^\circ\text{C}$  for 4 h are shown in Figure 2. In Figure 2a can be seen that obtained  $\text{SiO}_2/\text{C}_B$  composite has relatively uniform  $\text{SiO}_2$  distribution in pores. In some pores two or three shells of the  $\text{SiO}_2$  can be seen indicating each impregnation cycle. Obtained SiC ceramics (see Fig. 2b) consist of solid pore walls. Dimensions and shape of the pores are close to raw material ones. During  $\text{C}_B$  reaction with  $\text{SiO}_2$  some amount of carbon from pore walls is being loosed in form of gaseous  $\text{CO}$  and  $\text{CO}_2$  thus pore walls of final product become thinner than of  $\text{C}_B$  ones. For both  $\text{SiO}_2/\text{C}_B$  composite and SiC ceramics no cracks in cell walls was observed indicating that accurate temperature treatment was applied during pyrolysis and carbothermal reaction.

Geometrical density of obtained ceramics is  $0.35\text{ g/cm}^3$ . As the density of  $\beta\text{-SiC}$  is  $3.21\text{ g/cm}^3$ , overall porosity of the samples is around 89%.

**XRD analysis:** The XRD patterns of the  $\text{SiO}_2/\text{C}_B$  composite obtained at  $500^\circ\text{C}$  and the porous biomorphic SiC ceramics obtained at  $1600^\circ\text{C}$  are shown in Fig. 3.

It can be suggested that the broad peak centered at  $2\theta = 24^\circ$  is formed by overlying the  $\text{C}_B$  characteristic peak [11] and the amorphous  $\text{SiO}_2$  characteristic peak, both located at around  $2\theta = 24^\circ$  (Fig. 3a). In the XRD pattern of the products obtained at  $1600^\circ\text{C}$  (Fig. 3b) the peaks of the major phase cubic type  $\beta\text{-SiC}$  appear.

An additional diffraction peak (\* marked) is detected at  $2\theta = 33.68^\circ$  which is characteristic of stacking faults on the [111] planes in cubic SiC [17]. Diffraction peaks for crystalline  $\text{SiO}_2$  (cristobalite) is never observed, which indicates that nearly whole amount of silica has been consumed during the carbothermal reduction.

**FT-IR analysis:** Fig. 4 shows the FT-IR spectra of  $\text{SiO}_2/\text{C}_B$  composite after pyrolysis (Fig. 4a) and SiC ceramics

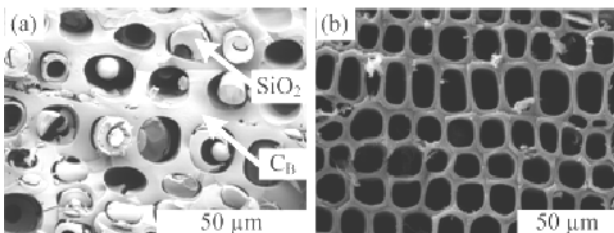


Fig. 2 SEM micrographs of (a)  $\text{SiO}_2/\text{C}_B$  composite and (b) obtained porous SiC ceramics

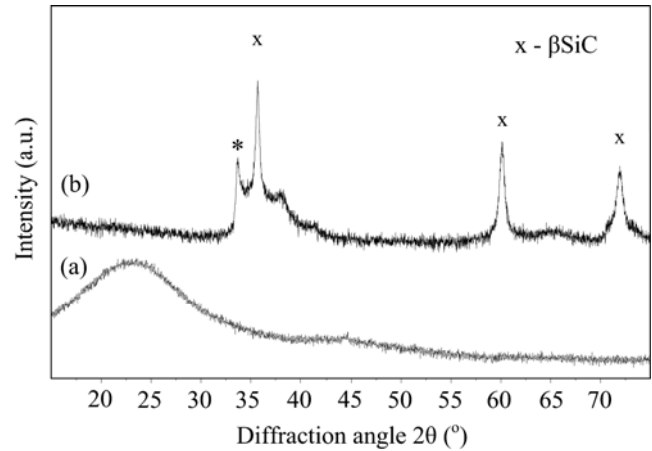


Fig. 3 XRD patterns of (a)  $\text{SiO}_2/\text{C}_B$  composite and (b) obtained porous biomorphic SiC ceramics

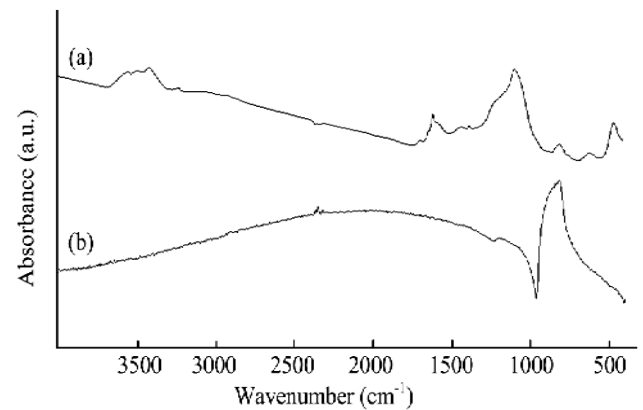


Fig. 4 FT-IR spectra of  $\text{SiO}_2/\text{C}_B$  composite after pyrolysis (a) and SiC ceramics obtained at  $1600^\circ\text{C}$  (b)

ics obtained at  $1600^\circ\text{C}$  in inert atmosphere for 4h (Fig. 4b). In the  $\text{SiO}_2/\text{C}_B$  composite spectrum asymmetric and symmetric stretching vibrations of Si-O-Si bonds at  $1090$ ,  $800$  and  $460\text{ cm}^{-1}$  and  $\text{C}_B$  characteristic C=C bond vibrations at  $1600\text{ cm}^{-1}$  can be observed. In the FT-IR spectrum of products obtained at  $1600^\circ\text{C}$  the peaks assigned to Si-O and C=C bond become meaningless, and nearly only the peaks ascribed to Si-C fundamental stretching vibration at  $825\text{ cm}^{-1}$  exist, suggesting that carbothermal reduction is nearly completed.

## IV. CONCLUSIONS

It is concluded that different wooden breeds has varieties in their microstructure and that is an advantage for obtaining porous biomorphic SiC ceramics having different pore

sizes and distribution. Pore microstructure of the obtained SiC ceramics are close to pyrolysed raw material. In present paper described ceramics obtaining technology is suitable for manufacturing of porous mainly  $\beta$ -SiC phase containing ceramics.

In further investigations also other wooden breeds will be converted into porous ceramics and biocompatibility of products obtained will be examined.

#### ACKNOWLEDGMENT

This work has been partly supported by the European Social Fund within the National Program "Support for carrying out doctoral study program's and post-doctoral researches" project "Support for the development of doctoral studies at the Riga Technical University".

#### REFERENCES

- Singh M, Salem J A (2002) Mechanical properties and microstructure of biomorphic silicon carbide ceramics fabricated from wood precursors. *J Europ Ceram Soc* 22:2709-2717
- Zawrah M F, El-Gazery M (2007) Mechanical properties of SiC ceramics by ultrasonic nondestructive technique and its bioactivity. *Mater Chem Phys* 106:330-337
- Guanjun Q, Rong M, Ning C, Chunguang Z, Zhihao J (2002) Microstructure transmissibility in preparing SiC ceramics from natural wood. *J of Mat Process Tech* 120:107-110
- Vogli E, Sieber H, Greil P (2002) Biomorphic SiC-ceramic prepared by Si-vapor phase infiltration of wood. *J Europ Ceram Soc* 22:2663-2668
- Munoz A, Fernandez J M, Singh M (2002) High temperature compressive mechanical behavior of joined biomorphic silicon carbide ceramics. *J Europ Ceram Soc* 22:2727-2733
- Esposito L, Sciti D, Pinacastelli A, Bellosi A (2004) Microstructure and properties of porous  $\beta$ -SiC templated from soft woods. *J Europ Ceram Soc* 24:533-540
- Klinger R, Sell J, Zimmermann T, Herzog A et al. (2003) Wood-Delivered Porous Ceramics via Infiltration of SiO<sub>2</sub>-Sol and Carbothermal Reduction. *Holzforschung* 57:440-446
- Herzog A, Klingner R, Vogt U, Graule T (2004) Wood-Derived Porous SiC Ceramics by Sol Infiltration and Carbothermal Reduction. *J Am Ceram Soc* 87:784-793
- Vogt U, Herzog A, Graule T et al. (2002) Porous Ceramics Derived from Wood. *Key Eng Mater* 206-213:1941-1944
- Zollfrank C, Kladny R, Sieber H, Greil P (2004) Biomorphous SiOC/C-ceramic composites from chemically modified wood templates. *J Europ Ceram Soc* 24:479-487
- Ota T, Takahashi M, Hibi T, Ozawa M, Suzuki S, Hikichi Y (1995) Biomimetic Process for Producing SiC „Wood“. *J Am Ceram Soc* 78:3409 - 3411
- Castro V, Fujisawa M, Hata T et al. (2004) Silicon Carbide Nanorods and Ceramics from Wood. *Key Eng Mater* 264-268:2267-2270
- Qian J M, Jin Z-H (2006) Preparation and characterization of porous, biomorphic SiC ceramic with hybrid pore structure. *J Europ Ceram Soc* 24:1311-1316
- González P, Serra J, Liste S, Chiussi S et al. (2003) New biomorphic SiC ceramics coated with bioactive glass for biomedical applications. *Biomaterials* 24:4827-4832
- Borrajó J P, Serra J, Liste S, González P et al. (2005) Pulsed laser deposition of hydroxylapatite thin films on biomorphic silicon carbide ceramics. *Appl Surf Sci* 248:355-359
- Rowell R (2005) *Handbook of wood chemistry and wood composites*, CRC Press, Florida
- Shin Y, Wang C, Samuels W D, Exarhos G J (2007) Synthesis of SiC nanorods from bleached wood pulp. *Mater Lett* 61:2814-2817

Author: Janis Locs  
 Institute: Riga Technical University, Riga  
 Biomaterials Innovation and Development Centre  
 Street: Pulka street 3/3  
 City: Riga  
 Country: Latvia  
 Email: janis.locs@rtu.lv

# Release of Quaternary Ammonium Antimicrobial Compounds from Acrylic Bone Cement

J.W. Nicholson<sup>1</sup>, M. Mathey<sup>1</sup> and V. Surana<sup>1</sup>

<sup>1</sup> University of Greenwich, School of Science, Chatham, Kent, UK

**Abstract** — Two quaternary ammonium compounds, namely benzalkonium chloride and cetyl pyridinium chloride, have been studied as additives for incorporation into acrylic bone cement (Palacos K-40) as anti-microbial agents. Each compound was added at 1% and 5% by mass. Setting time of the cement was 9.75 minutes. This was not altered by benzalkonium chloride (5%), but was shortened to 9.00 minutes by 5% cetyl pyridinium chloride.

Release was determined by measuring chloride release from set cement specimens with a chloride-ion selective electrode. Release was shown to occur but it did not follow simple diffusion-based kinetics. Rather it was a complicated process, and similar to that of gentamicin sulphate from bone cements.

The results show that these anti-microbial compounds can be incorporated into acrylic bone cement and then released satisfactorily, suggesting that these compounds have the potential to be used as active ingredients in orthopaedic cements.

**Keywords** — Acrylic bone cement, additives, anti-microbials, release

## I. INTRODUCTION

Acrylic bone cement is used extensively in orthopedic surgery to fix the components of the prosthesis to the bone in both total hip and knee arthroplasty [1]. Currently, the antibiotic, gentamicin sulphate is frequently added to the bone cement to reduce the incidence of post-operative infection [1].

Acrylic bone cement comprises two components, namely a powder consisting of pre-polymerised polymethylmethacrylate (PMMA) and a liquid component, methyl methacrylate monomer (MMA). Typically, the ratio of PMMA powder to MMA monomer used is 2:1. The initiator is benzoyl peroxide, in association with N, N-dimethyl-p-toluidine as accelerator which brings about setting through free radical polymerisation [1-2].

Gentamicin sulphate is added because it is effective in the treatment of several infections, including septicaemia. It is active against many strains of gram negative bacteria and *Streptococcus aureus*. However, it is inactive against anaerobes and only poorly active against *Streptococcus hemolyticus* and *Pneumococcus sp.* [3].

Gentamicin sulphate is typically released from bone cement in a biphasic fashion. This means that in the initial

time period, there is high release of the antibiotic, but later the release of antibiotic declines sharply, and long term release occurs at more moderate levels [4]. Although the release of gentamicin continues for a long period of time, it does not continue to completion. For example, one study showed that implanted bone cement released only about 20% of the total incorporated antibiotic after several months [5, 6].

Despite this retention, gentamicin sulphate is a successful additive to bone cements. Various studies have shown reductions in the incidence of infection when gentamicin sulphate is included in bone cement [7, 8].

However, there is a problem with gentamicin, namely that bacteria have developed to it. Resistant strains of *Staphylococcus sp.* are known and bacterial infections have been observed associated with acrylic bone cement in revision surgery [9].

Alternative antimicrobial compounds therefore need to be considered. In the current work, two such antimicrobials are considered, namely benzalkonium chloride and cetyl pyridinium chloride. These are similar compounds, in that they are quaternary ammonium compounds with some surfactant activity [10].

The current study employed these compounds at levels of 1% and 5% in a commercial acrylic bone cement, and was aimed at determining both the effect of incorporation of the antimicrobial on the setting behaviour of the acrylic cement and the nature and extent of release.

## II. MATERIALS AND METHODS

The bone cement used was Palacos-K40 (Schering-Plough Europe, Belgium). It was mixed in the ratio 2g powder to 1 cm<sup>3</sup> liquid in a glass beaker using a spatula, with mixing taking approximately 1 minute. The antimicrobial compounds used were benzalkonium chloride and cetyl pyridinium chloride [monohydrate] (Sigma-Aldrich, Poole, Dorset, UK). These were incorporated at levels of 1% and 5% by mass (*ie* 0.026 g or 0.144 g respectively for a 2 g/1cm<sup>3</sup> mixture).

Setting behaviour was determined by mixing a sample of cement, and once it attained a dough-like consistency, transferring it to a silicone rubber mould of dimensions

1 cm x 1 cm x 1 cm. A thermocouple was placed at the centre of the mass, and the temperature recorded every 15 seconds. From this data, a graph of temperature vs time was plotted and used to determine the setting time. This was carried out for the cement itself, and cement with 5% of each antimicrobial compound.

Release of chloride was determined from the parent cement and from cement containing antimicrobial compounds at 1% and 5% by mass. Specimens were prepared by mixing samples of cement with and without the antimicrobial compounds, and for each cement type, preparing six cylindrical specimens (6 mm high x 4 mm diameter). These were formed by transferring the cement at the dough stage to split stainless steel moulds of the appropriate size. Cements were allowed to set at room temperature for 20 minutes, then removed from the moulds and placed in individual 5cm<sup>3</sup> portions of deionised water in plastic storage bottles. The release of the chloride ions was detected using a chloride electrode (Model 7065, Electronic Instruments Ltd.) at time intervals of 15, 30, 45, 60, 120, 180, 240 minutes and 2 weeks, and results for amounts released were recorded as means and standard deviations.

Release vs. time was plotted for the 1% and 5% additive-loaded bone cements, in order to determine the nature of the release profiles of chloride from bone cement. In addition, release vs. (time)<sup>1/2</sup> graphs were plotted as required by Fick's second law to test whether release was a diffusion process.

Data on release were tested for significance using the Student-Neumann-Keuls test.

### III. RESULTS

Table 1 shows results for the setting time determined for the bone cement along, and with the addition of 5% by mass of each anti-microbial compound. There was no difference in the presence of benzalkonium chloride, which gave 9.75 minutes, compared with the control, but in the presence of cetyl pyridinium chloride, the working time was shortened slightly to 9.00 minutes.

Release profiles for the first 4 hours of release for benzalkonium chloride at 1% and 5% respectively; are shown in Figures 1 and 2.

Table 1: Working times determined from setting exotherms for cement with and without anti-microbial compound

Cement system	Setting time/min
Cement only	9.75
Cement + 5% benzalkonium chloride	9.75
Cement+ 5% cetyl pyridinium chloride	9.00

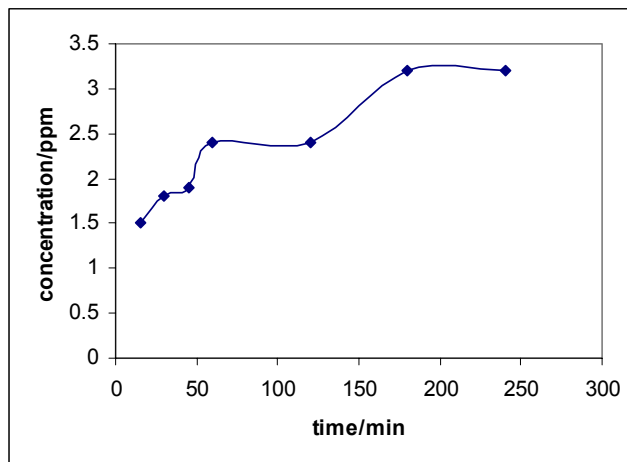


Figure 1: Release profile for 1% benzalkonium chloride

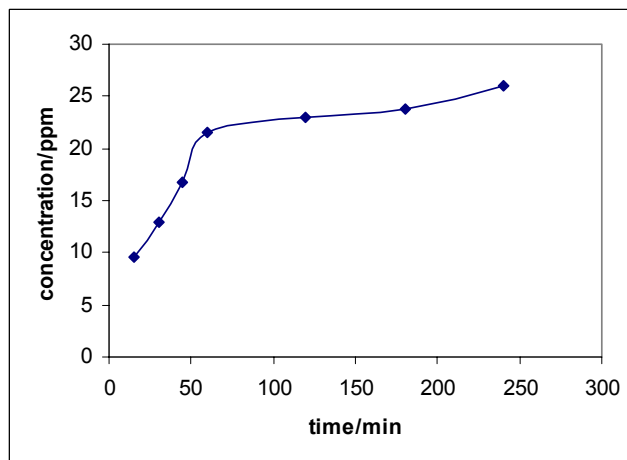


Figure 2: Release profile for 5% benzalkonium chloride

The plot for benzalkonium chloride at 1% concentration appears to show evidence of a two-stage release pattern. However, the release levels at the apparent step were 2.4 ppm (S.D. 1.1 ppm) at 120 s, and 3.2 ppm (S.D. 1.3 ppm), and the difference between these values is not statistically significant.

For benzalkonium chloride at 5%, release reached a plateau at 60 minutes. The actual mean values of release rose between that time and 240 minutes from 21.6 ppm (S.D. 7.8 ppm) to 26.0 ppm (S.D. 12.3 ppm), an increase that was not statistically significant.

Cetyl pyridinium chloride showed similar behaviour at both 1% and 5% levels, in that release rose to a clear plateau region, during which release levels rose by amounts that were small and not statistically significant. For the 1% level, this ranged from 2.5 ppm (S.D. 0.6) at 60 minutes to

2.9 ppm (S.D. 0.6 ppm) at 240 minutes. For 5%, it ranges from 25.3 ppm (S.D. 3.3 ppm) at 120 minutes to 26.6 ppm (S.D. 3.9 ppm).

Replotting these data as release vs. (time)<sup>1/2</sup> graphs did not give straight lines in any case, showing that release is not diffusion based for these compounds from acrylic cements.

#### IV. DISCUSSION

The inclusion of the candidate anti-microbial reagents was found to have little or no effect on the setting of the acrylic bone cement. The setting of methyl methacrylate occurs by an addition polymerization, typically initiated by benzoyl peroxide and accelerated by the presence of an amine [2]. The anti-microbials are both quaternary ammonium salts, so might possibly contribute to the accelerating effect. In fact, only cetyl pyridinium chloride showed any such effect, and then only to a small extent, shortening the setting time by a mere 45 seconds at the 5% level.

Both additives were shown to be released readily over periods of time of up to 2 weeks. The initial levels were studied for possible diffusion release, *ie* by plotting release against (time)<sup>1/2</sup>. However, these plots were not linear, showing that release was not a simple diffusion process in any of the four cases.

This is similar to the release of gentamicin sulphate from acrylic cements. For this substance, release has been shown to continue for at least 5 years [13], and to comprise three contributing mechanisms [14]. They are: (i) short-term initial elution through imperfections in the cement, (ii) stress-cracking due to ingress by aqueous medium, with resulting release of antibiotic, and (iii) permeation by surrounding aqueous medium, thus creating a series of interlocking channels through which the gentamicin sulphate is able to escape. This mechanism gives rise to complex kinetics, despite which the release of gentamicin is a controllable phenomenon and capable of being used in surgical practice.

Our experiments demonstrate some similarities with release of gentamicin sulphate. There is measurable release of anti-microbial from the earliest exposure of the acrylic bone cement to the aqueous storage medium, then a more complicated kinetic process than simple diffusion. This suggests that the release of benzalkonium chloride and cetyl pyridinium chloride may occur by a similar mechanism, as might be expected on the basis of their similar chemical nature.

More work is needed to fully characterise the experimental system we have studied. However, preliminary results are encouraging, and suggest that these compounds may be useful alternatives to the well-established gentamicin sulphate.

#### V. CONCLUSIONS

Both benzalkonium chloride and cetyl pyridinium chloride have been shown to be suitable for incorporation into commercial acrylic bone cement. They have little or no effect on the setting time, and can be released gradually over time from the set cement.

Chloride release from cement did not follow simple diffusion kinetics, but to be a more complicated process. This suggests that the mechanism of release is similar to that of gentamicin sulphate.

Overall, these results show that these anti-microbial compounds have the potential to be used in practical bone cements to prevent post-operative infection associated with hip or knee replacement surgery.

#### ACKNOWLEDGMENT

We thank the Heraeus Kulzer company (United Kingdom) for the gift of Palacos-K40 bone cement for use in these studies.

#### REFERENCES

- 1 Lewis G, Janna S and Bhattaram A, (2005). Antibiotic loaded bone cements in orthopaedic surgery, *J. Joint Bone & Spine*, 70(3): 4315-4325.
- 2 Kuhn KD, Bone cements, Springer-Verlag, Heidelberg, Germany, 2000.
- 3 Pascual B, Vazque B and Gurruchaga M (1996). New aspects of effect of size and size distribution on the setting parameters and mechanical properties of acrylic bone cement, *Biomaterials*, 17(5):509-516.
- 4 Corry D and Moran J (1998). Assessment of acrylic bone cement as a load delivery vehicle for the application of NSAID Drugs, *Biomaterials*, 19(14):1295-1301.
- 5 Hendriks JGE, Van Horn JR and Vandermei HC (2004). Backgrounds of antibiotic loaded bone cement and prosthesis related infection, *Biomaterials*, 25(3):545-556.
- 6 Wroblewski BM, Esser M and Srigley DW (1986). Release of gentamicin from bone cement. An ex-vivo study, *Acta Ortho. Scand*, 57(5):413-414.
- 7 Powles JW, Spencer RF and Lovering AM (1998). Gentamicin release from old cement during revision hip arthroplasty, *J. Bone Jt. Surg.* 80(4):607-610.
- 8 Passuti N and Guin F (2003). Antibiotic loaded bone cement in orthopaedic surgery, *J. Joint Bone & Spine*, 70(3):169-174.
- 9 Kalachandra S and Wilson TW (1992). Water sorption and mechanical properties of light-cured proprietary composite tooth restorative materials. *Biomaterials* 1992;13(2):105-109.
- 10 Van de Belt H, Neut D, Schenth W, Van Horn JR, Jim R. van Horn, Henny C. van der Mei and Henk J. Busscher (2001). Staphylococcus aureus biofilm formation on different gentamicin-loaded poly-methylmethacrylate bone cement, *Biomaterials*, 22(12):1607-1611.

- 11 Neut D, van der Belt H, van Horn JR, van der Mei HC and Bussler HJ (2001). Biomaterial-associated infection of gentamicin-loaded PMMA beads in orthopaedic revision surgery, *J. Antimicrob. Chemother.*, 47(6):885-891.
- 12 Tarbox BB, Conroy BP, Malicky ES, Mossaf FW, Hockman DE, Anglen JO, Simpson WA, Adelstein EH, Christensen G and Gainor BJ, (1998). Benzalkonium chloride: A potential disinfecting irrigation solution for orthopaedic wounds, *Clin. Orthop. Rel. Res.*, 346(1):255-261.
- 13 Neut D, van der Belt H, van Horn JR, van der Mei HC and Bussler HJ (2003). Residual gentamicin release from antibiotic-loaded polymethyl methacrylate beads after five years, *Biomaterials*, 24(10):1829-1831.
- 14 Frutos P, Diez-Peria E, Frutos G and Barrales-Rienda JM (2002). Release of gentamicin sulphate from a modified commercial bone cement, *Biomaterials*, 23 (18):3878-3897.

Address of the corresponding author:

Author: Professor John Nicholson  
Institute: University of Greenwich, School of Science,  
Medway Campus  
City: Chatham  
Country: UK  
Email: J.W.Nicholson@gre.ac.uk



# The Evaluation of Quality and Selection of TiNi Shape Memory Alloy for Medical Purpose

E.G. Novikova<sup>1</sup>, S.A. Atroshenko<sup>2</sup>

<sup>1</sup> St-Petersburg State University of Engineering and Economics, Saint-Petersburg, Russia

<sup>2</sup> Institute for Problems of Mechanical Engineering, Saint-Petersburg, Russia

**Abstract** — Two methods of estimation of quality of materials in conditions of high-speed loading are presented: differential method and a method of sector diagrams. The given methods allow to make an estimation of quality of materials applied in medicine, in particular stomatology.

**Keywords** — Shape memory alloy, shock loading, quality level, method, cobweb.

## I. INTRODUCTION

Now opportunities of application in medicine of new materials with the set properties (smart materials) are widely known. As these materials, as a rule, understand materials, which under action of external factors (temperatures, mechanical loading, etc.) can cardinaly change the properties in the necessary direction. Superelastic alloys concern to such shape memory materials. Shape memory alloys and, first of all, TiNi are more widely and more effectively used in various areas of medicine and stomatology, becoming a basis of new technologies and bringing exclusively positive results. In stomatology TiNi has found application at manufacturing endodontic instruments, systems and intrabone implant at prosthetics of support of a teeth and dental artificial limbs

Biological tolerance nickel-titanic shape memory alloys allows to use effectively them at a long finding and functioning of products from them in an organism. Alongside with a high level of biochemical and biomechanical compatibility, and to opportunities of self-fixing to these materials the same rheological laws of deformation are inherent, as in biological tissues that it makes TiNi superelastic shape memory alloys optimum at correction abnormal bite and precision prosthetics.

In some cases a product from such alloys during using can be exposed to actions of excited environments and shock loadings. This question is especially actual in stomatology, and, in particular, in prosthetics of teeth. The situation when own healthy teeth can break away or break at sharp movement or hit of a firm subject is frequent, therefore it is important, that implants could not only resist to similar influences alongside with a natural teeth, but also surpass the given characteristics. In this connection research these materials

and estimation of quality of TiNi shape memory alloys in conditions of shock loading is important. Results of a similar estimation help to carry out selection of various materials depending on final conditions of application.

The analysis and contrast of different materials are obstructed by the availability of large quantity of individual characteristics of them. It is necessary that materials evaluation was complex for solution of such kinds of problems. To present there are quite many different methods of evaluation of manufacturing product quality. But the quantity of special works concerning complex evaluation of technical materials quality is not enough.

For materials definite list of quality indicators exists. It is analogous the production quality ones. This list includes the following:

- function indicator;
- reliability indicator;
- safety indicator;
- aesthetic indicator;
- generalize indicator and so on.

But not all of these indicators can be applied in every specific case. The opportunity to use each indicator depends on the field of application and function of material.

The application of differential method of quality evaluation is the way for solution this problem.

The essence of differential method of evaluation of production quality consists of comparison of separate properties indicators of estimating specimen with correct indicators of basic specimen. During this procedure there are determined whether the correspondence of quality for estimating product to basic specimen quality is achieved in the whole, and what properties indicators of estimating product exceed or not correspond with basic specimen indicators and what extend analogous properties indicators differ one from another.

## II. EVALUATION OF QUALITY BY DIFFIRANCIAL METHOD

The value of total quality indicator, i.e. quality level  $L_T$  can be accounted as a definition of average arithmetical

magnitude of all levels of taking into account properties  $L_i$  of comparing (evaluating and basic) specimens as follows:

$$L_T = \frac{1}{n} \sum_{i=1}^n L_i, \quad (1)$$

where  $L_i$  – quality level of individual property can be determined according relation:

$$L_i = \frac{P_e}{P_b}, \quad (2)$$

where  $P_e$  – evaluating property and  $P_b$  – basic property.

But in the case of influence of shock wave testing on materials it is impossible to determine the basic value of properties. Therefore it is expedient in this case to use threshold values for basic properties.

Two TiNi shape memory alloys were used for analysis and estimation of quality. These materials containing 44,9% Ti, 55,1% Ni and with addition of 3%Cu were subjected explosive loading. The results of these testing are presented in Table 1.

Specimens-targets were in the form of disks 15 mm in diameter and parallelepipeds 23x18 mm<sup>2</sup> in square and with a thicknesses of 1,6 - 4,5 mm. Load pulses of different durations were created by impact of aluminum flyer-plates with a thicknesses of 0,2 - 4,0 mm. Backside spallation was realized under uniaxial strain conditions within the velocity range 600-700 m/s [1].

According with the experimental data basic indicators are accepted as follows:

- specimen thickness – 1,5 mm;
- flyer thickness – 2 mm;
- loading velocity – 700 m/s;
- pull-back velocity – 300 m/s;
- spall strength – 10 GPa.

Table 1 Primary data

Material	Specimen thickness H, mm.	Flyer thickness h, mm.	Loading velocity V, m/s	Pull-back velocity W, m/s	Spall strength $\sigma$ , GPa
1. Ti-Ni	1,61	0,2	600	94	3,177
2. Ti-Ni-Cu3	1,6	0,2	600	268	9,058
3. Ti-Ni-Cu3	3,96	0,4	630	230	7,774
4. Ti-Ni-Cu3	4,42	2	700	180	6,084
5. Ti-Ni-Cu3	4,5	2	700	100	3,38

Table 2 Values for quality levels

Material	L(H)	L(h)	L(V)	L(W)	L( $\sigma$ )	Quality level $L_T$
1. Ti-Ni	0,93	0,1	0,86	0,31	0,32	0,50
2. Ti-Ni-Cu3	0,94	0,1	0,86	0,89	0,91	0,74
3. Ti-Ni-Cu3	0,38	0,2	0,9	0,77	0,78	0,61
4. Ti-Ni-Cu3	0,34	1	1	0,60	0,61	0,71
5. Ti-Ni-Cu3	0,33	1	1	0,33	0,34	0,60

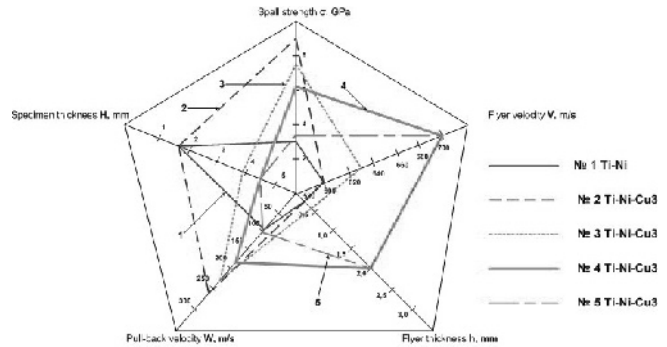


Fig. 1 The quality cobweb for nitinol

The values of quantity levels accounted according with relations (1) and (2) are presented in Table 2.

Specimens 2 and 4 with additions of copper in their contents have the highest quality level as it is seen from Table 2. These data are in agreement with quality cobweb (Figure 1) where it is clearly seen what approach is better and in what way.

The quality cobweb for definition of quality level for nitinol specimens is presented in Figure 1. It is received in accordance with experimental and accounted indicators using fifth basic properties presented at the fifth qualimetric scales.

Approach N1: Low spall strength, Low flyer velocity, Low pull-back velocity

Approach N2: High spall strength, Low flyer velocity, High pull-back velocity

Approach N3: Medium spall strength, Low flyer velocity, Medium pull-back velocity

Approach N4: Medium spall strength, High flyer velocity, Medium pull-back velocity

Approach N5: Low spall strength, High flyer velocity, Low pull-back velocity

The values of properties indicators are registered at the appropriate scales. Their points are joined together and five polygons are formed. It is seen from the cobweb that square occupied by polygons N2 and N4 is the largest and by poly-

gon N1 is the smallest. It is testified that quality level of material N2 is the best on complex properties in spite of the value of separate indicators are minimum. Besides the quality level of specimen N2 can be considered the best because this sample has maximum value of spall strength. The spall strength in this case is the determinative indicator. On account of this reason specimen N4 is inferior in sample N2 because it has less value of spall strength. It is obviously the minimum of quality level value for specimen N1 without copper addition. At the cobweb this sample forms polygon with the smallest square. It is caused by minimum values of practically all parameters.

Thus, differential method of quality evaluation is reasonable for quality estimation of materials underwent high-strain-rate loading. Given method allows us to account total quality indicator of specimen or quality level. At the same time this method admits us to present in diagram form how and what extend various specimens differ each other.

As can be seen in Figure 1, five different approaches are generally possible with respect to the good quality of material.

Approach N1, which involves a low spall strength, has the disadvantage that the damage arrest requirements may not be fulfilled.

Approach N2, which involves a highest spall strength, ensures excellent resistance for damage as well as fully satisfactory other properties, despite the relatively low flyer velocity. The spall strength should therefore be considered acceptable for the purpose of current standardization.

Experience gained meanwhile indicates that Approach N2 is the best choice. This approach enables the desired property profile to be achieved through an optimized spall strength.

It is necessary to note, that for stomatologic implants strength is important at sharp shock influences. Therefore in this case the priority and important characteristic is spall strength. Therefore the alloy with approach № 2 is the best variant in the given conditions.

### III. EVALUATION OF QUALITY BY ALTERNATIVE METHOD

Alternative way of representation of quality level during the estimation of quality of materials can be use of sector diagrams [2]. Sector diagrams are plotted by relative parameters of quality and their weight numbers. Each parameter is represented on the diagram in the form of circular sector which radius is equal to value of a parameter concerning the chosen analogue, and the central corner - to the weight number expressed in degrees or radians. Base values of all parameters are represented by a circle with radius

Table 3 Data for quality level of the sample 4

№ pp	Sample	Basic values	№ 4	Relative value, $r_i$	Weight number, $\alpha_i$	$\varphi$ , degree
1.	Specimen thickness H	1,5	4,42	0,34	0,19	68
2.	Flyer thickness h	2	2	1,00	0,07	25
3.	Loading velocity V	700	700	1,00	0,21	76
4.	Pull-back velocity W	300	180	0,60	0,2	72
5.	Spall strength $\sigma$	10	6,084	0,61	0,33	119
	Sum	-	-	-	1	360

Table 4 Data for quality level of the sample 2

№ pp	Sample	Basic values	№ 4	Relative value, $r_i$	Weight number, $\alpha_i$	$\varphi$ , degree
1.	Specimen thickness H	1,5	1,6	0,94	0,19	68
2.	Flyer thickness h	2	0,2	0,10	0,07	25
3.	Loading velocity V	700	600	0,86	0,21	76
4.	Pull-back velocity W	300	268	0,89	0,2	72
5.	Spall strength $\sigma$	10	9,058	0,91	0,33	119
	Sum	-	-	-	1	360

equal to unit. The central corner for  $i$  parameter with weight number  $\alpha_i$  is defined as  $\varphi = 2\pi\alpha_i$  rad ( $\varphi_i = 360^\circ\alpha_i$ , degree).

The quality level is defined on the basis of the complex average weighed parameter  $L_q$  called by an average weighed circular parameter. It is equal to radius of a circle which area is equal to the sum of the areas of sectors of the diagram. Its estimation can be made with the formula (3):

$$L_q = \sqrt{\sum_{i=1}^n \alpha_i r_i^2}, \tag{3}$$

where  $n$  – number of relative parameters of quality;

$\alpha_i$  – weight number;

$r_i$  – value of  $i$  parameter.

It's probably to compare by this technique 2 best samples which were defined by a differential method. Weight numbers are received by expert judgments- a method of ranging. The received values of samples № 4 and № 2 are presented accordingly in figures 2 and 3 (tables 3 and 4).

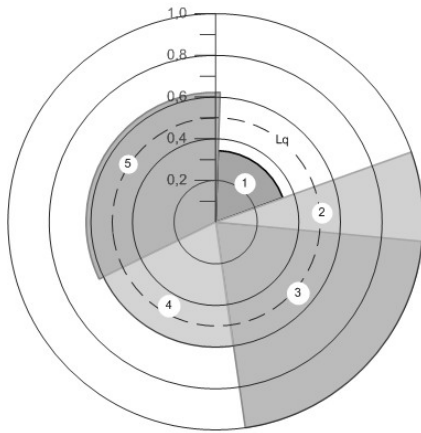


Fig. 2 Diagram of quality level for sample 4

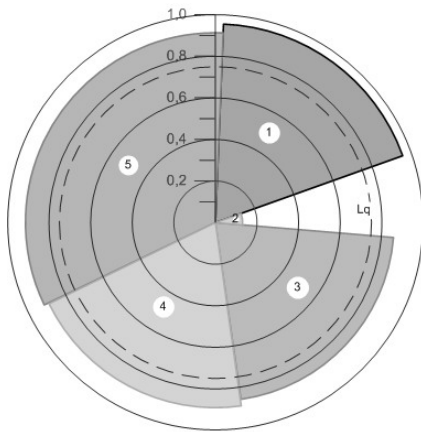


Fig. 3 Diagram of quality level for sample 2

$L_q$  is close to the average weighed arithmetic parameter. Value of the average weighed circular parameter graphically is presented by a circle in the form of a dashed line:

$$L_{q4} = \sqrt{0,19 \cdot 0,34^2 + 0,07 \cdot 1^2 + 0,21 \cdot 1^2 + 0,2 \cdot 0,6^2 + 0,33 \cdot 0,61^2} = 0,496$$

$$L_{q2} = \sqrt{0,19 \cdot 0,94^2 + 0,07 \cdot 0,1^2 + 0,21 \cdot 0,86^2 + 0,2 \cdot 0,89^2 + 0,33 \cdot 0,91^2} = 0,752$$

$Y_K < 1$  means that a quality level of the given sample below of basic one.

#### IV. RESUME

Thus, this estimation confirms earlier drawn conclusions that quality of the sample № 2 is better. Calculated with weigh numbers factors for two samples show that quality level of the sample № 2 on 65,9 % is more than quality level of the sample № 4. It is evidently visible on sector diagrams in what parameters one surpasses another.

#### REFERENCES

1. Atroshenko S.A., Barkova E.G., Razorenov S.V. Influence on shock loading on quality characteristics of shape memory alloys // Vestnik of engecon. Technical science series, 2006. V. 3 (12). pp. 160 – 163.
2. Zheleznov G.S. Graphical representation of quality level and quality index of production // Methods of quality management, 2002. № 12. pp. 26 – 27

Author: Novikova Evgeniya  
 Institute: St-Petersburg State University of Engineering and Economics  
 Street: Marata, 27  
 City: Saint-Petersburg  
 Country: Russia  
 Email: ebarkova@mail.ru

# Ions Release from Ti Implant Alloys in Simulated Bioliquids

M. Prodana<sup>1</sup>, M. Caposi<sup>1</sup>, D. Iordachescu

<sup>1</sup> University Polytechnica Bucharest/General Chemistry Department, Bucharest, Romania

<sup>2</sup> University of Bucharest/Biology Faculty, Bucharest, Romania

**Abstract** — The aim of this work was to evaluate the electrochemical behaviour of TiNiNb, TiAlV and TiAlZr in 0,9% NaCl (isotonic sodium chloride solution) and SBF (simulated body fluid). The surface of TiNiNb, TiAlV and TiAlZr alloys was mechanically polished and investigated with electronic microscopy. The hydroxyapatite (HA) layer appears on the surface of the samples due to the precipitation process from SBF. Their biocompatibility was demonstrated and sustained with cell cultures and the ion released concentrations were evaluated by inductively coupled plasma mass spectrometry ICP-MS measurements [1].

**Keywords** — TiNiNb, TiAlV and TiAlZr, surface treatments, electrochemical behavior, surface analyses, biocompatibility.

## I. INTRODUCTION

The release of nickel, vanadium and zirconium from titanium alloys is often responsible for allergic contact dermatitis despite the amounts of metal released from titanium alloys in trace amounts, taking into account the excellent corrosion resistance of the alloys.

Despite the excellent biocompatibility of thin native oxide film on titanium alloys implants, native titanium oxide is known as an inert ceramic biomaterial.

The success of many metallic biomaterials is in direct relation with surface treatments applied in order to improve cell adhesion and proliferation and immersion in SBF is a method of bioactivation.

However the stability of Ti alloys is a property desirable for an implant material, taking into account that even small amount of some ions are subject of toxic activity. This paper analyses the corrosion behavior and cations released from Ti alloys [1,2] in direct relation with their biocompatibility in terms of cell viability.

Since interactions between cells and titanium alloys implants (TiNiNb, TiAlV and TiAlZr) occur at their interfaces, surface characteristics of titanium alloys are essential.

## II. EXPERIMENTAL SETUP

### Materials:

The test solution used 0,9 % NaCl (isotonic sodium chloride solution) and SBF (simulated body fluid).

The studied alloys are TiNiNb, TiAlV and TiAlZr with a composition presented in table 1 as followings:

Table 1 Alloys composition

Alloy	Al	V	Zr	Ti	Nb	Ni
TiNiNb	1.06	-	-	42.36	10.75	42.23
Ti-6Al-4V	5.88	3.72	-	balance	-	-
Ti-6Al-4Zr	6.01	-	4.05	balance	-	-

The biomaterials samples were discs, mechanically polished with emery paper with different grain sizes, washed with distilled water, etched in 3% HF 20% HNO<sub>3</sub> for 3 min, degreased in benzene for 3 min, prolonged rinsed with distilled water and dried. The surface treatment was a deposition of Ca and P from SBF solution with a composition according to table 2.

After the surface preparation, each specimen was cleaned in deionized water for 5 min and dried in air.

**Methods:** -Electrochemical procedures;  
-Surface analysis;  
-Biocompatibility tests;  
-ICP-MS analysis.

### Electrochemical procedures:

The electrochemical measurements were conducted using a standard three-electrode cell. A Pt wire of large-enough area was used as auxiliary electrode, Ag/AgCl was the reference electrode and each Ti alloys as an working electrode.

Electrochemical measurements were carried out with a Voltalab 40 interfaced with a computer using Voltmaster 4 software for data acquisition and analysis and all the experiments were carried out at room temperature (20±2°C).

The electrodes were then treated by holding them at -800 V for 5 min to give a reproducible initial condition. Finally the scan was started at -800 V using a sweep rate of 2mV/sec and reversed at 1500 V.

Table 2 SBF composition

Medium	Ion concentration (mM)							
	Na <sup>+</sup>	K <sup>+</sup>	Ca <sup>2+</sup>	Mg <sup>2+</sup>	Cl <sup>-</sup>	HPO <sub>4</sub> <sup>2-</sup>	HCO <sub>3</sub> <sup>-</sup>	SO <sub>4</sub> <sup>2-</sup>
SBF	142	5.0	2.5	1.5	147.8	1.0	4.2	0.5

**Surface analysis:** Topographical features of alloys surface after immersion in studied solution were put in evidence using scanning electronic microscopy with an Environmental Scanning Electron Microscope FEI/Phillips XL30 ESEM. The ESEM equipment has an energy dispersive X-ray analysis module (EDAX) [4]. After 14 days SBF immersion revealed a presence of Ca and P ions over surface.

**Biocompatibility:**

In order to study the biocompatibility of the discs alloys after immersion in NaCl and SBF, the samples were sterilised in ultraviolet light, on the both sides and inseedinated with osteoblasts cells of the celular line G 292 (250 000 cells / Petri plate). The culture cells was monitorised 24 h. The citotoxicity and viability were investigated with a Olympus microscope in phases contrast with epifluorescence system with photo digital camera and quantified with MTT test. This method measures the proliferation and cell viability, and is based on the reduction of the yellow tetrazolium MTT (3-(4,5-dimethylthiazolyl-2)-2,5-diphenyltetrazolium bromide) to formazan, a purple compound.

**ICP-MS analysis:**

ICP-MS analysis performed with an ELAN DRC-e equipment permitted low concentration determination ( $\mu\text{gL}^{-1}$ ) of total metal content in fluids.

### III. RESULTS AND DISCUSSION

In figure 1 its shows the evolution of Ti alloys in NaCl 0,9% and SBF:

a) *Ti alloys in NaCl 0,9%:*

In the first minutes of Ti alloys immersion, the potential varying in very small limits, around -300mV. After 5000 minutes of immersion the potential for TiAlV has a remarkable variation, it begin to increase to a stable value around 20000 minutes, because of protective film on the Ti alloys surface. The stable potential value are for TiAlV around 200 mV, for TiAlZr around 100 mV and the TiNiNb around 50 mV. For the TiAlZr and TiNiNb, the potential increase in the first minutes of immersion to a very stable value. All the potential values are higher than the start potential values.

b) *Ti alloys in SBF:*

In the first hours after Ti alloys, exists a variation of the potential toward more electronegative values. After 15000 minutes of immersion, all potential values become positives due to reconstruction of the protective film on the Ti alloys surface.

Figure 1 (a-b): Open circuit potential for Ti alloys electrodes immersing in NaCl 0,9% and SBF solution.

Electrochemical behavior:

Figures 2 (a-b) present cyclic voltammograms of TiNiNb in 0,9% NaCl and SBF

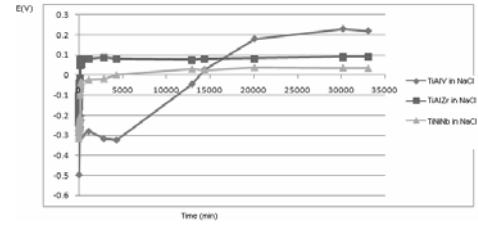


Fig. 1a Evolution of the electrode potential in open circuit for alloys electrodes immersing in NaCl 0.9%

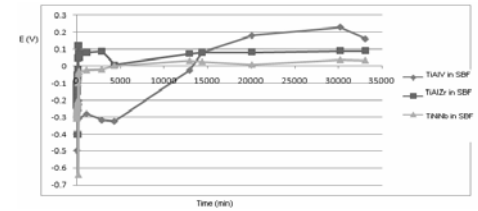


Fig. 1b Evolution of the electrode potential in open circuit for alloys electrodes immersing in SBF

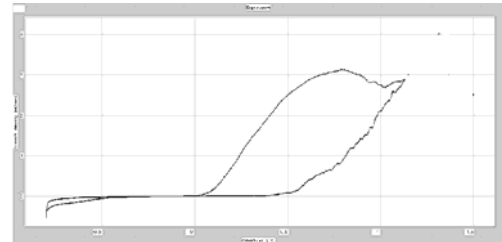


Fig 2a Cyclic voltammogram of TiNiNb in 0,9% NaCl

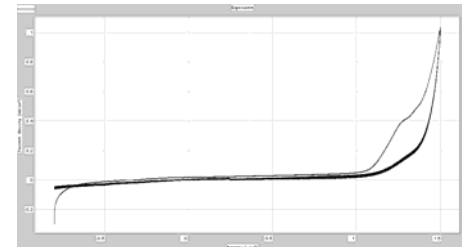


Fig.2b Cyclic voltammogram of TiNiNb in SBF

The corrosion resistance of titanium alloys, particularly TiNiNb, TiAlV, TiAlZr strongly depends on the performance of their protective passive film.

In table 3, the electrochemical parameters of Ti alloys in indicate electrochemical stability. The order of the electrochemical stability (S) of the Ti alloys is: S TiAlV>S TiAlZr> S TiNiNb.

The electrochemical parameters for Ti alloys in SBF are listed in table 4. The order of the stability is: S TiAlV>S TiAlZr> S TiNiNb.

Table 3 The main electrochemical parameters of Ti alloy in NaCl

Sample	$E_{cor}$ (mV)	$I_{cor}$ ( $\mu\text{A}/\text{cm}^2$ )	$V_{cor}$ ( $\mu\text{m}/\text{year}$ )
TiNiNb in NaCl	-38,4	2,14	20,55
TiAlZr in NaCl	-385	0,185	2,1
TiAlV in NaCl	-353	0,15	1,9

Table 4 The main electrochemical parameters for Ti alloys in SBF

Samples	$E_{cor}$ (mV)	$I_{cor}$ ( $\mu\text{A}/\text{cm}^2$ )	$v_{cor}$ ( $\mu\text{m}/\text{an}$ )
TiNiNb in SBF	-33	1,59	16,12
TiAlZr in SBF	-294	0.178	2,0
TiAlV in SBF	-250	0.12	1,2

Higher  $i_{corr}$  values for alloy in NaCl suggest that its surface is less corrosion resistant than alloy in SBF.

The behavior of the TiAlZr alloy in 0,9% NaCl present a passive region with lower passive current density. It can be observed for the TiAlZr in SBF a lower value for current density, confirming the beneficial effect of the immersion in SBF.

The presence of SBF puts in evidence the decreases of corrosion current and also, the decreases of corrosion rate. The composition of thin layer was obtained from the EDAX spectrum (fig. 5); this spectrum confirms that the depositions on TiAlZr surface were composed of calcium and phosphorous elements due to the precipitation process [6].

To study the effect of the cyclic polarization test on the surface morphology of the samples, SEM micrographs of the sample surface were captured after the test.

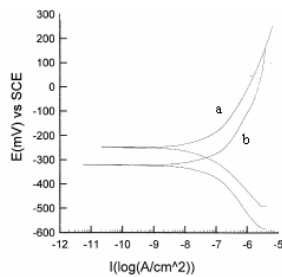


Fig 3 The allure of anodic polarization curves for TiAlZr a) in SBF, b) in NaCl

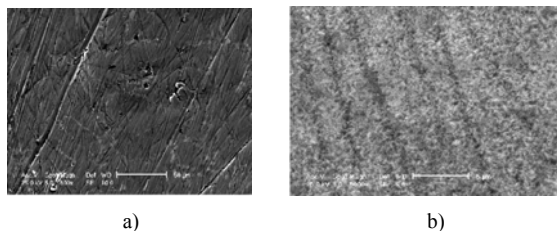


Fig. 4 SEM imagine of: a) TiAlZr in NaCl; b) TiAlZr in SBF after cyclic polarization

SEM images are according to electrochemical data, on the surfaces after polarization not exist local corrosion forms (pitting).

Fig. 5 presents the EDAX spectrum and put in evidence the change of the composition of thin films. The oxygen content marked an increase while titanium and nickel a decrease. These changes have implications on the electrochemical properties.

Figure 6 shows SEM [8] for TiNiNb mechanically polished and figure 7 the EDAX for TiNiNb mechanically polished after cyclic polarization in NaCl 0,9%.

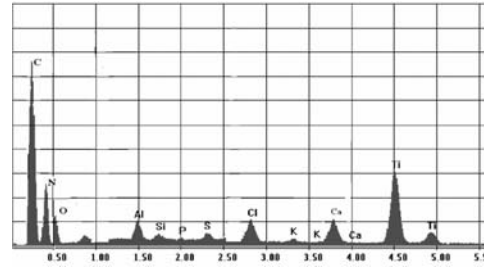


Fig. 5 EDAX spectrum for TiAlZr in SBF

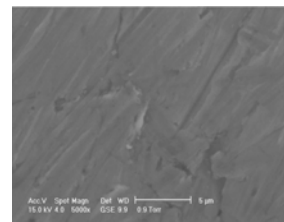


Fig 6 SEM for TiNiNb in NaCl

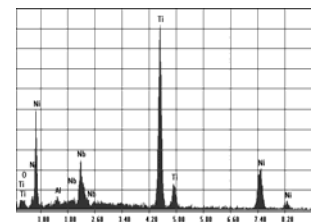


Fig.7 EDAX for TiNiNb in NaCl

Citotoxicity tests:

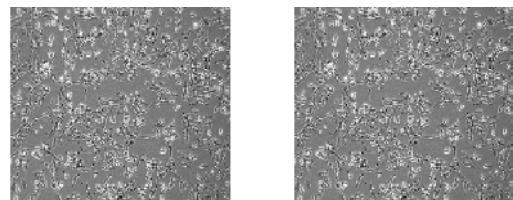


Fig. 8 Control sample

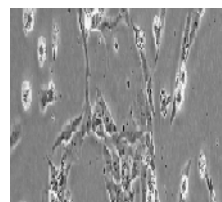


Fig. 9 TiAlZr in NaCl

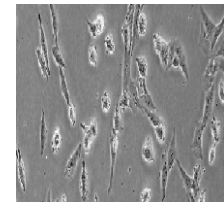


Fig. 10 TiAlZr in SBF

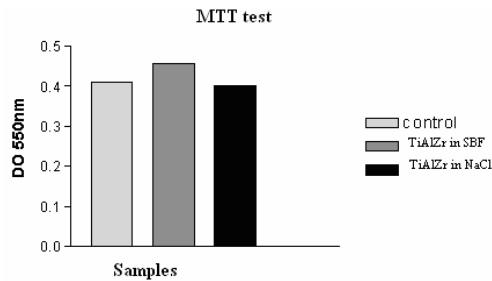


Fig.11 MTT test for cells viability

Table 5 MTT test parameters

Sample	DO 550 nm	viability %
Control	0,4097	100 %
TiAlZr in SBF	0,4579	112 %
Ti Al Zr in NaCl	0,4023	98 %

Table 6 Ions release quantity from titanium alloys

Samples	Period of time	Ions release concentration ppb			
		Ti	Al	V	Ni
TiNiNb in 0.9%NaCl	after 2 weeks	2.6	-	-	10.7
	initial	1.8	-	-	8.9
TiNiNb in SBF	after 2 weeks	1.3	-	-	8.5
	initial	0.8	-	-	6.4
TiAlZr in 0.9% NaCl	after 2 weeks	12.3	2.3	-	-
	initial	5.5	0.6	-	-
TiAlZr in SBF	after 2 weeks	5.7	1.4	-	-
	initial	1.2	0.2	-	-
TiAlV in 0.9% NaCl	after 2 weeks	4	1.5	7.5	-
	initial	3.2	0.6	3.1	-
TiAlV in SBF	after 2 weeks	0.9	1.1	5.7	-
	initial	-	0.2	3.2	-

The samples are not cytotoxic, the MTT test put in evidence close values of optical density DO (fig.11). We can say that the samples have a high biocompatibility degree.

After 2 weeks of immersion the quantity of Fe, Al, Ni, V released was higher in 0.9% NaCl than in SBF for all the alloys samples [9]. The ions release amount for the Ti alloys in SBF are lower than for NaCl immersion. The Ti ions released into SBF were much lower than in 0.9% NaCl. The layer has a positive effect on corrosion resistance of metallic substrate, and decreases the corrosion current density being a distinct advantage for prevention of ion release [1,7].

#### IV. CONCLUSIONS

For the Ti alloys samples in SBF, the corrosion current and the corrosion rate evaluated by electrochemical techniques show that the presence of the calcium phosphate on the surface improves the corrosion resistance of metallic substrate. The corrosion current and the corrosion rate are lower for the alloys samples in SBF than for the alloys samples in NaCl 0.9%.

The studied alloys present low corrosion currents densities in the tested media and a electrochemical stability.

SBF testing incorporate inorganic ions in superficial layer (Ca and P), this phenomena contributes to a increasing of the cellular viability. Ca and P presence on the surface as a result of bioactivation procedure induced and increase in biocompatibility values.

ICP-MS measurements indicate smaller ion released amounts.

#### ACKNOWLEDGMENT

Special thanks to Prof. Dr. Ing. D. Bojin for SEM analysis.

#### REFERENCES

- Hanawa T (2004) Metal ion release from metal implants. *Materials Science and Engineering C24*: 745-752
- Harding I S, Rashid N, Hing K A (2005) Surface charge and the effect of excess calcium ions on the hydroxyapatite surface. *Biomaterials* 26: 6818-6826
- Ibrektsson, T (1998) *J Oral Maxillofac Surg.* 56: 1312-1326
- Lim, Y J, Oshida, Y, Andres, C J, Barco, M T (2001) *Int J Oral Maxillofac Implants*, 16: 333-342
- Wu, Y, Yang, B C, Lu J, Gu Z W, Zhang X D (2007) *Key Engineering Materials* 330-332: 581-585
- Prodana M, Bojin D, Ionita D, Popa M, Vasilescu E, Drob P (2008) Biomimetic Hybrid Inorganic/Organic Coatings in the Increasing of the Integration Capacity of TiAlVZr Bioalloy. *Mol. Cryst. Liq. Cryst.* 486: 133-139
- Ionita D, Ciohodaru L, Prodana M, Demetrescu I, (2008) Metallic Ion Release from Titanium Alloy and Stainless Steel Coated With Electrolytic Calcium Phosphate (HA). *Key Engineering Materials* 361-363: 729-732
- Caposi M, Ionita D, Miculescu F, Demetrescu I, (2007) Surface Treatments in Electrochemical Behaviour of TiNi Wires for Implant Purposes. *Revista de Chimie* 9:875-879
- Ionita D, Man I, Demetrescu I (2007) *Key Engineering Materials* 330-332: 545-549.

Author: Mariana Prodana  
 Institute: University Politehnica Bucharest  
 Street: Polizu, No. 1  
 City: Bucharest  
 Country: Romania  
 Email: prodana\_mariana@yahoo.com



# Stress-Strain State of System “Bone-Implant” Analyzed by FEM and its Comparison with Experimental Results

L. Rupeks, V. Filipenkovs, I. Knets, J. Laizans, V. Vitins

Riga Technical University, Institute of Biomaterials and Biomechanics, Riga, Latvia

**Abstract** — In the last fifty years in medicine, engineering and other sciences widely is used finite element method (FEM), it is cost-effective alternative to the experimental approach for solving wide range of implant-biological tissue issues [1,2]. This method is applied for determination of stress-strain states in different systems. In the present study a stress-strain state of reconstruction system bone-implant was determined in theory by finite element program ANSYS. In order to solve this problem the mechanical characteristics of bone tissue were taken from literature [3], but characteristics of implants were obtained in experimental way in biomechanics laboratory in Riga Technical University. Afterwards obtained results were compared with the experimental ones.

In our experimental work two types of new composite implant materials are investigated. The first type of the biomaterials is based on silicate glass (SG) and hydroxyapatite. Both, the natural (NHAp) and synthetic hydroxyapatite (HAp) were used. The second type of the biomaterials made from ultrahigh molecular mass polyethylene (UHMMPE) and the natural hydroxyapatite. Their mechanical characteristics, biocompatibility and the dynamics of bond strength between the bio composites and live bone tissue are determined.

**Keywords** — bond strength, implantation, finite element method, biocompatibility.

## I. INTRODUCTION

Various biomaterials, such as alumina, hydroxyapatite, titan, Co-Cr-Mo and Ti-Al-V alloys, methyl methacrylate, polyethylene, composites based on porous nanohydroxyapatite, collagen and alginate, as well as many other play an important role in the creation of artificial materials for replacing bone tissue [4,5]. In this case, of first importance is the problem of designing material close to natural bone tissue in its mechanical characteristics and biocompatibility. Such materials include polyethylene and silicate glass (SG), reinforced with hydroxyapatite [6].

In the present study, a procedure is described for obtaining NHAp and artificial HAp hydroxyapatites, as well as composite materials based on them, namely ultrahigh molecular mass polyethylene UHMMPE-NHAp, SG-NHAp and SG-HAp.

The structure of bone tissue before and after deproteinization and the structure of composite materials

based on UHMMPE and NHAp (with different percentage) were investigated by the method of scanning electron microscopy[5]. Some mechanical characteristics of UHMMPE-NHAp, SG-NHAp and SG-HAp biocomposite materials and the bond strength between a live bone tissue of rabbits and SG(60)-HAp(40), SG(60)-NHAp(40), UHMMPE(70)-NHAp(30) and UHMMPE(50)-NHAp(50) composites were determined.

Also in the present study a stress-strain state of reconstruction system bone-implant was determined in theory by the finite element program ANSYS.

## II. PROCEDURE

The stress-strain state of reconstruction system *bone-implant* was determined by the finite element program ANSYS. Solving this theoretical problem values of characteristics of mechanical properties such as elastic modulus (E), Poisson's ( $\mu$ ) ratio were taken from literature and tests. For cortex bone tissue E was taken from 7 to 14 GPa, and  $\mu$  was taken from 0.3 to 0.4 [3]. For implantation material E was taken 0.385 GPa and 6.0 GPa, and  $\mu$  was taken 0.35 respectively [5].

The callus was located between bone tissue and implantation material in FEM model. It was as interface between bone tissue and implantation material. Values of E and  $\mu$  for callus were taken from 0.000005 to 14 GPa, and from 0.49 to 0.3 respectively. Displacement's value was taken 0.1 mm. This problem was solved several times using different values of E and  $\mu$ .

The natural hydroxyapatite for biomaterials was obtained from the bone tissues of cattle. Then the NHAp and UHMMPE particles were mixed for 10 min at  $t=180-200$  °C. Detailed methodology of preparation of NHAp is described in [5].

The characteristics of mechanical properties of these materials are shown in Table 1.

The structure of bone tissue before and after deproteinization, as well as the structure of compositions based on UHMMPE and NHAp (with different percentage), was investigated by the method of scanning electron microscopy [5].

Table 1. Mechanical characteristics of composite materials based on UHMPE and NHAp.

Material, wt.%	$\sigma_1^*$ , MPa	$E$ , MPa	$\varepsilon_1^*$ , %
UHMPE(70)-NHAp(30)	50.6±2.1	327±27	229±10
UHMPE(60)-NHAp(40)	35.2±3.7	368±45	161±25
UHMPE(50)-NHAp(50)	29.5±1.9	385±123	9±4

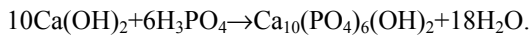
Table 2. Comparison between the experimental and calculated data by Eq. (1) elastic moduli (MPa) of composite materials based on silicate glass and hydroxyapatite

Material, wt %	Experiment	Calculation by Eq. (1)	Difference, %
SG(80)-HAp(20)	3282±701	3877	15.35
SG(60)-HAp(40)	6929±987	6677	3.64
SG(40)-HAp(60)	4516±429	5388	16.18
SG(80)-HAp(20)	3674±730	4332	15.19
SG(60)-HAp(40)	6235±1301	6606	5.62
SG(40)-HAp(60)	4899±1028	5418	9.6
SG(80)-NHAp(20)	3321±755	3979	16.54
SG(60)-NHAp(40)	5967±1150	6202	3.79
SG(40)-NHAp(60)	4059±437	4621	12.16
SG(60)-NHAp(40)	5772±359	5663	1.89
SG(40)-NHAp(60)	3277±271	3053	6.83

Table 3. Mechanical characteristics of composite materials based on silicate glass and hydroxyapatite.

Material, wt. %	$\sigma_1^*$ , MPa	$E$ , MPa	$\rho$ , g/cm <sup>3</sup>	Manufacturing temperature of materials, °C
SG(80)-HAp(20)	42.05±10.48	3282±701	1.146	800
SG(60)-HAp(40)	263.7±73.3	6929±987	2.110	800
SG(40)-HAp(60)	95.49±29.9	4516±429	1.830	800
SG(80)-HAp(20)	59.50±4.93	3674±730	1.280	750
SG(60)-HAp(40)	196.1±98.95	6235±1301	2.088	950
SG(40)-HAp(60)	109.7±73.26	4899±1028	1.840	950
SG(80)-NHAp(20)	35.98±12.79	3321±755	1.199	750
SG(60)-NHAp(40)	179.6±92.8	5967±1150	2.043	850
SG(40)-NHAp(60)	97.57±7.91	4059±437	1.680	850
SG(60)-NHAp(40)	161.0±20.7	5772±359	1.866	950
SG(40)-NHAp(60)	103.78±11.2	3277±271	1.110	950

The HAp was synthesized in laboratory conditions from Ca(OH)<sub>2</sub> and H<sub>3</sub>PO<sub>4</sub> as a result of the reaction



During the experiment, it was found that the mechanical properties considerably depended on the material density, which, in turn, was determined by the temperature at which they were manufactured. Taking into account the change in the density of the composite materials because of the porosity arising in their producing, the E of the materials can be calculated theoretically from the formula

$$E_{c.m} = (E_m + (E_f - E_m)V_f)k_\rho, \quad (1)$$

where  $E_m$  and  $E_f$  are the elastic moduli of the matrix and filler;  $V_f$  is the volume content of filler;  $k_\rho$  is the coefficient determining the relation between the true  $\rho$  and theoretical  $\rho_t$  density of the material:

$$k_\rho = \frac{\rho}{\rho_t}, \text{ where } \rho_t = \frac{\rho_m V_m + \rho_f V_f}{V_m + V_f}.$$

Here,  $\rho_m$  and  $\rho_f$  are the densities of the matrix and filler, and  $V_m$  is the volume content of the matrix. The test results and the values calculated from formula (1) are given in Table 2. From the data in this table, it is seen that the difference between the experimental and calculated values of elastic modulus is about 10% on the average.

The biocompatibility and bond strength between the artificial biomaterials and a live bone tissue were tested on adult rabbits. In the femur of rabbits was implanted following biocomposites: SG(60)-HAp(40), SG(60)-NHAp(40), UHMMPE(70)-NHAp(30), and UHMMPE(50)-NHAp(50). The specimens were cylinders 3 mm in diameter and 3 mm in height. The biocomposites were implanted in 48 rabbits.

### III. RESULTS

When an implant is applied to the bone surface, the bond strength between the bone tissue and the implant is one of the most important factors indicative of the reliability of fixing the implant to the bone tissue.

Figure 1. shows theoretical results of stress-strain state of reconstruction system *bone-implant* by using  $E_{bone} = 14 \text{ GPa}$ ,  $\mu_{bone} = 0.3$ ,  $E_{implant} = 6 \text{ GPa}$ ,  $\mu_{implant} = 0.35$ ,  $E_{callus} = 5 \text{ GPa}$ ,  $\mu_{callus} = 0.49$

The theoretical data of stress-strain state of reconstruction system *bone-implant* show that the stresses increase in the system with the increases of elastic modulus and shear modulus of callus. Also these data demonstrate that the punching out force reaches almost its maximum at  $E_{zz(callus)} = 5 \text{ GPa}$

$$(G_{yz} = \frac{E_{zz}}{2(1 + \mu)} = \frac{5}{2(1 + 0.49)} = 1.678 \text{ GPa}).$$

A value of the punching out force does not increase significantly when elastic modulus of callus reaches the value of the elastic modulus of the implant (Fig.2).

All the specimens implanted were punched out from the bone tissue in 2, 4, 10, and 25 weeks after implantation. The data in Fig. 3 show that the bond strength between the UHMMPE(50)-NHAp(50), SG(60)-HAp(40), and SG(60)-NHAp(40) composite biomaterials and the surface of the cortical bone increases considerably in four weeks after the implantation, and reaches almost its maximum in 10 weeks.

The SG(60)-HAp(40), SG(60)-NHAp(40), and UHMMPE(50)-NHAp(50) composites, having sufficiently good mechanical properties and a good bond strength with the cortical bone tissue, can be recommended as implant

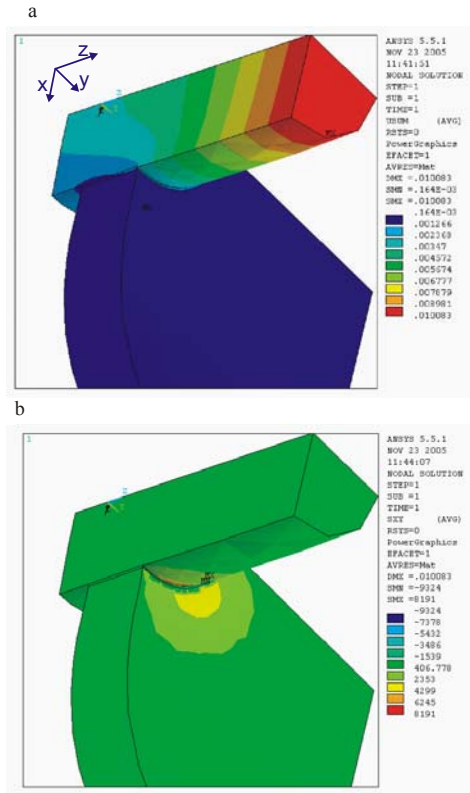


Fig. 1. The stress-strain state of reconstruction system *bone-implant*: a- total displacement; b-shear in XY plane.

materials for covering bone defects in order to create a new bone structure after orthopedic interventions.

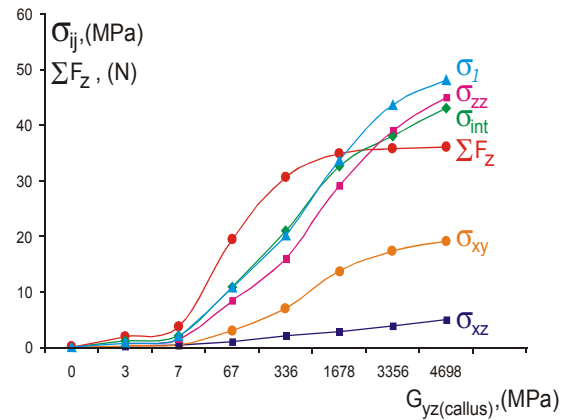


Fig. 2. The relationship of  $\sigma_{ij} - G_{yz(callus)}$  and  $\sum F_z - G_{yz(callus)}$  in the reconstruction system *bone-implant*.  $\sigma_1$  - maximal main stress;  $\sigma_{zz}$  - maximal normal stress;  $\sigma_{int}$  - maximal general stress;  $\sum F_z$  - total force in knots;  $\sigma_{xy}$  and  $\sigma_{xz}$  - maximal tangent stress

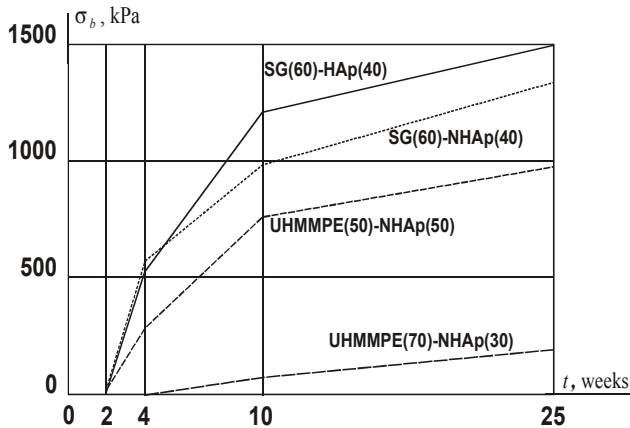


Fig. 3. Bond strength  $\sigma_b$  between the bone tissue and implants at various instants of time after implantation  $t$ .

A comparison between the composites based on UHMMPPE and NHAp has shown that a change in the matrix-filler ratio changes the mechanical characteristics of this material. A greater percentage of filler increases the E and decreases both the breaking strength and the strain at break.

As seen from the data in Table 3, mechanical characteristics of composite materials based on SG-HAp and SG-NHAp, such as the breaking stress in compression and the elastic modulus, depend on the density of the materials.

The results obtained show that the bond strength of composite biomaterials based on SG-HAP and SG-NHAp with bone tissue is better than that of the materials based on UHMMPPE-NHAp.

## REFERENCES

1. DeHoff P. Kenneth J. Anusavice J. Gotzen N. (2006) Viscoelastic element analysis of an allceramic fixed partial denture. *J. of Biomechanics* 39: 40-48
2. Shefelbine J. Augat P. Claes U. (2005) Trabecular bone fracture healing simulation with finite element analysis and fuzzy logic. *J. of Biomechanics* 38: 2440-2450
3. Natali A. N, Meroi E. (1989) A review of the biomechanical properties of bone as material. *J. Biomed. Eng.* Vol. 11, 266-276.
4. Duan Y. R, Wang Y, Chen J. (2005) Dynamic study of calcium phosphate formation on porous HA/TCP ceramics. *Materials in Medicine*: 795-801.
5. Filipenkov V, Knets I. (2005) Technology and some mechanical properties of biocomposites based on mineral components. *J. mechanics of Composite materials*, Vol. 41, 273-282.
6. Genovese K, Lamberti L, Pappalettere C. (2005) Finite element analysis of new customized composite post system for endodontically treated teeth. *J. of Biomechanics* 38: 2375-2389.

Author: Lauris Rupeks  
 Institute: Riga Technical University,  
 Institute of Biomaterials and Biomechanics.  
 Street: Kalku 1, LV 1648  
 City: Riga  
 Country: Latvia  
 Email: victor@ktf.rtu.lv

# Fourier Transform Infrared Spectra of Technologically Modified Calcium Phosphates

K. Salma, N. Borodajenko, A. Plata, L. Berzina-Cimdina, A. Stunda

Riga Biomaterials Innovation and Development Centre, Riga Technical University, Riga, Latvia

**Abstract** — Calcium phosphate powders were synthesized by wet-chemical precipitation method using  $\text{CaCO}_3$  and  $\text{H}_3\text{PO}_4$  as starting materials. Influence of technological parameters on chemical composition of as-prepared and thermal treated calcium phosphate samples were investigated. The following technological parameters were varied: temperature of the suspension during the process of synthesis ( $T$ , °C), ending pH value, aging time of suspension ( $\tau$ , h) and thermal processing ( $T$ , °C;  $\tau$ , h). The obtained calcium phosphates powders were identified and characterized using Fourier transform infrared spectroscopy method and X-ray diffraction. FTIR spectra of as-synthesized calcium phosphate powders showed characteristic chemical bands of hydroxyapatite ( $\text{PO}_4^{3-}$ ,  $\text{OH}^-$ ,  $\text{H}_2\text{O}$  absorbed,  $\text{CO}_3^{2-}$ ,  $\text{HPO}_4^{2-}$ ) at definite wave number ranges. Carbonate and  $\text{OH}^-$  absorbed bands disappear after calcination above 900°C. The experimental results of FTIR spectra X-ray diffraction showed biphasic mixtures containing HAp and  $\beta$ -tricalciumphosphate ( $\beta$ -TCP). The secondary phase ( $\beta$ -TCP) was formed after calcination HAp samples at 1000°C and above.

**Keywords** — calcium phosphates, synthesis, infrared spectra.

## I. INTRODUCTION

Various calcium phosphate-based bioceramics have been used as implantation materials for more than twenty years. There is a great interest in the preparation of biphasic ceramics from calcium phosphates such as hydroxyapatite (HAp) and a more resorbable  $\beta$ -tricalcium phosphate ( $\beta$ -TCP) in different proportions depending on the characteristics required for the specific application [1].

Several techniques have been utilized for the preparation of hydroxyapatite and biphasic calcium phosphates (BCP). The specific chemical, structural and morphological properties of calcium phosphates are highly sensitive to the changes in synthesis conditions such as the temperature of suspension in process of synthesis ( $T$ , °C), ending pH value of the suspension, thermal treatment etc. [2].

In this work calcium phosphates were obtained using wet-chemical precipitation method that is simple and inexpensive.

## II. MATERIALS AND METHODS

### A. Calcium phosphates synthesis

Calcium phosphate powders were synthesized by wet-chemical precipitation method using  $\text{CaCO}_3$  and  $\text{H}_3\text{PO}_4$  as starting materials. These synthesis series varied with following technological parameters: temperature of the suspension during the process of synthesis ( $T$ , °C), ending pH value, aging time of suspension ( $\tau$ , h) and thermal processing ( $T$ , °C;  $\tau$ , h).

During the synthesis such technological parameters as rate of acid solution addition, mixing speed and time, final pH of the calcium phosphate suspension, thermal conditions, were controlled.

The final pH was stabilized in the range of 6-11 using phosphoric acid solution. The temperature of suspension during synthesis was varied in the range of 20 to 70°C. The calcium phosphate suspensions were aged for 24 h at room temperature and then filtered. The filtered precipitates were dried at 105°C for 24 h and then pressed into sample tablets. The obtained powder samples were calcined in temperatures ranging from 800 to 1300°C for 1 h.

### B. Characterization of synthesized calcium phosphates

All of the as-dried and heat treated calcium phosphate powder chemical composition was identified and characterized using Fourier transform infrared spectroscopy (FTIR) and phase analyzed with X-ray diffraction (XRD).

FTIR was used to determine the various functional groups in the synthesized and calcined calcium phosphate powders. X-ray diffraction patterns showed that all as-dried and calcined calcium phosphate samples consisted of HAp and  $\beta$ -TCP phases.

X-ray diffractograms of all samples were recorded on X'Pert PRO PAN Analytical diffractometer. IR spectra were measured on Scimitar Series model Varian 800 FTIR spectrometer in the wave number region 400-4000  $\text{cm}^{-1}$ . All IR measurements were carried out at room temperature using the KBr pellet technique.

### III. RESULTS AND DISCUSSION

Seven technologically modified calcium phosphate syntheses series were studied by X-ray diffraction and FTIR analysis. X-ray diffraction patterns of as-synthesized calcium phosphates showed that all powders were partially crystalline. All as-prepared calcium phosphate powders consisted of single phase - HAp as indicated by XRD (Fig. 1).

FTIR spectra of calcium phosphates synthesized with different ending pH value of calcium phosphate suspensions (which was varied from 6 to 11) are shown in Fig. 2. All these IR spectra showed the vibration modes of  $\text{PO}_4^{3-}$  ions at 460, 550-600, 960 and 1020-1100  $\text{cm}^{-1}$ ,  $\text{OH}^-$  groups (630 and 3570  $\text{cm}^{-1}$ ) of the hydroxyapatite phase for all syntheses [3]. The presence of absorbed water could also be detected from FTIR spectra – respectively in the region around 3300-3500  $\text{cm}^{-1}$ . Some bands derived from ions  $\text{CO}_3^{2-}$  were observed at 875  $\text{cm}^{-1}$  and around 1420 and 1480  $\text{cm}^{-1}$ . It might be due to the absorption of atmospheric carbon dioxide during the sample preparation [4]. Low intensity  $\text{OH}^-$  ions derived bands at 630 and 3570  $\text{cm}^{-1}$ , which are typical of stoichiometric HAp, are also observed [5]. It is shown that independently of the different ending pH value, all as-dried syntheses have characteristic chemical bands of hydroxyapatite at definite wave number ranges. The carbonate bands for HAp prepared with pH 11 have showed stronger peaks than syntheses with the pH value in the range of 6-9 (Fig. 2). Also, increasing ending pH value of synthesis induced the substitution of  $\text{PO}_4^{3-}$  ions with  $\text{CO}_3^{2-}$  ions [6, 7].

The IR spectra in Fig. 3 show that the obtained calcium phosphate synthesis product has a typical apatite structure. IR spectra of the HAp samples shown in Fig. 3 have been calcined in the temperature range of 800-1300°C. There are significant changes in intensity and appearance of the peaks corresponding to carbonate and hydroxyl groups. It was

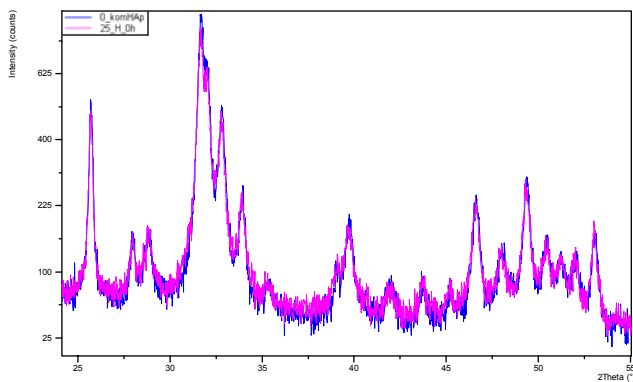


Fig. 1 X-ray diffraction pattern of as-synthesized calcium phosphate dried at 105°C 24 h in comparison with powder X-ray diffraction pattern of the commercial HAp

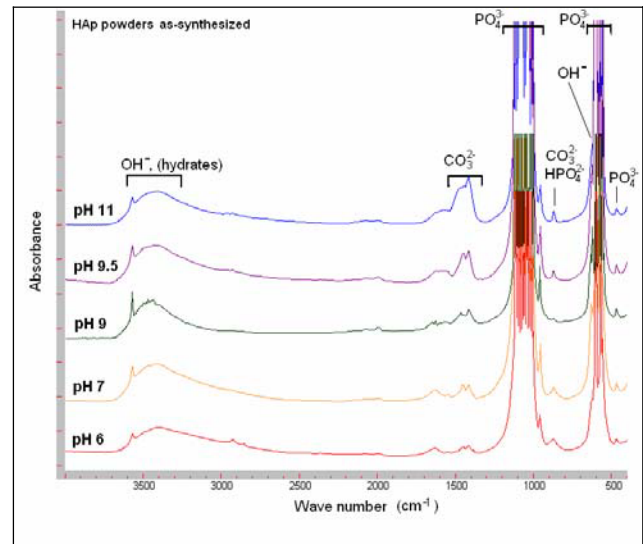


Fig. 2 IR spectra of as-synthesized calcium phosphate powders with different ending pH value dried at 105°C 24 h

found that, at 800°C, the carbonate ions were partially included in the apatite structure. At 1150°C the sample

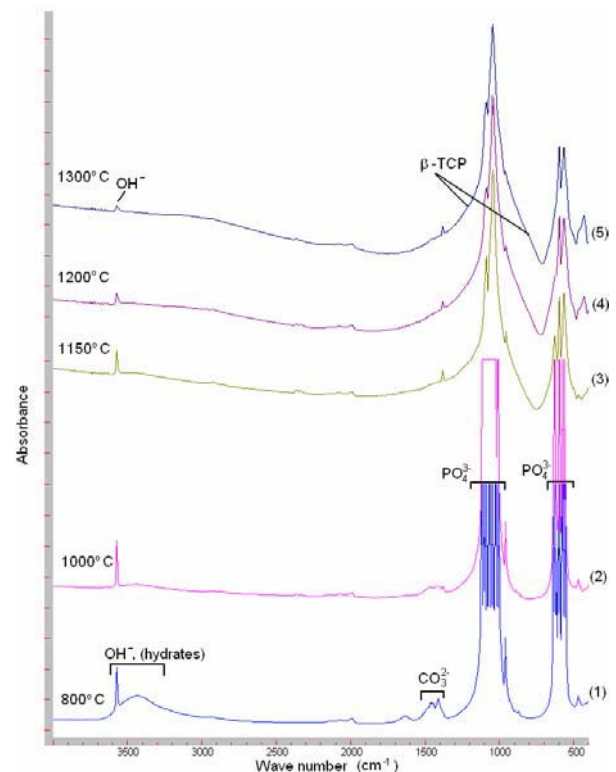


Fig. 3 IR spectra of calcium phosphate synthesis (ending pH=9, T=70°C, τ=24 h) product calcined at temperature range of 800 -1300°C

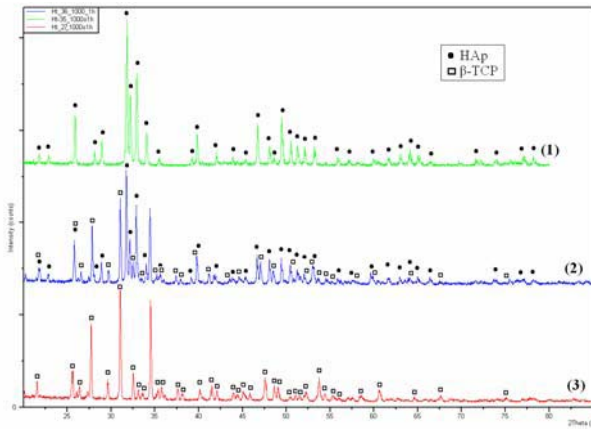


Fig. 4 X-ray diffraction patterns of 3 calcium phosphates syntheses obtained at different pH values and calcined at 1000°C for 1 h

became free of carbonate ions. Furthermore, it is important to point out that  $\text{OH}^-$  absorption bands were also affected by the elevated temperature. The  $\text{OH}^-$  peaks, at about  $3500\text{ cm}^{-1}$ , become narrower at  $1000^\circ\text{C}$ , indicating the removal of some amount of hydroxyl component such as water from the crystalline structure. After heat treatment at  $1150^\circ\text{C}$ , the  $\text{OH}^-$  absorption band disappeared and the IR spectrum in Fig. 3(3) some minor phase feature of  $\beta$ -TCP is present. It can be observed from the band shoulders around  $959$ ,  $975$  and  $1130\text{ cm}^{-1}$  [8].

As shown in Fig. 3(4)-(5), the characteristic peaks of  $\beta$ -TCP can be detected more obviously for the hydroxyapatite samples calcined at  $1200^\circ\text{C}$  and above, along with changes of the positions of the  $\text{PO}_4^{3-}$  vibration bands at  $571$  and  $601\text{ cm}^{-1}$  to  $569$  and  $602$ , as well as at  $1045$  and  $1089\text{ cm}^{-1}$  to new position at  $1051$  and  $1091\text{ cm}^{-1}$ . This indicates that hydroxyapatite has partially decomposed [8, 9].

The phase analysis of technologically modified calcium phosphate syntheses are shown in Fig. 4. The calcium phosphate sample XRD pattern in Fig. 4(1) synthesized at  $\text{pH}=9$  shows that the product calcined at  $1000^\circ\text{C}$  consists of a single well crystallized phase – hydroxyapatite (Fig. 4(1)) [10]. The XRD pattern of sample synthesized at  $\text{pH}=6$  (Fig. 4(2)) shows that this sample is a biphasic mixture of hydroxyapatite and  $\beta$ -TCP.

The FTIR spectra of two calcium phosphate powder samples synthesized at different pH and calcined at  $1200^\circ\text{C}$  for 3 h (Fig. 5) have different phase composition. The sample (Fig. 5(1)) is hydroxyapatite and sample, Fig. 5(2) is biphasic mixture of HAp and  $\beta$ -TCP.

FTIR studies have shown that the ending pH value can significantly change the phase composition of calcium phosphates. Therefore, the  $\beta$ -TCP content in HAp powder is found to be highly dependent on the changes in

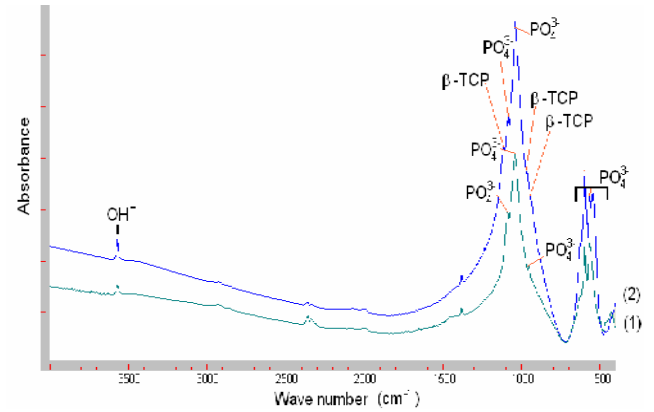


Fig. 5 IR spectra of two calcium phosphates syntheses obtained at different pH values ( $\text{pH}=9$  (1),  $\text{pH}=6$  (2)) and calcined at  $1200^\circ\text{C}$  for 3 h

technological parameters and it can be controlled with ending pH value and thermal treatment. The results of our studies have confirmed the influence of the synthesis conditions on the synthesis product of calcium phosphates.

#### IV. CONCLUSIONS

In this study, calcium phosphate powders were successfully synthesized using a modified wet-chemical precipitation method and excellent HAp,  $\beta$ -TCP and HAp/ $\beta$ -TCP was obtained.

The ending pH values for synthesis and the temperature of calcination were varied. HAp,  $\beta$ -TCP and their biphasic mixture formation parameters were investigated for each composition.

Pure  $\beta$ -TCP was successfully synthesized if the ending pH value was 6.8-7. In order to synthesize biphasic HAp/ $\beta$ -TCP composite powders, the ending pH value should be smaller than 7.

The phase composition of synthesized calcium phosphates depends on calcination temperature. Stable stoichiometric hydroxyapatite can be obtained if ending pH is 9 and above and calcination temperature is  $1000^\circ\text{C}$ .

#### ACKNOWLEDGMENTS

This work has been partly supported by the European Social Fund within the National Programme „Support for the carrying out doctoral study programm’s and post-doctoral researches” project „Support for the development of doctoral studies at Riga Technical University.

## REFERENCES

1. Peña J, Vallet-Regí M et. al. (2003) Hydroxyapatite, tricalcium phosphate and biphasic materials prepared by a liquid mix technique. *J Eur Ceram Soc* 23: 1687-1696
2. Smičiklas I et. al. (2005) Experimental design approach in the synthesis of hydroxyapatite by neutralization method. *Separat and Purificat Tech* 44: 97-102
3. Kwon S H et. al. (2003) Synthesis and dissolution behavior of  $\beta$ -TCP and HA/  $\beta$ -TCP composite powders. *J Eur Ceram Soc* 23: 1039-1045
4. Ślósarczyk et. al. (2005) FTIR and XRD evaluation of carbonated hydroxyapatite powders synthesized by wet methods. *J Mol Struct* 744-747: 657-661
5. Kumata P N et. al. (2005) Nanostructured calcium phosphates for biomedical applications: novel synthesis and characterization. *Acta Biomaterialia* 1: 65-83
6. Liu J et. al. (2003) The influence of pH and temperature on the morphology of hydroxyapatite synthesized by hydrothermal method. *Cerami Int* 29: 629-633
7. Mostafa N Y (2005) Characterization, thermal stability and sintering of hydroxyapatite powders prepared by different routes. *Macromol Chem Phys* 94: 33-341
8. Meejo S et. al. (2006) Phase and thermal stability of nanocrystalline hydroxyapatite prepared via microwave heating. *Thermochim Acta* 447: 115-120
9. Rapacz-Kmita A et al. (2005) FTIR and XRD investigation on the thermal stability of hydroxyapatite during hot pressing and pressureless sintering processes. *J Mol Struct* 744-747: 653-656
10. Kuriakose T A et. al. (2004) Synthesis of stoichiometric nano crystalline hydroxyapatite by ethanol-based sol-gel technique at low temperature. *J Cryst Growth* 263: 517-523

Author: Kristine Salma  
Institute: Riga Biomaterials Innovation and Development Centre  
Street: Pulka Str. 3/3  
City: Riga  
Country: Latvia  
Email: kristine.salma@rtu.lv



# Reactogenicity of Synthetic Hydroxyapatite (HAp) Ceramic Materials Implanted in Rabbits Jaws

I. Salma<sup>1</sup>, M. Pilmane<sup>2</sup>, J. Vetra<sup>2</sup>, L. Berzina-Cimdina<sup>3</sup>, G. Salms<sup>1</sup>, A. Skagers<sup>1</sup>

<sup>1</sup> Riga Stradins University, Department of Oral and Maxillofacial Surgery, Riga, Latvia

<sup>2</sup> Riga Stradins University, Institute of Anatomy and Anthropology, Riga, Latvia

<sup>3</sup> Riga Technical University, Center for Innovation and Development of Biomaterials, Riga, Latvia

**Abstract** — Experimental comparing of morphofunctional changes in implant contact tissue with same tissue involved in surgical intervention of same manner without insertion of artificial materials can clarify specific reactogenicity of implant and/or material. To evaluate early reactogenicity of porous synthetic HAp ceramic implants inserted in holes of rabbit upper jaw assessment of inflammatory response and regeneration in contact bone and soft tissue using histological and immunohistochemical methods was done. Our results demonstrated stimulation of TGFB and FGFR1 in bone after HAp implantation indicating possible osseoinductive role for the same Hap implants. Also moderate apoptosis and rich expression of FGFR1 in connective tissue around HAp implants commonly indicated intensive regeneration ability of the soft tissue with such cell death type that does not cause the fibrotic changes. Neuropeptide-containing innervation was not involved in healing processes after HAp implantation.

**Keywords** — hydroxyapatite ceramic, reactogenicity, growth factors, apoptosis

## I. INTRODUCTION

Early stages in osseointegration of bone substitutes run in close interaction of inflammatory and regenerative processes. Biomaterials of different origin as natural and synthetic have different mechanisms of host response. Synthetic HAp is artificially created main mineral constituent of bone and as such has no biological ingredients possible to initiate immunological response. Synthetic calcium phosphate ceramic bone substitutes as hydroxyapatite (HAp) and tricalcium phosphate (TCP) are used in restoration of lost jaw bone especially in preprosthetic surgery to provide size and quality for osseointegrating structures with dental implants. It is based on osteoconductive properties and even osteoinductive action of HAp proven by osteogenesis after implantation far away from bone [1, 2, 3, 4]. Porosity and pore size of biomaterials play a role for tissue ingrow resulting in formation of stable but remodeling hybrid structure of living tissue and bioceramics [5, 6]. Our results may enhance comprehension on reactogenicity of HAp bioceramic implants as bone substitutes. To evaluate early reactogenicity of porous synthetic HAp ceramic implants

inserted in holes of rabbit upper jaw assessment of inflammatory response and regeneration in contact bone and soft tissue using histological and immunohistochemical methods was done.

## II. MATERIALS AND METHODS

Porous hydroxyapatite (HAp) ceramics were obtained from HAp powder synthesized in Riga Technical University using wet chemical method from  $\text{Ca}(\text{OH})_2$  and  $\text{H}_3\text{PO}_4$  solutions and calcinated at 800 °C. The synthesized powder was marked as HAp-L29. Commercial HAp powder (Riedel – de Haën® 04238) was used for comparison. To form green bodies HAp powder was mixed with paraffin wax and gelatin (70:25:5) and uniaxially pressed in form of cylinder 2 mm diameter. The green bodies were sintered at 1100°C. The sintering temperature was chosen according to optical dilatometry data (Fig. 1).

The porosity of obtained ceramics was 25% – 30 %, water uptake 10 – 13% from mass and volume mass 2.1 – 2.2 g/cm<sup>3</sup>. XRD analysis patterns of the HAp-L29 sintered porous ceramic were compared with commercial HAp powder. XRD analysis of the powder of the HAp-L29 ceramic showed narrower more intensive peaks (Fig. 2). This indicates higher

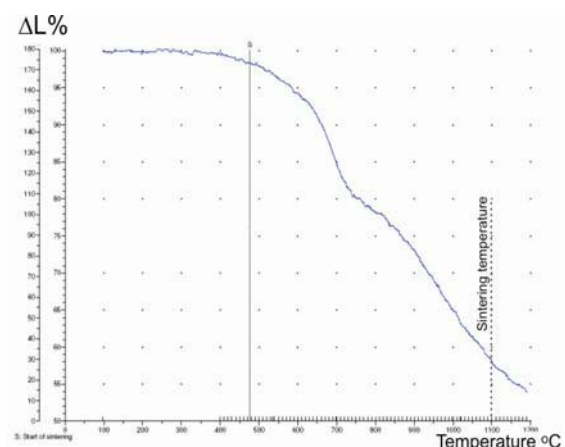


Fig. 1. Heating microscope image analysis of sample HAp L29.

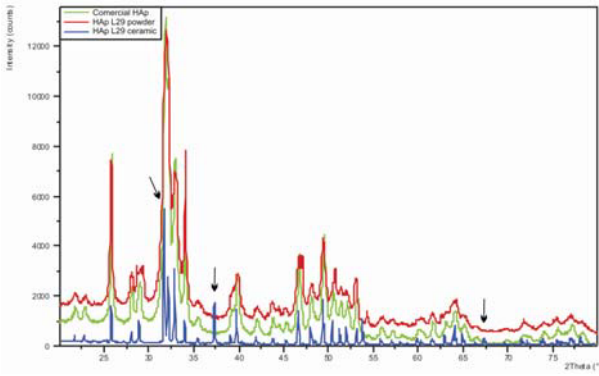


Fig. 2. XRD patterns HAp L29 of the sintered porous ceramic, typical of HAp crystal structure.

material crystallinity, which is linked with the thermal treatment of standards. In this XRD pattern some CaO→(ref. code 01-077-2010, 01-086-1199) peaks are seen maintaining some deviation from HAp stoichiometry.

With permission of Animal Ethics Committee of Latvian Food and Veterinary Administration experimental operations on 8 New Zealand male rabbits was done. After rising of mucoperiosteal flap in edentulous part of upper jaw right side hole 1.5 mm diameter was drilled, HAp cylinder 2 mm diameter inserted and wound closed in two layers. On the left side the same operation without insertion of HAp implants were done. After two weeks euthanasia was done. Blocks of soft tissue and bone were fixed in Stefanini solution. Sections done with EXACT Grinding system and from paraffin blocks were stained with hematoxylin/eosin

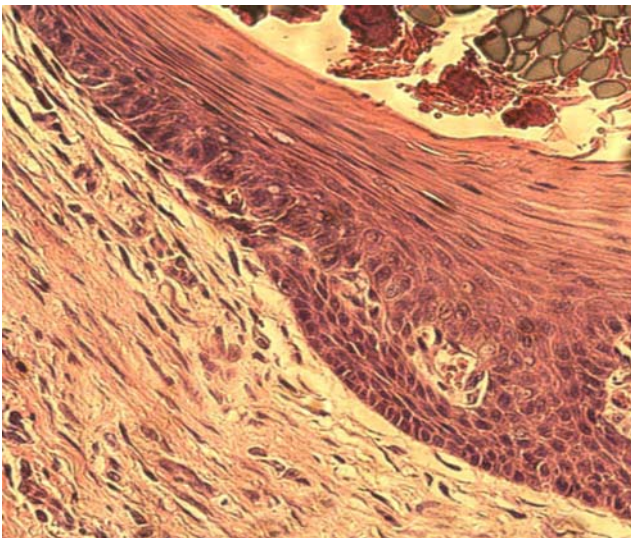


Fig.3. Soft tissues around implant without signs of inflammations (hematoxylin and eosin, x250).

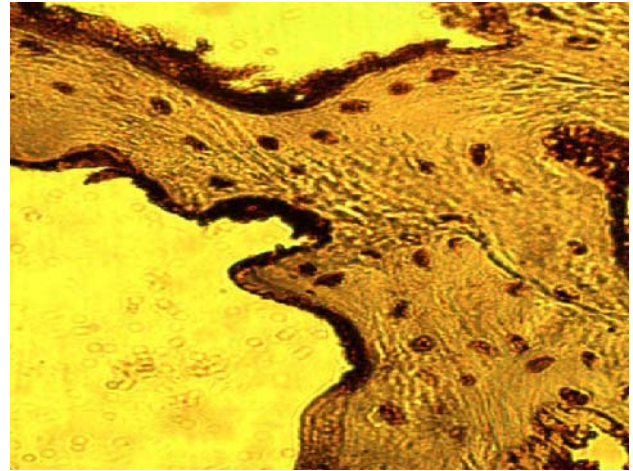


Fig.4. FGFR 1 expression in maxillary bone experiment side (FGFR IMH x250).

and using biotin and streptavidin immunohistochemical methods. In bone/HAp implant samples on expression of MMP2 (AF902, 1: 50, RD Systems, UK), MMP9 (AF 909, 1: 100, RD Systems, UK), TGFβ (1279, 1: 1000, Cambridge Science Park, UK), FGFR1 (10646, 1: 100, Cambridge Science Park, UK), barx1 (1: 250, Abcam, UK) were prepared and evaluated. For contact soft tissue besides previous techniques expression and distribution of TNFα (1: 200, Cambridge Science Park, UK), NGFRp75 (M3507, 1:150, Dako Cytomatin, Denmark), PGP 9.5 (Z5116, 1:150, Dako Cytomatin, Denmark), IL10 (ab34843, 1:400, Abcam, UK) was checked. TUNEL method was used for evaluation of apoptosis (Negoescu et al., 1998). Semiquantitative analysis of data was used (Pilmane, 1998).

### III. RESULTS

Any inflammatory response was not observed in soft tissue around the HAp ceramic implants (Fig.3).

MMPs2 and 9 were not seen in hard tissue of both – control and experimental side. Bone showed rich expression of FGFR1 in experimental and control side (Fig. 4).

TGFβ was same intensively expressed in endosteum of both side sections, but in bone around HAp implants expression of TGFβ was seen in moderate up to numerous number of bone cells while in control side there was no expression at all (Fig.5).

In all soft tissue sections was few PGP 9.5-containing nerve fibers seen and complete negative NGFRp75 expression. Apoptotic cells showed moderate number in experimental side, and only few cells were detected in control side (Fig.6).

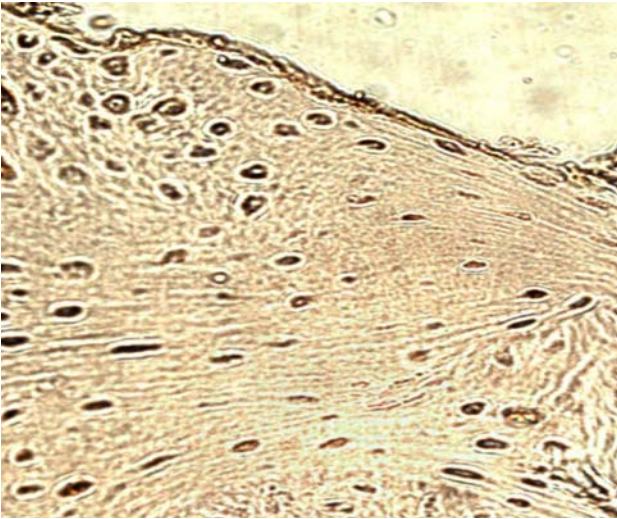


Fig.5. TGFβ expression in maxillary bone experiment side (TGFβ IMH x250).

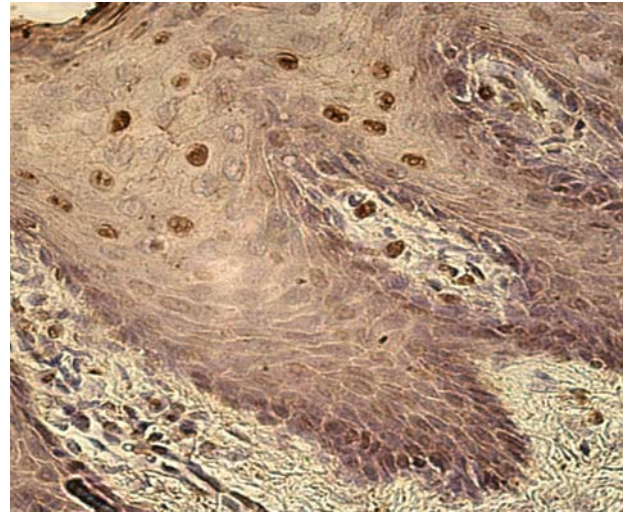


Fig.6. Apoptotic cells in soft tissue experiment side (TUNEL IMH x250).

IL10 was positive in moderate number of cells without difference between sides (Fig.7).

Small expression of TGFβ was observed only in experimental side. FGFR1 had rich expression around HAp implants down to few cells in control side. MMP2 showed expression in all cases but more intensive in cells of connective tissue at control side. MMP9 was found in few cells of connective tissue close to HAp implants. TNFα was positive in few connective tissue cells on both sides.

#### IV. DISCUSSION

TGF β plays an important role in the balance between bone resorption and subsequent bone formation [7]. Our results show significant increase of TGF β expression in bone after HAp ceramic implantation. It can be concluded that the effects of TGF β on bone formation and resorption, both *in vitro* and *in vivo*, must be evaluated in view of the presence of other cytokines and hormones, which modulate or are modulated by TGF β signaling in a number of ways.

Apoptosis is defined as a mechanism of genetically programmed cell death without inflammation of the surrounding tissue and is different from cell necrosis in morphology and biochemistry [8]. Apoptotic cells were in moderate number in experimental side, which approve that HAp implantation causes probably exchange of cell death type. As it is known that usually fibrosis does not follow to the programmed cell death HAp implantation seems might cause rather compensatory and/or adaptive than long-lasting connective tissue changes.

FGF stimulates the migration and regeneration of endothelial cells, is promoter of angiogenesis and stimulates wound healing [9]. We observed rich expression of FGFR1 around HAp implants in soft and hard tissues that prove to the above mentioned role of FGFs in regenerative mechanisms of tissues.

MMP are the group of enzymes that cleaves components of extracellular matrix and growth factors. Kherif contributes the expression of MMP 9 with the inflammation. This assumption matches with our results as we observed no inflammation.

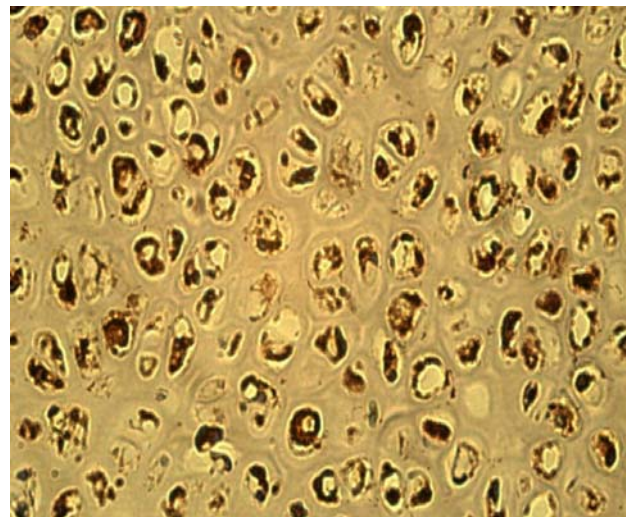


Fig.7. IL10 expression in connective tissue experiment side (IL10 IMH x250).

Nerve growth factor receptor p75 belongs to the group of TNF receptors. In adults it is expressed in several pathological conditions as neural degeneration [10].

We did not observe the expression of NGFRp75, it confirms that HAp did not causes significant changes in nerve tissues. We assume that in our experiment apoptosis was not induced by NGFRp75.

## V. CONCLUSIONS

Distinct higher expression of TGF $\beta$  in bone cells surrounding HAp implants may confirm osseoinductive activity of HAp. Implantation of HAp ceramic causes also common impressive FGFR1 expression in bone.

The intensive expression of FGFR1 and moderate apoptosis in soft tissues around the HAp implants indicate stimulation of adaptive/compensatory mechanisms of regeneration and probably better cell death type (without fibrotic complications) in connective tissue.

Indistinct TGF $\beta$  expression in soft tissue, few PGP 9.5-containing nerve fibers and lack of NGFRp75 demonstrate no involvement of the above mentioned growth factor and neuropeptide-containing innervation in morphopathogenetical regenerative mechanisms after HAp implantation.

Inflammation and/or tissue degeneration enzymes are not characteristic morphofunctional features in the tissue after HAp implantation.

## REFERENCES

1. Ripamonti U, Crooks J, Kirkbride AN. (1999) Sintered porous hydroxyapatite with intrinsic osteoinductive activity: Geometric induction of bone formation. *S Afr J Sci* 95:335-339
2. Yuan H, Kurashina K, de Bruijn JD, LI Y, De Groot K, Zhang XA. (1999) A preliminary study on osteoinduction of two kinds of calcium phosphate ceramics. *Biomaterials* 20:1799 – 1806
3. Yuan H, van Blitterswijk CA, de Groot K, de Bruijn JD. (2006) A comparison of bone formation in biphasic calcium phosphate (BCP) and hydroxyapatite (HA) implanted in muscle and bone of dogs at different time periods. *J Biomed Mater Res* 78:139-147
4. Gosain AK, Song L, Riordan P, Amarante MT, Nagy PG, Wilson CR, et al. (2002) A 1-year study of osteoinduction in hydroxyapatite-derived biomaterials in an adult sheep model. *Plast Reconstr Surg* 109:619-630
5. Rosa AL, Beloti MM, van Noort R. (2005) Osteoblastic differentiation of cultured rat bone marrow cells on hydroxyapatite with different surface topography. *Dent Mater* 19:768-772
6. Jones AC, Arns CH, Sheppard AP, Hutmacher DW, Milthorpe BK, Knackstedt MA. (2007) Assessment of bone ingrowth into porous biomaterials using MICRO-CT. *Biomaterials* 28:2491-2504
7. Sporn M, Roberts A. (1992) Transforming growth factor  $\beta$ : recent progress and new challenges. *J Cell Biol* 119(5):1017-1021
8. Twomey C, McCarthy J. (2005) Pathways of apoptosis and importance in development. *J Cell Mol Med* 9(2):345-59
9. Szebenyi G, Fallon JF. (1999) Fibroblast growth factors as multifunctional signaling factors. *Int Rev Cytol* 185:45-106
10. Dechant G, Barde YA. (2002) The neurotrophin receptor p75: novel functions and implications for diseases of the nervous system. *Nat Neurosci* 5(11):1131-6

Autor: Pilmane Mara  
 Institute: Institute of Anatomy and Anthropology  
 Street: Kronvalda 9  
 City: Riga  
 Country: Latvia  
 Email: mpilmane@latnet.lv

# Biomechanical Properties of Two Synthetic Biomaterials for Ventricular Septal Defect Closure in Infancy

L. Smits, I. Ozolanta, V. Ozolins, A. Lacis, V. Kasyanov

Riga Stradins University, Riga, Latvia

**Abstract** — Ventricular septal defect (VSD) is the most common congenital heart disease (15–20%). The traditional treatment is surgical repair – VSD closure using the autologous pericard or synthetic material – polytetrafluorethylene.

The aim of this research is to investigate the biomechanical properties of two synthetic materials and to biomechanically compare the properties of the PTFE (polytetrafluorethylene) material patches – *GORE TEX* and *BARD* *in vitro* studies the elastic modulus  $E$  (MPa), ultimate stress  $\varepsilon$  (%) and ultimate strain  $\sigma$  (MPa) of both. We suspect that knitted material (BARD) would be more appropriate for myocardial tissues.

Two types of PTFE patches were investigated: *GORE TEX Cardiovascular Patch* (GRTX), and *BARD Edwards Outflow Tract Fabric knitted PTFE Patch* (BARD). Every type of patch was divided into 3 subgroups: I subgroup – fresh material, II subgroup – 1 month exposed, III subgroup – exposed for 3 months in sterile saline 0,9% at 37°C. The testing data were recorded with software (Testexpert 11.02, Zwick-Roell).

For non-treated GRTX material  $\sigma_{\max}$  decreased after three months treatment from  $8.62 \pm 0.21$  MPa to  $7.36 \pm 1.45$  MPa ( $p < 0.05$ ).  $\varepsilon_{\max}$  increased from  $16.52 \pm 1.76\%$  to  $17.26 \pm 3.54\%$  ( $p = 0.05$ ). Modulus of elasticity ( $E$ ) of GRTX material decrease from  $84.46 \pm 11.8$  MPa (for non-treated) to  $59.65 \pm 5.03$  MPa ( $p < 0.05$ ). There are statistical differences between II and III subgroup of  $E$ :  $79.24 \pm 16.82$  MPa and  $59.65 \pm 5.03$  MPa ( $p < 0.019$ ).

$\sigma_{\max}$  for non treated BARD material decreased after three months from  $11,19 \pm 1,03$  MPa to  $8,55 \pm 0,62$  MPa ( $p < 0.05$ ).  $\varepsilon_{\max}$  increased from  $48.38 \pm 2.32\%$  to  $69.55 \pm 3.67\%$  ( $p < 0.05$ ) after.  $E$  modulus decreased from  $15.12 \pm 0.75$  MPa to  $8.12 \pm 0.48$  MPa ( $p < 0.05$ ).

After three months of treatment by saline the  $\varepsilon_{\max}$  of BARD material is  $48.38 \pm 2.32\%$ , but  $\varepsilon_{\max}$  of GRTX is  $17.26 \pm 3.54\%$  ( $p < 0.05$ ). Results show that BARD patch is not so stiff as GRTX patch, and is more suitable for the VSD closure in the first year life of children.

**Keywords** — polytetrafluorethylene, biomechanical properties, ventricular septal defect, infant.

## I. INTRODUCTION

Ventricular septal defect (VSD) is most common congenital heart disease (15–20%) [1][2] and about 70% of these are perimembranous (PmVSD). The traditional treatment, if necessary, is surgical repair – VSD closure using

the autologous pericard or synthetic material such as polytetrafluorethylene (PTFE). There are two types that are commonly in use – *GORE TEX Cardiovascular patch* (GRTX) and *BARD Edwards Outflow Tract Fabric knitted PTFE* (BARD).

For surgical operation there are usually used synthetic patch, uninterrupted (continuous) and interrupted suture technique, and transatrial access with cardiopulmonary bypass, cardioplegia in aortic root and local myocardial hypothermia. Most patients undergo the operation in the first year of life, therefore the structure of the myocardial tissues is softer [3] in contrast with a two year old or more, child's myocardial tissues characteristics, concerning material used for VSD closure. At the moment, of VSD exposure, considering localization, size and shape of the VSD, we made a decision of which material is more suitable in a specific case. We suspect that knitted material (BARD) would be more appropriate and with greater accordance to myocardial tissues as well as having the advantage of making less myocardial and conduction tissue trauma and being more fitted for good shaping of VSD patch to avoid residual defects [4].

The aim of this research is to investigate the biomechanical properties of two synthetic materials, such as the PTFE material patches – GRTX and BARD *in vitro*, and compare the main biomechanical parameter of these materials.

## II. MATERIAL AND METHODS

Two types of PTFE patches were used: a *GORE TEX Cardiovascular Patch* (thickness of the material is 0.4 mm), and a *BARD Edwards Outflow Tract Fabric knitted PTFE* (thickness of the material is 0.55 mm) cardiovascular knitted patch.

Two groups of specimens were investigated: GRTX and BARD patches. These two groups were divided into 3 subgroups of each patch type, and in total 30 specimens were investigated.

Specimens were cut 5.0 mm wide and up to 25 mm long. Throughout the process of preparation procedure of the specimens and their storage the aseptic obstacles were taken into account. Each group of GRTX and BARD patches were divided into 3 subgroups: fresh (non-treated) specimens - I subgroup; II subgroup – specimens with 2 months treated in ster-

ile saline 0.9% at 37°C in thermostat, and III subgroup – specimens with 3 months treated in sterile saline 0.9% at 37°C in thermostat. Subsequently all specimens in II and III subgroups were placed into sterile test-glasses with sterile saline 0.9% and were stored in thermostat at constant temperature 37°C.

Biomechanical tests were performed using a tensile testing machine *Zwick-Roell Z010* (*Zwick-Roell*, Germany), and the testing data was recorded with the accompanying software package (*Testexpert 11.02, Zwick-Roell*).

Uniaxial tensile tests were performed to examine the deformability and strength of the specimens (GRTX and BARD). Force-elongation curves were recorded at an elongation rate of 5 mm min<sup>-1</sup>. Ultimate stress  $\sigma_{\max}$  (MPa) and strain  $\epsilon_{\max}$  (%) were determined and modulus of elasticity E (MPa) at stress level 1MPa was calculated.

For pair-wise comparisons, Student *t* – tests were used to determine the significance in differences between the group means. Statistically, different pairs were defined as having  $p < 0.05$ .

Initial thickness of the samples GRTX and BARD was measured by cathetometer *MK-6 (LOMO)*, the precision of measurements is  $\pm 0.001$  mm. The wall thickness of the GRTX patch was  $0.4 \pm 0.006$  mm and the wall thickness of the BARD patch was  $0.55 \pm 0.008$  mm.

### III. RESULTS

Results of experimental investigations show, that mechanical strength and deformability for both materials decrease during the time of saline treatment (Table 1, 2). For example, ultimate stress for non-treated GRTX material decrease after three months of saline treatment from  $8.62 \pm 0.21$  MPa to  $7.36 \pm 1.45$  MPa, respectively ( $p < 0.05$ ). Ultimate strain for this material increase after three months of treatment in the saline from  $16.52 \pm 1.76\%$  to  $17.26 \pm 3.54\%$  ( $p = 0.05$ ). Modulus of elasticity of GRTX material during treatment also decrease from  $84.46 \pm 11.8$  MPa (for non-treated material) to  $59.65 \pm 5.03$  MPa (after three months of treatment), respectively ( $p < 0.05$ ). There is a statistical differences between modulus of elasticity of II and III subgroups also:  $79.24 \pm 16.82$  MPa and  $59.65 \pm 5.03$  MPa, respectively ( $p < 0.019$ ).

The treatment of BARD material in saline influenced the biomechanical properties as well (Tab. 2). Ultimate stress for non treated BARD material decreased after three months of saline treatment from  $11.19 \pm 1.03$  MPa to  $8.55 \pm 0.62$  MPa, respectively ( $p < 0.05$ ). Ultimate strain for BARD material increased after three months of treatment in the saline from  $48.38 \pm 2.32\%$  to  $69.55 \pm 3.67\%$ , respectively ( $p < 0.05$ ). Modulus of elasticity of BARD patch during treatment de-

Table 1. The main biomechanical parameters for GTRX material.

Parameters	$\sigma_{\max}$ (MPa)	$\epsilon_{\max}$ (%)	$E_t$ (MPa)
Expon. time			
Non-treated	$8,62 \pm 0,21$	$16,52 \pm 1,76$	$84,46 \pm 11,8$
1 month	$9,08 \pm 0,71$	$13,70 \pm 2,06$	$79,24 \pm 16,82$
3 months	$7,36 \pm 1,45$	$17,26 \pm 3,54$	$59,65 \pm 5,03$

Table 2. The main biomechanical parameters for BARD material.

Parameters	$\sigma_{\max}$ (MPa)	$\epsilon_{\max}$ (%)	$E_t$ (MPa)
Expon. time			
Non-treated	$11,19 \pm 1,03$	$48,38 \pm 2,32$	$15,12 \pm 0,75$
1 month	$9,87 \pm 0,79$	$45,19 \pm 2,46$	$15,37 \pm 3,01$
3 months	$8,55 \pm 0,62$	$69,55 \pm 3,67$	$8,12 \pm 0,48$

crease from  $15.12 \pm 0.75$  MPa (for non-treated material) to  $8.12 \pm 0.48$  MPa (after three months of treatment), respectively ( $p < 0.05$ ). There is no statistical differences between modulus of elasticity of I and II subgroup:  $15.12 \pm 0.75$  MPa and  $15.37 \pm 3.01$  MPa, respectively ( $p > 0.05$ ).

The BARD material in all subgroups has a higher ultimate stress then GRTX. For non-treated materials, there is  $8.62 \pm 0.21$  MPa and  $11.19 \pm 1.03$  MPa ( $p < 0.05$ ), respectively. Ultimate strain of BARD material in all subgroups is higher than of GRTX material (see Table 1, 2). For example, after three months of treatment by saline the ultimate strain of BARD material is  $48.38 \pm 2.32\%$ , but ultimate strain of GRTX is  $17.26 \pm 3.54\%$  ( $p < 0.05$ ), respectively. Making a comparison between experimental data for modulus of elasticity of these two materials may see, that modulus of elasticity of BARD material is essentially lower then of GRTX material. For example, for non-treated materials there is  $15.12 \pm 0.75$  MPa and  $84.46 \pm 11.8$  MPa, respectively ( $p < 0.05$ ). This difference retains for treated materials also: after three months of treatments the values are  $8.12 \pm 0.48$  MPa and  $59.65 \pm 5.03$  MPa, respectively ( $p < 0.05$ ).

Experimental results show that BARD material has preferable mechanical properties than GRTX material: higher ultimate stress and strain than GRTX material. The modulus of elasticity of BARD material is lower than modulus of elasticity of GRTX. It means that the BARD patch is not so stiff as the GRTX. The BARD patch is more suitable for VSD closure in child's first year of life. The mechanical testing of the materials showed that the stress – strain relationship for GRTX and BARD patch is non-linear. The shape of these curves differ from each other (Fig. 1, 2).

The main parameters of biomechanical properties for the two patches are shown in Table 1. and Table 2.

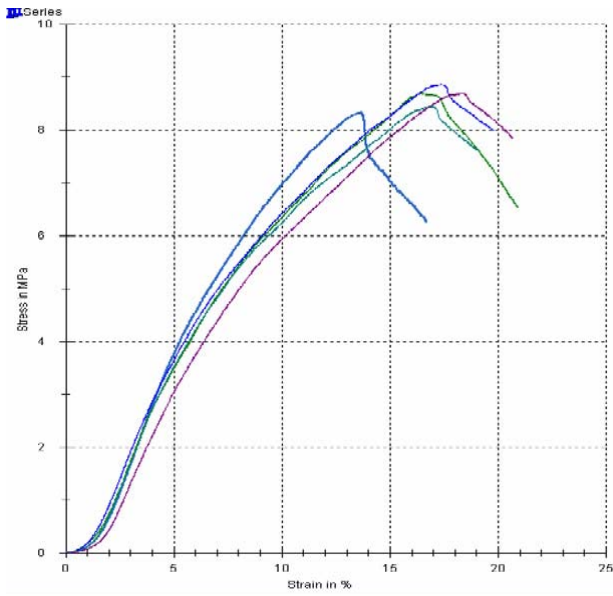


Fig. 1. Stress – strain relationship for GRTX patch (non treated material).

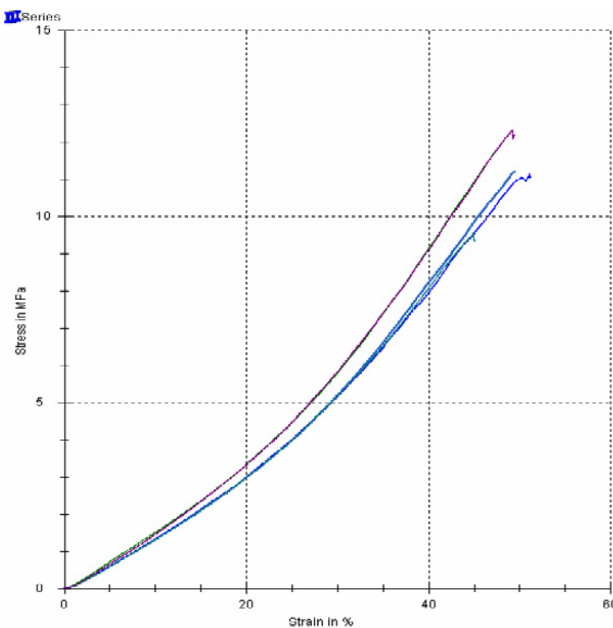


Fig. 2. Stress – strain relationship for BARD patch (non treated material).

#### IV. DISCUSSION

Due to the development of invasive cardiology, the management of VSD closure transcatheter or using the perventricular [5] hybrid method, has become more suitable [6] for children at a young age, even for the subaortic positioned

VSD. Despite this, there still remains the importance, to close VSD using the synthetic patch or autologous pericard, in situations where the child is too small for procedure, when the shape, configuration or localization of the defect is not suitable [7] for interventional closure or when this procedure has not been established yet. Therefore, the materials, having the more appropriate biomechanical properties to cardiac tissue (e.g. BARD), are more preferred for the VSD closure, especially in VSD management of infants, where the stiffness of the patch (e. g. BARD) is important to reach less trauma of myocardial tissues, conduction tissues, less possibility of residual VSD and it does not diminish functional characteristics of the ventricles as well. There is a lot of research to discover new biodegradable patch biomaterials [8] (e. g poly-l-lactide and polyester urethane urea) used to repair heart defects and would be more appropriate biomechanically and biocompatible, than PTFE material in the future, to become a suitable patch for surgical repair.

#### V. CONCLUSIONS

Experimental results show that BARD material has preferable mechanical properties than GRTX material: higher ultimate stress and strain than GRTX material. The modulus of elasticity of BARD material is lower than the modulus of elasticity of GRTX. It means that the BARD patch is not so stiff as the GRTX and it is more suitable for the VSD closure in the child's first year of life. The main biomechanical parameters of BARD material show that this material is a much better match to the biological soft tissue than that of GRTX.

#### REFERENCES

1. Hoffman, Julien IE, Samuel Kaplan. ( 2002 ) The incidence of congenital heart disease. *Journal of the American College of Cardiology* 39: 1890–1900
2. Bacha, Emile A, et al. ( 2003 ) Periventricular device closure of muscular ventricular septal defects on the beating heart: technique and results. *Journal of Thoracic and Cardiovascular Surgery* 126: 1718–23
3. Stark J, Sethia B. ( 1986 ) Closure of ventricular septal defect in infancy. *J Card Surg.* 1: 135–150
4. Fujimoto, Kazuro L, et al. ( 2007 ) In vivo evaluation of a porous, elastic, biodegradable patch for reconstructive cardiac procedures. *Annals of Thoracic Surgery* 83: 648–654
5. McCarthy KP, Ching Leung, PK, Ho SY ( 2005 ) Perimembranous and muscular ventricular septal defects- morphology revisited in the era of device closure. *J Interv Cardiol.* 18: 507–513
6. Arora R, et al. ( 2003 ) Transcatheter closure of congenital ventricular septal defects: experience with various devices. *J Interv Cardiol.* 16: 83–91

7. Ozawa, Tsukasa, et al. ( 2002 ) Histologic changes of non-biodegradable and biodegradable biomaterials used to repair right ventricular heart defects in rats. *Journal of Thoracic and Cardiovascular Surgery* 124: 1157–1164.
8. Lacis A, Smits L, Zidere V, Lubaua I, Lace I, Auzins J, Straume Z. ( 2003 ) Surgical closure of ventricular septal defects under cardiopulmonary bypass within the first year of life. *Acta Chirurgica Latviensis* 3: 88–93

Author: Lauris Smits  
Institute: Riga Stradins University  
Street: Dzirciema Street 16.  
City: Riga  
Country: Latvia  
Email: smits@bkus.lv



# Development of Poly(vinyl alcohol) Based Systems for Wound Dressings

J. Stasko, M. Kalnins, A. Dzene and V. Tupureina

Institute of Polymer Materials, Riga Technical University, Riga, Latvia

**Abstract** — Poly(vinyl alcohol) hydrogels are of special interest for the application in medicine (mainly for therapeutic systems) due to their biocompatibility and excellent ability to absorb water. The water absorption of different gels prepared by freezing/thawing method was studied in the presented work.

**Keywords** — Poly(vinyl alcohol), gels, water absorption

## I. INTRODUCTION

Besides such qualities as ability to guarantee temporary physiologic wound covering as well the protection from mechanical trauma, the therapeutic systems must efficiently absorb the exudates, thereby providing the necessary conditions for successful wound healing - normal moisture level at the bad of the wound [1].

Therefore, the water absorption of different PVA hydrogels prepared by freezing/thawing method was studied.

## II. EXPERIMENTAL PART

### A. Base materials

The choice of PVA primarily was determined by its water solubility which facilitates incorporation of therapeutic substances (most of them are water soluble) and secondly by the ability of this polymer comparatively easy to form cross-linked structures in process of sequential freezing/thawing cycles [2]. It is essential for hydrogel preparation.

Several samples of partially crystalline PVA were used: PVA I: mol. weight 130 000, melting temperature 225.8°C, glass transition temperature 76.6°C (DSC), PVA II: mol. weight 145 000; both supplied by *Merck Schuchardt* with degree of hydrolyzation calculated on anhydrous substances  $\geq 98\%$ , PVA III: mol. weight 88 000, degree of hydrolyzation  $\geq 88\%$ , and PVA IV: mol. weight 25 000 both from *Acros Organics*.

Some PVA samples were plasticized by glycerol as one of the most suitable PVA plasticizer [3,4].

PVA water solutions (15 wt%) (without and with glycerol; content of glycerol, 30 wt% from PVA) were used for gel preparation.

### B. Preparation of gel systems

PVA distilled water solution (15 %) was poured out on the glass vessels and exposed to from 1 to 3 subsequent cycles of freezing for 12 h at -20°C and thawing at 25°C (12 h).

### C. Gel content

Cross-linking does not occur entirely. Besides gel certain portion of PVA macromolecules stays un-crosslinked and forms sol. The gel content  $G$  in hydrogels was estimated as:

$$G(\%) = \frac{W_1}{W_d} \times 100 \quad (1)$$

where  $W_1$  – the weight of the dry sample before the immersion in the distilled water;  $W_d$  – the weight of the dried samples after water absorption and simultaneous separation of soluble part (sol).

### D. Determination of equilibrium water content ( $W_{eq}$ )

Swelling characteristics of samples were measured at several temperature levels: 20°C, 25°C, 30°C and 37°C (the last level simulates water absorption at the temperature of human body) in the thermostatically controlled chamber to the equilibrium state. Completely dry gel samples (0.5 g) were immersed into distilled water. The swollen samples were removed and immediately weighted (after the superficial water was wiping using absorbent paper) and dried at 30°C till the constant weight. Then water absorption experiments were carried out repeatedly.

The  $W_{eq}$  percentage was calculated:

$$W_{eq}(\%) = \frac{W_s - W_d}{W_s} \times 100 \quad (2)$$

where  $W_s$  is swollen weight of gels at equilibrium state and  $W_d$  is weight of dry gels [5].

## III. RESULTS AND DISCUSSION

Yield of gel strongly depends on the type of polymer and number of freezing/thawing cycles (Table 1). Thus poly-

Table 1 Gel fraction results for polymers PVA I (130 000M), PVA II (145 000M), PVA III (88 000M), PVA IV (25 000M) as function of number of cycles.

Number of freezing/thawing cycles	G, %			
	PVA IV	PVA III	PVA I	PVA II
1	does not form gel	-	68,81	82,35
2		-	71,01	83,50
3		≈ 70	82,30	87,70

mers with small value of molecular weight (PVA 4 and PVA 3) poorly form gel (polymer PVA 4 doesn't form gel at all). The gel content of polymers with higher molecular weight increases with number of freezing/thawing cycles. Satisfactory values of gel fraction could be reached even at the first freezing/thawing cycle.

Water absorption of dry gels turned out to be quite rapid. Values of water content close to the equilibrium value  $W_{eq}$  can be reached in 2 – 4 hours of exposure (Fig. 1).

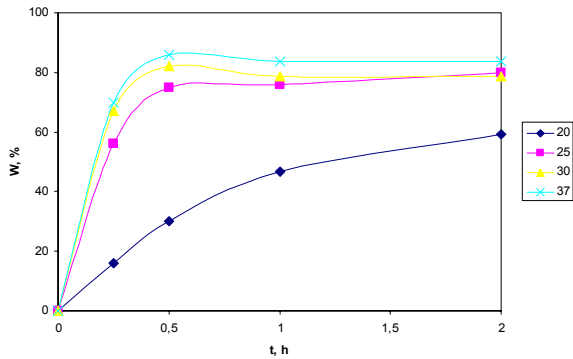


Fig. 1 W dependence from exposure time (initial two hours) for PVA I gels (1 freezing/thawing cycle).

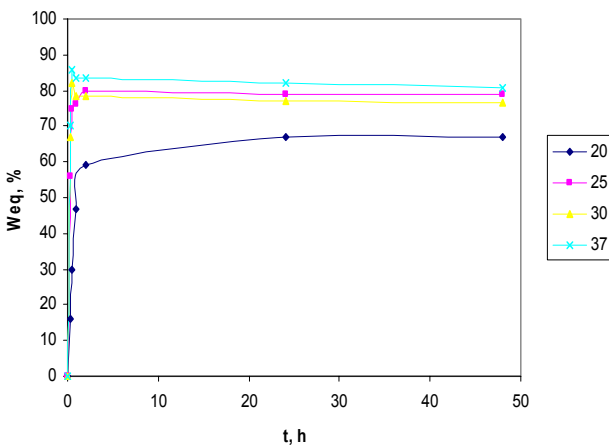


Fig. 2  $W_{eq}$  dependence from exposure time for PVA I gels (1 freezing/thawing cycle).

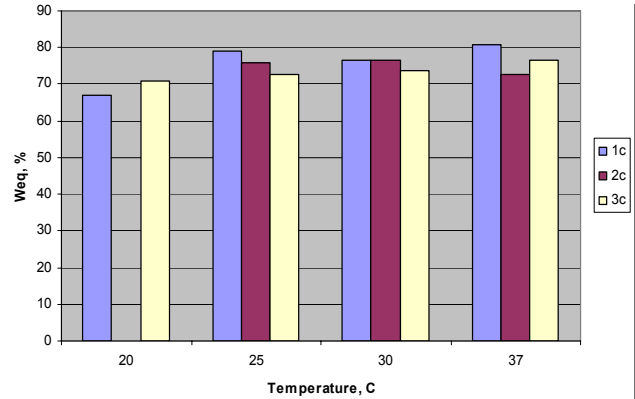


Fig. 3  $W_{eq}$  values for PVA I gels at different temperatures and number of freezing/thawing cycles.

There is increase of absorption rate (Fig.1) and equilibrium value of water content  $W_{eq}$  (Fig.2) with the exposure temperature. The main reason seems to be the increase of compliance of the cross-linked network.

Water absorption curves for elevated exposure temperature values show maxima, followed by slight decrease of  $W$  values (2-3%) most probably due to loss of not-crosslinked part of polymer, which dissolve in water.

It was observed that the number of freezing/thawing cycles affect  $W_{eq}$  values negligibly (Fig. 3).  $W_{eq} > 70\%$  can be obtained already at the first cycle.

Glycerol containing PVA gels absorb water more slowly, comparing with pure PVA gels  $W_{eq}$  are less too (Fig. 4).

Water absorption capability of PVA gels is hindered in presence of glycerol. Glycerol molecules either may occupy the free space between the molecular chains or take part in the formation cross-linked network.  $W_{eq}$  values increase with number of freezing/thawing cycles (Fig. 5).

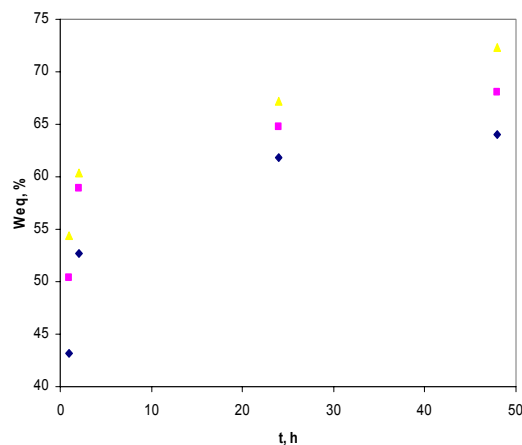


Fig. 4  $W_{eq}$  dependence from exposure time for PVA I systems with glycerol at temperature 30°C (number of freezing/thawing cycles -1, 2 and 3).

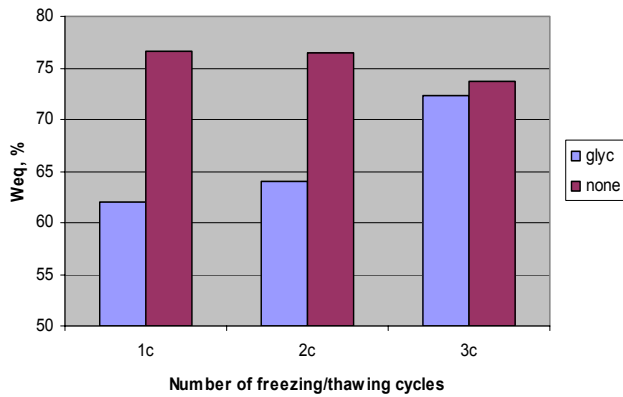


Fig. 5  $W_{eq}$  as function of number of freezing/thawing for plasticized and non-plasticized PVA systems.

Table 2  $W_{eq}$  as function of number of freezing/thawing cycles for polymers PVA I and PVA II at different exposure temperatures (ratio  $W_{eq}^2$  to  $W_{eq}^1$  in brackets)

Number of freezing/thawing cycles	PVA I		PVA II	
	First immersion, $W_{eq}^1$	Repeated immersion $W_{eq}^2$	First immersion $W_{eq}^1$	Repeated immersion $W_{eq}^2$
30 °C				
1	76,6	80,3 (1,05)	-	-
2	76,5	80,5 (1,05)	76,5	76,7 (~1)
3	73,8	77,6 (1,05)	74,2	76,4 (1,03)
37 °C				
1	80,9	87,2 (1,08)	78,0	77,8 (~1)
2	72,5	84,0 (1,16)	77,5	76,6 (~1)
3	76,4	81,0 (1,06)	77,9	77,8 (~1)

It was of special interest to check reversibility of water absorption. Swelled samples were dried at room temperature and repeatedly immersed into the distilled water.  $W_{eq}^2$  values were determined.

Repeated water absorption shows that  $W_{eq}^2$  values are higher than  $W_{eq}^1$  values for both high molecular polymers (Table 2). It indicates that obtained gel structures are stable enough.

## REFERENCES

1. Greidane J, Dzene A, Loginova N, Tupureina V, Dzenis M, Savenkova L (2006) Macromolecular Therapeutic Systems. Scientific issue of publications Faculty of Material Science and Applied Chemistry 12
2. Peppas N A, Mongia N K (1997) Ultrapure poly(vinyl alcohol) hydrogels with mucoadhesive drug delivery characteristics. Eur J Pharm Biopharm 43:51-58.
3. Sakellariou P, Hassan A, Rowe R C (1993) Plasticization of aqueous poly(vinyl alcohol) and hydroxypropyl methylcellulose with polyethylene glycols and glycerol. Eur Polym J 29:937-943.
4. Zhyravleva I I, Laktionov V M (1999) Выбор пластифицирующих агентов для временных съёмных покрытий на основе поливинилового спирта. *Plast.Massy* 2:16 -18 (in Russian).
5. Kokabi M, Sirousazar M, Hassan Z M (2007) PVA-clay nanocomposite hydrogels for wound dressing. Eur Polym J 43:773-781.

Author: Jolanta Stasko  
 Institute: Institute of Polymer Materials  
 Street: Azenes 14/24  
 City: Riga  
 Country: Latvia  
 Email: Jolanta.Stasko@rtu.lv

# Apatite-based Biomaterials Synthesized in Saline Melts

S.O. Tarasenko<sup>1</sup>, V.F. Zinchenko<sup>1</sup>

<sup>1</sup>A.V. Bogatsky Physical-chemical Institute of NAS of Ukraine/  
Department of chemistry of functional inorganic materials, Odessa, Ukraine

**Abstract** — An essentially new method of synthesis of apatite – based materials in saline melts at moderate temperatures (500-700°C) is developed. The method combines in itself the advantages of the ways of hyper-thermal hydrolysis (a "dry" method) and precipitation from aqueous solutions (a "wet" method). The thermodynamic estimation of efficiency of the interaction between components allowed optimizing the composition of a reaction mixture. As a reaction media the chloride melt of the equimolar NaCl-KCl composition as well as eutectics of the  $\text{Li}_2\text{CO}_3\text{-Na}_2\text{CO}_3\text{-K}_2\text{CO}_3$  composition were used. The obtained materials were identified with a method of the X-ray phase analysis. A mechanism of the synthesis of apatites in saline melts basing on solubility of the components was proposed. The capability to form of mechanically strong and porous items (tablets) directly in the process of synthesis of calcium hydroxiapatite in the molten carbonate eutectics was established. The developed method of synthesis of the biocompatible nano-scale materials and composites from them is a rather effective and accessible way to practical usage in stomatology, orthopaedics and other areas of medicine.

**Keywords** — Calcium apatites, synthesis, saline melts, biomaterials.

## I. INTRODUCTION

To apatites belong compounds with general formula  $\text{M}_{10}(\text{PO}_4)_6\text{X}_2$ , where M - Ca, Sr, Ba, Pb; X - OH, F, Cl. Apatites due to their universality are applied in the many fields of activity. They can be used as sensor controls, sorbents, phosphors and as biocompatible implants, etc. There are rather widespread Calcium apatites which are components of bones and teeth of the vertebrates in the nature. Available methods of the reception of synthetic apatites [1,2] have a number of characteristic lacks: thus solid-phase synthesis ("dry" method) of apatites is to be spent at rather high temperatures (more than 1200°C), and its product is characterized by a gradient of composition in a grain of the material; another method of synthesis via precipitation from aqueous solution (a "wet" method) occurs throughout a long period of time (10 hours and more), and often results in an amorphous and non-stoichiometric product.

We have developed an essentially new way of obtaining Calcium Hydroxylapatite (CaHap),  $\text{Ca}_{10}(\text{PO}_4)_6(\text{OH})_2$  and Calcium Fluorapatite (CaFap),  $\text{Ca}_{10}(\text{PO}_4)_6\text{F}_2$  in saline melts at moderate temperatures. The saline melts as media for

synthesis (basically of complex oxides) and growing-up of single crystals is known enough for a long time [3]. Their use leads to an intensification of the process of synthesis, due to an acceleration of the movement of particles in the melt in comparison with a solid state.

## II. EXPERIMENTAL PART

### A. Thermodynamical evaluation, and experimental methods

Previously we estimated by a routine procedure the thermodynamic probability of the CaHap and CaFap formation in the various reactions. Thermodynamic data for CaHap and CaFap were taken from the book [2]. As one can see from the Tab. 1, the most effective reactions should be 1,2 for CaHap and 5,6 for CaFap. Use of sodium metaphosphate is more preferable in comparison with potassium metaphosphate from the thermodynamic point of view.

Nevertheless in the developed ways of the synthesis [4-7]  $\text{KPO}_3$  was successfully used. Before using it was melted for elimination of water admixture. As media for synthesis the saline melts of composition: NaCl-KCl (50 mol.%,  $T_{\text{mp}}=665^\circ\text{C}$ ) and  $\text{Li}_2\text{CO}_3\text{-Na}_2\text{CO}_3\text{-K}_2\text{CO}_3$  (27; 28 and 45 mol. %, respectively,  $t_{\text{mp}}=390^\circ\text{C}$ ) were used. The high-purity salts were melted in the required ratios in the muffle furnaces at 800°C and 500°C, respectively. For carrying out the synthesis of apatites in the NaCl-KCl melt as initial Ca-containing components  $\text{CaCO}_3$ , CaO and  $\text{Ca}(\text{OH})_2$  in case of CaHap) or  $\text{CaF}_2$  (in case of CaFap) were used. The synthesis was carried out at 700°C during 2 hours.

At the synthesis of apatites in the carbonate melt  $\text{Ca}(\text{OH})_2$  (CaO in another variant),  $\text{KPO}_3$  for CaHap and  $\text{CaF}_2$ ,  $\text{KPO}_3$  for CaFap as initial components were used. The synthesis was carried out at 500°C during 2 hours.

At carrying out the research of apatites and their synthesis, the methods of thermal analysis (TA), X-ray phase analysis (XRPA) and chemical analysis were used. Thermograms and thermogravimetric curves were recorded with a device Derivatograph-1000 (MOM, Hungary) in a mode of permanent heating with a speed of 10 °C/min. A weight of the probes for researches laid within the limits of 500-1000 mg.

Diffraction patterns of the samples that have passed through thermal processing both during TA and synthesis were re-

Table 1 Thermodynamic evaluation of formation of calcium apatites in the various reactions

#	Equation of the reaction	$\Delta G_{r,298}^{\circ}$ , kJ/mole	Probability of the reaction
1	$6\text{KPO}_3 + 6\text{CaO} + 3\text{CaCO}_3 + \text{Ca}(\text{OH})_2 \rightarrow \text{CaHap} + 3\text{K}_2\text{CO}_3$	1048	successful
2	$6\text{NaPO}_3 + 6\text{CaO} + 3\text{CaCO}_3 + \text{Ca}(\text{OH})_2 \rightarrow \text{CaHap} + 3\text{Na}_2\text{CO}_3$	1188	successful
3	$6\text{KPO}_3 + 9\text{CaCO}_3 + \text{Ca}(\text{OH})_2 \rightarrow \text{CaHap} + 6\text{CO}_2\uparrow + 3\text{K}_2\text{CO}_3$	265	possible
4	$6\text{NaPO}_3 + 9\text{CaCO}_3 + \text{Ca}(\text{OH})_2 \rightarrow \text{CaHap} + 6\text{CO}_2\uparrow + 3\text{Na}_2\text{CO}_3$	358	possible
5	$6\text{KPO}_3 + 10\text{Ca}(\text{OH})_2 \rightarrow \text{CaHap} + 6\text{KOH} + 6\text{H}_2\text{O}\uparrow$	178	possible
6	$6\text{NaPO}_3 + 10\text{Ca}(\text{OH})_2 \rightarrow \text{CaHap} + 6\text{NaOH} + 6\text{H}_2\text{O}\uparrow$	316	possible
7	$6\text{KPO}_3 + 6\text{CaO} + 3\text{CaCO}_3 + \text{CaF}_2 \rightarrow \text{CaFap} + 3\text{K}_2\text{CO}_3$	1109	successful
8	$6\text{NaPO}_3 + 6\text{CaO} + 3\text{CaCO}_3 + \text{CaF}_2 \rightarrow \text{CaFap} + 3\text{Na}_2\text{CO}_3$	1199	successful
9	$6\text{KPO}_3 + 9\text{CaCO}_3 + \text{CaF}_2 \rightarrow \text{CaFap} + 6\text{CO}_2\uparrow + 3\text{K}_2\text{CO}_3$	329	possible
10	$6\text{NaPO}_3 + 9\text{CaCO}_3 + \text{CaF}_2 \rightarrow \text{CaFap} + 6\text{CO}_2\uparrow + 3\text{Na}_2\text{CO}_3$	419	possible

corded on the device DRON-3 with a filtered  $\text{CuK}_{\alpha}$ -radiation. The size of the particles was estimated by means of scanning electron microscopy (SEM) (the microscope ULTRA-55, Zeiss, Germany).

### B. Results

The series of endotherms and exotherms, which appears in DTA curves (Fig.1), indicates on the processes of interaction in the investigated systems. As it could be seen from the thermogravimetric curves (TG), the process proceeds in two stages in NaCl-KCl melt (a) and in one stage in  $\text{Li}_2\text{CO}_3$ -

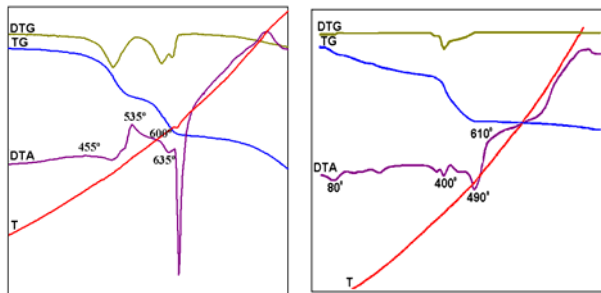


Fig.1 TA curves of the mixtures:

- a –  $\text{CaF}_2 + \text{CaCO}_3 + \text{NaPO}_3$  in NaCl-KCl system,  
 b –  $\text{CaF}_2 + \text{KPO}_3$  in  $\text{Li}_2\text{CO}_3$ - $\text{Na}_2\text{CO}_3$ - $\text{K}_2\text{CO}_3$  system

Table 2 Conditions and results of synthesis of calcium apatites in saline melts

Initial reagents	Composition of the saline melt	Processing temperature, °C	Products (XRPA data)
$\text{Ca}(\text{OH})_2$ , CaO, $\text{KPO}_3$ , $\text{CaCO}_3$	NaCl - KCl	700	$\text{Ca}_{10}(\text{PO}_4)_6(\text{OH})_2$ (tiny powder)
$\text{CaF}_2$ , CaO, $\text{KPO}_3$ , $\text{CaCO}_3$	NaCl - KCl	700	$\text{Ca}_{10}(\text{PO}_4)_6\text{F}_2$ (tiny powder)
$\text{Ca}(\text{OH})_2$ , $\text{KPO}_3$	$\text{Li}_2\text{CO}_3$ - $\text{Na}_2\text{CO}_3$ - $\text{K}_2\text{CO}_3$	500	$\text{Ca}_{10}(\text{PO}_4)_6(\text{OH})_2$ (strong material)
CaO, $\text{KPO}_3$	$\text{Li}_2\text{CO}_3$ - $\text{Na}_2\text{CO}_3$ - $\text{K}_2\text{CO}_3$	500	$\text{Ca}_{10}(\text{PO}_4)_6(\text{OH})_2$ (tiny powder)
$\text{CaF}_2$ , $\text{KPO}_3$	$\text{Li}_2\text{CO}_3$ - $\text{Na}_2\text{CO}_3$ - $\text{K}_2\text{CO}_3$	500	$\text{Ca}_{10}(\text{PO}_4)_6\text{F}_2$ (tiny powder)

$\text{Na}_2\text{CO}_3$ - $\text{K}_2\text{CO}_3$  melt (b). After entire melting of the systems (about 700°C in first case and 500°C in second case the process practically finishes.

The XRPA data suggest formation of the well-crystallized products; CaHap and CaFap, in the saline melt NaCl-KCl (Tabl.2). The washed out powders consist of nano-scale particles, associated into the stick-like aggregates of various sizes – from 1 to 5  $\mu\text{m}$  in a length (Fig.2). Generally, the fraction of nano-sized aggregates in case of CaFap is much more than for CaHap.

In case of the carbonate melt as a medium of the reaction, ( $\text{Ca}(\text{OH})_2$  or  $\text{CaF}_2$  as reactants), XRPA of products revealed, in addition to the phases of CaHap and CaFap, also phases of uncertain structure. At use of CaO as a reactant the phase of apatite was not found out at all.

Surprisingly, after washing out and drying of the samples, XRPA revealed only phases of apatites in all cases. In the process of development of a way of the synthesis of CaHap in the carbonate melt a possibility of obtaining it in the form of a strong ceramics has been found out (Tabl.2).

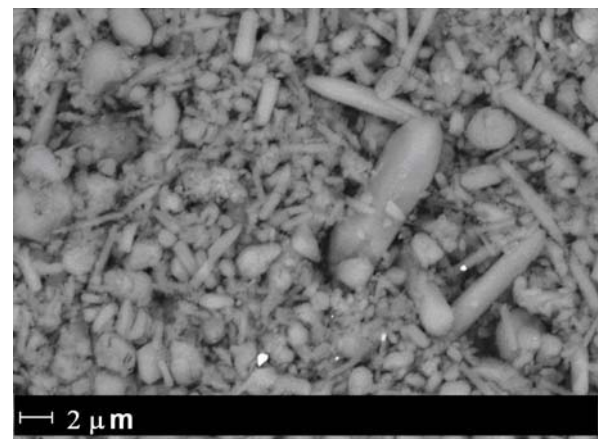


Fig.2 A SEM-microphoto image of the CaHap powder synthesised in the NaCl-KCl melt.

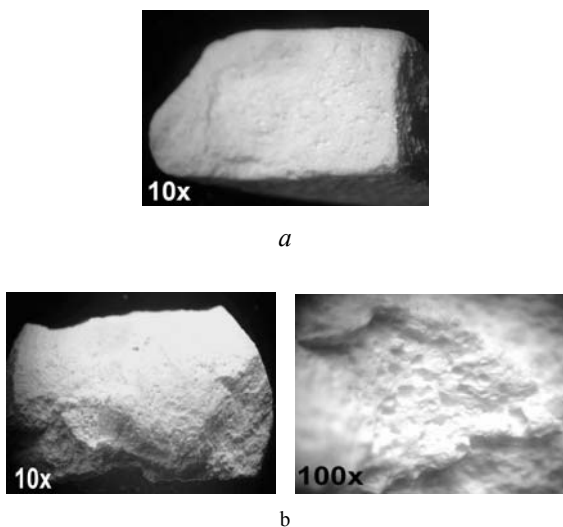


Fig.3 Microphotos of the samples of a CaHap ceramics synthesised in the  $\text{Li}_2\text{CO}_3\text{-Na}_2\text{CO}_3\text{-K}_2\text{CO}_3$  melt:  
a – washed out in water, b – washed out in glycerine

The obtained ceramical specimens were washed from the saline melt in two ways – in water, as usually, and in glycerine. After finishing of washing up, the ceramical items were extra washed out with ethanol and carefully dried up on air. As one could see from fig.3, the sample washed out in glycerine has more porous structure; it was also stronger in comparison with the sample washed out in water. So, we could recommend glycerine as a medium for soft washing up of the biomaterials based on apatites.

### III. DISCUSSION

The most simple explanation of the considerable acceleration (more than one order) of the processes in saline melts in comparison with the solid-phase synthesis consists of an essentially high solubility of the components in the synthesis medium (a saline melt). Meanwhile a solubility of the products of the synthesis should be significantly lower compare to the initial components. In the monograph [8] data on the solubility of oxigen-containing compounds (oxides and oxosalts) in the saline melts have been analyzed basing on an oxo-acidity position. Particularly, the work gathered the data on the solubilities of alkaline-earths (Mg, Ca, Sr, Ba) oxides and carbonates in the melts of alkaline halides and relative systems, which could be of interest for clearing the mechanism of the synthesis of apatites. In the recently published work [9] we reported data on the solubility of the initial components and of the reaction products (CaHap and CaFap) in the saline melt NaCl-KCl at 700°C. These data are recorded in Tab.3. As one could see, the

Table 3 Experimental data on the solubilitis in NaCl-KCl melt at 700°C

The probe	Chemical analysis results, wt. %	
	Ca <sup>2+</sup>	PO <sub>4</sub> <sup>3-</sup>
CaCO <sub>3</sub>	0,493	–
Ca(OH) <sub>2</sub>	0,245	–
CaF <sub>2</sub>	0,507	–
CaHap	0,018	0,031
CaFap	0,220	0,092

solubility of CaHap and CaFap is much lesser than the solubility of their components. The ratios Ca<sup>2+</sup>/PO<sub>4</sub><sup>3-</sup> indicate on an approximately congruent character of the solubility of CaHap and incongruent one of CaFap (nevertheless it is much more compare to CaHap). The mechanism of solubility of compounds in the saline melts, proposed by us, presumes an availability of the cation exchange reaction between solutes (oxides, oxo-salts, or fluorides) and solvents (saline melts). The calculated and experimental data on the solubilitis qualitatively coincide one with another, providedly at taking into account complexing processes in the saline melts.

### IV. CONCLUSIONS

An essentially new way of the synthesis of CaHap- and CaFap-based biomaterials in saline melts is developed. On the basis of a concept of solubility of the components and products in the alkaline halides melts, the mechanism of the synthesis is being proposed. This mechanism reveals the possibilities of obtaining of biocompatible items (teeth, bones) directly via the one-stage synthesis.

### ACKNOWLEDGEMENTS

Authors acknowledge the support and permanent attention to our work from Prof. Yu. Dekhtyar (Riga Technical University).

### REFERENCES

1. Kanazava T (2002) Inorganic phosphatic materials. Naukova dumka, Kiev [in Russian].
2. Shpak A P, Karbovsky V L, Trachevsky V V (2002) Apatites, Academicperiodika, Kiev [in Russian].
3. Belyayev I N, Evstifeyev E N (1975) Ionic melts as media for synthesis of inorganic substances. Naukova dumka, Kiev, Iss. 3 [in Russian].
4. Patent №69746A Ukraine. A way of the reception of hydroxyapatite / Zinchenko V F, Efruyushina N P, Stamikosto O V, Eryomin O G, Kovalevska I P. Appl. 28.11.2003; Publ. 15.09.2004 [in Ukraine]

5. Patent №72729A Ukraine. A way of the reception of fluorapatite / Zinchenko V F, Efyushina N P, Stamikosto O V, Eryomin O G, Kovalevska I P. Appl. 28.11.2003, Publ. 15.03.2005. [in Ukraine]
6. Declarative Patent on useful model № 13247 Ukraine. A way of the reception of fluorapatite. / Tarasenko S O, Eryomin O G, Zinchenko V F, Stamikosto O V. Appl. 14.10.2005, Publ. 15.03.2006. [in Ukraine]
7. Patent №78156 Ukraine. A way of the reception of hydroxyapatite / Tarasenko S O, Zinchenko V F, Eryomin O G, Stamikosto O V [in Ukraine]
8. Cherginets V L (2004) Chemistry of oxo-compounds in ionic melts. Kharkov, In-te of Single Crystals [in Russian]
9. Zinchenko V F, Stoyanova I V, Stamikosto E V, Tsyplakova N S, Tarasenko S A, Sadkovskaya L V (2008) Solubility of apatites and their components in the NaCl-KCl melt. Rasplavy (Melts) 1:36-43 [in Russian]

Author: Svitlana Oleksandrivna Tarasenko;  
Viktor Fedosiyovych Zinchenko  
Institute: A.V. Bogatsky Physical-chemical Institute of NAS of  
Ukraine  
Street: 86 Lustdorfska Doroga Str  
City: Odessa, 65080  
Country: Ukraine  
Email: svetata@ukr.net; vfzinchenko@ukr.net

# Degradation of Bone Material in Time

Yu. Dekhtyar<sup>1</sup>, V. Zemite<sup>1</sup> and H.J. Hein<sup>2</sup>

<sup>1</sup> Riga Technical University, Riga, Latvia, <sup>2</sup> Martin Luther University of Halle-Wittenberg, Germany

**Abstract** — Archaeology and anthropology are deeply interested in new technologies on reliable identification of belonging of excavated humans' skeletons of middle centuries. The investigations are devoted to detect the irreversible structural changes in bones, what form up in time. Taking into account that bone as a material relaxes in time, the work is targeted to find physical methods for characterizing structurally depended relaxing physical properties of human bones from the XIII-XVIII centuries compared with the eligible specimens from the XX - XXI centuries. The research of physical properties for characterizing degradation processes in time is targeted at macro-, micro and nano- scales: 1) for estimating of bones at macro structural scale X-ray computer tomography is used, 2) for investigation of several century human bones at micro structural level and micro-hardness, micro indentation measurement techniques were applied. 3) for examination at nano- scale Fourier transform infrared spectroscopy (FTIR), and Photo thermo stimulated electron emission (PTSEE) analysis measurement techniques were applied. The radiographic density changes measured in Hounsfield units obtained from computer tomography, have not dependence from time (centuries). The HV and E of several centuries' human bones obtained from micro hardness measurements have linear correlation with time (centuries). FT-IRS provides a maximum at line at  $2350\text{ cm}^{-1}$  and minimum at  $1726\text{ cm}^{-1}$  typical for the bones belonged to the XX century in contrast with specimens from other centuries. PTSEE has supplied a correlation of emission current derivation on the time (century).

**Keywords** — human bone, time, degradation.

## I. INTRODUCTION

Osteologists, archaeologists, specialists in forensic medicine are almost never able to estimate the age of bones - the time passed after the person death, the time of keeping underground. At present exists different dating methods of human bones – radiocarbon dating [8], thermoluminescence [1], electron spin resonance [4], amino acid racemisation dating [6], what characterise processes taking place in bones after person's death at time thousands years. In this study we interested in processes occurred at time measured hundred years.

Taking into account that bone as a material relaxes in time, the work is targeted to find physical methods for characterizing structurally depended relaxing physical properties of human bones from the XIII-XVIII centuries compared with the eligible specimens from the XX - XXI centuries.

## II. MATERIALS

In our investigation the femur, the longest, heaviest and strongest bone in the skeleton was selected, because there have been survived and unbroken. The integrity of a bone sample can be compromised by soil acidity, water damage, temperature and soil dwelling microorganisms.

Archeologically excavated human bones (femur) was used, all samples dated from the XIII-XVII century from cultural layer at the courtyard of Riga's Dome cloister (cathedral) in Latvia was obtained. The excavation is performed by specialists in archaeology and anthropology of Museum of the History of Riga and Navigation. For reference anatomically similar bones belonging to the XX and XXI century were selected for analysis too. These samples we obtained from Riga Stradins University (RSU), Institute of Anatomy and Anthropology.

From archaeological studies an archaeological age (century) was defined. The age of the graved person, as well his/her gender was recognized from anthropological studies. The age range of bones, what was choused for measurements was 30 – 50 years. The bones did not have visible paleopathological changes.

### A. Preparation of sample

For measurements of micro scale the surface of samples have to be very smooth without mechanical scrapes or gaps and parallel. The bone tissue was embedded in polymethyl methacrylate (PMMA), after fixation, dehydration and cleaning with 70% ethanol. The goals of embedding bone are avoids vibration and fracture during the sectioning process. For cutting of specimens the "Exact Trennschleifsystem" technique was used. Specimens were cut from diaphysis perpendicular to the longer bone axis. With this technique the bone samples was cut very thick slices, and during this process the samples was continuously cooled by water flow to prevent some thermal defects. The sections should be cut with slow, steady cutting stroke. The specimens were polished from one side to stick on the microscopic slide, and then specimens were polished from the other side parallel to foot. For grinding the "Exact Mikroschleifsystem" was used. This side was polished by water-proof silicon carbide paper FEPA from number 1200 (grain size  $18,0\text{ }\mu\text{m}$ ), 2400 and 4000, to get a sufficient polished



sample surface. During grinding specimen was continuously cooled by water flow to prevent some thermal defects on specimen surface. The samples was polished by polishing spray of 0,1  $\mu\text{m}$  and 0,25  $\mu\text{m}$  diamond grain size, to get a sufficient polished sample surface. The polishing machine PHOEMIX 300, Germany was in use.

The technology to prepare specimens for measurements at nano scales is described in [2]. The bones were cut transversally to their longitudinal axis by means of a stainless steel surgical saw. The obtained chips were polished with a silicon carbide papers with grain size 18  $\mu\text{m}$  and 1 $\mu\text{m}$ , washed in alcohol and dried in air at room temperature. The thickness of the specimens was reached around 2 mm ( $\pm$  0.1mm). The differences between individual samples were supplied less than 2% ( $\sim$  0.16 mm). As the result, the specimens became smooth (tested by an optical microscope  $\sim$  200 x) as good as possible.

### III. METHODS

The research of physical properties for characterizing processes, what taking place in bone material in length of time (in century), is targeted at macro-, micro and nano- scales.

For estimating of bones at macro level X-ray computer tomography (CT) is used. CT was acquired from spiral "General Electric Hi Speed DX/I" unit at the hospital "Latvijas Jūras Medicīnas centrs" (energy of photons 120 keV, current of exciting electrons 20...350 mA, soft – "Auto mA: MAX"). Measurements had been reduplicate on the CT technique "General Electric Medical System Light Speed Pro 16, CT 99\_OCO", what taking place at Hospital of Riga "Gaiļezers".

For investigation of several century human bones at micro level micro indentation measurement techniques were applied. For microindentation ultramicrohardness device UMH-10R was used. The LVH program (device software) controlled, make data recording and visualization of land penetration depth curve. Microindentation tests were done at the Martin Luther Halle/Wittenberg University.

For examination of several century human bones at nano level Fourier transforms infrared spectroscopy (FTIR), and Photo thermo stimulated electron emission (PTSEE) analysis measurement techniques were applied.

FT-IR measurements were carried out at the Martin Luther Halle/Wittenberg University room temperature on a "Bruker IR Scopell" FTIR equipped with a Cadmium Telluride detector. The spectra were measured at the range from 4000  $\text{cm}^{-1}$  up to 400  $\text{cm}^{-1}$ . To get reliable results, a total of 256 sample's scans and 256 reference's scans were taken for each spectrum by using a shuttle device. Dry air was constantly purged into the spectrophotometer to eliminate water vapor. All spectra were processed using OPUS/MAP Software.

PTSEE for *exoemission* control was used. Such a spectrometer was discussed in a great detail, for instance, in [3,5,7]. The device consists of a vacuum system, a complex of electronic devices for the PTEE intensity registration and the record of the received information blocks of photo- and thermo stimulation. Optimal methodology of photoemission test for the bone specimens was exploited in [2].

## IV. RESULTS

### A. Estimation of human bone at macro scale:

The parameter of measurements at macro scale was density. The radiographic density measured in Hounsfield units (HU) was obtained from computer tomography. The standard HU unit is assumed as the density of water – 0 HU ( $\pm$  10 HU), while air is -1000 HU. The measured area was between 18 – 80  $\text{mm}^2$ . The observed difference of HU between the specimens for each area was covered by measured values deviation. The results of CT measurements showed at fig. 1.

The results of measurements show no differences in densities of different centuries human bones.

### B. Estimation of human bone at micro scale:

Measurements at the micro scale are targeted to test morphology and local mechanical properties, for that microindentation measurement technique were applied.

We used the modified Vickers method for detection of recording microindentation and load-penetration depth-

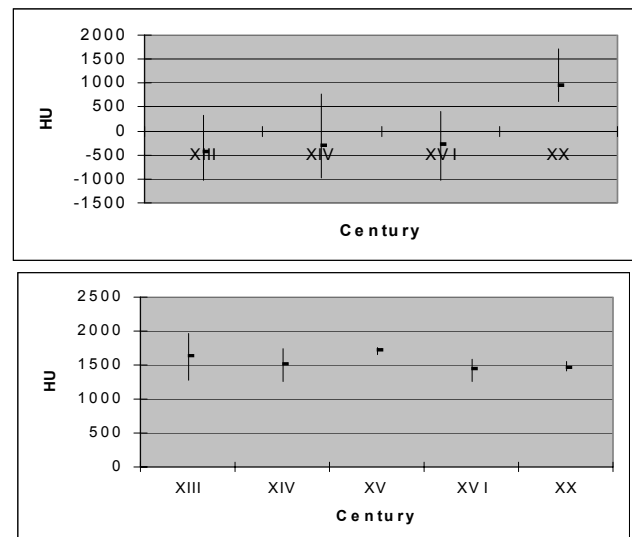


Fig. 1. Densities of several centuries' human bones measured by CT: at trabecular tissues (above) and cortical tissues (below).

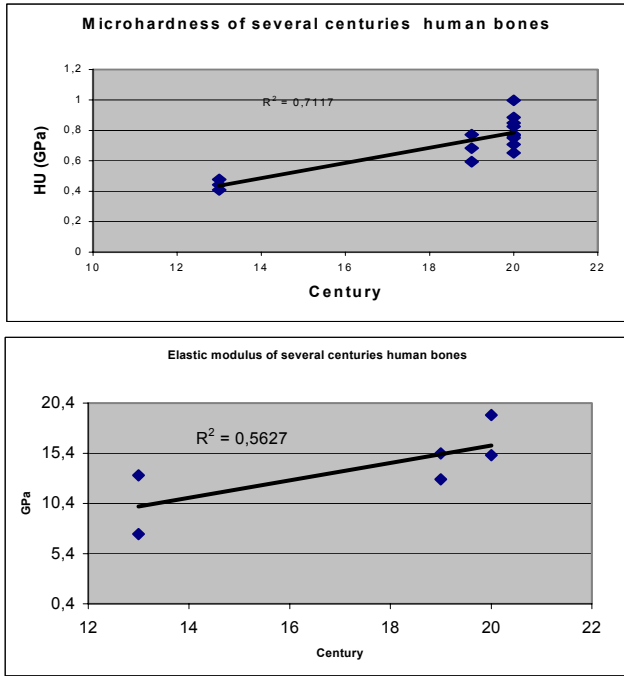


Fig. 2. Microhardness HU (above) and elastic modulus E (below) of several centuries' human bones.

curve. For calculation conventional Vickers hardness test use formula:

$$HV = k (P_{max} / h^2) \tag{1}$$

where  $P_{max}$  maximal load in our case 1 [N],  $k$  – indenter geometric constancy,  $d^2$ - indenter diameter, which is measured by optical microscope and software program LVH, [ $\mu\text{m}$ ]. Recording hardness calculation during by:

$$HU = k(P_{max} / h_{max}), \tag{2}$$

where  $h_{max}$  - is penetration depth [ $\mu\text{m}$ ],  $k$ - is indenter geometric constancy, for diamond 1854,4.

For measurements the load ( $P_{max}$ ) 1N and penetration velocity 20  $\mu\text{m}/\text{min}$  was used.

The results of elastic modulus, microhardness measurements showed in fig.2

The analysis of correlation showed that the HV and E of several centuries' human bones have linear correlation with time (centuries).

### C. Investigation of human bone on nano scale

#### 1. FT-IR measurements

FT-IR spectroscopy was applied to identify the presence of certain functional groups in a molecule and to notice changes in chemical structure of the sample.

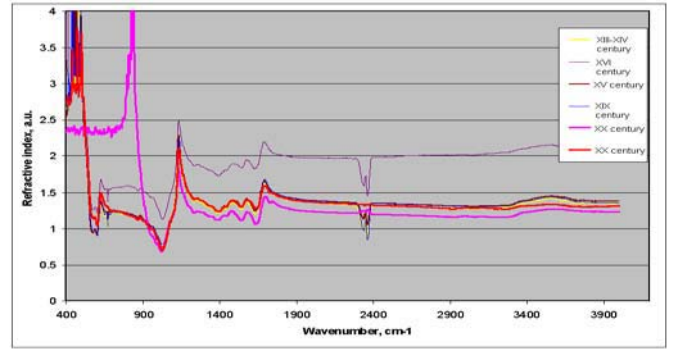


Fig. 3. The FT-IR spectra of several centuries' human bones.

Fig.5. shows infrared typical spectra of XX and XIII – XIX centuries human bones, with a minimum at wave numbers 2350  $\text{cm}^{-1}$ . For XX century human bones this peculiarity is not observed. This drop of refractive index is connected to disruption of bonds between collagen and HAP, probably C-H bonds.

At 1726  $\text{cm}^{-1}$  wavenumbers distinctive slight minimum for human bones from XX centuries, what for XIII – XIX centuries human bones is missed. According to this are collagen amide vibrations.

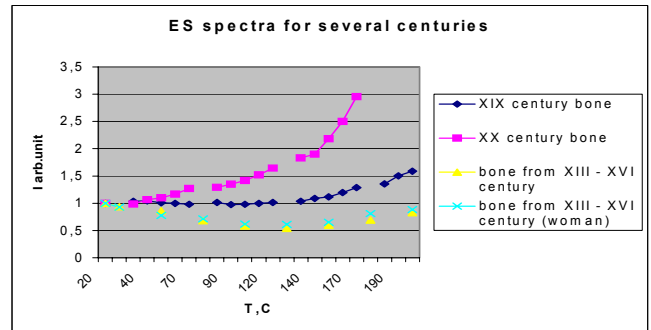


Fig. 4. Typical PTSEE spectra from several centuries' human bones.

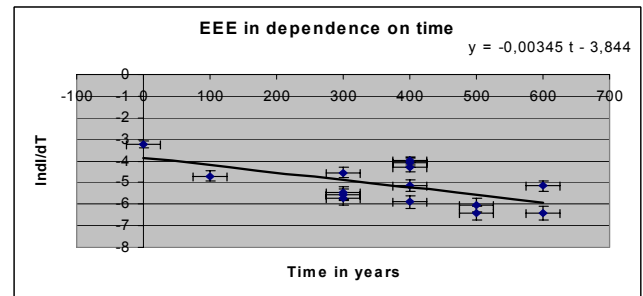


Fig. 5. Dependence of PTSE current on time.

## 2. The photo thermostimulated electron emission analysis

Because all materials are relaxing in time concentration of imperfections could become different in dependence on century. To estimate concentration of imperfections exoemission analysis having high sensitivity ( $\sim 10^{-4}$  atomic %) [6] was employed.

The samples were heated from the room temperature to  $+200^{\circ}\text{C}$  with rate  $15^{\circ}\text{C}/\text{min}$ . The error of I and T measurements did not exceed 5 % and 2% and  $\pm 1^{\circ}\text{C}$ , correspondingly [12]. The magnitude of I has a non-monotonic regularity in dependence on the specimen temperature (T). Measurements were employed in vacuum of  $10^{-4}$  Tor. Energy of photons for photo stimulation was selected 6,2 eV/200nm and the spot of the light on the specimens surface had a size  $1 \times 3 \text{ mm}^2$ . The results are provided in Figure 4. According to [3]

$$\frac{dI}{dT} = f(t) \quad (3.)$$

Because the concentration of relaxing imperfections has a direct influence on its relaxation rate the index  $dI/dT$  was in use.

$$\frac{dI}{dT} \approx \frac{dC}{dT} = -A[C(T)]^l \exp\left(-\frac{E}{kT}\right) \quad (4.)$$

the index  $dI/dT$  was in use to characterise the above. The C is the concentration of imperfections, A is a pre-exponential multiplier, l is the order of the relaxation reaction, E is activation energy and k is the Boltzman constant.

It has been found, that  $dI/dT$  correlates with  $t^*$  - archaeological age of bone. The  $dI/dT$  as function of  $t^*$  has been approximated as:

$$\frac{dI}{dT} = 0,02e^{-\frac{t}{290}} \quad (5)$$

PTSEE dependence on time (centuries) is showed at the Figure 5.

From (5), archaeological age interval that may be evaluated by means of PTEE method is approximately 580 years.

The inaccuracy of photo-thermo stimulation equals  $\pm 26$  years.

## V. CONCLUSIONS

1. The radiographic density measured in Hounsfield units obtained from CT have not difference among centuries
2. The HV and E of several centuries' human bones have linear correlation with time (centuries).
3. FT-IR provides a maximum at line at  $2350 \text{ cm}^{-1}$  and minimum at  $1726 \text{ cm}^{-1}$  typical for the bones belonged to the XX century in contrast with specimens from other centuries.
4. For estimation of several century human bones the better sensitivity of PTEE analysis, the "deepness" of this method is 580 years, the uncertainties  $\pm 26$  years.

## REFERENCES

1. Aitken M. *Thermoluminescence Dating*, 1985, Academic Press;
2. Bogucharska T., Dekhtyar Yu., Katashev A. et al Technology of preparing bone samples for exoemission tests / Latv. Journ. of Physics and Techn. Sc. Proceed. of the 13<sup>th</sup> Internat. Symp. on Exoemis. and Relax. Phenom. Jurmala, Latvia, August, 2000, 6. Supplement;
3. Dekhtyar Yu. Thesis. Riga, 1981, p. 205.
4. Ikeya, M., Miki, T., 1980. Electron spin resonance dating of animal and human bones // *Science* 207, 977-979;
5. Katashev A. Ph.D.Thesis Photothermostimulated exoelectron emission of bone tissue, Riga, 1989, p.62;
6. Robins J. Jones M. and Matisoo-Smith E. *Amino Acid Racemization Dating in New Zeland: An Overview*, 2001;
7. Sagalovich G. L., Malaxin V.P., Dekhtyar J.D. Exoelectron spectroscopy of solid state defects. Liesma: Riga, 1981, p. 77,.
8. Taylor, R.E., *Radiocarbon dating of bone: To collagen and beyond.* / Taylor R.E. et al. *Radiocarbon after four decades: An Interdiscipl. Perspective*, Springer-Verlag: New York, 1992, pp 375-402;

Author: V.Zemite  
 Institute: Riga Technical University  
 Street: 1. Kalku street  
 City: Riga  
 Country: Latvia  
 Email: vzemite@latnet.lv

# Real-Time EEG Parameterization for Shunt Decision Supporting System During Carotid Endarterectomy

A. Accardo<sup>1</sup>, M. Cusenza<sup>1</sup> and F. Monti<sup>2</sup>

<sup>1</sup> DEEI, University of Trieste, Trieste, Italy

<sup>2</sup> Clinical Neurophysiological Unity, University Hospital Cattinara, Trieste, Italy

**Abstract** — Intraoperative EEG monitoring during carotid endarterectomy (CEA) is the common operation used to reduce the risk of brain ischemia. Beside visual assessment of the EEG, some quantitative parameters, based on spectral information, have been recently suggested as additional criteria for shunt need decision. In this paper we explore spectral power-based parameters and some non linear parameters, like zero crossing (ZC) and beta coefficient, in order to find the parameter/s that could constitute a good decision support system in shunt decision. The results, compared with those supplied by the Brain Symmetry Index, suggest that the ZC represents the best parameter in a real time analysis of EEG during CEA.

**Keywords** — EEG monitoring, carotid endarterectomy, zero crossing, spectral analysis.

## I. INTRODUCTION

Carotid endarterectomy (CEA) is a well-known surgical procedure for the prevention of stroke in patient with high-grade carotid stenosis. Since routine shunting may increase the risk of perioperative stroke, CEA is generally performed with selective shunting. However, it is dependent on a reliable and accurate criterion able to identify those patients at risk for cerebral ischemia and stroke during carotid clamping if no shunt is used. Among the various criteria utilized to decide if shunting is indicated, the intra-operative EEG monitoring represents the commonest method to reduce the risk of brain ischemia [1].

Beside visual assessment of the EEG, subject to human error, some quantitative spectral parameters have been recently suggested as additional criteria for shunt need evaluation [2-4]. In this paper we explore if other parameters can be used for a real-time decision support system. In particular we examined the spectral power in the traditional EEG-ranges (delta 0.5-4Hz, theta 4-8Hz, alpha 8-13Hz and beta 13-18Hz bands) and the ratio between the power in the 8-15Hz and in the 0.5-5Hz (HF/LF) bands, following the hypothesis that in presence of brain suffering the spectral power decreases in the medium-high frequency band and could increase in the low frequency band.

Beside these linear parameters we also investigated some non linear ones like the Zero Crossings count (ZC) and the

power law beta scaling exponent (Beta exponent) that showed to be sensible to different EEG comportamental states bringing complementary information in respect to those carried out by a linear examination [5-7].

## II. MATERIALS AND METHODS

A large number (110) of EEGs derived from patients (35 females and 75 males) who underwent CEA procedure at the Neurophysiological Unity of Trieste were retrospectively examined.

Ten bipolar EEG derivations (F4-C4, C4-P4, P4-O2, F8-T6, T6-O2, F3-C3, C3-P3, P3-O1, F7-T5, T5-O1) were sampled at 128Hz and used for the analysis. Each of these was digitally filtered (0.4Hz high pass and 40Hz low pass) and divided into 50% overlapping sections of 20s. For each interval we computed the zero crossing (ZC), by counting the number of baseline crossings, the power spectral density (PSD) after a Hamming windowing and the Beta exponent by calculating the slope of the linear regression curve of the PSD represented in a double logarithmic plot.

For each parameter, the mean value calculated in the three minutes before clamping was considered as a baseline. Then the percent relative variations of each parameter after carotid clamping with respect to the baseline were calculated for each hemisphere, every 10 seconds.

We compared the behaviour of these indexes to that of the Brain Symmetry Index (BSI) suggested by van Putten [2]. The BSI index is a normalized measure for interhemispheric spectral symmetry defined as:

$$BSI = \frac{1}{N} \sum_{i=1}^N \left\| \frac{1}{M} \sum_{j=1}^M \frac{R_{ij} - L_{ij}}{R_{ij} + L_{ij}} \right\|$$

with  $R_{ij}$  ( $L_{ij}$ ) the Fourier coefficient belonging to frequency  $i=1, \dots, N$  of right (left) hemispheric bipolar derivations  $j=1, \dots, M$ . In our case  $M=5$  and  $N=50$  (frequency range 1-25Hz, with spectral bandwidth of 0.5Hz). It represents a measure of the hemispheric symmetry estimated from the absolute value of the relative difference of the average spectral density of the right and left hemisphere. A perfect symmetry for all channels corresponds to  $BSI=0$ .

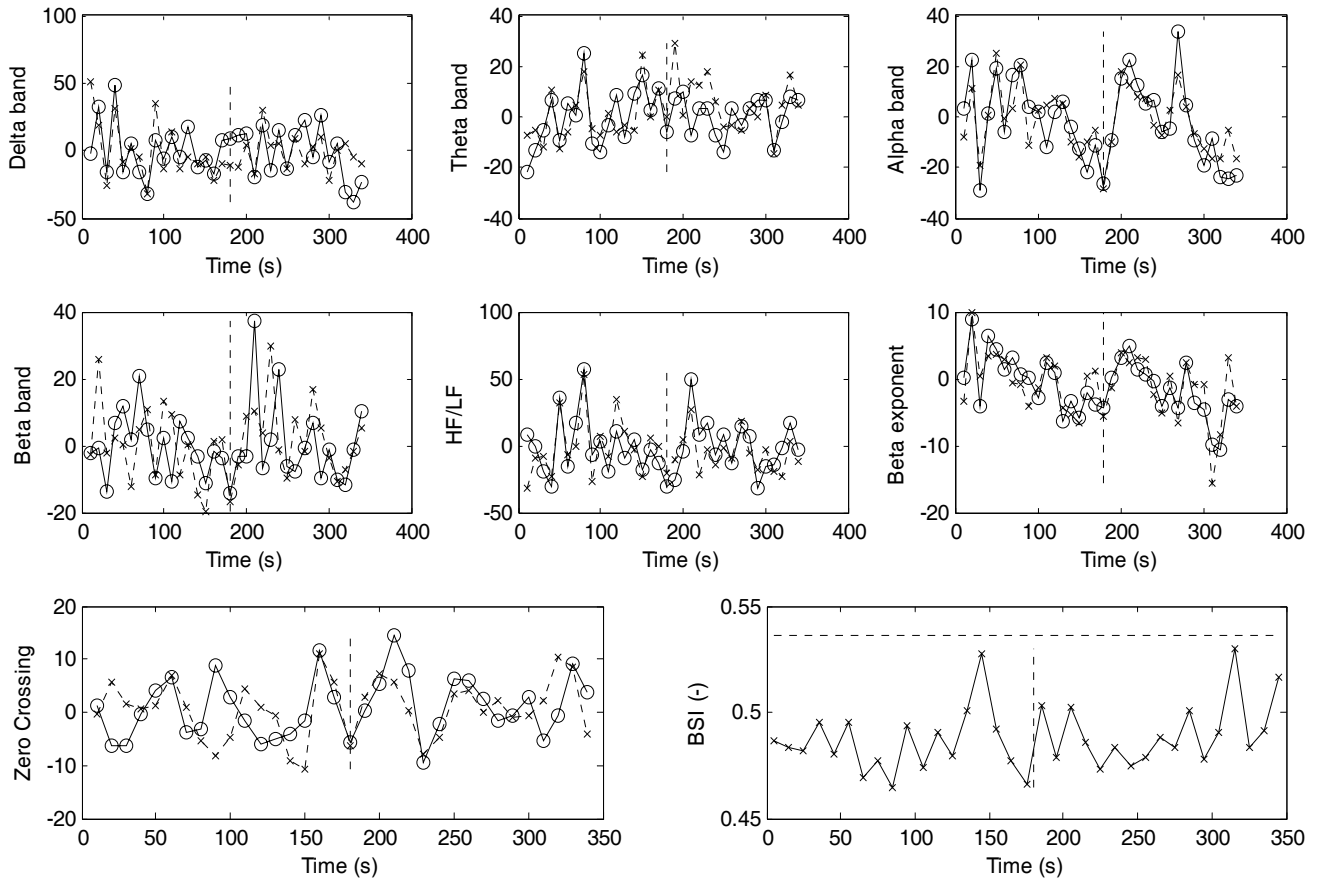


Fig.1 Example of parameter behaviours in a patient without shunting. The vertical line represents the start of clamping procedure. Crosses represent right side and circles represent left side responses. In the BSI parameter, the dashed horizontal line corresponds to the threshold calculated as in [2].

### III. RESULTS

Analysis of EEGs showed that hypoperfusion was generally accompanied by a decrease (monolateral or diffuse) of the power in the alpha and beta bands and frequently also by an increment in the delta band, confirming previous results [8-9]. ZC and HL/LF ratio also decreased during sufferece, correctly identifying all the situations of the examined patients. On the contrary, the Beta exponent as well as the BSI parameter were not able to recognize more than 40%/60% (respectively) of shunted cases while all the normal situations were correctly identified.

Examples of parameters time courses in three patients who underwent a carotid endarterectomy are shown in Figs.1, 2 and 3.

The patient in Fig.1 did not need the shunt. All the spectral parameters as well as the beta exponent and the zero crossing did not show any change. At the same way also the BSI parameter did not exceed the threshold.

The patients in Figs.2 and 3, on the contrary, represent cases with asymmetric suffereces that needed a shunt. In both cases, many parameters, immediately (10-20s) after the begin of the clamping procedure (vertical bar), presented very evident changes: the power in the high frequency bands (alpha and beta bands) abruptly decreased as well as partially happened also in the theta band, while the delta band did not show any significant variation. The HF/LF, the Beta coefficient and the zero crossing displayed a similar response, also maintaining the asymmetric characteristic. The BSI, instead, presented an ambiguous behaviour: in the patient of Fig.2 it noticed the asymmetry while in the patient of Fig.3 it did not exceed the threshold and consequently it did not signal the risk of a possible ischemia.

In both cases, after about 60s, due to the cerebral sufferece, the clamping procedure was interrupted. In fact all the considered parameters slowly turn back to the baseline values (in the last case a second clamping attempt was made).

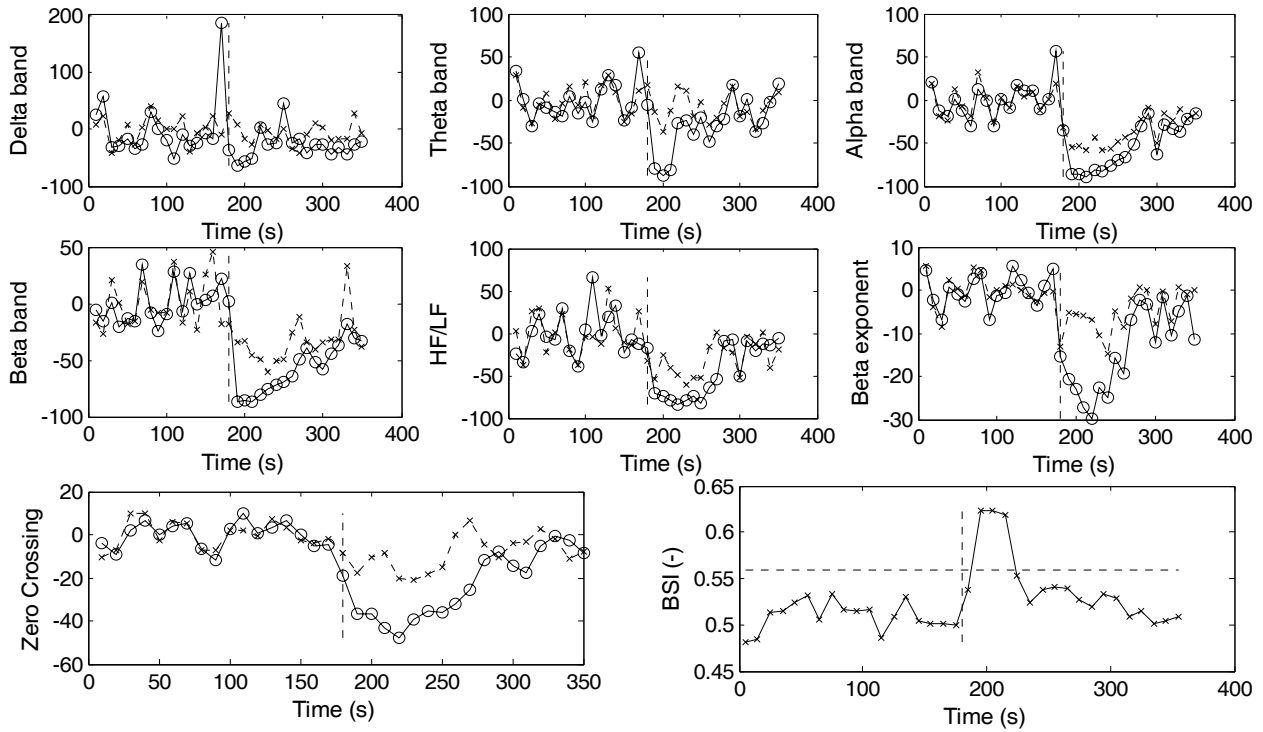


Fig.2 Example of parameter behaviours in a patient that needed shunting. The vertical line represents the start of clamping procedure. Crosses represent right side and circles represent left side responses. In the BSI parameter, the horizontal dashed line corresponds to the threshold calculated as in [2].

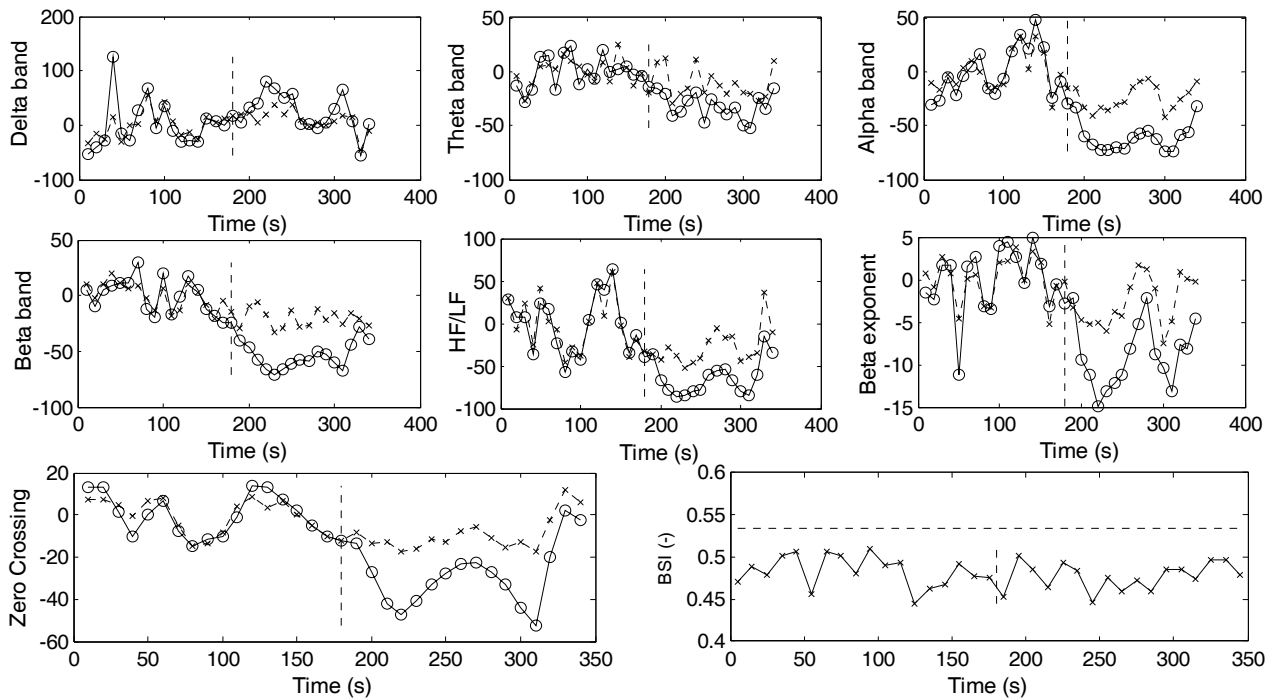


Fig.3 Example of parameter behaviours in another patient that needed shunting. In this case the BSI parameter did not signal the risk.

#### IV. DISCUSSION

Although the visual analysis of the EEG represents the standard method to decide when the shunt is needed during CEA, quantitative real-time EEG analysis represents a useful additional information assisting in the decision for selective shunting. In literature some parameters have been proposed even if their validity has been evaluated only preliminarily on few cases [2-4]. In this paper we examined, on a large number of CEA cases, some new parameters helpful in the monitoring of cerebral hypoperfusion due to artery clamping.

Our results confirm that medium-high frequencies are more sensitive to cerebral ischemia than other spectral bands. In any case, the HF/LF ratio is the linear parameter that better recognized hypoperfusion. On the contrary, theta power parameter seems to have no clinical significance.

ZC parameter proved to be a measure capable to sense reduction of fast activity as well as of possible slow activity changes. In fact, like HF/LF ratio, it always decreased after artery clamping in shunted patients. Similar results (but with about 40% of errors) were achieved by the Beta scaling exponent. The results obtained by using these parameters were compared with those achieved by the Brain Symmetry Index recently proposed by van Putten [2]. We found that this parameter alone is not able to identify the suffering, showing intrinsic limitation due to the demand of very altered EEG symmetry in order to operate in a correct way.

Finally we would underline that the ZC parameter is very easy to calculate directly from temporal signals and it does not need power spectrum evaluation of EEG (as spectral-based parameters like HL/LF ratio does); hence it is suitable for a real time implementation and its time course, added as a further signal in the visualization of EEG derivations, may permit the successful outcome of the surgical procedure.

#### V. CONCLUSION

EEG monitoring by means of suitable parameters quantifying the EEG changes proved to be useful in shunt decision during CEA.

The results reported in this paper show that the HL/LF ratio and the ZC indexes are able to correctly identify cases presenting mono- or bi-lateral hemispherical changes capturing both asymmetric and diffuse suffering situations. In

fact, in our retrospective analysis, those patients for which the visual EEG analysis showed significant changes (and a shunt was advised) also presented values of the HF/LF ratio and the ZC parameters that quickly decreased after the start of clamping.

In conclusion we think that the percent relative variation function of the ZC parameter represents the best choice both for a correct classification and for the possibility of a real time implementation. Thus we propose to use the ZC parameter to support the visual assessment of the EEG during CEA, offering a quantitative measure for EEG alterations due to cerebral hypo-perfusion.

#### REFERENCES

1. Pinkerton JA (2002) EEG as a criterion for shunt need in carotid endarterectomy. *Ann Vasc Surg* 16:756-61
2. van Putten MJAM, Peters JM, Mulder SM, de Haas JAM, Bruijninx CMA, Tavy DLJ (2004) A brain symmetry index (BSI) for online EEG monitoring in carotid endarterectomy. *Clin Neurophysiology* 115:1189-94
3. Cursi M, Meraviglia MV, Fanelli GF et al (2005) Electroencephalographic background desynchronization during cerebral blood flow reduction. *Clin Neurophysiol* 116: 2577-2585
4. van Putten MJAM (2006) Extended BSI for continuous EEG monitoring in carotid endarterectomy. *Clin Neurophysiol* 117:2661-6
5. Garrett D, Peterson DA, Anderson CW, Thaut MH (2003) Comparison of linear, nonlinear, and feature selection methods for EEG signal classification. *IEEE Trans Neural Syst Rehabil Eng* 11:141-4
6. Carrozzi M, Accardo A, Bouquet F (2004) Analysis of sleep-stage characteristics in full-term newborns by means of spectral and fractal parameters. *Sleep*. 27:1384-93
7. Acharya U R, Faust O, Kannathal N et al (2005) Non-linear analysis of EEG signals at various sleep stages. *Comput Methods Programs Biomed*. 80:37-45
8. Visser GH, Wieneke GH, van Huffelen AC (1999) Carotid endarterectomy monitoring: patterns of spectral EEG changes due to carotid artery clamping. *Clin Neurophysiol* 110:286-94
9. Minicucci F, Cursi M, Fornara C et al (2000) Computer-assisted EEG monitoring during carotid endarterectomy. *J Clin Neurophysiol* 17:101-7

Corresponding author:

Author: Agostino Accardo  
 Institute: DEEI-University of Trieste  
 Street: Via Valerio, 10  
 City: Trieste  
 Country: Italy  
 Email: [accardo@deei.units.it](mailto:accardo@deei.units.it)

# Automatic Quantification of Handwriting Characteristics Before and After Rehabilitation

A. Accardo<sup>1</sup> and I. Perrone<sup>2</sup>

<sup>1</sup> DEEI, University of Trieste, Trieste, Italy

<sup>2</sup> Dept. of Development Age, ULSS 7, Pieve di Soligo (TV), Italy

*Abstract* — Handwriting represents a complex motor behaviour recently analysed by using direct measurements carried out by digitizing tablets. This technology allows objective quantitative kinematic analyses of the quality of writing and can be used to study handwriting disturbances, that can be found in primary school-aged children, as well as the effects of a rehabilitation treatment.

The aim of this paper is to present a system able to analyse handwriting movements produced by children presenting dysgraphia, submitted to a rehabilitation treatment. The writing task consisted of a sequence of ‘lelele’, written by the subjects before and after a suitable spatio-temporal rehabilitation treatment (Terzi’s method). Handwriting samples from 14 non-proficient handwriters children attending primary school were collected before and after rehabilitation, with the aid of a digitizing tablet (Intuos3®, Watcom). The movements were segmented and each identified stroke was analysed by a suitable ad hoc software that calculated a series of static and kinematic parameters linked to pressure, trajectory and velocity features of the tract, in order to measure the procedure efficacy.

By means of the realized system significant differences in handwriting characteristics estimated before and after treatment were found. In particular a significant increase of the mean pressure calculated on each stroke ( $p < 0.001$ ) as well as an increment of the mean velocity during single stroke ( $p < 0.02$ ) and the mean width of a stroke ( $p < 0.02$ ) were pointed out. Significant differences were also found for the mean velocity along the whole curvilinear written tract ( $p < 0.02$ ) between the two conditions. On average the subjects improved in speed of writing after the intervention period thus demonstrating the efficacy of the Terzi’s method therapy.

These results demonstrated the potential of the realized system that provides quantitative spatio-temporal measures of handwriting performance, useful for the evaluation and treatment assessment of handwriting difficulties.

*Keywords* — Handwriting, Rehabilitation, Terzi’s method, spatio-temporal treatment, dysgraphia, kinematic analysis, children.

## I. INTRODUCTION

Handwriting represents a specific motor task in which the movement is realized by following a precise spatio-temporal sequence. In this process particular care must be

placed both in the correct automation of each grapheme and in the ergonomic aspect of the posture.

Both the main handwriting actions (“inscription” and “progression”) require a correct coordination among fine movements and the progression of wrist, forearm and shoulder. The automation of these movements permits the child to become more and more speedy and regular in the tracts execution.

On the other hand, disturbance in the neuromotor efficiency affects pattern velocity and regularity as well as the correctness and legibility of writing [1]. In particular dysgraphia, that represents a learning disability resulting from the difficulty in expressing thoughts in writing, refers to the poor handwriting that can be found in primary school children.

In the last years, the writing analysis has been carried out by using a direct measurement of handwriting movements acquired by digitizing tablets. This technology also allows objective quantitative kinematic analyses of the quality of writing and it has recently been used to characterize the handwriting process in children [1] as well as in elderly subjects [2] and in Parkinson’s disease [3].

The aim of this study is to develop an instrument to evaluate a rehabilitation process for graph-motor disorders treatment, starting from handwriting characteristics of primary school children. Parameters linked to the velocity profiles of strokes are used to verify how treatment modifies particular kinematic characteristics. The Terzi’s rehabilitation program, a spatio-temporal approach to the treatment of dysgraphia, is in particular examined.

## II. MATERIALS AND METHODS

The handwriting of 14 non-proficient handwriters children (aged 9-12 years) attending primary school studies were acquired, before and after a rehabilitation program, at the Dept. of Development Age (ULSS 7) of Pieve di Soligo (TV), by means a digitizing tablet (Wacom, Inc., Vancouver, WA, Model Intuos 2).

Pen displacement across the tablet is recorded at 100Hz sampling frequency both in the horizontal and vertical directions with a spatial resolution of 0.01 mm.



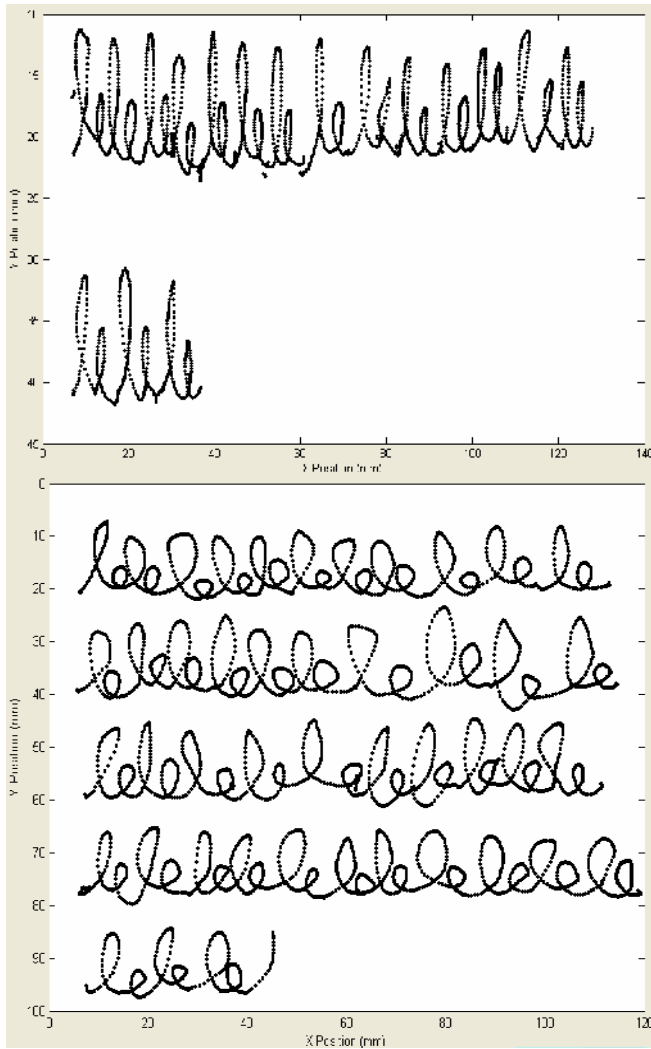


Fig.1 Example of writing test ('lelele') in a child before (top) and after (bottom) the rehabilitation program. In both cases the subject wrote for one minute.

A simple writing exercise mainly involving motor abilities was required. The task consisted of a one-minute continuous sequence of 'lelele'. This pattern represents an almost pure grapho-motor task, not involving significant words, permitting the identification of possible handwriting difficulties.

An user friendly device [4], based on the GUI (Graphical User Interface) tool of MATLAB® (Mathworks), allowing the analysis of handwriting data both in spatial and time domains was used and further developed. In particular it permits the movement segmentation, automatically identifying strokes starting from the curvilinear velocity curve; the curvilinear motion has been reconstructed in the x-y plane starting from the X and Y components. The procedure de-

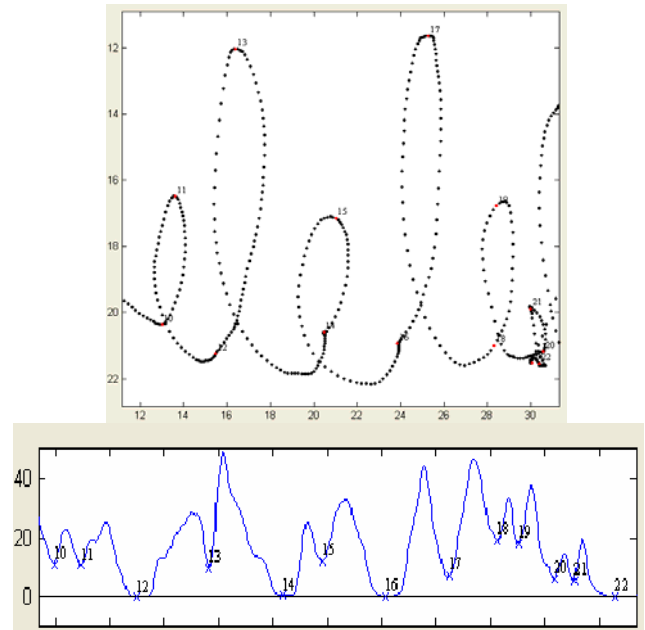


Fig.2 Top: Example of some strokes identification in the writing of Fig.1 (before treatment). The starting point of each stroke is progressively numbered. The horizontal and vertical scales are in mm. Bottom: Curvilinear velocity profile corresponding to the top x-y spatial tract. The numbering is the same of the top panel. Horizontal scale: 1 tick= 1/2 s; vertical scale in mm/s.

terminates points of minimal curvilinear velocity (Figs. 2 and 3, bottom), hypothesizing that each velocity minimum corresponds to a different motor stroke, as claimed by the bell-shaped velocity profile theory [5]. Stroke identification numbers superimposed on the velocity profiles allow comparison of spatial and temporal elements (see examples in Figs. 2 and 3). A series of static and kinematic parameters linked to pressure, trajectory and velocity features of each stroke are calculated, in order to measure the procedure efficacy and to evaluate what parameters are more sensitive to the recovery process.

The rehabilitation program is based on a cognitive-motor methodology (Terzi's approach [6]) that permits to develop the ability to obtain aware of the spatio-temporal information reaching cerebral structures from peripheral perception in order to correctly process and integrate them for a conscious use of the body during movement. The treatment affects the organization of both the personal (posture, pen hold) and extra-personal (metrical representation) spaces. In particular a geometrical re-construction of graphomotor patterns is carried out.

All children undergo the treatment for at least 15 sessions of 45' each, and their handwriting were recorded before and after the conclusion of the rehabilitation program.

### III. RESULTS AND DISCUSSION

Figure 1 shows the x-y handwriting tests of a child before (top) and after (bottom) the rehabilitation program. Since in both cases the subject wrote for one minute, it is evident that after the treatment the total number of written letters is more than doubled. At the same way also the curvilinear velocity (Figs. 2 and 3) is about doubled.

Moreover, after rehabilitation (Fig.3), the motor planning is different than before (Fig.2) changing from a single letter programming to multiple letter planning. This can be deduced from the instants in which the curvilinear velocity is near zero. More time the velocity is maintained high, more following strokes programming are superimposed demonstrating a higher automation of the motor action.

By means of the realized system we quantified these modifications founding significant differences in handwriting characteristics estimated before and after treatment. In particular a significant increase of the mean velocity during single stroke ( $p < 0.02$ ) and the mean width of a stroke ( $p < 0.02$ ) were pointed out (Fig.4). At an individual level, three out of the fourteen children after the treatment showed a little velocity reduction rather than the increment. The

increment of the velocity in the stroke production is an index of the old motor program substitution with another more automated that is able to produce a more fluent tract. On the other hand, the velocity decrement present in some subjects is compatible with the hypothesis that these children require a longer time for consolidate the new motor programs, still not at all automated.

Significant differences between the two conditions were also found for the mean velocity along the whole curvilinear written tract ( $p < 0.02$ ). On average the subjects improved in speed of writing after the intervention period. Moreover, an increment of the mean pressure calculated on each stroke ( $p < 0.001$ ) was generally found (Fig. 5).

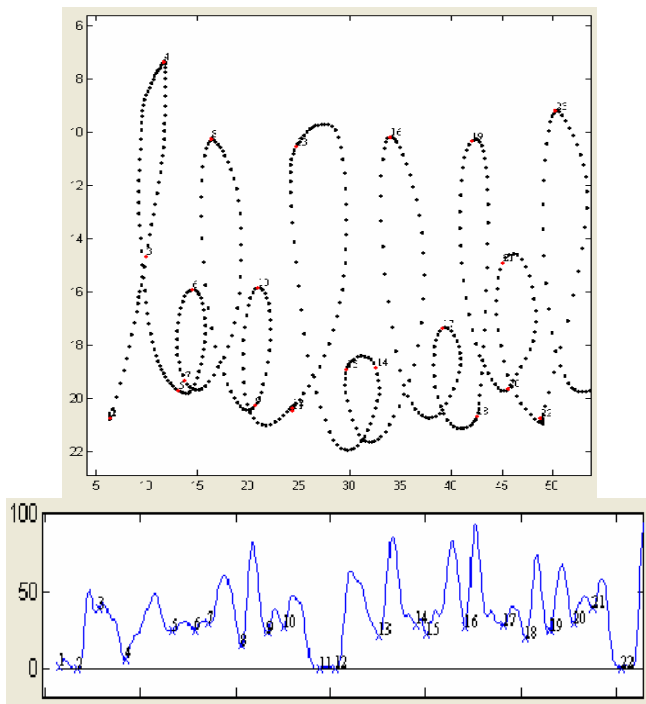


Fig.3 Top: Example of some strokes identification in the writing of Fig.1 (after treatment). The starting point of each stroke is progressively numbered. The horizontal and vertical scales are in mm. Bottom: Corresponding curvilinear velocity profile and stroke numbering. Horizontal scale in sec; vertical scale in mm/s.

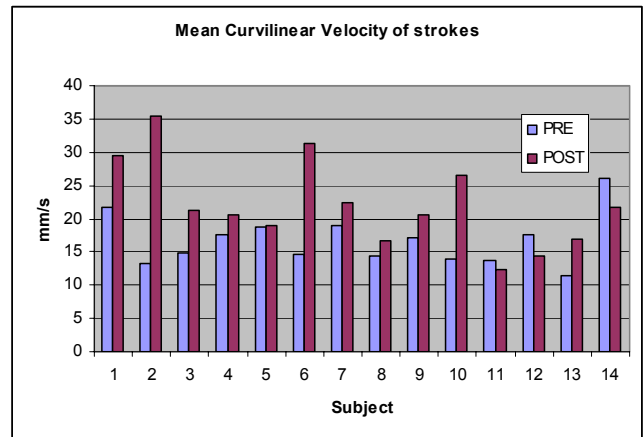


Fig.4 Mean curvilinear velocity of strokes in the considered children before (PRE) and after (POST) the rehabilitation treatment. Generally the velocity significantly increased, in a subject unchanged and in three children decreased.

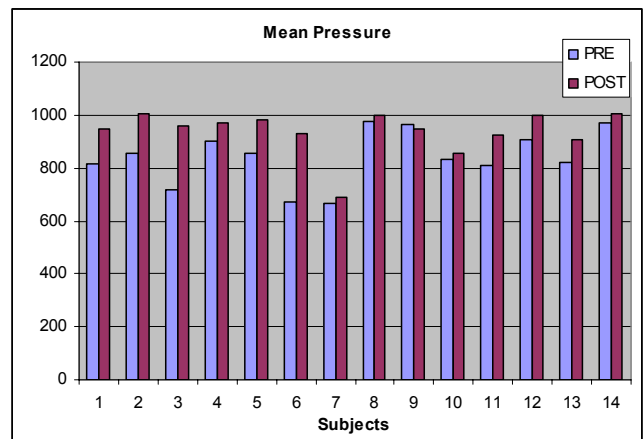


Fig.5 Mean pressure values in the children before (PRE) and after (POST) the rehabilitation treatment. Only in five cases the pressure remains about unchanged.

The pressure increase do not correspond to an excessive muscular tone rather to a passage from a muscular hypotonicity with a fluttering tract to a more checked pressure determining greater accuracy in the production of the graphic tract.

#### IV. CONCLUSIONS

The results, confirming previous preliminary findings [7], demonstrate the potential of the realized system that provides quantitative spatio-temporal measures of handwriting performance, useful for the evaluation and treatment assessment of handwriting difficulties, and can assist for a more comprehensive understanding of handwriting difficulties. The kinematic analysis of handwriting, carried out by the system, not only provides important information about the processes and strategies involved in learning and controlling handwriting but also constitutes a useful support for monitoring progress during the treatment of dysgraphia. In particular, the specific application of the system reported in this study suggests that the application of the Terzi's rehabilitation method improves the graphomotor patterns of the letter especially increasing the stroke speed of children initially identified as having poor handwriting quality.

#### ACKNOWLEDGMENT

The authors thank the working group of the Dept. of Development Age of the ULSS 7 for the valuable suggestions.

Work partially supported by the Dept. of Development Age, ULSS 7, Pieve di Soligo (TV), Italy.

#### REFERENCES

1. Rosenblum S, Chevion D, Weiss PL (2006) Using data visualization and signal processing to characterize the handwriting process. *Pediatric Rehabil.* 4:404-17
2. Rosenblum S, Werner P (2006) Assessing the handwriting process in healthy elderly persons using a computerized system. *Aging Clin Exp Res.* 18(5):433-9
3. Tucha O, Mecklinger L, Thome J et al (2006) Kinematic analysis of dopaminergic effects on skilled handwriting movements in Parkinson's disease. *J Neural Transm.* 113(5):609-23
4. Accardo A., Chiap A., Borean M. et al (2007) A device for quantitative kinematic analysis of children's handwriting movements. *Proceed of MEDICON, Ljubljana 26-30 june 2007*, 445-8
5. Plamondon R (1991) On the origin of asymmetric bell-shaped velocity profiles in rapid-aimed movements. In J.Requin and GE Stelmach (Eds) *Tutorial in motor neuroscience*, Kluwer Academic Publishers, Dordrecht, 283-295
6. Terzi I (1995) *Il Metodo Spazio-Temporale*. Ed. Ghedini, Milano, Italy
7. Bravar L, Borean M, Zin R, et al. (2005) Use of a graphic tablet in the evaluation of handwriting skills, before and after a movement-based treatment, in a group of children with dysgraphia. *6th Int. Conf. on Develop. Coord. Disorder (DCD)*, Trieste, Italy, May 17-20

Author: Agostino Accardo  
 Institute: DEEI-Dept of Electronics  
 Street: Via Valerio, 10  
 City: Trieste  
 Country: Italy  
 Email: [accardo@deei.units.it](mailto:accardo@deei.units.it)

# Reciprocating Orthotics Complex (ROC) for Children Suffering from Cerebral Paralysis and Spinal Diseases

E. Dukendjiev<sup>1</sup>

<sup>1</sup> Atypical Prosthesis Laboratory Latvia, Riga

**Abstract** — In order to dissociate pathologic interaction of executive periphery and cerebral structures and to induce formation of new reflex bonds strengthened during treatment, it is necessary to produce mechanically forced targeted corrected locomotive motions by external energy. Thus, to provoke inborn reflexes and synergy (background levels) and to form forced (within the norm) dominants of highly automatic movements.

**Keywords** — palsy, treatment, reciprocal, gate, synergy

## I. INTRODUCTION

For treatment of the mentioned above groups of diseases all known methods such as “Adeli”, Botatov’s, Peto’s, Voity’s, Koziavkin’s, etc. are based on the patient’s self-energy. Competence limit is determined by physical and control abilities of the patient, i.e. the process of treatment in its essence is passive and very variative and needs clinic department.

At both characteristic groups of diseases patients often suffer from vertigo, pallor, weakness, up to syncopes and fainting when getting up from the lying or sitting position (orthostatic hypotonia).

The methods of body verticalization, standing training do not improve the patient’s condition and do not contribute to ambulation and even vice versa. The reason lies in the essence of the process – body statics does not cause afferent muscular activity and causes little afferent control activity.

In order to dissociate pathologic interaction of executive periphery and cerebral structures and to induce formation of new reflex bonds strengthened during treatment, it is necessary to produce mechanically forced targeted corrected locomotive motions by external energy. Thus, to provoke inborn reflexes and synergy (background levels) and to form forced (within the norm) dominants of highly automatic movements.

## II. METHOD

The method is formed on the level of microstructure of movement control [2]. In the phase of muscles stimulation locomotor centers release from the inhibitory influence and

become available for correction measures. Due to motoneuron pools, spinal interaction can be realized, which organize throbbing like stepping ones. The final aim of the method is to influence the slow moving units by compulsory extension.

What is the “material basis” of the author’s idea?

For example, only in the gastrocnemius muscle there are more than 800 slow moving units, and in every moving unit there are about 2000 muscle fibres. Within the skeletal muscular system function hundreds of thousands of moving units and millions of muscular fibres, i.e. quite a mighty basis for the implementation of the method!

**Biomechanical elements.** The smallest anatomically independent structural unit of the muscular system is skeletal muscle tissue. Muscle and other cells are included into the structure of muscle tissue - *smooth (nonstriated) and cross-striped (striated)*. Striated muscles activate bones, actively change human body position.

**Bioelectronics elements.** The smallest anatomically independent unit of nervous system is a nerve cell (neuron) with branching processes. The cell is dynamically polarized that is able to let pass the nervous impulse only in one direction, from the dendrite to the axon. In the nervous system the neurons form chains, which transfer stimulation from the point of appreciation of the stimulation to the central nervous system and further to the working organ. There are three main types of neurons:

1. Sensory, receptor perceive stimulation in the tissues of the bodies themselves, they are located in muscles, tendons, ligaments, fascias, bones, articular capsules, etc.
2. Intercalary neuron realizes transmission of the stimulation from the sensory neuron to the motor one. Intercalary neurons are located within the central nervous system.
3. The bodies of efferent neuron are located in the central nervous system. Their axons spread to the working organs. Nerve endings of the axons of efferent neurons can be of two types: motor and secretory. Motor ones have their endings in muscle fibers forming *neuromuscular synapses*.

**Biomechatronical elements.** There is an end bud and a *neuromuscular synapse* in each muscle fibre, which are the means of transmission of the impulse to traction. The moving units are motoneurons (the smallest functionally

independent unit of biomechanotronics) which innervate the group of muscular fibers.

The degree of muscle contraction is controlled by three mechanisms:

- active moving units (motoneurons) regulation of the given muscle;
- regulation of the method of their work (motoneurons impulse frequency)
- regulation of temporary connection of moving units activity (motoneurons).

Recruitment phenomenon of motoneurons happens according to their size, i.e. slow, type I moving units muscles are active in any tension.

Slow motoneurons prevail, especially in childhood. It's necessary to influence them mechanically forcibly, hence their number constitutes more than 50 % of the total amount and they influence the generation of induced signals.

**Movements control.** Simple reflexes are effected by "lower parts of the central nervous system, i.e. spinal cord. The simplest reflex arch consists from two neurons, sensory and motor. Most often the reflex arch consists of many neurons. Then intercalary neurons are located between the afferent and efferent neurons. In such reflex arch the stimulation from the sensory neuron is transferred along its central process to one or several intercalary neurons.

Ukhtomsky A.A [3]. discovered the principle of domination. Functional systems combine all subordinate structures. In certain conditions the dominant nerve center can head the reflex action on the dominant enhancement and inhibition of other activities.

Later Anokhin P.K. [4] created the functional system theory. Anokhin P.K. understood "a range of certain physiological manifestations connected with performing some certain function (the act of breathing, the act of swallowing, locomotor act, etc.)" under the functional system.

Anokhin P.K. and his students proved the presence of the so called feedback of the working organ with the nerve centres, i.e. "reciprocal afferentation" in the course of experiments. The moment the efferent impulses from the nervous system centres reaches executive organs, the response appears (movement or secretion). This working effect stimulates the receptors of the executive organ itself. The impulses which appeared as a result of these processes go back to the centres of the spinal cord or the cerebrum along afferent ways in the form of information about the completion by the organ of a certain action at every certain moment. Thus, the ability of precise registration of the accuracy of orders execution in the form of nervous impulses, coming to the working organs from nerve centres, and their continuous correction is created. The existence of bilateral signaling in closed circular or annular reflex

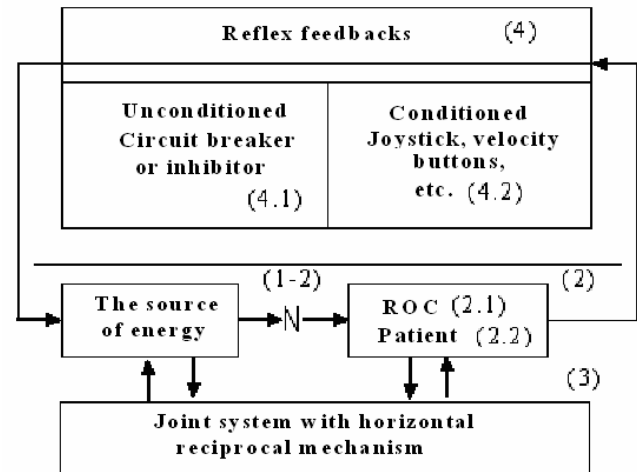


Fig.1. Reciprocal orthosis complex (ROC).

nervous chains of the "reciprocal afferentation" allows to hold constant continuous corrections of the organism responses to any changes in ambient and internal conditions.

The objective: in the canals of the "reciprocal afferentation", transferring to the brain the distorted because of MAD and attack angle sensor (AAS) information, it's necessary to bring in the correct information, which in course of time will become dominant.

The objective: synthesis of the mechanical system with smooth movements – reciprocal orthosis complex, realizing:

- kinematic interdependency between large joints;
- kinematic interdependency between lower extremities, body and upper extremities.

In the phase of muscles stimulation (forced by ROC) locomotor centers release from the inhibitory influence and become available for correction measures.

### III. RESULTS

The ROC developed by the author can be conditionally called an "artificial locomotion apparatus", which works at the expense of external energy with full deficits of muscular and control activity, i.e. with minimal, purely organic participation of brain in the process of walking.

ROS [1] is suspended with the help of a spherical junction in the common center of weights several millimeters higher of treadmill and the toes of both legs are fixed firmly by horizontal reciprocal yoke.

This provides [5]:

- Sequence of contact of a left and right leg with a moving belt;

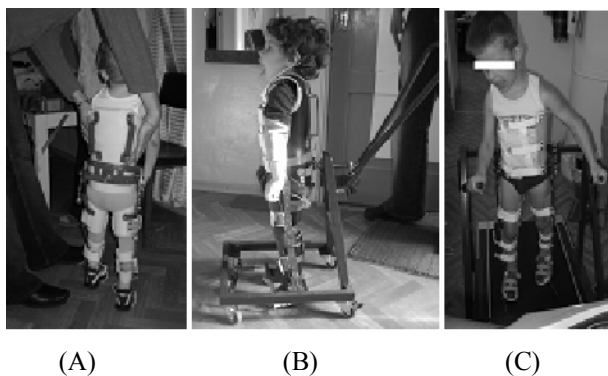


Fig.2. The developed ROC.

- transformation of external energy pathway, produced with the principle of a flat type flywheel clutch – ROS soles in the result of the frictional force are forced to move reciprocally;
- kinematic synchronization of three reciprocal mechanisms – for upper lower and extremities and feet, thus providing dimensionally balanced motions of the whole body.

The developed ROC which unites ROS (Fig.2.A) for the whole body with verticalization chair with a horizontal reciprocal mechanism (Fig.2.B) and treadmill (Fig.2.C) is a device stimulating artificial locomotion which works on the basis of external energy at complete deficit of muscle and control activity.

ROC can be regulated to the height, clasps “velcro” provides fast system removal/putting on. It can be used at home and in clinics.

In several months, after the muscles are strengthened, the treatment is continued only with the use of ROS with own muscle abilities.

ROC were constructed for 15 patients: ICP-7, spina bifida-2, spinal traumatism-2, paraparesis after tick-borne encephalitis-1, hypoxic ischemic damages of CNS-1, multiple congenital anomalies-1, arthrogryposis-1.

#### IV. DISCUSSION

With the help of mechanical force realized on the macro level of the reciprocal ортезного complex with the use of internal source of energy to cause changes in the reflex influence changes from the spindles and tendinous Goldgi's receptors, so that to get any activity flexors and extensor muscles ratios, observing the mechanism of reciprocal antagonist inhibition.

The source of forced bioelectric activity is afferentation going from any receptors, which inform about the course of

biomechanical task solution when mechanically forced. It incorporates into action any reflexes. Repeated reiteration cyclic actions along one and the same joints trajectory forcibly form synergies, creating and improving walking skills. The program of movements is worked out which mobilizes all necessary for the act of movement arsenal of levels and particular physiological mechanisms.

The author method has several aspects with different weight values in the process of movement realization - bioelectric, hemodynamic, biochemical.

Bioelectric aspect is the most important as with the help of the aspect the correct long-term movement stereotypes are formed. The processes of transformation of the external mechanical energy begin from the reaction of proprioceptors of muscle cells and tissues for forced extension. Under normal conditions the micro movement of one bone to the other bone is the result of muscle-antagonists work, regulated by the reciprocal reflex. The succession is as follows: agonist actively contracts and antagonists relax. In case of cerebral palsy spinal column and cord traumas the normal activities of the movement units are violated - they are contracted simultaneously generating trembling movement of six moves per second amplitude. The proposed inversion of "cause-consequence" of movement solves the problem - the "solid" links of the biokinematic chain of a limb after the external mechanical forced extension become the "cause" of the movement and antagonist muscles are forced to relax/contract passively without usage of inner energy, so they become "consequence"/ In such transformation the significant part of the inner energy is redirected to compensate MAD.

Haemodynamical aspect of the method is based on the structure of the arterial walls and muscle type veins. In arteria myocytes are 2-3 times bigger than in vein. That is why in MAD activities the blood system is also works abnormally not even considering orthostatic hypotonia. The forced extension of muscles by external energy beside negative effects generates peristaltic transversal muscle waves directed from microvasculature to heart. In other words so called "vein pump" activates. This "pump" corresponds to normal pressure up to 40% of the rising blood flow in very intensive muscle activity.

Biochemical aspect of the method is related to the cell metabolism. The weak flow among patients suffering from MAD and CAD is not sufficient to remove carbon dioxide from tissues and therefore lactic acid is accumulated and acid substances level sharply increases. This complex of factors causes cerebral type diatonic reaction, oxygen deficiency and so on. The forced extension of muscle fiber inverts the succession in the contraction/relaxation cycle where the most important factor is the reversible change of characteristics - electric polarization and penetrability of

muscle fiber membrane and intracellular membrane and reversible change of Calcium free ions concentration in cell fluid. As the result the usage of the rosette-forming cells causes significant acceleration and improvement of metabolism.

**Biomechanical aspect.** The lower extremities are not crossed and do not rotate inside, a rotation of pelvis is provided, as well as dimensional balance of the whole body in the process of locomotion, walking speed and gait phases are changed.

Registered: increase of growth and weight, increase of miopotentials, support ability is achieved and the skill of cyclic motion in ROS and without it, the speech, sense of vision and orexia are improved, the level of verbality and social activity is improved.

Reciprocate orthosis complex can be prescribed for:

- spina bifida;
- sklerosis multiplex, cerebrospinalis;
- paraparesis extremitatum inferiorum;
- ataxia cerebellaris;
- anomalia systematis nervosum centrale congenita;
- meningomyelocele regionis lumbosacralis;
- hydrocephalia congenita;
- paraplegia spinalis;
- functio laesa organum plevis;
- insufficientia musculorum;
- paresis/paralysis cereбрalis;
- fracturae corporis vertebrarum thoracicae/lumbalis;
- fractura osseum non consolidata (pseudoarthrosis).

Author's method is contra-indicated with epilepsy, vegetative disfunctions, spasms, intoxications, infectious diseases, repeated brain traumas, hereditary diseases of neural system, spinal cord or peripheral nerves affections, schizophrenia, hypertension.

## V. CONCLUSION

The method and ROC replace wheelchairs securing movement activities of handicapped person with non-amputated limbs on a principally higher level.

The method does not apply medicines, pharmaceutical preparations, surgery, soft and hard bandages, food supplements, electric medical devices and equipment.

Method is non-invasive, and application of ROC does not harm a patient.

From the economic point of view, the method and ROC are on the whole much cheaper than classic rehabilitation including multiple treatment courses, transportation and etc.

The results decisively depend on day-to-day application of ROC.

## REFERENCES

1. Dukendjiev E. Method for the reciprocal control of the human body and total-body reciprocal orthosis system (Paņēmiens cilvēka kustību recīprokālai vadībai un recīprokāla ortožu sistēma visam ķermenim) Latvia. Patent № LV13100 B (in Latvian)
2. Дюкенджиев Е. Method to compensate muscular and control deficiency by the external energy (Метод компенсации дефицита мышечной и управляющей активности внешней энергией) International Conference on Bionics Prosthetics, Biomechanics and Mechanics, mechatronics and robotics. June 5 -6, 2006 Varna, Bulgaria pp 5-13. (in Russian)
3. Ukhtomsky A.A . Principle of dominant (Принцип доминанты. Собр.соч. Т 1). Collecton of works, Vol.1, Leningrad, LGU, 1950 (in Russian)
4. Anokhin P.K Problems of the higher nervous activity (Проблемы высшей нервной деятельности), Academy of Science publishing, Moscow, 1949
5. 3. Dukendjiev E. Reciprocal orthotic complex for the children with cerebral paralysis and spinal diseases. (Recīprokāla ortožu kompleks bērnēm ar cerebrālo trieku un spinālām slimībām). Latvijas Ārsti, №5, p 42.

Author: Evgueni Dukendjiev  
 Institute: Atypical Prosthesis Laboratory  
 Street: 3 Liepajas Street, LV-1002  
 City: Riga  
 Country: Latvia,  
 Email: e-mail: dukendjiev1@inbox.lv

# Muscle Movement and Electrodes Motion Artifact during Vibration Treatment

A. Fratini<sup>1</sup>, P. Bifulco<sup>1</sup>, M. Cesarelli<sup>1</sup>, M. Romano<sup>1</sup>, G. Pasquariello<sup>1</sup>, A. La Gatta<sup>1</sup> and G. Gargiulo<sup>2</sup>

<sup>1</sup> University “Federico II” of Naples / Dept. of Electronic and Telecom. Engineering, Naples, Italy

<sup>2</sup> University of Sidney / School of Electrical and Information Engineering, Sydney, Australia

**Abstract** — Vibration treatment by oscillating platforms is more and more employed in the fields of exercise physiology and bone research. The rationale of this treatment is based on the neuromuscular system response elicited by vibration loads. surface Electromyography (EMG) is largely utilized to assess muscular response elicited by vibrations and Root Mean Square of the electromyography signals is often used as a concise quantitative index of muscle activity; in general, EMG envelope or RMS is expected to increase during vibration. However, it is well known that during surface bio-potential recording, motion artifacts may arise from relative motion between electrodes and skin and between skin layers. Also the only skin stretch, modifying the internal charge distribution, results in a variation of electrode potential. The aim of this study is to highlight the movements of muscles, and the succeeding relevance of motion artifacts on electrodes, in subjects undergoing vibration treatments.

EMGs from quadriceps of fifteen subjects were recorded during vibration at different frequencies (15-40 Hz); Triaxial accelerometers were placed onto quadriceps, as close as possible to muscle belly, to monitor motion. The computed muscle belly displacements showed a peculiar behavior reflecting the mechanical properties of the structures involved. Motion artifact related to the impressed vibration have been recognized and related to movement of the soft tissues. In fact large artifacts are visible on EMGs and patellar electrodes recordings during vibration. Signals spectra also revealed sharp peaks corresponding to vibration frequency and its harmonics, in accordance with accelerometers data.

**Keywords** — vibration treatment, muscle movement, electromyography, motion artifact.

## I. INTRODUCTION

The use of vibration training is growing in the fields of sport and rehabilitation medicine either for training or for rehabilitation purposes. The treatment is based on the hypothesis that vibration loads induce specific responses from the neuromuscular system [1, 3, 13,14]. Usually, vibrations are delivered to the patient body by means of a platform oscillating at different frequencies (10-80Hz).

Surface Electromyography (SEMG) is largely utilized to assess muscular response elicited by vibrations and Root Mean Square (RMS) of the EMG signal is often used as a concise quantitative index of muscle activity; in general,

EMG envelope or RMS is expected to increase during vibration [2, 6, 12].

It is also well known that during surface bio-potential recording, motion artifacts may arise from relative motion between electrodes and skin and also between skin layers. The only skin stretch, modifying the internal charge distribution, results in a variation of electrode potential [4, 9].

However on electrodes, vibration generates large motion artifacts that are not confined below 15/20 Hz and can not be eliminated by the use of standard high-pass filters [11].

This study aims to analyze the motion of muscles subjected to vibration treatments and the relevance of motion artifacts arising on electrodes.

Spectral analysis of the EMG reveals sharp peaks superimposed to the classical EMG spectrum: they exactly correspond to the mechanical stimulus frequency and some higher harmonics. Analyzing the recorded raw EMG data a remarkable amount of motion artifact was found: the percentage of power content associated to motion-related frequencies resulted, on average, about 30% of the total power of the raw signal. This is reasonable considering the typical non-linear behavior of the skin and other soft tissues.

The knowledge of skin motion could help in a better description of motion artifact origin and in filter-out motion-related electrode signals.

## II. METHODS

### A. System set-up

The device used to deliver vibration to the subjects was a vibrating platform (TSEM S.p.A., Padova - Italy). The platform was modified for our purpose by the manufacturer to allow remote control of the principal parameters (i.e. vibration frequency and intensity) from an external PC. Vibrations impressed by the platform were exclusively vertical; platform displacement was sinusoidal with an intensity (peak-to-peak displacement) set to 1.2 mm and with a frequency ranging from 10 to 80 Hz.

### B. Subjects

Fifteen healthy males (age  $24.6 \pm 4.9$  years, height  $175.17 \pm 5.83$  cm, weight  $74.17 \pm 9.09$  kg) were voluntarily



involved in the study and gave their informed, written consent to participate. All of the subjects were not athletically trained.

### C. Data recording and processing

Signals from the Rectus Femoris (RF) of the dominant leg were collected. In addition, a couple of supplementary electrodes was mounted on the patient's patella, supposing no EMG contribution at this site, to assess nature and magnitude of motion artifact on recordings (see Figure 1). Signals were recorded using small disc Ag/AgCl electrodes (5mm in diameter, inter-electrode distance of 20 mm arranged in the direction of the muscle fibres). Electrode skin areas were shaved and cleaned before the placement of electrodes and conductive paste was used. Electrodes positioning was realized in accordance with the guidelines of SENIAM Project [Hermens et al, 1999].

Patellar electrodes were arranged vertically using the same inter-electrode distance (see Figure 1). All the electrodes and cables were secured (specific adhesive tape was used) to prevent the cables from swinging and from causing induced artifact. Reference electrode was located on the ankle of the same leg. EMG signals were amplified using a multi-channel, isolated biomedical signal amplifier (Biomedica Mangoni, Pisa, Italy - model. BM623; input impedance > 10 MOhm; CMRR > 100 dB). The gain was set to 1000 V/V and a band pass filter (-3dB frequency 10 - 500 Hz) was applied; no notch filters were used to suppress line interference.

A tiny and lightweight (less than 10g) three-axial MEMS accelerometer (Freescale semiconductors) was used to measure accelerations on the patient's skin, at RF EMG electrodes level (Fig.1); the sensor was set to measure accelerations within  $\pm 6g$  range. An MEMS accelerometer was

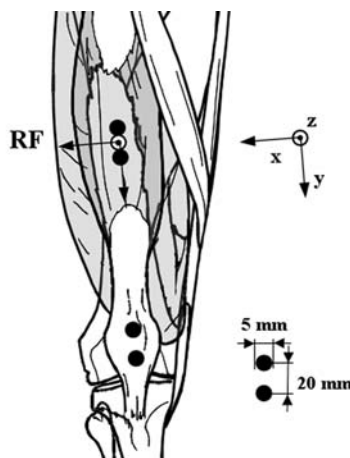


Fig. 1 : Electrodes and accelerometer arrangement.

stuck onto the skin as close as possible to the electrodes. Acceleration signals provide information related to the patient's RF muscle belly oscillation; they were pre-processed in order to exclude influence of gravity.

For gravitational acceleration  $g$ , a value of  $9.81 \text{ m s}^{-2}$  was used. Muscle displacement was computed integrating twice the acceleration data after gravity contribution removal on each axis. The initial conditions (position  $s_0$ , velocity  $v_0$ ) were set to zero and a time interval of 0.5 sec was selected for integration.

A PC multi-channel 16-bit data acquisition card (National Instruments DAQCard 6251) was used to acquire SEMG and acceleration signals and to drive the vibrating plate. Specific software was designed on purpose using the Lab-Windows/CVI (National Instruments) environment. All signals were sampled at 1536 Hz. A set of consecutive 20-second vibrations at different frequencies: 17.9, 23.3, 28.5, 33.9, 39.2 Hz, spaced with 30 seconds rest intervals, was delivered to patient. During rest intervals the patient stood up; five seconds before stimulus he reached the hack squat position. To minimize fatigue-related effects, the vibration frequencies order was randomized.

### III. RESULTS

Muscle motion resulted relatively complex: it is three-dimensional and hardly ever purely sinusoidal.

In order to better describe muscle movement the estimated displacements on the three axis were combined to show the trajectories of muscle belly on the three anatomical planes. Figure 3 shows an example of typical trajectory patterns at different stimulation frequencies.

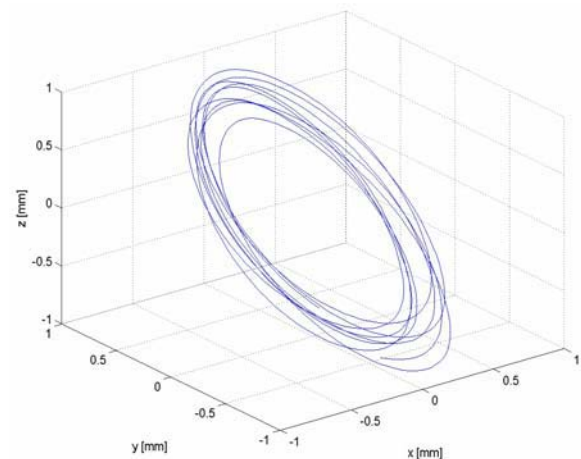


Fig. 2 : Three dimensional displacement of RF muscle belly under vibratory stimulation. The figure corresponds to a time interval of 0.5 sec and to a stimulation frequency of 17.9Hz.

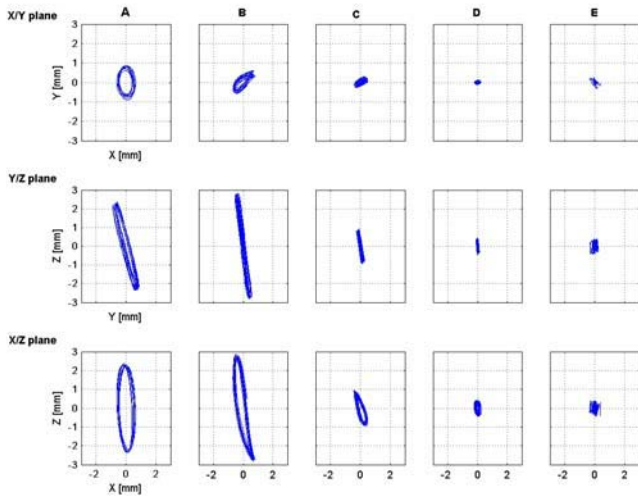


Fig. 3: RF muscle belly trajectories over the (x,y), (y,z) and (x,z) planes, on different stimulation frequencies (A=17.9 Hz, B=23.3 Hz, C=28.5 Hz, D=33.9 Hz, E=39.2 Hz).

From Figure 3 it is also easy to note a classic resonance-like behavior with a maximum amplitude displacement (in this case) at 23.3 Hz.

Figure 4 shows the collected SEMG and the estimated RMS from the same subject of Figure 3. The example was made on purpose to compare the electrical and mechanical muscular responses. From the figure it is also possible to

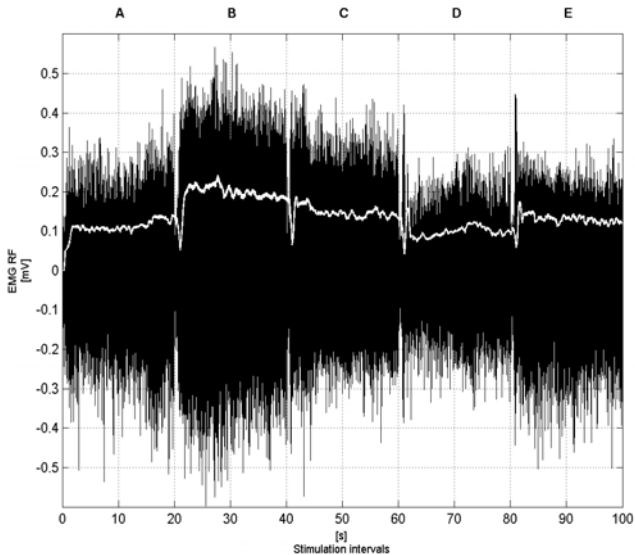


Fig. 4 : EMG signal (and its related RMS in white) collected on the RF muscle during vibration at different frequencies A=17.9 Hz, B=23.3 Hz, C=28.5 Hz, D=33.9 Hz, E=39.2 Hz.

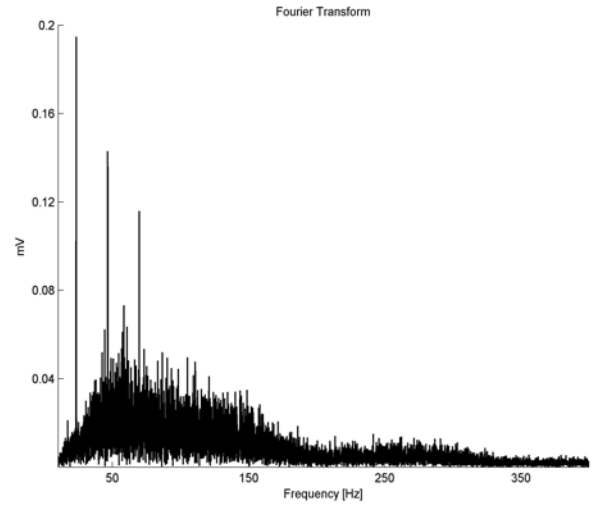


Fig. 5 : Typical (whole: 0-400 Hz) SEMG spectrum recorded from quadriceps (RF) during vibratory stimulations.

identify the same resonance behavior noticed on RF muscle trajectories over the frequency range explored.

Raw EMG signal spectrum clearly showed the presence of sharp peaks: the taller at a frequency coinciding to that mechanical chosen on vibrating platform and relatively smaller contributes related to even and odd harmonics.

In Fig. 5 it is visible the characteristic spectrum of the EMG interference pattern with three, vibration-related sharp peaks superimposed. Filtering out the narrow bands in which the peaks were present with a Matlab standard iirnotch filter (bandwidth=1.5Hz centered in  $f_0$ ,  $2f_0$  and  $3f_0$ ,

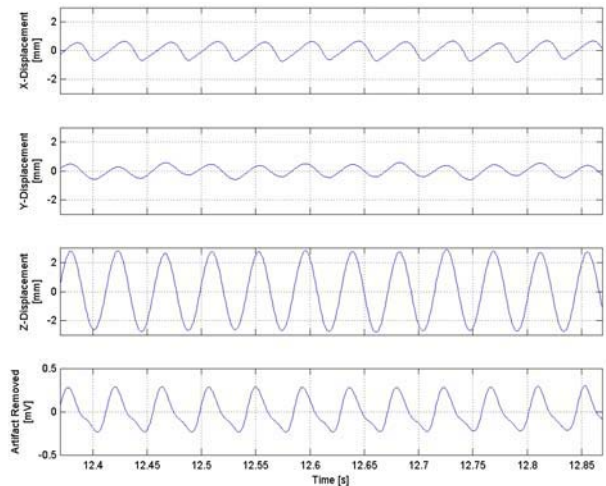


Fig. 6 : Comparison of quadriceps (RF) displacement estimation of on the 3 different axis (x,y and z) and the filtered-out part from the raw EMG signal.

were  $f_0$  is the stimulation frequency) the EMG increment reduced extremely. In Figure 6 instead is possible to see the three displacement components over the  $x$ ,  $y$  and  $z$  axis. In the figure is also presented the signal obtained as difference between the filtered and the raw EMG signal. The filtered-out component of raw EMG signal resulted not sinusoidal and its trend is obtainable as a combination of the  $x$ ,  $y$ ,  $z$ , axis displacements.

#### IV. CONCLUSIONS

The mechanical oscillation of a specific muscle depends on different parameters: its anatomy, tension, surrounding soft tissues properties, spatial orientation and kinematic chain on which vibration propagates, etc [10, 13, 14].

The three acceleration signals recorded onto muscle belly generally results not in phase between each other, they showed also different amounts of harmonics. Peak to peak amplitude values of acceleration depends on frequency; in some cases a resonant-like profile of amplitudes can be observed: the resonant frequency depends on subject.

Electrodes motion artifact seemed to be related to the muscle displacements, being its increasing consistent in a resonant-like conditions. The patellar signal confirmed the presence of motion artifact at electrode levels due to soft tissue motion during vibrations.

Although it is not possible to exclude a-priori that the true EMG power spectrum shows components at the vibration frequency and its harmonics, the presence of motion artifact if not considered, can lead to misinterpretation of the neuromuscular activity in response to vibratory stimulations.

Further studies are planned to investigate in more details the motion of different muscles and body parts of a patient subjected to whole body vibrations. More people will be involved in the experimentations. A multiple configuration is being set up in order to measure contemporarily SEMG from vastus medialis and vastus lateralis and their movements. Multiple knee angles will be considered. Approximate information about geometric anatomy of muscle involved (such as muscle length, diameters of the leg, etc. ) will be considered.

Summarizing this study analyzed the motion of muscles subjected to vibration treatments and revealed the relation between mechanical and electrical behavior. This study also underline the relevance of motion artifacts arising on electrodes as one of the possible reason for the large inter-studies differences about vibration treatments.

#### ACKNOWLEDGMENT

Authors are grateful to TSEM S.p.A. for providing the vibration training device and customer hardware modifications.

#### REFERENCES

1. Bosco C, Colli R, Introi E. Adaptive responses of human skeletal muscle to vibration exposure. *Clinical Physiology* 1999;19(2):183-87
2. Bosco C, Cardinale M, Tsarpela O. Influence of vibration on mechanical power and electromyogram activity in human arm flexor muscles. *European Journal of Applied Physiology and Occupational Physiology* 1999;79(4):306-11
3. Bongiovanni LG, Hagbarth KE. TVR elicited during fatigue from maximal voluntary contractions in man. *Journal of Physiology* 1990;423:1-14
4. De Talhouet H, Webster JG. The origin of skin-stretch-caused motion artifact under electrodes. *Physiological Measurement* 1996;17(2): 81-93
5. Hermens HJ, Freriks B, Merletti R, Stegeman D, Blok J, Rau G, Disselhorst-Klug C, Hägg G. *European Recommendations for Surface ElectroMyoGraphy, Results of SENIAM Project*. 8<sup>th</sup> ed. Enschede: Roessingh Research and Development, 1999
6. Lebedev M.A., Polyakov A.V. Analysis of surface EMG of human soleus muscle subjected to vibration. *Journal of Electromyography and Kinesiology* 1992, 2 (1), 26-35
7. Martin BJ, Park HS. Analysis of the tonic vibration reflex: Influence of vibration variables on motor unit synchronization and fatigue. *European Journal of Applied Physiology* 1997; 75(6):504-11
8. Mester J, Kleinoder H, Yue Z. Vibration training: benefits and risks. *Journal of Biomechanics* 2006; 39:1056-65
9. Ödman S, Åke Öberg P. Movement-induced potentials in surface electrodes. *Medical and Biological Engineering and Computing* 1982;20(2),159-66
10. Orizio C, Diemont B, Esposito F, Alfonsi E, Parrinello G, Moglia A, Veicsteinas A. Surface mechanomyogram reflects the changes in the mechanical properties of muscle at fatigue. *European Journal of Applied Physiology and Occupational Physiology* 1999;80(4):276-84
11. Roy SH, De Luca G, Cheng M S, Johansson A, Gilmore LD, De Luca CJ. Electro-mechanical stability of surface EMG sensors. *Medical and Biological Engineering and Computing* 2007; 45(5):447-57
12. Wakeling JM, Liphart A. Task-specific recruitment of motor units for vibration damping. *Journal of Biomechanics* 2006;39(7):1342-346
13. Wakeling JM, Nigg BM. Modification of soft tissue vibrations in the leg by muscular activity. *Journal of Applied Physiology* 2001;90(2):412-20
14. Wakeling JM, Nigg BM, Rozitis AI. Muscle activity damps the soft tissue resonance that occurs in response to pulsed and continuous vibrations. *Journal of Applied Physiology* 2002;93(3):1093-103

Author: Antonio Fratini

Institute: Dept. of Electronic and Telecommunications Engineering - D.I.E.T. - University "Federico II" of Naples

Street: Via Claudio, 21

City: Naples

Country: Italy

Email: a.fratini@unina.it

# Mandible and Temporomandibular Disc Movements on Physiological Subjects with Use of MRI

M. Fricova<sup>1</sup>, J. Krystufek<sup>1</sup>, Z. Horak<sup>1</sup>, V. Peterova<sup>2</sup> and S. Konvickova<sup>1</sup>

<sup>1</sup>Laboratory of Biomechanics, Department of Mechanics, Biomechanics and Mechatronics, Faculty of Mechanical Engineering, CTU in Prague, Czech Republic

<sup>2</sup>Department of MRI, Radiodiagnostic Clinic, 1st Faculty of Medicine, Charles University in Prague, Czech Republic

**Abstract** — The aim of this paper was to claim or disclaim if the jaw movement differs significantly between right and left side among young physiological subjects. Relative displacement of the temporomandibular (TM) disc and the mandible during mouth opening was determined. The movement of the TM disc was studied using a magnetic resonance imaging (MRI) quasi-static scan sequence with a customized mono-directional “spreader” device. A number of sagittal static images in revolved sections of the temporomandibular joint (TMJ) were obtained in various positions of jaw opening from 0 to 50 mm. The results provided a description of the TM disc displacements as a function of jaw opening. The anatomical marker movement data was observed with the assumption of fixed skull. Motions of the TM disc and the mandible were found out. The maximum average displacements of the mandible and the TM disc were about 16 mm (x-direction) and 6 mm (mean value) respectively at mouth opening of 50 mm. The maximum average rotation of the mandible was 32°. While the movement of the mandible has already been published, though only for a small mouth opening, the behavior of the disc during the same movement has not been well depicted. The results of these measurements can be used for clinical diagnostics and also as inputs for finite element analysis (FEA).

**Keywords** — magnetic resonance imaging, temporomandibular joint, motion, disc displacement, kinematics.

## I. INTRODUCTION

The question of face and jaw disorders is extensive and complex. It requires much effort to elaborate and implement new curative procedures and renew the function and shape of the orofacial area for a patient. Several studies have reported disc perforations and degeneration of the articulating surfaces [1]. Any TM disc motion divergence within the subject's sides during mouth opening will significantly influence temporomandibular disorders (TMD).

The movement of the TM disc during jaw opening and closure is very sophisticated. It was difficult to depict its motion exactly, because the disc shape changes significantly during the motion. The number of experimental studies is limited, because it is difficult to insert experimental devices, such as strain gauges, into the joint without causing damage to its tissues and influencing their mechanical behavior. In

several studies, condylar motion has been studied directly with the use of MRI [2, 3, and 4], videoanalysis [5], or ultrasound imaging [6]. [3] analyzed the displacement of the mandibular condyle. The data obtained from this experimental measurement during jaw opening was measured only for a maximum distance between central lower and upper incisors of 17 mm. In fact, the maximum comfortable mouth opening is greater (approx. 30-50 mm). In addition, there were no references to TM disc displacement. Experimental and numerical studies concerning jaw movement and the distribution of the loads in the TMJ have been performed in many models [7, 8, 9, and 10]. However, the TM disc is crucial for proper TMJ function, and it has been omitted or simplified in many numerical models and experiments [11, 4, and 12].

## II. MATERIALS AND METHODS

The experimental measurements were carried out at the Radiodiagnostic Clinic of the 1st Medical Faculty at Charles University. The magnetic resonance images were obtained using an Intera 1.5 T MR Scanner (Philips, the Netherlands). The TMJs of the subjects were scanned into 3 mm thick slices with the fast field echo (FFE) quasi-static scan sequence in the image plane of the slices [13]. The parameters of the head coil are shown in Table 1. The head was fixed to avoid major movements; smaller movements caused by swallowing and position discomfort of the head were corrected using the geometric transformation. The image plane was rotated from a mid-sagittal plane of 12-20°

Table 1 Parameters of head coil - Philips Intera 1.5 T

TR (repetition time)	135.74 ms
TE (echo time)	13.81 ms
FoV (field of view)	160 mm
Matrix	256/256
THK (slice thickness)	3 mm
NSA (slice acquisition number)	2
examination time	5:15 min
pixel size	0.625 mm

(depending on the subjects' anatomical condition) in the direction of the jaw. Image plane sections of TMJ were scanned in the specified location of jaw opening from 0 to 50 mm (distance between central lower and upper incisors) using a customized mono-directional "spreader" device. We used a Vernier caliper design and proposed an appropriate shape for convenient mouth opening. This device was made with rapid prototype technology. Ten (for first subject six) static mouth opening positions were obtained, starting with maximum jaw opening (50 mm) and proceeding to closure (0 mm), and an MR image of the TMJ was taken for each position. It was necessary to minimize the imaging time over which the patient must keep the jaw open. This can be uncomfortable for the patient in the supine position, as saliva collects in the back of the pharynx [14 and 2].

By reason that the accurate location of the TMJ components should be known the contours had to be traced. Tracing was carried out manually by imprinting. On the basis of the MR images, the TMJ contours were defined for the skull, the mandible condyle and the TM disc (Fig. 1) [13].

The displacements for each part of the TMJ were obtained from the contour transformation sequence. First, the transformation described the position of all reference points into the local Cartesian coordinate system (CCS) of the skull (index S). A global (index G) CCS was chosen to coincide with the CCS in the MR image. The first MR image (assigned as the n-th index – for maximum mouth opening) was established as a reference image. Second, all markers were transformed from the local coordinates (from the above-mentioned transformation) into the global CCS for all mouth opening positions; the temporal bone points A, B

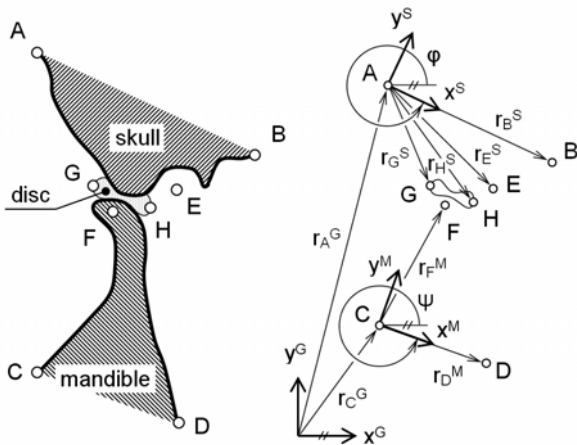


Fig. 1 Contours of part of TMJ with assigned reference points from A to H for maximum mouth opening (on the left); defined coordinate systems, upper index G – global CCS, upper index S – local CCS of the skull and upper index M – local CCS of the mandible (on the right); lower index A – H indicates corresponding curve characteristic point.

and E were identical for all positions. This was essential, because although the head was fixed, the skull might move towards the skin during the examination. The third step was the transformation of point F into the coordinate system from the global CCS to the local CCS of the mandible (index M). Finally, point F (local CCS of the mandible) was translated and rotated into the global coordinate system for all mouth opening positions. [15]

Movements of the mandible and TM disc reference points after the transformation were observed and graphically depicted in two directions, and for the mandible reference point rotation in angle  $\alpha$  was described. Fig. 3 is an example which shows the dependence of the reference point on the mouth opening for the measured TM disc. Fig. 3 includes the curves of the measured values as well as the curve of the average values. Due to the different anatomical distances among individual subjects, we proposed to normalize this data. The difference of the maximum and the minimum movement distances was set. Each value was divided by the difference. For example, for the values on the x-axis:

$$\bar{x}_i = \frac{x_i}{x_{\max} - x_{\min}} \quad (1)$$

### III. RESULTS

The results of the experimental measurements showed the motion of the TM disc and the mandible reference points during mouth movement. Figure 2 shows an example of the motion path of the reference points. We observed the relative motion of the TM disc and the mandible in the x-axis and in the y-axis (Fig. 3) and - for the mandibular reference point also the rotation depending on the mouth opening.

An example of TM disc movement, displacement of reference point H, is shown in Fig. 3, which show the TM disc behavior during jaw motion. The maximum average displacements of the TM disc points differ between the anterior (G) and the posterior (H) point due to the soft and changeable structure of the disc, and, above all, because of the individual features of the volunteers. The paths of the TM disc reference point differ slightly from volunteer to volunteer, but - significantly - the tendency has the same character.

The motion of the mandibular condyle was investigated in the x, y directions and one angle  $\alpha$ . The initial position was established for a closed mouth, where angle  $\alpha$  was chosen as  $0^\circ$  towards global CCS, so that the displayed angle was absolute. The average maximum displacement in

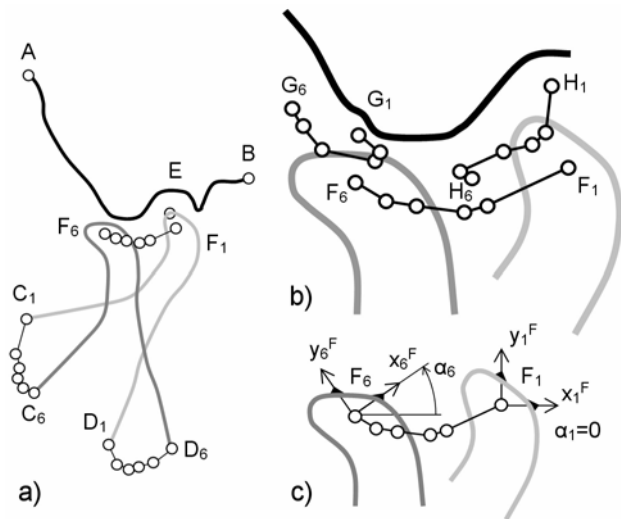


Fig. 2 Scheme of the reference point motion (index 1 mouth is closed, index 6 mouth is opened to the maximum): (a) scheme of the mandibular condyle movement, (b) image detail of the TM disc reference point movement, (c) coordinate system for graphic interpretation of the reference point motion and rotation  $\alpha$  on the mandibular reference point.

the x-direction was 16 mm, and in the y-direction it was 5 mm. The average maximum rotation of the mandibular condyle was  $32^\circ$ .

#### IV. DISCUSSION

The TM disc plays a crucial role in TMJ motion; it is therefore necessary to know its mechanical behavior as well as its movement. The displacement of the mandibular condyle was described in [3] for maximum mouth opening of 17 mm. This is not the maximum comfortable mouth opening, so it was necessary to extend these measurements. In addition, there was no investigation of TM disc movement. The results for mouth opening of 17 mm have been used for computing FEA [10], so that the results of this analysis describe only part of the general jaw movement. Our measurement method is based on [3], but we obtained a more complex description of the mandible and especially of TM disc behavior. Our study provided the displacement of the TM disc and of the mandible condyle in relation to mouth opening. The maximum mouth opening was 50 mm; this distance was defined between the lower and upper incisors.

Adjusting the MRI device was crucial. There are many scanning techniques, but in most of them the disc is not easily observed. Next, there can be significant loss due to slice thickness. Several experiments with MR specialists led to an appropriate scanning sequence. The precision of the

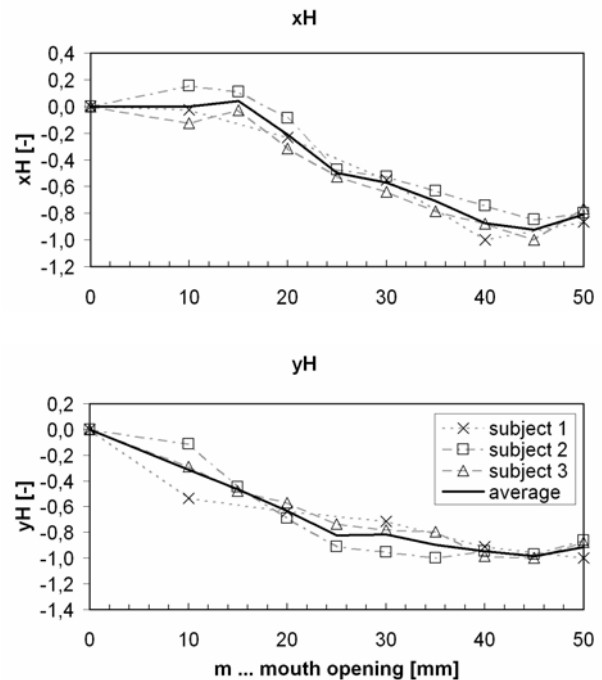


Fig. 3 Displacement of the reference point on the TM disc motion of reference point H in two directions depending on mouth movement.

results is also limited by the quality of the MR images and by the accuracy of the contours of the TMJ part.

Segmentation had to be prepared very conscientiously, because a negligible difference in point position definition could make significant differences. All parts were shaped according to their anatomical geometry, in cooperation with an experienced dentist.

One of the main disadvantages was that the individual quasi-static images that were analyzed in this initial study did not capture everything that was truly seen when examining the TMJ in motion. In [3] the motion of the mandibular condyle was studied for the reference point defined on the condyle, which does not seem to be precise. In our approach, the centre of the curvature should be a more exact description of the reference point. It should be pointed out that the approach is only two-dimensional. We suggest processing of the TMJ movement on dynamic MRI where we could observe the whole motion in the 3D and without any blank positions during the jaw movement path. The spatial conception needs to be more accurate, due to the extremely complex shape of the TM disc.

Left and right sides within one subject doesn't have significant differences. The subject were young and without any TMD. We suppose the differences are obvious with some pathology within the joint. For the future we prepare measurements even for subject with TMD.

Individual dimensions and also individual movements were the most important differences among the subjects. This data was therefore normalized, in an attempt to show more precise relations. In spite of these differences, all reference points in particular directions have more or less the same tendency. This seems to be a significant finding.

## V. CONCLUSIONS

The motion of the TM disc and the mandible during mouth movement was observed with use of MRI on young volunteers. The results showed the behavior of the TM disc and the mandible during jaw movement. This differs slightly from individual to individual, due to different shapes and properties of the soft tissues but the tendency has always the same character which claims our considerations. Based of our knowledge, the method proposed here was found new and appropriate, although it is only two-dimensional. We suggest processing of the TMJ movement on dynamic MRI where we could observe the whole motion in the 3D. The spatial conception needs to be more accurate, due to the extremely complex shape of the TM disc. We also intend to investigate more volunteers, and we will also try to investigate a non-physiological subject in order to define possible defects.

## ACKNOWLEDGMENT

This research was supported by project no. MSM 6840770012 of the Ministry of Education: Transdisciplinary Research in Biomedical Engineering II, and by the Czech Science Foundation project: "Application of synthetic biomaterials for replacement of orofacial parts of skull", No. CSF 106/07/0023.

## REFERENCES

1. Drace J E & Enzmann D R (1990) Defining the Normal Temporomandibular Joint: Closed-, Partially Open-, and Open-Mouth MR Imaging of Asymptomatic Subjects. *Radiology*, 177 (1), 67-71
2. Jergenson M & Barton J (1998) The occurrence of TMJ disc perforations in an aging population. *Journal of Dental Research*, 77(5), 264
3. Chen J & Buckwalter K (1993) Displacement Analysis of the Temporomandibular Condyle from Magnetic Resonance Images. *Journal of Biomechanics*, 26 (12), 1455-1462
4. Peterova V, Jirman R, Mazanek J & Seidl Z (2004) The Examination of the Temporomandibular Joint on 1,5T Magnetic Resonance. *Prague Medical Report*, 105 (4): 29-34
5. Yatabe M, Zwijnenburg A, Megens C C E J & Naeije M (1997) Movements of the Mandibular Condyle Kinematic Center during Jaw Opening and Closing. *Journal of Dental Research*, 76 (2), 714-719
6. Braun S & Hicken J S (2000) Ultrasound imaging of condylar motion: a preliminary report. *Angle Orthodontist*, 70 (5), 383-386
7. Beek M, Koolstra J H et al. (2000) Three-dimensional finite element analysis of the human temporomandibular joint disc. *Journal of Biomechanics*, 33 (3), 307-316
8. Choi A H, Ben-Nissan B & Conway R C (2005) Three-dimensional modeling and finite element analysis of the human mandible during occlusion. *Australian Dental Journal*, 50 (1), 42-48
9. Donzelli P S, Gallo L M, Spilker L R et al. (2004) Biphasic finite element simulation of the TMJ disc from in vivo kinematic and geometric measurement. *Journal of Biomechanics*, 37 (1), 42-48
10. Perez del Palomar A & Doblare M (2006) 3D Finite Element Simulation of the Opening Movement of the Mandible in Healthy and Pathologic Situations. *Journal of Biomechanical Engineering*, 128 (2), 242-249
11. Beek M, Aarnts M P, Koolstra J H et al. (2001) Dynamic properties of the human temporomandibular joint disc. *Journal of Dental Research*, 80 (3), 876-880
12. Perez del Palomar A & Doblare M (2006) The effect of collagen reinforcement in the behavior of the temporomandibular joint disc. *Journal of Biomechanics*, 39 (6) 1075-85
13. Fricova M, Krystufek J, Horak Z, Peterova V, Konvickova S (2007) Evaluation of the Temporomandibular Joint Disc Movement during Mouth Opening on Young Volunteers. 6th Youth Symposium on Experimental Solid Mechanics, Vrnjačka Banja, Serbia, Faculty of Mechanical Engineering, Kraljevo, ISBN 978-86-82631-39-2, pp 43-46
14. Katzberg R W (1989) Temporomandibular Joint Imaging. *Radiology*, 170 (2), 297-307
15. Stejskal V & Valasek M (1996) Kinematics and dynamics of machinery, Marcel Dekker Inc., New York (NY), USA, ISBN 0-8247-9731-0

Address of the corresponding author:

Author: Martina Fricova  
 Institute: Laboratory of Biomechanics, Faculty of Mechanical Engineering, Department of Mechanics, Biomechanics and Mechatronics  
 Street: Technicka 4  
 City: 166 07, Prague 6  
 Country: Czech republic  
 Email: martina.fricova@fs.cvut.cz

# Choice and Impact of a Non-Newtonian Blood Model for Wall Shear Stress Profiling of Coronary Arteries

L. Goubergrits<sup>1</sup>, E. Wellnhofer<sup>2</sup> and U. Kertzscher<sup>1</sup>

<sup>1</sup> Charité-Universitätsmedizin Berlin/Biofluid Mechanics Laboratory, Berlin, Germany

<sup>2</sup> German Heart Institute Berlin/Cardiology, Berlin, Germany

**Abstract** — the modelling of the in-vivo physiological situation is complex and time-consuming. Methodological simplifications are desirable. The aim of this study was to investigate the impact of non-Newtonian blood modelling and to determine the best suitable blood model. This study simulates numerically steady blood flow in an anatomically realistic model of the left coronary artery main bifurcation. The geometry was reconstructed from a post-mortem vessel cast. Three non-Newtonian (Casson, Walburn-Schneck and Generalized Power Law) as well as the Newtonian blood models were compared. First we tested the ability of the models to fit different experimental data performed with different hematocrit and total protein minus albumin (TPMA) concentration values under different temperatures. It was found that wall shear stress (WSS) is influenced by the used model. However, only the Walburn-Schneck model revealed significantly varied WSS distribution (mean difference of about 30% measured point by point) and magnitude (17% higher mean WSS) if compared with Newtonian model. The adapted Generalized Power Law (GPL) model allows the best fitting to the known experimental data with a Pearson's coefficient of  $R=0.9998$ . This is especially valid for fitting the flattening of the viscosity curve to very low shear rate values under pulsatile flow conditions. An adapted GPL model which includes the dependence of hematocrit, temperature and TPMA concentration is proposed. The impact of the non-Newtonian blood model in WSS profiling of coronary artery flow may be neglected for clinical studies with normal or obstructive (narrowed) coronary arteries. However, for dilated (enlarged) coronary arteries, the non-Newtonian blood model is significant and should be included in the numerical model of the coronary flow.

**Keywords** — coronary artery, non-Newtonian blood model, wall shear stress, computational fluid dynamics.

## I. INTRODUCTION

Clinical studies suggest that local wall shear stress (WSS) patterns modulate the site and the progression of atherosclerotic lesions [1]. Recent advances in the development of computational fluid dynamic (CFD) programs, hardware and non-invasive imaging techniques (multi-slice CT, MRI, biplane angiography, 3D IVUS and 3D rotational angiography) allow a patient-specific profiling of the endothelial WSS and their derivatives (WSS gradient, WSS angular deviation or oscillating shear index) in anatomically

realistic reconstructed vessel geometries. However, the modelling of an in-vivo physiological situation is complex and time-consuming. Methodological simplifications are desirable in porting this approach from bench to bedside. One simplification which was controversially debated in the literature is the use of non-Newtonian blood models. Based on these earlier studies we could not decide whether the use of non-Newtonian blood modelling is necessary or not and which model is preferable for the endothelial hemodynamic profiling of the coronary artery flow. The performed study is a numerical simulation of steady blood flow in an anatomically realistic model of the left coronary artery (LCA) main bifurcation including the left main (LM), the left anterior descending (LAD) and the left circumflex (LCX) coronary arteries. A Newtonian and three non-Newtonian blood models were compared. The comparisons were performed for the WSS distribution.

## II. MATERIALS AND METHODS

### A. LCA model

The vessel cast (see fig. 1) of the LCA bifurcation was manufactured post mortem in the Pathology of the Finlay Hospital, Havana, Cuba under a defined transmural pressure of 100 mmHg in a specially constructed apparatus using the polymer Technovit 7143 (Heraeus Kulzer GmbH, Wehrheim, Germany). The apparatus and the procedure of the vessel cast fabrication were presented in our earlier paper [2]. The resulting diameter of the LM inlet segment of the vessel cast was 4.25 mm. The cast of the LCA was digitized using an optical method. This digitalisation was carried out by GFal (Gesellschaft zur Förderung angewandter Informatik e.V., Berlin, Germany). The “greycodeshift” method, using an apparatus developed by GFal, was applied. The collected data set representing a cloud of approximately  $10^6$  vertices was processed with the software FinalSurface2, developed by GFal. A surface with a resolution of 0.1 mm was generated from the resulting vertices according to the “marching cubes” method. This surface was used to generate a basic computer model of the LCA for numerical flow study.



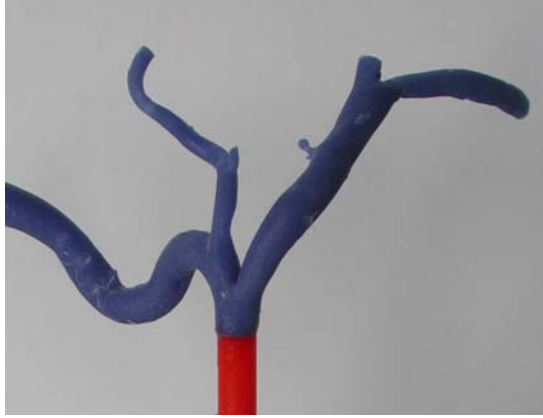


Fig. 1 Cast of the investigated left coronary artery.

### B. Non-Newtonian blood models

Three different non-Newtonian blood models were used in our study: Casson, Walburn-Schneck (WS) and Generalized Power Law (GPL). All of these models are a modification of the Power Law model, which itself is a modification of Newtonian blood model with the strain rate raised to a power:

$$\mu = m \cdot \dot{\gamma}^{n-1} \quad (1)$$

The parameter  $m$  is a consistency index, the parameter  $n$  is a non-Newtonian index and  $\mu$  is the viscosity. The main goal of non-Newtonian blood modelling - as it was found in studies - is to simulate shear-thinning that means a non-Newtonian index  $n < 1$ . The models used in this study are:

The Casson model modified by Fung [3] that enables the inclusion of hematocrit dependence:

$$\mu = \left( \sqrt{\mu_{\infty}} + \sqrt{\frac{\tau_y}{\dot{\gamma}}} \right)^2 \quad (2)$$

where  $\mu_{\infty} = \mu_0 \cdot (1 - H)^{-2.5}$  and

$$\tau_y = 0.01 \cdot (0.625 \cdot H)^3.$$

$H$  is the hematocrit ( $0 < H < 1$ ). Fung proposed a model with  $\mu_0 = 0.0012$ . Both hematocrit dependences were fitted to experimental data from Chien et al. and Cokelet et al. [3, 4].

Walburn and Schneck fitted their experimental data obtained from anticoagulated blood with four constants and two parameters (hematocrit  $H$  and the sum of fibrinogen and globulin concentrations  $TPMA$ ) [5] to the equation:

$$\mu = 0.1 \cdot C_1 \cdot \exp(C_2 \cdot H) \cdot \exp\left(C_4 \cdot \frac{TPMA}{H^2}\right) \cdot \dot{\gamma}^{-H \cdot C_3} \quad (3)$$

where the four constants are  $C_1=0.0797$ ,  $C_2=0.0608$ ,  $C_3=0.00499$  and  $C_4=14.585$ . They proposed a blood model with  $H=40\%$  and  $TPMA=25.9$  g/l.

The Generalized Power Law model incorporates the Power Law model at low shear rates, the Newtonian model at mid-range and high shear rates and the Casson model as a special case [6]:

$$\begin{aligned} \mu &= 0.1 \cdot \lambda_* \cdot \dot{\gamma}^{n_*-1} \\ \lambda_* &= \mu_{\infty} + \Delta\mu \cdot \exp\left(-\left(1 + \frac{\dot{\gamma}}{a}\right) \cdot \exp\left(\frac{-b}{\dot{\gamma}}\right)\right) \\ n_* &= n_{\infty} - \Delta n \cdot \exp\left(-\left(1 + \frac{\dot{\gamma}}{c}\right) \cdot \exp\left(\frac{-d}{\dot{\gamma}}\right)\right) \end{aligned} \quad (4)$$

where  $\mu_{\infty}=0.035$ ,  $n_{\infty}=1.0$ ,  $\Delta\mu=0.25$ ,  $\Delta n=0.45$ ,  $a=50$ ,  $b=3$ ,  $c=50$  and  $d=4$  which is the best fitting of different experimental data from Chien et al., Merrill et al., Walburn et al. and Cokelet et al. [6].

It was noted in the literature that the GPL model allows the best fitting to the experimental data [6], but the model do not include hematocrit dependence. The ideal non-Newtonian blood model should fulfil the following set of requirements:

- Simulate the shear-thinning effect.
- Include the hematocrit dependence for males ( $41\% < H < 55\%$ ) and females ( $37\% < H < 47\%$ ).
- Include the temperature dependence.
- Include the dependence of protein concentration and
- Consider the flow conditions. Most rheological studies of the blood were performed under steady flow conditions. However, we have pulsatile flow conditions.

### C. CFD

The numerical solution of steady Navier-Stokes equations were solved by a control volume finite element method (FEM) implemented in FLUENT 6 (ANSYS-Fluent Inc., Lebanon, USA).

The surface of the model was triangulated with a node distance between 0.1 and 0.2 mm. The number of the surface elements (triangles) was about 50,000. Based on the mesh independency study, we generated a mesh which was refined in the near wall region. A boundary layer was generated consisting of 3 rows, with a growth factor of 1.2 (ratio between two consecutive layers near the wall) and a total depth of 0.2 mm. The resulting number of grid volume elements was approximately 800,000 cells (prisms and tetrahedrons).

The steady laminar flow was simulated presuming rigid motionless walls. A no-slip condition was assumed at the

wall. A second order discretization scheme and a SIMPLEC model for pressure flow coupling were used. A plug velocity profile was assumed at the inlet. A 50/45/5 flow rate relation was assumed between the three outlet vessels of the LCA bifurcation. The mean flow rate at the inlet of the LCA was estimated based on literature data using 150 ml/min.

The results for WSS distributions were compared using a point by point method for all 24,000 surface nodes of the LCA model. Furthermore, the analysis included the measurement of the surface area averaged WSS value and an assessment of the areas with WSS values divided into the following three ranges:  $\tau < 0.4$  Pa,  $0.4$  Pa  $< \tau < 1.5$  Pa and  $\tau > 1.5$  Pa.

### III. RESULTS

#### A. Fitted Non-Newtonian blood models

First the three non-Newtonian models were fitted to selected experimental data [7-9].

The Casson and the Walburn-Schneck models already include the dependence of hematocrit. Hence the fitting should be done for one coefficient  $\mu_0$  for the Casson model and four coefficients  $C_i$  ( $i=1, \dots, 4$ ) for the Walburn-Schneck model. The fitting of the Casson model results in the parameter  $\mu_0=0.001674$ . The fitting of the Walburn-Schneck model results in the following four coefficients:  $C_1=0.000617$ ,  $C_2=0.0608$ ,  $C_3=0.00399$  and  $C_4=19.225$ .

The GPL model does not primarily include the dependence of hematocrit  $H$ . In order to incorporate the hematocrit dependence, we propose to model all eight coefficients of the GPL model as quadratic functions of  $H$ . Additionally; we incorporate a linear dependence of the temperature  $T$  that is known from the literature:

$$C_i = c_{1i} \cdot H^2 + c_{2i} \cdot H + c_{3i} \cdot T + c_{4i} \quad (5)$$

where  $C_i$  are the eight GPL coefficients ( $\mu_\infty$ ,  $n_\infty$ ,  $\Delta\mu$ ,  $\Delta n$ ,  $a$ ,  $b$ ,  $c$  and  $d$ , see eq. 4).

The experimental data of Thurston were used as the main reference, since he performed his experiments under pulsatile flow conditions. The experimental data under pulsatile flow conditions revealed a characteristic flattening of the curve at very low shear rates ( $\dot{\gamma} < 1.0$  s $^{-1}$ ). In order to fit the GPL model we used all of the experimental data. The fitting process was performed iteratively using a method of least squares. A correlation between experimental data and models was estimated by a Pearson's coefficient  $R$ .

The fitting of three non-Newtonian blood models to the selected experimental data revealed the good ability of all models to fit a shear rate dependence of the blood viscosity with high Pearson's coefficients  $R > 0.95$ . However, the GPL model shows the highest Pearson's coefficient.

#### B. Non-Newtonian vs. Newtonian blood models

Figure 2 shows the WSS distribution resulting from a CFD simulation of the steady flow in the Newtonian model (upper) and in the Walburn-Schneck model (down). A qualitative (visual) comparison shows no significant differences between these two WSS distributions. The same result was found for simulations with the two other non-Newtonian blood models.

Figure 3 shows normalized relative differences between WSS distributions resulting from CFD simulations with Casson model vs. a simulation with a Newtonian blood model. The mean relative difference for the Casson model with standard deviations is  $8.83\% \pm 5.52\%$ . The maximal deviation found was 121%. The mean relative difference for the Walburn-Schneck model with standard deviations is at  $29.9\% \pm 23.45\%$  significantly higher than for the Casson model. The maximal deviation found was 712%. The mean relative difference for the GPL model with standard deviations was at  $7.6\% \pm 9.9\%$  that is slightly lower than for the Casson model. The maximal deviation found was 172%.

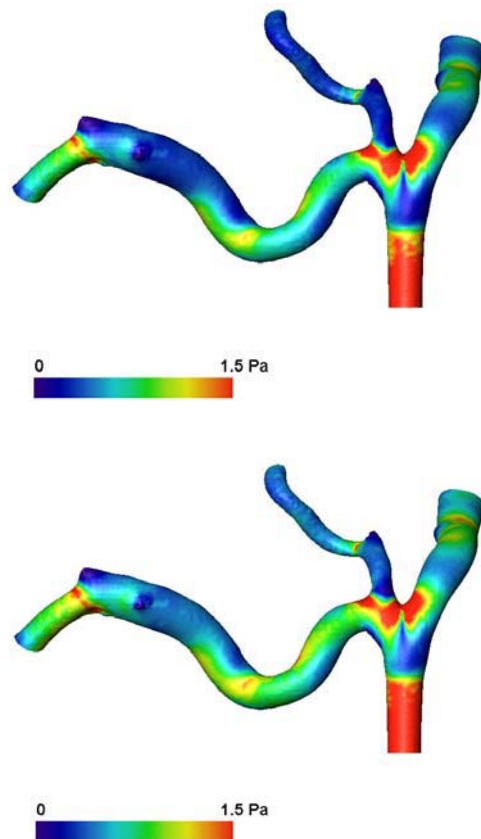


Fig. 2 Upper: WSS-distribution for Newtonian blood model. Lower: WSS-distribution for the Walburn-Schneck blood model.

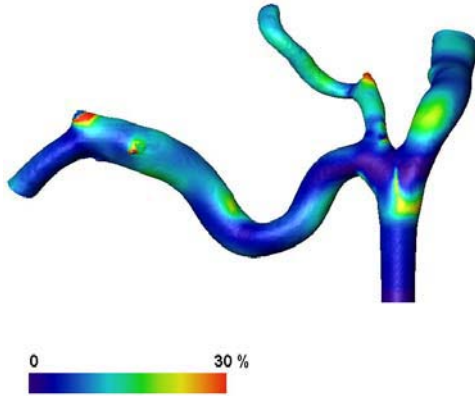


Fig. 3 Relative difference for the Casson blood model.

Finally, we decided to modify the GPL model in order to include hematocrit, temperature and TPMA dependencies. The resulting model which we propose to use in our studies is:

$$\mu = C_2 \cdot \exp\left(C_1 \cdot \frac{TPMA}{H^2}\right) \cdot (\mu_0 \cdot (1-H)^{-2.5} + \Delta\mu \cdot \exp\left(-\left(1 + \frac{\dot{\gamma}}{A}\right) \cdot \exp\left(-\frac{B}{\dot{\gamma}}\right)\right)) \quad (7)$$

$$A = a_1 \cdot H^2 + a_2 \cdot H + a_3 \cdot T + a_4$$

$$B = b_1 \cdot H^2 + b_2 \cdot H + b_3 \cdot T + b_4$$

where  $\mu_0=0.0008585$ ,  $\Delta\mu=0.00707$ ,  $C_1=0.0019225$ ,  $C_2=0.7639$ ,  $0<H<1$  and TPMA is measured in g/l. The constants  $a_i$  and  $b_i$  are following: 0.14054375, -14.7089379, 1.3072387, 383.039 and -0.02162045, 2.1138407, -0.193464, -41.2627. The proposed model is stable within the wide range of hematocrit and TPMA values, and is the best fitting for a set of experimental data.

#### IV. CONCLUSIONS

A comparative numerical study of the steady flow in the anatomically realistic left coronary artery main bifurcations with three non-Newtonian and one Newtonian blood models were performed.

According to the fitting analysis, the GPL model is the best model which should be used for modelling the non-Newtonian blood behaviour. This is especially valid for fitting the flattening of the viscosity curve for very low shear rate values. The impact of the GPL blood model in the WSS profiling of the coronary artery flow may be neglected for clinical studies with normal or obstructive (narrowed)

coronary arteries. However, for dilated coronary arteries, the non-Newtonian blood model should be included in the numerical model of the coronary flow.

The adapted GPL model (see eq. 6) is proposed for numerical modelling of the non-Newtonian blood behaviour. The model includes hematocrit and TPMA dependence, the two main parameters influencing the viscosity under constant temperature. Using these two parameters we can consider the blood variability from patient to patient in our studies. Our general recommendation is to use the proposed non-Newtonian blood model in clinical studies of the WSS profiling.

#### ACKNOWLEDGMENT

This study was supported by German Research Foundation (DFG). We thank Dr. Jose Fernandez-Britto, Dr. Finlay Hospital, Havana, Cuba, who fabricated the cast.

#### REFERENCES

1. Stone PH, Coskun A et al. (2003) Prediction of sites of coronary atherosclerosis progression: In vivo profiling of endothelial shear stress, lumen, and outer vessel wall characteristics to predict vascular behavior. *Curr Opin Cardiol* 18(6):458–470
2. Affeld K, Goubergrits L et al. (1998) Variability of the geometry of the human common carotid artery. A vessel cast study of 31 specimens. *Pathol Res Pract* 194(9):597–602
3. Fung YC (1993) *Biomechanics. Mechanical properties of living tissues.* Berlin: Springer
4. Chien S, Usami S et al. (1966) Effect of hematocrit and plasma proteins on human blood rheology at low shear rates. *J Appl Physiol* 21(1):81–87
5. Walburn FJ and Schneck DJ (1976) A constitutive equation for whole human blood. *Biorheology* 13(3):201–210
6. Ballyk PD, Steinman DA, and Ethier CR (1994) Simulation of non-newtonian blood flow in an end-to-side anastomosis. *Biorheology* 31(5):565–586
7. Brown RI (1989) The physics of continuous flow centrifugal cell separation. *Artif Organs* 13(1):4–20
8. Thurston GB (1979) Rheological parameters for the viscosity viscoelasticity and thixotropy of blood. *Biorheology* 16:149–162
9. Pelletier GA and Merrill EW (1967) Viscosity of human blood: transition from newtonian to non-newtonian. *J Appl Phys* 23:178–182

Author: Dr. L. Goubergrits

Institute: Charité – Universitätsmedizin Berlin,  
Biofluid Mechanics Laboratory

Street: Thielallee 73

City: 14195 Berlin

Country: Germany

Email: leonid.goubergrits@charite.de

# Validation of Individual Calibration Procedure in Prediction of One Repetition Maximum in Bench Press

M. Hannula<sup>1</sup> and A. Hirvikoski<sup>1</sup>

<sup>1</sup> Medical Engineering R&D Center, Oulu University of Applied Sciences, Finland

**Abstract** — In literature various studies about application of accelerometer sensors in analysis of weight lifting performance can be found. One specific application is prediction of one repetition maximum (1-RM) from submaximal lift, where the 1-RM is estimated on the basis of submaximal weight and acceleration values occurring during the lift. The prediction accuracy has been found to be good at a large subject group level. However, differences between individual subjects may result in inaccurate prediction in occasional cases. Therefore utilization of anthropometric data or information of weight lifting experience of the individual could improve the accuracy of the prediction. To evaluate this, in this study individual calibration of the prediction algorithm was evaluated in case of accelerometer based 1-RM prediction in bench press. The calibration procedure was tested with a total of 30 subjects (15 females, 15 males). The data analysis showed excellent correlation coefficient  $R$  of 0,99 ( $p < 0,001$ ) between the predicted 1-RM and the actual 1-RM in the validation phase of the study. Relative absolute error of 1-RM was 4,6 % for bench press. Without use individual calibration the correlation coefficient would have been 0,99 ( $p < 0,001$ ) and the relative absolute error would have been 9,2 %. The results clearly show the individual calibration increase significantly the 1-RM prediction accuracy.

**Keywords** — 1-RM, accelerometer, calibration

## I. INTRODUCTION

The one-repetition maximum (1-RM) is the maximum amount of weight lifted one time with correct in a standard weightlifting exercise [1,2,3,4]. There exists various methods for indirect estimation of 1-RM without performing actual 1-RM measure [1,5,6,7,8,9]. One new emerging application in this field is a method which predicts the 1-RM on the basis of submaximal weight and acceleration values occurring during the submaximal lift [10]. This method applies a specific accelerometer sensor measurement system in its function. The accuracy and applicability of this method has been studied in previous studies [9,11,12].

From the application point of view the idea of the new accelerometer-based 1-RM prediction method is to develop a personal wristwatch-type sports computer, which would be used for the 1-RM prediction in various types of gym exercises, Fig. 1. In athlete training a handy 1-RM predic-

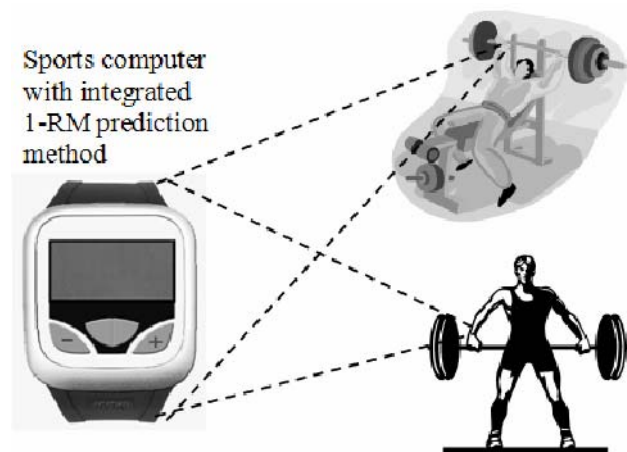


Fig. 1. Application examples of the accelerometer based 1-RM prediction method (sports computer picture: Juho Saavalainen).

tion device would be beneficial in monitoring the effect of the training program. In rehabilitation use it would be used for monitoring the progress of training without risk of injury. The device could be beneficial also for subjects for whom direct 1-RM performance testing is undesirable, for example elderly, hypertensives and cardiac patients.

The principle of the accelerometer-based 1-RM prediction method is to estimate the 1-RM on the basis of only two factors: submaximal weight and accelerometer values occurring during the submaximal lift. This results in satisfactory accuracy in prediction of 1-RM at the average level among large test subject population. However, the differences between individuals cause inaccurate prediction results in occasional cases. The accuracy of the prediction of one repetition maximum could be improved by taking into account also individual physiological factors such gender, age, weight and height, and information of training background of the subject. For example, both men and woman typically achieve their maximum muscular strength between ages 20 to 30 years, when muscle cross-sectional area achieves maximum size and strength then tend to decrease with age because of a reduction in muscle mass [13]. Further, gender differences in strength clearly emerge especially in upperbody strength evaluations. Muscular training may have a great effect on body composition, which may vary highly between subjects of the same height and weight

but different training history. Therefore standard “height-weight tables” reveal little about an individual's body composition and may vary considerably for any given body mass and stature [13].

In this study advantages of individual calibration of accelerometer-based 1-RM prediction in bench press were evaluated. The study consisted of two phases, calibration and validation phase. The study primarily investigates differences between non-calibrated and individually calibrated 1-RM prediction results. In addition, also connection between calibration parameters and anthropometric and training history data was considered.

## II. METHODS

The measurement system, shown in Fig. 2, consists of a wristwatch, including an integrated accelerometer (LIS3L02AQ 3-axis accelerometer, ST Microelectronics Inc., Switzerland), connected to a laptop computer which analyses the data in real time and shows resulting acceleration signal and 1-RM prediction result to the user.

The 1-RM prediction equation implemented in the system was

$$m_{1-RM} = \frac{(1,14 + k) * a_{max} \times m_{sub}}{g} \quad (1)$$

where  $m_{1-RM}$  is the 1-RM prediction result  
 $a_{max}$  is the maximum acceleration during the submaximal lift  
 $m_{sub}$  is the submaximal weight  
 $g$  is gravitation constant  $9,81\text{m/s}^2$  and  
 $k$  is calibration coefficient.



Fig. 2. The measurement system.

The Eq. (1) was developed on the basis of previous research project data, in which 1-RM prediction in bench press with the same measurement system was studied [14]. The calibration coefficient  $k$  in the equation made it possible to adjust the prediction individually for subjects.

The weight lift movement investigated in this study was bench press. This movement affects mainly on muscle groups of shoulder flexors and adductors. In the study a standard procedure of bench press was applied, where the bar was first lowered until it touches the chest, and next it was pushed up to the full elbow extension.

The study consisted of two phases, calibration and validation phase. In the calibration phase the subject's 1-RM was determined by adding weights to the bar until the maximum lift capacity was achieved. After a 5-10 min resting interval a submaximal weight (40-60% of the actual 1-RM result) was set to the bar and the subject was asked to pull the weights up as fast as possible. The accelerometer data during the lift was recorded to a computer and the maximum acceleration during the upward lift was defined. Next the calibration coefficient  $k$  from the Eq. (1) was calculated as follows:

$$k = \frac{m_{1-RM} \times g - 1,14 \times a_{max} \times m_{sub}}{a_{max} \times m_{sub}} \quad (2)$$

The  $k$  of individual subject was stored to a database of the measurement system together with information of subject's anthropometric data (gender, age, height, weight) and training activity history.

The validation phase of the study was done for each subject after an average of two weeks from the calibration. In this phase the subject was asked to perform one submaximal lift with the same submaximal weight as in the previous calibration phase. In the validation phase the actual 1-RM was not performed again, it was supposed to be the same as value determined in the first phase of the study.

After collection of data of all subjects the results were statistically analyzed. In those analyses correlation and relative error between predicted and actual 1-RM result with both calibrated and non-calibrated (where was  $k=0$ ) equation were investigated. Also, the relationship between anthropometric and training history data and the 1-RM prediction accuracy was shortly investigated.

## III. SUBJECTS AND DATA

The measurement system was built to a gym of School of Engineering of Oulu University of Applied Sciences. The test subjects consisted of voluntary students and personnel of the same organization. The total number of subjects was 30

(15 females, 15 males, age  $24\pm 5$  years, height  $171\pm 10$  cm, weight  $71\pm 16$  kg, all values mean $\pm$ std).

Before measurements in the calibration phase subjects were first explained how the measurements will be made. Next they were advised to warm up their muscles to obtain reliable results and to avoid injuries. Next the subjects answered in a survey about physiological factors (gender, height, weight, age) and training activity (estimate about how many years the subject has trained sports relating muscular training). Next the actual 1-RM value was determined by adding weight to the bar until the maximum was obtained, following typical procedure of 1-RM determination in the bench press. Then the subjects had a short rest interval. Then a submaximal weight (40-60% of the determined actual 1-RM value) was put to the bar, and the measurement wristwatch was attached to the bar. Then the subject made the submaximal lift as rapidly as possible. This was repeated few times to assure about a reliable result. The data of the last submaximal lift was used in the calibration coefficient calculation with help of Eq. 2.

After period of an average of two weeks from the calibration phase the validation phase was done for each subject. In this phase the subjects were first asked to warm up like in the calibration phase. Next the same submaximal weight that they had used in the calibration phase was put to the bar and the measurement wristwatch was attached to the bar. The subjects were then asked to lift the weights up like in the calibration phase. The data of the measurement was stored to the computer.

#### IV. RESULTS

Fig. 2 shows the 1-RM prediction result in validation phase, calculated by using individual calibration values.

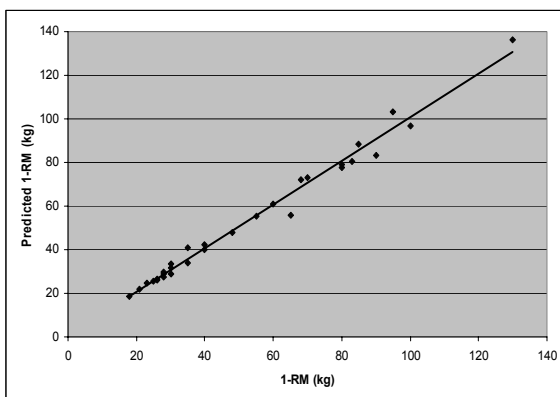


Fig. 2 The relationship between actual and estimated 1-RM values in bench press in validation phase.

Table 1 1-RM prediction accuracies for selected groups

Group	Absolute relative error (%)	R
Males (N=15)	4,6	0,98
Females (N=15)	4,6	0,96
>5 years training experience (N=19)	4,2	0,99
$\leq 5$ years training experience (N=11)	5,3	1,00
BMI $\geq 25$ (N=11)	5,5	0,99
BMI $< 25$ (N=19)	4,0	1,00
Age $\geq 24$ (N=11)	4,3	1,00
Age $< 24$ (N=19)	4,8	0,99

In Fig. 2 it can be seen clearly the accuracy of the prediction is good when using the calibration value. The Pearson's correlation coefficient R between the actual and predicted 1-RM was 0,99 ( $p < 0,001$ ) and the corresponding relative absolute error of the 1-RM prediction was 4,6%. Without use of the calibration value correction ( $k=0$ ), the corresponding results according to Eq. 1 would have been  $R=0,99$  ( $p < 0,001$ ) and 9,2%, respectively.

A short evaluation about relationship between anthropometric data, training history and the 1-RM prediction accuracy indicates differences between individuals in light of 1-RM prediction. Table 1 shows the correlation coefficients and relative absolute error of the 1-RM prediction for selected groups.

#### V. DISCUSSION AND CONCLUSION

In this study accuracy of a simple calibration procedure in prediction of 1-RM result from submaximal performance in bench press was validated. The results of this study show that the calibration procedure was advantageous, resulting in clearly smaller absolute error (4,6%), compared to non-calibrated result (9,2%).

The short evaluation of the correspondence between prediction accuracy and anthropometric or training history data showed slight differences between subjects with long and short training history. Differences in prediction accuracy in different anthropometric groups (gender, BMI, age) were smaller.

It is natural that the anthropometric data has some correlation with the 1-RM result of the subject. For example, in evaluation of subject's physical condition and performance the 1-RM results are often assessed related to the subject's weight. Further, the relationship between age muscle fibers is well known, and it should be taken into account especially if the 1-RM prediction is applied among elderly people.

In further studies it would be advantageous to collect data from large number of subjects of different kind of anthropometric and training history conditions, and then develop a method, which would automatically predict the correct calibration value  $k$  to the Eq. 1. This would make the prediction more applicable and usable because the prediction accuracy for the individual would appropriate accurate without need of calibration.

To conclude, the results of this study clearly show the individual calibration increase the significantly the 1-RM prediction accuracy with the method applied in this study.

## REFERENCES

1. Berger RA (1961) Determination of the resistance load for 1-RM and 10-RM. *J Assoc Physi Ment Rehab* 15, 1961, 108-110.
2. Chapman PP, Whitehead JR, Binkert RH (1998) The 225-lb Repts-to-Fatigue Test as a Submaximal Estimate of 1-RM Bench Press Performance in Col-lege Football Players. *J Strength Cond Res.* 12(4), 1998, 258-261.
3. Horvat M, Ramsey V, Franklin C, Gavin C, Palumbo T and Glass LA (2003) A method for predicting maximal strength in collegiate women athletes. *J Strength Cond Res.* 17(2), 2003, 324-328.
4. McArdle WD, Katch FI and Katch VL (1996) *Exercise physiology* Fourth Edition, Williams & Wilkins, Baltimore, 1996, 418, 571
5. Kim PS, Mayhew JL and Peterson DF (2002) A modified YMCA bench press test as a predictor of 1 repetition maximum bench press strength. *J Strength Cond Res.* 16(3), 2002, 440-445.
6. Mayhew JL, Ball TE and Arnold MD (1989) Prediction of 1-RM bench press from submaximal bench press performance in college males and females. *J Appl Sports Sci Res*, 53, 1989, S73.
7. Hoeger WWK, Hopkins DR, Barette SL and Hale DF (1990) Relationship between repetitions and selected percentages of one repetition maximum: A comparison between untrained and trained males and females. *Journal of Applied Sport Science Research*, 4, 1990, 47-54.
8. Cummings B, Finn KJ (1998) Estimation of a One Repetition Maximum Bench Press for Untrained Women. *J Strength Cond Res.* 1998, 12(4), 1998, 262-265.
9. Hannula M, Rontu J-P and Jauhiainen J (2007) Prediction of One Repetition Maximum in Weight Lifting with Multilinear Regression Model. *Proceedings of the Fifth IASTED International Conference on Biomedical Engineering.* - Innsbruck : IASTED, 2007.
10. Hannula M (2007) Evaluation method of a sports performance. Patent application n:o WO2007036611, World Intellectual Property Organization, 2007.
11. Salmi J, Rontu J-P, Hannula M, Leskinen S and Linnamo V (2007) 1-RM bench press performance estimated with accelerometer method. *Proceedings of the 12th Annual Congress of the ECSS*, 11-14 July 2007, Jyväskylä, Finland.
12. Hannula M, Jauhiainen J and Äijälä S (2006) One repetition maximum prediction from a submaximal performance in weight lifting. *Proceedings of 5th World Congress of Biomechanics*, Munich, Germany, 2006.
13. McArdle WD, Katch FI and Katch VL (2000) *Essentials of Exercise Physiology*, Second Edition, Lippincott Williams & Wilkins, Baltimore, 2000, 394-399, 559
14. Rontu J-P (2007) 1-RM Bench press performance estimated with a new accelerometer method, Master's Thesis, University of Jyväskylä, 2007.

Address of the corresponding author:

Author: Manne Hannula  
 Institute: Medical Engineering R&D Center, Oulu University of Applied Sciences  
 Street: Kotkantie 1  
 City: Oulu  
 Country: Finland  
 Email: manne.hannula@oamk.fi

# Prediction of One Repetition Maximum in Dumbbell Concentration Curl and Shoulder Press

M. Hannula<sup>1</sup>, A. Hirvikoski<sup>1</sup>, M. Isorinne<sup>1</sup> and J. Jauhiainen<sup>1</sup>

<sup>1</sup> Medical Engineering R&D Center, Oulu University of Applied Sciences, Finland

**Abstract** — In this study the prediction of maximum performance in dumbbell concentration curl and shoulder press was examined. The idea of the study was to predict the one repetition maximum (1-RM) with help of analysis of accelerations during a submaximal lift. In the study 30 gym trainees (all males, age  $26 \pm 7$  years, height  $179 \pm 6$  cm, weight  $77 \pm 10$  kg) performed dumbbell concentration curl and shoulder press exercises which all were accurately measured with help of a specific three-dimensional acceleration sensor based analysis system. The characteristics of the acceleration as a function of submaximal weight was analyzed and the prediction of one repetition maximum were evaluated. The data analysis resulted in 1-RM prediction mean absolute error of 2,8 kg for the dumbbell concentration curl and 12,3 kg for the shoulder press when using a simple linear prediction model. The detailed analysis showed that prediction mean absolute errors of 1,9 kg and 3,3 kg for dumbbell concentration curl and shoulder press would be achieved by adjusting the prediction model appropriately. The results show that it is possible predict the 1-RM with help of accelerometer from the submaximal performance in studied weight lifting exercises. However, the detailed prediction algorithm for 1-RM prediction requires further development.

**Keywords** — 1-RM, submaximal weight, accelerometer.

## I. INTRODUCTION

The one-repetition maximum (1-RM) determines the maximum performance of a subject in weight lifting. It is the absolute maximum load that a trainee can lift once [1,2,3]. In addition of being an indicator of maximum performance, the 1-RM is an important parameter in training program planning [4]. This means the 1-RM information is important not only for beginners who are tailoring training programs for themselves, but also for competition level athletes whose ranking may finally depend on their 1-RM result.

A number of different kinds of methods for predicting 1-RM can be found in the literature [1,5,6,7,8,9]. The prediction of 1-RM from submaximal exercise is challenging. Due to recent rapid development of sensor technology many new opportunities to evaluate weight lifting are currently available. Because of those trends also many kind of applications directed for ordinary trainees are soon emerging into con-

sumer markets. In this context this study is related to the previous studies about the use of accelerometer sensors in the prediction of 1-RM from submaximal exercise [9,10,11,12].

In this study the relationships between acceleration, submaximal weight and 1-RM in dumbbell concentration curl and shoulder press were studied with the help of a simple linear data analysis approach.

## II. METHODS

The measurement system used in this study is illustrated in Fig. 1. It consists of a wristwatch, including an integrated accelerometer (LIS3L02AQ 3-axis accelerometer, ST Microelectronics Inc., Switzerland), connected to a laptop computer which analyses the data in real time and shows the resulting acceleration signal and 1-RM prediction result to the user.

The measurement procedure was the following: first the wristwatch was attached to wrist and the submaximal weight was set by pushing the buttons of the watch. Next the system produced a beep, which indicated that the user should make the lift. After successful lift the system analysed the collected data and showed the result of the 1-RM prediction on the computer screen. The prediction of 1-RM from submaximal lift was based on analysis of maximum acceleration. Especially interesting in the prediction of 1-RM from the submaximal exercise is the relationship between submaximal load and maximum acceleration during the lift. In this study this relationship was examined in detail.

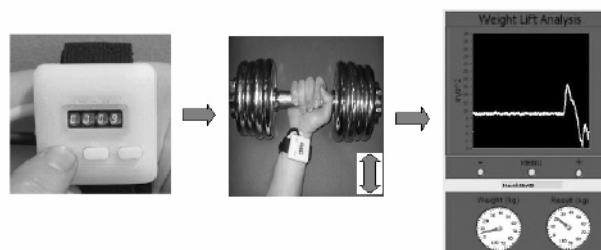


Fig. 1 Measurement system used in the study.



III. SUBJECTS AND DATA

The experimental data was collected from 30 men (age  $26 \pm 7$  years, height  $179 \pm 6$  cm, weight  $77 \pm 10$  kg). Every tester's age, weight and height were written down on a field book before measurements. Maximum acceleration of each weight was stored in the field book after every lift. Submaximal weight used on every lift and maximum result (= highest weight the trainee could lift) were also stored. Measurements were carried out at a gym called Ouluhalli.

The aim of the measurements was first explained to the test subjects. Then the subject was asked first to warm up muscles slightly and then accelerometer was set to the right wrist. After that the subject performed a dumbbell concentration curl in Scott-bench starting with a small weight and by increasing it until the limit was obtained. The applied weights were 3kg, 5kg, 6kg, 8kg, 12.5kg, 15kg, 17.5kg, 20kg, 22.5kg and 25kg. Testers made one repetition with each weight until the maximum weight was reached.

Measurements of the shoulder press were made the same way that dumbbell concentration curls except that the movements were made by both arms. Measurement wristwatch was fastened to the left wrist and lifts were made in standing position. The total number of submaximal lifts was 120 in dumbbell concentration curl and 207 in shoulder press.

In all measurements the aim was to give lifting instructions to the subjects in a way that the lifting technique would be similar among all the subjects.

IV. RESULTS

After measurements the maximum acceleration of submaximal lifts were analyzed. Fig. 2 shows the measured relationship between maximum accelerations and submaximal weights. The solid line shows the best linear fit between the measured values. The linear Pearson's correlation coefficient between the variables was  $R = -0.68$  in arm curl and  $R = -0.62$  in shoulder press, respectively.

It can be clearly seen from Fig. 2 that the maximum acceleration value diminishes as the submaximal weight increases. The 1-RM value is obtained when the acceleration reaches zero. Because the correspondence between the submaximal weight and maximum acceleration is linear, the maximum acceleration with weight  $m_{sub}$  can be calculated from equation  $a_{max} = k \times m_{sub} + b$ . By assuming the  $k$  is constant and  $b$  varies among subjects, the 1-RM value can be easily calculated by equation  $m_{1-RM} = \frac{-a_{max} - k \times m_{sub}}{k}$ . This value is the x-axis zero-crossing point of the line which has slope of  $k$ .

Next a simple linear 1-RM prediction model, which was based on the slope  $k$  in submaximal weight – maximum acceleration diagram, was evaluated. The prediction was done distinctly for dumbbell concentration curl and shoulder press by using all of the data in the prediction (total of 120 submaximal lifts in dumbbell concentration curl and 207 lifts in shoulder press). Fig. 3 shows the estimated 1-RM values calculated with the help of the linear equations shown in Fig. 2, where the  $k$  was  $-0.96$  in dumbbell concentration curl and  $-0.47$  in shoulder press. The corresponding mean absolute errors were 2.8 kg ( $R=0.38$ ) and 12.3 kg ( $R=0.42$ ) for the dumbbell concentration curl and shoulder press, respectively.

In Fig. 3 can be clearly seen, that especially in shoulder press the 1-RM estimates are systematically too high. Therefore the prediction accuracy was also evaluated by using in prediction  $k$  values, which would result in more accurate results. Fig. 4 shows the mean absolute error of

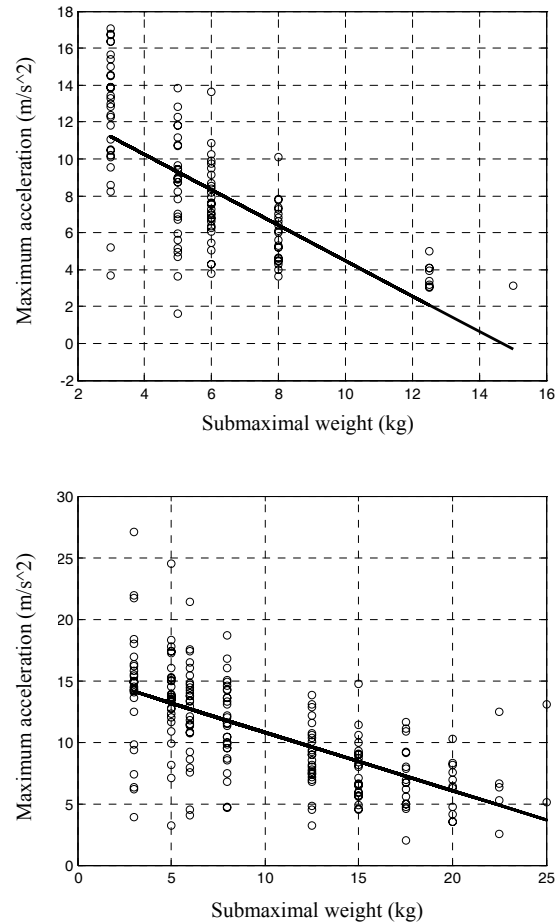


Fig. 2 Maximum accelerations and submaximal weights in dumbbell concentration curl (upper graph) and shoulder press (lower graph).

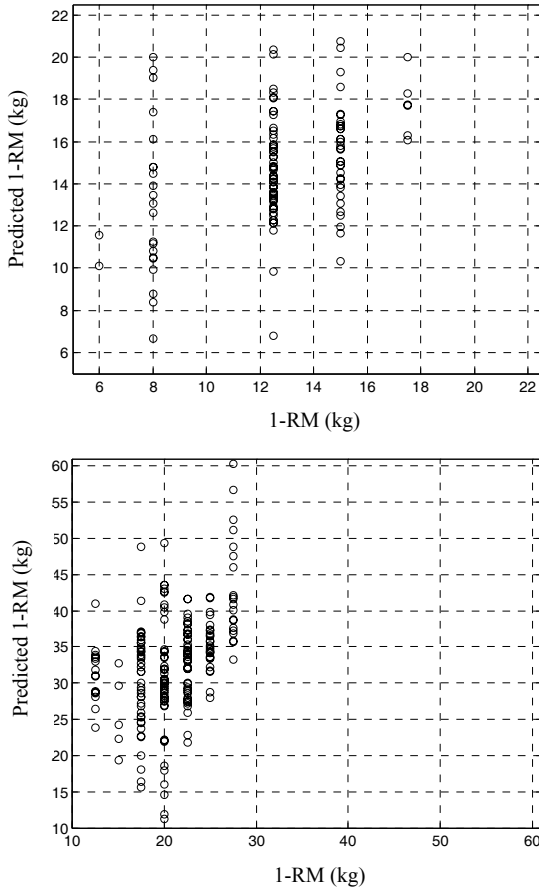


Fig. 3. The relationship between real and estimated 1-RM values in dumbbell concentration curl (upper graph) and in shoulder press (lower graph).

1-RM prediction in dumbbell concentration curl and shoulder press with  $k$  values between -0.5 and -1.5.

Fig. 4 illustrates the sensitivity of the 1-RM prediction to the value of  $k$  in the prediction equation. By selecting the optimal values for  $k$  in prediction the mean absolute errors of 1,9 kg and 3,3kg in dumbbell concentration curl and shoulder press would be achieved.

### V. DISCUSSION AND CONCLUSION

In this study the correlation between maximum acceleration and submaximal weight in dumbbell concentration curl and shoulder press was investigated. The study shows clearly that there is clear correspondence between the studied variables (Pearson’s correlation coefficients  $-0.62$  and  $-0.68$ ). However, the variability in the data is rather high, and direct use of the existing linear correlation feature does

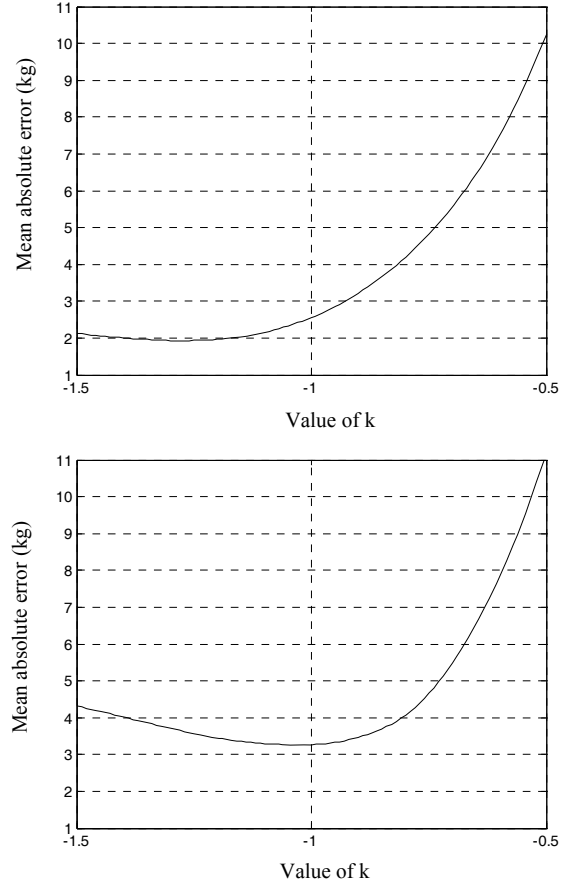


Fig. 4. The relationship between value of  $k$  and mean absolute error in 1-RM prediction in dumbbell concentration curl (upper graph) and in shoulder press (lower graph).

not produce accurate results for the prediction of 1-RM value from the submaximal performance.

In interpretation of the result it should be taken into account that this study was restricted to a very simple and straightforward data analysis. There were a total number of 30 subjects. Each of them produced one submaximal weight – maximum acceleration curve. If the individual features of each subject (e.g. anthropometric data) could be taken into account in data analysis, the result would be better. Further, in the data analysis a very simple approach for the prediction of the 1-RM was used: it was assumed to be in point where the submaximal weight – maximum acceleration line reaches value zero in the acceleration axis. It is highly probable that the near-zero “end” of the line is not linear. To investigate this, the relationship between weights which are very near to 1-RM and the corresponding acceleration values should be studied in more detail.

The 1-RM prediction in dumbbell concentration curl was much more accurate compared to the shoulder press. By using the  $k$  values determined directly with a simple linear model from Fig. 2, the mean absolute errors were 2,8 kg and 12,3 kg, and by selecting optimal  $k$  values from Fig. 4, the mean absolute errors were 1,9 kg and 3,3 kg, respectively. The most apparent reason for the clear differences is that in the measurements the dumbbell concentration curl the exercise setup was easier to regulate compared to the shoulder press. In the data collection phase it was found that in shoulder press, when subjects used submaximal weights near to their 1-RM amounts, they often tried to “help” the movement up with help of the body movement.

In conclusion, this study clearly illustrates that there is a correspondence between the submaximal weight and maximum acceleration in both dumbbell concentration curl and shoulder press. In further studies the focus is in development of accurate estimate of 1-RM value.

#### REFERENCES

- Berger RA (1961) Determination of the resistance load for 1-RM and 10-RM. *J Assoc Physi Ment Rehab* 15, 1961, 108-110.
- Chapman PP, Whitehead JR, Binkert RH (1998) The 225-lb Repts-to-Fatigue Test as a Submaximal Estimate of 1-RM Bench Press Performance in Col-lege Football Players. *J Strength Cond Res.* 12(4), 1998, 258-261.
- Horvat M, Ramsey V, Franklin C, Gavin C, Palumbo T and Glass LA (2003) A method for predicting maximal strength in collegiate women athletes. *J Strength Cond Res.* 17(2), 2003, 324-328.
- McArdle WD, Katch FI and Katch VL (2000) *Essentials of Exercise Physiology* (Second Edition, Lippincott Williams & Wilkins, Baltimore, 2000)
- Kim PS, Mayhew JL and Peterson DF (2002) A modified YMCA bench press test as a predictor of 1 repetition maximum bench press strength. *J Strength Cond Res.* 16(3), 2002, 440-445.
- Mayhew JL, Ball TE and Arnold MD (1989) Prediction of 1-RM bench press from submaximal bench press performance in college males and females. *J Appl Sports Sci Res*, 53, 1989, S73.
- Hoeger WWK, Hopkins DR, Barette SL and Hale DF (1990) Relationship between repetitions and selected percentages of one repetition maximum: A comparison between untrained and trained males and females. *Journal of Applied Sport Science Research*, 4, 1990, 47-54.
- Cummings B, Finn KJ (1998) Estimation of a One Repetition Maximum Bench Press for Untrained Women. *J Strength Cond Res.* 1998, 12(4), 1998, 262-265.
- Hannula M, Rontu J-P and Jauhiainen J (2007) Prediction of One Repetition Maximum in Weight Lifting with Multilinear Regression Model. *Proceedings of the Fifth IASTED International Conference on Biomedical Engineering.* - Innsbruck : IASTED, 2007.
- Salmi J, Rontu J-P, Hannula M, Leskinen S and Linnamo V (2007) 1-RM bench press performance estimated with accelerometer method. *Proceedings of the 12th Annual Congress of the ECSS*, 11-14 July 2007, Jyväskylä, Finland.
- Hannula M, Jauhiainen J and Äijälä S (2006) One repetition maximum prediction from a submaximal performance in weight lifting. *Proceedings of 5th World Congress of Biomechanics*, Munich, Germany, 2006.
- Hannula M (2007) Evaluation method of a sports performance. Patent application n:o WO2007036611, World Intellectual Property Organization, 2007.

Address of the corresponding author:

Author: Manne Hannula  
 Institute: Medical Engineering R&D Center, Oulu University of Applied Sciences  
 Street: Kotkantie 1  
 City: Oulu  
 Country: Finland  
 Email: manne.hannula@oamk.fi

# Feature Selection for Bayesian Evaluation of Trauma Death Risk

L. Jakaite and V. Schetinin

University of Bedfordshire/Department of Computing and Information Systems, Luton, UK

*Abstract* — In the last year more than 70,000 people have been brought to the UK hospitals with serious injuries. Each time a clinician has to urgently take a patient through a screening procedure to make a reliable decision on the trauma treatment. Typically, such procedure comprises around 20 tests; however the condition of a trauma patient remains very difficult to be tested properly. What happens if these tests are ambiguously interpreted, and information about the severity of the injury will come misleading? The mistake in a decision can be fatal – using a mild treatment can put a patient at risk of dying from posttraumatic shock, while using an over-treatment can also cause death. How can we reduce the risk of the death caused by unreliable decisions? It has been shown that probabilistic reasoning, based on the Bayesian methodology of averaging over decision models, allows clinicians to evaluate the uncertainty in decision making. Based on this methodology, in this paper we aim at selecting the most important screening tests, keeping a high performance. We assume that the probabilistic reasoning within the Bayesian methodology allows us to discover new relationships between the screening tests and uncertainty in decisions. In practice, selection of the most informative tests can also reduce the cost of a screening procedure in trauma care centers. In our experiments we use the UK Trauma data to compare the efficiency of the proposed technique in terms of the performance. We also compare the uncertainty in decisions in terms of entropy.

*Keywords* — Bayesian model averaging, MCMC, decision tree, trauma care, feature selection.

## I. INTRODUCTION

As it has been reported in [1], more than 70,000 people have been admitted into the UK hospitals with serious injuries. To make a reliable decision on the trauma treatment, a clinician has to urgently take a patient through a screening procedure which typically comprises around 20 tests [2]. However, the condition of a trauma patient is still very difficult to be tested properly. If the screening tests are ambiguously interpreted, and information about the severity of the injury is misleading, the mistake in a decision can be fatal; the choice of a mild treatment can put a patient at risk of dying from posttraumatic shock, while the choice of an overtreatment can also cause death [1]. How can we reduce the risk of the death caused by unreliable decisions?

It has been shown in [3 - 6] that probabilistic reasoning, based on the Bayesian methodology of averaging over deci-

sion models, enables to evaluate the uncertainty in decision making. The use of the Bayesian Model Averaging (BMA) over Decision Trees (DTs) makes decision models interpretable for clinicians as shown in [7]. The Bayesian averaging over DTs (BDTs) enables to select attributes which make the most significant contribution to decisions. Within the Bayesian DTs averaging we would expect that discarding weakest attributes would improve the performance. However, in our experiments, we observed that the performance decreased. Obviously, we can explain that this happened because the discarded attribute was still important for a small amount of the data. If this is the case, then we can expect that the replacement of this attribute by noise will further decrease the performance. Alternatively, we can assume that the weakest attribute makes a contribution to the BMA. Would it be possible to discard the weakest attribute without decreasing the performance? If so, then we can reduce the number of screening tests required for making reliable decisions within BDT methodology.

In theory, BMA methodology is immune to overfitting problem [3]. However, in some cases, overfitting was shown to affect the BMA performance [8]. Based on these results we can assume that if the replacement of the weakest attribute by noise does not decrease the BMA performance, this attribute, making negligible contribution, provides better conditions for mitigating BMA overfitting.

Based on these assumptions, in this paper we aim at selecting the most important screening tests, keeping the BDT performance high. This is important because selection of the most informative screening tests can reduce the cost of a screening procedure in trauma care centers. In our experiments we use the UK Trauma data to compare the efficiency of the proposed BMA technique in terms of the performance. We also compare the uncertainty in decisions in terms of entropy.

Section 2 of the paper describes the bases of BMA over DTs, and section 3 describes the Trauma data used for the experiments. The experimental results are presented in section 4, and section 5 concludes the paper.

## II. METHODOLOGY OF BAYESIAN MODEL AVERAGING

For a DT given with parameters  $\theta$ , the predictive distribution is written as an integral over the parameters  $\theta$

$$p(y | \mathbf{x}, \mathbf{D}) = \int_{\theta} p(y | \mathbf{x}, \theta, \mathbf{D}) p(\theta | \mathbf{D}) d\theta$$

where  $y$  is the predicted class ( $1, \dots, C$ ),  $\mathbf{x} = (x_1, \dots, x_m)$  is the  $m$ -dimensional vector of input, and  $\mathbf{D}$  are the given training data.

This integral can be analytically calculated only in simple cases, and in practice part of the integrand, which is the posterior density of  $\theta$  conditioned on the data  $\mathbf{D}$ ,  $p(\theta | \mathbf{D})$ , cannot usually be evaluated. However if values  $\theta^{(1)}, \dots, \theta^{(N)}$  are the samples drawn from the posterior distribution  $p(\theta | \mathbf{D})$ , we can write

$$\begin{aligned} p(y | \mathbf{x}, \mathbf{D}) &\approx \sum_{i=1}^N p(y | \mathbf{x}, \theta^{(i)}, \mathbf{D}) p(\theta^{(i)} | \mathbf{D}) \\ &= \frac{1}{N} \sum_{i=1}^N p(y | \mathbf{x}, \theta^{(i)}, \mathbf{D}) \end{aligned}$$

The above integral can be approximated by using Markov Chain Monte Carlo (MCMC) technique [3]. To perform such an approximation, we need to run a Markov Chain until it has converged to a stationary distribution. Then we can collect  $N$  random samples from the posterior  $p(\theta | \mathbf{D})$  to calculate the desired predictive posterior density.

Using DTs for the classification, we need to find the probability  $\phi_{jt}$  with which an input  $\mathbf{x}$  is assigned by terminal node  $t = 1, \dots, k$  to the  $j$ th class, where  $k$  is the number of terminal nodes in the DT. The DT parameters are defined as  $\theta = (s_i^{\text{pos}}, s_i^{\text{var}}, s_i^{\text{rule}})$ ,  $i = 1, \dots, k-1$ , where  $s_i^{\text{pos}}$ ,  $s_i^{\text{var}}$  and  $s_i^{\text{rule}}$  define the *position*, *predictor* and *rule* of each splitting node, respectively. For these parameters the priors can be specified as follows. First we can define a maximal number of splitting nodes, say,  $s_{\max} = n - 1$ . Second we draw any of the  $m$  predictors from a uniform discrete distribution  $U(1, \dots, m)$  and assign  $s_i^{\text{var}} \in \{1, \dots, m\}$ .

Finally the candidate value for the splitting variable  $x_j = s_i^{\text{var}}$  can be drawn from a discrete distribution  $U(x_j^{(1)}, \dots, x_j^{(L)})$ , where  $L$  is the number of possible splitting rules for variable  $x_j$ , either categorical or continuous. Such priors allow us to explore DTs which split data in as many ways as possible. However the DTs with different numbers of splitting nodes should be explored in the same proportions [3].

To sample DTs of a variable dimensionality, the MCMC technique exploits the Reversible Jump extension [3]. To implement the RJ MCMC technique, Denison *et al.* [3] and Chipman *et al.* [6] have suggested exploring the posterior probability by using the following types of moves:

1. *Birth*. Randomly split the data points falling in one of the terminal nodes by a new splitting node with the variable and rule drawn from the corresponding priors.

2. *Death*. Randomly pick a splitting node with two terminal nodes and assign it to be one terminal with the united data points.
3. *Change-split*. Randomly pick a splitting node and assign it a new splitting variable and rule drawn from the corresponding priors.
4. *Change-rule*. Randomly pick a splitting node and assign it a new rule drawn from a given prior.

The first two moves, *birth* and *death*, are reversible and change the dimensionality of  $\theta$ . The remaining moves provide jumps within the current dimensionality of  $\theta$ . Note that the *change-split* move is included to make “large” jumps which potentially increase the chance of sampling from a maximal posterior whilst the *change-rule* move does “local” jumps.

The RJ MCMC technique starts drawing samples from a DT consisting of one splitting node whose parameters were randomly assigned within the predefined priors. So we need to run the Markov Chain while a DT grows and its likelihood is unstable. This phase is said *burn-in* and it should be preset enough long in order to stabilize the Markov Chain. When the Markov Chain will be enough stable, we can start sampling. This phase is said *post burn-in*.

### III. THE PROPOSED METHOD

To test the assumptions made in section I, we propose two methods – the first is based on selection of DTs ensemble, and the second is based on the randomization of variables. The selection technique aims to omit the DTs which use the weakest variable. The randomization technique aims to provide better conditions for mitigating DT ensemble overfitting. In the following sections we test and compare these techniques on the Trauma data.

### IV. EXPERIMENTS AND RESULTS

#### A. Trauma Data

The Trauma data collected at the Royal London Hospital comprises 16 screening tests and attributes and the outcome (lived or died) for 316 injured patients. Among these variables 5 are continuous and 11 are categorical, see Table 1.

#### B. Variable's Importance

In our experiments we collected 10,000 DTs during post burn-in phase after sampling 200,000 DTs during burn-in phase. The sampling rate for post burn-in phase was 7; the number of minimal data instances allowed in DT nodes was 3; the acceptance rate was around 0.25.

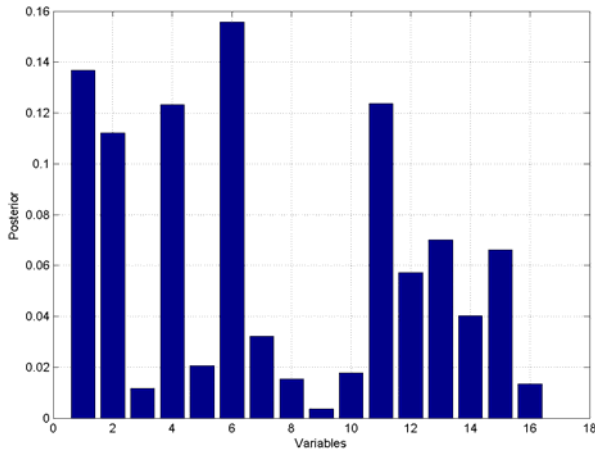


Fig. 1 Posterior probabilities of variables used in the ensemble

Table 1 Screening tests and attributes of the Trauma data

No	Screening Tests and Attributes	Type
1	Age	Continuous
2	Gender: Male = 1, Female = 0.	0,1
3	Injury type: Blunt = 1, penetrating = 0	0,1
4	Head injury, no injury = 0	0,1,2,3,4,5,6
5	Facial injury	0,1,2,3,4
6	Chest injury	0,1,2,3,4,5,6
7	Abdominal or pelvic contents injury	0,1,2,3,4,5
8	Limbs or bony pelvis injury	0,1,2,3,4,5
9	External injury	0,1,2,3
10	Respiration rate	Continuous
11	Systolic blood pressure	Continuous
12	Glasgow coma score (GCS) eye response	0,1,2,3,4
13	GCS motor response	0,1,2,3,4,5,6
14	GCS verbal response	0,1,2,3,4,5
15	Oximetry	Continuous
16	Heart rate	Continuous
17	Died = 1, living = 0.	0,1

Having obtained the ensemble of DTs, we estimated the importance of all 16 variables for the prediction. The estimates were calculated as the posterior probabilities of variables used in the DTs ensemble as shown in Fig. 1.

From Fig. 1 we can observe that the posterior probability of variable 9 is the smallest, around 0.005, while the maximal value is around 0.16 for variable 6. Therefore we can assume that the variable 9 makes negligible contribution to the ensemble’s outcome.

To test our assumptions, we aim to discard this variable from the Trauma data. Table 2 shows the maximal values of loglikelihoods calculated within 5-fold cross-validation for two sets including 16 and 16\9 variables. From this table, we can observe that the loglikelihood value for the 16\9 set becomes greater than that for the set of all 16 variables. However the performance of the ensemble using the set of 16\9 variables is slightly fewer than that using the set of 16

Table 2 Maximal loglikelihoods,  $L_{16}$  and  $L_{16\setminus 9}$ , performances and entropies of the ensembles using sets of 16 and 16\9 variables within 5-fold cross-validation

Fold	Loglikelihood ( $L_{16}$ )	Loglikelihood ( $L_{16\setminus 9}$ )
1	-36.14	-33.4
2	-44.29	-37.33
3	-37.23	-33.19
4	-36.24	-38.37
5	-37.98	-40.41
Loglikelihood	-38.37 ±3.39	-36.48 ±3.23
Performance, %	84.66 ±4.70	83.85 ±6.95
Entropy	29.8 ±2.1	30.0 ±4.7

variables. This can happen because the ensemble using the set of 16\9 variables becomes more overfitted to the training data. Thus, we can conclude that the weakest variable 9 provides better conditions for mitigating the DT ensemble overfitting.

### C. Selection of DT Ensemble

As shown above, the presence of the weakest variable has the positive effect on mitigating overfitting of the DT ensemble. This means that the DT ensemble should use all 16 input variables during sampling, but then we can exclude those DTs which use the weakest variable 9. After such selection of DTs there is no need to use the variable 9.

In our experiments this technique was tested within 5-fold cross-validation and results shown in Table 3 which compares the performance of the original DT ensemble using all 16 variables with the performance of the selected ensemble. This table also shows the number of DTs omitted after the selection.

This table show that the performance of the selected ensemble using 16\9 variables is the same as that of the original ensemble using all 16 input variables. The entropies in decisions are also the same. Thus from this experiment we can see that proposed technique allows us to use a reduced set of variables.

Table 3 Performances and entropies of the original and selected ensembles within 5-fold cross-validation

Fold	Original ensemble		Selected ensemble		
	Performance, %	Entropy	BDTs omitted	Performance, %	Entropy
1	85.93	26.47	314	85.93	26.46
2	80.95	28.89	467	80.95	28.91
3	84.13	31.80	217	84.13	31.79
4	82.54	32.05	631	82.54	32.04
5	87.30	31.44	336	87.30	31.46
	84.17±2.54	30.13±2.40	393±160	84.17±2.54	30.13±2.40

#### D. Addition of Noise to Variables

In our experiments some amount of noise added to a weak variable can provide better conditions for mitigating DTs ensemble overfitting. Therefore, we can assume that the addition of noise to all variables will further improve conditions for mitigating DTs ensemble overfitting.

To test this assumption we removed the variable 9 and added a uniform noise to the remaining 15 variables. The intensity of the noise was 0.01. Table 4 shows the performances of DT ensembles using the set of 16 variables and the set of 16\9 with the added noise compared within 5-fold cross-validation. This table shows that the performance of the DT ensemble using the set of 16\9 + noise is better on 2%, than that of the ensemble using the original 16 inputs.

Thus we can see that the addition of the noise to the set of 16\9 variables allows us to exclude the weakest variable 9 and, at the same time, this enables to improve the DT ensemble performance.

Table 4 Performance and entropy of the ensembles using 16 variables and 16\9 variables with noise estimated within 5-fold cross-validation

Fold	Trauma (16 variables)		Trauma (16\9 variables + noise)	
	Performance, %	Entropy	Performance, %	Entropy
1	84.37	26.63	85.93	26.52
2	79.36	28.70	80.95	30.31
3	84.12	32.54	88.88	32.47
4	88.88	31.24	90.47	32.00
5	88.88	28.11	88.88	32.65
	85.13± 7.94	29.4± 4.80	87.03± 7.54	30.8± 5.10

#### V. CONCLUSIONS & DISCUSSION

We have expected that discarding weakest attributes can improve the performance of the BDT ensemble. However, in our experiments, the performance has oppositely decreased. We have assumed that this happened because the discarded weakest attribute was still important for a small amount of the data. Alternatively, we have assumed that the weakest attribute makes a noticeable contribution to the BDT ensemble's outcome. The question was would it be possible to discard the weakest attribute without decreasing the performance? This is important for clinical practice if

the number of screening tests required for making reliable decisions within BDT methodology can be reduced.

Although BMA methodology in theory is immune to overfitting problem, in some cases, it was shown that overfitting affects the BMA performance. We have observed that the replacement of the weakest attribute by noise did not decrease the BDT performance, and therefore this attribute, making negligible contribution, provided better conditions for mitigating BDT ensemble overfitting.

In this paper we aimed at selecting the most important screening tests, keeping the BDT performance high. In our experiments we used the UK Trauma data to compare the efficiency of the proposed technique in terms of the performance. We also compare the uncertainty in decisions in terms of entropy.

As a result we found that the proposed techniques allow clinicians to reduce number of screening tests, keeping the performance and reliability of making decisions high. The optimized solutions can reduce the cost of a screening procedure in trauma care centers.

#### REFERENCES

1. Royal Society for the Prevention of Accidents available at <http://www.rospa.com/factsheets>
2. Trauma Audit and Research Network available at <http://www.tarn.ac.uk>
3. Denison D, Holmes C, Malick B, Smith A (2002) Bayesian methods for nonlinear classification and regression. Wiley
4. Breiman L, Friedman J, Olshen R, Stone C (1984) Classification and regression trees. Belmont, CA: Wadsworth.
5. Buntine W (1992) Learning classification trees. *Statistics and Computing* 2: 63-73
6. Chipman H, George E, McCulloch R (1998) Bayesian CART model search, *J. American Statistics*, 93: 935-960
7. Schetinin V et al. (2007) Confident Interpretation of Bayesian Decision Trees for Clinical Applications. *IEEE Transaction on Information Technology in Biomedicine*, Volume 11, Issue 3, 312-319
8. Domingos P (2000) Bayesian Averaging of Classifiers and the Overfitting Problem, *Proc. 17th International Conf. on Machine Learning*, San Francisco, CA, 2000, 223-230

Author: L Jakaite  
 Institute: University of Bedfordshire  
 Street: Park Square  
 City: Luton  
 Country: UK  
 Email: [Livija.Jakaite@gmail.com](mailto:Livija.Jakaite@gmail.com)

# Objective Evaluation of Stroke Patients' Movement

Á. Jobbágy<sup>1</sup>, P. Simon<sup>1</sup>, G. Fazekas<sup>2</sup>, P. Harcos<sup>3</sup>, Z. Grosz<sup>3</sup>

<sup>1</sup> Budapest University of Technology and Economics/Measurement and Information Systems, Budapest, Hungary

<sup>2</sup> Szent János Hospital/Dept. of Physical and Rehabilitation Medicine, Budapest, Hungary

<sup>3</sup> Szent Imre Hospital/Neurology Dept., Budapest, Hungary

**Abstract** — Different movement patterns of patients are analysed in health care. The aim is either to characterise the movement itself or to acquire information on disorders affecting the motor system. Probably the most frequently used examination is gait analysis but prosthesis adjustment, sports-, rehabilitation-, and ergonomic studies are also greatly helped by movement analysis. The early diagnosis and assessment of patients with brain disorders is more reliable if several movement patterns are involved in the test. The paper reports on the objective evaluation of the finger-tapping and pointing movement; the equipment used, the movement patterns, the tested persons, the recordings and the evaluation algorithms are described in detail. Twelve stroke patients and ten healthy control subjects were tested. Persons performed pointing tests on a hexagon and finger tapping tests. The tracking of markers has made it possible to characterise the performance of a person on the basis of the complete tapping and pointing movement. This is a substantial improvement compared to evaluation based on contact sensors. Parameters have been defined that characterise both the swiftness and the regularity of movements. Evaluation of the movements affirms that stroke patients have individual symptoms. The actual state of a patient as well as the change in it can be assessed objectively by movement analysis. The proposed tests are appropriate for use in clinical environment. Patients have found the tests challenging but not fatiguing. The tests can be used not only for rating the patients objectively but also to help their rehabilitation.

**Keywords** — movement analysis, finger-tapping, pointing.

## I. INTRODUCTION

Neurologists observed specific changes in the movement co-ordination of their patients – compared to healthy control subjects – a long time ago. In the early, preclinical phase the subtle changes cannot be detected by visual inspection. Similarly, variations in the performance of a patient resulting from slow progress of the disease remain undetected for the human observer. Evaluation of movement aids the diagnosis – even early diagnosis – and assessment of the actual state of patients if

- the movement patterns are defined in detail,
- movements are recorded with satisfactory sampling rate and spatial resolution,
- appropriate feature extraction methods generate meaningful parameters.

Neurologists use a number of movement patterns to test their patients. The recordings at Szent János Hospital and at the Department of Measurement and Information Systems revealed that the movement patterns are usually not defined accurately enough. This deteriorates the reproducibility of these tests.

Passive marker-based motion analysis is especially suitable for testing human movements. The markers are lightweight (1...10 gram), and no wires are needed between the markers and the analyser. The markers and the analysis cause absolutely no discomfort to the persons. The performance of commercially available motion analysers by far exceeds the requirements needed to record and evaluate the movement of patients with neural diseases. As a consequence, these devices are too expensive for the task. We developed a simple device that is applicable for movement analysis and affordable for routine medical and clinical use.

## II. MATERIALS AND METHODS

### A. Subjects

The paper reports the results of a measurement series taken at Szent János Hospital, Budapest, between 12<sup>th</sup> October 2007 and 12<sup>th</sup> March, 2008. 12 hemiparetic stroke patients were tested. In the tested group there were 8 males (age  $56.8 \pm 13.8$  years, time from onset  $14 \pm 16$  months), 4 females (age  $69.2 \pm 10$  years, time from onset  $37 \pm 42$  months.)

### B. Apparatus

The Passive Marker-based Movement Analyser (PAM) has been developed at the Dept. Measurement and Information Systems; based mainly on commercially available elements [1, 2]. PAM is simple-to-use, it is suitable for clinical application. The camera is on a tripod fixed to the tabletop. The stripes that should be touched during finger-tapping and the hexagon are also fixed to the tabletop. The distance between the camera and the fingers of tested persons varies only as a result of the movement. Thus, a single camera is enough to assess movements in three dimensions.



C. The finger-tapping test

Tested persons put their hands on the table in prone position, with fingers approximately 1 cm apart from each other. 9-mm diameter markers are attached to the middle phalanges of their fingers. Elbows are on the table. Persons lift their fingers (except thumbs) and then hit the table in the following order: little, ring, middle, and index finger. Persons are asked to perform the movement as fast as they can (most important instruction and expectation) so that they lift their fingers as high as they can. **The priority of speed must be explained.** Fig. 1. shows the trajectories of markers during finger-tapping movement of a newly diagnosed Parkinsonian patient.

Increasing the amplitude slows down the movement. However, persons should not try to increase speed by minimising the amplitude of finger lifting. The finger-tapping test was performed by the patients in three phases: only with the affected hand, only with the non-affected hand, and with both hands in parallel.

D. The pointing tests

Pointing tests included sliding along the edges of a hexagon (P1, Fig. 2.), touching its vertices one after the other

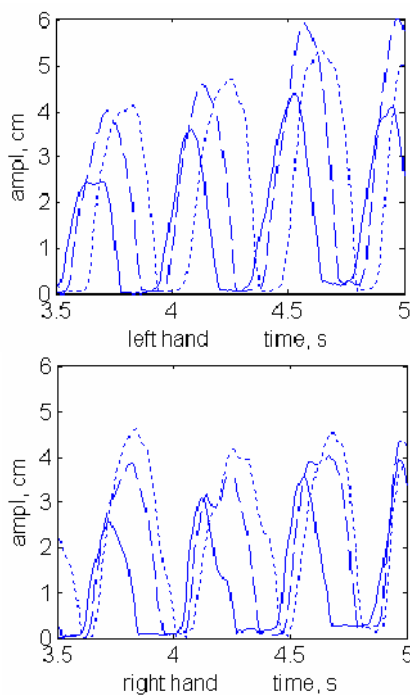


Fig. 1. Finger tapping movement of a newly diagnosed Parkinsonian patient. Affected hand below, non-affected one above. Solid = ring-, dashed = middle-, dotted = index finger.

(P2, Fig. 3.), and touching its vertices and the centre point alternately (P3, Fig. 4.).

Each movement lasted for twenty seconds, and was executed separately by both the affected and the other arm. The edge of the hexagon is 10 cm. The observing angle of the

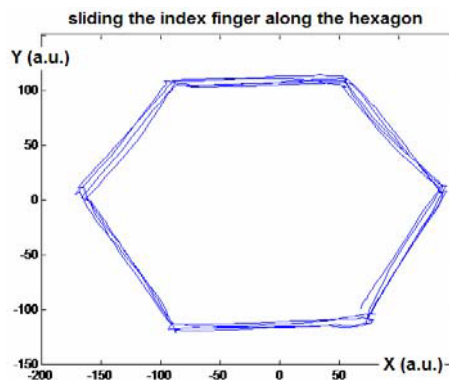


Fig. 2. Four cycles of sliding, healthy subject.

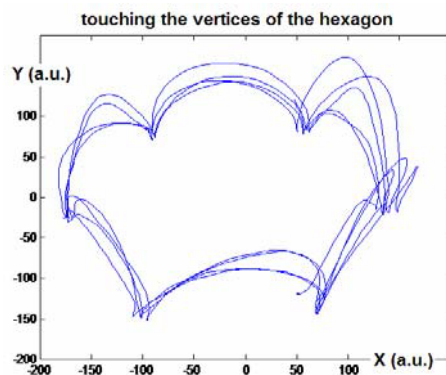


Fig. 3. Four cycles of touching the vertices, healthy subject.

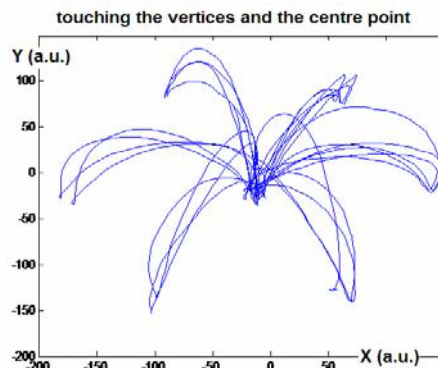


Fig. 4. Two cycles of touching alternately the vertices and the centre point, healthy subject.

camera is 45 degree thus the scaling in Figures 2-4 and 7-8 cannot be given in cm.

### E. Evaluation of movements

Evaluation of the tapping test is based on the regularity and speed of the movement. It is easier to execute the movement regularly at low speed. Consequently, the movement is characterized by the product of regularity and speed.

The *measure of periodicity, PM* of the quasi-periodic finger-tapping movement can be well quantified by using the singular value decomposition, SVD method [3]. Contrary to the Fourier analysis, the signal is broken down to periodic functions of any kind not only sinusoidal. The periodicity of movement (PM) is characterised by the relative weight of the dominant basis function within all basis functions necessary to describe the complete record, i.e. all periods. This is calculated on the basis of the weights ( $\sigma_i$ ) of all basis functions:

$$PM = \frac{\sigma_1^2}{\sum_{i=1}^n \sigma_i^2}$$

Greater amplitude or greater frequency during finger-tapping means faster finger movement, resulting in better performance. It is easier to execute the movement faster with smaller amplitude, the *amplitude \* frequency* of tapping is suggested as an appropriate parameter to characterise the speed. This feature, called *amxfr*, is determined for each tapping cycle and then averaged over the whole test.

The regularity of finger-tapping movement is characterised by calculating PM for each tapping finger. *The performance of a finger during the finger-tapping test is characterized by the product of the parameters expressing speed (amxfr) and regularity (PM)*. Having analysed more than 300 finger-tapping tests the Finger-Tapping Test Score [1] has been devised:

$$FTTS = (PM - 0.6) * amxfr.$$

Based on the scores of the fingers, scores can be calculated for the hands and for the person. One hand is characterised by adding up the results of the index-, middle- and ring fingers.

The pointing movement is characterized by the deviation from the pattern to be tracked (P1), the accuracy of touching the vertices and the centre point (P2, P3), the smoothness and speed of the movement (P1, P2, P3).

## III. RESULTS

### A. Finger-tapping

There are persons who need to perform the test several times to fully understand it and reach their normal result. This is called the *learning effect*. Fig. 5. shows the result of eight tests of parallel tapping during a two-week period for a young healthy female. From the third test on her results showed very low standard deviation. Fig. 6. shows the finger-tapping results of a stroke patient. The learning effect is present. The patient's standard deviation was much smaller for the affected (left) hand than for the other. During the first test the patient achieved better result with his affected hand! We can conclude that the finger-tapping test must be performed at least twice by a new subject before diagnostic information can be deduced from the results.

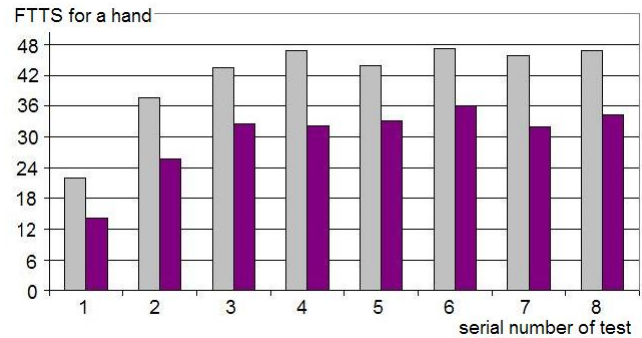


Fig. 5. FTTS scores for the parallel tapping hands of a young healthy subject during a 2-week period. Bright bars: left, dark bars: right hand.

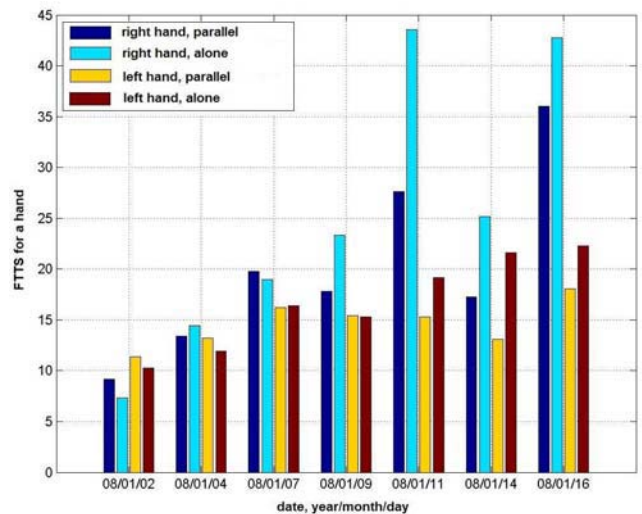


Fig. 6. FTTS scores for the hands of a stroke patient. Results of tapping with one hand only as well as together with both hands are shown.

The finger-tapping test is able to quantify how the movement of one hand influences the movement of the other hand. Tapping together with both hands (parallel tapping) is more sophisticated task than tapping with one hand only. Stroke patients achieved worse results with both hands during parallel tapping than during tapping with one hand alone. Fig. 6. shows seven sessions for a stroke patient.

During one session three movements were recorded: tapping alone with the affected side hand, tapping alone with the other hand and tapping together with both hands. After learning the movement the patient achieved better scores for both hands during tapping with one hand only.

### B. Pointing movements on a hexagon

The human image processing ability is excellent as far as still images are concerned and much less effective in evaluating movements. The pointing movement was carried out by both arms of each tested person. There were substantial differences between the affected side and the non-affected side. Trajectory of the sliding movement demonstrates the movement disorder and helps the evaluator assess it on a still image. The sliding movements of a stroke patient are demonstrated in Fig. 7. and 8., one sliding cycle is shown. The patient is a 50 year old male, 5 weeks after stroke, non-affected arm (left) is dominant, Rivermead motor assessment scale 13 for both arms. Barthel index was 45 at the time of test, in 6 weeks it improved to 95.

The vertical bars are proportional to the time the marker – and thus the index finger – spends at any given point. The movement slows down as the finger approaches a vertice. With the affected arm the movement from a vertice can also start slowly, see uppermost vertice in Figure 8. At different vertices the slowing down is also different. This is characteristic for a patient.

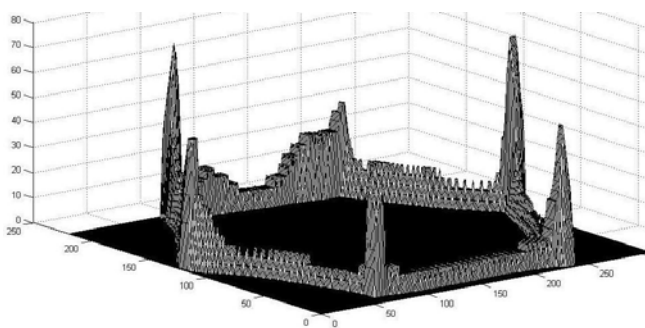


Fig. 7. Sliding along the hexagon, stroke patient, non-affected dominant arm.

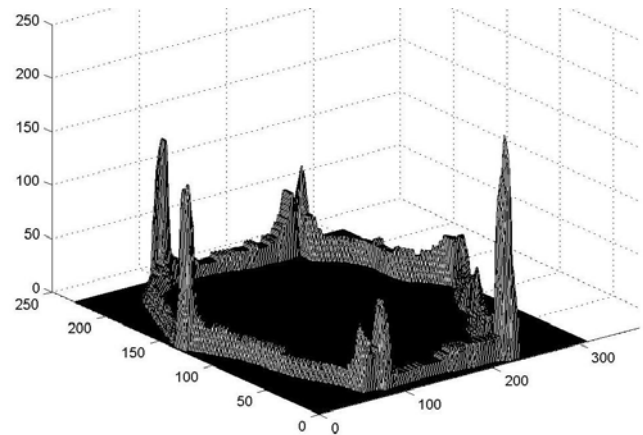


Fig. 8. Sliding along the hexagon, stroke patient, affected arm.

## IV. DISCUSSION

Objective evaluation of the movement of stroke patients gives diagnostic information. The finger-tapping and the pointing movements of the patients help assess their actual state.

## ACKNOWLEDGMENT

This study was supported by OTKA (Hungarian National Research Fund) project *Objective assessment of movement disorders* (T 049357, 2005- 2008).

## REFERENCES

1. Jobbágy Á, Harcos P, Karoly R, Fazekas G: Analysis of the Finger-Tapping Test. *Journal of Neuroscience Methods*, January 30, 2005. Vol 141/1, pp. 29-39.
2. Jobbágy Á, Hamar G: PAM: Passive Marker-based Analyzer to Test Patients with Neural Diseases. *Proc. of 26th Annual Conference of IEEE EMBS*, 1-5 Sept. 2004, San Francisco, CA USA, pp. 4751-4754.
3. Stokes V, Lanshammer H, Thorstenson A: Dominant Pattern Extraction from 3D Kinematic Data. *IEEE Tr. on BME*, 1999 January, pp. 100-106.

Author: Ákos Jobbágy  
 Institute: Budapest University of Technology and Economics  
 Street: Magyar Tudósok krt. 2.  
 City: Budapest  
 Country: Hungary  
 Email: jobbagy@mit.bme.hu

# Applying Consumer Technologies to Assistive Device Design

K. Kaneswaran and K. Arshak

Department of Electronic and Computer Engineering, University of Limerick, Limerick, Ireland

**Abstract** — Assistive Device Technology (ADT) helps people with disabilities to engage in everyday activities that might not otherwise be open to them. For people with severe paralysis or spinal injury ADT is a necessity, yet the cost associated with these technologies are still relatively high. In order to reduce these costs a mass – market consumer technology has been identified which can be applied to ADT and developed a new system for Electric Powered Wheelchairs which will allow a person with reduced mobility the capacity to control and navigate powered wheelchair systems using small finger movements. A prototype of the system has been developed and tested by able-bodied and disabled users.

**Keywords** — Rehabilitation, Capacitive Sensing, Assistive Devices, Joystick, Navigation.

## I. INTRODUCTION

Throughout history the application of technology has been used in ameliorating the problems of persons with disabilities. In the early 1890's the first hearing aid was patented [1]. Its major function the amplification of sound has not changed over the years but what has changed is the structure of these aids. Now they fit into the ear, amplify a wider range of sounds and are generally more effective. The same can be said for the joystick, designed in the early nineteen hundreds by the French pilot Robert Esnault-Pelterie [2] to control the equilibrium of airplanes. The electrical version was later used during World War II for guidance of anti-ship missile systems [3]. In recent times, the employment of joysticks has become common place in many industrial and manufacturing applications, such as; cranes, assembly lines, forestry equipment, mining trucks, and excavators. Specialist joysticks, classed as an assistive technology pointing device, are used to replace the computer mouse for people with fairly severe physical disabilities [4]. They are often useful to people with athetoid conditions, such as cerebral palsy, who find them easier to grasp than a standard mouse. Miniature joysticks are also available for people with conditions involving muscular weakness such as muscular dystrophy or motor neurone disease. They are also used on electric powered wheelchairs for control since they are simple and effective to use as a control method. The structure of the joystick has remained the same over the years, a lever on a pivotal base allowing us to control movement in the horizontal and vertical plane but due to recent technological advancements in areas of portable

electronics, the structure is now being replaced by newer contact and non-contact technologies such as capacitive controller systems. The successful integration of capacitive touch sensors into everyday consumer products such as MP3 players and mobile phones has caused consumer product development teams to reevaluate the use of capacitive sensor technology for improving the user interface and aesthetic look of their products. Mechanical switches are being replaced and restyled with highly reliable, attractive and cost effective capacitive interfaces. Although these new intuitive interfaces are designed for a mass portable device market their non mechanical nature may have more relevant use in Assistive Device Technology (ADT) for people with severe mobility conditions who do not possess the physical strength or dexterity to operate miniature joysticks. For this reason we have designed a capacitive interface which allows persons with muscular weakness the ability to navigate an electric wheelchair by small finger movements.

## II. DESIGN

### A. Rationale – choosing an Invacare based system

The Invacare Corporation is one of the world's leading manufacturers and distributors of health care products used in home. Today, Invacare has reached approximately \$1.5 billion in net sales and is the leading company in each of the following major, non-acute, medical equipment categories: power and manual wheelchairs, home care bed systems, and home oxygen system. Since many of the health care providers around the world mainly deal with Invacare products the prototype was designed around an Invacare wheelchair platform so that the finished product could reach the widest target audience.

### B. Prototype System Design

The prototype system comprised of Invacare's cruiser plus powered wheelchair, a touchpad controller which connects directly into the power supply module of the wheelchair and the touchpad. Invacare's products ranges are built around a proprietary communication channel known as the DX-Bus.

This is similar to the CAN Bus often found in vehicles. The DX-Bus allows connection of multiple input and output

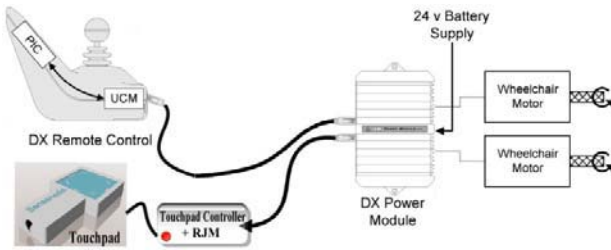


Fig.1 Prototype system

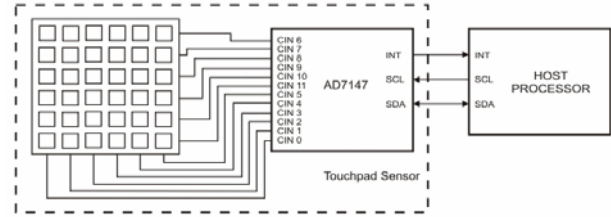


Fig. 2 AD7147 Connection Diagram

devices simultaneously to the Power Module (PM), fig.1. The power module (PM) regulates the power to these devices and also provides drive signals for the motors. As it is a proprietary product access to the DX-Bus is acquired by using a Remote Joystick Module (RJM). The RJM allows connection of an analog based joystick as a means of secondary remote while the wheelchair still retains its master joystick. The RJM can be purchased directly from Dynamic Controls Inc and support is provided for third party developers.

C. AD7147 based Touchpad Design

There are now several companies developing capacitive touch interface IC's, Analog Devices, Motorola, Cypress Semi-conductor and Quantum Technologies to name a few. Analog Devices have a range of capacitance to digital (CDC) converters suited for applications such as humidity, proximity, level, pressure and touch sensing. The AD7142/3/7 IC's are specifically designed for touch controller based systems but it is the unique features (Environmental calibration logic, single electrode systems for ultra thin portable applications, high resolution, on-chip self adjusting adaptive threshold and sensitivity algorithm) found in the AD7147 datasheet [5] which have led us to incorporate it in our prototype design. The AD7147 is mounted on a small PCB and connected to 12 rows of single layer electrodes. The configuration, fig.2, and a software algorithm contained in the firmware, running on the host microprocessor allow the detection of a user's finger in a 23 x 23mm area. The firmware is provided by Analog Devices for a range of 8051 based microprocessors royalty free which reduces coding time increasing time to market. The 23 x 23mm touchpad firmware requires 9.687 Kb of program memory and 545 bytes of RAM to implement the AD7147 register configuration, recalibration and touchpad algorithm on the host processor. It provides 199 positions on the x axis and 199 positions on the y axis. The position data is formatted in four 16 bit registers, table 1, which also contain commands useful for navigation of menu systems on a portable media device. Some of these commands are exploited for use in the navigation system as discussed later.

Table 1 ADI Register Descriptions

Bit	Register 0	Register 1	Register 2	Register 3
15	Active	Active	Not used	Not used
14	Tap		Not used	Not used
13	Go Left	Go Up	Not used	Not used
12	Go Right	Go Down	Not used	Not used
11	2 Fingers	2 Fingers	Not used	Not used
10	Large Finger	Large Finger	Not used	Not used
9	Touch error		Not used	Not used
8	Touch error		Not used	Not used
7	8 bit output*	8 bit output	8 bit output	8 bit output
6	-	-	-	-
5	-	-	-	-
4	-	-	-	-
3	-	-	-	-
2	-	-	-	-
1	-	-	-	-
0	Range 0-199	Range 0-199	0-127*	0-127*

\* The firmware can be edited to give a smaller resolution in the range of 50 to 199 positions on x and y axis, bits 7-0 gives a byte wide representation of this value. Register 0 and 1 are used for debugging in Labview while register 2 and 3 drive the DAC's.

The firmware also keeps track of environmental conditions such as change in temperature. This is useful as the algorithm can recalibrate sensor data when there is dirt or moisture on the sensors or when the temperature changes, causing sensor drift. This gives the touchpad system an advantage over other finger controllers such as VIC CCD finger controller [6] manufactured by HMC International. The algorithm also filters unwanted high amplitude noise on the sensor inputs and dynamically changes from interrupt to proximity detection mode to reduce power consumption when not in use.

D. Microprocessor selection for processing

There are several requirements for the host microprocessor system. In order to implement the analogue signals for the RJM the microprocessor must have some hardware means of generating analogue voltages. There must be enough code storage memory to implement the firmware for the AD7147, an I2C communication routine, debugging

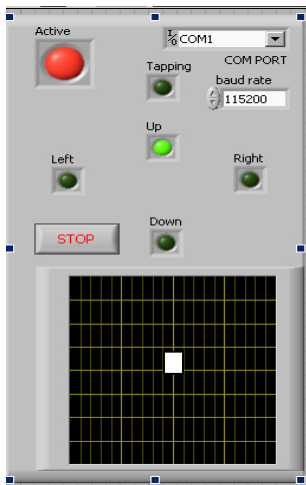


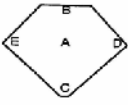
Fig. 3 Labview debugging of touchpad in real-time.

code and generation of the analogue voltages. The ADuC841 has the sufficient capacity to implement all these tasks. The dual on board 12 bit DAC's are set to 8 bit mode and are used to generate the voltage output. They are connected internally to the power rail of the system allowing a full voltage swing of 0 – 5V. An I<sup>2</sup>C driver allows communication from the microprocessor to the AD7147 thus requiring a further 726 bytes of code memory and 16 bytes of data memory taking advantage of the built in I<sup>2</sup>C hardware. The serial output port is used for debugging. Using the standard printf function calls in C, the values of ADIRegister 0 and 1 are transmitted to a PC running a Labview program, fig.3, which allows us to see the position of a user's finger on the pad in real time. The status bits up, down, left, right, active and tap are also displayed by the program. The up, down, left and right commands are activated when a user's finger reaches the extremities of the sensor pad, activating a scroll function to allow a user to scroll through a list box or menu system. The active and tap status show when the pad has detected a touch and whether or not the touch is an active movement or a tapping movement. The tap function can then be used to increment or decrement the profile function of the power wheelchair system as discussed in sub section E.

*E. RJM Module Specifications and use.*

The RJM allows any dual decode joystick to be connected directly to its input pins. The dual decode specification is outlined in table 2. The RJM also provides access to the DX Bus and the wheelchairs power supply providing up to 200mA regulated current. This provides sufficient power to run the microprocessor and the AD7147. Most wheelchairs come with several profiles programmed into the mas-

Table 2 Maximum input voltage levels for speed and direction on dual decode system with restrictor plate.

	Stick Position	V <sub>SPD</sub>	V <sub>DIR</sub>
	A	0°	0 ±.05
	B	17.5°	1.3 ±.06
	C	-20°	-1.5 ±.16
	D	20°	0 ±.17
	E	20°	0 ±.17

Voltage supply is 5V. All other voltages are with respect to 1/2 rail voltage.

ter joystick; this allows the user to change driving parameters for different surroundings. The RJM requires six control signals, power, ground, speed and direction, and speed and direction mirrors but will operate without the mirrors. The RJM has two pins which when toggled with a high pulse of 100ms duration increments or decrements the drive profile. These pins are used with the AD7147 tap output status. When a valid tap is detected on the lower/upper half of the touch pad we toggle the decrement/increment pins. Pull up resistors are used on the connections so that when the joystick power is recycled the pulse created does not increment or decrement the drive profile.

The output of the DAC's are buffered through op-amps and connected to a resistor network before connection to the RJM. The resistor network reduces the current input to the RJM and reduces the gain of the inputs. This is to keep the output range of a dual decode joystick between .5 and 4.5 volts.

*F. Software for positional information and DAC outputs*

The embedded firmware is assembled using the Keil µVision platform for C51 processors. The main loop in the code configures the DAC's to 8 bit asynchronous mode, configures serial port parameters and enables host external interrupt then sits in a while loop waiting for an interrupt. The routine services the interrupt by checking the status of the CDC values for all inputs, checking for high amplitude error signals, calculating absolute positions on the touchpad, and formatting the data into the four ADI Registers discussed earlier. This paper provides c-code required to implement the DAC output (1), profile down (2), serial output debugging (3), functions which require minimal code and data memory to implement. Once compiled the code is downloaded to the ADuC841 and is retained in the Flash EEPROM allowing the system to run as a standalone unit.

DAC output Example (1)

```

PLLCON = 0x00;           Ensures full clock speed 16.7Mhz
DACCON = 0xFF;          //DAC0 and 1 on 8-bit 0-VDD
DAC0L = 0x80;           //DAC0 mid scale
DAC1L = 0x80;           //DAC1 mid scale
    
```

```
//during the format position routine
ADIRegisters[2] = 0x1c+(XAxisPosition/ ScaledDownPositionRatioOnX);
ADIRegisters[3] = 0xE4-(YAxisPosition / ScaledDownPositionRatioOnY);
  if(TouchErrorOnX == 0){
  if(TouchErrorOnY == 0)
  {
  DAC0L = (unsigned char)ADIRegisters[3];//update dac
  DAC1L = (unsigned char)ADIRegisters[2];//update dac
  }
}
```

### Profile Down Example (2)

```
DPROFILE =0; //Down Profile pin is low.
if(TappingFlag==1) //Tapping flag computed by algorithm
{
  ADIRegisters[0] |= 0x4000;//Set tapping bit
  DPROFILE = 1;
  Wait(0xFFFF);
  DPROFILE = 0;
}
```

### Serial Debug Example (3)

```
printf("%04x%04x \n",ADIRegisters[0],ADIRegisters[1]);
```

## III. RESULTS

The touchpad signal on the left is converted to a drive signal on the right in each of fig. 4 and 5. The power supply module outputs a PWM signal with a duty cycle in proportion to the finger position on the pad. Each of the wheelchair joystick profiles has a max drive speed value which limits the output signal to the motors. In the both graphs we can see the full -24V to +24V swing. The system has been

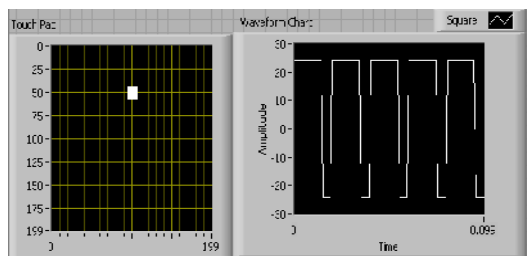


Fig. 4 PWM from motor with finger input position 100, 50.

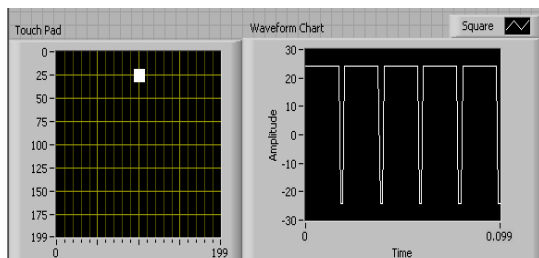


Fig. 5 PWM from motor with finger input position 100, 25.

tested with two end users who have successfully navigated an obstacle course but several user trials are envisaged in order to further evaluate the use of the assistive device as a replacement joystick.

## IV. CONCLUSION

The paper demonstrates how technology already available in many portable products can be used to improve accessibility and independence for persons with severe immobility.

The paper has identified a mass consumer technology that is easy to implement as an assistive device. Further improvements planned are to include Accelerometer and Electro Encephalogram (EEG) technologies into the touchpad system to implement an adaptive control algorithm to combat degenerative conditions.

## ACKNOWLEDGEMENTS

The authors would like to acknowledge and thank the following suppliers: Dynamic Europe Ltd, Stonebridge Cross Business Park, Droitwich, UK and Analog Devices, Raheen Industrial Estate, Limerick, Ireland. The authors would like to thank the Mid Western Health Board for the donation of the cruiser plus wheelchair platform. The authors would like to acknowledge Smile Rehab, UK for their valued consultancy. This research has been carried out under the Enterprise Ireland Commercialisation Fund.

## REFERENCES

1. Miltimore, A.E, "Magneto Telephone for Personal Wear", US Patent 466,725, Jan 05, 1892.
2. Zeller, T., "A Great Idea That's All in the Wrist", June 5, 2005, <http://www.nytimes.com/2005/06/05/weekinreview/05zeller.html?hp>
3. Kopp, C., "Dawn of the Smart Bomb", Air Power Australia, July 2006.
4. K.Arshak, D.Buckley, K. Kaneswaran, "Review of assisted devices for electric powered wheelchair navigation", pp13-23, Issue 13, May 2006.
5. Analog Devices AD7147 datasheet, pp 3 -25, September 2007, [http://www.analog.com/UploadedFiles/Data\\_Sheets/AD7147.pdf](http://www.analog.com/UploadedFiles/Data_Sheets/AD7147.pdf)
6. VIC CCD finger controller <http://www.hmc-products.com/fileadmin/PRODUCTS/InputDevices/0002-8001a-0201b.pdf>.

Author: Kelly Kaneswaran, Khalil ARshak  
 Institute: University of Limerick  
 City: Limerick  
 Country: Ireland  
 Email: [kelly.kaneswaran@ul.ie](mailto:kelly.kaneswaran@ul.ie), [khalil.arshak@ul.ie](mailto:khalil.arshak@ul.ie)

# Finite Element Analysis of Honeycomb-Core Foam on Shock-Absorbing Capability against Childhood Head Injury

C.Y. Lin<sup>1</sup>, L.T. Chang<sup>2</sup>, T.J. Huang<sup>3</sup>, K.H. Tsai<sup>4</sup>, C.S. Li<sup>5</sup> and G.L. Chang<sup>6</sup>

<sup>1</sup> Department of Pharmacy, Chia Nan University of Pharmacy and Science, Tainan, Taiwan

<sup>2</sup> Department of Childhood Education and Nursery, Chia Nan University of Pharmacy and Science, Tainan, Taiwan

<sup>3</sup> Department of Mechanical Engineering, National Cheng Kung University, Tainan, Taiwan,

<sup>4</sup> Graduate Institute of System Engineering, National University of Tainan, Tainan, Taiwan

<sup>5</sup> Department of Computer Science and Information Engineering, National University of Tainan, Tainan, Taiwan

<sup>6</sup> Institute of Biomedical Engineering, National Cheng Kung University, Tainan, Taiwan,

**Abstract** — This study developed a rubber foam model consisting of a surface layer of solid and a base layer of honeycomb core and used it to investigate head injury protective performance. An explicit finite element method based on the experimental data was used to simulate head impact on the rubber foam. The peak acceleration and head injury criterion (HIC) were employed to assess the shock-absorbing capability of the foam. This study supports the feasibility of using rubber foam with honeycomb core construction to improve shock-absorbing capability. The honeycomb-core structure provided an excellent cushioning effect via a lower axial shear stiffness of the surface layer and lower transverse shearing stiffness of the core. The core's dimensions were an important parameter in determining the shearing stiffness. The analysis suggested that the cushioning effect would significantly reduce the peak force on the head from a fall and delay the occurrence of the peak value during impact, resulting in a marked reduction in the peak acceleration and HIC values of the head.

**Keywords** — Head Injury, Impact, Protective Surfacing, Finite Element Analysis

## I. INTRODUCTION

Playgrounds are a fundamental part of the childhood experience. Equipment-related injuries, however, are a serious problem, with falls the most common cause of accidents [1-2]. A U.S. Consumer Product Safety Commission study found that 79% of equipment-related injuries involved playground falls [3]; specifically, 68% involved falls to the surface below the equipment. Among these equipment-related injuries, severe head injuries have the potential for serious long-term consequences or even death, with approximately two-thirds of mortalities involving a head injury [1-3]. To safeguard against falls, the need for protective surfacing around playground equipment to provide appropriate shock attenuation is generally emphasized.

Tiles made of rubber composite are widely used as a protective surfacing against head injury in playgrounds since they have good climate resistance and low maintenance costs.

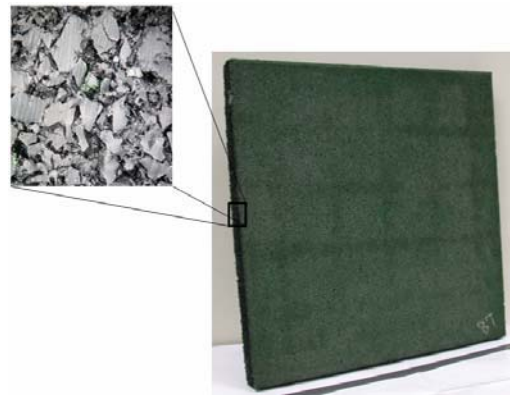


Fig. 1. A solid rubber tile with dimensions of 500×500×45 mm. Micrograph at 6.5× magnification shows the sponge-like structure of the matrix.

In general, these tiles are mainly made from rubber or recycled tires, which have been milled into shreds (length: 5~15 mm, width: 1~5 mm) or pellets and then mixed with resin to make tiles in a hot-press molding process (Fig. 1). Chang [4] established an experimental model for assessing the performance of rubber tiles, and showed that the shock-absorbing capability of tiles depended on the thickness and that a thickness less than 60 mm appeared to be insufficient for protection against falls from heights of more than 1.6 m.

The objectives of this research were to establish a finite element (FE) model of rubber tile based on shock-absorbing tests and to assess the protective performance of rubber tile against head injuries under honeycomb-core base construction.

## II. MATERIALS AND METHODS

### A. Finite element model

The FE model was established according to the standardize shock-attenuation test [5-6]. The model consisted of three components: 1) the headform; 2) the rubber tile;



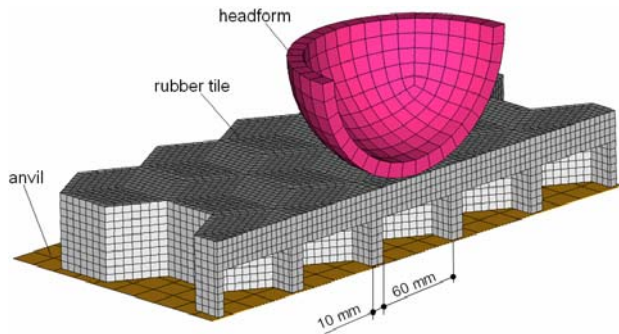


Fig. 2. Cross-sectional views of finite element mesh, a honeycomb core with ratio condition of 1:6.

and 3) the flat anvil. To enhance its shock-absorbing capability, the rubber tile model consisted of surface and base layers. The surface layer was solid with 20-mm thickness, and honeycomb-core constructions were employed in the base layer with 30-mm thickness. The magnesium alloy headform and the concrete anvil were assumed to be rigid bodies in the simulation; therefore, only one layer of elements was built for each structure. The headform and rubber tile consisted of eight-node solid elements, while the anvil consisted of four-node shell elements. The numbers of elements for each component were as follows: the rubber tile had 17440 elements, the headform had 300, and the anvil had 400. Contact elements were placed between the headform and the rubber tile, and between the rubber tile and anvil. The cross-sectional views of the mesh model are shown in Fig. 2. In order to investigate the influence of the honeycomb-core construction on head impact, we applied the explicit finite element code LS-DYNA for parametric analysis.

To evaluate the dynamic responses of the rubber tile, two drop heights of 1.8 m and 2.5 m (impact velocity of 6 m/s and 7 m/s, respectively) were employed. To reduce the computational time, the headform and rubber tile were placed very close to each other at the beginning of the simulation analysis. The drop height was produced by assigning an initial velocity to the headform. The peak acceleration on the headform and the head injury criterion (HIC) [7] were calculated to examine the protective performance of the tile against head injuries.

### B. Base structures

The honeycomb-core construction was employed in the base layer. The deformation of the plate in a honeycomb-core construction is caused by transverse shear force and can be characterized by the ratio of the diameter of the plate to the distance between two opposed plates [6] (Fig. 2). In this study, four ratio conditions were established in the

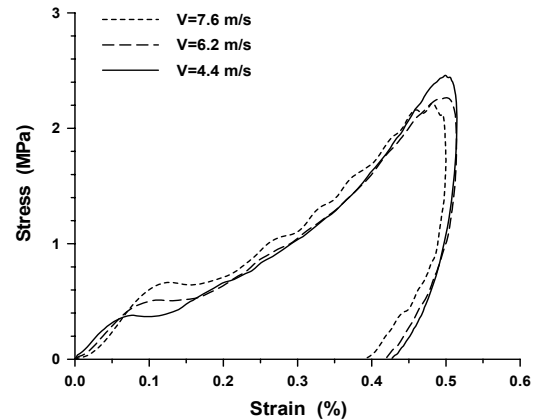


Fig. 3. Stress-strain curves of rubber-composite specimens (50×50×90 mm block) at impact velocities of 4.4, 6.2 and 7.6 m/s with impactor masses of 9.72, 4.86 and 3.24 kg, respectively.

honeycomb core, the ratio conditions of which were scaled by 1:3, 1:4, 1:5 and 1:6, respectively, with the latter representing the largest distance between two plates. To focus on the effects of the ratio condition, the diameters of all plates were adjusted to 10 mm.

### C. Material model

A micrograph of the rubber composite shown in Fig. 1 reveals its sponge-like structure. Analysis of the stress-strain curves of rubber-composite specimens revealed that the material is highly compressible (Fig. 3). Therefore, the constitutive model used for the rubber tile in DYNA was defined as “low density urethane foam”. This material required a curve of normal stress against strain to define its loading behavior (Fig. 3).

## III. RESULTS

The peak acceleration and HIC values of the headform at the drop height of 1.8 m (impact velocity of 6 m/s) are listed in Table 1. Even at this moderate drop height, peak acceleration and HIC values for the solid rubber tile with 50-mm thickness were up to 239 G and 2263, respectively (Table 1). They far exceeded the criteria of general protection standards [5,6]: 200 G for peak acceleration and 1000 for HIC. In the tile with honeycomb-core construction, when the ratio of the diameter of the plate to the distance between the two opposed plates increased, both indexes decreased. In general, HIC values were more sensitive to the ratio variation than the peak accelerations. The maximum variations of the peak acceleration and HIC values were 23% and 41%, respectively. At a drop height of 2.5 m (Table 2), both

Table 1. Peak acceleration (G) and HIC values of the headform at a drop height of 1.8 (impact velocity of 6 m/s)

Ratio*	Peak Acceleration				HIC			
	3:1	4:1	5:1	6:1	3:1	4:1	5:1	6:1
<b>Solid</b>	239				2263			
<b>Honeycomb</b>	204	185	177	166	1763	1496	1357	1247

\* The ratio of the diameter of the plate to the distance between two opposed plates

Table 2. Peak acceleration (G) and HIC values of the headform at a drop height of 2.5 m (impact velocity of 7 m/s)

Ratio*	Peak Acceleration				HIC			
	3:1	4:1	5:1	6:1	3:1	4:1	5:1	6:1
<b>Solid</b>	311				3903			
<b>Honeycomb</b>	269	235	222	204	3105	2180	1623	1334

evaluated indexes had a similar trend to those at the drop height of 1.8 m regardless of the ratio conditions. Among the ratio conditions, the maximum variations of the peak acceleration and HIC values were 32% and 133%, respectively.

#### IV. DISCUSSION

To evaluate the impact-absorbing properties of the protective surfacing around playground equipment necessary to prevent children's head injuries, standardized shock-attenuation tests [5,6] have been established in many countries. In these test procedures, a headform is used to strike the surfacing material, and the peak acceleration and HIC of the headform are determined. The critical height for a given surfacing is determined by peak acceleration and HIC values for the headform of less than 200 G and 1000, respectively. If a child falls from below this critical height, a life-threatening head injury would not be expected to occur. Hence, designers wishing to install protective surfacing around playground equipment should request the appropriate test data from the manufacturer, enabling them to design the installation so that the probable maximum fall height of children using the equipment does not exceed this critical value.

When the rubber tile base of 30 mm was replaced by the layer of honeycomb-core construction, the same tile thickness provided superior impact absorption in comparison to the solid variant (Table 1 and 2). Comparison of the tile with honeycomb-core base and solid constructions revealed that the maximum variations in peak acceleration and HIC values at the drop height of 1.8 m were 44% and 81%, respectively, and at 2.5 m increased to 52% and 193%, respectively. This was attributable to the excellent cushioning effect the honeycomb-core layer provided during impact. Inspection of the dynamic deformation of the tiles identified the following three mechanisms in the tiles with honeycomb-core constructions which absorbed the impact energy

in the loading process: 1) the axial bending deformation of the surface layer; 2) the transverse bending deformation of the plate in the base layer; and 3) the crushing of the plate in the base layer. These mechanisms reduced the peak acceleration of the headform and delayed the occurrence of the peak value (Fig. 4), thus markedly reducing both evaluated indexes of the headform. Both peak acceleration and HIC values decreased in the honeycomb-core construction as the ratio decreased (Table 1). This was attributed to the lower axial shear stiffness of the surface layer and lower transverse shearing stiffness of the core in the base layer under smaller ratio conditions. This effect considerably reduced the critical load, i.e. the force required to yield a bending deformation of the plate, and increased the headform displacement during impact (Fig. 5). Local buckling even occurred at interfaces between the surface layers and the plates of the honeycomb cores when the ratio conditions were less than 1:3. These findings support that when rubber tiles are used as a protective surfacing against head injury on playgrounds, a honeycomb-core construction in the base layer of the tile provides better shock-absorbing capability.

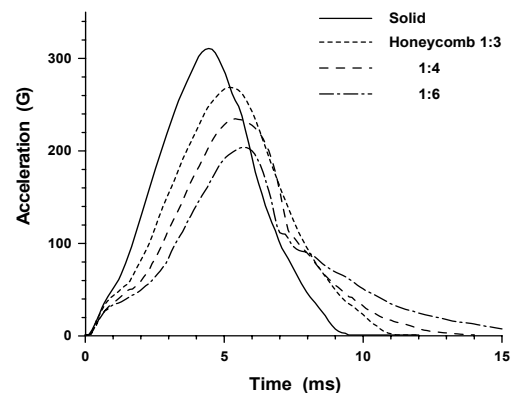


Fig. 4. Acceleration-time curve of the headform at the drop height of 2.5 m.

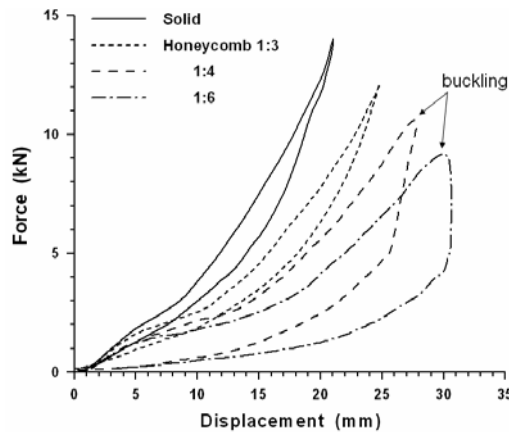


Fig. 5. Force-displacement curve of the headform with a honeycomb core at the drop height of 2.5 m.

The peak acceleration and HIC values for the solid rubber tile with 50-mm thickness at the drop height of 1.8 m far exceeded the criteria of general protection standards [5,6] (Table 1). Hence, Chang [4] suggested a solid rubber tile thickness of at least 60 mm for protective surfacing at playgrounds as the probable maximum fall heights are over 1.6 m. However, in this study, impact simulation at the drop height of 1.8 m showed that peak acceleration values were less than 200 G and HIC values exceeded slightly the criterion of 1000 when tiles with 50-mm thickness, 30-mm thickness honeycomb-core construction and a ratio condition less than 1:3 were employed. These findings indicate that with a critical height of over 1.8 m it may be possible to design a suitable rubber tile with 60-mm thickness.

## V. CONCLUSIONS

A rubber tile with plate-cell construction may be a suitable method for enhancing shock-absorption during head impact. In this study, the honeycomb-core construction provided an excellent cushioning effect due to the lower

axial shear stiffness of the surface layer and lower transverse shearing stiffness of the core. The core's dimensions were an important parameter in determining the shearing stiffness. In our simulations, the cushioning effect reduced the peak force to the head and delayed the occurrence of the peak value during impact, which markedly reduced the peak accelerations and HIC values.

## ACKNOWLEDGMENT

This study was supported by the National Science Council of the Republic of China (NSC-94-2213-E-041-002).

## REFERENCES

- Gallagher S, Finison K, Guyer B et al. (1984) The Incidence of Injuries among 87000 Massachusetts Children and Adolescents: Results of the 1980-81 Statewide Childhood Injury Prevention Program Surveillance System. *American Journal of Public Health* 74:1340-1347
- Rece R and Sege R (2000) Childhood Head Injuries: Accidental or Inflicted? *Archives of Pediatrics and Adolescent Medicine* 154:11-15
- Tinsworth D and McDonald J (2001) Injuries and Deaths Associated with Children's Playground Equipment. U.S. Consumer Product Safety Commission, Washington
- Chang LT, Tsai KH and Shiau JS (2004) Experimental Evaluation of the Impact-Absorption Properties of Rubber Tiles for the Playground. *Biomedical Engineering – Applications, Basis and Communications* 16:244-250.
- F 1292 (2004) Standard Specification for Impact Attenuation of Surface Systems under Around Playground Equipment, American Society for Testing and Materials, Pennsylvania, USA
- EN 1177 (2004) Impact Absorbing Playground Surfacing – Safety Requirement and Test Methods, British Standard Institution
- Versace J (1971) A Review of the Severity Index. Proceedings of 15<sup>th</sup> Stapp Car Crash Conference, New York
- Kollar L and Dulacska E (1984) Buckling of Shells for Engineers. John Wiley & Sons, New York

Author: Li-Tung Chang

Institute: Department of Childhood Education and Nursery, Chia Nan University of Pharmacy and Science

Street: 60 Erh-Jen Road, Section 1, Jen Te

City: Tainan

Country: Taiwan

Email: tchang@mail.chna.edu.tw

# Results of Reciprocal Orthosis System with Kinematic Interdependence used in Children with Children Cerebral Paralysis and Spinal Patients

V. Mihnovich, E. Dukendjiev

Atypical prosthetics laboratory Ltd.

**Abstract** — The paper is dedicated to the research in recovering the motional skills of patients using reciprocal orthosis system with kinematic interdependence, developed according to the method of reciprocal control by E. Dukendjiev. The reciprocal orthosis system with kinematic interdependence defines the picture of movements during a step cycle taking into account kinematic interdependence between large joints of a human body.

**Keywords** — reciprocal, orthosis, spinal, cerebral, paralysis.

## I. INTRODUCTION

There are neither investigations performed in restoration of the movements' ability in patients with the help of reciprocal orthosis systems (ROS) [1] including with kinematics interdependence between large lower extremity joints, nor certain methodology established for use. Results from long-term clinical studies are not available. It is necessary to develop passive measuring ROS [2], enabling to define an image of movements and interaction between all parts of the body in a certain time interval of a double step.

Such investigations enable to set administration and methodology for the ROS use, as well as to create more complete constructions of the ROS.

## II. METHOD

For evaluation of the results of using the reciprocal orthosis systems with kinematic interdependence (ROSKI), including use of the reciprocal electrostimulation of muscles (RESM) [3], a regular follow-up (once in two months) of the patients using ROSKI at home is carried out in the course of one year. A follow-up of 10 patients at the age from 1,5 to 10 years old having the following diseases: spina bifida, paraparesis, children cerebral paralysis, hydrocephalia, multiple inherent maldevelopment, arthrogriposis is carried out. 52 biomechanical parameters are registered: 7 linear and 11 circular antropometric measures, 12 electromyographic measurements, and 13 functionality parameters. Preliminary analysis of patient's protocols showed that there exist correlation between certain parameters in 72% of cases and correlation coefficient is 0,76. Therefore several

parameters for analysis from different groups were chosen (Table 1). Analysis was performed by evaluating the function of linear regression ( $Y=b+m*X$ ), where  $Y$  – linear function, characterizing the change of the present parameter,  $b$  – value of parameter at the first measurement, but evaluation of chosen parameter changes by the value of coef.  $m$  – with entrance time interval  $X$  (positive value  $m$  is evidence of improvement according to the present parameter). Characteristics of regression statistics by at each chosen parameter were evaluated:  $m$  – coef. corresponding to each independent changeable  $x$ ,  $s$  – standard error values for coef.  $m$ ,  $R^2$  – determination coef. Patients were divided into groups by following parameters: age, the main diagnosis, kind of the used ROS (Table 2).

Table 1. Choosing the follow-up's parameters for analysis

Group		Follow-ups' parameters
Circular measures	anthropometric	Circular measure of thigh
Linear measures	anthropometric	Shank length
Electromyographic measurements		Electrical activity of biceps muscle of thigh
Functionality parameters (ability to self-dependent movements)		Standing with support Standing at the table Walking with support and help for leg movement Walking with support Walking without assistance

Table 2. The follow-ups' and characteristics' results of regressive statistics of electrical activity of biceps muscle of thigh

Patient	1	2	3	4	5	6	7	8	9	10
Follow-up period in months	0	25	25	25	25	25	25	30	25	30
	2	25	30	25	30	25	25	30	30	30
	4	30	30	25	30	25	40	30	35	30
	6	30	35	30	30	30	45	30	50	30
	8	35	40	30	35	30	50	30	45	
	10	50	45	30						
	12	45		35						
<b>m</b>	<b>2,05</b>	<b>1,93</b>	<b>0,80</b>	<b>1,00</b>	<b>0,75</b>	<b>3,50</b>	<b>0,75</b>	<b>2,50</b>	<b>0,75</b>	<b>0,00</b>
<b>s</b>	0,42	0,19	0,16	0,29	0,25	0,58	0,25	0,82	0,43	0,00
<b>R<sup>2</sup></b>	0,83	0,96	0,84	0,80	0,75	0,93	0,75	0,76	0,60	1,00

Table 3. The values of coefficients m for various groups of patients

Parameter	Age groups		ROSKI types		The main diagnosis groups					
	Up to 5 years	Up to 10 years	ROSKI with RESM	ROSKI without RESM	Spina bifida	Paraparesis	Children cerebral I paralysis	Hydrocephalia	Multiple inherent maldevelopment	Arthrogriposis
Circular measure of thigh	0.234	0.071	0.192	0.113	0.232	0.093	0.118	-0.100	0.175	0.375
Shank length	0.0921	0.196	0.060	0.196	0.051	0.021	0.0411	0.050	0.050	0.000
Electrical activity of biceps muscle of thigh	1.013	1.664	2.494	0.936	2.054	1.929	1.311	1.000	2.500	0.000
Standing with support	1.676	0.988	1.193	1.294	1.607	1.571	0.591	0.000	2.750	3.750
Standing at the table	1.250	0.528	0.673	0.879	0.446	1.571	0.200	0.150	1.250	3.750
Walking with support and help for leg movement	0.467	1.103	1.089	0.745	1.375	1.643	0.713	1.250	0.650	0.000
Walking with support	0.475	0.960	1.120	0.615	0.768	1.643	0.920	0.000	0.650	0.000
Walking without assistance	0.188	0.221	0.443	0.107	0.000	1.329	0.000	0.000	0.000	0.750
<b>The average value according to all parameters</b>	<b>0.674</b>	<b>0.716</b>	<b>0.908</b>	<b>0.611</b>	<b>0.817</b>	<b>1.225</b>	<b>0.487</b>	<b>0.294</b>	<b>1.003</b>	<b>1.078</b>

### III. RESULTS

1. More intense development of circular body measures (Table 3), characterising the volume of the muscle mass, as well as standing function is found in patients from the first age group (up to 5 years).
2. More extensive linear body measures, electrical muscle activity that is related to muscle strength as well as significant improvement of walking skill learning are significantly increased.
3. Patients using ROSKI with RESM are showing better results in walking and electrical muscle activity parameters. The best result in comparison with cases without RESM was registered also by the average value.
4. The lowest results within the disease groups were found in groups of patients of hydrocephalia and children cerebral paralysis.

### IV. DISCUSSION

1. Antropometric data are showing increased patient body growth and total mass of patients. Decreased volume can be observed in some cases that is related to significantly increased physical load during exercises.
2. Significant increase of electrical muscle activity is observed in patients using ROSKI.
3. Following functional parameter changes are observed within the first and second months: increased muscle tone, improved trophics, vision, speech, appetite, that is related to verticalisation of the body, increased physical load as well

as with the fact that the child is aware of new possibilities of development. Supportive ability is increased during standing, skills of leg cyclic movements with ROSKI and without it are developing during walking within the time period of the second to the fourth month.

### V. CONCLUSION

Treatment by method of Dukendjiev is effective due to appearing of new functional condition, opening capabilities of faster motoric development of a child.

### REFERENCES

1. Dukendjiev E. Paņēmiens cilvēka kustību recīprokālā vadībai un recīprokālā ortožu sistēma visam ķermenim. Latvija. Patent Nr. LV 13100 B.
2. Michnovich, V. "Passive Exoskeleton Measurement System for Study and Correction of Movements". Medical & Biological Engineering & Computing. Vol.37, Supplement 1. Tallinn, 1999.
3. Dukendjiev E, Mihnovich V. New Approach to the Synthesis of Orthosis Systems for Spinal Patients. The 11<sup>th</sup> World Congress of the International Society for Prosthetics & Orthotics August 1-6, 2004, Hong Kong.

Author: Viktor Mihnovich  
 Institute: Atypical prosthetics laboratory Ltd.  
 Street: Pilsonu Street 13/30  
 City: Riga LV-1002  
 Country: Latvia  
 Email: viktor-m@inbox.lv

# Colorimetric Plantographic Diagnostics of Foot Pathology on the Footprint in Static and Dynamics

T. Ogurtsova<sup>1</sup>, E. Dukendjiev<sup>1</sup>

<sup>1</sup>Atypical Prosthesis Laboratory Latvia, Riga, e-mail: apl@stradini.lv

**Abstract** — The present paper reveals correlation between metrics (interaxial distances etc.) and kinematics (angles and dimensional interplacement) parameters of the support-movement apparatus and the plane foot print.

**Keywords** — foot imprints, analysis, walking.

## I. INTRODUCTION

An effective diagnostics is discussed without high requirements to specific knowledge in the sphere of foot with the help of equipment developed by the author VIDEOICHTNOGRAPH DEOT-1 (glass track on which a subject is walking and mobile video cameras connected to the computer and printer).

The objective of work:

1. To analyze condition of support-movement apparatus by foot sprints in dynamics process (during walking), including for people with amputation of one of lower extremities.
2. To work out the method for analysis of condition of support-movement apparatus by foot sprints in dynamics process.
3. To reveal correlation between metrics and kinematics of support-movement apparatus structure and planar foot print.

## II. METHOD

Three-dimensional supporting device is analyzed according to two-dimensional image with the help of space and color at the foot contact with the supporting surface while walking.

The plantogram divides the hind foot, midfoot and fore-foot, it contains beams along which a load is delivered to each toe while walking. A peculiar system of axes is created and when a foot print is placed therein an abnormality is observed.

The correlation of spaces of separate foot parts in [%] to the space of the whole foot is a factor specifying the type of abnormality.

The color of foot skin as the reaction on the load is a factor which is reflected in a color scale.

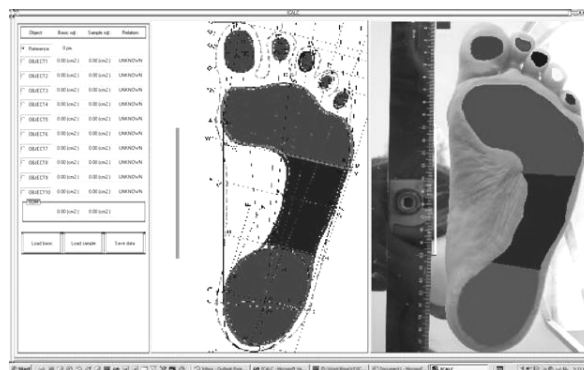


Fig. 1. Program at work

The automatic processing of digital pictures is performed with the program developed by the author - Image Calculator (ICALC), which calculates and presents the report in the file on the foot space (vertical projection contour) and the space of the supporting spot of the foot, as well as the percentage correlation of the separate parts of the plantogram.

## III. RESULTS

The coefficient  $K_2$ , which specifies the correlation of foot parts

Table 1.  $K_2 = l_{V1V2} / l_{V1+V1} = 0,47 \pm 0,02$  within the norm

Value $K_2$	Diagnosis
$K_2 = 0,46 \div 0,48$	Norm
$K_2 > 0,48$	Flat foot
$K_2 < 0,46$	Hollow foot

Table 2. (1) Valuation of condition of rear foot part  $\angle HC_2K$

Value $\angle HC_2U^*$	Diagnosis
$\angle HC_2K = 5^\circ$	Norm
$\angle HC_2K > 5^\circ$	Taliped foot
$\angle HC_2K < 5^\circ$	Flat foot

Table 3. (2) Valuation of condition of toes

Angle values	Diagnosis		
	= [°]	< [°]	> [°]
$\angle P_1*OP_5^* = 22^\circ$	Norm		
$\angle P_1*OP_2^* = 8^\circ$	Norm	<i>Hallux valgus</i>	<i>Spreading</i>
$\angle P_1*OP_3^* = 6^\circ$	Norm	<i>Hallux rigidus</i>	
$\angle P_1*OP_4^* = 5^\circ$	Norm	<i>Hallux rigidus</i>	
$\angle P_1*OP_5^* = 4^\circ$	Norm	<i>Hallux rigidus</i>	

Table 4. (3) Space of toes in % to the whole foot print

Value $f_i$ within the norm	Diagnosis		
	<i>Varus legs</i>	<i>Valgus legs</i>	<i>Hallux valgus</i> <i>Hallux rigidus</i>
$f_1 = 4.67\%$	$< f_1$	$> f_1$	$\gg f_1$
$f_2 = 1.31\%$	$< f_2$	$> f_2$	$< f_2$
$f_3 = 1.09\%$	$< f_3$	$> f_3$	$< f_3$
$f_4 = 0.83\%$	$< f_4$	$> f_4$	$< f_4$
$f_5 = 0.79\%$	$< f_5$	$> f_5$	$< f_5$
$\Sigma f_i =$ F1=8.69%			

Table 5.(4) Space of foot and dimensional position of a leg

Value $F_i$ within the norm	Diagnosis		
	<i>Varus legs</i>	<i>Valgus legs</i>	<i>Hallux valgus</i>
F1=8.69 %	$< F1$	$> F1$	$> F1$
F2= 37.5 %	$< F2$	$> F2$	$< F2$
F3= 23.6 %	$< F3$	$> F3$	$< F3$
F4= 31.21 %	$< F4$	$> F4$	$< F4$

Table 6. (5) Footprint spaces in percents

F1 = 0%	F1 = 0%	F1 = 10 %
F2 = 0%	F2 = 22%	F2 = 41%
F3 = 0%	F3 = 0%	F3 = 52%
<u>F4 = 25%</u>	<u>F4 = 0%</u>	<u>F4 = 35%</u>
$\Sigma 25\%$	$\Sigma 22\%$	$\Sigma 138\%$
<i>Pes calcaneus</i>	<i>Pes equinus</i>	<i>Pes planus</i>
F1 = 0%	F1 = 8%	F1 = 7%
F2 = 0%	F2 = 40 %	F2 = 38%
F3 = 32%	F3 = 30 %	F3 = 0 %
<u>F4 = 0%</u>	<u>F4 = 35%</u>	<u>F4 = 35%</u>
$\Sigma 32\%$	$\Sigma 113\%$	$\Sigma 80\%$
<i>Pes ecinovarus</i>	<i>Hallux valgus</i>	<i>Pes cavus</i>

Foot prints which are typical for the most frequently occurred foot abnormalities are analyzed.

#### IV. DISCUSSION

Combined deformations are observed more frequently: pes cavus-adductus-varus, pes planus-valgus-abductus, pes cavus-valgus, pes cavus-transversoplanus. Hallux valgus is usually combined with transverse flat foot (pes transversoplanus); as well as with the presentation of the forefoot (hallux varus; metatarsus varus)

#### V. CONCLUSIONS

It is marked, that the aims laid down in work are reached completely.

1. The condition of support – movement apparatus is analyzed by foot prints in dynamic process (during walking).
2. The method is developed for the analysis of condition of the support – movement apparatus by foot prints in dynamic process.
3. The correlation between the metrics and kinematics of structure of support – movement apparatus and plane prints of foot is revealed.

The diagnostics offered excludes the factor of subjectivity when analyzing foot condition and decreases the time for the examination of a patient.

#### REFERENCES

1. E. Dukendjiev, T. Ogurtsova. Planar geometry of imprints as the reflection of the structure and condition of locomotive system. 13th Nordic-Baltic Conference on Biomedical Engineering & Medical Physics June 13 - 17, 2005, Umeå, Sweden
2. T. Ogurtsova Начальный статистический анализ состояния опорного аппарата детей и школьников Латвии. International Conference on Bionics Prosthetics, Biomechanics and Mechanics, mechatronics and robotics. June 5 -6, 2006 Varna, Bulgaria.
3. E. Dukendjiev, T. Ogurtsova. Examination of Feet During Walking and Synthesis of Bionical Insoles The 11<sup>th</sup> World Congress of the International Society for Prosthetics & Orthotics August 1-6, 2004, China, Hong Kong
4. E. Dukendjiev, T. Ogurtsova. Express method for evaluation of the results of prosthetics and orthotics. 12th Nordic Baltic Conference on Biomedical Engineering and Medical Physics. June 18<sup>th</sup>-22<sup>nd</sup>, 2002 in Reykjavik, Iceland.

Author: Tatjana Ogurtsova, Evgueni Dukendjiev  
 Institute: Atypical Prosthesis Laboratory  
 Street: 13/30 Pilsonu Street  
 City: Riga  
 Country: Latvia,  
 Email: e-mail: apl@stradini.lv

# Biomechanical Properties of Glutaraldehyde Treated Human Pericardium

V. Ozolins, I. Ozolanta, L. Smits, A. Lacis, V. Kasyanov

Riga Stradins University, Riga, Latvia

**Abstract** — Autologous pericardium, for repair of congenital heart defects, can be used in its fresh non-treated state, or after chemical fixation with glutaraldehyde solution as a biomaterial for surgical repair of congenital heart anomalies. The aim of this experimental study is to investigate changes of biomechanical properties and resistance to proteolytic degradation of human pericardium, after harvesting with glutaraldehyde solution.

After taken out of a pericardium from anterior part of pericardial sac at the time of operation it was fixed with 0.2% solution of glutaraldehyde for 6 minutes.

Some glutaraldehyde treated and untreated samples were incubated in collagenase solution ( $100 \text{ Uml}^{-1}$ ) for 2 hours at  $37^\circ\text{C}$  and proteolytic effect was estimated with gravimetric method. For investigation of biomechanical properties uniaxial tensile tests were performed with testing machine Zwick-Roell Z010. There were set up 18 pieces of fresh human pericardium and 11 pieces of glutaraldehyde-treated human pericardium.

There is difference ( $p < 0.05$ ) of ultimate strain ( $\epsilon_{\max}$ ) between fresh pericardium  $\epsilon_{\max} = 0.119 \pm 0.037$  and glutaraldehyde treated human pericardium  $\epsilon_{\max} = 0.098 \pm 0.015$ , respectively. There is difference ( $p < 0.05$ ) of ultimate stress ( $\sigma_{\max}$ ) between non-treated pericardium  $\sigma_{\max} = 3.14 \pm 0.70 \text{ MPa}$  and glutaraldehyde treated human pericardium  $\sigma_{\max} = 6.20 \pm 1.47 \text{ MPa}$ . There is difference ( $p < 0.05$ ) of tangential modulus of elasticity ( $E$ ) between non-treated and glutaraldehyde treated human pericardium:  $98.67 \pm 20.75 \text{ MPa}$  and  $50.25 \pm 16.04 \text{ MPa}$ , respectively. Gravimetric data demonstrated that glutaraldehyde treatment resulted in statistically significant improvement in resistance of human pericardium to proteolytic degradation.

Material became stiffer and stronger after treatment with glutaraldehyde solution as well as more resistant to proteolytic degradation than non-treated one.

These biomechanical differences could be explained by formation of collagen crosslink after glutaraldehyde treatment. We conclude that treating with glutaraldehyde improve the application of autologous human pericardium as the plastic material for surgical repair of congenital heart anomalies by improving its biomechanical properties and increasing resistance to proteolytic degradation.

**Keywords** — Autologous pericardium, glutaraldehyde, biomechanical properties, proteolytic degradation, congenital heart defect

## I. INTRODUCTION

Pericardium is commonly used for repair of congenital heart defects worldwide for a long time [1]. Autologous

pericardium is one of the most useful materials for application as a patch or baffle [2]. There are wide range of other biomaterials used in congenital heart surgery – xenografts, homografts, synthetic and tissue engineering [3] patches and prosthesis.[4] Pericardium is excellent substitute for the atrial and ventricular septa, the aortic and ventricular walls, but not for a free atrial wall. The feasibility and the results of valvuloplasty with glutaraldehyde-treated autologous pericardium remain largely unknown [5],[1],[6]. It has several advantages including the fact that it is immediately available, sterile, non-immunoreactive and free. Autologous pericardium can be used in its fresh state, either pedicled or as a free graft, or it can be used as a free graft after fixation with glutaraldehyde. Whether fixed or unfixed pericardium has the important advantage that there is minimal bleeding through suture holes. The important argument for choose of the plastic material is influence of pressure. [7],[8]

Treatment of autologous human pericardium with glutaraldehyde at the time of operation is well-known method in congenital heart surgery [9],[10],[11], but there are not many studies about changes of biomechanical properties of human pericardium[12] after tanning with glutaraldehyde. There are controversial opinions between surgeons about using of chemical harvesting of pericardium. There is evidence-based methodology for bovine [13] and equine pericardium but not for autologous human pericardium.

Our experimental study was performed in biomechanical laboratory with previous experience on small size biomaterials. [14] The aim of this experimental study is to determine differences of biomechanical properties and resistance to proteolytic degradation of human pericardium after harvesting and treatment with glutaraldehyde.

## II. MATERIALS AND METHODS

The protocol of the study was approved by ethics committee on University Children's Hospital. Experimental studies of biomechanical properties was performed on human autologous pericardium, that was prepared as plastic material for closure of various congenital heart defects at the time of operation, but not used for various reasons. The removal of pericardium and tanning with glutaraldehyde was performed according to protocol used in Clinic of Pediatric Cardiology and Cardiac surgery, University Children's



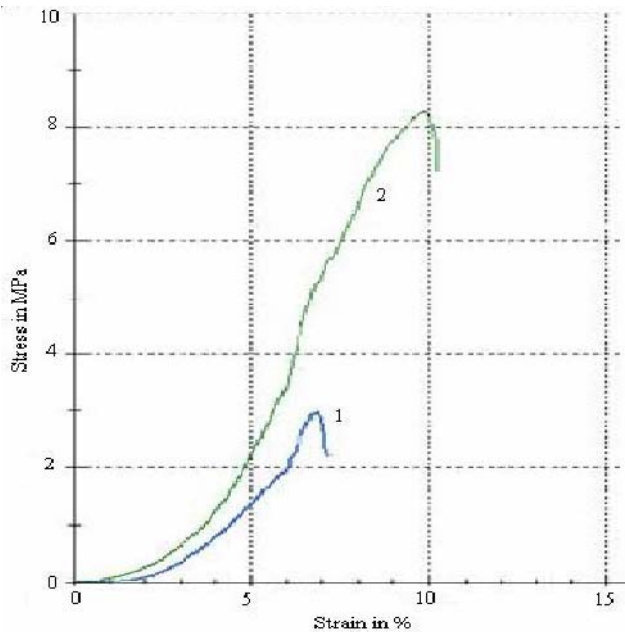


Fig. 1 Comparison of biomechanical properties between untanned and glutaraldehyde-treated human pericardium: Curve nr. 1 Fresh human pericardium; Curve nr. 2 Glutaraldehyde-treated human pericardium

Hospital. After taken out pericardium was fixed with 0.2% solution of glutaraldehyde for 6 minutes. Explored pericardium were stored in physiological sodium chloride solution at temperature  $+16 \pm 1^\circ\text{C}$  maximum for 12 hours. There were set up 18 pieces of fresh human pericardium and 11 pieces of glutaraldehyde-treated human pericardium for examination of biomechanical properties. Ten glutaraldehyde treated and untreated samples were incubated in collagenase solution ( $100 \text{ Uml}^{-1}$ ) for 2 hours at  $37^\circ\text{C}$  and proteolytic effect was estimated with gravimetric method. All samples were prepared with same width - 3.5 mm. Thickness of the samples of pericardium was measured with cathetometer KM-6 LOMO, Russia. The precision of measurements is  $\pm 0.005 \text{ mm}$ .

For investigation of biomechanical properties of human pericardium uniaxial tensile tests with computerized testing machine Zwick-Roell Z010 and data processing software package Testexpert 11.02, Zwick-Roell were used. Experimental data were analyzed with statistical method using built in MS Excel statistical function. For pair wise comparisons, Student t - tests were used to determine significance in differences between group means. Statistically different pairs were defined as having  $p < 0.05$ .

### III. RESULTS

Experimental data show, that there is statistically significant difference ( $p < 0.05$ ) of ultimate strain ( $\epsilon_{\text{max}}$ ) between fresh pericardium  $\epsilon_{\text{max}} = 0.110 \pm 0.037$  and glutaraldehyde treated human pericardium  $\epsilon_{\text{max}} = 0.098 \pm 0.015$ . There is statistically significant difference ( $p < 0.05$ ) of ultimate stress ( $\sigma_{\text{max}}$ ) between untanned pericardium  $\sigma_{\text{max}} = 3.14 \pm 0.70 \text{ Mpa}$  and glutaraldehyde treated human pericardium  $\sigma_{\text{max}} = 6.20 \pm 1.47 \text{ Mpa}$ . There is statistically significant difference ( $p < 0.05$ ) of modulus of elasticity (E) between untanned and glutaraldehyde treated human pericardium. For fresh pericardium  $E = 98.67 \pm 20.75 \text{ Mpa}$ . For glutaraldehyde treated human pericardium  $E = 50.25 \pm 16.04 \text{ Mpa}$ . There is no statistically significant difference ( $p > 0.05$ ) of thickness and cross - section square value between treated and fresh samples. Gravimetric data demonstrated that glutaraldehyde treatment resulted in statistically significant improvement in resistance of human pericardium to proteolytic degradation.

### IV. DISCUSSION

Using of maximal strain, maximal stress values and modulus of elasticity at strain level of 30% is appropriate way to determine and describe biomechanical properties of biomaterials. This experimental study certainly shows improvement of properties of human pericardium after treatment with glutaraldehyde from biomechanical point of view. The base of these biomechanical differences we found in literature - there is collagen crosslink formation after harvesting thereby is changed extracellular carcass of tissue.[9],[15] Influence of different concentration and exposition time of glutaraldehyde on human pericardium needs further investigation.[9],[16],[17],[18],[19] Other question is durability of implanted patches. Calcification [13],[20] is described in all xenotransplants and possible influence of glutaraldehyde[21] is meant. Human autologous pericardium has advantage when compared with xenopericardium because of lower rate of calcification. One of the most important basic principles of surgery for congenital heart disease is that operation should be designed to incorporate growth potential. This is still open for discussion. From one point of view, the pericardium cells are killed by glutaraldehyde and there is no growth potential. From other point of view the extracellular matrix is steel autologous and can potentially encourage growth. [22] There are different methods of detoxification process for glutaraldehyde-treated pericardium.[18]

## V. CONCLUSIONS

We conclude that human pericardium becomes harder and stronger, and more resistant to proteolytic degradation with statistical significance after tanning with glutaraldehyde (according to protocol used in Clinic of Pediatric Cardiology and Cardiac surgery of University Children's Hospital). These properties improve the application of autologous human pericardium as the plastic material in closure of congenital heart defects especially when there is relevant pressure effect. The treatment of autologous human pericardium with glutaraldehyde improves surgical administration (cutting, penetration with needle, shaping). The treatment of human pericardium with glutaraldehyde in congenital heart surgery is advisable from biomechanical point of view.

## REFERENCES

- Paez, J. M. G. and E. Jorge-Herrero. (1999) Assessment of Pericardium in Cardiac Bioprostheses: A Review. *J Biomater Appl* 13:351-388.
- Humphrey, J. D., R. K. Strumpf, and F. C. Yin. (1990) Biaxial mechanical behavior of excised ventricular epicardium. *Am J Physiol Heart Circ Physiol* 259:H101-H108.
- Yang, C., R. Sodian, P. Fu, C. Luders, T. Lemke, J. Du, M. Hubler, Y. Weng, R. Meyer, and R. Hetzer. (2006) In Vitro Fabrication of a Tissue Engineered Human Cardiovascular Patch for Future Use in Cardiovascular Surgery. *Ann. Thorac. Surg.* 81:57-63.
- Rubino, M., A. M. Hamad, F. Rea, and G. Gerosa. (2007) Reconstruction of the right atrium with pulmonary artery homograft after resection of right atrial lipomatosis. *Interact CardioVasc Thorac Surg* 15:359-381.
- Ng, C. K., J. Nesser, C. Punzengruber, O. Pachinger, J. Auer, H. Franke, and P. Hartl. (2001) Valvuloplasty with glutaraldehyde - treated autologous pericardium in patients with complex mitral valve pathology. *Ann. Thorac. Surg.* 71:78-85.
- Sharma, C. P. (2001) Blood-Compatible Materials: A Perspective. *J Biomater Appl* 15:359-381.
- Butera G, A. Y. B. D. B. P. (2001) Aneurysmal dilation of a pericardial patch prepared with glutaraldehyde and used for closure of a ventricular septal defect. *Italian Heart Journal* 2 : 317-318 .
- Kawashima, Y., S. Nakano, M. Kato, M. Danno, and K. Sato. (1974) Fate of pericardium utilized for the closure of ventricular septal defect. Postoperative ventricular septal aneurysm. *J. Thorac. Cardiovasc. Surg.* 68:209-218.
- Connolly, J. M., I. Alferiev, J. N. Clark-Gruel, N. Eidelman, M. Sacks, E. Palmatory, A. Kronsteiner, S. DeFelice, J. Xu, R. Ohri, N. Narula, N. Vyavahare, and R. J. Levy. (2005) Triglycidylamine Crosslinking of Porcine Aortic Valve Cusps or Bovine Pericardium Results in Improved Biocompatibility, Biomechanics, and Calcification Resistance: Chemical and Biological Mechanisms. *Am. J. Pathol.* 166:1-13.
- Hjelms, E., P. Pohlner, B. G. Barratt-Boyes, and J. B. Gavin. (1981) Study of autologous pericardial patch-grafts in the right ventricular outflow tracts in growing and adult dogs. *J Thorac Cardiovasc Surg* 81:120-123.
- Jayakrishnan, A. and S. R. Jameela. (1996) Glutaraldehyde as a fixative in bioprostheses and drug delivery matrices. *Biomaterials* 17:471-484.
- Boughner, D. R., M. Haldenby, A. J. Hui, J. Dunmore-Buyze, E. A. Talman, and W. K. Wan. (2000) The pericardial bioprosthesis: altered tissue shear properties following glutaraldehyde fixation. *J Heart Valve Dis* 9:752-760.
- Mavrilas, D., E. A. Sinouris, D. H. Vynios, and N. Papageorgakopoulou... (2005) Dynamic mechanical characteristics of intact and structurally modified bovine pericardial tissues. *J Biomech* 38:761-768.
- Stradins, P., R. Lacis, I. Ozolanta, B. Purina, V. Ose, L. Feldmane, and V. Kasyanov. (2004) Comparison of biomechanical and structural properties between human aortic and pulmonary valve. *Eur J Cardiothorac Surg* 26:634-639.
- Oswal, D., S. Korossis, S. Mirsadraee, H. Wilcox, K. Watterson, J. Fisher, and E. Ingham. (2007) Biomechanical characterization of decellularized and cross-linked bovine pericardium. *J Heart Valve Dis* 16:165-174.
- Chanda, J., R. Kuribayashi, and T. Abe. (1997) Concentration of glutaraldehyde in fixation of bioprosthetic valves. *J. Thorac. Cardiovasc. Surg.* 114:512.
- Duncan, A. C., D. Boughner, and I. Vesely. (1997) Viscoelasticity of Dynamically Fixed Bioprosthetic Valves. II. Effect of Glutaraldehyde Concentration. *J Thorac Cardiovasc Surg* 113:302-310.
- Stacchino, C., G. Bona, F. Bonetti, S. Rinaldi, L. Della Ciana, and A. Grignani. (1998) Detoxification process for glutaraldehyde-treated bovine pericardium: biological, chemical and mechanical characterization. *J Heart Valve Dis* 7:190-194.
- Vincentelli, A., R. Zegdi, A. Prat, P. Lajos, C. Latremouille, E. Le-Bret, G. De Boisbaudry, A. Carpentier, and J. N. Fabiani. (1998) Mechanical modifications to human pericardium after a brief immersion in 0.625% glutaraldehyde. *J Heart Valve Dis* 7:24-29.
- Srivatsa, S. S., P. J. Harrity, P. B. Maercklein, L. Kleppe, J. Veinot, W. D. Edwards, C. M. Johnson, and L. A. Fitzpatrick. (1997) Increased Cellular Expression of Matrix Proteins That Regulate Mineralization Is Associated with Calcification of Native Human and Porcine Xenograft Bioprosthetic Heart Valves. *J. Clin. Invest.* 99:996-1009.
- Gross, J. M. (2003) Calcification of bioprosthetic heart valves and its assessment. *J. Thorac. Cardiovasc. Surg.* 125:6S-8.
- Cheung, D. T., S. J. Choo, A. C. Grobe, D. C. Marchion, H. H. Luo, D. C. Pang, B. E. Favara, J. H. Oury, and C. M. G. Duran. (1999) Behaviour of Vital and Killed Autologous Pericardium in the Descending Aorta of Sheep. *J. Thorac. Cardiovasc. Surg.* 118:998-1005.

Author: Valts Ozolins  
 Institute: Riga Stradins University  
 Street: Dzirciema 16  
 City: Riga  
 Country: Latvia  
 Email: dr\_ozolins@inbox.lv

# Eye Kinematics of Athletes in Non-Familiar Sports Situations

R. Paeglis<sup>1</sup>, A. Spunde<sup>2</sup>, A. Klavinsh<sup>2</sup>, L. Vilkausha<sup>1</sup> and I. Lacis<sup>1</sup>

<sup>1</sup> Dept. of Optometry and Vision Science, University of Latvia, Riga, Latvia

<sup>2</sup> Dept. of Sports Games, Latvian Academy of Sports Education, Riga, Latvia

**Abstract** — Biological motion can hardly be imitated, starting from how a person observes and learns motor behaviour. We recorded eye movements of 13 female ball games athletes and 13 age-matched controls observing videos of unfamiliar sports. The athletes are better at alternating between faster and slower eye movement modalities. They initially use longer but fewer fixations than the non-athletes.

**Keywords** — Saccades, Infra-red eye-tracking, Direct matching, Karate, *iViewX*

## I. INTRODUCTION

We hypothesize that athletes, once sufficiently acquainted with a situation in a sport that they had not practiced before, will tend to implement the gaze shift patterns they use in their field of expertise. To test this hypothesis, we invited national level female basketball players to observe filmed situations in karate.

Visual skills are generally correlated to a person's performance in sports. This finding is revealed in a wide range of phenomena, ranging from those assessed in a routine visual testing [1] to gaze shift recorded by highly specialised equipment [2].

In their experiments, Flanagan and Johansson [3] demonstrate evidence for the "direct matching hypothesis". Their results witness that visually observed data are indeed mapped as motor representations in the observer's brain. In a real sports action the viewer's vision is involved in the task control, partly by monitoring own actions and partly by mirroring and predicting the movements of others. In a task that involves a motor action, the gaze is shifted to the points that are relevant for the procedure instead of the points of highest contrast or other remarkable physical features [4]. If the above findings are applied to sports, two different neural strategies could be implemented if a player aims to intercept a ball that he has just noticed or to block a power forward's shot. Likewise, a video where a ball is modelled on a screen [5] or fired by a machine [6], and a video with a person shooting the ball do not present equivalent information for neural processing. Only the cases with visible actors would activate any "mirror neurons" that are engaged in predicting the goal of action.

The time that a person looks at a point with suppressed eye movements is called a fixation and is related to informa-

tion processing demands, while the shift of a person's gaze, or saccade, is related to task and motivation specific factors [7]. Unlike in other voluntary movements, the velocity of rapid eye movements, or saccades, cannot be voluntarily controlled. Yet this velocity is correlated to the amplitude of eye movements, the "main sequence" relationship, and some factors, such as alertness or fatigue, can alter it [8]. Does this eye velocity and amplitude relationship change if an observed sports situation gets familiar?

## II. METHODS

Two groups of female volunteers, 13 athletes and 13 non-athletes, participated in the research. All participants were young adults, the average age of the athlete group was 18.5 years and that of the non-athletes was 19.8 years. The athletes participated were members of the Latvian National level basketball teams and students of the Latvian Academy of Sports Education. They were training 3 to 4 hours 4 to 5 days per week (in total at least 12 hours a week). The experimental protocol was in accordance with the Declaration of Helsinki. The participants joined the research voluntarily and provided written informed consent after the procedure was explained to them.

Movements of the right eye were tracked by an *iViewX Hi-Speed* system (*SensoMotoric Instruments*, Germany). It is a video-based setup that calculates the eye position from the 1<sup>st</sup> Purkinje reflection from the cornea and the centroid of the pupil image. The data were sampled 240 times per second. Saccades and fixations were identified by separate algorithms implemented in *BeGaze*, software provided by the eye-trackers' manufacturer. Simultaneously with the numerical data of gaze coordinates the eye tracker recorded the gaze video at a resolution of 768 by 576 pixels.

Identical films were demonstrated, every time with different instructions. The film was the karate 'kata', or individual learned sequence of movements. At first, the participants were asked to watch the video in order to assess the level of the performer (Is he a professional or novice? What level competitions could he take part in?). In the second task, the participants were asked to memorize the sequence of movements to compare to the next film. The third task was a 'change detection' task – were there any differences, compared to the previous film? The particular scene we

selected was a fragment of the “kata” named “Unsu” and was performed by a young expert who participated in the international competitions. In addition, the basketball players were shown a video of free shots by other female athletes. Their task thus was to guess and indicate if the shot will score. This task was devised to provide a reference level for the athletes.

### III. RESULTS

Saccade velocity depends on its amplitude, i.e., the larger the gaze shift is, the faster the eyes move. If the saccades were made to a target at a defined range of distances, the saccade velocities of the participants could be compared directly. Since the viewers explored a real action and the research intended to record their ‘natural’, unrestricted eye movements, a different route of the data processing was chosen. The ‘main sequence’ analysis relates the peak velocity of an eye movement to its amplitude over duration, or the average speed. Thus in the ‘main sequence’ plot saccades of different amplitudes and peak velocities align to a line, the slope of this line is denoted by Q. This linear relationship is observed for the amplitudes of up to 20 degrees, the range where saccades fall in this experiment.

We obtained the values of the maximum velocities of saccades times their duration and plotted them on the Y axis, whereas the X axis contained the corresponding saccade amplitudes. These points aligned to lines whose slope values, or Q values, and their standard errors were further calculated. We computed the ‘main sequence’ slopes for the 26 participants and calculated the average and the 95% confidence intervals for each group in every task (Fig. 1). In addition, we report these statistics for a control task, free

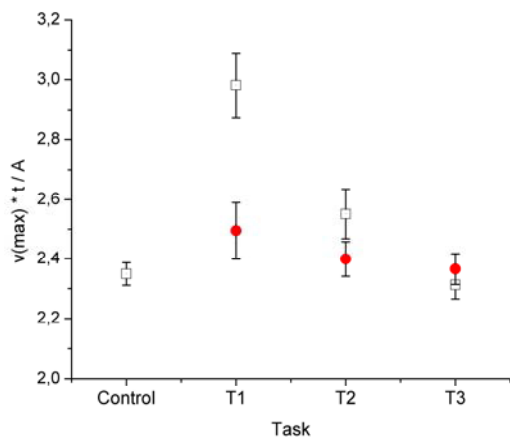


Fig. 1 Mean values of ‘main sequence’ slopes for the athletes (empty squares) and non-athletes (full circles). Bars, 95% confidence intervals

shots in basketball viewed as a reference only by the basketball players. In watching unfamiliar sport situations, the group of athletes can indeed be distinguished from the non-athletes, based on the eye velocity criteria. The same films were shown to the volunteers but with different instructions (estimate, memorize, compare) in the three experimental tasks (T1 through T3). In the first two tasks, the peak velocity over the average velocity ratio of the two groups differed significantly. Within the confidence intervals, the non-athletes did not respond significantly different in the first three tasks. On the other hand, the eye kinematics of the athletes was significantly different in these tasks. By task three, the Q values for the athletes have converged to ‘the baseline’ or the control situation of the basketball shots (‘Control’).

The first two tasks witnessed to high differences in the way eyes were accelerated; moreover, significant differences in gaze fixations were also found in these cases (Fig.2,3). The distribution of fixations did not match the normality criteria. This was supported by Kolmogorov-Smirnov normality test, for the fixation durations of the athletes it yielded  $D=0.099$  in Task 1 and  $D=0.094$ , Task 2, in both cases  $p<0.01$ . For the non-athletes we found  $D=0.132$  and  $0.121$  for Tasks 1 and 2 respectively, in both

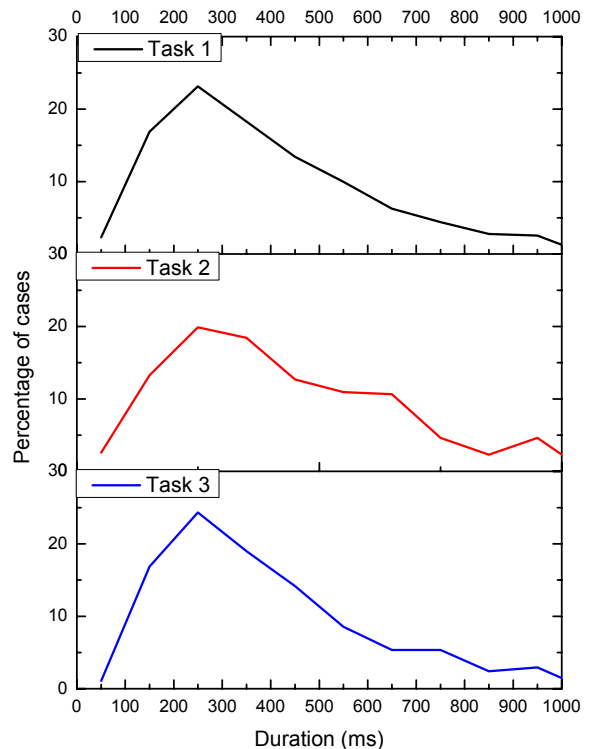


Fig. 2 Normalized distribution of fixations by their duration for the athletes

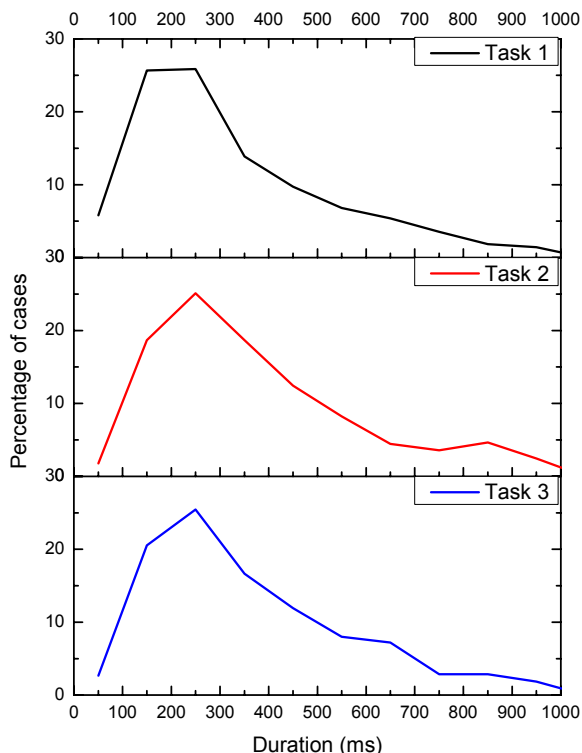


Fig. 3 Normalized distribution of fixations by their duration for the non-athletes

$p < 0.01$ . Therefore a non-parametric test was applied to compare the distribution of fixations. In the mastery estimation task (No. 1) the group of the athletes made 432 fixations (median 332 milliseconds), the non-athletes made 483 fixations (median 265 ms). The fixations were significantly different (Mann-Whitney  $U=122985$ ,  $p < 0.01$ ). In Task 2 (memorize the sequence of movements) the athletes made 347 fixations (median value 374 ms) and the non-athletes 450 (median value 315 ms). The groups were also significantly different ( $U=87915$ ,  $p=0.02$ ).

These findings, along with the upper two rows in Fig. 2 and Fig. 3, substantiate the conclusion that the athletes made fewer fixations, but their fixations were longer than those of the non-athletes.

#### IV. DISCUSSION

We conclude that the visual system advantages exist in athletes when a real situation is viewed. It was not obvious from the onset that eye kinematics of the athletes and non-athletes would form two distinct groups in any task. It could be equally well expected that the 'main sequence' lines would form one diffuse family. Since the two groups

were age and gender matched, we are inclined to assume that it is the adjustment of the visual system, rather than genetic factors or cognitive strategies, primarily explain for the differences between the groups. To answer the posed hypothesis, we indeed observed relatively higher eye movement velocities when the basketball players first observed the karate scenes. At further exposures, the "main sequence" relationship converged to that of watching basketball shorts and the confidence intervals of the two groups overlapped.

Our findings are in part contrary to the findings of Babu and colleagues [9] who found no significant differences in the kinematics of saccades between the athletes and non-athletes. There is no reason to assume that the type of sports of the athletes, the racquet sports or basketball, was the decisive factor. Possibly here we face a problem that is encountered in other types of eye movement research, namely, the human visual system tends to behave more efficiently on the natural rather than laboratory stimuli [10]. The performance advantages of the athletes may not be fully revealed in computer-generated abstract forms but appear whenever real situations are viewed. We also refer back to the "direct matching hypothesis [3]. According to it, the participants of our research mapped the observed movements of human actors to their motor cortex. The generated eye movements corresponded to their efforts to predict or reproduce the observed actions. The participants with a better trained kinaesthetic memory did it with significantly different saccades and fixations.

The above reasoning leaves unanswered the question of why does the kinematics of the athletes' eye movements in novel sports situations converge to the performance in their familiar basketball shots (Fig. 1). We hypothesize that athletes are also better accustomed to distinguish the situations that risk a failure and those that do not. An athlete is trained to use brief moments of the game to relax and restore performance. A non-familiar sports display, and non-customary task of watching videos at a scientific laboratory, could initially mobilize the athletes for tougher performance. Likewise, a decisive sports situation would cause much arousal. On the other hand, recorded basketball video, and dance that may not be perceived as 'a real sport' by the invited athletes, has been classified as 'non-threatening' by the athletes.

Comparing Tasks 1 and 2 in Figs. 2 and 3, the athletes use a smaller number of fixations that are longer than those of the non-athletes. Remarkably, at repeated exposure both groups watched the same video with relatively longer fixations. Thus the extent but not the nature of changes differed in both groups. In other words, the quantity and not the quality are of importance when an unfamiliar sport scene is tackled. No differences in fixations were found in the other

3 tasks, even though the last two differed significantly in eye kinematics. Furthermore, the unexpected shift in Task 5, where the non-athletes witnessed to relatively higher eye velocities times their duration, was not accompanied by any significant changes in the duration of fixations. This is not surprising since saccades and fixations are programmed independently and saccades alone can be used as a research tool [7].

A limitation of eye movement research in sports is that the fixations mark only the foveal vision. The field of view of up to 32 degrees is necessary for an efficient navigation if the contrast is sufficiently low. Before getting to fixate the target milliseconds before a shot, the player must traverse the playgrounds in a dynamic setting of team-mates and opponent players [12] before getting to the critical position [13]. The success of navigation determines if the 'quiet eye' [14] (Vickers, 1996) will be used at all, hence the rating of a player is determined by the entire course of action. Are there as yet incompletely described skills that must accompany the 'quiet eye' of a successful player? It may be further researched what preliminary information of the parafoveal vision is processed before the player gets to the 'ready position'.

#### ACKNOWLEDGEMENTS

The researchers have been inspired and consulted by karate trainer Zanna Vasilyeva (4th Dan). The authors express gratitude to Ivars Bacis.

The authors thank Dr Vyacheslavs Kashcheyevs for thoughtful remarks on calculations and Dr Ingvars Birznieks for comments on neurobiology. The researchers thank Prof. Uldis Rogulis for his scientist's and athlete's perspective on the manuscript.

This research has been supported by the European Social Fund.

#### REFERENCES

1. Jafarzadehpur E, Aazami N, & Bolouri B (2007) Comparison of saccadic eye movements and facility of ocular accommodation in female volleyball players and non-players. *Scandinavian Journal of Medicine & Science in Sports*, 17: 186-190.
2. Vickers J N (2006) Gaze of Olympic speedskaters skating at full speed on a regulation oval: perception-action coupling in a dynamic performance environment. *Cogn. Processing*: 102-105.
3. Flanagan J R & Johansson R S (2003) Action plans used in action observation. *Nature*, 424: 769-761.
4. Johansson R S, Westling G, Bäckström A, & Flanagan J R (2001) Eye-Hand Coordination in Object Manipulation. *The Journal of Neuroscience*, 21 (17): 6917-6932.
5. Brouwer A, Brenner E, & Smeets J B J (2002) Perception of acceleration with short presentation times: Can acceleration be used in interception? *Perception & Psychophysics*, 64: 1160-1168.
6. Land M F, & McLeod P (2000) From eye movements to actions: how batsmen hit the ball. *Nature neurosci.*, 3: 1340-1345.
7. Leigh R J, & Kennard C (2004) Using saccades as a research tool in the clinical neurosciences. *Brain*, 127: 460-477.
8. Snyder L H, Calton J L, Dickinson A R, & Lawrence B M (2002) Eye-Hand Coordination: Saccades Are Faster When Accompanied by a Coordinated Arm Movement. *J. Neurophysiology*, 87: 2279-2286.
9. Babu R J, Lillakas L, & Irving E (2005) Dynamics of Saccadic Adaptation: Differences Between Athletes and Nonathletes. *Optometry and Vision Science*, 82 (12): 1060-1065.
10. Peters R J, Gabbiani F, & Koch C (2003) Human visual object categorization can be described by models with low memory capacity. *Vis. Res.*, 43: 2265-2280.
11. Hassan S E, Hicks J C, Lei H, & Turano K A (2007) What is the minimum field of view required for efficient navigation? *Vis. Res.*, 47: 2115-2123.
12. Martell S G, & Vickers J N (2004) Gaze characteristics of elite and near-elite athletes in ice hockey defensive tactics. *Human Movement Science*, 22: 689-712.
13. Oudejans R R D, Michaels C F, & Bakker F C (1997) The effects of baseball experience on movement initiation in catching fly balls. *J. Sports Sci.*, 15, pp. 587-595.
14. Vickers J N (1996) Visual control when aiming at a far target. *Journal of Experimental Psychology: Human Perception and Performance*, 22: 342-354.

Author: Roberts Paeglis  
 Institute: Dept. of Optometry & Vision Science, University of Latvia  
 Street: 8 Kengaraga Str.  
 City: Riga  
 Country: Latvia  
 Email: Roberts.Paeglis@lu.lv

# Feasibility Experiment of Gait Training System Using Real-time Visual Feedback of Knee Joint Angle

J. Park<sup>1</sup>, J. Ku<sup>1</sup>, S. Cho<sup>1</sup>, D.Y. Kim<sup>2</sup>, I.Y. Kim<sup>1</sup> and S.I. Kim<sup>1</sup>

<sup>1</sup> Department of Biomedical Engineering, Hanyang University, Seoul, Korea

<sup>2</sup> Department of Physical Medicine and Rehabilitation, Yonsei Medical School, Seoul, Korea

**Abstract** — Patients with stroke exhibit a stiff-knee which characteristic is that knee flexion diminishes significantly during gait, particularly in the swing phase because loss of control ability. Ability of knee control is important during gait. In this paper we developed a Virtual Reality (VR) rehabilitation system for stroke patients who have a stiff-knee gait disorder. Developed VR rehabilitation system is able to measure knee joint angle and interact between system and patients using a marker-based measurement system composed of a PC and an IEEE1394 camera. To validate feasibility of VR system, we performed experiment using a treadmill with same speed (2.0 km/h) and various target angles (40 degrees, 50 degrees and 70 degrees). The purpose, we performed with various target angles, is that we ascertain that normal participants make a success of task with the abnormal target angle as well as the normal target angle. Four healthy male (age from 24 to 28 years) was recruited for this experiment. And experimental task was composed in three stages and we measured average of trial numbers for success in each stage. The trial numbers gradually decreased with each stage in 50 and 70 degrees. In conclusion we ascertained that VR system help with increasing control ability of knee joint of the participants at 50 and 70 degrees. From now on we expected that developed VR gait training is possible to use in practical gait training with stroke patients. Therefore we will need a clinical test to apply this system to stroke patients in hospital.

**Keywords** — stiff-knee, gait training, knee angle, virtual reality, rehabilitation

## I. INTRODUCTION

Knee flexion is very important in gait because knee joint participates to the shocking absorption, the stability of low limb, and prevention of catching the toe in normal gait phase [1]. Stroke patient exhibits stiff-knee which is at characteristic gait which is visible frequently from the stroke patient with stiffness paralysis gait. Characteristic of stiff-knee gait is that knee flexion during swing phase is significantly diminished [2][3][4].

In cause of stiff-knee gait, energy consumption is increased, and walking speed and step number per minute are decreased during walking. Also, stroke patient has frequently falling down. It can cause a wrist fracture, a pelvis fracture, the lower limb fracture, and the other body parts.

Moreover stroke patient has problem of the Activities of Daily Living [5]. For overcoming these problems, it is necessary that patient adjusts knee joint as a normal. Therefore the training of knee joint adjustment is required for adjusting normal knee angle in gait phase.

In conventional rehabilitation training, patient trained repeatedly by same treatment such as physiotherapy and treadmill training. Physiotherapy was used to enhance physical strength. And treadmill training was used to train patient to walking. The aims of gait rehabilitation training are to achieve the normal knee flexion and normal gait pattern. Patient needs a difference training level to achieve the aims because maximum knee joint angle of patient is different each other. Therefore we required to measure the knee angle to apply the appropriated training to patient.

The conventional rehabilitation training wasn't able to provide training which is to adjust knee angle which is suitable in gait because it wasn't able to measure knee angle in real-time. It is important that patient adjust suitable knee angle in gait cycle. In normal gait, knee has various angles according gait phase, but patient doesn't adjust knee angle because patient has stiff-knee gait. As a consequence, we needed a novel rehabilitation training which is able to measure knee joint angle and to apply interaction in real-time.

We suggested that Virtual Reality (VR) could be used in novel rehabilitation training. Practical advantages of using virtual reality for training include safety, time, space, and equipment cost efficiency using computed three dimensional (3D) Virtual Environment (VE), and subjective data analysis using computed data [6]. Also, VR is able to offer interaction, behavioral tracking and feed-back in real-time [7].

In this study we developed a VR rehabilitation training system which is able to measure knee joint angle and to interact in real-time. For the real-time interaction we used marker based knee angle measurement system. It was able to measure knee angle in real-time during swing phase. Therefore it induced to adjust knee angle according gait phase. The developed rehabilitation training system composed the scenario to performed task which was proper for the target of the training for the stiff-knee gait. We had a system feasibility experiment whether the developed rehabilitation training system will be able to apply it to practical

rehabilitation training. Also, we had a clinical test with three stroke patients in local rehabilitation hospital.

## II. METHODS

### A. Knee angle measurement system

The marker based knee angle measurement system composed a Personal Computer (PC), an IEEE1394 camera, and IEEE1394a interface card. The knee angle is calculated by relation between rotation values of two markers in real-time using captured image by IEEE1394 camera (Fig. 1).

### B. Virtual Reality Rehabilitation System

We created two trees, a background, and three stepping-stones using A6 Game Studio to apply into VR rehabilitation training system. The developed VR rehabilitation training system was composed of simple task which was crossing a stepping-stone. The stones putted with difference length each target angle to present more efficiency visual feed-back. For example length between two stepping-stones is short when target angle has a low value. On the other hand length between two stepping-stones is long when target angle has a high value (Fig. 2).

The red-cross image in VE moved according to knee angle which was measured in real-time. The participants could

target angle of knee angle, the red-cross image changed into foot image on the stepping-stone. Subsequently, if they maintained target angle during 0.1 seconds on the stone, the stepping-stone color changed into the yellow. Subsequently, if they dragged the stepping-stone to blue line, they succeeded a step (Fig. 3).

### C. Feasibility Experiment

Four normal male (age from 24 to 28 years) was participated in feasibility experiment. They performed task with same speed (2.0 km/h) of treadmill and various target angles (40 degree, 50 degree, 70 degree). The speed was established by a rehabilitation specialist. It is used in rehabilitation training with patients with hemiplegia being able to train using treadmill. In the event each participant performed task 3 times totally without break.

Experiment procedure was following:

- 1. Attach two markers to left knee of the participants.
- 2. Input information about participants, the region of measurement, movement mode, target angle, and successful number of times.
- 3. Perform a practice.
- 4. Perform the practical task : The success condition is that participants maintain the target angle during 0.17 seconds. The failure condition is that they don't maintain the target angle during 0.17 second.
- 5. Try repeatedly until successful number will be 30 times.

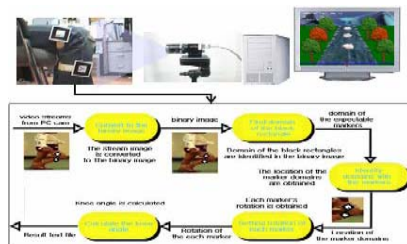


Fig. 1 Marker based knee angle measurement system

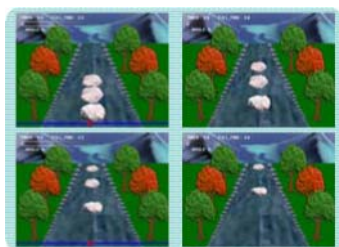


Fig. 2 Different length between two stepping-stones



Fig. 3 Task procedure ( clockwise from left upper )



Fig. 4 Experimental Environment

cross over next stepping-stone when they succeed maintaining target angle during the time of 0.1 seconds. If they made



We measured the times of trial until participants succeed each stepping-stone. We divided each task into three periods such the first stage which includes from first to tenth stone, middle stage which includes from eleventh to twentieth stone, and last stage which includes from twenty first to thirtieth stone.

Participants are asked to answer to the System Feasibility Questionnaire. The questionnaire scale was composed four items and five scale from 1 to 5 with responses “Strongly No,” “No,” “Maybe,” “Yes,” and “Strongly Yes.”.

*D. Clinical Experiment*

Three adults with stiff-knee gait disorder, treated at a local rehabilitation hospital, were participated in clinical test. They performed task with each speed appropriated their walking ability. The speed was established by a rehabilitation specialist. They performed one task with totally 25 stepping-stones with their maximum knee angle. Patients are asked to answer to the User Satisfaction Questionnaire to evaluate whether the developed system could be used to rehabilitation. The questionnaire scale was composed four

Table 1 Feasibility Questionnaire

Item Number	Question	Keyword
No. 1	It is difficult to control knee angle at the first time after starting walk.	control
No. 2	In the process of repeating performing, I could readjust knee angle to target angle.	trial number
No. 3	I felt that VR task is difficult.	task
No. 4	I thought that speed of treadmill is fast.	speed

Table 2 User Satisfaction Questionnaire

Item Number	Question	Keyword
No. 1	It is difficult to control knee angle at the first time after starting walk.	Control difficulty
No. 2	In the process of repeating performing, I could readjust knee angle to target angle.	Control ability
No. 3	I perfectly understand the method of going over stepping-stone.	Understanding of method
No. 4	I thought that speed of treadmill is fast.	Treadmill speed
No. 5	I thought that this system was able to improve gait pattern.	Help to gait
No. 6	I thought that walking with required target in this system was approximately normal gait pattern.	Natural gait pattern

items and five scale from 1 to 5 with responses “Strongly No,” “No,” “Maybe,” “Yes,” and “Strongly Yes.”.

III. RESULTS

*A. Feasibility Experiment*

In this experiment, we determined the feasibility of the developed VR rehabilitation training system for knee control ability.

This result showed the gait cycles to succeed the first stage, middle stage, and last stage in whole task. 50 and 70 degrees increased and 40 degrees increased between first stage and last stage (Fig. 5).

In the result of questionnaire, the mean score of the 70 degree was the highest and the 50 degree was the lowest in the first item. Also the mean score of the 50 degree was the highest and the 40 degree was the lowest in the second item. Also the mean score of the 70 degree was the highest and the 50 degree was the lowest in the third item. Also the mean score of the 70 degree was the highest and the 50 degree was the lowest in the ‘speed’ item.

*B. Clinical Experiment*

In the result of questionnaire, patients reported that ‘control difficulty’ was 3, ‘control ability’ was 4, ‘understanding of method’ was 5, ‘treadmill speed’ was 2.3, ‘help to gait’ was 4, and ‘natural gait pattern’ was 2.

Table 3 Mean and standard deviation of the Feasibility Questionnaire ‘Strongly yes’ score is 5

	control MEAN(SD)	trial number MEAN(SD)	Task MEAN(SD)	Speed MEAN(SD)
40 degrees	3.31(1.37)	3.00(1.15)	2.75(1.50)	2.00(1.41)
50 degrees	2.75(0.96)	3.75(0.50)	2.00(0.81)	1.75(0.50)
70 degrees	4.50(0.58)	3.50(1.00)	3.25(1.50)	2.25(1.26)

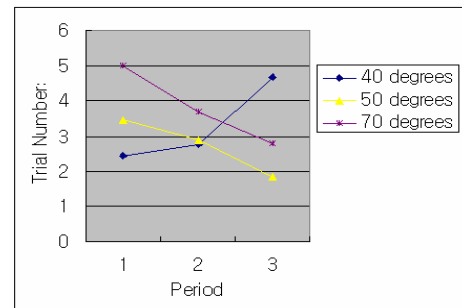


Fig. 5 Trial times to succeed each period

Table 4 Result of the User Satisfaction Questionnaire  
'Strongly yes' score is 5

	MEAN	SD
Control difficulty	3	0
Control ability	4	0
Understanding of method	5	0
Treadmill speed	2.3	0.6
Help to gait	4	0
Natural gait pattern	2	0

#### IV. DISCUSSION AND CONCLUSION

We developed VR rehabilitation training system for knee adjustment VR technology. Patient was able to perform task appropriated his/her maximum knee control ability using the developed VR rehabilitation training system..

Number of gait cycle to succeed each stage in whole task, in the system feasibility experiment, we knew that gait cycles from first stage to last stage at 50 and 70 degrees decreased. Therefore, we could think that the ability of knee control was increased by VR knee control training. The other side number of walking cycle at 40 degrees increased. In other words, there was no training effect of VR knee control training. We could explain the reason of this result by the system feasibility questionnaire. Score of 'control ability' of the system feasibility questionnaire was 3.0 point. It was the lowest point among the different target angles. It meant that the effect of knee control training was normal. Therefore, we could expect that the result of performing task at 40 degrees was no. The purpose of the developed VR rehabilitation training system was increasing the performance of knee adjustment ability. Therefore, in knee adjustment training, the target angle could be set up such as present ability or more. So, we interested in 50 and 70 degrees target angle. In conclusion we could expect that the developed VR rehabilitation training system will be able to be used in knee control training with suitable target angle of patient's ability. Therefore, we could expect that the developed VR rehabilitation training system would improve stiffness gait pattern of stroke patient.

We applied the developed VR rehabilitation training system to practical patients in the local rehabilitation hospital based on result of the system feasibility experiment. Patients reported that they were not difficult to adjust knee at

the first time after starting walking on a treadmill. We could expect the reason was because we measured maximum knee angle of patients before patients performed treadmill training. Also, patients reported that it was easy to understand the task, and that treadmill speed was not fast because the treadmill speed was decided by the rehabilitation specialist. The important finding, in this clinical test, was that patients reported that developed VR rehabilitation training system will be able to improve own gait pattern. This finding agreed with our ultimate expected effectiveness. But we could not assert that the developed VR rehabilitation training system would improve gait pattern of stroke patient because we just tested 3 patients at once for all. Therefore we will need a comparing group study between conventional rehabilitation training and VR rehabilitation training.

#### REFERENCES

1. Thiru M. Annaswamy, Candace J. Giddings, Ugo Della Croce, D. Casey Kerrigan (1999) Rectus femoris: its role in normal gait. *Arch Phys Med Rehabil* 80: 930-934
2. Sutherland DH, Santi M, Abel MF (1999) Treatment of stiff-knee gait in cerebral palsy: A comparison by gait analysis of distal rectus femoris transfer versus proximal rectus release. *J. Pediatric Orthoped*, 10: 433-441
3. Kerrigan DC, Gronley J, Perry J (1991) Stiff-legged gait in spastic paresis: A study of quadriceps and hamstrings muscle activity. *Am J Phys Med Rehabil* 70: 294-300
4. Waters RL, Garland DE, Perry J, Habig T, Slabaugh P (1979) Stiff-legged gait in hemiplegia: Surgical correction. *J Bone Joint Surg Am* 61: 927-933
5. Mireille Donkervoort, Joost Dekker, Groningen (2002) Sensitivity of different ADL measures to apraxia and motor impairments. *Clinical Rehabilitation* 16: 299-305
6. Holden MK, Todorov E (2002) Use of Virtual Environments in Motor Learning and Rehabilitation, *Handbook of Virtual Environments: Design, Implementation, and Applications (Human Factors and Ergonomics Series)*. LEA Inc., 999-1026
7. Albert Rizzo, and Gerard Jounghyun Kim (2005) A SWOT Analysis of the Field of Virtual Reality Rehabilitation and Therapy. *Presence* 14: 119-146

Author: Jeonghun Ku, Ph.D.  
 Institute: Department of Biomedical Engineering,  
 Hanyang University  
 Street:  
 City: Seoul  
 Country: Korea  
 Email: kujh@bme.hanyang.ac.kr

# Investigation of Biomechanical Properties of Different Elements of Human Mitral Valve

J. Pavars, P. Stradins, R. Lacis, I. Ozolanta, V. Kasyanov

Riga Stradins University, Riga, Latvia

**Abstract** — Mitral valvular heart disease is one of the major causes of morbidity and mortality all over the world. The optimal surgical strategy of treatment of valvular heart disease is repair or replacement. There is still ongoing research for optimal valve replacement options. Creation of new valve prosthesis is still a pressing problem. It is not enough information in publications about biomechanical properties of human mitral valve. We performed experimental studies of biomechanical properties of mitral valves on pathologically unchanged human heart valves, taken from 4 cadaveric hearts. Mitral valve construction elements were investigated using uniaxial tensile tests. It was established that an anterior chordae modulus of elasticity ( $477.28 \pm 24.322$  MPa), is greater than the one of anterior and posterior leaflet ( $43.48 \pm 15.97$  MPa and  $6.36 \pm 3.15$  MPa, respectively). These results correspond to previously published reports. Future valve sample radial direction investigations will provide more detailed information about it.

**Keywords** — mitral valve, anterior leaflet, posterior leaflet, chordae tendineae, modulus of elasticity.

## I. INTRODUCTION

Mitral valvular heart disease is one of the major causes of morbidity and mortality all over the world. A common method of treatment of valvular heart disease is surgery - repair or replacement [1, 2]. Up to now there is no perfect mode of surgery. Creation of new valve prosthesis is still a pressing problem. In literature it is available to find data about biomechanical properties of animal (porcine) native valves [3, 4] and human pathologically changed native valves [5, 6] but there are no data about biomechanical properties of different elements of normal human mitral valve. In order to create a novel artificial mitral valve we need exact information about biomechanical properties particularly in pathologically unchanged human heart valves. However, there is not enough published information regarding this issue. The aim of our study is to acquire detailed information about biomechanical properties of elements of human mitral valve.

## II. MATERIALS AND METHODS

Experimental studies of biomechanical properties of mitral valves were performed on pathologically unchanged

human heart valves, taken from 4 cadaveric hearts within 24 h of death. Donors age ranged from 36 to 44 years. Mitral valves were stored in a physiological sodium chloride solution at 20°C. Specimens of cusps were cut in circumferential direction 25 mm long and 3.5 mm wide. Specimens of chordae tendineae were cut 25 mm long. Initial thickness of samples was measured by cathetometer MK-6 (LOMO). All mitral valve construction elements were investigated using uniaxial tensile tests with material testing machine Zwick-Roell BDO-FB0.5TS. Maximum stress  $\sigma^*$  (MPa), maximum strain  $\epsilon^*$  (%), modulus of elasticity E (MPa) were measured. Modulus of elasticity is computed as the slope of the linear range of the curve stress – strain. Results were processed by specific software (Testexpert 11.02, Zwick-Roell).

## III. RESULTS

Experimental results are shown in Table 1. Maximum stress of anterior mitral leaflet in circumferential direction is  $1.99 \pm 0.24$  MPa, maximum strain  $5.97 \pm 1.47$  %, modulus of elasticity  $43.48 \pm 15.97$  MPa. Maximum stress of posterior mitral leaflet in circumferential direction is  $0.25 \pm 0.04$  MPa, maximum strain  $10.7 \pm 0.64$  %, modulus of elasticity  $6.36 \pm 3.15$  MPa. Maximum stress of anterior chordae tendineae is  $17.25 \pm 4.06$  MPa, maximum strain  $4.95 \pm 1.11$  %, modulus of elasticity  $477.28 \pm 204.32$  MPa. Ultimate stress of anterior chordae tendineae is higher ( $p < 0.05$ ) than ultimate stress of anterior and posterior leaflet ( $17.25 \pm 4.06$  MPa,  $1.99 \pm 0.24$  MPa and  $0.25 \pm 0.04$  MPa, respectively). Ultimate strain of posterior leaflet is higher ( $p < 0.05$ ) than anterior leaflet and chordae tendineae

Table 1 Main experimental parameters of human mitral valve

Parameters	Anterior Leaflet	Posterior Leaflet	Chordae Tendineae
Maximum stress $\sigma^*$ (MPa)	1.99±0.24	0.25±0.04	17.25±4.06
Maximum strain $\epsilon^*$ (%)	5.97±1.47	10.7±0.63	4.95±1.11
Modulus of elasticity E (MPa)	43.48±15.97	6.36±3.15	477.28±24.32

( $10.7 \pm 0.64$  %,  $5.97 \pm 1.47$  % and  $4.95 \pm 1.11$  %, respectively). Highest modulus of elasticity is for anterior chordae tendineae.

#### IV. CONCLUSION

Uniaxial tensile tests have shown that all elements of human mitral valve have different mechanical properties. Anterior chordae elasticity module is greater than the one of anterior and posterior leaflet. These results correspond to previously published reports. Future valve sample radial direction investigations will provide more detailed information about it.

#### REFERENCES

1. Kouchoukos NT, Blackstone EH, Doty DB, Hanley FL, Karp RB (2003) Acquired valvar heart disease in Kirklin/Barrat-Boyes Cardiac surgery, 3<sup>rd</sup> edition.
2. Savage EB, Bolling SF (2006) Atlas of mitral valve repair.
3. Ritchie J, Jimenes J, He Z, Sacks MS, Yoganathan AP (2006) The material properties of native porcine mitral valve chordae tendineae: An in vitro investigation. *J of Biomechanics*: 1129-1135.
4. Ritchie J, Warnock JN, Yoganathan AP (2005) Structural characterization of chordae tendineae in native porcine mitral valves. *Ann Thorac Surg*: 189-197.
5. Grande-Allen KJ, Barber JE, Klatka KM, Houghtaling PL, Vesely I, Moravec CS, McCarthy PM (2005) Mitral valve stiffening in endstage heart failure: Evidence of an organic contribution to functional mitral regurgitation. *J of Thoracic and Cardiovascular Surgery*: 783-790.
6. Barber JE, Kasper FK, Ratliff NB, Cosgrove DM, Griffin BP, Vesely I (2001) Mechanical properties of myxomatous mitral valves. *J of Thoracic and Cardiovascular Surgery*: 955-962.

Author: Janis Pavars  
 Institute: Riga Stradins University  
 Street: 16 Dzirciema, LV-1007  
 City: Riga  
 Country: Latvia  
 Email: jpvavars@yahoo.com

# Development of Research for Machining of Implants with Novel Materials for Bone Surgery

O.A. Rozenberg, S.V. Sokhan' and V.V. Voznyy

V.N. Bakul Institute for Superhard Materials/Department for Perspective Resource-saving Technologies of Machining by Tools with Super Hard Materials, National Academy of Science, Kyiv, Ukraine

**Abstract** — The paper is targeted to inform on the novel techniques and cutting machine for precision surfacing of hip joint heads of the new materials developed in Ukraine, like artificial sapphire, zirconium ceramics and the titanium alloy without vanadium and aluminum in its composition. These materials having favorable combination of their biocompatibility, toxicity, strength, wear resistance and life time in a living organism are used for a manufacture of femoral heads, acetabular cups in total hip-joint replacements.

Today next requirements to hip joint heads are considered as enough for successful functioning: sphericity less than 1.0  $\mu\text{m}$  and roughness of the polished surface Ra 0.010...0.020  $\mu\text{m}$ . However, for instance, anisotropy of properties of sapphire or low elastic properties of the titanic alloy essentially hampers machining of such products. Therefore, it was required to develop techniques and cutting machine for precision surfacing of hip joint heads of the new materials.

Suggested techniques includes preliminary shaping spherical surface of sapphire from cubic- or cylindrical-type blanks by circular diamond tool which has a feed under some angle to the axis of blank. Finish machining has several stages of fine grinding and lapping with diamond tools from micro- to nano powder. For this purpose special grinding and polishing machine was especially designed. Such approach provides making sapphire hip joint heads with a sphericity 0.4...1.0  $\mu\text{m}$  and roughness of polished surface Ra 0.006...0.015  $\mu\text{m}$ . Surface plastic deformation is provided preliminary and finish polishing finally for surfacing of hip joint heads of the new titanium alloy. Some aspects of developed techniques and cutting machine can be used for a manufacture of components of knee-joint prostheses from these materials.

**Keywords** — Sapphire, zirconium ceramics, titanium alloy, femoral heads for total hip joint replacements.

## I. INTRODUCTION

Perfecting of biomaterials is a major factor of advance in many fields of medicine, especially in surgery of joints. Any material implanted into a living organism is not absolutely bioinert – everyone invokes a response of a living tissue. A depth of a layer of the fibrous tissue which is isolating the material from remaining tissues of an organism can serve as a measure of bioactivity. For less bioinert materials (for example, stainless steels) depth of a layer of a

fibrous tissue is the tenth lobes of millimeter and more, whereas several molecular layers of such tissue are enough for the most bioinert materials (oxide ceramics, sapphire). Structural materials used for a manufacture of an implants in total hip-joint replacements should have favorable combination of their biocompatibility, toxicity, strength, wear resistance and life time in a living organism.

At last time for a manufacture of femoral heads or acetabular cups in hip joint replacements such structural materials as artificial sapphire, zirconium ceramics and titanium alloy which is not containing chemical elements V and Al are developed in Ukraine (Fig. 1).

Prostheses for total hip joint replacements with metallic-polymeric coupling "the femoral head – the acetabular cup" have demand due to rather low cost. But its basic disadvantage is a toxicity of usual metallic components and a short life of the polymeric insert that restricts the term between an initial and revision implantation for in 5-10 years in dependence on activity of the patient. New titanium alloy is less toxic than, for example, alloy  $\text{Ti}_6\text{Al}_4\text{V}$ .



Fig. 1 A blank of sapphire, hip joint heads from sapphire, zirconium ceramics (a) and titanium alloy without V and Al (b).

In comparison with metallic implanted materials bioinert ceramics is more biocompatible with a living organism and exerts smaller influence on immune system. However, a bioinactivity of the ceramics reduces because of impurities of silicon oxides and alkali metals which result to etching borders of grains at the long-lived stay in a living organism. Etching borders of grains augments a friction coefficient and wear of prosthesis of a joint. In this time sapphire having a structure of single crystal loses this disadvantage.

Today it has showed by novel research that the roughness of the polished surface on the hip joint head should be Ra 0.006...0.010  $\mu\text{m}$ , and a maximal deviation from sphericity in any measured 16 points of a sphere should not exceed 0.1-0.3  $\mu\text{m}$ . Satisfaction of these values depends on properties of materials and methods of machining. However, for instance, anisotropy of properties of sapphire or low elastic properties of the titanic alloy essentially hampers machining of such products.

The paper is targeted to inform on the novel techniques and cutting machine for precision surfacing of hip joint heads of the new materials developed in Ukraine, like artificial sapphire, zirconium ceramics and the titanium alloy without vanadium and aluminum in its composition.

## II. MATERIALS AND A METHOD OF MANUFACTURE OF FEMORAL HEADS FOR HIP JOINT REPLACEMENTS

### A. A novel bioinert materials for bone surgery

Sapphire heads are made of blanks of especially pure material – the crystals of alumina oxide synthesized at temperature  $>2000^\circ\text{C}$ . Sapphire has the same physical and mechanical properties as alumina ceramics. It is the best material for manufacture of implants. Etching of boundaries of grains in a biomedium does not happen at use of sapphire having structure of a single crystal. Therefore as contrasted to metal hip joint heads allergic responses of an organism are eliminated for sapphire head. However as the single crystal sapphire has strongly pronounced anisotropic properties. In addition it was required to manufacture sapphire hip joint heads from cubic- or cylindrical-type blanks. Sapphire hip joint heads are manufactured in Ukraine in common by V.N. Bakul Institute for Superhard Materials (ISM) and Institute for Single Crystals (ISC) of National Academy of Science (NAS) of Ukraine [1].

On biocompatibility the ceramics based on tetragonal zirconium dioxide stabilized by oxides of yttrium or cerium is close to alumina ceramics but has higher bending strength (up to 1200 GPa) and fracture strength (up to  $10 \text{ MPa} \times \text{m}^{-1/2}$ ). The new bioinert ceramic material which basis is nano crystalline powder  $\text{ZrO}_2$  is developed for hip joint

heads at the I.M. Frantsevich Institute for Problems of Materials Science (IPMS) NAS of Ukraine according to ISO 13356 [2].

As against the titanium alloy  $\text{Ti}_6\text{Al}_4\text{V}$  which is widely applicable in the medical practice and contains V and Al Prof. S.A. Firstov and associates are designing the titanium alloys of system Ti-Si at the IPMS of NAS of Ukraine and use alloying elements, completely inert to an organism of the person. Corrosion resistance of new alloys is much higher than one of alloy  $\text{Ti}_6\text{Al}_4\text{V}$ . Strength of new alloys is at a level 700-1100 MPa, plasticity of 9-20 %.

### B. A method of manufacture of hip joint heads for hip joint replacements

The indicated requirements to a spherical surface of hip joint heads are satisfied by successive use of two essentially different methods of machining: preliminary diamond grinding by the tubular tool on a method of "hard axes", and finishing diamond lapping surface. For this purpose special grinding and polishing machine was especially designed (Fig. 2).

The geometry of space cross of two bodies – the tubular tool with a narrow ring face surface and workpiece is in a ground of shaping spherical surfaces by the method of "hard axes". Both bodies are hardly bound to rotation axis which lay in one plane and intersected under some angle. At rotation of these bodies and transition of the tool along its axis to workpiece the ridge of the tool cuts a surface which all points lay on a circle formed by rotation of the tool in a body of a workpiece, and simultaneously same points form a body of rotation concerning an axis of a workpiece.

A precise shaping of spherical surface by diamond lapping is carried out at simultaneous rotation of a workpiece and ring lap elastically pressed to it which axis passes through rotation axis of a workpiece in center of a formed sphere. The hinging of lap ensures loose self-laying of its concave surface on a workpiece with contact immediately or through an abrasive interlayer. It is not required the forced rotation of lap because of an angle disposition of rotation axis. Finish machining has several stages of fine grinding and lapping with diamond tools from micro- to nano powder.

Process engineering is designed by Prof. O.A. Rozenberg and associates at the ISM of NAS of Ukraine for shaping high-precision ceramic workpiece of medical assigning and sapphire with a control modification of velocity and force parameters of diamond lapping. It is based on a solution of 3-dimensional contact for lapping process of ceramic or sapphire workpiece in accordance to interference of changed contact geometry, kinematics and dynamic of process owing to acting friction and abrasive wear of bod-



Fig. 2 Preliminary shaping by grinding (a) and finish lapping sapphire hip joint head (b).

ies. In such conditions leveling of entrance speed of diamond grains in a contact zone is ensured in a case when the absolute minimum of sliding speed is between outside and interior ridges of lap, and angular speeds of lap and workpiece coincide (Fig. 3).

At moving lap along a workpiece with even feed rate leveling of entrance speed of diamond grains in a contact zone is ensured at square-law association of reduction ratio  $v$  on angle  $\alpha$  of crossing axes of the tool and a workpiece with a maximal value near  $\alpha = 35^\circ$ . At moving lap along a workpiece with variable feed rate, but at stationary reduction ratio leveling of entrance speed of diamond grains in a contact zone is ensured with a modification of feed rate under the harmonic law, the close to sine, and with a maximal value of feed rate near  $\alpha = 35^\circ$ , and minimum – near  $\alpha = 1^\circ$  and  $\alpha = 80^\circ$ .

For leveling work removal parameter on a profile of a workpiece redistribution of contact pressure is used for increasing of the parameter in a necessary direction under acting of moment of force created by a hold-down tool [3].

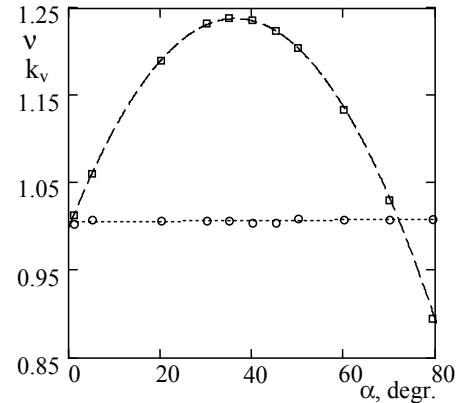


Fig. 3 The graph of association  $v$  and  $k_v$  from angle  $\alpha$  at  $\omega_1 = 104,7 \text{ c}^{-1}$  and  $r_2/R_1 = 0,982$ : □ –  $v$ ; ○ –  $k_v$ .

Surface plastic deformation is provided preliminary and finish polishing finally for surfacing of hip joint heads of the new titanium alloy.

### C. The measuring technique of a surface roughness and sphericity

Measuring of linear amplitude parameters  $R_a$ ,  $R_z$  of a surface roughness of the heads was carried out by a contact method on a device “Talyscan-5M-120”. Measuring of a surface roughness of the heads was carried out else by a contact method on a device “Talyscan-150” by scanning a site of a surface with a size  $1,0 \times 1,0 \text{ mm}$  or  $0,5 \times 0,5 \text{ mm}$ , filtrations of the shape and consequent calculation of parameters of grain  $S_a$ ,  $S_z$  and surface isotropy. Thus for detection of influence of anisotropy of sapphire measuring of the roughness parameters and surface isotropy was carried out both on all the scanned site of a surface, and on separate 8 its sites with a size  $0,25 \times 0,25 \text{ mm}$  posed on a circular line, for detection of the greatest and least values.

A deviation from sphericity on hip joint heads is measured on 3-dimensional measuring machine of modes PMM 12106 Leitz corporations in 45 points.

## III. RESULTS

Measuring of a surface roughness of the heads from sapphire, zirconium ceramics on a device “Talyscan-5M-120” has shown, that it is achieved a level of roughness  $R_a$   $0,006-0,020 \mu\text{m}$ .

Outcomes of measuring of a surface roughness of the heads from sapphire, zirconium ceramics on a device “Talyscan-150” are showed in Table 1.

Table 1 Amplitude roughness parameters and isotropy of surface.

Item	Sapphire			TZP
	General	Max.	Min.	General
Arithmetic Mean Deviation $S_a$ , $\mu\text{m}$	0.0704	0.0667	0.0497	0.073
Maximum height of summits $S_p$ , $\mu\text{m}$	0.437	0.365	0.295	0.333
Maximum height of valleys $S_v$ , $\mu\text{m}$	1.36	0.91	0.907	0.45
Ten Point Height $S_z$ , $\mu\text{m}$	1.42	0.977	0.978	0.701
Isotropy, %	1.18	4.39	12.2	0

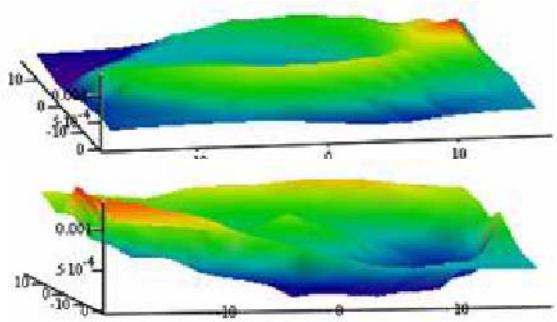


Fig. 4 Surfaces showing a deviation from sphericity of sapphire heads.

Showed on Fig. 4 surfaces showing a deviation from sphericity of the heads (0,5-1,0  $\mu\text{m}$ ) illustrate an influence of anisotropy of sapphire on its surface geometry.

#### IV. DISCUSSION

The process engineering and diamond tool designed at the ISM allow to manufacture hip joint heads from the mentioned materials with a deviation from sphericity in limits 0,5-1,0  $\mu\text{m}$  and grain Ra 0,01-0,02  $\mu\text{m}$ .

#### V. CONCLUSIONS

Thus, designed process engineering and diamond tool allow implementing the new concept of manufacture individual sapphire-metal endoprostheses for total hip joint replacements [1].

On their basis the endoprostheses for total hip joint replacements has designed with the sapphire head of heightened wear resistance which consists of a metal leg, the sapphire head, interlayer between them from extremely-macromolecular polyethylene and acetabular cup (Fig. 5-6).

To the present time it is carried out already over 10 successful operations of a total hip joint replacement with use of endoprostheses with the sapphire head.



Fig. 5 An overview of hip joint endoprosthesis with sapphire head.



Fig. 6 X-ray pictures of a patient before operation (a) and after its (b).

Some aspects of developed techniques and cutting machine can be used for a manufacture of components of knee-joint prostheses from these materials.

#### REFERENCES

1. Mamalis A G, Ramsden J J, Grabchenko A I et al. (2006) A novel concept for the manufacture of individual sapphier-metallic hip joint endoprostheses. Kharkiv, Ukraine, Journal of Biological Physics and Chemistry, 6(2006):113-117
2. Shevchenko A V, Dudnik E V, Dubok V A et al. (2006) Bioinert implants based on nano crystalline powders  $\text{ZrO}_2$ . Moscow, Russia, Technics of mechanical engineering, 2(58):32-35
3. European patent application EP 1 563 953 A1, 7 B 24 B 11/10. The way of machining of spherical surfaces and the device for its realization. A.G. Mamalis, N.V. Novikov, O.A. Rozenberg, S.V. Sokhan. 10.10.2003; Publish. 17.08.2005, Bulletin 2005/33

Author: Oleg A. Rozenberg, Prof.,  
Sergiy V. Sokhan, Dr Eng,  
Vjacheslav V. Voznyy, Ph. D  
Institute: V.N. Bakul Institute for Superhard Materials  
Street: 2 Avtozavodskaya  
City: Kyiv  
Country: Ukraine  
Email: ism20@ism.kiev.ua



# The Artificial Larynx: A Review of Current Technology and a Proposal for Future Development

M.J. Russell<sup>1</sup>, D.M. Rubin<sup>1</sup>, B. Wigdorowitz<sup>1</sup> and T. Marwala<sup>1</sup>

<sup>1</sup> School of Electrical and Information Engineering, University of the Witwatersrand, Johannesburg, Johannesburg, South Africa

*Abstract* — The loss of speech following a laryngectomy presents substantial challenges, and a number of devices have been developed to assist these patients, ranging from the electrolarynx to the unidirectional valve used in Tracheoesophageal speech. However, all of these devices have concentrated on producing the sound from the patient's vocal tract.

A brief review of the current state of the artificial larynx will be presented, followed by an introduction and system-level overview of a new type of artificial larynx currently in the early stages of research and development by our group. This new device will utilize dynamic measurement of tongue position to infer intended speech, and will transmit these signals to an electronic unit for near-real-time speech synthesis. The dynamic tongue measurement is achieved with the use of an existing palatometer and pseudopalate. This device, consisting of over 100 contact sensors spread over the palate, detects the exact tongue-palate contact pattern in speech. The tongue contact positions as a function of time are presented as a 2-D time-space plot. A brief summary of the planned future work will be given, which will include proposals for traditional image processing techniques amongst others to be used for extraction of information. The extracted features will be fed into a suitably designed Artificial Neural Network. By using a combination of data from the palatometer and from other biological signals it should be possible to infer what the patient is saying. Other methods for data presentation, feature extraction and signal processing will also be considered.

It is anticipated that the intended speech will be reconstructed using Artificial Intelligence techniques, and that this information will be streamed to a speech-synthesizer. Algorithms will ultimately be developed to achieve a synthesized voice pattern as close to the patient's original sound as possible.

*Keywords* — Artificial Larynx, Electropalatograph, Automatic Speech Recognition

## I. INTRODUCTION

The ability to communicate vocally is a skill many people take for granted. However some people lose their ability to talk due to a laryngectomy. A laryngectomy is an operation in which the larynx (or "voice box") is removed from a patient due to laryngeal, oesophageal or pharyngeal cancer [1]. A number of alternatives are available to the patient to give them a means to communicate, however none of these devices produce natural sounding speech.

In this paper a brief review of the current types of available artificial larynxes is given, as well as an introduction to a new type of artificial larynx. In section II the anatomy of the larynx and the laryngectomy procedure are discussed. The current available options for phonation are also reviewed. In section III the new artificial larynx is introduced and the various aspects of its design are outlined.

## II. THE CURRENT STATE OF THE ARTIFICIAL LARYNX

### A. Details of a Laryngectomy

The larynx is part of the conducting tube that joins the pharynx and the trachea. It has two main functions [2]:

1. To prevent food or drink from entering the trachea and lungs during swallowing
2. To produce sound

It is made up of a number of different cartilages and muscles which hold the larynx open during breathing and which close the laryngeal opening (glottis) during swallowing and in speech. The epiglottis is a spoon-shaped structure that aids in closing the glottis during swallowing. The vocal folds in the larynx are controlled by muscles and are used in sound production [2].

A laryngectomy is a procedure used to remove the larynx (see Fig. 1). In a laryngectomy, the entire larynx including the thyroid and cricoids cartilages is removed [3]. Once this has been done the upper part of the trachea is attached to the front of the neck to create a permanent opening (the tracheostoma) [4]. The tracheostoma is mainly for breathing purposes. The laryngectomy results in the patient being totally unable to phonate; this is due to the complete removal of the vocal cords.

### B. Current options for Phonation

There are multiple ways in which a patient can attempt to regain his/her voice. However Oesophageal and Tracheoesophageal speech are the most common with Tracheoesophageal speech fast becoming considered as the gold-standard in artificial speech production. Some of the common methods are:

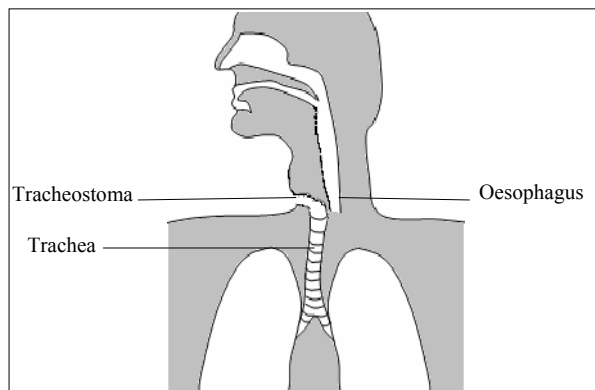


Fig. 1 Basic anatomy after a laryngectomy (Adapted from [2])

1. *Electrolaryngeal Speech:* This involves the use of an electrolarynx, which is a battery-powered transducer that directs a buzzing noise into the patient's vocal tract [1]. The sound can be introduced via the neck using a handheld device or into the oral cavity using an intraoral device. Patients then articulate the sound into words using their mouth. Pitch-controllable and volume-controllable devices are available [4]. This form of rehabilitation has a short learning time and the ability to use the device immediately after the operation. It is also readily available and has a low-cost. However, this device produces a mechanical sound and is dependent on batteries and maintenance of the intraoral tubes [5].
2. *Pneumatic Artificial Laryngeal Speech:* This device is coupled to the tracheostoma on the patient's neck. When the patient wants to talk, air from the lungs is sent into the device which causes a rubber reed to vibrate and produce sound. This sound is then directed into the patient's mouth via a plastic tube for modulation [4]. This device has a short learning time and is low-cost but it produces a reedy sound and is conspicuous. It also requires maintenance of the intraoral tubes. This method is generally seen as obsolete.
3. *Oesophageal Speech:* This type of phonation requires no external device. The upper part of the patient's oesophagus serves as an air reservoir. When the patient wishes to communicate, this air is ejected from the oesophagus causing the pharyngo-oesophageal segment to vibrate, thus producing sound which the patient can modulate using their mouth [4]. This form of artificial speech is less conspicuous than the electrolarynx. It also requires no batteries, is not mechanical sounding, and is not manual. There is a large variation in the success rate of this method (14-76% reported success rates [6]) with some users abandoning the technique due to heartburn and bloating from the swallowed air [7].

4. *Tracheoesophageal Speech:* This is currently the most popular restorative option. A hole during (primary oesophageal puncture) or after (secondary oesophageal puncture) the laryngectomy operation is created between the trachea and the oesophagus. A unidirectional valve is then fitted into the hole that allows air to enter the oesophagus from the trachea. When the patient wants to phonate, the tracheostoma is blocked and air travels from the trachea into the oesophagus. This causes vibration and a source of sound that the patient can modulate [4]. This method has a good success rate (95% of patients achieve effective conversational speech with 88% achieving good voice quality [8]). This method requires manual covering of stoma during speech and regular maintenance and replacement of the prosthesis.

Despite the different options above, a significant percentage, 7-40%, of patients never regain any form of speech [1].

A number of novel artificial larynxes have been proposed in recent literature. Research is being done into a new vibration source for Electrolarynxes by using PZT ceramics [9]. By studying the changes in magnetic field during speech, a system was developed to detect words from a volunteer that wore magnets on the lips, teeth and tongue [10].

### III. A NEW ARTIFICIAL LARYNX DESIGN

A new artificial larynx is currently being developed by the Biomedical Research Group at the University of the Witwatersrand, Johannesburg. The new artificial larynx will utilize dynamic measurement of tongue position to infer intended speech and will transmit these signals to an electronic unit for near-real-time speech synthesis. The dynamic tongue measurement will be achieved with the use of a LogoMetrix Electropalatograph system consisting of a palatometer and pseudopalate (LogoMetrix, Arizona). By using a combination of data from the palatometer and from other biological signals, it will be possible to infer what the patient is saying

#### A. The LogoMetrix Electropalatograph (EPG) System

The LogoMetrix system uses a pseudopalate to give dynamic, real-time information about tongue-palate contact during speech. This data is collected by the pseudopalate which has 118 gold touch sensors spread over the palate (see Fig. 2). Palate data is sampled at 100Hz. A pseudopalate is custom made for each user's mouth thus ensuring correct fit.

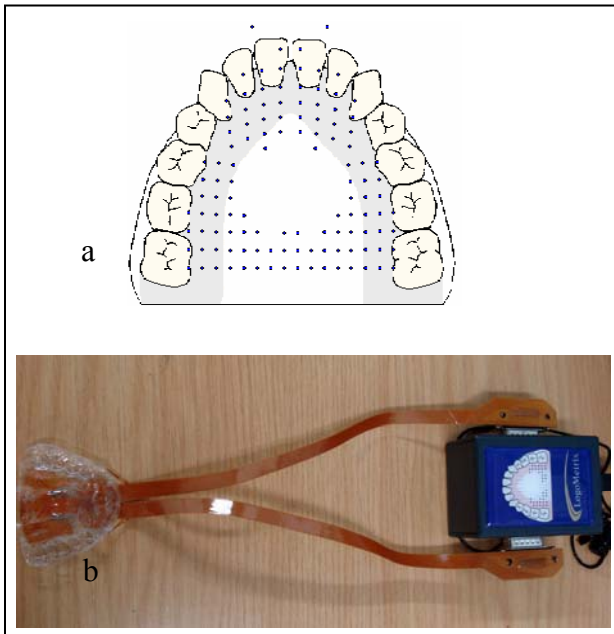


Fig. 2 a) Screen shot of the Logometrix system showing placement of sensors on the LogoMetric pseudopalate. b) The Logometrix system showing the pseudopalate and the palatometer

### B. Data Representation

Data for 200 common words were recorded using the pseudopalate system. The pseudopalate contact patterns were then separated from the audio signal. These signals were then formed into a 2-D space-time plot using MATLAB (see Fig. 3). In this way, the dynamic nature of the signals is preserved and standard image processing techniques can be applied.

### C. Image Recognition

Using a variety of image descriptors, unique information about the 2-D space-time images will be fed into a multi-layer perceptron (MLP) neural network. This will be trained to associate the various image descriptors with specific words in the vocabulary of the system. A HMM (Hidden Markov Model) may be used in order to anticipate the words and allow for a real-time output of the words. Other artificial intelligence and pattern recognition techniques will also be considered in the future.

### D. Speech Synthesis

The outputs from the MLP and HMM will be sent to a word synthesizer. Algorithms will be included to achieve a synthesized voice pattern as close to the patient's original sound as possible. This will be done by sending other physiological signals (such as jaw opening, lip movement etc.) to the synthesizer to modulate the output. According to [11] the magnitude of jaw-opening corresponds to increasing syllable magnitude and emphasis. In [12] it was shown that the fundamental frequency ( $F_0$ ) in vowel production decreases as jaw opening increases. Inhalation and exhalation may also be used for timing. This information will all be useful in making the tone and quality of the synthesized voice as real and lifelike as possible,

## IV. CONCLUSION

A plan for the development of a novel artificial larynx is given and current technology is briefly reviewed. It is hoped that this artificial larynx will be developed into a viable option for laryngectomy patients.

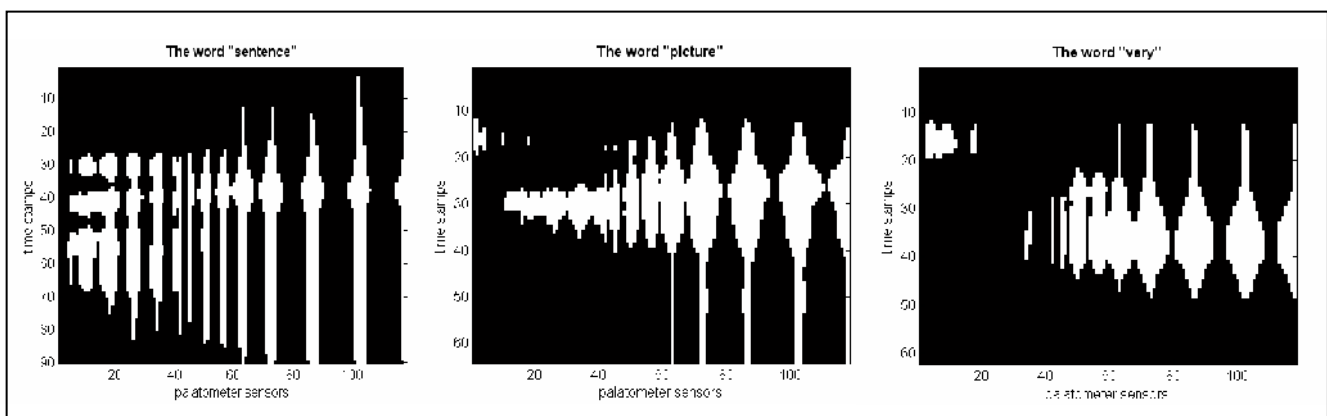


Fig. 3 Space-time representation for the words "sentence", "picture" and "very"

## REFERENCES

1. Takahashi H, Nakao M, Kikuchi Y and Kaga K, "Alaryngeal speech aid using an intra-oral electrolarynx and a miniature fingertip switch", *Auris Nasus Larynx*, Vol. 32, 2005, pages 157-162
2. Van De Graaf, K. M, "Human Anatomy", 6<sup>th</sup> ed. New York: McGraw-Hill Higher Education, 2002
3. Shoureshi R. A, Chaghajerdi A, Aasted C and Meyers A, "Neural-based Prosthesis for Enhanced Voice Intelligibility in Laryngectomees", *Proc. IEEE EMBS Conference on Neural Engineering*, March, 2003, pages 173-176
4. Ng M. L, Kwok C. I and Chow S. W, "Speech performance of adult Cantonese-speaking laryngectomees using different types of alaryngeal phonation", *Journal of Voice*, Vol. 11, No. 3, 1997, pages 338-344
5. Liu H. and Ng M, L, "Electrolarynx in voice rehabilitation", *Auris Nasus Larynx*, 34, 2007, pages 327-332
6. P Jassar, R J A England and N D Stafford "Restoration of voice after laryngectomy", *J R Soc Med*, 92, 1999, pages 299-302
7. Putney F.J. "Rehabilitation of the postlaryngectomized patient." *Ann Otol Rhinol Laryngol*, 67, 1958 pages 544-549
8. Op de Coul BMR, Hilgers FJM, Balm AJM, Tan B, van den Hoogen FJA, van Tinteren H. "A decade of postlaryngectomy vocal rehabilitation in 318 patients. A single institution's experience with consistent application of Provox indwelling voice prostheses." *Arch Otolaryngol Head Neck Surg*, 126, 2000, pages 1320-1328
9. Ooe K, Fukuda T and Arai F, "A New Type of Artificial Larynx Using a PZT Ceramics Vibrator as a Sound Source", *IEEE/ASME Transactions on Mechatronics*, Vol. 5, No. 2, June 2000
10. Fagan MJ, Ell SR, Gilbert JM, Sarrazin E and Chapman PM, "Development of a (silent) speech recognition system for patients following laryngectomy", *Med Eng Phys*, 2007, in press
11. Menezes C., Erickson D. and Fujimura O, "Contrastive Emphasis: Comparison of Pitch Accents with Syllable Magnitudes", *Proc. Of Speech Prosody*, France, April, 2002
12. Lim M, Lin E. and Bones P, "Vowel Effect on Glottal Parameters and the Magnitude of Jaw Opening", *Journal of Voice*, Vol. 20, No. 1, 2006, pages 46-54

Author: Megan J. Russell  
 Institute: School of Electrical and Information Engineering,  
 University of the Witwatersrand, Johannesburg  
 City: Johannesburg, 2050  
 Country: South Africa  
 Email: m.russell@ee.wits.ac.za

# Power Density Spectra of the Velocity Waveforms in Artificial Heart Valves

A.A. Sakhaeimanesh

Biomedical Engineering Group, Faculty of Engineering, University of Isfahan, Isfahan, Iran

**Abstract**— To find the possible frequencies induced by the vibration of the flexible membrane of the Jellyfish valve, power density spectra of the the valvular velocity waveforms were carried out.

Most of the spectral energy was contained in frequencies lower than 11 Hz and all spectra exhibited pronounced peaks which implied wave motions in the preferred frequency range.

Two distinct peak frequencies, 1.2 and 2.4 Hz, were observed downstream of the Jellyfish valve which qualified as the frequencies of fundamental harmony of the waveform velocity and one of its sub harmonics.

Effect of oscillation on elevating turbulent shear stresses through the jellyfish and St.Vincent valves has also been investigated. Laser Doppler Anemometry (LDA) was employed to determine the velocity and shear stress distributions at various locations downstream of the valves. Comparison between two valves revealed that at 0.5D downstream of the valves the magnitude of shear stresses in the Jellyfish valve were much higher than those of the St. Vincent valve at cardiac outputs of 4, 5.5 and 7 l/min.

The cause of high shear stresses in close proximity to the Jellyfish valve could be attributed to the oscillation of the membrane which in turn generated a wake downstream of the valve (in the core of valve chamber) and produced a wide region of disturbance further downstream. This resulted in further pressure drag and consequently, higher pressure drops across the valve and higher shear stresses downstream of the valve.

**Keywords**— Power density spectra, Heart valves, shear stresses, oscillation, LDA technique

## I. INTRODUCTION

Prosthetic heart valves are commonly used for replacement of natural valves, in ventricular assist devices (VADs) and total artificial hearts (TAHs). In artificial heart valves, the problems of haemolysis, platelet destruction, thrombus formation, perivalvular leakage, tissue over growth and endothelial damages are directly related to the fluid dynamic characteristics of flow past artificial heart valves ([1], [2], [3]). The presence of the prosthetic valve as a stenosis disturbs the blood flow and produces regions of high turbulent shear stresses, jetting and flow stagnation which, in turn cause pathological problems such as haemolysis and thrombosis. Blood cells in the region of

high shear stresses are exposed to a distribution of shear stresses over their entire membrane which causes the blood-cell membrane to be stretched and cause harmful changes to its essential function and eventually rupture the cells. Therefore, haematologically, it is highly desirable that a valve design shouldn't produce excessive turbulence, which may cause haemolysis ([2], [3], [4], [5]). In this study power density spectra of the valvular velocity waveforms were carried out and the effect of oscillation on elevating turbulent shear stresses and pressure drops through the jellyfish and St.Vincent valves has been investigated. Laser Doppler Anemometry (LDA) was employed to determine the velocity and shear stress distributions at various locations downstream of the valves.

## II. METHOD

Power density spectra of the valvular velocity waveforms were carried out. The fast Fourier transform (FFT) was implemented by FLOWare to calculate spectral estimate of the valvular velocity waveforms over the entire cycle to produce the power spectra density.

Mean spectral or power spectral density can be estimated as:

$$S_T(f)_{FFT} = \frac{T}{N^2} \left\{ \left| \sum_{i=1}^N u_i e^{j2\pi f t_i} \right|^2 \right\} \quad \&$$
$$\bar{S}_T = \frac{1}{M} \sum_{m=1}^M S_{Tm}$$

where  $S_T(f)$  is spectral estimate,  $\bar{S}_T(f)$  is mean spectral estimate or power spectral density,  $S_{Tm}$  is the spectral estimate  $S_T$  calculated from the mth blocks of data, M is the total number of blocks, T is duration of block during which N spherical samples occur and  $u_i$  is axial velocity component of  $i^{\text{th}}$  particle.

Two valves, namely Jellyfish and St.Vincent valves were selected. Jellyfish valve consist of a thin flexible membranous occluder made of Polyurethane and attached centrally to a rigid frame which have several spokes to protect against prolapse of the membrane.

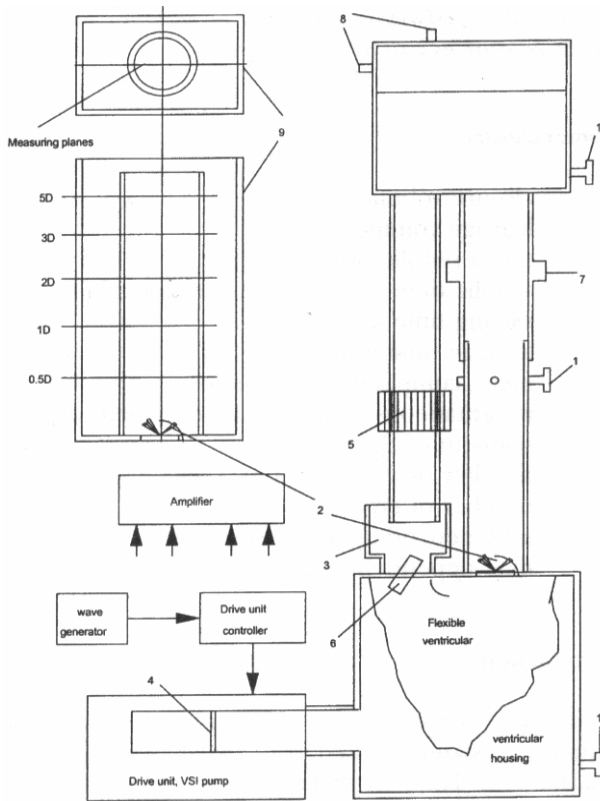


Fig. 1: Diagram of the pulse duplicator used in this study (not in scale), (1) ventricular, aortic and compliance pressure taps; (2) aortic valves; (3) mitral chamber; (4) pump piston; (5) adjustable resistance; (6) mitral valve; (7) electromagnetic flow meter probe; (8) air releaser and air pump; (9) index matching box.

A blood analogue fluid of water-saline solution was contained inside the ventricle chamber and was separated from the piston pump by the polymeric flexible ventricle. Blood analogue fluid provided a transparent and easy handling situation for velocity measurements with Laser Doppler Anemometry. In the inlet of the flexible ventricle chamber (mitral position) a Björk-Shiley tilting disc valve was installed.

An electromagnetic square-wave flowmeter, which was calibrated before measurement, was installed 8D downstream of the valve so that the instantaneous flow rates could be determined.

The pressure pulses were measured by three disposable and physiological blood pressure transducers in the left ventricle, downstream of the aortic valve and in the compliance chamber. Flow measurements were done at cardiac outputs of 4, 5.5 and 7 l/min.

A Dantec (Skovlunde, Denmark) two-component LDA system was used to determine the flow field at various locations downstream of the valve.

Data was collected in continuous mode over 100 to 200 cycles, depending on the collected data rate to ensure that at least 1000 samples would be collected during every 5 ms of the forward flow phase. After collecting data over complete cycles, data from each cycle is divided into 168 sample windows, each 5 ms duration. Then data belong to  $n$ th sample window of each cycle was compiled into  $n$ th bin and averaged to yield fluctuating and mean components. Mean components over 100 to 200 cycles (depending on data rate collection) can be manipulated into one representative cycle as follows:

$$S_n = \frac{\sum_{i=1}^n \sum_{j=1}^m S_{ij}}{nm}$$

where  $S_n$  is the mean component of  $n$ th sample window,  $S_i$  are the instantaneous components contained within a sample window,  $n$  is the number of data points in a sample window and  $m$  is the number of cycles measured.

All possible sources of error were carefully examined and having ensured that all recommendations concerning optical component alignment, seeding, filtering, signal processing, and calibration were carried out, the estimated measurement error of the mean velocity is  $\sim 3\%$  and that in the rms is  $\sim 7\%$ .

Diagram of mock circulatory system is shown in figure 1 and more details of it and LDA technique are given somewhere else ([6] and [7]).

### III. RESULTS AND DISCUSSION

#### A. Spectrum analysis

To find the possible frequencies induced by the vibrations of the flexible membrane of the Jellyfish valve, power density spectra of the valvular velocity waveforms were carried out. The random nature of the LDA prohibits sampling at regular and equi-spaced intervals which presents additional variability of the spectral estimator. In order to reduce this variability, spectral analysis of data was performed according to the method of direct Fourier transform of short blocks of data by FLOWare by implementing the re-sampling of the signals for data that were not collected in the dead time mode.

Important and useful information about dominant frequency peaks and preferred mode which exist in the flow

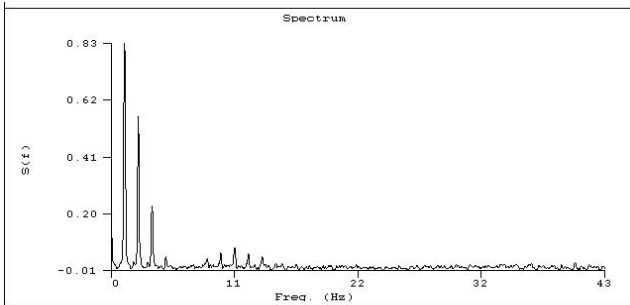


Fig. 2: power density spectra of waveform velocity estimated at 0.5D downstream of the Jellyfish valve in the region of Jetting at cardiac output of 6.5 l/min under pulsatile flow condition.

can be derived from the spectral information. Figures 2 and 3 show typical energy spectra measured at downstream locations of the Jellyfish and St. Vincent valves in the regions of stagnation and jetting at cardiac output of 6.5 l/min.

Most of the spectral energy was contained in frequencies lower than 11 Hz and all spectra exhibited pronounced peaks which implied wave motions in the preferred frequency range.

Two distinct peak frequencies, 1.2 and 2.4 Hz, were observed downstream of the Jellyfish valve which qualified as the frequencies of fundamental harmony of the waveform velocity and one of its sub harmonics.

Another distinct peak, between 3 and 4 Hz, with the power of 0.2 was observed at 0.5D of the jellyfish valve (figure 2). This frequency peak may qualify as the second sub harmonic frequency of the velocity waveform or, together with other higher frequency peaks, may qualify as the product of the membrane induced vibration peaks. The same results were found downstream of the Jellyfish valve at the other cardiac outputs. These are not presented here due to similarity in the results.

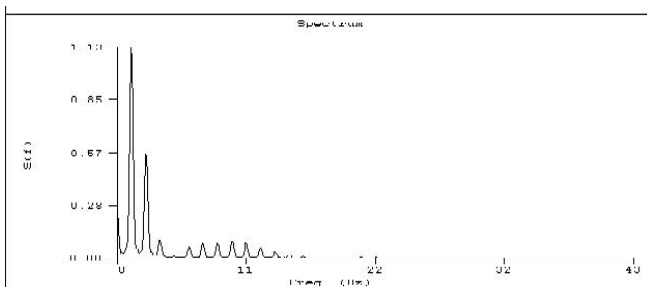


Fig. 3: power density spectra of waveform velocity estimated at 0.5D downstream of the St. Vincent valve in the region of Jetting at cardiac output of 6.5 l/min under pulsatile flow condition.

Behind the occluder and in the jetting region of the St. Vincent valve, two distinct peak frequencies of the fundamental and its sub harmonics of the velocity waveform motion were observed (figure 3). A third distinct peak frequency, between 3 and 4 Hz, which was observed at downstream of the Jellyfish valve did not exist at downstream of the St. Vincent valve. This can be described in terms of solidarity of the occluder of the St. Vincent valve, which does not induce vibration in the flow.

Comparison between two valves revealed that at 0.5D downstream of the valves the magnitude of shear stresses in the Jellyfish valve were much higher than those of the St. Vincent valve at cardiac outputs of 4, 5.5 and 7 l/min. Furthermore, at 3D and 5D downstream of the Jellyfish valve the magnitudes of shear stresses reduced dramatically to 6 and 1 N/m<sup>2</sup> respectively at cardiac output of 7 l/min. At 3 and 5D downstream of the St. Vincent valve, on the other hand, showed maximum shear stresses of the values of 49 and 17 N/m<sup>2</sup> respectively at the same cardiac output

It is hypothesized that the cause of high shear stresses in close proximity to the Jellyfish valve was due to the oscillation of the membrane which in turn generated a wake downstream of the valve (in the core of valve chamber) and produced a wide region of disturbance further downstream. This resulted in further pressure drag and consequently, higher pressure drops across the valve and higher shear stresses downstream of the valve.

This idea was supported by the results of shear stress (table 1) and pressure drop measurements (Figure 4). Maximum and mean shear stresses at 0.5D downstream of the Jellyfish valve were about twice those of the St. Vincent valve and pressure drops across the Jellyfish valve were up to 93 % higher than those of the St. Vincent valve under steady flow rates between 10 to 26 l/min.

The effect of oscillation can also be seen from the results of turbulence intensities. Maximum and mean turbulent intensities 0.5D downstream of the Jellyfish valve were as high as 781 and 273 % respectively at cardiac output of 7 l/min (605 and 212% at cardiac output of 5.5 l/min and 440 and 145 % at cardiac output of 4 l/min respectively). At 3D downstream of the valve, maximum and mean turbulent intensities reduced dramatically to 19 and 8 % respectively at cardiac output of 7 l/min. Reduction in turbulence, and consequently in shear stress estimation in the 3D and 5D downstream measuring planes of the Jellyfish valve, indicated that the effect of the membrane oscillation decayed beyond 1D at all cardiac outputs. The consequence of such a reduction in turbulence was low shear stress estimations in these measuring planes (less than 5 N/m<sup>2</sup>) at cardiac output of 7 l/min.

Table 1: Mean and maximum values of shear stresses, turbulent intensities and r.m.s of axial velocities of the Jellyfish and St. Vincent valves at cardiac outputs of 7 l/min at different downstream locations.

Distance, in diameter	Jellyfish valve			St. Vincent valve		
	0.5D	3D	5D	0.5D	3D	5D
Max shear stress, N/m <sup>2</sup>	155	5	1	88	49	21
Mean shear stress, N/m <sup>2</sup>	62	1	0.3	19.4	18.5	5.5
Max turbulent intensity, U %	781	19	17.7	118	37.8	33
Mean turbulent intensity, U %	273	8	6	47	24.5	17

Despite the eccentricity of the flow at downstream of the St. Vincent valve, turbulent intensities at close vicinity of the St. Vincent valve (0.5D) were much less than those of the Jellyfish valve (table 1). This can be attributed to the fact that solid occluder of the St. Vincent valve did not produce vibration in the downstream flow field which consequently resulted in low shear stress estimations.

At 3 and 5D downstream of the St. Vincent valve, eccentricity of flow still existed. This meant that flow become a fully developed beyond 5D. Maximum and mean turbulent intensities of the values of 33 and 17 % respectively were found 5D downstream of the St. Vincent valve. These were twice the values found at 5D downstream of the Jellyfish valve (17 and 6 %) at cardiac output of 7 l/min. Such a disturbed flow at 3 and 5D downstream of the St. Vincent valve produced maximum shear stresses in the range of 21-49 N/m<sup>2</sup> (compare to 1-5 N/m<sup>2</sup> in The Jellyfish valve). A summary of the data are presented in table 1 for cardiac outputs of 7 l/min. Similar trends and results were

found at mid acceleration and deceleration but are not presented here due to their similarity with the peak systole results.

## REFERENCES

1. Hanle D.D., Harrison E.C., Yoganathan, A.P., et al. (1989), In vitro flow dynamics of four prosthetic valves, a comparative analysis, *J. Biomechanics*, 22: 597-607.
2. Reul H., Van Son Jaques A.M., et al. (1993), In vitro comparison of bileaflet aortic heart valve prostheses- St. Jude Medical, CarboMedics, Modified Edwards-Durmedics and Sorin-Bicarbon valves. *J of Thoracic and Cardiovascular Surgery*, 106: 412-420.
3. Yoganathan A.P. (1995) Cardiac Valve prostheses, In: J.D. Bronzino (ed), *The Biomedical Engineering Handbook* (CRC and IEEE presses, 1847-1870).
4. Ruel H. (1983), In vitro evaluation of artificial heart valves., In: D.N. Ghista, O. Hamilton, (eds). *Advance in Cardiovascular physics* (Basel New York, Karger, 5)
5. Shim H.S., Lenker J. A. (1988) Heart valve prostheses, In: Webster J.G., (ed), *Encyclopedia of Medical device and instrumentation* (John Wiley and sons, Inc., 3: 1457-1473)
6. Sakhaeimanesh A.A., Morsi Y.S. (1999) Analysis of regurgitation, mean systolic pressure drops and energy losses for two artificial aortic valves. *Journal of Medical Engineering and Technology*, 23(2): 63-68.
7. Morsi Y. S., Sakhaeimanesh A. A (2000) Flow characteristics past jellyfish and St. Vincent valves in the aortic position under physiological pulsatile flow conditions. *Artificial Organs*, Volume 24(7): 564-574.
8. Bluestein D, Einav S (1994) A modified stability diagram of pulsatile flow through heart valves based on improved spectral estimations of LDA data, *American Society of Mechanical Engineers: Laser Anemometry, Advance and Application*, Volume 191: 125-133.

Author: A. A. Sakhaeimanesh  
 Institute: Biomedical Engineering Group, Faculty of Engineering,  
 University of Isfahan  
 Street: Hezar Jarib Street  
 City: Isfahan  
 Country: Iran  
 Email: sakhaei@eng.ui.ac.ir

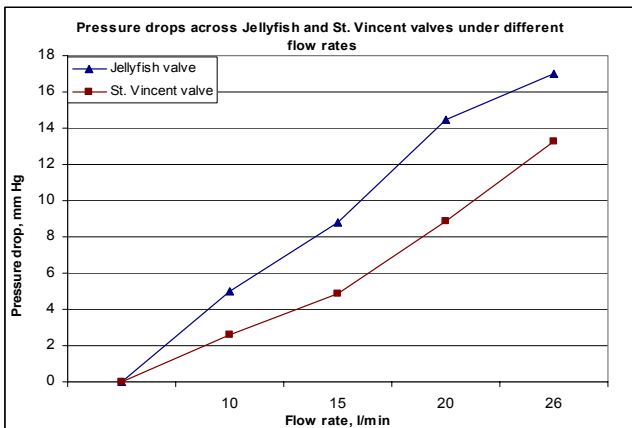


Fig. 4: pressure drops across the Jellyfish and St. Vincent valves under different flow rates.



# Development of a Generic Assistive Platform to Aid Patients with Motor Disabilities

F. Senatore<sup>1</sup>, D.M. Rubin<sup>1</sup> and G.J. Gibbon<sup>1</sup>

<sup>1</sup> School of Electrical and Information Engineering, The University of the Witwatersrand, Johannesburg, South Africa

*Abstract* — The development of a generic platform, which can assist patients suffering from a range of motor disabilities to perform everyday tasks is described. Methodologies were established, whereby the design could be made sufficiently flexible, that it could be programmed to suit people with a wide variety and with varying severity of motor disabilities, in terms of their needs and level of functional impairment. This needed to be achieved without redesigning the system for each person. Suitable sensors were chosen to detect the residual motor function of the disabled individual, while being non-invasive and safe for use. These sensors were connected to a signal selection and conditioning circuit and an analogue-to-digital converter (ADC). This served as an interface between the hardware and a stand-alone software application, developed to provide all the customisability and functionality for the system. The software application allowed the user to customise the digital signal processing of the various input signals, as well as allowing a user to calibrate the level at which the input from a particular sensor, triggered an output response. This helped ensure that only voluntary actions resulted in an output response. The software also facilitated the user customising the output function required. The proof-of-concept was tested by setting up the system to allow the user to operate a computer. By having volunteers with disabilities test the system, it was determined that the assistive platform was, in general, capable of satisfying various users' diverse requirements.

*Keywords* — customisable platform, assistive device, disabilities, sensors.

## I. INTRODUCTION

Physical disability can impose substantial individual and family burdens, as well as major economic consequences [1]. Physical disability may result in pain, and difficulty with motor control and speech. Examples of conditions that result in motor disability include cerebral palsy and spinal cord injury (SCI), resulting in the loss of central nervous system control of motor function. [2]. The range of resulting clinical manifestations include, but are not limited to, quadriplegia and paraplegia.

In many cases motor disorders are severely incapacitating, and the patient may not be able to perform the most basic of tasks. There is therefore a need to assist patients who suffer from these particular disabilities, in any way possible, to help them achieve a better quality of life and better social and professional integration.

The essential objective of this project was to develop a device (generic assistive platform) which could be customised to assist people with a fairly wide range of motor disabilities, to perform common tasks. This needed to be achieved without redesigning the system for each person. Most importantly the design had to be non-invasive and safe.

## II. DESIGN AND IMPLEMENTATION

The device design needed to behave as a stand-alone generic system, which could be adaptable to the end-user's requirements.

### A. The Input Stage

Suitable sensors were chosen for the system on the basis that they were **capable of detecting the residual motor functions of people with a diverse range of motor disabilities**, for use on the upper extremities of these individuals. For this study, the input sensors were restricted to the following:

1. *Movement sensors*: The Analog Device™ ADXL210 Dual-Axis Accelerometer [3].
2. *Touch sensors*: The QProx™ QT160D 6-Key Charge-Transfer QTouch™ Sensor IC [4].
3. *Blink/Wink sensor*: The Tash™ Self-Calibrating Auditory Tone Infrared (SCATIR) Switch [5].

These sensors were positioned to efficiently detect residual movements of the subjects. The placement of the sensors, for the purpose of this study, were restricted to sensing arm (dual-axis accelerometer) or finger movements (touch sensors), head and neck movements (accelerometer) and blink/wink and/or eye-brow movements (SCATIR switch).

### B. The Signal Selection and Conditioning Stage

Signal conditioning and the sampling rate constituted the primary hardware concerns for reading the input signals from the input sensors mentioned above [6]. The performance of the analogue to digital conversion (ADC) needed to be taken into account when designing the signal conditioning unit. This was needed to determine the characteristics of the anti-aliasing filter [7]. This particular design utilises a

single signal conditioning unit, which provided the analogue filtering and anti-aliasing, as well as the amplification of the various input signals which were connected to multiple input channels. The input stage, coupled with the signal selection and conditioning stage are illustrated in Figure 1 below, following the general scheme of [8].

C. The Data Acquisition (DAQ) and Control Stage

This stage centered on the A/D conversion, which behaves as an interface between the software application and the analogue signals outputted from the signal conditioning unit. This stage also determines the accuracy and predictability of the input signal, required to produce the correct output action at a specific time, as illustrated in Figure 2.

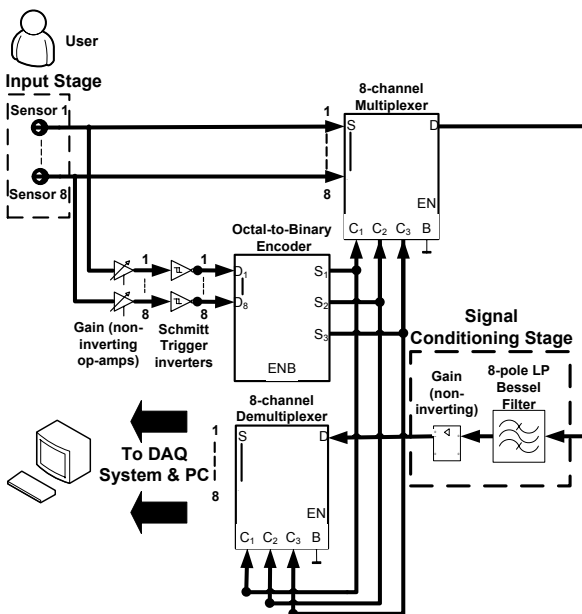


Fig. 1 Input, signal selection and signal conditioning stages

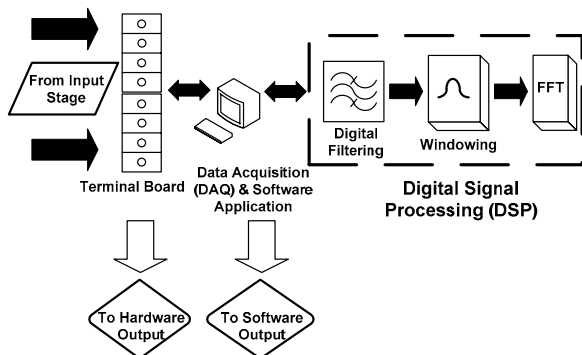


Fig. 2 The data acquisition (DAQ), DSP and Software Application Stages

D. The Software Design Stage

This involved the development of a stand-alone "Generic Assistive Software Application", which would provide most of the customisability to the system. The software application allows a user to customise the digital signal processing of the various input signals, by allowing the user to alter the digital filtering/windowing behaviour as well as certain timing parameters. The system was calibrated to achieve triggering of an output response only when the input occurs above a specified peak magnitude within a pre-defined frequency range. The basic functionality diagram for the application is illustrated in Figure 3.

E. The Output Stage

The system should be customisable in terms of controlling different environments (hardware/software). The device had been designed to control the output using the "Generic Assistive Software Application". To control the hardware devices, the user would need to customise the signal type and amplitude required to operate these devices. These signals may be output in analogue and/or digital form via the DAQ card. The output software applications, to be controlled by the system, must be written such that they interface with the generic software application.

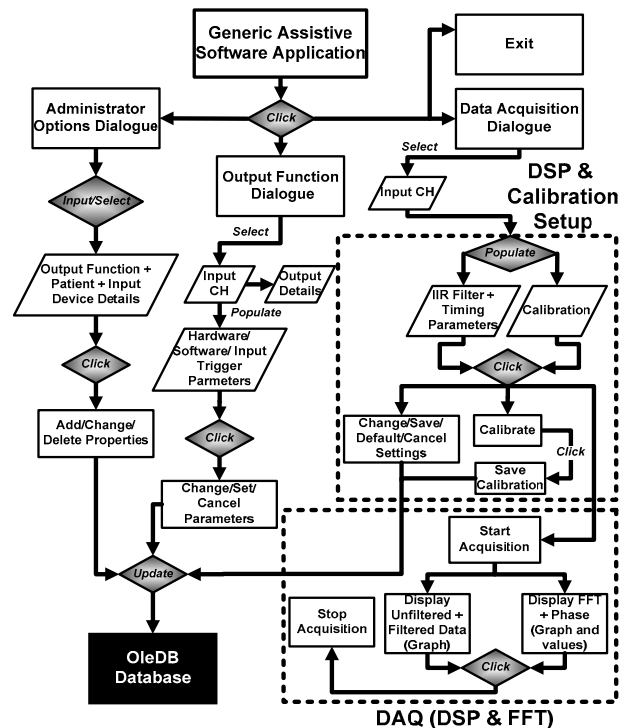


Fig. 3 Simplified Functionality Diagram of the Software Application

F. The Design Implementation and Functionality Testing

This formed the final stage of the design. The hardware components were implemented on PCB circuits. Testing was performed throughout the design process, on the separate components constituting the system. The design was finally concluded by performing functionality testing and validation on the full system, while first ensuring that it is non-invasive and safe for use by all prospective subjects.

III. TESTING AND RESULTS

A. The Testing Procedure

A total of 5 volunteers participated in the study and were chosen with different classifications and levels of disability, as shown in Table 1 below.

The subjects performed a set of tests, by utilising all or some of the input sensors provided and were selected based on their suitability for the subjects' retained functions, which may have been residual in nature. The volunteers were subsequently asked to answer a questionnaire, concerning their assessment of the performance and potential usefulness of the system. The only subject information recorded was the extent of the volunteers' motor disabilities. The topics covered are summarized in Table 2 and are discussed in more detail in the results section which follows.

B. Results

Figure 4 shows the average scores given by the volunteers. The questions related to the ease of use, comfort level, performance and predictability, and fatigue levels. Figure 5

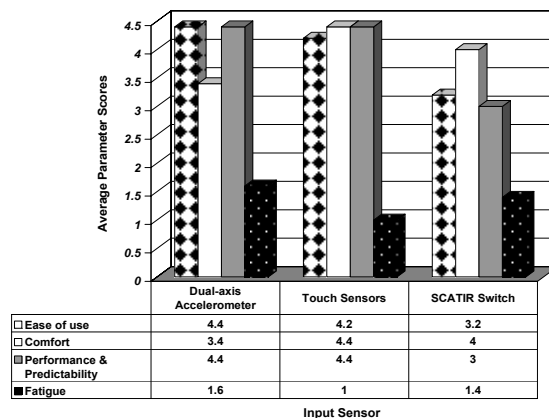


Fig. 4 Average parameter scores relating to the input sensors

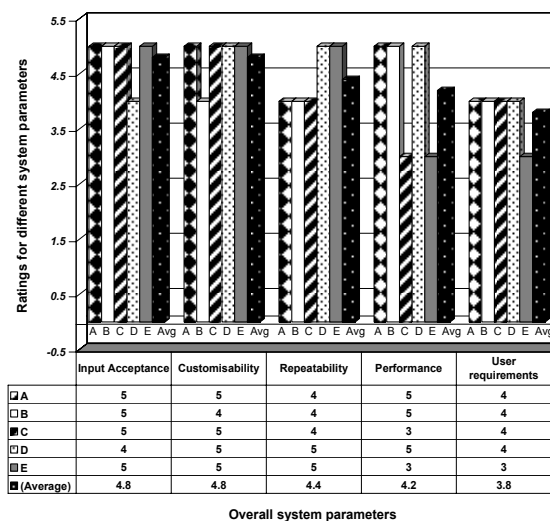


Fig. 5 System parameters used for the overall assistive system

Table 1 Subject Classification and Level of Lesion

Subject	Disability
Subject A	Quadriplegic – C4/C5
Subject B	Muscular Dystrophy
Subject C	Quadriplegic – C6/C7
Subject D	Cerebral Palsy
Subject E	Quadriplegic – C5/C6

Table 2 Questions asked during the testing phase

Input Sensor Characteristics	Overall System Characteristics
a) Ease of Use	e) Input Acceptance
b) Comfort Level experienced	f) Customisability
c) Performance & Predictability	g) Repeatability
d) Fatigue experienced	h) Performance
	i) User Requirements

shows the various system parameters, which have been used to determine the viability of the overall assistive system. All scores for both graphs were rated out of 5.

C. Analysis of Results

Input Sensor Characteristics

It is evident from Figure 4, that all the sensors were relatively *easy to use*, with the dual-axis accelerometer achieving the highest average score of 4.4. The touch sensors and SCATIR switch scored well with mean scores of 4.2 and 3.2 respectively. The touch sensors and SCATIR switch were the most *comfortable* sensors to use, with mean scores of 4.4 and 4 respectively. The accelerometer was the least comfortable to use, averaging 3.4. From the data in Fig. 4, it

appears that the ease of use and comfort levels show some correlation.

Good to excellent results were scored for the *performance and predictability*. The accelerometer and touch sensors scored the highest, with both averaging 4.4. The SCATIR switch scoring the lowest averaging 3. Fatigue was measured on an inverted scale where the least fatigue was 1 and the most was 5. Generally low levels of fatigue were experienced. The touch sensors scored the best with a perfect average of 1, meaning that no fatigue was experienced by the users, throughout the duration of testing. The SCATIR switch and dual-axis accelerometer also scored well, with overall mean scores of 1.4 and 1.6 respectively.

Comparison of the fatigue with the performance and predictability levels, suggests that they are correlated. This is especially the case with the SCATIR switch, which was the least predictable of all the sensors used. In this case, the subjects were required to perform winking actions multiple times to activate an output response, which increased the level of fatigue experienced by the facial muscles. By comparing the input sensor parameters, one can determine that the **touch sensors** averaged the best, of all the sensors used.

#### *The Overall System Characteristics*

Figure 5 demonstrates that the system accepted all or most of the input sensors as required, with an overall average score of 4.8, for “*Input acceptance*”. “*Customisability*” determines the customisability of the system, in terms of providing a specific output for a specific and voluntary input. This scored very high, with a mean score of 4.8. A good mean score of 4.4 was given for the system *repeatability*, meaning that the system is capable of repeating specific tasks multiple times and with fair accuracy.

The system *performance* scored a mean of 4.2. This score could be improved by implementing more efficient coding methods and by using a less graphics-intensive interface (GUI). The “*User Requirements*” determined whether the system could potentially meet the various users’ specific requirements. This scored the lowest of the overall system parameters with a mean score of 3.8, as only a few output function examples were provided for proof of concept.

#### *Suggested System and Design Improvements*

More useful technologies, which would better suite the requirements of the various users, could include the use of an eye-gazing sensor, tracker-ball mouse and a voice activation system and can be used by a wide variety of disabled people; even those suffering with severe motor deficiencies.

## IV. CONCLUSIONS

The essential research objective was the development of a single generic assistive platform, which could accommodate various patients suffering from a wide range of motor disabilities and fairly diverse requirements. This was established by assessing and characterizing a limited set of motor disabilities, and thereafter developing the system to maximize the retained motor function of the disabled individual.

Methodologies were developed to establish whether the design could be made sufficiently flexible to accommodate people in terms of their needs and level of motor disability. This needed to be achieved without re-designing the system for each person. It was concluded that the system was capable of satisfying a range of users’ diverse requirements, thereby establishing feasibility for further research.

## ACKNOWLEDGMENT

I would like to thank all of the volunteers, and Mr. Vincent Gore for his advice and assistance on various issues relating to this project.

## REFERENCES

1. S. J. Church, “Knowing About Disabilities,” in *The Student With a Physical Disability in the Regular Classroom: A Handbook for the Classroom Teacher and School Counsellor*, SSTA Research Center Report No. 91-05, SSTA Research Center, 1991.
2. I. Bromely, *Tetraplegia and Paraplegia - A Guide for Physiotherapists*. Edinburgh: Churchill Livingstone, fifth ed., 1998.
3. “Low Cost  $\pm 2g/ \pm 10g$  Dual Axis iMEMS R Accelerometers with Digital Output - ADXL202/ADXL210,” at <http://www.analog.com>.
4. “QProx™ QT160/QT161 6 Key Charge-Transfer QTouch™ Sensor IC,” at <http://www.qprox.com>.
5. “SCATIR Switch User Guide,” June 2005 at <http://www.tashinc.com>.
6. R. J. Hansman Jr., “Characteristics of instrumentation,” in *The Measurement Instrumentation and Sensors Handbook*, CRC Press LLC, 2000.
7. R. Jamal and R. Steer, “Filters,” in *The Measurement Instrumentation and Sensors Handbook*, CRC Press LLC, 2000.
8. P. Horowitz and W. Hill, *The Art of Electronics*. Trumpington Street, Cambridge: Cambridge University Press, second ed., 1997. pp 2-54.

Address of the corresponding author:

Author: Franco Senatore  
 Institute: School of Electrical & Information Engineering,  
 The University of the Witwatersrand Johannesburg  
 Street: Private Bag 3, 2050  
 City: Johannesburg  
 Country: South Africa  
 Email: f.senatore@ee.wits.ac.za

# Usability Evaluation of Three Unilateral – Propelled Wheelchairs for Hemiplegic Patients

K.H. Tsai<sup>1</sup>, C.Y. Yeh<sup>2</sup>, H.C. Lo<sup>3</sup>, L.T. Chang<sup>4</sup>, J.S. Lee<sup>5</sup>, C.T. Lee<sup>1</sup>

<sup>1</sup> Graduate Institute of System Engineering, National University of Tainan, Taiwan, ROC

<sup>2</sup> School of Physical Therapy, Chung Shan Medical University, Taiwan, ROC

<sup>3</sup> Institute of Biomedical Engineering, National Cheng Kung University, Taiwan, ROC

<sup>4</sup> Department of Childhood Education and Nursery, Chia Nan University of Pharmacy and Science, Tainan, Taiwan, ROC

<sup>5</sup> Department of Computer Science and information Engineering, National University of Tainan, Taiwan, ROC

*Abstract* — Most hemiplegic patients use the unaffected arm and leg to propel wheelchair. The asymmetrical forces may cause the wheelchair to stray toward the affected side on level surface, and even cause danger on a slope. Although a variety of designs from mechanical approach have been developed to improve propulsion efficiency and reduce injuries, such as hand-lever drive and crank propulsion, most of them were just designed for users having healthy upper limbs. The purpose of this study was to evaluate the usability and the physiological responses of each of the two new wheelchairs comparing with a commercial two-handrim propelled wheelchair at a rehabilitation center.

Two newly designed wheelchairs (ankle-propelled wheelchair (APW), knee-propelled wheelchair (KPW)) were recruited and compared with a commercial two-handrim propelled wheelchair (TPW). 15 stroke patients were recruited from the rehabilitation center of Chung Shan Medical University, Taichung, Taiwan. Subjects propelled the three wheelchairs along an oval-shaped pathway and videotape was made during test for analysis. The parameters, including total propelling time, deviation frequencies, deviation percentage, physiological cost index (PCI), maximum VO<sub>2</sub> (VO<sub>2</sub>max), and rating of perceived exertion (RPE) were measured and compared among the three types of wheelchair.

The results show that KPW had the best results in terms of performance evaluation among the three wheelchairs no matter in controllability, cardiopulmonary responses, or RPE. However, the gear ratio of force transmitting system of KPW was fixed, and some patients felt that the propulsion was heavy when starting KPW. It was more suitable and comfortable for hemiplegic patients to use KPW than to propel TPW and APW. If the adjustment of KPW were properly improved, it would be a comfortable device for movement for hemiplegic patients.

*Keywords* — wheelchair, leg-propulsion, oxygen consumption, stroke, rehabilitation

## I. INTRODUCTION

A wheelchair is important for people with hemiplegia to improve their mobility and avoid accidents during recovery. In general, most patients with hemiplegia use only their unaffected arm and leg to propel a wheelchair. To facilitate the propulsive pattern, the wheelchair's leg rest on the patient's

unaffected side is usually removed, and the patients are expected to stamp their unaffected foot on the ground to produce propulsive force and direct the wheelchair. Asymmetrical forces generated by this arrangement, however, may cause the wheelchair to stray toward the affected side on a level surface, which may be dangerous on a slope [1].

Leg control is another means of wheelchair propulsion. It should be more effective to propel a wheelchair with one's legs than with one's arms, because the leg muscles are stronger. Leg propulsion requires less than half the effort of arm propulsion for individuals with spinal cord injuries [2]. Furthermore, using the legs to propel a wheelchair increases the circulation and conditioning of the lower extremities for wheelchair users.

There have been many excellent studies [1, 3-4] evaluating the performance of manual wheelchairs for patients after stroke, but none have provided data on specialized wheelchairs for hemiplegia. We recently developed 2 types of unilaterally operated wheelchairs that allow patients with hemiplegia to move the wheelchair forwards and backwards and to make turns, using their unaffected lower legs [5]. The purpose of the present study was to evaluate the controllability and physiological responses of each new wheelchair and to compare them with those from a commercial 2-handrim propelled wheelchair.

## II. METHODS

### A. Wheelchairs

Two-hand-rim propelled wheelchair (TPW). The TPW was a commercial wheelchair (Sunrise Medical Inc., Torrance, CA, USA) with 2 hand-rims on the patients' unaffected side. The patient uses the unaffected hand to propel ambilateral wheels by pushing the 2 handrims.

Ankle-propelled wheelchair (APW). The patient uses the unaffected arm to turn the wheel on the unaffected side, and uses the unaffected foot to turn the other wheel by stepping on a modified footrest with the foot and ankle joint.

Knee-propelled wheelchair (KPW). The KPW uses a propulsion lever and a pedal to translate knee flexion and extension into wheelchair movement. To use this wheelchair the patient places the unaffected leg on the pedal and then extends the lower leg. The unaffected hand controls the direction of wheelchair by steering a handle module connected to the castors.

*B. Subjects*

A total of 15 stroke patients (8 men, 7 women, age range 45–73 years) (Table 1) were recruited from the Subsidiary Rehabilitation Center of Chung-Shan Medical University. All subjects signed an informed consent approved by the medical ethics committee of Chung-Shan Medical University. All the patients had right-side hemiplegia and were excluded if they had significant respiratory or musculoskeletal morbidity.

*C. Experimental protocol*

The field test included 2 phases. In phase 1 the patients propelled themselves forwards anticlockwise along an oval pathway 1 metre wide and 30 m from start to finish. The first lap was completed when the patients arrived at the starting position. In phase 2, after circumrotating the patients propelled themselves clockwise on the same pathway back to the start position. All patients were instructed to propel each wheelchair as fast as they could during the test.

For the controllability evaluation, a video record was made while patients were performing the tasks. Then the physical therapists watched the videos at least twice and calculated the total propulsion times, deviation frequencies, and deviation times for the 3 wheelchairs in the pathway. The definition of “deviation” was “both the castor and rear wheel of one side ran over the pathway boundary”, and the “deviation percentage” was defined by dividing the deviation time by the total propulsion time.

Table 1 Characteristics of the subjects

Item	
Age (years), mean (SD)	53.0 (9.5)
Gender (male/female)	12/3
Height (m), mean (SD)	1.6 (0.05)
Weight (kg), mean (SD)	68.9 (14.4)
Side of stroke (right/left)	15/0
Dominant side (right/left)	15/0
Onset time (month), mean (SD)	19.3 (9.7)
Smoking history (yes/no)	1/14
Wheelchair experience (yes/no)	15/0

For cardiopulmonary response measurements, before the test, the heart rate (HR, beats/min) and oxygen consumption (VO<sub>2</sub>, ml/min/kg) were measured for 2 min as rest HR and VO<sub>2</sub>, respectively. The VO<sub>2</sub> in the last 30 sec of the exercise test was measured. The physiological cost index (PCI, beats/m) was obtained by subtracting the HR at rest from the HR during the last 30 seconds and dividing the result by the average speed of the wheelchair [6]. In addition, a rating of perceived exertion (RPE) was used to measure subjective exertion at the end of each test and to compare the efforts during propulsion.

Statistics Package for the Social Sciences (SPSS, version 12; SPSS Institute, Chicago, IL, USA) was used for all statistical analysis. All parameters were compared between the 3 types of wheelchair using a 1-way ANOVA with repeated measures. A Scheffe post hoc test was used to detect statistically significant differences in the dependent variables across the tests. Statistical significance was set at  $p < 0.05$ .

III. RESULTS

All patients completed the 60-m tasks using the 2-hand-rim propelled wheelchair TPW, APW and KPW, and none reported any adverse reactions to the tasks. It took the patients significantly less time to propel the KPW than the TPW and APW around the test oval (Table 2). That means that the KPW was significantly faster than the TPW and APW.

The deviation frequencies of KPW took significantly less ( $p < 0.05$ ) than that of TPW and APW. Regarding deviation percentage, all 3 types of wheelchair revealed a higher percentage in the same pathway (Table 2). The deviation percentage of KPW appeared to be significantly lower than that of TPW and APW. The results meant that the APW and TPW went over the boundary more easily than the KPW.

Table 2 Results of controllability and cardiopulmonary response of the three types of wheelchair during the field test

	TPW	APW	KPW	<i>p</i>
Controllability				
Propulsion time (seconds)	369.1(86.8)	331.0(92.0)	163.2(41.6)	0.00*
Deviation frequency (beats)	19.4(5.9)	12.8(4.5)	4.2(1.9)	0.00*
Deviation percentage (%)	30.9(12.2)	26.0(18.5)	14.2(7.2)	0.06
Cardiopulmonary response				
VO <sub>2</sub>	5.8(2.6)	5.8(1.6)	4.8(1.7)	0.6
PCI (beat/m)	1.51(0.59)	1.35(0.56)	0.70(0.29)	0.03*
RPE	15.1(1.7)	14.8(1.6)	10.8 (1.5)	0.00*

There were no significant differences in  $VO_2$ , but the mean value of the  $VO_2$  of the KPW was the lowest of the 3 types of wheelchair (Table 2). The KPW took significantly ( $p < 0.05$ ) less PCI than the TPW and APW. The level of RPE of the KPW was significantly ( $p < 0.05$ ) less than that of the TPW and APW. These results indicated that the KPW was significantly easier to control and significantly more efficient than the other

#### IV. DISCUSSION

Type TPW. The most severe problem with the TPW was that it required more power to propel than our patients after stroke were able to provide. Insufficient arm strength may be more likely to result in upper extremity injuries in patients after stroke than in wheelchair users who have more strength and who are able to use both arms to propel the wheelchair. The second significant weakness of the TPW was direction control. The strong points of this wheelchair, however, are that it is foldable, portable and easy to get in and out of.

Type APW. The most serious problem with the APW was the propulsion skill required. Patients had to use the unaffected arm to propel the wheel on that side, and also use the unaffected foot to propel the wheel on the other side by pedaling a specialized footrest with their foot and ankle joint. The advantages of this design were that both the unaffected arm and leg could be used to propel the wheelchair, thus providing more power than possible with a TPW. However, most patients were unable, even after 3 weeks' training, to master the mode of propulsion sufficiently to allow them to operate the APW. Another design weakness of the APW was its loss of energy caused by the 4-bar linkage system on the drive mechanism. This energy loss was noticeable for most patients.

Type KPW. Hemiplegic patients using the KPW moved faster than those using the TPW and APW. This indicated that it was more efficient to propel the KPW than the TPW with only one arm and the APW with the unaffected hand and leg. Although both the APW and KPW require legs to propel them, the major muscles and joints used during propulsion are different. Muscles in the lower leg are used for the APW; however, muscles in both the lower and upper legs are used for the KPW. Furthermore, the controllability of the KPW was superior to that of the other 2 wheelchairs because the deviation frequency and deviation percentage were much lower. It was easier for patients with hemiplegia to control the KPW using a steering lever than using the unaffected leg and arm to control wheel speeds and direc-

tion adjustment while propelling the APW. On the other hand, some details of the KPW should be modified. A variable gear ratio is desirable. The ratio of the pedal and rear wheel rotation was fixed, and some patients felt that it took too much heavy pedalling to start the KPW.

#### V. CONCLUSION

The KPW gave the best performance evaluation results of the 3 wheelchairs tested in the present study. With suitable and necessary adjustments, the KPW would be suitable for use by patients with hemiplegia.

#### ACKNOWLEDGMENT

The authors thank the patients and staff who participated in this project. This research was supported by grant NSC 91-2614-E-218-001 from the National Science Council, Taiwan.

#### REFERENCES

1. Kirby RL, Ethans KD, Duggan RE. Wheelchair propulsion: descriptive comparison of hemiplegic and two-hand patterns during selected activities. *Am J Phys Med Rehabil* 1999; 78: 131–135.
2. Stein RB, Chong SL, James KB, Bell GJ. Improved efficiency with a wheelchair propelled by the legs using voluntary activity or electric stimulation. *Arch Phys Med Rehabil* 2001; 82: 1198–1203.
3. Pomeroy VM, Mickelborough J, Hill E, Rodgers P, Giakas G, Barrett JA. A hypothesis: self-propulsion in a wheelchair early after stroke might not be harmful. *Clin Rehabil* 2003; 17: 174–180.
4. Kirby RL, Adams CD, MacPhee AH, Coolen AL, Harrison ER, Eskes GA, et al. Wheelchair-skill performance: controlled comparison between people with hemiplegia and able-bodied people simulating hemiplegia. *Arch Phys Med Rehabil* 2005; 86: 387–393.
5. Tsai KH, Yeh CY, Lo HC. Applications of concurrent systematic design on assistive technology – a new wheelchair design for stroke patients. *FMBE Proceedings EMBEC '05, 3rd European Medical & Biological Engineering Conference* 2005; 11: 28.
6. MacGregor J, editor. The Objective measurement of physical performance with long-term ambulatory physiological surveillance equipment (LAPSE). *Proc 3rd Int Symp on Ambulatory Monitoring*. London: Academic Press; 1979, p. 29–39.

Author: Kueng Horng Tsai  
 Institute: Innovation Incubation Center  
 National University of Tainan  
 Street: 33, sec.2, Shu-Lin st  
 City: Tainan  
 Country: Taiwan ROC, 7005  
 Email: tsai kh@mail.nutn.edu.tw

# The Effect of Gait Speed on Pre- and Postoperative Analysis of Gait Parameters after Total Knee Arthroplasty

R. Ullmann<sup>1</sup>, M. Hildebrand<sup>2</sup> and S. Leuchte<sup>1</sup>

<sup>1</sup>Dept. of Sports, Institute of Media, Communication and Sports, Martin-Luther University Halle-Wittenberg, Germany

<sup>2</sup>Dept. of Orthopedic Surgery, Martin-Luther-University Halle-Wittenberg, Germany

**Abstract** — The objective of the study is to analyse the effect of gait speed on pre- and postoperative gait parameters after the implantation of total knee arthroplasty. The second objective is to compare the gait pattern of patients with total knee arthroplasty to the gait pattern of healthy control subjects.

43 patients with symptomatic unilateral gonarthrosis had undergone a total knee arthroplasty with a midvastus surgical approach. Gait analysis with various gait speeds took place prior to, as well as 6 and 13 weeks after surgical intervention. The motion of the knee joint, the spatial-temporal parameters of the gait cycle and the vertical ground reaction forces of the operated knee are discussed.

13 weeks after surgery, cadence and gait speed display a significant increase. Single support does not change significantly 6 weeks after the operation, as a sign of the lasting reduction of the physical abilities. A significant increase of single support time occurs 13 weeks after the surgical intervention. 13 weeks after the total knee arthroplasty, knee joint motion in the sagittal plane shows a remarkable improvement of maximum flexion at swing phase. The follow-up shows that the loading rate of the operated side is simultaneously reduced after 13 weeks, and could be interpreted as a relieving posture. Influence on gait speed shows changes in kinetic and kinematic parameters. SF-36 questionnaire indicates significant improvement in dimension of bodily pain after inpatient treatment. The results of the age-matched control group were not yet achieved 13 weeks after the total knee arthroplasty.

Restrictions of knee joint motion and physical capacity after the total knee arthroplasty follow from long-standing relieving posture as a result of weakened muscles, shortened sinews and ligaments („quadriceps avoided gait“).

**Keywords** — gait analysis, total knee arthroplasty, gait speed, knee

## I. INTRODUCTION

The rapid development of knee arthroplasty particularly results from so called minimally invasive surgical approaches, with less damage to soft tissues and muscles in combination with newly developed prosthesis. This makes early functional rehabilitation possible for patients after total knee arthroplasty. Kinetic, kinematic and spatial-temporal parameters are

essential in order to characterise gait patterns. Complex gait analysis presents itself as a tool to evaluate the rehabilitation process after orthopedic surgery.

In previous studies, patients walked at a self-selected walking speed on level ground. Speed-related changes in biomechanical parameters of gait have to be considered, because most of the biomechanical parameters depend on gait speed [1, 2]. The objective of the present study is to analyse the effect of gait speed on pre- and postoperative gait parameters in patients with total knee arthroplasty. The second objective is to compare the gait pattern of the patients with the gait pattern of the control group.

## II. MATERIALS AND METHODS

In the prospective current study 43 patients ( $62,7 \pm 8,1$  years, body mass index  $28,9 \pm 3,43$ ) with unilateral symptomatic gonarthrosis were investigated prior to, as well as 6 ( $6,3 \pm 0,6$ ) and 13 ( $13,2 \pm 1,0$ ) weeks after unilateral knee arthroplasty (Journey<sup>®</sup>, Smith & Nephew). The inclusion criteria for patient selection were primarily osteoarthritis of one knee without painful symptom of another joint in the lower limbs and the ability to walk without helping devices. The exclusion criteria were cardiovascular diseases or illnesses of the nervous system, gait influencing diseases or injuries.

The control group consists of 20 healthy subjects matching the age of patients ( $59,6 \pm 6,2$  years, body mass index  $25,6 \pm 2,5$ ). The gait data of the reference group were collected once. An informed written consent was obtained from all patients.

The first quantitative gait analysis was performed by asking the patients to walk at their own natural speed on a level walkway. Then the patients walked with different gait speeds (70 (slow), 90 (normal) and 110 (fast) steps per minute). The frequency was given by a metronome. The kinematics of knee were registered with a computerized motion analysis system (VICON system, 200 Hz), using 6 infrared video cameras that recorded the trajectories of the passive reflective markers. Ground reaction forces were measured with 2 force plates (AMTI, 1000 Hz) which were embedded in the walkway.



The passive markers were attached on the anterior and posterior superior iliac spines, thigh, lateral epicondyle, shank, lateral malleolus, heel and the second metatarsal head in order to measure the kinematics of knee. The marker protocol was based on the Helen-Hayes model. Data on knee angle and ground reaction force were simultaneously obtained from 10-12 walk trials for each limb. SF-36 Health Survey questionnaire for the measurement of subjective pain and function was evaluated.

An analysis of variance (ANOVA) was conducted to study the effects of follow-up. Student's *t*-test was used to find out if patients reach the outcomes of the control group.  $p < 0.05$  was considered as significant.

### III. RESULTS

Before the implantation of the knee prosthesis, 74% of the patients were able to walk slowly (70 steps/minute) and 47% could walk at normal gait speed (90 steps/minute). 6 weeks after the surgery, the gait analysis was accomplished by 77% of the patients at slow gait speed and by 58% of patients at normal gait speed. 13 weeks after the surgery, all the patients could walk at slow gait speed on the walkway without problems. 67% of the patients were able to walk at 90 steps/minute. All healthy subjects and four patients (preoperative) were able to walk on the walkway at a frequency of 110 steps/minute, defined as the maximum frequency in the study (Fig. 1). Because of the small number of patients, this frequency is not discussed in this paper.

In the present paper, the operated side of the knee and the reference data are compared at free walking speed. 6 weeks after total knee arthroplasty, patients tended to have slower velocity (Fig. 2), less cadence, restricted extension in the terminal stance phase and flexion in the mid-swing phase of the knee joint, diminished ground reaction forces and loading- and push-off-rate than before the implantation of knee prosthesis, and compared to the normal group. The

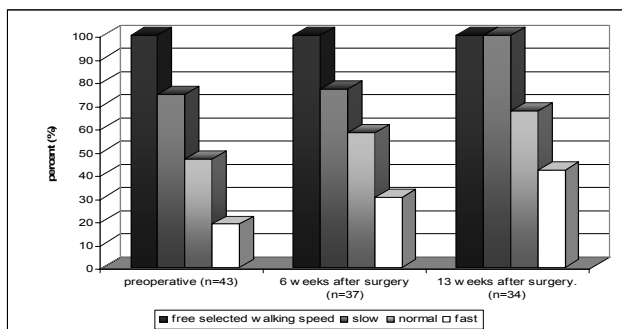


Fig. 1 Free walking speed and possible step frequencies of the patients

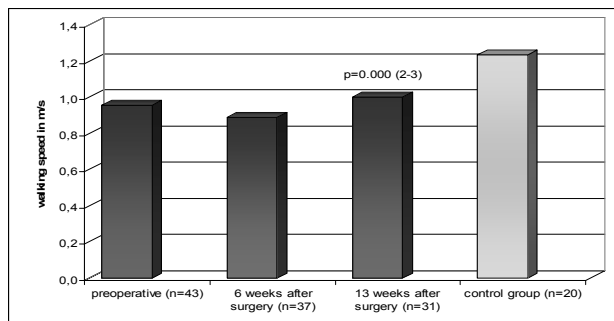


Fig. 2 Development of free selected walking speed of the patients and the control group

peak values of the vertical ground reaction forces barely reached body weight. Patients also demonstrated a shorter single support phase of the involved leg. Considering mean-values 13 weeks after total knee arthroplasty, patients improved in every parameter except for mid-stance peak flexion. In spite of this, the parameters between operated side and reference data differ significantly 6 and 13 weeks after the surgery. (Tab.1).

#### A. Temporal-spatial parameters

By analysing the changes of free walking speed and cadence in the course of time, it shows that the decisive improvement occurs between 6 and 13 weeks ( $p=0.000$ ,  $\eta^2=0.434$ ). Since frequency was controlled by means of a metronome, there are no statistical differences between the separate measuring times in slow (70 steps/minute) and normal (90 steps/minute) gait speed. Single support changes significantly in the course of time ( $p=0.004$ ,  $\eta^2=0.178$ ). Single support does not change significantly 6 weeks after the surgery, as a sign of the lasting reduction of the physical abilities. The decisive effect occurs between the 6<sup>th</sup> and the 13<sup>th</sup> week after the surgery ( $p=0.000$ ,  $\eta^2=0.441$ ) (Tab.2).

#### B. Kinematics during gait

Free-selected gait speed: The range of motion is the only parameter which shows significant improvements at all times and frequencies. That is not due to an increasing extension in terminal stance (not significant), but to distinct knee flexion during mid-swing. This parameter shows a significant improvement between the 6<sup>th</sup> and the 13<sup>th</sup> week ( $p=0.000$ ,  $\eta^2=0.429$ ). Between the preoperative and first postoperative gait analysis, there is no statistical significant tendency in mid-swing peak flexion. So the main effect obviously results from the essential changes between the 6<sup>th</sup> and 13<sup>th</sup> week. The peak flexion in mid-stance stays statistically unaltered in every frequency. This parameter does not change significantly.

Table 1 Differences in sagittal plane motion, vertical ground reaction forces (GRF) and temporal-spatial parameters between the patients and the normal group in free walking speed (fws)

Variable	preoperative			6 weeks postoperative		13 weeks postoperative	
	normal group	patients	p-value	patients	p-value	patients	p-value
Sagittal plane motion (°)							
Mid-stance peak flexion	21.23 ± 5.44	18.43 ± 7.76	n.s.	17.73 ± 6.78	n.s.	18.88 ± 6.12	n.s.
Terminal stance peak extension	3.62 ± 2.84	9.55 ± 6.78	0.000	10.46 ± 5.94	0.000	10.22 ± 5.13	0.000
Mid swing peak flexion	64.31 ± 5.72	55.16 ± 10.72	0.001	50.84 ± 9.89	0.000	56.97 ± 7.93	0.001
Range of motion	60.69 ± 3.89	45.61 ± 11.89	0.000	40.38 ± 11.20	0.000	46.75 ± 9.91	0.000
Vertical GRF (% BW)							
Weight acceptance peak force	110.79 ± 6.37	101.36 ± 6.46	0.000	99.57 ± 4.94	0.000	101.05 ± 6.18	0.000
Mid-support force	74.46 ± 6.47	87.07 ± 6.43	0.000	87.55 ± 5.20	0.000	85.28 ± 6.26	0.000
Push off peak force	112.76 ± 5.47	101.60 ± 3.86	0.000	100.76 ± 4.17	0.000	101.98 ± 3.19	0.000
Loading rate	8.02 ± 0.99	6.36 ± 1.58	0.000	6.00 ± 1.29	0.000	6.53 ± 1.42	0.000
Push off rate	7.73 ± 0.93	6.07 ± 0.97	0.000	5.86 ± 1.04	0.000	6.32 ± 0.86	0.000
Gait speed (m/s)	1.24 ± 0.14	0.96 ± 0.20	0.000	0.89 ± 0.16	0.000	1.00 ± 0.15	0.000
Cadence (steps/min)	111.64 ± 7.46	98.15 ± 14.55	0.000	92.70 ± 11.72	0.000	99.36 ± 10.74	0.000
Single support (%)	38.62 ± 0.99	36.28 ± 1.64	0.000	35.47 ± 2.19	0.000	36.67 ± 1.44	0.000

n.s. not significant

Table 2 Main effects (time) (Greenhouse-Geisser) and effects at week 6 and 13 in vertical ground reaction force (GRF), knee angle and temporal-spatial parameters by various gait speeds (in brackets: effect size:  $\eta^2$ )

Variable	main effect (1-3)			effect at week 6 (1-2)			effect at week 13 (2-3)		
	fws n=31	slow (70) n=23	normal (90) n=12	fws	slow (70)	normal (90)	fws	slow (70)	normal (90)
Sagittal plane motion (°)									
Mid-stance peak flexion	n.s.	n.s.	n.s.	n.s.	n.s.	n.s.	n.s.	n.s.	n.s.
Terminal stance peak extension	n.s.	n.s.	n.s.	n.s.	n.s.	0.040 (0.331)	n.s.	n.s.	n.s.
Mid-swing peak flexion	0.011 (0.164)	0.003 (0.129)	n.s.	n.s.	0.028 (0.110)	0.041 (0.327)	0.000 (0.429)	0.001 (0.229)	n.s.
Range of motion	0.006 (0.188)	0.001 (0.150)	0.032 (0.302)	0.045 (0.131)	0.013 (0.137)	0.016 (0.029)	0.000 (0.522)	0.000 (0.289)	0.029 (0.365)
Vertical GRF (%BW)									
Weight acceptance peak force Fz1	n.s.	n.s.	n.s.	0.038 (0.136)	n.s.	n.s.	n.s.	n.s.	n.s.
Mid-support force Fz2	0.017 (0.138)	0.009 (0.204)	n.s.	n.s.	0.004 (0.314)	n.s.	0.001 (0.296)	n.s.	n.s.
Push off peak force Fz3	0.048 (0.106)	n.s.	n.s.	n.s.	0.047 (0.168)	n.s.	0.004 (0.243)	n.s.	n.s.
Loading rate Fz1-tFz	n.s.	n.s.	n.s.	n.s.	0.006 (0.298)	n.s.	0.027 (0.153)	n.s.	n.s.
Push off rate Fz3-tFz3	n.s.	n.s.	n.s.	n.s.	n.s.	n.s.	0.042 (0.131)	n.s.	n.s.
Gait speed (m/s)	0.004 (0.181)	n.s.	n.s.	n.s.	n.s.	n.s.	0.000 (0.434)	n.s.	n.s.
Cadence (steps/min)	0.013 (0.140)	n.s.	n.s.	n.s.	n.s.	n.s.	0.001 (0.299)	n.s.	n.s.
Single support (%)	0.004 (0.178)	n.s.	n.s.	n.s.	n.s.	n.s.	0.000 (0.441)	n.s.	n.s.

n.s. not significant

Slow gait speed: Joint motion of knee shows a remarkable improvement in knee flexion in mid-swing at a frequency of 70 steps/minute between measuring time 1 and 2 and measuring time 2 and 3. Mid-stance peak flexion remains reduced throughout the follow-up examinations.

Normal gait speed: Peak extension in terminal stance phase shows a significant effect ( $p=0.040$ ,  $\eta^2=0.331$ ) at normal gait speed. Patients extend their knees more in the terminal stance phase when walking faster than at a free and slow gait speed (Tab. 2).

### C. Kinetics during gait

The vertical ground reaction forces were all normalized to body weight.

Free-selected gait speed: Mid-support force and push off peak force exhibit a main effect in course of time. The decisive effect occurs between the 6<sup>th</sup> and the 13<sup>th</sup> week after surgery. 6 weeks after the total knee arthroplasty, no statistically significant tendencies were determined in loading parameters, besides weight acceptance peak force ( $p=0.038$ ,  $\eta^2=0.136$ ).

Slow gait speed: Mid-support force shows a main effect at slow gait speed ( $p=0.009$ ,  $\eta^2=0.136$ ). No main effects were determined in weight acceptance peak force, push off peak force, push-off-rate and loading rate. However, significant differences were found in push off peak force and loading rate between 6 and 13 weeks after surgery. ( $p=0.047$ ,  $\eta^2=0.168$ ,  $p=0.006$ ,  $\eta^2=0.298$ ).

Normal gait speed: 13 weeks after surgery, there is no main effect in the course of time and there are no significant changes concerning loading parameters between the different measuring times (Tab. 2).

The evaluation of health-survey questionnaire (SF-36) shows significant changes ( $p=0.000$ ) in the dimensions of bodily pain (Fig. 3) and physical functioning, as well as remarkable effect sizes ( $\eta^2=0.353$ ,  $\eta^2=0.222$ ) throughout the period. Already 6 weeks after surgery and inpatient treatment a significant improvement could be detected in the dimension of bodily pain ( $p=0.001$ ,  $\eta^2=0.244$ ). At first, the dimension of physical functioning remains unchanged 6 weeks after total knee arthroplasty. Only after 13 weeks a significant change occurs ( $p=0.001$ ,  $\eta^2=0.222$ ).

### IV. DISCUSSION

Finally, the results demonstrate clearly that the change of gait parameters is dependent on gait speed. Range of motion changes significantly between the different gait analyses independent of gait speed. Mid-swing flexion is also not affected by the gait speed. However, the single support is strongly related to walking speed. 6 and 13 weeks after total knee arthroplasty there are still differences in the motion of knee joint. The bodily pain is reduced but does not reach the level of the control group 13 weeks after surgery.

The effect of inpatient rehabilitation on reaching a dynamic gait pattern is very low, regarding gait parameters 6 weeks after total knee arthroplasty. This is often caused by persistent swelling and painful knees after surgery. After total knee

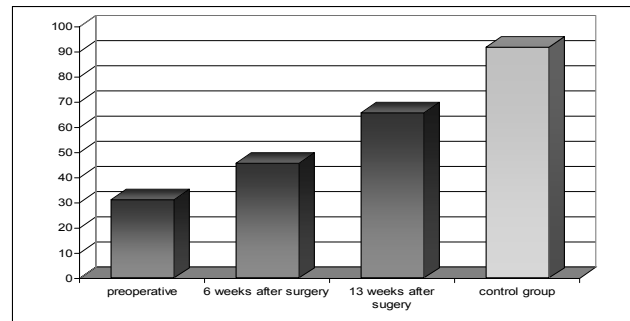


Fig. 3 Results of bodily pain dimension compared to the control group (SF-36)

arthroplasty, restrictions in motion of knee joint and poor physical capacity follow from long-standing relieving posture as a result of weakened extensors, shortened sinews and ligaments („quadriceps avoided gait“) [3].

### V. CONCLUSION

The study shows the development of free walking speed as well as the influence on gait speed by metronome in order to compare the gait parameters within the patients. Gait speed can significantly influence the biomechanical parameters of gait. So gait speed should be considered as a part of clinical gait analysis studies, although it is a very time-consuming examination. Further gait analysis 26 and 52 weeks after the operation is planned in order to demonstrate the improvement of the gait patterns.

### REFERENCES

- 1 Jordan, K, Challis, JH, Newell, KM (2007) Walking speed influences on gait cycle variability. *Gait & Posture* 26: 128-134.
- 2 Chiu, MC, Wang, MJ (2007). The effect of gait speed and gender on perceived exertion, muscle activity, joint motion of lower extremity, ground reaction force and heart rate during normal walking. *Gait & Posture* 25: 385-392.
- 3 Pap, G, Machner, A, Awiszus, F (2000) Funktionelle Veränderungen des Quadriceps Femoris Muskels bei Patienten mit Varusgonarthrose. *Z Rheumatol* 59: 380-387.

Author: Regina Ullmann  
 Institute: Department of Sports, Institute of Media, Communication and Sports  
 Street: Selkestr. 9  
 City: 06120 Halle  
 Country: Germany  
 Email: regina.ullmann@medizin.uni-halle.de

# Quantitative Analysis of the Activation Strategies during Freezing in Parkinson's Patients

A. Accardo<sup>1</sup>, S. Mezzarobba<sup>2</sup>, M. Millevoi<sup>2</sup> and F. Monti<sup>3</sup>

<sup>1</sup> Department of Electronics, DEEI, University of Trieste, Trieste, Italy

<sup>2</sup> Laboratory of gait analysis, School of Physiotherapy, University of Trieste, Trieste, Italy

<sup>3</sup> Clinical Neurophysiological Unity, University Hospital Cattinara, Trieste, Italy

**Abstract** — Freezing of Gait (FOG) is a symptom usually observed in the advanced stage of the Parkinson's Disease (PD). During it the subject suddenly becomes unable to start walking or to continue to move forward. Little is known about the gait of the subjects presenting FOG. In order to accurately analyse the alterations in the muscular activation strategies so as to evaluate hypotheses about the ON freezing generation in PD, in this paper we describe a system able to quantify the electromyographic activity of the distal and proximal muscles as well as of the basographic temporal patterns.

Signals were recorded by using a portable commercial system that acquires surface electromyographic (sEMG) bilateral data coming from tibialis anterior (TA), gastrocnemius (GS), gluteus maximus (GX) and gluteus medius (GM) muscles together with basographic signals that was used for the identification of the four gait phases. The system presents the plot of all the signals during gaits just before freezing in order to easily analyse the characteristics of the activation patterns.

To test the system, ten PD patients, presenting FOG in the ON phase of the medication cycle, were examined while performing normal walking or subject to freezing.

Results showed that significantly abnormal timing occurred in the TA and GS muscles with overall preserved reciprocity. Before freezing, TA and GS swing activities already started prematurely during the pre-swing phase. Similar timing alterations were present in GX and GM activities with significant pattern inversions between omo- and contra-lateral muscles during swing phase. The analysis of these altered patterns, highlighted by the realized system, can contribute in the explanation of the muscular activation strategies that produce FOG.

**Keywords** — Parkinson's disease, freezing in ON, FOG, gait analysis, EMG.

## I. INTRODUCTION

Patients with Parkinson's disease (PD) often experience freezing of gait (FOG) that represents one of the most disabling and least understood symptoms in PD. It is usually observed in the advanced stages (Hoehn & Yahr stage III-IV, 1967) of the disorder after a mean disease duration of at least five years [1-3]. During FOG the subject suddenly becomes unable to start walking or to continue to move forward [2].

FOG can be experienced on turning, in narrow spaces, whilst reaching a destination, in stressful situations as well as in dual tasking (cognitive load). It is relevant to distinguish between the two forms in which the FOG can be observed: the OFF state, the commonest form in which the medication effects are low (as it happens at the end of medication cycle), and the ON state during which the medication effects are high. The last condition can appear also during early phase of PD.

Hence, the FOG does not depend only on the dopamine level but also on cognitive and sensorial inputs a patient is submitted. The FOG and other gait alterations present in PD subjects in ON state induce to hypothesize that these phenomena could be due to different alterations at the central level of nervous system. Little is known about the gait of the subjects presenting FOG and recently it was hypothesized that the dyscontrol of the cadence of walking in freezing could contribute to this symptom [4-7].

Moreover, the kinematics analysis of gait pointed out that the steps of PD patients with FOG present, during their 'normal' walk, alterations that are common for all PD subjects: reduced velocity and step width, altered anticipatory corrections both laterally and antero-posteriorly [4, 8].

In order to evaluate hypotheses about the ON freezing generation in PD, in this paper we describe a system able to quantify the electromyographic activity of the distal and proximal muscles just before freezing as well as of the basographic and trunk accelerometric temporal patterns. The system can help in the analysis of the alterations in the muscular activation strategies that could produce FOG.

## II. MATERIALS AND METHODS

Signals are recorded by using a portable commercial system (PortiLab2®, TMSi) that acquires and transmits (via bluetooth) eight surface electromyographic (sEMG) bilateral data coming from tibialis anterior (TA), gastrocnemius (GS), gluteus maximus (GX) and gluteus medius (GM) muscles together with six basographic (footswitches) and three accelerometric (3D sensor) signals.

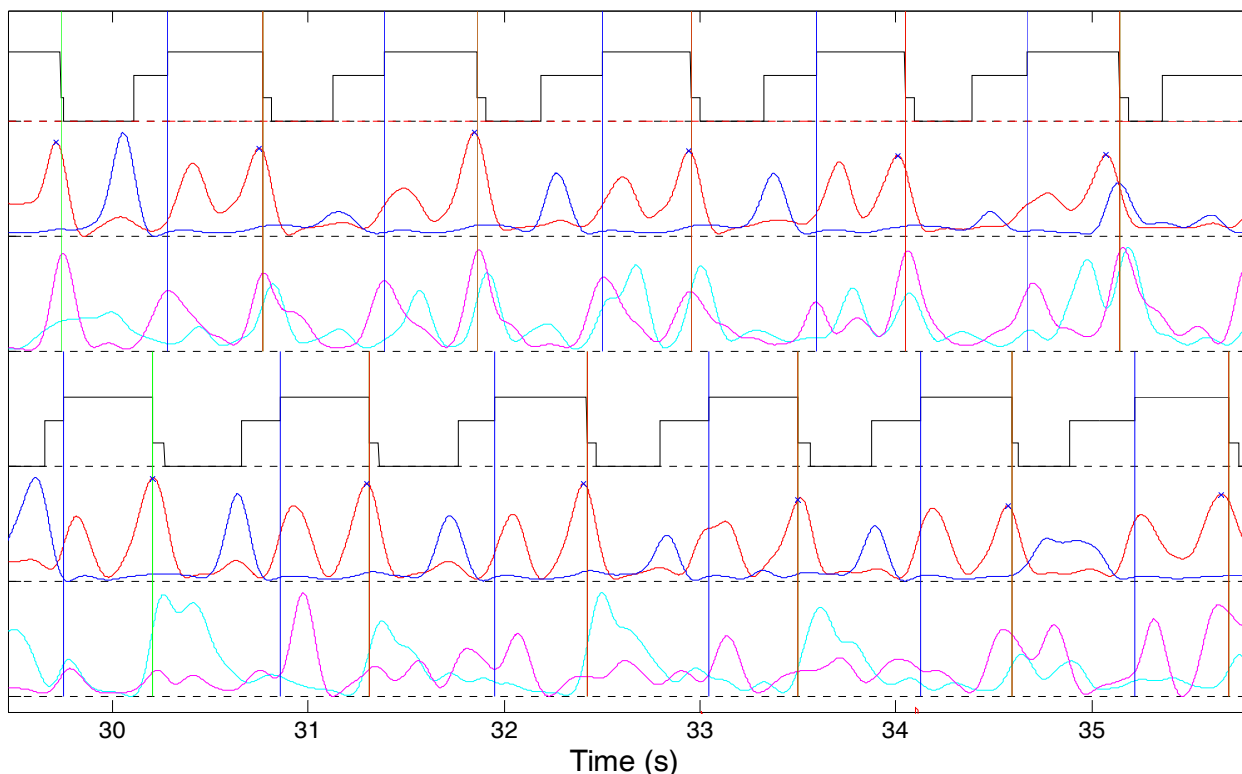


Fig.1 Example of sEMG envelopes sequence for left and right sides in a Normal subject. From top to bottom: gait phases, extracted from the basographic response, for right side (lowest level=stance, low level=heel-strike, high level=toe-off, highest level=swing); sEMG envelope of the right TA (red), GS (blue), GX (magenta) and GM (cyan) muscles; gait phases for left side; sEMG envelope of the left TA (red), GS (blue), GX (magenta) and GM (cyan) muscles.

The system samples all the signals at 1024 Hz and an ad-hoc software (written in MATLAB®) digitally filters (bandpass: 10Hz-500Hz) each sEMG signal, then rectifies and smooths in order to obtain the sEMG envelopes. The sEMG signals can be also expressed as a percentage of the gait cycle. The four gait phases (heel-strike, mid-foot, toe-off and swing) are identified from the combination of the three basographic signals. The sEMG signals are then synchronized with gait phases and the characteristics of the patterns (sEMGs, gait phases and accelerometric signals) during gaits just before freezing are visualized and easily analysed (Fig. 2). Moreover, sEMG peaks are determined using a preset threshold and, if necessary, corrected after visual inspection. The same system is also used to analyse the gait of normal subjects (Fig. 1) in order to compare the step of PD patients and to point out the alterations present during walking.

To test the system, some normal subjects as well as ten patients presenting a mean Unified Parkinson Disease Rating Scale (UPDRS) score of 15,4 (SD 5.9) and a mean FOGQ of 14.3 (SD 4.09), in the ON phase of the medication

cycle, were recruited. They performed several trials of normal walking and PD patients were also exposed to freezing-provoking circumstances.

### III. RESULTS

Fig.1 shows an example of the regular patterns present in a normal subject for all the sEMG envelope signals recorded during walking. The gait phases for both right and left sides follow the expected sequence and the sEMG envelopes show the correct number of peaks and timing.

Fig. 2 shows an example of the gait signals of a PD patient immediately before a freezing phenomenon.

The arrows, in Fig.2, indicate the progressive anticipation of the TA activation that immediately precedes the freezing. The example shows that significantly abnormal timing occurred in the TA and GS muscles with overall preserved reciprocity. Before freezing, TA and GS swing activities already start prematurely during the pre-swing phase.

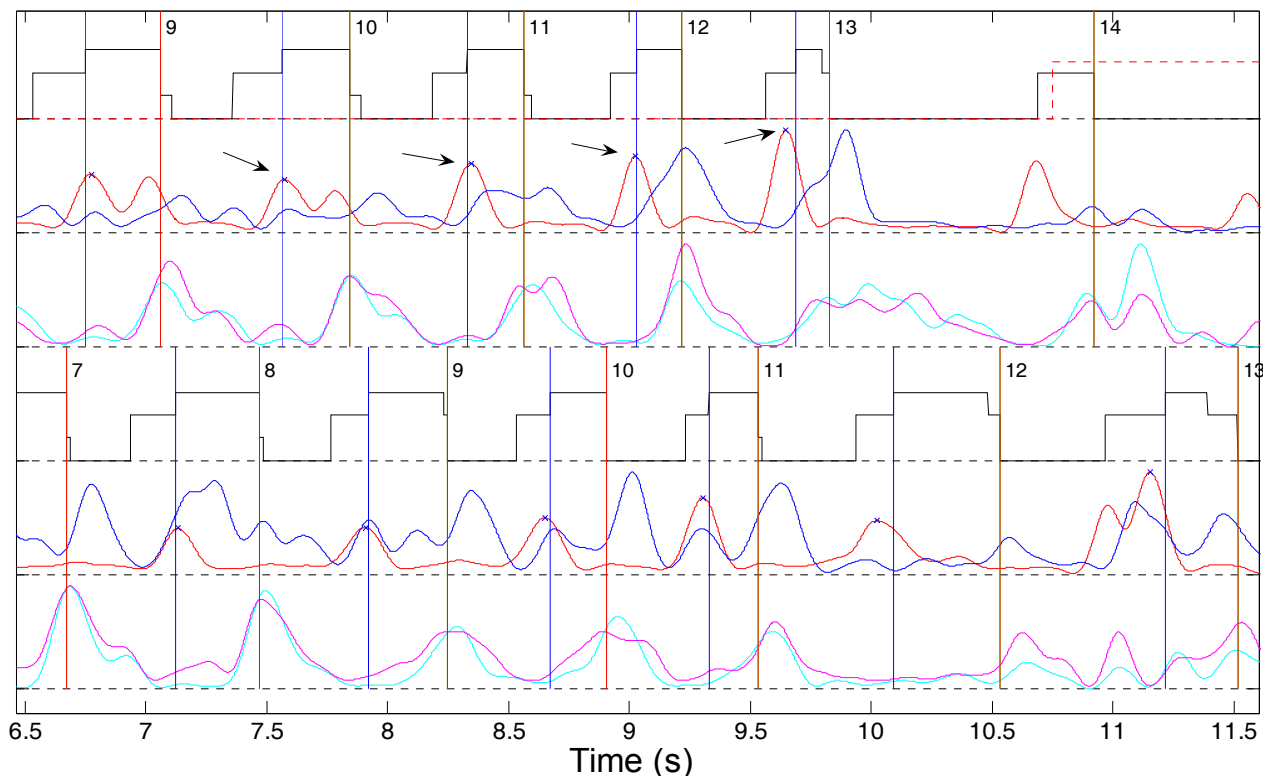


Fig.2 Example of sEMG envelopes for left and right sides in a Parkinson's patient. From top to bottom: gait phases for right side (lowest level=stance, low level= heel-strike, high level=toe-off, highest level=swing); sEMG envelope of the right TA (red), GS (blue), GX (magenta) and GM (cyan) muscles; gait phases for left side; sEMG envelope of the left TA (red), GS (blue), GX (magenta) and GM (cyan) muscles. Each step is numbered progressively and separately for the right and left side. The arrows indicate the progressive anticipation of the TA activation that immediately precedes the freezing (starting after the step #13 of the right side)

Similar timing alterations are present in all the examined PD patients that also presented GX and GM activities with significant pattern inversions between omo- and contra-lateral muscles during swing phase. The premature pattern, present also at the proximal level, could contribute to insufficient forward progression, progressively prevent the advancing of the contra-lateral limb.

Moreover, this pattern of altered activation is mainly present on the side more compromised by PD, that is also the side where freezing starts.

#### IV. DISCUSSION

The results obtained by using the system show that PD subjects with FOG have a continuous gait disturbance. The ability to regulate the stride-to-stride variations in gait timing and to maintain a stable walking rhythm is markedly impaired in subjects with FOG suggesting that the inability to control temporal co-ordination of muscles in lower limb and cadence might play an important role in this debilitating

phenomenon. These outcomes confirm previous reported hypothesis [4] supported by basographic data alone, correlating the stride-to-stride variability also with sEMG data (in particular those coming from the proximal muscles in lower limb) and freezing episodes.

Furthermore, these findings also support the hypothesis that the freezing in ON is not a sudden phenomenon, as it could seem to the clinical observation, but rather it is compatible to a progressive disorganization in the gait planning, not clinically evident, that can be initially compensate by the adaptation of the motor control.

In conclusion, the possibility, allowed by the realized system, to investigate the specific strategies of altered muscular activation patterns producing the freezing in ON demonstrates the utility of this instrument. The quantitative analysis of the precise activation timing can permit a more correct characterization of the alterations present in the gait of a specific subject and consequently a more considered decision of the best rehabilitative intervention to be carried out. Finally, the system can be also used for verifying the efficacy of the rehabilitation treatment.

## REFERENCES

1. Okuma Y, (2006) Freezing of gait in Parkinson's disease. *J Neurol*, 253 Suppl 7:VII27-32
2. Giladi N, Gurevich T, Shabtai H et al (2001) The effect of botulinum toxin injections to the calf muscles on freezing of gait in parkinsonism: a pilot study. *J Neurol.*, 248(7):572-6
3. Giladi N, Treves TA, Simon ES et al (2001) Freezing of gait in patients with advanced Parkinson's disease. *J Neural Transm*, 108(1): 53-61
4. Hausdorff JM, Schaafsma JD, Balash Y et al, (2003) Impaired regulation of stride variability in Parkinson's disease subjects with freezing of gait. *Exp Brain Res*, 149(2):187-94
5. Nieuwboer A, Dom R, De Weerd W et al, (2001) Abnormalities of the spatiotemporal characteristics of gait at the onset of freezing in Parkinson's disease, *Mov Disord*, 16(6):1066-75
6. Nieuwboer A, Dom R, De Weerd W et al (2004) Electromyographic profiles of gait prior to onset of freezing episodes in patients with Parkinson's disease. *Brain*, 127:1650-60
7. Macht M, Kaussner Y, Möller JC et al, (2007) Predictors of freezing in Parkinson's disease: a survey of 6,620 patients. *Mov Disord*, 22(7):953-6
8. Vaugoyeau M, Viallet F, Mesure S, Massion J, (2003) Coordination of axial rotation and step execution: deficits in Parkinson's disease. *Gait Posture* 18(3):150-7

Corresponding author:

Author: Agostino Accardo  
 Institute: DEEI-University of Trieste  
 Street: Via Valerio, 10  
 City: Trieste  
 Country: Italy  
 Email: [accardo@deei.units.it](mailto:accardo@deei.units.it)

# Precise Positioning of Electrodes at Transesophageal Atrial Stimulation Using Multichannel Transesophageal Pacemaker and Lead

A. Anier<sup>1</sup>, J. Kaik<sup>1</sup> and K. Meigas<sup>1</sup>

<sup>1</sup> Technomedicum of Tallinn University of Technology, Tallinn, Estonia

**Abstract** — To evaluate the dependence of pacing threshold current from electrode position a special study in 15 patients was performed. Computer controlled switch was used to select different active electrodes out of 9-channel pacing lead. Our results show that optimal mean position of esophageal lead is 1 cm distal to the maximal unipolar atrial electrogram registration point. Removal of lead position in the proximal direction is accompanied with significant elevation of pacing threshold, the same is noticed if the anode is placed in the distal direction for more than 2 cm from maximal atrial electrogram location. In 8 patients out of 15 individual optimal position differs from mean position. Precise positioning of pacing lead according to individual optimum allowed reduction of pacing current threshold 20% in average over standard bipolar transesophageal method at approximately 50% of patients.

**Keywords** — transesophageal pacing, threshold current

## I. INTRODUCTION

Transesophageal atrial stimulation (TAS) is widely used in evaluation and treatment of supraventricular (SV) arrhythmias. It can yield important information in most situations where invasive atrial stimulation is usually done, but is safe, rapid, inexpensive and can often be performed in an outpatient setting. TAS can initiate and terminate SV tachycardias [1, 2] and atrial flutter [3], and predict the risk of potentially lethal SV arrhythmias in asymptomatic WPW syndrome patients [4].

TAS is feasible because of the proximity between the esophagus and the posterior wall of the left atria – the distance (approximately 5-6 mm) remains constant in patients with age and weight differences [5]. Atrial capture can be obtained in more than 95% of patients. Pacing usually produces certain thorax discomfort, mainly burning chest sensation, that most patients tolerate, but nevertheless minimizing of pacing threshold is highly desirable and corresponding studies have been performed from the very early years of invention of this method [6]. Widely studied methods of reducing the stimulus current include finding the optimal position for the pacing electrode, the patient [7, 8] and the geometrical modification of the electrode.

In this paper we propose a multichannel transesophageal pacemaker and a method utilising it to reduce pacing current threshold and patient discomfort.

## II. MATERIALS AND METHODS

### A. Multichannel transesophageal pacemaker

The main components of the laboratory device (Fig. 1) are a transesophageal catheter with multiple electrodes; programmable commutator controlled by programmer, which allows each electrode or combinations of electrodes to be connected to a current pulse generator. The current pulse generator has interfaces to specify pulse current and length. The main principles of the laboratory device are protected under useful model no. EE 00542 U1.

A standard PC, National Instruments peripheral devices, programmable current pulse generator E53002-01 and self-made programmable commutator were used to implement the laboratory device. The application software was developed using the LabView development environment.

### B. Precise positioning of pacing dipole

To evaluate the dependence of the pacing threshold current on electrode position, a special study was performed in 15 patients who underwent routine electrophysiological study in the Department of Cardiac Arrhythmias of Estonian Institute of Cardiology. The intermediate electrode (denoted

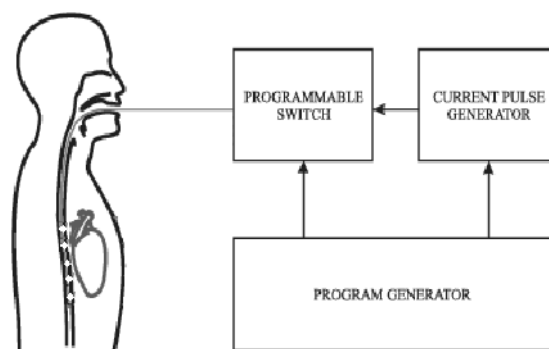


Fig. 1 Multichannel transesophageal pacemaker



as Lead 0) was positioned in the process of localization of maximal unipolar atrial electrogram (Fig. 2).

By gradually increasing pacing current until stable capture of atrial pacing was confirmed by surface ECG, the pacing threshold for all 9 electrode positions was found.

The dependence of threshold current on anode position is shown on Fig. 3.

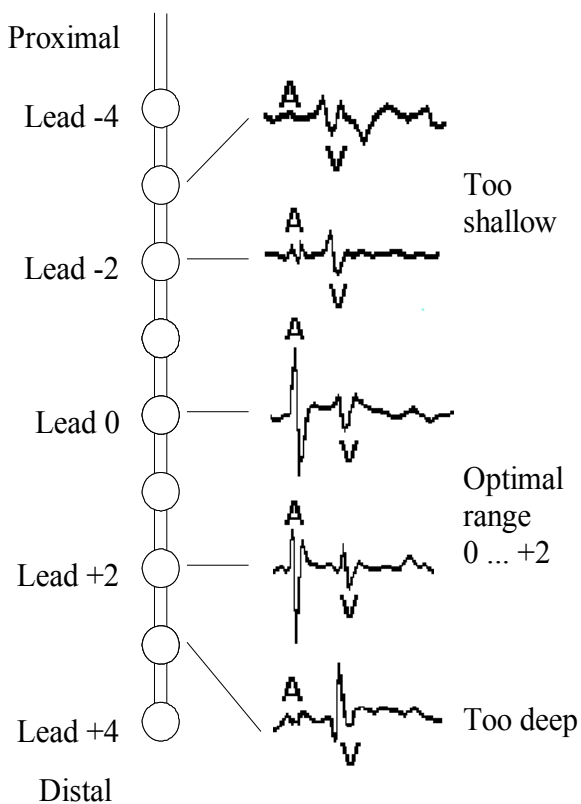


Fig. 2 Catheter positioning

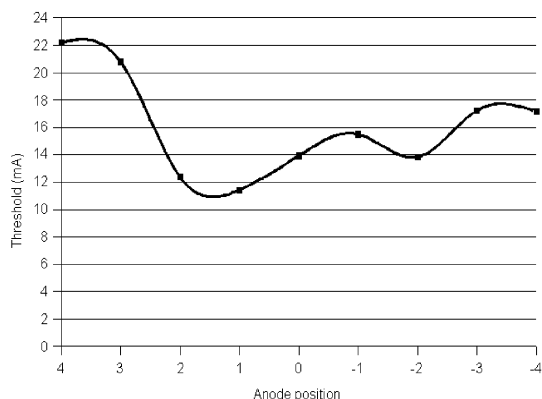


Fig. 3 Pacing threshold dependence on anode position

Anode position 0 denotes the intermediate electrode of multichannel pacing lead positioned at the localization of maximal unipolar atrial electrogram. Positive numbers represent anode positions distal to position 0 in centimeters. Negative numbers represent anode positions proximal to position 0 in centimeters. Stimulation points 1 cm to distal or proximal to optimal position also assure acceptable pacing thresholds. Removal of anode position in the proximal direction is accompanied by significant elevation of pacing threshold; the same is noticed if the anode is placed more than 2 cm distal from the maximum atrial electrogram location.

### III. RESULTS

Our results show that the optimal position of esophageal lead is patient-dependent and is located 0 to 2 cm distal to the maximal unipolar atrial electrogram registration point (Table 1). Highlighted cells show the optimal lead position

Table 1 Optimal lead position dependence on patient

Patient #	Lead position			Reduction %
	-2	-1	0	
1	8	9	12	12,5 %
2	16	13	25	
3	13	13	15	
4	9	14	14	55,6 %
5	13	13	25	
6	12	10	9	11,1 %
7	11	12	17	9,0 %
8	13	8	7	14,3 %
9	12	13	11	18,2 %
10	10	17	16	
11	20	18	15	20,0 %
12	14	13	25	
13	13	9	16	
14	13	11	12	
15	22	17	20	
<b>Tot/Avg</b>	<b>4</b>	<b>7</b>	<b>4</b>	<b>20,10%</b>

for each patient. In 8 of 15 patients, the individual optimal position differs from average. By selecting lead configuration according to the individual patient, pacing current threshold was reduced in 8 of 15 patients by 9- 55%, 20% on average.

#### IV. DISCUSSION

There are two main sources of discomfort in TOE electrophysiological study -- the initial introduction of the pacing catheter into the esophagus and the burning sensation caused by the pacing current. The pacing threshold (and current strength) can be reduced by modifying certain parameters: the position of pacing electrodes, construction of electrodes, distance between electrodes, and the duration and shape of the pulse.

The proposed multichannel transesophageal pacemaker with multichannel catheter allows the best position of electrodes (and inter electrode distance) for successful atrial pacing to be quickly scanned without moving the catheter inside the esophagus causing extra patient discomfort. Initial catheter depth of insertion (DOI) for middle electrode (Lead 0) could be calculated using formula  $DOI = \text{patients height} / 5 + 5 \text{ cm}$  [9].

#### V. CONCLUSIONS

The optimal lead position in transesophageal atrial stimulation is patient dependent and varies 0 to 2 cm distal to location of maximal unipolar electrogram. The multichannel transesophageal pacemaker developed allows to quickly scan for the best set of active electrodes of multichannel transesophageal pacing lead for successful atrial pacing.

#### ACKNOWLEDGMENT

This study was supported by Estonian Competence Centre Programme and the Estonian Science Foundation grant ETF7506.

#### REFERENCES

1. Brockmeier K, Ulmer HE, Hessling G (2002) Termination of atrial reentrant tachycardias by using transesophageal atrial pacing. *J Electrocardiol.*, 35 Suppl: 159-163
2. Kesek M, Sheikh H, Bastani H, et al. (2000) . The sensitivity of transesophageal pacing for screening in atrial tachycardias. *Int J Cardiol.*, 72: 239-242
3. Rostas, L, Antal K, Puterek Z. (1999) "Transesophageal pacemaker therapy in atrial flutter after procainamide pretreatment. *Am J The.*, 6: 237-240,
4. Fenici R, Brisinda D, Nenonen J, Fenici P. (2003) Noninvasive study of ventricular preexcitation using multichannel magnetocardiography. *Pacing Clin Electrophysiol.*, 26:431-435
5. Crawford TM, Dick M, Bank E, Jenkins JM. (1986) Transesophageal atrial pacing: importance of the atrial-esophageal relationship. *Med. Instrum.*, 20: 40-44
6. Benson DW Jr, Stanford M., Dunnigan A., Benditt DG. (1984) Transesophageal atrial pacing threshold: role of interelectrode spacing, pulse width and catheter insertion depth. *Am J Cardiol.* 53: 63-67
7. Pehrson S, Wedekind T, Madsen B, et al. (1999) The optimal oesophageal pacing technique – the importance of body position, interelectrode spacing, electrode surface area, pacing waveform and intraoesophageal local anesthesia. *Scand Cardiovasc J*, 33: 103-109
8. Schwann NM, Maguire DP, Roth JV, et al. (2001) Evaluation of transesophageal atrial pacing in the prone and lateral positions. *J Cardiothorac Vasc Anesth*, 15 : 192-196
9. Roth JV, Brody JD, Denham EJ (1996) Positioning the pacing esophageal stethoscope for transesophageal atrial pacing without P-wave recording: implications for transesophageal ventricular pacing. *Anesth Analg*, 83(1):48-54

Author: Andres Anier  
 Institute: Technomedicum of Tallinn University of Technology  
 Street: Ehitajate tee 5  
 City: 19086 Tallinn  
 Country: Estonia  
 Email: andres.anier@mail.ee

# Automated multi-parametric label free 24 channel real-time screening system

B. Becker<sup>1</sup>, V. Lob<sup>1</sup>, N. Janzen<sup>1</sup>, D. Grundl<sup>1</sup>, F. Ilchmann<sup>1</sup> and B. Wolf<sup>1</sup>

<sup>1</sup> Heinz Nixdorf-Chair for Medical Electronics at the Technical University of Munich (www.lme.ei.tum.de)

**Abstract** — In research, pharmacological drug-screening and medical diagnostics, the trend towards the utilization of functional assays using living cells persists. As they are very sensitive, cells are used as signal transducers. For this purpose our research group has developed an automated high-content online measurement system, which is described in this paper. The system is comprised of a pipetting robot sensors for measurement of pH, pO<sub>2</sub>, electric signals and cell adhesion, a digital microscope and a climate chamber. The robot is used to supply the cells with nutrient solution or active agents that are to be tested, while the sensors monitor the acidification of the medium, the uptake of oxygen and the adhesion of the cells to the substrate. Reflected light as well as fluorescence imaging during the course of an experiment are possible due to the included microscope. Cells and sensors are arranged in a special 24-well micro plate that is placed at a fixed position within the system. Oxygen and pH values are usually measured every 5 to 15 seconds. The running software also allows planning of experiments over a long period of time (several days), which makes the system suitable for applications like pharmaceutical drug screening, in vitro chemo-sensitivity assays, toxicological studies and analytical histopathology.

**Keywords** — online measurement, cells, chemosensitivity, automated

## I. INTRODUCTION

The major science of the twenty-first century, biology, is changing paradigmatically from the pure analysis of molecular components to the comprehension and analysis of complex interrelations and functions within cells, organs, and even entire organisms [1].

Pharmacology continuously pushes the development of biomedical equipment. Miniaturization and automation has already made possible the ultra high throughput screening of isolated targets on a molecular level with hundreds of thousands of samples a day [2, 3]. Thus, a steadily increasing number of potential drug candidates are identified and enter the later pre-clinical phases. In reducing these to only a few promising leads, cell based (in vitro) methods are meanwhile often replacing assays restricted to the screening of isolated targets [4].

Other reasons for the success of in vitro cell testing are the increased requirements for animal testing and clinical trials. Here, cell based assays can be used for the determination of the correct dosage, medication intervals and side

effects of potential drug candidates. Taking into account the importance of reproducible and statistically significant large datasets, automation plays an increasingly central role. When interpreting numerous cellular assays, it is necessary to observe that the function of a cell is primarily characterized by highly complex mechanisms of parallel transmission of information and metabolic signals.

Micro-sensor technology provides a tool to overcome difficulties in the assessment of basic functional parameters of living cells cultures. Biochips offer an ideal minimally invasive measurement platform to obtain precise and reproducible measurement results. Global cell metabolic activity, the rate of mitochondrial oxygen consumption, cell growth, morphological changes and patterns of electric activity are the parameters that are typically investigated [5, 6]. Cells are able to respond in an extremely sensitive way to changes in their environment. Electronic or optic micro-sensors can be utilized to analyze such responses. While yielding significantly more specific information, cell-based assays are more expensive and time consuming [7].

## II. MATERIALS AND METHODS

### A. General setup

The IMR (Intelligent Microplate Reader) System has a strictly modular setup. It is comprised of a pipetting robot, sensors for measurement of pH, pO<sub>2</sub>, bioelectric signals and cell adhesion, a digital microscope, and a climate chamber. The sensors are arranged on a modified micro-well-plate. The robot is used to supply the cells with nutrient solution or active agents that are to be tested, while the sensors monitor the acidification of the medium, the uptake of oxygen and the adhesion of the cells to the substrate. The latter is achieved by an interdigitated electrode structure (IDES), whereas the chemical changes are detected by optodes. Reflected light, as well as fluorescence imaging during the course of an experiment are possible due to the included microscope. All components are arranged in a climate chamber, which provides sterility and keeps environmental parameters (gas, humidity, temperature) constant.

Two setups of the IMR System are used in parallel. One uses an electro-optical system to read out the optodes in the measurement volumes. The other one applies a microscope

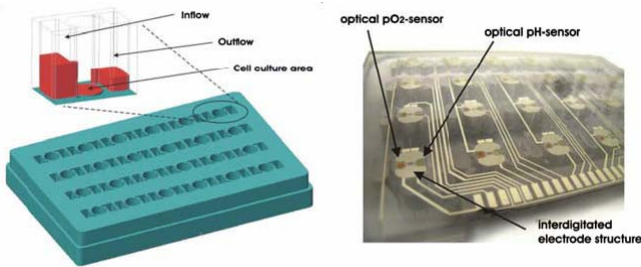


Fig. 1 Micro-well-plate; the 3 chambers (inflow, outflow and cell culture area) are shown on the left side whereas the glass plate with sensors (optical and electric) is shown on the right.

to access a big variety of optical analysis methods. In both setups the IDES sensor is available for impedance measurements.

A third setup with an additional multi-electrode-array (MEA) will be available. Here, potentials, firing- and burst-rates of nerve cells will be measured under the influence of specific drugs.

### B. Micro-well-plate

At the heart of the IMR, a sensorchip-based micro-well-plate with integrated micro fluidics for measurements on living cells is placed at a fixed position within the device. Made of a polymer block that is bonded to a glass plate with a sensor array for 24 wells, it provides a means for a well-controlled fluid exchange for every individual cell culture well. Each well consists of three chambers (Fig. 1), at which the central chamber holds cells and sensors. It possesses a very small volume of only 23  $\mu\text{l}$  to allow a higher sensitivity to changes in cell metabolism, and is equipped with micro structured channels for fluid exchange with the other two chambers. The bottom of the micro cell culture chambers is enclosed by the glass sensorchip (Fig. 1).

### C. Pipetting Robot

Automation of the platform is achieved using the pipetting robot. It is able to move in three degrees of freedom and therefore can access every position and height on the ground plate. Using a 24 channel pipetting head, the fluids in all wells of the micro-well-plate can be replaced in parallel. The pipettes can hold volumes of up to 250  $\mu\text{l}$ .

The robot's ground plate provides seven additional positions for standard cell culture plates (one position is used for the measurement micro-well-plate), but in exchange also pipette racks, waste volumes or a washing station can be placed according to the planning of the experiment.

### D. Sensor systems

pH- and  $\text{pO}_2$  values are determined by an electro-optical system of the Precision Sensing GmbH (Regensburg, Germany) [8], that is reading out the optodes using optic fibers. The quenching of a fluorescence signal is measured and concentrations can then be calculated. The measurement range comprises of pH-values from 6.5 to 8.0 and oxygen air saturations from 0 % to 250 %.

Growth in cell number and changes in cell adhesion are measured with the IDES structure, which is in principal a capacitor. The impedance is measure separately in each well with 24 channel circuitry by RAW Electronic GmbH (Weiler im Allgäu, Germany).

Both sensor systems are usually used to generate measurement results every 5 to 15 seconds. Faster measurement rates are possible, but rarely practical.

### E. Microscope

A novel scaleable and modular microscopy system is used within the IMR that especially meets the requirements of automated microscopy [9]: iMIC [10]. In order to allow the integration of this inverted microscope into workstations and/or product lines, the microscope's components were highly integrated into one embedded module. The objective carousel, the filter changer(s) (e.g., needed for fluorescence microscopy) and the focus drive were therefore seamlessly integrated into an octagonal shaped microscopic building block.

The greatly reduced size and weight of the microscope allows movement of the microscope instead of the micro-well-plate, therefore eliminating stress caused to cells by acceleration and vibrations. In order to obtain movement of the probe relative to the optics, the entire microscope is set on a base that can be moved in x and y direction underneath the static stage.

### F. Course of an experiment

Cells are transferred to the central chamber of the micro-well-plate and incubated for at least two days to assure proper growth. After that the measurement plate is placed in the IMR, where the climate chamber of the IMR is set according to the desired climate settings (usually 37°C).

Recording of measurement values begins immediately after insertion of the plate. After a set period of time, the robot replaces the fluids in the cell culture wells. This replacement is repeated periodically as a proper metabolic rate of the investigated cell culture has to be ensured at all times. Therefore the programmed test procedure is divided into several maintenance cycles. Within one cycle metabolic

by-products are flushed out of the micro reaction chamber and replaced by fresh nutrient solution, which takes only a few seconds. Two important aspects make this investigation method important: The reaction chamber with the living cells has to be so small that changes in the extra cellular medium can be easily detected. Therefore, an increase of the relative volume of the specimen compared to the volume of the culture medium by limiting the size of the reaction chamber leads to an increased resolution of the monitored cell activity parameters. Furthermore, flushing the reaction chamber with fresh nutrient solution once every maintenance cycle guarantees constant starting conditions and makes the measured cell parameters comparable to each other. The aim of a series of measurements is to guarantee stable and constant conditions for the desired measurement time.

### III. RESULTS

Two different cell types were tested in the IMR: MCF-7 breast cancer and CaCo-2 colon cancer cells. In each case  $0.4 \cdot 10^5$  cells were seeded per well of the micro-well-plate. All 24 wells were used. After two days of incubation the cells covered about 80-95 % of the well's ground area. In this state the experiments were started.

Fig. 2 and 3 show the first experiment with MCF-7 cells. The robot was used to maintain a fluid exchange every 10 minutes. In each cycle 250  $\mu$ l (of 260  $\mu$ l whole volume) of nutrition medium were replaced. After 3 hours 10 minutes a prolonged maintenance cycle of 29 minutes was tested.

The tested drug in this case was 0.2 % of Triton X 100. It was added to the nutrient medium after 4 hours and 10 minutes and causes a disintegration of cell membranes and thereby a cessation of cell metabolic activity.

The recorded parameters of pH-value and oxygen saturation are shown (both in well C2).

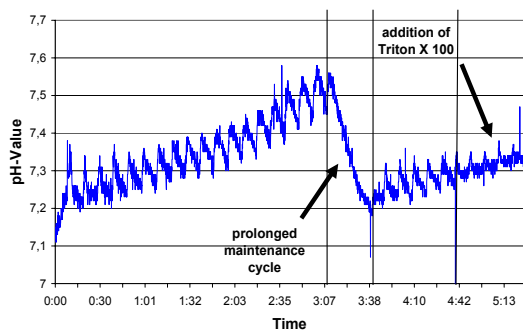


Fig. 2 pH-Values (MCF-7 cells) during 10 minute maintenance cycles, a prolonged cycle and after the addition of Triton X 100 (0.2%).

The second experiment is shown in Fig. 4 & 5. The setup is identical to the first test case but CaCo-2 as well as MCF-7 cells were investigated. Triton X 100 was added after 1:28 and 0:45 hours, respectively. The maintenance interval of 10 minutes persisted. Impedance values were measured every 5 seconds.

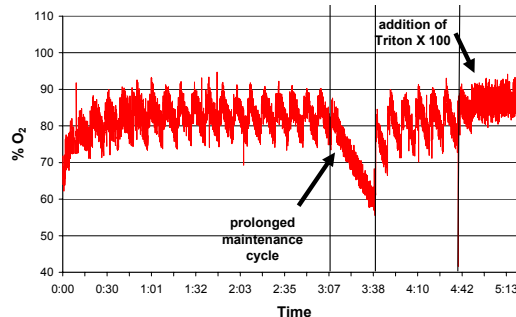


Fig. 3 O<sub>2</sub>-Values (MCF-7 cells) during 10 minute maintenance cycles, a prolonged cycle and after the addition of Triton X 100 (0.2%).

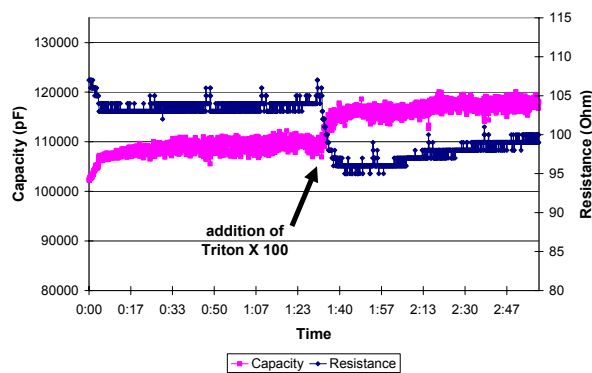


Fig. 4 Impedance Values (CaCo-2 cells) before and after the addition of Triton X 100 (0.2%) to the maintenance cycle of 10 minutes.

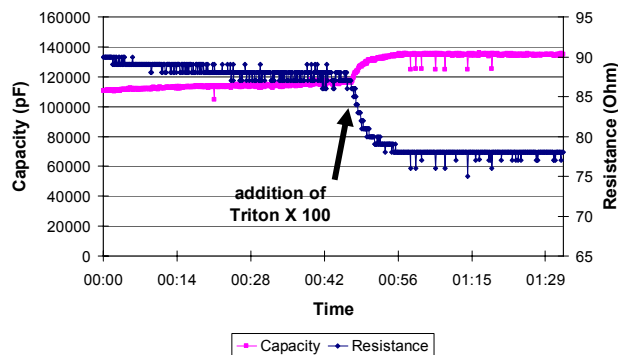


Fig. 5 Impedance Values (MCF-7 cells) before and after the addition of Triton X 100 (0.2%) to the maintenance cycle of 10 minutes.

## IV. DISCUSSION

### A. Experiment results

Measuring the metabolic rate using the parameters of pH and pO<sub>2</sub> makes it possible to see the impact of drugs on cell metabolism. The uptake of oxygen and the acidification of the medium with metabolic products can be quantified. After the addition of the drug, the change in uptake and acidification rates is visible.

Changes in morphology and cell number can be detected via the impedance values. After the addition of Triton X the cells disintegrate, which is leading to a reduction of resistance between the IDES structures as cells possess isolating characteristics. At the same time capacity is rising due to the higher dielectric constant of water compared to cells.

### B. General discussion

The state of the art in functional analysis of living cells is the use of micro-test-plates in combination with various optical readout systems. However, since no truly appropriate optical techniques are available for studies on cell adhesion, cell metabolic activity or electric signals, sensor based readout systems appear to a complementary tool, particularly with respect to their real-time monitoring capabilities.

Automation of the entire system is the key to the ability to screen large numbers of drug targets. Even testing of multiple doses of the same drug is possible as capacities are rising.

The field of application for cell-based assays is as large as the variety of different cell types to investigate. For medium- and long-term assays on chips, a liquid handling system is necessary to adjust and to maintain the required physio-chemical parameters and, eventually, drug concentrations of the medium. To ensure sensitive measurements of metabolic rates, small, closed micro-volumes for the cell cultures are necessary: only when a sufficiently high ratio of cell number to medium volume is achieved, those rates can be recorded precisely. This brings about an additional requirement, namely the repeated exchange of cell culture media (with cycle times of some minutes) while retaining the cells in the micro chambers.

In order to achieve relevant high quality results, a major challenge is to improve the in vitro analysis methods. Ideally, the in vitro test-environment reproduces the in vivo conditions as good as possible. This paper describes an analysis concept for living cells and a method to get significant data of living cells close to in vivo conditions. The system offers the possibility to adjust individual measurement cycles to analyze cell response profiles on various active agents.

## V. CONCLUSION

Currently planar non-enzymatic sensors are used to detect several extra-cellular parameters. The presented system is able to monitor up to 3 parameters (pH-, pO<sub>2</sub>-, and impedance-value) in parallel and automated for a long period of time without the need for interference of personal.

In most systems only one kind of signal is measured. End-point measurements are also a common means. However, the higher effort for a more complex system pays off with new insights to cellular mechanisms and better and more consistent (online and real-time) data.

The presented system could become an enabling technology for future screening assays, especially in the field of pharmacological drug screening, screening for toxic effects of chemical compounds and in applications of individualised in vitro chemosensitivity testing of cancer patients.

## REFERENCES

1. Kraus M, Wolf B (1995) Structured biological modelling—a new approach to biophysical cell biology. CRC Press, Boca Raton
2. Entzeroth M (2003) Emerging trends in high-throughput screening. *Curr Opin Pharmacol* 3:522–529
3. Hertzberg RP et al (2000) High-throughput screening: new technology for the 21st century. *Curr Opin Chem Biol* 4:445–451
4. Moore K et al (2001) Cell-based versus isolated target screening: how lucky do you feel? *J Biomol Screen* 6:69–74
5. Brischwein M, Motrescu ER, Otto AM, Cabala E, Grothe H, Wolf B (2003) Functional cellular assays with multiparametric silicon sensor chips. *Lab Chip* 3(4):234–240
6. Wiest J et al (2005) Cellular assays with multiparametric bioelectronic sensor chips *Chimia* 59:243–246
7. Brischwein M, Grothe H, Otto AM, Stepper C, Motrescu E, Weyh T, Wolf B (2004) Living cells on chip: bioanalytical applications. In: Mirsky VM (ed) *Ultrathin electrochemical chemo- and biosensors*. Springer, Berlin, pp 159–180
8. Arain S et al (2006) Characterization of microtiterplates with integrated optical sensors for oxygen and pH, and their applications to enzyme activity screening, respirometry, and toxicological assays. *Sens Actuators B* 113:639–648
9. Geisler T et al (2006) Automated multiparametric platform for high-content and high-throughput analytical screening on living cells. *IEEE Trans Autom Sci Eng* 3:169–176
10. Constans A (2004) Automated microscopy gets a new shape. *Scientist* 18:41–43

Author: Dipl.-Ing. Bernhard Becker  
 Institute: Lehrstuhl für Medizinische Elektronik der TU München  
 Street: Theresienstr. 90 Geb. N3  
 City: 80333 München  
 Country: Germany  
 Email: becker@tum.de

# Decentralized Multi-channel Digitizing of Bioimpedance Signals

I. Bilinskis<sup>1</sup>, Y. Artyukh<sup>1</sup> and M. Min<sup>2</sup>

<sup>1</sup>Institute of Electronics and Computer Science, Riga, Latvia

<sup>2</sup>Tallinn University of Technology, Tallinn, Estonia

*Abstract* — As bioimpedance data more often than not have to be acquired from a number of signal sources scattered over some area, multi-channel data acquisition scheme has to be implemented and that typically is realized on the basis of multiplexers. However connecting a multitude of distanced analog signal sources to a multiplexer causes a number of problems. To avoid them, an alternative approach to decentralized bioimpedance data acquisition is suggested and discussed. It is shown that the centralized multiplexing of input signals can be replaced by decentralized remote sampling of the bioimpedance signals performed in the close proximity of the respective signal sources. That leads to a number of advantages, including reductions in design complexity and power consumption of the front-end remote sampling devices. The suggested digitizing of bioimpedance signals is based on application of a distributed analog/digital converter containing a number of remote samplers that might be placed near to the signal sources. The functions of sampling and data acquisition from multiple sources then are performed specifically. The algorithms for processing the data acquired in this way, matched to these specifics, and the significant benefits achievable in the described way are described and discussed.

*Keywords* — Bioimpedance, data acquisition, remote sampling.

## I. INTRODUCTION

Bioimpedance signals usually have to be picked up from electrodes located outside and/or inside of a biological object at a number of places (e.g. 12-lead impedance cardiograph, post-surgery cardiac monitor, different implantable pacemakers and cardioverters). Therefore, there is a multitude of these signals that have to be acquired and analysed by a multi-channel system. The number of channels, the excitation frequency and other conditions for bioimpedance analysis might vary in a large range. All these conditions for analysis of the bioimpedance signals complicate the task of multi-channel data acquisition, demodulation and bioimpedance estimation. One of the basic issues, important for organizing bioimpedance data acquisition in a rational way, is the necessity of arranging the bioimpedance data acquisition in a way providing for obtaining the information about the respective biomedical processes of interest simultaneously in parallel from all available signal sources. To do that in a way ensuring high

performance of the involved data acquisition system is not so easy. The traditionally used approach to multi-channel data acquisition based on using a multiplexer for switching the analog input signals to a central ADC for digitising them has serious drawbacks. Specifically, the wires used for connecting the multiplexer with the distributed over some area signal sources typically are not so short. Therefore it is not easy to protect the analog input signals from the corruption due to the impact of the ambient noise. Next, the multiplexer performs switching of these signals and the transients related to this represent yet another error source. The mentioned problems become really difficult whenever the number of the bioimpedance signal sources become large, as it is in some application cases, for example, in the case of bioimpedance tomography when a hierarchy of multiplexers has to be used. An obvious alternative is to use multiple ADC placed close to the signal sources and then to multiplex their digital outputs. While that would help in achieving better accuracy, the design of front-end devices of the data acquisition system then would become relatively complicated and, what is especially problematic, the power consumption level of them then often would not be acceptable.

An alternative approach to decentralized simultaneous bioimpedance data acquisition from a large number of signal sources in parallel is suggested and discussed in this paper. It is based on the concept of distributed analog/digital conversions [1].

## II. BASIC STRUCTURE FOR DATA ACQUISITION

Although the further described method and algorithm for digitising, demodulation and pre-processing of bioimpedance carriers are rather specific, the classical approach to bioimpedance measurements, in general, remains the same. Some excitation signals, as usual, have to be generated, applied to the biological object being investigated and then reactions to the excitations have to be measured. The suggested approach considered in this paper concerns the measurement part of the whole process. To carry out bioimpedance measurements, it is suggested to use the Digital Alias-free Signal Processing (DASP) technology, as it is highly flexible and meets the

requirements of multi-channel bioimpedance measurements. The focus is on bioimpedance carrier digitizing, special digital representation of bioimpedance signals, reconstruction and pre-processing of them. As these issues are discussed in the context of bioimpedance data acquisition from a number of signal sources, let us start this discussion by explaining the basic structure of the subsystem performing the measurements. Actually it is the structure of the distributed analog-to-digital converters (ADC) partly embodied in active electrodes – see Figure 1, where a joint system for electro- and impedance cardiography (ECG/ICG) is depicted.

The active chest electrodes ( $C_1$  to  $C_6$ ), also the right and left arm and leg electrodes (RA, LA and RL, LL) contain remote samplers. A logic circuitry is used for collecting the output signals of the samplers and then they are transmitted over a wire or wireless transmission lines to the master part of this structure. The sampled signals received there are demodulated, reconstructed and transferred to a computer. At the first glance, the structure of the distributed ADC is simple enough. It contains  $n$  front-end devices, which are used for performing the operation of input signal sampling, data transmission line and the master part of the converter. However digitizing of the bioimpedance signals according to this scheme actually is carried out in an unusual decentralized way. To implement this approach, sampling of the input signals apparently has to be performed closely to the respective signal sources. In other words, remote sampling has to be used. It means that the sampling and quantizing operations, traditionally fulfilled closely together within a structure of an analog-to-digital converter, have to be separated and carried out at different locations with some transmission lines inserted between them. That makes sense only if the sampled signals are represented and encoded in a way suitable for safe transmission of this information over a relatively short distance. Transmission of the usually taken sample values of analog signals obviously is not acceptable.

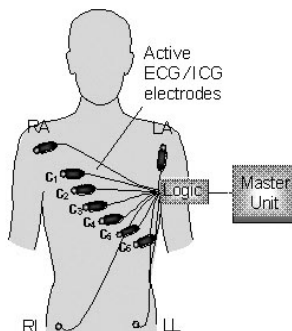


Figure 1. A joint electro/impedance cardiograph (ECG/ICG).

Therefore to implement and use the remote sampling idea, the signal sampling operation has to be carried out in way differing from the traditionally performed sampling. So specific sampling techniques are used to satisfy this requirement.

### III. REMOTE SAMPLING

To perform the considered remote sampling operation, a reference function  $r(t)$  with given and stable parameters is generated, compared with the input signal  $x(t)$  and sampling is carried out specifically as an operation of detecting the time instants  $\{t_k\}$  when crossings of the input signal  $x(t)$  and the reference function  $r(t)$  occur [2-5]. A sine-wave is generated and used as the reference function. Therefore  $r(t) = A_r \sin(2\pi f_r t + \varphi_r)$ , where  $A_r$ ,  $f_r$ , and  $\varphi_r$  are the amplitude, frequency and phase angle of the reference function, respectively. Block diagram of a group of this type of remote samplers is given in Figure 2 (a). The sampling concept according to which this type of the remote sampler operates plays an essential role for the whole structure and performance of the described distributed ADC. In particular, it defines the digital signals representing the original analog input signals [4, 5]. The digital signals in this case are sequences of the crossing instants  $\{t_k\}$ . This information might be carried either by trains of appropriately positioned in time short pulses (Figure 2 (d)) or by digital value sequences of these time instants (Figure 2 (e)). The first type of the information encoding by pulse positioning modulation is used for transmission of information from the sampler outputs to the central master part of the distributed ADC. There the received sampled signals are converted into the digital signals of the type shown in Figure 2 (e) by using the second digital encoding mode fulfilled as time-to-digital conversions.

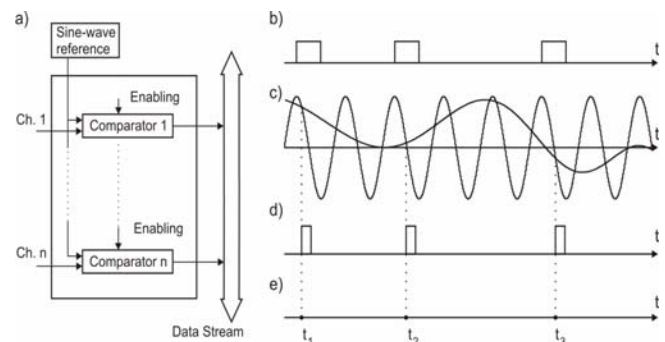


Figure 2. Block diagram of the front-end devices performing the remote sampling function within the structure of the distributed ADC.



The suggested approach to building electronic systems for the bioimpedance measurements on the basis of remote sampling distributed ADC is well suited for meeting the requirements of this application and it has a number of advantages. First, digitising of bioimpedance signals is then decentralised. It means that sampling of signals is performed closely to the signal sources. That helps to minimize distortions due to the ambient noise. Next, the design of the remote samplers, used as the front-end devices, is very simple. The most responsible basic element of the sampler is a comparator used for detecting the time instants  $\{t_k\}$  when the values of the input signal  $x(t)$  and the reference function  $r(t)$  become equal, when the equality  $x(t_k) = r(t_k)$  holds.

As the design of the samplers is simple, the power consumption of these front-end remote sampling devices, might be very low. Actually achieving of low power consumption depends on at least three factors. In addition to the design simplicity, sequential enabling of the remote sampling devices is performed instead of switching analog signals by a multiplexer. Therefore each of the front-end devices is not active for most of the time. The third power saving technique used is economic encoding of the sampled signal. Each single pulse generated at the comparator output to mark in time a particular event of the signal and the reference intersection typically carries 8 to 12 bit information.

On the other hand, this approach to signal sampling is specific. The signal sampling process then is nonuniform and that has to be taken into account at processing the acquired bioimpedance data. Fortunately, that does not represent a special problem if the demodulation and bioimpedance signal parameter estimation is carried out on the basis of the existing DASP methods and algorithms [1, 2, 3]. Moreover, using of the suggested digital representation of bioimpedance signals leads to complexity-reduced signal processing algorithms as it is shown below.

#### IV. PREPROCESSING OF DATA

Thus the signal sampling operation is carried out in a way ensuring that the information carried by each input signal  $x(t)$  is fully transferred to the sampled signal given as the sequence of crossing time instants  $\{t_k\}$ . The sequences of the appropriately positioned in time pulses, received at the master part of the distributed ADC, are transformed into digital sequences by performing time-to-digital conversions. After that there are basically two options how to proceed with preprocessing of the multi-channel bioimpedance data represented as  $n$  digital sequences  $\{t_k^n\}$  of crossing instants.

These digital signals could be either (1) used for reconstructing the sample values of the original signal and then to process them, or (2) they could be preprocessed directly.

Reconstructing of signal sample values do not represent a problem [2, 3]. The instantaneous values of the reference function  $r(t_k) = A_r \sin(2\pi f_r t_k + \varphi_r)$ , corresponding to the time instants  $\{t_k\}$ , obviously defines the sequence  $x(t_k)$  of the instantaneous values of a particular input signal. However the second option, direct processing of the digital sequences  $\{t_k^n\}$  of crossing instants, fully representing the respective bioimpedance signals, is more rational. To illustrate this, let us consider bioimpedance measurements performed in a single channel case under the conditions where the excitation current  $i(t)$  contains components at  $M$  frequencies  $f_m$ . Variations of bioimpedance typically lead to the amplitude and phase modulation of this information carrier. To estimate the reaction of the biological object being tested to this excitation, a voltage waveform  $v(t)$  is picked up and then sampled according to the signal and reference crossing discussed above. The sequence of the crossing time instants  $\{t_k\}$  then represents the waveform  $v(t)$  and it could be written that the discrete values of this voltage

$$v(t_k) = \sum_{m=1}^M [a_m \cos(2\pi f_m t_k) + b_m \sin(2\pi f_m t_k)], \quad (1)$$

where  $a_m$ ,  $b_m$  are Fourier coefficients characterizing the quadrature components of the object reaction to the excitation current component at the frequency  $f_m$ .

To carry out the demodulation, parameters  $a_m$ ,  $b_m$  have to be estimated as the basis for calculation of the digital amplitude and phase angle values of the modulated carrier. Usually these estimates  $\hat{a}_m$ ,  $\hat{b}_m$  are calculated in the standard way according to the following equations:

$$\hat{a}_m = \frac{2}{N} \sum_{k=0}^{N-1} v(t_k) \cos(2\pi f_m t_k) \quad (2)$$

$$\hat{b}_m = \frac{2}{N} \sum_{k=0}^{N-1} v(t_k) \sin(2\pi f_m t_k)$$

Most of the multi-bit number multiplication operations needed for performing the bioimpedance signal analysis then are related to the calculation of these estimates. Using of the crossing instant sequence  $\{t_k\}$  for digital representation of the bioimpedance signal  $v(t)$  makes it possible to reduce the complexity of this analysis significantly. Then the indicated Fourier coefficients could

be estimated in a much simpler way [1]. In this case the estimates  $\hat{a}_m$ ,  $\hat{b}_m$  could be calculated on the basis of the following equations not requiring multi-bit number multiplications:

$$\begin{aligned}\hat{a}_m &= \frac{1}{N} \sum_{k=0}^{N-1} (\sin 2\pi(f_r - f_m)t_k + \sin 2\pi(f_r + f_m)t_k) \\ \hat{b}_m &= \frac{1}{N} \sum_{k=0}^{N-1} (\cos 2\pi(f_r - f_m)t_k - \cos 2\pi(f_r + f_m)t_k)\end{aligned}\quad (3)$$

Thus the complexity of bioimpedance data pre-processing might be considerably reduced and that clearly represents an advantage. However, the fact remains that the signal sampling is nonuniform and that leads to some risks of getting errors due to the irregularities of the sampling process which would corrupt the bioimpedance measurements. To avoid this, processing of the digital bioimpedance signals apparently always has to be matched to the specifics of sampling and this requirement should not be ignored. Various aspects of rational pre-processing of the considered type of digital signals have been studied and are discussed in [2-5]. To obtain good results, the whole process of bioimpedance data acquisition, encoding and pre-processing, including generation of the reference sine-wave and the procedures of enabling the samplers, has to be appropriately arranged.

## V. CONCLUSIONS

The described approach to decentralized acquisition and pre-processing of bioimpedance data is recommended first

of all for applications in the bioimpedance measurement cases where it is essential to acquire data from a relatively large number of bioimpedance signal sources under conditions seriously limiting power consumption. The frequency range that could be relatively easily covered by bioimpedance measurement systems of this type stretches from very low frequencies up to about 10 MHz.

## REFERENCES

1. Bilinskis I. *Digital Alias-free Signal Processing*, John Wiley & Sons, Ltd (UK), 2007, 430 p.
2. Bilinskis I., Sudars K. Processing of signals sampled at sine-wave crossing instants. Proceedings of the "2007 Workshop on Digital Alias-free Signal Processing", 2007, London, UK, pp 45-50.
3. Artyukh Y., Bilinskis I., Sudars K., Vedin V., Multi-channel data acquisition from sensor systems, Proc. the 10-th International Conference "Digital Signal Processing and its Applications", Moscow, Russia, 2008, vol. X-1, pp 117-119.
4. Bilinskis I., Sudars K. Digital representation of analog signals by timed sequences of events, "Electronics and Electrical Engineering", No. 3(83), 2008, pp 89-92.
5. Bilinskis I., Sudars K. Specifics of constant envelope digital signals, "Electronics and Electrical Engineering", No. 4(84), 2008, accepted for publication.

Author: Ivars Bilinskis  
 Institute: Institute of Electronics and Computer Science  
 Street: 14 Dzerbenes Street  
 City: Riga  
 Country: Latvia  
 Email: bilinskis@edi.lv

# Design and Implementation of Textile Sensors for Biotelemetry Applications

M. Cerny<sup>1</sup>, L. Martinak<sup>1</sup>, M. Penhaker<sup>1</sup> and M. Rosulek<sup>1</sup>

<sup>1</sup> VSB - Technical University of Ostrava/Department of Measuring and Control, Ostrava, Czech Republic

**Abstract** — The sensing of biological signals is very actual theme. Especially bioelectrical signals are commonly measured for the evaluating a health status of a man. This article is focused on the analysis and design of sensing electrodes by the use of unconventional materials for a long term bioelectric activity measurement with advanced capabilities in a transmission of signal, time-impedance stability and low half cell voltage.

The principle of electrodes is conducting polymers which can be built-up on a textile or other non primary conducting materials. These types of sensors could be used among other ones in mobile human's telemetry systems. The sensors were tested in our laboratory and used in this telemetry project.

**Keywords** — Sensor, Biotelemetry, Polymers.

## I. INTRODUCTION

There are a lot of physiological parameters to measure from and on the human body. Generally there are signals obtained invasively or none invasively. Consequently there are signals discrete or continuous which can be divided concerning sensing procedure. Generally human body produces a lot of different signals, from the electrical to impedance, magnetical, biomechanical, acoustical, optical and chemical ones. Especially an electrical signal called the bioelectrical signal is very important for clinicians to determine patient's condition. In a long term measurement of bioelectrical activity there should be a problem with standard types of electrodes which has a time variable parameters.[1] [8] [9]

### A. Biopotential electrodes

Electrodes (second class leader) have to make a quality conductive connection of these two types' line wires regarding to the fact that the tissue (first class leader) is a conductor of a different type that leads electricity by available ions. That is why the electrodes are supplemented with conductive gels that generate electrolyte to transmit passage electrode – skin. The electrolyte creates surrounding body fluids to undersurface electrodes. [1] [3]

Biopotential electrodes are active sensors – source of an electrical current, source of signal.

General requirements are: high-quality conductive connection skin- instrument, nontoxic and nonirritating for

skin, chemical stability, sterility for invasive use, disinfection potentiality.

The biopotential electrode can be as an electrochemical half cell. In contrast of a chemical cell the polarity isn't constant. There are proceeding reducing oxidative reactions. At the electrochemical cell the half cell potential is the goal and instead at biopotential electrodes this is unwanted necessity. During a measurement on a human there is potential difference between electrodes and skin which we would like to measure. Regarding to ignorance and inability to measure the half cell voltage of electrodes exactly the irremovable error is added during measurement. That is why the evaluation of biosignals is not processed absolutely, but also is compared signal from more places and frequency analysis is provided. [2]

## II. METHODS

Conducting polymers are composed of long repeated constitutional group of chain. Common polymers like polyetylen or polyvinylchloride are non-conducting and they are usually use as an insulating material. However there has been a group of polymers which is chemically conducting.

From that reason of long term monitoring and sensing of biological data there is necessary to find out new materials and conception of sensing to obtain validate data. In this case the conducting materials like textile, polymers and conducting rubber is a way how to realize it. [4]

Conductive polymers are forming system conjugate dual structures, i.e. in their structure regularly diversify simple and dual bindings.

Except conjugation there is another necessary presumption seat electrical conductivity present bearers bullet that

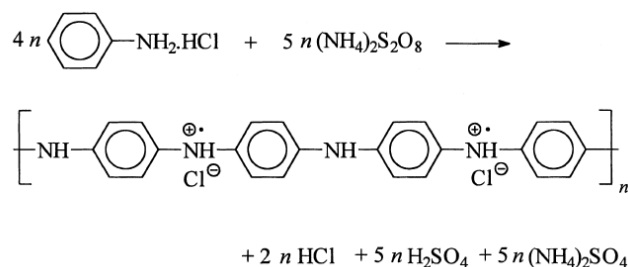


Fig. 1 Oxidation of aniline hydrochloride with ammonium peroxydisulfate yields polyaniline (emeraldine) hydrochloride. [4]

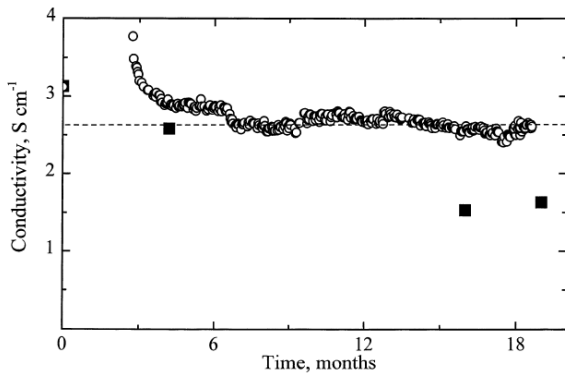


Fig. 2 Conductivity aging of polyamynil - hydrochloride as a pellet (open circles) and as a powder occasionally compressed into a set of pellets (full squares). [4]

the mediating his transport through chains. They are rising which is in an analogy with classical semiconductor given a name geed - up. However substantial discrepancy is between geed - up organic and inorganic semiconductors. In polymers it is for example higher concentration than in inorganic semiconductors. [5]

Electric conductivity of those group of polymers is at the level  $0,01 - 30 \text{ S.cm}^{-1}$ , i.e. it is compare with conductivity inorganic solid - state materials, as is for example germanium. Conductivity is then manifold lower in comparison with metals, as is copper or silver, overleaf is but heaps order higher, than it is customary near common polymers. [6] [7]

### III. IMPLEMENTATION ANALYSIS

The sensor design is a part of the process called implementation analysis. This is set from the implementation layers:

- Knowledge model
- Sensitivity analysis
- Sensor design
- Tests

At the beginning there is necessary to collect the knowledge model. This contains the information about what type of sensor is designed on, what sort of measured variables is measured and the explicit expression of models. Knowledge model is very important for other implementation layers.

The layer of sensitivity analysis consists in an assessment of their relevant changing factors. In the layer of sensor designed is made a list of existing sensors or rules of relevant factors to design new one.

The test layer verifies the quality of the chosen or designed sensor concerning required factors. Also there is a

possibility to adjust the knowledge model and sensitivity analysis entry conditions to improve the sensor characteristics.

### IV. KNOWLEDGE MODEL

Knowledge model specify of physician-expert requirement for measuring the specific biosignals. In our case it is bioelectric signal measure none invasively on the skin. The input information's are:  $0,1 - 50\text{mV}$  voltage range,  $0 - 1000$  Hz frequency range,  $40 - 100\%$  humidity range,  $2,1 - 7,8$  pH range,  $-40 - 50$  °C temperature range etc..

From the physician requirements are not specified the information about accuracy and resolution of bioelectrical signal. These properties have to be linguistic expression and they are input of sensitivity analysis.

### V. SENSITIVITY ANALYSIS

Sensitivity analysis establishes an important parameter for sensor selection or new design. In the sensitivity analysis we got layers up from linguistic expression and also from principles of physical measurement. The result is sensitivity level influence of an assigned value. It means that the sensitivity of input/output transmission has the desired value.

Biosignals desired value is deterministic. Most of them are time variable in spite of all regulated fixed factors. That is why it is necessary to reflect some of the criterions like: sensitivity, error, range, resolution, accuracy, time response and others.

In the dependence on a sensor type we can also distinguish from proper and mediate biosignals types, measurement methods and sensor utilization in medical diagnostics.

General requirements on bio-sensors are:

- Explicit input/output sensitivity
- Preferably linear dependence
- Maximal sensitivity
- Acceptable transfer function modality
- Time stability of sensor
- Minimal parasitic dependence
- Minimal measured object stress
- Maximal reliability
- Minimal energy consumption
- Simple construction and maintaining

Sensitivity analysis is mostly done by expert access. Outgoing list then specifies an important respect of sensor selection/design as: speed of response, material, dimension, cable length, impedance and other related aspect for example sensor placement, case making, etc..

### A. Deterministic method of sensitivity analysis

Deterministic method is based on partial derivation of input particular parameters implied function.

There can be set a partial derivation in an analytical way for more simple models. For a complex one it can be done by numerical approximation.

By system's analyzing and synthesis there are used mathematical models which are taken to be well known. In reality the real system can not be identified accurately. It is not possible to solve most of tasks without model's simplification. The sensitivity knowledge on parameters change should be necessary piece of every task of identification, analysis, synthesis and also optimization.

Mathematical model is assigned to a certain variable to parameter vector  $\mathbf{g}$ . The variable can be temperature, electrical potential, pH, impedance etc. The parameters are material, response, accuracy, resolution, etc. In certain conditions of continuity assignment can be make out matrix function  $\mathbf{S}$ . This function is sensitivity function.

Vector of parameters is defined by:

$$\mathbf{g}(\mathbf{a}): \mathbb{R}^m \times \mathbb{R}^n \rightarrow \mathbb{R}^m \quad (1)$$

$$\mathbf{g} = \{g_1(\mathbf{a}), g_2(\mathbf{a}), g_3(\mathbf{a}), \dots, g_m(\mathbf{a})\} \quad (2)$$

Sensitivity function is generally defined as Jacobian:

$$S_{i,j} = \frac{\partial g_i(\mathbf{a})}{\partial a_j} \quad i = 1, 2, \dots, m \text{ and } j = 1, 2, \dots, n \quad (3)$$

The  $\mathbf{S}$  function is except a parameters also generally dependent on time, frequency, input quantity, etc.. That is why  $\mathbf{S}$  function is not matrix coefficient but sensitivity function.

For sensitivity function there stand the same rules as for partial derivations. Sensitivity functions in time realm are actually time behaviors of a function. They can be easily simulated by sensitivity models. The functional can be defined to sensitivity functions. They characterize the sensitivity globally by one number that is called sensitivity rate.

## VI. SENSORS DESIGN

A great problem occurs at the ECG measurement. The medical instrument should be transportable and that's why the electrodes has to be part to not to manipulation illimitability. The problem rises how to create the electrodes which can by only put on the skin and not to be stick by conducting stick or gel (dry electrode). As a result it is clear that the designed electrode should be no metal or gel one. For the construction of this kind of electrode the same principles

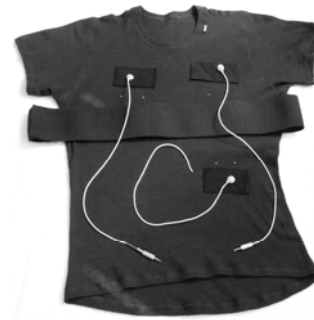


Fig. 3 Distribution of ECG electrodes on the T- shirt

were used as in common electrode. Also the interface skin - electrolyte (gel) – metal. Instead the electrolyte there was used material referred to conducting polymer (Figure 3.). It is a mixed conductor. There is neither first-order conductor nor second-order one.

From that reason the polyamide is suitable for making dry biopotential electrode. Their conductivity is  $4 \text{ S.cm}^{-1}$  is sufficient because they are settled in thin film form with thickness 100nm.

The production of this type of electrode takes apx. 15 minutes and there is also the need of another 12 hours for desiccation. The production is very cheap and easy to attach for a single use. The price of one polymer electrode realization is apx. 0.25 EUR. For the electrodes manufacturing we can use them with an advantage that there isn't registered any toxic or irritable character.

We can qualify it as a harmless electrode. Another advantage is that the utilization of the material can be manufactured electrode on any matter to resisted acidic medium. Textile materials are easy to use and that is why the electrodes on Velcro fastener were made. Velcro both side fastener is covered by polyanilin Figure 3.

## VII. RESULTS PRESENTATION

The testing layer serves for verifying of designed procedures and also for function testing. This can also improve obtaining of valid information about measured value.

During the testing on three leads ECG there was found out that manufactured electrodes are well usability. The measurement were done by ECG being short (pectoral) bipolar placement gained by bioamplifier g.BSamp, 16 channels from g.tec medical engineering GmbH and digitalized by A/D card NI DAQPad-6052E. The results were measured with common attached electrodes on computer at the same time. The measured results were mathematically compared and results were presumable and plausible.

Electrodes were mounted on flexible t-shirt made on elastics fiber. Adherence pressure was too small to well connect skin with electrode and that is why the great interference voltage arose. Consequently there was added the elastic belt on thoraxes to improve adherence pressure of the electrodes Figure 3.

For impedance characteristics measurement Eval AD5933 module was used. The measurement of impedance was done in frequency range 700 Hz to 15 kHz. The testing voltage was 2 V.

Impedance characteristics measured on AG/AgCl electrode with the gel RED Dot 2570 and Polyaminil covered textile. Both were measured on six samples each. Results evaluation was compared by value of standard deviation  $\sigma$  (4). The range of  $\sigma$  were between 0,006 to 0,015  $\Omega$ .

$$\sigma = \sqrt{\frac{1}{N} \sum_{i=1}^N \left( X_i - \bar{X} \right)^2} \quad (4)$$

where:  $X_i$  - difference between Ag/AGCl and Polyaminil textile; N - number of values of impedance record (N=14300)

### VIII. DISCUSSION

We are able to mention that polyamides are suitable material for biopotential electrodes construction from acquired results of our experiments. But there is a need to concentrate on parameters' measuring and monitoring in long term firmness - both an electro technical and a mechanical. From the point of view the tissue feature that changes its acidity and pH, there can be changes in electrical features of biopotential electrodes in specific circumstances. That is why it is also important to concentrate on materials mechanical resistance.

Also a wide range of sensor design methods can be discussed. Except deterministic method we can use also statistical, graphical and others based on fuzzy, neural network and chaos theory. This has to be verified because probably none of them are multi-purpose for all physical variables.

### IX. CONCLUSIONS

In the present time the health telemetry systems create an integral part of our everyday lives. The sensors are the primary part of these systems and also the improvement on design, new materials, constructions and sensor disposition are actual nowadays. Our research and tests enabled us to

find out that electrochemical allied substances seem to be appropriate for the future applications.

### ACKNOWLEDGMENT

Many thanks to Mr. Jaroslav Stejskal PhD. and Mrs. Eleně Konjušenko from Academy of science, The work and the contribution were supported by the project Grant Agency of Czech Republic – GAČR 102/08/1429 Safety and security of networked embedded system applications.

This work was partially supported by the faculty internal project, "Biomedical engineering systems IV"

### REFERENCES

1. Bronzino, J. D. (1995). *The Biomedical Engineering Handbook*, CRC Press
2. Washburn, E.W. et al. (2003) International Critical Tables of Numerical Data, Physics, Chemistry and Technology. 1st Electronic Edition. Knovel, ISBN 1-59124-491-9.
3. Penhaker, M., Imramovský, M., Tiefenbach, P., Kobza, F. (2004). *Lékařské diagnostické přístroje učební texty*, VŠB – TU Ostrava
4. Stejskal, J., Gilbert, R. G.: Polyaminil. Preparation of a Conducting Polymer, *Pure Appl. Chem.* 74, 857 (2002).
5. Stejskal, J., Sapurina, I.: Polyaminil: Thin Films and Colloidal Dispersions, *Pure Appl. Chem.* 77, 815 (2005).
6. Brožová L., Holler P., Kovářová J., Stejskal J., Trchová M.: The Stability of Polyaminil in Strongly Alkaline and Acidic Aqueous Media, *Polym. Degrad. Stab.* 93, 592–600 (2008).
7. Blinova N.V., Stejskal J., Trchová M., Čirić-Marjanović G., Sapurina I.: Polymerization of Aniline on Polyaminil Membrane, *J. Phys. Chem. B* 111, 2440–2448 (2007).
8. Mrázová, J. (2005). Bio-signals classification into groups, In *TRANSCOM Section 5*
9. Noury, N., From Signal to Information : the smart sensor. Applications in Industry and Medicine Habilitation a diriger des recherches, France: Grenoble, 2002.
10. Randy, F. Understanding Smart Sensors. London: Artech House, 1996. ISBN 0-89006-824-0
11. Julian W. Gardner, *Microsensors: Principles and Applications*, John Wiley & Sons Ltd, 1999
12. Ryoji Ohba, *Intelligent sensor technology*, John Wiley & Sons Ltd, 1992
13. Scanaill, C.N., Carew, S., Barralon, P. Noury, N. Lyons, D. And Lyons, G.M. A Review of Approaches to Mobility Telemonitoring of the Elderly in Their Living Environment *Annals of Biomedical Engineering*, Vol. 34, No. 4, April 2006 ( C\_ 2006) pp. 547–563 , ISSN 0090-6964 (Print) 1573-9686 (Online)
14. Martinák, L. Implementační analýza snímáču teploty a pohybu pro použití v telemedicině, 2006, PhD. thesis,

Address of the corresponding author:

Author: Ing. Marek Penhaker, Ph.D.  
 Institute: VSB – TU Ostrava  
 Street: 17. listopadu 15  
 City: Ostrava - Poruba  
 Country: Czech Republic  
 Email: marek.penhaker@vsb.cz

# The Suitability of Silver Yarn Electrodes for Mobile EKG Monitoring

A. Comert<sup>1</sup>, M. Honkala<sup>2</sup>, M. Puurtinen<sup>1</sup> and M. Perhonen<sup>3</sup>

<sup>1</sup> Department of Biomedical Engineering/TUT, Tampere, Finland

<sup>2</sup> SmartWear Lab/TUT, Tampere, Finland

<sup>3</sup> CorusFit Oy, Jyväskylä, Finland

**Abstract** — The use of textile electrodes in wearable EKG monitoring systems is presented. We show that if motion does not exist, textile electrodes offer comparable quality to medical grade electrodes. Upon solving problems and artifacts arising mainly due to motion, textile electrodes can be a basis for a more user friendly long and short term monitoring garment.

**Keywords** — EKG, wearable, mobile, smart textile, textile electrode

## I. INTRODUCTION

Mobile monitoring of EKG in healthy subjects and patients under risk is catching interest in the areas of sports, emergency care, and preventive care. Medical electrodes used today pose a number of problems, making it necessary to provide a new solution to the electrode level of a monitoring system. For a wireless-wearable EKG monitoring project, we have been using silver yarn embroidered onto textile as electrodes, and this setup proves to be promising.

Cabling and glue in the medical electrodes of present makes them unsuitable for long term mobile monitoring in a way that patient discomfort is present. A way to integrate electrodes into an EKG monitoring garment without making the electrodes distinguishable from the worn fabric would increase wearing comfort considerably and also reduce the patients' feeling of being monitored. This can be achieved by using textile electrodes made from conductive fibers or yarns, and by attaching them onto the garment in a user friendly way. Different manufacturing methods of textiles can all offer potential means to produce suitable electrode structures. It is however important that the conductivity of the electrode is as consistent as possible also during possible extensions of the electrode structure. In our work we have studied the feasibility of conductive silver yarns in achieving reliable and comfortable electrode system. Silver has the advantage of being non-irritating and also it is suitable for EKG monitoring during exercise because of its anti-bacterial properties, as well as the material having appropriate electrical properties.

Commercial medical electrodes use gel and are attached to the skin via glue, to allow high signal quality. The textile electrodes to be used will have no such attachment

possibilities and also will function as dry electrodes when the person is not sweating. This causes low quality measurement in extreme motion cases if the electrode-skin contact is affected. We have anyway found that, at present, textile electrodes provide reliable measuring opportunities in situations where the body is still, or body motion at the electrode location is kept at minimum. Currently there are few heart rate monitors available which utilize silver textiles for heart rate monitoring [1,2], but these do not need to be as reliable as EKG monitoring and electrode locations are different than unconventional EKG measurements. For wearable EKG monitoring, EMG artifacts, motion artifacts and the necessary cabling generate different problems than those a simple chest belt based heart rate monitoring device experiences.

Thus, in this study we have demonstrated that textile electrodes are suitable to be used in wearable EKG monitoring, if the effects of motion can be further reduced. Solutions to reduce these effects of motion will in turn be presented in upcoming papers, so this one can be taken as an introductory text.

## II. TEXTILE ELECTRODES

Electrodes tested in this study are comprised of 234 dtex silver yarn sewn or embroidered onto different types of textiles, or woven into different types of narrow fabrics. The conductive yarn is silver plated high grade multifilament nylon (polyamide 6.6) yarn.

In the experiments reported in this paper we have used the Lead I of a three lead system, which runs from the Right Arm (RA) to the Left Arm (LA). In different experiments we have been also using the precordial leads V3, V4 and V5 locations, but they are left out for the sake of simplicity. The reason for the complexity is that the electrode structure is different due to different anatomical requirements of these locations.

For RA we have used the midpoint of the upper right arm, for LA, the respective location on the left arm. (Fig. 1) We have not used the wrist as an electrode location since a short sleeved vest or t-shirt is more user friendly and more versatile than a longer sleeved one when thinking about a

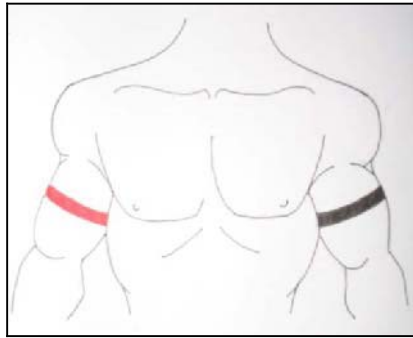


Fig. 1 Textile electrode locations

sports environment at room temperature. The reason for not using a shoulder electrode location close to the clavicle is the immense difficulty in attaching a dry electrode to that location without using glue.

The arm electrode is a stretchable ribbon type electrode fully circumventing the arm.. The electrode can stretch up to about 160% of its original length, retaining the same electrode area during the stretch. The 3 cm wide ribbon has 5 mm margins without silver yarns, and into the remaining area 10 silver yarns are embedded in a way that the conductive silver pattern does not affect the stretchability. The length of the ribbon varies depending on the size of the specific garment. (Fig. 2).

To further complete the system setup, the textile electrodes are connected to the amplifier via textile cables.

The signals are amplified with a two stage EKG amplifier, where the first amplifier stage is realized with INA126 instrumentation amplifier. Signals are filtered with 1-40 Hz band pass filter and sampled with 16-bit AD-converter using 250 Hz sampling frequency. The signals are then transferred wirelessly to a PC.

### III. COMPARISON OF ELECTRODES

To compare the functionality of textile electrodes with commercial medical electrodes, we present two experiments.

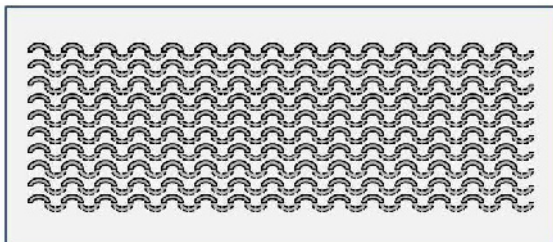


Fig. 2 Electrode structure

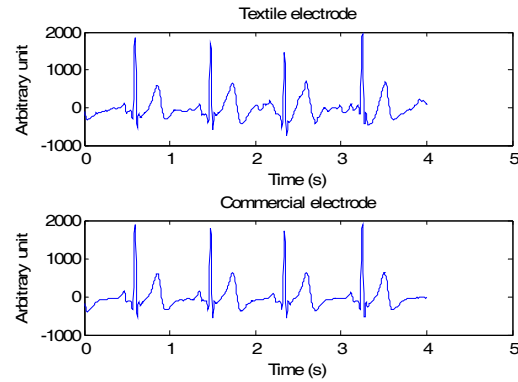


Fig. 3 Resting condition

In both of the experiments the measurements from the electrodes have been done by identical amplifiers simultaneously. The shown EKG signals are synchronized.

The signals both undergo band pass filtering between 1Hz and 35Hz. This is the only signal processing done on the signals.

#### A. Signal when totally relaxed

This is a comparison between the commercially available medical electrodes when the person is sitting on a chair, without motion in the body or the extremities. The muscles are relaxed.

As can be seen in the Figure 3, the EKG signal quality of the two electrode types are comparable, and if no motion would be present, the medical electrodes could be exchanged with the textile electrodes, resulting only in a small amount of quality degradation.

For all the following graphs, the textile electrode’s signal will be the top part of the figure.

#### B. Signal when EMG present

For this test, these two muscle groups have been contracted separately and simultaneously:

- Biceps
- Triceps

The biceps muscle is contracted so that the elbow joint is bent at 90 degrees and the forearm is parallel to the ground. The contraction is isometric and is done at 30 percent of the maximum weight the subject can lift without breaking proper form (Fig. 4).

The triceps muscle is contracted so the arm stays in the same position as in the biceps contraction test, and again we used 30 percent of the maximum weight the subject can press on the triceps press machine (Fig. 5).



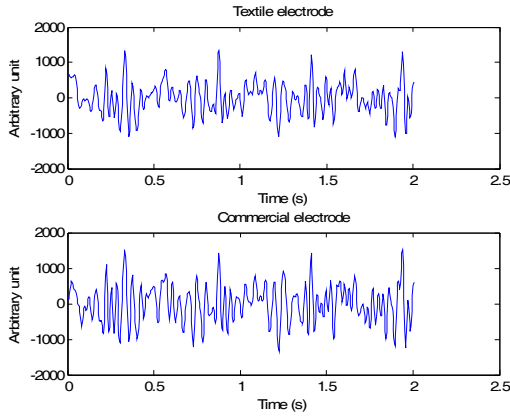


Fig. 4 Biceps muscle contraction

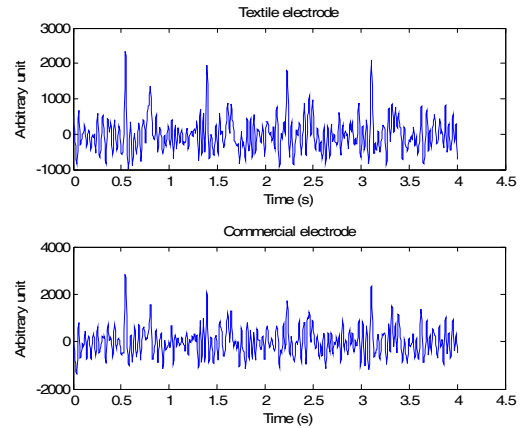


Fig. 6 Isometric contraction of both muscle groups

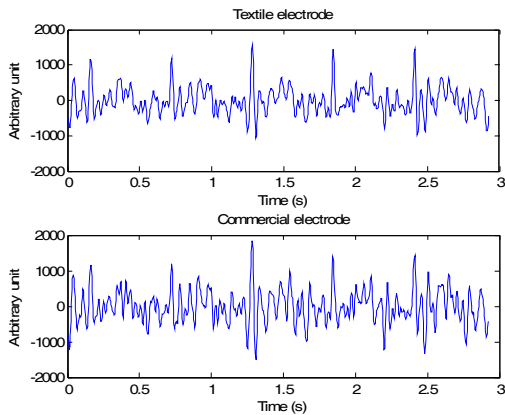


Fig. 5 Triceps muscle contraction

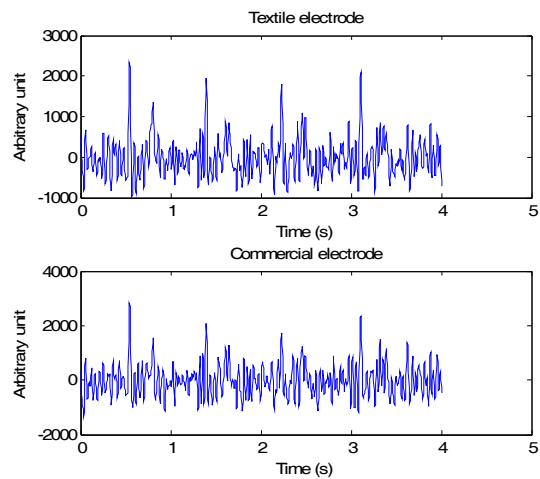


Fig. 7 Isometric contraction of both muscle groups when sweat is present on the skin.

A third experiment has been conducted so that the elbow joint is at 90 degrees, forearm parallel to the ground, and the subject is performing isometric contraction of both muscle groups at the same time, just under the level where the arm would start shaking (Fig. 6).

As one intended application area for a garment incorporating these textile electrodes is sports, it would be useful to demonstrate the effect of sweat on the comparison of the textile electrodes to the commercial electrodes. (Fig. 7)

#### IV. RESULTS

The analysis of the four tests under dry conditions reveals that in the selected locations the EMG effect on the textile electrodes is not significantly different compared to the conventional ones.

This result is also obtained from the frequency domain analysis of the signals. To provide an example, in Figure 8

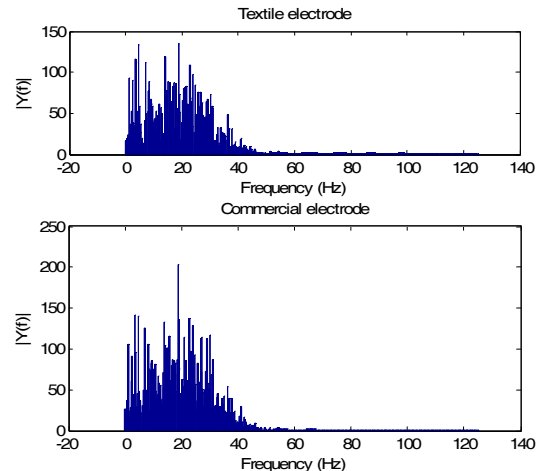


Fig. 8 Frequency domain analysis of the signals during isometric contraction

we show the frequency domain analysis for the isometric contraction. Except the dominant 20Hz component of the commercial electrode's signal, the signals show a clear similarity.

An additional result would be that the textile electrodes show a minor superiority to the commercial electrodes in sweaty conditions. This is due to the fact that even if sweat does not affect the already gelled commercial electrode, it significantly increases the conductivity of the dry textile electrode.

## V. CONCLUSION

According to our experiments, textile electrodes can be used even though the motion artifact is a challenge. The signal quality under no-motion conditions is comparable to commercial electrodes. The EMG has a similar effect on both types of electrodes in dry conditions, while the signal-to-noise ratio is better for textile electrodes when the skin is damp or sweaty.

The biggest challenge textile electrodes face is the motion artifact. Since they are dry electrodes and not

attached to the skin via glue, these electrodes are highly susceptible to the effects of motion. Probably different structures of electrodes located at carefully selected anatomical locations could eliminate or minimize the effects of motion to a degree where textile electrodes will be used instead of present day's commercial electrodes.

## ACKNOWLEDGEMENT

The authors would like to acknowledge CorusFit Ltd. for the financial support of this study.

## REFERENCES

1. Polar Wearlink, <http://www.polarusa.com>
2. AdiStar Fusion, <http://www.adidas.com>

Author: Alper Cömert  
Institute: Department of Biomedical Engineering  
Street: P.O.Box 692  
City: Tampere 33101  
Country: Finland  
Email: [alper.comert@tut.fi](mailto:alper.comert@tut.fi)

# Drawback of ICA Procedure on EEG: Polarity Indeterminacy at Local Optimization

F. Cong<sup>1</sup>, I. Kalyakin<sup>1</sup>, T. Ristaniemi<sup>1</sup> and H. Lyytinen<sup>2</sup>

<sup>1</sup>School of Information Technology, University of Jyväskylä, Jyväskylä, Finland

<sup>2</sup>Department of Psychology, University of Jyväskylä, Jyväskylä, Finland

**Abstract** — Independent component analysis (ICA) has been extensively applied to reject artifacts in electroencephalography (EEG) signal processing. The first step is to extract the independent component activations from the electrode records, and then project the desired components back to the electrodes. After the composition of the projected component is analyzed in details under ICA procedure, this study shows that since ICA may extract some source components at the local optimization in high-dimensional EEG signal space, the artificial polarity indeterminacy may happen on the projected component at some electrodes. By numerical simulations, this issue also exhibits that this polarity ambiguity occurs. Hence, we conclude that the abnormal polarity reversal should be corrected, and that without prior knowledge on the desired target activation or the artifacts, the polarity of the projected component may be not reliable under ICA procedure.

**Keywords** — ICA, projection, polarity, local optimization

## I. INTRODUCTION

Electroencephalography (EEG) collected from any point on human scalp includes activity generated within a large brain area because of the distance between the skull and brain and their different resistivities [1,2]. This spatial smearing of EEG data by volume conduction does not involve significant time delay, and the linear transform model of latent variables fits the EEG data in a trial,

$$z_i(t) = \sum_{j=1}^n a_{ij}s_j(t) + n_i(t), \quad (1)$$

where,  $z_i(t)$  is the record at the electrode  $i$ ,  $t$  is the time index,  $t = 1, \dots, T$ ,  $s_j(t)$  is the activation sent by the neuron  $j$ ,  $a_{ij}$  is the constant spatial scalp map coefficient from the neuron  $j$  to the electrode  $i$ ,  $n_i(t)$  is the sensor noise and is of the Gaussian distribution. This EEG data model has been generally acknowledged by the experts in EEG signal processing, and adopted by the well-known EEGLAB-open source Matlab toolbox for electrophysiological research [3]. In the past tens of years, independent component analysis (ICA) [4] has been extensively applied to reject the artifacts since Makeig and colleagues published their articles [1,2]. ICA procedure on EEG includes two steps. The first is to

extract the independent components from the electrode records, and the second is to project the desired components back to the electrodes.

Most ICA algorithms are adaptive and optimized through various gradient descent methods. Since the objective function may possess many locally optimized points, the performance of these algorithms heavily relies on the random initial point. This determines a direction to optimize the objective function. When ICA is applied to EEG, it is usually the case of a very high-dimensional signal space, and the probability to find the global optimal algorithms should be rather low. However, if some prior knowledge of sources can be supplied, for example, the similar distribution of the source, even at the local optimization, a component or a subset of the components may be accurately estimated. Therefore, to assess the algorithmic reliability of the estimated components, it is reasonable to run the estimation algorithm many times, using different initial values, and assessing which of the components are found in almost every run. This is the basic principle of ICASSO procedure [5]. However, what it extracts from the mixtures may also at the local optimization for some bad index qualities. This means that the global matrix of ICA is not a matrix with just only one nonzero element in each row and each column, but an element of the comparatively large absolute value. Under such a local optimal solution, after the desired target component activation is projected back to electrodes, the projected component activation may possess the abnormal polarity reversal at some electrodes. We will make explanations on it in details at part two.

To some EEG signals, the polarity is very significant. For example, the mismatch negativity (MMN) is a component of auditory event-related potentials, and is a tool for studying how the human brain detects deviations within sequences of repeated auditory stimuli. When all electrode locations were referred to the tip of the nose the MMN had negative amplitude in frontal, central, and parietal locations and positive amplitude in mastoid locations [6].

In this study, we focus on discussing the polarity of a projected component when the component is estimated from the local optimization. Next, we first analyze the composition of the projected components, and conclude that the projected components may possess polarity indeterminacy.

Then we design a simulation of the ICA procedure under the local optimization, and find the abnormal polarity reversal. Finally, we make conclusions on ICA procedure to EEG.

## II. COMPOSITION OF A PROJECTED ACTIVATION

If sensor noises could be omitted, then, the EEG data may be modeled as

$$\mathbf{x}(t) = \mathbf{A}\mathbf{s}(t). \quad (2)$$

ICA is to find such an unmixing matrix  $\mathbf{W}$  to transform  $\mathbf{x}(t)$  into

$$\mathbf{y}(t) = \mathbf{W}\mathbf{x}(t). \quad (3)$$

In EEG,  $\mathbf{y}(t)$  are called the component activations and they are the time courses of relative strengths or activity levels of the respective independent components, and the columns of the inverse of an unmixing matrix give the relative projection strengths of the respective components onto each of the scalp sensors. These may be interpolated to show the scalp map associated with each component [1,2]. In this paper, we assume  $n$  sources and  $n$  sensors. The projection of the  $k^{th}$  independent component back onto the original electrodes is given by the outer product of the  $k^{th}$  row of the component activation matrix with the  $k^{th}$  column of the inverse unmixing matrix, and is in the original units (microvolts). The projection  $k^{th}$  independent component to the electrode  $i$  can be mathematically expressed as

$$\mathbf{W}\mathbf{A} = \mathbf{C}. \quad (4)$$

$$\mathbf{B} = \mathbf{W}^{-1}, \quad (5)$$

$$e_i(t) = b_{ik}c_{km}s_m(t) + \sum_{j=1, j \neq m}^n b_{ik}c_{kj}s_j(t), \quad (6)$$

where,  $b_{ik}$  is the element of projection matrix  $\mathbf{B}$ , and  $c_{km}$  is the element of global matrix  $\mathbf{C}$ , moreover,  $c_{km}$  is assumed to possess the largest absolute value among elements of the  $k^{th}$  row of  $\mathbf{C}$ , and  $s_m(t)$  is the target activation. In this study, we denote the  $b_{ik}$  and  $c_{km}$  as the projection factor and separation factor respectively.

In theory,  $\mathbf{C} = \mathbf{P}\mathbf{D}$ , where  $\mathbf{P}$  is a permutation matrix, and  $\mathbf{D}$  is a diagonal matrix. As a result,  $\mathbf{C}$  is a matrix that has only one nonzero element in each row and each column. Thus, the second part of the right side at the equation (6) will disappear, and the projected component activation is equal to the mapped activation

$$e_i(t) = a_{im}s_m(t). \quad (7)$$

In practice, since the equation (3) is possibly under the local optimization,  $\mathbf{C}$  may be a matrix that has only one element with the comparatively large absolute value in each row and each column. This may also cover the local optimal case. Thus, from equations (4) and (5), we can conclude that the sign of the product of projection factor  $b_{ik}$  and the separation factor  $c_{km}$  will be random. As a result, the polarity of the projection activation will be indeterminate according to the equation (6). Moreover, projected components should consist of the mapped target activation and the sum of the other mapped activations.

According to the equation (6), the equation (2) can be rewritten as

$$x_i(t) = a_{im}s_m(t) + \sum_{j=1, j \neq m}^n a_{ij}s_j(t). \quad (8)$$

The equations (6), (7) and (8) describe the projected activation, mapped activation, and mixed activation at the electrode  $i$ . The mapped activation determines the polarity of the record at the electrode. However, it is impossible to obtain the exact mapped activation with the equation (7) in practice. Fortunately, the EEG signal is of a high-dimensional space, and the second item in the right part of the equation (8) is the sum of the undesired mapped activations. According to the central limit theory, this item should be of the Gaussian distribution. Hence, due to the constant map from the neuron to the electrode, averaging over many trials can also reveal the essence of the target activation under the equation (8) [7]. This method is extensively adopted in the society of psychology [6]. With the development of advanced signal processing techniques, we can obtain the projected activation through the equation (6). In contrast to the equation (8), the advantage of the equation (6) is that the signal to interference ratio (SIR) should be greatly improved since  $c_{km}$  is assumed to possess the largest absolute value among all the elements of the  $k^{th}$  row of  $\mathbf{C}$  but  $a_{im}$  is not of such characteristic; since ICA could possibly extract the target activation under the local optimization, the disadvantage is that the signs of the projection factor  $b_{ik}$  and separation factor  $c_{km}$  may be random. We define that the polarity indeterminacy appears when polarities of the projected activation and the mapped activation are not identical at the same electrode. It is artificial, so it should be corrected. Through averaging over thousands of trials, the equation (8) may supply the reliable infomax on the polarity of the mapped activation. Then, this prior knowledge may assist to correct the polarity of the projected activation.

### III. SIMULATION RESULTS

In this part, we simulate the ICA procedure on EEG from the equation (2) to (8). For better understanding, the SIR of the mixed activation is defined as below,

$$SIR_{mix} = \frac{1}{n} \sum_{i=1}^n 10 \log_{10} \frac{\sum_{t=1}^T [a_{im} s_m(t)]^2}{\sum_{t=1}^T \left[ \sum_{j=1, j \neq m}^n a_{ij} s_j(t) \right]^2} \quad (9)$$

The SIR of the projected activation is set as

$$SIR_{proj} = 10 \log_{10} \frac{\sum_{t=1}^T [c_{km} s_m(t)]^2}{\sum_{t=1}^T \left[ \sum_{j=1, j \neq m}^n c_{kj} s_j(t) \right]^2} \quad (10)$$

The SIR improvement is calculated as

$$SIRI = SIR_{proj} - SIR_{mix} \quad (11)$$

Six artificial sources with unit variance are produced as Fig.1. The second source is named as the sole target activation. The mixing matrix is randomly generated. During the simulation, we do not run any ICA algorithm, but generate the global matrix  $\mathbf{C}$ , and let  $\mathbf{C}$  have only one element with the comparatively large absolute value in each row and each column. This may also cover the local optimal case. Fig.2 describes the mixing matrix and global matrix. Fig.3 is the waveforms of projected activations and mapped activations. In the Fig.3, the solid line is the projected activation, and the dash-dot line is the mapped activation at each electrode. At the second electrode in Fig.3, the abnormal polarity reversal (APR) of the projected activation occurs in contrast to the mapped activation, and at other electrodes, projected activations are very close to mapped activations. In this

example, the  $SIR_{mix}$  is -13.9dB,  $SIR_{proj}$  is 32.3dB, and  $SIRI$  is 46.1dB. From the view of ICA, Fig.2 and Fig.3 imply the performance should be good enough. However, even under such good performance, the APR still appears.

Fig.2 and Fig.3 are only the single run results. In order to make our conclusion more believable, we mix sources 100 times with different mixing matrices, and for each mixing matrix, ICA procedure on mixtures is run 1000 times.

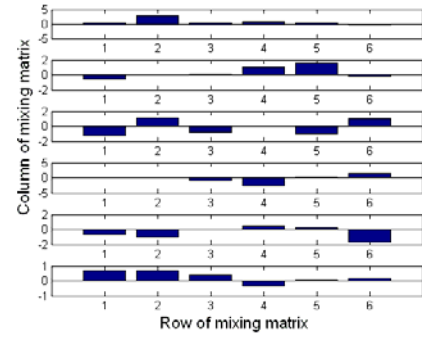


Fig. 2. (a) mixing matrix

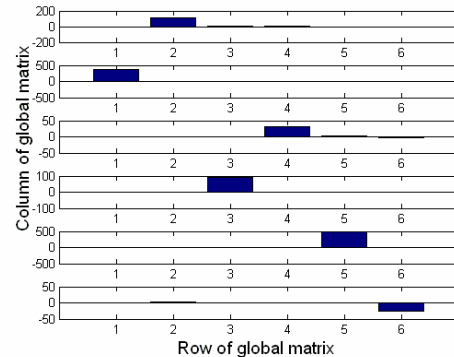


Fig. 2. (b) global matrix

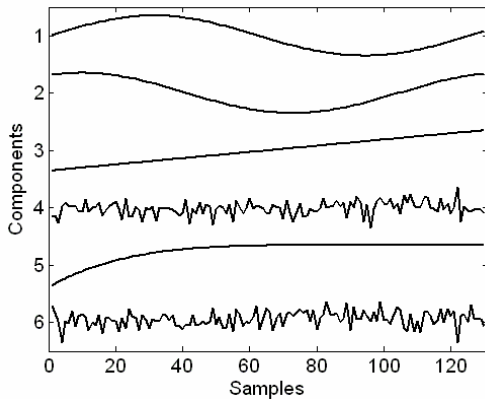


Fig. 1. Waveforms of six sources

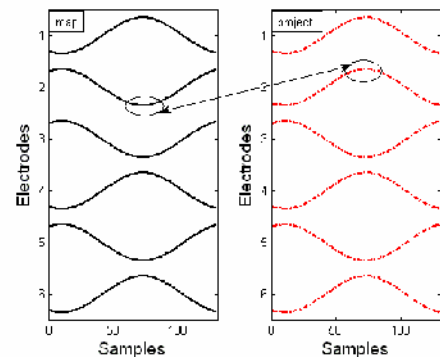


Fig. 3. Waveforms of six projected and mapped activations

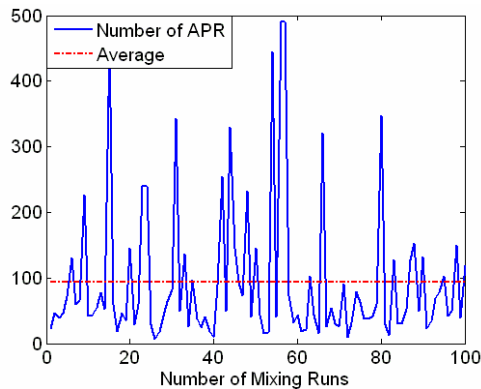


Fig. 4. Number of APR occurrence among 1000 ICA procedure runs under each mixing matrix

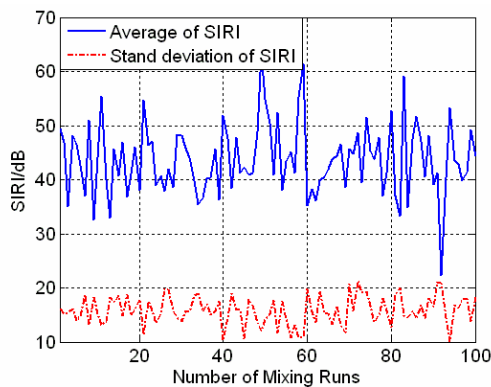


Fig. 5. SIR improvement under each mixing matrix

Fig.4 is the mixing SIR under each mixing matrix, and describes how many runs the APR happens. The solid line is the number of APR occurrence among 1000 ICA procedure runs under each mixing matrix, and the dash-dot line is for its average. Corresponding to Fig.4, Fig.5 shows the SIR improvement under the runs that APR appears. In Fig.5, the solid line and dash-dot line are respectively the average SIR and its deviation. Fig.4 shows that APR happens nearly in one tenth of all runs. This ratio is not low. In Fig.5, average SIRI is beyond 30dB under most mixing matrices. This number means the ICA performance should be good enough. Averaging increases the SIR by an amount proportional to the square root of the number of trials [7]. In order to obtain the same SIRI, 900 trials are required for the mixed activation. However, this simulation exhibits that with the projected activation much less trials can also contribute to the higher SIR. This is the advantage of ICA procedure on EEG. In practice, sources and the mixing matrix are unknown, and it is impossible to know the SIR. This simulation just describes that the polarity indeterminacy

may happen in the ICA procedure on EEG, but it does not necessarily occur under our simulation conditions. In fact, the higher SIRI is, the lower the possibility of the APR occurrence is.

#### IV. CONCLUSIONS

In high-dimensional signal space, ICA may extract the desired target activation under the local optimization with high possibility, and the global matrix of ICA can not have just one nonzero element in each row and column, but one element with comparatively large absolute value. Hence, the sign of the product of the projection factor and separation factor may be indeterminate under the ICA procedure on EEG. This can directly result in the polarity indeterminacy of the projected activation at some electrodes. If the prior knowledge of the target activation is available, the polarity ambiguity can be corrected. To unknown activations, what ICA procedure estimates may be not reliable in the polarity.

#### REFERENCES

1. Makeig, S., Bell, A. J., Jung, T.P., et al. (1996) Independent component analysis of electroencephalographic data. In D. Touretzky, M. Mozer, & M. Hasselmo (Eds.), *Advances in Neural Information Processing Systems*, Cambridge, MA, USA: MIT Press, 8 : 145-151
2. Makeig, S., Westerfield, M., Jung, T.P., et al. (1999) Functionally independent components of the late positive event-related potential during visual spatial attention. *Journal of Neuroscience*, 19: 2665-2680.
3. Delorme A., Makeig S. (2004) EEGLAB: an open source toolbox for analysis of single-trial EEG dynamics. *Journal of Neuroscience Methods*, Vol.134, pp.9-21.
4. Comon P. (1994) Independent component analysis, a new concept?. *Signal processing*, 36 (3) :287-314.
5. Himberg J., Hyvärinen A., Esposito F. (2004) Validating the independent components of neuroimaging time-series via clustering and visualization. *NeuroImage*, 22(3):1214-1222.
6. Näätänen, R. (1992) *Attention and brain function*, Hillsdale, NJ: Lawrence Erlbaum Associates Publishers.
7. Harmony T. (1984) Neurometric assessment of brain dysfunction in neurological patients. In E. R. John & R. W. Thatcher (Eds.). *Functional Neuroscience: Vol. III*. Hillsdale, NJ: Lawrence Erlbaum Associates Publishers.

Address of the corresponding author:

Author: Fengyu Cong  
 Institute: University of Jyväskylä  
 Street: POBox 35 (Agora)  
 City: Jyväskylä  
 Country: Finland  
 Email: fecong@jyu.fi

# Empirical Mode Decomposition on Mismatch Negativity

F. Cong<sup>1</sup>, X. Xu<sup>2</sup>, T. Ristaniemi<sup>1</sup> and H. Lyytinen<sup>3</sup>

<sup>1</sup> School of Information Technology, University of Jyväskylä, Jyväskylä, Finland

<sup>2</sup> Hangzhou Applied Acoustic Institute, Hangzhou, China

<sup>3</sup> Department of Psychology, University of Jyväskylä, Jyväskylä, Finland

**Abstract** — Empirical mode decomposition (EMD) has been applied in the various disciplines to extract the desired signal. The basic principle is to decompose a time series into intrinsic mode functions (IMFs) and each IMF corresponds to an oscillation phenomenon. A statistical description of the oscillatory activities of the EEG has been well known. It is desired to extract single oscillatory process from the EEG by EMD. Mismatch negativity (MMN) can be automatically elicited by the deviant stimulus in an oddball paradigm, in which physically the deviant stimulus occurs among repetitive and homogeneous stimuli. MMN thus reflects the ability of the brain to detect changes in auditory stimuli. So, the MMN trace indeed is the superposition of different event related potentials (ERPs). In theory, different ERPs correspond to different oscillatory phenomena. We assume each oscillatory activity corresponds to an IMF. Hence, EMD can decompose the MMN trace into different IMFs. Based on the timing, spectral and time-frequency infomax of MMN, a MMN detector is also designed to choose the MMN-like IMF. In contrast to the classic methods—averaging and optimal digital filtering (ODF), the EMD can cancel the ERPs overlapped with MMN both in the time and frequency domain. In the computation on the MMN experiment dataset, EMD outperforms averaging and ODF with about 3dB higher support to absence ratio.

**Keywords** — EMD, IMF, MMN, time-frequency, SAR

## I. INTRODUCTION

With the development of the recognition on human brains, scientists have gradually begun to agree millions of neurons self-organize into transient networks that synchronize in time and space to produce a mixture of short bursts of oscillations. These periodic vibrations can be observed and detected in the electroencephalogram (EEG) [1-4]. Mismatch negativity (MMN) belongs to the event-related potential (ERP), and can be automatically elicited by the deviant stimulus in an oddball paradigm, in which physically the deviant stimulus occurs among repetitive and homogeneous stimuli. MMN thus reflects the ability of the brain to detect changes in auditory stimuli. As a result, the MMN trace indeed is the superposition of different ERPs. In this study, we define each ERP as an oscillatory phenomenon. Thus, MMN trace can be regarded as mixtures of different oscillatory phenomena.

In order to extract the MMN-like oscillatory from the mixtures at a single channel, the averaging, band pass digital filtering and wavelet filtering have been extensively used. In the society of the psychology, averaging over trials is a very popular algorithm to improve the signal to noise ratio. The averaging algorithm assumes that at different trials, the desired target signal is invariant, and no artifacts are produced, and noises are Gaussian distribution [5]. Under such an assumption, the signal to noise ratio could be improved via an amount proportional to the square root of the number of trials [6]. However, this assumption does conflicts to the reality. During eliciting MMN, the brain may also generate many spontaneous ERPs, moreover, the MMN at different trials could be somewhat different. Hence, the performance of averaging should degenerate. A band pass digital filtering is an extremely easily implemented method and it can delete the frequency components out of a certain frequency band. Nevertheless, when the ERPs overlap in the frequency domain, such a filter can not separate the overlapping. Another problem is that the frequency resolution needs longer time series. This requirement can not be met when the desired ERP is transient. To resolve this problem, the wavelet filter has been developed and become very popular in many disciplines from the end of 1980s. Indeed, it is very useful in analysing data with gradual frequency changes. Since wavelet transformation has an analytic form for the result, it has attracted extensive attention of the applied mathematicians. Although wavelet filtering is versatile, the disadvantage is that wavelet filter is not an adaptive methodology. The selection of the wavelet is too vital to make the method very strict to data.

Empirical mode decomposition (EMD) was first formulated by Huang and his colleges [7]. As they have defined that EMD is an adaptive method to identify the intrinsic oscillatory modes by the characteristic time scales in the data empirically, and then decompose the data accordingly, and that the decomposition is according to the straightforward extraction from the signal energy based on the various intrinsic time scales, and that this technique adaptively decomposes non-stationary signals into a set of intrinsic time scales, and that in contrast to previously discussed methods, EMD is intuitive, direct, *a posteriori* and adaptive, with the basis of the decomposition based on, and derived

from, the data. EMD has been applied in the biomedical engineering [8-12].

In the present study, EMD is applied to find the MMN-like IMF, and the artefacts are rejected simultaneously. The methods will be introduced in the second part, and results are reported in the third part. As last the discussion of EMD on MMN is given.

## II. METHOD

MMN is usually elicited in a passive oddball paradigm presenting an uninterrupted sound consisting of two alternating tones (600Hz and 800Hz) of the same duration (100ms) with infrequent shortenings of one of the 600Hz tones (50ms or 30ms) [13]. The experiment paradigm is shown in Fig.1.

Due to the limited length of the paper, the participants, MMN eliciting paradigm and EEG recordings are not exactly stated. Please refer to the [14, 15]. There were totally 98 subjects, 9 channels, two MMN deviations and 350 trials for each participant at each electrode. The sampling frequency was 200Hz, and each trial lasted 650ms, i.e., 130 samples were available in each trial.

ERP is time-locked; therefore, the time-frequency analysis may describe ERP more accurately than the spectral or waveform information. After time-frequency analysis is performed, the one-dimensional signal is transformed to be the two-dimensional image, and a data matrix with dimensions of time by frequency is generated. In this matrix, the frequency range should correspond to the spectral feature. From the view of time, the time range of a trace where the event related potential is present will be called its support, and others of the trace are called its absence [5]. Then, we define the support to absence ratio (SAR) in the time-frequency plane as below,

$$SAR = 20 \log_{10} \left( \frac{TF_s}{TF_A} \right),$$

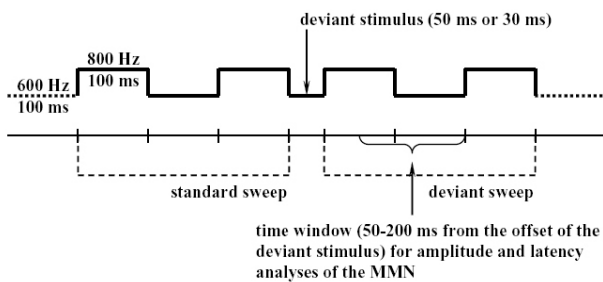


Fig.1 Illustration of the MMN eliciting experimental paradigm

$$TF_s = \frac{1}{T_s} \sum_{f=F_L}^{F_H} \sum_{t=T_1}^{T_2} |F(f, t)|,$$

$$TF_A = \frac{1}{T - T_s} \sum_{f=F_L}^{F_H} \left[ \sum_{t=1}^T |F(f, t)| - \sum_{t=1}^{T_s} |F(f, t)| \right],$$

where,  $F(f, t)$  is the time-frequency analysis of a trial's trace,  $T$  is the length of the trace,  $[F_L, F_H]$  is the ERP optimal frequency band,  $[T_1, T_2]$  is the time interval of ERP. SAR can reflect the characteristics of support signal based on its timing and spectral features. The larger SAR is, the better support signal is obtained. This is the MMN detector hereinafter. Exactly, in our MMN experiment, the sampling frequency is 200Hz, and the optimal frequency band is 2-8.5Hz. In each trial, we obtain 130 samples in our dataset. For the 50ms deviation, the MMN starts from 80<sup>th</sup> sample and ends at 110<sup>th</sup> sample. In this study, the Morlet wavelet transformation was adopted for the time-frequency analysis [16]. The half length of Morlet wavelet was 6.

On the basis of the visual, distribution and possibility inspection of the EEG data, four excision principles were set up to rule out the artifacts in this paper. The first was that a trial exceeds  $\pm 100V.$ , which was to cancel the EOG-artifacts [14]; the second was that the trace of a trial was a straight line, which was to delete the trials with null information; thirdly, the kurtosis of a trial was larger than 10, which was to remove the trials with impossible distributions; at last, the entropy of a trial was larger than 35, which was to reject trials with impossible data. Criteria of kurtosis and entropy had been used in the popular software—EEGLAB [17]. So, we applied them for the trials excision principles in this paper. The number of included trials per subject varied from 181 to 346 trials. The average number was 331 trials. 4.5% trials were rejected.

After the data reduction, the averaging over the left trials was implemented at each electrode for each subject, and the first 300ms samples were formulated for the baseline. Hereinafter, the baseline of the averaged trace was removed. Then, the EMD was performed on the averaged trace to acquire IMFs. Next, the SAR was computed for each IMF. Finally, the IMF with the largest SAR was chosen as the MMN-like IMF. This IMF is the output of the EMD on MMN. Please refer [7-12] for the EMD algorithm due to the length limitation.projected activation.

## III. RESULTS

As the original dataset was the same to the one used by Kalyahin et al.[15], and the little difference was only that we rejected few trials and they adopted all trials, some basic results were shown by Kalyahin et al., and not discussed



here. This paper was focused on the main effect of different methods. The result consisted of 98 subjects by 9 channels by two deviations by three methods. Fig. 2 was the image trace of all subjects at Fz electrode under 50 ms deviation. The horizontal ordinate was the sample, and the vertical ordinate was the subject, and the color in the image denoted the trace amplitude. The color bar showed the trend of the amplitude with the color. For better display, the value of each sample was multiplied by minus one before the plot-

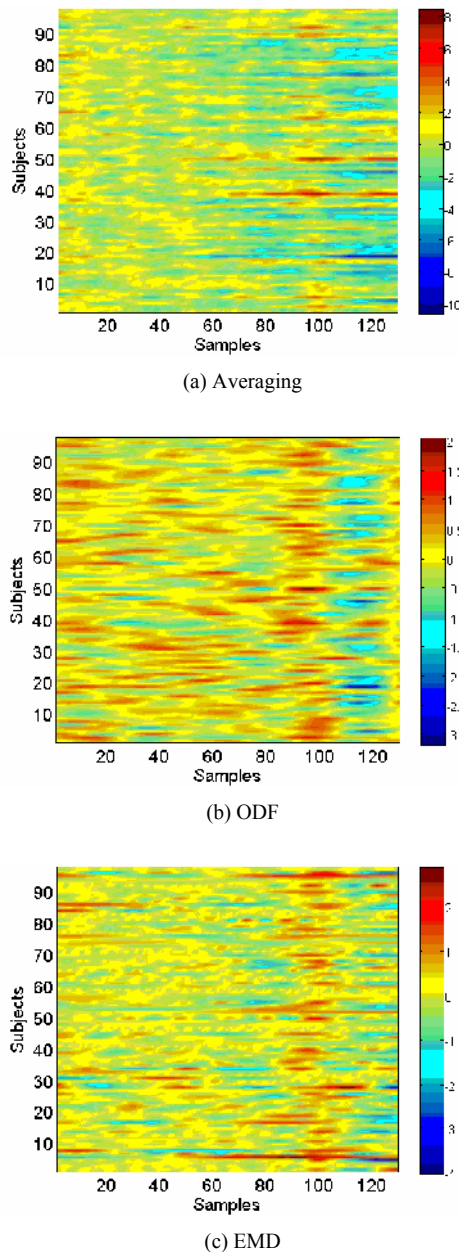
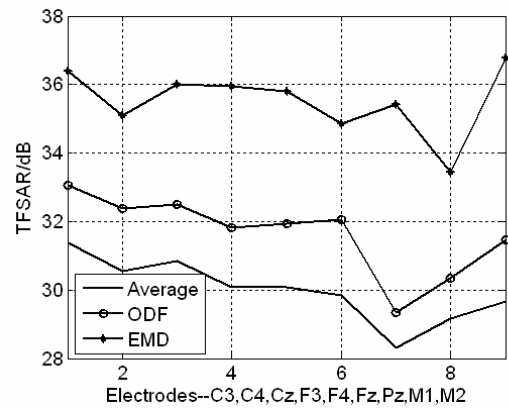


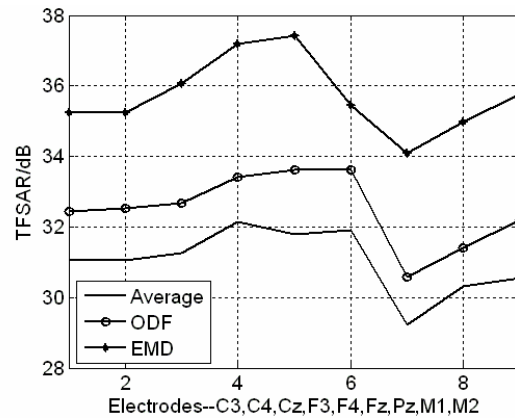
Fig.2 trace image at Fz electrodes under 50 ms deviation

ting. Fig. 2.1 2.2 and 2.3 corresponded to the averaging, ODF and EMD respectively. Apparently, compared to ODF, Fig. 2 demonstrated that EMD filtered out more response to repeated stimuli from the original averaging trace, and the MMN was much clearer. Fig. 3 was the SAR. Fig. 3.1 and 3.2 corresponded to the two deviations respectively. The horizontal ordinate was the electrode, and the vertical ordinate was the SAR in dB. The value is the mean of all 98 subjects. The statistical tests of the SAR at each electrode under each deviation were also computed. The independent variables were methods (three levels). For the length limitation, the statistical results were only shows the C-channels.

In fact, the differences were all significant in all channels. The statistical test demonstrated that the results in Fig. 3 were reliable. More over, the SAR at the 30ms deviation was larger than the one at 50ms deviation. This corresponds to the theoretical expectation, i.e., the larger deviation elicits larger MMN [13].



(a) 50ms deviation



(b) 30ms deviation

Fig.3 SAR of averaged, ODF and EMD traces at nine electrodes

Table 1: Statistical tests of SAR at C-electrode under each deviation.

Electrode	C3	C4	Cz
Deviation-50ms			
F(2,194)	36.9	28.7	21.5
p	0.00	0.00	0.00
Deviation-30ms			
F(2,194)	34.1	59.9	54.3
p	0.00	0.00	0.00

#### IV. DISCUSSION

In the MMN experiment, each trial contained the response to repeated stimuli, transient MMN, other event-related potentials, and background noises. The classic data analysis methods include averaging and digital filtering. However, these two methods are not suitable to evaluate the transient signals. The present contribution demonstrated that EMD was appropriate to decompose the mismatch negativity trace and to show the effectiveness of EMD under comparison with averaging and optimal digital filtering.

However, the amplitude of the MMN peak was not analyzed in this study because the IMF has the characteristic that at any point, the mean value of the envelope defined by the local maxima and the envelope defined by the local minima is zero. This is quite different with the baseline removal. This is the disadvantage of MMN.

While, the peak amplitude of MMN computed from the ODF has a almost equal mean value and variance. This implies that the data quality is not good under the criterion of the peak amplitude. This study gives another parameter—SAR. The variance is about 3 at all the channels among all the subjects. Compared to the mean value of the SAR, this number is small. Then the statistical analysis is more significant to reflect the quality of the data and the advantage of EMD than ODF and averaging.

As Table 1 and Fig.3 demonstrated, the larger deviation corresponds to the larger SAR. This keeps consistent to the theoretical expectation on MMN peak amplitude. So, it is possible to use SAR to evaluate the quality of the MMN instead of the MMN peak amplitude. To find another parameter in the time-frequency plane is necessary to give the judgment on the MMN latency. This will be our future work.

#### V. ACKNOWLEDGEMENT

Authors thank Mr. Igor Kalyakin very much for his valuable report and discussion.

#### REFERENCES

- Lopes da Silva, F., (1987). EEG analysis: theory and practice. In: Neidermeyer, E., Lopes da Silva, F. (Eds.), *Electroencephalography*. Urban and Schwarzenberg.
- Lachaux, J.P., Rodriguez, E., Martinerie, J., Varela, F.J.,(1999). Measuring phase synchrony in brain signals. *Hum. Brain Mapp.* 8, 194–208.
- Varela, F., Lachaux, J.P., Rodriguez, E., Martinerie, J., 2001. The brainweb: phase synchronization and large-scale integration. *Nat. Rev. Neurosci.* 2:229– 239.
- Olbrich E. and Achermann P. (2004). Oscillatory events in the human sleep EEG-- detection and properties. *Neurocomputing*, Volumes 58:129-135.
- Möcks, J., Gasser, T., & Köhler, W. (1988). Basic statistical parameters of event-related potentials. *Journal of Psychophysiology*, Vol.2:61-70.
- Harmony, T. (1984). Neurometric assessment of brain dysfunction in neurological patients. In E. R. John & R. W. Thatcher (Eds.), *Functional Neuroscience: Vol. III*. Hillsdale, NJ: Lawrence Erlbaum Associates Publishers.
- Huang N.E., Shen Z., Long S.R., et al, (1998). The empirical mode decomposition and the Hilbert spectrum for nonlinear and non-stationary time series analysis. Volume 454: 903-995.
- Li X., Sleight J., Voss L, et al. (2007). Measure of the electroencephalographic effects of sevoflurane using recurrence dynamics. *Neuroscience Letters*, Volume 424, Issue 1: 47-50.
- Li X. (2004). Temporal structure of neuronal population oscillations with empirical model decomposition. *Physics Letters A*, Volume 356, Issue 3:237-241
- Liang H., Bresser S., Desimone R., et al (2005). Empirical mode decomposition: a method for analyzing neural data. *Neurocomputing*, Volumes 65:801-807.
- Liang H, Lin Z., McCallum R.W.(2000). Artifact reduction in electrogastrogram based on the empirical model decomposition method, *Medical and Biological Engineering and Computing*, Vol. 38:35-41.
- Huang, W., Shen, Z., Huang, N. E. and Fung, Y. C. (1998). Engineering analysis of biological variables: an example of blood pressure over 1 day. *Proc. Nat. Acad. Sci. USA*, 95, pp. 4816-4821.
- Pihko, E., Leppäsaari, T., & Lyytinen, H. (1995). Brain reacts to occasional changes in duration of elements in a continuous sound. *NeuroReport*, 6, 1215-1218.
- Huttunen, T., Halonen, A., Kaartinen, J., & Lyytinen, H. (2007). Does mismatch negativity show differences in reading disabled children as compared to normal children and children with attention deficit? *Developmental Neuropsychology*, Vol. 31, No. 3: pages 453-470.
- Kalyakin, I., González, N., Joutsensalo, J., Huttunen, T., Kaartinen, J., & Lyytinen, H. (2007). Optimal digital filtering versus difference waves on the mismatch negativity in an uninterrupted sound paradigm. *Developmental Neuropsychology*, Vol. 31, No. 3: pages 429-452.
- Burrus CS, Gopinath RA, Guo H (1998). *Introduction to Wavelets and Wavelet Transforms: A Primer*. New Jersey: Prentice Hall.
- Delorme A., Makeig S. (2004). EEGLAB: an open source toolbox for analysis of single-trial EEG dynamics. *Journal of Neuroscience Methods*, 134:9-21.

Author: Fengyu Cong  
 Institute: University of Jyväskylä  
 Street: POBox 35 (Agora)  
 City: Jyväskylä  
 Country: Finland  
 Email: fecong@jyu.fi

# Measurement and Control of Ultra-Low Liquid Flowrates for Drug Delivery Application

C. Damiani, S. Klein, D. Wuttig and B. Nestler

Lübeck University of Applied Sciences/Center of Biomedical Engineering, Lübeck, Germany

**Abstract** — Implantable, gas-driven drug pumps are safe, cost-effective and do not require internal batteries like their motor-driven counterparts. However, their flow rate cannot be changed after implantation. This work focuses on the development of an adjustable micro-flow regulator to be used in a programmable gas-driven pump. Several concepts of flow-restrictors made of microstructured silicone-elastomers have been evaluated and the manufacturing techniques have been optimized. Currently, fixed flowrates down to 250 nl/min can be achieved for a pressure drop of  $3,4 \times 10^5$  Pa. Development of prototypes with adjustable flowrate is in progress. A test bench based on optical front-tracking for dynamic flowrate-analysis down to 10 nl/min has also been implemented. This enables an independent calibration of thermal micro-flow sensors as well as wide-range, low impedance flowrate measurements.

**Keywords** — microfluidic, flow measuring, flow regulator, flow restrictor, implantable pumps.

## I. INTRODUCTION

The market for implantable infusion systems has grown significantly during the last years because of their advantages compared to oral drug delivery (no drug loss by re-sorption, topic drug delivery). These devices are mainly used for pain and spastic therapy.

Among the implantable medicament pumps, those driven by a constant-pressure chamber (two phase mixture) are the most widely used. They are more reliable, have less moving parts and cost a fraction of their motorized counterparts. Their flow-rate, however, is fixed after implantation and dosage changes are not possible. Moreover, new highly-effective drugs (e.g. Piralt) require flow rates as low as 15 nl/min. To provide long-time, maintenance-free operation of the implants at such low flow ranges new adjustable flow regulators have been developed and first results are here presented.

Several effective methods for measuring flow are available [1,2,3,]. However, current Standards for measuring micro-flowrates (for example gravimetric methods) are tedious and not reliable for variable flows. Thermal micro-flow sensors promises a better alternative [4], but they need a fluid-specific calibration and have usually a high flow impedance. A validated measuring method with

accuracy within a few nl/min and low impedance is therefore essential to calibrate microfluidic parts before implantation. The development of such a system is also discussed in this work.

## II. MATERIALS AND METHODS

Different combinations of inner and outer spiral-channel microstructures have been evaluated for the construction of the flow regulator. Also several materials (silicone elastomer, TiAl6V4, brass, PEEK, PMMA) and manufacturing methods (shape cutting, pressure moulding, casting) were tested. The current system consists of a microstructured biocompatible silicone part (Nusil) with outer spiral channels fabricated by pressure moulding. In contrast to standard MEMS solutions consisting where mostly combinations of hard materials are used (silicon, metals, hard plastics), elastomers allow to change the flow-impedance through mechanical deformation of the parts without compromising the tightness of the system. The smallest channels achieved are currently 45  $\mu\text{m}$  deep and 130  $\mu\text{m}$  wide, have a curvature radius of 50  $\mu\text{m}$  and a pitch of 250  $\mu\text{m}$ . The silicone screw fits into a PMMA housing which seals the channels and provides inlet and outlet connectors for the fluid (Figure 1).

To change the flow impedance of the system, a modified regulator which allows a radial elastic deformation of the channels is under development.

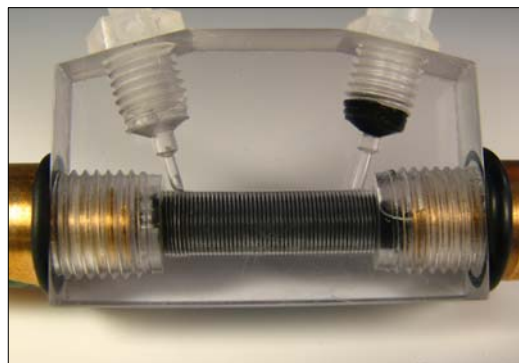


Fig. 1 Flow regulator for Laboratory tests



Fig. 2 Front-Tracking System

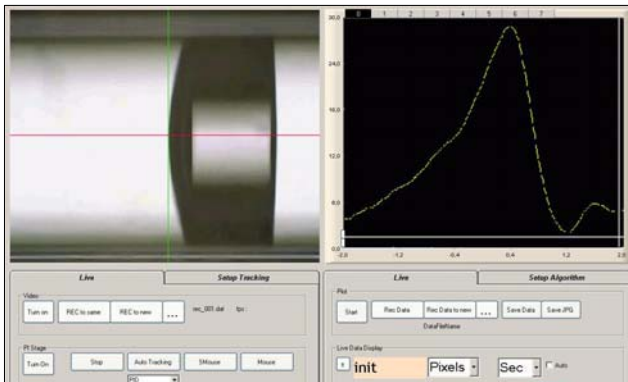


Fig. 3 Front-Tracking software with flow velocity profile

A custom flow-measuring setup based on optical front-tracking has been developed (Figure 2)

It comprises a high precision glass capillary attached to the outlet of the system which flow-rate has to be determined, a digital zoom-microscope (Keyence, VHX 600) mounted on a micro-motion stage (PI) and a custom-made image processing software. The motion of the interface between the fluid and the air is detected by the software (Figure 3), which in turn controls the motion of the motorized stage through a PID algorithm to keep the front centered on the image. The flow is calculated from the velocity of the front and the diameter of the glass capillary.

The whole system is assembled on top of an air-damped table to reduce the effects of vibrations. Accuracy can be increased by choosing higher magnifications or smaller capillary internal diameters. In the first case the stability of the system has to be increased (vibration damping); in the second the maximum allowable measuring time is reduced (capillary length is fixed).

Capillary tubes are 25cm long and the following inner diameters are available to achieve a broad range of flow-rate accuracy and maximum measuring times: 80 μm, 150 μm,

300 μm, 600 μm and 1000 μm. Inner diameter tolerances are under 5% in all cases. Thermal expansion effects of the glass near RT are negligible.

With the optical zoom (20x-200x) resolutions between 1,7 μm and 17 μm per pixel can be freely chosen. Calibration is made automatically from the software using a high resolution linear optical encoder integrated in the motion stage (0.1 μm accuracy).

Time uncertainty during the determination of the front position is under 50ms (Windows XP SP2, intel Pentium 4, 1 GB RAM, no other programs running, CPU usage ca. 10%).

Stable flows to test the equipment were generated using fixed pressure drops (water column method).

Thermal flow sensors (Sensirion, Switzerland, model SLG 1430-025) were also compared against the front-tracking method. The minimum calibrated flow than can be measured with these sensors is 50nl/min.

### III. RESULTS

Repeatable flowrates down to 250 nl/min have been obtained for a pressure drop of  $3,4 \times 10^5$  Pa with silicone-based regulators using ultra pure water (Figure 4).

With the Front tracking system flow measurements with 5% accuracy down to 10 nl/min and much lower impedance than the thermal methods are possible.

Figure 5 shows a comparison between the “out-of-the-box” readings of the thermal sensor and that of the front-tracking software. Discrepancies were below 1 % down to 40 nl/min (capillary diameter of 300 μm, resolution 3,4 μm per).

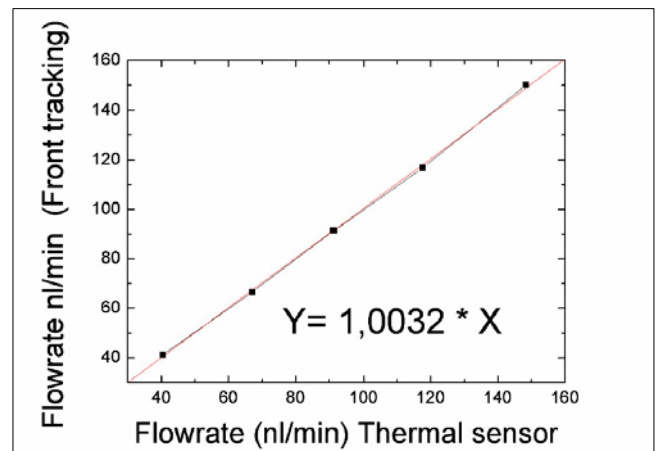


Fig. 4 Flow-rate as a function of the housing diameter

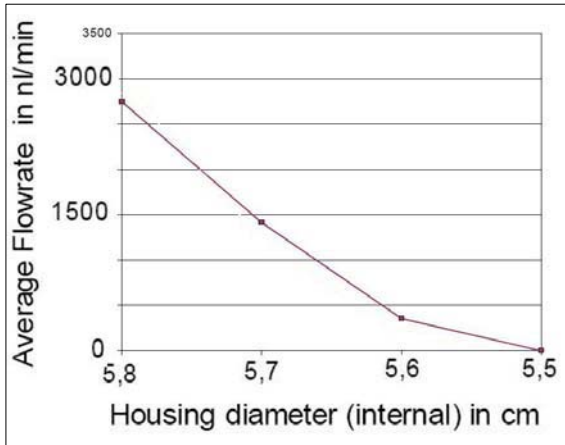


Fig. 5 Reading of the thermal sensor vs. reading of the Front-Tracking System

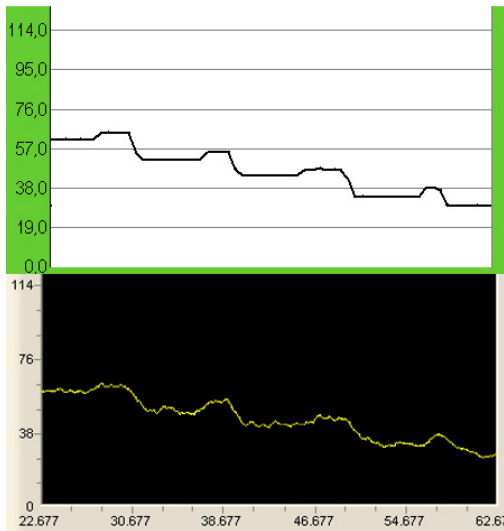


Fig. 6 Variable flow-rate profiles. Above: thermal Sensor, below: Front-Tracking System. X-axis: time in seconds, Y-Axis flow-rate in nl/min

Response to changing flow-profiles showed also a good agreement (**Figure 6**).

One thermal flow sensor showed a drift of the reading under constant flow and temperature. A restart of the sensor

was required to eliminate the drift. Such problems were not observed with the front-tracking system.

Integration times of ca. 1 second or the equivalent to 10 pixels of motion of the front (the larger of the two values was selected) were necessary reduce the noise of the flow curves due to pixel discretization. For the thermal sensors, integration times of 0,7 seconds were used. Under these circumstances the noise of the thermal sensors was lower than that of the front-tracking system. Reaction times (to sudden changes in the flow) were similar.

#### IV. CONCLUSIONS

A micro-flow regulator has been successfully fabricated using implantable materials (Nusil silicone®). Designs of adjustable microflow regulators are in progress.

Ultra low flow-rates down to 10nl/min have been successfully measured with a custom-made optical system.

Thermal sensors available on the market do not reach such low values and need fluid-specific calibrations.

#### ACKNOWLEDGMENT

The authors thank the Innovation Foundation of the State of Schleswig-Holstein (ISH) and the State of Schleswig-Holstein for funding their work.

#### REFERENCES

1. Upp, L., LaNasa, P.(2002): Fluid Flow Measurement - A Practical Guide to Accurate Flow Measurement; 2. Aufl., Gulf Professional Publishing
2. Fraden, J.(2004): Handbook of Modern Sensors. 3.Aufl., Springer
3. Wackerle, M. et al.(2002), Sub-nl flow measurement method for microfluidic actuators. Proc. Actuator 2000, Bremen
4. US-Patent 6813944: Flowsensor

Author: Christian Damiani  
 Institute: Fachhochschule Lübeck  
 Street: Mönkhofer weg 239  
 City: Lübeck  
 Country: Germany  
 Email: damiani@fh-luebeck.de

# Hardware Embedded System on a Chip for the Normal ECG Recognition

A.C. Dimopoulos, C. Pavlatos, G. Papakonstantinou

National Technical University of Athens/ School of Electrical and Computer Engineering, Athens, Greece

**Abstract** — This paper proposes a highly efficient embedded system, implemented entirely in reconfigurable hardware, for the extraction of electrocardiogram (ECG) measurement parameters and the recognition of the normal ECG. The entire process takes place on an FPGA and is based on the syntactic pattern recognition approach. The underlying model for this system is that of Attribute Grammars (AG), whose descriptive power allows the concurrent recognition and measurement of the input ECG. The proposed generic platform for syntactic pattern recognition applications, is using the fastest parallel Context Free Grammar parsing algorithm in the bibliography.

**Keywords** — ECG, Attribute Grammars, FPGA, SoC

## I. INTRODUCTION

In this paper a generic platform for coping with Syntactic Pattern Recognition applications [1], [2] is presented. The underlying model for accomplishing this task is that of Attribute Grammars [3]. The entire process is based on the syntactic pattern recognition approach and takes place on an FPGA board. Our implementation makes use of the fastest parallel Context Free Grammar parsing algorithm [4] in the bibliography, implemented entirely in hardware [5]. Moreover, all the computations imposed by the input data are done by dedicated hardware modules, eradicating the need for a microprocessor existence, contrary to previous attempts where a general purpose processor, softcore [6] or external [7] was needed.

As an example application, the automated recognition of the normal Electrocardiogram (ECG) is chosen, for which, an automated System on a Chip (SoC) is proposed. The proposed system inputs the ECG measurements and not only recognizes the normal ECG but additionally, outputs various parameters regarding the measured heart beat. In this way, the proposed system can not only acquire the ECG, extract its features and make measurements but furthermore, it recognizes and diagnoses whether the examined ECG is a normal one or not.

In the case of Syntactic Pattern Recognition applications such as the ECG, a pattern grammar is utilized, which describes the patterns to be recognized in a formal way. Furthermore, this pattern grammar is augmented with extra attributes, thus extending into an Attribute Grammar [3]. These attributes are evaluated constantly throughout the parsing process, giving values that allow a more accurate

measurement of the ECGs and the recognition of the normal ones.

In our approach, the biomedical input waveform must undergo a first process in order to have the primitive patterns extracted. These primitive patterns are described by the pattern grammar proposed by Trahanias et al [9] and constitute the input string to be parsed by our hardware parser [5]. A separated module on the chip is responsible for this task. Once the input string is defined, it can be submitted to the hardware parser. During the parsing process, for each input string, the corresponding attributes are evaluated allowing a real time analysis of the original waveform.

The proposed architecture has been implemented in synthesizable Verilog in the Xilinx ISE 9.1 [10] environment, while the generated source has been simulated for validation, synthesized and tested on a Xilinx Virtex-5 ML506 FPGA.

The rest of the paper is organized as follows. In section II the necessary theoretical background is specified, while in section III an overview of the proposed system is given and the example implementation of the normal ECG recognition SoC is presented in Section IV. Finally, section V summarizes the proposed implementation and outlines directions for future work.

## II. THEORETICAL BACKGROUND

Attribute Grammars (AG) were devised by D. Knuth [8] as a tool for formal languages specification extending Context Free Grammars (CFG). Specifically, semantic rules and attributes are added to CFGs augmenting their expressional capabilities. Knowledge can be represented in AGs, using syntactic and semantic (attribute evaluation rules) notation.

A CFG is a quadruple  $G = \{V, N, R, S\}$ , where:  $V$  is the finite set of grammar symbols,  $N$  is the set of non-terminal symbols (NT),  $R$  is the finite set of rules and  $S$  is the start (nonterminal) symbol of the grammar. In addition,  $T = V - N$  is the set of terminal symbols. Rules are in the form  $A \rightarrow \alpha$ , where  $A \in N$  and  $\alpha \in V^*$ ;  $A$  is called the left hand side symbol (lhss) and  $\alpha$  is the string of the right hand side symbols (rhss) of the specific rule. Rule  $A \xrightarrow{*} \alpha$  means that  $\alpha$  can derive from  $A$  after the application of one or more rules. Let  $S \xrightarrow{*} \alpha$ , be a derivation in grammar  $G$ . The correspond-

ing derivation (parsing) tree is an ordered tree with root  $S$ , leaves the terminal symbols in  $\alpha$ , and nodes the rules that are used for the derivation process. The process of analyzing a string for syntactic correctness is known as parsing. A parser is an algorithm that decides whether or not a string  $\alpha_1\alpha_2\alpha_3\dots\alpha_n$  can be generated from a grammar  $G$  and simultaneously constructs the derivation (or parse) tree.

An AG is also a quadruple  $AG = \{G, A, SR, d\}$ , where  $G$  is a CFG,  $A = \cup A(X)$  where  $A(X)$  is a finite set of attributes associated with each symbol  $X \in V$ . Each attribute represents a specific context-sensitive property of the corresponding symbol. The notation  $X.a$  is used to indicate that attribute  $a$  is an element of  $A(X)$ .  $A(X)$  is partitioned into two disjoint sets; the set of synthesized attributes  $A_S(X)$  and the set of inherited attributes  $A_I(X)$ . Synthesized attributes  $X.s$  are those whose values are defined in terms of attributes at descendant nodes of node  $X$  of the corresponding semantic tree. Inherited attributes  $X.i$  are those whose values are defined in terms of attributes at the parent and (possibly) the sibling nodes of node  $X$  of the corresponding semantic tree. The start symbol does not have any inherited attributes. Each of the productions  $p \in P$  of the CFG is augmented by a set of semantic rules  $SR(p)$  that define attributes in terms of other attributes of terminals and on terminals appearing in the same production. The way attributes are being evaluated depends both on their dependencies to other attributes in the tree and also on the way the tree is traversed. Finally  $d$  is a function that gives for each attribute  $a$  its domain  $d(a)$ .

The parallel Earley's parsing algorithm, implemented on hardware [5] decides whether an input string  $a_1a_2\dots a_n$  of length  $n$  is a sentence of a CFG. The parsing task is reduced to the procedure of filling a two dimension table (parse

table) of size  $(n+1) \times (n+1)$ . Only the elements on or above the diagonal are used, hence the number of needed processing elements is  $(n+1) \times (n+2)/2$ . Every processing element is computing one cell  $pt(i, j)$  in each execution time and at the next execution time is used again to compute the cell that belongs to the same column and is one row higher  $pt(i-1, j)$ . After the end of each execution step  $k$  ( $t_{ek}$ ), the computation of one parsing processing element terminates. At the next execution step this processing element transmits the computed cells, to the next processing ( $t_{ek}$ ). Each processing element repeatedly calculates a cell, checks if it should transmit any cells and then if it should receive any. All the above are illustrated in Figure 1, for an input string of length 2.

### III. EXTENDING THE PARSER

As already analyzed, the parser presented in [5] can only deal with CFG and not AGs, since it has no attribute evaluation abilities. For this reason, it was crucial to extend the parser so as to tackle with attributes. In order to succeed that, for each entry of the parse table, extra data (come from - CF) must be kept, pointing for every rule to the cell it was created. The origin of each produced rule is encoded in a bit-vector, since it is crucial to maintain the combinatorial nature of the parser, responsible for the high circuit efficiency. The produced parse table is filled starting from its most left column and continuing to the right successively and based on the CF data, the parse tree can easily be constructed.

Once the parse table is constructed, based on it, the parse tree must be constructed and traversed once. During this traverse, the final scope – that of semantic evaluation - takes place on a dedicated hardware module. Inside this module, a stack-based approach is used to transfer the attributes from a tree node to its descendant nodes (for inherited attributes) and to its parent node (for synthesized attributes). For each attribute a stack is defined, and data are pushed or popped according to specific rules. In addition, operations between attributes are executed on dedicated arithmetic modules, based on the semantic rule corresponding to each syntax rule. The basic idea of the algorithm is to first evaluate all the subnodes of a node, before evaluating the node itself. To signify the stack-based approach, a simple example using only a synthesized attributes is explained: Consider the syntax rule  $L \rightarrow R_1 \dots R_i \dots R_n$ , with the corresponding semantic rule  $L.s = f(R_1.s; \dots; R_n.s)$ , where  $f$  is a function of  $R_1.s, \dots, R_n.s$ . In the parser tree, the NT symbols  $R_1, \dots, R_n$  are descendants of the NT  $L$  and as a result, before evaluating the attributes of  $L$ , the attributes of the descendant nodes have already been evaluated and stored at consequent places

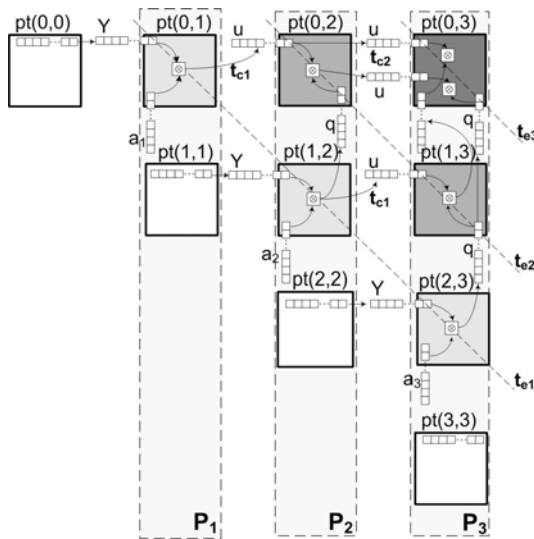


Fig. 1 Parser Architecture for constructing the Parse Table

into the top of the stack. Hence, by popping  $n$  times the stack, the attributes are passed to the dedicated arithmetic module and the result is pushed again into the stack.

Therefore, the proposed system is consisting of three major modules, the extended parser, the tree constructor and the attribute evaluator. The parser handles the recognition task and constructs the parse table. When the parsing process is over, the parse tree is constructed and afterwards, while being traversed, the corresponding attributes are evaluated. The first two modules are automatically produced by the platform, based on the given AG. The last module follows a generic architecture for the attribute handling, which is independent to the grammar but for the arithmetic expressions, dictated by the semantics, special submodules are required. Therefore, these submodules responsible for the arithmetic calculations cannot yet be produced automatically but have to be application specific functions provided by the user.

#### IV. A REAL-LIFE EXAMPLE

In order to present the SoC abilities, a real-life example from the area of biomedicine has been chosen, that of normal ECG recognition. For almost a century, the health care community has a strong ally in its arsenal of monitoring aids, the ECG. An ECG monitor can accurately define the duration and the frequency of the heart beat, as well as any variations. Furthermore, by the usage of ECG, medical conditions such as arrhythmia or deviation from the normal heart beat can be diagnosed and the cause for these anomalies can be further explored.

The ECG is the electrical potential between various body points, which can be measured by the usage of suitable equipment when the electrode leads are properly attached to the patient body. The measured voltage is directly linked to the muscle activity of the heart. Thus, at the beginning of the heart stimulation a positive electrical deviation is measured, this is called a P wave. Next, as the stimulation starts to extend initially a negative wave (Q) appears which is followed by a large and fast inversion (R wave). As the stimulation reaches its end, another negative wave appears (S wave). Finally, the repolarization of the ventricles is marked by a positive wave, the T wave.

For the linguistic representation of an ECG waveform, an AG presented by Trahanias et al [9] is being used. Due to space limitations the AG rules are not quoted here. The grammar has the terminal symbols  $\{K^+, K^-, E, \Pi\}$ , where  $K^+$  denotes positive peaks,  $K^-$  negative peaks,  $E$  straight line segments and  $\Pi$  parabolic segments. Thus, every ECG waveform is transformed to a string of the abovementioned symbols. For each input string seven attributes (both inher-

ited and synthesized) are evaluated i.e. the number of cardiac waves, the number of QRS classes, the duration of left/right arm of a peak, the height of the left/right arm of a peak and finally a candidacy for a peak as a P or a T. Therefore, based on the so far proposed methodology, seven stacks will be used for the storage of those attributes. The operations between the attributes are for the most rules simple assignments and additions with the exception of five rules, where apart from the adder circuit, an accumulator and a comparator are imposed by the semantic rules.

The prospective is to have a dedicate module to cope with acquisition of the ECG data from a source and supply a next module responsible for the primitive extraction from the raw ECG data in real-time, based on piecewise linear approximation methods. However, at this stage, in order to test the platform efficiency, artificial ECG primitive data have been used as input string and not real ECG data. The input string is being processed in bursts, therefore to facilitate a pipelined collaboration of the primitive extraction module and the parser, a shared memory buffer is used by both modules. The input string length, due to the grammar nature, must be long enough to contain at least one cardiac cycle, therefore depending on the sample ratio, the buffer size can be decided upon.

Once the input string is determined, the parsing process begins outputting the parse table. Following the CF data stored in the parse table, the corresponding parse tree is build and traversed. The tree is decorated with the semantics top down and from left to right. At each leaf of the tree a synthesized attribute is evaluated and the result is pushed into the corresponding stack. This is the simplest case, where a value is merely pushed in. During the semantic evaluation of the tree nodes, arithmetic operations must be carried out between attributes. In such cases, the corresponding attributes are popped out of their stack and send to the hardware module responsible for the arithmetic operations together with the proper control signal. The result is then pushed into the related stack. When the whole tree is decorated with the attributes, the endmost module is triggered that based on the calculated attributes, carries out the three important tasks:

1. QRS Detection and Recognition: Consecutive peaks are recognized as a QRS complex based on a threshold value and the angle between the right and the left arm of two consecutive peaks. The morphology of the QRS is determined by the alternative of the syntactic rule that matches the QRS.
2. P, T Detection and Recognition: One ore two consecutive peaks are recognized as a P or a T complex by thresholding their width and amplitude, depending on the syntactic rule being evaluated.



3. QRS Classification: the distance between a given QRS complex and a given class of QRS complexes is computed, based on morphological (structural) and quantitative (statistical) features.

All the output information is transmitted from the FPGA to a computer via a serial cable and by the same mean, the input data is transmitted to the FPGA. At all stages of the parsing and attribute evaluation, the circuit retains its combinatorial nature and therefore its remarkable speedup as proved in [5]. In addition, the arithmetic operations between the attributes and the concluding task of recognition, detection and classification are all handled by dedicated hardware modules, eradicating the need for a microprocessor and thus the delay imposed is minimal.

## V. CONCLUSIONS

Due to the combinatorial nature of the proposed system, a remarkable speedup is achieved as compared to the pure software implementation or to implementations based on soft-core general purpose processor of similar approaches [11] resulting in a speedup counted in orders of magnitude. Therefore, the contribution of this paper can be summarized in the followings: Firstly, a generic platform is proposed for syntactic pattern recognition applications, using the fastest parallel Context Free Grammar parsing algorithm [4], [5] in the bibliography. Additionally, the hardware implementation of the SoC is, to the best of our knowledge, the first hardware implementation for the recognition and diagnosis of the normal ECG using a syntactic pattern recognition approach. And finally, the flexibility, rapid prototyping and efficiency of the implementation, attributable to the high level description (AGs) of the problem and the generic nature of the platform.

Our future work remains focused on implementing the proposed architecture shown in Figure 2, where real-time ECG data, such as those obtained from PhysioBank [12], will be inputted to the SoC, the primitive patterns will be automatically extracted and after the process the ECG will be recognized and evaluated data will be given. In every case, the overall system must not lose its combinatorial nature, responsible for the speedup compared to conventional approaches. Once the system is complete, comparison with other ECG recognition systems can occur by using specific test ECG sequences as benchmark.

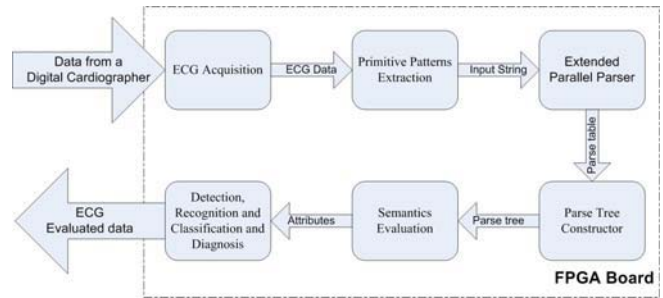


Fig. 2 SoC for the real time normal ECG Recognition

## REFERENCES

- Vitulano D (1999) A syntactic approach applied to materials degradation. *Pattern Recognition Letters*, 20(1), January.
- Colin de la Higuera (2005) A bibliographical study of grammatical inference. *Pattern Recognition*, 38:1332–1348
- Paakki J (1995) Attribute grammar paradigms - a high-level methodology in language implementation. *ACM Comput. Surv.*, vol.27, no.2: 196-255
- Chiang Y, Fu K (1984) Parallel parsing algorithms and VLSI implementation for syntactic pattern recognition. *IEEE Trans. Pattern Anal. and Mach. Intell.* PAMI-7
- Pavlatos C, Dimopoulos A, Koulouris A, Andronikos T, Panagopoulos I, Papakonstantinou G (2007) Efficient Reconfigurable Embedded Parsers. *Computer Languages, Systems & Structures*, in press
- Pavlatos C, Dimopoulos A, Papakonstantinou G (2005) An embedded system for the electrocardiogram recognition, *EMBE'05*, Prague, Czech Republic
- Pavlatos C, Dimopoulos A, Papakonstantinou G (2005) An Intelligent Embedded System for Control Applications, *Workshop on Modelling and Control of Complex Systems*, Cyprus
- Knuth D E (1971) Semantics of context free languages. *Math. Syst.Theory*, vol.2, no.2: 127-145
- Trahanias P, Skordalakis E (1990) Syntactic pattern recognition of the ECG. *IEEE Transactions on Pattern Analysis and Machine Intelligence*, vol. 12, issue 7: 648-657
- Xilinx Official WebSite, <http://www.xilinx.com>
- Khatib I Al, Poletti F, Bertozzi D, Benini L, Bechara M, Khalifeh H, Jantsch A, Nabiev R (2006) A multiprocessor system-on-chip for real-time biomedical monitoring and analysis: architectural design space exploration. *DAC '06*, San Francisco, pp.125-130
- PhysioBank at <http://www.physionet.org/physiobank/>

Address of the corresponding author:

Author: Alexandros C. Dimopoulos  
 Institute: National Technical University of Athens/ School of Electrical and Computer Engineering,  
 Street: Iroon Polytechniou 9  
 City: Athens  
 Country: Greece  
 Email: alexdem@cslab.ece.ntua.gr

# Slit-lamp Based Ocular Fluorometry Scanning

J.P. Domingues<sup>1,2</sup>, M. Alberto<sup>1</sup>, C. Correia<sup>1</sup>, J. Cunha-Vaz<sup>2</sup>

<sup>1</sup> Physics Department/University of Coimbra, Coimbra, Portugal

<sup>2</sup>IBILI – Biomedical Institute for Research on Light and Image - Faculty of Medicine/University of Coimbra, Portugal

**Abstract** — The aim of this work is to develop and present new slit-lamp based instrumentation and methods to measure anterior segment ocular fluorescence with clinical significance, mainly in diabetic patients. With those measurements we have been able to quantify both endogenous and exogenous fluorescence (after systemic tracer administration, in the last case) and to detect alterations in Blood-Ocular Barriers (BOB) permeability.

Increased vascular permeability in diabetes is one well accepted alteration affecting the whole vascular system. In the eye an alteration of both the Blood-Aqueous Barrier (BAB) and the Blood-Retinal Barrier (BRB) have been shown to be one of the earliest alterations occurring in diabetes. BAB is the main target of our study and both oral and intravenous tracer administration have been used.

**Keywords** — Blood-Ocular Barriers, Ocular Fluorescence, Diabetes, Slit-Lamp, Data Acquisition.

## I. INTRODUCTION

In a recent study by our group, looking at the initial stages of diabetic retinal disease in a prospective two-year follow-up study, the increase in Blood-Aqueous Barrier permeability paralleled the increase in Blood-Retinal Barrier permeability and the progression of the retinopathy judged by stereofundus photography [1]. Also alteration of the BAB, measured by aqueous spot fluorometry, is a sensitive indicator of ocular inflammation [2].

A new light detection and data acquisition system has been developed to perform ocular fluorescence quantitative measurements (PAF – Photodiode Array Fluorometer, US patent 06,013,034, European patent EP 0 656 759 B1). The system is based on an ophthalmic slit-lamp to produce excitation with appropriate filter selection and, to collect fluorescence through the objective, additional optics and adequate emission filters are used. The detector is a solid state multi-element image detector. With this apparatus it is possible to quantify BAB Fluorescein diffusion coefficient by measuring fluorescence both in aqueous and in blood plasma over time.

A clinical *in vivo* study using both PAF and Fluorotron Master™ (Ocumetrics, USA) – a commercialized standard instrument - has been performed both with oral and IV administration of Fluorescein regarding BAB permeability

assessment with results that assure the reliability of this new and simpler method. Finally, a new microcontroller-based interface has been developed – and will be described - that offers the system increased flexibility and portability along with faster and more sensitive measurements.

## II. MATERIALS AND METHODS

The PAF ocular fluorometer is optically and mechanically coupled to an ordinary slit-lamp. The excitation source is the slit-lamp tungsten-halogen lamp used together with optical filters to select the appropriate wavelengths to fluorescence excitation. Fluorescence light coming from different eye structures or fluids is collected by the slit lamp objective. Emission filters are there placed to prevent collection of reflected light. A beam-splitter then directs the collected light to image formation optics (spherical lens) and to a solid state linear image sensor. Cylindrical optics is also used to maximize image size and photosensitive area matching.

Data Acquisition and Processing is accomplished by the use of two main electronic modules. A dedicated PC board and a detector board. The PC board has local processing capabilities provided by a Digital Signal Processor (DSP) and memory. From the PC point of view this is a simple memory and I/O board. A protocol has been established between PC and the DSP to assure that the host can only interrupt the DSP when it is not executing important activity that cannot be interrupted. This module provides also the basic timing signals for sensor driving and for A/D conversion and all the electronics for temperature reading and control. The Interface to the sensor board is a parallel 12 bit data interface with timing control signals and some power lines.

The detector board, connected to the above described PC board by means of a 50 way flat cable, provides the driver/readout circuit for the sensor, the amplification electronics to fit the sensor output to the input range of the ADC used, the ADC itself and the power electronics to drive the TE cell responsible for the sensor cooling. The module is to be adapted to the ocular piece of an ordinary slit lamp that provides the optics (lenses and filters) for both excitation and fluorescence collection. A set of

interchangeable excitation and emission filters can be used. The overall system diagram is depicted in Fig. 1. The hardware/software system allows great flexibility in acquisition parameters programming and data storage and analysis and the IBM compatible environment offers good computational possibilities for graphical analysis of data.

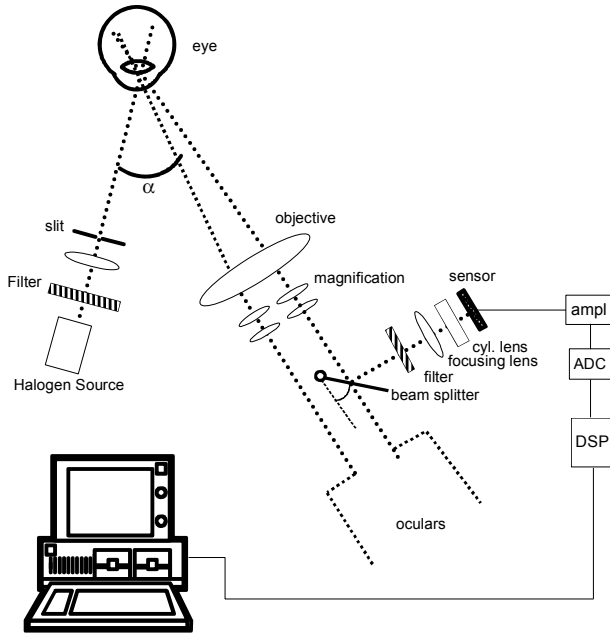


Fig. 1 – PAF Fluorometer

The detector choice for this application was a self-scanning type PDA (Hamamatsu Mos Linear Image Sensor series). Among the important parameters in imaging applications of PDA's are: Sensitivity, response uniformity, dark current, pixel size (spatial resolution), quantum efficiency, saturation signal, linearity and maximum and minimum data rate. In order to evaluate detector performance by measuring some of these parameters the data acquisition system must be flexible, fast, highly programmable even for long term operation and data storage and analysis tools must be available. As we are dealing, in ocular fluorometry, with very low light levels, special care must be focused on the quality of electronics for amplification and A/D conversion. Some signal processing techniques as simple as signal averaging must also be used. The system we have developed fulfils those requirements.

Fluorotron Master™ is the *gold standard* reference commercial ocular fluorometer, capable of measuring ocular fluorescence over the entire ocular axis from retina to anterior segment by spot measurements in different

positions determined by a scanning lens mechanical displacement [3].

The Diffusion Coefficient,  $K_d$ , calculated is the rate of appearance of fluorescein in the anterior chamber after intravenous or oral administration is compared to the concentration decay of the non-protein bound fluorescein (NPBF) in plasma [4]. It is defined as the ratio from the fluorescein concentration in the anterior chamber and the time integral of NPBF in plasma.

The increase of NPBF concentration in the anterior chamber can be written as:

$$\frac{dC_a}{dt} = K_d(C_p - C_a) - K_f(C_a - C_h) - K_{a.ca}(C_a - \frac{C_c}{r_{ca}}) \quad (1)$$

where  $C_a$ ,  $C_p$ ,  $C_h$  and  $C_c$  are the NPBF concentrations respectively in anterior chamber, plasma, aqueous humour and cornea.  $K_d$  is the diffusion coefficient from plasma to anterior chamber (the parameter we are interested in),  $K_f$  is the loss coefficient due to aqueous flow and  $K_{a.ca}$  the aqueous to cornea diffusion coefficient.  $r_{ca}$  is simply a correction factor [3]. After integration of both sides we can approximate  $K_d$  as:

$$K_d = \frac{C_a(t_m)}{\int_{t_d}^{t_m} C_p dt} \quad (2)$$

Different groups from different countries reached standard protocols and methodologies for anterior segment fluorometry based on intravenous (IV) administration. For oral not much experience is available and we followed the same approach with required adaptations.

A commercial curve fitting package (curve expert 1.3) has been used and additional software for automatic calculation of plasma integral and diffusion coefficient in Blood – Aqueous Barrier for endovenous and oral administration has been developed.

A new version of data acquisition system (Fig. 2) has been developed to incorporate new technology developments and to improve sensitivity, measurement resolution, portability and to increase programmability. This is achieved by using a dsPIC Microcontroller (dsPIC30F6012A, Microchip, USA) together with a 16-bit, 1.25 MSPS ADC. The communications with the PC are done either by USB or RS-232 and a robust power supply has been coupled. No other computer dedicated boards are needed and PIC programming and data reading are made by serial interface. Next picture depicts a simplified block diagram. Basic *in vitro* performance tests are now being performed with this new architecture.

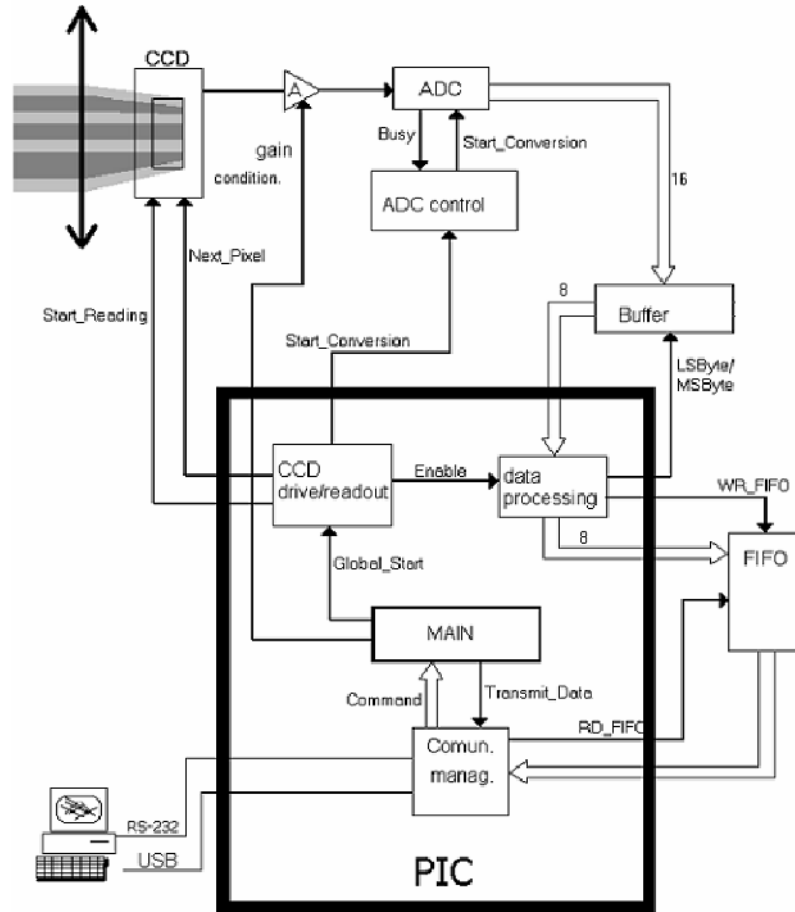


Fig. 2 – Data Acquisition Architecture

### III. RESULTS

A clinical study was performed using both endovenous and oral administration of sodium fluorescein. All patients (10 normal volunteers and 22 diabetic patients) were examined (fluorophotometry by both FM and PAF) in two visits separated by two weeks minimum. Fig. 3 shows some results obtained by PAF after oral tracer administration.

Both endovenous and oral examinations presented no statistically relevant deviations between FM and PAF results using Spearman Rank Order Correlations (SROC), and Wilcoxon Matched Paired Tests (WMPT) methods. For example, intravenous results of diabetic group gave  $p < 0.001$  (SROC).

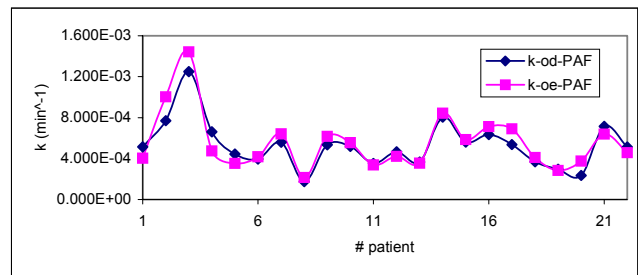


Fig. 3 – Example of Oral  $K_d$  results (OD vs OE). X-axis indicate patient number

Reproducibility, calculated by:

$$\frac{1}{n} \sum_n \frac{|K_1 - K_2|}{(K_1 + K_2) / 2} \quad (3)$$

where  $K_1$  e  $K_2$  are the  $K_d$  of first and second visit respectively, was found to be less then 8% for FM and less then 10% for PAF. Intravisit reproducibility was found to be  $3.6\% \pm 1.6\%$ .

With endovenous administration good correlation PAF-FM was achieved and no significative difference between

$K_d$  of first and second visit (both PAF and FM) was obtained as validated by Spearman Rank Order Correlation and Wilcoxon Matched Paired Tests.

One important objective of the study was to define a protocol for ocular fluorometry after oral tracer administration. Although a more complex plasma concentration profile with time, we were able to develop curve fitting and calculation methods to evaluate plasma concentration time integral.

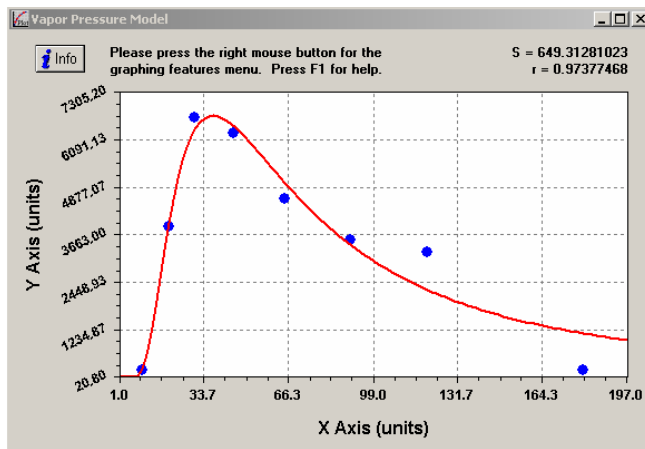


Fig. 4 - Curve fitting for calculation of plasma concentration time integral

Fig. 4 shows one particular curve where experimental points were adjusted to a vapour pressure model given by the following equation

$$y = e^{a + \frac{b}{x} + c \ln x} \quad (4)$$

where a, b and c are adjustable parameters.

Several curve fitting models were compared and trapezoidal methods were also evaluated.

#### IV. DISCUSSION

Intravenous administration is a well established procedure and data collected gave simply the opportunity to compare measurements made with both equipments.

Taken the FM as gold standard the new equipment – PAF – proved to be reliable as data collected from both fluorometers are correlated ( $r = 0.872$ ;  $p < 0.001$ ). This is achieved for both visits and for both measurement times (30' and 60' in case of IV). Good reproducibility was achieved (4% intra-visit, 9% inter-visit) and correlation with Gold Standard Instrument results has been proved.

The safer oral administration of fluorescein (no patient adverse reactions) together with a simplification of the procedure in order to increase patient comfort can lead this technique to a clinical routine use. But there are some limitations: Plasmatic concentration curve is less predictable in comparison with EV case (more samples and care with food ingestion must be taken); long examinations (more then 90 min); Work proceeds towards simpler but reliable procedures. Attempts have been made to consider only anterior chamber concentration (either rise or wash out phases) independently of plasma measurements. That seems to be a promising direction.

Other ocular fluorometry applications like cornea and lens autofluorescence are also easily implemented with the apparatus herein described.

#### REFERENCES

1. Ribeiro M, Lobo C, Figueira J, et al. Correlation between Progression of Retinopathy and Metabolic Control in a Two-year Follow-up Study of Mild Nonproliferative Retinopathy in Subjects with Type 2 Diabetes. Invest. Ophthalmol. Vis. Sci. 2003 44: ARVO E-Abstract 3980
2. Streilein, JW (ed): Immune Response and the Eye. Chem Immunol. Basel, Karger, 1999, vol 73
3. José Cunha-Vaz, Ocular Fluorometry: standardization and Instrumentation Development, International Ophthalmology, 17, 147-153, 1993
4. Franco Docchio, editor – Introduction to Ocular Fluorometry – European Concerted Action on Ocular Fluorometry, Coimbra – Portugal, 1997

Author: José P. Domingues  
 Institute: IBILI – Biomedical Institute for Research on Light and Image  
 Street: Az. Sta Comba - Celas  
 City: Coimbra  
 Country: Portugal  
 Email: jpd@ibili.uc.pt

# Epicardial Acceleration Signal Measured Using a Single Chip 3-axis Accelerometer

L.A. Fleischer<sup>1,2</sup>, P.S. Halvorsen<sup>3</sup>, L. Hoff<sup>1</sup>, E. Fosse<sup>3,4</sup> and O.J. Elle<sup>3</sup>

<sup>1</sup> Faculty of Science and Engineering, Vestfold University College, Horten, Norway

<sup>2</sup> Department of Informatics/Faculty of Mathematics and Natural sciences, University of Oslo, Horten, Norway

<sup>3</sup> The interventional Centre, Rikshospitalet, Oslo, Norway

<sup>4</sup> Faculty Division Rikshospitalet, Faculty of Medicine, University of Oslo, Oslo, Norway.

**Abstract** — This study was part of a major effort to study epicardial acceleration as a mean to monitor myocardial function. This article presents new epicardial acceleration data measured with a commercially available capacitive 3-axis accelerometer. The single chip accelerometer was packaged in medical grade silicon and approved for use in clinical trials. The sensor was used to measure heart motion in an animal model. The acceleration signal was integrated to velocity and position using numerical integration. The new recordings of epicardial acceleration showed good details.

**Keywords** — Accelerometer, epicardial acceleration, heart motion.

## I. INTRODUCTION

This article presents new recordings of epicardial acceleration using a 3-axis accelerometer.

Graft occlusion immediately after coronary surgery is a serious and well known problem. Hol et al has reported there was a 4% chance of coronary bypass graft occlusion immediately after closure of the wound, obtained by using angiography in the operating theater [1]. An accurate tool for online monitoring of myocardial function may give the physician an opportunity to revise occluded grafts before departure from the hospital.

Since heart wall motion is directly linked to cardiac function, echocardiography is a commonly used method for studying regional myocardial dysfunction [2]. However, echocardiography gives only intermittent readings, and the method is time consuming.

The goal of this effort was to use accelerometers to achieve inexpensive, simple and continuous measurement of heart wall motion, in order to monitor myocardial function. Several studies have used epi- or endocardial acceleration to study the origin of heart sound [3][4][5][6][7], and to monitor contractility by measuring vibrations associated with the first heart sound [8].

An earlier study from this group demonstrated how 3-axis accelerometers can be used to detect coronary occlusion interpreted using short-time Fourier transform [9]. The sensor was a hybrid 3-axis sensor made by mounting two 2-axis sensors perpendicular to each other. The sensors used

were the ADXL-202 from Analog Devices (Analog Devices Inc, Norwood, MA, USA) and the samplings frequency was 250Hz.

Another study demonstrated how the acceleration signal could be used to approximate velocity and position [10]. This study also used a hybrid 3-axis sensor made up of two 2-axis accelerometers (ADXL311)(Analog Devices Inc, Norwood, MA, USA). The bandwidth of this was limited to 50Hz and the sampling frequency was 250Hz. This method allowed the comparison of information with signals obtained from echocardiography, e.g. tissue velocity imaging [2].

A result of these studies was that accelerometers seem to be sensitive in detecting changes in myocardial movement pattern, but there are some challenges that need to be overcome in order to use accelerometers for continuous monitoring of heart condition.

This article presents acceleration data measured with a new commercially available, single chip, micro machined, 3-axis capacitive accelerometer. The chip was packaged in a biocompatible material and connected to a five lead cable. The packaging was designed with holes in each corner to suture the sensor securely to the heart surface. This sensors advantage was its size, weight, thin cable and its holes dedicated to sutures. This allowed the sensor to follow the epicardial movement with good accuracy. The sensor was tested on a pig model to visualize its ability to measure heart movement.

## II. METHOD

### A. Animal protocol

In a pig model, access to the heart was achieved through a median sternotomy after anesthesia. Anesthesia was induced with intravenous pentobarbital (2-3 mg kg<sup>-1</sup>) and boluses of morphine (0.05 mg kg<sup>-1</sup>), titrated to no reaction to skin incision and maintained by continuous inhalation of isoflurane 0.5-1.5% and intravenous infusion of morphine 0.15-0.2 mg kg<sup>-1</sup> h<sup>-1</sup>. The animal was ventilated using a respirator with a frequency of ca. 20 respiration per minute. One accelerometer was attached to the surface of the left

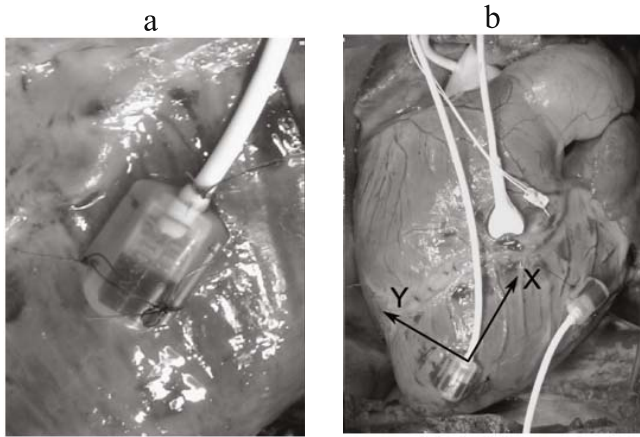


Fig. 1. Image a) shows how the encapsulated sensor was sutured to the epicardium. Image b) shows how two sensors were positioned on the left ventricle. The arrows in the right image marked X and Y, shows the longitudinal and transversal sensor directions relative to the heart surface. The last direction, Z, was perpendicular to the heart surface.

cardiac ventricle, anteriorly, near the apex by Prolene 5-0 epicardial sutures (Fig. 1). The study was performed in one animal according to a protocol approved by the institutional Animal Care and Use Committee at Rikshospitalet described in previous work [9]. The animals used were Norwegian land pigs of either sex, with a weight of 51.0kg.

### B. Accelerometer

Acceleration was measured with a commercially available triple-axis miniature accelerometer (Kionix KXM52-1050, Kionix Inc. Ithaca, NY, USA), mounted on an alumina substrate and encapsulated in medical grade silicone [11](Figure 1 a)). Key parameters for the sensor are listed in Table 1. The accelerometer was calibrated using earth gravitational field. Capacitors of 47nF were connected to each of the outputs of the sensor, reducing the bandwidth to 105 Hz and limiting the output noise from the sensors. The encapsulation of the sensor was designed with one hole in each corner to be able to securely fasten the sensor to the epicard with sutures.

Table 1 Specification of the capacitive accelerometer KXM52-1050, as used in the described setup.

Parameters	Units	KXM52-1050(xyz)
Range	g	$\pm 2$
Sensitivity	V/g	1@ Vcc=5,0V
Operating Voltage	V	5.0
Noise @500Hz	mg/Hz <sup>1/2</sup>	0.5(x & y), 0.8(z)
Bandwidth (-3dB)	Hz	0-105 (Limited)
Cross-axis sensitivity	%	2

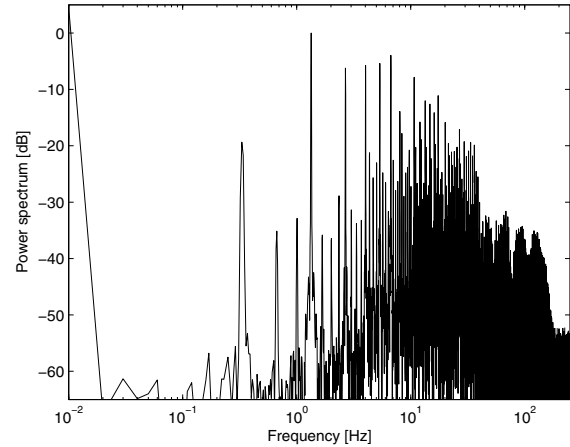


Fig. 2. This figure shows the power spectrum of the unfiltered acceleration signal from the longitudinal axis. This frequency spectrum from the other axis showed similar results.

### C. Data acquisition and hardware

The signals from the accelerometer and the ECG were recorded simultaneously. Data was recorded at a sampling rate of 500 Hz using a NI USB 6009 AD-Converter (National Instruments Inc. Austin, TX, USA) connected to a computer running the LabVIEW software (National Instruments Inc.). The full-scale resolution of the converter was 13bit, but with the described setup and signal levels, the effective resolution was approximately 10bit.

The ECG signal was recorded to relate the acceleration to the cardiac cycle. A Dräger Siemens SC 9000XL monitor (Siemens AG, Germany) was used as a signal condition unit, and output from this monitor was recorded in parallel with the accelerometer signals, using the same AD-board and software. The output from the monitor was delayed compared to the input ECG signal. This delay was experimentally measured to 22ms, and was compensated for in the processing of the data.

### D. Signal processing

The acceleration signal was high-pass filtered using a 4th order Butterworth digital filter with a cutoff frequency of 0.71Hz. The filter was applied in both directions to remove phase differences.

The velocity was approximated by trapezoidal numerical integration. The integration constant was approximated by assuming no velocity below the cutoff frequency. This was done by high-pass filtering after the integration. Position was approximated from velocity in the same manner.

The frequency spectrum of the unfiltered acceleration signal was calculated and presented in Figure 2. The accel-

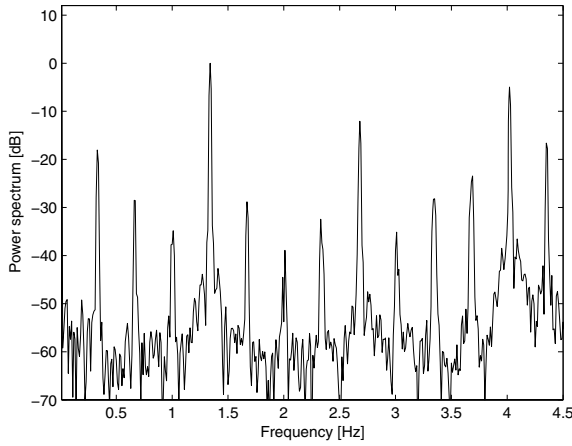


Fig. 3 This figure shows the power spectrum of the acceleration plotted with a linear frequency scale. This figure shows the heartbeat and respiration frequency and the unlinear mixing between them.

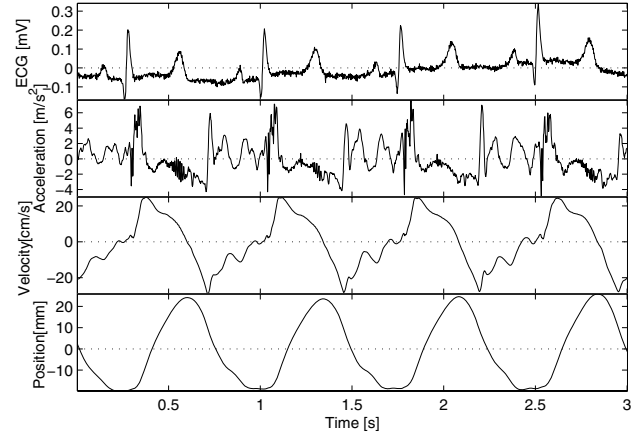


Fig. 5 This figure shows a tree second time trace. It shows the ECG and the acceleration and approximated velocity and position from the transversal accelerometer axis.

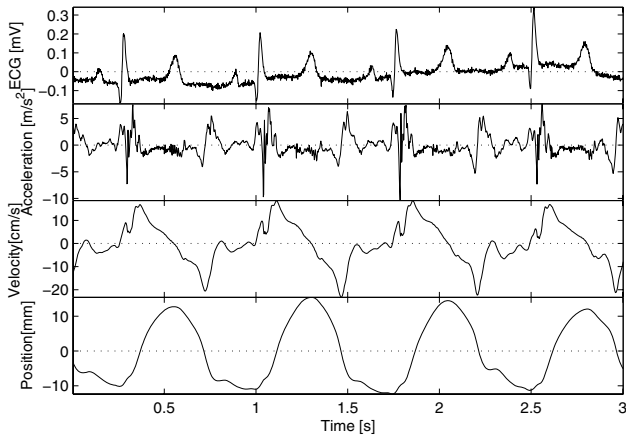


Fig. 4 This figure shows a tree second time trace. It shows the ECG and the acceleration and approximated velocity and position from the longitudinal accelerometer axis.

eration was from the accelerometers y-axis (Fig. 1 b)), with a sensing direction transversal to the heart surface. The frequency spectrum in the chosen axis was a typical representation of all the axes. The amplitude of the frequency specter was normalized to the amplitude of the heart rate frequency. A Hanning window was used during Fourier transform and the frequency band covered was 0-250Hz.

A tree second time trace of the ECG, high-pass filtered acceleration and the approximated velocity and position, was presented in Figure 3, 4 and 5. The tree figures presented data from all tree axes in the 3-axis accelerometer. Figure 3 presented data from the x-axis, longitudinal to the heart, and Figure 4 presented data from the y-axis, transversal to the heart (Fig. 1 b)). Data from the z-axis, perpendicular to the heart, was presented in Figure 5.

### III. RESULTS

In the frequency plot it was to identify the heart rate and its higher order components, starting at 1.34Hz (Fig. 2). It was also possible to identify the respiration and one of its higher components, starting at 0.33Hz. This frequency corresponded to the rate the animal was ventilated with. There was also possible to identify an unlinear mixing between the heart rate and the respiration rate ( $1.34-0.33=1.01\text{Hz}$ ,  $1.34+0.33=1.68\text{Hz}$  and  $1.34+2*0.33=2.01\text{Hz}$ ).

### IV. DISCUSSION

The filter coefficients were chosen to reduce the gravity and respiration component in the acceleration signal. The filtering was important in order to approximate the velocity and position.

The approximated velocity has similarities with tissue velocity echocardiography, and some of its typical features may be identified. In all the figures showing the different axis, something similar to an ejection and early filling phase may be identified. In the time trace plot it may be possible to identify the ejection phase in the approximated velocity as the phase with a positive velocity immediately after the peak R-wave in the ECG signal. It may also be possible to identify the ejection phase in the approximated position as the upward stroke.

#### A. Limitations

According to Einstein's principle of equivalence, rotation in a gravitation field and acceleration can not be distin-



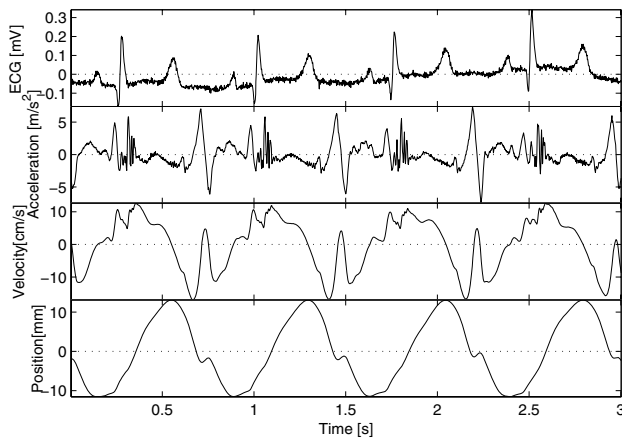


Fig. 6 This figure shows a three second time trace. It shows the ECG and the acceleration and approximated velocity and position from the perpendicular accelerometer axis.

guished. This may be relevant when using accelerometers on the heart since the heart twists and rotates the apex during a cardiac cycle [12]. This rotation will occur at the same frequency as the heart rate, hence, can not be removed by filtering in the frequency domain.

## V. CONCLUSIONS

The new single chip micro machined 3-axis accelerometer measured epicardial acceleration recording with good details and resolution.

## REFERENCES

1. Hol P K, Lingaas P S, Lundblad R et al (2004) Intraoperative angiography leads to graft revision in coronary artery bypass surgery, *Ann. Thor. Surg.* 78:502–505.

2. Edvardsen T, Skulstad H, Aakhus S et al. (2001) Regional myocardial systolic function during acute myocardial ischemia assessed by strain Doppler echocardiography, *J. Am. Coll. Cardiol.* 37:726-730.
3. Ishimitsu T, Smith D, Berko B and Craige E (1985) Origin of the third heart sound: comparison of ventricular wall dynamics in hyperdynamic and hypodynamic types, *J. Am. Coll. Cardiol.* 5:268-272.
4. Ozawa Y, Smith D and Craige E (1983) Origin of the third heart sound. I. Studies in dogs, *Circulation* 67:393-398.
5. Ozawa Y, Smith D and Craige E (1983) Origin of the third heart sound. II. Studies in human subjects, *Circulation* 67:399-404.
6. Wood J C, Buda A J and Barry D T (1992) Time-frequency transforms: a new approach to first heart sound frequency dynamics, *IEEE. Trans. Biomed. Eng.* 39:730-40.
7. Wood J C, Festen M P, Lim M J et al. (1994) Regional effects of myocardial ischemia on epicardially recorded canine first heart sounds, *J. Appl. Physiol.* 76:291-302.
8. Theres H P, Kaiser D R, Nelson S D et al. (2004) Detection of acute myocardial ischemia during percutaneous transluminal coronary angioplasty by endocardial acceleration., *Pacing clin. electrophysiol.* 27 621.
9. Elle O J, Halvorsen S, Gulbrandsen M G and Fosse E (2005) Early recognition of regional cardiac ischemia using a 3-axis accelerometer sensor, *Physiol. Meas.* 26:429-440.
10. Hoff L, Elle O J, Grimnes M J et al. (2004) Measurements of heart motion using accelerometers, *Proc. of 26. ann. internat. conf. IEEE Eng. in Med. and Biol. Society* 26:2049-2051.
11. Imenes K, Aasmundtveit K, Husa E M et al. (2007) Assembly and packaging of a three-axis micro accelerometer used for detection of heart infarction, *Biomedical Microdevices*, Springer Netherlands, in press, online publication 10.1007/s10544-007-9082-2.
12. Marcelli E, Plicchi G, Cercenelli L and Bortolami F (2005) First Experimental Evaluation of Cardiac Apex Rotation with an Epicardial Coriolis Force Sensor, *ASAIO Journal* 51:696-701.

Author: Lars Albert Fleischer  
 Institute: Vestfold University College  
 Street: P.O.Box 2243  
 City: N-3103 Tønsberg  
 Country: Norway  
 Email: Lars.A.Fleischer@hive.no

# Novel Conducting Polymer Composite pH Sensors for Medical Applications

E.I. Gill<sup>1</sup>, A. Arshak<sup>1</sup>, K. Arshak<sup>2</sup> and O. Korostynska<sup>2</sup>

<sup>1</sup> Department of Physics, University of Limerick, Limerick, Ireland

<sup>2</sup> Department of Electronic and Computer Engineering, University of Limerick, Limerick, Ireland

**Abstract** — Sensors for pH measurements in the pH range of human blood (pH7.0-pH8.0) is reported. The sensors comprise of a gold interdigitated electrode structure with a novel polyaniline-based composite thick film as the sensing layer. The sensors showed a sensitivity of approximately 10  $\Omega$ /pH unit, when in contact with the test solutions. Due to the permanent effects of the pH of the solution on the films, the resistance of the films (after removal from the solution) varied over several orders of magnitude. The sensors demonstrated a repeatable response.

**Keywords** — Polyaniline, Resistance, Thick Films, pH, Blood

## I. INTRODUCTION

Conducting polymers (CPs) are a novel brand of materials, whose unique electrical properties are only beginning to be fully appreciated. Polymers belonging to this group of normally insulating materials are being exploited on a large scale, in many different applications, including batteries, light emitting diodes, electro-optic and optical devices [1]. Another important area in which CPs have found use is in chemical sensing devices, such as those to detect glucose [2] and urea [3] levels in the body.

The pH of bodily fluids is also important to the health of a patient. Devices designed to measure the pH levels in human patients need to have a higher sensitivity and be more reliable than standard pH sensors. Some CPs, such as Polyaniline (PANI) and Polypyrrole (PPy) [4, 5], show promise in such pH-sensing applications.

This work shows how conductimetric sensors, employing novel polymer composite materials as their sensing layers can be successfully developed for medical applications. Conductimetric sensors have appeared frequently in the literature, measuring pH, glucose and so forth [6-9]. In this work, a conductimetric sensor based on an interdigitated (IDE) gold electrode structure in conjunction with a PANI based composite thick film sensing layer can be employed to measure the pH of solutions in the pH range of pH7.0-pH8.0, a significant pH range as the pH of human blood is maintained in this region.

Polyaniline is exploited as a pH-sensitive material, as its conductivity is governed by the pH of the solution. Previous work by the authors [5] has found that this conductivity

varies with the pH of the solution it is in contact with; with the conductivity decreasing as the pH of the solution increases (becomes more alkaline).

## II. EXPERIMENTAL

The PANI Emeraldine Salt (ES) was purchased in powder form from Sigma Aldrich and underwent no further purification. First, 1.0 g of the PANI ES powder was placed in a 60 mL glass jar, along with 10 wt.% of polyvinyl butyral (PVB), which acts as a binder and Hypermer PS3 (surfactant) and manually stirred with a spatula until well mixed. Once the mixture is ready, a suitable amount of solvent (ethyleneglycolmonobutylether) was manually mixed into the composite polymer mixture. Once sufficient rheological properties have been achieved, the mixture is ready for screen-printing.

The IDE structure was screen-printed onto pre-cleaned alumina substrates (CeramTec UK Ltd.) using a DEK 1202 automatic screen-printer. The material used for the electrodes was Au thick film conductive paste (Heraeus Materials). After screen-printing, the substrates were placed into an oven at 80°C for 2 hours to facilitate the initial drying of the paste. In this step, the remaining solvent in the thick film paste evaporates, leaving the dried pattern on the substrate. The devices are next placed into a multi-chamber belt-furnace for a much higher temperature (850°C) cycle. In this step, any remaining organic binder is removed and the metal frit is sintered into one solid structure. This step also allows the electrode pattern to settle to its final thickness and resistivity values.

The thickness of the Au thick film is 9  $\mu\text{m}$  and was measured using a Dektak Surface Profile Measuring System.

Once the electrode structures are ready, the composite polymer is screen-printed over the IDE structure. These devices are then placed into an oven at 80°C for 12 hours to ensure complete solvent evaporation. After 12 hours, the devices are ready for testing and link wires are soldered directly to the bond pads of the IDE structure.

The DC and AC electrical characteristics of the sensors were examined to determine the stable operating region for the devices, and to determine the conduction mechanism in the films. A National Instruments Data Acquisition (DAQ) card controlled by LabWindows/CVI software and driven by

customized electronics hardware measured the current voltage characteristics of the sensors. This equipment was also used to measure the resistance of the sensors at various temperatures.

AC characteristics were monitored using a HP 4192A Low Frequency Impedance Analyzer (50 mV, 10 Hz – 10 MHz), using LabView software to log the results.

Testing the pH sensitivity of the devices was achieved by submerging the film into 20 mL of test buffers (Sigma Aldrich Hydrion® (pH2-11) and Trizma® Hydrochloride-Base mixtures (pH7.0-pH8.0) (also from Sigma Aldrich)). The change in the electrical parameters of the sensors was recorded using the HP4192A Impedance Analyzer. After the test is complete, the sensor is rinsed in de-ionised water and dried. The electrical parameters of the film are again examined to establish any permanent effects the pH of the test buffers may have on the composite polymer films.

### III. RESULTS AND DISCUSSION

#### A. AC and DC Electrical Characteristics of Composite Thick Films

In order to understand the reactions taking place between the test solutions and the thick films, it is necessary to study the electrical characteristics of the film before exposure to any solutions. It was found that the composite thick films had a low resistance value of approximately 5  $\Omega$ , and when a sweeping voltage was applied to the sensor, the resultant current was ohmic in nature (Fig. 1). It was also observed that the film resistance increased with increasing temperature, suggesting a conduction that is metallic in nature.

The resistance of the films also did not vary considerably with frequency, further supporting metallic conductivity (Fig. 2). These results are supported by some of the theoretical treatment of conducting polymers, which refer to these

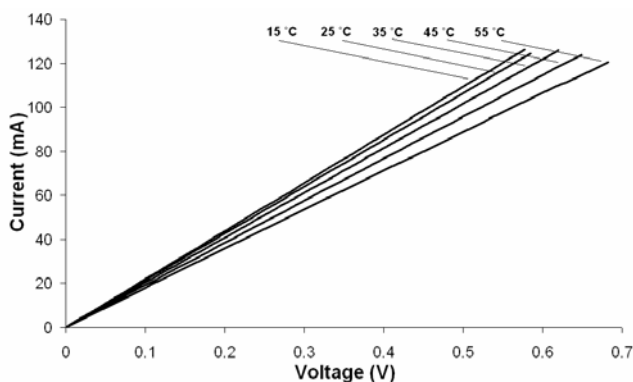


Fig. 1. Current-Voltage Characteristics of composite thick films.

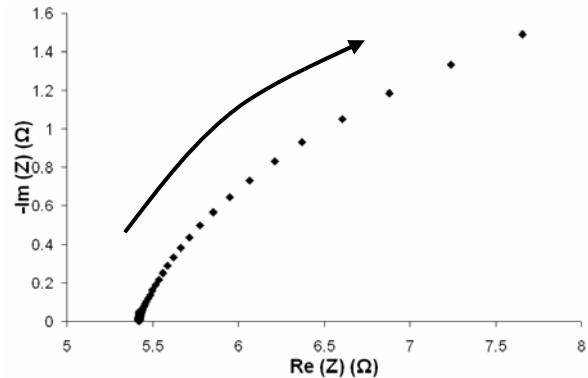


Fig. 2. Real versus Imaginary Impedance components of untested composite thick film before testing. The arrow represents the direction of increasing frequency.

polymers as organic semiconductors [1]. In this treatment, when the band-gap between the valence and conduction bands disappear (due to doping), the two bands overlap leading to a conduction mechanism which is metallic in nature.

#### B. Results and Discussion

Upon immersion into the test solutions, the resistance of the film undergoes an immediate change. The sensor was allowed to rest in the solutions for five minutes, and then it was placed into the next buffer. This was repeated for all test buffers in the pH range pH7.0-pH8.0, with the pH increasing in increments of 0.1 of a pH unit. Fig. 3 shows the resistance of the film while in contact with the solution taken after five minutes.

The change in resistance of the film is attributed to the de-protonation of the polymer back-bone, with the resulting loss of charge carriers. Previous work by the authors has established this fact [5]. The composite thick films are essentially PANI particles held together by the polymer binder. The film

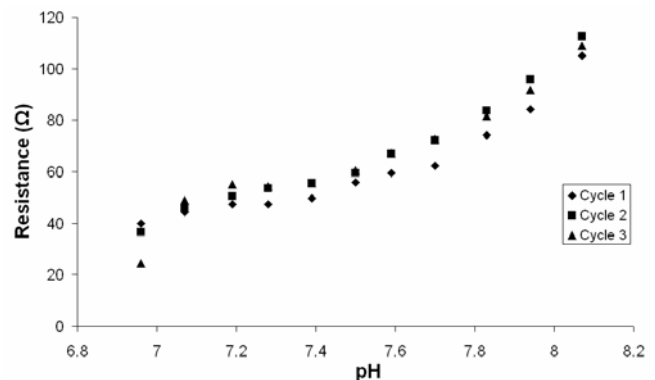


Fig. 3. Composite thick film resistance versus solution pH. Measurements are taken after five minutes of film contact with the test solution.

is porous in nature, allowing the solution to penetrate into the film and interact with the PANI particles. Conduction through the film occurs at the points where these particles meet. As contact between the film and solutions of alkaline pH cause the removal of the charge carriers in these regions, the resistance of the film increases. The extra information in Fig. 3 shows the sensors have good repeatability. After stepping the sensor through each buffer, starting at pH7.0 and increasing to pH8.0, the sensor is allowed to soak in an acidic buffer (pH2.0) for 10 minutes. This restores the resistance to its pre-test value and the experiment can be repeated. The data in Fig. 4 shows the reprotonation of the film.

From the reviewed literature and previous work by the authors [5-6, 11], it is known that the resistance of the composite thick film varies over several orders of magnitude. The reason that the resistance of the film (while in contact with the test solutions) remains relatively low is that once the deprotonation process is underway, the dominant conduction in the film-solution system is changed from a film-dominant conduction process to a joint film and solution conduction process. The charge carriers that are lost in the film are replaced by the ions in the solution. However, when we compared the conductance of the solution to the conductance of the film, it was found that the ions in the solution only contribute a “background” conductance, and that the overall conductance of the film is not dominated by the solution ions.

By taking the above conclusions into consideration, it was decided to investigate the permanent effect of the solution on the resistance of the sensor. By soaking one sensor in each buffer for 12 hours, it was possible to investigate these effects. Once removed from the solution, the sensors were rinsed thoroughly in de-ionised water (to remove any remaining solution) and dried for several hours in an oven at 80 °C. The electrical properties of the sensors were measured over the same frequency range as before.

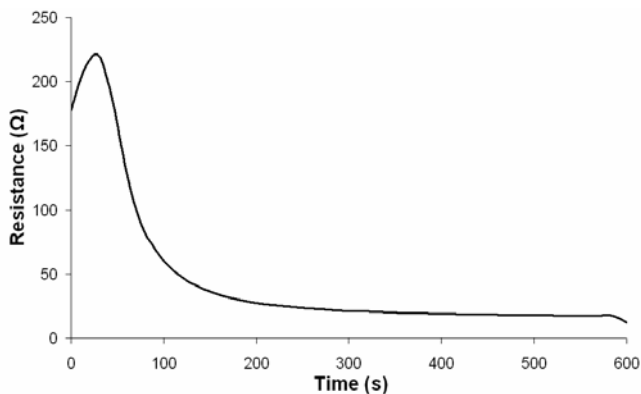


Fig. 4. Reprotonation of the composite polymer thick films after first experiment.

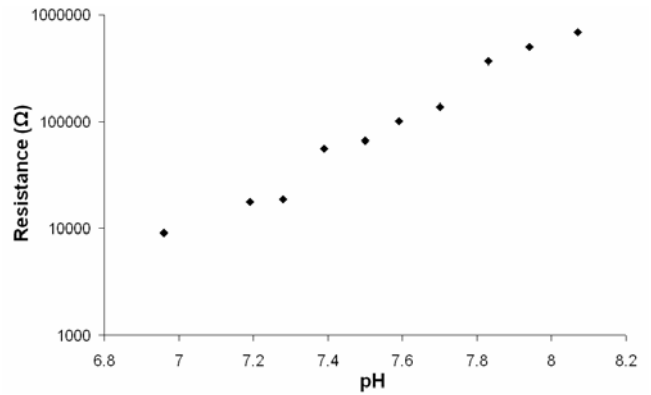


Fig. 5. Resistance of composite thick films after 12 hour soak in buffers of different pH values.

It was found that the long term effects of the solutions on the films dramatically affected the resistance of the films (Fig. 5). The resistance values recorded after this experiment demonstrates the large changes in magnitude experienced by the sensors, when solution conductance is not taken into consideration.

By examining the impedance spectra of the different samples (same as used in Fig. 5), it was found that the electrical conduction taking place in the films had changed considerably (Fig. 6).

The curves seen in Fig. 6, correspond very closely to the examples given by MacDonald [11]. In his work, impedance plane plots of the same shape are attributed to a common RC circuit, i.e. a resistor and a capacitor in parallel with each other. In this case, the capacitance arises from the insulating media now present in the film (PANI particles devoid of charge carriers). In effect, the film has become a disordered, inhomogeneous semiconductor. It is also evident from Fig. 6 that the difference in magnitude of both

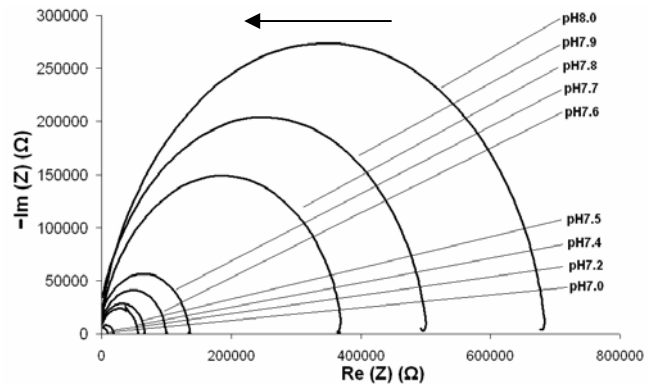


Fig. 6. Cole-Cole plots of samples after 12 hour soak in buffers of different, known, pH values. The arrow indicates the direction of increasing frequency.

the real and imaginary components of the impedance is large for devices tested under different pH conditions.

#### IV. CONCLUSIONS

The sensor developed in this work has successfully demonstrated its suitability as a device to measure the pH of a solution in the biologically significant pH region pH7.0-pH8.0. By the deprotonation of the polymer back-bone, the resistance of the film was seen to increase with increasing pH. The sensor resistance varied over a range of approximately 100  $\Omega$  when the sensor is in contact with the test buffers and over several orders of magnitude when not in contact with the solution. It was also discovered that the overall conduction mechanism in the film changes as the pH of the test solution is increased. The new conduction mechanism can be approximated by an equivalent RC circuit. The sensors also demonstrated good repeatability and reproducibility.

#### ACKNOWLEDGMENT

This research was supported by the Irish Research Council for Science Engineering and Technology (IRCSET): funded by the National Development Plan.

#### REFERENCES

1. Chandrasekhar, P. (1999) *Conducting Polymers, Fundamentals and Applications: A Practical Approach*. Kluwer Academic Publishers, Boston.
2. Shan, D., Wang, S., He, Y., Xue, H. (2008) Amperometric Glucose Biosensor Based on In Situ Electropolymerised Polyaniline/ Poly (acrylonitrile-co-acrylic acid) composite film. *Mat. Sci. and Eng.* In Press.
3. Castillo-Ortega, M.M., Del Castillo-Castro, T., Ibarra-Bracamontes, V.J. (2007) Urea sensing film prepared by extrusion from DBSA-doped polyaniline-poly(styrene-co-potassium acrylate) in a poly(n-butyl methacrylate) matrix. *Sens. and Act. B: Chem* 125:538-543 DOI 10.1016/j.snb.2007.02.049
4. Korostynska, O., Arshak, K., Gill, E., Arshak, A. (2007) Review on state-of-the-art in polymer based pH sensors. *Sensors* 7:3027-3346
5. Gill, E., Arshak, A., Arshak, K., Korostynska, O. (2007) pH sensitivity of novel PANI/PVB/PS3 composite films. *Sensors* 7:3329-3346
6. Gill, E., Arshak, K., Arshak, A., Korostynska, O. (2007) Mixed metal oxide films as pH sensing materials. *Microsys. Techn.* 14:499-507
7. Sheppard, N.F., Tucker, R.C., Salehi-Had, S. (1991) Design of a conductimetric sensor based on pH-sensitive polymer hydrogels. *Annual International Conference of the IEEE Engineering in Medicine and Biology Society* 13:1581-1582.
8. Arnold, F.H., Zheng, W., Michaels, A.S. (2000) A membrane-moderated, conductimetric sensor for the detection and measurement of specific organic solutes in aqueous solutions. *Journ. of Memb. Sci.* 167:227-239 DOI 10.1016/S0376-7388(99)00283-5
9. Gallardo Soto, A.M., Jaffari, S.A., Bone, S. (2001) Characterization and optimization of AC conductimetric biosensors. *Biosens. and Bioelectr.* 16:23-29 DOI 10.1016/S0956-5663(00)00119-6
10. Macdonald, J.R. (1987) *Impedance Spectroscopy: Emphasizing Solid Materials and Systems*, John Wiley & Sons, New York.
11. Arshak, K., Gill, E., Arshak, A., Korostynska, O. (2007) Investigation of Tin Oxides as Sensing Layers in Conductimetric Interdigitated pH Sensors. *Sens. and Act. B.* 127:42-53

Author: Dr. Arousian Arshak  
 Institute: University of Limerick  
 Street: Plassey Technological Park  
 City: Limerick  
 Country: Ireland  
 Email: rousian.arshak@ul.ie

# Future Trends in Robotic Neurosurgery

T. Haidegger<sup>1,2</sup>, L. Kovacs<sup>1</sup>, G. Fordos<sup>1</sup>, Z. Benyo<sup>1</sup> and P. Kazanzides<sup>2</sup>

<sup>1</sup> Budapest University of Technology and Economics / Department of Control Engineering and Information Technology - Laboratory of Medical Informatics, Budapest, Hungary

<sup>2</sup> Johns Hopkins University / Center for Computer Integrated Surgical Systems and Technology, Baltimore, USA

**Abstract** — Computer Integrated Surgery has only existed for two decades, however it has already spread out world wide, with well over 100.000 operations performed. In the near future, newly developed robotic systems may conquer even the most challenging fields—such as neurosurgery—to provide better patient care and medical outcome. This paper presents the major systems and different strategies applied in robotic neurosurgery. Besides appropriate design, adequate control strategies are required to ensure maximal safety. This makes automated neurosurgery a technologically challenging area for researchers. It is also important during the design phase to consider market aspects. We anticipate that the future trends of clinical applications are outlined by the current leading research directions. The conclusions of the past years of innovation will lead forward on the path of further improvement.

**Keywords** — Computer Integrated Surgery, robotic surgery, neurosurgery

## I. INTRODUCTION

Robotic surgery is entering its adulthood due to the continuous development made by research groups all over the world. From the close co-operation of engineers and physicians great medical robotic innovations were born. It was first proven more than thirty years ago that robotic tools can extend human capabilities, as a brain biopsy procedure (manipulating biopsy cannulae with a PUMA 560 robot) was successfully performed in 1985 [1]. General purpose laparoscopic multi-manipulators—such as the da Vinci—have performed thousands of operations so far; however, more emphasis has been put on gastro-intestinal, cardiovascular and orthopaedic surgery.

Neurosurgery is one of the most demanding areas for Computer Integrated Surgery (CIS), where the complexity of the anatomical regions and the high sensitivity of the tissues require fine accuracy and high precision. In the mean time, robot-aided procedures offer remarkable advantages both for the patient and the surgeon. The ability to perform a surgery in smaller scale with robots makes microsurgery a reality. The use of mechatronic devices can increase the stability and robustness of the system, give increased accuracy to navigate based on medical images and help position-

ing the surgical tool to the target point. Furthermore, there is the option to introduce advanced digital signal processing and control or to record the spatial points-of-interest and motions. This can be useful for surgical simulation and risk-free training. Finally, robotized equipment can greatly add to the ergonomics of the procedure, especially in the case of minimally invasive surgery (MIS).

CIS promises significant results in the case of brain procedures mainly for two reasons: the skull gives a rigid frame, therefore it is easier to register real world structures to preoperative scans of the patient. (This is the basis of effective image-guided surgery). Second, the compactness of the head allows less soft tissue motion during the intervention, enabling a more accurate use of pre-operative planning. However, once the skull is open during the procedure, there may be significant tissue motion. Compensating for brain shift is a major field of research.

We can categorize surgical robots based on their different roles in the OR [2]. Passive robots only serve as a tool holding device once directed to the desired position. Semi-active devices perform the operation under direct human control (e.g. in compliant mode). Active devices are under computer control, and automatically perform certain interventions (e.g. bone machining). Beyond this, surgical robots can be involved in the procedure with different level of autonomy [3]. Systems that are able to perform fully automated procedures—such as CT-based biopsy or cutting—are called autonomous, or supervisory controlled. (A human supervisor would always be close to the robot, but does not intervene, as long as everything goes according to the surgical plan.) On the other hand, if the robot is entirely remote-controlled, and the surgeon is in charge of every single motion of the robot, we may call it a teleoperated system. The latter can be realized by a master-slave manipulator system for example. Modifying this control paradigm, we can introduce compliant (co-operative) control. It means that the surgeon is directly giving the control signals to the machine, while leaving some space for automation. This is called the hands-on technique, as the human is always in contact with the robot.

Table 1. Major neurosurgical robotic projects and most important features. (CA = commercially available)

Project [ref.]	Category	Institute, company	Main features
Alpha robot [1]	Active, teleoperated	MicroDexterity Systems Inc.; Albuquerque, NM, USA	5 DOF parallel manipulator mounted on the stereotactic frame, CA
Cranio [11]	Active, automated	RWTH-Aachen / Lehrstuhl für Biomedizinische Technik; Aachen, DE	Craniectomy with 6 DOF hexapod robot
Cyberknife [12]	Active, automated	Accuray Inc.; Sunnyvale, CA, USA	Image guided radiotherapy, tumor irradiation, CA
Evolution 1 [13]	Semi-active, automated	Universal Robot Systems; Schwerin, Germany	6 DOF hexapod robot for pedicle screw placement and adenoma dissection, CA
JHU project w/ NeuroMate [9]	Co-operative control	Johns Hopkins University; Baltimore, MD, USA	Skull base drilling with force based co-operative control with Virtual Fixtures
KineMedic [15]	Active, teleoperated	DLR / BrainLAB AG, Feldkirchen, Germany	Light-weight, high payload 7DOF robot for MIS neurosurgery, CA
MARS robot (SmartAssist) [16]	Active, automated	Mazor Surgical Technologies Inc.; Caesarea, Israel	FDA approved, light-weight, head mountable robot for needle insertion
Minerva [17]	Active, automated	Lab. of Microengineering, Swiss Federal Inst. of Tech.; Lausanne, CH	Real time frameless stereotactic instrument guidance in CT scanner
MRI compatible robot [7]	Semi-active, automated	Harvard Medical School; Boston, MA, USA	5 DOF robot for percutaneous procedures, driven by ultrasonic motors
neuroArm [8]	Active, teleoperated	University of Calgary; Canada	MRI compatible complete multi-manipulator
NeuRobot [18]	Active, automated	Computer Integrated Medical Intervention Laboratory; Singapore	Instrument guidance, skull-base surgery
NeuroMaster [19]	Active, automated	Robotic Institute Beihang University; Beijing, China	6 DOF robot for stereotactic procedures
NeuroMate [10]	Passive, automated	IMMI / ISS / Schaerer Mayfield NeuroMate Sarl; Lyon, France	Cannulae positioning for biopsy, neuroendoscopy, CA
PathFinder [6]	Active, automated	Prosurgics Ltd. (formerly Armstrong Healthcare Ltd.); High Wycombe, UK	6 DOF manipulator for instrument guidance, CA
Raven [20]	Active, teleoperated	University of Washington; WA, USA	6 DOF general surgery, automated suction
RAMS [21]	Active, teleoperated	NASA JPL; Pasadena; CA, USA	6 DOF manipulator for eye and brain surgery with motion scaling and tremor filtering
Steady Hand System [14]	Co-operative control	Johns Hopkins University; Baltimore, MD, USA	7 DOF robot with advanced tremor filtering for MIS needle driving

## II. CURRENT ROBOTIC APPLICATIONS IN NEUROSURGERY

In the past decades, several different robotic neurosurgical devices have been created, and a couple have reached the market (Table 1).

In fact, none could move on towards real mass production and achieve the success of the well-known da Vinci teleoperated system. We cannot talk about a major financial breakthrough because of certain functional limitations and the higher investment/ maintenance costs. However, the new systems offer even more significant clinical advantages that may well compensate for their high cost.

Table 1. lists the major neurosurgical robotic systems and their main features. Beyond these, several other research projects exist, as listed in the MEDical Robotics DATABASE (MERODA [4]).

## III. FUTURE OF NEUROSURGICAL ROBOTS

Present research projects are focusing on three major areas for improvement. One is to increase the overall accuracy and/or efficacy of the classic stereotactic systems, another is to increase the added-value of the equipment and the third is

to further enhance the capabilities of the human surgeon. The following ongoing research examples give a good insight how these trends are realized and what are benefits for future patients. Safety is paramount, and may always determine the way research is conducted. In the discussed three cases, patient safety is addressed differently in each system.

#### A. Improvement of stereotactic surgery

The European Union's most recent initiative, the Robocast project aims to augment existing image-guided surgery techniques and to find new ways to perform high-precision keyhole neurosurgery [5]. The Robocast systems will use optical trackers for patient safety (to monitor and compensate for any change in the patient's position) and provide visual information of the surgical field. Given an accurate registration, the controller will use the preoperative diagnostic information to plan the path of the intervention. The modular system to be built will consist of two manipulators and one smaller probe, actively cooperating in a biomimetic sensory-motor integrated framework. The PathFinder system (Prosurge Inc., UK) forms the basis of the bigger positioning robots. The stereotactic 6 degree-of-freedom (DOF) PathFinder is already available on the European market. It works with the CT or MRI images of the patient and automatically registers the position of the probe (with at least 1.25 mm accuracy). In general practice, it is capable of aligning the surgical tools within 1 mm to the target. In 2003, real-life experiments showed that the application accuracy was  $0.44 \pm 0.02$  mm (mean  $\pm$  standard deviation) using the robot,  $0.98 \pm 0.02$  mm with stereotactic frame and the error was  $1.96 \pm 1.6$  mm in with a standard (frameless) navigation system [6].

Improving the efficiency and precision of stereotactic surgery will lead to more gainful treatment of certain brain tumors and lesions. Deep brain stimulation electrodes could be placed very accurately with this kind of system, resulting in the routine treatment of Parkinson and similar diseases. Effective percutaneous brachytherapy could be achieved, where radioactive seeds are implanted to kill the cancer cells. Based on the preoperative images, blood clots could also be removed. Robocast is planned to be used to inject stem cells into the brain to treat Alzheimer's and other diseases [7].

#### B. Integrating imaging devices

The other main direction of development is to integrate the robots with advanced imaging devices to increase their utility by allowing intraoperative imaging. This can be very challenging technically, but offers the highest level of added-value to the procedure. Magnetic resonance imaging

(MRI) gives a fine resolution picture of soft tissues, with acceptable rate, while it does not expose the patient and the surgeon to radiation. MRI compatible robotics has been in the focus of research interest since the mid 90s.

NeuroArm [8] is a recent teleoperated anthropomorphic robot from a University of Calgary led consortium. The MRI compatible robot (up to 1.5 Tesla magnetic field) is made for stereotaxy and microsurgery. Beyond motion scaling and high definition visual feedback, the neuroArm is able to provide very accurate 3D information of its two 7 DOF arms. It uses three displays to give a complete visual coverage on the operating environment, showing in parallel the 3D stereoscopic view of the operation, the MR image of the patient and the control panel. The system has been used on one human patient so far, further clinical trials will begin shortly, and the robot may hit the market in the next years.

#### C. Hands-on surgery

The ongoing neurosurgical research project at the Johns Hopkins University (JHU) is a good example of the cooperative control concept. The system is based on a modified NeuroMate surgical robot that is capable of helping and increasing the performance of human surgeons [9].

The NeuroMate robot was the first neurosurgical robotic device to get CE mark in Europe, and then the US Food and Drug Administration's (FDA) approval in 1997 for stereotactic neurosurgical procedures. (After having performed over 3000 operations, it was approved for frameless stereotactic surgery as well in 1999.) It also has a CE mark for neuro-endoscopic applications. Originally developed at the Grenoble University and produced by Innovative Medical Machines International (Lyon, France), the 5 DOF NeuroMate provided an accurate and trusted assistance for supervised needle positioning for brain biopsy. The technology was bought and commercialized by Integrated Surgical Systems Inc. (Sacramento, CA, USA) in 1997 and later acquired by Shaerer Mayfield NeuroMate Sarl (Lyon, France). The robot's reported intrinsic accuracy is 0.75 mm, with a repeatability of 0.15 mm. In real-life stereotactic surgical setup, the overall application accuracy was measured to be  $1.95 \pm 0.44$  mm [10].

Beyond the robot, the JHU system (Figure 1.) consists of an FDA approved, widely used treatment guidance system—StealthStation (Medtronic Navigation, Louisville, CO, USA)—and the 3D Slicer open source software ([www.slicer.org](http://www.slicer.org)). To the last link of the NeuroMate robot, a 6 DOF force sensor (JR3 Inc., Woodland, CA, USA) was attached, and the end-effector is a high-speed bone drilling surgical instrument (Anspach eMax drill, Palm Beach Gardens, FL, USA). Optical tracking is made possible by passive visual markers mounted on the robot and on the patient.



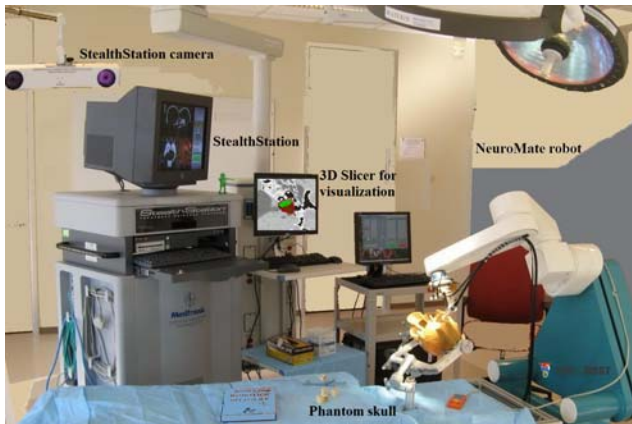


Figure 1. Robotic neurosurgery setup at the Johns Hopkins University with a modified NeuroMate robot, a StealthStation surgical navigation system and the 3D Slicer software.

The NeuroMate is guided in cooperative control mode for removal of cranial bone on the skull base. This means that the readings of the force sensor are directly coupled back to control the robot. Depending on the direction of the force applied by the surgeon, the robot moves in the defined direction, and its speed is proportional to the force.

The JHU system has three major advantages. It offers the visualization features used in stereotactic surgery: the tool's position can be followed on the 3D model of the patient, acquired from pre-operative CT scans. Second, the surgical tool is mounted on the rigid robot, thereby improving its stability. The surgeon is still holding the classic drill tool, and directs its movement; he or she can release the tool any time, take a rest, or position it arbitrarily. The most important advantage, and the real novelty of the application, is that the surgeon can define virtual boundaries on the CT scan, prior to the operation. These are called Virtual Fixtures (VF), and once registered to the robot, they are used to prevent the tip of the tool from going beyond the defined safe area in any direction. The VFs are defined using the editing and model creation tools of the 3D Slicer software. These features together greatly increase the safety and the reliability of the procedure, easing the surgeon's task, and therefore potentially reducing the operating time.

Experimental results have been acquired through foam block cutting and cadaver tests. The application accuracy of the system was measured to be  $0.79 \pm 0.82$  mm in phantom experiments with foam blocks, and the typical overcut on cadaver test samples was 1.5 mm, with a maximum of 2.5 mm. This shows that the system can be considered for serious applications, especially with the further improvement of the registration procedures' accuracy.

Hands-on surgery is providing an ergonomic and safe way for surgeons to operate. Force readings can be effec-

tively used to control such a system, allowing the introduction of advanced computer control. Further extensions of the concept will allow the integration of dynamic Virtual Fixtures that may be used for automated motion compensation of human body organs.

#### IV. CONCLUSION

Robotic neurosurgery has already proved its utility in the case of several applications from biopsy to skull base drilling. Systems currently under development are about to deliver high clinical advantages and improved safety features providing better procedures for both the patient and the surgeon. Three directions of development presented in the paper, the improvement of accuracy in stereotactic procedures, the close integration with imaging devices and the use of hands-on surgery concept will greatly improve the overall quality of computer integrated neurosurgery. It is believed that through improved quality of future healthcare, the higher costs of robotic interventions will pay off.

#### ACKNOWLEDGMENT

The research was partially funded by the NSF EEC 9731748 grant and the Hungarian National Scientific Research Foundation, Grant No. OTKA T69055.

#### REFERENCES

1. P. B. McBeth et al. (2004) Robotics in Neurosurgery; *The American Journal of Surgery*, 188
2. Robotics in Surgery: History, Current and Future Applications, Editor: R. A. Faust; Nova Science, 2007; ISBN: 1-60021-386-3
3. N. Nathoo et al. (2005) In Touch with Robotics: Neurosurgery for the Future; *Journal of Neurosurgery* 56: 421-433
4. MeRoDa: <http://www.ma.uni-heidelberg.de/apps/ortho/meroda/>
5. ROBOCAST Project (EU - FP7): <http://www.robocast.eu/>
6. M. S. Eljamel (2007) Validation of the PathFinder neurosurgical robot using a phantom; *Int. J. of Med Robotics Comput Assist Surg* 2007, 3
7. M. S. Eljamel (2007) Robotic Applications in Neurosurgery; *Medical Robotics*, edited by V. Bozovic, ISBN 978-3-902613-18-9, I-Tech Education and Publishing
8. G.R. Sutherland et al. (2008) An Image-guided MR Compatible Surgical Robot: Rapid Communication; *Neurosurgery* 62: 286-293
9. P. Kazanzides et al. (2008) A Cooperatively-controlled Image Guided Robot System for Skull Base Surgery; *Proc. of the 16th MMVR conference*, Long Beach, CA, USA, 2008
10. Q. H. Li et al. (2002) The Application Accuracy of the NeuroMate Robot—A Quantitative Comparison with Frameless and Frame-Based Surgical Localization Systems; *Computer Aided Surgery* 7:90–98
11. A. Popovica et al. (2003) CRANIO—computer-assisted planning for navigated and robot-assisted surgery on the skull; *International Congress Series* 1256; 1269–1275
12. A. Muacevic et al. (2001) Cyberknife Radiosurgery; *Touch – Neurosurgery*, Online Journal

13. C. S. Karas (2007) Neurosurgical robotics: a review of brain and spine applications; *J of Robotic Surgery*, 1:39–43; DOI 10.1007/s11701-006-0006-6
14. M. Matinfar (2007) Robot-Assisted Skull Base Surgery; *Proc. IEEE Intl. Conf. on Intelligent Robots and Systems (IROS)*, 2007
15. T. Ortmaier (2005) KineMedic: Robot Assisted Placement of Pedicle Screws; *Proc. 2nd Summer European University*, Montpellier, France
16. R. Shamir (2005) A miniature robot system for keyhole neurosurgery; MS thesis, Hebrew University of Jerusalem, Jerusalem, Israel
17. N.Villotte et al. (1992) Conception of Stereotactic Instruments for the Neurosurgical Robot Minerva; *Proc. IEEE ICRA*, 1992
18. D. Handini et al. (2004) System Integration of NeuroBot – A Skull-Base Surgical Robotic System; *Proc. IEEE ICRA*, 2004
19. J. Liu et al. (2006) The Application Accuracy of NeuroMaster: a Robot System for Stereotactic Neurosurgery; *Proc. IEEE/ASME ICME*
20. M.J.H. Lum et al. (2007) Telesurgery Via Unmanned Aerial Vehicle; *Proc. 15th MMVR - Medicine Meets Virtual Reality*, Long Beach, CA, 2007
21. H. Das et al. (1997) Robot Assisted Microsurgery Development at JPL; *Proc. Workshop on Medical Application of Virtual Reality*

Author: Tamas Haidegger  
Institute: The Johns Hopkins University / BME  
Street: 3400 N. Charles Street  
City: Baltimore, MD  
Country: USA  
Email: haidegger@jhu.edu

# Development and Evaluation of One Arm Electrode Based ECG Measurement System

M. Hannula<sup>1</sup>, H. Hinkula<sup>1</sup> and J. Jauhiainen<sup>1</sup>

<sup>1</sup> Medical Engineering R&D Center, Oulu University of Applied Sciences, Finland

**Abstract** — In this work we have developed an electrocardiogram (ECG) measurement system, which measures ECG by two electrodes attached to the left arm of the subject. The measurement system consists of wrist and upper arm electrodes connected to an amplifier, which is further connected via data acquisition card to a laptop-computer. The computer included Labview® and Matlab® based integrated real-time analysis software, which reads, filters and analyzes the ECG signal. In the implementation of the system specific solutions to the amplifier and analysis software were built to be able to measure and interpret the very weak and noisy ECG signal originating from the electrodes. The measurement system was evaluated by comparing the heart rate interval data calculated from the new ECG measurement system to Polar S810i heart rate meter and Biopac M35 measurement system. The results showed that the new ECG measurement system yielded equal results compared to the reference measurements for subjects at rest. For moving subjects the reliability of the new measurement system reduced due to artefacts. The application experiences about the system were especially encouraging. The usability of the system was excellent due to simple one-arm electrode solution.

**Keywords** — biopotential, heart rate, validation, clinical engineering.

## I. INTRODUCTION

Electrocardiogram (ECG) is one of the most typical measurements in clinical engineering. It offers a very illustrative way to monitor electrical activity of the heart [1]. The typical measurement setups in the ECG measurement are measurements with three or twelve leads, attached to different standardized sites of the body [1]. However, in previous studies [2,3] we have found that it is possible to measure some essential features of the ECG signal with electrodes attached to the left arm of the subject only. Those studies concentrated mainly on electrode placement and comparison of different electrode materials. Both studies [1,2] proved that the commercially available amplifier systems performed poorly these kinds of measurements. They are not designed for two-electrode measurement configuration in case where the electrodes locate in the same arm very near to each other. Therefore there was a need to develop a measurement system which is capable of efficiently measuring the ECG signal in this case.

Traditionally in ECG signal measurement systems operational amplifier based designs use reference electrode and measure ECG signal between reference level, positive and negative electrodes. This arrangement prevents signal drifting which is a typical problem in noisy environments, caused e.g. by EMG artefacts or other electromagnetic interferences. In this basic measurement arrangement, if the reference is removed or connected in negative electrode, the ECG signal tends to drift between positive and negative supply voltages.

Because of those challenges in the ECG signal measurement with one arm electrode configuration, we decided to develop a specific measurement system for this purpose. The amplifier of the measurement system was built according to an efficient amplifier construction found from literature [4] and the data from the amplifier was filtered and analyzed in real time with a specific computer software.

In the study the new ECG measurement system was built and its accuracy and reliability was evaluated by using commercial reference measurement systems as a reference.

## II. MEASUREMENT SYSTEM

The objective of the measurement system development was to build a real time ECG measurement system which detects the R-peaks of the QRS complex reliably with help of two electrodes attached to the left arm of the subject. The Fig. 1 illustrates the measurement system setup, which includes electrodes, amplifier (AMP), data acquisition card (DAQ) and a laptop computer for the real time analysis of the data.

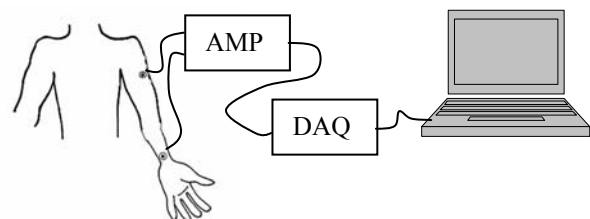


Fig. 1 Measurement system setup.

The electrodes applied in the measurement were wrist-band-type textile electrodes, which were found applicable for this purpose in previous studies [3].

The amplifier was built according to Dobomir Dobrev's two-electrode biopotential amplifier [4]. Its design includes self-leveling feature which establish removal of the reference electrode from the ordinary ECG measurement setup. The Dobrev's amplifier was equipped with an additional Sallen-Key [5] type low-pass filter to remove mains based interferences from the signal. This filter works also as a buffer to balance measurement impedances before amplifier's connection to the data acquisition card.

The data acquisition card was type NI USB-6009 (National Instruments, USA). This card was connected to the USB port of the laptop computer.

The laptop computer used in the study was a standard office laptop of type Fujitsu-Siemens Lifebook equipped with 1.6 GHz processor and 512 MB RAM. The laptop computer included a Labview® (National Instruments, USA) and Matlab® (Mathworks Inc, Natic, MA, USA) based software, which acquired the data from the amplifier via the data acquisition card with sampling rate of 200Hz. The software first filters the signal with suitable bandstop and bandpass filters. Next the software stores the filtered signal temporarily to a database. When the required amounts of data points are obtained, the ECG data is put through a MathScript algorithm which mathematically detects the QRS complex from the signal and then enhances R spikes from it. The time intervals between R spikes are used to calculate the heart rate. Simultaneously, the software shows the ECG signal in real time on the screen of the computer, together with the R-R interval based heart rate value.

The idea in the construction of the measurement system was to keep the hardware based filtering in minimum because it was possible to implement efficient filtering and analysis to the system with help of the software of the system. This made it possible to easily make changes to the system.

### III. EXPERIMENTAL RESULTS

To preliminary evaluate the performance of the measurement system the system was tested with experimental measurements. The test subject was healthy 28-years-old male volunteer. His height was 180 cm and weight 97 kg. Measurements were conducted in Medical Engineering R&D laboratory of Oulu University of Applied Sciences. The results were analyzed by Matlab® and Microsoft Excel® software.

The first phase of the experiment was to measure the ECG of the subject with Biopac M35 (Biopac Systems Inc,

CA, USA) by using a regular three electrode configuration. The result of the measurement is shown in Fig. 2.

In the next phase of the experiments the electrodes were moved to the left arm so that the positive electrode was placed on the upper part of biceps, and the negative and reference electrode were placed on a wrist. The determination of this placement was based on previous studies [2,3]. By using this electrode arrangement the ECG measurements were performed first with Biopac M35 system and then with the developed new system. Fig. 3 shows the result of the Biopac M35 and Fig. 4 shows the result of the new system.

Finally, to evaluate the performance of the new measurement system in heart rate measurement, comparison between the new system and a Polar S810i (Polar Electro Oy, Finland) heart rate monitor was done. In the measurements the heart rate was measured simultaneously with the new and Polar S810i heart rate monitor. The results of the measurements are shown in Fig. 5. The y-axis shows the heart rate determined by the new system and the x-axis shows the corresponding heart rate value of the Polar 810i heart rate monitor.

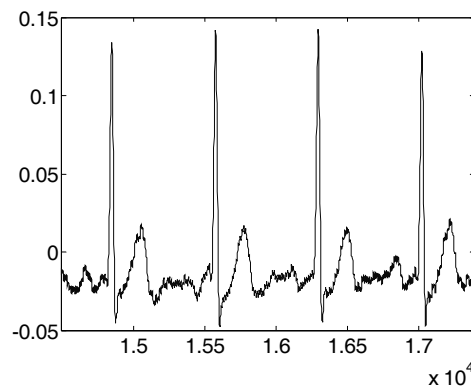


Fig. 2 ECG measurement with a regular three electrode configuration with Biopac M35.

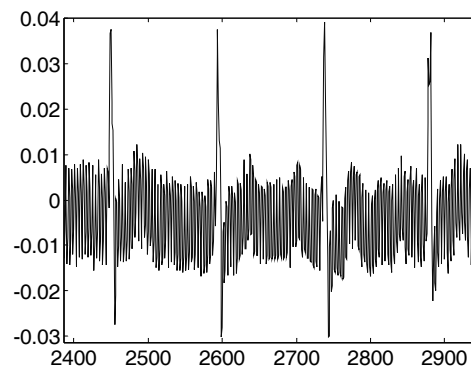


Fig. 3 ECG measured with two electrode configuration with the Biopac M35.

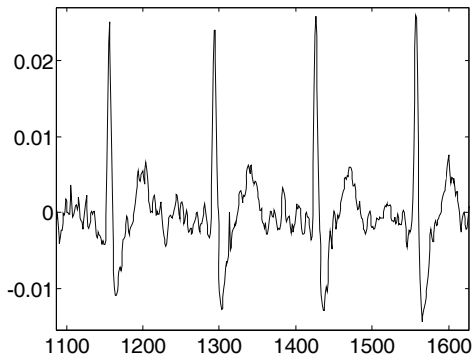


Fig. 4 ECG measured with two electrode configuration with the new system.

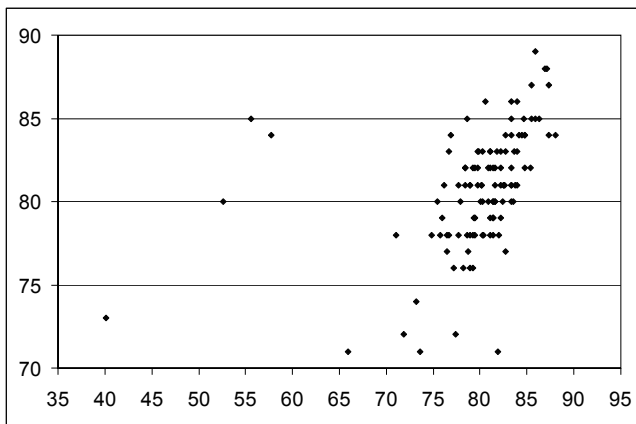


Fig. 5 Comparison of the heart rate, measured by the new system and the Polar S810i heart rate monitor.

#### IV. DISCUSSION AND CONCLUSION

The aim of this study was to develop and evaluate a system which has capability to measure ECG signal with electrodes attached to one arm of the subject. The development of the system was challenging due to low signal-to-noise ratio of the signal and due to theoretical restrictions of the electrode configuration.

The system was developed by utilizing the latest knowledge and literature on ECG measurement systems and by applying efficient software based real time analysis tool for filtering and analyzing the signal.

The developed system was evaluated preliminarily with the help of experimental measurements. In the measurements the characteristics of the measurement signal were compared to commercial reference measurement devices. First, Fig. 2 shows the ECG measured with the standard 3 lead electrode arrangement. This is the signal characteristics

which is the “ideal”. By comparing the Fig. 4 result with this signal, it can be said that the results are rather near to each other. Thus, it seems that the two-electrode arrangement does not result in essentially different signal compared to the result originating from the three-electrode arrangement. Further, when comparing the Fig. 3 with the Fig. 4 it is clearly seen that the Biopac M35 system without the proper reference electrode results in a noisy and unstable signal. Only the R-peaks of the ECG signal can be clearly seen. The same measurement with the new measurement system, seen in Fig. 4, results in a clear signal. Thus, from this point of view the design and application of the measurement amplifier and signal processing methods the proposed new measurement system works appropriately.

The developed new system was evaluated also in its application in heart rate measurement. This measurement can be argued to be the most appropriate application of the system, due to the theoretical restrictions of the ECG signal propagation in the body, because the R-peak is the most evident signal which can be measured with two electrodes only. The heart rate measurement evaluation result, shown in Fig. 5, illustrates clearly the correlation between the new measurement system heart rate value and the Polar S810i heart rate monitor. The heart rate values clearly correlate with each other, however, some artefacts can be seen.

It should be noted that the evaluation done in this study was restricted; it was done by one test subject only. In further studies the system has to be evaluated with the help of a large subject group to obtain more reliable results. In addition, the evaluation measurements were done at rest, where e.g. the interference from the EMG signals is small. One topic for further studies could be to evaluate performance of the new system with walking or running subjects.

In conclusion, the principle operation of the one arm electrode based ECG measurement system developed in this study works well. The short evaluation of the system indicates the system works well compared to the reference systems. Due to simple and innovative one-arm electrode arrangement the system has a high potential to develop new user friendly ECG measurement applications

#### REFERENCES

1. Webster JG et al (1998) *Medical Instrumentation, Application and Design*. Third edition, John Wiley & Sons, Inc.
2. Hannula M and Heikkinen P (2006) Experimental determination of minimum distance between wrist and body electrodes in ECG measurement. *Proceedings of 29th Conference of the Canadian Medical and Biological Engineering Society, Vancouver, Canada, 2006*.
3. Keskitalo A (2007) *EKG-mittaus käsivarresta vaihtoehtoisilla elektrodinatkaisuilla*. Bachelor's Thesis, Oulu University of Applied Sciences, 2007.

4. Dobrev D (2003) Two-electrode non-differential biopotential amplifier. *Medical and Biological Engineering and Computing* 40(5): 546-549.
5. Sallen RP and Key EL (1955) *A Practical Method of Designing RC Active Filter*. IRE Transactions on Circuit Theory 2 (1): 74-85.

Address of the corresponding author:

Author: Manne Hannula  
Institute: Medical Engineering R&D Center, Oulu University  
of Applied Sciences  
Street: Kotkantie 1  
City: Oulu  
Country: Finland  
Email: manne.hannula@oamk.fi

# Diagnosing Acute Liver Graft Rejection: Experimental Application of an Implantable Telemetric Impedance Device in Native and Transplanted Porcine Livers

J.H. Harms<sup>1,2</sup>, A. Schneider<sup>2</sup>, M. Tautenhahn<sup>1</sup>, J. Henke<sup>3</sup> and R. Busch<sup>4</sup>

<sup>1</sup>Klinik für Visceral-, Transplantations-, Thorax- u. Gefäßchirurgie, Universitätsklinikum Leipzig AöR, Leipzig, Germany

<sup>2</sup>Institut MiTi, Technische Universität München, München, Germany

<sup>3</sup>Institut für experimentelle Therapieforchung, Technische Universität München, München, Germany

<sup>4</sup>Institut für Statistik und Epidemiologie, Technische Universität München, München, Germany

**Abstract — Background and aims:** Diagnosis of acute rejection is a complex and persistent problem in liver transplantation. Focused on the use of proprietary impedance technology a porcine liver model was designed to provide immediate information for differentiation of normal and rejecting tissue by an implantable telemetric device. **Methods:** Electrical impedance was analysed by electrodes implanted *in vitro* and *in vivo* in the liver of pigs, where impedance is derived from measurements of voltage transients produced in response to programmed current pulses. Consequent electric recordings in porcine livers after transplantation and after mere laparotomy were evaluated in relation to biochemical parameters and histological results of liver biopsies. **Results:** Acute rejection was correctly predicted in all cases and excluded in the remaining 32 biopsy related impedance recordings ( $p < 0.004$ ). Impedance measurements not only correlated with the diagnosis from liver biopsy specimen ( $r = 0.84$ ,  $p < 0.0001$ ) but also exemplified the severity of acute rejection. **Conclusion:** Impedance analysis reveals evident physiologic relation of acute liver graft rejection and electrical organ properties. Electrodes implanted in transplanted porcine livers allow running less invasive monitoring and thus early detection of rejection. The technology may have broad value in providing an immediate diagnosis of acute rejection, reducing unnecessary patient anxiety and eliminating the significant expenses associated with multiple referrals, expensive sample handling and tissue analysis.

**Keywords —** liver transplantation, impedance, acute rejection, devices, telemetry.

## I. INTRODUCTION

Large-scaled allograft monitoring to prevent postoperative liver transplant failure merits a problem for health care. According to literature reports, over 50% of the liver grafts will have one or more episodes of acute rejection [1]. Because advanced stages of acute rejection are difficult to treat, it is important to detect graft rejections at their earliest stages. It has been shown that neither the absolute level nor the change of biochemical parameters can differentiate acute rejection from other causes of graft dysfunction [2,3]. Radiologic imaging may represent an essential tool but is

also not able to verify the diagnosis. Liver transplant histology is the most specific improvement. However, liver core biopsy is invasive. Problems arise from the limited availability, the necessity for patient transfer, the timing, the biopsy sampling error and psychological burden to the patient [2,4]. The use of nonproprietary computer network solutions facilitates the ability to gain a stream of trended data in a way that was previously unrealizable [5]. Considering the basic research on hepatic impedance and the results from intramyocardial electrocardiogram monitoring of cardiac transplant recipients, a prototype of an implantable bioelectrical impedance analyzer was evaluated in native porcine livers and transplanted pigs for the diagnosis of acute rejection [6].

## II. MATERIAL AND METHODS

### A. Experimental setup

The experiments conducted were designed to test whether the impedance monitor can detect and differentiate acute allograft rejection from normal functioning grafts and native livers. As acute rejection of liver grafts in pigs is less frequent and severe, genetically different Pietrain pigs served as liver donors. Animals were handled in accordance to the principles of laboratory animal care (NIH publication No. 86-23, revised 1985). To enhance the probability of acute rejection, no immunosuppression with the exception of a single intraoperative steroid pulse (250 mg prednisolone, Urbason<sup>®</sup>) prior graft reperfusion was administered. Biochemical measurements included blood counts; electrolytes, urea, creatinine, total bilirubine, serum glutamic-pyruvic transaminase (SGPT), serum glutamic-oxalacetic transaminase (SGOT) and serum glutamic-dehydrogenase transaminase (SGLDH), alkaline phosphatase (AP) and gamma-glutamyltranspeptidase ( $\gamma$ -GT).

### B. Impedance device

Arranged in parallel, the impedance electrodes were designed with two outer and inner voltage pins. The length

and penetration depth of the four puncture electrodes was 4 mm. Protected by a silicone priming tube the matched coaxial cables were linked with the input of the battery and the impedance registration unit. Voltage electrodes were connected with a differential amplifier of high input impedance. Probes were pricked into the right liver lobe. The distance between the probes was 2–3 cm. Dislocation was prevented by sealing with a fibrin-glue-coated adhesive sheet. Impedance recordings were obtained 6 times per hour in 16.0 ms intervals. Through the two outer electrodes a rectangle impulse current of 40 mA, with a frequency 0.0625 Hz to 140.4 kHz, outlasting 16 ms was applied. By means of the two inner electrodes the voltage drop was registered in 7.813 ms intervals up to a total of 62.5 ms. The size and design of the 54.4 g weighing telemetric chamber is comparable with a cardiac pacemaker. The telemetric chamber was implanted extraperitoneal between the muscle layers of the abdominal wall. Main item of the telemetric chamber is an application specific integrated circuit component (ASIC). Following inductive connection of an extracorporeal magnetic spool data were transferred via the long-wave band from the intra- to the extracorporeal control unit. Using a modem as a server data were transferred via telephone to a central data collecting and analyzing registry. To avoid artificial interferences during impedance registrations all interrogations were performed with the animal asleep or resting quietly during recordings. To establish longitudinal daily analysis, data were imported to a computerized calculation program. Regardless of the experimental setting, the results from biopsy evaluation and blood chemistry, impedance data were analyzed by a qualified computer operator.

### C. Liver transplantation group

German landrace pigs were used as transplant recipients. Non-related pure bred Pietrain pigs served as liver donors. In total 10 liver transplantations were performed. Liver donors and recipients were only matched for weight. Ex-vivo flush perfusion of the graft consisted of 2000 cm<sup>3</sup> cold (4°C) histidine–tryptophan–ketoglutarate solution (Custodiol®) and 1000 cm<sup>3</sup> of saline solution. Transplantation was performed orthotopic without veno-venous bypass [7,8]. Only survivors of more than 24 h were included. 8 transplants met the requirements. Because of cardiac and neurological complications, 4 animals had to be excluded from evaluation. Proven acute rejection was found in all of the remaining 4 liver grafted pigs. Median survival of these pigs was 4 days (2–6 days). Altogether 11 liver biopsies were performed in the 4 animals that exhibited acute allograft rejection.

### D. Native liver group

11 German landrace pigs were operated upon. 2 animals were excluded from final evaluation because of a technical default. Median survival of the 9 animals meeting the requirements was 10 days (8–12 days). 25 liver biopsies were obtained in the native liver group.

### E. Histologic monitoring

Liver biopsy specimens were evaluated unaware of animal assignment to the control or transplantation group by a single pathologist. Samples were graded with the use of the Birmingham Score (BH-score); (4). Based on quantitative scoring on a scale from 0–3 histologic features were added to produce a final score and classified as none, BH-score 0–2, borderline, BH-score 3, severe rejection, BH-score 4–5.

### F. Data processing

Preliminary in vitro testing of physical variables revealed that the offset of the impedance measurements was only influenced by external factors. In accordance to in vitro studies the most sensitive interval for postprocessing and quantitative analysis was located between 7.813 and 62.5 ms, frequency of 128 and 16 kHz of the 16 ms lasting cycle. The data input per day accounted a volume of 1.2 megabyte (MB). As a common postoperative phenomenon first baseline measurement could be conducted 12–24 h postoperatively. During the subsequent period coherent measurements were possible. For this reason the offset of day 0 was set to 100%. The absolute of the mean of subsequent bisensoric (left and right impedance sensor) recordings for running analysis were referenced in percent to the offset of day 0 and defined as the absolute impedance gradient (IG). For quantitative description of daily discrepancies the relative IG was introduced as the percentile difference of between absolute IGs of consecutive days.

### G. Statistical analysis

Biochemical parameters and the postoperative courses of relative IG's were expressed as means  $\pm$  SD. Differences between groups were assessed by the Kruskal–Wallis or Mann–Whitney test. Exact 95% confidence intervals were determined for proportions. All *P*-values are two sided, a *P*-value of less than 0.05 was considered to indicate statistical significance. Correlation between impedance recordings and the results of biochemical and histological data were evaluated with the Pearson correlation coefficient. As a measure of proximity between both variables we demanded that the correlation coefficient should be  $> 0.7$  (which for  $n=14$  cor-



responds to a  $P < 0.001$ ). Receiver operating characteristic analysis (ROC) was performed to illustrate how good impedance recordings discriminate rejecting from non-rejecting forms and to discriminate the optimal cut-off allowing a diagnosis of acute rejection. The analysis was performed using the software package SPSS V8.0.

### III. RESULTS

#### A. Impedance in non-transplanted porcine livers

The time-course of the relative IG discrepancies from native livers and liver transaminases and total bilirubin with a peak value on the day of surgery returned to normal until the 2<sup>nd</sup> postoperative day. IG recordings required a duration of 1–2 days to stabilize. With postoperative recovery and prolonged survival, approximation of interindividual relative IG discrepancies were assigned. Once reaching a postoperative plateau relative IG's during histologic quiescence revealed gradual stability over the median of 10 experimental days. Correlation of relative IG discrepancies with liver transaminases showed evident coherence with SGLDH ( $r=0.5$ ,  $P<0.001$ ) and SGPT ( $r=0.5$ ,  $P<0.04$ ).

Invasive examinations of the liver, such as biopsies, were generally associated with a uniform, non-significant and reversible positive increase of relative IG discrepancies. Compared with measurements preceding the day of biopsy the median increase of the relative IG accounted +5.3% (+2.4% to +10.5%). With a subsequent negative increase of IG recordings normalized after a mean duration of 10 h following core biopsy. In correspondence with the findings of IG analysis 24 of the 25 biopsies in the control group, consisting of 2.9 per specimen, were judged free of evidence of rejection. The median BH-score was 1 (range 0–3). The median of the biopsy related day-to-day variability of relative IGs was +6.4% (-2.2% to +11.4%). On the basis of ROC-analysis all recordings were correctly analyzed for the exclusion of acute rejection yielding a sensitivity and specificity of 96%.

#### B. Impedance analysis in porcine liver transplants

Uncompromised function of the liver grafts characterized the initial course of the 4 animals meeting the objective of terminal acute allograft rejection. In conjunction with operative trauma and graft reperfusion a common positive increase of relative IG's and of liver transaminases with a maximum on the 2<sup>nd</sup> postoperative day was observed. A synchronous negative increase of relative IG's and liver transaminases characterized graft recovery. Corresponding to the observations of the native liver group relative IG dis-

crepancies in transplants did not drop below the 100% offset during histologic quiescence. With a median BH-score 2; 6 of the biopsies obtained during the initial postoperative course were assumed positive for the exclusion of acute rejection. The median variability of biopsy related relative IG accounted -9.1% (+1% to -12.3%).

Histology of rejecting biopsy specimens in subsequent biopsies was characterized by infiltration of portal tracts by lymphocytes, mononuclear cells and eosinophils. As rejection progressed endothelialization of hepatic venules coincide with infiltration and spread into the parenchyma, necrosis of hepatocytes and disruption of the lobular architecture. The aggressive course of acute rejection correlated with the degree of negative increase of relative IG's in each specimen. Progression of acute rejection with a median BH-score 5 at the end of the experimental period was joined with a median of -47% (+1.8 to -92.9%) negative increase of relative IG's.

Altogether statistical analysis emphasized significant interrelation between the negative increase of relative IG discrepancies and the results of liver biopsies ( $r=0.96$ ,  $P<0.001$ ). In borderline rejection the relative bisensoric IG was -6.5%. Unisensoric recordings were heterogeneous, yielding a decline of -27% versus an increase of +14%. The fact may find explanation in correspondence to the supposition of heterogeneous initialization and manifestation of onsetting acute rejection. Biochemical accounts did not predict the individual fate of the transplanted livers and revealed any statistical correlation with the results of biopsies or with the courses of impedance recordings during onset and/or progress of acute rejection.

Considering the small number of animals meeting acute rejection the reliability of impedance recordings was tested by inter-group analysis. All measurements were analyzed for the absence ( $n=90$ , median relative IG +2.2%) or the presence of acute rejection ( $n=4$ , median relative IG 48.7%). Non-parametric two-tailed analysis revealed significant difference between both ( $P<0.004$ , Mann-Whitney Test). There was significant correlation between the scored results of liver biopsies and the changes of relative IG discrepancies. The observation also implied that the severity of a rejection episode can be described by the degree of negative percent increase of relative IG's ( $r=0.84$ ,  $P<0.0001$ ). With regard to biochemistry significant differences were only ascertained for bilirubin ( $P<0.002$ , Mann-Whitney Test).

### IV. DISCUSSION

Acute rejection remains a threat to graft survival. Electrical impedance analysis to monitor organ damage during

ischemia, organ preservation and acute rejection has been introduced in recent years in heart, liver and kidney [9,10]. Today, there is virtually no implantable and automatized sensor technique that can be used for less invasive diagnosis of acute rejection in liver transplants. Electrical impedance of living tissues gives access to tissue compartment parameters which are telemetrically sent within seconds using minimally invasive, simple metallic electrodes.

Liver transplantation in pigs however merits the problem that acute rejection is less often [7,10,11,12]. Nevertheless, the anatomic similarities of porcine and human livers render the pig model favourable for establishment of the technical feasibility and general applicability of electrical impedance analysis for detection of rejection, particularly since genetic differences between pig races allow enhancement of rejection. Organ temperature, configuration of the liver capsula, regional blood flow and local pressure to the liver surface by the impedance electrodes all influence the individual offset and the course of impedance reactance [6,9,11]. To abolish systemic errors of impedance measurements in the given experimental setting the characteristics of the animals and the fixation technique of the sensoric leads to the liver were standardized. Considering the influencing effects the independent method of gradient calculation was used for comparative quantification.

In-vitro pretesting studies confirmed addiction of impedance recordings to organ temperature. During pathologic conditions, changes of passive hepatic electric conductance as attributed by *Kehrer et al.* are traced back on dynamic ionic shifts affecting the hepatocyte- and endothelial membrane complexes, the intra- and extracellular spaces and their interspheric gap junctions. Temporary and/or reversible changes of impedance recordings otherwise mirror both destructive and regenerative processes of the intra- and extracellular components of the hepatocyte and the sinusoidal lining cells [6]. In transplanted animals a uniform and negative increase of relative IG's characterized acute rejection. This consistency and stability of relative IG's during functional and morphologic quiescence in native and transplanted livers implies evidence of interrelation between histologic, and the passive electrophysiological changes. Proven by ROC-analyses diminution of relative IG discrepancies of -24% of the preceding day served as a diagnostic criterion for acute rejection in pigs. Correlation between the negative increase of relative IG's and the severity of acute rejection suggested that not only the onset, but also the progressive course of rejection can be monitored by trended impedance data. A non-linear negative increase of unipolar lead impedance recordings, exhibiting a borderline-lesion on microscopic examination may indicate the supposition of

inhomogeneous onset of graft rejection. Because of the disparate cellularity, inhomogeneous distribution of necrosis and fibrosis it is not improbable that heterogeneity of spatial tissue characteristics can alter regional differences of electrical conductance. It can be stated that continuous impedance recordings with the technical equipment used can be done without the loss of information. Theoretically, on-line liver graft monitoring can be conducted over an unlimited period. The technique of computerized clinical data processing is simple and thus can be applied in clinical routine. The next step for this technology, which has not been implemented yet is to establish its value in monitoring effects of anti-rejection treatment, to differentiate rejection from preservation injury and viral hepatitis.

## REFERENCES

1. Hall BM, Suranyi M (1995) In: Wood, K. (Ed.), Understanding rejection: The handbook of transplant immunology, 1. Medi Science, London, Vol.1, 1st.:113-115.
2. Freese D, Ascher NL, Bloomer J (1987) The role of liver biopsy in the accurate evaluation of the post-liver transplant patient. *Gastroenterology*. 86 (5,Pt.2):1318
3. Geest S, Vanhaecke J (1999) Methodical issues in transplant compliance research. *Transplant Proc.* 31(4A): 81-83.
4. Hübscher S (1996) Diagnosis and grading of liver allograft rejection: a european perspective. *Transplant Proc.* 28 (1):504-507.
5. Merion RM (1996) Transplant information transfer and analysis in cyberspace. *Transplant Proc.* 28 (4): 2026-2028.
6. Kehrer G, Aminalai A, Bürger et al (1993) Interrelations between electrical and biochemical processes in ischemic porcine livers at low temperature. *Z. Gastroenterol.* 31: 171-178.
7. Calne, RY, Yoffä, DE, White HJO et al (1968) A technique of orthotopic liver transplantation in the pig. *Br. J.Surg.* 55 (3), 203-206.
8. Dent DM, Hickman R, Uys, CJ et al (1971) The natural history of liver and autotransplantation in the pig. *Br. J. Surg.* 58:407-413.
9. Erhard J, Lange R, Gersing E et al (1993) Die Impedanz-messung zur Beurteilung von Ischämieschäden der humanen Leber in der Vorbereitung zur Transplantation. *Langenb Arch Chir* 378: 233-238.
10. Gerhäuser A, Reichel T, Neukomm PA (1997) Rejektionsdiag-nostik nach Nierentransplantation über Impedanzspektroskopie mit einem implantierbaren Meßsystem. *Biomed. Tech.* 42:160- 162.
11. Eisele Ph, Woddle ES, Hunter GS et al (1986) Anesthetic, pre-operative considerations for liver transplantation in swine. *Lab Anim.Sci* 36:402-405.
12. Oldhafer KJ, Hauss J, Gubernatis G et al (1993) Liver transplantation: a model for studying reperfusion injury. *J Invest Surg* 6:439- 450.

Author: Jens Harms MD  
 Institute: University of Leipzig  
 Street: Liebigstraße 20  
 City: Leipzig  
 Country: Germany  
 Email: dr.jens.harms@gmx.de

# Augmentation Index in Different Severity Coronary Heart Disease Patients

I. Hlimonenko<sup>1</sup>, K. Meigas<sup>1</sup>, M. Viigimaa<sup>1,2</sup> and K. Temitski<sup>1</sup>

<sup>1</sup>Department of Biomedical Engineering, Technomedicum of Tallinn University of Technology, Ehitajate tee 5, 19086 Tallinn, Estonia

<sup>2</sup>Department of Cardiology, Tallinn North – Estonian Regional Hospital, J. Sütiste tee 19, 13419, Estonia

**Abstract**— The objective of the present study was to compare augmentation index (AI) in coronary heart disease (CHD) patients and healthy volunteers.

In the present study twenty seven subjects were investigated. Augmentation Index was measured using the TENSIOmed Arteriograph (TensioMED Ltd., Hungary).

The major finding of this study was that patients with CHD had increased AI compared with healthy subjects ( $P<0.01$ ). We studied also difference of AI in patients depending on disease severity. Patients were classified into 2 groups: patients with arteriosclerosis grade from 1 to 6 and patients with arteriosclerosis grade from 7 to 10. Results didn't show significant difference between CHD patients and healthy volunteers. Also difference of AI in patients with and without diabetes was analyzed. No significant difference was found. Difference of AI in patients with and without myocardial infarct was investigated. There was no significant difference found.

**Keywords** — atherosclerosis, coronary heart disease, Augmentation Index, aortic stiffness, risk factors

## I. INTRODUCTION

The endothelium modulates arterial stiffness, which precedes overt atherosclerosis and is an independent predictor of cardiovascular events [1]. Dysfunction of the endothelium may be considered as an early and potentially reversible step in the process of atherogenesis. Numerous methods have been developed to assess endothelial status and large artery stiffness, including PWV and augmentation index measurements. The endothelium dysfunction is accompanied by an increased total peripheral vascular resistance (TPR). The augmentation index among several other factors is largely influenced by the actual TP.

## II. METHODS

### A. CHD patients and healthy volunteers

The clinical characteristics of the study population are summarized in Table 1. In the present study twenty seven subjects were investigated (13 males, 14 females); their mean age was 59.5 years (range 24-81 years). Group of

CHD patients consisted of 17 patients treated in the Department of Cardiology of the North-Estonian Regional Hospital from January to March 2007. CHD was confirmed by coronary angiography. Twelve patients out of 17 have been suffered from myocardial infarction. In 8 patients diabetes has been diagnosed and 13 were hypertnsives.

Systolic ( $150.0\pm 26.8$  mm Hg) and diastolic ( $90.5\pm 13.6$  mm Hg) blood pressure were significantly higher in the CHD patients compared to healthy subjects.

The healthy group consisted of 10 subjects (3 males, 7 females) who were considered as persons without any cardiovascular disease or complication. Their main age was 27.5 years (in range 24-36).

### B. Coronary Angiography

In all CHD patients coronary angiography was performed by Siemens digital angiograph. Severity of coronary artery stenosis was graded from grade I (up to 25%) to grade 6 (100%, total occlusion). Atherosclerosis grade (from 1 to 10) was evaluated based on number of damaged coronary artery segments and stenosis severity.

Table 1 Characteristics of the study population

	CHD patients (n=17)	Healthy volunteers (n=10)	P value
Age	66 (49-81)	27.5 (24-36)	
Men	55%	30%	
Diabetes	47%	-	
Hypertension	76%	-	
Myocardial infarction	70%	-	
Systolic Blood Pressure (mmHg)	150.0±26.8	122.0±14.8	<0.01*
Diastolic Blood Pressure (mmHg)	90.5±13.6	70.5±6.9	<0.01*

Data are mean ± SD.

\*  $P<0.01$ , difference is statistically significant

### C. Augmentation Index

Measurements were performed one after another in a laboratory conditions in the supine positions for about 15 minutes.

The Augmentation Index was measured using the TENSIOmed Arteriograph (TensioMED Ltd., Hungary). The measurement is based on the fact that during systole, the blood volume having been ejected into the aorta generates pulse wave (early systolic peak). This pulse wave runs down and reflects from the bifurcation of aorta, creating a second wave (late systolic peak). The difference between first and reflected systolic waves (in msec) is related to the stiffness of the aorta. The difference of the amplitudes of the first and second systolic waves (Augmentation Index) depends on the tone of the peripheral arteries (endothelial function). According to the TENSIOmed Arteriograph data: optimal Augmentation Index is  $< -30\%$ . The Arteriograph measures endothel/vascular dysfunction by measuring total Augmentation Index (further Augmentation Index).

### D. Statistical Analysis

All data analysis was performed using the program SPSS 10.0 for Windows. Data was expressed as the mean  $\pm$  SD. Multiple linear regression analysis (Pearson correlation) was used for the relationships between risk factors and PWV, and between pulse wave velocities measured in different sites of arterial tree. A value of  $P < 0.05$  was considered statistically significant.

## III. RESULTS

The results of the study are summarized in Table 2. Augmentation index was significantly increased as well in the CHD group compared with that in the healthy group.

We also studied the difference of AI in patients depending on disease severity. Patients were classified into 2 groups: patients with arteriosclerosis grade from 1 to 6 and patients with arteriosclerosis grade from 7 to 10. AI didn't show significant difference between patients with different severity coronary heart disease. The results are shown in Table 3.

Difference of AI in patients with and without diabetes was also analyzed. No significant difference was found (Table 4).

The difference of AI in patients with and without myocardial infarction was investigated. There was no significant difference found (Table 5).

Table 2 AI in CHD and healthy groups

	CHD patients (n=17)	Healthy volunteers (n=10)	P value
Augmentation index (%)	0.2 $\pm$ 38.3	-73.3 $\pm$ 20.4	<0.001*

Data are mean  $\pm$  SD.

\*  $P < 0.01$ , difference is statistically significant.

Table 3 AI in CHD patients with different atherosclerosis grade

Atherosclerosis grade	[1-6] n=7	[7-10] n=10	P value
Augmentation index (%)	13.8 $\pm$ 37.4	-24.3 $\pm$ 40.0	NS

Table 4 AI in CHD patients with and without diabetes

	Diabetic patients n=8	Non-diabetic patients n=9	P value
Augmentation index (%)	-24.2 $\pm$ 40.5	13.8 $\pm$ 41.6	NS

Table 5. AI in CHD patients with and without previous MI

	MI patients n=12	Non-MI patients n=5	P value
Augmentation index (%)	-24.3 $\pm$ 41.8	0.5 $\pm$ 27.8	NS

## IV. DISCUSSION

The objective of this study was to examine arterial stiffness in relation to some indicators of atherosclerosis at different sites of arterial tree. Because endothelial dysfunction reflects a systemic vascular abnormality, we can indirectly evaluate the endothelial function of the coronary arteries by examining aortic stiffness or elastic properties of arterial arteries.

The major finding of this study was that patients with CHD had increased AI compared with healthy subjects. This demonstrates that patients with CHD have impaired endothelial function compared with healthy subjects, and are consistent with previous studies [2-5].

The strong association of aortic stiffness with atherosclerosis at various sites of the arterial tree suggests that aortic stiffness can be used as an indicator of generalized atherosclerosis [3]. The findings of our study confirm the same.

In our study healthy group was significantly younger than the patients. Increased of AI in CHD patients group

is expected when the arteries become less distensible due to structural changes that take place with age.

Our study showed that difference in AI between CHD patients with different atherosclerosis grade was not significant. Also there was no difference between diabetic and non-diabetic patients and in group with or without previous myocardial infarction. This can be explained by the fact that in our patients atherosclerosis was advanced and in all patients atherosclerotic changes were already present.

Previous studies using intravascular ultrasound (IVUS) have revealed that atherosclerotic process first starts in the arterial wall. This disease is primarily not a disease of the lumen, but a disease of the vessel wall. It is the atheroma in the vessel wall that determines the natural history and pathophysiology of the disease. A vessel that appears completely normal (ie, no luminal narrowing) on angiography is often found to be burdened with atheroma on IVUS. IVUS can image lesion characteristics more reliably than angiography and has shown that atherosclerotic burden begins earlier in life than expected [6]. This shows that formation of atherosclerotic plaques happens in later stages. Patients for our study were chosen based on angiography investigation that means with late stages of atherosclerosis. But analysis of AI allows detecting early phase of atherosclerosis. Recent 2007 European Guidelines for the Management of Arterial Hypertension are first time advising to use PWV measurement for assessment of cardiovascular risk and subclinical organ damage. European SCORE-chart is widely used for estimation of cardiovascular risk [7]. Individuals with a 10-year risk of fatal cardiovascular disease higher than 5% belong to the high-risk group.

IVUS is expensive and complicated technology to perform in all patients. So, noninvasive simple AI analysis method is needed to be able select patients with early phase of atherosclerosis. Further AI studies should be focused on patients with pronounced risk factors but without established cardiovascular disease.

## V. CONCLUSION

The major finding of this study was that patients with CHD had increased AI compared with healthy subjects. Our study showed that difference in AI between CHD patients with different atherosclerosis grade was not significant. Also there was no difference between diabetic and non-diabetic patients and in group with or without previous myocardial infarction. Further AI studies should be focused on patients with pronounced risk factors but without established cardiovascular disease that allow us to select patients with early phase of atherosclerosis.

## ACKNOWLEDGMENT

This research has been supported by Estonian Science Foundation, Grant No. 7506.

## REFERENCES

1. Nichols, W. W., O'Rourke, M. F. McDonalds' blood flow in arteries: theoretical, experimental and clinical principles, 4<sup>th</sup> Ed. Arnold, London, 1998.
2. Van Popele, N., Grobbee, D. Association between arterial stiffness and atherosclerosis: the rotterdam study. *Stroke*, 2001, **32**, 454-460.
3. Weber, T., Auer, J. Arterial stiffness, wave reflections, and the risk of coronary artery disease. *Circulation*, 2004, 184-189.
4. Kovaite M, Petrulioniene Z et al. Relationship of arterial wall parameters to cardiovascular risk factors and cardiovascular risk assessed by SCORE system. *Medicina (Kaunas)*. 2007;43(7): 529-41
5. Uzun M, Ozkan M et al. The value of augmentation index and myocardial performance index obtained from cardiac catheterization pressure recordings in predicting coronary artery disease. *Anadolu Kardiyol Derg*. 2006 Jun;6(2):121-5.
6. Nissen, S. E. IVUS is redefining atherosclerotic disease. *The American Journal of Managed Care*, 2003.
7. European Guidelines on Cardiovascular disease prevention in clinical practice: executive summary. *European Journal of Cardiovascular Prevention and Rehabilitation*, 2007, 14.

Author: Irina Hlimonenko  
 Institute: Technomedicum of Tallinn University of Technology  
 Street: Ehitajate tee 5  
 City: Tallinn  
 Country: Estonia  
 Email: irina\_hlimonenko@hotmail.com

# Photoplethysmographic Measurements and Analysis

M.J. Huotari, V. Lantto

University of OULU, Finland

Department Electrical and Information Engineering, Microelectronics and Materials Physics Laboratories

**Abstract** — Human arteries stiffen and cause health problems all over the world, also in younger age. Arterial stiffening can be determined with means of photoplethysmography (PPG). By PPG device we determine heart generated pulse wave velocity (PWV) in, e.g., in the peripheral organs, fingers and toes, noninvasively. According to PPG measurements blood vessels can be classified according to their physical properties, e.g. elasticity. Conventional elasticity measurements are complex and time consuming, eg. ultrasound. Many studies have shown that PWV values depend on subject under study, arterial properties and blood viscosity, blood vessel diameter, wall structure, arterial stiffness, body mass index, and age. We are developing a stiffness measurement system. In this system the PPG waveforms can be rapidly and simply acquired by detecting with a PIN photodiode the reflection of infra-red LED light from the skin of the forefinger and the second toe. Here the waveforms are fitted using Origin 7.5 software. According to the fittings we are able to separate the waveforms belonging to different waveform classes, e.g., direct wave, and reflected waves. These waveforms are characteristics for the young persons and elderly persons. The more template waveforms we take in to the consideration for different reflected waveforms the more accurate results we get. However, there are a certain limit number of reflected waves. Here we compare the limit numbers of three and four.

**Keywords** — Photoplethysmography (PPG), pulse wave velocity, fit, lognormal distributions.

## I. INTRODUCTION

The photoplethysmographic (PPG) pulse waveforms are known to reflect the flow and blood vessels waveforms at the throughput organs, e.g. fingers or toes. Our purpose was to clarify the usefulness of PPG waveforms recorded from the fingers and toes for detecting cardiac function and arterial stiffness (Awad et al, 2007).

The contour of the PPG waveform is characterized by 2 distinct waves, an early systolic peak caused by direct pressure transmission along the arterial tree followed by a second or more peaks caused by the pressure waves reflected at sites of impedance mismatch, mainly in the lower limb. Increased arterial stiffness of large conduit vessels leads to earlier return of the reflected wave, resulting in elevated pulse wave velocity (PWV) values and more complex waveforms to be decomposed. The PWV is based upon the

vessel length divided by the time of the differences of the individual pulse wave pairs in a single recording.

PWV, the speed of propagation of arterial flow waves through the arterial tree, is related to arterial stiffness and is an important marker for cardiovascular risk events.

## II. MATERIALS AND METHODS

### A. The volunteers for the photoplethysmographic recording

The photoplethysmography recordings were obtained from the male and female volunteers in the supine position at a quiet room. The volunteers were aging between 15 and 81 (one person) years. The PPG recording time was between 100 and 200 s after a rest period of at least 10 min in the mornings. The room temperature was about 22 °C.

### B. Photoplethysmographic recording

A custom-made instruments, sensor construction (LED-PIN photodiode) and amplifiers, are used for photoplethysmographic recording of heart generated pulses from finger and toe vessels simultaneously on the surface of skin in reflectance mode. As a detector we have also used OxyTip 10 pulse oximetry sensor for comparison in the transmittance mode. All these components are compact, sensitive, and have very fast rise times. Near infrared (NIR) LEDs and responding photodetector were encapsulated in the sensor probes for finger and toe, respectively. The PIN photodiode connects to a noiseless ac transimpedance amplifier. The waveforms were stored on a dynamic digital signal analyzer (HP 35665A) and/or a TEAC DAT recorder for later decomposition, spectral and cross-correlation analysis. Here we introduce the factorizing or decomposition analysis based on the Origin 7.5 software package (Microcal, Massachusetts, USA).

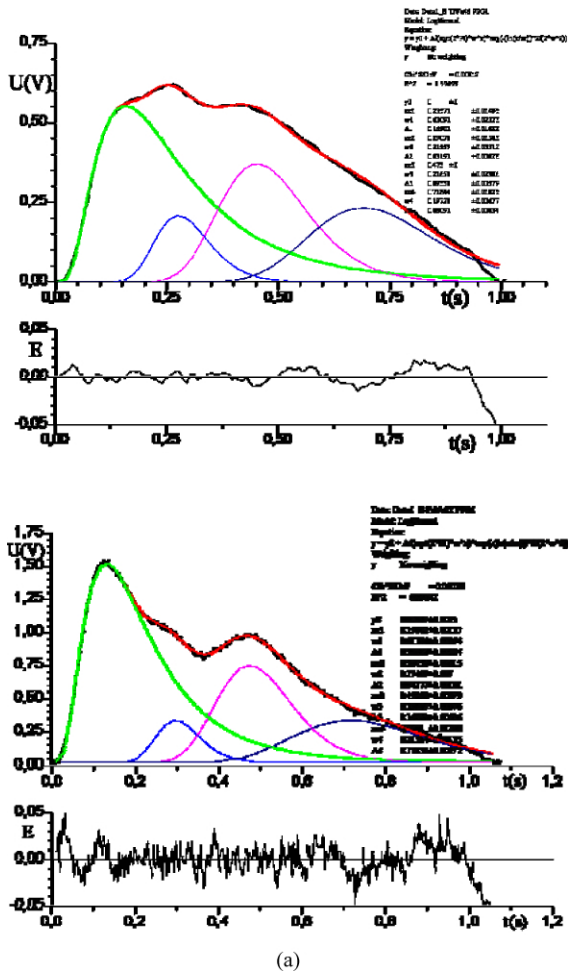
### C. Pulse wave analysis

The PPG signal is associated with changes in peripheral and central blood flow circulation, the blood vessel condition and persons health status. The complexity of the waveforms has been asked and applied many methods to open this question in practice when recording from fingers and

lower limbs. Here we work with the PPG signals by fitting them for decomposing the signal into its primaries, and by analyzing the residuals obtained after the summed signal reconstruction with the best and informative fit. Our purpose is directed for reconstructing a signal that preserves the basic characteristics of the PPG waveform by using a limited number of primary functions, also in theory, namely the log normal distribution functions family. In addition, information of the residuals we use in the conclusion phase.

III. RESULTS AND DISCUSSION

Fig. 1 shows two pairs of typical PPGs measured from a forefinger of a) a father (48 years) and his son (22 years) and b) a father (59 years) and his son (35 years), respectively.



The upper waveforms have become from the elder persons and they have the process of triangular in the beginning. However, the younger persons (the sons) have the three reflected peaks, in addition to the direct pulse, which are clearly separable. In pulse wave analysis we have separated peripheral arterial pulses into its primaries. This allows us to distinguish the origin of each wave that contributes to the characteristic waveform in any blood vessel, e.g., in this case the radial arteries.

IV. CONCLUSIONS

PPG and especially arterial stiffness determination system can also be used to extract illness of blood vessels and

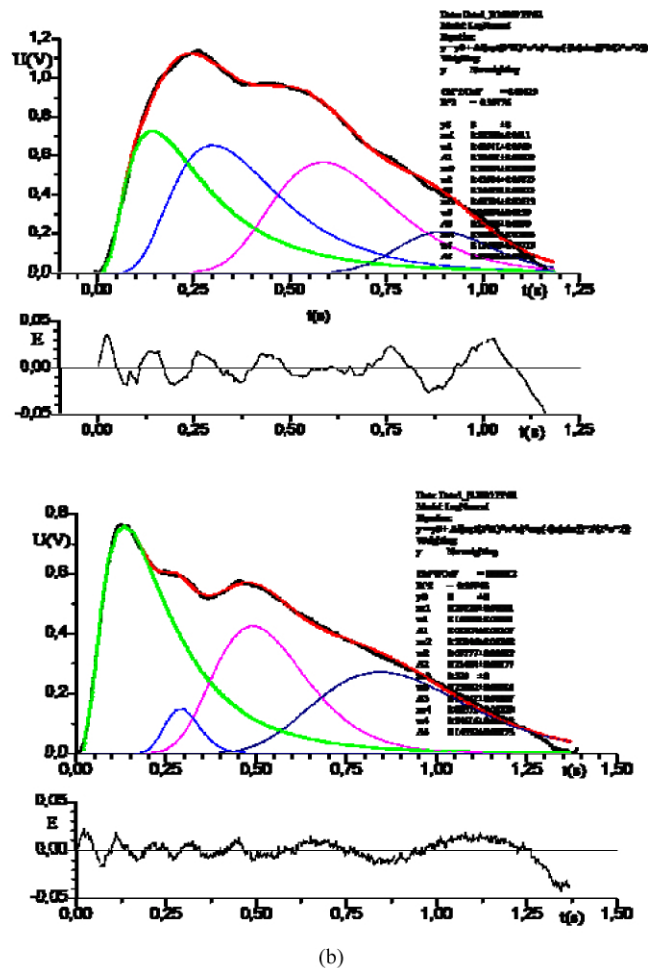


Fig. 1. Finger photoplethysmographic waveforms from (a) father (48 years) and his son (22 years) and (b) father (59 years) and his son (35 years) fitted by four lognormal distribution functions, respectively. Below there are the corresponding error between the measured PPG signal and the fitted sum function.

the information before any other method could give so easily this information. PPG is well suited and patient-friendly for the simplification of the sensor construction. Degradation of the signal quality of PPG due to motion artifact should be reduced before it is adopted for our arterials stiffness measurements. The data indicate that the finger pulse photoplethysmographic waveform can be more sensitive to changes in arterials during aging than the other devices. This information can be used to assess the overall status of the arterial wall. An appreciation of changes in pulse waveform may provide valuable evidence also with respect to changes in peripheral blood flow. However, before this no simple and economic principles trying to separate the direct and reflected waveforms have not been introduced.

#### ACKNOWLEDGMENT

We acknowledge the Department of Electrical and Information Engineering, University of OULU, Workshop for ideas and construction many PPG sensors for PPG research.

#### REFERENCES

1. Awad AA, Haddadin AS, Tantawy H, Badr TM, Stout RG, Silverman DG,
2. Shelley KH. (2007) The relationship between the photoplethysmographic waveform and systemic vascular resistance. *J Clin Monit Comput*; 21:365–372.

Author: Matti Huotari  
Institute: University of OULU  
Street: Erkki Koiso-Kanttilan katu 1  
City: 90570 OULU  
Country: Finland  
Email: matti.huotari@ee.oulu.fi



# Noninvasive Measurement of the Pressure Gradient between the Radial and Finger Arteries

K. Jagomägi, R. Raamat, J. Talts and U. Ragun

Institute of Physiology, University of Tartu, Tartu, Estonia

**Abstract** — Non-invasive mean blood pressure (MAP) recorded at radial artery by the Vasotrac monitor was compared with MAP from finger arteries recorded by the differential oscillometric device in 14 healthy subjects. Simultaneous spontaneous fluctuations in the skin microcirculation were obtained by the Laser Doppler Flowmetry (LDF). The MAP values measured at radial artery were  $4.8 \pm 6.0$  mm Hg higher than those measured on fingers. Pearson correlations between the LDF signal and MAP were  $-0.40$  for the Vasotrac and  $-0.65$  for finger mean pressure, while the difference between the radial and finger mean blood pressures has positive correlation ( $r=0.37$ ) with the LDF signal. The individual correlation coefficients between the pressure difference and LDF signal ranged from  $-0.21$  to  $0.71$ .

**Keywords** — Mean arterial pressure, non-invasive blood pressure, differential oscillometric method, Vasotrac, LDF.

## I. INTRODUCTION

The newly designed Vasotrac device (Medwave, Arden Hills, MN) allows non-invasive measurement of arterial blood pressure (BP) and arterial waveform. Using a patented method of measuring radial artery waveforms, the Vasotrac system calculates systolic, diastolic and mean pressures. It takes approximately 15 seconds to obtain and display a new measurement. The Vasotrac does not provide continuous beat-to-beat measurements; it is able to record data more frequently than the standard oscillometric device. The Vasotrac has been compared to both a radial artery catheter [1-5] and arm-cuff BP [4, 5] in various settings and found to have a good agreement with them.

No studies, however, have been carried out so far on measurements comparing continual blood pressure obtained by the Vasotrac with non-invasive beat-to-beat blood pressure values from fingers. The objectives of this study were to compare the Vasotrac readings with an oscillometric monitor for the measurement of beat-to-beat mean arterial pressure in the finger arteries and to assess whether spontaneous fluctuations in the skin microcirculation, obtained by LDF, are related to the wrist-finger pressure gradient.

## II. MATERIALS AND METHODS

The subjects were 14 students, eight females and six males, aged from 19 to 24. They had no history of vascular disease and gave their informed consent to participate in the study. The study was approved by the Ethics Committee of the University of Tartu. The mean subject height and weight were  $175 \pm 8.4$  cm and  $71.4 \pm 17.8$  kg, respectively.

*Study protocol:* The subject rested for 10 min in the supine position, after which resting blood pressure in the both brachial arteries was measured using an appropriately sized cuff and an ordinary sphygmomanometer (Omron M4). If the blood pressure differed by more than 5 mm Hg, the subject was not included in the study. During the following 8-minute data collection period the volunteers lay still and breathed normally; physical and mental stimulations were reduced to a minimum to avoid sympathetic activation. Room temperature ranged between 21 and 24 °C.

*Radial mean arterial pressure:* Periodic readings of the radial MAP were obtained approximately every 15 seconds by means of the Vasotrac APM205A Monitor. After a successful self-calibration check the Vasotrac sensor was placed over the left radial artery in the manner described by the manufacturer [7]. Data were collected with the Vasotrac in continuous mode.

*Beat-to-beat finger mean arterial pressure:* Finger arterial blood pressure was measured by the UT9201 physiograph, University of Tartu, Estonia. This instrument applies the oscillometric method for measuring beat-to-beat finger arterial pressure. This method needs a servosystem to control the counter pressure in the finger cuff [6]. In the modified oscillometric instrument the cuff pressure level is kept constant during the systolic part of every cardiac cycle (measuring) and is changed during the diastolic part of the cycle (regulating). By modulating the counter pressure level according to the criterion of getting maximum volume oscillations in the cuff in every cardiac cycle, the counter pressure in the cuff is kept equal to the mean arterial pressure (MAP) in the finger arteries. For a higher reliability the control system is made differential, and it operates with two cuffs on adjacent fingers with pressures shifted from the mean pressure value in both directions for a constant difference. In this 'differential' version the principle of maximum oscillations becomes

the principle of the equality of the amplitudes of the simultaneous volume oscillations in the two adjacent finger cuffs.

Two cuffs of the UT9201 instrument were attached to the middle and ring fingers of the right hand. Special attention was paid to a proper attachment of finger cuffs to avoid tight or loose fixation.

To avoid differences of readings due to the hydrostatic pressure differences, the sensors of both BP measuring devices were carefully kept at the same level.

*Laser Doppler Flowmetry (LDF):* Skin blood flow was recorded by a laser Doppler instrument (MBF3D, Moor Instruments, Axminster, Devon, UK). The bandwidth of the instrument was set at its highest level (21 kHz), the filter time constant on 0.5 s; the emitted wavelength was 820 nm. LDF flux signal was used to reveal intensive vasoconstrictions capable of affecting the accuracy of the finger blood pressure measurement. The laser Doppler probe was attached with double adhesive tape to the skin on the thumb pulp of the right hand.

For detecting single rapid and deep inspirations, which result in arteriolar vasoconstriction [8], a perimetric pneumatic transducer was applied to record the respiratory movements of the chest during the whole experiment. A single investigator placed all the units on the subjects to ensure uniformity.

*Signal processing and data analysis:* Simultaneous recordings of the Vasotrac, beat-to-beat finger MAP, laser Doppler in-

strument and respiratory trace were A/D converted at a sample rate of 100 Hz and input into a personal computer with custom-made software for subsequent analysis.

Because there were varying numbers of paired measurements among subjects, the differences between the two methods were also determined separately for each person and then averaged across all the subjects to avoid weighting some subjects more than others.

To test for the presence of significant differences in the readings obtained by the Vasotrac and UT9201 monitor, Student's paired *t*-test was used. To test all the hypotheses, a level of significance of 0.05 was applied. Data are expressed as mean and standard deviation.

Data were averaged within each volunteer, and then averaged among the volunteers. The overall processing was performed using custom made software.

### III. RESULTS

Data were obtained in 14 healthy persons; a total of 383 pairs of Vasotrac and finger mean blood pressure measurements were analyzed. Figure 1 is an example of an original recording in one individual (subject F). It demonstrates that the proximal (radial) and distal (finger) mean pressures follow each other quite well, the radial pressure being systematically slightly higher than the digital pressure.

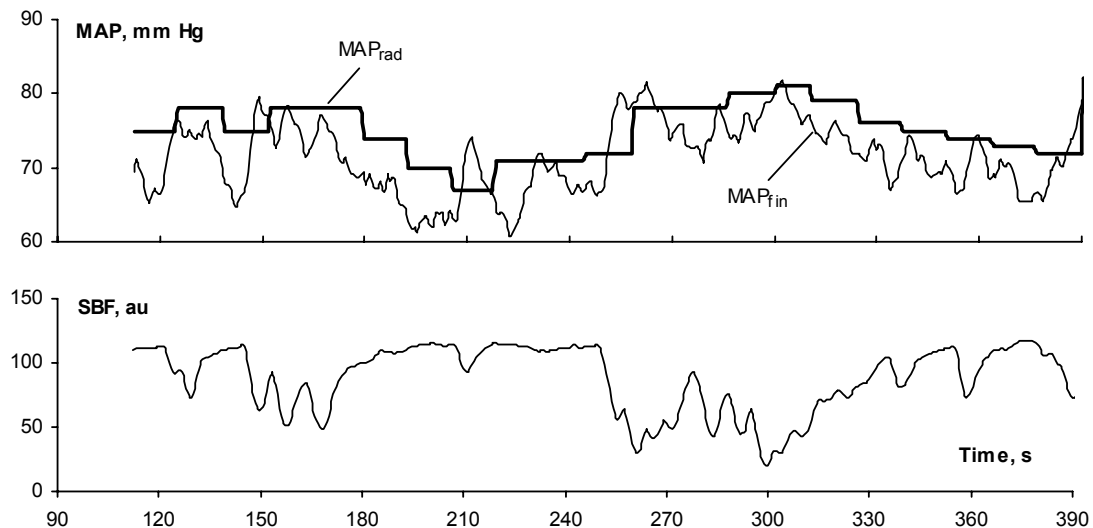


Fig. 1. Example of original recording in subject F. Vasotrac mean blood pressure ( $MAP_{rad}$ ), oscillometric mean blood pressure ( $MAP_{fin}$ ) and fingertip skin blood flow (SBF) are shown.

Table 1. Results of MAP measurement by the two devices in 14 individuals

	Vasotrac MAP	Finger MAP	Difference (rad-fin)	LDF
A	75.2±3	76.9±2.6	-1.7±2.4	135±26.7
B	94.4±3.8	82.7±3.3	11.7±3.1	124.2±31.1
C	93.5±4.5	93.2±4.7	0.3±1.9	16.1±10.5
D	75.7±7.8	60.4±3	15.3±2.6	23.6±13.1
E	92.4±2.9	90.4±2.6	2±1.7	68.3±27.6
F	75.1±3.7	71.7±4.2	3.4±2.1	88.6±24.7
G	95.4±2.6	85.2±2.7	10.2±1.9	67±15.2
H	86.3±4.5	85.9±4.5	0.4±2.6	63.4±23.4
I	83.5±5.2	76.1±4.3	7.4±4.2	133.5±10.3
J	76.2±6.7	75.4±4.5	0.8±5.4	125.6±32.4
K	81.2±3.1	70.9±3.3	10.3±1.8	78.6±18.8
L	79.5±2	74.2±2.3	5.3±1.8	51.2±17
M	72.7±2.7	75.4±3.9	-2.7±2.6	143.4±32.4
N	73.9±5.2	69.4±6.7	4.5±3.7	97.4±31

Values are mean±SD, MAP in mm Hg, LDF in arbitrary units a.u.

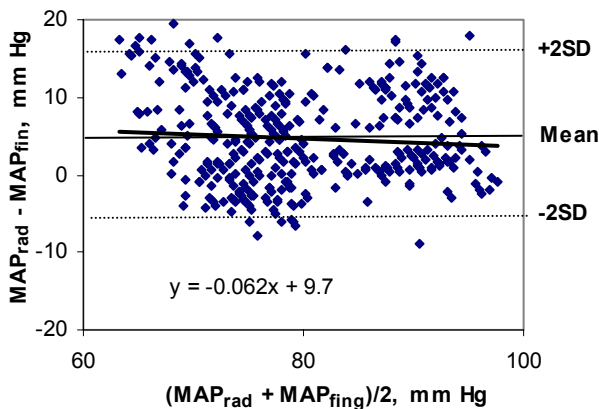


Fig. 2. Bland-Altman bias plot for mean blood pressure showing bias (solid line) and limits of agreement (broken lines).

The Bland-Altman bias plot is shown in Figure 2. Pearson correlations between the MAP values from the Vasotrac device and the differential oscillometric device were  $r=0.79$ .

At the same time individual subject correlation coefficients ranged between 0.50–0.91.

Based on all 383 paired measurements, without considering individual persons separately, the Vasotrac measurements for MAP (mean±SD) were  $4.8±6.0$  mm Hg higher than the MAP values obtained by the oscillometric device.

Pearson correlations between the LDF signal and MAP were  $-0.40$  for Vasotrac and  $-0.65$  for finger mean pressure, while the difference between the radial and finger mean blood pressures has positive correlation ( $r=0.37$ ) with

the LDF signal. The individual correlation coefficients between the difference and LDF signal ranged from  $-0.21$  to  $0.71$ .

#### IV. DISCUSSION

In our study the MAP values measured by the Vasotrac were  $4.8±6.0$  mm Hg higher than values measured on fingers by the oscillometric device. Several factors could contribute to the differences between these measurements: different sites of pressure measurement (finger versus radial artery), technical limitations of the devices, interference from the vasomotor activity of small finger arteries and natural side to side difference.

*Different sites:* Mean finger pressure is lower than radial arterial pressure as a result of a pressure gradient across the vascular tree caused by flow. According to published data the finger mean pressure may be some 8–10 mm Hg less than the brachial values [9-11]. A new development is the reconstruction of radial pressure based on a finger-to-radial autoregressive exogenous model [12]. The pressure decay related to flow in arteries depends on the degree of peripheral constriction. Wesseling et al have found that the change in the difference between full constriction and maximal dilation is 8 mm Hg [9]. In our study the vascular tone was estimated using Laser Doppler Flowmetry. Both MAP values are inversely related to the Laser Doppler signal; the mean correlation coefficient between skin blood flow (SBF) and MAP was  $-0.65$  for finger and  $-0.40$  for radial artery pressure. This is in accordance with published data [9, 13]. The difference between the radial and finger mean blood pressures has positive correlation ( $r=0.37$ ) with the LDF signal.

*Technical limitations:* In two subjects (A and M) of our study the mean finger pressure (MAP) was 2 mm Hg lower than the radial mean arterial pressure, which may reflect a technological error. From a physiologic point of view this is not possible, because radial MAP must be slightly higher than mean finger artery pressure for blood flow to circulate.

*Vasomotor activity of small finger arteries:* Peripheral vasoaction may be distorting the measurement of blood pressure at fingers [14]. In condition of peripheral vasoconstriction the differential oscillometric device tends to overestimate the finger mean blood pressure [15]. The Vasotrac (Medwave, Arden Hills, MN) does not offer truly simultaneous pressure data. This device averages 12 to 15 beats and reports updated pressure intervals; therefore it is not possible to investigate the influence of short lasting vasoconstrictions on the level of radial artery mean pressure.

*Natural side to side difference:* We consistently used the Vasotrac device on the left arm and the differential oscillometric

device on the right. Any side to side difference in the arterial blood pressure time course would be recorded as a difference between the two machines. However, in our young healthy volunteers contralateral (left versus right arm) oscillometric BP difference was less than 5 mm Hg. We therefore think that side to side difference is very unlikely to be the explanation for the differences that we have observed.

## V. CONCLUSIONS

Both recorded non-invasive mean blood pressures follow each other well. The Vasotrac averages 12 to 15 beats and reports updated pressure intervals, therefore it is not possible to investigate the influence of short lasting vasoconstrictions on the level of radial artery mean pressure.

## ACKNOWLEDGMENTS

This work was supported by Grant 6947 from the Estonian Science Foundation.

## REFERENCES

1. Belani K, Ozaki M, Hynson J et al. (1999) A new noninvasive method to measure blood pressure: results of a multicenter trial. *Anesthesiology* 91:686–692
2. Belani KG, Buckley JJ, Poliac MO (1999) Accuracy of radial artery blood pressure determination with the Vasotrac. *Can J Anaesth* 46:488–496
3. Thomas SH, Winsor GR, Pang PS et al. (2004) Use of a radial artery compression device for noninvasive, near-continuous blood pressure monitoring in the ED. *Am. J Emerg Med* 22:474–478
4. Thomas SH, Winsor G, Pang Pet al. (2005) Near-continuous, noninvasive blood pressure monitoring in the out-of-hospital setting. *Prehosp. Emerg. Care* 9:68–72
5. Cua CL, Thomas K, Zurakowski D et al. (2005) A comparison of the Vasotrac with invasive arterial blood pressure monitoring in children after pediatric cardiac surgery. *Anesth Analg* 100:289–294
6. Reeben V, Epler M (1983) Indirect Continuous Measurement of Mean Arterial Pressure. in D.N.Ghista (ed.) *Advances in Cardiovascular Physics*, vol.5, Cardiovascular Engineering. Part II: Monitoring (Karger, Basel) 90–118
7. Vasotrac at <http://www.vasotrac.com/>
8. Allen J, Frame JR, Murray A (2002) Microvascular blood flow and skin temperature changes in the fingers following a deep inspiratory gasp. *Physiol Meas* 23:65–73
9. Wesseling KH, Settels JJ, van der Hoeven GMA et al. (1985) Effects of peripheral vasoconstriction on the measurement of blood pressure in a finger. *Cardiovasc Res* 19:139–145
10. Lal SK, Henderson RJ, Cejnar M et al (1995) Physiological influences on continuous finger and simultaneous intra-arterial blood pressure. *Hypertension* 26:307–314
11. Bogert LW, van Lieshout JJ (2005) Non-invasive pulsatile arterial pressure and stroke volume changes from the human finger. *Exp Physiol* 90:437–446
12. Guelen I, Bogert LWJ, Van Beek M et al. (2004) Reconstruction of radial artery pressure from non-invasive finger arterial pressure measurements in patients with ischemic heart disease. *J Hypertens* 22:S280–S281.
13. Lossius K, Eriksen M, Walloe L (1993) Fluctuations in blood flow to acral skin in humans: connection with heart rate and blood pressure variability. *J Physiol* 460:641–655
14. Birch AA, Morris SL (2003) Do the Finapres and Colin radial artery tonometer measure the same blood pressure changes following deflation of thigh cuffs? *Physiol Meas* 24:653–660
15. Raamat R, Jagomägi K, Talts J (2000) Different responses of Finapres and the oscillometric finger blood pressure monitor during intensive vasomotion. *J Med Eng Technol* 24:95–101

Address of the corresponding author:

Author: Jagomägi K  
 Institute: University of Tartu  
 Street: 19 Ravila Str.  
 City: Tartu  
 Country: Estonia  
 Email: kersti.jagomagi@ut.ee

# A Multicenter Study of Removed Uric Acid Estimated by Ultra Violet Absorbance in the Spent Dialysate

J. Jerotskaja<sup>1</sup>, F. Uhlin<sup>2</sup> and I. Fridolin<sup>1</sup>

<sup>1</sup> Department of Biomedical Engineering, Tallinn University of Technology, EST-19086 Tallinn, Estonia

<sup>2</sup> Department of Nephrology, University Hospital, Linköping, S-581 85 Linköping, Sweden

**Abstract** — The aim of this study was to investigate the relation between removed uric acid (UA) and measured ultra violet (UV) absorbance of the spent dialysate during dialysis.

Ten uremic patients from Tallinn and ten from Linköping, during 30+40 haemodialysis treatments, were followed at the Departments of Dialysis and Nephrology at North-Estonian Medical Centre and at Linköping University Hospital. The dialysate samples were taken and analyzed by means of UA concentration at the chemical laboratory and with a double-beam spectrophotometer. UV absorbance at the wavelength of 297 nm was transformed into UA concentration in the spent dialysate using the regression model from the total material, noted as general model.

Mean concentration of UA was  $53,4 \pm 22,7$  micromol/l measured at the chemical laboratory, and  $53,4 \pm 21,4$  micromol/l determined by UV-absorbance. The results were not significantly different ( $p < 0.05$ ). The concentrations found did differ less than 10%.

Our study indicates that the removed UA can be reliably estimated in different dialysis centres by the UV technique.

**Keywords** — Haemodialysis, spent dialysate, absorption uric acid, spectrophotometry.

## I. INTRODUCTION

Uric acid (UA) is a water-soluble compound (molecular weight of 168.1) that is the final metabolite of purine in humans. Evaluations of UA in blood are common in patients with kidney diseases as well as in those treated with dialysis. Urea, creatinine and UA have for a long time been known to accumulate in the bodies of haemodialysis (HD) patients. UA is removed from plasma in a similar manner as urea during dialysis treatment [1] but so far has not been investigated concerning patient outcome, compared to urea. UA is mostly associated with gout, but studies have found that UA affects biological systems [2], [3] and could also cause higher mortality in dialysis patients [3].

Earlier a good correlation between ultra-violet (UV)-absorbance in dialysate and the concentration of several solutes both in the spent dialysate and in the blood of the dialysis patients has been shown, indicating that the technique can be used to estimate the removal of retained

substances [4]. Also, the possibility to estimate dialysis dose (urea- $Kt/V$ ) [5] and total removed urea by UV-absorbance [6] has been presented.

The aim of this study was to investigate the amount of removed UA during the dialysis estimated by measured ultra violet (UV) absorbance of the spent dialysate with different countries/dialysis centres involved.

Compared to earlier results, a present study shows that a selected wavelength from a scanned range of wavelengths also can be used to build models that can estimate total removal of UA. It also gives opportunity to in detail test which wavelength(s) that is the best to use online or even for other solutes in the future.

## II. MATERIALS AND METHODS

This study was performed after approval of the protocol by the Ethics Committee, at University Hospital of Linköping, Sweden and by the Tallinn Medical Research Ethics Committee at the National Institute for Health Development, Estonia. An informed consent was obtained from all participating patients.

Ten uremic patients, three females and seven males, mean age  $62.6 \pm 18.6$  years, were included in the study at the Department of Dialysis and Nephrology, North-Estonian Medical Centre, Estonia and 10 uremic patients, four females and six males, mean age  $62.8 \pm 20.9$  years were included at the Department of Nephrology, University Hospital of Linköping, Sweden.

All patients were on chronic thrice-weekly haemodialysis. The patients were monitored during three dialysis treatments in Tallinn and four dialysis treatments in Linköping with duration from 240 to 270 minutes (totally 70 haemodialysis sessions). The studied treatments were consecutive in Tallinn and not consecutive in Linköping but were performed within three weeks for each patient.

The schematic clinical set-up of the experiments is shown in Figure 1.

In Linköping an althane dialyser was used with the effective membrane area of 1.8 m<sup>2</sup> (AF180, Ahlthin Medical, Ronneby, Sweden). The dialysate flow was 500

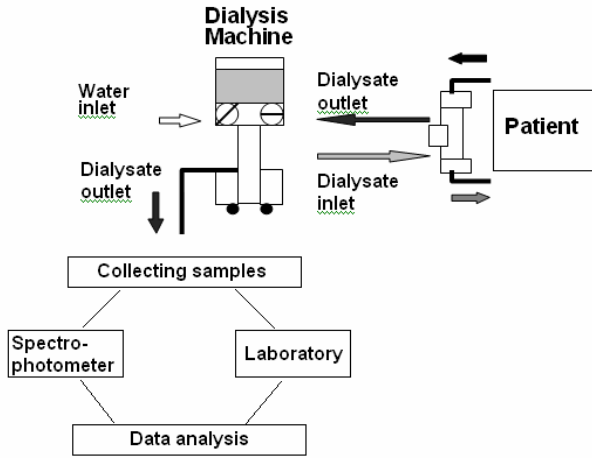


Fig. 1 Schematic clinical set-up of the experiments.

mL/min and the blood flow was 300 mL/min except in one session (250 mL/min) due to temporary access (needle) problems. Two types of machines were used, AK 200 (Gambro Lundia AB, Sweden) and Fresenius 4008H (Fresenius Medical Care, Germany).

In Tallinn F8 HPS (N=14), F10 (N=3), and FX80 (N=13) (Fresenius Medical Care, Germany) with the effective membrane area of 1.8 m<sup>2</sup>, 2.2 m<sup>2</sup>, and 1.8 m<sup>2</sup> were used, respectively. The dialysate flow was 500 mL/min and the blood flow varied between 245 to 350 mL/min. The type of dialysis machine used was Fresenius 4008H (Fresenius Medical Care, Germany).

Dialysate samples were taken before dialysis (pure dialysate), used as the reference solution, when the dialysis machine was prepared for starting and the conductivity was stable, and after 5 (only in Linköping OIL), 10 (only in Tallinn), 15 (OIL), 30 (OIL), 60, 90 (OIL), 120, 180 minutes after the start of the dialysis session and at the end of the session (210, 240 or 270 minutes).

The concentration of UA was determined at the Clinical Chemistry Laboratory at North-Estonian Medical Centre and at the Clinical Chemistry Laboratory at Linköping University Hospital using standardized methods.

Double-beam spectrophotometers (UVIKON 943, Kontron, Italy) in Linköping and (SHIMATSU UV-2401 PC, Japan) in Tallinn were used for the determination of UV-absorbance. Spectrophotometric analysis over a wavelength range of 190 - 380 nm was performed by an optical cuvette with an optical path length of 1 cm. The obtained UV-absorbance values were processed and presented on the computer screen by a PC incorporated in the spectrophotometer using UV-PC software (UV-PC personal spectrophotometer software, version 3.9 for Windows). The final data processing was performed in

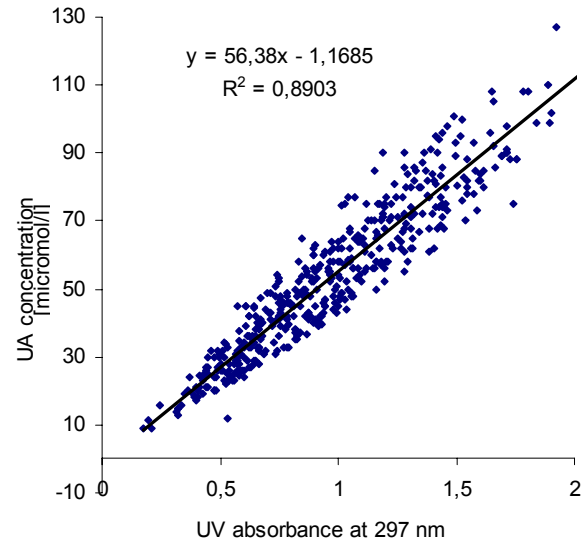


Fig. 2 A regression line between uric acid (UA) concentration in dialysate and UV-absorbance at 297 nm ( $R = 0.9436$ ,  $N = 450$ , totally 70 haemodialysis sessions).

EXCEL (Microsoft Office Excel 2003). The absorbance  $A$  of a solution, obtained by the spectrophotometer using the pure dialysate as the reference solution, was determined as:

$$A = \log \frac{I_r}{I_{r+s}} \tag{1}$$

where  $I_r$  is the intensity of transmitted light through the reference solution (pure dialysate) and  $I_{r+s}$  is the summated intensity of transmitted light through the reference solution containing the solutions under study (pure dialysate + waste products from the blood).

Regression line for the collected dialysate samples and corresponding UV-absorbance values at the wavelength 297 nm was assessed to transform UV-absorbance into UA concentration (Figure 2). Figure 2 shows that a good linear relationship exists between UV-absorbance and dialysate UA concentration. The obtained relationship was used for generating a model,  $y = 56,38x - 1,1685$ , (general model) to estimate UA concentration in different centres.

### III. RESULTS

Figure 3 shows the mean values of the concentrations of the UA measured at the laboratory and UA calculated from the general model.

The mean concentration in  $\mu\text{mol/L}$  of UA determined at the laboratory was (mean  $\pm$  SD)  $53,4 \pm 22,7$  for the total

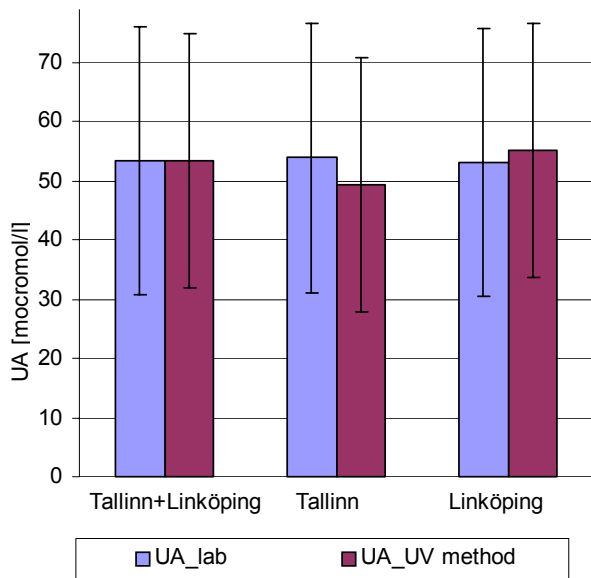


Fig.3 Mean values of UA for the total material and for different centres respectively.

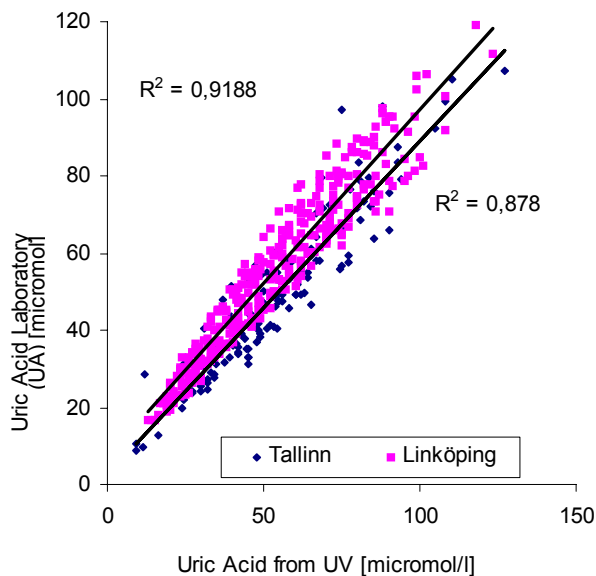


Fig. 4 The regression line between laboratorial UA concentration in dialysate and calculated UA from UV-absorbance, Linköping ( $R=0,9585$ ;  $N=316$ ) and Tallinn ( $R=0,9370$ ;  $N=134$ ), respectively.

material ( $N=450$ ),  $53,2 \pm 23,1$  for Linköping ( $N=316$ ), and  $53,9 \pm 21,8$  for Tallinn ( $N=134$ ).

The mean concentration of UA  $\pm$  SD in  $\mu\text{mol/L}$  calculated by the general model using the UV-absorbance was  $53,4 \pm 21,4$  for the total material ( $N=450$ ),  $55,1 \pm 21,8$  for Linköping ( $N=316$ ), and  $49,3 \pm 20,1$  for Tallinn

( $N=134$ ). The concentrations found did differ less than 10%.

Figure 4 shows the regression line between laboratorial UA concentration in dialysate and calculated UA from UV-absorbance for the particular centre.

Applying the obtained center-specific models to the UA calculations from UV-absorbance  $53,2 \pm 22,2 \mu\text{mol/L}$  for Linköping ( $N=316$ ), and  $53,9 \pm 20,4 \mu\text{mol/L}$  for Tallinn ( $N=134$ ) is obtained. This means that if the transformation model for specific centre is utilised the UA concentrations estimated by UV-absorbance has the same mean value as the UA determined at the laboratory.

#### IV. DISCUSSION

The presented results show the possibility to estimate UA concentrations with UV-Absorbance technique generated model in different dialysis centres.

A good agreement using the general model utilised to calculate UA concentration is demonstrated in the two dialysis centres. The greatest difference was seen in Tallinn, (Fig. 3) when the general model was used to estimate UA. One explanation is probably the differences in dialysis filters used. In Linköping only one type of filters was used but in Tallinn three different filters were used, and the difference in membrane permeability of solutes may have caused this difference. Another explanation could be that two different spectrophotometers have been used to measure the absorbance (one in Tallinn and one in Linköping). Absorbance may differ due technical differences between spectrophotometers. This is shown in Fig. 4, and even if the correlation to UA is similar at the two centres the difference is more obvious when putting the data together.

A solution to increase the accuracy is probably to calculate a general model for each dialysis filter in the future. This could be done by the manufactures at the same time as clearance for different solutes is measured and later presented in the manual to the filters.

The values of UA obtained using the general model of UV-absorbance measurements were in the same order as UA measured at the laboratory (Fig. 3). Also, the SD of the mean value for the compared methods was of the same magnitude. A good correlation between UV-absorbance and UA could be explained by relatively high millimolar extinction coefficients with three distinct maxima around 202, 235 and 292 nm and two minima around 220 and 260 nm in the wavelength range from 200 to 380 nm [7]. The absorbance around 292 nm is characteristic for UA and is utilised for UA concentration determination by the enzymatic degradation method [8]. The reason why a

wavelength of 297 nm was chosen in this study was the opportunity to compare these results with on-line monitoring data in next studies, were 297 nm has been used.

A relatively dominant absorbance for UA and creatinine, compared to other compounds in different fluids (serum, spent dialysate, urine), is confirmed by several HPLC studies at the wavelength 254 nm [10, 11]. UA, being a small solute, is also removed from the blood by haemodialysis in a similar manner as urea, the traditional marker for dialysis efficiency, and is associated with disturbances of calcitriol production and metabolism [2]. Since the spent dialysate contains many UV-absorbing compounds, a summated effect of the compounds must be regarded.

The fact that the UV-method has similar results as the standard methods at the chemical laboratory indicates that the removal rate of UV-absorbing solutes is comparable to a solute like UA during haemodialysis. This is also confirmed by a very good correlation between several small molecular weight waste products and the UV-absorbance [4] and similar concentration changes during dialysis for several azotemic markers (e.g. urea, creatinine, UA and pseudouridine) as reported earlier [12], [1]. The elimination of such a small molecular weight waste product as UA can therefore be assessed by the UV-technique. As a consequence, this makes it possible to determine UA concentration and calculate total removed UA even when the technique does not measure solely UA.

The clinically aim in the future is to develop an on-line monitoring system that could offer an estimation of the removal of several clinical important solutes during haemodialysis. The UV technique may be the monitoring tool in the future that ensures dialysis quality by evaluating the delivery of the prescribed treatment dose and immediately identifying and being alert for any deviations in dialysis treatment.

## V. CONCLUSION

The results show the possibility to estimate total removed UA using a general model based on UV-absorbance at the wavelength of 297 nm. The mean values of UA obtained using the general model were very close to UA measured at the laboratory, even if the pure UA concentration is measured in the spent dialysate at the chemical laboratory, while the UV method measures all UV-absorbing compounds in the spent dialysate. The assumption that UV-absorbing solutes are removed in a similar manner compared with UA seems to be valid in this material. Also the possibility to estimate total removal

of other solutes, e.g. those presented by the EUTox group [13] may be used as a measure of dialysis adequacy in the same manner as UA should be validated. This information will be useful as a source for analysing and revising haemodialysis quality and existing standards and methods to ensure treatment quality and patient welfare.

## ACKNOWLEDGEMENTS

The authors wish to thank all dialysis patients who participated in the experiments, Per Sveider, Jan Hedblom and Rain Kattai for skilful technical assistance, and Dr. Merike Luman and Galina Velikodneva for assistance during clinical experiments, and Kai Lauri for assistance during the laboratory analysis. Supported in part by the Swedish CompetenceCentre for Non-invasive Medical Measurements, NIMED and in part by the Estonian Science Foundation Grants No 5871 and No 6936.

## REFERENCES

- [1] R. C. VANHOLDER, R. V. DE SMET, and S. M. RINGOIR, (1992): 'Assessment of urea and other uremic markers for quantification of dialysis efficacy', *Clin Chem*, **38**, pp. 1429-1436
- [2] R. DE SMET, G. GLORIEUX, C. HSU, and R. VANHOLDER, (1997): 'p-cresol and uric acid: two old uremic toxins revisited.', *Kidney Int*, **Nov**; **62**, pp. S8-11
- [3] T. S. PERLSTEIN, O. GUMIENIAK, P. HOPKINS, L. MURPHEY, N. BROWN, G. WILLIAMS, H. NK, and N. FISHER, (2004): 'Uric acid and the state of intrarenal renin-angiotensin system in humans', *Kidney Int*, **66**, pp. 1465-1470
- [4] I. FRIDOLIN, M. MAGNUSON, and L.-G. LINDBERG, (2002): 'On-line monitoring of solutes in dialysate using absorption of ultraviolet radiation: technique description', *The International Journal of Artificial Organs*, **25**, pp. 748-761
- [5] F. UHLIN, I. FRIDOLIN, L.-G. LINDBERG, and M. MAGNUSON, (2003): 'Estimation of delivered dialysis dose by on-line monitoring of the UV-absorbance in the spent dialysate', *American Journal of Kidney Diseases*, **41**, pp. 1026-1036
- [6] F. UHLIN, I. FRIDOLIN, L. G. LINDBERG, and M. MAGNUSON, (2005): 'Estimating total urea removal and protein catabolic rate by monitoring UV absorbance in spent dialysate', *Nephrol Dial Transplant*, **20**, pp. 2458-2464
- [7] I. FRIDOLIN and L.-G. LINDBERG, (2003): 'On-line monitoring of solutes in dialysate using absorption of ultraviolet radiation - wavelength dependence', *Medical & Biological Engineering & Computing*, **41**, pp. 263-270
- [8] E. PRAETORIUS and H. POULSON, (1953): 'Enzymatic determination of uric acids', *Scand. J. Clin. Invest.*, **5**
- [9] W. W. E. SIMONS, (1979): 'The Sadtler Handbook of Ultraviolet Spectra. Philadelphia, Pennsylvania: Sadtler. Heyden, pp. 1016
- [10] A. GORDON, J. BERSTRÖM, P. FÜRST, and L. ZIMMERMAN, (1975): 'Separation and characterization of uremic metabolites in biologic fluids: a screening approach to the definition of uremic toxins', *Kidney International*, **2**, pp. 45-51
- [11] P. FÜRST, L. ZIMMERMAN, and J. BERGSTRÖM, (1976): 'Determination of endogenous middle molecules in normal and uremic body fluids', *Clinical Nephrology*, **5**, pp. 178-88.



- [12] G. GAL, J. GROF, and E. KISS, (1983): 'Continuous monitoring of the efficiency of haemodialysis by recording the UV transmittance of the dialysis solution', *Acta Chir Hung*, **24**, pp. 231-239
- [13] R. VANHOLDER, R. DE SMET, G. GLORIEUX, et al. (2003): 'Review on uremic toxins: classification, concentration, and interindividual variability', *Kidney International*, **63**, pp. 1934-1943

Author: Jana Jerotskaja  
Institute: Department of Biomedical Engineering, Technomedicum,  
Tallinn University of Technology  
Street: Ehitajate tee 5  
City: 19086 Tallinn  
Country: Estonia  
Email: jana@cb.ttu.ee

# Comparison of Tibial Nerve Somatosensory Evoked Potential Signal-to-Noise Ratios During Anaesthesia

A.S. Joutsen<sup>1</sup>, P. Puumala<sup>2</sup>, L-P. Lyytikäinen<sup>2</sup>, O. Pajulo<sup>3</sup>, A. Etelämäki<sup>4</sup>, J. Jurva<sup>2</sup>, V. Jäntti<sup>2</sup> and H. Eskola<sup>1</sup>

<sup>1</sup> Department of Biomedical Engineering, Tampere University of Technology, Tampere, Finland

<sup>2</sup> Department of Neurophysiology, Tampere University Hospital, Tampere, Finland

<sup>3</sup> Department of Surgery, Tampere University Hospital, Tampere, Finland

<sup>4</sup> Department of Anaesthesiology, Tampere University Hospital, Tampere, Finland

**Abstract** — Monitoring the function of the central nervous system of a patient during a surgery where an injury to the nerves can occur is important in securing the safety of the patient. The somatosensory tract of patients undergoing corrective surgery for scoliosis were monitored using tibial nerve somatosensory evoked potentials (tSEP) by stimulating the tibial nerve from the ankle and recording the responses from electroencephalography (EEG) electrodes placed on the scalp of the patient.

The recorded EEG was segmented off-line into different epochs on the basis of spontaneous neuronal activity overlaying the tSEPs. The epochs were: bursts, suppressions, spindles and technical artefacts. Ensemble averaging was carried out over the epochs to discover how quickly the overall tSEP signal-to-noise ratio (SNR) increases as a function of N.

The tSEP SNR increased most rapidly during the suppression epochs which contain only little spontaneous EEG activity in comparison with the tSEPs recorded during the burst and spindle epochs. Fast and reliable results can be achieved in the operating room by using deep propofol anaesthesia where the spontaneous EEG activity is mostly low, selecting only high SNR epochs and using ensemble averaging on those to form the overall tSEP response.

**Keywords** — Somatosensory evoked potentials, Signal-to-noise ratio, Ensemble averaging, Anaesthesia.

## I. INTRODUCTION

Somatosensory evoked potential (SEP) study is a neurophysiological examination method that can be used for detecting nerve conduction problems in peripheral and central nervous system in humans. The method is nowadays used routinely to diagnose for example multiple sclerosis, spinal stenosis and neuropathies. It is also useful in intraoperative monitoring (IOM) to ensure patient safety when there is a high risk of damaging the spinal cord due to a surgical operation [1].

The data for our study consists of 7 channels of EEG with tSEP:s synchronized to a trigger signal used to deliver the electric stimuli to the tibial nerve of the patient. The data has been recorded during scoliosis surgery. For each patient

an optimal tSEP channel was found comparing response amplitudes [2].

The tSEP responses, which are embedded in the EEG, have a very low amplitude, just a few  $\mu\text{V}$ , where as the noise may range from  $\mu\text{V}$  to hundreds of mV. This leads to a poor signal-to-noise ratio in the measurement.

There are many ways for improving the signal-to-noise (SNR) ratio of the tSEP during anaesthesia. The signal is generated by the somatosensory cortex of the brain and has a relatively constant waveform, and thus little can be done to enhance that. Most of the artificial noise can be reduced by using shielded equipment, braided cables and proper grounding. Filtering the EEG with tSEPs using a band pass filter of 30 – 200 Hz rejects the low and high frequency components that are not of interest to tSEP IOM. Physiological noise can be reduced using muscle relaxants and burst suppression level anaesthesia. The de-facto method for improving the SNR is to use ensemble averaging during the recording and add new responses as they come available.

In this work we evaluate the effect of different kind of EEG activity which overlaps with the tSEP responses in the gamma band 25 - 100 Hz. Due to the frequency content of the different types of physiological noise they have unique delaying effects on the SNR increase and thus the formation of the final result.

## II. MATERIAL AND METHODS

The 8 patients selected for this study were operated in Tampere University hospital during 2006 and 2007 for idiopathic scoliosis. tSEPs were used during the operations to monitor the integrity of the somatosensory tracts and to warn the surgeon about possible arising complications of the spinal cord.

The monitoring device was Endeavor Bravo intraoperative monitoring system (Viasys Healthcare, PA, USA). The acquired EEG was sampled at 8 kHz. The tSEP stimulation frequency was 3,1 Hz. After recording the EEG was moved to off-line analysis with Matlab (Mathworks, MA, USA),

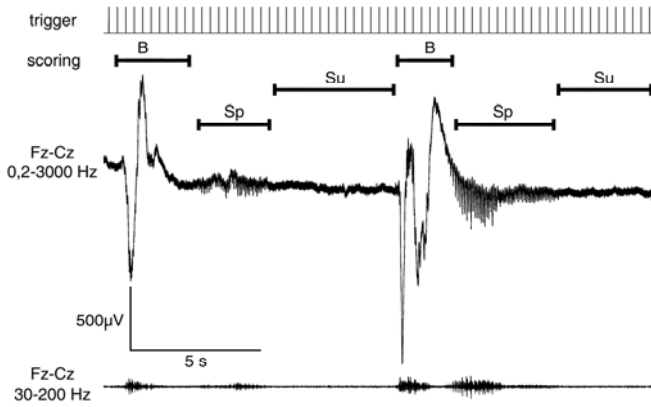


Fig. 1 This is an example of typical anaesthesia burst suppression EEG with spindles. From top to bottom: tSEP trigger, segmentation scoring, raw EEG from the Fz-Cz channel derivation and the same band pass filtered. In the scoring B, Su and Sp denote burst, suppression and spindle respectively.

where it was band pass filtered with 30 to 200 Hz to reject high and low frequency noise not associated with the tSEP. The EEG was visually scored using Somnologica Studio (Embla, Co, USA) to bursts, suppressions and spindles [3,4] and technical artifacts, which were omitted from the study (Fig. 1). The EEG contained some 50 Hz mains artifact. An optimal tSEP channel was calculated for each patient by selecting the EEG derivation yielding the highest tSEP responses [2]. Channels used were the derivations of standard 10-20 EEG locations [5], from which Fz-Cz or C3-C4 was most frequently selected. The tSEP responses occurring during the three EEG epochs were separated to their respective datasets and ensemble averaging with a rejection criterion of 200  $\mu\text{V}$  peak-to-peak per single response was used to improve the SNR inside the sets.

Ensemble averaging is based on a simple signal model in which the potential  $x_i$  of the  $i^{\text{th}}$  stimulus is assumed to be additively composed of a deterministic, evoked signal component  $s_i$  and a random noise  $n_i$  which is asynchronous to the stimulus (Eq 1).

$$x_i = s_i + n_i \quad (1)$$

The noise is assumed to have zero mean and it is uncorrelated between measurements. Noise and signal need to be uncorrelated and the signal needs to have constant waveform morphology [6]. The first three requirements are fulfilled, but in IOM sudden changes in the tSEP response need to be detected, as these may be caused by conduction problems in the somatosensory tract of the patient. In our data there was no physiological signal loss.

The SNRs of the averaged tSEPs were calculated using the  $\pm$  reference that estimates the residual noise in evoked potentials by subtraction of two separate averages: one consisting of the odd-numbered sweeps ( $\bar{x}_1$ ), the other of

the even-numbered sweeps ( $\bar{x}_2$ ). We can calculate these averages by

$$\begin{aligned} \bar{x}_1 &= \frac{1}{k} \left( \sum_{i=1}^{2k-1} (s_i + n_i) \right) \\ \bar{x}_2 &= \frac{1}{l} \left( \sum_{i=1}^{2l} (s_i + n_i) \right) \end{aligned} \quad (2)$$

$$k = \begin{cases} N/2 & N = \text{even} \\ (N+1)/2 & N = \text{odd} \end{cases}$$

$$l = \begin{cases} N/2 & N = \text{even} \\ (N-1)/2 & N = \text{odd} \end{cases}$$

where N is the total number of sweeps. As all single responses  $s_i$  are assumed to be identical during the recording no response will remain after the subtraction

$$\bar{x}'_N = \bar{x}_1 - \bar{x}_2 \quad (3)$$

The subtraction of the noise terms  $n_i$  results in a noise estimate with a mean value of zero and a variance  $\sigma_n^2$ . The expected residual noise power equals  $\sigma_n^2 / N$ . The variance of the averaged signal  $\bar{x}$  divided by the variance of the  $\pm$  reference  $\bar{x}'$  results in a true SNR power ratio

$$P = \frac{\text{var}\{\bar{x}(t)\}}{\text{var}\{\bar{x}'(t)\}} \quad (4)$$

where P equals to SNR [7]. SNRs are calculated for burst, suppression and spindle sets for every patient.

### III. RESULTS

The results of the study are shown in Fig. 2 and Table 1. In Fig. 2 the ensemble averaged responses from 1 to 256 for an example patient are shown.  $N=256$  was chosen as an endpoint of the process because little change in wave morphology or SNR was detected after that. The used arithmetic mean smoothes the waves heavily and only the main deflection of tSEP around 30 to 40 ms is visible when N grows over 128. On the other hand the SNR of the result is ideally proportional to the square root of N [8], which means that when the innate SNR is 0,1 during the EEG bursts of the example patient, increasing it tenfold requires N to be 100.

The EEG noise was much higher during bursts and spindles than during suppressions which can be seen as the forming of the characteristic tSEP response wave shape

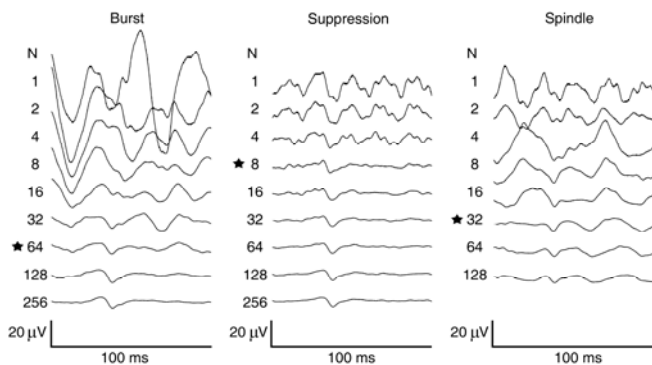


Fig. 2 The results of ensemble averaging of the data of an example patient with burst, suppression and spindle sets after N responses. ★ signifies when the tSEP response has formed. The example patient had enough spindle responses only for N=128.

during suppressions when N is 8 and during bursts and spindles when N is significantly higher, 64 and 32, respectively (Fig. 2). With the 3,1 Hz tSEP stimulation frequency it takes 2,6 seconds to acquire 8 responses, in comparison to 20,6 s and 10,3 s of 64 and 32 responses. During high noise segments an acceptable result may need hundreds of responses leading to minutes of acquisition time. The maximum amplitude of the response lowers somewhat when N is high because of small amplitude and latency variations (jitter), in the single responses  $s_i$  (Eq 1).

The same trend as in Fig. 2 can be seen in the SNR in Table 1, which shows the minimum and maximum SNR among the 8 patients as a function of N. The tSEP SNR increase is significantly faster during suppressions when compared to bursts and spindles. The large inter-patient SNR distribution is due to different patient tSEP physiology [2] and their reaction to the anaesthetic agent propofol. Changing IOM conditions also may contribute to the result as a fluctuation of the SNR in consecutive Ns.

#### IV. CONCLUSIONS

The physiological noise caused by bursts and spindles have components that overlap with the tSEP in the EEG-gamma band 25-100 Hz. Using burst suppression level of anaesthesia and selecting epochs, where the noise level consisting of unrelated physiological activity, mostly EEG, and technical artifacts is low, seems to yield high tSEP SNRs and thus enables faster detection of response loss than when monitoring during continuous EEG and accepting all the responses under the 200 μV rejection criterion. The conclusions are somewhat limited by the number of patients, which was 8. Further studies are needed to expand the results and conclusions.

Table 1 The minimum and maximum SNRs

N	Burst	Suppression	Spindle
2	0,32 - 3,44	0,73 - 3,22	0,98 - 2,47 (5)
4	0,46 - 6,90	0,54 - 3,57	0,61 - 3,18 (5)
8	0,21 - 3,11	0,37 - 4,45	0,52 - 1,17 (4)
16	0,57 - 3,45	1,15 - 7,80	0,89 - 1,40 (4)
32	0,71 - 3,99	0,69 - 26,29	0,37 - 9,08 (3)
64	0,37 - 9,53	1,77 - 63,30	0,41 - 3,49 (2)
128	0,75 - 28,10	1,29 - 135,32	1,58 (1)
256	1,32 - 32,86	5,44 - 398,08	

The amount of patients in burst and suppression set was 8. The amount of patients decrease in spindle column (shown in parenthesis) as N grows, because simultaneous spindles and tSEP responses were rare in this set of patients.

#### ACKNOWLEDGEMENT

This study was funded by the Finnish Ministry of Education through the International Graduate School in Biomedical Engineering and Medical Physics in the Tampere University of Technology. The use of the patient material was approved by the chief administrative medical officer of Tampere University Hospital (decision number R0853).

#### REFERENCES

- Marc R. Nuwer, Edgar G. Dawson, Linda G. Carlson, Linda E. A. Kanim and John E. Sherman (1995) Somatosensory evoked potential spinal cord monitoring reduces neurologic deficits after scoliosis surgery: results of a large multicenter survey, *Electroencephalography and Clinical Neurophysiology/ Evoked Potentials* 96:6-11.
- MacDonald DB, Al Zayed Z, Stigsby B (2005) Tibial somatosensory evoked potential intraoperative monitoring: recommendations based on signal to noise ratio analysis of popliteal fossa, optimized P37, standard P37, and P31 potentials. *Clin Neurophysiol.* 116:1858-69
- Huotari AM, Koskinen M, Suominen K, Alahuhta S, Remes R, Hartikainen KM, Jääntti V (2004) Evoked EEG patterns during burst suppression with propofol. *Br J Anaesth.* 92:18-24.
- Jääntti V, Yli-Hankala A, Baer GA, Porkkala T (1993) Slow potentials of EEG burst suppression pattern during anaesthesia. *Acta Anaesthesiol Scand.* 37:121-3
- Klem G, Lüders H, Jasper H, Elger C (1999) The ten-twenty electrode system of the International Federation. The International Federation of Clinical Neurophysiology *Electroencephalogr Clin Neurophysiol Suppl.* 52:3-6.
- Sörnmo L, Laguna P (2005) *Bioelectrical Signal Processing in Cardiac and Neurological Applications*, Academic Press, New York
- Schimmel H, Rapin I, Cohen MM (1974) Improving evoked response audiometry with special reference to the use of machine scoring. *Audiology*, 13:33-65
- Luck S (2005) *An introduction to event-related potential technique*, MIT Press, Cambridge

Author: Atte Joutsen  
 Institute: Department of Biomedical Engineering / Tampere University of Technology  
 Street: Biokatu 6, 4<sup>th</sup> floor  
 City: Tampere 33520  
 Country: Finland  
 Email: atte.joutsen@tut.fi

# Phase Coupling in EEG Burst Suppression during Propofol Anesthesia

F.E. Kapucu<sup>1</sup>, T. Lipping<sup>2</sup>, V. Jäntti<sup>3</sup> and A.-M. Huotari<sup>4</sup>

<sup>1</sup> Department of Biomedical Engineering, Tampere University of Technology, Tampere, Finland

<sup>2</sup> Information Technology, Pori, Tampere University of Technology, Pori, Finland

<sup>3</sup> Department of Clinical Neurophysiology, Tampere University Hospital, Tampere, Finland

<sup>4</sup> Department of Anesthesiology, Oulu University Hospital, Oulu, Finland

**Abstract** — This work analyzes the quadratic phase coupling between EEG rhythms during burst suppression period of propofol anesthesia. The main goal is to specify the phase relation between different EEG rhythms and search for possible systematic behavior. In order to achieve this, the presented work focuses on the detection of quadratic phase coupling (QPC) based on bispectral analysis. The study indicates that frequencies of the dominant components of the bursts vary, so the detection of QPC is practically not as simple as detecting synchrony between couples of well defined rhythms.

**Keywords** — bispectrum, propofol anesthesia, quadratic phase coupling (QPC), higher order spectrum (HOS), EEG-burst-suppression.

## I. INTRODUCTION

Burst suppression is a pattern formed by burst periods – high-voltage slow waves superimposed by sharp waves-sequentially alternating with suppressed background activity [1]. The pattern is observed during deep anesthesia and its appearance is often suggested as a specific endpoint in the continuum of deepening anesthesia. Furthermore, virtually all the commercial depth-of-anesthesia monitoring algorithms are capable of detecting this pattern and use the relative proportion of the period of suppressed EEG (called Burst Suppression Ratio) as an indicator of level of drug induced coma in very deep anesthesia [2].

The behavior of the pattern and its contents can potentially reveal the underlying physiological mechanisms. It is also possible to uncover the interactions of different brain regions with each other by observing the interrelations of frequency components measured from corresponding EEG channels. The study by Witte et. al [3] aimed at defining the degree of interrelations between the lower frequency components 0-2.5 Hz and the frequencies 3-7.5 Hz and 8-12 Hz. Their results indicate coherence between mentioned components and the authors concluded that there may be regional physiological interaction. The study hypothesized that the waves of frequencies of 3-7.5 and 8-12 Hz are originated from the interactions between reticular thalamic, thalamocortical and corticothalamic neurons and may be modulated by cortically generated low frequency oscillations.

Bispectrum analysis or generally higher order spectrum (HOS) analysis has prospect to expose the mechanisms underlying these interactions due to its ability to preserve phase information.

Quadratic Phase Coupling (QPC) has been analyzed using bispectrum estimation previously in several studies. According to [4], there are various conditions in which QPC detection in the EEG signal can be useful. One of the first studies in this area is the work of Huber et al. [5]. In this work the phase relations of EEG are tested by means of bispectrum analysis. Non-linear mechanisms of EEG and auditory evoked potentials (AEPs) are analyzed using bispectrum in [6]. As a result, the existence of QPC at low frequency components has been detected. The Gaussianity and linearity of the EEG acquired from different brain regions and different conditions (eye-closed and eye-opened), is analyzed by quantifying the level of QPC in [7]. The relative non-linearity and non-Gaussianity of eye-closed condition is stated in conclusion whereas different characteristics were obtained from different brain regions. Higher order spectrum is applied to characterize the sleep spindles in [8]. Time domain analysis has been performed by means of second and third order correlations to detect the transitions between multiple activities and frequency domain analysis by means of spectrum and bispectrum allows the description of frequency interactions related with nonlinearities.

In this paper, similar kinds of interactions have been investigated by looking at bispectral information of the burst components.

## II. MATERIALS AND METHODS

### A. Data Characteristics and Selection Criteria

The EEG data in this study was recorded during propofol induced anesthesia. Propofol infusion lasted until burst suppression patterns were observed. The signals were recorded continuously using NeuroScan Synamp amplifier (Neuroscan, El Paso, TX, USA). The signal was initially filtered using a bandpass filter of 0.05-1000 Hz and digitized with a sampling rate of 5000 Hz. Before the analysis

presented in this study, the signal was decimated to 500 Hz sampling rate. EEG was recorded from Fp1, Fp2, Fz, F3, F4, F7, F8, Cz, C3, C4, CPz, CP3, CP4, T3, T4, T5, T6, Pz, P3, P4, O1 and O2 unipolar channels according to the 10-20 system with the reference at FCz. Detailed description of the recording setup as well as the neurophysiological findings can be found at [9].

Initial purpose of recording the data was analyzing evoked EEG patterns during burst-suppression period of propofol anesthesia. Evoked potentials were elicited by electrically stimulating the median nerve. Medelec ST-10 stimulator (Medelec, Old Woking, UK) was used by applying surface electrodes at the wrist. Pulses of 0.1 ms and 100 mA were triggered during the EEG suppression manually [9].

Bursts can be seen either as a response to the stimulation or they can occur spontaneously in deep anesthesia, thus the bursts can be classified into two groups such as spontaneous bursts and stimulated bursts. The selection of the burst segments has been done manually indexing the start and end points of the bursts and all the calculations performed on these selected patterns. The duration of the burst is another criterion for the selection. The bursts lasting less than one second (500 samples) were excluded. Total number of the bursts selected is 32 while 11 of them are occurred spontaneously and 21 were stimulated. Fig.1 shows examples of selected bursts.

The channels F3-C3 and F4-C4 were used to calculate bipolar EEG. Selection was maintained unilaterally considering the study presented in Hagihira et al. [10].

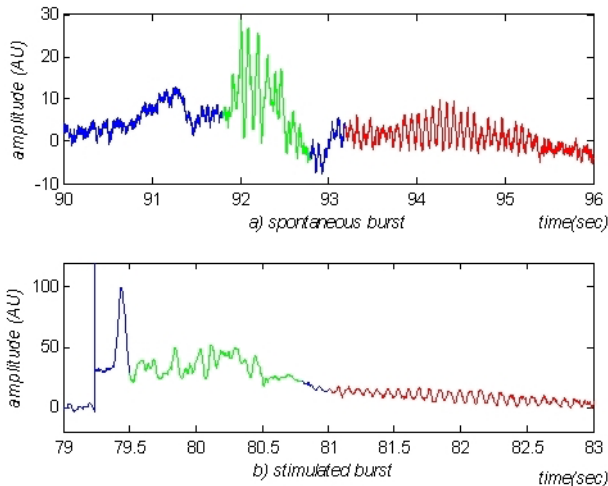


Fig. 1 Selected burst examples a) spontaneously occurred burst pattern b) stimulated burst pattern; burst (green) and the following spindle (red).

## B. Principles of Bispectrum and Quadratic Phase Coupling

The term higher order spectra could be understood by first defining the “cumulants” or “moments”.

If  $\{X(k)\}, k = 0, \pm 1, \pm 2, \pm 3, \dots$  is a real stationary discrete-time signal and its  $n$ th order moment exists, then the  $n$ th order moment function could be expressed as [11]:

$$m_n^x(\tau_1, \tau_2, \dots, \tau_{n-1}) \triangleq E\{X(k)X(k+\tau_1)\dots X(k+\tau_{n-1})\} \quad (1)$$

In the special cases where  $n = 3, 4$  the  $n$ th order cumulants of a non-Gaussian random stationary signal  $\{X(k)\}$  can be written as:

$$c_n^x(\tau_1, \tau_2, \dots, \tau_{n-1}) = m_n^x(\tau_1, \tau_2, \dots, \tau_{n-1}) - m_n^G(\tau_1, \tau_2, \dots, \tau_{n-1}) \quad (2)$$

where  $m_n^G(\tau_1, \tau_2, \dots, \tau_{n-1})$  is the  $n$ th order moment function of a Gaussian signal which has the same mean value and autocorrelation as  $\{X(k)\}$ .

As it is presented below, the  $n$ -th order moment/cumulant spectrum is defined as  $(n-1)$ -th dimensional Fourier transform of the  $n$ -th order cumulant.

Power Spectrum:  $n = 2$

$$C(w_1) = \sum_{\tau_1=-\infty}^{+\infty} c_2(\tau_1) \exp\{-j(w_1\tau_1)\} \quad (3)$$

Bispectrum:  $n = 3$

$$C(w_1, w_2) = \sum_{\tau_1=-\infty}^{+\infty} \sum_{\tau_2=-\infty}^{+\infty} c_3(\tau_1, \tau_2) \exp\{-j(w_1\tau_1 + w_2\tau_2)\} \quad (4)$$

Trispectrum:  $n = 4$

$$C(w_1, w_2, w_3) = \sum_{\tau_1=-\infty}^{+\infty} \sum_{\tau_2=-\infty}^{+\infty} \sum_{\tau_3=-\infty}^{+\infty} c_4(\tau_1, \tau_2, \tau_3) \exp\{-j(w_1\tau_1 + w_2\tau_2 + w_3\tau_3)\} \quad (5)$$

To understand the phase coupling better, the following example demonstrated previously by Nikias et al. would help [12]:

Let

$$X_1(k) = \cos(\lambda_1 k + \varphi_1) + \cos(\lambda_2 k + \varphi_2) + \cos((\lambda_1 + \lambda_2)k + \varphi_3)$$

and

$$X_2(k) = \cos(\lambda_4 k + \varphi_4) + \cos(\lambda_5 k + \varphi_5) + \cos((\lambda_4 + \lambda_5)k + (\varphi_4 + \varphi_5))$$

where the values  $\varphi_1, \varphi_2, \varphi_3, \varphi_4, \varphi_5$  are independent and uniformly distributed random variables over  $[0, 2\pi]$  and  $\lambda_1, \lambda_2, \lambda_3$  and  $\lambda_4, \lambda_5, \lambda_6$  are harmonically related. As

phase information is lost while calculating the power spectrum, the power spectra of these signals are identical, however, their bispectrum shows totally different results. See Fig.2 for demonstration.

An example signal based on synchronized frequency components is generated which has phase coupled harmonics, at 0.15 Hz and 0.30 Hz.

Additionally, there is one uncoupled harmonic of 0.20 Hz. Fig.3 presents the power spectrum and bispectrum magnitude. The third harmonic which arises from the phase coupling of 0.15 and 0.30 Hz components can be seen at 0.45 Hz in the power spectrum. The only possible explanation for this is that the second coupled harmonic, 0.30 Hz, is the summation of 0.15 Hz by itself.

Direct method [11] is used to estimate bispectrum in this study. The algorithm of Matlab function, *bicohere* [13] is applied. Mean of the signal is subtracted as an initial step of the algorithm. Secondly, the data is divided into segments. Number of the segments depends on the window size, over-

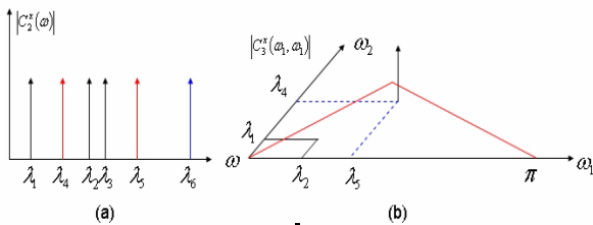


Fig. 2 a) Spectral representation: the black components are independent where the blue component is a result of phase coupling between red components b) Bispectral representation: phase coupling of  $\lambda_1$  and  $\lambda_3$  generates a peak. Quadratic Phase Coupling is estimated inside triangular region.

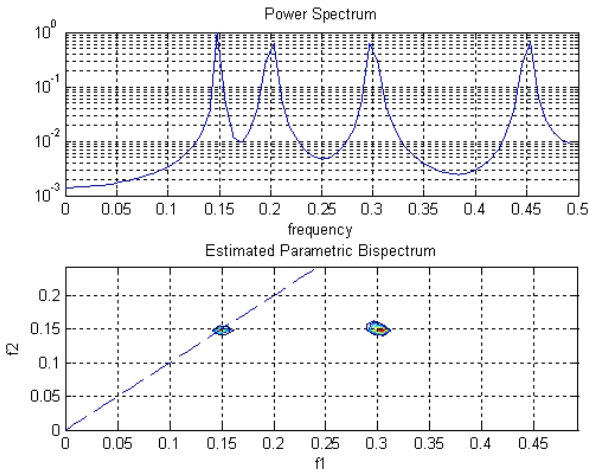


Fig. 3 Bispectrum precisely plots the phase relation between the coupled components where there is no effect of the uncoupled component placed at 0.20 Hz. Additionally, there is a peak at the point (0.15 Hz; 0.15 Hz).

lapping ratio and the length of the burst. The resolution of the calculation was kept maximal by taking the window size as small as possible. In the application, window length was selected as 256 samples and window type was selected as Hamming. The computational superiority of the direct method against the indirect method in bicoherence estimation is primarily caused by the utilization of the frequency domain representation by the direct method. Frequency spectra of the segments and later the power spectra are calculated by the *fft* function. The bispectrum is calculated according to Eq.6.

$$\hat{B}_3^i(\omega_1, \omega_2) = \frac{1}{\Delta^2} F^i(\omega_1)F^i(\omega_2)F^{i*}(\omega_1 + \omega_2) \quad (6)$$

where  $F^i(\omega)$  is the Fourier transform of each record, \* denotes the complex conjugate and  $\Delta$  is the spacing between the frequency samples in the bispectrum domain. The average bispectrum is obtained by dividing the sum of the bispectra of the individual segments by the number of segments (Eq.7).

$$\hat{B}_3(\omega_1, \omega_2) = \frac{1}{K} \sum_{i=1}^K \hat{B}_3^i(\omega_1, \omega_2) \quad (7)$$

Finally, bicoherence is estimated by normalizing the magnitude squared bispectrum by the squared power spectrum (Eq. 8).

$$Bic(\omega_1, \omega_2) = \frac{|B(\omega_1, \omega_2)|^2}{P(\omega_1)P(\omega_2)P(\omega_1 + \omega_2)} \quad (8)$$

where  $B(\omega_1, \omega_2)$  is the final estimate of the bispectrum and  $P(\omega)$  is the power spectrum.

### III. RESULTS

The results of the power spectrum and bicoherence analysis for each spontaneous and stimulated burst are separately studied. Fig. 4 demonstrates the results of some particular bursts. Average results of stimulated and spontaneous bursts from different bipolar channel combinations are shown in Fig. 5.

### IV. DISCUSSIONS AND CONCLUSIONS

Phase synchronization between the frequency components around 10 Hz and 0.5 Hz during EEG burst suppression was previously discussed by Steriade [1; 14; 15]. At the beginning of this research, the principal aim was stating

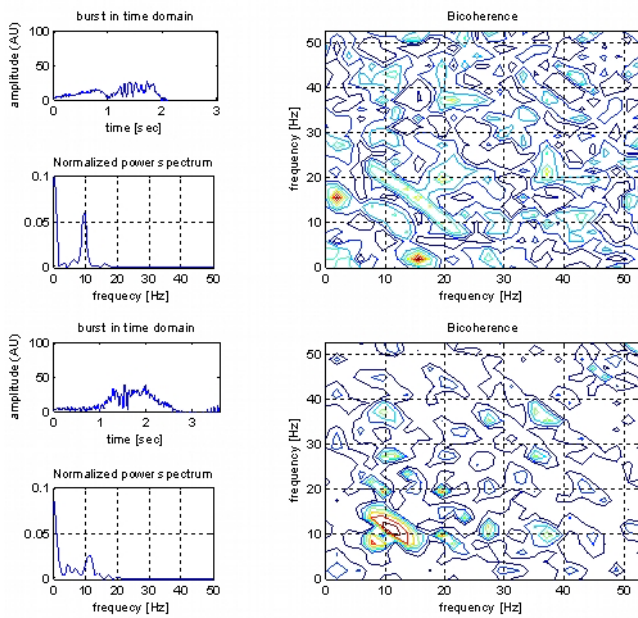


Fig. 4 Power spectrum and bicoherence demonstration of selected bursts.

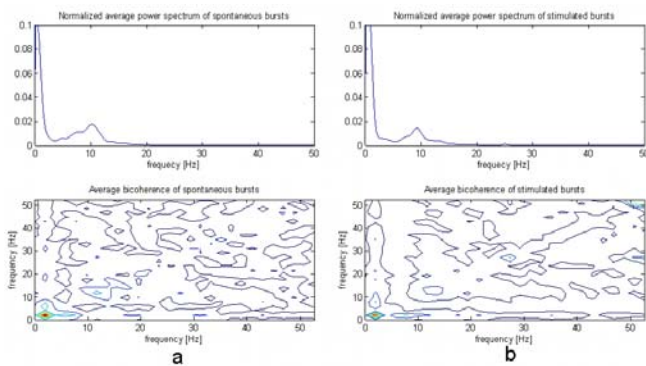


Fig. 5 a) Averaged power spectrum and bicoherence results for spontaneous bursts from channel F4-C4 b) Averaged power spectrum and bicoherence results for stimulated bursts from channel F3-C3.

these phase relations by analyzing third order spectrum characteristics of the signal.

Bispectrum detects certain phase couplings of unsophisticated signals precisely; however the method provides ambiguous results in the case of studying more complex signals as in this study. Despite the variety in bicoherence results for individual bursts, there is no significant difference observed regarding the type of the bursts. In other means spontaneous and stimulated bursts can not be classified based on the bicoherence results. Finally, in case of

having reliable method for detecting synchrony, stating phase relations of burst patterns during anesthesia is still a feasible research. Further studies may address cross-bicoherence between different channels or phase synchronization during anesthesia infused by different anesthetics.

## REFERENCES

1. Steriade M, Amzica F, Contreras D et al. (1994) Cortical and thalamic cellular correlates of electroencephalographic burst-suppression. *Electroencephalography and Clinical Neurophysiology* 90:1-16
2. Witte H, Schack B, Helbig M et al. (2000) Quantification of transient quadratic phase coupling within EEG burst patterns in sedated patients during electroencephalic burst-suppression period. *Journal of Physiology* 94:427-434
3. Witte H, Schelenz Ch, Specht M et al. (1999) Interrelations between EEG frequency components in sedated intensive care patients during burst-suppression period. *Neuroscience Letters* 260:53-56
4. Hadjileontiadis L J, Rekanos I T, Panas S M, (2006) Higher-order statistics, *Encyclopedia of Biomedical Engineering*. Wiley and Sons, New York
5. Huber P J, Kleiner B, Gasser T et al. (1971) Statistical methods for investigating phase relations in stationary stochastic process. *IEEE Transactions on Audio Electroacoustic* 19:78-86
6. Ademoglu A, Demiralp T (1992) Quadratic phase coupling of electroencephalogram (EEG) and evoked potentials (EP). *Proc. of International Biomedical Engineering Days, 1992* pp 146-150
7. Haejeong P, Kwangsuk P (1994) A study on the stochastic properties of the EEG using bicoherence. *IEEE/EMBS Proc. vol.2 16<sup>th</sup> Annual International Conference, 1994* pp. 1314-1315
8. Akgül T, Sun M, Scabassi R J et al. (2000) Characterization of sleep spindles using higher order statistics and spectra. *IEEE Transactions on Biomedical Engineering* 47(8):997-1009
9. Huotari A-M, Koskinen M, Suominen K et al. (2004) Evoked EEG patterns during burst suppression with propofol. *British Journal of Anaesthesia* 92(1):18-24
10. Hagihira S, Takashina M, Mori T et al. (2004) Bispectral analysis gives us more information than power spectral-based analysis. *British Journal of Anaesthesia* 92(5):772-773
11. Nikiyas C L, Mendel J M (1993) Signal processing with higher-order spectra. *IEEE Signal Processing Magazine* 10:10-37
12. Nikiyas C L, Raghuveer M R (1987) Bispectrum Estimation: A Digital Signal Processing Framework. *Proc. IEEE* 75:869-891
13. Ananthram Swami, HOSA – Higher Order Spectral Analysis Toolbox at <http://www.mathworks.com>
14. Steriade M, Gloor P, R. Llinas R R et al. (1990) Basic mechanisms of cerebral rhythmic activities. *Electroencephalography and clinical Neurophysiology* 76:481-508
15. Steriade M (1993) Cellular substrates of brain rhythms, *Encephalography: Basic Principles, Clinical Applications and Related Fields*. Williams & Wilkins

Author: Fikret Emre Kapucu  
 Institute: Tampere University of Technology  
 Street: Biolaaketieteen Tekniikan Laitos  
 City: Tampere PL 692 33101  
 Country: Finland  
 Email: emre.kapucu@tut.fi



# Rhythmic Fluctuations in Intracellular $Mg^{2+}$ in Spontaneously Beating Cultured Cardiac Myocytes

K. Kawahara, R. Sato, D. Matsuyama and S. Iwabuchi

Graduate School of Information Science & Technology/Laboratory of Cellular Cybernetics, Hokkaido University, Sapporo, Japan

**Abstract** — Magnesium ions ( $Mg^{2+}$ ) play fundamental role in cellular function, but the cellular dynamic changes of intracellular  $Mg^{2+}$  remains poorly delineated. In this study, we performed noise analysis of the fluctuations in the concentration of intracellular  $Mg^{2+}$  in spontaneously beating cultured cardiac myocytes from neonatal rats. The concentration of intracellular  $Mg^{2+}$  was estimated by loading of cells with either Mg-fluo4/AM or KMG-20/AM. The results revealed that the intensity of Mg-fluo-4 or KMG-20 fluorescence cyclically fluctuated in association with rhythmic contraction of cardiac myocytes. In addition, the simultaneous measurement of Fura2 and Mg-fluo-4 fluorescence revealed that there were phase differences between the dynamics of two signals, suggesting that the cyclic changes in the Mg-fluo-4 or KMG-20 fluorescent intensity actually reflected the changes in intracellular  $Mg^{2+}$ . Treatment of cultures with 2,3-butanedione monoxime (BDM), a reversible blocker of cardiac contraction, for 20 min resulted in the complete termination of spontaneous rhythmic contractions while both  $Ca^{2+}$  and  $Mg^{2+}$  oscillations were still observed, suggesting that the intracellular  $Mg^{2+}$  oscillation did not result from mechanical movements in association with the spontaneous rhythmic contraction of cardiac myocytes. The present study demonstrated that the concentration of intracellular  $Mg^{2+}$  changed in association with spontaneous, cyclic contractions and intracellular  $Ca^{2+}$  oscillation of cardiac myocytes. Noise analysis of the subtle changes in the fluorescence intensity may lead to the elucidation of novel functional roles played by changes in intracellular  $Mg^{2+}$  in cells.

**Keywords** — cardiac myocytes, spontaneous beating,  $Ca^{2+}$  oscillation,  $Mg^{2+}$  oscillation

## I. INTRODUCTION

The magnesium ion,  $Mg^{2+}$ , is one of the most abundant divalent cations within mammalian cells [1]. Although much is now known about the pathways responsible for the regulation of intracellular  $Ca^{2+}$ , the factors affecting intracellular  $Mg^{2+}$  remain poorly understood [2], mostly because the techniques available for measuring  $Mg^{2+}$  are a far cry from those available for measuring other cations [1]. Another important reason is that the concentration of free  $Mg^{2+}$  in cells is high, several orders of magnitude greater than that of  $Ca^{2+}$  or  $H^+$ . Therefore, even large changes in intracellular  $Mg^{2+}$  represent only a small fraction of the background concentration [1]. Previous studies, however, have revealed

that intracellular free  $Mg^{2+}$  plays a fundamental role in a variety of cell functions. Changes in the concentration of intracellular  $Mg^{2+}$  are involved in the modulation of the activity of L-type  $Ca^{2+}$  channels [3],  $Na^+/Ca^{2+}$  exchangers [4], cardiac ryanodine receptors in the sarcoplasmic reticulum [5], and mitochondrial  $F_1F_0$ -ATPase/synthase [6]. Thus, it seems increasingly important to clarify the changes in the concentration of intracellular  $Mg^{2+}$ .

In this study, we performed a noise analysis of the fluctuations in the concentration of intracellular  $Mg^{2+}$  in spontaneously beating cultured cardiac myocytes from neonatal rats. Here we show that the concentration of intracellular  $Mg^{2+}$  possibly changes in association with spontaneous, cyclic contractions and the intracellular  $Ca^{2+}$  oscillation of cardiac myocytes.

## II. MATERIALS & METHODS

### A. Culture of cardiac myocytes

The method of culture was described elsewhere in detail [7-9]. In short, cardiac myocytes were prepared from ventricles of 1 to 3-day old neonatal Wistar rats removed after decapitation. The ventricles were rinsed in a 25 mM HEPES-buffered minimum salt solution (MSS) to remove contaminating blood cell components and then minced with scissors into fragments to be digested with 0.1% collagenase (Wako Chemical, Tokyo, Japan) in MSS at 37 °C for 10 min. The digested fragments were centrifuged at 1000 rpm for 2 min (LC-100, TOMY, Japan) and precipitated cell components were washed twice with MSS to terminate the effects of collagenase. The cell components were suspended in MCDB 107 (Research Institute for Functional Peptides, Yamagata, Japan) containing 5% FCS (MBL, Nagoya, Japan), and then passed through a wire mesh screen (90  $\mu$ m porosity) to remove large aggregates of cells; the filtered suspension contains cardiac myocytes and fibroblasts. To separate cardiac myocytes from fibroblasts based on the selective adhesion technique, the cell suspension was poured into petri dishes ( $\phi$  60 mm, Falcon), and incubated for 60 min at 37 °C, in 5%  $CO_2$  and 95% air. By virtue of the procedure, most of the fibroblasts adhere to the dish. After the incubation, the suspension, mostly containing

cardiac myocytes, was collected. The suspension was centrifuged at 700 rpm for 5 min to separate the remaining blood cell components in the supernatant. The precipitated cells were resuspended in MCDB 107 containing 5% FCS, transferrin (10 µg/mL, Sigma, St. Louis, MO), and insulin (10 µg/mL, Yamanouchi, Tokyo, Japan). The cell suspension was passed through a fine wire mesh screen (25 µm porosity) to remove remaining small aggregates of myocytes, and finally the isolated myocytes remaining were cultured at a density of about  $3.0 \times 10^5$  cells/ml in a petri dish ( $\phi$  30 mm, Falcon) coated beforehand with fibronectin (10 µg/mL, Sigma).

### B. Measurement of cellular Mg<sup>2+</sup> and Ca<sup>2+</sup>

For the measurement of changes in cytosolic free Mg<sup>2+</sup> and Ca<sup>2+</sup>, Mg-fluo-4/AM or KMG-20/AM, and Fura2/AM were used, respectively. For the simultaneous measurement of cellular Mg<sup>2+</sup> and Ca<sup>2+</sup>, cardiac myocytes were first loaded with the fluorescent calcium indicator by incubating them with Fura2/AM (5 µM; Molecular probes, Eugene, OR, USA) in MCDB medium for 40 min at 37 °C, in 5% CO<sub>2</sub> and 95% air. After a washout with PBS, the cardiac myocytes were then incubated with Mg-fluo-4/AM (10 µM; Molecular probes) in MCDB for 40 min at 37 °C, in 5% CO<sub>2</sub> and 95% air. After another washout with PBS, the medium was replaced by MCDB and incubated for 20 min at 37 °C, in 5% CO<sub>2</sub> and 95% air. The cells in a dish were then placed on the stage of an inverted microscope (IX 70, Olympus, Tokyo, Japan). Fura2 was excited at 340/380 nm, and emission intensity was measured at 520 nm. Mg-fluo-4 was excited at 488 nm, and the emission intensity was measured at 520 nm. In some of the experiments, the concentration of intracellular Mg<sup>2+</sup> was also estimated by using KMG-20/AM (Wako Chemical, Tokyo, Japan). Cardiac myocytes were incubated with KMG-20/AM (10 µM) in MCDB for 40 min at 37 °C, in 5% CO<sub>2</sub> and 95% air. KMG-20 was excited at 440 nm, and the emission intensity was measured at 515 nm. Fluorescent images were acquired with a cooled CCD camera (C4880-80; Hamamatsu Photonics, Hamamatsu, Japan) through an image intensifier (C8600-05; Hamamatsu Photonics) to amplify the fluorescence. An analysis of the acquired images was done with an image processing and measuring system (AQUACOSMOS; Hamamatsu Photonics). Fluorescent intensity (F) was normalized with the initial value (F<sub>0</sub>), and the changes in the relative fluorescent intensity (F/F<sub>0</sub>-1) from which both a DC component and a high-frequency noise were removed with a band-pass filter (0.1–2.0 Hz) using a software for the time series analysis (Kyowa Electronic Instruments, Tokyo, Japan) to estimate changes in the

concentrations of intracellular free Ca<sup>2+</sup> and Mg<sup>2+</sup>. In some cases, DC recordings were made to estimate the changes in Mg-fluo-4 fluorescence with time.

### C. Statistics

The data are expressed as the mean±S.D. Comparisons were performed using a paired t-Test. A *P* value of less than 0.05 was considered statistically significant.

## III. RESULTS

Isolated and cultured neonatal cardiac myocytes started to contract spontaneously and cyclically usually after 2 to 4 days *in vitro* (2-4 DIV). We first investigated whether the intensity of Mg-fluo-4 fluorescence actually fluctuated in spontaneously beating cultured cardiac myocytes (Fig. 1). At first sight, the Mg-fluo-4 fluorescence of cardiac myocytes did not seem to fluctuate at all (Fig. 1A). However, the relative Mg-fluo-4 fluorescence (Fig. 1B) as well as an auto-correlation analysis of the time series (Fig. 1C) suggested regularity to the fluctuations. A spectral analysis of the de-trended fluorescent signals revealed that the dominant frequency of the fluctuations was about 0.6 Hz (Fig. 1D).

We next tried to clarify whether the fluctuations in fluorescent intensity were derived from the changes in the concentration of intracellular Mg<sup>2+</sup> by exploiting the simultaneous measurement of changes in the fluorescent intensity of Fura2 and Mg-fluo-4 in cardiac myocytes (Fig. 2). A spec-

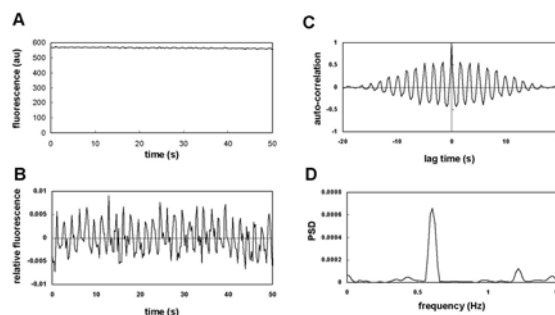


Fig. 1 Fluctuations in the intensity of Mg-fluo-4 fluorescence in spontaneously beating cardiac myocytes in cultures. The Mg-fluo-4 fluorescence in cultured neonatal cardiac myocytes at 4 days *in vitro* (4 DIV) was measured. Cyclic changes in the intracellular concentration of free Mg<sup>2+</sup> were estimated by loading myocytes with the fluorescent Mg<sup>2+</sup> probe Mg-fluo-4/AM (10 µM). Figures A & B show changes in the intensity of Mg-fluo-4 fluorescence with time. Auto-correlation analysis of the changes in the intensity of Mg-fluo-4 fluorescence (C) revealed the fluctuations had some periodicity. A spectral analysis of the fluctuations demonstrated that the dominant frequency of the cyclic changes in the intensity of Mg-fluo-4 fluorescence was about 0.6 Hz (D).

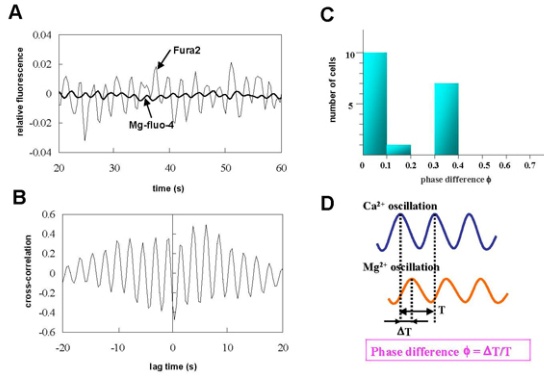


Fig. 2 Simultaneous measurement of fluctuations in the intensity of Fura2 and Mg-fluo-4 fluorescence in spontaneously beating cardiac myocytes in cultures. Cells were double-loaded with Fura2/AM (5  $\mu$ M) and Mg-fluo-4/AM (10  $\mu$ M). Figures A and B indicate the existence of a phase difference between the cyclic changes in Fura2 and Mg-fluo-4 fluorescence. Figure C shows the distribution of the phase difference between the cyclic changes in Fura2 and Mg-fluo-4 fluorescence ( $n=18$  cells in 6 different cultures).

tral analysis of fluctuations of Fura2 and Mg-fluo-4 fluorescent intensity in single cardiac myocytes demonstrated a common dominant frequency of about 0.45 Hz (data not shown). However, there was a phase difference between the two signals (Fig. 2A). A cross-correlation analysis also showed the existence of a phase difference (Fig. 2B). Figure 2C shows the distribution of the phase difference between Fura2 and Mg-fluo-4 fluorescence in 18 cells tested. Phase difference  $\phi$  was calculated from the formula,  $\phi = \Delta T / T$ , as is schematically illustrated in Fig. 2D. These results further supported that fluctuations in Mg-fluo-4 fluorescence reflected changes in the concentration of  $Mg^{2+}$ , not of  $Ca^{2+}$ .

The amplitude of cyclic changes in Mg-fluo-4 fluorescence was very small compared with the DC level of the fluorescence due to the relatively high resting concentration of intracellular  $Mg^{2+}$ , about 1.0 mM [10], as is evident from Fig. 1A. Although the fluctuations in the fluorescence of Mg-fluo-4 reflected changes in the concentration of intracellular  $Mg^{2+}$  in association with the spontaneous contraction of cardiac myocytes, the possible contribution of mechanical factors such as changes in cell volume caused by spontaneous rhythmic contraction to the changes in fluorescence still remained to be solved; that is, it is possible that the fluctuations in Mg-fluo-4 fluorescence were an artifact. Our previous studies have demonstrated that treatment of cultures with an uncoupler of E-C coupling results in a cessation of the spontaneous contraction of cardiac myocytes, but does not abolish cyclic changes in the concentration of intracellular  $Ca^{2+}$  [8, 11]. Therefore, we next performed a simultaneous measurement of Fura2 and

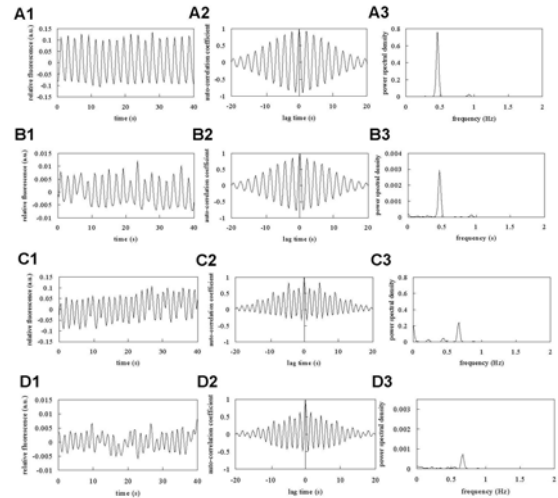


Fig. 3 Persistence of rhythmic changes in both Fura2 and Mg-fluo-4 fluorescence in quiescent cultured cardiac myocytes treated with BDM. The spontaneous rhythmic contraction of a cultured cardiac myocyte was almost completely terminated by the loading of cells with 7.5 mM BDM for 20 min. Figures A1-A3 and C1-C3 show the analysis of Fura2 fluorescence of the cell before the onset of BDM treatment (control) and 20 min after the treatment, respectively. Figures B1-B3 and D1-D3 show the analysis of Mg-fluo-4 fluorescence of the same cell before the onset of BDM treatment (control) and 20 min after the treatment, respectively.

Mg-fluo-4 fluorescence when the spontaneous contraction of cardiac myocytes was terminated by treatment of cultures with 7.5 mM 2,3-butanedione monoxime (BDM), a blocker of cardiac contraction that does not block electrical activity [12] (Fig. 3).

Treatment of cultures with 7.5 mM BDM terminated spontaneous rhythmic contractions in almost all the cardiac myocytes, but cyclic changes in both Fura2 (Figs. 3C1-3C3) and Mg-fluo-4 (Figs. 3D1-3D3) fluorescence were still observed. The termination of spontaneous contractions did not result in significant changes in the amplitude or the interval of Fura2 and Mg-fluo-4 fluorescence (data not shown). These results suggested that mechanical factors caused by spontaneous cyclic contraction were not responsible for the cyclic changes in Mg-fluo-4 fluorescence.

#### IV. DISCUSSION

The present noise analysis of the fluctuations in Mg-fluo-4 and KMG-20 fluorescence showed that the concentration of intracellular  $Mg^{2+}$  possibly changed in association with spontaneous, cyclic contractions of cardiac myocytes. The question then arises as to what mechanisms are responsible for the cyclic changes in the concentration of intracellular  $Mg^{2+}$ . The exact mechanisms are currently unknown, but one possibility is that the cyclic changes of intracellular

Mg<sup>2+</sup> result from the rhythmic contraction-associated changes in the concentration of intracellular Ca<sup>2+</sup>. Although the termination of spontaneous rhythmic contractions of cardiac myocytes by treatment with BDM, an uncoupler of E-C coupling, did not affect the cyclic changes in Ca<sup>2+</sup> or Mg<sup>2+</sup> (Fig. 3), treatment of cardiac myocytes with 1.0 μM of verapamil, a blocker of L-type Ca<sup>2+</sup> channels, for 20 min resulted in the suppression of cyclic Mg<sup>2+</sup> changes (data not shown). This concentration of verapamil almost completely terminated the spontaneous rhythmic contraction and Ca<sup>2+</sup> oscillation [8]. In addition, the peak in the cyclic changes of intracellular Mg<sup>2+</sup> was almost always delayed by the peak in those of intracellular Ca<sup>2+</sup> (phase delay) (Fig. 2C). In some of the cardiac myocytes examined, the phase difference between the peaks of Mg<sup>2+</sup> and Ca<sup>2+</sup> was zero, but Mg<sup>2+</sup> peaks never preceded the Ca<sup>2+</sup> peaks (Fig. 2C), suggesting that the cyclic changes of intracellular Mg<sup>2+</sup> were caused by the rhythmic changes in the concentration of intracellular Ca<sup>2+</sup>. If this is the case, the question then arises as to what mechanisms are responsible for the Ca<sup>2+</sup>-induced changes in intracellular Mg<sup>2+</sup>. Further studies will be needed to clarify this issue.

## V. CONCLUSION

The present noise analysis of the fluctuations in the intensity of fluorescent Mg<sup>2+</sup> indicators has demonstrated that the concentration of intracellular Mg<sup>2+</sup> possibly changes cyclically in association with rhythmic contractions and intracellular Ca<sup>2+</sup> oscillations in spontaneously beating cardiac myocytes in culture. This finding suggests that the concentration of intracellular Mg<sup>2+</sup> is dynamically regulated, and such cellular Mg<sup>2+</sup> dynamics are crucially involved in the regulation of a variety of cell functions.

## ACKNOWLEDGMENT

This work was supported by grants-in-aid for scientific research from the Ministry of Education, Science, and Culture of Japan (16300145, 19300153) to KK.

## REFERENCES

1. Romani A, Scarpa A (1992) Regulation of cell magnesium. *Arch Biochem Biophys* 298:1-12
2. Murphy E (2000) Mysteries of magnesium homeostasis. *Circ Res* 86:245-248
3. White RE, Hartzell HC (1988) Effects of intracellular free magnesium on calcium current in isolated cardiac myocytes. *Science* 239:778-780
4. Wei S-k, Quigley JF, Hanlot SU et al. (2002) Cytosolic free magnesium modulates Na/Ca exchange currents in pig myocytes. *Cardiovasc Res* 53:334-340
5. Valdivia HH, Kaplan JH, Ellis-Davies GCR et al. (1995) Rapid adaptation of cardiac ryanodine receptors: Modulation by Mg<sup>2+</sup> and phosphorylation. *Science* 267:1997-2000
6. Ko YH, Hong S, Pedersen PL et al. (1999) Chemical mechanism of ATP synthase. *J Biol Chem* 274:28853-28856
7. Kawahara K, Hachiro T, Yokokawa T et al. (2006) Ischemia/reperfusion-induced death of cardiac myocytes: possible involvement of nitric oxide in the coordination of ATP supply and demand during ischemia. *J Mol Cell Cardiol* 40:35-46
8. Nakayama Y, Kawahara K, Yoneyama M et al. (2005) Rhythmic contraction and intracellular Ca<sup>2+</sup> oscillatory rhythm in spontaneously beating cultured cardiac myocytes. *Biol Rhythm Res* 36:317-326
9. Nakayama Y, Kawahara K, Hachiro T et al. (2007) Possible involvement of ATP-purinoreceptor signaling in the intercellular synchronization of intracellular Ca<sup>2+</sup> oscillation in cultured cardiac myocytes. *BioSystems* 90:179-187
10. Silverman HS, Lisa DF, Hui RC et al. (1994) Regulation of intracellular free Mg<sup>2+</sup> and contraction in single adult mammalian cardiac myocytes. *Am J Physiol* 266:C222-C233
11. Kawahara K, Nakayama Y (2007) Fluctuations in the concentration of extracellular ATP synchronized with intracellular Ca<sup>2+</sup> oscillatory rhythm in cultured cardiac myocytes. *Chronobiol Intern* 24:1-14
12. Cheng Y, Mowrey K, Efimov IR et al. (1997) Effects of 2,3-butanedione monoxime on atrial-atrioventricular nodal conduction in isolated rabbit heart. *J Cardiovasc Electrophysiol* 8:790-802

The address of the corresponding author:

Author: Koichi Kawahara, Prof.  
 Institute: Hokkaido University  
 Street: Kita 14, Nishi 9, Kita-ku  
 City: Sapporo  
 Country: Japan  
 Email: kawahara@ist.hokudai.ac.jp

# Importance of Nonlinear Signal Processing in Biomedicine

W. Klonowski<sup>1,2</sup>

<sup>1</sup> Institute of Biocybernetics and Biomedical Eng., Polish Academy of Sciences, Warsaw

<sup>2</sup> GBAF-SENSATION, Medical Research Center, Polish Academy of Sciences, Warsaw

**Abstract** — Many biomedical researchers are ‘infected with HLV – “Human Linearity Virus”. They ‘think linearly’, and ignore the facts that human body, and, particularly, human brain are complex nonlinear systems. These complex nonlinear systems generate non-stationary nonlinear signals, and appropriate analysis of such signals does need new nonlinear methods.

**Keywords** — Nonlinear Dynamics, Deterministic Chaos, Higuchi’s Fractal Dimension, Symbolic Methods

## I. INTRODUCTION

We do need new nonlinear methods of Biosignal analysis; otherwise while living in XXI century, we will still be plunged in XIX century ‘linear science’ of Fourier and Markov.

Linear methods such as FFT may give very misleading results. E.g. if in a measured signal one observes regular waves of frequency 12 Hz with amplitude modulated with frequency 1 Hz, then Fourier decomposition of this signal leads to two components, each of amplitude equal half of that of the analyzed signal, with frequencies 11 Hz and 13 Hz respectively:

$$\begin{aligned} [2 \cdot \cos(2\pi \cdot 1 \cdot t)] \cdot \sin(2\pi \cdot 12 \cdot t) = \\ = \sin(2\pi \cdot 11 \cdot t) + \sin(2\pi \cdot 13 \cdot t) \end{aligned}$$

while the basic frequency of the analyzed signal (12 Hz) does not appear at all in the Fourier spectrum. One also often forgets that methods like FFT do not work properly for nonstationary signals.

## II. NONLINEAR VS LINEAR METHODS

Nonlinear models and nonlinear methods of data processing are much more appropriate in Biomedicine than ‘classical’ linear methods. Even European Parliament has emphasized the importance of nonlinear dynamics, in particular of the deterministic chaos methods, in biomedical research [1]. Unfortunately, linear methods are rooted in medical tradition whereas nonlinear methods are not. That is why in 2007 I founded a new *open access* journal *Nonlinear Biomedical Physics* [2].

We use methods of nonlinear dynamics, deterministic chaos theory, and of symbolic dynamics in analysis of biosignals, in particular of EEG and HRV (examples of application of nonlinear signal processing in Biomedicine and Biomedical Engineering cf. [3], [4]). These methods may be also applied in hybrid modeling of biomedical systems for improving quality of life and elimination of experiments on animals [5].

Here the following case studies are presented:

1. Monitoring the depth of anaesthesia and of sedation;

Brain electrical activity in patients was measured continuously with an A-2000 BIS Monitor (software version: XP, Aspect Medical Systems, Newton, MA, USA) and bispectral index (BIS) was recorded every 10 seconds. The bispectral index is commonly accepted as a measure of hypnosis during anaesthesia, but the algorithms the BIS Monitor uses are not in public domain. In addition, depth of anaesthesia was continuously tested and classified by a specialist-anaesthesiologist to six OAA/S (Observer’s Assessment of Alertness and Sedation) levels; patients were judged to be conscious if the OAA/S score was between 3 – 5 and unconscious if the OAA/S score was less than 3. We analyzed EEG-signals post-operatively. The results were averaged every 10 s for epochs 30 s long. Since  $1 \leq D_f \leq 2$  the fractal dimension value has been presented to adjust the scale for better comparison with BIS. We demonstrated that the fractal dimension corresponds to the depth of anaesthesia and we applied for a patent for this new method of anaesthesia monitoring. In addition we have used a new symbolic dynamics method to calculate another measure of the depth of anaesthesia, called SDI.

2. Bright Light Therapy (BLT) and Seasonal Affective Disorder;

When an eyes-opening event occurs fractal dimension of EEG-signal grows from 1.1–1.3 to 1.5–1.6 in the occipital channels and even to 1.8 in the frontal channels – this increase is denoted  $\Delta_o$ ; when eyes remain open fractal dimension diminishes, to rise again when an eyes-closing event occurs; when eyes remain closed, it diminishes again – this decrease is denoted  $\Delta_c$ . We define  $\Delta_o/\Delta_c$  as open-/closed-eyes fractal dimension ratio (FD-ratio). We observed that in EEG of healthy subjects this ratio shows values close to 1. For SAD patients the FD-ratio was compared with HDRS before and after BLT.

### 3. Analysis of posturographic signals.

Position of the center-of-mass in relation to the base of support (COM signal) and that of the center of foot pressure (COP signal), both of  $x$  (anteroposterior, AP) and  $y$  (mediolateral, ML) components of each - may contribute towards better understanding of postural control. - cf. [4] and references therein).

### 4. Evoked EEG and photo-stimulation.

Higuchi's fractal dimension may also be used for analysis of biosignals evoked by external stimuli, e.g. of EEG evoked by photo-stimulation that is routinely performed in EEG-examinations, in increasing as well as in decreasing frequency order (from 3 Hz to 27 Hz every 3 Hz) of the stimuli; each stimulus consisting of light flashing for 5 seconds with given frequency; there is one-second break between subsequent stimuli. Performing fractal analysis one can notice clear dependence of fractal dimension on frequency of photo-stimulation with the maximum for 18 Hz. Higher frequencies cause more rapid changes in fractal dimension value than lower frequencies. In power spectra of the evoked EEG one cannot notice practically any relative differences for various frequencies of stimulation that are so clearly noticeable in fractal dimension - cf. [4] and references therein;

### 5. Influence of electromagnetic fields generated by cellular phones.

While linear spectral analysis suggests that Influence of electromagnetic fields (EMF) generated by cellular phones are eliminated by using a 'neutralising protective device (NPD)' fractal analysis shows that EMF of cellular phones have rather small influence on EEG of majority of persons (thanks God!!), no matter if the phone is equipped with such an 'NPD' or used without it, while there are some persons (1 out of 6 in our investigation) who might be seriously influenced by EMF of a cellular phone even one equipped with an 'NPD' - cf. [4] and references therein).

## III. CONCLUSIONS

Unlike it is often thought by HLV-infected scientists and doctors, we will show that many nonlinear methods must not be more complicated than widely used linear methods, like FFT or wavelet decomposition. The benefits for patients may include better diagnostics and better assessment of applied therapy. Benefits for basic and ap-

plied research are obvious. For example, geocentric system as proposed by Ptolemy seemed to have worked quite well and everybody could observe 'obvious fact' that Sun turns around Earth; it took years and years to accept genius of Copernicus and his not so obvious model of Solar System. Linear models and linear methods of biosignal processing may be compared with geocentric model. .

## ACKNOWLEDGMENT

GBAF acknowledges support by European Union FP6. IP SENSATION under grant IST-507231 and by SPUB of the Polish Ministry of Education and Science. This work was partially supported by IBBE PAS under St/24/2007 and by grant COST/190/2006 (142/COS/2006/01) of the Polish Ministry of Science and Higher Education.

## REFERENCES

1. European Parliament, Directorate General for Research, Division Industry, Research and Energy, Scientific and Technological Options Assessment (STOA) (2001) The Physiological and Environmental Effects of Nonionising Electromagnetic Radiation, Final Study. *Working document for the STOA Panel PE 297.574/Fin.St. Luxembourg*, 5, 14, [http://europarl.eu.int/stoa/publi/pdf/00-07-03\\_en.pdf](http://europarl.eu.int/stoa/publi/pdf/00-07-03_en.pdf)
2. *Nonlinear Biomedical Physics*, BioMed Central, London, <http://www.nonlinearbiomedphys.com/edboard>
3. Klonowski W (2007) The Metaphor of "Chaos", in: *Systems Biology. Principles, Methods and Concepts*, Konopka AK, Ed., CRC Press, Boca Raton, London, New York, pp.115-138.
4. Klonowski W (2007) From conformons to human brains: an informal overview of nonlinear dynamics and its applications in biomedicine, *Nonlinear Biomedical Physics*, 1, 5, BioMed Central, London, <http://www.nonlinearbiomedphys.com/content/1/1/5> ;
5. Klonowski W., Stepien R, Darowski M, Kozarski M (2007): Chaotic Data Analysis and Hybrid Modeling for Biomedical Applications, in: 'Recent Advances in Stochastic Modeling and Data Analysis', Skiadas CH, Ed., World Scientific, Singapore, London, pp. 338-341

Author: Włodzimierz Klonowski  
 Institute: IBBE PAS  
 Street: 4 Trojdena St.  
 City: 02-109 Warsaw  
 Country: Poland  
 Email: [wklon@ibib.waw.pl](mailto:wklon@ibib.waw.pl); [wklon@gbaf.eu](mailto:wklon@gbaf.eu)

# An Intelligent Method for Identifying Cardiac Cycles from Tracheal Sounds during Sleep

A. Kulkas, E. Huupponen and S.-L. Himanen

Department of Clinical Neurophysiology, Medical Imaging Centre, Pirkanmaa Hospital District, Tampere, Finland

*Abstract* — The prevalence of sleep disorders is increasing and they are becoming more and more complex public health problems. Auscultation of the heart is a common procedure of medical practitioners, though it is highly subjective and depends on the expertise of the doctor. In this paper, we present a new method for identifying the cardiac cycles from the tracheal sound signal during sleep. Polysomnographic recordings of 4 female and 8 male subjects were analyzed. The tracheal sound signal was measured with a sampling rate of 11025 Hz. As the first step in the present development, the tracheal sound signal was low-pass filtered with a cut-off frequency of 50 Hz. Then, the Hilbert transform was performed to obtain the envelope, which was further smoothed with moving average filtering. Additionally, a local maximum signal was extracted from the smoothed envelope and cardiac cycles were detected at the time instances when the maximum signal value equaled the envelope value. Beat-to-beat intervals of the cardiac cycle were determined as the time between two consecutive cardiac cycle detections. The beat-to-beat intervals obtained with the developed method and from the reference method (electrocardiogram, R-R interval) were determined and collected to separate pools. Median values and 25% and 75% percentiles of beat-to-beat durations were extracted for evaluation. The method presented here provided high concordance with the reference method in all subjects. The developed method seems to be a promising tool for identifying cardiac cycles from tracheal sounds. Thus, analysis of tracheal sounds can be utilised in monitoring of the cardiovascular system with methods such as presented here. Analysis of tracheal sounds offers an interesting modality for evaluating the cardiovascular system during sleep.

*Keywords* — Tracheal sound, cardiac cycle, Hilbert transform, automated detection, beat-to-beat interval.

## I. INTRODUCTION

Heart sound signal is perhaps the most traditional biomedical signal indicated by the fact that stethoscope is widely used by physicians. Sounds recorded from the chest have been reported to have a frequency band extending up to 250 Hz [1]. This band contains muscle, breathing and heart activity. The sounds recorded from the chest are filtered considerably by the tissues. Sounds recorded over the trachea are considered to be less filtered and are therefore reported to contain frequencies up-to 1200 Hz [1]. The

tracheal sounds originate from the vibrations of the tracheal wall and surrounding soft tissues, caused by pressure fluctuations [1,2]. From the sounds recorded over the trachea, first (S1) and second (S2) heart sounds stemming from the heart valve activity [3] can be identified as low frequency vibrations [4].

The prevalence of sleep disorders is increasing and they are becoming more and more complex public health problems. Patients with respiratory disturbances during sleep have a higher risk of coronary artery disease, stroke, myocardial infarction and hypertension [5]. Heart rate variability analysis (obtained from cardiac cycles) is a well-established non-invasive method applied extensively in general medicine [6] and also in sleep medicine. The objective of the present work was to develop a new method for detecting cardiac cycles utilising tracheal sounds during sleep.

## II. METHODS

### A. Recordings

In the present study, the data from polysomnographic recordings of 4 female and 8 male subjects were analyzed. The median age of the subjects was 35.5 years (range 16 – 53), the median body mass index (BMI) was 24.7 kg/m<sup>2</sup> (range 22 – 44.6). All the polysomnograms were recorded in the sleep laboratory of Tampere university hospital in the Pirkanmaa Hospital District and approved by the local ethical committee. A digital polysomnographic recorder Embla N7000 and Somnologica studio software (Medcare®, Iceland) were used as the recording system. The recording montage consisted of six electroencephalography derivations (Fp1-A2, Fp2-A1, C3-A2, C4-A1, O1-A2, O2-A1), two electro-oculography channels and submental electromyography (EMG), electrocardiography (ECG), nasal pressure, thermistor, thoracic and abdominal respiratory movements, body position, anterior tibialis muscle EMG, blood oxygen saturation (SaO<sub>2</sub>) and pulse rate by a finger pulse oximeter (Nonin XPOD®, Nonin Medical Inc, USA), transcutaneous measurement of carbon dioxide (TcCO<sub>2</sub>, Tina TCM4, Radiometer, Denmark), the Emfit sleep mattress (Emfit Ltd, Vaajakoski, Finland) and a tracheal sound recorder. The sampling rate of 1 Hz was used

for TcCO<sub>2</sub> measurements, 2 Hz for oximetry (SaO<sub>2</sub> and pulse), 10 Hz for respiratory movements, 500 Hz for ECG, 11025 Hz for tracheal sound and 200 Hz for all other signals.

Tracheal sound recordings were performed with a small electret microphone, Panasonic WM-60A (Matsushita, Osaka, Japan) The microphone has a 3 mm deep conical air cavity of 25 mm in diameter. The sensitivity of the microphone is 10 mV/Pa and the frequency range is 20 Hz - 20 kHz [7]. The microphone is attached to the skin in the suprasternal notch with an adhesive tape ring with additional taping on the top. The measured sound signal is amplified with a preamplifier unit. After that the signal is fed into a sound card USB Sound Blaster Audigy 2 NX (Creative Labs, Singapore) for 24-bit A/D conversion followed by USI-01 USB isolator (MESO, Mittweida, Germany) providing galvanic isolation between the patient and the recording equipment. SuperHeLSA software (Pulmer, Helsinki, Finland) records the raw signal from the sound card. For the analysis, the raw data is converted into Embla data format.

The visual scorings of the present work were performed in consensus of two experienced clinical neurophysiologists from the conventional polysomnography. Breathing was explored in more detail by analysing the flow shapes of the nasal pressure signal. Each inspiration was labeled either as a round (considered normal) or non-round (disturbed) flow signal shape [8,9]. A 10-min section of regular respiration was accepted when the percentage of round flow shapes exceeded 80%. One 10-min section of regular respiration was included in the analysis from each subject. Data recorded from one female and one male subject (totalling 1307 cardiac cycles) was used in the development stage of the algorithm (training data). Training subjects were randomly selected among genders. The recordings from 3 females and 7 males served as an independent test data (totalling 6863 cardiac cycles).

### B. The detection algorithm

In the present work, an algorithm for the identification heart sounds from the tracheal breathing sound signal is developed.

#### Step 1. Filtering of the tracheal sound signal

A 6001 tap finite impulse response (FIR) filter with a pass-band of 0-50 Hz is used to filter the raw sound signal, denoted as  $r(n)$ , where  $n$  denotes the discrete time index. The resulting signal is denoted as  $c(n)$ . The 3 dB cut-off frequency of the FIR filter is set at 55 Hz and the attenuation in the stop-band exceeds 85 dB. The band of 0-50 Hz preserves the low frequency heart sounds [10]

while excluding main tracheal breathing sound signal components [1].

#### Step 2. Envelope extraction

Hilbert transform for a continuous-time signal  $x(t)$  is defined as follows:

$$H\{x(t)\} = \frac{1}{\pi} \int_{-\infty}^{\infty} x(\tau) \frac{1}{t-\tau} d\tau. \quad (1)$$

A thorough presentation of the theory of the Hilbert transform is presented, for instance, in [11]. Here, the Hilbert transform is used to extract the envelope of the filtered sound signal  $c(n)$ . The  $c(n)$  is divided into 3-s segments, denoted as  $c_{seg}(n)$ , advancing at 1-s steps. Each segment is Hilbert transformed resulting in a 3-s segment  $c_H(n)$ . The corresponding envelope is obtained as follows:

$$c_e(n) = \sqrt{c_H(n)^2 + c_{seg}(n)^2}. \quad (2)$$

From  $c_e(n)$ , only the middle-most 1-s part is stored at each step. This overlapping processing is done to ensure an accurate result of the Hilbert transform (and the envelope) also at the edges of the stored 1-s segment. An example of the resulting envelope signal  $c_e(n)$  is shown in Fig. 1.

The  $c_e(n)$  is then smoothed and down-sampled with a moving average window of length 360 ms advancing at 2 ms steps. The resulting smoothed envelope signal is denoted as  $c_s(n)$ . The smoothing is an essential part of the

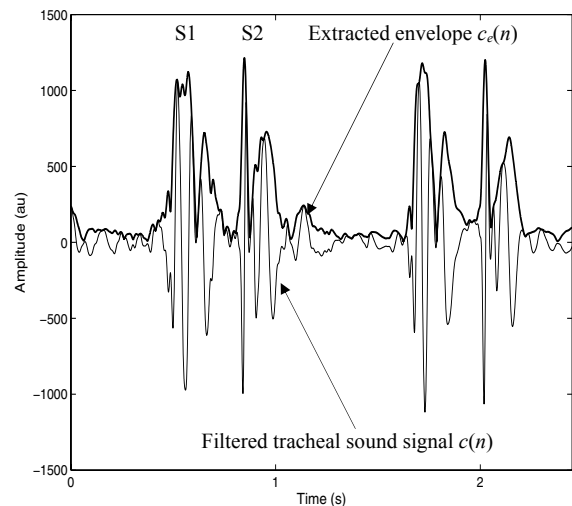


Fig. 1 Low-pass filtered tracheal sound signal  $c(n)$  and its envelope  $c_e(n)$ , obtained utilising the Hilbert transform. Both signals are presented during two cardiac cycles. "S1" and "S2" denote the first and second heart sounds, respectively.



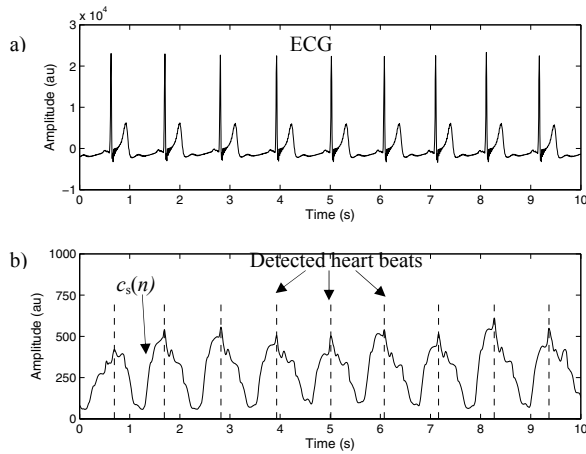


Fig. 2 Detection of cardiac sound peaks. ECG in panel a) and smoothed envelope  $c_s(n)$  in panel b) are seen during nine cardiac cycles. The detected cardiac sound peaks, labeled as “Detected heart beats”, are indicated with dashed vertical lines in panel b).

present development. The length of 360 ms was experimentally selected using the training data and it is in line with the time-scale of the cardiac cycle. The down-sampling from 11025 to 500 Hz was done here merely to conform with the reference method, ECG, sampled with 500 Hz.

### Step 3. Identification of cardiac sound peaks based on local maximum

First, a local maximum signal is extracted from the  $c_s(n)$  using a moving 0.5-s window. The resulting signal is denoted as  $c_{\max}(n)$ . A cardiac sound peak, indicating heart beat, is then identified as point where  $c_{\max}(n)$  equals  $c_s(n)$ . These are the peaks illustrated in Fig. 2 b). Length of 0.5-s was chosen based on the time-scales of the cardiac cycle and experiences on the training data.

### C. Performance evaluation

Reliability of the developed method was evaluated by comparing the beat-to-beat intervals of detected cardiac beats with the R-R-intervals determined from the reference method ECG. The duration of each beat-to-beat interval detected from tracheal sounds and from the reference method were determined and collected to separate pools. Median values and 25% and 75% percentiles were extracted for evaluation.

## III. RESULTS

An example of the detected beat-to-beat intervals obtained with the developed method and the reference method

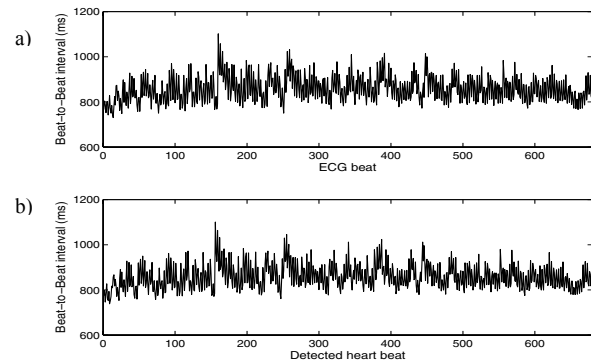


Fig. 3 An example of beat-to-beat intervals of a) ECG and b) the developed tracheal based sound method. The observed beat-to-beat interval variability of the two methods seems to correspond well even at individual cycle level.

is seen in Fig. 3. The beat-to-beat intervals concentrate around 900 ms in this example. The interval durations obtained with the developed method compare favorably with the reference method.

The results of the accuracy of the beat-to-beat interval determination can be seen in Fig. 4. There is considerable individual variation in the interval durations but despite of this the method is reliable in performance and accuracy among all subjects.

## IV. CONCLUSIONS

In the present work, a new tracheal sound based method for identifying the cardiac cycles during sleep was developed. The developed method is designed to work considering individual differences in the recorded sounds and offers high reliability and accuracy. Here the detection method was compared to the standard method of measuring beat-to-beat intervals through ECG signal [6,12].

The developed method is independent of sound amplitude levels and therefore aims to be independent on individual differences. One limitation of the method is that the cardiac sound phenomenon is not as unambiguous in the time localization as the R wave of the ECG signal. The developed method detects the cardiac cycles but the accuracy of the time localization of each individual beat should be explored further. In any case, already the present evaluation of the beat-to-beat intervals showed high concordance with the reference method ECG.

The prevalence of sleep disordered breathing increases and it is becoming a more and more complex public health problem [13-15]. Due to the adaptive nature of the developed method presented here and the simplicity of the recording equipment, it could perhaps be applied to a larger

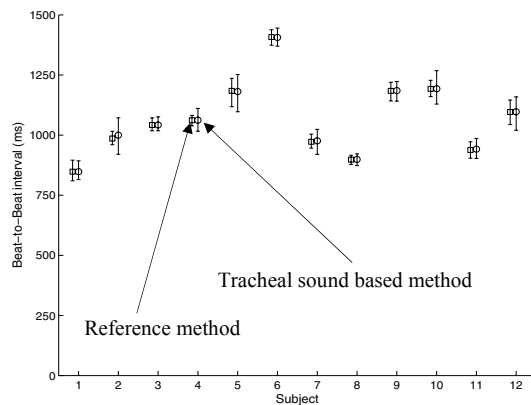


Fig. 4 Median durations and 25% and 75% percentiles of the beat-to-beat intervals derived from the reference method and from the developed method. Median values are indicated with squares and with circles, respectively. Median values of beat-to-beat intervals are seen to range from 800 to 1400 ms and despite this variability the method provides high concordance with the reference method.

clinical population to provide support for the diagnosis and treatment planning of sleep disorders. Computational analysis of tracheal sounds seems to offer an interesting modality for analyzing the cardiovascular system during sleep.

#### ACKNOWLEDGEMENTS

This study was financially supported by the National Technology Agency of Finland, the Research fund of the Tampere University Hospital, the Jenny and Antti Wihuri foundation, the Tampere Tuberculosis foundation, the Emil Aaltonen foundation, the Finnish Cultural foundation as well as the Instrumentarium Science foundation.

#### REFERENCES

1. Sovijärvi A, Malmberg L, Charbonneau G et al. (2000) Characteristics of breath sounds and adventitious respiratory sounds. *Eur Respir Rev* 10:591-596

2. Beck R, Rosenhouse G, Mahagnah M et al. (2005) Measurement and theory of normal tracheal breath sounds. *Ann Biomed Eng* 33:1344-1351
3. Kirby B, MacLeod K (2006) Clinical examination of the heart. *Medicine* 34:123-128
4. Kaniusas E, Pfurtner H, Saletu B (2005) Acoustical signal properties of cardiac/respiratory activity and apnea. *IEEE Trans Biomed Eng* 52:1812-1822
5. Roux F, D'Ambrosio C, Mohsenin V (2000) Sleep-related breathing disorders and cardiovascular disease. *Am J Med* 108:396-402
6. Kobyashi H, Ishibashi K, Noguchi H (1999) Heart rate variability: An index for monitoring and analyzing human autonomic activities. *Appl Human Sci* 18:53-59
7. Sovijärvi A, Helistö P, Malmberg L et al. (1998) A new versatile PC-based lung sound analyzer with automatic crackle analysis (HeLSA); repeatability of spectral parameters and sound amplitude in healthy subjects. *Technol Health Care* 6:11-22
8. Rauhala E, Himanen S-L, Saastamoinen A et al. (2007) Prolonged spiking in the Emfit sensor in patients with sleep-disordered breathing is characterized by increase in transcutaneous carbon dioxide. *Physiol Meas* 28:1163-1173
9. Calero G, Farre R, Ballester E et al. (2006) Physiological consequences of prolonged periods of flow limitation in patients with sleep apnea hypopnea syndrome. *Respir Med* 100:813-817
10. Earis J, Cheatham B (2000) Current methods used for computerized respiratory sound analysis. *Eur Resp Rev* 10:586-590
11. Benitez D, Gaydecki P, Zarch A et al. (2001) The use of the Hilbert transform in ECG signal analysis. *Comput Biol Med* 31:399-406
12. American Academy of Sleep Medicine (1999) Sleep related breathing disorders in adults: Recommendation for syndrome definition and measurement techniques in clinical research. *Sleep* 22:667-689
13. Gibson G (2004) Obstructive sleep apnoea syndrome: underestimated and undertreated. *Br Med Bull* 72:49-64
14. Peter J, Koehler U, Grote L et al. (1995) Manifestations and consequences of obstructive sleep apnoea. *Eur Respir J* 8:1572-1583
15. Wittmann V, Rodenstein D (2004) Health care costs and the sleep apnea syndrome. *Sleep Med Rev* 8:269-279

Author: Antti Kulkas

Institute: Department of Clinical Neurophysiology, Medical Imaging Centre, Pirkanmaa Hospital District

Street: Biokatu 6

City: Tampere

Country: Finland

Email: antti.kulkas@pshp.fi

# Ultrasonic Non-invasive Investigation of Arterial Elasticity

I. Kupciunas, A. Kopustinskas

Kaunas University of Technology, Kaunas, Lithuania

**Abstract** — Arterial wall elasticity is relevant property closely related to artery physiology. Supposedly, decrease of arterial wall elasticity leads to serious diseases of blood vessel system. Possibility to assess parameters of artery wall elasticity *in vivo* would contribute significantly to early diagnostics of atherosclerosis, stenosis and other pathologic lesions. Despite the efforts made by numerous investigators widely accepted and in clinical practice used non-invasive approach still doesn't exist.

In this paper original method for the estimation of artery wall elasticity using non-invasive ultrasound technique is proposed. Method is based on the indirect simultaneously measurements of blood pressure and movement of artery wall. Algorithm for the investigation of arterial diameter and wall dynamics using ultrasound M-scan technique is created. Algorithm enables to detect dynamics of blood-intima, media-adventitia boundaries and intima-media thickness in human carotid artery. Blood flow velocity Doppler measurement for the indirect estimation of blood pressure is employed.

Method for the elasticity estimation was evaluated in a *in vivo* study on the common carotid artery of 5 volunteers. Results show that proposed methodology provides valuable information on mechanical properties, i.e. artery wall elasticity and has a high potential for routine clinical usage. Further investigations for the detailed analysis of adequacy and validation using human artery phantom and larger population study are planned.

**Keywords** — artery, elasticity, ultrasound, evaluation, method.

## I. INTRODUCTION

Arterial wall elasticity is relevant mechanical property closely related to artery physiology. Therefore artery behaviour during blood circulation depends greatly on its elastic properties. Numerous studies have demonstrated that both long-term and transient blood flow or pressure changes can result in adaptive vascular remodelling. In many cases this readjustment appears as morphologic restructuring of vessel wall composition and configuration, i.e. variation of artery mechanical characteristics. It is believed that artery wall elasticity alterations emerge not only during normal adaptive remodelling, but also in early pathologic state, leading to serious diseases of blood vessel system. Hence possibility to assess parameters of artery wall elasticity *in vivo* would contribute significantly to early diagnostics of atherosclerosis, stenosis and other pathologic lesions.

Various methods for elasticity estimation have been proposed in the past. Most elasticity parameters require determination of pressure change during heart beat. Although often used, measurement of pressure alterations in brachial artery is rather rough and not always acceptable approximation. Important index of arterial stiffness is pulse wave velocity (PWV) or pulse transit time (PTT) [1]. The use of PWV technique has the advantage that no arterial pressure recordings are necessary. Nevertheless precise and sophisticated measurements are required in order to define time delay between two simultaneously recorded pressure or distension waves. Even more important, pulse wave velocity provides averaged elasticity value of artery segment in study. Using this technique early local elasticity changes can be left unnoticed. Recently few non-invasive techniques have been developed to explore mechanical properties of blood vessels. Promising results have been announced using ultrasound-stimulated vibro-acoustography and measurement of artery wall thickness change during heartbeat [2], [3]. Unfortunately all above mentioned techniques require special equipment, which is commercially unavailable at this time. Despite the efforts made by numerous investigators widely accepted and in clinical practice used non-invasive approach still doesn't exist.

In this paper original method for the estimation of arterial wall elasticity is proposed. Essential parameters, characterizing artery elasticity, are acquired by means of non-invasive ultrasound. M-mode ultrasound images are used to evaluate cross-sectional area changes of carotid artery. Intima-media thickness is also measured as a reference of artery state. Method enables to estimate blood pressure in indirect manner. For this purpose blood flow velocity measurements are employed [4]. Technique for the elasticity estimation was evaluated in a *in vivo* study on the common carotid artery.

## II. METHOD

### A. Elastic modulus estimation

Assuming that the arterial wall is relatively thin and incompressible, one can use LaPlace's Law to derive the following expression for the elastic modulus:

$$E = \frac{r^2}{h} \frac{\Delta P}{\Delta r}, \quad (1)$$

where  $r$  and  $h$  is the internal radius and wall thickness, respectively, and  $\Delta r$  and  $\Delta P$ , are the change in internal radius and transmural pressure.

It is obvious that transmural pressure change ( $\Delta P$ ) can be defined as the force change ( $\Delta F$ ) per cross-sectional area ( $A$ ):

$$\Delta P = \frac{\Delta F}{A}. \quad (2)$$

Moreover, we know there are three main forces, related to the pressure change during heartbeat:

$$\Delta F = \Delta F_1 + \Delta F_2 + \Delta F_3. \quad (3)$$

First sum component is responsible for the inertance effect and can be derived using Newton's Law relating force change,  $\Delta F$ , mass,  $m$  and the maximum rate of change of blood velocity, which is the acceleration,  $a$ :

$$\Delta F_1 = ma = \rho V_M a = \rho AL_M \left. \frac{dv(t)}{dt} \right|_{MAX}, \quad (4)$$

where  $\rho$  and  $V_M$ , are blood density and blood volume, which is accelerated during the systolic period. Blood volume or artery volume is expressed in terms of artery cross-sectional area ( $A$ ) and vessel length ( $L_M$ ). Furthermore artery volume and length can be written as:

$$V_M = \bar{A} L_M = \bar{A} \int_0^{T_C} \bar{v}(t) dt, \quad (5)$$

$$L_M = \int_0^{T_C} \bar{v}(t) dt = \bar{V} T_C, \quad (6)$$

where  $\bar{v}$  and  $\bar{V}$  is the mean cross-sectional and mean blood velocity during pulse period, respectively  $\bar{A}$  and  $T_C$ , are the mean cross-sectional area of artery and duration of heart pulse period.

Blood flow frictional force component is obtained as:

$$\Delta F_2 = \eta \bar{v}(t) = \eta \frac{L_M}{T_C}, \quad (7)$$

where  $\eta$  is coefficient of friction.

The influence of the frictional force is rather small if compared to other components of the sum, thus will be neglected in this case.

The last component of the sum characterizes whole peripheral resistance of vascular tree and is the most difficult to estimate. Using Ohm's Law peripheral resistance force change can be derived as follows:

$$\Delta F_3 = \Delta P A = R_{TP} \bar{Q} A, \quad (8)$$

where  $R_{TP}$  and  $\bar{Q}$  are the artery hemodynamical resistance and mean blood flow.

Hemodynamical resistance can be expressed in terms of geometric artery parameters:

$$R_{TP} = \frac{8\mu L_M}{\pi r^4}, \quad (9)$$

where  $\mu$  is blood viscosity.

Mean blood flow is given by:

$$\bar{Q} = A \frac{1}{T_C} \int_0^{T_C} \bar{v}(t) dt = \frac{AL_M}{T_C}. \quad (10)$$

Substituting equations (9) and (10) into (8), we obtain expression for peripheral resistance force as follows:

$$\Delta F_3 = \frac{8\mu L_M^2 A^2}{\pi r^4 T_C}. \quad (11)$$

Pressure change in (1) is expressed using (2). Finally, equation of elasticity modulus is obtained substituting (4) and (11) into (3) and (3) into (1):

$$E = \frac{r^2 L_M}{h \Delta r} \left( \rho \left. \frac{dv(t)}{dt} \right|_{MAX} + \frac{8\mu L_M}{r^2 T_C} \right). \quad (12)$$

From the expressions (12), (6) one can see, that elastic modulus estimation requires knowledge of geometrical parameters of the artery, blood velocity time function and period of the heart beat. These delineated parameters may be measured using only a non-invasive ultrasound technique.

### B. In vivo study

Elastic modulus calculation method was investigated experimentally using *in vivo* study data of 5 volunteers. Pathological artery wall changes were observed for all subjects during earlier routine medical examinations. All required data was acquired using a commercial GE Vingmed ultra-

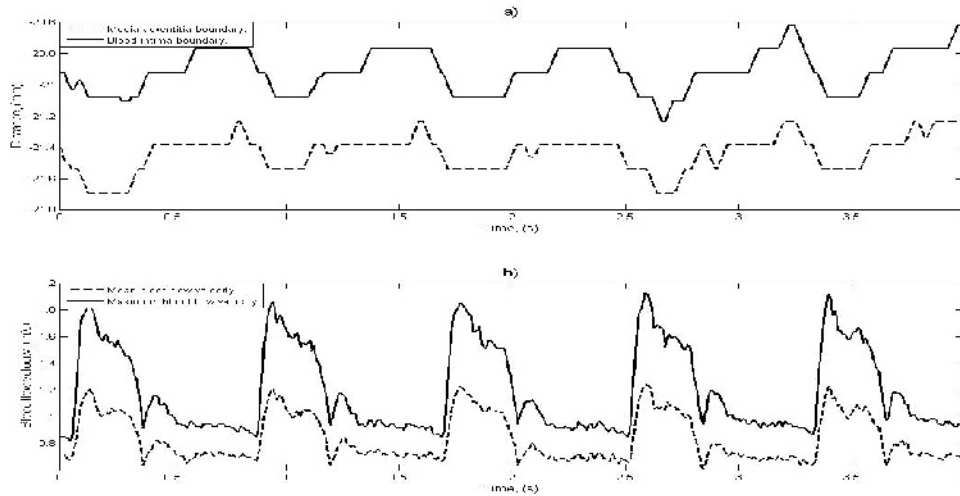


Fig. 1 Typical common carotid artery far wall boundaries displacement (a) and blood flow velocities (b)

sound system. The system was equipped with 10 MHz transducer. Volunteers were asked to lie down and after 5min., their left and right common carotid arteries were analyzed at locations about 2 cm proximal to the bifurcation. Ultrasound M-mode was applied to obtain ultrasound images of artery far wall changes in time.

Algorithm was developed for the detection of dynamical geometrical parameters of blood vessel cross-section. Employing MATLAB program displacement of far wall blood-intima and media-adventitia boundaries was evaluated from ultrasound M-mode images (Figure 1 a). Intima-media thickness was also calculated. Immediately after acquisition of M-mode ultrasound images, Doppler flow velocity and auscultatory blood pressure measurements were performed. Algorithm was developed and MATLAB program used for the extraction of maximum and mean blood flow velocity time functions (Figure 1 b) from the acquired Doppler spectrogram.

### III. RESULTS

Results obtained in the *in vivo* study are summarized in Table 1. Two important elasticity indexes, elastic modulus and area compliance, were calculated in this study. Widely in clinical practice used intima-media thickness is also presented. Intima-media thickness gives the initial idea of the artery lesion state. From the results we see that artery wall thickness is reflected in area compliance and elasticity modulus. Area compliance value increase should be interpreted as a reduction of artery’s ability to distend during systole phase, i.e. decrease of elasticity related artery properties. Conversely, elastic modulus value increase describes artery elasticity rise. It is important to note that compliance does not characterize the material, i.e. artery wall, properties. This parameter characterizes overall structural behaviour of a blood artery. Thus area compliance and elastic modulus can’t be directly compared with each other as a

Table 1 Results of *in vivo* study on the common carotid artery of 5 volunteers

Volunteer no.	Internal radius ( $r$ ), mm	Internal radius change ( $\Delta r$ ), mm	Pressure change ( $\Delta P$ ), mmHg	Intima-media thickness( $h$ ), mm	Area compliance( $C_A$ ), m Pa <sup>-1</sup>	Elastic modulus ( $E_1$ ), Pa	Elastic modulus ( $E_2$ ), Pa
1	3,62±0,54	0,46±0,09	38±2	1,1±0,14	1,63 10 <sup>-8</sup>	1,31 10 <sup>5</sup>	1,67 10 <sup>5</sup>
2	3,54±0,51	0,31±0,08	56±2	0,46±0,1	1,05 10 <sup>-8</sup>	6,56 10 <sup>5</sup>	1,54 10 <sup>6</sup>
3	3,23±0,49	0,31±0,08	50±2	1,08±0,13	9,84 10 <sup>-9</sup>	1,4 10 <sup>5</sup>	7,19 10 <sup>4</sup>
4	3,46±0,5	0,62±0,11	50±2	1,05±0,13	1,13 10 <sup>-8</sup>	1,23 10 <sup>5</sup>	1,2 10 <sup>5</sup>
5	3,38±0,5	0,54±0,1	54±2	0,77±0,12	9,97 10 <sup>-9</sup>	1,98 10 <sup>5</sup>	2,3 10 <sup>5</sup>

equivalent parameters of artery elasticity. Elastic modulus ( $E_2$ ) values, acquired using in this paper proposed method, agree rather well with those ( $E_1$ ), calculated employing common LaPlace's Law derivative (1). Obtained maximum  $E_2$  value ( $1,54 \cdot 10^6$  Pa) corresponds to maximum  $E_1$  value ( $6,56 \cdot 10^5$  Pa). Highest  $E_1$  and  $E_2$  values indicate highest artery wall elasticity of all the subjects under study. Moreover, this assumption is confirmed by relatively small intima-media thickness ( $0,46 \pm 0,1$  mm) and area compliance ( $1,05 \cdot 10^{-8}$  mPa $^{-1}$ ). For all calculations blood density assumed equal  $1 \text{ gcm}^{-3}$ , blood viscosity  $\mu=4 \cdot 10^{-2}$  P. Axial resolution of the ultrasound images – 0,07 mm.

#### IV. DISCUSSION

Proposed blood vessel elastic modulus estimation technique has two main advantages.

Firstly, blood vessel is investigated locally. Thus parameters, characterizing a specific segment of vessel under investigation are obtained.

Secondly, all measurements are done using only a non-invasive high resolution ultrasound technique. Required magnitude change of blood pressure is estimated in an indirect manner using a dynamic feature of blood flow and peripheral resistance.

Important advantage of the method is employment of commercially available non-invasive ultrasound equipment. However it is important to mention that derived peripheral resistance force expression (11) is more suitable for the general case. Doubtful accuracy of this component requires detailed analysis to be carried out in the future.

This work is currently being extended to detailed analysis of method adequacy and validation. Human artery phantom is being constructed for this purpose. Future work also includes larger population *in vivo* study of not only affected, but also presumably healthy human common carotid arteries.

#### V. CONCLUSIONS

The blood flow time function, acquired in the vessel during the heart beat, depends on the mechanical parameters of

the vessel itself and physiological blood pressure changes. Simultaneous analysis of blood flow and diameter time functions allows to evaluate mechanical parameters of the blood vessel. A novel method for the estimation of artery wall elasticity was proposed in this paper. Employing this method relevant artery elasticity parameter – elastic modulus can be estimated avoiding direct blood pressure measurements. The *in vivo* study has demonstrated that important artery mechanical parameters can be obtained using only non-invasive ultrasound. Possibility to utilize widely outspread commercial equipment for the proposed method emerge high potential for routine clinical usage.

#### ACKNOWLEDGMENT

The authors are greatly acknowledged to dr. Jolanta Marcinkeviciene and dr. Renaldas Jurkevicius from cardiology clinic of Kaunas University Hospital for providing data of the *in vivo* study. This work was partly supported by the Lithuanian State Science and Studies Foundation under project No. T-68/07, 2007.

#### REFERENCES

1. Foo J Y A, Wilson S J (2005) Development of a non-intrusive system to monitor radial pulse wave velocity, IEEE-EMBS Proc., Engineering in Medicine and Biology Conference, Shanghai, China, 2005, pp 7505-7508
2. Heikkila J, Karjalainen T, Hynynen K (2004) 3D simulations of difference frequency effects on a blood vessel in ultrasound-stimulated vibro-acoustography. IEEE International Ultrasonics, Ferroelectrics, and Frequency Control Joint Conference, Montreal, Canada, 2004, pp 1247-1250
3. Hasegawa H, Kanai H, Koiwa Y et al. (2002) Measurement of elastic moduli of tissue components in atherosclerotic plaques by ultrasonic phased tracking method. IEEE Proc. vol. 2, Ultrasonic Symposium, 2002, pp 1847-1850
4. Kopustinskas A, Kopustinskiene G (2004) Application of ultrasound Doppler technique for blood velocity evaluation. Ultrasound 52:47-52

Author: I. Kupciunas  
 Institute: Kaunas University of Technology  
 Street: Studentu st. 50-303r.  
 City: Kaunas LT-51368  
 Country: Lithuania  
 Email: Irmantas\_k@yahoo.com

# EEG-fMRI Ballistocardiogram Removal: A New Non-linear Dynamic Time Warping Approach

A.J.L. Kustra<sup>1</sup>, J.M. Fernandes<sup>1,2</sup> and J.P.S. Cunha<sup>1,2</sup>

<sup>1</sup> IEETA, University of Aveiro, Aveiro, Portugal

<sup>2</sup> DETI, University of Aveiro, Aveiro, Portugal

**Abstract** — Functional Magnetic Resonance Imaging (fMRI) is a promising technique to spatially identify activated areas. However, because of its limited time resolution (about one volume every 3 seconds), integration with a high temporal resolution method (Electroencephalography (EEG)) has shown to be promising. Two main artifacts rise on the EEG in this setup: The imaging artifact and the Ballistocardiogram artifact (BCG). The focus of this paper is to present a new approach for BCG removal. The most common method for its removal is based on average wave shape subtraction. This method assumes a deterministic approach to the BCG, which, as every analog biomedical signal, is not a good assumption. In this paper we present and evaluate, for the first time, a Ballistocardiogram removal adaptive algorithm based on dynamic time warping (DTW)[1]. Although for stable pulse this method can slightly distort the wave shape, we believe it can be reliable to deal with greater BCG time variations, like in the presence of arrhythmia, or during emotion stimulation.

**Keywords** — electroencephalography, functional magnetic resonance imaging, multimodal, ballistocardiogram, dynamic time warping

## I. INTRODUCTION

fMRI is a relatively new magnetic resonance imaging (MRI) based technique that allows monitoring of the brain activation patterns by measuring the magnetic variation induced by changes in the blood flow associated to brain neural activity. The neural activity produces an increase in blood flow (with a delay of about 2 seconds) richer in oxyhemoglobin to compensate the increase in oxygen consumption. This change in oxyhemoglobin is called the Blood Oxygen Level Dependent response or BOLD effect [2]. The local fluctuations in BOLD induce magnetic variations that are susceptible to be detected through T2-weighted gradient-echo echo-planar imaging[3]. When BOLD activations and deactivation are time related with specific events, they can be related to metabolic response in the brain. Therefore fMRI provides an indirect way of studying the brain activity[3]. Although it provides a good spatial resolution, the drawback of fMRI is its poor time resolution (typically one head volume acquisition every 3 seconds in a 1.5 T MRI machine), a limiting factor when observing the rapid brain

electrical dynamics. However, these can be reliably characterised through the electroencephalography (EEG) where electric potential variations, induced by electrical brain activity, can be measured on the scalp surface in high sampling frequencies ( $\geq 200\text{Hz}$ ). In contrast to the ability of capturing events in real time, EEG has a limited spatial resolution. Integrating both techniques (EEG-fMRI) represents an added value both in normal and abnormal brain activity characterisation[4]. This integration is not free from problems due to artifacts induced in EEG by magnetic field variations: EEG relies on cables connected to the subjects head to capture the electric potential over the scalp that, when acquired inside a MRI shielded room, are subjected to electric inductance generated by the very strong static and varying magnetic fields in fMRI sequences, obscuring the original EEG signal. In this environment the two most relevant artifacts are: the imaging artifact originated by magnetic field gradient fast alterations and the Ballistocardiogram (BCG) induced by heart pulse[4]. The removal of the BCG artifacts is the focus of the present work, where we present a new approach to address this problem. The BCG artifact occurs between two successive Electrocardiogram (ECG) R waves, and so it is associated with the subjects pulse. The pointed causes for its occurrence have been the subjects head motion, the expansion and contraction of the scalp arteries in the static magnetic field and the Hall effect when hemoglobin flows perpendicular to the static field[5-7]. This last source is believed to be very small, because of the approximate equal number of positive and negative ions in the circulation, and the random blood vessel distribution, that leads to a cancellation of the induced signals [8, 9]. Since this artifact obscures the underlying physiological EEG, methods for its removal have been proposed. The proposed methods rely on different techniques such as average artifact subtraction(AAS), Adaptive Filtering and independent component analysis(ICA)[10, 11]. Bonmassar *et al*[8] proposes a method to remove the BCG artifact based on the principle that the most significant contributions to the artifact are due to small movements in the scanner. By using a motion sensor in a target position on the subjects scalp, these are quantified, an adaptive noise cancellation algorithm was used and the system was modeled as a linear combination of the physiological contributions with the

induced artifact, similarly to the above explained methods. These artifact components are calculated based on the motion sensor output, producing a Finite Impulse Response (FIR) filter kernel which is used to estimate the noise signal that is subtracted from the acquired EEG. Although this method presented good results its setup is not trivial as it requires a motion sensor. The most widely used method for BCG removal is the one proposed by Allen *et al.*[5]. It relies on estimating the artifact wave shape by averaging several artifacts, followed by the subtraction of the averaged artifact template to each position. It is capable of successfully removing the artifact, as long as the artifact is assumed stable from frame to frame. However, the BCG results from the subjects physiological responses and to assume this signal is deterministic seems like an unrealistic approach[11]. An enhanced version of this algorithm is presented by Sijbers *et al*[7] where, prior to template averaging, time scaling of the artifacts to a fixed time interval is performed. Each artifact is then normalized with respect to mean and standard deviation. Also, it is subjected to a wavelet filter where the wavelet coefficients of the highest frequencies are set to zero. Although a variation in the artifact is assumed, it is still deterministic because it results from a linear wave shape variation, proportional to the R-R distance. This leaves no room for spontaneous wave shape warps, very common in physiological signals in many situations such as reaction to motor or visual stimulation. The approach taken in this paper is based on average artifact subtraction, and it is capable of adapting itself to each artifact epoch by applying Dynamic Time Warping (DTW)[1] prior to averaging the template and warping the template back before subtraction.

## II. MATERIALS AND METHODS

### A. Data

The algorithms were tested both on real EEG data acquired in an fMRI environment, and on simulated data. The EEG acquisition was performed on one healthy and two epileptic subjects. The EEG/fMRI consisted in 5 minutes of continuous acquisition in a 1.5T GE CVi/NVi scanner. The EEG was recorded at 1000 Hz through a set of AgCl electrodes connected to an amplifier located outside the scanner room through carbon fiber wires (MagLink, Neuroscan, El Paso, TX, U.S.A.). The data acquisitions were performed in three different occasions, each time on a different subjects, P1..P3. The patient identified as P1 was healthy, while P2 and P3 suffered from epilepsy. For each acquired channel, the gradient artifact was filtered by the method proposed by Allen *et al*[5], and the BCG was reduced using a simple AAS and our proposed DTW method. In the simulated data,

our goal was to get a close approach to the physiological signal with the Ballistocardiogram artifact and manipulate its characteristics to study the algorithm tolerance and performance to its change. The signal was simulated based on a random signal with a linear distribution. It was low pass filtered simulating a signal with a range of frequencies from 0 to 70Hz. The artifact was simulated by a *sinc* function ranging from  $-\pi$  to  $\pi$ . The standard length of the artifact was set to 1000 samples, in order to simulate a typical ECG R to R wave distance acquired at a sampling frequency of 1 kHz. To induce artifact timing variations, we generated an *artifact maximum variation* index ranged from 0.5% to 15%, with a linear distribution around the mean value. The amplitude of the artifact was set to twice the absolute mean value of the signal. For each maximum variation, a total of 1000 epochs were generated.

### B. Dynamic time warping

Dynamic Time Warping (DTW) is a technique for aligning two time series in order to find a dissimilarity measure using nonlinear temporal alignment. This algorithm has found its application in the solution of different problems such as handwriting recognition or speech recognition. Its use in the analysis of electrophysiological signals has been of great importance in the analysis of spike patterns, event related potentials and in the analysis of the ECG waveform. It provides the ability to compare two time series because it provides an index of the similarity of two time series. In order to calculate this index, the target time series is nonlinearly warped into the other, stretching and compressing along the X axis, providing a minimum cost alignment between two time series. The details of its implementation can be found in Keogh *et al*[1]. In this paper we present DTW as potential tool to improve the removal of the BCG by not blindly averaging to the template and subtracting it from the signal, but prior to those operations, dynamically warping the signals.

### C. Applying DTW to the average artifact subtraction

To deal with these variations, the template must dynamically adapt to every epoch. To solve this problem, the previously described DTW algorithm can be used. Therefore, before averaging each epoch, this is dynamically warped to the current template, obtaining the lowest cost alignment between the two signals. By adding this step, we avoid one portion of the signal averaging with *the wrong* part of the signal. The template achieved by this method is used, just like in AAS, to be subtracted to the signal at defined positions. However, prior to subtraction, the template, is warped to match the current signal position.



### III. RESULTS

For the validation of the results we compared our algorithm with AAS as proposed by Allen[5], which is the most commonly used approach. In the simulated data, we compared each reduced artifact, by calculating a correlation index for every original epoch (prior to adding the artifact) to the epoch after artifact removal with AAS and our DTW approach. An illustration of the resulting signals is presented on Fig. 1. In the presence of a perfect removal algorithm, the original and resulting signal after the algorithm application would be identical. In order to study the efficiency of both algorithms with different warping values, the simulation was repeated for warping variations between 0.5% and 15%. The resulting mean correlations are illustrated in Fig.2. Although for small artifact warping values (<3.5%) the AAS presents a higher mean correlation value between the original signal and the signal after artifact removal, this decreases as the warping increases. For the acquired data, we compared the template adaptation to each epoch. A better adapted template should better reduce the artifact while minimizing the distortion to the actual underlying physiological EEG. The Pearsons Correlation was calculated for each epoch (of 1000 samples) along every channel with the template at the epochs position. The values were calculated for the full available EEG time (50s, 50000 samples), and the results were averaged for each channel, and subsequently for each patient. As can be observed in Table 1, the DTW approach consistently presents higher values of correlation.

Table 1 Mean Correlation Values (EEG)

Subject	DTW		AAS	
	Correlation	$\sigma$	Correlation	$\sigma$
P1	0.61	0.17	0.55	0.16
P2	0.60	0.13	0.46	0.14
P3	0.54	0.14	0.40	0.15

### IV. DISCUSSION

The main goal in artifact removal methods is always the removal of the artifact while minimizing the distortions on the underlying signal. The most popular methods proposed for the BCG artifact removal, although providing an acceptable signal for some situations, and because of the simplicity of their implementation, are becoming a standard for the BCG removal but have been criticized because of the principle of its initial assumptions[11]. By assuming a periodicity in an artifact with a physiological source, we always end up distorting the underlying signal to a certain degree. Our goal is to provide an algorithm that shares the AAS

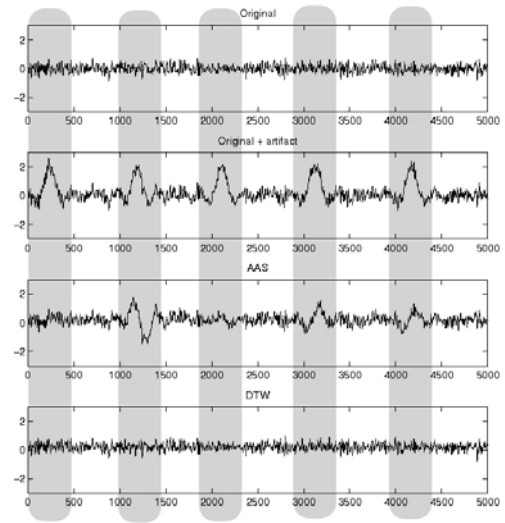


Fig. 1 A signal resulting from the simulation presenting the original simulated signal (5000 samples), followed by the signal with the added artifact (*sinc* function) with +5% artifact warping variation, the signal after application of the AAS algorithm and the signal after application of our DTW approach. The portions of the signal corresponding to the artifact highest amplitude peaks are highlighted

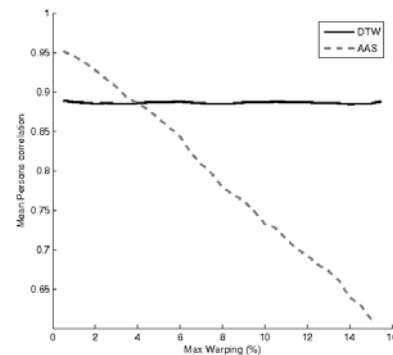


Fig. 2 The mean signal correlation (N=1000 artifact epochs of 1000 samples each) between the original signal (prior adding the artifact) and the signal after application of each algorithm (AAS and DTW). The DTW approach shows higher correlation value than the AAS when the time warping variation exceeds 3.5%

principles, but overcomes the problems resulting from its initial assumptions. The proposed algorithm is, contrary to the simple AAS, able to dynamically adapt the template time axis to each signal epoch between two successive R ECG waves. The assumption that the best artifact alignment is the one resulting from the application of the lowest cost function is acceptable as long as the artifact is larger in amplitude than the underlying physiological signal. The possible drawback of our proposed method is that by dynamically time warping the signal with a minimum cost

function, we could be distorting the signal to some degree. Our simulation results for different levels of signal variation show that our algorithm becomes more efficient in the artifact removal when signal warping was present, with a linear distribution over 3.5% the epoch length. For a basal ECG rhythm of 80bpm, a variation of just 3bpm or more in the rhythm will degrade the AAS performance in the BCG removal. Stimulation can induce this type of variation (emotional responses or hypopnea)[12]. In such situations, the use of DTW will enhance the results. For the real EEG data our DTW method was consistently superior by presenting better correlation values, suggesting that it is better for the BCG removal, even with small and spontaneous pulse variations. Since the adaptation improves with the increase of the artifact/signal ratio and for higher magnetic field strengths the amplitude of the BCG increases, our algorithm should further improve the quality of the template adaptation and further improve the BCG reduction in EEG-fMRI data from 3T or higher MRI machines. Because of the greater complexity of the algorithm and consequently a higher demand for processing power, a compromise between the artifact variation, desired removal quality and processing speed should be taken in account when applying the algorithm.

## V. CONCLUSIONS

The DTW approach for the removal of the BCG shows a very good potential to overcome the AAS limitations. More work is needed for the algorithm to be further explored with different static field strengths, where its amplitude ratio to the underlying physiological EEG should be higher, improving the template adjustment and consequently the BCG removal.

## ACKNOWLEDGMENT

We would like to thank the EpilBi project (POSC/EEA-CPS/60977/2004) and its funding institution, FCT (Portuguese Science and Technology Agency), IEETA (www.ieeta.pt), Alberto Leal, M.D. and Nicolas Lori for their contributions to the current work.

## REFERENCES

1. Keogh, E. and M. Pazzani, *Derivative Dynamic Time Warping*. 2001.
2. Oswaga, S., et al., Brain magnetic resonance imaging with contrast dependent on blood oxygenation, in *Proceedings of the National Academy of Sciences*. 1990. p. 9868--9872.
3. Cohen, M.S. and R.M. DuBois, Stability, repeatability, and the expression of signal magnitude in functional magnetic resonance imaging, in *Journal of Magnetic Resonance Imaging*. 1999. p. 33--40.
4. Salek-Haddadi, A., et al., EEG quality during simultaneous functional MRI of interictal epileptiform discharges, in *Magn Reson Imaging*. 2003. p. 1159--1166.
5. Allen, P.J., et al., Identification of EEG Events in the MR Scanner: The Problem of Pulse Artifact and a Method for Its Subtraction, in *NeuroImage*. 1998. p. 229--239.
6. Hill, R.A., et al., Hemodynamic and metabolic aspects of photosensitive epilepsy revealed by functional magnetic resonance imaging and magnetic resonance spectroscopy, in *Epilepsia*. 1999. p. 912--920.
7. Sijbers, J., et al., Reduction of ECG and gradient related artifacts in simultaneously recorded human EEG/fMRI data, in *Magnetic Resonance Imaging*. 2000. p. 881--886.
8. Bonmassar, G., et al., Motion and ballistocardiogram artifact removal for interleaved recording of EEG and EPs during MRI, in *NeuroImage*. 2002. p. 1127--1141.
9. Schomer, D.L., et al., EEG-Linked functional magnetic resonance imaging in epilepsy and cognitive neurophysiology, in *J Clin Neurophysiol*. 2000. p. 43--58.
10. Briselli, E., et al., An independent component analysis-based approach on ballistocardiogram artifact removing, in *Magnetic Resonance Imaging*. 2006. p. 393--400.
11. Nakamura, W., et al., Removal of ballistocardiogram artifacts from simultaneously recorded EEG and fMRI data using independent component analysis, in *IEEE Trans Biomed Eng*. 2006. p. 1294--1308.
12. Haag, A., et al., Emotion Recognition Using Bio-sensors: First Steps towards an Automatic System, in *International Tutorial and Research Workshop on Affective Dialogue Systems, Germany*. 2004. p. 36-48.

Author: Jacek Lukasz Kustra  
 Institute: IEETA – University of Aveiro  
 Street: Campus Univ. de Santiago  
 City: Aveiro  
 Country: Portugal  
 Email: jacek@ua.pt

# Local Filtered QRS Duration during Sodium-channel Blockade in Brugada Syndrome Patients

A.C. Linnenbank<sup>1,3</sup>, P.G. Postema<sup>2</sup>, M.G. Hoogendijk<sup>1</sup>, P.F.H.M. van Dessel<sup>2</sup>,  
H.L. Tan<sup>1,2</sup> and J.M.T. de Bakker<sup>1,3</sup>

<sup>1</sup> Academic Medical Center/Heart Failure Research Center, Amsterdam, The Netherlands

<sup>2</sup> Academic Medical Center/Cardiology Dept, Amsterdam, The Netherlands

<sup>3</sup> Interuniversity Cardiology Institute of the Netherlands, Utrecht, The Netherlands

**Abstract** — The Brugada syndrome is associated with sodium channel dysfunction and the characteristic ST segment elevation is thought to arise from the right ventricle. We hypothesized that sodium channel blockade in Brugada syndrome patients cause more activation delay in leads overlying the right ventricle than in other leads. ECG data were recorded during infusion of a sodium channel blocker in 17 family members of Brugada syndrome patients. Signal averaged and filtered signals from a number of body surface leads were investigated for small potentials that are generated by myocardium close to the recording electrode. ST segment elevation in V1 during sodium channel blockade was accompanied by pronounced activation delay in V1 after the end of the QRS complex in lead II ( $32 \pm 18$  ms), whereas activation in V6 was not later than end of QRS ( $12 \pm 13$  ms). The latest activation in V1 was delayed to a greater extent than in control patients without ST elevation during sodium channel blockade ( $151 \pm 17$  ms vs  $128 \pm 10$  ms,  $p < 0.005$ ). We conclude that the activation of the right ventricle in Brugada syndrome patients is more sensitive to sodium channel blockade compared to the left ventricle and compared to patients without ST segment elevation.

**Keywords** — Brugada Syndrome, Late potentials, Body surface mapping, Signal averaging

## I. INTRODUCTION

Brugada Syndrome (BrS) is characterized by specific ST-segment elevation in the right precordial ECG leads (V1-V3), syncope and sudden cardiac death secondary to ventricular tachyarrhythmias, in the absence of gross structural abnormalities [1]. Mutations in the cardiac sodium channel are found in 20-25% of BrS patients [2]. The amount of ST-segment elevation differs among patients and is highly variable within patients in time. Cardiac sodium channel blockers (e.g., ajmaline) may increase ST-segment elevations and can be used to uncover a hidden vulnerability. Because ST-segment elevation only arises in the right precordial leads, it is presumed that the process that generates the elevation

occurs in or close to the right ventricular outflow tract. It is, however, unclear whether this ST-segment elevation is the result of a local repolarisation or depolarisation disorder, or a combination. Studying low amplitude surface signals in right precordial and left lateral leads may give insight in the relation of late activation of the right ventricle and ST elevation.

## II. METHODS

Body surface ECGs from 65 leads (see Figure 1) were recorded during a provocation tests using ajmaline infusion in 17 relatives of BrS patients. Ajmaline was infused according to the consensus criteria at 10mg boluses every minute until a maximum of 1mg/kg body weight was reached or until the ECG criteria for the diagnosis of BrS were fulfilled. To assess whether conduction disturbances are correlated to the characteristic ST-segment elevation, we determined changes in local late activation during ajmaline infusion from the body surface electrograms.

All leads were individually averaged over 1 minute intervals using a time reference derived from crosscorrelating the QRS in V6.

ECGs were filtered between 25 and 200 Hz, and displayed as color-coded straps with 1-minute averages side by side (Fig. 2, left panel). The latest recordable signal in left and right precordial leads (V6 and V1) was determined in this graph by fitting a spline consisting of 5 cubic segments with 2<sup>nd</sup> order continuity (Fig. 3). As a measure of global conduction slowing, QRS width was determined in Einthoven lead II.

Latest activation during ajmaline infusion in lead V1 was compared between patients with and without STelevation ( $> 0.1mV$ ) in V1 and was related to latest activation in leads V6 and Einthoven II. The results are expressed as mean $\pm$ SD. Latest activations were compared using the unpaired Student t test

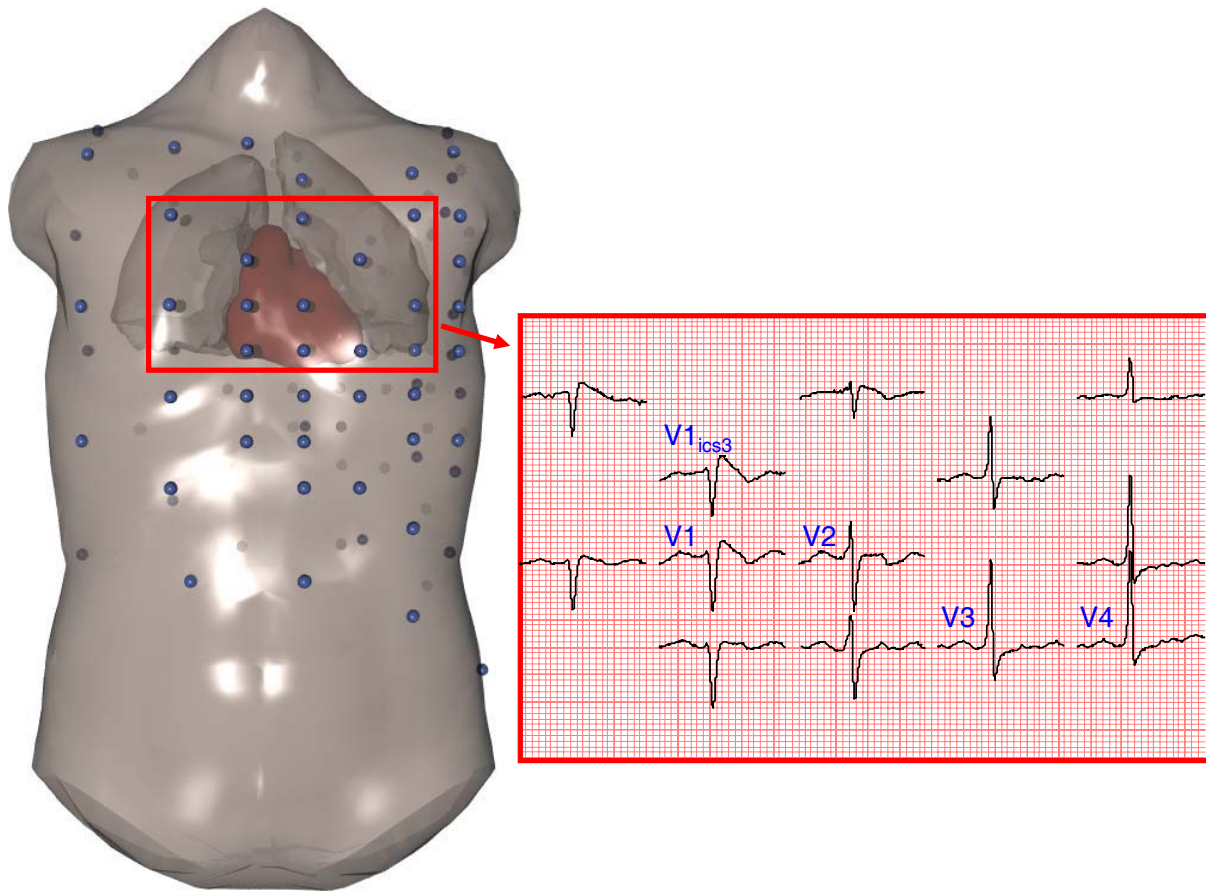


Fig. 1: Left panel: MRI based reconstruction of the torso of one of the patients. Right panel: Body surface electrograms recorded at the electrodes within the red rectangle.

### III. RESULTS

During ajmaline infusion the latest activation in V1 was always later than V6 in patients with ST elevation in V1. The latest activation in V1 was also significantly later than in patients without ST elevation ( $151 \pm 17$  ms vs  $128 \pm 10$  ms,  $p < 0.005$ ). In the patient group with ST elevation the latest activation in V1 is later than the end of QRS in lead II. The delay with respect to the end of QRS is different between both groups ( $32 \pm 18$  ms vs  $12 \pm 12$ ,  $p = 0.013$ ). In the same patient groups latest activation in V6 was no later than the end of QRS, neither in the group with nor in the the group without ST elevation. There is also no difference in delay between these groups. ( $12 \pm 13$  ms vs  $3 \pm 13$  ms,  $p = \text{ns}$ ).

The delay in V1 during peak ajmaline was  $17 \pm 14\%$  larger than expected based on general QRS widening as measured in lead II in patients with ST elevation. In patients without elevation the extra delay is only  $3 \pm 9\%$ . The difference between the groups is significant ( $p = 0.02$ ).

### IV. DISCUSSION

Traditionally, late potentials are assessed from the average of 300 or more beats. In our study, this was impossible because ajmaline serum levels changed continuously during the stepwise infusion, and because ajmaline has a serum half-life of only a few minutes. As a compromise between noise levels and stationarity of the signals, we averaged over 1-minute intervals. Another difference with traditional late potentials measurements is that we did not study the vector magnitude of the combined X,Y and Z leads but all surface leads individually [3]. This was done to assess local differences in activation of myocard close to the recording electrodes.

The non stationarity of the signal during ajmaline infusion hampers determining of the last activation. The global pattern was used as guidance and neighbouring leads were used to assess consistency of the small signals. We only analyzed signals that were consistent in morphology during

the entire procedure. Marked changes in morphology as a result of sodium channel blockade might result in underestimation of the time of latest activation.

Despite the limitations the filtered averaged signals provide a valuable insight in local phenomena close to the recording electrode, which can not be achieved in any other non-invasive way.

In patients with a positive test result the infusion was often terminated before the maximum dose was reached.

Therefore these patients had often a lower maximum serum level of ajmaline than patients with a negative test result.

Parts of the heart that are already activated late are even more delayed during sodium channel blockade. This observation is consistent with our previous results where we estimated the activation sequence at baseline and peak ajmaline in one of these patients using an inverse electrographic technique [4].

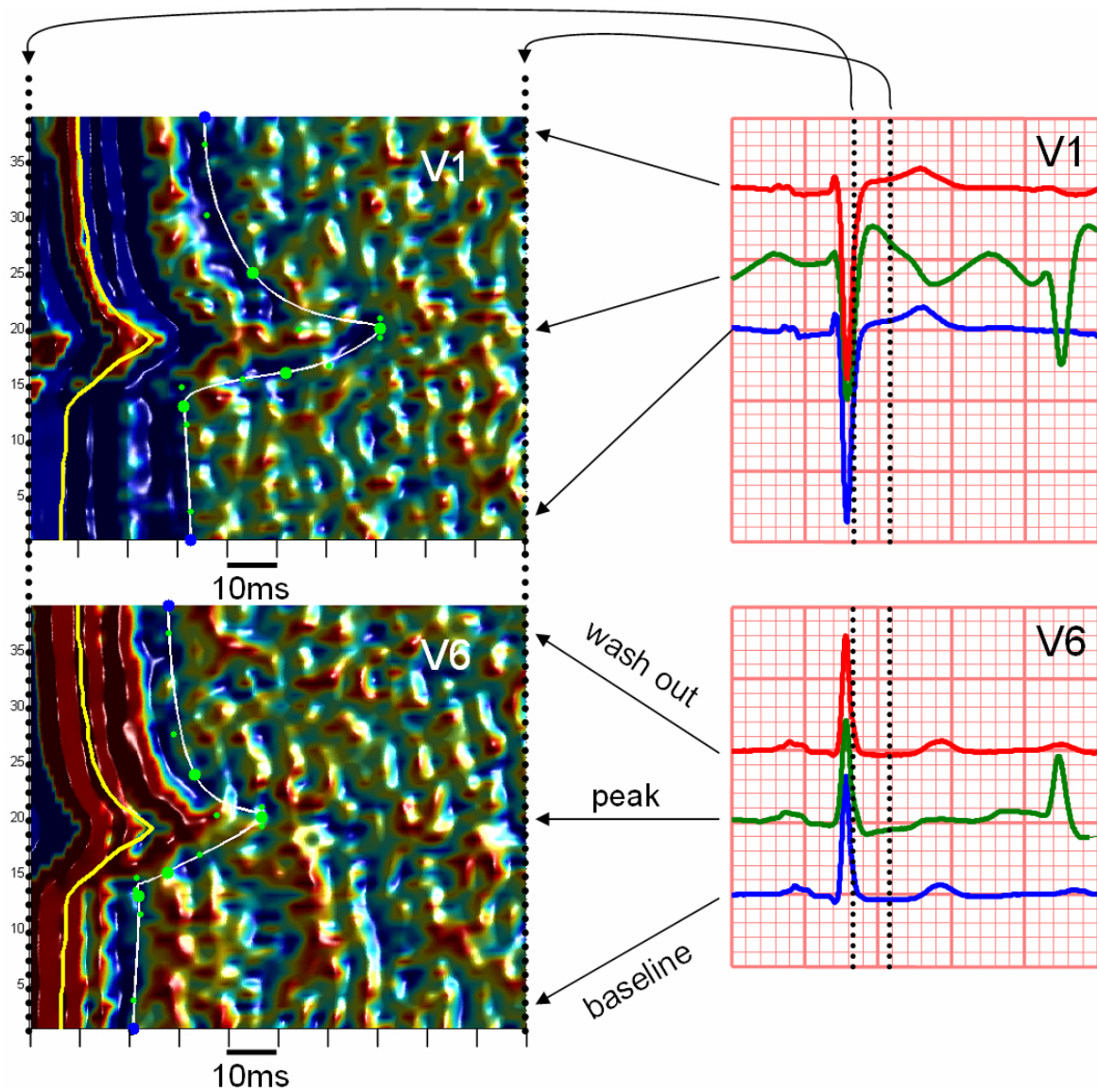


Fig. 2: The left panel shows the filtered terminal parts of the QRS in V1(top) and V6(bottom) during the entire 39 minute procedure from bottom to top. The infusion of the first bolus of ajmaline started at approximately 14 minutes and the last one was given at  $t=19$  minutes. After that the serum level dropped because the half life of ajmaline is only a few minutes. The white lines follow the moment of the latest measurable potentials in these leads. The yellow line in the left panels corresponds to the J point in Einthoven lead II.

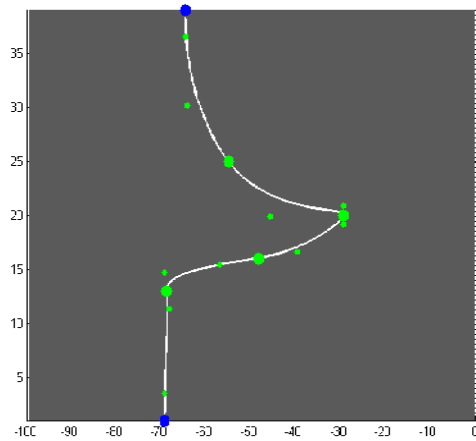


Fig. 3: Timing for every minute was estimated by manually adjusting 5 connected bezier splines with 4 control points. Splines are restricted to be 2<sup>nd</sup> order continuous at connecting points (larger green dots) by forcing the 3<sup>rd</sup> control point from one spline to be at the exact opposite position from the common point as the 2<sup>nd</sup> point on the next.

## V. CONCLUSIONS

The base of the right ventricle is activated markedly later in patients with Brugada-type ST elevation during sodium channel blockade than the global end of QRS as determined in lead II. In contrast, the left lateral lead V6 shows no sign of late activation after the QRS in these patients.

These findings support the idea that right ventricular activation delay plays a significant role in BrS.

## ACKNOWLEDGEMENTS

This study was supported by the Netherlands Heart Foundation grants 2002B087 and 2005B92

## REFERENCES

1. Antzelevitch C, Brugada P, Borggrefe M, Brugada J, Brugada R, Corrado D, Gussak I, LeMarec H, Nademanee K, Perez Riera AR, Shimizu W, Schulze-Bahr E, Tan H, Wilde A. Brugada syndrome: report of the second consensus conference. *Heart Rhythm*. 2005 Apr;2(4):429-40.
2. Antzelevitch C, Brugada P, Brugada J, Brugada R, Shimizu W, Gussak I, Perez Riera AR. Brugada syndrome: a decade of progress. *Circ Res*. 2002 Dec 13;91(12):1114-8
3. M.B. Simson,. Use of signals in the terminal QRS complex to identify patients with ventricular tachycardia after myocardial infarction. *Circulation*, 64:235-242,1981
4. A.C. Linnenbank, A. van Oosterom, T. Oostendorp, P.F.H.M van Dessel, A.C. van Rossum, R. Coronel, H.L Tan, J.M.T. de Bakker. Non invasive imaging of activation times during drug induced conduction changes, World Congress on Medical Physics and Biomedical Engineering 2006.

Author: A.C. Linnenbank  
 Institute: Heart Failure Research Center, AMC  
 Street: Meibergdreef 11  
 City: Amsterdam  
 Country: the Netherlands  
 Email: a.c.linnenbank@amc.uva.nl

# Development of Flexible Thin Film Microelectrode Arrays for Neural Recordings

S. Myllymaa<sup>1</sup>, K. Myllymaa<sup>1</sup>, H. Korhonen<sup>1</sup>, K. Djupsund<sup>2</sup>, H. Tanila<sup>2</sup> and R. Lappalainen<sup>1</sup>

<sup>1</sup> University of Kuopio/Department of Physics, Kuopio, Finland

<sup>2</sup> University of Kuopio/A. I. Virtanen Institute, Department of Neurobiology, Kuopio, Finland

**Abstract** — The design, fabrication and testing of flexible polyimide-based microelectrode arrays (MEAs) for neural recording is described. Several designs of MEAs were realized by varying layouts of arrays and electrode materials and insulating materials. Two different layouts were 8-channel and 16-channel MEAs consisting of round-shape microelectrodes with a diameter of 200  $\mu\text{m}$  and 100  $\mu\text{m}$ , respectively. Polyimide was chosen as a base material due to its suitable mechanical and dielectric properties and biocompatibility. Electrodes, transmission lines and connector pads were formed by sputter-deposition of gold (Au) or platinum (Pt) thin film together with underneath titanium (Ti) adhesion layer and patterned photolithographically via lift-off procedure. Photosensitive polyimide and epoxy-resist were tested as an insulation material. Microelectrode arrays were characterized *in vitro* by impedance spectroscopy in physiological saline solution (0.9 % NaCl) and tested *in vivo* by somatosensory evoked potential (SEP) recordings in rat cortex. The results from these preliminary tests indicate good electrochemical properties and spatiotemporal resolution of arrays. The polyimide-platinum-polyimide sandwich structure was found to be the most suitable alternative for flexible MEAs. In the future, this biocompatible fabrication protocol is possible to adapt for the development of different neural interfaces.

**Keywords** — Microelectrode array, neural recording, polyimide, thin film, photolithography

## I. INTRODUCTION

In clinical practice, electroencephalography (EEG) recordings are usually performed with different amount of electrodes attached to the scalp and measuring potential differences between electrodes. However, spatial resolution of scalp-EEG is quite poor. To achieve better source localization, it is advantageous to place the electrodes closer to the tissue. Penetrating electrode probes and non-penetrating electrode arrays placed on the surface of cortex offer possibilities to get detailed maps of brain. However, the use of penetrating electrode probes in humans is limited to the areas destined to surgical resection due to risk of damaging the brain tissue. Flexible subdural strip and grid electrodes placed on the surface of cortex are used as a less invasive method in some clinical cases, e.g. in epilepsy surgery [1].

Modern microfabrication techniques offer a great potential to develop novel implantable microsystems for the re-

ording of neural signals or electrical stimulation of nerves. For example, different lithographic and thin film techniques can be utilized in development of substrate-integrated electrodes with higher spatial resolution as present clinical subdural electrodes [2].

Neurophysiologists have performed multichannel cortical recordings in animal models by microwire bundles [3], [4] and various silicon probes and arrays. Michigan probes [5] and Utah arrays [6] are perhaps the most famous examples of microfabricated electrodes. Major advantages of the microfabricated electrode arrays over the microwire bundles are the high precise control of the electrode sizes and separation between themselves. However, there is a mismatch between mechanical properties of the brain tissue and silicon. The rigidity of silicon may cause tissue damaging, inflammation reactions and scar formation [7]. Recently, different flexible polymer materials have been studied as substrate materials in implantable neural interfaces [8]. Polyimide is one of the most potential materials due to its suitable mechanical properties and biocompatibility [9], and stability in wet microfabrication processes. Several polyimide-based microelectrode arrays have been developed for various neural applications [10]-[12], but only a few attempts have been reported to develop polyimide-based MEAs for cortical surface field recordings [13]-[15].

We hypothesized that it is possible to design and fabricate flexible thin film microelectrode arrays for stable neural recordings with high spatiotemporal resolution. The aim of this study was to find out the most suitable materials, designs and fabrication methods. A number of different prototypes were realized and their performance was evaluated *in vitro* by impedance spectroscopy in physiological saline solution and *in vivo* by somatosensory evoked potential (SEP) recordings in rat cortex.

## II. MATERIALS AND METHODS

### A. Array fabrication

The flexible microelectrode array is based on DC-sputter deposition (Stiletto Serie ST20, AJA International Inc., North Scituate, MA, USA) of electrochemically stable and biocompatible thin films (gold or platinum) on top of flexible polyimide base layer. UV- lithography (Karl Suss

MA45, Suss Microtec Inc., Waterbury Center, VT, USA) was used to pattern the metallization layer. Photosensitive polyimide Pyralin PI-2711 (HD Microsystems, Bad Homburg, Germany) and epoxy-resist SU-8 2003 (MicroChem, Newton, MA, USA) were tested as the materials for insulation layer. The photomasks needed in lithography processes were designed by CleWin layout software (WieWeb software, Hengelo, The Netherlands), and glass plates with a structured chrome layer were commercially fabricated by Mikcell Ltd. (Ii, Finland).

During a 2-year trial period, a number of different MEA prototypes were demonstrated. The most relevant variations are presented in Table 1. Two different layouts were 8- and 16-channel MEA with round-shape microelectrodes with a diameter of 200  $\mu\text{m}$  and 100  $\mu\text{m}$ , respectively [Fig. 1].

The fabrication of microelectrode arrays was accomplished on top of microscope glass slides, 76 x 51 mm, to ensure a rigid support during fabrication process. As a base layer in all the MEA prototypes were used 25  $\mu\text{m}$  thick DuPont's Kapton HN film (Goodfellow, Cambridge, UK) together with PI-2525 (HD MicroSystems GmbH, Bad Homburg, Germany). Adhesion promoter VM-651 (HD MicroSystems) was spun (Bidtec SP-100) onto the glass slide. Then, a piece of Kapton film was attached to the glass slide. The size of Kapton piece (about 66 x 42 mm) was little bit smaller than the slide to ensure that PI-2525 keeps the base layer tightly on the glass slide during the whole array process flow. PI2525 were spun with low acceleration rate and cured in oven according to manufacturer's guidelines. The final thickness of the base layer was about 30  $\mu\text{m}$ .

At first 20 % hexamethyldisilazane (HMDS) (Riedel-de Haen Laborchemikalien GmbH, Seelze, Germany) in xylene was spun upon the dry baked polyimide base layer to improve adhesion between polyimide and photoresist. A negative photoresist (ma-N 1420, Micro resist technology GmbH, Berlin, Germany) was patterned according to the basic steps of photolithographic process: spin coating, pre-bake, exposure, development, rinse and post-bake. Thin films of titanium (20-50 nm) and gold or platinum (250-280 nm) were sputtered onto a surface of patterned base layer. Titanium layer was sputtered to the surface of polyimide to achieve well-adhesive noble metal thin films. Metallization layers were structured via a lift-off procedure.

Photosensitive polyimide PI-2771 (HD MicroSystems) was used as an insulation layer in all prototypes except of type B. PI-2771 was coated with high spinning speed (5000 rpm) to achieve a thin and flat layer of polyimide. PI-2771 was then pre-baked on a hot plate and photo-structured. Finally, PI-2771 was cured in oven forming about 3  $\mu\text{m}$  thick electrically insulating layer everywhere else than the areas of electrodes and connection pads.

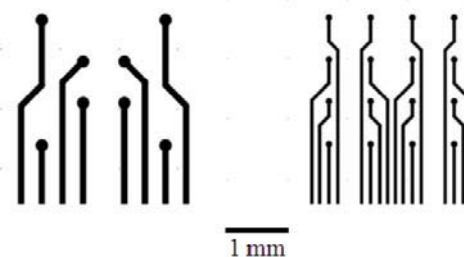


Fig. 1 The layouts of the 8- and 16- channel MEAs viewed at recording ends. The length of these arrays is 28 mm.

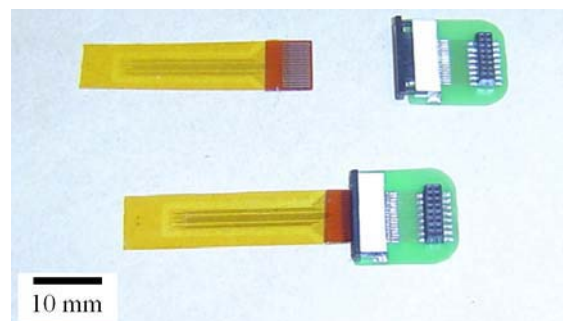


Fig. 2 Flexible MEA can be attached to a ZIF-type connector (not in final outer shape).

Table 1 Developed array prototypes

Type	Number of electrodes	Electrode material	Electrode size	Insulation material
A	16	Ti/Pt	100 $\mu\text{m}$	PI-2771
B	16	Ti/Pt	100 $\mu\text{m}$	SU-8
C	8	Ti/Pt	200 $\mu\text{m}$	PI-2771
D	8	Ti/Au	200 $\mu\text{m}$	PI-2771

In MEA type C epoxy-based negative photoresist, SU-8 2003 (MicroChem, Newton, MA) was used instead of PI-2771. SU-8 was spin coated, pre-baked on a hot plate, photo-structured and post-baked. Unexposed SU-8 areas were removed using propylene glycol methyl ether acetate (PGMEA) (Sigma-Aldrich) and sample was rinsed with isopropanol and de-ionized water. After hard-baking, SU-8 also formed about 3  $\mu\text{m}$  thick insulation layer.

MEAs were detached from the microscope glass slides and cut to their final outer shape using scissors and knife. Thin film connector pads were designed to fit into a 16-channel zero-insertion-force (ZIF) connector (JST Ltd., Halesworth, UK) [Fig. 2]. ZIF connectors were custom-soldered to commercially fabricated printed circuit board (PCB) adapters (KytKentälevy Ltd., Helsinki, Finland). In addition of the ZIF connector, PCB contains also 2 x 8 channel surface mount microsocket (CLM-serie, Samtec



Inc., New Albany, IN, USA) and via this socket MEA could be connected to the preamplifier and further to recording instrumentation. Casco strong epoxy-resin (Akzo Nobel Coating Ltd., Vantaa, Finland) was used as an encapsulant at the interface between MEA and ZIF connector and at signal tracks in PCB.

### B. Electrical characterization

MEAs were characterized by impedance spectroscopy in physiological saline solution (0.9 % NaCl) with one microelectrode at a time against the counter electrode with a much larger surface area (about 240 mm<sup>2</sup>). Counter electrodes were custom-made sputter-coated Au or Pt thin films upon the Kapton. Pt-counter electrode was used in determining electrode-electrolyte impedances of Pt-microelectrodes and Au-counter electrode for Au-microelectrodes, respectively. Impedance spectroscopy was carried out at frequencies between 50 Hz and 100 kHz by applying a sinusoidal signal of 100 mV without any offset using a LSR meter (HIOKI 3531Z HiTester, Koizumi, Japan). Measurements were also performed with two microelectrodes (MEA type A) in saline solution at the amplitude of 100 mV and frequencies between 100 Hz and 1 MHz. To determine the dielectric properties of polyimide insulation layer, a test structure was used. The layout of the test structure was similar to MEA type A, but insulating polyimide layer was not patterned, i.e. there was a continuous 3 μm thick layer of PI-2771 at the top of metallization layer.

### C. In vivo testing

MEA implantations and recordings were done in rats at University of Kuopio. All experiments were conducted in accordance with the Council of Europe guidelines and approved by the Institutional Animal Care and Use committee and the State Provincial Office of Eastern Finland.

Wistar rats (300g) were anaesthetized with 1.2 – 1.5 g/kg urethane intraperitoneally and placed in a stereotaxic apparatus. Holes for recording and reference screw electrodes were drilled on the same side of the animal. The ground electrode was placed at A1, L1 with respect to bregma.

The MEA (laid on the dura, over the pre- and postparietal cortices between lambda and bregma) were connected via a preamplifier (Neuralynx Inc., Bozeman, MT, USA) into the main amplifier (Grass Instruments, West Warwick, RI, USA) and data acquisition PC (running DataWave Sciworks). An isolated current source (WPI Inc., Sarasota, FL, USA) was used to generate current stimuli, a set of paired pulses with pulse intervals of 500 ms. The duration of individual square wave current pulse was 1 ms. The stimuli were delivered to the left front or back paw of the rat.

## III. RESULTS

Electrode-electrolyte interface impedances of MEAs' (A, C and D) microelectrodes were measured at frequencies between 50 Hz and 100 kHz. Twenty microelectrodes in both materials and both electrode sizes were examined. The mean impedances of MEA type C and D (Ø: 100 μm) at 1 kHz were 34 kΩ and 95 kΩ with standard deviations of 4 kΩ and 40 kΩ, respectively and for type A (Ø: 200 μm) the values were 98 kΩ and 18 kΩ, respectively. Impedance curves of a couple of Pt- and Au-electrodes (Ø: 200 μm) are presented in Fig. 3.

The impedance curve of an insulated test structure [Fig. 4] compared to non-insulated one indicates that dielectric properties of polyimide are good enough for high quality recordings in wet environment.

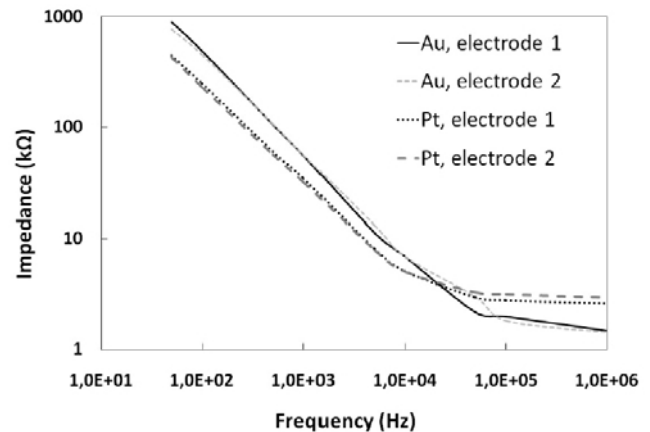


Fig. 3 Impedance curves of platinum and gold microelectrodes (Ø = 200 μm) in physiological saline solution. Twenty electrodes were examined, but only two curves per electrode material are presented here for clarity.

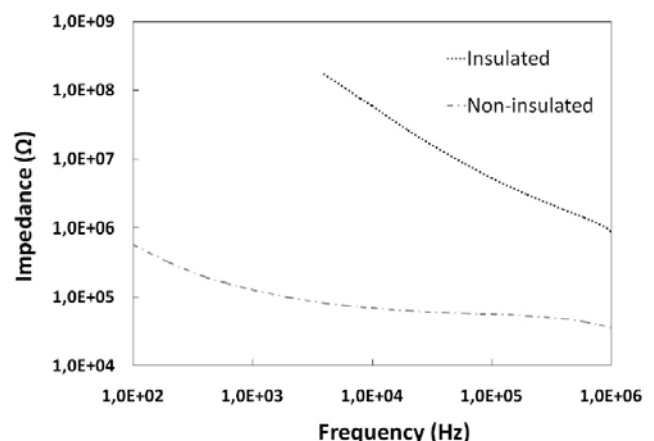


Fig. 4. Impedance curves of completely insulated and non-insulated test structure (Pt-electrodes, Ø: 100 μm) in physiological saline solution.

Preliminary *in vivo* recording tests showed promising results. Experiments with 8-channel platinum MEA yielded stable evoked potential recordings with maximum peak-to-peak amplitudes as high as 0.2 mV. Observed standard response parameters, such as latencies, onsets and decays of main components in voltage traces showed the good spatiotemporal performance of MEA.

#### IV. DISCUSSION

We described the design, fabrication, *in vitro* tests and *in vivo* experiments of flexible thin film MEA. The main aim of this study was to find out the most suitable materials, designs and fabrication methods for flexible electrode arrays. Modern microfabrication methods offer great possibilities to develop neural interfaces in microscale. Human body is a very demanding environment to implantable electrical microdevices due to moisture and salt ionics. All selected implant materials must also be compatible with biological tissue (tissue response, allergic response). We chose polyimide for the base material due to its excellent biocompatibility, mechanical properties and chemical stability. Sputtered platinum was found to be suitable material to neural recording. Platinum has much lower impedance level compared to gold especially at low frequencies below 1 kHz which are the most relevant in recordings of biological signals. Epoxy-resist SU-8 has been tested as an insulation material in corresponding flexible electrode arrays [14] and it was reported to be biocompatible [16]. Based on our brief mechanical bending tests, polyimide was noticed to be much better insulation material. Polyimide MEAs are very robust and they could be bent even into sharp angles without any cracks observed whereas the bending caused lots of cracks to SU-8 film and even delaminations of SU-8 film. However, SU-8 could also be a good candidate in some applications which do not require extreme bending capability.

#### V. CONCLUSIONS

Flexible thin film MEAs were designed and fabricated. Different variations and device materials were tested for aiming to find out the most functional MEA solution. *In vitro* electrochemical evaluations and preliminary *in vivo* recordings indicated good performance and potential of these arrays, especially in polyimide-platinum-polyimide sandwich realization.

#### ACKNOWLEDGMENT

Parts of this work has been supported by the TEKES (Finnish Funding Agency for Technology and Innovation project 70032/06 "Neurogrid". We are grateful to the staff of Microsensor laboratory of Savonia University of Applied Sciences, Kuopio, Finland. We also like to thank Dr. Markku Tiitta for help in impedance spectroscopy and Mr. Aimo Tiihonen for assembling connector boards.

#### REFERENCES

1. Nair D, Burgess R, McIntyre C et al. (2008) Chronic subdural electrodes in the management of epilepsy. *Clin Neurophysiol* 119:11-28
2. Kitzmiller J, Beversdorf D, Hansford D (2006) Fabrication and testing of microelectrodes for small-field cortical surface recordings. *Biomed Microdevices* 8:81-85
3. Williams J, Rennaker R, Kipke D (1999) Long-term neural recording characteristics of wire microelectrode arrays implanted in cerebral cortex. *Brain Res Brain Res Protoc* 4:303-313
4. Nicoletis M, Ghazanfar A, Faggin B et al. (1997) Reconstructing the engram: simultaneous, multisite, many single neuron recordings. *Neuron* 18:529-537
5. Najafi K, Wise K (1986) An implantable multielectrode array with on-chip signal processing. *IEEE J Solid-St Circ* 21:1035-1044
6. Campbell P, Jones K, Huber R et al. (1991) A silicon-based, three-dimensional neural interface: manufacturing processes for an intracortical electrode array. *IEEE T Bio-Med Eng* 38:758-768
7. Polikov V, Tresco P, Reichert W (2005) Response of brain tissue to chronically implanted neural electrodes. *J Neurosci Meth* 148:1-18
8. Cheung K (2007) Implantable microscale neural interfaces. *Biomed Microdevices* 9:923-938
9. Richardson R, Miller J, Reichert W (1993) Polyimides as biomaterials: preliminary biocompatibility testing. *Biomaterials* 14:627-635
10. Cheung K, Renaud P, Tanila H et al. (2007) Flexible polyimide microelectrode array for *in vivo* recordings and current source density analysis. *Biosens Bioelectron* 22:1783-1790
11. Boppart S, Wheeler B, Wallace C (1992) A flexible perforated microelectrode array for extended neural recordings. *IEEE T Bio-Med Eng* 39:37-42
12. Stieglitz T, Beutel H, Schuettler M et al. (2000) Micromachined, polyimide-based devices for flexible neural interface. *Biomed Microdevices* 2:283-294
13. Owens L, Denison T, Versnel H et al. (1995) Multi-electrode array for measuring evoked potentials from surface of ferret primary auditory cortex. *J Neurosci Meth* 58:209-220
14. Hollenberg B, Richards C, Richards R et al. (2006) A MEMS fabricated flexible electrode array for recording surface field potentials. *J Neurosci Meth* 153:147-153
15. Takahashi H, Ejiri T, Nakao M et al. (2003) Microelectrode array on folding polyimide ribbon for epidural mapping of functional evoked potentials. *IEEE T Bio-Med Eng* 50:510-516
16. Voskerician G, Shive M, Shawgo R et al. (2003) Biocompatibility and biofouling of MEMS drug delivery devices. *Biomaterials* 24:1959-67

Author: Sami Myllymaa  
 Institute: University of Kuopio  
 Street: Yliopistonranta 1 R  
 City: Kuopio  
 Country: Finland  
 Email: sami.myllymaa@uku.fi

# Prediction of Epileptic Seizures for On-Demand Vagus Nerve Stimulation

K.R. Nielsen<sup>1</sup>, C. Sevcencu<sup>1</sup>, A. Rasmussen<sup>2</sup> and J.J. Struijk<sup>1</sup>

<sup>1</sup> Center for Sensory-Motor Interactions (SMI), Aalborg University, Aalborg, Denmark

<sup>2</sup> Aalborg Hospital – Aarhus University Hospitals, Aalborg, Denmark

**Abstract** — Vagus nerve stimulation (VNS) is a therapy for refractory epilepsy. Typically, VNS is performed for 30 s every 5 min, and the therapeutic effect increases over a time scale of several months. In addition, VNS exerts an immediate seizure suppressing effect. To use this effect, VNS should be done on-demand, before or at the early start of seizures. This requires that seizures can be predicted or detected at an early stage. This study was performed to develop an epilepsy model suitable for identifying seizure predictors for use in an on-demand VNS system.

The present work was performed in 9 rats. Animals were anesthetized by continuous intravenous (I.V.) administration of a mixture of ketamine and xylazine. Seizures were induced by I.V. infusion of 50 mg/kg pentylenetetrazole (PTZ) over a 5 min period. During the experiments EEG, ECG and EMG (one animal) were recorded. Seizures were defined from the EEG activity and RR interval (RRInt) changes were investigated as a seizure predictor.

Four different stages of EEG activity were identified. Stage 2 was associated with the onset of the tonic phase of the seizure. Therefore the start of this EEG stage was defined as the onset of tonic seizure. In 78% of cases, it was possible to predict seizures based on significant changes in the RRInt. Predictions were done  $114 \pm 29$  s (mean  $\pm$  SD) prior to seizure onset. In 89% of cases tonic seizure was associated with bradycardia.

The results show that the model is suitable for identifying precursors for epileptic seizures. RRInt changes could be used as a predictor in the model, however, further work is needed to clarify if RRInt changes can be used for seizure prediction in other animal models or in human patients.

**Keywords** — Epilepsy, Vagus Nerve Stimulation, Animal model, RR interval, Heart Rate

## I. INTRODUCTION

VNS has been applied for the treatment of refractory epilepsy for more than 20 years. The typical treatment paradigm consists of stimulating the left vagus nerve for 30 s every 5 min with 20-30 Hz pulse trains at the highest tolerated intensity [1]. Studies have shown that in approximately 50 % of patients, seizure frequency is reduced by more than 50 % during VNS treatment [2]. The mechanisms supporting the observed seizure reduction is not fully understood. However, VNS seems to be effective at 3 different time scales: 1) it is able to abolish ongoing seizures [3], 2) it has a persistent effect lasting up to 10 min after stimulation

offset [4], 3) the seizure inhibiting effect increases over several months [5]. The currently used stimulation paradigms primarily exploit the latter two longer time scale effects. The efficiency of VNS might be increased by stimulating just before or in the early stage of a seizure, thus optimizing the timing of the seizure inhibiting mechanisms working on the short time scales, 1 and 2. However, to perform such on-demand VNS seizures must be predicted or at least detected early. Seizure detection has been investigated for more than 3 decades and research has mainly been focused on EEG recordings. However, methods still need be improved before they can be used in clinical practice. [6] On the other hand, studies have shown that seizures may be preceded by changes in the cardiac activity [7].

Therefore the aim of this work was to develop an animal model appropriate for finding a precursor of epileptic seizures and to investigate if changes in the RRInt could be used to predict the onset of seizures.

## II. METHODS

The present experiments were performed on 9 male Wistar (n=4) and Sprague Dawley (n=5) rats, 300-585 g weight. The animals were initially anesthetized with 2 intramuscular (I.M.) doses of ketamine/xylazine (45 mg/5 mg per kg) administrated 10 min apart. The level of anesthesia was afterwards kept constant by continuous I.V. administration of the same drugs (45 mg/5 mg per kg/hour) diluted in saline (total volume of 8.2 ml per kg/hour). After the experiment rats were killed using an overdose of anesthesia.

Temperature was monitored using a rectal probe and maintained at  $37 \pm 1$  °C using a heating pad. EEG was recorded via 2 stainless steel electrodes, which were screwed in the cranium 3 mm anterior (active) and 9 mm caudal (indifferent) to *bregma*. ECG was recorded using needle electrodes placed subcutaneously in lead II configuration. In one rat (rat number 8) additionally EMG was recorded from the left styloglossal muscle using stainless steel wire electrodes. EEG and ECG were sampled at a minimum of 1 kHz and EMG at 20 kHz. After the electrodes were inserted, the animal was left to stabilize for at least 15 min before any recordings were performed. Seizures were induced using PTZ diluted in saline (25mg/ml) and the mixture was ad-

ministrated I.V. for 5 min at a rate of 10 mg PTZ per kg/min (total of 50 mg/kg). This way of PTZ administration was applied for ensuring a consistent increase of plasma PTZ levels across rats.

The seizure onset was defined from the EEG recordings. RRInt were median filtered in 2 s bins to remove the influence of faulty R-peak detections caused by movement artefacts and to reduce variance. A 1 min RRInt baseline was considered immediately before the start of PTZ infusion. A seizure was regarded as detected when 3 consecutive RRInt deviated from the 95% confidence interval of the baseline in either positive or negative direction.

### III. RESULTS

#### A. Seizure Development

EEG could be divided into 4 consecutive stages, (Fig. 1): The baseline activity (stage 0), was defined as the activity before PTZ administration. This stage typically contains 1-2 Hz irregular waves and few spikes.

Stage 1 was characterized by an increase in the frequency and regularity of spikes. This spiky period developed gradually from the baseline activity, making it impossible to define the exact time of the onset of this stage. The transition from stage 1 to stage 2 was more well-defined and associated with a short period of myoclonic twitches (Fig. 2). These twitches started in the face, and then spread to the frontal and later the hind limbs.

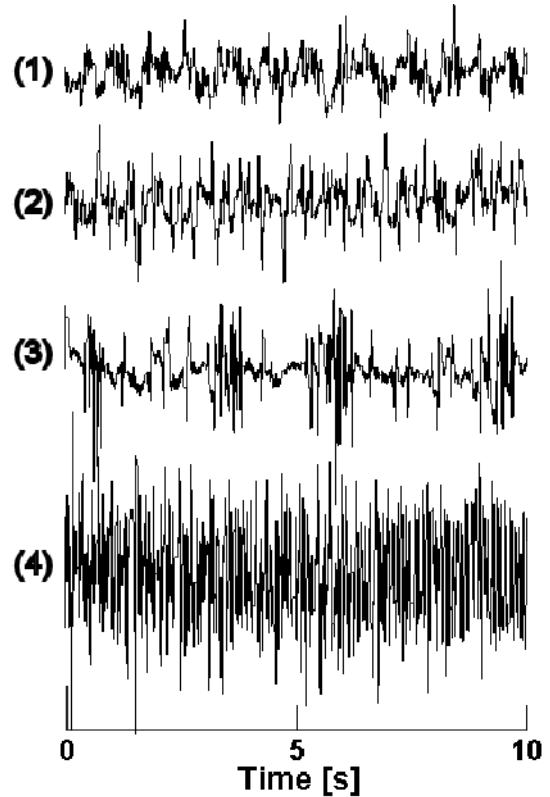


Fig. 2 EEG traces before and after PTZ administration in rat 9. Stage 0 show baseline activity and the subsequent stages show gradual seizure development. The stages are described in the text.

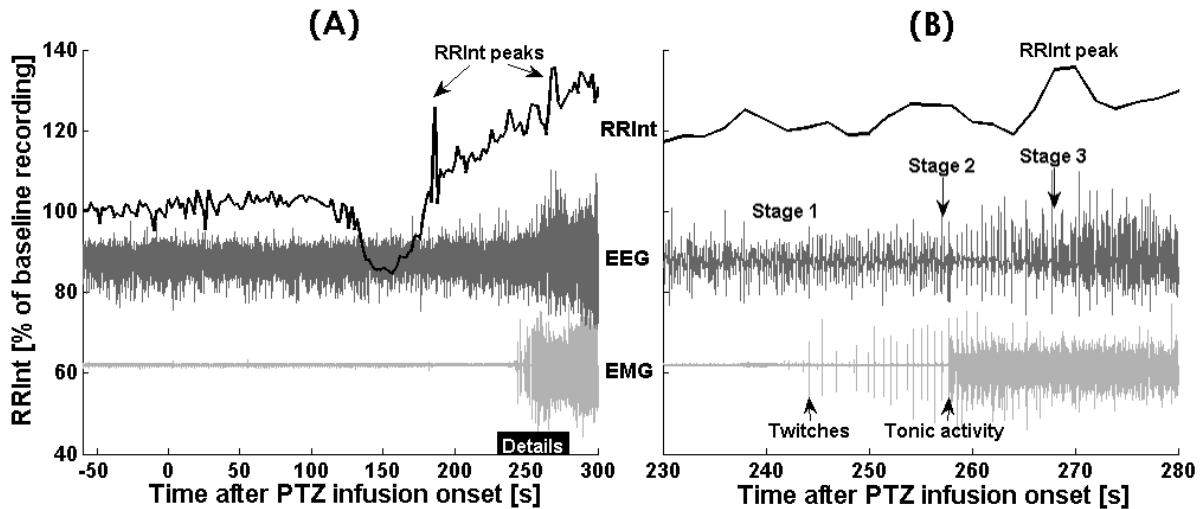


Fig. 1 (A) RRInt shown together with EEG and EMG traces, recorded in rat number 8. RRInt peaks occur at 186 s and 270 s after the onset of PTZ infusion. The black box in the bottom illustrates the part of the recording which is enlarged in the right plot. (B): Myoclonic twitches start 13 s prior to the onset of stage 2 EEG and tonic muscle activity. Note the latter RRInt peak, which coincides with the onset of stage 3 EEG activity.

In stage 2, the cortical activity assembles into clusters of 1-9 spikes firing at 8-10 Hz separated by ~0.5-1 s long quiet periods. Stage 2 was associated with the start of the tonic seizure (Fig. 2), it started  $206 \pm 43$  s after PTZ infusion onset and had a duration of  $24 \pm 16$  s.

Stage 3 was associated with ongoing tonic seizures and consisted of continuous large amplitude and high frequency (8-16 Hz) spikes and spike-and-wave discharges. Stage 3 started  $223 \pm 32$  s after the onset of PTZ infusion.

All rats displayed stage 1 to 3 activity, except rat 4 which did only reach stage 2 activity.

*B. The RR Interval in Relation to Seizure*

Using the RRInt as described in section Methods, seizures were predicted in 7 out of 9 rats (78 %),  $114 \pm 29$  s prior to the onset of stage 2 (Fig. 3). In 2 rats seizures were not detected until 20 and 30 s after stage 3 onset.

Out of the 7 predicted seizures, 5 predictions were based on pre-ictal bradycardia and 2 on tachycardia. In the 2 later cases (rats 7 and 8), animals recovered from tachycardia and developed bradycardia during the actual seizure. Bradycardia during seizure was observed in 8 out of 9 rats and the onset of stage 3 EEG activity was in 6 rats associated with an RRInt peak.

In general, bradycardia was more pronounced than tachycardia when occurring, thus RRInt increased by more than 5 % in 8 out of 9 animals, whereas only 2 rats showed an RRInt decrease of more than 5 %.

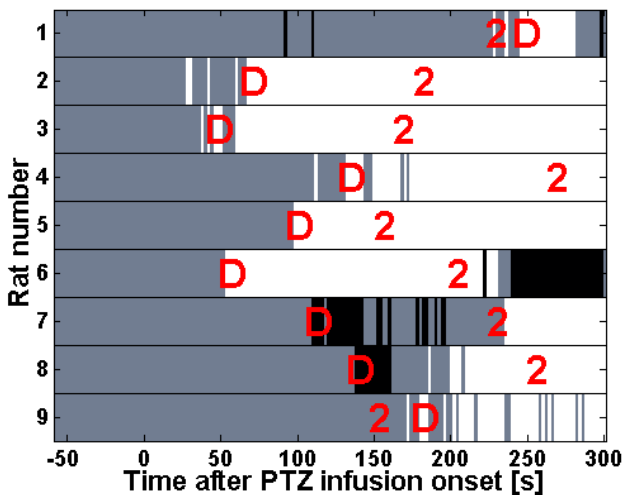


Fig. 3 Evaluation of RRInt changes as a predictor of tonic seizure. Every horizontal row illustrates one experiment over time. Gray tone indicates that the RRInt is within the 95% confidence interval of the baseline, which is defined from the 60 s just prior to start of PTZ infusion. White and black tones illustrate that the RRInt has significantly increased (bradycardia) or decreased (tachycardia), respectively. “D” shows when a pending seizure can be detected based on RRInt changes, and “2” refers to the EEG stage.

IV. DISCUSSION

An animal model of epilepsy was developed for investigating precursors for epileptic seizures. The start of tonic seizure was defined based on stage 2 EEG activity which occurred in all rats following PTZ administration.

Ono et al. suggested a 0 to 6 grading system for PTZ induced seizures in awake rats [8]. In their experiments seizures developed gradually and the EEG activity was correlated to observed symptoms. The gradings from 0 to 6 were associated with:

- Grade 0: occasional bursts of sharp EEG waves without any relation to seizure symptoms
- Grade 1-2: Ictal EEG events associated with symptoms as head twitches and myoclonic jerks.
- Grade 3-5: 1-9 Hz spike and wave activity were always present and associated with head twitching, clonic contractions of frontal limbs and kangaroo position.
- Grade 6: Tonic seizure. EEG could not be interpreted because of movement artifacts.

The findings are similar to those from our anesthetized model, where seizures also develop gradually and the first sign was an increased frequency of spikes. Later myoclonic twitches in the face, frontal and hind limbs and finally tonic seizure occurred.

When using both EEG and observations in the awake model, it was possible to distinguish more seizure stages, then when using EEG only in our anesthetized model. It might, however, be possible to further distinguish of seizure stages in an anesthetized model, e.g. by combining EMG recording from face and limbs with the EEG activity. Figure 2 illustrates that stage 1 activity can be divided into EEG activity with and without myoclonic twitches.

An anesthetized rat model has several advantages compared to an awake freely moving rat model. Measurements are easier to perform because of fewer requirements to insertion and equipment. In addition, there will be fewer movement artifacts, which is exemplified with the fact that Ono was not able to interpret EEG recordings from the tonic seizure phase. These advantages make an anesthetized rat model suitable for testing new measurements. Especially promising precursors found may later be tested in an awake model, to evaluate the robustness to noise.

Continuous I.V. maintenance of anesthesia, was applied instead of repeated bolus injections to avoid oscillating anesthetic levels in order to have a stable model (e.g. RRInt and EEG baseline activity), and to minimize the possible effect of ketamine on the seizure susceptibility [9].

PTZ was also continuously administered I.V. to minimize the effect of different wash out rates at a bolus injection.

tion site e.g. in a muscle. To the authors experience, I.M. administration of 50 mg/kg PTZ did not result in as distinct symptoms and EEG changes as when done I.V. over 5 min.

Novak et al. found changes in heart rate variability 30 s prior to and during temporal lobe seizures. In addition, heart rate started to rise (tachycardia) few seconds prior to seizure onset with a maximum during seizure [7]. In comparison, we were able to predict seizures ~4 times earlier, at  $114 \pm 29$  s prior to seizure onset. There are of course some obvious limitations in our results. As no control period has been evaluated it was not possible to evaluate the specificity of the RRInt based prediction algorithm. In addition the animals are anesthetized thus a stable RRInt was expected. This will normally not be the case during normal every day life activity in humans.

In humans, seizures are most frequently related to tachycardia, however, bradycardia is also reported. In our model seizures were mainly related to bradycardia, but there seems to be some discrepancy between PTZ models of epilepsy, described in the literature, where both bradycardia and tachycardia has been reported [10,11]. Further work is needed to elucidate these variations between experiments.

## V. CONCLUSION

A rat model of epilepsy for investigating seizure precursors was developed. EEG recordings showed that seizures developed gradually through 4 distinct stages from baseline to ongoing seizure. The late stages were accompanied by myoclonic twitches and finally tonic activity. RRInt changes could be used as a predictor for tonic seizures in the model. However, further work is needed to investigate if RRInt changes can be used for seizure prediction in other animal models or in human patients.

## ACKNOWLEDGEMENTS

This work was supported by the Danish National Advanced Technology Foundation.

## REFERENCES

1. Groves DA, Bowman EM, Brown VJ (2004) Recordings from the rat locus coeruleus during acute vagal nerve stimulation in the anaesthetized rat. *Neurosci Lett* 379: 174-179 DOI:10.1016/j.neulet.2004.12.055
2. De Herdt V, Boon P, Ceulemans B et al. (2007) Vagus nerve stimulation for refractory epilepsy: A Belgian multicenter study. *Eur J Paediatr Neuro* 11(5):261-269 DOI:10.1016/j.ejpn.2007.01.008
3. Zabara J. (1992) Inhibition of experimental seizures in canines by repetitive vagal stimulation. *Epilepsia* 33(6):1005-12 DOI:10.1111/j.1528-1157.1992.tb01751.x
4. Takaya M, Terry WJ, Naritoku DK. (1996) Vagus nerve stimulation induces a sustained anticonvulsant effect. *Epilepsia* 37(11):1111-6 DOI:10.1111/j.1528-1157.1996.tb01033.x
5. Labar D, (2004) Vagus nerve stimulation for 1 year in 269 patients on unchanged antiepileptic drugs. *Seizure* 13(6):392-8 DOI:10.1016/j.seizure.2003.09.009
6. Lehnertz K, Mormann F, Osterhage H et al. (2007) State-of-the-Art of seizure prediction. *J Clin Neurophysiol* 24(2):147-153
7. Novak V, Reeves AL, Novak P et al. (1999) Time-frequency mapping of R-R interval during complex partial seizures of temporal lobe origin. *J Auton Nerv Syst.* 77(2-3):195-202 DOI:10.1016/S0165-1838(99)00044-2
8. Ono J, Vieth FR, Walson PD. (1990) Electroencephalographical observation of seizure induced by pentylentetrazol (PTZ) injected in rats. *Funct Neurol* 5(4):345-352
9. Herink J. (1997) Effect of alprazolam and ketamine on seizures induced by two different convulsants. *Acta Medica (Hradec Kralove)*. 40(1):9-11
10. Beiga MI, Bhagata N, Talwara A et al. (2007) Simultaneous recording of electroencephalogram and blood pressure in conscious telemetered rats during ictal state. *J Pharmacol Toxicol Methods* 56(1):51-57 DOI:10.1016/j.vascn.2006.12.006
11. Lathers CM, Schraeder PL (1982) Autonomic dysfunction in epilepsy: characterization of autonomic cardiac neural discharge associated with pentylentetrazol-induced epileptogenic activity. *Epilepsia*. 23(6):633-647

Author: Kristian Rauhe Nielsen  
 Institute: Center for Sensory-Motor Interactions (SMI)  
 Street: Fredrik Bajers Vej 7D2  
 City: 9220 Aalborg  
 Country: Denmark  
 Email: krauhe@hst.aau.dk

# Apparatus for Short-Wave Inductothermy “Magnetotherm”

N.A. Nikolov<sup>1</sup>, V.E. Orel<sup>1</sup>, I.I. Smolanka<sup>2</sup>, N.N. Dzyatkovskaya<sup>1</sup>, A.V. Romanov<sup>1</sup>, Yu.I. Mel'nik<sup>1</sup>,  
M.Yu. Klimanov<sup>3</sup> and V.O. Chernish<sup>2</sup>

<sup>1</sup> State National Cancer Institute/Medical Physics & Bioengineering Department, Kyiv, Ukraine

<sup>2</sup> State National Cancer Institute/Department of Breast Cancer, Kyiv, Ukraine

<sup>3</sup> State National Cancer Institute/Department of Polyclinic, Kyiv, Ukraine

**Abstract — Aim.** This paper describes the design, technical parameters and clinical trials of apparatus “Magnetotherm” (Radmir, Ukraine) for short-wave moderate inductothermy with increased asymmetry of electromagnetic field. **Materials and methods.** The basic elements of apparatus are the power module, control and management device, high-frequency generator, devices of defence and management, co-ordinate device and inductive applicator for electromagnetic irradiation (EI). EI frequency was  $27.12 \pm 0.16$  MHz. The apparatus “Magnetotherm” was tested in cancer clinics. Temperature measured by infrared thermometer on the surface of exposed region was  $38.96 \pm 0.10$  °C. The patients with breast cancer (IIA and IIIB stages) were treated by standard treatment regimen of chemotherapy with 30 min EI. **Results.** Computer simulation and experimental researches testified an increase in asymmetry of electromagnetic field (EF) for frame applicator with the circular arc in profile compared to similar applicator with straight profile. It is accompanied by differing interaction characteristics of electric and magnetic fields for homogenous and heterogeneous structure of phantoms. There was registered the regression of primary tumours by 17% and regression of lymph nodes and metastases by 57% with the constancy of side effects. **Conclusion.** The use of local EI by new apparatus “Magnetotherm” for short-wave moderate inductothermy with increased asymmetry of EF during anticancer neoadjuvant therapy of patients with breast cancer increased the efficiency of the treatment.

**Keywords —** inductothermy, asymmetry of electromagnetic field, tumour.

## I. INTRODUCTION

The electromagnetic field (EF) in radiofrequency range is widely used in hyperthermia induction of malignant human tumour for anticancer neoadjuvant therapy. Malignant tumours have a very different sensitivity to EF. The external EF is partially transformed into the heat. Radiofrequency hyperthermia produces local heating (39–46 °C) of the tumours without generation of whole-body hyperthermia. The temperature in the centre of the heated tumour fluctuates within  $\pm 0.1$  °C, while the temperature uniformity within the tumour fluctuates within  $\pm 0.5$  °C [1]. Recently scientists have demonstrated that hyperthermia induced by

moderate temperature gradients can have significant biological effects. The heating of rodent tumours up to 39–42 °C was accompanied by continuous increase in blood flow and oxygenation in the tumour [2].

One of the branches in hyperthermia known as electrohyperthermia is based on the transfer of electromagnetic energy into tumour with the help of capacitive electrodes. This depolarizes and therefore destabilizes cell membranes and changes the active membrane transport, the membrane capacity, potential etc. The local electrohyperthermia treatment reduces the size and slows down the growth of the treated tumours compared to the control values for some tested tumours [3].

The second branch of hyperthermia known as inductothermia is based on the use of magnetic component of EF in the radiofrequency spectrum for the localization and the concentration of the heat during anticancer neoadjuvant therapy or activation of susceptor material implanted in the tumour [4].

The magnetic component of EF causes heating in tumour tissues through induced eddy currents that capable initiate adverse effects during the treatment too. Incorporation of antitumour agents into tumour cells is increased by eddy current stimulation induced by pulsing magnetic fields. Therefore, the cell cycle shifts from the non-proliferative to proliferative phase that lead to increased antitumour activity of the drug [5].

Cancer is often characterized as a chaotic, poorly regulated growth. Cancer can be viewed as a complex adaptive system [6]. Complex adaptive systems can be described mathematically by nonlinear (chaos) theory including fractal structures, autocorrelation analysis and asymmetry [7]. Atypical shape (heterogeneous) of tumour cells and chaotic structure of blood flow is one of the characteristic features for cancer process. In paper [8] it was suggested to produce asymmetric magnetic field pattern with eddy current orthogonal to the magnetic force lines during regionally-focused hyperthermia of heterogeneous malignant cells. However, the influence of electromagnetic local irradiation especially with increased asymmetry of EF during treatment of cancer patients was not studied yet.

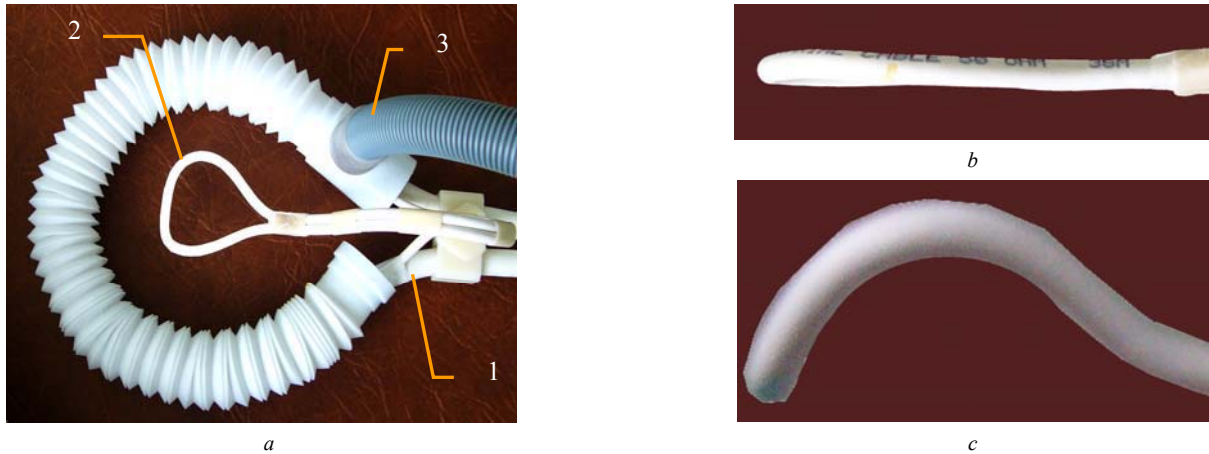


Fig.1 Original appearance of inductive applicator: 1 – major loop; 2 – complementary loop; 3 – aerial cooler; a – assemblage on a horizontal plan; b – complementary loop with the profile of straight-line segment; c – complementary loop with the profile of an arc of the circle

This paper describes the design, technical parameters and clinical trials of apparatus “Magnetotherm” (Radmir, Ukraine) for short-wave moderate inductothermy with increased asymmetry of electromagnetic field.

## II. MATERIALS AND METHODS

### A. The design and technical parameters

The basic elements of apparatus are the power module, control and management device, high-frequency generator, devices of defence and management, co-ordinate device and inductive applicator for electromagnetic irradiation (EI). EI frequency was  $27.12 \pm 0.16$  MHz. Original appearance of inductive applicator is shown at Fig. 1. Basic details of inductive applicator: major and complementary loops, aerial cooler.

### B. Computer simulation

EF isolines computed according to [9] are presented in Fig. 2. An asymmetry of electric ( $a_E$ ) and magnetic component ( $a_H$ ) of EI was calculated according to [10].

### C. Estimation of EF distribution

We estimated EF distribution of applicators according to their shape. The shape of major applicator was an ellipse on a horizontal plane. Complementary applicators were elliptic too and differed by profile geometry. In first case the profile of complementary applicator was a straight-line segment, in second case it was an arc of the circle with 2.3 cm in radius. Electric ( $E$ ) and magnetic ( $H$ ) components was estimated by

measuring elements connected to the amplifier, analog-to-digital converter and personal computer (DMPB-1, Ukraine).

### D. Patient population

Two groups of patients with breast cancer (IIA and IIIB stages) were studied. All diagnoses were morphological and histological verified. Main 1-st group included 15 patients treated by standard treatment regimen of polychemotherapy (PCT) with 30 min EI. Control 2-nd group included 14 patients treated by standard treatment regimen of PCT without EI. All groups consisted of women aged 42–68 years.

PCT included doxorubicin hydrochloride ( $70 \text{ mg/m}^2$ ), cyclophosphan ( $600 \text{ mg/m}^2$ ) intravenously with EI from first to seventh day. Three courses of PCT and EI were conducted with an interval in 21 day. Temperature measured by infrared thermometer Medisana AG (Hilden, Germany) on the surface of exposed region. Temperature on the skin surface in the area of EI increased from  $36.12 \pm 0.18$  °C to  $38.96 \pm 0.1$  °C after irradiation.

The efficiency of treatment estimated by an involution of primary tumour and the reduction of lymph nodes and metastases by means of mammography and histology.

## III. RESULTS AND DISCUSSION

### A. Computer simulation

EF isolines for applicators in  $10 \times 10$  cm irradiated region are presented at Fig. 2.



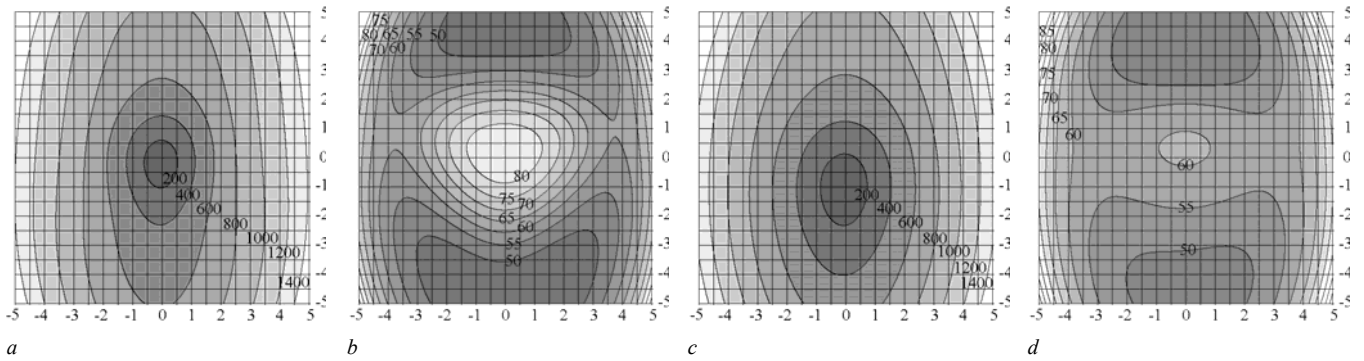


Fig. 2 EF isolines. The applicator with straight-line segment in profile: *a* – electrical component with  $a_E = 0.1$  a.u.; *b* – magnetic component with  $a_H = 0.64$  a.u. The applicator with an arc of the circle in profile: *c* – electrical component with  $a_E = 0.16$  a.u.; *d* – magnetic component with  $a_H = 1.42$  a.u. Distance to the plane of applicator was 0.5 cm; the values on isolines indicated the tension of electrical field in V/m and magnetic field in A/m; the distance in cm is indicated on the axis of abscissas and ordinates

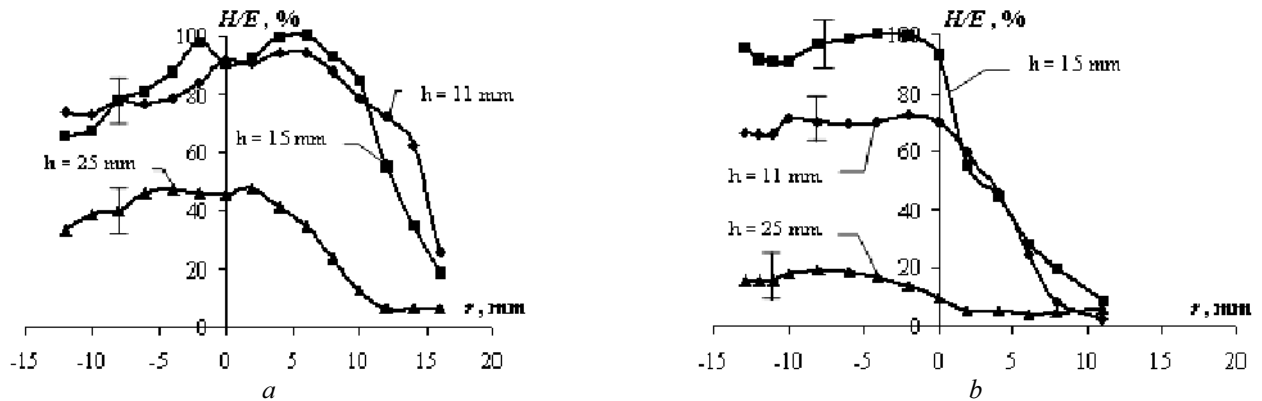


Fig. 3 Change (%) of ratio  $H/E$  for EF in the line of major axis on distance  $h$  to the plane of applicator: *a* – the applicator with straight-line segment in profile; *b* – the applicator with an arc of the circle in profile; the point (0, 0) is the geometric centre of applicator

The greatest coefficients of the asymmetry  $a_E = 0.16$  a.u. and  $a_H = 1.42$  a.u. were obtained for the applicator with the profile in the form of an arc of the circle.

*B. Experimental researches*

The change of the ratio  $H/E$  for EF on the line of major axis at different distances to the plane of main applicator is shown in Fig. 3.

It should be noted that ratio  $H/E$  in geometric centre for applicator with straight profile was diminished on 2.3% and 49% with increasing of distance from 11 mm to 15 mm and from 15 mm to 25 mm accordingly. For applicator with an arc of the circle in profile an increase on 40% of the ratio  $H/E$  in geometric centre was observed while the distance increased from 11 mm to 15 mm, with increasing of distance from 15 mm to 25 mm the ratio  $H/E$  was diminished more than in 8 times. The results of experiment

testified more expressed changes in the ratio  $H/E$  in the space near the applicator with profile in the form of circular arc. It confirms the results of above-mentioned computer simulation.

As it is mentioned above the structure of tumourous tissue as a rule is more heterogeneous compared to normal tissue. The change of EF asymmetry during regionally-focused EI may differ in the character of EF interaction with tumourous and normal tissues. To investigate this the distinctions of the ratios of electric and magnetic components for different phantoms were studied. In first case Petri dish of organic glass 38 mm in diameter, 10 mm in height with 7 ml normal physiological solution imitating homogeneous structure was used. In second case Petri dish of similar size contained the foam wadding impregnated with normal physiological solution imitating heterogenous structure. Fig. 4 shows the change of the ratios of electric field strength for the phantoms with normal physiological

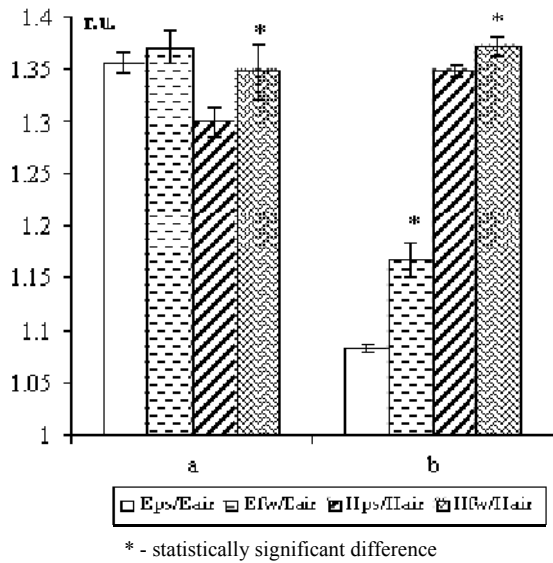


Fig.4 The change of the ratios  $E_{ps}/E_{air}$ ,  $E_{fw}/E_{air}$ ,  $H_{ps}/H_{air}$  and  $H_{fw}/H_{air}$  in geometric centre of the applicators after interaction EF with phantoms: a – the applicator with profile in the form of straight-line segment; b – the applicator with profile in the form of an arc of the circle

solution, foam wadding to electric field strength in the air under empty Petri dish ( $E_{ps}/E_{air}$ ,  $E_{fw}/E_{air}$ ) and ratios for magnetic field  $H_{ps}/H_{air}$  and  $H_{fw}/H_{air}$  depending on asymmetry of EF.

The results testified statistically significant decreasing of the ratio  $H_{ps}/H_{air}$  relative to  $H_{fw}/H_{air}$  after EI by the applicator with straight-line segment in profile. In case of the applicator with an arc of the circle in profile the ratios  $E_{ps}/E_{air}$  relative to  $E_{fw}/E_{air}$ , and  $H_{ps}/H_{air}$  relative to  $H_{fw}/H_{air}$  decreased with statistically significant difference. The ratios of EF components after interaction with foam wadding and saturated by physiological solution was greater than after interaction with physiological solution only in all traced experiments.

The results of computer simulation and experimental researches testified an increase in EF asymmetry for frame applicator with the circular arc in profile compared to similar applicator with straight profile. Symmetry of the magnetic field was more expressed. An interaction of EF with homogenous phantom structure differed from heterogeneous. The early was shown that the temperature distribution in the volume of physical phantom is qualitatively similar to the distribution of EF in the space. An increase of EF asymmetry increased the heterogeneity of heat generation structure in a tumour after local EI. [11].

In accordance with [12] the initiation of quasiregular cycles by external object in the chaotic dynamics of the system is possible. Therefore it is reasonable to use the

applicator with an arc of the circle in profile and increased asymmetry of EF for treatment of cancer patients.

### C. Clinical trials

The treatment effect on patients with breast cancer illustrated in Table 1.

Table 1. The treatment effect on patients with breast cancer

Group, treatment, patients number	Regression of tumours >50%, patients number, (%)	Regression of tumours <50%, patients number, (%)	Regression of lymph nodes and metastases, patients number, (%)
Main 1-st, PCT+EI, n = 15	9 (60%)	6 (40%)	14 (93%)
Control 2-nd, PCT, n = 14	6 (43%)	8 (57%)	5 (36%)

More than 50% regression of primary tumour was observed in 9 cases (60%) in the main group and in 6 cases in control group (43%). Regression of primary tumour less 50% it is marked in 6 cases (40%) in the main group and in 8 cases (57%) in control group. Regression of lymph nodes and metastases was marked in 14 cases (93%) in the main group and 5 cases (36%) in control group.

A morphological analysis demonstrated higher on 17% devitalization of primary tumour after treatment by PCT and inductotherapy compared to PCT only. There was diminishing of volume particle of viable tumour parenchyma on 51% after treatment by PCT with EI. At the same time after the use of PCT only it was evened 40%. Combined therapy that included inductotherapy and PCT does not led to the growth of side effects and postoperative complications, it was survived by cancer patients tolerantly.

It should be noted that greater regression of primary tumours, metastases and lymph nodes during treatment of patients with breast cancer was observed for combined PCT and EI by apparatus "Magnetotherm" compared to the use of PCT only.

### IV. CONCLUSION

New apparatus for short-wave moderate inductotherapy with the increased EF asymmetry "Magnetotherm" adds to the armamentarium of complex treatment of cancer patients. A thorough understanding of nonlinear dynamics (chaos theory) for application in oncology is required for its effective using. It has the potential to attain a place as a complementary tool with additional functionality among chemo- and radiation therapy of cancer patients.

## REFERENCES

1. Hugander A, Hafstrom L, Jonsson P E, Bolmsjo M, Persson B R, Stenram U (1984) Local hyperthermia in treatment of experimental liver tumours. *Cancer* 53:1686–1691
2. Song C W, Park H J, Lee C K, Griffin R (2005) Implications of increased tumour blood flow and oxygenation caused by mild temperature hyperthermia in tumour treatment. *Int J Hyperthermia* 21:761–767
3. Fiorentini G, Szasz A (2006) Hyperthermia today: Electric energy, a new opportunity in cancer treatment. *J Cancer Res Ther* ; 2: 401–6.
4. Storm F K, Elliott R S, Harrison W H, Kaiser L R, Morton D L (1981) Radio frequency hyperthermia of advanced human sarcomas. *J Surg Oncol* 17:91–98
5. Omote Y (1988) An experimental attempt to potentiate therapeutic effects of combined use of pulsing magnetic fields and antitumor agents. *Nippon Geka Gakkai Zasshi* 89:1155–1166
6. Coffey D S. (1998). Self-organization, complexity and chaos: The new biology for medicine. *Nature Medicine* 4:882–885
7. Mandelbort B B (1982) *The Fractal Geometry of Nature*. New York, W.H. Freeman
8. Boddie Jr A W, Frazer J W, Yamanashi W S. RF electromagnetic field generation apparatus for regionally-focused hyperthermia. United States Patent 4674481, 06/23/1987, Primary Class 600/10
9. Nikolskiy V V, Nikolskaya T I (1989) *Electrodynamics and radio-wave propagation*. Moscow: Nauka (in Russian)
10. Korn G A, Korn T M (1968) *Mathematical handbook for scientists and engineers*. New York, MacGraw-Hill Book Company
11. Orel V E, Dzyatkovskaya I I, Nikolov N A, Romanov A V, Kozarenko T M (2008, *in press*) Initiation of antitumor activity of doxorubicin by 40 MHz electromagnetic local irradiation with increased asymmetry of magnetic component during treatment of animals with doxorubicin-resistant Guerin's carcinoma. *Experimental Oncology*
12. Berzhe P, Pomo I, Vidal' K (1991) *Order in Chaos*. Moscow. Mir (in Russian)

Author: Valeriy E. Orel  
 Institute: State National Cancer Institute  
 Street: 33/43 Lomonosova Str  
 City: Kyiv  
 Country: Ukraine  
 Email: v-orel@i.com.ua

# What Conclusions does Rapid Image Classification by Eye Movements Provide for Machine Vision?

R. Paeglis, A. Kotelnikovs, A. Podniece and I. Lacis

Dept. of Optometry and Vision Science, University of Latvia, Riga, Latvia

**Abstract**— Human ability to rapidly classify images of natural objects has been a matter of study for more than a decade. Recently eye movements have been exploited as a behavioural response, which has led to alternative hypotheses of natural image processing. In this research, twelve volunteers made a movement towards a briefly displayed digital image if it was an animal, and a movement away otherwise. In both cases, the average response time was more than 400 milliseconds.

**Keywords**— VOG, *iViewX*, image categorisation, SRT

## I. INTRODUCTION

Machine vision experts look for image features that bring automated image segmenting closer to human performance. Image cues, such as brightness, colour, edges and texture, enable objects to be identified and classified by a computer [1]. Grouping images by the colour pixel distribution in a digital photograph has been shown to be a successful approach to rapidly categorise digital images [2], [3].

Computer vision is inspired by the findings of the human and animal vision. Thus in the categorization tasks the nature and limits of the human visual system are explored. It is done under conditions of short image presentation and the demand for a rapid behavioural response [4], increased number of simultaneously presented items [5], deteriorated image contrast [6] and other constraints.

At rapid sequential visual presentation of images psychophysical responses to classify images have the median reaction time of 445 milliseconds, with the shortest being below 400 milliseconds [7]. Research suggests that the differential neural activity, which is evoked by semantic categorization of objects into groups like natural objects (animals, plants) or man-made objects (furniture, clothing), is not task dependent [8]. If one compares the time for cortical processes for isolated objects as detected by Löw and collaborators, and that for objects in context [4], it can be argued that the context facilitates classification of object images but is not the decisive factor.

We followed the proposition of Kirchner and Thorpe [9] to use eye movements to categorise images. They report that eye movements may emerge as a faster way to respond in a classification task. With the minimum reliable saccade response time of 120 milliseconds, this is even faster than the

differences in the ERP [7] and has inspired possibilities that each pass of image processing actually uses a different neuronal path. Hypothetically, the image recognition and classification could act as an internal cue for the gaze stability before a conscious and voluntary action is performed. We also were interested in how rapid is the categorization process if it is not facilitated by the alternative forced choice paradigm and less trained by the number of images presented in sequence. We term a saccade towards the side of image presentation a pro-saccade, whereas an opposite movement an anti-saccade. Both of them are in fact voluntary saccades with a memory guided component [10].

## II. METHODS

### A. Participants

Twelve healthy volunteers (age 21 to 24), ten in the first stage of the research and two in the second, contributed to the research, having normal or corrected to normal near vision. The research was conducted in accordance to the ethical standards of the Declaration of Helsinki. All participants provided informed consent concerning the procedure but were naive to the purpose of the research.

### B. Eye-tracker

The images were presented on a PC (CPU: Intel Pentium 4, 3 Ghz; RAM: 1 GB) with a 17 inch LCD screen (Hyundai ImageQuest L72D, 1280 by 1024 pixels, refresh rate 60 Hz). Custom software was made in Visual Basic for image presentation. The actual time that the images were seen on the screen for the specified hardware and selected images was  $330 \pm 7$  milliseconds.

Eye position was detected by the *iViewX* infra-red eye tracking device (SensoMotoric Instruments, Germany). After a 13 point calibration every participant's eye was tracked with the data sampling frequency of 240 Hz.(precision 0.5 degrees, tracking accuracy for the screen and distance we used the tracking resolution lowers to 0.04 degrees). Gaze position data recording on the operator's PC was synchronised with the stimulus presentation on the participant's PC with the accuracy of 1 millisecond.

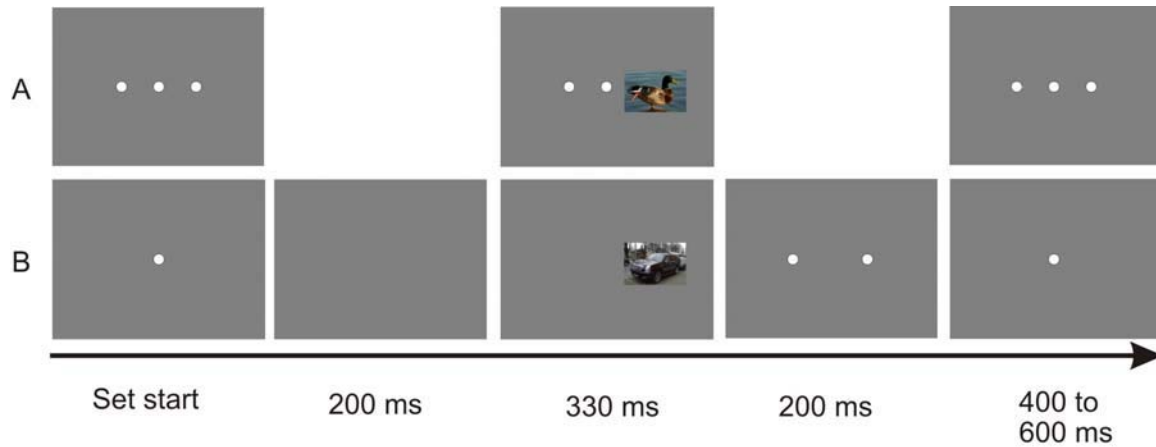


Fig. 1 Participant's screen in a single set of the overlap (A) and the gap (B) trials

### C. Procedure and images

A participant was seated at the eye tracking column and the person's head was stabilised on a chinrest. The demonstration screen was located 40 centimetres from the person's eye. The person fixated the gaze on a white central fixation point on a neutral grey screen. For the overlap paradigm, the central fixation point and two auxiliary points were on the screen during the entire procedure (Fig. 1), and 30 images were shown after practice. After a 30 + 30 image training a 90 image sequence was shown in the gap paradigm. The images were 300 pixels wide and 225 pixels high, or subtended 12 by 9 degrees, their left edge being located 7 degrees from the central fixation point. Colour photographs of objects were selected from a commercially available database. Images of animals in their natural habitats (e.g., a bird on a tree or a killer-whale in the water) were selected as the targets, which corresponds to the published approach [9].

Saccades and fixations were calculated separately by and *BeGaze* software provided by the manufacturer of the eye-tracker. The gaze position for a fixed time after the stimulus onset was extracted from the raw data by custom-made MATLAB 7.4 code. Statistical data processing was done in SPSS 16.0 and Origin 8.0 with alpha levels 0.01 if not specified otherwise.

## III. RESULTS

### A. Saccades to a single image

Ten volunteers observed a series of 30 images appearing to the right from the central fixation point. The saccades were further classified into correct responses (either a saccade to an animal image or an anti-saccade otherwise) and

erroneous responses. The sets where a participant failed to make an eye movement response in 1000 ms or made an eye movement sooner than 100 ms after the image appearance (express saccade time) were excluded from consideration. With these cases excluded, we obtained the mean saccade response time  $455 \pm 164.8$  ms for the correct responses, and  $362 \pm 228.9$  ms for the movements to a wrong direction. Since the distributions of the response times in both groups were normal (Kolmogorov-Smirnov,  $D(284) = 0.063 > 0.207$ ) but their variances were significantly different (Levene's test,  $F = 13.019$ ;  $p < 0.001$ ) we found that the correct and erroneous response times differ significantly by the Independent samples t-test assuming unequal variances,  $t(57; 317) = 2.311$ ;  $p = 0.024$ . This motivated us to make an experiment where saccades and anti-saccades could be distinguished in the correct and erroneous response groups.

### B. Overlap and gap paradigms contrasted

We developed the data analysis algorithm so that we could classify the responses into correct saccades, correct anti-saccades, erroneous saccades and erroneous anti-saccades. By these means we intended to search for possible indicators of the response before it is made, and to test if the saccade response time is correlated to the kinematics of the following eye move.

For the overlap paradigm, we calculated response times of  $460 \pm 73$  ms for correct pro-saccades and  $460 \pm 88$  ms for correct anti-saccades ( $370 \pm 114$  and  $450 \pm 81$  ms for erroneous pro-saccades and anti saccades respectively). In the gap paradigm, the participant made correct saccades in  $440 \pm 30$  ms and correct anti-saccades in  $420 \pm 42$  ms (accordingly, erroneous ones were made in  $420 \pm 15$  ms and  $390 \pm 34$  ms).

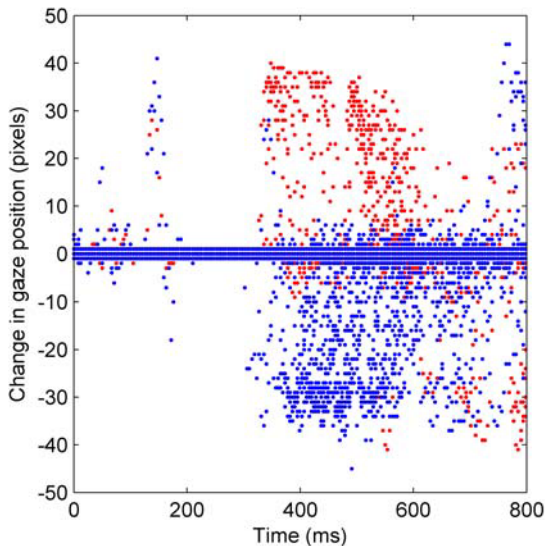


Fig. 2 Gaze stability for the participant AK (overlap paradigm) changes 160 ms after the image appearance.

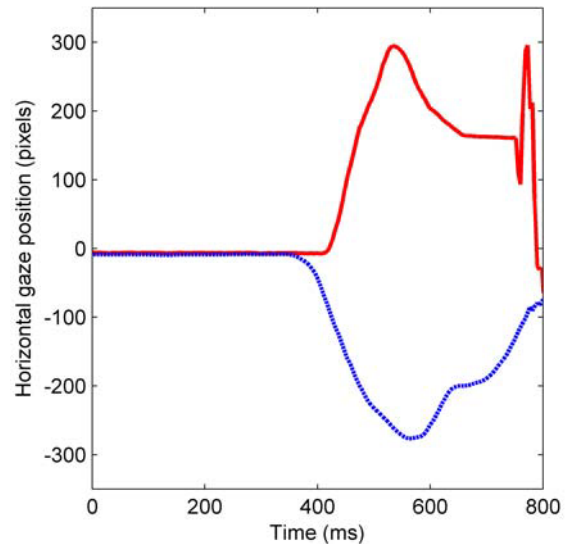


Fig. 3 Participant LV (gap paradigm) made voluntary saccades away from images (dotted line deviating down) faster than the saccades towards them

The maximum velocity of eye movements was correlated to its amplitude, Spearman's  $\rho = 0.549$  for the overlap paradigm and  $\rho = 0.751$  for the gap paradigm,  $p < 0.01$  in both cases. The other correlation, which we surmised at the beginning, is that the maximum velocity is correlated to the response time. Contrary to the predictions, this correlation is negative, i.e., the longer it takes to process an image and respond, the slower and 'hesitant' the response will be. Thus Spearman's  $\rho = -0.652$  ( $p < 0.01$ ) for the overlap paradigm and  $\rho = -0.733$  for the gap paradigm ( $p < 0.05$ ).

Saccade kinematics was searched for any potential correlations to the saccade response times. We found statistically significant correlations among the saccade amplitude and its peak speed ( $\rho = 0.613$ ), average speed (0.723) and duration (0.849) for the overlap paradigm, and the amplitude and peak speed ( $\rho = 0.788$ ) and duration (0.511) for the gap paradigm. In addition, we found a change in gaze stability some 160 ms after an image has appeared on the screen in the overlap paradigm (Fig. 2). An observation in the gap paradigm was that the anti-saccade response times can be faster than the pro-saccade response times (Fig. 3), which is not surprising since both groups in fact equally are voluntary saccades.

We have found that the gaze stability before an eye movement is made could be characterized by the Hilbert transform (Fig. 4). Similarly to the approach of Seo and Lee concerning eye movements in reading [11], we have calculated eye velocity and taken the absolute value of its Hilbert transform. In doing so, we have found that the eye is more volatile before an anti-saccade on average. Then, a reflexive

response must be suppressed and an opposite move should be generated. We could not argue of the exact timing of differences since the Hilbert transform is an integral over the entire period considered ( $\sim 300$  ms).

#### IV. DISCUSSION

The human visual system appears to respond at its extreme speed if two images present alternative forced choice [9]. In the case if a single image is presented that requires separate reaction, saccade response times are close to button release times. Since eye movements in terms of neural signal transmission are faster than moving fingers in button-release experiments, we hypothesize that the majority of the response time is spent for the image analysis. It can also be inferred that automated image search machines would benefit from hierarchical image categories rather than analyzing if a single image fits the proposed description. Machine learning could also be considered, since some of the faster response times in the preceding research [9], as contrasted to ours, could still be attributed to human learning in a larger image series.

The finding that saccade amplitudes are significantly correlated to the duration, peak speed and average speed (which is the amplitude divided by the duration) is a refection of the main sequence relations [10]. It is noted that there is some variability in the dynamics of saccades, which is linked to the participant's alertness and experimental conditions [10].

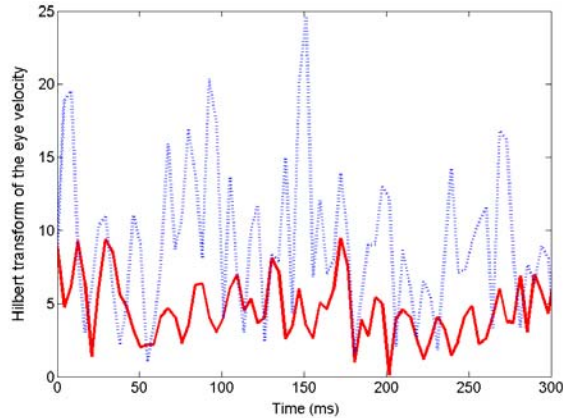


Fig. 4 Hilbert transforms of the average eye velocity before pro-saccades (solid line) and anti-saccades (dashed)

What was not anticipated is the fact that when outliers were removed and hardware delays taken into account, pro-saccades and anti-saccades as a rule were not launched during the image exposition. Rather it takes about 100 milliseconds after the image has been erased from the screen to launch a saccade, which is close to the express saccade response time [9],[10].

We have considered the Hilbert transform as an indicator of gaze stability and found that before an anti-saccade the gaze is less stable on average. The phase of this transform could be used in comparing the vertical and horizontal gaze stability in image classification tasks that have separate neural regulators.

To summarize, several differences in the experimental protocol may account for the fact that saccade response times are not much shorter than the manual response times published [10]. First, we used by angular extent smaller and more peripheral images than other research, yet they were not seen longer. Second, we observed the performance for one 90 image set instead of 10 sets by 80 images (for different conditions), although same images were presented after a week. Third, we tested both the overlap and gap paradigms and found no difference in response times. Next, and possibly the most influential difference is that we tested single side presentation instead of the alternative forced choice. Saccade response times are close to those of manual responses when single images are presented centrally [7]. This leaves us with the question of the possible mechanisms that can selectively activate the hypothesized faster image

processing and response, like V4 to the superior colliculus [9]? They then bypass the typical processing routes for some but not other experimental conditions. We also note that the saccade velocities are negatively correlated to their response times in our image classification task.

#### ACKNOWLEDGMENT

The research is supported by the European Social Fund.

#### REFERENCES

1. Shi J, Malik J (2000) Normalized Cuts and Image Segmentation. *IEEE Transactions on Pattern Analysis and Machine Intelligence* 22 (8): 888-905.
2. Greenspan H, Goldberger J, Ridel L (2001) A continuous probabilistic framework for image representation and matching. *Journal of Computer Vision and Image Understanding*, Dec., 84: 384-406.
3. Goldberger J, Gordon Sh, Greenspan H (2006) Unsupervised image-set clustering using an information theoretic framework, *IEEE Trans. on Image Processing*, 15(2): 449-458.
4. VanRullen R, Thorpe SJ (2001) Is it a bird? Is it a plane? Ultra-rapid visual categorization of natural and artificial objects. *Perception*, 30: 655-668.
5. Rousselet GA, Thorpe SJ, Fabre-Thorpe M. (2004) Processing of one, two or four natural scenes in humans: the limits of parallelism, *Vis. Res.*, 44: 877-894.
6. Macé M J-M, Thorpe SJ, Fabre-Thorpe M (2005) Rapid categorization of achromatic natural scenes: how robust at very low contrasts? *European Journal of Neuroscience*, 21: 2007-2018.
7. Thorpe S, Fize D, Marlot C (1996) Speed of processing in the human visual system. *Nature*, 381: 520-522.
8. Löw A, Bentin Sh, Rockstroh B, Silberman Y, Gomolla A, Cohen R, Elbert T (2003) Semantic Categorization in the Human Brain: Spatio-temporal Dynamics Revealed by Magnetoencephalography, *Psychological Science*, 14 (4), July: 367-372.
9. Kirchner H, Thorpe S (2006) Ultra-rapid object detection with saccadic eye movements: Visual processing speed revisited, *Vis. Res.*, 46: 1762-1776.
10. Leigh RJ, Kennard C (2004) Using saccades as a research tool in the clinical neurosciences, *Brain*, 127: 460-477.
11. Seo H, Lee C (2002) Head-free reading of horizontally and vertically arranged texts. *Vis. Res.* 42: 1325-1337.

Author: Roberts Paeglis  
 Institute: Dept. of Optometry & Vision Science, University of Latvia  
 Street: 8 Kengaraga Str.  
 City: Riga  
 Country: Latvia  
 Email: Roberts.Paeglis@lu.lv

# Analysis of Foveation Sequences in Congenital Nystagmus

G. Pasquariello<sup>1</sup>, P. Bifulco<sup>1</sup>, M. Cesarelli<sup>1</sup>, M. Romano<sup>1</sup>, A. Fratini<sup>1</sup>

<sup>1</sup> Dept. of Electronic Engineering and Telecommunication, Biomedical Engineering Unit, University "Federico II", Naples, Italy

**Abstract** — Congenital nystagmus (CN) is an ocular-motor disorder that appears at birth or during the first few months of life; it is characterised by involuntary, conjugated, bilateral to and fro ocular oscillations. Pathogenesis of congenital nystagmus is still unknown. Eye movement recording allow to extract and analyse nystagmus main features such as shape, amplitude and frequency; depending on the morphology of the oscillations nystagmus can be classified in different categories (pendular, jerk, horizontal unidirectional, bidirectional). In general, CN patient show a considerable decrease of the visual acuity: image fixation on the retina is disturbed by nystagmus continuous oscillations; however, image stabilisation is still achieved during the short foveation periods in which eye velocity slows down while the target image is placed onto the fovea. Visual acuity was found to be mainly dependent on foveation periods duration, but cycle-to-cycle foveation repeatability and reduction of retinal image velocities also contribute in increasing visual acuity. This study concentrate on cycle-to-cycle image position variation onto fovea, trying to characterise the sequences of foveation positions. Eye-movement (infrared oculographic or electro oculographic) recordings, relative to different gaze positions and belonging to more than 30 CN patients, were analysed. Preliminary results suggest that sequences of foveations show a cyclic pattern with a dominant frequency (around 0.3 Hz on average) much lower than that of the nystagmus (about 3.3 Hz on average). Sequences of foveations reveals an horizontal ocular swing of more than 2 degree on average, which can explain the low visual acuity of the CN patient. Current CN therapies, pharmacological treatment or surgery of the ocular muscles, mainly aim to increase the patient's visual acuity. Hence, it is fundamental to have an objective parameter (expected visual acuity) for therapy planning. The information about sequences of foveations can improve estimation of patient visual acuity.

**Keywords** — Congenital nystagmus, visual acuity, foveation, eye movement signal processing.

## I. INTRODUCTION

Congenital nystagmus (CN) is an ocular motor disorder which develops at birth or in the first months of life and persists all life long. Nystagmus consists essentially in involuntary, conjugated, horizontal (rarely vertical or rotatory) rhythmic movements of the eye. Nystagmus oscillations can persist also closing eyes, even if they tend to dump in absence of visual activity. Nystagmus can be idiopathic or associated to central nervous system alterations and/or

ocular system affections such as acromathopsia, aniridia and congenital cataract. Both nystagmus and associated ocular alterations can be genetically transmitted, with different modalities. According to some authors, occurrence of idiopathic CN would be 1 out of 1000 males and 1 out of 2800 females; CN is present in most cases of albinism.

In vertebrates, eye movements are controlled by oculomotor system in a complex manner, depending on the stimuli and viewing conditions. An attempt to bring the image of a target onto the retina can involve up to five oculomotor subsystems: the saccadic, smooth pursuit, vestibular, optokinetic and vergence systems. The vestibular system is driven by non-visual signals from the semicircular canals, while the other systems are driven by visual signals encoding target information [1]. Pathogenesis of the congenital nystagmus is still unknown; dysfunctions of at least one of the ocular stabilization systems was hypothesized.

Even in healthy subject, eye moves continually to keep the light from the object of interest falling onto the “fovea centralis”, a 0.3 mm diameter rod-free retina area with very thin, densely packed cones; this process is referred to as foveation. The diameter of the fovea corresponds to about 1 degree visual angle.

Resolution of details (visus) decreases sharply away from the fovea, and is also degraded if images slip over the fovea at velocities greater than a few degrees per second. Optimal visual performance is therefore only attained when images are held steady on this region.

Like all neurons, the cones need time to react to stimuli and this interval can be related to light response; it has been recently demonstrated that the photocurrent produced by iodopsin shows a response peak to dim light flash between 20 and 35 ms after the stimulus [2] (please note the similarity of this value to the time constant present in the subsequent formula).

Eye movement recording and estimation of concise parameters, such as shape, amplitude, frequency, foveation periods duration and foveation direction, are a strong support for an accurate diagnosis of CN, for patient follow-up and for therapy evaluation. Various techniques are currently used to measure and record eye-movements: electro-oculography (EOG), magneto-oculography (MOG), also known as scleral search coil system (SSCS), infrared oculography (IROG) and video-oculography (VOG). This methods differs in the principle used to quantify eye movements,



but each of them ensure a linearity from -30 to +30 degree on the horizontal plane and an accuracy, for research purpose, of less than a degree (typical 15 minarc).

According to bibliography, nystagmus can be classified in different categories (pendular, jerk, horizontal unidirectional, bidirectional) depending on the characteristics of the oscillations. Current therapies for CN, still debated, aim to increase the patient's visual acuity by means of refraction defects correction, drug delivery and ocular muscle surgery. In general, CN patients present a considerable decrease of the visual acuity (image fixation on the retina is obstructed by nystagmus continuous oscillations) and severe postural alterations such as the Anomalous Head Position, applied by patient to obtain a better fixation of the target image onto the retina. Indeed, often CN presents 'neutral zones' corresponding to particular gaze angles, in which a smaller nystagmus amplitude and a longer foveation time can be recorded; this zones correspond to position of maximum visual acuity. This led up to asses that visual acuity is mainly dependent on the duration of the foveation periods, but cycle-to-cycle foveation repeatability and eye velocity also contribute [3-4].

Moreover, in a previous work we found evidence of a slow eye movement oscillation superimposed to nystagmus, which we called Base Line Oscillation (BLO) [5]. Characteristics of such oscillation, concisely approximated by a sinusoid, have been extracted and analyzed. Frequency of this slow oscillation resulted  $0.36 \pm 0.11$  Hz on average, and the amplitude resulted correlated with that of the nystagmus waveform. The estimated relationship between mean nystagmus amplitudes and mean BLO amplitudes for each eye movement recording, showed an high correlation coefficient value ( $R^2 = 0.77$ ), suggesting an high level of interdependence between BLO and nystagmus amplitude [4].

Presence of this superimposed oscillation reduces substantially the visus, causing an increase of the Standard Deviation of position (SDp) during foveation, which in turn may hamper visual acuity.

Apart the usual technique to measure visual acuity, using Landolt C or other similar methods, a number of visual acuity predictor was developed by different research team [4,7]. Such functions are considered as an objective measure of the CN patients foveation ability and, therefore, of their potential visual acuity; they could be used to evaluate the effects of therapies applied to a patient or across patients.

Focus of this study is to compare results obtained using three different estimators of cycle-to-cycle foveation repeatability: standard deviation of all samples contained within the foveation, amplitude of the base line oscillation and standard deviation of a smoothing spline interpolation of the exact foveation points sequence.

## II. MATERIAL AND METHODS

Horizontal projections of eye movements were analyzed from CN patients, at different gaze positions. More than 30 CN patients, without additional sensory defects, ranging in age from 6 to 34 years participated in the study. They presented different types of nystagmus (pendular, jerk, dual jerk etc.) according to the classification proposed by Dell'Osso [8]. Binocular, horizontal eye movements, at different gaze positions, were recorded for each patient.

A standard visual acuity measurement was performed for each patient using a classical Landolt Cs technique. The visual acuity values measured (ranging from 0 to 1 with increments of 0.1) were expressed in tenths.

To record eye movement signals, the patients, sitting in a dimly lit room, were instructed to fixate a light stimulus presented using a LED bar at fixation distance of 1 meter. The device was able to provide stimuli in a range of 60 degrees of the field of vision ( $\pm 30^\circ$ ). Head movements were minimized using chin and head rests. Rarely, for very young children, a parent assisted in holding the patient's head.

The stimuli were sequentially presented at different gaze positions (sequence:  $0^\circ, 5^\circ, 10^\circ, 20^\circ, 30^\circ, 0^\circ, -5^\circ, -10^\circ, -20^\circ, -30^\circ, 0^\circ$ ) for 10 seconds each. Eye movements were detected using either an infrared limbal reflection technique apparatus (Oftalmograf, Universal Initram Corporation, El Paso) or an electro-oculography device (Gould ES 2000, Gould Instrument System with bio-signal amplifiers 11- 5407-58). Eye position signals were digitized at 200 Hz with a 16 bits resolution, using a PCI acquisition board (National Instruments NI PCI-6251), and stored on PC for off-line analysis.

Recorded data were filtered to reduce noise; a specific software, developed at our Lab, was used to recognize nystagmus waveforms and compute nystagmus parameters such as frequency, amplitude, intensity and waveform shape. The nystagmus cycles were detected automatically using a modified version of a previously utilized algorithm [9].

In congenital nystagmus the foveation is usually considered to occur at the end of the fast phase (which correspond to a swift repositioning of the target onto fovea, after the slow de-positioning of the eye from the target). More correctly, foveation is achieved whenever eye velocity is near  $0^\circ/s$  and the target is in a range of  $\pm 0.5^\circ$  in respect to eye position (roughly correspondent to visual angle covered by fovea). In this study we defined a "foveation window" considering the time interval in which eye velocity was lower than  $4^\circ/s$  [3, 10] and the eye position was contained within  $0.5^\circ$ , with respect to the local maximum (or minimum) of the eye position.

To recognize foveation direction (left or right) we separated automatically slow phases from fast phases for each nystagmus cycle; the slope of the fast phase was considered

a good approximation for the foveation direction (positive for right direction of vice-versa).

Once recognised foveation and computed average of foveation durations and cycle-to-cycle repeatability, the following relationship was used to estimate visual acuity:

$$NAEF = \exp(-SDp)[1-\exp(-Tf/\tau)] \quad (1)$$

where NAEF stands for Nystagmus Acuity Evaluation Function. In this relationship Tf is the average foveation time, SDp is the standard deviation of eye position during foveation and  $\tau$  was set to 33.3 ms.

Different approaches can be used to measure foveation time and cycle to cycle repeatability.

Once recognized the foveating points, a good approximation of the foveation window have to be evaluated. Velocity estimation was critical due to noise and few number of samples contained in each tract. A smoothed version of the position signal was then considered, computing a second order polynomial interpolation of the selected points; the derivative was evaluated. The foveation time was finally obtained considering the points meeting the requirements stated above (velocity less than 4°/s and eye position not more than 0.5° away from local point of fixation).

Base line oscillation was evaluated, as well as the smoothing spline (csaps.m MATLAB, p=0.85) interpolation of foveation points sequence.

The spline interpolation was considered a better estimation with respect to BLO of the standard deviation of position for CN eye movement signals

### III. RESULTS

An example of fast phases and slow phases detection in a CN eye movement recording generated by the described procedure are shown in Figure 1. Eye position and eye velocity are displayed: eye position corresponding to fast phases are painted in red, while the BLO is represented as a dashed black line.

In the specific tract represented in Fig.1 a few number of fast phase are opposed in direction in respect to the others (this is also evident in the velocity signal).

An example of the foveation points sequence (black stars), the BLO (red) and the spline computed curve (green) are shown in Figure 2.

The nystagmus frequencies resulted ranging from 3.1 to 4.6 Hz (average: 4.2 Hz) and amplitudes from 4.5 to 12.8 degrees (average: 7.6 deg.); the BLO frequencies resulted ranging from 0.15 to 0.36 Hz (average: 0.22 Hz), while BLO amplitudes resulted ranging from 0.5 to 3.4 degrees (average: 1.3 deg.). Nystagmus waveforms resulted of different types, mainly belonging to jerk types.

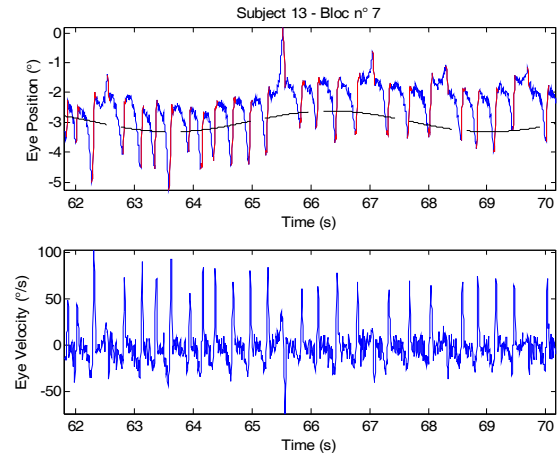


Fig.1 An example of the algorithm output (red) superimposed to the selected signal (blue). The picture also shows the BLO curve as a dashed black line and eye velocity.

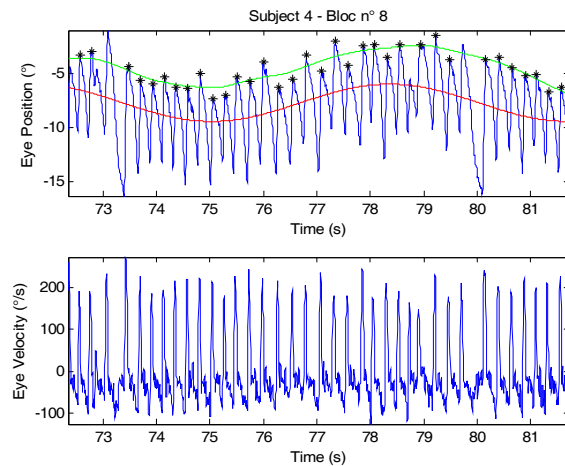


Fig. 2 An example of the spline (green) superimposed to the selected signal (blue) and the BLO (red). The picture also reports fixation points (black stars) and eye velocity.

The thirty selected patients have a measured visus very low, fifty percent of them (15 patients) have a visus of one on tenth. The estimated mean SDp for all these patients ranged from 0.3 to 1.55 degree. However, also fifty percent of patients with measured visus higher than 1 have a SDp higher than 1 degree. The low measured visus seems to depend mainly by the SDp in respect to foveation time.

A comparison between BLO SD and standard deviation of position computed on all the points in the foveation windows showed values 35% lower, while spline interpolation SD was two times more accurate, being 18% less than SDp computed on all points (the percentages refer to mean values computed on all thirty patients).

Foveation points sequence showed a non Gaussian distribution, but a sinusoidal-like behaviour. To quantify the SDp without determination of foveation points, we first identified the base line oscillation (a sinusoidal trend component); however BLO amplitude resulted not an accurate estimator.

Moreover use of a spline interpolation for the foveation sequence increased the accuracy in assessing SDp; the spline was able to fit better real data in most of the cases (containing more than one harmonic), it also resulted independent from definition of the foveation window.

#### IV. CONCLUSIONS

This study presents an analysis of nystagmus foveation sequences recorded during fixation on a fixed target, at different gaze positions in CN patients.

Current algorithms to predict visual acuity (such as NAEF) rely on standard deviation of position of all the samples used to assess the foveation time; use of a spline interpolation for the foveation sequences reduce the dependency of estimated SDp from the foveation criteria applied. This result in a large step forward from the original in both its applicability to most, if not all, CN recordings and in the reduction of the expertise necessary to accurately analyze eye movement.

The NAEF could be considered an objective measure of the foveation ability and, therefore, of the potential visual acuity. The NAEF could be used to determine the amount of broadening of the range of gaze angles of highest acuity produced by surgical treatment, like tenotomy. This measure is similar to the null-broadening hypothesized to be due to tenotomy but is more directly related to potential visual acuity than measurement of the null region based simply on CN amplitude.

#### REFERENCES

1. Akman O.E., Broomhead D.S., Abadi R.V., Clement R.A. (2005): Eye movement instabilities and nystagmus can be predicted by a nonlinear dynamics model of the saccadic system. *J. Math. Biol.*; 51, pp. 661–694
2. van Hateren J.H. , Lamb T.D. (2006): The photocurrent response of human cones is fast and monophasic *BMC Neuroscience*, 7 pp 34 -41.
3. Abadi R.V., Bjerre A. (2002): ‘Motor and sensory characteristics of infantile nystagmus’. *Br J Ophthalmol*; 86, pp. 1152-1160
4. Dell’Osso L.F. and Jacobs J.B. (2002): ‘An Expanded Nystagmus Acuity Function: Intra- and Intersubject Prediction of Best-Corrected Visual Acuity’. *Doc Ophthalmol.*; 104, pp. 249–276
5. Bifulco P., Cesarelli M., Loffredo L., Sansone M., Bracale M. (2003): ‘Eye Movement Baseline Oscillation and Variability of Eye Position During Foveation in Congenital Nystagmus’, *Doc Ophthalmol* 107, pp. 131-136.
6. Cesarelli M., Coppola P., Bifulco P., Romano M., Sansone M. (2005), ‘Slow Eye Movement Oscillation In Congenital Nystagmus’, *IFMBE Proc.* 2005 11(1), The 3rd European Medical and Biological Engineering Conference, Prague, Czech Republic, 2005, pp
7. Cesarelli M., Bifulco P., Loffredo L. and Bracale M. (2000): ‘Relationship between visual acuity and eye position variability during foveation in congenital nystagmus’. *Doc Ophthalmol* 101, pp. 59-72.
8. Dell’Osso LF, Darof RB. Congenital nystagmus waveform and foveation strategy. *Doc Ophthalmol* 1975; 39: 155–82.
9. Cesarelli M., Bifulco P., Romano M., Pasquariello G., Fratini A., Magli A., De Berardinis T., Boccuzzi D. (2007): Analysis of foveation duration and repeatability at different gaze positions in patients affected by congenital nystagmus, *IFMBE proc MEDICON 07*, Ljubljana, Slovenia, 2007, 26-30 pp. 426-429.
10. Dell’Osso LF, Van Der Steen J, Steinman RM, Collewijn H. (1992): Foveation dynamics in congenital nystagmus. I: Fixation. *Doc Ophthalmol* 1992; 79: 1–23.
11. Ukwade MT, Bedell HE. (1992): Variation of congenital nystagmus with viewing distance. *Optometry Vision Sci* 1992; 69: 976–85.

Author: Giulio Pasquariello  
 Institute: Department of Electronic and Telecommunication  
 Street: via Claudio, 21  
 City: Naples  
 Country: Italy  
 Email: pabifulc@unina.it

# Numerical Models of Skin Conductivity Changes during Electroporation

N. Pavšelj<sup>1</sup> and D. Miklavčič<sup>1</sup>

<sup>1</sup> University of Ljubljana, Faculty of Electrical Engineering, Ljubljana, Slovenia

**Abstract** — By exposing biological cells to electric pulses, we induce the electroporation of cell membrane, increasing its permeability for molecules that otherwise can not cross the membrane, such as drug molecules or DNA. Electroporation can also be used to enhance transdermal drug delivery and DNA transfection in skin. The experiments showed that skin layers below stratum corneum can be permeabilized in this way. The electroporabilization process in skin was described theoretically, by means of numerical modeling, leaning on data derived from the in vivo experiments published previously, and tissue conductivity data found in literature. The numerical models took into account the layered structure of skin tissue and macroscopical changes of its bulk electric properties during electroporation. The results obtained with the model were compared to the in vivo results of gene transfection in rat skin and a good agreement was found. Further, tissue conductivities and model geometry were varied to estimate their effect on the output of the model. The changes in the output electric current were still well in the range of the currents measured during the vivo experiments.

**Keywords** — electroporation, electroporabilization, skin, numerical modeling, finite elements

## I. INTRODUCTION

Cell membrane is, in general, impermeable for larger molecules; however, the application of electric pulses to cells results in electroporation of cell membrane, increasing its permeability and making it possible for molecules, such as drug molecules or DNA, to enter the cell [1]. Skin is an attractive target tissue for gene therapy for a variety of reasons. Its size and accessibility facilitates gene delivery. It can be used for the treatment of skin disorders or it can be used for systemic effect to treat diseases of other organs. Electroporation seems particularly effective to improve DNA transfection after intradermal and topical delivery without any significant alteration of skin structure and can be used to create aqueous pathways across the skin's outermost layer, the stratum corneum to enhance transdermal drug delivery [2]. Skin is also a very good target organ for DNA immunization because of the large number of potent antigen presenting cells, critical for an effective immune response [3]. In this report, electroporation of skin is described theoretically, by means of numerical modeling, based on data derived from the in vivo experiments resulting from our previous research [4].

Numerical modeling of the electric field and the electric current distributions inside the biological systems represents a useful tool for the research of the effects of the electromagnetic fields on cells, tissues and organs [5]. Such numerical models can provide a more in-depth understanding of electroporation. With a good model, we can predict the outcome of pulse delivery before the treatment, thus helping in optimizing/choosing the right protocols and pulse parameters and electrode geometries.

The numerical models presented in this report take into account the layered structure of skin and changes of its bulk electric properties during electroporation [6]. They are based on the tissue-electrode geometry and electric pulses used in our in vivo experiments [4] and tissue conductivity values found in literature [7-10].

The accuracy of a numerical model depends on many factors. First, the geometry of the model needs to be as close as possible to the in vivo geometry we are aiming to represent with the model. Second, the parameters of the model, in our case tissue conductivities and their changes during electroporation all have an effect on its accuracy. We thus varied the geometry and some of the parameters of the model to evaluate its robustness.

## II. MATERIALS AND METHODS

The numerical model was made by means of commercially available computer program COMSOL Multiphysics 3.3 (COMSOL, Los Angeles, CA, USA) based on the finite element method. This method solves partial differential equations by dividing the model into smaller elements where the quantity to be determined is approximated with a function or is assumed to be constant throughout the element. Finite elements can be of different shapes and sizes, which allows modeling of intricate geometries. Nonhomogeneities and anisotropies can also be modeled and different excitations and boundary conditions can be applied easily.

## III. THE NUMERICAL MODEL

In the past, we performed a series of in vivo experiments on rat skin [4]. The reporter gene used in the study was a gene coding for green fluorescent protein (GFP). Pulses

were delivered through external parallel plate electrodes (of 4 mm distance), using the square-wave generator Cliniporator. The results showed that the expression of GFP was enhanced by electroporation in both, dermis and the viable epidermis.

We constructed a numerical model of a skin fold with the geometry as close to the *in vivo* experimental tissue-electrode set-up as possible [11]. Four layers of skin were modeled: stratum corneum, epidermis, dermis and the subcutaneous layer of fat and connective tissue. The geometry of our numerical model is shown in Figure 1a. By using symmetry, only one quarter of the skin fold was modeled to decrease the number of finite elements. The boundary conditions had to be set accordingly (see Figure 1a). The geometrical representation of such a model needs to be as close to the real experimental tissue-electrode geometry as possible. As the geometry in Figure 1a did not take into account the presence of the injected plasmid, we varied the geometry of the numerical model, modeling also the plasmid injected at the top of the skin fold (Figure 1b and c), reflecting the situation closer to the *in vivo* experiments. To assess the influence of variations in geometrical representation on the accuracy of the model, two additional models were made, a simpler one (Figure 1b), and a more accurate one (Figure 1c).

Apart from a good geometrical representation, the electrical conductivities of the skin layers represented with such

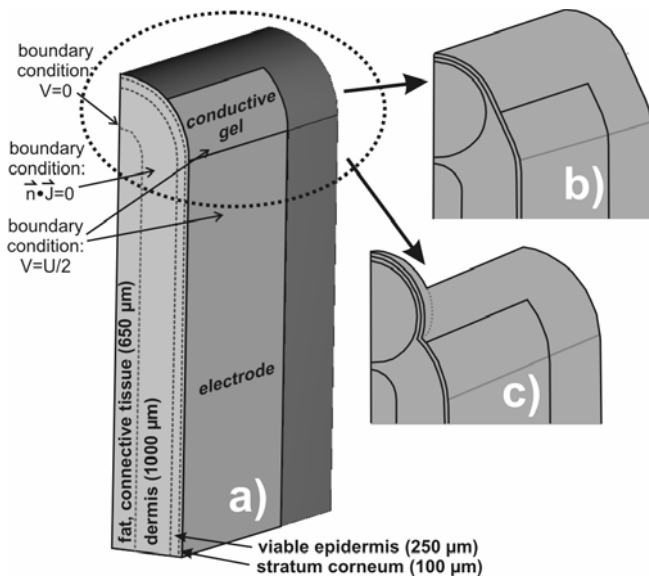


Fig. 1 a) Geometry of the skin fold finite element model made in COMSOL. Only one quarter of the skin fold was modeled to decrease the number of finite elements. The boundary conditions were therefore set as shown; b) The simpler variation of the skin fold geometry, with the plasmid injected at the top; c) The more accurate variation of the skin fold geometry, with the plasmid injected at the top.

a model have to be defined. Upon applying electric pulses, the voltage will be divided among different layers proportionally to their electrical resistivities, as in serially connected resistors. We get a certain electric field distribution; different layers are exposed to different electric field strengths. The voltage, and consequently the electric field will be the highest in the layer with the highest resistivity (the lowest conductivity). The stratum corneum will be exposed to the highest electric field, while the electric field in the target tissues (the dermis and the viable epidermis) stays too low for a successful electroporation-mediated DNA delivery to the dermis and the viable epidermis, confirmed *in vivo*, still possible when external plate electrodes are used. The answer lies in the conductivity increase of the permeabilized tissues. Namely, the high electric field in the stratum corneum is above the threshold causing its electroporation. As a consequence, the conductivity of the stratum corneum increases, and the electric field distribution is changed. In this way, the electric field high enough reaches the target skin layers below stratum corneum. Therefore, our numerical models are nonlinear, tissue conductivities are dependent on the electric field, thus the numerical analysis has to be performed in iterations.

Exactly how tissue conductivities ( $\sigma$ ) change with electric field ( $E$ ) is another poorly known parameter of tissue electroporation. Due to the non-uniformity of the cell size and shape in the tissue, not all the cells are permeabilized at the same time once the threshold electric field is reached [12, 13]. Therefore, we assumed a gradual increase of the conductivities with electric field. In our model, the conductivities were increased from their low to their high values in the range between 600 and 1400 V/cm of the electric field strength. The initial and the increased conductivities of all skin layers modeled are summarized in Table 1. The initial conductivities used in our model were in the middle of the value ranges found in the literature [7-10]. Although the dermis and the epidermis were modeled as separate layers, the same conductivity was assigned to both, due to the lack of impedance data on different skin layers. Plasmid conductivity used in the models in Figure 1b and c was set to 1.5 S/m.

The thickness of the stratum corneum in the model is set larger than in real skin (around 6 times). Namely, due to the

Table 1 Tissue conductivities used in the models on Figure 1 a), b) and c)

Tissue	$\sigma_0$ (S/m)	$\sigma_1$ (S/m)
Subcutaneous layer	0,05	0,2
Dermis, epidermis	0,2	0,8
Stratum corneum	0,0005	0,5

Table 2 Varied tissue conductivities used in the model in Figure 1a

Tissue		$\sigma_0$ (S/m)	$\sigma_1$ (S/m)
Subcutaneous layer	→ lower $\sigma_0$	0.01	0.04
	→ higher $\sigma_0$	0.2	0.8
	→ 3x $\sigma$ increase	0.05	0.15
	→ 5x $\sigma$ increase	0.05	0.25
Dermis, epidermis	→ lower $\sigma_0$	0.05	0.2
	→ higher $\sigma_0$	0.8	3.2
	→ 3x $\sigma$ increase	0.2	0.6
	→ 5x $\sigma$ increase	0.2	1
Stratum corneum	→ lower $\sigma_0$	0.00005	0.05
	→ higher $\sigma_0$	0.005	5
	→ 500x $\sigma$ increase	0.0005	0.25
	→ 2000x $\sigma$ increase	0.0005	1

large differences in layer thicknesses, numerical problems can occur and can make the calculation impossible. Therefore, the conductivity of this very resistive layer was also set higher (6 times).

The parameters such as conductivities of permeabilized and non-permeabilized tissue also have an effect on the output of the model. However, data are very scarce in the literature. In addition, large discrepancies can be found between various reports. Therefore, certain inaccuracies can not be avoided in the numerical model. We roughly estimated the error thus made by varying the tissue conductivities, assessing their influence on the output of the model. We varied initial conductivities and the conductivity increase of all skin layers (Table 2). Only one parameter at a time was changed in the model. The varied initial tissue conductivities and conductivity increases were chosen from the borders of the value ranges found in literature and derived from our in vivo experiments.

#### IV. RESULTS

Five different voltage amplitudes were used to permeabilize the skin during our in vivo experiments – 160, 280, 400, 520 and 700 V [4]. During the pulse, the voltage between the electrodes and the current through the skinfold were measured. The described numerical models were solved for the abovementioned voltage amplitudes and the currents obtained from the model were compared with our experimental data. Figure 2 shows the currents of the model compared to the currents measured in vivo during the pulse (grey diamonds). Black circles denote the output currents of the model in Figure 1a, computed with the conductivity values given in Table 1. The current-voltage dependence of the model seems to agree well with the current-voltage dependence we got from experiments. Further, the conduc-

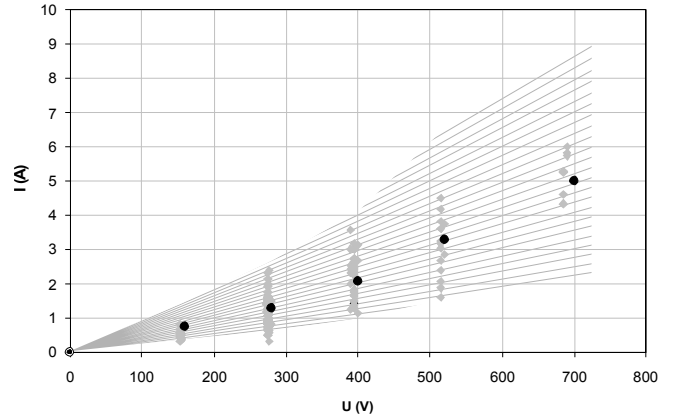


Fig. 2 Electric currents obtained with the model in Figure 1a, using the parameters in Table 1 (black circles), compared to the currents measured during the pulse delivered in vivo (grey diamonds), with respect to the applied voltages. The currents of all the varied models are inside the hatched area.

tivities of skin layers of the model in Figure 1a were varied (see Table 2), one at a time, while we kept the values of the rest of the layers as denoted in Table 1. Also, to assess the influence of variations in geometrical representation on the accuracy of the model, two additional models were made (Figure 1b and c). The currents of all the varied parameters described above were inside the hatched area in Figure 2. The changes in the geometry had only very limited effect on the output current. Also, using lower or higher conductivity increase, little difference was observed in the output current. The results showed that changing initial conductivity values of the layers below stratum corneum have the most influence on the output current.

#### V. CONCLUSIONS

The location of GFP expression shows that we successfully permeabilized viable skin layers below stratum corneum (the dermis and viable epidermis). We constructed a numerical model describing the nonlinear process of tissue conductivity changes during electroporation due to tissue permeabilization, using finite element method. The output of the model was compared with the current and the voltage measured during in vivo experiments and a good agreement was observed. Also, comparing the voltages needed for a successful electroporation as suggested by the electric field distributions in the model (data not shown), with voltages achieving good in vivo gene transfection, good agreement can be observed. For comparison we looked at both, the literature, as well as our own experiments. Further, tissue conductivities before and after electroporation were set with help from the literature and our own

experiments. However, data on conductivities of the permeabilized tissues is scarce, sometimes non-existent. Namely, the subject of tissue conductivity changes due to electroporation is still a rather unexplored area. Also, due to different measuring circumstances, measuring techniques and species used by different researchers, large discrepancies can be found in the reported data on tissue conductivities. Therefore, we evaluated the robustness of our model by varying initial conductivities and the conductivity increase of all skin layers. In addition, two variations of the numerical geometry were made, modeling also the plasmid injected at the top of the skin fold. The currents of all the varied models were in the range of the scatter of the currents measured *in vivo*.

By means of numerical modeling, we used the available data to describe the mechanism of the nonlinear process of skin electropermeabilization from the aspect of bulk conductivity changes. Such models, further improved and validated by more *in vivo* experiments can help us plan new experiments and protocols, design electroporation devices and can be used as a part of treatment planning.

#### ACKNOWLEDGMENT

This research was supported by the European Commission under the FP5 grant Cliniporator QLK-1999-00484, under the FP6 grant Angioskin LSH-2003-521217 and by the Slovenian Research Agency.

#### REFERENCES

1. Mir LM (2000) Therapeutic perspectives of *in vivo* cell electropermeabilization. Review article, *Bioelectrochemistry* 53: 1-10
2. Denet A-R, Vanbever R, Pr at V (2004) Skin electroporation for transdermal and topical delivery, *Adv Drug Deliv Rev* 56: 659-674
3. Zhang L, Widera G, Rabussay D (2004) Enhancement of the effectiveness of electroporation-augmented cutaneous DNA vaccination by a particulate adjuvant. *Bioelectrochemistry* 63: 369-373
4. Pavšelj N, Pr at V (2005) DNA electrotransfer into the skin using a combination of one high- and one low-voltage pulse. *J Cont Rel* 106: 407-415
5. Pavšelj N, Bregar Z, Cukjati D et al. (2005) The course of tissue permeabilization studied on a mathematical model of a subcutaneous tumor in small animals. *IEEE Trans Biomed Eng* 52(8): 1373-1381
6. Pliquett U, Langer R, Weaver JC (1995) Changes in the passive electrical properties of human stratum corneum due to electroporation. *BBA* 1239: 111-121
7. Yamamoto T, Yamamoto Y (1976) Electrical properties of the epidermal stratum corneum. *Med Biol Eng* 14(2): 151-158
8. Yamamoto T, Yamamoto Y (1976) Dielectric constant and resistivity of epidermal stratum corneum. *Med Biol Eng* 14(5): 494-500
9. Gabriel C, Gabriel S, Corthout E (1996) The dielectric properties of biological tissues: I. Literature survey. *Phys Med Biol* 41: 2231-2249
10. Gabriel S, Lau RW, Gabriel C (1996) The dielectric properties of biological tissues: II. Measurements in the frequency range 10 Hz to 20 GHz. *Phys Med Biol* 41: 2251-2269
11. Pavšelj N, Pr at V, Miklavčič D (2007) A numerical model of skin electropermeabilization based on *in vivo* experiments. *Annals Biomed. Eng.* 35: 2138-2144
12. Pavlin M, Pavšelj N, Miklavčič D (2002) Dependence of induced transmembrane potential on cell density, arrangement, and cell position inside a cell system. *IEEE Trans. Biomed. Eng.* 49: 605-612
13. Vali  B, Golzio M, Pavlin M et al. (2003) Effect of electric field induced transmembrane potential on spheroidal cells: theory and experiment. *Eur. Biophys. J.* 32: 519-528

Author: Nataša Pavšelj  
 Institute: University of Ljubljana, Faculty of Electrical Engineering  
 Street: Tržaška 25  
 City: Ljubljana, SI-1000  
 Country: Slovenia  
 Email: [natasa.pavselj@fe.uni-lj.si](mailto:natasa.pavselj@fe.uni-lj.si)

# An Experimental Study of PPG Probe Efficiency Coefficient Determination on Human Body

K. Pilt<sup>1</sup>, K. Meigas<sup>1</sup>, M. Rosmann<sup>2</sup>, J. Lass<sup>1</sup> and J. Kaik<sup>1</sup>

<sup>1</sup> Tallinn University of Technology/Department of Biomedical Engineering, Tallinn Estonia

<sup>2</sup> Tensiotrace Ltd., Tallinn, Estonia

**Abstract** — Some of the cardio vascular disease diagnostics need the long-term photoplethysmography (PPG) signal measurement session. For such kind of measurements, PPG probes have to be designed. In addition, the PPG signal shape, as diagnostic information carrier, is also dependent on probe location on human body. To make the PPG probe comparison, experiments were conducted, using PPG probes with different geometrical, optical and electrical parameters on different places of human body, where the signal under interest is measurable. The aim of the study is to design efficient PPG probe for each selected location on human body. As result for each probe, the efficiency-describing coefficient was calculated, which is the ratio of PPG AC component and diode current.

**Keywords** — Photoplethysmography, probe efficiency, AC component, LED current, PD current.

## I. INTRODUCTION

PPG is a non-invasive optical technique for measuring changes in blood circulation and has been used mainly for monitoring blood perfusion in skin. In PPG the optical radiation from a light source is emitted to the skin. The light, which is often red or infrared, is absorbed, reflected and scattered in the tissue and blood. Received light intensity changes are measured by photodetector (PD).

Mainly there are two ways to measure PPG signal: reflection and transmission mode. In reflection mode, a PD is placed adjacent to the light source and directed toward the skin. The PD receives the reflection of emitted light. In transmission mode, the PD and the light source are placed opposite sides of the measured volume. The PD measures the transmitted light intensity. In this work we are concentrated on reflectance sensor.

Measured PPG signal can be divided into two components: DC and AC component. The DC component of the signal varies slowly and reflects variations in total blood volume of the examined tissue. The AC component is synchronous with heart rate and depends on pulsatile pressure and pulsatile blood volume changes. The AC component can be more than ten times smaller than DC component. In number of noninvasive devices, where PPG signal is used to monitor cardiovascular parameters [1], such as pulse rate,

blood pressure, PWTT [2] etc., the AC component carries important information. During the poor perfusion state the PPG signal AC component can be affected by noises and it is hard to detect. It is necessary to find best combinations of PPG probes and their placement on human body to achieve enough good quality of the PPG signal for the diagnostics.

In previous studies there has been measured perfusion levels in different body locations, which is related to the measurement of AC component [3]. Recently there have been also conducted experiments to determine the optimal space between LED and PD in reflectance pulse oximetry [4]. In this study, we are measuring maximum amplitudes of PPG signal AC component from selected body locations, to design the efficient PPG probe for each of them.

## II. METHODS

To measure PPG signal in locations, where transmission probes cannot be placed, reflectance probes are used. The idea of measuring the amount of light reflected (back scattered) from the tissue, allows to measure PPG signal from virtually any point on the skin surface, where the probe can be placed.

Measured PPG signal AC component amplitude depends on the selection of probe light emitting diode (LED) wavelength, angular dissipation of LED and PD; distance between LED and PD; LED driving current and temperature of skin.

The light from LED is partially reflected, transmitted, absorbed, and scattered by the skin and other tissues and the blood before it reaches the detector. The light is scattered and reflected by both the moving red blood cells and the non-moving tissue, and a part of this back scattered and reflected light is detected by the PD.

In PPG related devices usually the wavelengths 600nm - 940nm are used. The red skin pigmentation absorbs a great amount of light at wavelength shorter than 600nm and therefore it is not desirable to measure PPG signal in this range. Haemoglobin is the main light absorber in human blood at given wavelengths range and its spectrum is influenced by its oxygenation level (Figure 1).



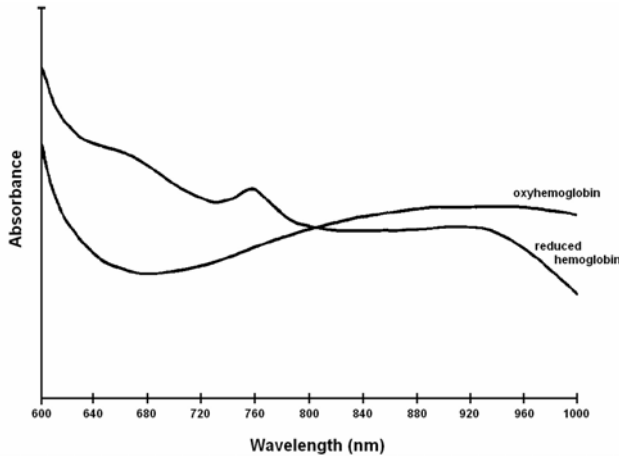


Fig. 1. Oxyhemoglobin and reduced hemoglobin absorption spectrum.

The intensity of the back-scattered light from the skin depends not only on the optical absorption spectrum of the blood but also on the structure and pigmentation of the skin. LED's wavelength influences the light penetration depth [5] in skin. It has been reported that light penetration into the tissue increases with increasing wavelength.

In past studies it has been proved through experiment, that PPG signal AC component is also skin temperature dependent [6]. By increasing the skin temperature from 34°C to 45°C, the AC component raises five times.

By increasing the LED current, the effective penetration depth in the skin is increased. With constant LED and PD separation distance, using higher light intensity, we can illuminate a larger pulsatile vascular bed [7]. As a result the PPG signal AC component will be larger. But, in practice, the LED driving current has to be limited, because of the power dissipation of the LED.

One of the major design considerations in designing a PPG reflectance sensor is determination of the optimum separation distance between the LED and PD. In case the LED intensity is kept constant and the radial distance be-

tween the LED and PD is increased, the AC component decreases roughly exponentially. In past studies it has been also shown, that the depth of the light penetration is increased with increasing the distance between the light source and the PD [8, 9]. Still if we place the PD too close to the LED, the PD will be saturated as a result of the large DC component obtained by the multiple scattering of the incident photons by the blood-free stratum corneum and epidermal layers in the skin.

The simple PPG measuring system is given on Figure 2. It consists of operational amplifier circuit configuration, which changes PD current into voltage. The relation between input current and output voltage is described by (1):

$$I_{PD} = -\frac{V_{OUT}}{R}, \quad (1)$$

where  $I_{PD}$  is the PD current,  $V_{OUT}$  is the output of current to voltage converting operational amplifier and  $R$  is feedback resistor. By measuring maximum PPG signal AC component amplitude, we can convert it into PD current.

PPG probe efficiency constant calculation is based on the PPG AC component current amplitude ratio to LED driving current:

$$\alpha = \frac{I_{PD}}{I_{LED}}, \quad (2)$$

where  $I_{PD}$  and  $I_{LED}$  are currents of PD and LED. As the light propagation in tissue depends on many factors, the maximum value of AC component in each location of the body is measured. In this way we can assume, that the maximum amount of photons were reflected and caught by PD. To compare the efficiency constant between different body locations and different subjects a large number of measurements should be carried out.

### III. RESULTS

Two different LED wavelengths were chosen for PPG probes - 640nm and 880nm. All LED and PD angular dissipations were the same for all probes. LED and PD separation distances were 7.5mm, 12.5mm and 17.5mm. In total six different reflectance probes were compared (Figure 3). LED current 11mA was chosen for all experiments. The experiments were carried out on 5 healthy subjects with normal weight and in the room with constant air temperature. The PPG signal was measured from left hand thumb, index and middle finger tip; and three points from forehead - left and right side of the temple; and from the center. Body locations are numbered and pointed out on Figure 4. The subjects were in resting position during experiment.

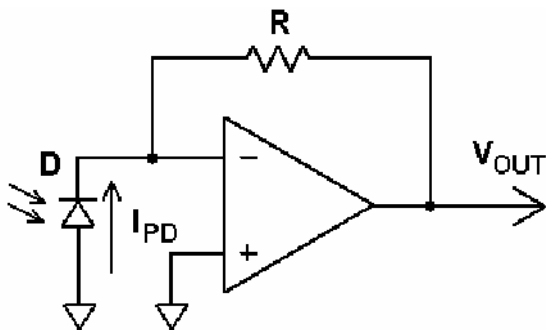


Fig. 2. Simplification of the PPG signal measurement circuit.



Fig. 3. Reflectance probe for PPG signal measurements.

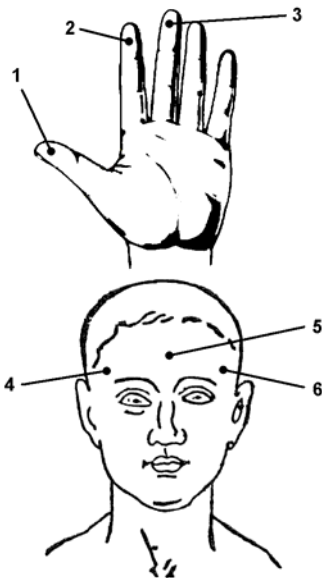


Fig. 4. Body locations identified by site number, where PPG signal measurements were performed.

PPG signals were measured with self-made circuit, which simplified version was also described before. The DC component was eliminated with RC filter, which cut-off frequency was chosen on 0.1Hz. PPG signals were digitalized and analyzed by using LabView environment and National Instruments DAQCard6034. The maximum amplitudes of the AC component were detected in real time.

The results are shown in Table 1. Each probe with its wavelength ( $\lambda$ ) and distance ( $d$ ) characteristics got ID number. In following columns coefficients are calculated according to the equation (1). The mean value is taken over the experiments for each location and probe. For better overview, all coefficients are multiplied with  $10^6$ .

To make afterward comparisons the LEDs and PD were placed up against and the PD currents were measured in case

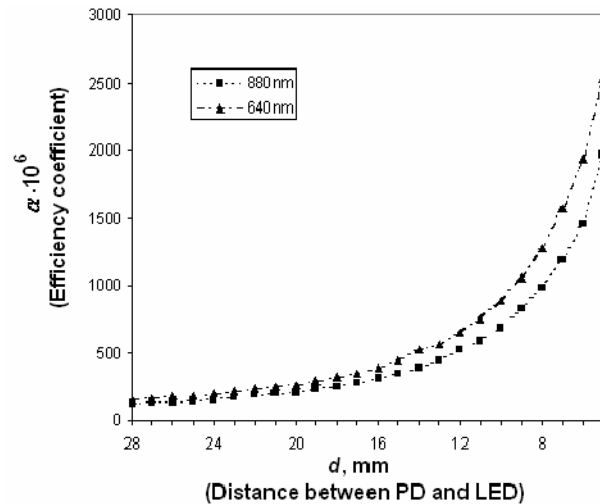


Fig. 5. An efficient coefficient in case of LED and PD is placed up against to each other and the distance between them is changed. For better overview coefficients are multiplied with  $10^6$ .

of 11mA LED current. The efficiency coefficient was calculated in different distances between LED and PD. The distances were varying between 5mm up to 28mm. All coefficients were multiplied with  $10^6$  for better comparison and plotted on Figure 5. By closing PD to LED, the efficiency coefficient is raising exponentially. Similar behavior was mentioned before, when LED and PD was closed to each other in case of reflectance sensor. From Figure 5 we can conclude, that LED with wavelength of 660nm has better efficiency than LED with wavelength of 880nm with given PD.

From Table 1 it is visible, that coefficients in forehead have more than twice difference. It may be because of the tissue parameters and low concentration of blood in forehead. Standard deviation (SD) is equal or over 10% in the experiments with probes 1, 2, 4 and 5. High SD is caused by the low SNR, which in most of the cases increases with the distance between PD and LED. For the future study the number of subjects has to be increased to lower the SD.

In all body locations the PPG probe with ID number 6 had the best efficiency coefficient. Also all probes with wavelength of 880nm had higher coefficients than probes with 640nm respectively to each body location. It is opposite, what was concluded from Figure 5. It means, that due to wavelength, the probes with 880nm LED have higher efficiency coefficients.

#### IV. CONCLUSIONS

PPG probe characteristics, in the point of view measuring high quality PPG signal AC component, was discussed. Six

Table 1. Efficiency coefficient,  $\alpha$ , determination experimental results for six PPG probe (mean  $\pm$  SD).  
For better overview coefficients are multiplied with  $10^6$ .

Probe ID	$\lambda$ , nm	$d$ , mm	Thumb(1), $\alpha$	Index finger(2), $\alpha$	Second finger(3), $\alpha$	Right temple(4), $\alpha$	Center forehead(5), $\alpha$	Left temple(6), $\alpha$
1	640	17,5	1,4 $\pm$ 0,2	1,0 $\pm$ 0,1	1,7 $\pm$ 0,2	0,4 $\pm$ 0,05	0,3 $\pm$ 0,03	0,4 $\pm$ 0,1
2	640	12,5	4,5 $\pm$ 0,5	4,7 $\pm$ 0,6	4,7 $\pm$ 0,6	1,5 $\pm$ 0,2	0,4 $\pm$ 0,1	0,7 $\pm$ 0,1
3	640	7,5	16,9 $\pm$ 0,9	12,4 $\pm$ 0,9	17,0 $\pm$ 1,1	4,3 $\pm$ 0,3	3,9 $\pm$ 0,3	4,7 $\pm$ 0,4
4	880	17,5	2,7 $\pm$ 0,3	3,2 $\pm$ 0,5	3,6 $\pm$ 0,4	1,0 $\pm$ 0,1	0,9 $\pm$ 0,1	0,9 $\pm$ 0,1
5	880	12,5	7,0 $\pm$ 0,7	8,2 $\pm$ 1,0	8,0 $\pm$ 0,7	1,6 $\pm$ 0,2	0,8 $\pm$ 0,1	0,9 $\pm$ 0,1
6	880	7,5	29,9 $\pm$ 1,1	26,6 $\pm$ 0,8	34,4 $\pm$ 1,4	10,0 $\pm$ 0,5	5,8 $\pm$ 0,3	6,9 $\pm$ 0,3

different probes were prepared. Experiments to determine the PPG probe efficiency coefficient was carried out in different body locations. The probe, with highest coefficient value was determined. Also the LED and PD characteristics variability should be increased.

#### ACKNOWLEDGMENT

This work was supported in part by the Estonian Science Foundation under Grant G7506.

#### REFERENCES

- Pilt K., Meigas K., Lass J., Rosmann M., Kaik J. (2007) Analogue step-by-step DC component eliminator for 24-hour PPG Signal Monitoring. Conf. Proc. IEEE Eng. Med. Biol. Soc. 1006-1009
- Meigas K., Hindrikus H., Kattai R., Lass J. (2003) Self mixing in a diode laser as a method for cardiovascular diagnostics. J of Biome. Optics 8:152-160
- Tur E., Tur M., Maibach M. D., Guy R. H. (1983) Basal perfusion of the cutaneous microcirculation: measurements as a function of anatomic position. J Invest Dermatol 81: 422-446
- Hickey M., Kyriacou P. A. (2007) Optimal spacing between transmitting and receiving optical fibers in reflectance pulse oximetry. J of Phys: Conf Ser 85
- Anderson R. R., Parrish J.A. (1981) The optics of human skin. J Invest Dermatol 77:13-19
- Mendelson Y., Ochs B. D. (1988) Noninvasive pulse oximetry utilizing skin reflectance photoplethysmography. IEEE Trans. Biomed Eng 35:798-806
- Webster J. J. (1997) Design of pulse oximeters. Bristol: Institute of Physics Publishing
- Fridolin I., Lindberg L. G. (2000) Optical non-invasive technique for vessel imaging: I. Experimental results. Phys Med Biol 45:3765-3778
- Fridolin I., Hansson K., Lindberg L. G. (2000) Optical non-invasive technique for vessel imaging: II. A simplified photon diffusion analysis. Phys Med Biol 45:3779-3792

Author: Kristjan Pilt  
 Institute: Department of Biomedical Engineering  
 Street: Ehitajate tee 5  
 City: Tallinn, 19086  
 Country: Estonia  
 Email: kristjan.pilt@gmail.com

# Non-linear Assessment of Heart Rate Variability in Ovo-lactovegetarians, Vegans and Omnivores during Oral Glucose Tolerance Test

T. Princi<sup>1</sup>, I. Fabbro<sup>1</sup>, D. Peterec<sup>2</sup>, M. Fonda<sup>3</sup>, L. Cattin<sup>3</sup> and A. Accardo<sup>4</sup>

<sup>1</sup> Dept. Physiology and Pathology, University of Trieste, Italy

<sup>2</sup> Institute of Physiology, University of Ljubljana, Slovenia

<sup>3</sup> Diabetes and Metabolic Diseases Center, Azienda Osp. Universitaria, Trieste, Italy

<sup>4</sup> D.E.E.I., University of Trieste, Italy

**Abstract** — Although the health benefits of vegetarian diets have been well documented, the exact mechanisms of health benefits of vegetarian diets on the cardiovascular system remain unclear. Autonomic nervous system (ANS) activity is influenced by food ingestion. Carbohydrate but not fat or protein ingestion affects the cardiac ANS by increasing the sympathetic activity. In this study we aimed to investigate the cardiac ANS activity in 7 ovo-lactovegetarians, 8 vegans and 5 omnivores by means of heart rate variability (HRV) non-linear (Poincaré plot and fractal dimension - FD) analysis. Heart rate (HR) was recorded continuously at baseline and during oral glucose tolerance test (OGTT-75 gr of glucose) (90 min) by using Polar S810 HR monitor. The series of consecutive R-R interval (tachogram) in function of beat numbers was extracted, linearly interpolated and resampled at 2 Hz for further processing. Non-linear parameters of HRV were calculated at baseline and during OGTT. This study demonstrated in all three groups, both at baseline and during the OGTT, a similar value of RR interval as well as a not significant difference of FD, which is considered as a possible indicator of complexity of inputs to HR controllers. On the contrary, the Poincaré plot analysis revealed, both at baseline and during the OGTT, a difference in the SD1 and SD2 parameters values, comparing omnivores to vegetarians and vegans, with the highest values in omnivores. At baseline and during the OGTT (30 min) the SD1 and SD2 parameters in normalized units (n.u.) as well as the SD1/SD2 ratio, as expression of vago-sympathetic balance, were statistically different between omnivores and vegans. In conclusion, non-linear Poincaré plot analysis suggested a different cardiac ANS function in vegans and ovo-lactovegetarians in comparison to omnivores at baseline as well as during the OGTT.

**Keywords** — Vegetarian diets, OGTT, heart rate variability.

## I. INTRODUCTION

The health benefits of vegetarian diets have been well documented [1]. As compared with omnivores, vegetarians have lower blood pressure [2-4] and lower risk of cardiovascular disease and stroke [5]. However, the exact mechanisms of health benefits of vegetarian diets on the cardiovascular system remain unclear. Since there is not one

homogeneous group of vegetarians and vegetarians consume widely divergent diets, a differentiation between various types of vegetarians diets is necessary. In fact, a lot of misunderstandings concerning vegetarianism are due to scientific data from studies without this differentiation [6].

Autonomic nervous system (ANS) activity is influenced by food ingestion [7]. Among the main dietary components, carbohydrate ingestion, but not fat or protein ingestion, is accompanied by increased sympathetic nervous system (SNS) activity [8-10]. The carbohydrate consumption [11] and in particular the glucose administration [12, 13] affected also the cardiac ANS activity. Beat-to-beat spontaneous oscillations in R-R intervals (heart rate variability – HRV) depend on autonomic nervous system activity on the cardiac function and pacemaker properties of myocardium [7]. The analysis of HRV is recognized as a powerful non-invasive assessment that reflects brain - heart interaction [14] and in particular sympathetic and parasympathetic nervous control of the myocardium [15].

The HRV evaluation has mainly been used in the prediction of mortality in patients with cardiovascular diseases as well as in the healthy population [16, 17]. The Framingham Heart Study reported that HRV low values were associated with the risk of cardiac events in healthy adults examined regularly over a long period [16]. It is reasonable that measurement of HRV by either linear or non-linear methods is a useful research tool for detecting modifications in cardiac neural regulation in various clinical settings [18].

In this study we aimed to evaluate the cardiac ANS activity by means of HRV non-linear analysis (Poincaré plot, fractal dimension – FD) in ovo-lactovegetarians, vegans and omnivores at rest and during oral glucose tolerance test (OGTT).

## II. MATERIALS AND METHODS

The study was performed on 20 healthy young male volunteers (aged 18-33), who have been on a vegetarian diet for at least 5 years, divided into 5 omnivores, 7 ovo-lactovegetarians and 8 vegans. Heart rate (HR) was re-

corded continuously at baseline and during oral glucose tolerance test - OGTT (90 min) by using Polar S810 HR monitor. From the HR recordings, the series of consecutive R-R intervals (tachogram) in function of beat numbers were extracted. All artifacts arising during the registration were removed by passing the time R-R series through a filter that eliminated noise and substituted premature beats (if deviated from previous qualified interval by more than  $2 \cdot SD$ ) with an interpolated value computed from the neighboring 10 beats. In order to sample at regular time intervals, the series were linearly interpolated and resampled at 2 Hz for further processing.

Non-linear Poincaré plot parameters (SD1, SD2) of HRV were calculated on the whole recording at baseline and during three consecutive intervals of 30 min each in the 90 min OGTT (75 gr of glucose) test. The Poincaré plot represents a diagram in which each R-R interval of the tachogram is plotted as a function of the previous R-R interval. This method is able to measure the differences among R-R intervals due to changes in vagal and sympathetic modulation, without the requirement for the stationarity of the data [19]. From the Poincaré plot analysis, SD1 parameter is used as a marker of vagal influence, whereas SD2 parameter represents the more delayed R-R interval changes correlated to sympathetic activity, and SD1/SD2 ratio indicates the vagal/sympathetic balance, being SD1 and SD2 the two axes of the best-fit ellipse that contains the Poincaré points.

The fractal dimension (FD) of the HRV was investigated as a possible indicator of the complex interaction that might reflect the number of inputs to HR controllers [20, 21]. The FD, which is considered to be indicative of the complexity of a given time series, was evaluated on tracts of 120 consecutive R-R interval samples, by means of Higuchi's algorithm [22] based on the measure of the mean length of the curve by using a segment of  $k$  samples ( $k$  varying from 1 to 6) as a unit of measure. The mean value of FD was considered in the analysis.

In order to compare the HRV non-linear parameters, evaluated at baseline as well as at 30 min intervals during 90 min OGTT, the Student's t-test was applied. A  $p < 0.05$  was adopted as statistically significant.

### III. RESULTS

Table 1 summarizes the results of HRV non-linear analysis performed in 3 groups of subjects following different diets. In all analyzed omnivores, ovo-lactovegetarians and vegans the R-R intervals presented similar values at rest (baseline) as well as at three different intervals (30 min, 60 min and 90 min) during the OGTT.

Also the FD did not show any significant difference comparing the values detected in the same group at different conditions as well as comparing the different groups (omnivores, ovo-lactovegetarians and vegans) at the same condition.

At all evaluated conditions the Poincaré plot SD1 and SD2 values, expressed in absolute units (ms), presented the highest values in omnivores, whereas similar lower values were observed in both vegetarians groups, at rest and during the OGTT. On the other hand, the SD1 and SD2 parameters, expressed in normalized units, as well as the SD1/SD2 ratio, which indicates the vago-sympathetic balance, presented a statistically significant difference between omnivores and vegans both at baseline and at 30 min interval during the OGTT.

### IV. DISCUSSION

A growing body of scientific evidence indicates the health benefits of vegetarians diets [1-5] with positive effects on the cardiovascular system, but the exact mechanisms are poorly understood. Furthermore, since vegetarians consume widely divergent diets, a differentiation between various types of vegetarian diets is necessary. Indeed, many contradictions and misunderstandings related to vegetarianism are due to scientific data from studies without this differentiation [6]. In general, vegetarian diets are based on cereals, pulses, nuts, vegetables and fruits, and may also include dairy products and eggs. Ovo-lactovegetarians do not consume any meat, poultry or fish, but do include dairy products and eggs in their diet. Vegans do not consume any foods of animal origin [23].

To our knowledge this study is the first one, which reports cardiac ANS activity evaluation comparing omnivores with volunteers, divided into ovo-lactovegetarians and vegans, who have been on a vegetarian diet for at least 5 years. In all subjects the cardiac ANS function was analyzed by means of HRV non-linear assessment both at baseline in rest condition and during oral glucose tolerance test (OGTT). Our data demonstrated no significant difference in the HR between the different subjects compared at the same condition. Thus, it is likely that a vegetarian diet does not exert any relevant effect on this cardiac parameter, considering healthy young subjects at rest condition. After the glucose ingestion along the OGTT no significant modification of the HR was detected in any of these subjects, in contrast with Paolisso et al. (2000), who observed in old subjects, during OGTT, an increase of HR as well as a sympathoexcitation.

In our study, at baseline as well as during the OGTT, the non-linear Poincaré plot SD1 and SD2 parameters (absolute units) showed higher values in omnivores compared to both

vegetarians groups, probably due to higher cardiac sympathetic and vagal modulation in this group (Table 1). On the other hand, the SD1 and SD2 parameters (n.u.) as well as SD1/SD2 ratio revealed a statistically significant difference

between omnivores and vegans at baseline and at 30 min intervals of OGTT, indicating a shift of sympatho-vagal balance towards a more sympathetic and less parasympathetic activity in vegans.

Table 1 Mean values (SD) of RR intervals, Poincaré plot SD1 and SD2 parameters (ms, n.u.), SD1/SD2 ratio, fractal dimension (FD) at rest (baseline) and 30-60-90 min after glucose administration during oral glucose tolerance test (OGTT) in omnivores, vegans and ovo-lactovegetarians. \*Statistically significant difference between omnivores and vegans at p<0.05

	Omnivores (n=5)		Vegans (n=8)		Ovo-lactovegetarians (n=7)	
baseline	Mean value	SD	Mean value	SD	Mean value	SD
RR interval (ms)	997	115	995	146	960	105
SD1 (ms)	28	11	14	4.8	17	5.1
SD2 (ms)	149	59	83	20	92	19
SD1 (n.u.)	16	0.40	14*	2.2	15	2.2
SD2 (n.u.)	84	0.40	86*	2.2	84	2.2
SD1/SD2	0.19	0.01	0.17*	0.03	0.19	0.03
FD	1.42	0.16	1.51	0.16	1.44	0.07
30 min						
RR interval (ms)	1057	86	992	133	966	84
SD1 (ms)	35	23	17	6.4	17	5.5
SD2 (ms)	153	102	90	19	88	32
SD1 (n.u.)	18	1.6	15*	3.6	17	1.7
SD2 (n.u.)	82	1.6	85*	3.6	83	1.7
SD1/SD2	0.23	0.02	0.18*	0.05	0.20	0.03
FD	1.46	0.13	1.50	0.16	1.46	0.10
60 min						
RR interval (ms)	990	165	961	134	985	104
SD1 (ms)	22	12	15	5.7	19	6.2
SD2 (ms)	108	36	95	31	102	19
SD1 (n.u.)	17	2.5	14	3.2	15	2.9
SD2 (n.u.)	83	2.5	86	3.2	85	2.9
SD1/SD2	0.20	0.04	0.16	0.05	0.18	0.04
FD	1.46	0.13	1.52	0.12	1.44	0.09
90 min						
RR interval (ms)	1037	144	983	122	971	85
SD1 (ms)	26	12	16	7.4	20	8.3
SD2 (ms)	136	49	101	33	100	33
SD1 (n.u.)	16	2.1	14	4.7	16	1.8
SD2 (n.u.)	84	2.1	86	4.7	84	1.8
SD1/SD2	0.19	0.03	0.17	0.06	0.20	0.03
FD	1.42	0.18	1.50	0.16	1.45	0.08

No statistically significant difference was detected comparing FD values between different groups in all analyzed conditions.

In conclusion, the HRV analysis, assessed in omnivores, ovo-lactovegetarians and vegans by means of Poincaré plot non-linear analysis, suggests, at rest, a different sympatho-vagal modulation in omnivores compared to these two vegetarian groups. Furthermore, comparing omnivores with vegans, i.e. subjects being on two extremely different diets, the difference in cardiac ANS activity appears statistically significant.

#### ACKNOWLEDGMENT

The study was partially supported by Associazione Amici del Cuore (Trieste, Italy).

#### REFERENCES

- Lin CL (1997) Vegetarianism. *Tzu Chi Med J* 9:81-89
- Rouse IL, Beilin LJ, Armstrong BK, Vandongen R (1983) Blood-pressure-lowering effect of a vegetarian diet: controlled trial in normotensive subjects. *Lancet* 1:5-10
- Margetts BM, Beilin LJ, Vandongen R, Armstrong BK (1986) Vegetarian diet in mild hypertension: a randomised controlled trial. *Br Med J* 293:1468-1471
- Appleby PN, Davey GK, Key TJ (2002) Hypertension and blood pressure among meat eaters, fish eaters, vegetarians and vegans in EPIC-Oxford. *Public Health Nutrition* 5(5):645-654 DOI 10.1079/PHN2002332
- Hu FB (2003) Plant-based foods and prevention of cardiovascular disease: an overview. *Am J Clin Nutr* 78(suppl 3):544S-551S
- Leitzmann C (2005) Vegetarians Diets: What are the Advantages? Diet Diversification and Health Promotion. *Forum Nutr. Basel, Karger* 57:147-156
- Akselrod S, Gordon D, Ubel FA, Shannon DC, Barger AC, Cohen RJ (1981) Power spectrum analysis of heart rate fluctuations: A quantitative probe of beat-to-beat cardiovascular control. *Science* 213:220-222
- Young JB, Landsberg L (1977) Stimulation of the sympathetic nervous system during sucrose feeding. *Nature* 269:615-617
- Berne C, Fagius J, Niklasson F (1989) Sympathetic Response to Oral Carbohydrate Administration. Evidence from Microelectrode Nerve Recordings. *J Clin Invest* 84:1403-1409
- Welle S (1995) Sympathetic nervous system response to intake. *Am J Clin Nutr* 62(suppl 5):1118S-1122S
- Tentolouris N, Tsigos C, Perea D, Koukou E, Kyriaki D, Kitsou E, Daskas S, Daifotis Z, Makrilakis K, Raptis SA, Katsilambros N (2003) Differential Effects of High-Fat and High-Carbohydrate Isoenergetic Meals on Cardiac Autonomic Nervous System Activity in Lean and Obese Women. *Metabolism* 52(11):1426-1432
- Paolisso G, Manzella D, Ferrara N, Gambardella A, Abete P, Tagliamonte MR, De Lucia D, Furgi G, Picone C, Gentile S, Rengo F, Varricchio M (1997) Glucose ingestion affects cardiac ANS in healthy subjects with different amounts of body fat. *Am J Physiol* 273 (Endocrinol Metab 36):E471-E478
- Paolisso G, Manzella D, Rizzo MR, Barbieri M, Gambardella A, Varricchio M (2000) Effects of glucose ingestion on cardiac autonomic nervous system in healthy centenarians: differences with aged subjects. *Eur J Clin Invest* 30:277-284
- Singh RB, Kartik C, Otsuka K, Pella D, Pella J (2002) Brain-heart connection and the risk of heart attack. *Biomed Pharmacother* 56(2):257s-265s
- Malliani A, Pagani M, Lombardi F, Cerutti S (1991) Cardiovascular neural regulation explored in the frequency domain. *Circulation* 84:482-492
- Tsuji H, Larson MG, Venditti FJ, Manders ES, Evans JC, Feldman CL (1996) Impact of reduced heart rate variability on risk for cardiac events. The Framingham Heart Study. *Circulation* 94:2850-2855
- Wichterle D, Simek J, La Rovere MT, Schwartz PJ, Camm AJ, Malik M (2004) Prevalent low-frequency oscillation of heart rate: novel predictor of mortality after myocardial infarction. *Circulation* 110(10):1183-1190
- Lombardi F, Mäkikallio TH, Myerburg RJ, Huikuri HV (2001) Sudden cardiac death: role of heart rate variability to identify patients at risk. *Cardiovascular Research* 50:210-217
- Tulppo MP, Mäkikallio TH, Takala TES, Seppanen T, Huikuri HV (1996) Quantitative beat-to-beat analysis of heart rate dynamics during exercise. *Am J Physiol* 271:H244-H252
- Nakamura Y, Yamamoto Y, Muraoka I (1993) Autonomic control of heart rate during physical exercise and fractal dimension of heart rate variability. *J Appl Physiol* 74(2):875-881
- Goldberger AL (1996) Non-linear dynamics for clinicians: Chaos theory, fractals, and complexity at the bed-side. *The Lancet* 347:1312-1314
- Higuchi T (1988) Approach to an irregular time series on the basis of the fractal theory. *Physica D* 31:277-283
- Key TJ, Davey GK, Appleby PN (1999) Health benefits of a vegetarian diet. *Proc of the Nutrition Society* 58:271-275

Author: Princi Tanja  
 Institute: Department of Physiology and Pathology  
 Street: Via A. Fleming, 22  
 City: 34127 Trieste  
 Country: Italy  
 Email: princi@dfp.units.it

# Photoplethysmography Analysis of Artery Properties in Patients with Cardiovascular Diseases

U. Rubins<sup>1</sup>, A. Grabovskis<sup>1</sup>, J. Grube<sup>1</sup> and I. Kukulis<sup>2</sup>

<sup>1</sup> Institute of Atomic Physics and Spectroscopy, University of Latvia, Riga, Latvia

<sup>2</sup> Institute of Cardiology, University of Latvia, Riga, Latvia

**Abstract** — In this study arterial parameters of healthy subjects were compared to those of patients with cardiovascular diseases. The photoplethysmography (PPG) measurements of blood volume pulsations have been performed. Using a novel algorithm for analysis of simultaneously measured ear and finger PPG signals, arterial parameters were evaluated in representative groups of healthy subjects and patients with cardiovascular diseases. Digital volume pulse (DVP), pulse cycle duration (T), augmentation index (AIx), reflection index (RI) and transit time of reflected wave (RTT) were evaluated in every heartbeat cycle. Correlations between the AIx and RI, T and RTT, AIx and standard deviation of AIx, RTT and standard deviation of RTT showed differences between the healthy subjects and patients.

**Keywords** — photoplethysmography, non-invasive diagnostics, bio-signal processing, vascular assessment, arterial stiffness.

## I. INTRODUCTION

The analysis of peripheral blood volume pulse helps to understand arterial pathologies, a major contributor to cardiovascular diseases, which is a common cause of death in modern society. The risk factors for cardiovascular diseases are associated with the increasing stiffness of the arterial wall [1,2].

Photoplethysmography (PPG) is an optical non-invasive measuring technique that can be used to detect blood volume changes in the peripheral vessels at different body locations (fingers, earlobes, toes etc) [3-5]. The blood volume pulsations, produced by heart, propagate through the arterial tree and are affected by reflected waves from the arterial branching sites. Most reflecting site is bifurcation of aorta in the lower body, so aortic pressure waveform is affected mainly by reflected wave from the lower body. Aortic waveform is similar to PPG pulse contour at the finger or ear and contains several peaks. Analyzing time intervals between the peaks of forward and reflected waves and the amplitude relation of peaks gives arterial parameters [6,7].

This study mainly focused on the arterial parameters, which were evaluated from simultaneously detected finger and ear PPG signals taken from healthy subjects and pa-

tients having cardiovascular diseases. Using a novel signal processing algorithm, these arterial parameters were evaluated in representative groups of patients and healthy subjects, with further correlation analysis of the obtained data. The diagnostic potential of the proposed methodology is discussed as well.

## II. METHODS

### A. Design of the device

The PPG device used in the study is shown in Fig. 1a. It comprises two pulse oximeter contact probes (DS-100A, Nellcor, USA), a signal acquisition circuit and portable computer with software (written in Visual Basic). Both sensors were fixed onto the measurement site by clips (Fig. 1b). The analogue signals from the PPG contact probes were digitized by a 15-bit analogue-to-digital converter (sampling rate 200 Hz) and transferred to the computer. The PPG signals were saved in data files after each measurement.

### B. Subjects

A total of 174 volunteers were included in the study – 46 healthy subjects of age range 23-35 years, 26 healthy subjects of age range 63-76 years and 102 patients of age range 60-80 years with diagnosed cardiovascular diseases



Fig. 1 The PPG device (a) and sensors applied to finger and ear (b).



(27 subjects with coronary occlusion, 63 subjects with peripheral arterial occlusion in the legs and 12 subjects with carotid artery occlusion).

### C. The protocol of measurements

The measurements were performed in hospital conditions at room temperature ( $22 \pm 1$  °C). Before the measurements the subjects were asked to relax for 3 minutes in a sitting position. During the experiment, patients were asked to sit normally and quietly with their forearm lying on the legs. Measurements were performed continuously in a sitting position during 1 minute.

### D. Signal processing

Data from each measurement were processed offline by computer program written in Matlab. DC and slow varying components (0-0.1 Hz) were removed by subtracting the mean-averaged PPG from the signal (Fig. 2). Random noise ( $>15$  Hz) was removed from the signal by a Savitsky-Golay smoothing filter. All feet of the PPG pulses (signal minima) were found, and the normalized digital volume pulse (DVP) was calculated for each heartbeat cycle, as well as the pulse cycle duration (T). The feet of the DVP of the ear and finger were offset in time to start always at time  $t=0$  (Fig. 3a).

Typically, the DVP is formed by a direct pressure wave that propagates from the heart to the finger and ear, and a delayed component that is reflected backward from peripheral arteries [6,7]. In our calculations we assumed that a part of the reflected wave appears in the systole and another part appears in diastole of the DVP. One direct wave and three reflected waves were considered in the model calculations.

The following calculations were performed for both ear and finger DVP. Firstly, the second derivative of the DVP was calculated (Fig. 3a). Then, two inflection points where the second derivative crosses zero, near the local maximum (in the time interval 0.2 – 0.4 s) were found. The DVP waveform was separated into two parts: a systolic part from the foot of the DVP to the first inflection point, and a diastolic part from the second inflection point to the end of the DVP. Secondly, each part of DVP was fitted with the sum of two Gaussian functions (Fig. 3b). The amplitudes of these Gaussian functions were evaluated independently for ear and finger DVP, but the positions of the Gaussians were the same for ear and finger DVP.

The model parameters were evaluated by means of a least square minimization of the following sum:

$$\sum_{j=1}^N (DVP_{j,n} - p_j)^2 \rightarrow \min \quad (1)$$

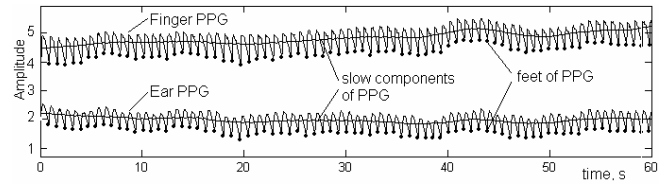


Fig. 2 PPG signals measured from the ear and finger. Dots indicate the positions of the feet.

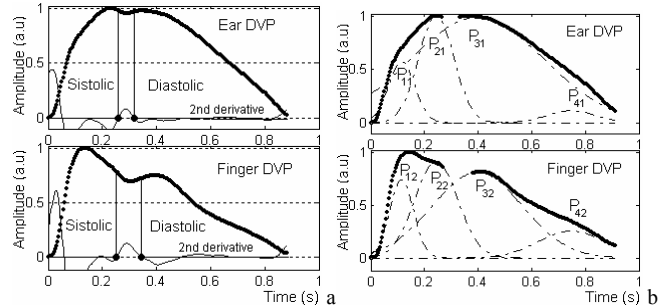


Fig. 3 Separation of systolic and diastolic parts (a) and evaluation of the inflection points of the DVP by Gaussian fitting (b). Bold dots represent the DVP, dotted lines – Gaussians.

where DVP is the systolic ( $n=1$ ) or diastolic ( $n=2$ ) part of the DVP data,  $p$  – the model fitted to data,  $N$  – the number of data points. The model is fitted to data by solving the following system of equations:

$$p_m = \sum_{k=1}^2 P_{(k+2n-2),m} \exp \left[ -\frac{(t - \tau_{(k+2n-2)})^2}{2b^2_{(k+2n-2),m}} \right] \quad (2)$$

where  $b$  – Gaussian width,  $\tau$  – Gaussian time shift,  $P$  – Gaussian peak amplitude,  $m=1$  for ear,  $m=2$  for finger DVP, and  $k$  refers to the Gaussian that belongs to the fitting function of that part of the DVP.

Solving (1) and (2) gave values of  $P_{12}, P_{22}, P_{32}, P_{42}$  which correspond to the amplitudes of the finger DVP at the three inflection points at time positions  $\tau_1, \tau_2, \tau_3, \tau_4$  which are common for ear and finger DVP (Fig. 3b).

Arterial parameters – transit time of the reflected wave RTT, augmentation index AIX and reflection index RI are calculated from equations (3), (4) and (5):

$$RTT = \tau_3 - \tau_1 \quad (3)$$

$$AIX = \frac{P_{12} - P_{22}}{P_{12}} \quad (4)$$

$$RI = \frac{P_{32}}{P_{12}} \quad (5)$$

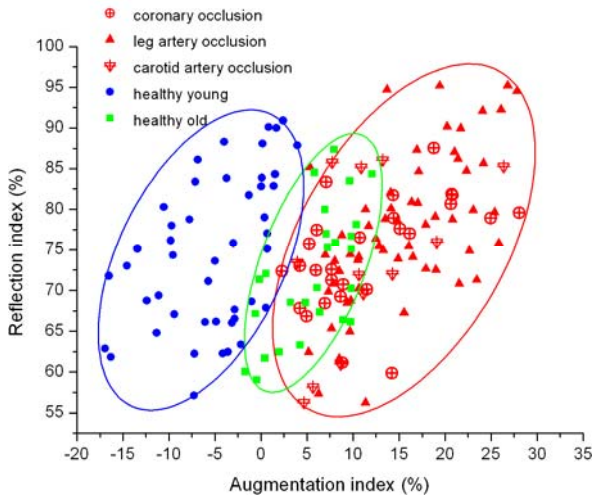


Fig. 4 The correlation of augmentation index (AIx) and reflection index (RI) for five groups of subjects. Each dot represents separate heartbeat.

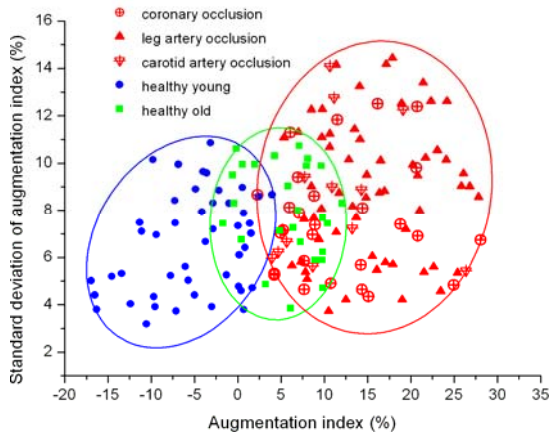


Fig. 5 The correlation of augmentation index (AIx) and standard deviation of AIx. Each dot represents separate heartbeat.

III. RESULTS

Fig. 4-7 shows the correlations between the arterial parameters and its standard deviations. The parameters of five subject groups are showed in graphs: 1) healthy young, 2) healthy elderly, 3) carotid artery occlusion, 4) leg artery occlusion, 5) coronary occlusion. From the Fig. 4-7 is seen a clear difference between the three patient groups – healthy young, healthy elderly and patients with cardiovascular diseases. Ellipse lines around the data points represent the borders of data.

Fig. 4 shows the dependence of AIx and RI. Correlation between these parameters is linear for all subject types. For older and more diseased patients AIx showed higher values

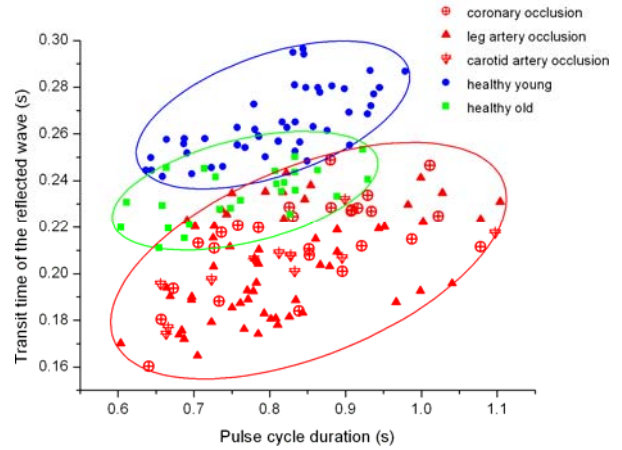


Fig. 6 The correlation of pulse cycle duration (T) and transit time of the reflected wave (RTT) for five groups of subjects.

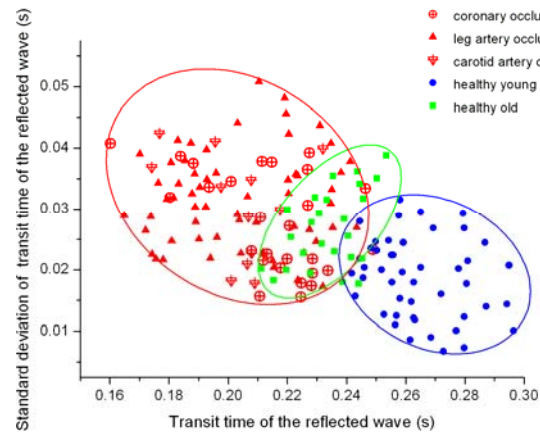


Fig. 7 The correlation of transit time of the reflected wave (RTT) and standard deviation of RTT for five groups of subjects.

compared with young subjects (Fig. 4, Fig. 5). Fig. 6 shows dependence of pulse cycle duration (T) and RTT during a single pulse cycle. The values of RTT decreased for higher pulse rates (or lower T) and showed lower values for patients. Standard deviation of RTT shows greater value for patients (Fig. 7).

IV. DISCUSSION

The results obtained in this study showed a correlation between the arterial parameters AIx, RI, RTT and T. This means that all parameters are somehow related to each other. AIx and RI are related to amplitude of reflected pulse waves, but RTT depends of transit time of propagated pulse wave [6,7]. These parameters are related to compliance of

aorta and large arteries [2], which depends of various factors such as hypertension and high arterial stiffness. Changes in the vascular tone induce changes in the amplitude of the wave reflected from the periphery. When the arteries become stiffer, the amplitude of the reflected wave increases. This leads to higher AIx and RI values. Both AIx and RI are related with cardiovascular risk factors [1,2]. Fig. 4 and Fig. 5 show increased values of AIx for older and diseased subjects while increasing of RI is negligible. This means that AIx can be better in diagnosis of cardiovascular diseases.

Arterial stiffness is also associated with peripheral vascular tone. Changes in pulse rate can affect peripheral vascular tone and therefore change the arterial stiffness [8]. Therefore, RTT decreases due to increasing vascular tone and higher pulse wave velocity in the arteries. Our results showed correlation between the pulse cycle duration and RTT, with lower RTT values for patients than for healthy subjects (Fig. 6, Fig. 7).

The DVP shape can be adequately fitted with a superposition of four Gaussians, which may be efficiently used to estimate the arterial parameters, especially when the DVP is weak and noisy or in cases when the diastolic part of the DVP is damped out. Compared with the standard method [6,7,9,10] when the inflection points of the DVP are calculated using the first or higher derivatives, the Gaussian fitting method is more sensitive. In addition, this method becomes more attractive when two or more DVP from different body sites are fitted by superposition of Gaussians. One should note that the inflection points of DVPs measured at different body sites are common in time but differ in amplitude. Therefore, additional measurements give greater certainty about the location of the inflection points.

## V. CONCLUSIONS

The results of this study show that the PPG technique may have the potential to detect and assess arterial diseases associated with increasing arterial stiffness.

The obtained results demonstrated differences among the correlations in arterial parameters RTT, AIx, and RI of healthy subjects and patients. This indicates to their potential to be used as risk factors in fast non-invasive primary vascular diagnostics. The novel algorithm for the analysis of

simultaneously measured ear and finger PPG allows the evaluation of arterial parameters of patients whose pulse contour is difficult to analyze with traditional means.

## ACKNOWLEDGMENT

This project has been supported by European Social fund.

## REFERENCES

1. Laurent S, Cockcroft J, Bortel L V, Boutouyrie P, Giannattasio C, Hayoz D, Pannier B, Vlachopoulos C, Wilkinson I, Srujker-Boudier H (2007) Abridged version of the expert consensus document on arterial stiffness. *Artery Research* 1:2-12
2. Nürnberg J, Keflioglu-Scheiber A, Opazo Saez A M, Wenzel R R, Philipp T and Schäfers R F (2002) Augmentation index is associated with cardiovascular risk. *J. Hypertension* 20:2407-14
3. Spigulis J (2005) Optical non-invasive monitoring of skin blood pulsations. *Appl. Opt* 44:1850-57
4. Spigulis J, Erts R, Kukulis I, Ozols M, Prieditis K (2004) Optical multi-channel sensing of skin blood pulsations. *Proc.SPIE* 5459:46-53
5. Allen J, Murray A (2003) Age-related changes in the characteristics of the photoplethysmographic pulse shape at various body sites. *Physiol. Meas.* 24:297-307
6. Millaseau S C, Ritter J M, Takazawa K and Chowienczyk P J. (2006) Contour analysis of the photoplethysmographic pulse measured at the finger. *J. Hypertens* 24:1449-56
7. Millaseau S C, Kelly R P, Ritter J M and Chowienczyk P J (2002) Determination of age-related increases in large artery stiffness by digital pulse contour analysis. *Clinical Science* 103:371-77
8. Lantelme P, Mestre C, Lievre M, Gressard A, Milon H (2002) Heart rate: an important confounder of pulse wave velocity assessment. *Hypertension* 39:1083-87
9. Takazawa K, Tanaka N, Fujita M, Matsuoka O, Saiki T, Aikawa M, Tamura S and Ibukiyama C (1998) Assessment of vasoactive agents and vascular aging by the second derivative of photoplethysmogram waveform. *Hypertension* 32:365-70
10. Karamanoglu M (1997) A system for analysis arterial blood pressure waveforms in humans. *Computers and Biomedical research* 30:244-55

Address of the corresponding author:

Author: Uldis Rubins  
 Institute: University of Latvia  
 Street: Raina Blv.19  
 City: Riga  
 Country: Latvia  
 Email: rubul@lanet.lv

# Dialysis Adequacy On-line Monitoring Using DiaSens Optical Sensor: Technique and Clinical Application

A. Scherbakov<sup>1</sup>, I. Fridolin<sup>1</sup>

<sup>1</sup> Tallinn University of Technology, Estonia

**Abstract — Background:** DiaSens is an optical sensor that uses UV-light to measure the rate of substances removal from the blood during dialysis thus being able to monitor the dialysis quality. DiaSens is connected to the drain output of the dialysis machine with dialysate passing through its flow-through optical cell. The concentration of substances in spent dialysate is directly proportional to the light absorbance. The sensor working principle is based on Beer-Lambert's law.

**Objective:** Evaluate DiaSens measurement results in comparison with blood urea measurements.

**Methods:** The study included 19 treatments in total from 5 uremic patients, both male and female. All patients were on chronic thrice-weekly haemodialysis therapy and standard procedure duration varied from 180 to 300 minutes. Study included both stable and unstable treatments.

**Results:** The mean values of the estimated parameters (mean  $\pm$  SD) were: (1) Kt/V was  $1,07 \pm 0,14$ , (N = 11), spKt/V was  $1,13 \pm 0,20$ , (N = 11), and eKt/V was  $1,07 \pm 0,12$ , (N = 11) from DiaSens, and (2) Kt/V was  $1,15 \pm 0,15$ , (N = 11), spKt/V was  $1,20 \pm 0,14$ , (N = 11), and eKt/V was  $1,14 \pm 0,14$ , (N = 11) from the blood sample analysis. Difference between the Kt/V, spKt/V and eKt/V obtained from the blood sample analysis and DiaSens was approximately 10% from the corresponding DiaSens average absolute values being stably 0.07 lower comparing to the blood urea tests.

**Conclusion:** The measurement results obtained by DiaSens have a strong and stable relationship with those received using the reference laboratory technique. DiaSens could be used in hospitals for routine dialysis adequacy monitoring to complement or replace blood sampling method.

**Keywords —** DiaSens, optical dialysis monitoring, Kt/V, dialysis quality, dialysis adequacy.

## I. INTRODUCTION

Dialysis dose has been reported to have great significance for the outcome of dialysis treatment. Many studies have shown a relationship between dialysis dose, measured as Kt/V and morbidity and mortality among haemodialysis patients.

Recently an optical method for on-line monitoring of solutes in the spent dialysate utilizing the UV-absorbance has been developed, enabling one to follow a single haemodialysis session continuously and monitor deviations in dialysis efficiency. The UV-method does not need blood sam-

ples, no disposables or chemicals, is fast, and allows to continuously measure the elimination of the substances that are retained in the uremic patients. The method, contributing to the identification, characterization, and evaluation of uremic retention solutes, offers new perspectives to ensure dialysis adequacy and quality.

DiaSens is a commercially available optical monitoring device that uses UV-radiation for constant monitoring of haemodialysis treatment.

DiaSens utilizes double-channel optical system with LED as a light source and two gallium nitride based photo-diodes as detectors. Wavelength used in DiaSens is  $\lambda = 280$  nm.

## II. MATERIALS AND METHODS

The study was performed after approval of the protocol by the Ethics Committee of Estonian Ministry of Health (approval no.1229).

The study included 19 treatments in total from 5 uremic patients. All patients were on chronic thrice-weekly haemodialysis therapy and standard procedure duration varied between 180 and 300 minutes.

For determination of UV absorbance DiaSens was connected to the drain tube of the dialysis machine. The absorbance A [a.u.] of a solution, obtained using pure dialysate as a reference solution, is given by the Beer-Lambert law as

$$A = \log \frac{I_0}{I_{r+s}} - \log \frac{I_0}{I_r} \quad (1)$$

where

$I_0$  is the intensity of incident light from the light source

$I_r$  is the intensity of transmitted light through the reference solution

$I_{r+s}$  is the summated intensity of transmitted light through the reference solution mixed with the solution under study

Several treatment results were excluded from the study because of nurse or laboratory errors or DiaHub failures.

Blood samples were taken before the beginning of the treatment and 5 minutes prior to its end and then analyzed

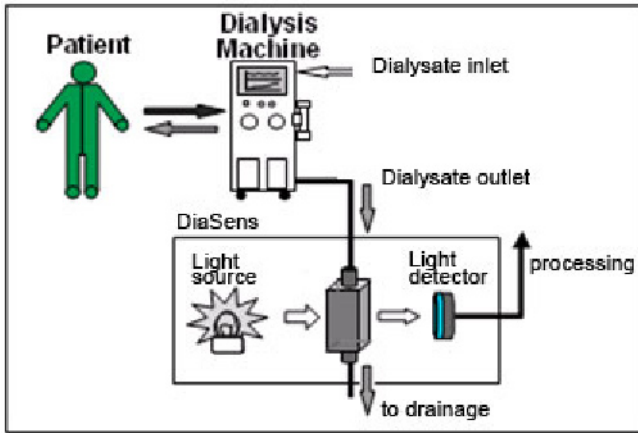


Fig. 1 Experiment setup

in the laboratory to determine the concentration of urea and uric acid.

Logs of each procedure including all changes in the procedure course were taken by the nurses and analyzed afterwards.

Kt/V value for blood samples was then calculated according to the (equation 2) and using the absorption curve slope (K/V) for DiaSens (equation 3)

$$\frac{Kt}{V} = \ln\left(\frac{C_0}{C}\right) \quad (2)$$

$$Kt/V = S_a * t \quad (3)$$

Calculation of spKt/V was performed using the following formulas for blood samples

$$spKt/V = -\ln\left(\frac{C_t}{C_0} - 0.008 \frac{t}{60}\right) + \left(4 - 3.5 \frac{C_t}{C_0}\right) \left(\frac{UF}{W}\right) \quad (4)$$

and for DiaSens

$$spKt/V = -\ln\left(e^{\frac{Kt}{V}} - 0.008 * \frac{t}{60}\right) + \left(4 - 3.5 * e^{\frac{Kt}{V}}\right) * \frac{UF}{W} \quad (5)$$

where

$C_0$  – initial concentration of urea (mmol/l)

$C_t$  – concentration at arbitrary moment (mmol/l)

UF – ultrafiltration volume (litres)

W – end-session body weight (kg)

t – treatment time (min)

K – dialyser clearance (ml/min)

V – urea distribution volume (litres)

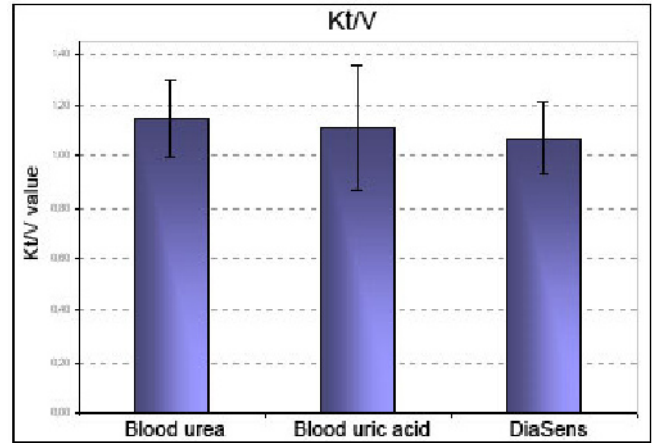


Fig. 2 Kt/V values for blood samples and DiaSens

Equilibrated Kt/V was calculated using the following equation

$$eKt/V = spKt/V - \left(\frac{0.6}{t/60} * spKt/V\right) + 0.03 \quad (6)$$

where t is treatment time in minutes.

### III. EXPERIMENT RESULTS

The method of processing of the experimental data was adopted from an article “Estimation of Delivered Dialysis Dose by On-Line Monitoring of the Ultraviolet Absorbance in the Spent Dialysate” by F. Uhlin, I.Fridolin et al [21].

Several treatment sessions were excluded from the study due to obvious laboratory errors (2 treatments) or DiaSens software failures (1 treatment).

The results are presented as mean value + SD (Table 1).

The results are depicted on figures 2, 3, 4.

From the abovementioned figures it can be noted that DiaSens values are generally lower than those obtained from blood samples. The stability of this tendency suggests that the difference can be removed with DiaSens pre-calibration.

The figures above show that deviation values themselves may vary greatly mostly due to treatment instabilities.

Table 1 Experiment results

	Blood urea	Blood uric acid	DiaSens
Kt/V	1.15 ± 0.15	1.10 ± 0.24	1.07 ± 0.14
spKt/V	1.20 ± 0.14	1.17 ± 0.28	1.13 ± 0.20
eKt/V	1.14 ± 0.14	1.10 ± 0.23	1.07 ± 0.12

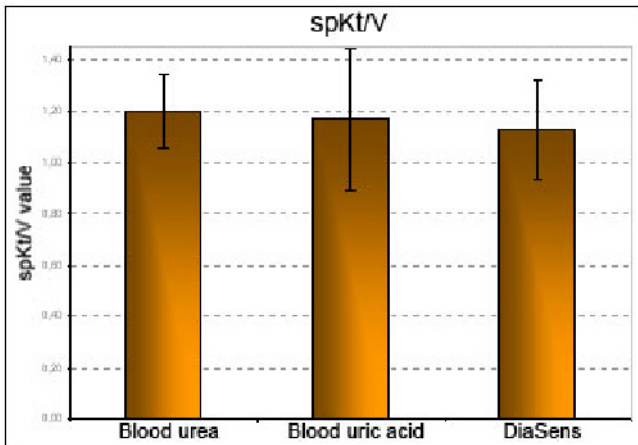


Fig. 3 Single-pool Kt/V values for blood samples and DiaSens

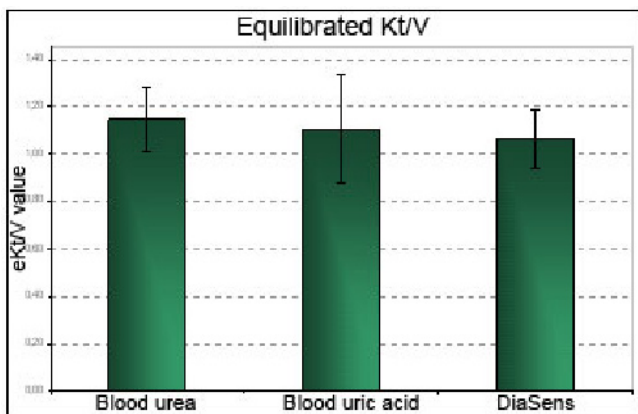


Fig. 4 Equilibrated Kt/V values for blood samples and DiaSens

#### IV. DISCUSSION

It is for many years that a possibility of using ultraviolet optical monitoring for dialysis treatment is known, but the purpose of this experiment was to demonstrate the work of the device that is not only based on the principles of UV-monitoring, but ready to be installed in clinics and operate on a daily basis.

DiaSens implements all the advantages of the optical method over its competitors, such as precision, simplicity and ability to operate in such conditions where other semi-online methods [3,4,5,22] fail. It provides continuous online measurement and immediately identifies any changes in dialysis machine performance.

As it can be clearly observed difference between blood analysis and DiaSens readings exists with DiaSens having an obvious tendency of understating treatment results.

The lower mean Kt/V value of the UV-method may be explained by a lower clearance of these UV-absorbing higher molecular weight solutes compared to that of urea as indicated by removal of uric acid in this study. The fact that urea-based methods have differences similar to the UV-method indicates that the removal rate of UV-absorbing solutes is comparable to a non-UV-absorbing solute like urea during haemodialysis.

The accuracy of the DiaSens described in this study shows a non-systematic error of approximately 10 % (100% \* difference in SD/mean), which is similar to the errors of the other methods and studies described above. A way to further minimize the SD value for differences between blood-urea and the UV method is probably to apply appropriate calibration (Fridolin 2006). Nevertheless, it still seems quite difficult to achieve a low SD even using the standard methods, indicating that HD is a complicated clinical treatment where the measurement situation is cumbersome.

Another explanation of the fact that some patients show high deviation might be that both stable and unstable treatments we put into the same statistical group. Procedure is classified as “unstable” if some unexpected events occurred during its course (Figure 8). Those can be blood flow changes, machine pump stops due to many reasons, poor vascular access, dialysis machine malfunction, pressure changes etc. Due to this fact changes in substances concentration in spent dialysate may change significantly. These abrupt changes are easily recognizable but still they are the source of an additional error in the final results of the experiment.

Nevertheless, it is during unstable treatments where DiaSens becomes the most valuable asset. Blood sample analysis method does not give any information about the procedure course, but rather only its start and end points. The UV-technique, on the other hand, gives the possibility to follow each dialysis treatment continuously, due to the very high sampling frequency, allowing the monitoring of any deviations on-line and the presentation of the data in an appropriate way on a screen. The method offers the possibility to create a database where valuable information about each dialysis treatment can be first saved and analyzed afterwards. The application could be especially suitable for following the patients during home-HD. This information can be a useful source for analyzing and revising treatment quality and existing standards and methods to ensure treatment quality and patient welfare.

## REFERENCES

1. Fridolin, I., F. Uhlin, et al. (2006). "Accurate Estimation of Delivered Dialysis Dose by On-Line Ultra Violet Absorbance in the Spent Dialysate." *Nephrol Dial Transplant*. Vol 21(Nr 7 July): ERA/EDTA XLIII Congress (abstract), Glasgow
2. Cogan M. G. and P. Schoenfeld (1991). *Introduction to Dialysis*. New York Edinburgh London Melbourne Tokyo, Churchill Livingstone Inc.: 1-44.
3. Kuhlmann U, Goldau R, Samadi N, et al: Accuracy and safety of online clearance monitoring based on conductivity variation. *Nephrol Dial Transplant* 16:1053-8., 2001
4. Di Filippo S, Andrulli S, Manzoni C, Corti M, Locatelli F: On-line assessment of delivered dialysis dose. *Kidney International* 54:263-267, 1998
5. Manzoni C, Di Filippo S, Corti M, Locatelli F: Ionic dialysance as a method for the on-line monitoring of delivered dialysis without blood sampling. *Nephrology Dialysis Transplantation* 11:2023-2030, 1996
6. Depner, T., P. Keshaviah, et al. (1996). "Multicenter clinical validation of an on-line monitor of dialysis adequacy." *Journal of the American Society of Nephrology* 7(3): 464-471.
7. Depner, T. A., T. Greene, et al. (1999). "Imprecision of the hemodialysis dose when measured directly from urea removal. Hemodialysis Study Group." *Kidney Int* 55(2): 635-47.
8. Fridolin, I. (2003). *Photon propagation in tissue and in biological fluids applied for vascular imaging and haemodialysis monitoring*. Dept. of Biomed. Eng., PhD Thesis, Dissertation No. 818, Linköping University, ISBN: 91-7373-638-4: 248.
9. Fridolin, I. and L.-G. Lindberg (2003). "On-line monitoring of solutes in dialysate using absorption of ultraviolet radiation - wavelength dependence." *Medical & Biological Engineering & Computing* 41: 263-270.
10. Fridolin, I., M. Magnusson, et al. (2002). "On-line monitoring of solutes in dialysate using absorption of ultraviolet radiation: technique description." *The International Journal of Artificial Organs* 25(8): 748-761.
11. Gotch, F. A. and M. L. Keen (1991). *Care of the patient on hemodialysis*. Introduction to Dialysis. M. G. Cogan and P. Schoenfeld. New York Edinburgh London Melbourne Tokyo, Churchill Livingstone Inc.: 101-176.
12. Keen, M. L. and F. A. Gotch (1991). *Dialyzers and delivery systems*. Introduction to Dialysis.
13. HabelKeen, M. (2002). *Understanding Urinalysis, RnCeus Interactive,LLC*. 2004.L.
14. Kaye, D. (1968). "Antibacterial Activity of Human Urine." *The Journal of Clinical Investigation* 47: 2347-2390
15. Keshaviah, P., J. Ebben, et al. (1995). "On-line monitoring of the delivery of the hemodialysis prescription." *Pediatric Nephrology* 9 Suppl: S2-S8.
16. Mann, C. K., T. J. Vickers, et al. (1974). *Ultraviolet-visible absorption spectroscopy*. Instrumental Analysis. New York, Evanston, San Francisco, London, Harper & Row, Publishers: 427-452.
17. Kouri, T. (2000). *European Urinalysis Guidelines*, European Confederation of Laboratory Medicine, ECLM: 145.
18. Vanholder, R., A. Schoots, et al. (1989). *Uremic toxicity. Replacement of Renal Function by Dialysis: A textbook of dialysis*. J. F. Maher. Dordrecht Boston Lancaster, Kluwer Academic Publishers: 4-19.
19. Mann, C. K., T. J. Vickers, et al. (1974). *Ultraviolet-visible absorption spectroscopy*. Instrumental Analysis. New York, Evanston, San Francisco, London, Harper & Row, Publishers: 427-452.
20. NKf-DOQI (1997). "NKf-DOQI clinical practice guidelines for hemodialysis adequacy." *American Journal of Kidney Diseases* 30(3, suppl 2): S1-S64.
21. Tortora, G. J. and S. R. Grabowski (1993). *Principles of Anatomy and Physiology*. New York, HarperCollins College Publisher.
22. Uhlin, F., I. Fridolin, et al. (2003). "Estimation of delivered dialysis dose by on-line monitoring of the UV-absorbance in the spent dialysate." *American Journal of Kidney Diseases* 41(5 (May)): 1026-1036.
23. , F., I. Fridolin, et al. (2006). "On line monitoring using ultraviolet absorption for surveillance of clinical events during haemodialysis" *Journal of Renal Care*, 2006 Jul-Sep; 32(3):141-6.

Author: Aleksei Scherbakov  
 Institute: Tallinn University of Technology  
 Street: Ehitajate tee 5  
 City: Tallinn  
 Country: Estonia  
 Email: aleksei@bambus.ee

# Effects of ROI Size on Correlation between ROISR and SNR

L. Sinkkila<sup>1</sup>, J. Vaisanen<sup>1</sup>, O. Vaisanen<sup>1</sup> and J. Hyttinen<sup>1</sup>

<sup>1</sup> Department of Biomedical Engineering, Tampere University of Technology, Tampere, Finland

**Abstract**— In electroencephalography (EEG) measurements the highest possible signal-to-noise ratio is always sought in order to achieve measurement results of as high quality as possible. In an ideal measurement the sensitivity of the measurement should focus on the region of interest (ROI) in comparison to other source areas inside the volume conductor. A parameter called region of interest sensitivity ratio (ROISR) has been previously introduced by Vaisanen et al. for analyzing the sensitivity distribution of an EEG measurement. They have found that the ROISR parameter correlates with signal-to-noise ratio (SNR). The correlation is highest in an optimal case when all the signal sources are located within the ROI and all the noise sources are located outside the ROI in other parts of the volume conductor. In this paper we studied the effect of the size of the ROI on the correlation with multilead VEP measurements performed on three testees. The results show that when the ROI location and general measurement settings are chosen carefully, the ideal ROI radius in a VEP experiment is 20 mm. Further on, since the correlation is highest when the measurement parameters are ideally chosen the experiments indicate that the ROISR parameter could be used for optimising EEG measurement set-ups and it could also have applications in source localization.

**Keywords**— region of interest sensitivity ratio, signal-to-noise ratio, sensitivity distribution

## I. INTRODUCTION

In electroencephalography (EEG) measurements an optimal electrode configuration and the highest possible signal-to-noise ratio (SNR) is significant. To achieve a high SNR the measurement sensitivity should be concentrated accurately on the region of interest (ROI). The signal sources should locate inside the ROI volume and the noise sources outside the ROI volume within the nonROI volume. In practise it would be convenient to be able to evaluate the sensitivity properties of a measurement in advance to achieve the best possible results.

Only a few methods for analysing the sensitivity distributions of an EEG measurement have been introduced. One of them is the half-sensitivity volume (HSV), which is used to define a volume in which the measurement sensitivity is concentrated [1]. Another method previously introduced in [2] utilizes a parameter called region of interest sensitivity ratio (ROISR) [2]. ROISR characterises how well the sensitivity of a bipolar EEG lead is concentrated within the ROI in comparison with other source regions inside the volume

conductor. In optimal situation the signal measured is generated by the sources inside the ROI and the sources outside the ROI produce noise to the measurement.

The correlation between ROISR and SNR in multichannel p100 visual evoked potential (VEP) measurements has been previously demonstrated in [2]. The magnitude of the correlation in various source distribution models has been examined in a stimulation study [3]. When the signal sources are located within all points of the ROI and the noise sources in all other points of the brain the correlation in an ideal case is close to 100 %.

The VEPs in [2] were measured with a 256-channel Neuroscan measurement cap with an electrode corresponding to Cz of the internationally standardized 10-20 system as a reference. The sensitivity distributions of 254 channels were calculated within the brain volume of a three-layer spherical head model with an analytical method introduced by Rush and Driscoll [4]. Based on the studies it is evident that the ROI size and location have an effect on the correlation between ROISR and SNR. In the calculation of ROISR the ROI was selected to have a constant 20 mm radius and its' location was varied in the model around the cortex. The results showed that the correlations are high (>90%) when the ROI is located near the posterior part of the head model where the primary visual cortex is located.

In the present paper we further evaluate the effect of the ROI radius on the correlation and seek the most optimal radius length in a VEP experiment by comparing the measured correlations between ROISR and SNR using the same measurement settings as in [2].

The objective of this study is to examine the effect of the ROI size on correlation between ROISR and SNR in VEP multichannel measurements and to evaluate the feasibility of the ROISR method in analysing EEG measurement systems.

## II. METHODS

### A. Sensitivity distribution

In an EEG measurement the sensitivity distributions of a measurement configuration can be described with lead fields defined by McFee and Johnston [5]. When the field point is fixed in a certain location the length and direction of the lead vector receive different values as a function of source location. The value of the lead vector can be deter-



mined for each source location while the lead detects the source with different sensitivity depending on it. Each lead vector represents the sensitivity of the lead to the specific dipole source as a function of its location and direction. This distribution over the volume conductor is called the sensitivity distribution [5].

The lead vectors define the relationship between the signal measured in the lead and the current sources in the volume conductor. This is described in equation 1.

$$V_{LE} = \int \frac{1}{\sigma} \bar{J}_{LE} \cdot \bar{J}^i dv = \int \frac{1}{\sigma} \cdot |\bar{J}_{LE}| \cdot |\bar{J}^i| \cdot \cos(\alpha) dv \quad (1)$$

, where  $V_{LE}$  is the lead voltage,  $\sigma$  is the conductivity at the source point,  $\bar{J}_{LE}$  is the lead field and  $\bar{J}^i$  is the impressed current source density and  $\alpha$  is the angle between the lead vector and the source vector. The lead voltage is expressed as the scalar product of the source density and the lead field current density through the entire volume source [5].

The lead field theorem is originally based on the reciprocity theorem introduced by Hermann von Helmholtz in 1853. It denotes that the lead field  $\bar{J}_{LE}$  equals the electric current density field through a volume conductor when a reciprocal unit current ( $I_R=1$  A) is fed to the measurement leads. [6]

### B. Spherical head model

A three-layer spherical Rush and Driscoll head model [4] was used to calculate the sensitivity distributions of 254 bipolar EEG leads. The model takes into consideration three major tissue types. These are the scalp, the skull and the brain. The radii of the three layers are 92, 85 and 80 mm, respectfully. The resolution of the model is 2mm x 2mm x 2mm and it contains in all 267 730 nodes. Every node expresses an 8 mm<sup>3</sup> volume in the brain region.

### C. The concept of ROISR

A modelling related parameter called ROISR has previously been introduced in [2]. It describes how well the sensitivity of an EEG measurement is concentrated within the ROI in comparison with other source areas inside the volume conductor referred to as nonROI. In an EEG measurement, ROISR is defined as a ratio between the average sensitivity of a ROI volume and the average sensitivity of a nonROI volume as described in equation 2.

$$ROISR = \frac{\frac{1}{V_{ROI}} \int |\bar{J}_{LE}| dv}{\frac{1}{V_{nonROI}} \int |\bar{J}_{LE}| dv} = \frac{\frac{1}{V_{ROI}} \int |\bar{J}_{LE}| \cdot \cos(\alpha) dv}{\frac{1}{V_{nonROI}} \int |\bar{J}_{LE}| \cdot \cos(\alpha) dv} \quad (2)$$

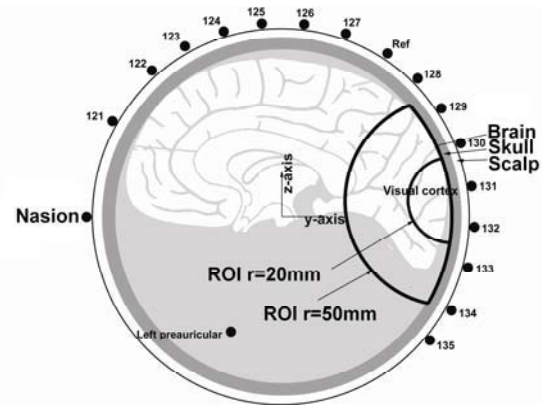


Fig. 1 A cross-section of the spherical head model representing two ROI areas with radii of 20 mm and 50 mm. The numbers on the surface indicate the measurement electrodes on the centerline of the measurement cap.

where  $V_{ROI}$  is the ROI source volume,  $V_{nonROI}$  is the nonROI source volume and  $\alpha$  is the angle between the lead vector and the source vector.

The latter part of the equation describes a case where the directions of the sensitivities inside the ROI and the nonROI are known. In practise the directions of the noise sources are almost impossible to know and therefore the worst-case scenario where they are oriented parallel to the lead vectors is usually chosen. If the directions inside ROI are known they are used in the calculations.

In this experiment the effects of the ROI size were studied by calculating the sensitivity distributions as earlier described. The ROI was chosen to be the shape of a partial sphere, restricted by the surface of the brain layer of the three-layer spherical head model on the outer side. Its size was varied by altering its radius between 5 to 50 mm with steps of 5 mm. The shape and the location of the ROI volumes inside the head model are represented in Fig. 1. Its location was chosen to where the primary visual cortex and hence the signal sources were assumed to be [7]. Since the SNR values are presumed to be highest near the source region, the centre of the ROI location was set on the brain layer directly underneath the electrode with the highest SNR [2]. After defining the ROI parameters, the correlations between ROISR and SNR were calculated, differences between radius lengths evaluated and the optimal radius defined.

### D. Measurements and clinical data

For the clinical experiment we performed a multichannel p100 VEP measurement on three healthy testees; one male and two females. The measurements were conducted twice on each testee producing six individual measurement examinations. The VEPs were measured with a Neuroscan 256-channel EEG cap. The experiment was based on a

checkerboard stimulation [8] produced with Stim from Neuroscan. The stimulus was repeated 200 to 300 times. After collecting the data electrode locations were digitised and fitted on the head model surface. The continuous data was then processed and cut into series of sweeps called epochs. Channels and epoch of poor quality were removed and finally the data was averaged.

### E. Analysis

The ROISR parameter has a notable correlation to the SNR since the ROI volume is assumed to contain the signal sources and the nonROI volume the noise sources [3]. In this study we have calculated the SNR with a natural SNR estimator introduced by Raz, Turetsky and Fein [9]. We further calculated the correlation between ROISR and SNR for all EEG channels by using equation 3.

$$\text{correlation} = \frac{n \sum (XY) - \sum X \sum Y}{\sqrt{\left[ n \sum X^2 - \left( \sum X \right)^2 \right] \left[ n \sum Y^2 - \left( \sum Y \right)^2 \right]}} \quad (3)$$

where X corresponds to the individual SNRs of the measurement leads, Y corresponds to the ROISRs of the measurement leads and n is the total number of the leads (254). The higher the correlation is, the better the calculated SNR and ROISR values correspond to each other.

## III. RESULTS

The results of the effects of the ROI radius on the correlation are presented in Table 1. The correlations of the six measurements are averaged separately for each radius length. The variation of the correlations amongst the six measurements is also presented.

The results show that on average the ROI volumes with radii of 20 mm give the highest correlations between ROISR and SNR. Therefore the optimal ROI radius of a

Table 1 Correlations between ROISR and SNR

ROI radius (mm)	Average correlation (%)	Variation (%)
5	90	86-95
10	92	88-96
15	92	88-96
20	93	88-96
25	92	88-96
30	92	87-95
35	91	86-94
40	89	84-93
45	88	82-92
50	86	79-90

VEP experiment can be estimated to be 20 mm. The correlations with this radius were between 88 - 96%. In comparison, the correlations with 5mm and 50mm radii were between 86 - 95% and 79 - 90%, respectively. The average correlation for the 20 mm radius is 93 %. For the smaller radii the correlations are very similar but as the ROI volume increases the correlation significantly decreases.

## IV. DISCUSSION

### A. Findings of the study

When the ROI volume is chosen correctly the correlation between ROISR and SNR is high. In an optimal situation the ROI volume contains all the signal sources and none of the noise sources. In this study we chose a constant location and varied the ROI radius in a VEP experiment. The results of this study indicate that the optimal radius length is 20 mm, which is close to the reported size of the cortical volume where p100 components are produced [10].

If the highest correlations in a measurement are received with a ROI having a larger radius (>20 mm), it can be assumed that the location of the ROI has not been optimal. The volume does not include all the signal sources while some noise sources are included instead. On the other hand if the highest correlations are received when the ROI radius is smaller than 20 mm the results suggest that the actual signal sources are located on a smaller area.

### B. Limitations of the study

In this study we used the spherical head model, which does not correspond a real human head very accurately. Its shape is very simplified and it only represents the three major tissue types. Therefore higher correlations might have been achieved with a more realistic head model. We chose the ROI locations for each testee by approximating the location of the primary visual cortex. Since the location of this area might vary between testees it was based on choosing the electrode with the highest SNR. By using a more precise method to evaluate the location could have an effect on the results.

Another important factor is the electrode configuration. In this study we used an electrode corresponding the Cz electrode of the international 10-20 system as a reference. Testing various reference sites and combinations could give higher correlations. All of these factors could be taken into account in future studies to improve EEG measurements.

### C. Future considerations

In EEG measurements it is important that the optimal electrode configuration is selected in order to achieve high

quality results. The results imply that since the ROISR parameter has high correlation with SNR while the ROI has been chosen correctly, with a constant ROI the effects of different electrode configurations on the correlation could be examined. By finding the setting with the highest correlation the most appropriate settings for each study could be chosen. The correlations are highest when the location and size of the ROI volume are optimally chosen and when the electrode configuration is also optimal. By evaluating the differences in the correlation while varying the ROI parameters, ROISR could also be utilized in source localization purposes.

## V. CONCLUSION

In EEG measurements it is important to choose the correct measurement settings in order to receive optimal results. In the present paper we defined the optimal ROI radius of a VEP experiment by applying the ROISR parameter and calculating its correlation with SNR. The results indicate that for this specific measurement the ROI radius which should be applied in ROISR calculations is 20 mm. When the ROI volume is correctly localized the ROISR parameter can be used to analyse EEG measurement systems by testing various measurement settings and choosing the setting with the optimal sensitivity distribution. Since a high correlation between ROISR and SNR is evident when the ROI is correctly chosen, the method could also be utilized in source localization.

## REFERENCES

1. J. Malmivuo, V. Suihko, H. Eskola (1997) Sensitivity distributions of EEG and MEG measurements. *IEEE Trans Biomed Eng* 44:196-208.
2. J. Vaisanen, O. Vaisanen, J. Malmivuo, J. Hyttinen (2008) New method for analysing sensitivity distributions of electroencephalography measurements. *Med Biol Eng Comput* 46:101-108.
3. J. Vaisanen, J. Hyttinen, J. Malmivuo (2008). Correlations between signal-to-noise ratios and region of interest sensitivity ratios of bipolar EEG measurements. *Med Biol Eng Comput* 46:381-389.
4. S. Rush, D. A. Driscoll (1969) EEG electrode sensitivity--an application of reciprocity. *IEEE Trans Biomed Eng* 16:15-22.
5. J. Malmivuo, R. Plonsey (1995). *Bioelectromagnetism; Principles and Applications of Bioelectric and Biomagnetic fields*. Oxford University Press.
6. R. McFee, F. D. Johnston (1953). Electroencephalographic leads: I. Introduction. *Circulation* 8:554-568.
7. Tobimatsu, G. G. Celesia (2006). Studies of human visual pathophysiology with visual evoked potentials. *Clin Neurophysiol* 117:1414-1433.
8. G.G. Celesia, I. Bodis-Wollner, G. E. Chatrian, G. F. Harding, S. Sokol, H. Spekreijse (1993). Recommended standards for electroretinograms and visual evoked potentials, Report of an IFCN committee. *Electroencephalogr Clin Neurophysiol* 87:421-436.
9. J. Raz, B. Turetsky, G. Fein (1988). Confidence intervals for the signal-to-noise ratio when a signal embedded in noise is observed over repeated trials. *IEEE Trans Biomed Eng* 35:646-649.S.
10. T. J. Andrews, S. D. Halpern, D. Purves (1997). Correlated Size Variations in Human Visual Cortex, Lateral Geniculate Nucleus, and Optic Tract. *J. Neurosci.* 17:2859-2868.

Author: Juho Väisänen

Institute: Department of Biomedical Engineering, Tampere University of Technology

Street: Korkeakoulunkatu 3

City: Tampere

Country: Finland

Email: juho.vaisanen@tut.fi

# Effect of Microwave Radiation on EEG Coherence

A. Suhhova<sup>1</sup>, M. Bachmann<sup>1</sup>, K. Adamssoo<sup>2</sup>, Ü. Võhma<sup>2</sup>, J. Lass<sup>1</sup> and H. Hinrikus<sup>1</sup>

<sup>1</sup>Department of Biomedical Engineering, Technomedicum of Tallinn University of Technology, Tallinn, Estonia

<sup>2</sup>Clinic of Psychiatry, North Estonian Regional Hospital, Tallinn, Estonia

**Abstract** — The aim of this study was to investigate the changes in the EEG coherence produced by microwave exposure for healthy and depressive persons. The experiments were carried out on two groups of volunteers: a group of healthy subjects and a group of patients with major depressive disorder. Each group consisted of 18 female subjects. During 30 min experiment volunteers were exposed to 450 MHz microwave radiation modulated at 1000 Hz. The field density at the scalp was 1,6 mW/cm<sup>2</sup>. The coherence values were calculated for FP1-T3 – FP2-T4, T3-P3 – T4-P4 and P3-O1 – P4-O2 channel pairs. The EEG theta (4-8 Hz), alpha (8-13 Hz), beta1 (13-20 Hz) and beta2 (20-40 Hz) frequency bands were selected for analysis. Statistical analysis of calculated parameter for individuals with post-hoc Bonferroni correction was applied. The experiments demonstrated no significant changes in the EEG coherence between exposed and not exposed conditions for healthy as well as depressive group. However, the results showed significant changes produced by exposure in the EEG coherence for a part of subjects. In the healthy group: 1) an increase occurred in the EEG coherence in theta and alpha rhythms, and the differences were statistically significant over the frontal and temporal regions in theta (3 subjects, 16 %) and alpha (2 subjects, 11 %) rhythms, 2) decrease in alpha (2 subjects, 11%) rhythm was statistically significant over the parietal and occipital regions. In the group of patients with major depressive disorder microwave exposure caused statistically significant changes in the EEG coherence in beta2 rhythm (2 subjects, 11 %) over frontal and temporal regions and in alpha (3 subjects, 16 %) over temporal and parietal regions.

**Keywords** — microwave radiation, depression, EEG analysis, coherence.

## I. INTRODUCTION

The increasing applications of telecommunication devices roused problem of possible effects of the radio frequency electromagnetic, especially microwave field on human brain physiology. This effect can be different for healthy persons and persons with mental disorders as probably more sensitive to external stressors.

The diagnosis of depression as a mental disorder is based on evaluation of the intensity of subjective and clinical symptoms by psychiatrists (M.I.N.I interview, Hamilton test etc.). Prolonged electroencephalographic (EEG) studies have found the abnormalities in brain functioning in patients

with depressive disorder. Based on these studies it was supposed that left frontal hypoactivation is distinctive for depressed individuals, being characterized by relatively more left alpha activity [1, 2, 3]. Moreover, frontal alpha asymmetry seems to characterize also recovered depressives [2, 3]. In addition, absolute and relative power in beta band appeared to differentiate patients and controls, with patients exhibiting more power than controls [1]. The findings above suppose that characteristic changes in the EEG pattern in patients with depressive disorder are related to spatial phenomena in the brain. Brain spatial behaviour can be measured not only by the asymmetry of energy but also by the inter-hemispheric EEG coherence.

EEG coherence is a sophisticated technique that quantifies the similarity between EEG waveforms generated at a pair of electrodes and is considered to be an indicator of interdependence between those sites [4]. EEG coherence studies with patients with depressive disorder had reported reduced coherence values compared to healthy controls [1, 5].

The recent results of effect of microwave exposure on brain functioning have reported that exposure to a low-level microwave produces alterations in the resting electroencephalographic signal and/or brain behaviour [6, 7, 8, 9]. Authors of other studies have demonstrated that exposure to pulse-modulated microwave alters not only EEG but also regional cerebral blood flow [8, 10, 11]. Patients with major depressive disorder have shown to be more sensitive to low-level microwave exposure than healthy subjects [12].

The measures for detection of the effect of microwave exposure to the brain applied in these studies were based on energy of the EEG or intensity of the blood flow. The measures based on spatial correlation in the brain as coherence can provide additional information about microwave effects on brain bioelectrical activity.

The aim of this study was to investigate the effect of modulated microwave exposure on the EEG coherence. Inter-hemispheric coherence between frontal, temporal, parietal and occipital channels was considered.

## II. MATERIALS AND METHODS

### A. Subjects

The experiments were carried out on two groups of volunteers: a group of patients with major depressive disorder and a group of healthy subjects. Each group consisted of 18 female subjects, mean age 39 years, standard deviation 10 years.

The study was conducted in accordance with the Declaration of Helsinki and has formally approved by the local Medical Research Ethics Committee.

Subjects with major depressive disorder were selected for hospital inpatient unit. Subjects with non/psychotic major depressive disorder as defined by ICD-10 criteria and determined by 17-item Hamilton Depression Rating Scale (HAM-D) score more than 14 were eligible. The average score for the group was 21 (SD 3.3). Subjects were without antidepressant treatment, only regular (same dosage for more than 3 weeks) benzodiazepine use was allowed.

All the subjects passed two experimental procedures – with exposure and sham. During each test session, the succession of exposure-sham was randomly assigned. The subjects were not informed of their exposure; however, they were aware of the possibility of being exposed.

### B. Microwave exposure

The 450 MHz microwave radiation was generated by the Rhode & Swartz (Germany) signal generator model SML02. The RF signal was 100% pulse modulated by the modulator SML-B3 at 1000 Hz frequency (duty cycle 50 %). The generator signal was amplified with the Dage Corporation (USA) power amplifier model MSD/2597601 and additional laboratory amplifier (Miteq-Eesti, Estonia). The generator and amplifier were carefully shielded and located in the laboratory room. The 10W EMF output power was guided by coaxial to the quarter-wave antenna NMT450 RA3205 by Allgon Mobile Communication AB, Sweden, located at 10 cm from the skin from the left side of the head.

The spatial distribution of the microwave power density was measured by the Fieldmeter C.A 43 Chauvin Arnoux (France) field strength meter. The calibration curves of the field power density dependence on the distance from the radiating antenna were obtained from these measurements performed in the real condition of the experiment. During the experiments, the stability of the microwave level was monitored by the IC Engineering (USA) Digi Field C field strength meter. Estimated by the measured calibration curves, the field power density at the skin from the left side of the head was 1, 6 mW/cm<sup>2</sup>. The SAR value, calculated based on the maximum field power density, is 0,3 W/kg.

### C. Experimental procedure and EEG recording equipment

The study consisted of two experimental procedures identical for all subjects. The first protocol included continuous EEG recording during 30 minutes.

The 450MHz 1000 Hz modulated microwave exposure is switched on during all recording. The second protocol is the same except that the microwave exposure is switched off.

The Cadwell Easy II EEG measurement equipment was used for the EEG recordings. The EEG was recorded using 32 electrodes, which were placed on the subject's head according to the international 10-20-electrode position classification system. The channels for analysis were chosen to cover the entire head: frontal – FP1, FP2; parietal - P5, P4, temporal – T3, T4; occipital – O1, O2 and the reference electrode Cz. The EEG recordings were stored on a computer with a 400 Hz sampling frequency.

### D. EEG analysis

The dynamics of the EEG energy of the theta (4-8 Hz), alpha (8-13 Hz), beta1 (13-20 Hz) and beta2 (20-40 Hz) frequency bands were analyzed.

The 30 min signal was divided into overlapping epochs (50%), with the length of 1024 points. Epochs were extracted through a Hanning window and submitted to Fast Fourier Transform (FFT).

Segment of the EEG recordings with the length of 10 minute were selected for analysis.

Coherence values were computed using the next formula:

$$Coh_{xy}(w) = \frac{|P_{xy}(w)|^2}{P_{xx}(w) \cdot P_{yy}(w)}, \quad (1)$$

where  $P_{xy}$  is the cross-spectrum of two signals and  $P_{xx}$ ,  $P_{yy}$  the power spectrum of each signal. The coherence values for specific frequency band were calculated

$$C_{xy}(k_1, k_2) = \frac{(\sum_{k=k_1}^{k_2} S_{xy}(k))^2}{\sum_{k=k_1}^{k_2} S_{xx}(k) \cdot \sum_{k=k_1}^{k_2} S_{yy}(k)}, \quad (2)$$

where  $k_1$  and  $k_2$  are the lowest and highest frequency in specific frequency band, respectively. The coherence values were calculated for FP1-T3 – FP2-T4, T3-P3 – T4-P4 and P3-O1 – P4-O2 channel pairs. To estimate the long-term effect of microwave exposure to EEG coherence the difference between last 10 min and first 10 min of recorded EEG signal was selected for analysis.

Signal processing and calculation of parameters were performed in the LabView programming and signal processing environment.

The statistical analysis of calculated parameter for individuals with post-host Bonferroni correction was applied.

### III. RESULTS AND DISCUSSION

Coherence values were calculated for FP1-T3 – FP2-T4, T3-P3 – T4-P4 and P3-O1 – P4-O2 channel pairs for all subjects for microwave exposure and sham recordings.

Average coherence values for healthy participants in sham conditions are presented in Fig. 1. Fig. 2 presents average coherence values for healthy participants in microwave exposure condition.

As can be seen, the biggest differences are in frontal and temporal regions. Alpha rhythm is more influenced in P3-O1 and P4-O2 channel pairs. In case of microwave exposure in frontal-temporal region coherence values are increased; the decrease of coherence values occurred in parietal-occipital region.

For sham recordings, there were no significant results for individuals estimated by the ratio of computed coherence

differences to the standard deviation (calculated on the basis of sham signals). For recordings using microwave exposure, the differences were significant in FP1-T3 and FP2-T4 channel pairs in theta rhythm in 3 cases (16%) and in alpha rhythm in 2 cases (11%). The significant differences in T3-P3 - T4-P4 and P3-O1 – P4-O2 were in 2 cases (11%) for alpha rhythm.

Fig. 3 presents the average coherence values for different EEG frequency bands for depressive group in sham condition and Fig. 4 presents microwave exposure condition.

Differences between coherence in microwave exposed and sham recordings are much less than in the case of healthy persons. The biggest differences occur in temporal-parietal regions. The relative changes in other brain regions caused by microwave exposure are within 2% and caused by natural variability of the EEG.

For sham recordings, there were no significant differences. In case of microwave exposure, the significant differences were in FP1-T3 and FP2-T4 channel pairs in 2 cases (11%) for beta2 rhythm. In T3-P3 and T4-P4 channel pairs significant differences were in 3 cases (16%)

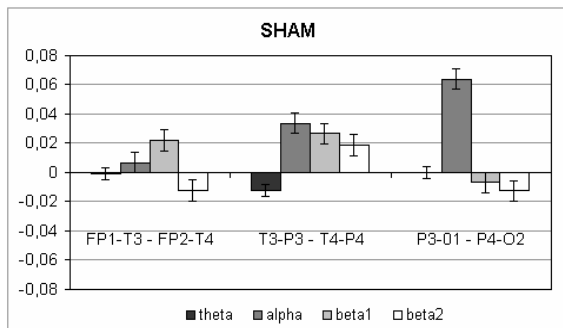


Fig. 1 The average coherence values for different EEG rhythms for healthy group in sham condition.

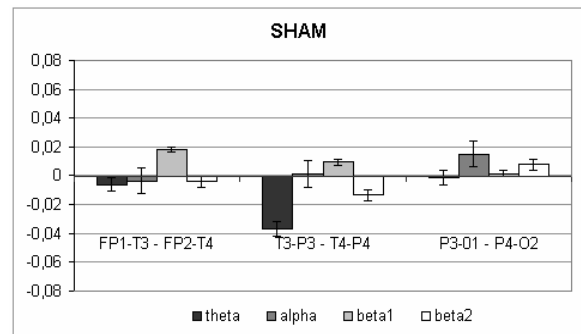


Fig. 3 The average coherence values for different EEG rhythms for depressive group in sham condition.

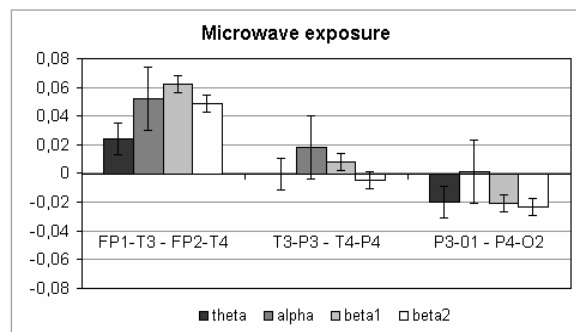


Fig. 2 The average coherence values for different EEG rhythms for healthy group in microwave condition.

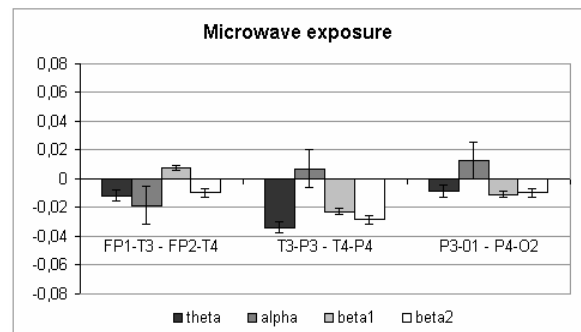


Fig. 4 The average coherence values for different EEG rhythms for depressive group in microwave exposure condition.

for alpha rhythm. In P3-O1 and P4-O2 channel pairs there were no significant differences.

#### IV. CONCLUSION

Exposure to 450 MHz microwave radiation modulated at 1000 Hz did not caused significant changes in EEG coherence for a group of healthy persons as well as depressive patients.

The rate of individual subjects affected by microwave exposure is the same for healthy and depressive group.

#### REFERENCES

- 1 Knott, V., Mahoney, C., Kennedy, S., Evans, K., 2001. EEG power, frequency, asymmetry and coherence in male depression. *Psychiatry Research: Neuroimaging Section* 106 pages 123 – 140.
- 2 Allen, J., Urry, H., Hitt, S., Coan, J., 2004. The stability of resting frontal electroencephalographic asymmetry in depression. *Physiology* volume 41 issue 2, page 269. Flor-Henry, P., Lind, J., Koles, Z., 2004. A source – imaging (low – resolution electromagnetic tomography) study of the EEGs from unmedicated males with depression. *Psychiatry Research: Neuroimaging* pages 191 – 207.
- 3 Sritharan, A., Line, P., Sergejew, A., Silberstein, R., Egan, G., Copolov, D., 2005. EEG coherence measures during auditory hallucinations in schizophrenia. *Psychiatry Research* 136, 189-200.
- 4 Yamada, H., Kimura, H., Mori, T., Endo, S., 1995. EEG power and coherence in presenile and senile depression. Characteristic findings related to differences between anxiety type and retardation type. *Nippoo Ika Daigaku Zasshi*, 62(2): 176-85.
- 5 Leszczynski, D., Joenväeä, S., Reivinen, J., Kuokka, R., 2002. Non-thermal activation of the hsp27/p38MAPK stress pathway by mobile phone radiation in human endothelial cells: molecular mechanism for cancer- and blood brain barrier-related effects. *Differentiation* 70, 120-129.
- 6 Krause, C.M., Sillanmäki, L., Koivisto, M., Häggqvist, A., Saarela, C., Revonsuo, A., Laine, M., Hämäläinen, H., 2000. Effects of electromagnetic field emitted by cellular phones on the EEG during a memory task. *NeuroReport* 11: 761-764.
- 7 Curcio, G., Ferrara, M., Moroni, F., D’Inzeo, G., Bertini, M., De Gennaro, L., 2005. Is the brain influenced by a phone call? An EEG study of resting wakefulness. *Neuroscience Research* 53: 265–270.
- 8 Hinrikus, H., Bachmann, M., Lass, J., Tomson, R., Tuulik, V., 2008. Effect of 7, 14 and 21 Hz modulated 450 MHz microwave radiation on human electroencephalographic rhythms. *International Journal of Radiation Biology*, vol. 84, pp.66-79.
- 9 Huber, R., Treyer, V., Borbely, A.A., Schuderer, J., Gottselig, J.M., Landolt, H.P., Werth, E., Berthold, T., Kuster, N., Buck, A., Achermann, P. 2002. Electromagnetic fields, such as those from mobile phones, alter regional cerebral blood flow and sleep and waking EEG. *Journal of Sleep Research* 11: 289–295.
- 10 Huber, R., Treyer, V., Schuderer, J., Berthold, T., Buck, A., Kuster, N., Landolt, H. P., Achermann, P., 2005. Exposure to pulse-modulated radio frequency electromagnetic fields affects regional cerebral blood flow. *The European Journal of Neuroscience*. 21: 1000–1006.
- 11 Bachmann, M., Hinrikus H., Aadamsoo K., Võhma Ü., Lass, J., Rubljova J., Suhhova A., Tuulik, V., 2007. Modulated microwave effects on individuals with depressive disorder. *The Environmentalist*, vol.27, pp. 505-510.

Address of the corresponding author:

Author: Anna Suhhova  
 Institute: Technomedicum of Tallinn University of Technology  
 Street: 5 Ehitajate road  
 City: Tallinn  
 Country: Estonia  
 Email: anna@cb.ttu.ee

# Stress Stages and Changes on EEG by low-level Physical (EMF) and Chemical Stressors

V. Tuulik, J. Lass and M. Bachmann

Department of Biomedical Engineering, Technomedicum, Tallinn University of Technology, Tallinn, Estonia

**Abstract** — The psychosocial, physical and chemical factors, which affect the human organism on the workplace or in environmental, are considered by some authors [1, 2, 3] as stress factors which affect the functional state [FS]-vigilance level- of the central nervous system (CNS) and can cause the changes of this by developing of three stages of stress according to the stress theory H. Selye: hypersthenic, hyposthenic and organic psychosyndrome [4]. To characterise the low –level effects of chemical or physical factors on the vigilance level of CNS according to stress theory stages we have used the different psychological/ psychometrical tests and EEG analyzing methods. By using for the investigation of low–level impact of occupational chemical stressors on the vigilance level of CNS we have used the different methods as questionnaires, psychometric tests (827 workers) and analyzing of the EEG date (77 workers). As low-level physical factor we have used modulated electromagnetic radiation at different rhythms [14, 15, 16] and analyzed the changes on the EEG data of different groups of 77 volunteers. This data have showing the changes of the beta- and alpha-activities depending of the modulation frequencies and associated with data of the neuropsychological tasks [16]. This investigations have showing that for the analyzing of changes in EEG by impacting of modulated electromagnetic radiation at different rhythms is possible to use the stress theory stages for the understanding of impacting this low level physical factor on the vigilance level of CNS. In conclusion: to analyze the low level chemical and physical factors impacting on the vigilance level CNS by using the psychological/psychometrical and electrophysiological (EEG) data we found the acceptable to use the stress theory and developing of the stress stages H. Selye to characterizes the development of CNS vigilance level changes.

**Keywords** — vigilance level, low-level effects, physical and chemical stressors, modulated microwaves

## I. INTRODUCTION

Psychosocial, physical and chemical factors which affect the human organism in industry or in environment are considered by some authors as stress factors which change the functional state (FS)-vigilance level- of the central nervous system (CNS) or which change the cerebral homeostasis [1, 2, 3]. Cerebral homeostasis is understood to be the ability of the nervous system to maintain the optimum levels of excitability, reactivity and liability, which are adequate for a given situation [4, 5]. According to contemporary research

data, it possible to determine the level of stability or instability of cerebral homeostasis, to characterize the changes in the FS-vigilance level- of the CNS on low-level impacting of occupational or environmental physical and chemical stressors. According to Anokhin's theory of functional systems and Ashby's theory of the mechanism of the regulation of cerebral activities and the stabilization of its systems, the nervous system works like a complex integral self-regulating system [6, 7]. The functional state (FS)-vigilance level- of the central nervous system (CNS) is a complex concept and therefore cannot be expressed by a sole indicator. By the using the complex of the different quantitative methods [8] – psychometric and psychological methods and electrophysiological methods as electroencephalography (EEG) – vigilance level of the CNS can be measured [9]. The neuropsychological theory of localization and equipotentiality [10] the psychic functions and understanding of brain – behavior relationship can be useful for the analyzing of the low-level effects (LE) on vigilance level CNS by impacting of physical and chemical stressors. By Luria's theory the psychophysiological data are intercorrelated by three cerebral blocks [10]: the block of reception, the block of processing and retaining of the exteroceptive information, and the block of programming, regulation, and control of cognitive activities. Luria's concept of a system provides a means of classifying functions into three major types. It is accepted consist of breaking down compound functions into their elementary components [9]. Various tests and procedures can be designed to separate different elementary functions in compound function- that is to use component analyses [9]. By this the general compound functions as mental speed and attention are generally more sensitive to brain damage anywhere in the brain than are tests of an elementary function. The general function and general effects of brain damage is one in which a lesion produces nonspecific impairment on test related to many areas of the cortex [8]. The elementary function as components of a total functional system may be analyzed on the psychometric level as isolated components of function. It means, we would like to find nonspecific effects by investigation of general functions (speed and attention as mental function) and use the possibilities to measure the isolated components of psychic function process as specific effects for low-level stressors. By this we must accept the fluidity and plasticity of mental



functions in CNS. By the using of the neurophysiologic method as EEG for the detecting changes of the vigilance level of CNS by impacting different low-level stressors is accepted but it must be used combination of different analyzing methods to provide most reliable results

## II. METHOD AND EQUIPMENT

The aim of our work was: to analyze and characterize the changes of the vigilance level of CNS by low-level effects of the chemical (organic solvents, heavy metals) and physical stressors (modulated microwaves); to characterize the changes of vigilance level CNS - nonspecific and specific symptoms- by development the stress stages by impacting low-level chemical and physical stressors.

To characterize the low-level effects of the chemical and physical factors we have analyzed with the different statistic methods data of the psychometrical and psychological investigations and electrophysiological (EEG) data of the two groups: group of workers who have been exposed to different low-level occupational neurotoxic agents and by experimentally exposed to the modulated microwave as low-level physical factor -the group of healthy volunteers. Groups of workers who have been exposed to different occupational low-level neurotoxic agents were investigated: 402 workers had occupational contact with lead, 96 with styrene, 252 with oil-shale products, and 77 with organic solvents. A control group of 145 workers was also investigated. Occupational health services provided the information about the occupational neurotoxic agents on the workplaces. All workers were also examined clinically and tested by psychological methods on different groups by accepting of age and sex. The clinical examination was evaluated with the occupational history, analyzing of subjective syndrome [by using of special questionnaires], and the accepting by hygienists of the exposure of the low-level chemical factors on the working places and with the neurological examination of all neurological subsystems. Reaction time was measured to light and sound stimuli where the tasks become more complicated during the experiment. The methods of Bourdon-Wiersma, Ratten, Benton, Schulte, Kohc'cubes, Kraepelin and Luria were used. All data of psychometric tests were analyzed by accepting of age, sex, clinically diagnosed syndromes. The results of psychometric tests we analyzed the speed, the successful and accuracy using different statistic methods (Pearson's correlations, methods of information coefficients of Hoolma and Peterson etc) [11].

By using EEG were investigated 77 workers with low level contact with the occupational chemical stressor and statistic analyzing of the data of the EEG energy (epoch 20s) on the main EEG frequencies. This data's were the

basis for the developing a perception based neural network method diagnosing different syndrome classes (on the basis of the data 77 persons with low-level chemical stressors contact and 10 healthy subjects) [12].

For the detecting low-level effects of the physical stressors were analyzed EEG data of the 77 healthy volunteers (the Cadwell Easy HEEG measurement equipment was used with the international 10-20-electrode position classification system), by modulated 450MHz microwave exposure [13]. Microwave exposure conditions were the same for all subjects, except modulation frequencies. The 450MHz microwave radiation was modulated at 7, 14, 21, 40, 70, 217 or 1000Hz frequencies. For the statistical analyzing and were used different methods [13].

## III. RESULTS

By the statistical analyzing of the data psychometric tests of workers, who have been exposed to different occupational neurotoxic agents on the low-level concentrations, was find the decreasing of speed of psychic activities investigated workers what correlated with the length of exposure to toxic substances ( $r=0.45 - 0.53$  by  $p<0.05$ ) The increasing of the numbers of mistakes in the psychometric tests (learning-test "Labyrinth", reaction time, Kraepelin test, Schulte) have given information about decreasing of vigilance level and attention concentration disorders and with the increasing of functional disorders of CNS ( $r=0.50$ ;  $p<0.005$ )[3]. The changes on the psychometric tests were correlated with the changes on the vigilance level and bioelectrical activity on the different frequencies EEG statistically accepted on the level alpha- and beta frequencies [3]. The correlation analysis has showing the decreasing of the bioelectrical activity (BA) EEG of the brain, related to the changes of the vigilance level of CNS [3]. The changes of the BA at different frequency ranges energy and EEG leads have been correlated with the diagnosed changes of the vigilance at the syndrome level: the first changes were detected -mainly in the range of the beta activity, and by developing the changes of vigilance level -in the alpha-activity [3]. The first changes by the development of the low-level chemical effect on the CNS were finding on the frontal and temporal EEG leads [3]. According to the results of the analyzed database-psychometric and neurophysiologic database[EEG] by impacting of chemical low-level stressor-the changes on the vigilance level correspond to the developing universally recognized stress stages H. Selye [4]: hypersthenic syndrome-mobilization due to the alarm of the adaptation possibilities, hyposthenic syndrome- stage of stress development, organic psychosyndrome-stage of exhaustion.

As low-level physical factor we have used modulated electromagnetic radiation at different rhythms and analyzed the changes on the EEG data of 77 healthy volunteers [14, 15, 16]. By using different statistic methods for the detecting changes on the EEG rhythms was showing the changes of the beta and alpha-activities depending of the modulation frequencies and associated with data of the neurophysiologic tasks [16].

#### IV. DISCUSSION

The first low-level effects and symptoms and/or syndromes of the changes of vigilance level CNS by impacting low-level physical and chemical occupational or environmental stressors is possible diagnose by using with complex of different psychometrical and electrophysiological (EEG) methods. The developing of changes on vigilance level is depended of the characteristics of physical and chemical stressors. By using of the stress theory of H. Selye (1950) the stress stages characterize the development the changes on vigilance level by impacting low-level physical and chemical environmental or occupational stressors. The non-specific symptoms by impacting of low-level occupational chemical and physical stressors are the changes of more general characteristics of psychic functions: the nonstability of psychic functions, decreasing of vigilance level and attention concentration. It means, it is possible to diagnose the changes in functional state of the first block (by Luria), calling by us as hypersthenic syndrome of stress – the mobilization due to the alarm of the adaptation possibilities of the organism reserves – by H. Selye. The hypersthenic syndrome – it is mild changes on the vigilance level, irregular speeds of cognitive activity, disturbed attention, increase in the number of errors in the tests; no memory disorders; increased variability in reaction time [3].

By the continue the low-level occupational or environmental stressor develops the hyposthenic syndrome – moderate changes of the vigilance level: decreased speed in cognitive activity, decreased results in tasks requiring long-term effort, decreased speed of psychic processes and attention; modal-nonspecific memory changes, prolonged RT and increased its variability, complaints of headaches, sleeping disorders, changes in emotional level.[3]

By the analyzing of the data of the psychometric tests we had conclude, that the first changes in the psychic activity by low-level effects of physical and chemical stressors are the disorders of more complicated psychic functions, what is possible to diagnose with most complicated psychometric tests and with the increasing of numbers of mistakes in this; by the developing of the stress was possible the decreasing of vigilance level and successful of psychometrical tests results [3].

The specific symptoms of stress developing depends of the specificity [of character of psychical or chemical stressor] of stressors and can be diagnosed by the more complicated psychometrical tests [3].

For the developing of nonspecific and specific symptoms – what is related to characteristics of stressor – specify of psychic activity is important the impacting of the stressors to the different functional systems in CNS. Developing of specific symptoms by low-level effects depends from the specific impacting on the specific functional systems or from the specific disorders in metabolism of different functional systems in CNS,

We concluded that the physical and chemical stress, caused by low-level effects of physical and chemical stressors on the workplaces or in the environment at every stage of its development produces both nonspecific, as well as the relatively specific changes of the vigilance level of the CNS. Functional changes in the nervous system by low-level effects of occupational physical and chemical stressors develop as the hypersthenic syndrome, the hyposthenic syndrome and, the organic psychosyndrome, The effects on the EEG- by the low-level impacting of chemical occupational stressor - by using of neural network method [12] identified the three stages on the EEG data: the first changes on the level of beta-activity in the hypersthenic stage and the decreasing of the alpha-activity by the developing of chemical stress –in hyposthenic stage. The changes on EEG by impacting of the low-level physical stressor - as modulated microwave radiation- correspond to the developing changes on EEG by hypersthenic syndrome [14, 15, 16].

#### V. CONCLUSION

This investigation have showing that for the analyzing of changes in EEG by impacting of modulated electromagnetic radiation at different rhythms is possible to use the stress theory stages for the understanding of impacting this low level physical factor on the vigilance level of CNS.

In conclusion: to analyze the low level chemical and physical factors impacting on the vigilance level CNS by using the psychological /psychometrical and electrophysiological (EEG) data we found the acceptable to use the stress theory and developing of the stress stages H. Selye to characterizes the development of CNS vigilance level changes.

#### ACKNOWLEDGMENT

I am thankful for the co-work of my colleagues and Professor Hubert Kahn of the data collection in Occupational Health Departments of Institute of Experimental and Clinical Medicine.

## REFERENCES

1. O'Hanlon, J.F. (1978). Neurophysiological reactions to stress: Psychosocial, physical and chemical stressor at work. *Scandinavian Journal of Psychology*, 12, 157-159.
2. Lindström, K., Mäntusalo, S.(1987). Physical and chemical factors that increase vulnerability to stress and act stressors at work. In: *Psychosocial Factors at Work*, 3, 112-123.
3. Tuulik, V. (1996) The Functional State of the Central Nervous System in Chemical Stress. *International Journal of Stress Management*. Vol. 3. Nr. 2, pp 107-115.
4. Selye, H.(1950). The psychology and pathology of exposure to stress. *Acta Inc. Med. Publ. Montreal*.
5. Livanov, M.N., Russinoff, V.S., Simonov, P.V. et al. (1988). Diagnosis and prognosis of the functional state of the human brain. *Medicina, Moscow*.
6. Anokhin, P.K. (1998). *Cybernetics of functional system*. Moscow, Medicine, 400 p.
7. Ashby, R. (1966). *Design for a Brain*. Chapman Hall Ltd., London, ISBN 0-412-20090-2
8. Bleecker, M.L. (1994). *Clinical Presentation of Selected Neurotoxic Compounds*. *Occupational Neurology and Clinical Neurotoxicology*, 207-234, Williams&Wilkins, Baltimore.
9. Russell Elbert W. (1986). *The Psychometric Foundation of Clinical Neuropsychology*. *Handbook of Clinical Neuropsychology*. Vol. 2. John Wiley & Sons, 45-80.
10. Luria, A.R. (1973). *The functioning brain*. Basic Books, New York. O'Hanlon, J.F. (1978). Neurophysiological reactions to stress: Psychosocial, physical and chemical stressor at work. *Scandinavian Journal of Psychology*, 12, 157-159.
11. Hoolma, M., Petersen, I. (1981). *Computer analysis of data*. Valgus, Tallinn, 112.
12. Tuulik, V. et al.(1997). Neural Network method to determine the vigilance level of the chronic chemical stress. *Technol. Health Care*, 5, 243-251.
13. Bachmann, M et al.(2007) Individual changes in human EEG caused by 450 MHz microwave modulated at 40 and 70 Hz. In: *Environmentalist*, 27:511-517.
14. Hinrikus, H.; Bachmann, M.; Lass, J.; Tomson, R.; Tuulik, V. (2008). Effect of 7, 14 and 21 Hz modulated 450 MHz microwave radiation on human electroencephalographic rhythms. *International Journal of Radiation Biology*, 84(1), 69 - 79.
15. Hinrikus, H.; Parts, M.; Lass, J.; Tuulik, V (2004). Changes in human EEG caused by low level modulated microwave stimulation. *Bioelectromagnetics*, 25(6), 431 - 440.
16. Lass, J.; Tuulik, V.; Ferenets, R.; Riisalo, R.; Hinrikus, H (2002). Effects of 7 Hz-modulated 450 mhz electromagnetic radiation on human performance in visual memory tasks. *International Journal of Radiation Biology*, 78(10), 937 - 944.

Author: V. Tuulik

Institute: Department of Biomedical Engineering, Technomedicum,  
Tallinn University of Technology

Street: Ehitajate tee 5

City: Tallinn

Country: Estonia

Email: viiu@cb.ttu.ee

# Body Surface Potential Mapping for Noninvasive Ischemia Detection

M. Tysler<sup>1,2</sup>, P. Kneppo<sup>2</sup>, V. Rosik<sup>1</sup>, S. Karas<sup>1</sup>, E. Heblakova<sup>1</sup> and J. Muzik<sup>2</sup>

<sup>1</sup> Institute of Measurement Science, Slovak Academy of Sciences, Bratislava, Slovakia

<sup>2</sup> Faculty of Biomedical Engineering CTU in Prague, Kladno, Czech Republic

**Abstract** — Portable body surface potential mapping system and method for early noninvasive detection of local ischemia is introduced.

Mapping system with intelligent data acquisition unit enables simultaneous recording of up to 128 ECG leads. Active electrodes, powering from Li-ion battery and optical connection to USB port of the controlling notebook help to reduce noise in ECG and guarantee patient safety. Modular software for ECG recording and body surface potential mapping is applicable for more detailed cardiac diagnostics.

Method for ischemia detection is based on dipolar model of the cardiac electric generator. It uses alterations in time integrals of surface potentials connected with changed repolarization of ischemic myocardial cells together with information on torso volume conductor for estimation of an equivalent dipole representing the ischemic lesion. Testing of the method on patients after myocardial infarction that underwent successful percutaneous cardiac intervention and patients with suspected ischemia suggest that ECG mapping connected with such simplified inverse solution might be a useful tool for non-invasive identification of repolarization changes connected with local ischemia.

**Keywords** — Body surface potential mapping, inverse solution, equivalent dipole model, early detection of local ischemia.

## I. INTRODUCTION

Body surface potential (BSP) mapping is a non-invasive electrocardiographic method for detailed registration of surface cardiac potentials using high number of sensing electrodes. It was shown elsewhere [1] that use of high quality BSP maps can help in more precise clinical diagnostics of cardiac diseases. However, several studies proved that BSP maps together with information on torso volume conductor obtained from MR, CT or ultrasound imaging systems can be used for more advanced diagnostic methods based on inverse solutions and enable non-invasive model based assessment of abnormal electrical sources in the cardiac tissue [2, 3].

In this paper a high resolution ECG mapping system for BSP based cardiac diagnostics is introduced and possibility to use the system for noninvasive identification of local ischemic heart region is analyzed.

## II. METHODS AND MATERIAL

### A. ECG mapping device

Based on our previous experience [4], ProCardio 8 mapping device was developed to acquire high quality multi-channel ECG recordings and to compute BSP maps suitable for direct clinical diagnostics or for advanced model-based interpretation of the mapped data. The device consists of a set of active electrodes, data acquisition unit and a notebook computer used for data acquisition control, processing of measured ECG signals and for their analysis and electrophysiological interpretation.

ECG signals are sensed by active electrodes formed by disposable passive electrodes attached to active adapters made in SMD technology (Fig.1). While use of quality disposable Ag-AgCl electrodes guarantees low noise, minimal polarization potentials and eliminates risk of patient infections, high input and very low output impedance of the active adapter (with OP07 amplifier) effectively reduces disturbing signals often induced in electrode cables.

Modular data acquisition unit is placed in a patient terminal box and consists of several measuring boards plugged into a motherboard containing microcontroller, USB interface and switched power supply module (Fig. 2). Each measuring board has 16 analog input channels connected to two robust Centronix connectors. All signals are measured relatively to a common mode sense (CMS) electrode that can be attached to the patient's body so that the interference from the common mode is minimal.



Fig. 1 Active electrodes are composed of quality Ag-AgCl disposable electrodes and active electrode adapter.

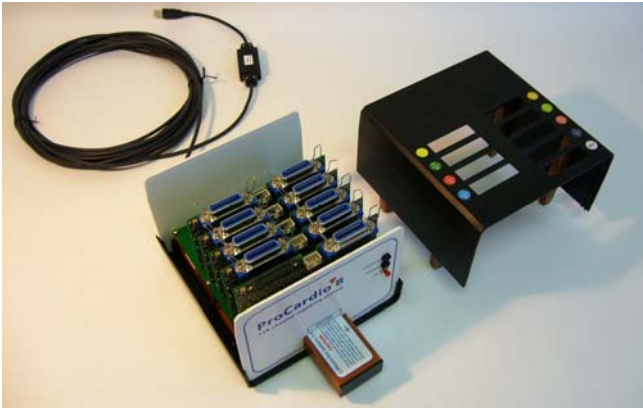


Fig. 2 Opened patient terminal box with one reference and four 16-channel boards, optical interface cable and Li-ion battery module.

One of the boards is configured as reference board and is used for recording of signals from limb leads R, L and F. Signal of the Wilson's central terminal (WCT) that is commonly used as the reference for all unipolar ECG leads is also generated. Remaining 12 channels on the board can be used for additional unipolar leads. The board contains circuitry for the CMS electrode and driven right leg (DRL) electrode that provides “active grounding” of the patient and further reduces the common mode voltage. Resistor in the DRL circuit limits maximum current through the patient body to  $\pm 50 \mu\text{A}$  and protects the patient in case of electrical defects in the unit. Additional protection circuit generates a power-down signal if the current is steadily close to  $50 \mu\text{A}$ .

Each low noise ( $< 1.0 \mu\text{V}_{\text{RMS}}$ ) measuring channel has fixed gain of 40 and is equipped with a DC-coupled instrumentation amplifier (AD621) and a 22-bit  $\Delta\text{-}\delta$  A/D converter (AD7716). Sampling frequency can be selected between 125 and 2000 Hz resulting in effective dynamic converter resolution between 19 and 16 bits.

The data acquisition system is controlled by 16-bit CISC microcontroller (Fujitsu MB96340). Its internal flash memory, 4 UARTs and a DMA controller are used to control the multi-channel measuring unit and to communicate with the host computer. Selection of measured channels, desired sampling rate and formatting of sampled data is controlled by commands received from the host computer.

Serial data sampled from analog channels are streamed to the host computer over an USB FIFO circuit (FTDI FT245R) that provides bidirectional data transfer with rates of up to 1 MB/s. To minimize capacitive coupling between the patient terminal and the host computer USB port, a fiber optic USB extension cable is inserted.

The patient terminal is powered by Li-ion battery module. Thanks to advanced power management the battery has to be replaced or recharged approximately once a day.

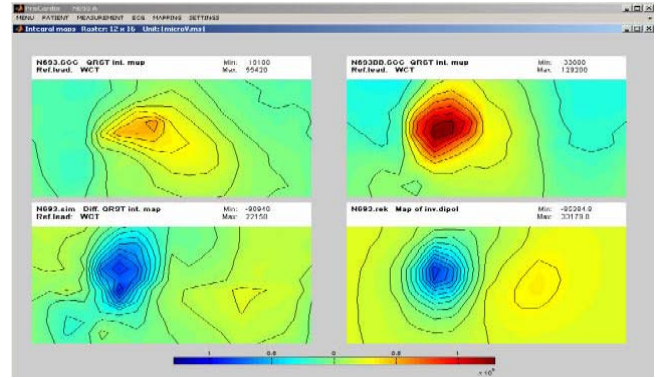


Fig. 3 Maps of surface potentials integrated over the QRST interval in a MI patient. Left part of each map represents anterior chest, right part the back. Maps before and after coronary intervention are shown (top left and right). Their difference (bottom left) represents changes in the surface electrical field caused by the reduction of the ischemic lesion. In case of small lesion, these changes can be satisfactorily reproduced by an equivalent dipolar electrical generator (bottom right).

ProCardio 8 application software is running under Windows/XP and was developed in Matlab environment.

Measuring program controls the data acquisition unit, checks electrode contacts, reads data stream with ECG and control data, displays ECG signals on computer screen and stores them on disk as a GDF (general data format for biosignals) file.

Data processing and evaluation programs include pre-processing of ECG signals (baseline correction and filtering routines) and mapping of body surface potentials or their time integrals. 2D presentation or 3D projection of obtained maps on the torso surface is possible. In Fig. 3 is example of 2D surface integral maps of the QRST interval with and without manifestation of ischemia that were recorded in the same patient. Their difference may be regarded as contribution of pathological sources within the ischemic lesion that can be approximated by equivalent model generator as described in following paragraphs.

### B. Model based identification of ischemic lesion

Differences between surface potentials under normal conditions and during ischemia that are caused by myocytes action potential alterations during the repolarization phase are projected into difference QRST integral maps (DI maps). These maps were used for noninvasive assessment of the region with the ischemic lesion.

Supposing a small region, differences in body surface potentials can be interpreted as being caused by single dipolar generator located at the centre of the region. To guarantee localization of the dipole within the heart walls we used fixed dipole model located at one of predefined locations in

the myocardium. For each of these locations  $i=1,2,\dots,n$ , an equivalent dipole (ED) source representing changes in body surface potentials was estimated using the formula:

$$D_i = T_i^+ \Phi \quad (1)$$

where  $D_i$  is an estimate of the dipole moment of an ED located in the  $i$ -th predefined position that in fact represents integral of the dipole moment of physical current dipole during the QRST (depolarization-repolarization) period,  $T_i^+$  is pseudoinverse of a transfer matrix representing relation between position of the  $i$ -th dipole and surface potentials and reflects only geometrical and electrical properties of the torso volume conductor,  $\Phi$  are differences in QRST integrals of surface potentials in mapped surface points. To solve the inverse problem of  $D_i$  estimation, pseudo-inverse  $T_i^+$  was computed for each possible dipole location  $i$  using singular value decomposition of  $T_i$ .

To find the location of an ED that best represents changes in surface potentials, minimal rms difference  $R_D$  between the original DI map (values  $\Phi_n$ ) and a map generated by the ED (values  $F_n$ ) in the same torso surface points was used:

$$R_D = \frac{\sqrt{\sum_n (F_n - \phi_n)^2}}{\sqrt{\sum_n \phi_n^2}} \quad \text{for } n=1,2,\dots,l \quad (2)$$

where  $l$  is number of ECG leads (torso surface points).

Magnitude of  $R_D$  can also serve as a measure showing to which extent the ED is able to represent an ischemic region.

### C. Measured data

To data sets were used for testing of the above method:

*Set 1:* ECG data were taken from 12 patients (9 men, 3 women, age 45-69) after myocardial infarction (MI) that underwent coronary intervention (PCI) on single coronary vessel. QRST integral maps before and after the intervention were computed from 32 ECG leads measured in the Lux32 lead set [5]. Impact of the reperfusion on the surface potentials was analyzed in this group. It was hypothesized that regions with changed repolarization will be identified near the infarcted tissue due to revascularization and reduction or disappearance of the ischemia.

*Set 2:* Averaged ECG data from 4 healthy persons and 7 patients suffering from effort angina pectoris were taken using Amsterdam lead system with 62 surface electrodes. Two patients were taking no medication, 3 patients were taking beta blockers. One ECG record of 1 minute length was taken before and five records every 3 minutes after sublingual nitroglycerine application. Difference QRST

integral maps between the first record and all records after nitroglycerine application were computed and evaluated.

For both sets, maps were corrected for QT interval length if it varied more than 5% between the measurements. Common realistic inhomogeneous torso and heart model geometry were used to find an ED representing the region with changed repolarization. Possible positions of ED were defined at gravity centers of 28 anatomical segments of an analytical heart model.

## III. RESULTS

From the 12 tested MI patients of set 1, the PCI was successful in 11 patients. In one patient where the PCI failed, changes in the surface potentials and estimated dipole moment of the ED source were very small. Changes in QRST integral maps were noticeable in patients after successful PCI. In 8 of them measured DI maps could be reasonably represented by single ED. In 6 cases relative rms error between the measured DI maps and maps generated by the ED was  $< 35\%$ , in another 2 patients it was  $< 56\%$ . In remaining 3 patients, rms error of the DI map approximation was higher than 56% and they were excluded from further analysis because single dipole was probably not appropriate model for these cases. In 7 of 8 analyzed patients, positions of estimated ED well matched with the region supplied by the treated vessel. Dipole moments were directed inwards the ventricle suggesting changes near the endocardial wall (Fig. 4). In 1 patient after PCI on right coronary artery the ED was incorrectly located in mid anterior left ventricular wall.

In all persons from set 2, except one healthy subject that was excluded from further evaluation, nitroglycerine administration was followed by increase of heart rate with peak effect predominantly 3-6 minutes after application.

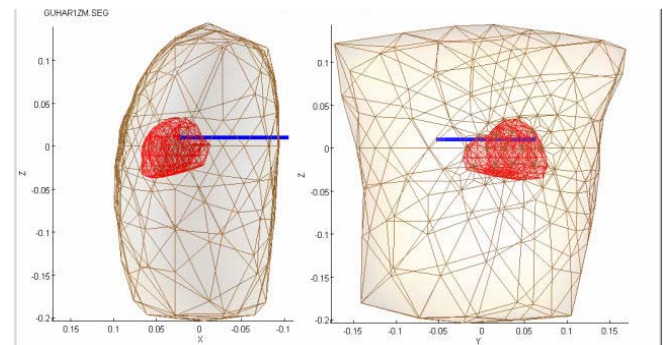


Fig. 4 Result of non-invasive localization of area with changed repolarization in a MI patient after successful PCI. Single dipole model was used as an equivalent generator representing locally changed electrical properties of the myocardium. Position and orientation of the ED is marked by a line.

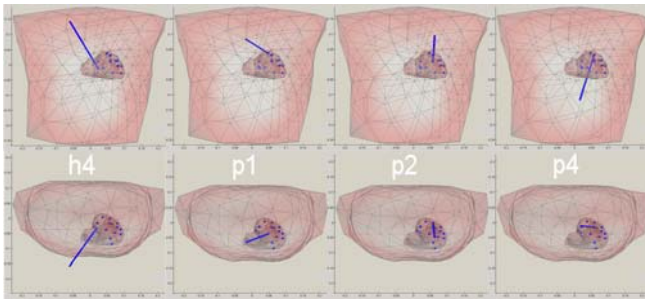


Fig. 5 Inversely estimated EDs representing possible locations of ischemic lesions in one healthy subject and three patients with effort angina pectoris.

Relevancy of DI maps for inverse identification of local ischemia was examined by evaluation of relative rms differences between QRST integral maps from records before and after nitroglycerine application. To account for possible intra-individual variability in averaged QRST integral maps, only rms differences greater than 15% were considered significant. One “healthy” subject (h4) and three patients without medication (p1, p2, p4) fulfilled this condition and their DI maps were inversely approximated by single ED. Relative rms error between measured DI map and map produced by the ED was 33% for h4 subject and 51%, 60% and 31% for patients p1, p2 and p4, respectively (Fig. 5).

#### IV. DISCUSSION AND CONCLUSIONS

Our attempts to detect ischemic regions by using departure integral maps [6] showed that changes in BSP are small when compared with normal inter-individual fluctuations and can hardly be detected by departures from mean normal maps. However, computer simulations [7] suggested that relative differences between normal and ischemic QRST integral maps can be 20-45% rms, correlations .45- .99. These are greater than observed intra-individual variability in healthy subjects (5-20% rms, correlations >.98) what, in principle, allows ischemia identification. Simulations also showed that use of the proposed method might be not appropriate for identification of larger and transmural lesions where the single dipole model is not adequate and its localization may not be in correspondence with the real lesion. Moreover, transmural lesions produce smaller differences in DI maps and their identification is more difficult.

Simulated ED localization from 32 ECG leads provided slightly worse results than from 62 or 192 leads. Hence more than 32 leads should be used in future measurements. Use of a high resolution mapping system with sufficient

number of measuring channels therefore seems to be crucial for practical implementation of the proposed method.

No individual torso geometry was available when the method was tested on real patients and common model geometry had to be used. Use of individual geometry should improve accuracy of the lesions localization [8].

Despite these limitations our results indicate that the developed ECG mapping device could be useful tool for clinical implementation of ECG mapping methods, helping in non-invasive cardiac diagnostics using common BSP mapping methods. Moreover, it can help to identify small ischemic regions with changed repolarization using model-based interpretation of difference QRST integral maps.

#### ACKNOWLEDGMENT

This work was supported by grants 2/7092/27 from the VEGA grant agency, APVV-51-059005 from the APVV agency, ESF project Meditech SORO/JPD-26/2005 and grant MSM 6840770012 from the Ministry of Education, Youth and Sports of the Czech Republic.

#### REFERENCES

1. De Ambroggi L, Musso E, Taccardi B (1989) Body surface mapping. In: Comprehensive Electrocardiology. Pergamon Press, New York, 1015-1049
2. Geselowitz DB(1963) The concept of an equivalent cardiac generator. In: Biomedical Science instrumentation, Plenum, New York, 325-330
3. Gulrajani RM, Roberge FA, Savard P (1989) The inverse problem of electrocardiography. In: Comprehensive Electrocardiology. Pergamon Press, New York, 237-288
4. Rosik V, Tysler M, Jurko S, Raso R, Turzova M (2002) Cardio 7 - Portable System for High Resolution ECG Mapping. Studies in Health Technology and Informatics 90: 41-46
5. Lux RL, Smith CR, Wyatt RF, Abildskov JA (1978) Limited lead selection for estimation of body surface potential maps in electrocardiography. IEEE Biomed Eng BME-25: 270-276
6. Filipova S, Tysler M, Turzova M, Rosik V (2003): Reference ECG-mapping etalons improve the diagnostic accuracy of myocardial ischemia according to departure isointegral surface maps Int. J. of Bioelectromagnetism 5: 369-370
7. Tyšler M et al. (2007) Non-invasive Assessment of Local Myocardium Repolarization Changes using High Resolution Surface ECG Mapping. Physiological Research, 56: Suppl 1, S133-S141
8. Tysler M, Turzova M, Svehlikova J, Heblakova E, Filipova S (2005) Noninvasive detection of ischemic regions in the heart. IFMBE Proceedings 11: 2207

Author: Dr. Milan Tysler  
 Institute: Institute of Measurement Science SAS  
 Street: Dubravská cesta 9  
 City: Bratislava  
 Country: Slovakia  
 Email: tysler@savba.sk

# Effect of Lead Orientation on Bipolar ECG Measurement

J. Vaisanen, M. Puurtinen and J. Hyttinen

Department of Biomedical Engineering, Tampere University of Technology, Tampere, Finland

**Abstract** — The objective of the study was to evaluate the effects of bipolar ECG lead orientation on the morphology and amplitudes of the ECG. We studied the differences between horizontal and vertical bipolar leads by analyzing body surface measurements of 236 normal patients. In this study we had 42 horizontal and vertical bipolar leads located on the anterior thorax. We calculated correlations and mean square differences (MSD) between horizontal and vertical lead orientations. The results of the study show that there are only a few lead locations in the left mid-thoracic region where horizontal and vertical orientations provide similar ECG morphology. There are also leads which produce high negative correlation which implies that only the phase of the signal changed. The study also shows that in most of the leads in the thoracic region the correlation between horizontal and vertical orientation is poor.

**Keywords** — Bipolar, ECG, lead, orientation

## I. INTRODUCTION

Various electrode systems are available for measuring the electrical activity of the myocardium by electrocardiography (ECG). The 12-lead ECG system, introduced in the 1940s, is considered a standard system and remains the electrode system most commonly applied in clinical use. For decades it has been debated whether the 12-lead system is the best and most optimal for detecting different cardiac symptoms and abnormalities. Number of studies has sought one way or another to establish how many leads are needed for different measurement purposes and where they should be located. Trägårdh and colleagues [1] have recently published a good review of these clinical studies.

Interest towards light weight, wearable and implantable electrocardiography (ECG) measurement devices has been continuously increasing during the 21st century [2-5] because the multilead ECG recordings such as 12-lead ECG are not feasible in sports and long-term measurements. Light weight monitoring systems typically provide 1 or 2 bipolar leads [4-7] and many of these devices are designed, not only to measure heart rate, but also to analyze the morphology of the ECG.

It is well-known that the electrode distance and orientation of the lead have major effects on morphology and amplitudes of the measured ECG and further to the outcome of the diagnosis. The importance of electrode positioning increases when only one lead, two electrodes, is applied in the

measurement and especially when implantable monitors are applied. In case of implantable monitors the location is permanent and thus it has to be carefully selected beforehand. Previously van Dam [8] and Zellerhoff [9] have analyzed effects of implantable ECG monitors lead orientation on measured ECG.

Objective of the present paper was to study the effects of bipolar lead orientation on the morphology of ECG. We have applied in this study body surface potential measurements of 236 normal healthy patients. The analysis of the effects is based on the correlations and mean square differences between 42 vertical and horizontal bipolar leads.

## II. MATERIAL AND METHODS

### A. Data

The data used in this study was a set of clinical BSPM data on 120-lead ECG acquired from 236 normal patients. The data is provided by Professor Fred Kornreich, Vrije Universiteit Brussel, Belgium and recorded with Dalhousie body surface lead system [10].

Data contained pre-processed and parameterized unipolar signals recorded with Wilson's central terminal as a reference. Each 120 leads from each subject comprised ensemble averages of 52 time points set in a time-normalized P-to-T complex waveform [11]. For this study we constructed 42 horizontal and vertical bipolar leads by subtracting the signals from adjacent electrodes. The studied leads are located on the anterior side of the thorax. Fig. 1 presents electrode locations from Dalhousie lead system which were applied in this study to obtain 42 bipolar sets. It also shows examples of how vertical and horizontal leads were constructed from individual leads. The electrode distances of the bipolar leads constructed from the BSPM are approximately 46 mm.

### B. Analysis

The effects of lead orientation on the ECG morphology were analyzed by calculating correlations between signals horizontal and vertical bipolar leads. Equation 1 presents the correlation, where  $X$  is the signal of horizontal lead,  $Y$  is the signal vertical lead and  $n$  is total number of samples 52. The correlation 1 refers to identical morphology but not necessarily identical amplitudes.



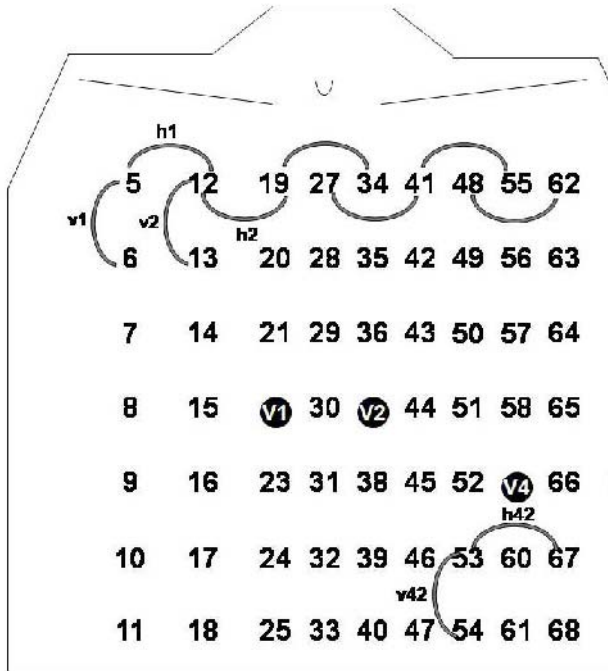


Fig. 1 Electrode locations of Dalhousie lead system applied to construct 42 horizontal and vertical bipolar leads. E.g V1 corresponds to vertical lead measured between electrodes 5-6 and H1 to horizontal bipolar lead measured between 5-12.

$$correlation = \frac{n \sum (XY) - \sum X \sum Y}{\sqrt{\left[ n \sum X^2 - \left( \sum X \right)^2 \right] \left[ n \sum Y^2 - \left( \sum Y \right)^2 \right]}} \quad (1)$$

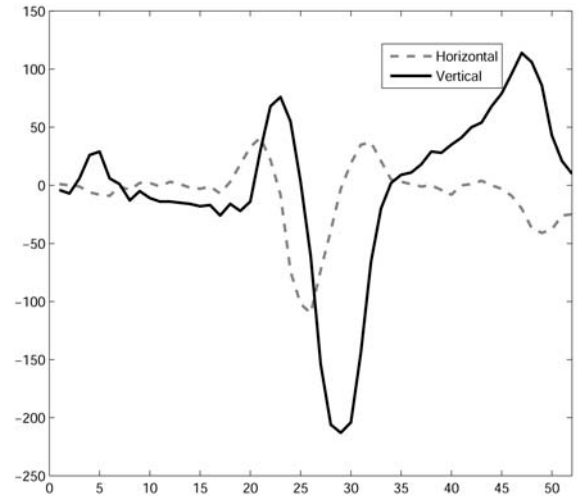
The effects of orientation on the amplitudes were analyzed by calculating the mean square difference (MSD) between the two orientations. MSD is also known as mean square error and presented in Equation 1. From (1), we can express that the ECG measured with horizontal lead orientation is  $z_{horz}[n]$  and  $z_{vert}[n]$  is the ECG measured with vertical orientation. The smaller is MSD the more similar are the amplitudes of signals.

$$MSD = \frac{E[(z_{horz}[n] - z_{vert}[n])^2]}{E[z_{vert}[n]^2]} \quad (2)$$

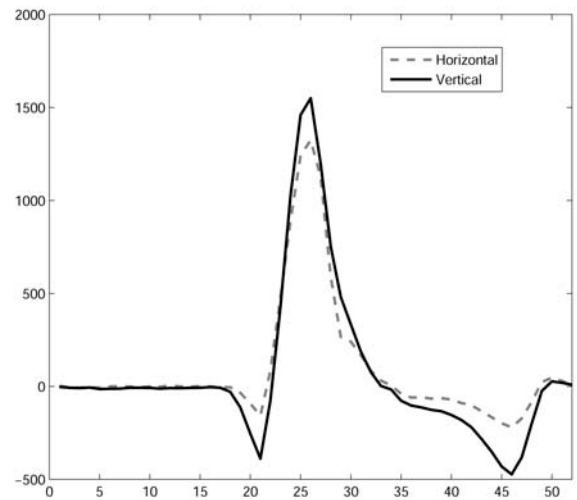
### III. RESULTS

We calculated correlations and MSDs between horizontal and vertical orientations for each of the 42 lead locations of 236 patient. Fig. 2 presents horizontal and vertical bipolar ECGs from two locations of one patient. Fig.2A presents

signals measured between electrodes 6-13 (horizontal) and 6-7 (vertical) and Fig. 2B presents signals measured between electrodes 44-58 (horizontal) and 44-45 (vertical). It can be seen that the morphologies of vertical and horizontal signals are very different in Fig. 2A and quite similar in Fig.2B. The correlations in these locations between horizontal and vertical orientations were -0.02 and 0.99, respectively. The MSDs of these signals are 1.2 and 0.06, respectively.



a)



b)

Fig. 2 Examples of signals with bipolar leads obtained from one patient. (A) Bipolar leads between electrodes 6-13 (horizontal) and 6-7 (vertical). (B) Bipolar leads 44-58 (horizontal) and 44-45 (vertical). The correlations between these leads are -0.02(A) and 0.99 (B). The MSDs are 1.2 and 0.06, respectively.

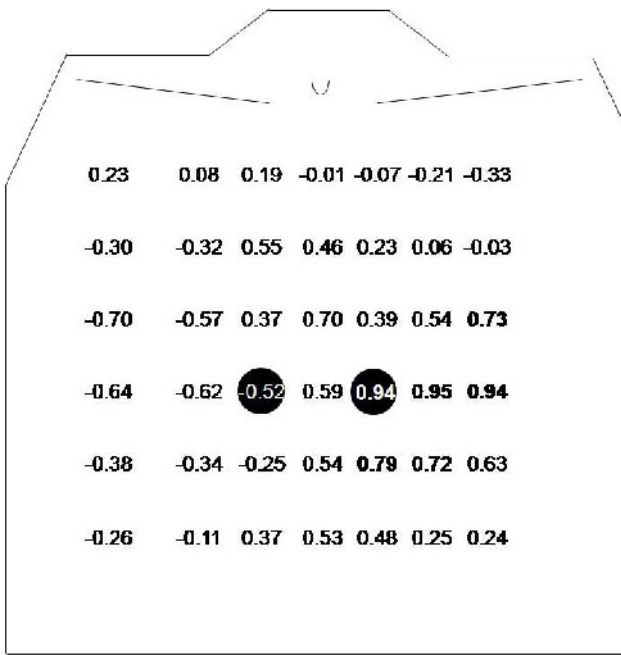


Fig. 3 Median correlations between vertical and horizontal bipolar leads (n=236).

We calculated the medians of the correlations and MSDs in each lead location among the 236 patients. Fig. 3 presents

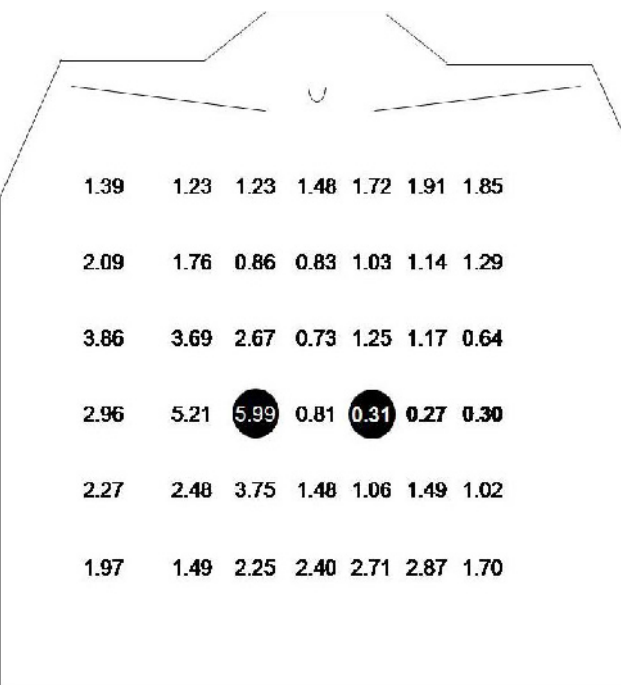


Fig. 4 Median MSDs between vertical and horizontal orientations (n=236).

the median correlations in 42 lead locations. Fig. 4 presents the median MSDs in 42 lead locations.

In the studied data set the highest correlation (0.95) between horizontal and vertical orientation was achieved in the lead located on the left mid thoracic region where horizontal lead was measured between electrodes 44-58 and vertical lead between electrodes 44-45. Examples of signals in the same location are presented in Fig. 2B. This location is close to the locations of V2 and V3 of standard 12-lead ECG. In this lead location 89 percent of the study population has correlation higher than 0.7 and 67% has correlation over 0.9. In the same location the median of MSDs was (0.27). 50% of study population has lower than 0.3 MSD and 23% have lower than 0.1 MSD in this lead.

The median correlation in location which example was presented in Fig. 2A was -0.3 and only 4.2% of population had over 0.7. The median MSD in this location was 2.09 and 0.4% of the population has under 0.3 MSD and 13% under 1 MSD.

The lowest median correlation (-0.70) was in the location on the right mid thoracic region between horizontal (electrodes 7-14) and vertical leads (electrodes 7-8). Half of the study population has correlation lower than -0.7 in this lead. If the correlation is close to -1 the morphology of the signals is otherwise identical but they are in opposite phase.

#### IV. DISCUSSION

In the present paper we have analyzed effects of bipolar ECG leads orientation on the ECG. In the present study we have applied 117 electrode BSPMs of 236 normal patients and constructed 42 horizontal and vertical bipolar leads. The effects were analyzed by calculating correlation and MSDs between horizontal and vertical ECGs.

The results of the study show that among the whole population there are only few lead locations on the anterior thorax where both orientations give similar morphologies to the measured ECG. These locations are on left-mid thoracic region around V2 and V3 leads of standard 12-lead ECG. In all other locations the morphologies are notable different and changes between orientations vary more between individuals. It is worth noticing that there is not a wide area or clear pattern of locations where morphologies are similar or differ widely for all patients. The best correlation in the location around V2 and V3 could be explained by considering the mean electrical axis of the heart. If the axis is normal (between 0-90 degrees) then the horizontal and vertical leads are oriented in such fashion that their ECG would be similar. If the similarity in ECG would based only on the deviation of the heart axis we could assume that same behavior would be in all the leads nearby, above and below

this lead. The correlations are notably lower in the leads above and also on the mid thoracic region at the same intercostal level (between locations of V1 and V2) the correlation is much lower.

The limitations of the study are in the data set and electrode configurations. The exact electrode locations for each patient were not known the accuracy of leads is based on the Dalhousie BSPM. On the other hand the number of patients is high and thus the results presented can be assumed to be reliable. Other limitation related to the applied data set is that we could not separate male and female patients. Thus we cannot state how the effects of lead orientations differ between genders. The number of samples in ECG is low (52) which affects the accuracy of the correlation and MSD calculations.

In the present paper we have not studied the effects of lead orientation in case of pathologies or cardiac diseases. It would be valuable to have knowledge on how the lead orientations affect the measured ECG in cases of different cardiac abnormalities.

As a conclusion the study shows that for all people there are only a few locations on the anterior thorax where the leads can be oriented either horizontally or vertically without major changes in morphology of the ECG. But in most of the locations the changes in ECG morphology are generally dramatic if lead orientation is changed from horizontal to vertical.

#### ACKNOWLEDGEMENT

The authors would like to express their gratitude to Professor Friedrich Kornreich, MD, for providing the valuable clinical data

#### REFERENCES

1. E. Tragardh, H. Engblom, O. Pahlm (2006) How many ECG leads do we need? *Cardiology Clinics* 24(3): 317-330
2. A. Vehkaoja, J. Leikkala (2004) Wearable wireless biopotential measurement device. 26th Annual International Conference of the IEEE Engineering in Medicine and Biology Society 2004, pp 2177-2179
3. J. Riistama, J. Väisänen, S. Heinisuo, et al. (2007) Wireless And Inductively Powered Implant For Measuring Electrocardiogram. *Med Biol Eng Comput* in press
4. B. Gyselinckx, J. Penders, R. Vullers (2007) Potential and challenges of body area networks for cardiac monitoring. *J Electrocardiol* 40(6 Suppl): S165-8
5. J. K. Russell, S. Gehman (2007) Early experience with a novel ambulatory monitor. *J Electrocardiol* 40(6 Suppl): S160-4  
<http://www.alivetec.com> <http://www.alivetec.com>
6. <http://www.alivetec.com>
7. <http://www.cardguard.com> <http://www.cardguard.com>
8. P. M. van Dam, A. van Oosterom (2007) Analysing the potential of Reveal for monitoring cardiac potentials. *Europace* 9 Suppl 6(vi119-23)
9. C. Zellerhoff, E. Himmrich, D. Nebeling, et al. (2000) How can we identify the best implantation site for an ECG event recorder? *Pacing Clin Electrophysiol* 23(10 Pt 1): 1545-9
10. T. J. Montague, E. R. Smith, D. A. Cameron, et al. (1981) Isointegral analysis of body surface maps: surface distribution and temporal variability in normal subjects. *Circulation* 63(5): 1166-72
11. F. Kornreich, T. J. Montague, M. Kavadis, et al. (1989) Multigroup diagnosis of body surface potential maps. *Journal of Electrocardiology* 22 Supplement(169-178)

Author: Juho Väisänen

Institute: Department of Biomedical Engineering, Tampere University of Technology

Street: Korkeakoulunkatu 3

City: Tampere

Country: Finland

Email: [juho.vaisanen@tut.fi](mailto:juho.vaisanen@tut.fi)

# On the Mechanism of Low Frequency Bioelectromagnetism

J. Valdmanis, A. Cipijs

Institute of Physics University of Latvia, Salaspils, Latvia

**Abstract** — Results of investigations using simple physical models were presented. It is shown that physically exist small models that intensified low frequency electromagnetic field (EM). There are individual modes with definite symmetry. In the model cases we need some small background field for generations but in biological systems maybe there is some stabilizations factor. Experimental results and their biophysical aspects were discussed.

**Keywords** — Electromagnetic field, rhythmical oscillation, resonance, electromagnetism.

## I. INTRODUCTION

There are many studies on rhythmical low frequency bioelectromagnetism ( $\alpha$ ,  $\beta$ ,  $\Delta$  rhythm and others) but the generations mechanisms is not definitively clear. It is claimed that role in generations made electron processes including straight electron transportations [1]. Such realization could be through conductive zone or by electron jumping between albumens shoots due to quantum mechanical interaction. The question is how such electron current could generate low frequency electromagnetic field because the wave length is very long. It needs to be some resonance mechanism. The question is also interested from physical point of view. Could we make some simple small element that are active in 50 Hz EM waves range and lower? In that cases active mean ability to intensify external EM field.

## II. EXPERIMENTAL RESULTS

In physics the simplest model is harmonic oscillator that is anything that can vibrate back and forth with periodic motion. Element activity could be stimulated by resonance process. The problem is that smaller the EM frequency, the larger the wave length. Really the EM antennas geometry is comparable to wave length. Because for 50 Hz frequency wave length is some thousands km we need new ideas.

On fig.1 model of such active element for 50 Hz frequency is given. It is special coil of wire that is active to 50 Hz EM external field. On Fig. 2 voltage- frequencies characteristics of model Fig. 1 are given. The voltage of sin-type EM field generator is  $\sim 32$  volts. Maximal intensification is  $\sim 5$ . There are also some higher modes, with the same symmetry but the



Fig. 1. Model, that resonate at 50 Hz.

intensification in that cases is smaller. Changes in model connection allow to receive resonant frequency 2.69 kHz. Really 50 Hz is asymmetrical mode and 2.69 kHz symmetrical one.

The excitation process Fig. 2 is realized by straight contact element – generator. The same results are if we excite element by electric or magnetic induction. It is without straight contacting.

In experiment HAMEG type oscillograph were used. Its electrical resistance  $10\text{ M}\Omega$  and capacity  $C=12\text{ pF}$ . Influence of measuring process changes a little characteristics. For

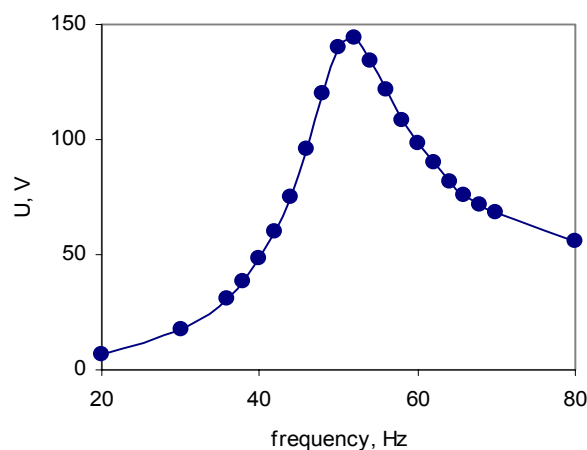


Fig. 2. Voltage- frequency characteristic for element fig.1.

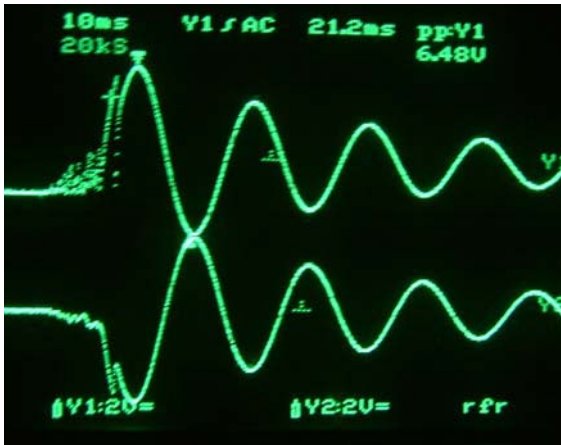


Fig. 3. Model excitation by EM pulse.

asymmetrical mode (50 Hz) no changes, but for symmetrical resonance in straight contacting 2.69 kHz without contacting – 2.90 kHz.

On Fig. 3 the situation when oscillator are excited by pulse EM field are shown. At starting time there are chaotic higher modes but than process goes to main 50 Hz mode. Because there are some dissipation process the sin-type oscillations decrease in time.

On Fig. 4 the same excitation for symmetrical mode are shown.

Really model Fig. 1 has double spiral wire form. That is one of the points that allow thinking about analogy between biological systems.

Resonant characteristic for model Fig. 2 is given for double spirals one side. On Fig. 5 the generators voltage at

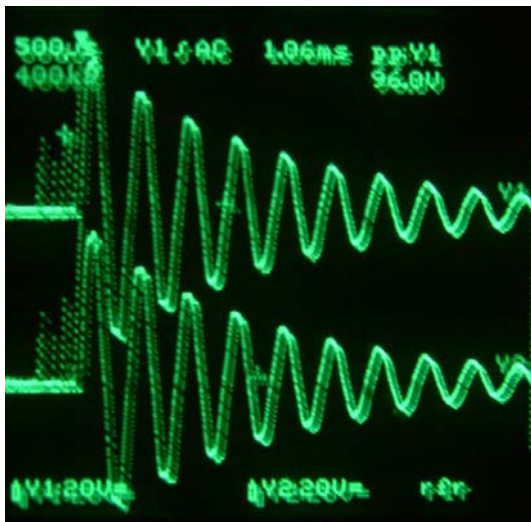


Fig. 4 Symmetrical mode excitation by EM pulse.

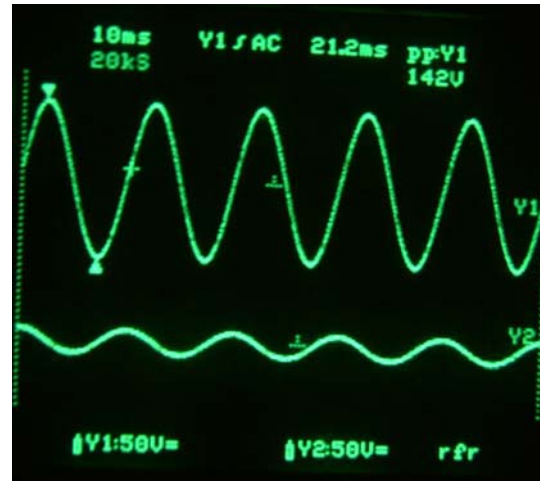


Fig. 5. Results of voltage intensifications at double spirals one side.

one spirals end is given (second channel). Intensified voltage at other end is shown on oscillographs channel one. Because the 50 Hz mode is asymmetrical the voltage in double spiral next side is in opposite phase. Really it is in opposite end also. On Fig. 6 the voltage at both ends of double spiral are given. That situation corresponds to maximal voltage point Fig. 2. Taken into account opposite character of signals the intensification is two times larger, it is  $\sim 10$ .

Of course in our cases active oscillation process is due to electron current interacting with EM field. In organisms there are double spiral systems and some ideas about electron transportation [1]. Before discussion we will summarize main conclusions about model experiment.

- ❖ Active response of EM field.
- ❖ Resonant modes discreteness.
- ❖ Chaotic higher modes generation when pulse EM field excitation take place.
- ❖ Double spiral character of model.
- ❖ Double spiral geometry can generate situation, when EM field electric or magnetic component are dominant.

Because we are no specialists in biological process it is worth discuss only some questions. The 50 Hz model was investigated because that is main background frequency. No principal problems to decrease frequency. The same (approximately) results give the model for 25 Hz. Returning to the  $\alpha$ ,  $\beta$  and  $\Delta$  type rhythm it looks that taking into account the dimensions and perfectiveness it is possible generate such frequencies. We made experiments at room temperature. In those cases we need some small external field to realize resonant process. Maybe decreasing temperature the background field is enough to generate

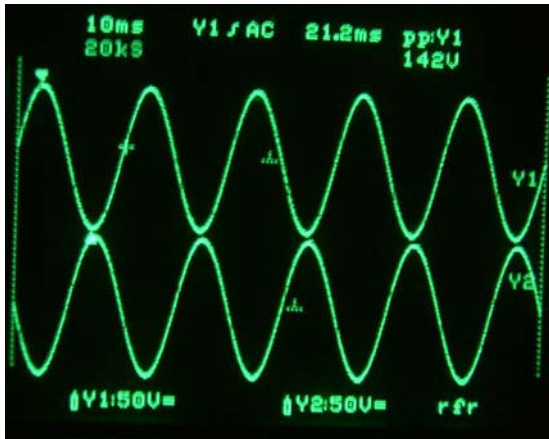


Fig. 6. Voltage at double spirals opposite sides. Generator voltage 32 V.

resonant frequency. Model Fig. 1 as well as biological systems are electrically nonhomogenous. That is one of the reasons of active character of EM process. Maybe the brain conscious activities are regulated by the low frequency rhythmical oscillations. External EM with long wavelength made correlated activities in process on mycro levels. If brain is in active phase, there is one rhythm . In sleeping phase dominant is the other frequency type.

Very important is the question about influence of external EM field and interaction process between models. Because the excitation process is resonant the permissible exposure levels (PEL) could be strictly individual. In those cases we need to take in to account discreteness of resonant frequencies as well as their changes in time. As the experiments shown the interaction process between models is intensified if models are strictly identical. In organisms resonances could be fine-tuned and sharp. . For highest frequencies the measuring process can change the results of interaction. It was demonstrated on model experiments for kHz wave range.

On Fig. 7 voltage frequency characteristic for symmetrical mode is given when one oscillographs channels straight contacting is used. Resonance frequency is 2.69 kHz. Without contacting 2.90 kHz. When both channels by straight contact are used ,  $f_r$  is 2.46 kHz.

Another question is known difference between low frequency electric and magnetic encephalograms components in living organisms. Measuring process to

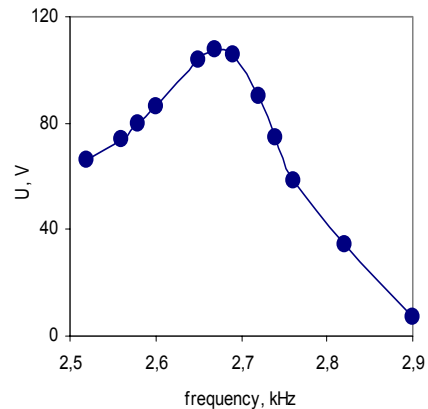


Fig. 7. Voltage frequency characteristic for symmetrical mode.

receive qualitative magneto encephalogram is more complicated compare with one for encephalogram .

In model Fig. 1 double spiral is regular and coil windings induced magnetic field summarizes. When the spiral winds chaotic the total magnetic component decreases. Maybe that is the case in brain rhythms processes.

### III. CONCLUSIONS

Received results is based on some analogy of physical processes in model experiments and living organism.

Principally it is possible to realize model that has main resonant frequencies that is the lowest in brain or other rhythms. In that case we could investigate higher modes and compare results with real one. But that is for future investigations and could be realized only in co-operation between corresponding specialists.

### REFERENCES

1. Давыдов А.С. (1979) Биология и квантовая механика, „Наукова думка”, стр.296.

Author: Janis Valdmanis Aleksandrs Cipijs  
 Institute: Institute of Physics University of Latvia  
 Street: Miera Str. 32  
 City: Salaspils LV-2169  
 Country: Latvia  
 Email: jvaldman@sal.lv

# The Effect of Electrode Size on Cortical EEG Sensitivity Distributions

K. Wendel and J. Malmivuo

Tampere University of Technology/Department of Biomedical Engineering, Tampere, Finland

**Abstract** — We investigated the influence of electrode contact size on cortical electroencephalogram (EEG) sensitivity distributions. We focused this investigation on the fifth sensitivity volume (FSV) of mapping the lead field in the cortex. We evaluated the cortical sensitivity in concentric spheres and realistic models, using electrode diameters of 1 mm, 5 mm, 10 mm, and 15 mm. We found that when electrodes were spaced farther apart than the bipolar pair of the 128-channel montage, real dimensional electrodes should be used rather than point electrodes in the simulation studies.

**Keywords** — EEG, sensitivity, electrode, model.

## I. INTRODUCTION

Traditionally, the analytical model, surface Laplacian, and many numerical solutions use point electrodes in their models [1] although some two-dimensional and three-dimensional electrode models show that volumetric electrodes alter the spatial sensitivity distribution. Ollikainen et al. [2] recommended using the point electrode model (PEM) for EEG studies using less than 50% coverage of the scalp. They based their conclusion on three-shell two-dimensional spherical models that used the highly contested scalp-to-skull conductivity ratio of 80:1 [3].

Counter to the PEM, Law et al. [4] obtained optimal results for their surface Laplacians on spherical and ellipsoidal surfaces using 10 mm diameter electrodes. We modeled our electrodes as simple recessed electrodes i.e. cylinders [5]. We examined the volumetric changes of the cortical sensitivity distributions with respect to changing electroencephalogram (EEG) contact electrodes on head volume conductor models. This investigation is an extension of our previous work [6] that evaluated electrodes according to the half sensitivity volume (HSV) [7]. Our current investigation concentrates on the sensitivity within the cortex, which is volumetrically measured by the fifth sensitivity volume (FSV) [8].

## II. MATERIALS AND METHODS

We constructed spherical models and realistic models from the Visible Human Woman (VHW). Our electrode diameters measured 1 mm, 5 mm, 10 mm, and 15 mm. We varied the thickness of the cerebrospinal fluid (CSF) within our models. We set the average CSF thicknesses to 0 mm,

2.0 mm, 3.5 mm and 0 mm, 2.0 mm, 2.8 mm for the spherical and realistic models, respectively, to determine whether this highly conductive layer masked the volumetric electrodes. Our common parametric conductivity values were 0.45 S/m, 0.025 S/m, 1.79 S/m, 0.25 S/m and 0.25 S/m for the scalp, skull, CSF, gray matter and white matter, respectively, across all models [9]. Lastly, we moved a pair or bipolar electrodes long the central sulcus according to the 10-20 and 5-5 standard EEG measurement locations [10].

We obtained our cortical sensitivity distribution results by feeding a reciprocal unit current through the bipolar electrode pair. The distribution of the current density  $\mathbf{J}$ , where

$$\mathbf{J} = -\sigma \nabla \Phi + \mathbf{J}^c, \quad (1)$$

maps the sensitivity of the lead pair as a function of the scalar potential  $\Phi$  and the externally applied current density  $\mathbf{J}^c$  assuming quasistatic conditions [6]. We analyze these simulations according to the FSV [8] to measure the volume where the top 20% of the current density flows within the brain – namely the cortex.

## III. RESULTS

The results (Fig. 1) reveal more fluctuation in volumetric cortical sensitivity than our previous study [6] evaluated according to the half sensitivity volume (HSV), i.e. the top 50% of the current density volumetrically within the brain [7]. The FSV concentrates within the cortex i.e. localized to the gray matter, while the HSV measures up to 1 cm beneath the cortex. The spreading of the three CSF-thickness sets of trends begins at 20°, which centers between 64 and 128-channel montages. In addition, the set with the thickest CSF (3.5 mm) yields the most variation between the 15 mm and 1 mm electrodes.

Our previous results [6] addressed the region mapped by the HSV, which is the region that identifies where 50% of the current density flows. In order to indicate the impact of the influence of these different sensitivity volumes, we report the ratio of the HSV to the FSV as 12.5 and 8.5 for bipolar pairs of the 256- and 64-channel montages, respectively. High resolution EEG results namely the 256-channel, bipolar pairs showed negligible results in volumetric sensitivity changes, whereas, the standard 10 mm 10-20 EEG montage i.e. 21-channel, bipolar pairs yielded up to 47%

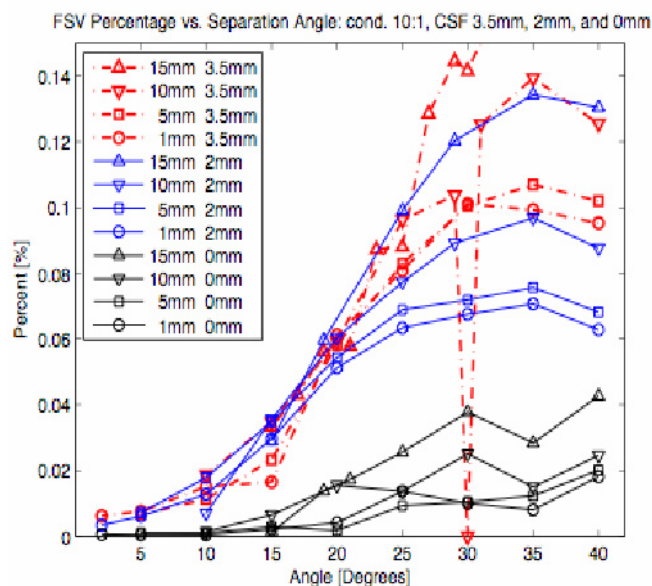


Fig. 1 Spherical fifth sensitivity volume (FSV) percentage occupying the brain: Scalp electrodes move laterally apart across the central sulcus. Angles 11°, 18°, 23°, and 31° approximate 256, 128, 64, and 32 channel EEG montages [8,10]. Legend: (left value) electrode diameter and (right value) CSF thickness.

change in cortical sensitivity volume for the medium CSF thickness. The increased CSF thickness had more variation, 47% versus 31%, than the same electrode pairs of medium thickness (2 mm).

Additional realistic FSV percentage results at 35° diminish as follows: 1.09%, 1.05%, 0.97%, 0.93%, 0.88%, and 0.86% for 2.8 mm-CSF of electrode diameters of 5 mm and 10 mm, and 2.0 mm-CSF of electrode diameters 5 mm, 10 mm, and 15 mm, and 0 mm-CSF of electrode diameter of 10 mm, respectively.

#### IV. DISCUSSIONS

The increased variation of the FSV results is counter to the results of the HSV in [6] because the CSF absorbs and channels the flow of the reciprocal current [8], thus concentrating it near the cortex. We reported that the HSV maps a region approximately ten times larger than the FSV so naturally the HSV would be less sensitive to volumetric changes. Together these two sensitivity volume measurements identify the macroscopic and microscopic significance of what the lead pair measures. In the interest of cortical changes, the FSV evaluation indicates the need for three-dimensional electrodes representative of the physically measured situation.

The finer the desired resolution of measurement the more the investigator should expect fluctuation in the measurement. This current study does not address movement of the brain or the size of different gyri in the cortex but indirectly addresses these issues through shrinking the CSF to zero. The thickness of the CSF does contribute to channeling the reciprocal current; therefore, it invariably shapes the sensitivity distribution according to the localized situation thereby affecting the measurement lead.

#### V. CONCLUSIONS

We recommend that EEG head model studies investigating less than 128-channels, evoked potential studies, or neural stimulation studies incorporate electrodes with real dimensions instead of using the point electrode model.

#### ACKNOWLEDGMENT

We would like to thank Nathaniel G. Narra and Markus Hannula for providing the segmentation of the Visible Human Woman dataset. This work was supported by the International Graduate School of Biomedical Engineering and Medical Physics, Finland.

#### REFERENCES

1. Nunez PL and Srinivasan R (2006) *Electric Fields of the Brain: The Neurophysics of EEG*. 2<sup>nd</sup> ed. Oxford University Press, 2006.
2. Ollikainen J, Vauhkonen M, Karjalainen P, Kaipio J (2000) Effects of electrode properties on EEG measurements and a related inverse problem. *Med. Eng. & Phys.*, vol. 22, pp. 535 – 545, 2000.
3. Huiskamp G (2008) Interindividual variability of skull conductivity: an EEG-MEG analysis. *Intl. J. of Bioelectromag.* Vol. 10, no. 1, pp. 25 – 30, 2008.
4. Law S, Nunez P, Wijesinghe R (1993) High-resolution EEG using spline generated surface Laplacians on spherical and ellipsoidal surfaces. *IEEE TBME*, vol. 40, no. 2, pp. 145 – 153, Feb. 1993.
5. Suesserman M, Spelman F, Rubinstein J (1991) In vitro measurement and characterization of current density profiles produced by nonrecessed, simple recessed, and radially varying recessed stimulating electrodes. *IEEE TBME*, vol. 38, no. 5, pp. 401 – 408, May 1991.
6. Wendel K, Narra NG, Hannula M, Kauppinen P, Malmivuo J (2007) The Influence of Electrode Size on EEG Lead Field Sensitivity Distributions. *Intl. J. of Bioelectromag.*, vol. 9, no. 2, pp. 116 – 117, 2007.
7. Malmivuo J, Suihko V, Eskola H (1997) Sensitivity distributions of EEG and MEG measurements. *IEEE TBME*, vol. 44, no. 3, pp. 196 – 208, March 1997.
8. Wendel K, Narra NG, Hannula M, Kauppinen P, Malmivuo J (2008) The Influence of CSF on EEG Sensitivity Distributions of Multilayered Head Models. *IEEE TBME*, vol. 55, no. 4, pp. 1454 – 1456, April 2008.



9. Ferree T, Eriksen K, Tucker D (2000) Regional head tissue conductivity estimation for improved EEG analysis. *IEEE TBME*, vol. 47, no. 12, pp 1584 – 1592, Dec. 2000.
10. Oostenveld R (2001) The five percent electrode system for high-resolution EEG and ERP measurements. *J. of Clin. Neurophysiology*, vol. 112, pp. 713 – 719, 2001.

Author: Katrina Wendel  
Institute: Department of Biomedical Engineering  
Tampere University of Technology  
Street: Korkeakoulunkatu 3, P.O. Box 692  
City: FI-33101 Tampere  
Country: Finland  
Email: [Katrina.wendel@tut.fi](mailto:Katrina.wendel@tut.fi)

# Measurement of Dissolved Oxygen with Lab-on-Chip Systems

J. Wiest<sup>1,2</sup>, M. Brischwein<sup>2</sup>, H. Grothe<sup>2</sup> and B. Wolf<sup>2</sup>

<sup>1</sup> Innovationszentrum Medizinische Elektronik - cellasys GmbH, München, Germany

<sup>2</sup> Heinz Nixdorf-Lehrstuhl für Medizinische Elektronik, Technische Universität München, Germany

**Abstract** — Measurement of dissolved oxygen with lab-on-chip systems or cell based assays reflects the metabolic activity of living cells cultivated on such devices. This information together with other data from the cells (e.g. extracellular acidification, morphological changes) allows interpretation of cellular vitality and analysis of their interaction with drugs or pollutants. In this work the state of the art of measurement of dissolved oxygen is presented. The most important principles of the measurement methods of dissolved oxygen are presented. Example measurements with lab-on-chip systems from applications as environmental monitoring and chemosensitivity of cancer cells are shown. These measurements were performed at the IMOLA, a lab-on-chip system which was developed at the Heinz Nixdorf-Lehrstuhl für Medizinische Elektronik. IMOLA is a modular cell based approach where multiparametric electrochemical biosensors are used to monitor the vitality of living cells without the use of markers. Environmental monitoring was performed using algae as signal transducer for environmental pollutants. In case of chemosensitivity results from an effectiveness test of a chemotherapeutic are presented. Here the vitality of cancer cells is compared between treated and untreated cells in an online experiment. Finally the emerging importance of a cell based approach in pharmacology and cancer research is discussed.

**Keywords** — biosensor, IMOLA, dissolved oxygen, cell based assay, cellular respiration.

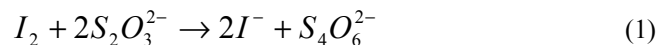
## I. INTRODUCTION

For better understanding of system biology, the label-free investigation of living cells is a promising method. Applications of this field are the development of new therapies against diseases as cancer [1,2], pharmacological research [3], alternative methods for animal experiments [4] or the introduction of new biosensors using living cells as signal transducers [5-7]. Different parameters as acidification, growth rate or cellular respiration are used to monitor metabolic and morphological changes of living cells and their interaction with drugs or toxins [8,9]. Amongst these parameters the cellular respiration takes an important place, because it shows the mitochondrial activity i.e. the aerobic energy conversion of eukaryotic cells [10]. The relevance of the cellular respiration can be deduced from our atmosphere. Their actual composition is based on the starting of photosynthetic active cells 1.5 billion years ago. Before this

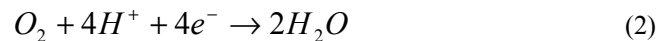
cellular energy conversion was based on anaerobe metabolism. Due to this evolution many cells can switch between the more energy efficient aerobic respiration and anaerobe metabolism [1].

Measurement of cellular respiration is done via measurement of the oxygen consumption of the cells under investigation. Usually the cells are cultivated in cell culture media, i.e. the dissolved oxygen (DO) in the cell culture media has to be measured. First the development of the DO-measurement and the different methods are described briefly.

The measurement of dissolved oxygen started historically in 1888 with the Winkler-titration method [11]. Here titration of thiosulfate into the measurement solution until change of color is done. According to equation 1 the dissolved oxygen in the solution can be calculated by counting the amount of titrated thiosulfate.



At the beginning of the 20<sup>th</sup> century, different physical methods as cartesian divers [12] (a buoyancy based method) or a vacuum extraction method [13] were investigated. In the middle of the 20<sup>th</sup> century different electrochemical methods such as the dropping mercury electrode [14] or the Mackereth-sensor [15] for measurement of dissolved oxygen were investigated. The most popular electrochemical sensor for measurement of dissolved oxygen is the Clark-sensor which was patented by L.C. Clark in 1959 [15]. This sensor works on an amperometric basis. Usually a voltage of -600mV is applied to a set of electrodes and the resulting current is measured. This current is equivalent to the electrons in equation 2. The generated electrons correspond to the consumed oxygen. Using this method it is important to choose the dimensions of the electrodes small enough to avoid a disturbance of the DO in the solution by the oxygen consumed at the electrodes.



At the end of the 20<sup>th</sup> century so called optical sensors were introduced by Wolfbeis [16]. This method is based on fluorescence quenching. DO-sensors based on this method are mainly based on ruthenium [17], porphyrin [18] or pyrens [2]. Two measurement methods are common. Either

Table 1 Methods for dissolved oxygen measurement and ability for measurement of cellular respiration.

Method	Continuous measurement	Biocompatibility	Cost / complexity
Chemical	No	No	Medium
Physical	No	No	Medium
Electrochemical	Yes	In vitro, in vivo	Low
Optical	Yes	In vitro	Low
Magnetic	Yes	In vivo	High

the intensity [19] or the decay time [20] of the fluorescence is detected. Latest developments in this field are methods based on the magnetic effects of dissolved oxygen [21] or modifications of electrochemical sensors with substances as carbon nanotubes [22] or vitamins [23]. Table 1 summarizes the available methods for measurement of DO and evaluates their ability for measurement of cellular respiration.

Based on these considerations, different lab-on-chip systems are under investigation at the *Heinz Nixdorf-Lehrstuhl für Medizinische Elektronik* of the *Technische Universität München*. In this work the electrochemically based intelligent mobile lab (IMOLA) which was spun-off to *cellasys GmbH* ([www.cellasys.com](http://www.cellasys.com)) was used for the measurements. Development and research on the IMOLA was performed by the authors at the *Technische Universität München*.

## II. MATERIALS AND METHODS

IMOLA is a modular solution for monitoring the vitality and morphology of living cells. This is done non-invasive, label-free, real-time, multi-parametric and with an integrated cell culture media delivery system. The details of the system have been described elsewhere [24].

In this work only the properties which are related to DO measurement are described. Figure 1 shows the BioChip-C which is used at the IMOLA system. It is packaged sterile and has to be handled under sterile conditions. In the middle of the chip the DO sensor is realized in thin film technology. It is a membrane-free, amperometric electrochemical DO sensor with three electrodes. The working electrode has an area of 1.1 mm<sup>2</sup> and an auxiliary electrode is used to keep the reference electrode current-free [25].

The amperometric measurement principle with a three electrode setup is shown in Figure 2. This principle was used by the authors to allow measurement of DO with the IMOLA system. The three electrodes were fabricated in thin film technology at the BioChip-C and the geometry was optimized toward low noise and high signal to noise ratio [13].



Fig. 1 Sterile packaged BioChip-C with microsensors for measurement of dissolved oxygen, pH, impedance and temperature. The side length of the chip is 24 mm.

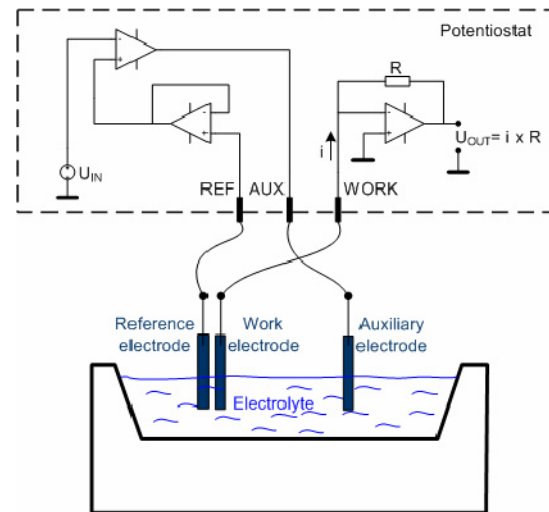


Fig. 2 Principle of the amperometric measurement principle. Between a work and a reference electrode the voltage  $U_{IN}$  is applied and the resulting current in the nA range is measured. To avoid ageing of the reference electrode the current is directed via the auxiliary electrode.

During the development of the IMOLA device, different parameters had to be considered to allow long term monitoring of living cells. To maintain sterility a closed fluidic system is implemented which works in suction mode. Pressure adaptation is realized via a sterile filter. The suction mode was implemented to maintain a small under-pressure. This and proper temperature handling is necessary to avoid gas-bubbles in the system. A bubble on one of the microsensors would disturb the measurement. To maintain the cells with fresh cell culture media and to be as close as possible to in vivo conditions the fluidic is driven in a stop and go mode. A cycle with 3 min pump on and 7 min pump off is repeated over the whole measurement period. The detailed description of the different experiments, the used

cell culture media, chemotherapeutic or drug and the cells have been described in different publications for environmental monitoring [6,26] and for chemosensitivity analysis [8,27,28]. Due to the modular IMOLA concept it was easily possible to design a system for mobile environmental monitoring and another setup which is used as a stationary six channel laboratory setup.

### III. RESULTS

In Figure 3 the photosynthetic activity of algae is shown. For this measurement the IMOLA has been extended with a light module which contains two light emitting diodes. With the light module the algae are triggered to produce oxygen which can be monitored with the DO microsensor.

The cellular respiration of cancer cells is shown in Figure 4. Here the raw data of the measurement are evaluated and only the effect of the drug doxorubicin toward the respi-

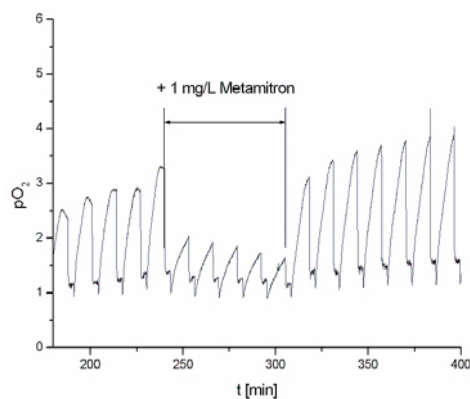


Fig. 3 Environmental monitoring measurement example (raw data). The decreased photosynthetic activity of the algae *Chlorella kessleri* due to contamination of their microenvironment with the herbicide metamitron is shown.

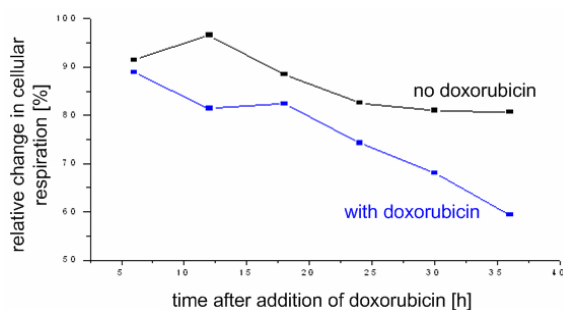


Fig. 4 Measurement example from chemosensitivity analysis (evaluated data). The reduced cellular respiration of the mama-carcinoma cell line MCF-7 after exposure toward the chemotherapeutic drug doxorubicin is shown.

ration activity of the cells is displayed. Two experiments are shown in the diagram. One with treated and another one with untreated cells. It can be clearly concluded that the drug reduces the vitality of the cancer cells.

### IV. DISCUSSION

Different methods for measurement of cellular respiration are available and evaluated in this work. The use of electrochemical microsensors has proven to be adequate for measurement of dissolved oxygen in the microenvironment of living cells. Furthermore it is important to have a sophisticated fluidic system to provide devices for sterile, long term analysis of cellular respiration. The application in the field of chemosensitivity shows the feasibility and opens the application field toward pharmacological studies or basic cell-biological research. With the application in environmental monitoring the functionalization of living cells as signal transducers was shown. This shows the ability of the IMOLA-platform as real biosensor for applications as point-of-care diagnostic or homeland security. The application as water quality monitoring system has recently become more important. In our modern society residues of medicine products which are not decomposed in our sewage plants are becoming an increasing problem. E.g. the hormone 17 $\alpha$  ethinylestradiol (which is used in the birth control pill) accumulates in the rivers of big cities and intervenes with the fish population [6].

Furthermore in the field of pharmacology the cost for DNA and protein based analysis methods are immense and do not result in the expected licensing of new drugs. In this field a whole cell approach could be useful to complete the spectrum of development tools. For the developing research area of system biology the IMOLA tool also should be considered.

### ACKNOWLEDGMENT

Authors like to thank “Bayrische Forschungsstiftung”, “Deutsche Forschungsgemeinschaft”, “Heinz Nixdorf-Stiftung” and “Bund der Freunde der Technischen Universität München“ for support of the ongoing project.

### REFERENCES

1. Alberts B, Bray D and Lewis J (2002) Molecular Biology of the Cell. Taylor & Francis, London.
2. Basu BJ, Thirumurugan A, Dinesh AR, Anandan C and Rajam KS (2005) Optical oxygen sensor coating based on the fluorescence quenching of a new pyrene derivative. Sensors and Actuators B: Chemical 104: 15-22.

3. Geisler Th, Ressler J, Harz H, Wolf B and Uhl R (2006) Automated Multiparametric Platform for High-Content and High-Throughput Analytical Screening on Living Cells. *IEEE Transactions on Science and Engineering* 3: 169-176.
4. Otto AM, Brischwein M, Motrescu ER, Cabala E, Grothe H, Stepper Ch and Wolf B (2004) Chips statt Mäuse: Zellen auf bioelektronischen Sensorchips als Alternative zu Tierversuchen. *ALTEX* 21: 70-76.
5. Védrine Ch, Leclerc J-C, C.Durrieu and C.Tran-Minh (2003) Optical whole-cell biosensor using *Chlorella vulgaris* designed for monitoring herbicides. *Biosensors & Bioelectronics* 18: 457-463.
6. Stadthagen, T. Entwicklung eines online Gewässermonitoringsystems mittels Biosensorchips zum Nachweis ausgewählter Xenobiotika. 2007
7. Podola B and Melkonian M (2005) Selective real-time herbicide monitoring by an array chip biosensor employing diverse microalgae. *Journal of Applied Phycology* 17: 261-271
8. Wolf B, Brischwein M, Lob V, Ressler J and Wiest J (2007) Cellular signaling: aspects for tumor diagnosis and therapy. *Biomedizinische Technik* 52: 164-168.
9. Wiest J, Brischwein M, Ressler J, Otto AM, Grothe H and Wolf B (2005) Cellular Assays with Multiparametric Bioelectronic Sensor Chips. *Chimia* 59: 243-246.
10. Hoinkis J and Lindner E (2001) *Chemie für Ingenieure*. WILEY-VCH, Weinheim.
11. Winkler LW (1888) Die Bestimmung des im Wasser gelösten Sauerstoffes. *Berichte der Deutschen Chemischen Gesellschaft* 21: 2843-2854.
12. Glazer BT, Marsh AG, Stierhoff K and Luther III GW (2004) The dynamic response of optical oxygen sensors and voltammetric electrodes to temporal changes in dissolved oxygen concentrations. *Analytica Chimica Acta* 518: 93-100.
13. Hitchman ML (1978) Measurement of Dissolved Oxygen. *Chemical Analysis* 49: 1-246.
14. Laitinen HA, Higuchi T and Czuha M (1947) Potentiometric Determination of Oxygen Using the Dropping Mercury Electrode. *Journal of the American Chemical Society* 70: 561-565.
15. Oehme F and Schuler P (1983) *Gelöst-Sauerstoff-Messung*. Dr. Alfred Hüthig Verlag GmbH Heidelberg, Heidelberg.
16. Wightman RM (2006) Probing cellular chemistry in biological systems with microelectrodes. *Science* 311: 1570-1574.
17. Lochmann C, Hansel T, Haupt T and Beuthan J (2006) An oxygen imaging system for medical applications: preliminary results. *Biomedizinische Technik* 51: 111-115.
18. O'Riordan TC, Buckley D, Ogurtsov V, O'Connor R and Papkovsky DB (2000) A Cell Viability Assay Based on Monitoring Respiration by Optical Oxygen Sensing. *Analytical Biochemistry* 278: 221-227.
19. Gillanders RN, Tedford MC, Crilly PJ and Bailey RT (2003) Thin film dissolved oxygen sensor based on platinum octaethylporphyrin encapsulated in an elastic fluorinated polymer. *Science Direct* 502: 1-6.
20. Holst G, Glud RN, Kühl M and Klimant I (1997) A microoptode array for fine-scale measurement of oxygen distribution. *Sensors and Actuators* 38-39: 122-129.
21. Gallez B, Baudalet C and Jordan BF (2004) Assessment of tumor oxygenation by electron paramagnetic resonance: principles and applications. *Nmr in Biomedicine* 17: 240-262.
22. Ye J-S, Wen Y, De Zhang W, Cui H-F, Gan LM, Xu GQ and Sheu F-S (2003) Application of multi-walled carbon nanotubes functionalized with hemin for oxygen detection in neural solution. *Journal of electroanalytical chemistry* 562: 241-246.
23. Lin MS, Leu HJ and Lai CH (2006) Development of Vitamin B12 based disposable sensor for dissolved oxygen. *Analytica Chimica Acta* 561: 164-170.
24. Wiest J, Stadthagen T, Schmidhuber M, Brischwein M, Ressler J, Raeder U, Grothe H, Melzer A and Wolf B (2006) Intelligent mobile lab for metabolics in environmental monitoring. *Analytical Letters* 39: 1759-1771.
25. Wiest J, Brischwein M, Grothe H, Otto AM and Wolf B (2005) Planar Microsensors for measurement of cellular respiration. *SENSOR 2005 Proceedings II*: 249-254.
26. Wiest, J., Schmidhuber, M., Grundl, D., Brischwein, M., Grothe, H., and Wolf, B. Environmental Engineering using Living Cells as Signal Transducers. [IEEE Africon 2007]. 2007. Windhoek/Namibia, IEEE Catalog number: 04CH37590C.
27. Brückl, M., Grundl, D., Otto, A. M., Schmidhuber, M., Wiest, J., and Wolf, B. Real-time analysis of tumor cell metabolism and chemosensitivity testing using multiparametric sensor chips. 2007. Munich, Germany. Integrative Cancer Genomics.
28. Wiest, J., Brückl, M., Schmidhuber, M., Grundl, D., Lob, V., Brischwein, M., Grothe, H., and Wolf, B. Multiparametric, six channel, online analysis of MCF-7 cells. 2007. MIPTEC 2007.

Author: Dipl.-Ing. Joachim Wiest  
 Institute: Innovationszentrum Medizinische Elektronik –  
 cellasys GmbH  
 Street: Karlstrasse 96  
 City: 80335 München  
 Country: Germany  
 Email: wiest@cellasys.com

# Effects of Optical Radiation on the Healing of Bone Defect in Rabbits

Yu. Dehkyar<sup>1</sup>, A. Katashev<sup>1</sup>, J. Katasheva<sup>2</sup> and I. Ozolanta<sup>2</sup>

<sup>1</sup>Riga Technical University, Riga, Latvia

<sup>2</sup>Riga P. Stradina University, Riga, Latvia

**Abstract** — Hypothesis, that optical radiation is able to alter surface electrochemical potential and due to this affect bone remodeling processes have been proposed. Besides, researches, being done beforehand, in majority used laser radiation of single wavelength; the latter usually does not match well with optical absorption bands of the bone, obtained in a series of *in-vitro* experiments. The goal of the present work was to evaluate *in-vivo* influence of the optical light of different wavelength on the bone remodeling / reconstruction process. For this, artificial defect have been made at the mandible bone of female rabbits. During operation and 10 days after surgery operation site was irradiated with optical radiation with either long (550 – 5000 nm) or short (350 – 550) wavelength. Results demonstrated that light treatment suppresses rate of healing of the bone defect for both experimental groups comparing with the control. The suppression effect is more expressed for short-wavelength irradiation.

**Keywords** — bone remodeling, optical radiation, fracture healing.

## I. INTRODUCTION

Optical radiation is known to be able to change physical properties of semiconductor surface, providing surface charge and altering surface electrochemical potential. The bone had been demonstrated as a material, having an energy gap at resembling semiconductor [1]. This means, that electron transitions in bone may cause alteration of the bone surface charge.

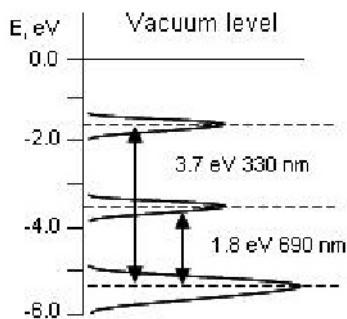


Fig. 1. Bone electronic structure, following [2]. Arrows indicate electron transitions.

That is why hypothesis arose, that optical radiation may alter bone surface properties (including electrochemical potential), hereby affecting ion exchange between bone and bone cells and influencing bone remodeling.

In the previous works, structure of electron states levels of bone has been studied [2]. Two distinct energy levels exist in bone (Fig.1). The energy of electron transitions between these levels are about 1.8 and 3.7 eV, that corresponds to the photon wavelengths 690 nm and 330 nm [pavlenko]. If optical radiation indeed alters bone remodeling, the effect must be most expressive at the wavelengths that correspond to bone electron transition band.

The number of research, targeted to explore influence of the optical radiation on remodeling and reconstruction of bone, has been already reported. Reported results was both positive, declaring that irradiation facilitates bone remodeling [3, 5, 6] and negative, demonstrated longer bone repair after optical laser treatment [4]. Besides, in majority, these researches applied high or low intensive laser radiation with a wavelength in the red and near infrared range. This wavelength, usually, did not match well electronic (i.e electron absorption bands) structure of the bone.

The goal of the present work was to evaluate influence of the optical light of different wavelength, that are selected to excite electron transitions in bone on the bone remodeling / reconstruction process *in-vivo*.

## II. MATERIALS AND METHODS

### A. Bone defect treatment

Experiments have been carried out with 4-month female rabbits. Animals were randomly divided into three groups: control, experimental group I and experimental group II. Animals assignment to groups is summarized at Table 1. For every animal surgery was performed under anesthesia to make a Ø3 mm semi – circular defect at the right lower side of mandible (Fig.2). For the procedure, Ø3 mm bore had been used.

During manipulation, before the wound was closed by tissue and sutured, the defect for experimental group I was illuminated using Xe arc lamp through the orange filter.



Fig. 2. Artificial bone defect.

Table 1. Experiment design

Group	Procedure	Animals N°
Control	-	9, 10, 11
Experimental I	Irradiation using filter OS-12 (> 550 nm), 10 sek	3, 8, 12
Experimental II	Irradiation using filter SZS-21 (350 – 550 nm), 30 sek	1, 4, 7

Animals N° 2, 5 and 6 have been euthanized for histological evaluation. Corresponding data were censored out from the consideration.

The filter had transmission spectral band 550 – 5000 nm; irradiation time selected to be 10 sec. For experimental group II defect was irradiated through the blue – green filter, having transmission band 350 – 550 nm. Irradiation time was 30 sec. The time of irradiation was adjusted to deliver the same energy flux to the wound in both cases. The fluxes through the both filters were compared in arbitrary units, using non-calibrated thermopile. Evaluated by calculations value of the delivered energy was 1 – 2 J/cm<sup>2</sup>. The wavelength bands were selected in accord with known electron structure of the bone to excite electron transitions via the energy gap [2]. For the control group, the defect was left intact, with no irradiation.

For experimental groups, the defect sites were irradiated every day through the skin at the same modes 10 days after surgery. To prevent bias between control and experimental groups due to stress, related to handling, animals from control group were submitted to the same manipulations with the Xe lamp switched off.

*B. Evaluation of the healing process*

Because of proposed hypothesis, that electron transitions in bone may be responsible for alteration of bone remodeling, X-ray evaluation of the defect healing was not appropriate. X-ray photons itself are able to modify bone electronic structure, due to this causing uncontrolled bias in the results.

Ultrasound technique has been demonstrated to be able to visualize and evaluate size of open edge bone defects [7].

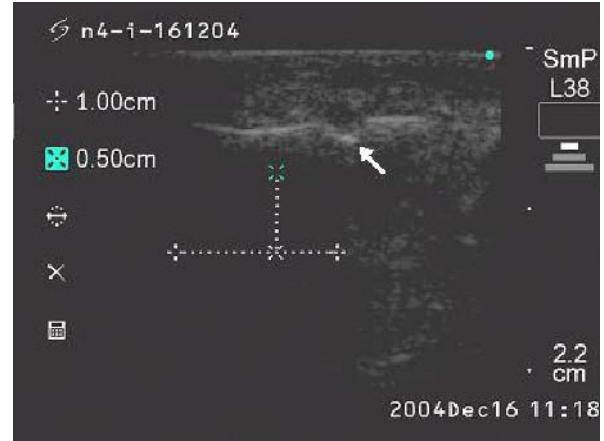


Fig. 3. US image of the bone defect (arrow).

Therefore, the healing of the defect was evaluated non-invasively, using US imaging equipment “SonoSite 180Plus” equipped with the 10MHz linear array transducer. Before surgery, US images of intact rabbit mandibles were obtained for each animal. After the surgery, US images were obtained 2 – 3 times per week. Figure 3 depicts typical US image of the bone defect. The area of the defect, seen at the image, was used as the measure of the defect size. For the number of animals, excessive mass of bone was formed over the defect site. For such cases, the area of excessive bone were calculated and used for further analysis with negative sign. To evaluate defect size measurement uncertainty, areas had been measured several times in a random-fashioned order. The average standard deviation of the calculated defect area values was 0.40 mm<sup>2</sup>.

To evaluate defect healing process, determined from US images defect areas were plotted against the time passed after surgery (Fig.4). Resulting curves were approximated

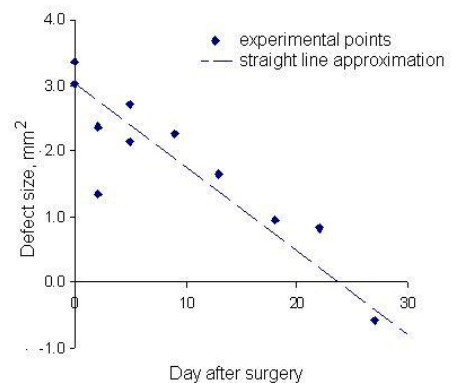


Fig. 4. Typical change of the defect side over time. Negative numbers correspond to excessive bone mass formation.

with the straight lines using least square method. The slope of the line was taken as a measure of the healing rate. The standard deviation for the calculated healing rates was  $0.01 \text{ mm}^2/\text{day}$ . Healing rates were compared for control and both experimental groups.

### III. RESULTS AND DISCUSSION

Experimental results are summarized in the Table 2. To evaluate, whether there is any relationship between initial defect size and defect healing rate, the correlation coefficient between those parameters was calculated. Both graphic presentation (Fig.5) and the value of correlation coefficient suggested, that healing rate does not depend on initial defect size.

Figure 6 shows distribution of healing rates between experimental groups. Distributions demonstrated that healing rate tends to be lower at irradiated groups. The average healing rate for each group was  $0.12 \text{ mm}^2/\text{day}$  for control group,  $0.10 \text{ mm}^2/\text{day}$  for experimental group I and  $0.08 \text{ mm}^2/\text{day}$  for experimental group II. Such a result is reasonable, because group II was irradiated with short – wavelength light that has higher energy of photons and may induce more noticeable changes.

Single factor ANOVA [8] was applied to compare difference between groups with scattering within the groups. The corresponding P – value was 0.14. The difference in average healing rate therefore is significant only at the 15% level of significance, that does not allow make sound conclusion whether irradiation affect average bone healing rate. But, one has to take into account, that analysis used small experimental groups.

Figure 6 suggests that, alongside with average healing rate, the variability of the healing rate differs for different groups. Healing rate standard deviation was equal to  $0.004 \text{ mm}^2/\text{day}$  for control group,  $0.03 \text{ mm}^2/\text{day}$  for experimental group I and  $0.04 \text{ mm}^2/\text{day}$  for experimental group II. Fisher test (F-test, [8]) was used to compare standard deviation in each ex-

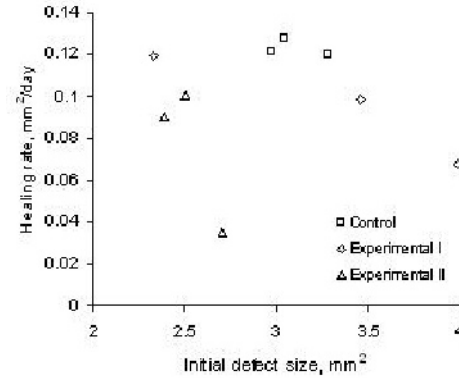


Fig. 5. Correlation between healing rate ad initial bone defect size.

perimental group with control one. Corresponding P – values for the difference between experimental group variance and control group variance was 0.02 and 0.01 for experimental group I and II, correspondingly. Statistically significant difference in variances makes any conclusion, made on the base of ANOVA useless, because analysis of variance requires equality of group standard deviations [9].

Therefore, one may come to conclusion, that optical radiation affected bone remodeling process in both experimental groups, more likely inhibiting it. Inhibition effect was expressed in a greater extent in experimental group II, irradiated with shorter wavelengths light. This is in favor of the proposed hypothesis, that irradiation causes electron transition in bone and hereby alter bone electrochemical properties. One may note, that inhibition effect of the optical laser radiation has been reported previously as well [4]

The present work attempted just to demonstrate influence of optical radiation on the bone defect healing and does not answer most important question, is the effect appeared due

Table 2. Experimental data on defect healing rate

Group	Animal N <sup>o</sup>	Initial defect size, mm <sup>2</sup>	Healing rate, mm <sup>2</sup> /day
Control (no irradiation)	9	3.0	0.13
	10	3.3	0.12
	11	3.0	0.12
Experimental I (550 nm <)	3	4.0	0.07
	8	3.5	0.10
	12	2.3	0.12
Experimental II (350 – 550 nm)	1	2.4	0.04
	4	2.5	0.09
	7	2.7	0.10

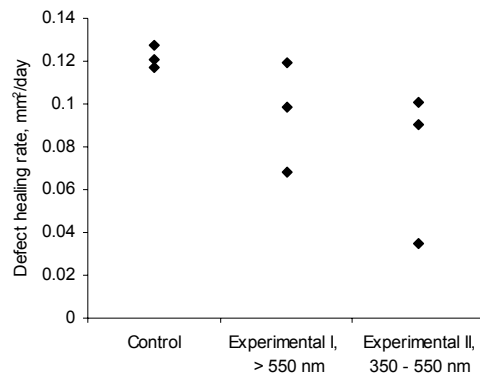


Fig. 6 Variation of defect healing rate for different groups.



to irradiation of bone itself or it is a systemic effect due to irradiation of wound covering soft tissue.

#### IV. CONCLUSIONS

The results demonstrated that wound treatment with optical radiation suppresses healing of the bone defect in rabbits. The suppression effect is more expressed for the group, irradiated with short wavelength light

#### ACKNOWLEDGMENT

Authors are deeply indebted to the staff of veterinary clinic "KAVET" for unlimited access to the operation facilities and to the company NMS Diagnostika for rent of US equipment.

#### REFERENCES

1. Dekhtyar Yu, Katashev A, Pavlenko A. (1997) Long-living electron states and energy gap in bone Proc. Of the 12<sup>th</sup> International Symposium Exoemission and its applications, Polanica Zdroj, Poland, 1997, pp 135-138
2. Arwin H, Bogucharska T, Hill R.M et al. (2001) Structure and electron properties of bone surface, Proceedings of the European Society of Biomechanics 2001 conference, London, UK, 2001, p124
3. Yaakobi T, Maltz L, Oron U.(1996) Promotion of bone repair in the cortical bone of the tibia in rats by low energy laser (He-Ne) irradiation.. *Calcif Tissue Int.* 1996 Oct;59(4):297-300
4. Friesen LR, Cobb CM, Rapley JW, Forgas-Brockman L, Spencer P. (1999) Laser irradiation of bone: II. Healing response following treatment by CO<sub>2</sub> and Nd:YAG lasers. *J. Periodontol.* Jan;70(1):75-83
5. Kawasaki K, Shimizu N. (2000), Effects of low-energy laser irradiation on bone remodeling during experimental tooth movement in rats. *Lasers Surg Med.*;26(3):282-91.
6. Barbos Pinheiro AL, Limeira Júnior Fde A, Márquez Gerbi ME, et.al. (2003) Effect of 830-nm laser light on the repair of bone defects grafted with inorganic bovine bone and decalcified cortical osseous membrane. *J Clin Laser Med Surg.* Dec;21(6):383-8.
7. Dekhtyar Yu, Derjugina I, Katashev A. et.al. (2002) Evaluation of the size of local bone injuries by means of ultrasound. *Polish journal on medical physics and engineering*, V.8, N.3: 165.-171
8. Mould R.F. (1998) *Introductory medical statistics*, IoP, Bristol and Philadelphia
9. Ivanova, V.M, Kalinina V.N, Neshumova L.A et .al, (1981) *Mathematical statistics*, "Vysshaya shkola" Moscow (in Russian)

Address of the corresponding author:

Author: Alexei Katashev  
 Institute: Riga Technical University  
 Street: 1 Kalku street  
 City: Riga  
 Country: Latvia  
 Email: katashev@latnet.lv

# Transmyocardial Laser Revascularization in Patients with Diffuse Coronary Artery Disease

E. Freilibs<sup>1</sup>, R. Lacis<sup>1</sup> and U. Strazdins<sup>1</sup>

<sup>1</sup>Pauls Stradins Clinical University Hospital/ Center of Cardiac Surgery, Riga, Latvia

**Abstract — Objective:** The standard revascularisation methods have not proved effective enough in situations of very diffuse coronary artery disease (CAD). One of the methods to solve this situation is transmyocardial laser revascularization (TMLR). **Methods and results:** 20 patients have undergone surgical treatment since November 2003. All operations had done TMLR as an adjunct to coronary artery bypass graft surgery (CABG). All patients had 3 vessels disease. At a median follow up 6 months after operation 81 % of patients were free of angina pectoris. All patients before operation were in III and IV Canadian Cardiovascular Society (CCVS) angina class, after operation at follow up time were in class 0 – I CCVS. Myocardial perfusion scintigraphy demonstrated significant improvement of myocardial perfusion. In control group were 30 patients after on- pump isolated CABG. No statistical significant differences were found in Troponin I level, postoperative bleeding compared with isolated CABG. **Conclusions:** TMLR is minimally traumatic and effective treating method in combination with CABG.

**Keywords —** transmyocardial laser revascularization, coronary artery disease, coronary artery bypass graft surgery, Canadian cardiovascular society angina class

## I. INTRODUCTION

Coronary artery disease is the leading cause of death worldwide. Cardiovascular diseases cause 42% of all deaths in the European Union (EU): 46% of deaths (women) and 38% deaths (men). 4 million Europeans are dying each year from cardiovascular diseases [1].

There are three main treating methods for CAD: medical therapy, percutaneous interventions (PCI), and coronary artery bypass graft surgery (CABG). In patients with severe diffuse coronary artery atherosclerosis it is not possible to do complete revascularisation with PCI or CABG (we can predict it in coronary angiography). If these patients have severe angina that persists despite maximal medical therapy we have to look at other treating methods. One option is TMLR. The first time TMLR was done by Mirhoseini et al. to animals in 1981 [2-4]. It was done for the first time to people by Okada et al. in 1986 [2-4].

The technical idea of method is to create the channels through myocardium with laser energy. Hypothesis of TMLR are – blood flow to the myocardium through channels and initiate the wound healing process with associated

angiogenic response (angiogenesis) and (or) regional myocardial denervation. [5] Mechanism of revascularization with TMLR is still unclear. Several randomized, controlled, multicenter trials have established the clinical efficacy of sole therapy TMLR [2-4, 6, 7]. Our aim is to do TMLR as an adjunct to CABG and to assess the effect of operation.

## II. MATERIALS AND METHODS

20 patients were operated on in our hospital by TMLR plus CABG. The operations took place from November 2003 to 2008. 10 patients were women and 10 men. The average age was 64 years old (46- 75). All patients had three vessels severe diffuse coronary artery atherosclerosis disease. One or two main coronary arteries were non amenable for PCI or CABG. It was diagnosed preoperatively angiographically or intraoperatively. For TMLR we use Cardiogenesis „TMR 2000,, Holmium: yttrium – aluminum – garnet (Ho: YAG). Ho: YAG is pulsed mid – infrared laser. The average amount of channels was 10 to a patient. Mostly channels were done to anterior wall of the left chamber.

50 % of patients were examined before and 6 months after operations with myocardial perfusion scintigraphy. Patients were checked for their CCVS class pre and 6 months postoperatively.

We controlled Troponin I postoperatively.

We checked postoperative bleeding.

In control group were 30 patients with three vessels disease, all patients were after isolated CABG operated on pump.

## III. RESULTS

Survival after operations was 95%. 1 patient died 9 days after the operation; the cause was acute respiratory virus infection (ARVI). All patients were in class III-IV CCVS preoperatively. After operations 81 % of patients were in class 0 (CCVS). 19 % of patients were in class I, 6 months after the operations.

Average Troponin I after operations was 23.3 ng/ml. Average Troponin I in the control group was 15.5 ng/ml.

The incidence of myocardial infarction postoperatively was 5 % in TMLR group. 6.6 % myocardial infarction postoperatively in the control group.

No reoperations caused by postoperative bleeding in both groups.

Myocardial perfusion scintigraphy showed perfusion improvement in myocardium after operation; however some patients still had ischemic regions in myocardium.

#### IV. CONCLUSIONS

TMLR in combination with CABG is an effective treating method at the end stage medically refractory coronary artery disease.

It is not easy to conclude that the improvement of angina and myocardial perfusion due to TMLR was because we did TMLR in combination with CABG.

TMLR is a minimal traumatic method - no reoperations due to bleeding, the Troponin I level and incidence of myocardial infarction postoperatively was approximately the same in the control group.

The number of patients is too small to draw a statistically accurate conclusion.

#### REFERENCES

1. Coronary Heart Disease Statistics at <http://www.annecollins.com/nutrition/heart-facts.htm>.
2. Allen KB, Dowling RD, Fudge TL, et al., Comparison of transmyocardial revascularization with medical therapy in patients with refractory angina. *N Engl J Med* 1999; 341:1029-36
3. Frazier OH, March RJ, Horvath KA. Transmyocardial revascularization with a carbon dioxide laser in patients with end-stage coronary artery disease. *M Engl J Med* 1999;341:1021-8
4. Jones JW, Schmidt SE, Richman BW, et al. Holmium: YAG laser transmyocardial revascularization relieves angina and improves functional status. *Ann Thorac Surg* 1999; 67:1596-601
5. Charles R.Bridges, Keith A.Horvath, Ray Chu-Jeng Chiu (2006). Myocardial laser revascularization. Blackwell
6. Schofield PM, Sharples LD, Caine N, et al. Transmyocardial laser revascularization in patients with refractory angina: a randomized controlled trial. *Lancet* 1999; 353:519-24
7. Burkhoff D, Fisher PE, Apfelbaum M, et al. Histological appearance of transmyocardial laser channels after 4 weeks. *Ann Thorac Surg* 1996; 61:1532-6

Address of the corresponding author:

Author: Edgars Freilibs  
 Institute: Pauls Stradins Clinical University Hospital/ Center of Cardiac Surgery  
 Street: Pilsonu Street 13  
 City: Riga  
 Country: Latvia  
 Email: [edgars.freilibs@inbox.lv](mailto:edgars.freilibs@inbox.lv)

# Evaluation of a Fiber-Optic Based Pulsed Laser System for Fluorescence Spectroscopy

N. Haj-Hosseini<sup>1</sup>, S. Andersson-Engels<sup>2</sup> and K. Wårdell<sup>1</sup>

<sup>1</sup> Linköping University/ Department of Biomedical Engineering, Linköping, Sweden

<sup>2</sup> Lund University of Technology/ Department of Physics, Lund, Sweden

**Abstract** — A fiber optic based continuous wave laser setup has been developed to record the 5-aminolevulinic (5-ALA) induced Protoporphyrin IX (PpIX) fluorescence signals from cerebral gliomas. To reduce the energy delivered to the tissue as well as suppression of the ambient lamp artifact from the recorded spectra, a pulsed laser setup has been developed and evaluated. This setup has been calibrated and first evaluations were performed on the 5-ALA treated skin showing PpIX fluorescence peaks from the ALA treated skin at 635 and 704 nm wavelengths. The system controls laser pulses through a computer interface and LabVIEW software package. Pulses as short as 50 ms over a period time of 500 ms are generated and optimally detected. The results from primary measurements on skin show an effective suppression of room fluorescent lamp artifact from the recorded spectra.

**Keywords** — Fluorescence spectroscopy, Pulsed laser modulation, 5-aminolevulinic acid induced fluorescence, Glioma resection, Intraoperative optical guide

## I. INTRODUCTION

The highly malignant brain tumor, glioblastoma multiforme, is difficult to totally resect due to its infiltrative way of growing and its morphological similarities to surrounding functioning brain under direct vision in the operating field. MR and/or CT images are taken before and after surgery for observing the location and form of the tumor but still the important task of identifying tumor margins is based on visual inspection and palpation of tissue.

Optical measurements may offer a precise, safe and spatially beneficial option for intraoperative measurements. Thus the goal of this study has been to develop a system that assists the neurosurgeons with delineating the border between normal and malignant tissue during tumor resection. Although some research groups [1,2,3,4] have reported competitive studies of cerebral tumor demarcation using different detection methods of endogenous and exogenous fluorescence, quantitative tracing of 5-ALA induced fluorescence in cerebral tumors have remained unexplored.

The general idea is that about 3 hours prior to surgery the patient receives orally a low dose of 5-aminolevulinic acid

(ALA) which passes the defect blood-brain barrier in the tumor and is converted to the fluorescence tumor marker protoporphyrin IX (PpIX) in the malignant cells to facilitate tumor demarcation via the tissue fluorescence signal. Laser light at 405 nm is absorbed by the PpIX and a fluorescence emission spectrum with peaks at 635 nm and 704 nm can be collected. PpIX is a natural substance in the haem cycle which is rapidly eliminated from the body. Stummer et al [5] have conducted extensive research on detection of cerebral glioma through oral administration of ALA reporting a higher resection rate by using PpIX fluorescence microscopy. The inspection done through a microscope, is based on visual judgement of the surgeon.

A study has been previously conducted using a compact fiber optic based fluorescence spectroscopy system using an LED at 395 nm both on skin and during neurosurgical resection procedure [6]. Results indicate that PpIX fluorescence and brain tissue autofluorescence can be recorded with the help of the developed system intraoperatively during resection of glioblastoma multiforme. To omit the undesired effect of superimposed unsuppressed operating lamp noise on the recorded spectra, a non-transparent funnel had been previously used in the measurements. Though this funnel effectively restricts the ambient light artifact, it blocks the view of the surgeon which is of a great disadvantage during operation.

To restrict the sensitivity of the collected fluorescence to the ambient light and to avoid excessive bleaching of the protoporphyrin IX marker under exposure to laser as well as reducing the measurement time, a system based on a pulsed mode laser at 405 nm (50 mW peak power) and a spectrometer has been developed and evaluated on skin prior to clinical measurements.

## II. SYSTEM AND SETUP

The different components of the system, as described below, are mounted in a compact box of 31×25×21 cm which is easily carried on a trolley to the operation theater (Fig 1). The total weight of the box is 4.6 kg.

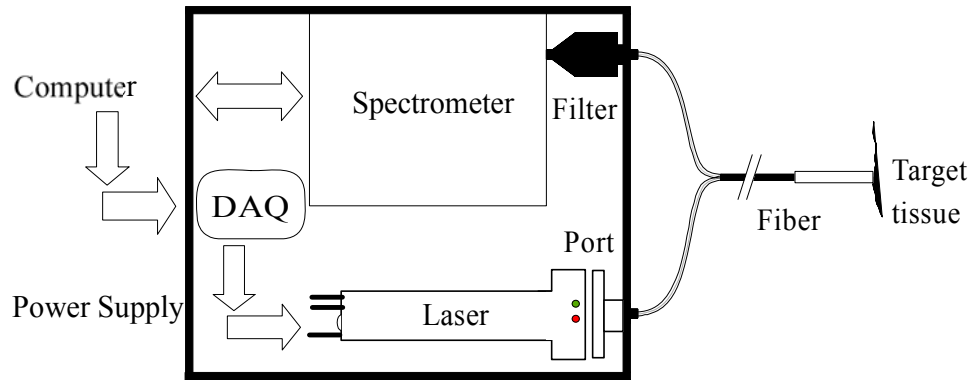


Fig. 1 Fiber optic based pulsed system design.

### A. System components

**Laser:** Near-UV laser diode module with the maximum excitation light at 405 nm and maximum power of 50 mW was acquired (Oxxius, Inc., CA). The laser operates both in modes of continuous wave and pulsed modulation. Shortest generated pulse may have a width of 7  $\mu$ s. Relatively small mechanical dimensions make the packaging of this laser very handy.

**Spectrometer:** The spectrometer (EPP 2000, Stellarnet) uses 2048 element CCD in the range of 200-850 nm wavelengths with a practical resolution of 2 nm, though the theoretical resolution is higher. The minimum reliable integration time of the spectrometer is 30 ms.

**Filter:** As the reflection from the laser light saturates the spectrometer, a long pass cut off filter of 450 nm (Schott CG-GG-475-0.50-3, CVI, USA) is fixed before the detector slit of the spectrometer.

**Fiber optical probe:** Excitation light is brought to the tissue through a hand-held optical fiber probe with core and total diameter of 600 and 950  $\mu$ m and numerical aperture of 0.37. This excitation fiber is surrounded by 9 other fibers of

200  $\mu$ m core diameter and numerical aperture of 0.22 which collect the light from the measurement site and transfer it to the spectrometer (Fig. 2 a). The optical fibers are arranged to match the slit configuration of the spectrometer at the detector end (Fig. 2 b and c). However, some light at the upper and lower fibers at the detector end are lost (Fig. 2 b).

**Fiberport:** A miniature micropositioner (OFR Inc., Caldwell, NJ) has been mounted at the interface of laser and fiber probe to allow the alignment of the laser light. The maximum attenuation of light through the fiberport is 25%.

### B. Pulse generation and spectrum collection

The system controls generation of laser light pulses and the spectrometer through a computer interface and labview software package. The concept is to have a simultaneous pulse generation and spectrum collection. The pulse and laser pulsewidth should be a trade off of the integration time of the spectrometer, minimum energy given to the tissue and the time needed to keep the ambient light sensitivity at minimum while collecting detectable amount of light. The software is programmed such that pulses are generated as a function of given spectrometer integration time and period time. However, the execution time of the loops in the software package do not allow setting of the period time below a certain level with the current design.

### C. Calibration

**Calibration:** The system is calibrated with the coefficients specific of the spectrometer against the fluorescent lamp to make sure of the validity of the recorded wavelengths. Before each set of measurements a dark spectrum is recorded to measure the background level of the system without light input. All measured spectra are corrected for this background. The spectral sensitivity of the system needs to be taken into account in subsequent data analysis

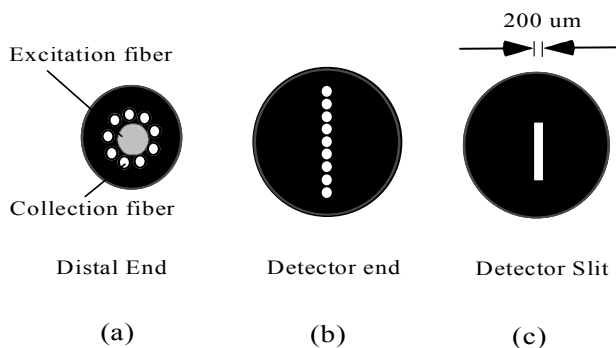


Fig. 2 Fiber probes (a) distal end of the fiber probe (b) detector end connected to the spectrometer and (c) detector slit.

by recording the spectrum from a National Institute of Standards and Technology (NIST) traceable stable calibration light source.

A fluorescent plastic is used for fluorescence intensity calibration to check the absolute level of the recorded spectra before each set of measurements.

### III. SYSTEM EVALUATION

#### *Undesired spectra from the continuous wave laser mode:*

The background superimposed on the measured spectra due to the room fluorescent lamps during measurements with the 405 nm laser in continuous mode is shown in Fig. 3.

*Evaluation on skin:* Methylaminolevulinat (METVIX® 160 mg/g, Photocure ASA, Norway) cream was applied on the skin 3-4 hours prior to the measurements. The skin was

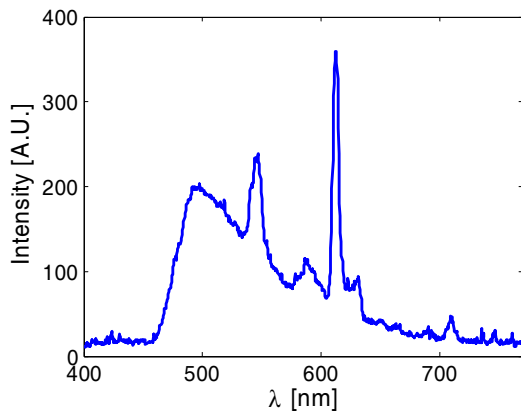


Fig. 3 Spectrum recorded with no mechanical suppression of room fluorescent tube lamp using the continuous wave laser (405 nm) system. The artifact is superimposed on the tissue autofluorescence.

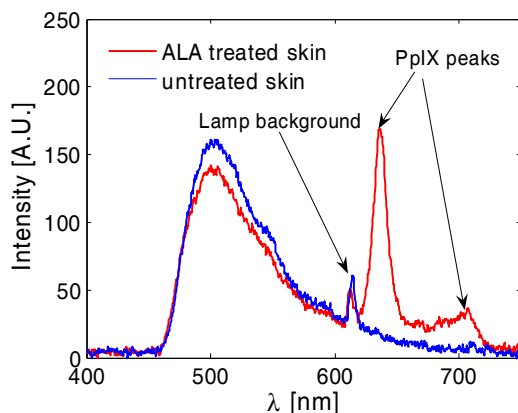


Fig. 4 Fluorescence signals detected from the ALA treated and untreated skin with pulsed mode laser system with the room lamps on. Pulse width of 50 ms over a duty cycle of 0.1 was applied.

covered to avoid exposure to the light and thus prevent bleaching of the fluorophores. The aminolevulinic acid in this cream changes to PpIX in the skin and exhibits fluorescent peaks at 635 and 704 nm wavelengths. Measurements were performed on the untreated and ALA treated skin. Fig. 4 shows the fluorescence recorded from the untreated skin and the fluorescence from the treated skin, using the developed pulsed system. Pulses of 50 ms long with a duty cycle of 0.1 have been chosen and evaluated. The power was set to 1 mW. These values were chosen as an obtained compromise between the desired features mentioned earlier.

### IV. DISCUSSION

The system offers a quantitative measurement method of the fluorescence in malignant glioma brain tissue compared to the microscope based inspection reported by Stummer et al. [5].

We have observed negligible traces of ambient light in the collected fluorescence spectra. This helps the visual supervision of the surgeon to a great extent compared to the previous measurements with continuous wave excitation laser. In the continuous wave mode the measurement site has to be covered with a non-transparent funnel and the lamps should be directed away from the surgery site. As the operation lamp and microscope lamp also exist in addition to the fluorescence lamp tubes in the operation theater, the sensitivity of the system to the background light of the mentioned lamps should be considered in the next step of the system performance evaluation.

Further work will include optimization of pulse generation and detection at the software level as well as averaging of the collected pulses for visualization of a more stable fluorescence spectra intensity. Clinical measurements on brain gliomas would follow the completion of the system.

### V. CONCLUSION

Using the developed fiber optic based pulsed fluorescence spectroscopy system, it has been shown that PpIX fluorescence signals can be quantitatively detected on ALA treated skin and the artifact of the ambient fluorescent lamps are effectively omitted. However, further optimization and evaluation of the pulsed fluorescence detection system is necessary before clinical trials.

### ACKNOWLEDGMENT

We would like to thank Carina Fors for her skillful programming and Dr. Johan Richter for his valuable neurosur-

gical cooperation. Technical support of research engineers at the department of biomedical engineering at Linköping University, Per Sveider and Bengt Ragnemalm, in mechanical system setup has been of great value to us.

#### REFERENCES

1. S. Andersson-Engels, Å. Elner, J. Johansson, S.-E. Karlsson, L. G. Salford, L.-G. Strömblad, K. Svanberg, and S. Svanberg, "Clinical recording of laser-induced fluorescence spectra for evaluation of tumour demarcation feasibility in selected clinical specialities," *Lasers Med. Sci.* 6, 415-424 (1991).
2. Toms S A, Lin W C, Weil R J, Johnson M D, Jansen E D, Mahadevan-Jansen A (2005) Intraoperative optical spectroscopy identifies infiltrating glioma margins with high sensitivity, *Operative Neurosurgery J 4*, vol. 57: 382-391
3. Chung Y G, Schwartz J A, Gardner C M, Sawaya R E, Jacques S L (1997), Diagnostic potential of laser-induced autofluorescence emission on brain tissue, *J Korean Med Sci* 12(2):135-142.
4. Bogaards A, Varma A, Collens S P, Lin A, Giles A, Yang V X D, Bilbao J M, Lilge L D, Muller P J, Wilson B C (2004), Increased brain tumor resection using fluorescence image guidance in a pre-clinical model, *Lasers in surgery and medicine* 35:181-190.
5. W. Stummer, U. Pichlmeier, T. Meinel, O. D. Wiestler, F. Zanella, and H.-J. Reulen, "Fluorescence-guided surgery with 5-aminolevulinic acid for resection of malignant glioma: a randomised controlled multicentre phase III trial," *The Lancet Oncology*, vol. 7, pp. 392, 2006.
6. Ilias A M, Richter J, Westermark F, Brantmark M, Andersson-Engels S, and Wårdell K (2007) Evaluation of a fiber-optic fluorescence spectroscopy system to assist neurosurgical tumor resections, *SPIE* vol. 6631:66310W-1-8

Author: Neda Haj-Hosseini  
 Institute: Linköping University  
 Street: University hospital, 58185  
 City: Linköping  
 Country: Sweden  
 Email: nedha@imt.liu.se

# Effect of Light Scattering Simulation in the Eye on Different Color Stimuli Perception

G. Ikaunieks<sup>1</sup> and M. Ozolinsh<sup>1</sup>

<sup>1</sup>Department of Optometry and vision science, University of Latvia, Riga, Latvia

**Abstract** — One of the factors which influences visual functions is intraocular light scattering. To assess the effect of light scattering and stimulus color on visual functions, visual acuity and retinal straylight were measured with and without light scattering occluder. For visual acuity measurements black Landolt optotypes on red, green and blue background were used. Retinal straylight was measured with a direct compensation method using the same colors stimuli. For one subject straylight was measured with 5 different light scattering levels of eye occluder.

All subjects showed the best visual acuity with black optotypes on red background and the lowest visual acuity values on blue background with and without light scattering occluder.

At all occluder scattering levels retinal straylight values were highest for blue color. At high light scattering levels retinal straylight values were smallest for red color. For low light scattering levels straylight values were smallest for green color. Results show, that simulation of different light scattering levels changes spectral dependence of intraocular light scattering. These changes have no direct effect on visual acuity results; however they can affect other visual functions. Optical factors which can induce these spectral changes are discussed.

**Keywords** — intraocular light scattering, visual acuity, colors

## I. INTRODUCTION

Intraocular light scatter is the phenomenon when a part of the light reaching the retina does not participate in normal image formation [1]. Main sources for intraocular light scattering in healthy eye are light reflectance from cornea, lens, retina and light penetrating through sclera and iris [2, 3]. Light scattering in the eye increases if there are pathological (corneal dystrophy etc.) or age related changes in optical parts of the eye (cataract) [1, 4]. There are discussions about importance of measuring straylight in clinical practice [5], because straylight can effect such visual functions as contrast sensitivity, visual acuity, especially in mesopic and scotopic conditions in the presence of light source away from fixation point in the visual field [6, 7].

Another question, which was discussed for a long time, is the straylight spectral dependence. Two main theoretical models of intraocular light scattering are Mie and Rayleigh light scattering models. Mie scatter is not strongly wave-

length dependent. Many clinical studies showed, that straylight is not depending on wavelength and thus is predominantly of Mie form [8, 9]. However newer research has showed that in young and well pigmented eye light scattering was close to Rayleigh scattering [10]. This type of light scattering is strongly wavelength dependent ( $\alpha\lambda^4$ ) and thus it is the greatest for short wavelengths visible light (blue). If eye is not well pigmented long wavelengths light (red light) penetrate through ocular wall and straylight increase. Results also showed that intraocular straylight is less wavelength dependent with increasing age[10].

The main purpose of our studies was to find out changes in straylight values, when high degree cataract is stimulated with a light scattering plate.

## II. METHOD

Two experiments were done: measurements of intraocular straylight and visual acuity threshold measurements. For intraocular straylight measurements the direct compensation method was used [1]. In this method a concentric annulus is shown on computer screen (Fig. 1). The annulus width was 4.7 degrees and diameter ( $\theta$ ) 5.7 degrees. During measurements the annulus color changed from black to colored (red, green or blue) with frequency 8Hz. Due to light scattering in the eye subjects perceived flickering in the test field (center of annulus).

It is possible to neutralize this flicker by showing a counter phase modulating light in the test field (centre). Subject task is to find compensation luminance value, at which flicker in the center disappears or is the weakest. The luminance L which is needed to cancel flickering in the

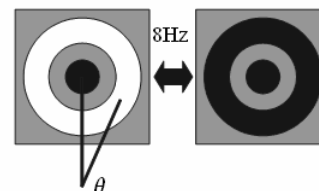


Fig. 1 Test stimulus in direct compensation method.



center is related with light scattering value in the eye. Exact light scattering value is calculated from formula

$$s = \frac{\theta^2 L}{E}, \tag{1}$$

where L – compensating luminance of the test field, E – the illuminance at the pupil plane caused by straylight source,  $\theta$ - angular distance (degrees) of glare source from fixation point. At least 5 light scattering measurements were done with each color stimuli.

The “Freiburg Visual Acuity Test” [11] was used for visual acuity measurements. Stimuli were black Landolt C optotypes on colored background (red, green and blue). Monitor with separate inputs for red, green and blue canals to change color background was used to demonstrate stimuli. Luminance for all backgrounds was 22cd/m<sup>2</sup> (Minolta CS-100). The distance from monitor was 4m.

The CIE xy coordinates for colors used in both experiments were 0.59, 0.36 for red, 0.30, 0.59 for green and 0.16, 0.12 for blue, respectively. Stimuli were shown on CTX PR960F 19" monitor. All experiments were done with right eye. Left eye was covered.

Experiments were done in two conditions, normal and high degree light scattering condition. A polymer dispersed liquid crystal (PDLC) plate was used for simulating high degree light scattering condition. Light scattering inside the plate is caused by the difference in refractive index of crystal droplets and polymer which surround these crystals [12]. Thickness of plate was ~2,5mm. Applying AC voltage it is possible to improve light transparency of the PDLC plate.

For all subjects measurements were done with minimal light transparency level (0.4) of PDLC occluder (without applying AC voltage). PDLC plate was placed in front of the right eye.

For one subject additional intraocular straylight measurements were done with 5 different levels of light transparency of PDLC plate. Improved direct compensation method - compensation comparison method [13] - was used for this experiment.

4 subjects (GA,VA, SE, VE) age ranging from 21 to 28 years participated in experiment. Refractive errors ranged from 0D to -2.0D for sphere, cylinder was smaller than 1.0D.

### III. RESULTS

Results of visual acuity and intraocular straylight for all subjects are showed in Fig. 2.

In visual acuity measurements without light scattering occluder there is significant difference between results of

red, green and blue color background stimuli for each subject, except for subject VE red and green background color data is not statistically different. The highest visual acuity is for black Landolt stimuli on red color background and the lowest for stimuli on blue background.

Results with the light scattering occluder show significant reduction of visual acuity for all subjects. Only for subject VA visual acuity for red color is similar with data obtained without eye occluder. Data between different color backgrounds show the same tendency as in measurements without PDLC occluder – the best visual acuity is for red color and the worst for blue color. Similar results were obtained in our previous measurements [14, 15]. One of the factors which influences visual acuity for stimulus with different color background is retinal receptive fields. They

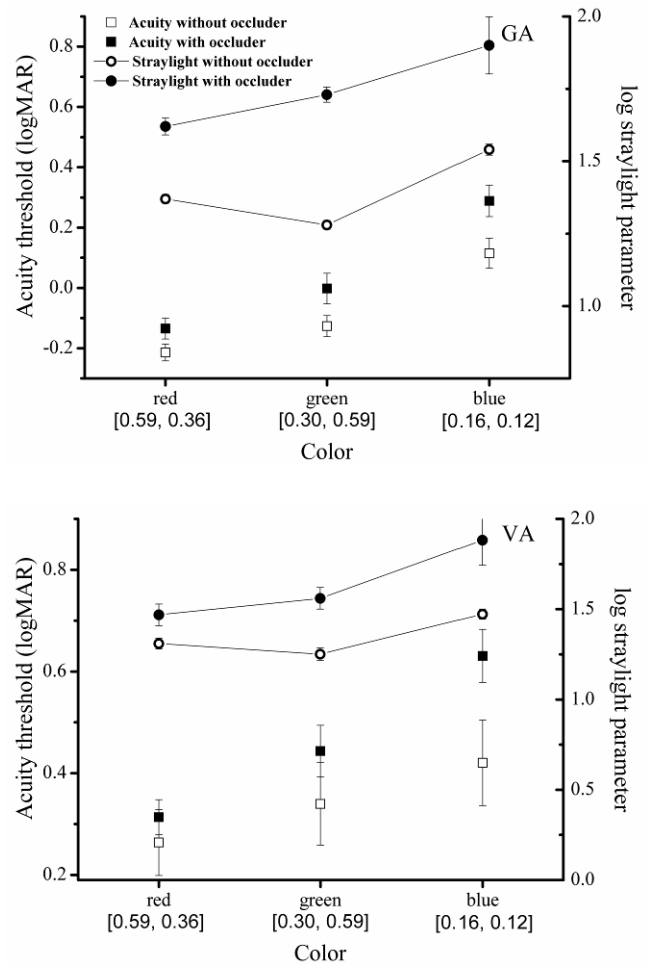


Fig. 2 Visual acuity and straylight parameter for all subjects (GA, VA, SE, VE) depending on stimulus background color in acuity measurements and of straylight source color in intraocular light scatter measurements. CIE coordinates are given for each color.

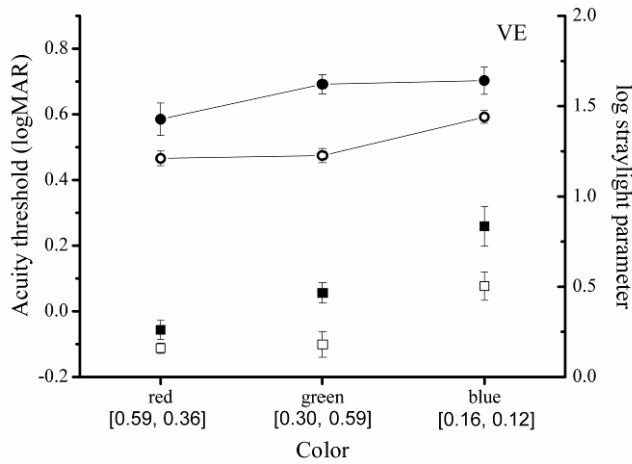
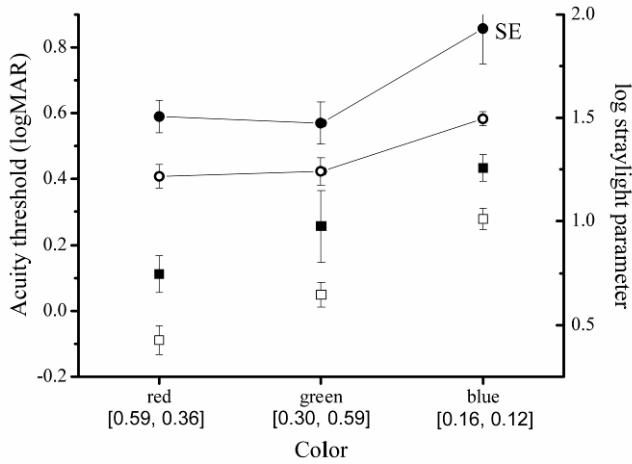


Fig. 2 Visual acuity and straylight parameter for all subjects (GA, VA, SE, VE) depending on stimulus background color in acuity measurements and of straylight source color in intraocular light scatter measurements. CIE coordinates are given for each color.

have different sizes. In periphery receptive fields are larger and being more efficient in discriminating of blue–yellow, whereas in the central part of the retina they are smaller and more efficient in discriminating of green–red stimuli [16].

Intraocular straylight values with and without PDLC occluder are the greatest for blue color. Ratio of red and green color stimuli values differs between subjects. There are significant greater values for red stimuli comparing with green color for 2 subjects (GA, VA) in measurements without PDLC occluder. For subjects SE, VE results for red and green color stimuli are not significant different. These results are in correspondence with results in previous studies, which showed the highest straylight values for short wavelengths stimuli (blue color) and individual variations in ratio of red and green color [10].

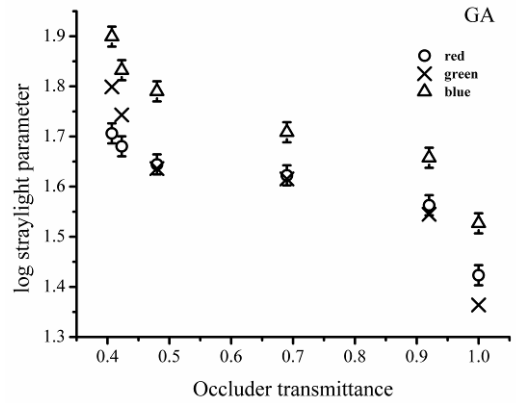


Fig. 3 Straylight parameter with different PDLC occluder transmittance and different color stimuli for one subject.

Using PDLC occluder data for green color are greater than for red color for 3 subjects. Only subject SE shows similar results for both colors stimuli.

Fig. 3 shows more detailed dependence of straylight parameter from light transparency level in PDLC plate for different color stimuli. These data are obtained for subject GA. The greatest straylight values are for blue color for all transparency levels. For high transparency levels intraocular straylight is the smallest for green color, but for low transparency levels the smallest values are for red color stimuli.

#### IV. DISCUSSION

There could be several reasons why intraocular straylight is greater for green than for red color with high light scattering level (low transparency) of eye occluder and is smaller when occluder is more transparent. One of the factors which could influence these changes is the spectral transparency of occluder. PDLC occluder has the greatest transparency for long wavelengths and smallest for short wavelengths [16, 17]. It means that green light is scattered more than red light. Spectral dependence of transmittance of PDLC plate is greater when average transparency of the plate is the highest and keeps almost constant for all wavelengths when the average transparency is the smallest. However the transmittance for red light is larger than for green with all transparency levels of the plate.

As mentioned previously, important source of straylight in the eye is light which penetrate trough the sclera and iris. Penetration is highest for long wavelengths (red) light [10]. When plate with low light transparency is in front of the eye, there is less light falling on the eye. Thus PDLC plate reduce the amount of light which penetrates trough the ocular walls and iris. If illuminance of the eye decrease pupil become wider and relative amount of light which

enters into the eye through the pupil increase. These two factors could be main reasons for spectral changes of light scattering.

Spectral changes for the red and green color stimuli have no direct effect on visual acuity. Visual acuity is the best for the stimulus on red color and the worst on blue background in all light scattering conditions. In all measurements CRT monitor was used for showing stimulus. Light which come from monitor is not monochromatic. This factor could be one of the reasons why effect is not so great.

Previous researches showed that contrast sensitivity is more affected than visual acuity when cataract is stimulated with light scattering occluder [4]. If there is no effect on visual acuity we can't conclude that there is no effect on contrast sensitivity. Additional experiment should be done to evaluate this effect.

## V. CONCLUSIONS

Light scattering occluder (polymer dispersed liquid crystal plate) changes spectral dependency of intraocular straylight – intraocular light scattering increases for green light and reduces for red light. One of the factors which causes these changes is spectral transparency of occluder. PDLC occluder has the greatest transparency for long wavelengths and smallest for short wavelengths. Another factor could be the changes in amount of light which penetrate through ocular wall and which is important source of straylight for red light. These changes have no direct effect on visual acuity for colored stimuli.

## ACKNOWLEDGMENT

Gatis Ikaunieks is supported by European Social Fund

## REFERENCES

1. Van den Berg T J (1986) Importance of pathological intraocular light scatter for visual disability. *Doc Ophthalmol* 61:327-33
2. Van den Berg T J, Ijspeert J K, de Waard P W T (1991) Dependence of intraocular straylight on pigmentation and light transmission through the ocular wall. *Vision Res* 31:1361-1367
3. Yuan R, Yager D, Guethlein M et al. (1993). Controlling unwanted sources of threshold change in disability glare studies: a prototype apparatus and procedure. *Optom Vis Sci* 70:976–81
4. Elliott D B, Bullimore M A, Patla A E et al. (1996) Effect of a cataract simulation on clinical and real world vision. *Br J Ophthalmol* 80:799-804
5. Aslam T M, Haider D, Murray I J (2007) Principles of disability glare measurement: an ophthalmological perspective. *Acta Ophthalmol Scand* 85:354-60
6. Van den Berg T J (1991) On the relation between glare and straylight. *Doc Ophthalmol* 78:177-81
7. Vos J J (2003). On the cause of disability glare and its dependence on glare angle, age and ocular pigmentation. *Clin Exp Optom* 86:363–70
8. Wooten B R, Geri G A (1987) Psychophysical determination of intraocular light scatter as a function of wavelength. *Vision Res* 27:1291–1298
9. Whitaker D, Steen R, Elliott D B (1993) Light scatter in the normal young, elderly, and cataractous eye demonstrates little wavelength dependency. *Optom Vis Sci* 70:963–968
10. Coppens J E, Franssen L, Van den Berg T J (2006) Wavelength dependence intraocular straylight. *Exp Eye Res* 82:688–692
11. Bach M (2007) The Freiburg Visual Acuity Test-Variability unchanged by post-hoc re-analysis. *Graefes Arch Clin Exp Ophthalmol* 245:965-71
12. Ozolinsh M, Papelba G (2004) Eye cataract simulation using polymer dispersed liquid crystal scattering obstacles. *Ferroelectrics* 304:207–212
13. Franssen L, Coppens J E, van den Berg T J (2006) Compensation comparison method for assessment of retinal straylight. *Invest Ophthalmol Vis Sci* 47:768-76
14. Ozolinsh M, Ikaunieks G, Bueno J M et al. (2004) Human eye photoreceptor acuity at different colour contrast stimuli, Proc., Conference “Basic Problems of Optics”, St. Peterburg, Russia, 2004, pp. 34-35
15. Ozolinsh M, Colomb M, Ikaunieks G et al. (2006) Colour stimuli perception in presence of light scattering. *Vis Neurosci* 23:597–601
16. Blatherwick P, Hallett P E (1992) The discrimination of blur in peripheral colored borders. *Vision Res* 32:1719–1727
17. Bueno J M., Berrio E, Ozolinsh M et al. (2006) Optical properties of a polymer dispersed liquid crystal to be used on visual testing, Proc., ICO Topical Meeting on Optoinformatics/Information Photonics, St. Peterburg, Russia, 2006, pp. 276-278

Author: Gatis Ikaunieks  
 Institute: Department of Optometry and vision science,  
 University of Latvia  
 Street: Kengaraga 8  
 City: Riga  
 Country: Latvia  
 Email: gatis.ikaunieks@lu.lv

# Diffuse Reflectance Spectroscopy During Experimental Radio Frequency Ablation

J.D. Johansson<sup>1</sup>, A. Zerbinati<sup>2</sup> and K. Wårdell<sup>1</sup>

<sup>1</sup> Department of Biomedical Engineering, Linköping University, Linköping, Sweden

<sup>2</sup> Politecnico di Torino, Turin, Italy

**Abstract** — The aim of the study was to investigate the spectral changes during heating and to estimate threshold temperatures for initiation of the thermal coagulation. A brain electrode with optical fibers was used to generate lesions in *ex-vivo* porcine white and gray matter as well as in fat and meat from pork chop. Radio frequency ablation (60 s, 48 – 90 °C, steps of 2-10 °C) was performed while simultaneous spectroscopy measurements were made in the range 490 – 900 nm.

The optical signal recorded from porcine gray and white brain matter was unstable with the reflected light intensity fluctuating a lot. Nevertheless an abrupt increase in light intensity during coagulation in gray matter was found at  $48 \pm 6$  °C ( $n = 21$ ), probably indicating onset of coagulation. The reflected light intensity from white matter showed no consistent behavior during coagulation.

The results for pork chop meat and fat were considerably more consistent. The reflected light intensity from pork chop meat stayed stable up to a mean temperature of  $42.5 \pm 3.5$  °C ( $n = 11$ ). Above this temperature it abruptly increased for all wavelengths. The reflected light intensity from pork chop fat dropped over all wavelengths immediately as the temperature increased and remained low as the fat cooled ( $n = 8$ ).

In conclusion diffuse reflectance spectroscopy appears to be suitable to detect onset of coagulation in muscle tissue and gray matter. The estimated initiation temperature of coagulation varied and was dependent on tissue type.

**Keywords** — radio frequency ablation, diffuse reflectance spectroscopy, brain, muscle, fat

## I. INTRODUCTION

Radio frequency (RF) ablation, or RF lesioning, is a common technique for temperature-controlled thermocoagulation of malfunctioning tissue. It is used in a wide area of organs such as the brain, the heart and the liver. It can be used to disrupt local overactivity that is characteristic to certain forms of heart arrhythmias [1] and neural diseases such as Parkinson's disease [2]. It is also useful for destroying tumors that are not feasible for resection [3]. An alternating current with a sufficiently high frequency not to stimulate nerves or muscles is used to heat up a small volume of tissue around an electrode tip containing a temperature sensor. The measured temperature of the tip is then used to control the current to a desired target temperature in

order to obtain a satisfactory destruction without boiling the tissue.

Recent development of RF-electrodes in our group has implemented optical fibers along the shaft. This makes it possible to perform either reflection spectroscopy or laser Doppler perfusion monitoring simultaneously to RF-lesioning [4]. Our group has also performed modeling and simulation studies on RF lesioning in the brain where a threshold temperature of 60 °C was assumed for onset of coagulation [5, 6] and we would now like to test the validity of this assumption. Optical methods are expected to be suitable for detection of this threshold of coagulation due to the blanching usually induced.

The aim of the study was to investigate the spectral changes of white and gray brain matter as well as pork chop meat and fat during heating and to estimate a threshold for initiation of the coagulation when possible.

## II. MATERIAL AND METHOD

### A. Experimental set-up

A custom-made monopolar RF electrode with optical fibers was used to coagulate the tissue, see Fig. 1. The electrode tip dimensions (length = 2.0 mm, diameter = 1.6 mm) had been specially requested by a neurosurgeon in order to be small without being easily bent. A hole in the bottom of the tip provided a window for 4 parallel optical glass fibers (core diameter = 200  $\mu\text{m}$ , cladding diameter = 230  $\mu\text{m}$ , numerical aperture = 0.22). The electrode was connected to an RF generator (Leksell Neuro<sup>®</sup> Generator, Elekta Instrument AB, Sweden) for temperature-controlled thermocoagulation. Two adjacent fibers were used for spectroscopy. One of the fibers was used to emit white light from a white halogen lamp (AvaLight-Hal-S, Avantes BV, The Netherlands) and the other to collect the diffusely reflected light to a spectrometer (AvaSpec-2048-2, Avantes BV, The Netherlands). This combination of lamp and spectrometer gave spectra that were considered acceptable between the wavelengths,  $\lambda$ , 490 – 900 nm. Temperature,  $T(t)$  (°C), and light intensity of the raw spectra,  $I_{\text{raw}}(\lambda, t)$  (a.u.), over time,  $t$  (s), were recorded to a personal computer using software written in LabView 6.1 (National Instruments Corporation, U.S.).

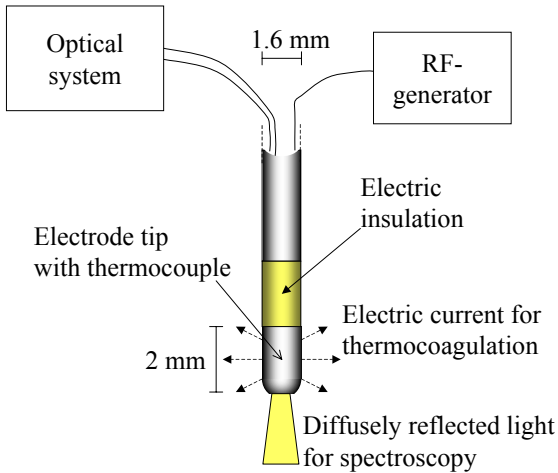


Fig. 1 The RF electrode with optical fibers.

Thermocoagulations were performed in three porcine brains obtained from a slaughterhouse (use approved by the Swedish board of Agriculture, D.O. 38-6097/05) and in pork chops obtained from a local grocery store. The tissue was removed from the storage fridge for some hours prior to the experiments in order for it to obtain an even room temperature. Stable room temperature of the tissue during the measurement series was verified with frequent thermocouple readings (type K, TMD90, Meterman Test Tools). 52 thermocoagulations were performed at temperatures between 50 – 90 °C in steps of 2 – 6 °C in the brain tissue, 11 between 48 – 80 °C in steps of 2 – 10 °C in pork chop meat and 8 between 50 – 80 °C in steps of 10 °C in pork chop fat. The temperature was allowed to rise at a rate of at most 6 °C/s. Thermocoagulations in the pork chop fat were made near muscle tissue and with the tissue soaked by a tiny amount of 0.9 % NaCl solution in order to obtain sufficient electric contact. 5 of the brain thermocoagulations were performed in the cortex.

Calibration measurements,  $I_{cal}(\lambda)$ , were made against a white reference tile (WS-2, Avantes BV, The Netherlands) at a fixed distance in a closed reference model that shut out any background light. Measurements of the dark current level,  $I_{dark}$ , were also made with the lamp blocked.

### B. Data analysis

Data analysis was made in MatLab 7.5 (The Mathworks Inc., U.S.). Normalized intensities,  $I(\lambda, t)$ , for each measurement were made according to

$$I = \frac{I_{raw}(\lambda, t) - I_{dark}}{I_{cal}(\lambda) - I_{dark}} \quad (1)$$

Brain tissue with similar mean  $I$  before heating as cortex tissue was assumed to be gray. Brain tissue with twice the  $I$  of cortex tissue before heating was assumed to be white. Rapid changes in light intensity were noted and compared to the measured temperature of the electrode tip at the same time. Coagulation onset was assumed to appear as a rapid and irreversible increase in  $I$ . Mean values and standard deviations (mean  $\pm$  s.d.) of the temperatures for such increases were calculated for the different tissue types.

## III. RESULTS

Changes in reflected light intensity were very similar for all measured wavelengths. A somewhat different behavior of wavelengths beneath 600 nm corresponding to high light absorption in blood could be seen however. Examples of temperature and mean reflected light intensity in the wavelength bands 560 – 585 nm,  $I_{560-585}$ , and 770 – 790 nm,  $I_{770-790}$ , are presented for the different tissue types in Fig. 2 – 5.

Abrupt increases of  $I$  for brain, see Fig. 2, could be seen in 21 thermocoagulations at threshold temperatures of  $48 \pm 6$  °C. All these were corresponding to gray matter with a target temperature of at least 60 °C.  $I$  also increased for 2 gray matter coagulations at a target temperature of 56 °C but no abrupt threshold could be seen. 15 coagulations were estimated to be in white brain matter. While  $I$  changed during heating, see Fig. 3, no obvious pattern could be seen and  $I$  could be both higher and lower after coagulation compared to before.

Abrupt increases of  $I$  for pork chop meat, see Fig. 4, could be seen in all 11 thermocoagulations at threshold temperatures of  $42.5 \pm 3.5$  °C.  $I$  immediately decreased

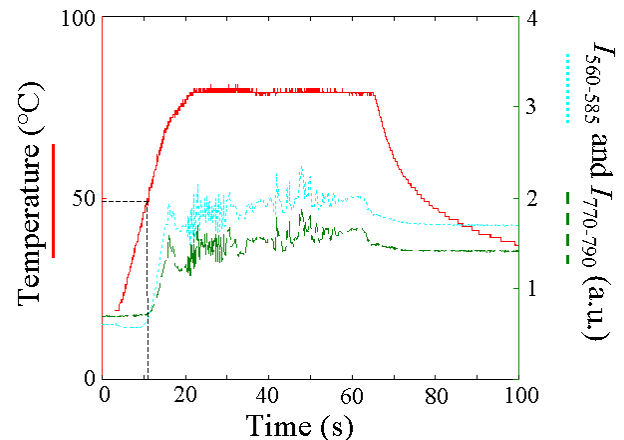


Fig. 2 Example of heating in gray brain matter. The reflected light intensity remains stable until a threshold temperature is reached where it increases abruptly. The signal is fairly unstable thereafter.

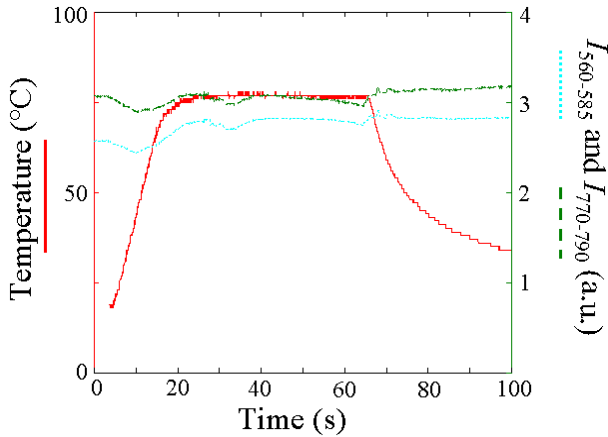


Fig. 3 Example of heating of white brain matter. No larger typical changes in light intensity were found in this study.

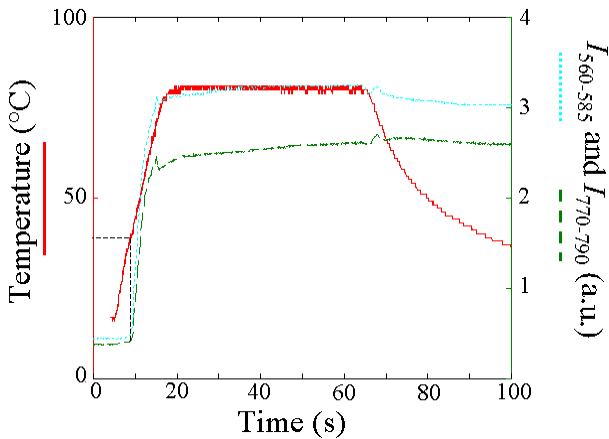


Fig. 4 Example of heating in pork chop meat. The reflected light intensity remains stable until a threshold temperature is reached where it increases abruptly. The signal is fairly stable thereafter.

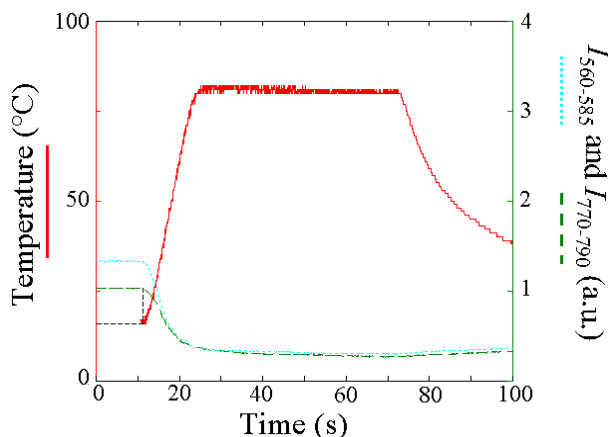


Fig. 5 Example of heating in pork chop fat. The reflected light intensity immediately drops when heating starts and remains stable thereafter.

upon onset of heating and remained lower after cooling for all 8 measurements in pork chop fat, see Fig. 5.

#### IV. DISCUSSION

Skeletal muscle tissue has high protein content (reported values of ~17.9 – 21.3 %) and low lipid content (~1.6 – 6.8 %). Gray brain matter has lower but still quite high protein content (~8 – 12 %) and low lipid content (~5.3 %) while white brain matter has a quite high content of both proteins (~11-12 %) and lipids (~18 %) [7]. The reflected light intensity,  $I$ , from the pork chop meat and gray brain matter increased due to the thermocoagulation while it decreased for the pork chop fat. A hypothesis for the lack of detectable coagulation threshold for white matter may thus be that the effects of heating on the proteins and lipids cancel each other out to varying degrees here. A study on created mixtures with varying controlled protein and lipid content may be useful for testing this.

The coagulations in gray matter are difficult to see visually unless a target temperature of 70 °C or more is used, hence the choice of such temperatures. The optical fibers however are much more sensitive and the onset of coagulation seems to be considerably lower. For future studies a lower temperature range thus is recommended.

The temperature measured in the electrode tip may be somewhat behind in time compared to the temperature of the surrounding tissue. It is thus possible that this study underestimates the threshold temperatures for onset of coagulation. It may be preferable to lower the rate of the increase towards the target temperature in order to reduce such potential errors. Nevertheless, it seems likely that the assumed temperature of 60 °C for coagulation earlier used by us in simulation studies may be too high for porcine gray matter.

Spectroscopy by our group before and after thermocoagulation in porcine thalamus has showed a similar behavior as this study in the wavelength range 500 – 1000 nm with an even increase in light intensity above 600 nm and a somewhat larger increase at 500 – 600 nm after coagulation [8]. The deviating behavior at 500 – 600 nm could be due to residual blood in the *ex-vivo* tissue. Thermocoagulation has also been shown to increase the scattering properties of heart [9] and liver tissue [10] in this wavelength range.

#### V. CONCLUSIONS

The optical electrode seems suitable for verification of coagulation in gray brain matter and muscle tissue but not in white brain matter. Estimated threshold temperatures for

gray matter and pork chop meat were  $48 \pm 6$  °C and  $42.5 \pm 3.5$  °C respectively but these may be underestimations.

#### ACKNOWLEDGMENT

We would like to thank Blå kustens kontrollslakteri AB (Sweden) for provision of the brains and M.Sc. Carina Fors for aid with programming in MatLab and LabView.

#### REFERENCES

- [1] S. Martin-Suarez, B. Claysset, L. Botta, M. Ferlito, D. Pacini, C. Savini, G. Marinelli, and R. DiBartolomeo, "Surgery for atrial fibrillation with radiofrequency ablation: four years experience", *Interact Cardiovasc Thorac Surg*, vol. 6, pp. 71-6, 2007.
- [2] E. Cosman, "Radiofrequency lesions", in *Textbook of Stereotactic and Functional Neurosurgery*, P. L. Gildenberg and R. Tasker, Eds. Kingsport: Quebecor Printing, 1996, pp. 973-985.
- [3] S. N. Goldberg, "Radiofrequency tumor ablation: principles and techniques", *Eur J Ultrasound*, vol. 13, pp. 129-147, 2001.
- [4] J. Antonsson, *On optical methods for intracerebral measurements during stereotactic and functional neurosurgery*, PhD dissertation No. 1070, Department of Biomedical Engineering, Linköping University, Linköping, 2007.
- [5] J. D. Johansson, O. Eriksson, J. Wren, D. Loyd, and K. Wårdell, "Radio-frequency lesioning in brain tissue with coagulation-dependent thermal conductivity - modelling, simulation and analysis of parameter influence and interaction", *Medical & Biological Engineering & Computing*, vol. 44, pp. 757-766, 2006.
- [6] J. D. Johansson, D. Loyd, K. Wårdell, and J. Wren, "Impact of cysts during radio frequency (RF) lesioning in deep brain structures - a simulation and in-vitro study", 2006.
- [7] A. F. Duck, *Physical properties of tissue*. Cambridge: The University Press, 1990.
- [8] O. Eriksson and K. Wårdell, "Optical changes as a marker for lesion size estimation during radio frequency ablation: a model study", presented at Biomedical Diagnostic, Guidance, and Surgical-Assist Systems III, San Jose, CA, USA, pp. 164-171, 2001.
- [9] J. Swartling, S. Palsson, P. Platonov, S. B. Olsson, and S. Andersson-Engels, "Changes in tissue optical properties due to radio-frequency ablation of myocardium", in *Medical & Biological Engineering & Computing*, vol. 41, 2003, pp. 403-409.
- [10] Roggan, *Dosimetrie thermischer Laseranwendungen in der Medizin*. Berlin: ecomed.

Address of the corresponding author:

Author: Johannes D. Johansson  
 Institute: Linköping University  
 Street: Department of Biomedical Engineering  
 City: Linköping  
 Country: Sweden  
 Email: johjo@imt.liu.se

# Closed-Feedback Control of Laser Soldering of Rat Skin Using Diode Laser

M.E. Khosroshahi<sup>1</sup>, M.S. Nourbakhsh<sup>1</sup>, S. Saremi<sup>1</sup> and F. Tabatabaee<sup>2</sup>

<sup>1</sup>Faculty of Biomedical Engineering, Amirkabir University of Technology, Tehran, Iran

<sup>2</sup>Biomechanics Department, University of Social Welfare & Rehabilitation Sciences, Tehran, Iran

**Abstract** — Tissue laser soldering is a method of closure of incisions that in principle may have advantages over conventional closure methods. It is a non-contact technique, continuous and watertight and the procedure is faster and requires less skill to master. However, in practice there have been difficulties in obtaining strong and reliable welding. The quality of the weld depends on the ability to monitor and control the surface temperature of soldering zone during the procedure. Our goal was to use laser soldering to seal cuts in rat skin under temperature feed-back control and compare the results with standard sutures. Full-thickness incision created on the dorsum of rats and albumin solder with Indocyanine-Green (ICG) dye was added between the incision edges and photothermally coagulated with diode laser. We have developed an automated soldering system based on diode laser, IR detector, photodiode, digital thermocouple and camera. The true temperature of the heated tissue was determined by using and improved calibration software method. Laser soldering was carried out spot by spot until it reached a preset value of 70-75°C at each point. The tensile strength of laser soldered cuts was measured after 2-10 days postoperatively and was found comparable to that of sutured cuts. Histopathological studies showed better healing and less inflammatory reactions than that caused by standard sutures after 7<sup>th</sup> day.

**Keywords** — Laser soldering, Feedback control, Histopathology, Wound Healing

## I. INTRODUCTION

Advanced systems are currently being evaluated for real time monitoring and control in medical procedures involving laser [1]. These systems generally consist of a sensor capable of rapidly measuring a tissue parameters coupled to a feedback loop that adjusts the laser parameters. The response time of this type of system can usually be significantly fast.

Sensor can be used to monitor tissue parameters not visually discernible. One such parameter being studied for feedback control is surface temperature [2].

In these procedures a laser is used as a source of heat to cause thermal denaturation of the illuminated tissue proteins. In the case of tissue photocoagulation, several variables can influence the clinical results.

For instance, disparities in tissue properties can cause differences in the absorption characteristics. The fluence in

the tissue can vary significantly for identical procedures, if the laser spot sizes or energy delivery rate is varied. These differences will cause the tissue temperature to fluctuate during laser procedure. Since the thermal damage to the irradiated tissue is strongly dependant on the evaluated temperature achieved during the laser soldering process, hence the resultant surgical outcome is highly variable [3].

A typical endpoint for laser soldering is the bleaching of tissue which occurs when soft tissue is heated above its denaturation temperature. This is not instantaneous at temperature below 90° C but occurs after a time delay, which increases with decreasing temperature [4]. Visual control of photocoagulation at tissue temperatures above 90°C is likewise extremely difficult and can often lead to tissue charring which can result in impaired healing at repaired site.

This study describes the use of closed feedback control systems for an ex-vivo laser soldering of skin. We believe that temperature dependence of laser soldering could be quantified by studying the biomechanical properties of tissue. In addition the histopathological evaluations were also performed to determine the pattern of wound headlining.

## II. MATERIAL AND METHODS

We developed a system for real time monitoring and control of the temperature of spot in tissue surface (Figure 1).



Fig. 1 An example of experimental setup for rat irradiation



The heated spot emits an infrared radiation whose intensity (I) is determined by temperature (T). The intensity is monitored and a feedback loop controls the laser power so that the surface temperature is stabilized at some set value.

The system includes the following: (1) a diode laser with emission at  $\lambda=810$  nm, (2) a pyroelectric IR detector which converts the emitted intensity (I) to an electrical signal. This signal is proportional to the tissue surface temperature (T), (3) a photodiode, (4) a computer which analyses the signal and determines the correct surface temperature. The temperature control is based on the feedback algorithm which sends a signal defined and varies correspondingly by the laser power.

8 male rats weighing 250-300 gr were used. They were divided to two groups of 4. The rats were anesthetized with Ketamine (90mg/kg). Their dorsal skin was shaved and depilated using Nair cream. Four cuts, each 2cm long were made on the upper and middle portions using 11" blades. Two of cuts were laser soldered and other two which served as a control group were sutured. For laser soldering the cut edges were brought close using a small clam on the distal portion of the cut. A drop of solder (1.25mg/cc ICG + 1.25gr/cc albumin) was placed upon the cut line. The temperature control was preset to 70°C. The bonding technique used was spot soldering. For the control group the cuts were sutured with silk.

The animals were anesthetized after 2, 5, 7 and 10 days postoperatively. An area of the skin with the repaired (soldered or sutured) incision in the middle was harvested. Some sections were used for biomechanical measurement and other for histological examinations.

The 16 healed skin specimen were tested using a load machine (Zwick/Roell, HCT 25/400 series). Strips were inserted into the head of loading machine and tensile strength measurement was carried out at a rate of 5mm/min. For histological examination, sections of the soldered tissue were first fixed in 10 % formaldehyde solution and routinely processed. They were then stained by hematoxyline and eosine for histological examination.

### III. RESULTS

The yield strength,  $\sigma_t$ , was measured for the 16 sections that were harvested between day 2 and day 10 postoperatively (2 samples in each subcategory).  $\sigma_t$  of soldered and suture cuts are shown in Figure 2. At first day the  $\sigma_t$  of soldered repairs was lower than sutured cuts but increased rapidly after day 7.

The energy of rupture of the repaired skin is shown in Figure 3. It shows that the skin tenacity of soldered skin is more similar to the normal skin and has a linear behavior,

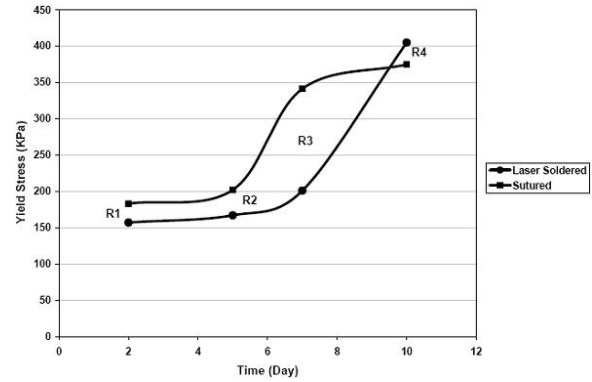


Fig. 2 Yield strength of soldered versus sutured rat skin

but in the case of sutured skin the skin tenacity highly fluctuated.

We found the soldered scar were cosmetically better looking than sutured scars. Pathological results showed a significant difference between collagen structural formation in soldered and sutured cuts.

The pathological results for laser soldered and sutured skin after 10 days are shown in Figure 4 and 5. Very mild thermal injury was seen on day 2 in soldered scars, but from day 7 on, there was no evidence of thermal damage in all to the tissues. No carbonaceous substance was seen over the epidermis. Albumin was seen at day 2 in about 40% of the soldered cuts, but from day 7 on there was no evidence of its presence. The degree of re-epithelization was similar in both soldered and sutured scars, and it reached its maximal degree on day 7 postoperatively.

Overall, in the soldered scars, the process of wound healing is faster and more effective, which is one of the many advantages of our technique

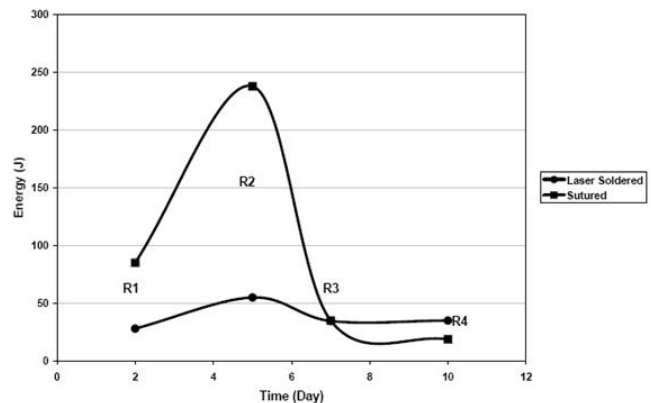


Fig. 3 Energy of rupture for soldered and sutured cuts

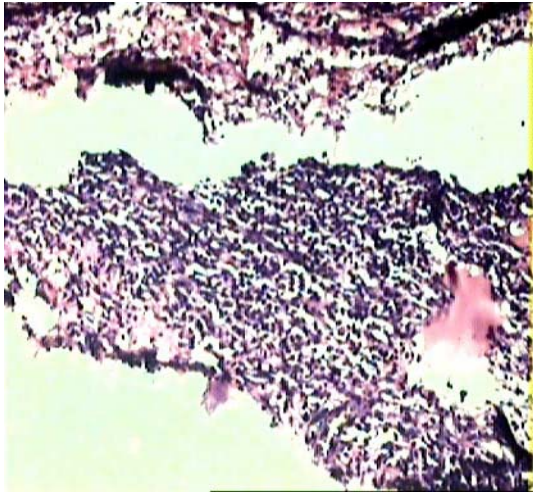


Fig. 4 Wound healing after 10 days in soldered scar

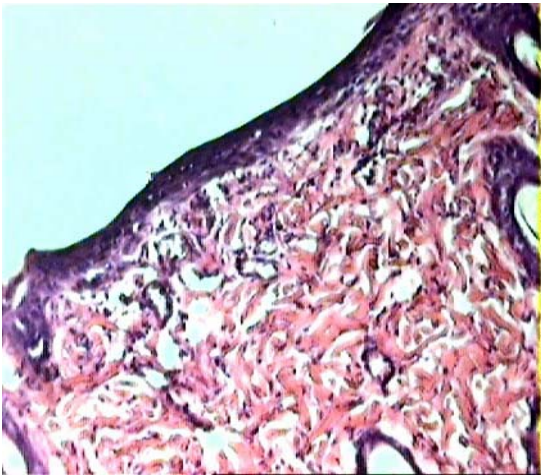


Fig. 5 Wound healing after 10 days is sutured scar

#### IV. DISCUSSION

One of the important factors to be considered for soldering is the type of laser being used. In this work a diode laser with wavelength 810nm which is highly absorbed by ICG was chosen. The absorption coefficient  $\alpha_{ab}$  of ICG for this wavelength is  $2 \times 10^5 \text{ cm}^{-1}/\text{Mol}$ [5].

Tensile strength was measured on the days 2, 5, 7 and 10. We found on day 2 post operatively a tensile strength of 150

Kpa which is to the best of our knowledge sufficient to hold tissue together [6].

The average value of  $\sigma_t$  for the soldered cut was comparable to the sutured cuts from day 2 to day 10. We did not observe any rupture of scars in our rats. The scars showed very good overall uniformity in tensile strength.

#### V. CONCLUSION

The main goal of this study was to test a closed feedback controlled laser soldering system in order to accomplish reliable, fast and strong bonding of cuts in skin. We demonstrated that our laser soldering technique for bonding cuts in skin is practical. It is better than standards suturing technique as far as healing, scar formation, inflammation and the operation time are concerned. The performance of the laser soldering system was reliable and it produced reproducible uniform results.

#### ACKNOWLEDGMENT

The authors are grateful to the High-Tech Industries Center-Optics group of Iran for supporting this work.

#### REFERENCES

1. Dix P, Poppas, Robert B. et al (1996) Temperature-controlled laser photocoagulation of soft tissue: In vivo evaluation using a tissue welding model. *Lasers in Surgery and Medicine* 18: 335-344
2. Bernard Lobel, et al (2000) Temperature controlled CO2 laser welding of soft tissues: Urinary bladder welding in different animal models (rats, rabbits, and cats). *Lasers in Surgery and Medicine*.26:4-12
3. Yoko Kamegaya, William A. Farinelli (2005), Evaluation of photochemical tissue bonding for closure of skin incisions and excisions. *Lasers in Surgery and Medicine* 37: 264-270.
4. D. Simhon, A. Ravid et al.(2001), Laser soldering of rat skin, using fiberoptic temperature controlled system. *Lasers in Surgery and Medicine* 29,267-273
5. Optical Absorption of ICG at <http://omlc.ogi.edu/spectra/icg>
6. Maish GO III, Shumate ML, Ehrlich HP, Cooney RN(1998). Tumor necrosis factor binding protein improves incisional woundhealing in sepsis, *J Surg Res* 78:108-117.

Author: M.E.Khosroshahi  
 Institute: Amirkabir University of Technology  
 Street: Hafez Ave  
 City: Tehran  
 Country: Iran  
 Email: khosro@aut.ac.ir

# Characterization of Input-Output Relations in Single Neurons using Spatiotemporal Photo-stimulation

M. Krumin<sup>1</sup> and S. Shoham<sup>1</sup>

<sup>1</sup> Technion – IIT, Faculty of Biomedical Engineering, Haifa, Israel

**Abstract** — We are pursuing a hybrid optical-electrophysiological-computational approach for studying and modeling neuronal input-output transformations in CNS neurons *in vitro* under increasingly realistic conditions. Our approach combines two-photon glutamate uncaging, which enables non-invasive stimulation of neurons with single synapse specificity, and rapid three-dimensional hopping between many different uncaging locations (termed "patterned uncaging"). The input sequences used are doubly stochastic Poisson point processes with predefined custom auto- and cross-correlation functions, generated using a new method we developed.

Our experiments quantitatively analyze the role of the input correlation structure on dendritic integration in CNS neurons by experimentally mimicking natural synaptic activity while simultaneously electrically measuring the output soma potentials.

**Keywords**— two-photon, glutamate uncaging, dendritic integration, correlations, doubly stochastic Poisson

## I. INTRODUCTION

The functional properties of Central Nervous System neurons are the subject of numerous experimental and computational investigations. A major theme in these studies is an attempt to capture the integrative properties (input-output relationship) of neurons using a relatively simple reduced mathematical model, which can then be used in network models[1]. These studies typically involve complex multi-compartment biophysical model simulations [2], or *in vitro* electrical stimulation experiments[3]. Computational studies on complex models give an opportunity to conduct arbitrarily sophisticated 'experiments'. However, these complex multi-compartment biophysical models may have hundreds to thousands of specific parameters that are not sufficiently constrained by existing experimental data.

The powerful technique of two-photon glutamate uncaging enables non-contact stimulation of neurons with single synapse specificity[4]. Rapid hopping with high temporal resolution between many different uncaging locations (termed "patterned uncaging"[5]) on the *three-dimensional* dendritic tree expands the ability of this technique to mimic natural synaptic activity with high spatial and temporal resolution. This paper presents an outline of our approach: combining patterned two photon uncaging with a new ap-

proach for flexibly controlling the multi-correlation structure of input firing patterns.

## II. EXPERIMENTAL SETUP

Our experimental system consists of a custom-made two-photon laser scanning microscope [6], integrated with a brain-slice electrophysiology system. Our optical system (Fig. 1) uses a tunable Ti:Sapphire mode-locked femtosecond laser (Mai Tai, Spectra Physics; wavelength range: 710-920nm). Two dimensional scanning (in imaging mode) and 2D random-access hopping (in photo-stimulation mode) is achieved by steering the incident beam with galvanometric mirrors (Model 6210, Cambridge Technologies). Precise, rapid motion in the axial dimension is achieved by a piezoelectric element (MIPOS 500 model, piezosystem jena GmbH, Jena, Germany) with a travel range of 500 $\mu$ m that is mounted on the objective lens (Nikon CFI APO x60 water immersion NA 1.0). A Pockels cell EOM is used for laser intensity attenuation and rapid laser shuttering during photo-activation with microsecond precision. The system also includes an IR imaging "Dodt tube", which provides a high-quality phase contrast capability for neuron visualization and targeting.

Custom software written in Matlab (MathWorks Inc., Natick, MA) and based on ScanImage [7] is used to control

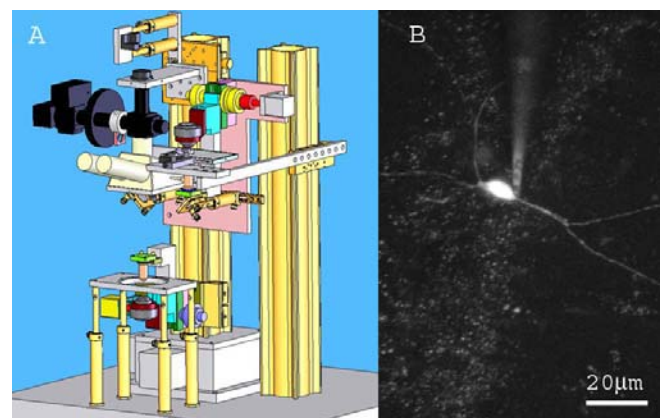


Fig. 1. Optical system. A. The microscope's CAD model . B. Image of a neuron intracellularly stained with the fluorescent dye Alexa 488.

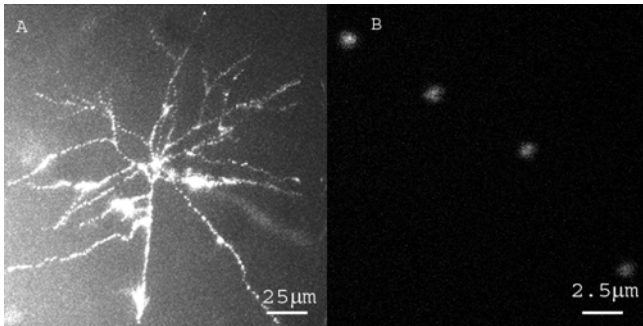


Fig. 2. Targeted random-access Uncaging. A. A sample containing dry caged fluorescein was uncaged by 710nm laser pulses at the predefined locations and then imaged at 920nm. Only regions where uncaging occurred are fluorescent. Roughly a thousand of uncaging locations are distributed in 3D creating complex predefined three-dimensional pattern. Depth of z-axis  $\sim 150\mu\text{m}$ . B. A small number of locations, sub-micron resolution of uncaging is achieved.

the system, acquire images and perform patterned photo-stimulation through data acquisition boards and serial communication PC ports using a single graphical user interface (GUI). A second User Interface is used to control the electrophysiology system.

This experimental system can perform rapid patterned photo-stimulation with sub millisecond temporal and sub-micron spatial precision (Fig. 2).

### III. CONTROLLING INPUT CORRELATIONS

Emerging evidence indicates that information processing as well as learning and memory processes in both the network and single- neuron levels are highly dependent on the correlation structure of multiple spike trains. There is therefore much interest in how the correlation structure of pre-synaptic activity affects the way neural input is processed by the dendrites of single cells. In order to conduct a systematic study of these effects we need the ability to provide neural input with specific and tunable degrees of correlation. The main difficulty in this task is that neural activity has a sparse structure (spike trains; mathematically: point processes) for which classical signal processing tools are typically inapplicable. The generation of spike trains with controlled mean rates and pre-defined *correlation coefficients* (reflecting an overall level of synchrony) has recently been addressed by Niebur[8]. The more general (and interesting) case includes pre-defined *correlation functions* between spike trains (allowing for temporally structured correlations). We have developed a strategy for generating stationary and non-stationary doubly stochastic Poisson

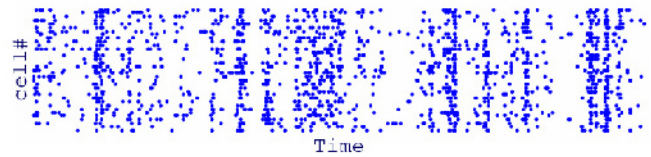


Fig. 3. Presynaptic network activity. Firing of 35 cells was generated with a predefined multi-correlation structure that results in spontaneous synchronization between spike trains.

point processes with controlled mean rates and predefined auto- and cross-correlation functions (manuscript in preparation). Our approach enables flexible control over the correlation structure of simulated presynaptic activity. This method allows us to address the question of the impact of input correlations on dendritic integration in a systematic and quantitative way.

### ACKNOWLEDGMENT

This work is supported by Israeli Science Foundation grant # 1248/06. We thank Avner Shimron for valuable assistance and discussions.

### REFERENCES

1. Hausser, M., and Mel, B. (2003). Dendrites: bug or feature? *Current Opinion in Neurobiology* 13, 372-383.
2. Poirazi, P., Brannon, T., and Mel, B. W. (2003). Pyramidal Neuron as Two-Layer Neural Network. *Neuron* 37, 989-999.
3. Magee, J. C. (2000). Dendritic Integration of Excitatory Synaptic Input. *Nature Reviews Neuroscience* 1, 181-190.
4. Matsuzaki, M., Ellis-Davies, G. C. R., Nemoto, T., Miyashita, Y., Iino, M., and Kasai, H. (2001). Dendritic spine geometry is critical for AMPA receptor expression in hippocampal CA1 pyramidal neurons. *Nat Neurosci* 4, 1086-1092.
5. Shoham, S., O'Connor, D. H., Sarkisov, D. V., and Wang, S. S. H. (2005). Rapid neurotransmitter uncaging in spatially defined patterns. *Nat Meth* 2, 837-843.
6. Tsai, P. S., Nishimura, N., J., Y. E., Dolnick, E. M., White, G. A., and Kleinfeld, D. (2002). Principles, Design, and Construction of a Two-Photon Laser-Scanning Microscope for In Vitro and In Vivo Brain Imaging. In *In Vivo Optical Imaging of Brain Function*, R. D. Frostig, ed. (CRC Press), pp. 113-171.
7. Pologruto, T., Sabatini, B., and Svoboda, K. (2003). ScanImage: Flexible software for operating laser scanning microscopes. *BioMedical Engineering OnLine* 2, 13.
8. Niebur, E. (2007). Generation of Synthetic Spike Trains with Defined Pairwise Correlations. *Neural Comp* 19, 1720-1738.

Author: Shy Shoham  
 Institute: Faculty of Biomedical Engineering, Technion IIT  
 City: Haifa  
 Country: Israel  
 Email: sshoham@bm.technion.ac.il

# Sensor for Measurement of Wear in Total Hip Arthroplasty

D. Mandat<sup>1</sup>, M. Hrabovsky<sup>1</sup>, V. Havranek<sup>1</sup>, M. Pochmon<sup>1</sup>, T. Rossler<sup>2</sup>, J. Gallo<sup>3</sup>

<sup>1</sup> Joint laboratory of optics UP and FZU AS CZ, Olomouc, Czech Republic

<sup>2</sup> Palacky Univ./ Fac. of Natural Sciences/Dept. of Experimental Physics, Olomouc, Czech Republic

<sup>3</sup> University Hospital, Palacky Univ., Fac. of Medicine and Dentistry/ Department of Orthopedics, Olomouc, Czech Republic

**Abstract** — This article treats of measurements of the total deformation of polyethylen cotyles ABG I of coxa by means of the optical topography method. The total deformation is considered as a combination of the plastic deformation and the real diminution of the artificial cotyle material due to usage of a hip replacement. We use 3D scanning topography to measure surface geometry of cotyle. The sensor consists of optical source, digital camera, rotating stage and linear stage. We use LabView to control the measurement and Matlab to compute the result. We want to measure the set of more then 200 cotyle samples.

**Keywords** — Cotyle ABG I, 3D Topography, LabView, Matlab, total deformation.

## I. INTRODUCTION

Total hip arthroplasty significantly improves the quality of life in majority of patients with osteoarthritis. However, prosthetic wear is a problem because of inducing the development of aseptic loosening and periprosthetic osteolysis which needs revision surgery. The paper gives principles of one method usable for construction of a device for the non-contact prosthetic wear measurement. We tested three possible measuring methods. 3D scanning topography, Fourier profilometry and measuring microscope. From the point of view of the repeatability, the scanning profilometry is more acceptable.

## II. ARTHROPLASTY

Total hip arthroplasty is one of the most successful therapies with regard to achieved quality of life and risk-benefit analysis. Previously it was found that polyethylene wear particles initiate cascades of events at the bone-implant interface that result in development of aseptic loosening and osteolysis. At first non-radiologic (in vitro) and radiologic (in vivo) methods for polyethylene wear quantification were proposed. The volumetric wear can be obtained by mathematical conversion based on the most linear shift of femoral head in the cup. In vivo using X-ray scan (the sensitivity and accuracy is very low). This method can be used for periodic control during patient usage. In vitro methods are based on contact or noncontact measurements.



Fig. 1 Hip arthroplasty

With regard to geometry of cotyle we decided to use 3D topography. The cotyle is axially symmetrical (e.g. Fig. 1). We can rotate with the sample and measure topography of the cotyle. The principle of wear measurement is based on the determination of the 3D profile map of retrieved cup. The full wear map is obtained by comparing shape of the post-used cup with the shape of original one.

## III. 3D SCANNING TOPOGRAPHY

The 3D scanning topography is based on laser beam passes through an optical system. This optical system transforms the laser beam to a strip, focused in the tangential plane close to the reference plane (e.g. Fig. 2). The knowledge of the strip shape in the detection plane enables us to determine the surface shape of the measured object. Experimental setup by Asundi [1].

The topographic depth  $\Delta r$  can we write as:

$$\Delta r = c_1 \Delta u - c_2 (\Delta u)^2, \quad (1)$$

or:

$$\Delta r = \frac{\Delta u}{b + a \Delta u}, \quad (2)$$

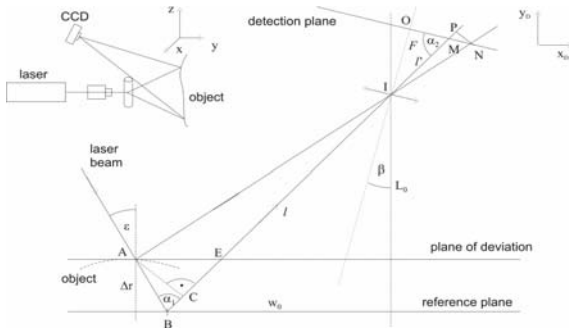


Fig. 2 Setup of the experiment

$a, b$  are parameters of the mapping algorithm,  $c_1, c_2$  are parameters of sensitivity.

Measurement error  $\delta(\Delta r)$  is given to expression:

$$\delta(\Delta r) = |c_1 - 2c_2\Delta u| \delta(\Delta u) + |\Delta u| \delta c_1 + (\Delta u)^2 \delta c_2 \quad (3)$$

For example: experimental values  $\Delta u = 50$  pix,  $c_1 = 0.410$  mm/pix,  $c_2 = 0.000010$  mm/pix<sup>2</sup>,  $c_2 = 0.000043$  mm/pix<sup>2</sup>. The estimate of the mean square error  $\delta(\Delta r)$  is then equal to 0.475 mm. That value includes the sensitivity of the experimental setup  $c = 0,410$ mm.

The calculation of the wanted surface deviation  $\Delta r$  is carried out as the arithmetic mean of measured values  $\Delta r_i$  relative to each reference plane defined at calibration. The typical plane number is twenty. This way we are able to make the measurement accuracy better and to get under the sensitivity threshold  $c$  of the experimental setup.

The first step of this experiment is the calibration of the configuration [2]. We move a calibration object to define reference planes. The second step is the capturing of the object profiles. The last step is the computing of the dimension.

The analysis consists of following steps:

- Threshold and removal of spurious bright grains by means of morphology,
- Determination of the strip centre by means of weight averaging,
- Analysis of the strip position on the socket and its approximation by a polynomial of first degree,
- Determination of the centre of the cotyle image and of the scale factor,
- Completion of missing points in the cotyle image in case of shading.

The cup or the strip is rotated to cover the whole area of the measured surface. The magnitude of step influences the resolution and sensitivity of the method. The record and the analysis are repeated consequently. The result whole-field profile is obtained connecting the individual linear profiles.

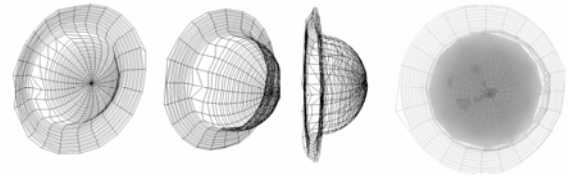


Fig. 3 WRML model of cotyle (last model with spherical etalon)

The result of this proceeding is a file of points on the surface with three dimensional coordinates. The very last step is the visualization of the scanning object. We use an international language to make virtual models WRML (e.g. Fig. 3). In some cases we put the data from measured object and an etalon object in this virtual space to see differences between their surfaces.

#### IV. THE SENSOR

We have a set of more than 200 cotyles to compute the material loss. Automation of the measurement process increase time of analysis. We developed new sensor for 3D automation measurement of used cotyles. The sensor consists of 2 motorized axis, motion control unit, digital camera, light source, computer and software. The calibration process uses motorized translation stage to capture and then compute the calibration planes. Rotary stage is used during data measurement process. We rotate with the sample around it's axis of symmetry in range of  $0 \div 179$  degrees. Whole system is controlled by LabView (e.g. Fig. 4) and analysis by Matlab. We synchronize movement of the sample with digital camera. The picture of single profile is analyzed using out personal Matlab scripts. The program calculates the capacity of measured cotyle. Comparing with etalon (unused one) we get the value of material loss.

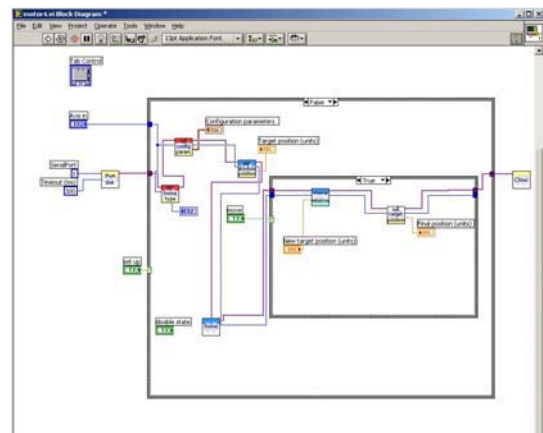


Fig. 4 LabView motion control software for rotary stage

## V. CONCLUSIONS

Primary the fact that the repeatability is lower together with simpler image and data processing and acceptable accuracy led us to the decision to construct the sensor of the total wear based on the principle of the scanning profilometry. The automation of rotating of the specimen and the coordination with recording by the camera will be carried out to decrease the total duration of the whole measurement process.

## ACKNOWLEDGMENT

That results of the project 1M06002 was supported by The Ministry of Education of the Czech Republic. That results of the project OC168 COST was supported by project of The Ministry of Education of the Czech Republic.

## REFERENCES

1. Asundi A, Sajan M R, . (1999) Mapping algorithm for 360-deg. Profilometry with time delayed integration imaging.. *Optical Engineering* 38, 339-343.
2. Rossler T, Pochmon M, . (2006) Calibration of topographic and profilometric methods using the prism normal measurement. In Miler, M (eds) 15<sup>th</sup> Czech-Polish-Slovak Conference of quantum and..., SPIE vol. 6609, ISBN 9780819467485
3. Mandat D, Rossler T, Pochmon M,. Validation of 3D scanning profilometry using total knee arthroplasty sample. In Miler, M (eds) 15<sup>th</sup> Czech-Polish-Slovak Conference of quantum and..., SPIE vol. 6609, ISBN 9780819467485

Author:

Institute: Joint Laboratory of Optics UP and FZU ASCZ

Street: 17. Listopadu 50

City: Olomouc

Country: Czech Republic

Email: [mandat@jointlab.upol.cz](mailto:mandat@jointlab.upol.cz)

# Effects of Static and Dynamic Modes on Laser Tissue Soldering: An In-vitro Study

M.S. Nourbakhsh<sup>1</sup>, M.E. Khosroshahi<sup>1</sup>, S. Saremi<sup>1</sup> and F. Tabatabaee<sup>2</sup>

<sup>1</sup>Faculty of Biomedical Engineering, Amirkabir University of Technology, Tehran, Iran

<sup>2</sup>Biomechanics Department, University of Social Welfare & Rehabilitation Sciences, Tehran, Iran

**Abstract** — Laser tissue soldering based on protein as biological glues and other compounds can provide greater bond strength and less collateral damage. Endogenous and exogenous materials such as indocyanine green (ICG) are often added to solders to enhance light absorption. The purpose of this study was to examine the impact of static and dynamic modes of laser soldering on the thermo-physical properties of the sheep skin. A mixture of albumin solder and ICG was prepared with the ratio of 1000:1 and then the coated samples were irradiated by a diode laser ( $\approx 800\text{nm}$ ) at different conditions. Temperature rise, number of scan (Ns), and scan velocity (Vs) were investigated in dynamic mode. The results showed that at each laser power density (I) the tissue tensile strength ( $\sigma_t$ ) of cuts repaired in dynamic mode is higher than static mode. However, in practice to have an optimal condition for skin closure the above parameters must be carefully studied. In our case, the results showed that the  $\sigma_t$  increases by increasing both Ns and I. But, also it has been equally shown that at lower Vs, hence higher temperature, a higher value of  $\sigma_t$  is achieved. It is therefore imperative to consider the trade off between the scan and the surface temperature for achieving the optimum operating condition. Finally, it is tentatively concluded that the skin temperature should not exceed  $90^\circ\text{C}$  at any time of work, then the acceptable conditions in our experiment correspond to  $I = 47 \text{ Wcm}^{-2}$ ,  $\sigma_t = 300\text{gr}$ ,  $Ns = 8$ ,  $Vs = 0.3\text{mm}^{-1}$ .

**Keywords** — Tissue soldering, Diode laser, ICG, Tensile strength, Static and dynamic mode

## I. INTRODUCTION

There have been two fundamental approaches to laser – assisted bonding of tissue: laser welding which is heating the approximated edges of cuts in tissue by a laser beam and laser soldering which involves heating a biological solder on the approximated edge of tissue. Both techniques are very promising surgical techniques [1, 2]. They are in principle, faster and easier to master than suturing and to form an immediate water-tight seal. Also they are less traumatic to tissue because they cause much less foreign body reactions.

Laser soldering has been carried out using various types of solders. In some cases a colouring dye was added to the solder, to increase the absorption of the laser irradiation in the solder [3, 4]. McNally et al. [5] used laser soldering with

dye enhanced albumin of different concentrations. They found that the highest immediate tensile strength (measured by weight bearing system) was achieved with 60% bovine serum albumin, when the surface was heated to  $85^\circ\text{C}$ .

There are three main drawbacks to laser welding: (a) the immediate tensile strength, during the first few days is low [6, 7]; (b) there is often a noticeable thermal damage; (c) the results are frequently inconsistent. The addition of chromophore-enhanced protein solders to augment laser repair procedures significantly reduces the problems of low strength and thermal damage associated with laser tissue welding techniques. The most notable of these is an indocyanine green (ICG) - doped albumin protein solder used in conjunction with an 808nm diode laser to repair tissue [8, 9, 10].

The purpose of this study was to use 810nm diode laser with biological solder combination of ICG and BSA for closure of an incision in the model of sheep skin and evaluate the effect of laser parameters, number of scans and scan velocity on the tensile strength of the soldered incision.

## II. MATERIALS AND METHOD

A piece of sheep skin was obtained from a slaughter house and depilated suitably, using a depilation cream (Nair). After preparation, a full thickness  $2.20 \text{ mm}^2$  cut was made on the skin using 11" blades. Protein solder solution was prepared from 25% BSA (Sigma Chemical Co.) and 0.25 mg/ml ICG dye (Sigma Chemical Co.) mixed in deionized water. The protein solder was stored in a light-proof plastic vial in a refrigerator prior to its use. The set up of system is shown in Figure.1. The system includes the following: (1) a diode laser with emission at  $\lambda = 810 \text{ nm}$  with a linear beam profile with dimensions of  $1 \times 7 \text{ mm}^2$ , (2) a stepper motor that scans the laser probe on the skin surface with variable speed, (3) a digital thermometer (CHY502A1) that measures the skin surface temperature during laser soldering, (4) computer analysis of thermometer signals and recording system, (5) a CCD (Dynamic wv-CP450) camera to observe and record the skin changes during the laser soldering.

The protein solder solution was placed in the incision for 5 min and then irradiated with different power densities in



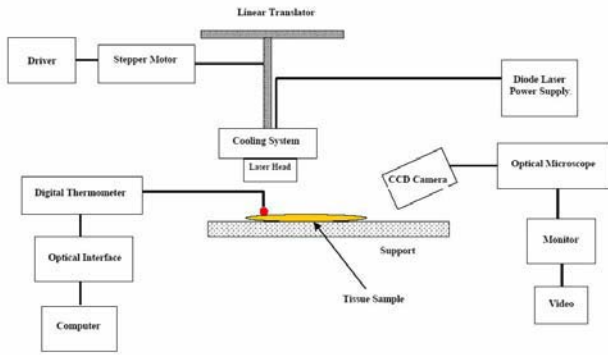


Fig. 1 Experimental setup

the static and dynamic modes. In the static mode the incision was same as the laser output profile and the laser head was positioned statically at the surface of incision and irradiate with different power densities for 4 minutes. In the dynamic mode, however the laser probe was located perpendicularly to the incision and scanned the surface with a predefined speed until the soldering was finished set by upper temperature limit. Tensile strength measurements were performed to test the integrity of the resultant repairs immediately following the laser procedure using a gravity-based instrument. The repaired specimen was then mounted between two metal grips which one was fixed and the other was allowed to move. The defined weights were added to moving grip until the first rupture occurred in the repaired skin.

### III. RESULTS AND DISCUSSION

The effect of laser power densities on the tensile strength of tissue repair in static and dynamic modes is shown in Figure 2. As it is seen from this figure,  $\sigma_t$  increases by increasing the power density for both static and dynamic modes.

The temperature rise at the skin was measured with a digital thermometer. The laser beam moved from one place to the next, along the cut line, so that each line slightly overlapped the previous one. The schematic of the temperature rise of skin during laser soldering using 36 W/cm<sup>2</sup> is shown in Figure 3 where each peak was achieved when the laser beam was coincided on the tip of thermometer. Clearly each scan can contribute to temperature rise by an increment as residual heat which accumulated on the previous scan effect. This, in turn implies that by varying the scanning velocity the distance between peaks and their amplitude can change, hence controlling the final temperature rise.

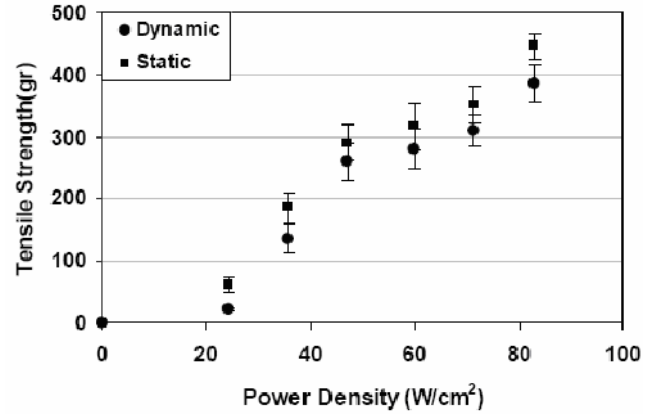


Fig. 2 The effect of power densities on the tensile strength of soldered skin

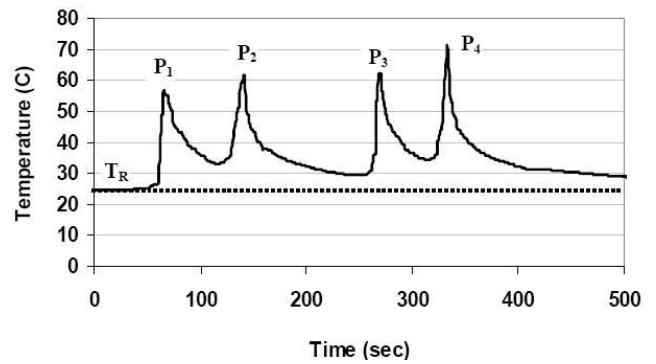


Fig. 3 Surface Temperature rise in dynamic mode of soldering

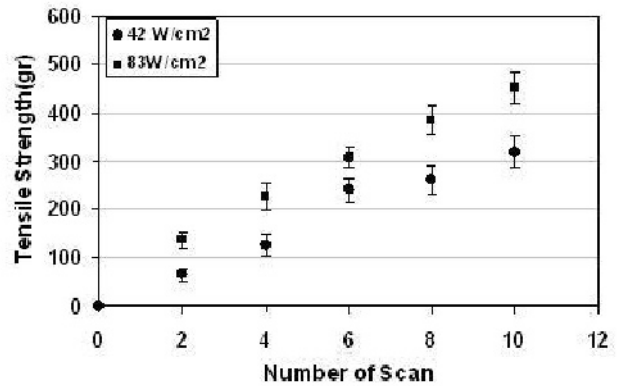


Fig. 4 The effect of number of scans on the tensile strength

The effect of number of scan on the tensile strength of repaired skin for two different power densities illustrated in Figure 4. For each power density,  $\sigma_t$  increases by increasing the number of scan.

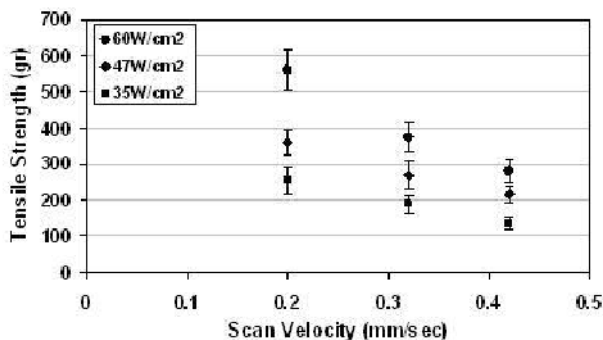


Fig. 5 The effect of scan velocity on the tensile strength

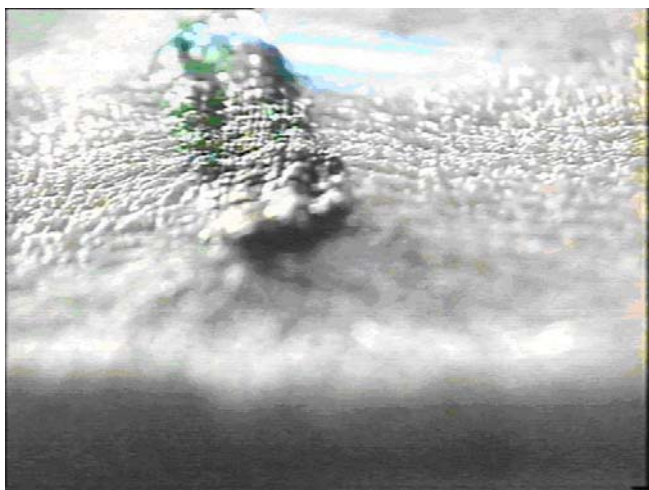


Fig. 6 An example of incision healing in dynamic mode at 60W/cm<sup>2</sup> after 8 scans

Figure 5 shows the effect of scan velocity on the  $\sigma_r$  of the healed wound at different power densities for 8 scans. As shown in this figure the  $\sigma_r$  of repair decreases by increasing of scan velocity which is likely due to less heating of solder.

An image of healed wound at 60 W/cm<sup>2</sup> captured by CCD camera is shown in Figure 6. During the operation tissue colour changes from green (ICG) to brown indicating the heating effect.

#### IV. CONCLUSIONS

The results showed that the tensile strength of the repaired skin increased by increasing the power density in both static and dynamic mode. But because of thermal damage of tissue due to high temperatures at high power densi-

ties, an optimum value must be selected. By increasing the scan velocity the tensile strength of repair and operation time decreases which also must be taken into account in any operation. Thus, it can tentatively be concluded that since the skin temperature should not exceed ~80C at any time of work, then the acceptable conditions in our experiment would correspond to  $I \sim 47 \text{ Wcm}^{-2}$ ,  $\sigma = 300 \text{ gr}$ ,  $N_s = 8$ ,  $V_s = 0.3 \text{ mm s}^{-1}$ .

#### ACKNOWLEDGMENT

The authors are grateful to the High-Tech Industries Center of Iran for supporting this work.

#### REFERENCES

1. Bass LS. Laser tissue welding (1995): a comprehensive review of current and future clinical applications. *Lasers Surg Med* 17:315-349
2. Forber B, Vasilyev, T, Brosh T. (2005) Repair of pig dura in vivo using temperature-controlled CO2 laser soldering. *Lasers Surg Med* 37 : 286-92
3. Simhon D, Brosh T, Halpern M, Ravid A, Vasilyev T, Kariv N, Katzir A, Nevo Z. (2004) Closure of skin incisions in rabbits by laser soldering: I: Wound healing pattern. *Lasers Surg Med*. 35:1-11
4. Fried NM, Walsh JT (2000). Laser skin welding :In vivo tensile strength and wound healing results. *Lasers Surg Med* 27:554-65
5. McNally KM, Sorg BS, Welch AJ, Owen ER (1999). Photothermal effects of laser tissue soldering. *Phys Med Biol* 44:983-1002
6. Savage, Howard E.; Lee, John; Halder, Rabindra; McCormick, Steven A.; Paul, M. Alfano, R (2003) Near-infrared laser welding of aortic and skin tissues and microscopic investigation of welding efficacy. *SPIE - The International Society for Optical Engineering*, 49: 182-185
7. Hoffman GT, Byrd BD, Soller EC, Heintzelman DL, McNally-Heintzelman KM. (2003) Effect of varying chromophores used in light-activated protein solders on tensile strength and thermal damage profile of repairs. *Biomed Sci Instrum* 39:12-7
8. Wolf, Roman F.; Bartels, Kenneth E.; Shivakoti, Suman; Liu, Hong (2004); Selective photo thermal tissue interaction using 805-nm laser and indocyanine green in tissue welding. *Journal of X-Ray Science and Technology*, Vol 12:117-126
9. Brosh T, Simhon D, Halpern M, Ravid A, Vasilyev T, Kariv N, Nevo Z, Katzir A (2004). Closure of skin incisions in rabbits by laser soldering II: Tensile strength. *Lasers Surg Med* 35:12-7
10. Gulsoy M, Dereli Z, Tabakoglu HO, Bozkulak O (2006) Closure of skin incisions by 980-nm diode laser welding. *Lasers Med Sci* 21:5-10

Author: M.S.Nourbakhsh  
 Institute: Amirkabir University of Technology  
 Street: Hafez Ave  
 City: Tehran  
 Country: Iran  
 Email: S\_nourbakhsh@aut.ac.ir

# Photoplethysmography Device for Detection of Changes in the Vasomotor Parameters of Small Laboratory Animals

J. Paturskis<sup>1</sup>, V. Veliks<sup>2</sup>, M. Ozols<sup>1</sup>, I. Svikis<sup>2</sup>, R. Erts<sup>1</sup>, J. Spigulis<sup>1</sup>

<sup>1</sup>Institute of Atomic Physics and Spectroscopy, University of Latvia, Riga, Latvia

<sup>2</sup>Faculty of Biology, University of Latvia, Riga, Latvia

**Abstract** — A device for observation of changes in vasomotor parameters of small laboratory animals with limited blood amount has been developed. The device contains cw laser sources (635 nm, 650nm or 980 nm), photodetector, amplifier of the absorption photoplethysmography signal and special software for data recording.

Use of pigtailed laser diode with optical fibre output allows avoiding thermal influence on the blood flow. Another advantage of the device is the possibility to record the received signal indirectly via the optical fibre to photodiode, or directly to photodiode. The described design allows to investigate the influence of magnetic fields in combination with optical microscopy, in particular -to record the changes of blood flow in a single vessel or in tissue with relatively small blood volume.

**Keywords** — Photoplethysmography, optical bio-sensing, cardio-vascular assessment.

## I. INTRODUCTION

Main goal of the study is detection of variations in blood flow at single blood-vessels or in tissues with low blood amount in small laboratory animals under influence of external fields. There is a need to register changes in blood pressure for animals with relatively little amount of blood – rats and frogs. Photoplethysmography (PPG) signals may be recorded via optical fibres without any interference with magnetic or electro-magnetic fields. Due to large size and insufficient sensitivity of commercially available PPG devices (for example Blood Volume Pulse (BVP) Sensors: SA9308M (manufactured by Thought Technology Ltd.), NX32-BVP1A, (manufactured by Stens Biofeedback - Stens Corporation) combined laser Doppler and pressure system PRM2™ (manufactured by Moor Instruments Ltd.), it is impossible to use them in this experimental branch of physiology. We used non-invasive photoplethysmography method for studies of the blood volume pulsations by detection and analysis of the absorbed optical radiation [1]. Blood pumping and transport dynamics has been monitored at various locations on animals' body, for example on legs or tail.

## II. DESIGN OF THE MEASUREMENT SYSTEM

The measurement system consists of the source of light signal (1), fibre-optic PPG absorption probe (2), photosignal amplifier (3), signal measurement and recording device (4). Figure 1 represents the fitted drawing of the measurement system.

As a source of the signal were used pigtailed laser diodes, manufactured by AOE (Associated Opto-Electronic, China) with fiber diameter 65  $\mu\text{m}$  and maximum output power 5 mW. We controlled blood volume changes at conditions of small available blood and tissue amounts. In our tests we measured the light intensity temporal variations caused by pulsatile blood absorption in tissue. In order to reduce the DC component of the measured signal, we reduced output power at the fibre output connector to 2 mW.

Tests were conducted with red-emitting laser diodes, wavelengths 635 nm (AL635T5MF) and 650nm (AL650T5MF), as well as in the near infrared range - wavelength 980 nm (AL980T5MF2).

Signal after propagation through the tissue was detected by a custom-made PPG device. While choosing elements for PPG contact probe we met the necessity to minimize impact of external electromagnetic noise at light frequencies as well as at radio frequencies. In the case with small blood amount, the variable component of PPG signal is very low and any noise significantly influences detection of the wanted signal.

As a result of series of experiments using different photo elements (BPW21, S1336-18BQ, TSLR257 color sensor red, BP104F photodiode selective, S2381 avalanche

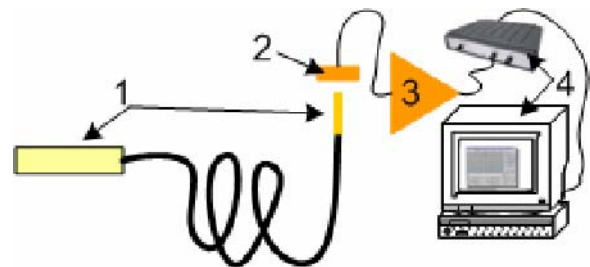


Fig. 1. Scheme of the measurement system.

photodiode), we have chosen a light-voltage converter OPT 101P [2] with built-in amplifier. It allowed us to enhance the measured signal level thus reducing the impact of external electromagnetic noises.

Maximum sensitivity of the probe has been obtained at the infrared range (Figure 2). OPT 101P ensures small deviations of angle of incidence of light (till 10°) that is very important working with our objects. (Figure 3).

The OPT 101 is a monolithic photodiode with on-chip transimpedance amplifier. Output voltage increases linearly with light intensity.

The integrated combination of photodiode and transimpedance amplifier on a single chip eliminates the problems commonly encountered in discrete designs such as leakage current errors, noise pick-up and gain peaking due to stray capacitance. The 0.09 x 0.09 inch photodiode is operated in the photoconductive mode for excellent linearity and low dark current. The OPT 101 operates from +2.7V to 36V supplies quiescent current is only 120µA. Temperature range is 0°C to 70°C.

Bipolar power supply Circuit Connections (Figure 4.) were used because it was found more efficient than unipolar

one for the detection of extremely low signals. The OPT101 is capable of driving load capacitances of 10nF without instability. However, dynamic performance with capacitive loads can be improved by applying a negative bias voltage to pin 3 (Figure 4.). This negative power supply voltage allows the output to go negative in response to the reactive effect of a capacitive load. An internal JFET connected between pin 5 (output) and pin 3 allows the output to current leakage. The benefits of this are shown on the typical performance curves Small Signal Response.

Amplifier is designed on the basis of operation amplifier with inverting shutter and consists of 2 stages. First stage consists of OP U2A, feedback potentiometers R5 and R6, which can change the gain of the first stage approximately from 1 to 500. Potentiometers R1, R2 and resistor R3 are

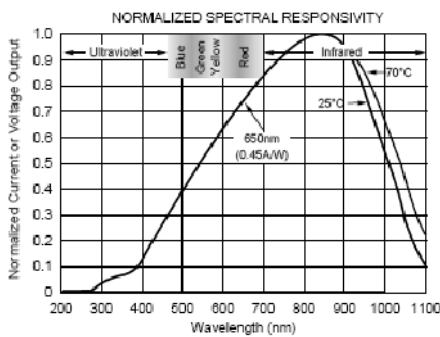


Fig. 2. Normalized spectral responsivity.

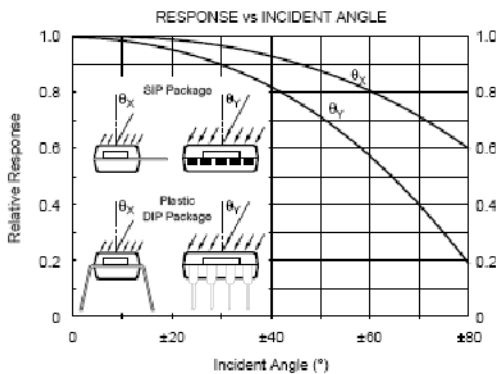


Fig. 3. Response depending on incident angle.

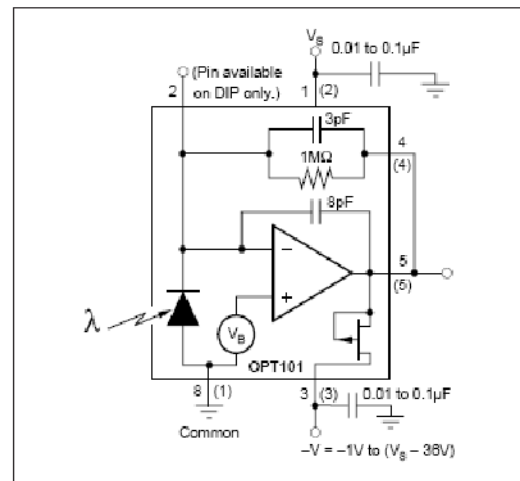


Fig. 4. Bipolar power supply circuit connections.

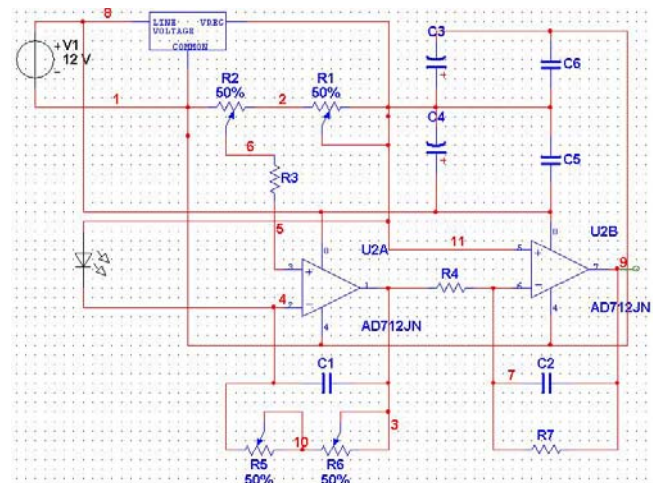


Fig. 5 Fitted drawing of the received signal amplifier.

used to compensate the constant component of the input signal, as we are interested in the variable component only. The second amplifier stage consists of U2B, R4, R7 and C2 and provides gain  $R7/R4=100$ . Capacitors C1 and C2 filters out high frequency noise. Total gain of the amplifier ranges from 100 to 5000.

During experiments it was found that the ratio between constant and variable components of the signal at different locations of frog's body differed by 100-150 times. Therefore for the purpose of signal measurements at very low blood volume we made short circuit by shunting potentiometers R1 and R2.

Connection of probe and amplifier was realized by means of special electrical cable with shielded central signal wire and additional common shielding to protect signal from the external electromagnetic noise.

Velleman PCS500 PC based digital storage oscilloscope [3] was used as amplified electrical signal measurement and recording device. It uses a computer and its monitor to display waveforms. All standard oscilloscope functions are available in the Windows program supplied with the oscilloscope. The operation is just like a normal oscilloscope. The PCS500 has two completely separate channels with a sampling frequency of up to 1Ghz. Connection is through the computer parallel port, the scope is completely optically isolated from the computer port.

### III. BIOLOGICAL EXPERIMENT

*Animals.* Experiments were carried out on 5 common frogs (*Rana temporaria* L.), males in weight of 25-40 gram. Observations were carried out in the period of hibernation. In the winter period frogs were kept in glass reservoirs with a small amount of water, without access of light, at temperature  $+5\text{ }^{\circ}\text{C}$ ; water was changed two times per week. Before experiments frogs were taken from refrigerator and placed for heating to room temperature in a dry bath. After 30 minutes animals were anaesthetized with Ether (Peaxum, Cehija) by inhalation for 5 minutes. Frogs were placed on their spine on a specific table with mounted laser diodes on its surface, optical sensor for recording of photoplethysmographical data was placed on the upper part of the frogs' body. Altogether three body parts were observed: chest over heart with relatively high amount of the blood, on thigh muscle, and on leg foot with relatively small amount of blood.

Photoplethysmogram was recorded for at least two minutes on each part. During the laser diode change frogs were placed in a moist bath.

### IV. RESULTS

Recorded photoplethysmogrammes were processed using Fourier spectral analysis in Matlab using routine procedure.

Surprisingly, from the data of the observation with laser diode with wavelength 650 nm it was unable to detect heart rhythm on frog's legs, therefore the data recorded over heart was not analyzed and showed in the article.

The visibly detectable heartbeat record we managed to record only in the heart area. For typical photoplethysmographical signal record with detectably heart rhythm see Figure 6.

Clear heartbeat signals were always recorded from the chest area. Although heartbeat signals were easily detectable in all wavelengths, better signal was obtained

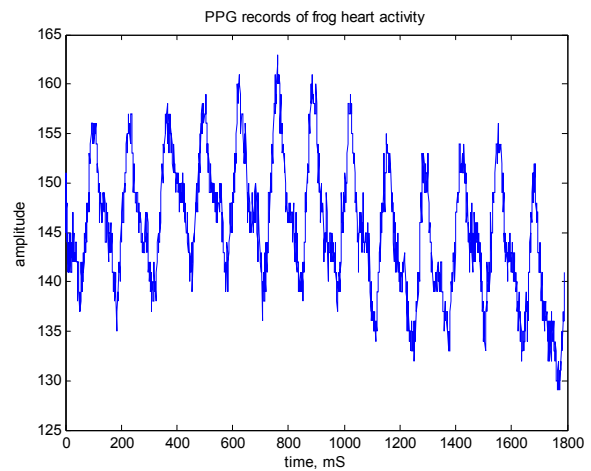


Fig. 6 Photoplethysmographical heartbeat activity record, x-axes time in mS, y-axes signal relative amplitude.

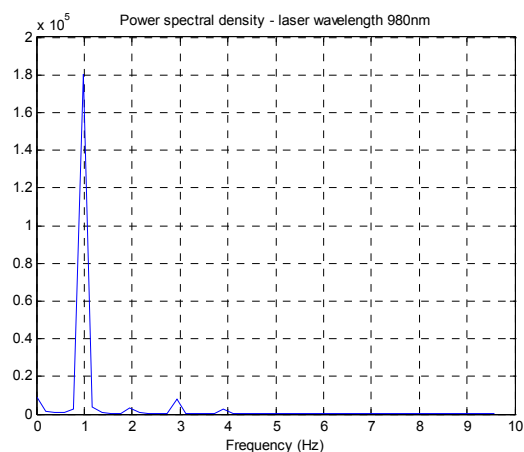


Fig. 7 Frog heartbeat with frequency of 60bpm or 1Hz, x-axes frequency Hz, y-axes signal relative power.

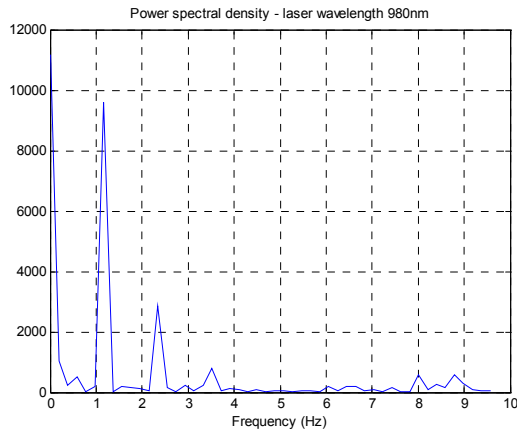


Fig. 8 Frog heartbeat with frequency 1.2Hz recorded with laser of 980nm wavelength recorded on leg foot, x-axes frequency Hz, y-axes signal relative power.

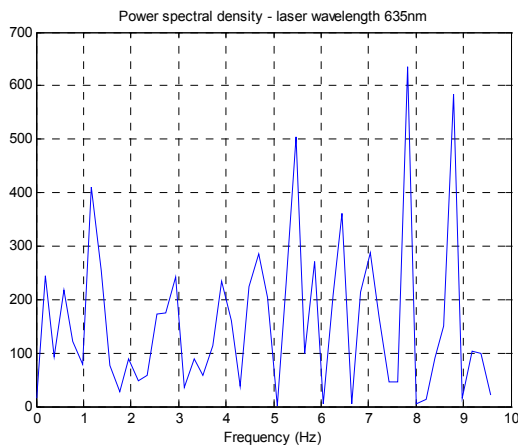


Fig. 9 Frog heartbeat with frequency 1.2Hz recorded with laser of 635nm wavelength recorded on leg foot, x-axes frequency Hz, y-axes signal relative power.

using laser with wavelength 980 nm. The signal has good signal/noise ratio and clearly shown heartbeat, for example, in Figure 7 frog has heartbeat of 60 bpm or 1 Hz.

The signal on legs was weak and noisy. Heartbeats were detectable only using Fourier analysis procedure. Better results again were obtained with laser of wavelength 980nm, it seems that light from laser with wavelengths 650 and 635 nm goes not only through the body but goes around the body, thus in the result the noise level in the record increases. Figure 8 shows records from leg foot recorded when laser with wavelength 980 nm was used and Figure 9 recorded from the same point with laser of 635 nm wavelengths.

## V. CONCLUSIONS

The developed design makes it possible to record the changes of blood flow in a single blood vessel or in tissue with relatively small blood volume.

Better results were obtained using laser with wavelength of 980nm.

## VI. ACKNOWLEDGMENT

Work was done with support of the ESF.

## VII. REFERENCES

1. J. Spigulis, M. Ozols, R. Erts, K. Prieditis, "A portable device for optical assessment of the cardiovascular condition", Proc. SPIE 5123, pp. 313-319, 2003.
2. Texas Instruments on <http://focus.ti.com/docs/prod/folders/print/opt101.html>
3. Velleman on <http://www.vellemanusa.com/us/enu/product/view/?id=351379>

Author: Juris Paturskis1  
 Institute: Institute of Atomic Physics and Spectroscopy,  
 University of Latvia  
 Street: Skunu 4  
 City: Riga  
 Country: Latvia  
 Email: jurpat@unistars.lv

# Potentialities of Wear Measurement in Total Knee Arthroplasty

M. Pochmon<sup>1</sup>, T. Rössler<sup>2</sup>, J. Gallo<sup>3</sup>, M. Hrabovský<sup>1</sup>, D. Mandát<sup>1</sup> and V. Havránek<sup>1</sup>

<sup>1</sup> Joint Lab. of Optics of the Palacky Univ. and the Inst. of Physics of the Acad. of Sciences of the Czech Rep., Olomouc, Czech Republic

<sup>2</sup> Palacky Univ./ Fac. of Natural Sciences, Dept. of Experimental Physics, Olomouc, Czech Republic

<sup>3</sup> University Hospital, Palacky Univ./Fac. of Medicine and Dentistry, Department of Orthopedics, Olomouc, Czech Republic

**Abstract** — The contribution describes two optical and one contact measuring method used to measure the wear of polyethylene insert of knee implants. These implants are under stress in patient body and therefore they suffer from wear. The purpose of these measurements is the creation of sensor intended to measure a statistic file of damaged implants and compare this file with way of life and other parameters of patients, who used them.

**Keywords** — Total endoprosthesis, phase-shifting profilometry, 3D laser scan profilometry, contact surface measurement.

## I. INTRODUCTION

Total knee arthroplasty is the best method to heal the arthritis of knee joint [1]. Today, in most cases are used implants with polyethylene insert, which suffer from wear. The size of this wear depends on the patient's age, sex, activity, weight, way of life, etc. By measuring of enough amounts of used knee implants, it is possible to create a statistic file of these implants and classify each wear according to specific patient.

The wear is depended upon the shape of polyethylene insert, too. There are several manufactures, that produce these insert, and each of these producer has its own shape of knee implant insert that differ a little from another ones. Another purpose of wear measurement is to discover, which shape is more resistant to wear.

In this paper, three 3D measuring methods are described. One contact method and two optical methods, 3D laser scan profilometry and phase-shifting profilometry. In conclusion, the advantages and disadvantages of these methods will be discussed and one of them will be chosen for building sensor, which will serve to measure the file of worned implants.

Every method measures the surface of used implant insert, and the result is then subtracted from the reference unused implant insert. This way, the wear is achieved.

## II. KNEE IMPLANT

The knee implant is created of polyethylene insert, that is connected to shin-bone (see fig.1) and metal part connected to thigh-bone. At fig.2 it is possible to see polyethylene

insert from other manufactures. The shape difference between them can be well seen.

The wear of polyethylene insert has two origins, loss of material because of using and little fragments and grooves, made by extraneous objects and by material defect. These small defects are very small compared to wear caused by attrition of metal and polyethylene parts.



Fig. 1 The polyethylene insert of knee implant.



Fig. 2 The polyethylene insert of knee implant – other producer.

### III. CONTACT MEASURING METHOD

This method is based on scanning of the surface of measured object by contact sensing head [2]. For measurement, the Talysurf from Tyler-Hobson was used. Resolution of the measurement was approximately 50  $\mu\text{m}$ . The implant insert is put under the sensing head and it is scanning insert's surface in premeditate determined plains. The more plains are defined, the more time measurement takes. The speed of the sensing head is about 2 mm per second. Results of the contact measurements are shown at fig.3 and fig.4.

### IV. 3D LASER SCAN PROFILOMETRY

This 3D optical non-coherence method is based on projecting of linear laser stripe on the measured object [3]. This stripe is deformed by the surface of the object and saved into computer by CCD camera. Because the calibration of the deformations of laser line is done, the height variation through the laser line can be computed. The whole surface is measured, when the laser line is shifted over whole measured area in defined steps (for examples 1 mm). The area between two nearby lines is approximated. The resolution

of this method is about 100  $\mu\text{m}$ . The deformed linear laser stripe is shown in fig.5, the result of measurement is shown in fig.6.

### V. PHASE-SHIFTING PROFILOMETRY

This optical 3D non-coherence method is based on evaluating of change of phase of sinusoidal pattern. These patterns are projected on the reference plain and measured object, each one shifted from another. If there are used N patterns, each pattern is shifted by  $2\pi/N$  and all of them are saved into computer by CCD camera. After computing algorithm, which gives a change of phase in whole measured area, it is possible to compute height variation in each pixel of CCD chip and whole profile of measured object is achieved. The resolution of that method is about 100  $\mu\text{m}$ . For the result, it is necessary to take at least 4 snapshots of

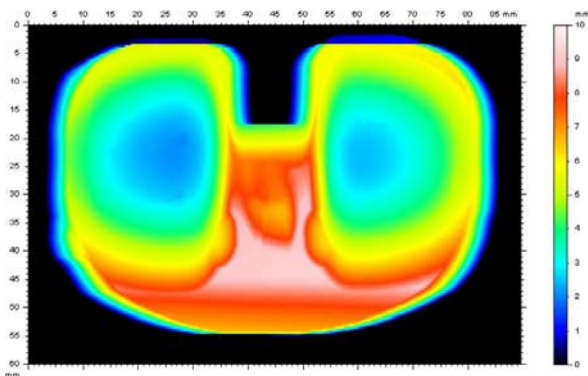


Fig. 3 The result of contact polyethylene insert measurement.

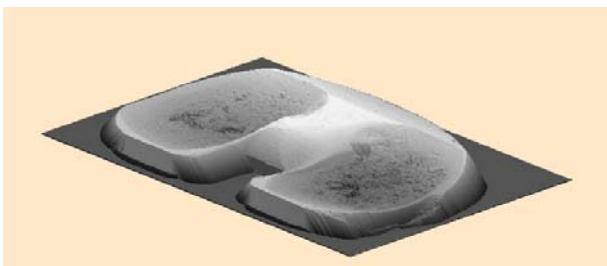


Fig. 4 The result of contact polyethylene insert measurement – other visualization.

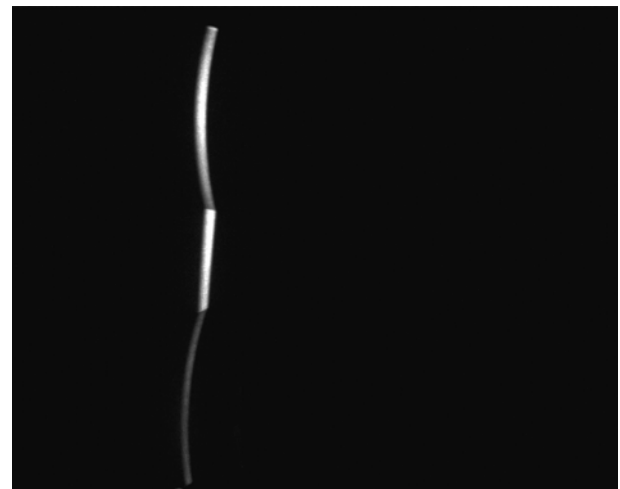


Fig. 5 The linear laser stripe deformed by measured surface.

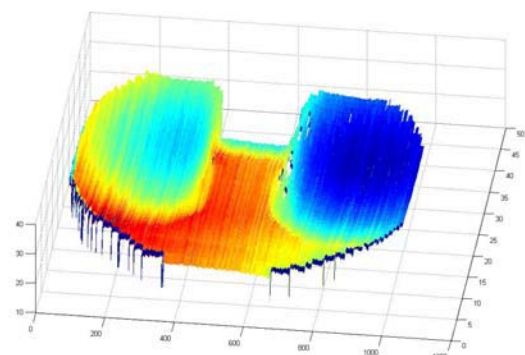


Fig. 6 The result of measurement using 3D laser scan profilometry.



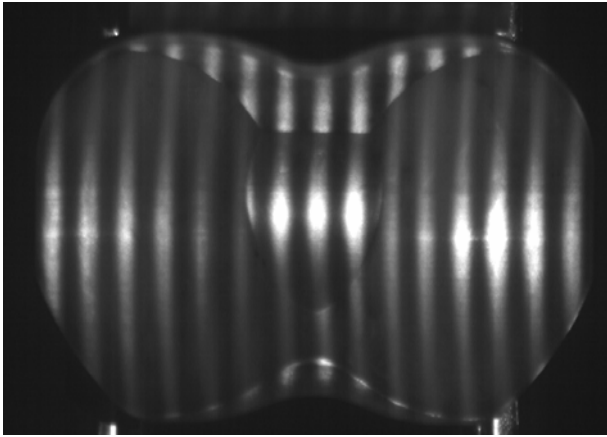


Fig. 7 Sinusoidal pattern projected on the knee implant insert.

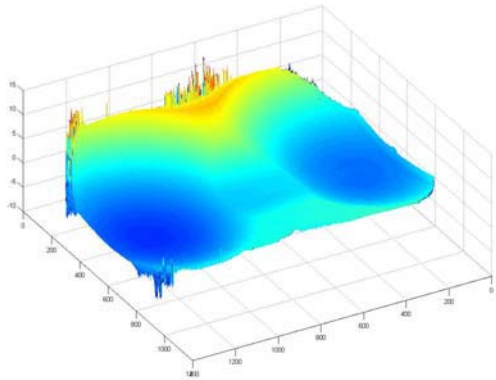


Fig. 8 Result of phase-shifting profilometry.

patterns on measured object and 4 snapshots of patterns on reference plain. The sinusoidal pattern is shown in fig.7 and in fig.8 is shown the result of knee insert measurement.

## VI. CONCLUSIONS

It is obviously, that contact method is the most accurate method for measuring of knee implant inserts. On the other

side, one measurement takes too much time – about hours. And for this kind of application, its superior resolution is not necessary.

3D laser scan profilometry has sufficient resolution, but it is time-consuming measurement. The width of knee insert is about 7,5 cm, it means 75 position changes and 75 snapshots during one measurement with 1 mm step.

For this kind of surface, the most proper measuring method is phase-shifting profilometry. It has sufficient resolution, its projected optical structure covers whole measured area and it takes only 4 snapshots of measured object. The measurement can be done during few seconds and is enough accurate for its purpose.

Another step will be construction of measuring sensor and creation of large statistic file of knee implant inserts. This will lead to improve insert's shape, quality of its material, and its lifetime.

## ACKNOWLEDGMENT

These results of the project 1M06002 was supported by The Ministry of Education of the Czech Republic.

These results of the project OC168 was supported by The Ministry of Education of the Czech Republic.

## REFERENCES

1. Gallo J, Havránek V, Čechová I, Zapletalová J (2006) Wear measurement of retrieved polyethylene ABG 1 cups by universal measuring microscope and x-ray methods. Biomed Pap Med Fac Univ Palacky Olomouc Czech Repub 150(2):231-236.
2. Havránek V, Gallo J (2007) measurement of the polyethylene liner wear of the extracted total knee substitute. Fine mechanics and optics 52(11-12):316-320.
3. Mandát D, Rössler T, Hrabovský M, Gallo J (2006) Optical topographical methods in medical practice. Acta mechanica Slovaca 10(1):327-332.

Author: Pochmon Michal

Institute: Joint Lab. of Optics of the Palacky Univ. and the Inst. of Physics of the Acad. of Sciences of the Czech Rep.

Street: Tr. 17 listopadu 50a

City: Olomouc

Country: Czech republic

Email: michal.pochmon@upol.cz

# Optical Non-contact In-vitro Measurement of Total Hip Arthroplasty Wear

T. Rössler<sup>1</sup>, J. Gallo<sup>2</sup>, M. Hrabovský<sup>3</sup>, D. Mandát<sup>3</sup>, M. Pochmon<sup>3</sup> and V. Havránek<sup>3</sup>

<sup>1</sup>Palacky Univ./ Fac. of Natural Sciences, Dept. of Experimental Physics, Olomouc, Czech Republic

<sup>2</sup>University Hospital, Palacky Univ./Fac. of Medicine and Dentistry, Department of Orthopedics, Olomouc, Czech Republic

<sup>3</sup>Joint Lab. of Optics of the Palacky Univ. and the Inst. of Physics of the Acad. of Sciences of the Czech Rep., Olomouc, Czech Republic

**Abstract** — Total hip arthroplasty significantly improves the quality of life in majority of patients with osteoarthritis. However, prosthetic wear is a problem because of inducing the development of aseptic loosening and periprosthetic osteolysis which needs the revision surgery. Thus, the polyethylene wear measurement is the central to contemporary orthopaedics. Various in vivo methods have been developed offering the ability to determine and study the prosthetic cup linear wear before the revision surgery. The radiological methods are the most available but the accuracy and related relationship between measured linear wear and true value of volumetric wear is the problem. As the “golden” standard the in vitro methods can be employed. This contribution gives the review of previously published study concerned with the accuracy of three radiological techniques (Livermore, Charnley, and Dorr methods) based on the using the universal-type measuring microscope in vitro method. Moreover, this paper introduces the comparison of results obtained by the previously used microscope method and the newly developed optical scanning profilometry in vitro method. Results of the comparison shows the using of this optical method can specify and spread the mentioned study.

**Keywords** — Total hip arthroplasty, polyethylene wear measurement, radiographic techniques, microscope method, scanning profilometry

## I. INTRODUCTION

The study focused on the accuracy of three radiological techniques (Livermore, Charnley, and Dorr methods) was performed and results were published [1]. Wear was measured manually in 80 patients by a single observer according to the Livermore, Charnley, and Dorr description. A multi-component statistical analysis was used to test the hypothesis that the Livermore technique was superior. In vitro data obtained from a Universal-type measuring microscope served as a gold standard.

In vitro measurement showed an average linear wear of 0.363 mm per year (0.000–0.939, SD 0.241) with a corresponding volumetric wear rate of 161 mm<sup>3</sup> per year (0–467, SD 118.2). The Livermore technique showed the least deviation from the optical reference standard and a superior position from the viewpoint of error analysis but the correlation coefficient was slightly less ( $r=0.761$ ) in comparison

with the Dorr and Charnley techniques ( $r=0.795$  and  $r=0.778$ , respectively). In addition, the mean error of the Dorr method differed significantly from zero ( $p=0.036$ ). Overall, the Livermore technique was the most accurate method for polyethylene wear measurement regardless of the abduction angle of the cup. The Livermore technique performed manually was more accurate than the Charnley and Dorr methods. Nevertheless, authors considered the Dorr technique an adequate tool for day-to-day wear measurements, mainly due to its simplicity.

## II. PRINCIPLES OF OPTICAL IN VITRO METHODS

As it was said, the Universal-type measuring microscope method was used to obtain the reference data for radiological methods evaluation. The reference data can be obtained also employing the other optical method – newly developed scanning profilometric method. The principle of both follows.

### A. Universal-type measuring microscope method

This method is based [1,2] on the determination of the post-use and manufactured positions of the prosthetic head inside polyethylene cups as follows from Fig.1. Thus, the reliability and precision of measurement strongly depends on the precision of that positioning.

With the help of the measuring microscope the number of 3D coordinates on the surface of the prosthetic ball in both positions is measured (See Fig.2).

Finally, the ball centers are converted into linear values of wear using a computational algorithm [3] and serve for

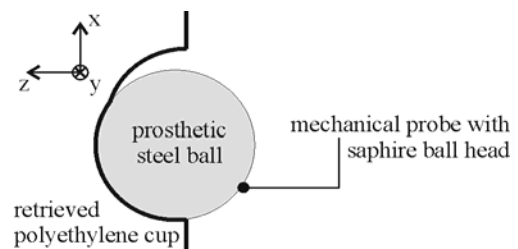


Fig. 1 Using a Universal-type measuring microscope.

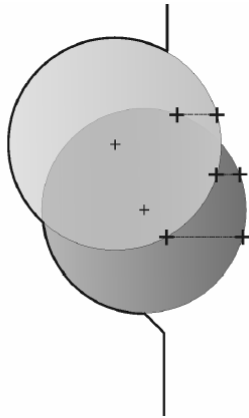


Fig. 2 Principle of wear measurement.

the determination of total wear using the next special mathematical algorithm.

*B. Optical scanning profilometric method*

This optical method [4] belongs to the group of profilometric methods. The general principle of these methods is the projection of optical structure (grating, speckle, strip, point, etc) onto the measured surface. This structure is influenced (deformed etc) by the shape of surface. It is recorded by the camera and the structure is analyzed to obtain z-coordinates in the regular or irregular system of point given by the x- and y-coordinates.

With respect to the implant shape the one strip projection is better to use instead of other projection types. The principle of method is clear from Fig.3.

The projected linear strip is deformed by the measured surface. The example of the strip deformation is shown on the Fig. 4. The profile in one direction is computed from this strip deformation.

The cup or the strip is rotated to cover the whole area of the measured surface. The magnitude of step influences the resolution and sensitivity of the method. The record and the

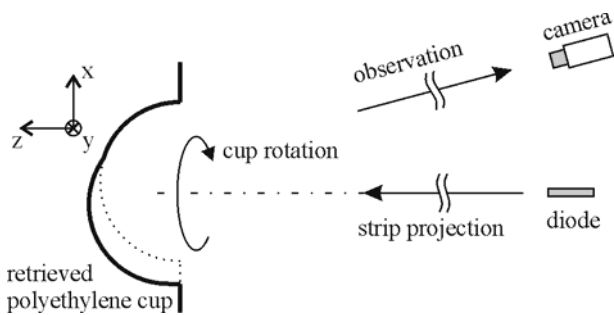


Fig. 3 Optical scanning profilometric method.



Fig. 4 Recorded digital image of the linear strip deformed by the surface.

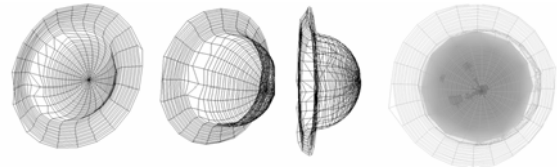


Fig. 5 Resulting WRML map of the cup.

analysis are repeated consequently. The result whole-field profile is obtained connecting the individual linear profiles. The resulting wired model of the cup is shown on Fig.5.

The usual data format of the resulting profile map can be obtained using the standard conversion of this format.

III. COMPARISON OF METHODS

Concerning the measurement process both methods are not the real-time ones. In case of microscope method the two positions should be found with the high precision to eliminate the systematic error. The points on the ball captured inside the cup are measured manually and consequently. The whole procedure is time-consuming like in the case of the scanning profilometry. In this case, the total duration depends on the duration of the positioning (rotating) the measured cup (or projected) and recording and processing of number of strips. But the total duration of measurement can be improved to the acceptable short time using the automation and synchronization of the rotating, recording and data processing. From the point of view of measurement process this method is the more use-friendly.

To compare the quality and limits of both methods, several cups with the simulated wear were measured. The principle of simulation [5] is shown on the Fig.6.

Milling parameters were chosen based on the experience from clinical practice. Wear was simulated by the milling cutter under the direction of 0, 30 and 50 degrees. These angles simulate the abduction angle of really-worn cups. That means this is the wear direction simulation. For each of this direction, the deepness of milling was chosen to simulate

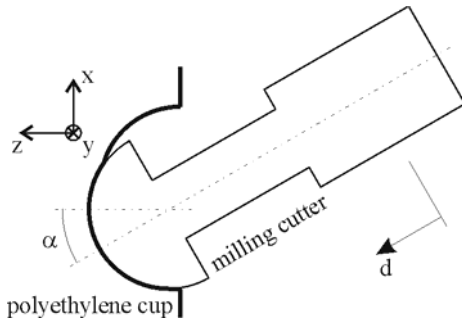


Fig. 6 Mechanical simulation of wear, geometry of milling.

the linear wear. Three practically important values of the total wear were obtained for each direction – low, medium and high. The choice was carried out based on the estimation of resulting simulated values of wear using their computation.

Cups prepared by such a way were measured employing the previously mentioned methods and the total wear values were determined. The way to validate the compare both methods consists in the comparison of these computed values with ones obtained by the other reference way. In fact, the gravimetric method was employed for the measurement of the removed mass of implant caused by the milling.

Every cup was weighed before and after milling and the removed mass was identical to the difference of weighs. In brief, the volume decrease was equal to wanted total wear and could be computed using that difference and known density of material. Absolute values of wear are introduced on Fig.7. The relative differences of methods under the study and gravimetric results as a percentage of gravimetric values are introduced on the Fig.8.

angle [deg]	0		
depth [mm]	0,5	1,5	2,0
gravimetry	253,4	865,5	1147,6
microscope	-	-	-
scanning	268,3	843,7	1197,6
angle [deg]	30		
depth [mm]	0,5	1,0	2,0
gravimetry	259,5	510,6	1084,6
microscope	-	316	484
scanning	276,4	465,2	998,7
angle [deg]	50		
depth [mm]	0,5	1,5	2,5
gravimetry	234,3	730,0	1269,2
microscope	222	620	1263
scanning	218,5	658,0	1224,1

Fig. 7 Absolute values of wear (in mm<sup>3</sup>) measured by both methods and gravimetry in dependence of wear direction and value of linear wear.

angle [deg]	0		
depth [mm]	0,5	1,5	2,0
microscope	-	-	-
scanning	5,9	-2,5	4,4
angle [deg]	30		
depth [mm]	0,5	1,0	2,0
microscope	-	-45,5	-58,7
scanning	6,5	-8,9	-7,9
angle [deg]	50		
depth [mm]	0,5	1,5	2,5
microscope	-5,2	-15,1	-0,5
scanning	-6,7	-9,9	-3,6

Fig. 8 Relative percentage differences of both methods according to gravimetry.

The important conclusion follows from previous lists of results. The measuring microscope method gives worse or no results under the condition of small angle. The lower the angle is, the worse results are. It follows from the principle of method, the lower the angle is the smaller part of original non-worn surface is available to capture the prosthetic ball inside the cup in one of the two positions.

#### IV. CONCLUSIONS

Results achieved by using of the microscope measuring method are of good quality under the condition of the sufficiently great value of cup abduction angle. However, this method does not fully address all problems associated with prosthetic wear measurement such as the low-wear condition, the complex wear mode or the wear anisotropy.

On the other hand, the method of scanning profilometry offers primary the 3D map of whole-area of a cup. Its mathematical processing gives the information not only about the magnitude of total wear but also about the contribution of wear what is useful to determine the various other parameters such as the maximum strain areas, the strain direction or the wear anisotropy. Results introduced in this paper give the hypothesis the clinical study can be expanded with the low-worn and low-angled cups. Thereby, the number of cups available for study increased to more than 200. The results will be presented soon.

#### ACKNOWLEDGMENT

These results of the project OC168 was supported by The Ministry of Education of the Czech Republic.

These results of the project 1M06002 was supported by The Ministry of Education of the Czech Republic.

## REFERENCES

1. Gallo J, Havránek V, Čechová I, Zapletalová J (2006) Wear measurement of retrieved polyethylene ABG 1 cups by universal measuring microscope and x-ray methods, Biomed Pap Med Fac Univ Palacky Olomouc Czech Repub 150(2):231-236.
2. Havránek V (2002) Measurement by universal microscope, Fine Mechanics and Optics 47:20-22.
3. Gallo J, Havranek V, Hrabovsky M (2003) Measurement of retrieved polyethylene cup by universal microscope, Fine Mechanics and Optics 48:333-338.
4. Asundi A, Sajan M R (1999) Mapping algorithm for 360-deg. Profilometry with time delayed integration imaging, Optical Engineering 38, 339-343.
5. Rossler T, Pochmon M, Mandat D, Havranek V, Hrabovsky M and Gallo J (2007) Validation of the measurement of the prosthetic wear of the total hip arthroplasty by means of the optical 3D methods, DAS Proc., Symposium on Developments in Experimental Mechanics, Sibiu, Romania, 29-30.

Author: Tomas Rössler  
Institute: Palacky Univ./ Fac. of Natural Sci., Dept. of Exp. Physics  
Street: av. 17.listopadu 50a  
City: Olomouc  
Country: Czech Republic  
Email: tomas.rossler@upol.cz

# Spectroscopic Studies on Binding of Cationic Pheophorbide-a Derivative to Model Polynucleotides

O.A. Ryazanova<sup>1</sup>, I.M. Voloshin<sup>1</sup>, I.Ya. Dubey<sup>2</sup>, L.V. Dubey<sup>2</sup> and V.N. Zozulya<sup>1</sup>

<sup>1</sup> Dept. of Molecular Biophysics, B. Verkin Institute for Low Temperature Physics and Engineering, NAS of Ukraine, Kharkiv, Ukraine

<sup>2</sup> Dept. of Nucleotide Chemistry, Institute of Molecular Biology and Genetics, NAS of Ukraine, Kiev, Ukraine

**Abstract** — The binding of new cationic Pheophorbide-a derivative to double-stranded poly(A)-poly(U), poly(G)-poly(C) and four-stranded poly(G) was investigated in buffered solutions, pH6.9, of low ionic strength (2 mM Na<sup>+</sup>) by methods of absorption and polarized fluorescence spectroscopy in a wide range of molar phosphate-to-dye ratios (P/D). Two types of CatPheo-a binding to polynucleotides were revealed: (i) dye intercalation between the nucleic bases; (ii) cooperative binding with stacking of chromophores caused by electrostatic attraction of the dye to polynucleotide backbones. The last type is predominant for double-stranded polynucleotides. However in the case of four-stranded poly(G) containing system the external binding prevails only at low P/D, whereas under high P/D values the intercalative binding mechanism is mainly realized. Fluorescent techniques was revealed to be efficient for recognition of binding mode because of the dye emission increases upon chromophore intercalation and quenches strongly upon the outside binding accompanied with the dye stacking-association. The spectroscopic characteristics of complexes formed were obtained.

**Keywords** — Pheophorbide-a, polynucleotides, outside binding, intercalation, fluorescence.

## I. INTRODUCTION

A great interest to the photophysical properties of porphyrin dyes is caused by their use in molecular biology and medicine as photosensitizers [1-3]. The Pheophorbide-a (Pheo-a) is an anionic porphyrin derivative which can be easily prepared from chlorophyll [4]. It is used in photodynamic therapy [2,5] of tumors and psoriasis because of its high photosensitizing activity *in vitro* and *in vivo* [6-9]. The photophysical properties of the Pheo-a were investigated earlier [10, 11]. It was established that Pheo-a selectively accumulates in tumor cells [12] and has a high extinction coefficient in the red region of spectrum where the transparency of tissues to light increases considerably. However its photodynamic activity is predominantly determined by monomeric dye molecules and involves indirect reactions mediated by reactive oxygen species, including singlet oxygen [10,12] and direct electron transfer between DNA bases and Pheo-a singlet excited state. The dimerization [13] or aggregation of the dye in water-containing solutions strongly reduces its photodynamic activity. Anionic charac-

ter and very low water-solubility of Pheo-a prevents it from interaction with negatively charged nucleic acids. Therefore the modification of Pheo-a was carried out [14] to obtain a water-soluble cationic derivative (CatPheo-a, Fig.1), which is capable for polyanion binding.

It is known that cationic porphyrins bind to DNA by means of intercalation, groove binding and outside electrostatic binding to phosphate DNA backbone [15-19]. The last one is accompanied by the formation of  $\pi$ -stacked aggregates. Earlier a pure external electrostatic binding of CatPheo-a to polyanionic chain of nucleic acids was modeled [14] by the dye interaction with inorganic polyphosphate in aqueous buffered solution (pH6.9) of low (2 mM Na<sup>+</sup>) and physiological (0.15M Na<sup>+</sup>) ionic strength.

In the present work the binding of CatPheo-a with synthetic double-stranded poly(A)•poly(U) and poly(G)•poly(C) polynucleotides, as well as four-stranded poly(G) one has been studied in aqueous buffered solution (pH6.9) of low (2 mM Na<sup>+</sup>) ionic strengths in a wide range of molar phosphate-to-dye ratios, P/D, using absorption and polarized fluorescent spectroscopy techniques. The aim of work was to determine types of CatPheo-a binding modes depending on P/D and to establish the absorption and fluorescent characteristics of the complexes formed.

## II. MATERIALS AND METHODS

### A. Chemicals

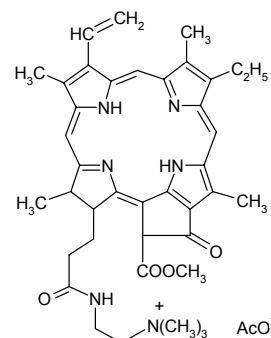


Fig. 1 Molecular structure of CatPheo-a.

The CatPheo-*a* (Fig. 1) was synthesized from Pheophorbide-*a* (Frontier Scientific Inc., Logan, Utah) according the procedure [14]. Poly(A)·poly(U), poly(G)·poly(C), poly(G) polynucleotides from Sigma Chemical Co. were used as received. The 2 mM sodium cacodylate buffer pH6.9, prepared from deionized water, was used as a solvent.

The CatPheo-*a* solution was prepared according with [14]. Polynucleotide concentrations were determined spectrophotometrically in aqueous solution using the following extinction values:  $\epsilon_{260} = 7140 \text{ M}^{-1} \text{ cm}^{-1}$  for poly(A)·poly(U),  $\epsilon_{260} = 7900 \text{ M}^{-1} \text{ cm}^{-1}$  for poly(G)·poly(C),  $\epsilon_{252} = 9900 \text{ M}^{-1} \text{ cm}^{-1}$  for poly(G). The CatPheo-*a* solution was titrated with increasing amounts of the polymer solution containing the same concentration of the dye to achieve the desired P/D value in the final solution. The concentration of the dye was  $1.3 \cdot 10^{-5} \text{ M}$  in all samples.

### B. Apparatus and techniques

Electronic absorption spectra were measured in 0.5 and 1 cm quartz cells, on SPECORD M40 (Carl Zeiss, Germany) spectrophotometer. The intensity and polarization of fluorescence were measured in  $1 \times 0.5$  cm quartz cell with a laboratory spectrofluorimeter, constructed on the basis of a double monochromator DFS-12 (LOMO, Russia), by the method of photon counting. The apparatus and procedure of measurements were described earlier [20]. The He-Ne laser was used as a light source for the fluorescence excitation ( $\lambda_{\text{ex}} = 633 \text{ nm}$ ). The intensity of the laser radiation has been reduced by a neutral color filter. The emission was observed at an angle of  $90^\circ$  from the excitation beam, and obtained fluorescence spectra were corrected for a spectral sensitivity of the spectrofluorimeter. For melting experiments the cuvette was located in copper cell which temperature was changed by Peltier element. The thermal cell can be inserted alternately both into the spectrophotometer and into spectrofluorimeter.

## III. RESULTS AND DISCUSSION

### A. Electronic absorption and fluorescence spectra of CatPheo-*a* in water

The visible electronic absorption spectrum of CatPheo-*a* in water consists of the intense Soret band (B-band) located at 380 nm and four Q-bands, most intensive of which is located at 682 nm (Fig. 2). We assumed that under investigated concentration of  $1.3 \cdot 10^{-5} \text{ M}$  the spectrum corresponds mainly to dimeric form of the dye. The temperature dependence of absorption changes at 380 nm shows that a disintegration of the dimers is started only at  $T > 70^\circ \text{C}$  (Fig. 3).

The 10-fold dilution of the dye solution induces the moderate hyperchromism of the spectrum as well as an appearance of blue-side shoulder of longwave Q-band corresponding to the monomeric form of dye. The absorption spectrum of the sample recorded at the temperature of  $90^\circ \text{C}$  shows that this transition is accompanied by hyperchromism and 20 nm red shift of Soret band as well as 20 nm blue shift of the longwave absorption band to 663.5 nm (Fig. 2). After a time after cooling the dimerization arises again. Thus, in spite of its good water solubility at the room temperature in aqueous solution CatPheo-*a* exists in a form of dimers, as it was earlier observed for Pheo-*a* [13]. For comparison the absorption spectrum of CatPheo-*a* in ethanol is presented in Fig.2, since it corresponds to monomeric form of the dye.

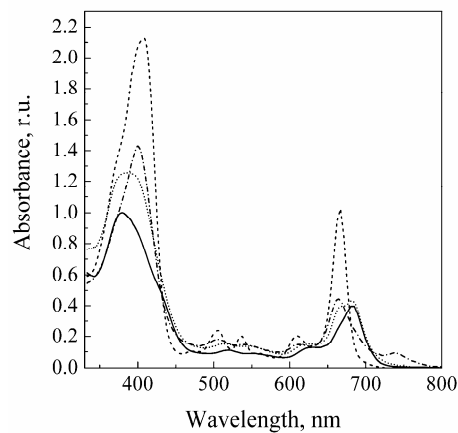


Fig. 2 Normalized absorption spectra of CatPheo-*a* in ethanol (---) and water (—) at  $20^\circ \text{C}$  under the dye concentration of  $1.3 \cdot 10^{-5} \text{ M}$ . Also the normalized absorption spectra of CatPheo-*a* measured in water under the dye concentration of  $1.3 \cdot 10^{-6} \text{ M}$  at  $20^\circ \text{C}$  (.....) and at  $85^\circ \text{C}$  (-·-·-·) were represented being multiplied by 10 times.

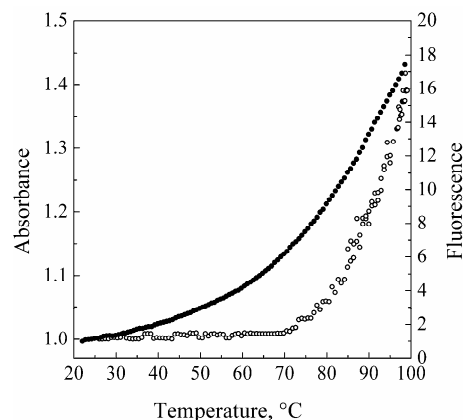


Fig. 3 Temperature dependence of the CatPheo-*a* absorption at 384.6 nm (O) and fluorescence intensity in the maximum of emission band (●). The data are normalized for their values observed at  $25^\circ \text{C}$ . The measurements were carried out in water,  $C_{\text{dye}} = 1.3 \cdot 10^{-5} \text{ M}$ . Excitation wavelength is 633 nm.

The fluorescence spectrum of the CatPheo-*a* in aqueous solution recorded at the room temperature represents a broad band with a maximum at 668 nm [14]. It is positioned in more shortwave region relatively to the longwave absorption band (682 nm) which is attributed to dimeric form of the dye, since the emitting species is a monomer. The temperature dependence of the CatPheo-*a* fluorescence intensity shows that the transition of the dye from dimeric to monomeric form is accompanied by the substantial increase of its emission (Fig.3).

### B. Binding of CatPheo-*a* with double-stranded polynucleotides

The fluorescent titration curves of CatPheo-*a* by double-stranded poly(A)·poly(U) and poly(G)·poly(C) were plotted as a dependence of fluorescence intensity,  $I/I_0$ , (Fig. 4A) and fluorescence polarization degree,  $p$ , (Fig. 4B) measured in the dye emission maximum on P/D. It is seen that binding of the dye is accompanied by strong fluorescence quenching (Fig. 4A) as well as by increase in  $p$  caused by the chromophore immobilization under self-aggregation or a decrease in the fluorescence lifetime. (Fig. 4B). The lowest value of residual fluorescence intensity observed at P/D = 4 is ~8.3% of that for the free dye.

The linear initial part of the fluorescent titration curves observed under P/D < 1 (Fig. 4C) is typical for strongly cooperative binding of cationic dyes to linear polyanions caused by Coulomb interaction [21]. It corresponds to the binding saturation, when CatPheo-*a* forms continuous stacking associates on the polyanionic matrix of the polynucleotide, as was observed earlier for CatPheo-*a* – single-stranded polyphosphate system [14]. For this binding mode a number of binding sites per monomer unit of polymer is 1. The increase of P/D results in gradual rise of the emission reaching at P/D = 330 of 21% from its initial value (Fig.4A). Fluorescence maxima for dye complexes are 15

nm red shifted as compared to that for the free dye (not shown). Gradual increase of  $I/I_0$  allows us to assume that under high P/D stacking associates disintegrates and CatPheo-*a* molecules intercalates into the double helix. This is confirmed by increase in  $p$  from 0.015 for the free dye to 0.21 at P/D = 330 (Fig. 4B) However even under high P/D values the external binding still makes essential contribution to complex formation.

### C. Binding of CatPheo-*a* with four-stranded poly(G)

The study of CatPheo-*a* binding to poly(G) is of great interest as this polynucleotide is capable to form four-stranded structure. So it is suitable for the modelling of the sections of telomeric DNA molecules called G-quadruplexes. The formation of four-stranded structure was proved by the melting experiments with the registration of the temperature dependence of absorbance at 295 nm [22].

The fluorescent titration experiments show that initial part of titration curve at P/D < 1 is coincident to those for the double-stranded polynucleotides (Fig.4C). It evidences the dye outside binding under low P/D values. The value of residual fluorescence intensity at P/D = 1 is 7.5% of that for the free dye. However, in contrast to single- and double-stranded-systems, in the case of poly(G) under P/D > 1 drastic rise of fluorescence intensity was observed reaching the value of  $I/I_0 = 4.4$  under P/D = 385 (Fig. 4A). It is accompanied by ~13 nm red shift of the Soret band maximum, as well as 15 nm red shift of fluorescence band (not shown). In the initial P/D range from 1 to 10 the fluorescence polarization degree rises from 0.01 to 0.28 and then, at P/D > 10, it levels off 0.29 (Fig. 4B). Such high value of  $p$  confirms intercalation of dye chromophores between guanine quartets of poly(G). Increase in CatPheo-*a* fluorescence yield upon its intercalation into poly(G) is of interest, since guanine residues effectively quench fluorescence of most dyes [23,24].

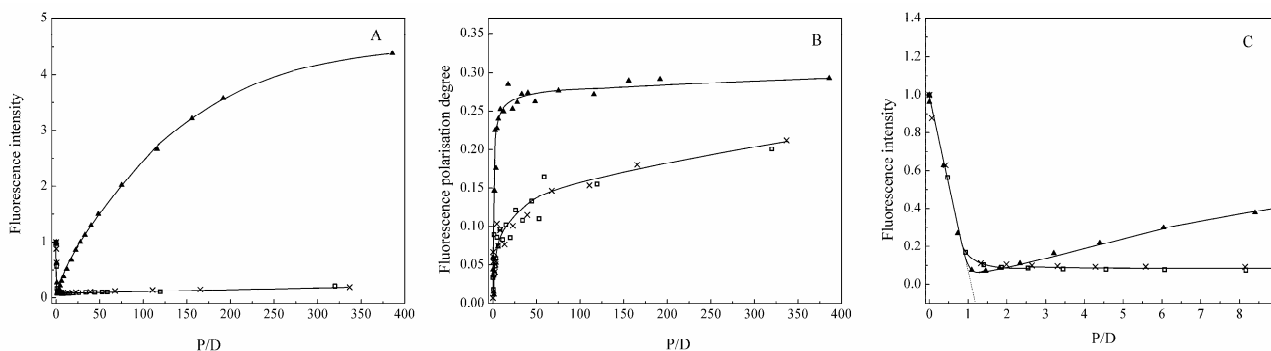


Fig. 4 Dependence of normalized fluorescence intensity (A, C) and fluorescence polarization degree (B) of CatPheo-*a* on polymer/dye ratio upon titration by poly(G)·poly(C) (□), poly(G) (▲) and poly(A)·poly(U) (×) polynucleotides measured in the maximum of emission band in aqueous buffered solution containing 2 mM Na<sup>+</sup>, C<sub>dye</sub> = 1.3·10<sup>-5</sup> M. Fluorescence excitation wavelength is 633 nm



In such a way two binding modes for CatPheo-a with poly(G) were observed: at low P/D values ( $P/D < 5$ ) the outside binding predominates, while the P/D increase results in the dissociation and prevalence of intercalative binding mechanism. In this case the total transition of dye from stacking associates to intercalated state was realized.

#### IV. CONCLUSIONS

The investigation of CatPheo-a binding to double-stranded poly(A):poly(U) and poly(G):poly(C) polynucleotides, as well as to four-stranded poly(G), shows that for all systems the highly cooperative outside binding occurs under low  $P/D < 3$  values. It is accompanied with the chromophore stacking association, which is characterized by the strong quenching of CatPheo-a fluorescence. Under high P/D ratios the disintegration of aggregates takes place and intercalative binding is occurred. In the four-stranded poly(G) containing system the intercalating binding mode was observed under  $P/D > 5$  being confirmed by substantial increase of fluorescence intensity and polarization degree. In the case of the double-stranded polynucleotides the intercalative binding of CatPheo-a is weak. Its saturation does not occur even under high P/D values. It was revealed that the fluorescent technique is efficient for the recognition of the binding mode since CatPheo-a emission increases substantially upon the dye intercalation, while it is quenched upon the stacking-association.

It was established that CatPheo-a binds effectively to four-stranded poly(G) by the intercalation of its chromophore between guanine quartets. The improved photodynamical activity for CatPheo-a in comparison with that for Pheo-a is expected because of a good water solubility of CatPheo-a, the absence of high-order dye aggregates formation in a wide concentration range, and the efficient dye binding with polyanionic biopolymers. Thus, CatPheo can be proposed for use as an anticancer agent for photodynamical therapy and it can be considered as a possible fluorescence probe for recognition of G-quadruplex structures.

#### ACKNOWLEDGMENT

This work was partially supported by Science and Technology Center in Ukraine (STCU grant #3172).

#### REFERENCES

- Owens J W et al. (1998) Photophysical properties of porphyrins, phthalocyanines, and benzochlorins. *Inorg. Chim. Acta* 279:226–231
- Dougherty T Jr et al. (1998). Photodynamic therapy. *J Natl Cancer Inst* 90: 889–905

- Ricchelli F (1995). Photophysical properties of porphyrins in biological membranes. *J Photochem Photobiol B: Biol* 29: 109–118
- Willstatter R and Stoll A (1913) *Untersuchungen über Chlorophyll. Methoden und Ergebnisse.* Springer, Berlin
- MacDonald I J and Dougherty T Jr (2001) Basic principles of photodynamic therapy. *J Porphyrins Phthalocyanines* 5: 105-129
- Röder B (1990) Photosensitizing properties of phorbides. *J Photochem Photobiol B: Biol* 5: 519-521
- Röder B (1990) Tetrapyrroles: a chemical class of potent photosensitizers for the photodynamic treatment of tumours. *Lasers Med Sci* 5: 99-106
- Roeder B (1998) Pheophorbides. *In Photodynamic Tumor Therapy: 2nd and 3rd Generation Photosensitizers.* J.G. Moser, Ed.: 35-42 Harwood Academic Publishers. Amsterdam.
- Hajri A, Wack S et al. (2002) In vitro and in vivo efficiency of photofrin and pheophorbide a, a bacteriochlorin in photodynamic therapy of colonic cancer cells. *Photochem Photobiol* 75: 140-148
- Krasnovsky A Jr et al. (1990) Photophysical studies of pheophorbide a and pheophytin a. Phosphorescence and photosensitized singlet oxygen luminescence. *J. Photochem Photobiol. B: Biol.* 5: 245-254
- Roeder B (1998). Photobiophysical parameters. *In Photodynamic Tumor Therapy: 2nd and 3rd Generation Photosensitizers.* J.G. Moser, Ed.: 9-19. Harwood Academic Publishers. Amsterdam.
- Tanielian C, Kobayashi M, Wolf C (2001) Mechanism of photodynamic activity of pheophorbides. *J Biomed Opt* 6: 252-256
- Eichwurz I, Stiel H, Roeder B (2000) Photophysical studies of the pheophorbide a dimer. *J Photochem Photobiol B: Biol* 54: 194-200
- Ryazanova O, Voloshin I, Dubey I, Dubey L and Zozulya V (2008) Fluorescent studies on cooperative binding of cationic pheophorbide-a derivative to polyphosphate. *Annals NYAS* (in press)
- Fiel R (1989) Porphyrin-nucleic acid interactions: a review. *J Biomol Struct Dyn* 6:1259–1274
- Pasternack R, Gibbs E, Villafranca J (1983) Interactions of porphyrins with nucleic acids. *Biochemistry* 22: 2406–2414
- Pasternack R, Gibbs E, Villafranca J (1983) Interactions of porphyrins with nucleic acids. *Biochemistry* 22: 5409–5417
- Bennett M. et al. (2000) A DNA–porphyrin minor-groove complex at atomic resolution: The structural consequences of porphyrin ruffling. *Proc Natl Acad Sci USA* 97: 9476–9481
- Ford K et al. (1987) DNA sequence preferences for an intercalating porphyrin compound revealed by footprinting *Nucleic Acids Res* 15: 2221 – 2234
- Zozulya V et al. (1997) Fluorescence and binding properties of phenazine derivatives in complexes with polynucleotides of various base compositions and secondary structures. *Biophys Chem* 65: 55-63
- Schwarz G, Klose S, Balthasar W (1970) Cooperative binding to linear biopolymers 2. Thermodynamic analysis of the proflavine - poly(L-glutamic acid) system. *Eur J Biochem* 12: 454-460.
- Mergny J, Phan A, Lacroix L (1998) Following G-quartet formation by UV-spectroscopy. *FEBS Letters* 435: 74-78
- Löber G, Kittler L (1978) Redox mechanism involved in the fluorescence quenching of dyes bound to deoxyribonucleic acid (DNA). *Stud. Biophys.* 73(1): 25-30
- Seidel C, Schulz A, and Sauer M (1996) Nucleobase-specific quenching of fluorescent dyes. 1. Nucleobase one-electron redox potentials and their correlation with static and dynamic quenching efficiencies. *J. Phys. Chem.* 100: 5541-5555

Author: Olga Ryazanova  
 Institute: B. Verkin Institute for Low Temperature physics and Engineering of NAS of Ukraine  
 Street: 47 Lenin ave.  
 City: Kharkov  
 Country: Ukraine  
 Email: ryazanova@ilt.kharkov.ua

# ICT and Knowledge Management for the ISO 9001:2000 Standards Compliance of I.R.C.C.S. “Burlo Garofolo” Maternal-children Hospital

M. Bava<sup>1</sup>, E. Danielli<sup>1</sup>, A. Orsini<sup>2</sup>, D. Tarticchio<sup>2</sup>, L. Vecchi Brumatti<sup>1</sup>, R. Zangrando<sup>1</sup>, F. Zennaro<sup>1</sup> and A. Accardo<sup>2</sup>

<sup>1</sup> Maternal-children I.R.C.C.S. “Burlo Garofolo”, Trieste, Italy

<sup>2</sup> Department of Electronics, DEEI, University of Trieste, Trieste, Italy

**Abstract** — The I.R.C.C.S. “*Burlo Garofolo*” is a maternal-children’s Hospital and Clinical Research Institute located in Trieste, which must comply with ISO 9001:2000 standards for Health Processes, as required by Italian Law (D.L.vo 288/2003). This paper describes the design and the development of the intranet portal of the hospital, built in accordance with regulations and especially to enhance the internal communication among the Hospital units.

**Keywords** — LAMP open source technology, Joomla! CMS, ISO 9001:2000 quality standards.

## I. INTRODUCTION

In order to comply with ISO 9001:2000 standards for Health Processes, as required by Italian Law (D.L.vo 288/2003), the IRCCS “*Burlo Garofolo*” started the re-organization of the clinical research and medical practice according to the international healthcare standards.

An I.R.C.C.S. is a particular kind of hospital in the Italian health care system where healthcare and scientific research are conducted simultaneously and are managed at the same level.

An intranet portal, built in accordance with regulations and especially to enhance the internal communication among the hospital units, has been recognized by the Hospital Strategic Direction as an innovative tool to be designed, developed and maintained.

The Quality Assurance Office and the Hospital Information System collaborated to establish the portal to improve the distribution of internal documentation, especially guide lines, procedures and protocols.

The availability of such a portal represents a platform used as a common dashboard where it is possible to retrieve the documentation in force, which is the electronic expression of the corporate knowledge. The subsequent exploitation of this knowledge allows to evaluate globally the production of procedures, guide lines and protocols by the different wards, avoiding redundancies and enabling work sharing, improving integration and harmonization of the corporate processes.

The portal encourages communication through the use of an internal blog in which users with accounts may transmit in real time necessary information to get the expected results in a more effective and efficient manner.

## II. SYSTEMS AND TECHNOLOGIES

The intranet portal is based on a popular free open-source CMS, “Joomla!” (stable version 1.0.12), revised according to the requirements suggested by the “*Burlo Garofolo*’s” Strategic Direction.

In order to accomplish the proposed objectives, the typical structure of Joomla! [1] has been applied to map both the functional organization of the clinical departments and the major quality items as considered in the Quality Program Document.

The platform, developed and managed by an internal team of professionals, is realized using LAMP technology and is housed in a hospital dedicated server.

The operating system is Linux Debian 4.0 Stable [2], installed on a vintage double Pentium II processor system equipped with four SCSI hard drives. Debian recognized very well the RAID 0+1 configuration of the server, obtained through an Adaptec AHA 27040 control card.

Apache 2.0 [3] is the web server used for the intranet portal; it was developed and sponsored by Apache Software Foundation both as source code and binary code. The database server is MySQL 5.1 [4] developed by MySQL AB, and as server side scripting language is used PHP 4.4.

The first intranet web site in 2004 was a static home page located on a machine with a private ip address, reachable only from the internal hospital subnets. The only dynamic tool was the corporate phone book realized using FileMaker Pro 5 and the built-in proprietary web server.

Joomla! offers a friendly user interface and a simple configuration control panel to update the contents and the corporate documentation. The control panel can be easily understood, and its use can be taught to the internal personnel in the wards or in the administrative offices.

III. DESIGN AND IMPLEMENTATION

A. General structure

As shown in Fig.1 the main menu of the intranet home page was structured into three macro “areas”, the first two designed according to the content structure of Joomla! itself, which is based on the division in sections, categories and articles.

The first “area” is constituted by common interest corporate subjects as:

1. On-line and pdf downloadable address book
2. Guidelines and rules regarding the day hospital activity
3. pharmaceutical vade-mecum
4. hospital forms catalogue
5. stationery catalogue
6. quality programme
7. budget programme

These subjects reflect the needs both to communicate and to validate general procedures, guide lines and protocols at the corporate level, avoiding redundancies and promoting work sharing to improve the corporate processes and their integration.

The second “area” lists the Hospital Departments and offices reflecting the organization chart, and is composed of:

1. Strategic Office
2. Scientific Office
3. Sanitary Office
4. Administrative Office
5. Paediatrics Department
6. Obstetrical and Gynaecological Department
7. Surgery Department
8. Laboratory and molecular medicine Department

The structures listed above are organized following a general scheme built on the Joomla! “sections -> categories

-> articles -> elements” scheme. In this model the sections are the Departments or the Offices; the categories are the functional structures composing the single Department or Office; the articles are organized for every structure following the scheme shown in the table below.

In the third “area” of the menu the links to a variety of services related to the intranet are found, using it as a unified and common platform as shown in Fig. 2.

The articles of each area listed in Table 1 are further organized in a table in with every element (a specific protocol or guide line or procedure) is identified as shown in Fig. 3.

Table 1

Articles	Date of upload	Author	Contacts
Guidelines	dd/mm/yyyy	admin	n
Projects and programs			
Reports			
Lists			
Plans			
Objectives			
Procedures			
User manuals			
Rules			
Newsletters			



Fig. 1 Intranet home page

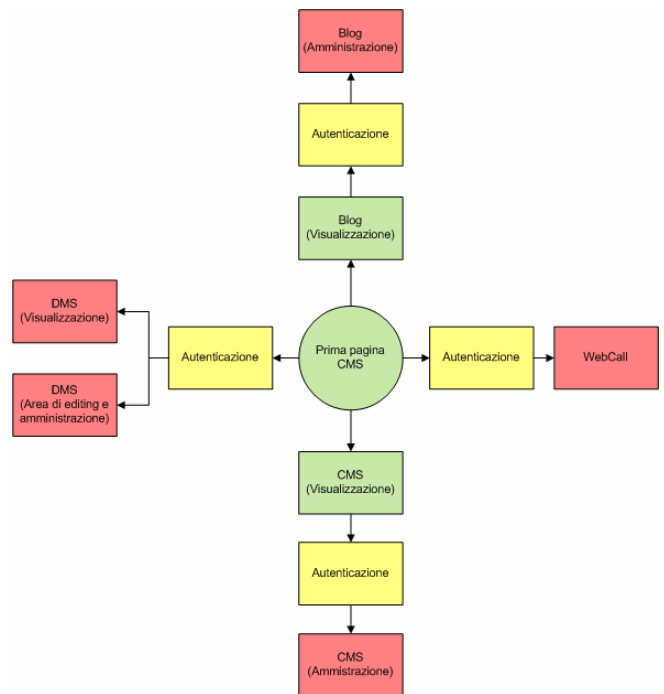


Fig. 2 Intranet common platform

TYPE	COD	REV	DATE	SUBST.	SUBST. BY	STATUS	TITLE	DEPT/ DIR	STRUCT/ SERV
LEG	LEG.01	0	08/01/2008	\	\	VIG	LEGEND	DSN	DSN
PR	PR CAT VESC	0	ott-97	\	\	VIG	Protocollo di assistenza al paziente portatore di catetere vescicale	DSN	INF OSP
LETT	LETT Prof. N 5367/Cla sse: DS/8	0	22/04/2004	\	\	VIG	Lettera esplicativa al Protocollo di assistenza al paziente portatore di catetere vescicale	DSN	INF OSP
PR	PR MRSA	0	nov-02	\	\	VIG	Protocollo per la prevenzione della diffusione dello <i>Staphylococcus aureus</i> Meticillino Resistente (MRSA)	DSN	INF OSP

Fig. 3 Common “elements” page

The table format was chosen and internally standardized for every article published on the intranet web site.

### B. Specific implementations

Joomla! is a CMS widely available by the community and developed to offer a large number of modules, mambots and features. It is possible to customize the web pages, their contents and the tools for navigation, visualization and use of the web sites in which is implemented.

During the design and the development of the intranet web site, the Hospital Information System with the collaboration of university students and personnel started to test and use some of Joomla!’s built-in tools and many of the community developed tools to enhance the basic modules provided with the installed release 1.0.12.

The aim of the experimentation was to better understand the potential of Joomla! itself, to respond to the needs which emerged during the interviews performed in the analysis phase of the project.

From the beginning of the design of the platform, for example, it was necessary to unify, organize and make available the entire Hospital paper documentation in electronic format. This documentation can now be consulted and downloaded in the first area section named “hospital forms catalogue”.

Joomla!’s built-in address book module was immediately suitable for the on-line address book allowing an easy search of internal personnel (telephone number, e-mail address, location) and structures.

The portal offers as many services as the Hospital wards or structures require to archive, publish and visualize their documentation.

During the test time an easy-to-use chat system has been available to enhance the internal communication, and the RSS feed engine has been proposed for each ward or structure that needs to collect specific web sites news.

### C. Accesses and permissions

The access to the front-end of the platform is free although limited to the internal machines located in private subnets. Thus the access is ip-filtered. The back-end of the platform is accessed only by the administrators who control and manage the entire system and by a restricted user of the Technical Office that has been trained to update the list of the technical interventions performed.

### D. The “Burlo’s Blog”

An internal blog has been created using Wordpress 2.01 [5] to allow better interaction among the Hospital’s personnel regarding the corporate objectives and the discussion around five topics:

1. job organization
2. instrumentation and informatics
3. legal features
4. guide lines (add, modify, update, etc...)
5. chain of responsibilities

The common blog’s home page is reachable from the intranet portal; to add or update some of the contents concerning the topics listed above, a list of users with different privileges has been prepared, according to the possibilities offered by Wordpress. Rules have been stipulated for access and for etiquette to continue using the system. The Blog is fully moderated by an internal consultant who acts as a filter for the contents to be published.

## IV. RESULTS AND DISCUSSION

After the introduction of the platform in 2007 a more appropriate use of the hospital correct forms and a more punctual diffusion of information (such as the new Corporate Act or the new information Policies) has been quantified.

The possibility of a continuous update of the contents and of the documentation complies with the ISO 9001:2000 standards for Health Processes, allowing to know the review number, the author and the date of the document.

Finally, implementing the intranet has achieved a first step to diffuse explicitly corporate knowledge (both administrative and medical) that was previously hidden or implicit [6]. This is a process that should be continued, converting more and more of the medical and administrative information into shared knowledge, and even including in this path the peculiar scientific and research aspects of the I.R.C.C.S..

Apart from these results remain at least two critical situations.

The first regards the extension of the information tools which may introduce more complexity to the system and to the regular and consolidated procedures.

The second class of problems is related to the first and regards the formation and the training of the personnel in using the information tools correctly and effectively. This represents a challenge at the organizational level especially because it involves the employment of internal technical competencies and human resources.

## V. CONCLUSIONS

Beyond the continuous update of both the corporate documentation and the CMS managed by an internal team composed by IT and healthcare specialists, the future will be characterized by implementing an effective knowledge management system (KMS) by which the ISO 9001:2000 certified wards may control their quality documentation and to review and to update this documentation systematically and safely.

In recent months such a system has been studied, and testing some commercial and open-source products has

begun. The “Knowledge Tree” [7] Document Management System has been used to archive and manage the documentation of one of the ISO 9001:2000 certified wards, the paediatrics Radiology structure.

Further developments are expected, especially in modeling through UML data and resources fluxes of additional certified wards.

## REFERENCES

1. Joomla! at <http://www.joomla.it>
2. Debian at <http://www.debian.org>
3. Apache web server at <http://www.apache.org>
4. MySQL database at <http://www-it.mysql.com>
5. Wordpress at <http://www.wordpress-it.it>
6. Van Bommel J H, Musen M A. (1999) Handbook of medical informatics. MIEUR.
7. Knowledge Tree at <http://www.knowledgetree.com>

Author: Michele Bava

Institute: Clinical engineering and medical informatics - I.R.C.C.S.  
“Burlo Garofolo”

Street: Via dell’Istria 65/1

City: Trieste

Country: Italy

Email: [bava@burlo.trieste.it](mailto:bava@burlo.trieste.it)

# Biotelemetry

M. Cerny<sup>1</sup>, M. Penhaker<sup>1</sup>

<sup>1</sup>Department of Measuring and Control/Faculty of Electrical Engineering and Computer Science,  
VSB - Technical University of Ostrava, Ostrava, Czech republic

*Abstract* — **The biotelemetry is more common application of biomedical engineering and telemetry in our professional life. By this reason the biotelemetry is taught in our bachelor study program Biomedical technology from its beginning. These lessons are focused on the basics of networks, wired communications and wireless communication standards. Students learn systematically grounds of modern telemetry in the application in the biomedical engineering. The paper is focused on system of lectures and system of practical laboratory exercises.**

*Keywords* — **Biotelemetry, wireless communication, bachelor's education**

## I. INTRODUCTION

The biomedical engineering is taught in our university till beginnings of faculty of electrical engineering and computer science in 1990. It was the five year master study program first. Afterwards this program was divided to three years bachelor study program and two years master study program in 2004. The bachelor study program is named Biomedical technology. There are taught basics of medical science and basics of biomedical engineering. The subject Biotelemetry is taught in bachelor study branch Biomedical technology from beginnings of this study branch in 2004. The Biotelemetry is taught in the fifth semester of study. Even if it is optional subject it is fully occupied each year. Thanks to ESF funds were last year issued learning texts.

This article is focused on the structure of lesson and practical measurements.

## II. LESSONS STRUCTURE

The lessons are divided into ten chapters, which correspond to number of lectures per semester. The first four chapters are pursued history of telemetry, biosignals, techniques of biosignal measurement, basics of biomedical sensors and standards for signal modulation. Next chapter deals about steps of analog to digital conversion. The basics of the communication are taught as following. There are lectured differences between parallel and serial data transmission, between synchronous and asynchronous data transmission. The methods of transmission methods like multiplexing, networks taxonomy, network topology and the ISO- OSI reference model.

Afterwards, there is a chapter, which deals about technologies for wired data transmission. Students can learn about standards RS232, for parallel communication, USB, FireWire, GPIB and Ethernet.

The following chapter about wireless communication technologies deals about Infrared, Bluetooth, ZigBee, Wi-Fi, WiMAX, GPS, and GPRS.

The last chapter is engaged to applications of biotelemetry in HomeCare projects and similar projects for wireless monitoring of base life functions.

Because students of these lessons are in bachelor study program, the one half of the lectures time is intended for practical exercises.

The next part of this article deals about realized practical exercises.

## III. PRACTICAL EXERCISES

Students can verify their knowledge of the signal modulation standards, of conditions of A/D conversion, of RS 232, of Bluetooth, of ZigBee and radio modems. They can see application of all used devices in the real project - remote HomeCare. Each used technology is used in real application with medical measuring device. All designed and used devices are finished in our biomedical engineering laboratory; mostly there are used OEM modules for measure biological signals like temperature, blood pressure, plethysmography and ECG. Wireless communication is mostly realized by commercial wireless modules, which are in-built in measuring devices. At receiving side (PC) are used development boards, to can see students the real hardware. Each exercise is targeted to another problematic, but there is something like red sewing. Student can identify differences between similar technologies, their ranges and power consumption. The used devices are designed more robust not only to be safe for students, but to can be used in future.

### A. Amplitude and frequency modulation

This practical exercise allows to students to understand to basics and difference between amplitude and frequency signal modulation. They have to measure in frequency and amplitude modulated signal. The modulated signal is speci-

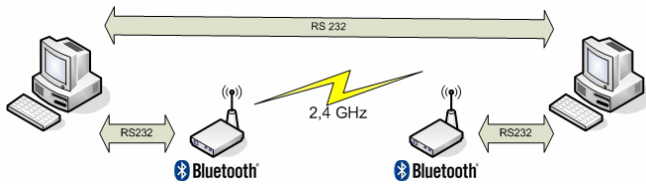


Fig. 1 The RS232 and Bluetooth emulation exercise scheme

fied before each practical lesson for each group has different one.

Students have to know how to work with the Matlab (The Matlab is taught in previous semester). Students have to know how to work with modern signal generator and spectral analyzer. Even if the basics of the measuring devices are taught in the pervious semester, the control of spectral analyzer is not easy for students. They have to study how to work with it before practical measurement at home (The simple manual is provided them).

The results from measurement can students verify in the program in Matlab after real measurement.

#### B. RS232 and RS232 emulation using Bluetooth module

The students have to try a RS232 communication between two PC using standard RS232 cable. The two cables are provided to students. One cable has the crossed connection between connectors; the second has the straight connected connectors. Students are testing which cable is suitable for data transmission between two PCs. Afterwards they test RS232 communication between two PC with different settings of RS232.

The last part of this exercise is devoted to RS232 emulation by Bluetooth. The OEMSPA-13i Bluetooth module from ConnectBlue with their setting program is used. Students set up the parameters of RS232 communication and set up the Bluetooth pairing procedure between used Bluetooth modules. The Fig.1 shows the scheme of this exercise.

The power consumption of Bluetooth modules is measured too.

#### C. The wireless measurements – Bluetooth

This exercise is focused on correct measurement of analog input signal. The signal is measured by the BluesenseAD Bluetooth module. The measured data are wirelessly transmitted to PC. Students have to set up the Bluetooth communication and learn about parameters setting up of BluesenseAD module. This module has included 8 channels 12-bit A/D converter with maximal sample frequency or one channel 4 kHz. The parameters of Bluetooth module can be set up wirelessly. Students measure the signal gener-

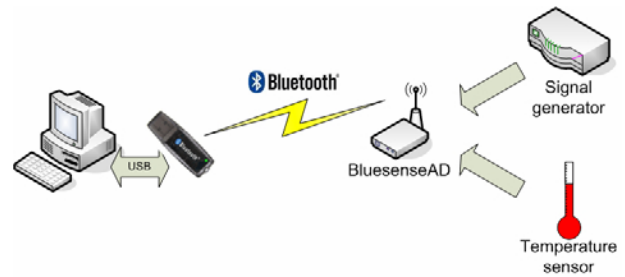


Fig. 2 Bluetooth measurements exercise scheme

ated by signal generator first. They have to try different set up of sampling frequency – It is the way how student can verify the Shannon theorem “in vivo”. Afterwards they connect the temperature sensor to BluesenseAD. They start the temperature measurement. They have to receive several data packets and decode these packets themselves. Afterwards they can count the measured temperature. The scheme of this exercise is shown on the Fig.2.

The power consumption of Bluetooth module is measured too.

#### D. Bluetooth application in biotelemetry

In the frame of this exercise students work with medical devices which communicate using Bluetooth technology. The Bluetooth technology could be replaced by ZigBee in several lessons.

The OEM modules for non-invasive blood pressure and ECG measurement are used. Students have to set up Bluetooth connection, verify the Bluetooth communication and afterwards receive and decode data packets from the both OEM measuring devices. Afterwards the real measuring with both devices in the same time could be realized. Students have to try the Bluetooth range too. The range measurement is only rough; they only take the device as far as possible till the measuring falls. The realized measuring devices are powered by accumulators; it allows moving with the measuring devices during the measuring.

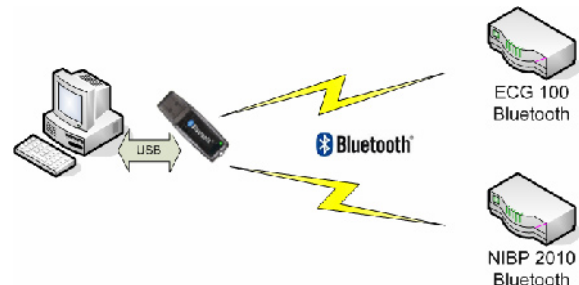


Fig. 3 The Bluetooth application in biotelemetry - exercise scheme

Students have to open and discover the measuring devices to they recognize parts of electrical circuits realized inside of measuring device.

The scheme of this exercise is shown on the Fig.3.

*E. The ZigBee application in biotelemetry*

This exercise is focused on emulation of wired communication by ZigBee. The ZigBee is realized by XBee ZigBee modems from Maxstream. It is easy to configure these modems because the official configuration software is used.

There is measured pulse oximetry using OEM module ChipOx.

Students have to teach themselves how to work with ChipOx, after they realize wired communication between PC and ChipOx. They have to recognize data packet and decode it themselves (The ChipOx communication protocol is provided.) Afterwards the wired communication is replaced by ZigBee communication. Students have to set up the parameters of ZigBee modules

The rough range measurement is realized. The power consumption of ZigBee modules is measured too.

The scheme of this exercise is shown on the Fig.3.

*F. The radio modems – AC4868*

This exercise is focused on the using of radio modems in the Biotelemetry. They have been intended for data transmission for longer distances using ISM band.

Students have to teach themselves how to work with radio modem AC4868 from Aerocomm. They will try the range of the radio data transmission with various antennas. The output transmitting power can not be set up to maximal value, because the maximal range is up to 10 km (in line of sight).

The spectral analyzer is used for the measurement of the real data transmission band.

The power consumption of radio modules is measured during data transmission too.

*G. The biotelemetry application – HomeCare Project*

The HomeCare system is designed, developed and realized in our laboratory. It is remote monitoring system of base life functions, which takes care about alone living elderly people. Not only standard monitored biosignals can give us the valuable information about the change in the state of the health of the monitored person. In cooperation with Ostrava University (Medical-social faculty) it was realized the Testing Flat for HomeCare technologies.

The last practical exercise in frame of Biotelemetry is held in this Testing flat. There are mounted every devices

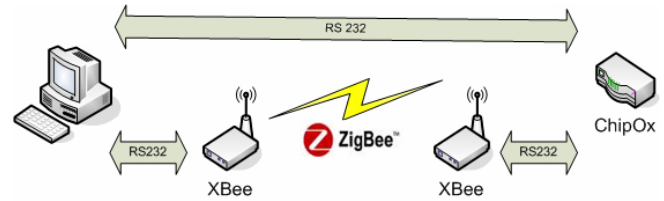


Fig. 4 The ZigBee application in Biotelemetry – exercise scheme

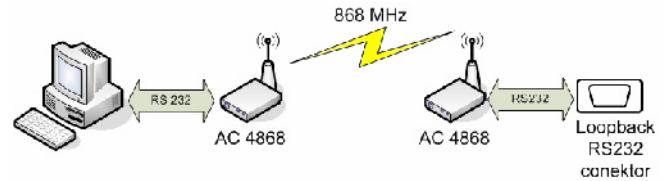


Fig. 5 The radio modems - exercise scheme

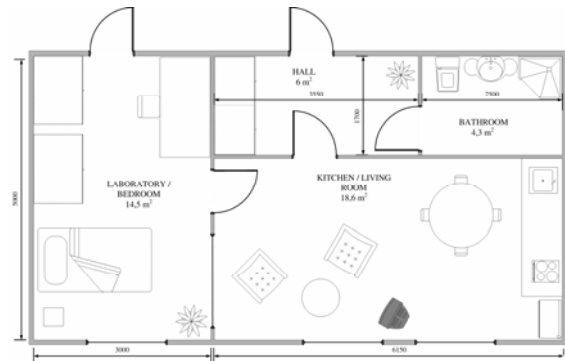


Fig. 6 The HomeCare Testing Flat (layout)

which were designed for HomeCare application in our laboratory. Students can see the devices used in the biotelemetry exercises in real applications, some new devices are mounted there too.

The movement monitoring system is mounted in the Testing flat too. In the frame of this last exercise students can try the movement monitoring system in the Testing flat. Before this exercise is realized, students has to design they own Homecare system. These student’s designs could be very usable for us project.

IV. CONCLUSIONS

Even if the Biotelemetry lectures are optional, the capacity of the lectures is fully took each year. This subject is useful for students of our bachelor study program Biomedical technology. Biotelemetry lectures provides them information about modern communication technologies and know how to use them in the biomedical engineering.



We can better get to know our students of bachelor study branch. The best students of Biotelemetry lectures are mostly asked to work in our HomeCare project; they can realize their bachelor works in frame of this project.

Nowadays the Biotelemetry lectures are translated to English language, to can be taught in English study programs in our university. New practical exercises are in progress now; to can we react to evolution in telemetry.

#### ACKNOWLEDGMENT

This work was supported in part by grant GACR 102/05/H525: The Postgraduate Study Rationalization at Faculty of Electrical Engineering and Computer Science VSB-TU Ostrava, ESF fund. No. 96/2004 Sb.

CZ.04.1.03/3.2.15.1/0020 and by the faculty internal project Biomedical engineering systems IV.

#### REFERENCES

1. Cerny, M., Penhaker, M.: Biotelemetry - lectures, VSB TU Ostrava 2007 ISBN: 978-80-248-1605-0
2. Cerny, M., Penhaker, M.: Biotelemetry - exercises, VSB TU Ostrava 2007 ISBN: 978- 80-248-1606-7

Author: Martin Cerny  
Institute: VSB – Technical University of Ostrava  
Street: 17.listopadu 15  
City: Ostrava Poruba  
Country: Czech Republic  
Email: martin.cerny@vsb.cz

# Five Year Biomedical Engineering Curriculum – Experiences and Results from the First Eight Years

K. Dremstrup and P. Elberg

Aalborg University, Department for Health Science and Technology, Aalborg, Denmark

**Abstract** — A full M.Sc- curriculum in Biomedical Engineering and Informatics was established at Aalborg University in 2000. The curriculum reflects the multidisciplinary composition of Biomedical Engineering and it consists of elements from engineering, informatics, medical and natural sciences as well as of elements from the social sciences.

The education follows the AAU problem-based learning (PBL) study paradigm with project-organized studies. The first students graduated as M.Sc. in June 2005. We have an average annual uptake of app. 35 students of which 25 - 40% are female students.

By establishing a full graduate curriculum in BME with intake directly from the high school level we believed, and have proved, that it is possible to attract more students due to larger visibility of the BME-program as opposed to classical graduate. It has been shown that the curriculum and study form equips the student well for future jobs – all candidates from the first three years have jobs.

Several student projects have taken awards; some student projects have lead to patents and some student projects are being transferred to private companies. Both hospital, industry and academia are giving very positive testimonials about the first candidates.

**Keywords** — BME, Education, Problem Based Learning

## I. INTRODUCTION

Biomedical Engineering (BME) most often exists as a candidate specialization build upon a classical engineering bachelor degree. This was also the case in Aalborg from 1978 to year 2000 where AAU introduced a full 5-year BME curriculum. The background for this introduction was an expressed need for highly trained candidates from the Danish BME industry and from politicians.

In a historical perspective BME has emerged from several different parent-fields: Electrical engineering, chemical engineering, mechanical engineering, physics, and other areas. They have all developed their applications in medicine and biology. Consequently, in most of the places in the world where BME is a graduate program it is typically embedded in one of these fields.

This strategy raises problems. In order to deliver a Biomedical Engineer, it is not optimal first to provide e.g. electrical engineering for three years and then building BME on

top of that. From a student's point of view the road to BME through e.g., electrical engineering is a long one. Many students simply do not even start on that road, or have no idea that it exists. This means that an enormous potential is lost. Biomedical engineering need and deserves a better focus from the start of the education.

As a consequence Biomedical Engineering is now establishing itself as an independent discipline. There are now well over 20 universities with undergraduate Biomedical Engineering programs in the USA. In Europe besides Aalborg, full five year programs have now emerged in The Netherlands and in Copenhagen.

The first BME candidates from Aalborg University graduated in summer 2005.

## II. TO BE TAUGHT OR TO LEARN - THAT IS THE QUESTION

The BME curriculum follows the AAU study paradigm with problem-based and project-organized studies with the student groups as the fundamental structural and pedagogical entity, see Fig. 1.

This study form has proven to secure a more efficient throughput in terms of study-time and percentage of students finalizing their study compared to the classical auditoria-based study forms.

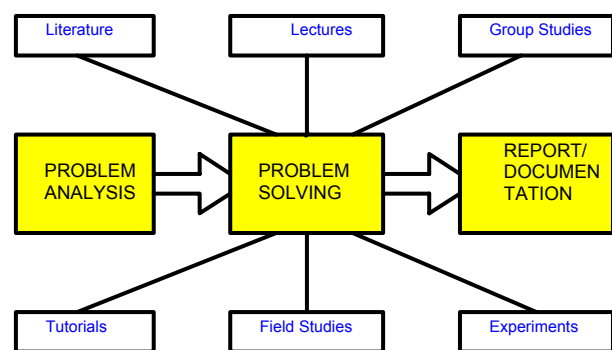


Figure 1: Principles of problem-based and project organized learning. The outcome from the project work is typically a prototype device/system demonstrated at the examination and documented in a report of size 100-150 pages.

The back-spine of the PBL study-form is the project where the students work with real-world problems, typically from the clinic, which are analysed, solved fully or partially, and finally documented, presented and defended at the examination [1, 2].

Each semester, lasting 5 month, consists of 30 ECTS units divided between course and project work. The workload of the course work and project work changes over the semester as illustrated on Fig.2 with more and more time devoted to the project. Five to seven students work together on a project solving a problem originating either from a hospital department, a company or a research group at the university. The group is allocated a supervisor, a professor from faculty, acting as a consultant - not a problem solver! The groups are allocated a work room (app. 18m<sup>2</sup>) at campus, this serve as their personal.

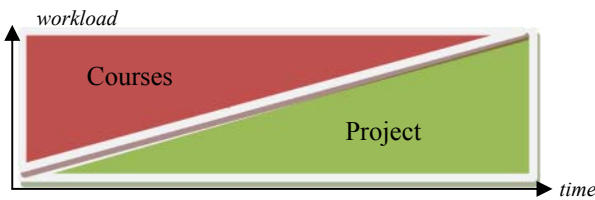


Figure 2: Composition of workload over time in the semester with one big project per semester. Note that half or more of the time is devoted to the project.

The students typically meet in their group room on a daily basis e.g. from 8 am to 4 pm. So from day one in their study time the students adapt to the working conditions most of them will meet as candidates. The group will have their internal meetings and meetings with their supervisor in the group room. Course examinations throughout the education are on individual terms. The projects are presented on a group basis, but the students are given individual examination and marks.

### III. CURRICULUM COMPOSITION

The curriculum in BME reflects the multidisciplinary of Biomedical Engineering and contains elements from medical and natural sciences, classical electronic engineering, as well as parts from humanities and social sciences. The study is divided into a bachelor part including a clinical external ship at the hospital, a candidate specializations with a final master thesis year, see fig.3.

### IV. BACHELOR AND CLINICAL YEARS

The first three bachelor years in the curriculum are comprised of a freshman year, a discipline oriented year and a clinical year. The freshman year provides the students with basic skills in mathematics, biology and computer science (Matlab and C++-programming) as well as with concepts of social science with emphasis on technology and society. The principles of Health Technology Assessment are introduced and applied in the projects. Through the BME-projects often made in close collaboration with the hospital, the students are introduced to the problem-oriented and project-organized paradigm as well as to the health sector. The projects are supported with courses in introduction to BME, biochemistry and modeling (Matlab based) and in courses on how to manage projects, cooperate in groups and how to learn



Figure 3: BME-MSc-programme composition. MS: Medical Systems, MI: Medical Informatics, BM: Biomechanics, DTT: Drug and Tissue Technology.

Project examples are: Influence on false alarms on patients and personnel in the ICU, Home care technologies and Work related EMG Measurements. Centrally for the projects is a certain level of empirical work at the hospital or in a laboratory. The groups are allocated two supervisors during the freshman year. Two professors, one with BME background, the main supervisor, and one with background in social sciences are allocated [1, 2].

The theme for third semester is: "Recording and presentation of biological signals". The semester introduces human anatomy and physiology. Medical instrumentation including safety aspects in the laboratory and measurement techniques is introduced. Examples of typical third semester projects are: "ECG-pulse measurement", "Body impedance measurements device" and "Stimulator for functional electrical stimulation". The projects on third semester all include bio-instrumentation, safety aspects and measures one or more biological variable from patients or subjects - often the students. As in all semester projects the students must

construct a demonstrator - here a physical device that must be proved to function and documented appropriately.

Fourth semesters theme is: "Processing of biological signals" and it focuses on physiology, application of microcontrollers, programming and signal processing in biomedicine. Project examples are: "EMG-controlled Mouse", "ECG-monitor" and "Digital stethoscope". The 4th semester projects use a microcontroller as the core of the problem solution. The students will construct an appropriate interface and program the microcontroller in C. The user interface is typically made on a PC connected to the microcontroller system using Labview. Fig. 4 illustrates the compositions of the bachelor semesters [5].

Courses on third and fourth semesters are Mathematics including continuous and discrete calculus, Electric Circuit Theory, Physiology and Anatomy, physiological modeling, Bioinstrumentation, Electromagnetism, Microcontroller architecture, Signal Processing and C-programming.

On 3rd and 4th semesters the students have to build and document an operable prototype which they will demonstrate at the examination.

Fifth semester focuses on the clinical work at the hospital departments. The projects take place at different hospital departments at Aalborg Hospital and the students have group rooms at the hospital. The students follow the daily routine at the department they are allocated. The projects have out-spring in the clinical problems from the departments and the students are assigned a clinical as well as a faculty supervisor. Examples of projects are: Diagnosis of Hydrocephalus, Data Flow in a Hospital Department, Temperature measurement in children

On the sixth semester the students are still physically located at the hospital. But where the projects on 5th semester mostly are of analytical nature, the students are supposed to design solutions on the sixth semester. Courses on the clinical year covers: Internal medicine and surgery, theory of science, organization theory, ethics, hospital hygiene, microbiology, homeostasis, hospital information systems, imaging and OO-design and programming (UML and Java).

V. SPECIALIZATIONS AND M.SC.-THESIS YEARS

In the last two years the students are specialized but a common course core exists to ensure that all students manage central topics. Four specializations are offered for the time being: Medical Informatics, Medical Systems, Biomechanics and Drug delivery and Tissue Engineering. On the specialization semesters most of the projects are part of ongoing research projects and provide the students with insight in scientific research planning and execution.

Many of the students choose to spend up to a full semester abroad on another university on the last part of the education. A one-year project within one of the research groups at the Department of Health Science and Technology or the hospital makes the final specialization. The final projects are made by individual students or two students together. Courses in the specialization years cover the different specializations and span from neurophysiology over stochastic mathematics and biostatistics to medical image analysis and medical information systems. Also topics such as medical standards and regulations, ethics and entrepreneurship are covered.

Some projects are started during a stay abroad and finished during the last semester. For example several students have been introduced to Natural Language Processing techniques in Sydney, Australia, and these methods have been used in order to retrieve specific information from electronic patient records in a Danish setting during the final semester project [3, 4, 5].

VI. EIGHT YEARS OF EXPERIENCES

By establishing a full graduate curriculum in BME with intake directly from the high school level we believed, and have proved, that it is possible to attract more students due to larger visibility of the BME-program as opposed to classical graduate programs where students have to "pass" a traditional engineering study before reaching the BME-specialization. The student intake in 2000 was 32 and 27 students in 2007, see Table 1. Saturation has seemingly occurred and the level of intake will probably stabilize between 30 and 40 students per year. The size of the annual uptake is probably influenced by the start of competing programs both in Copenhagen and in Aarhus, the two largest cities in Denmark. Internal competition for students cannot be excluded as reason either, as AAU started a Medical education with industrial specialization in 2006 with an annual uptake of around 100 students.

A positive bonus of the BME-program is that the percentage of female students is much higher than seen on eg. electronic engineering. The first year 50 % of the uptake

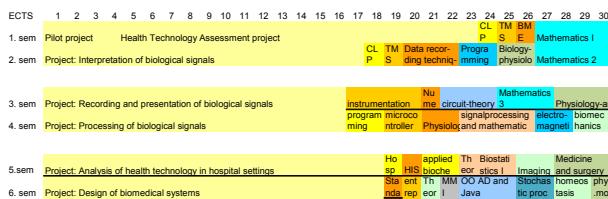


Figure 4. Composition of the bachelor part of BME. Each semester consists of 30 ECTS, the size of the projects (pale yellow) are between 16 and 23 ECTS units. The coloured modules are different supporting courses taught ex auditorium.

Table 1 Annual uptake on BME

Year	Number of students
2000	32
2001	46
2002	50
2003	40
2004	57
2005	38
2006	34
2007	27

was female, this has now settled to 25 %. Still a very high percentage compared to the normal level of <5% female students on the electronic engineering study. The decline may be explained by the above mentioned new Medical program. Many female students probably consider this education an alternative to BME.

What is of course very interesting for a new program is that it has shown that the curriculum and study form equips the student very well for future jobs. All candidates of the first three years graduating in 2005-2007: 18, 27 and 29 have been employed. The education focused on three main areas for employment: Industry, hospitals and academia. Candidates have been employed in all three areas. A large group continued in a phd-study program, another large group got employment as R&D's in industry – from medical informatics companies to device companies. The third group is more diverse with jobs in hospitals, patent companies and in BME sales and marketing functions.

Several student projects have taken awards; some student projects have been so promising that patents are applied for; some projects are being handed over to private companies. A single project initiated at the first 7th semester has been so successful that a patent has been filed and a license contract with a world leading company has been established. Some of the students have established private companies - even before graduation.

Six of the first candidates have pursued their carrier as innovators in a newly established incubator at the Department for Health Science and Technology [6].

## VII. CONCLUSIONS

The BME curriculum is now adapted to the Bologna model and some of it will be taught in English, making it possible to exchange students with universities abroad. It has been shown that the BME curriculum implemented at

AAU full-fill the requirements from the relevant consumers of the candidates, i.e. the BME-industry, the health sector and the academia with respect to factual knowledge within biomedical engineering, medicine and informatics etc. We are convinced that the ability to crack real-life problems, to document the process and solutions, to collaborate with peers and colleagues with different background as taught and **learned** using the Problem Based Learning paradigm ensures that the candidates significantly contribute to the companies and departments where they get employment and thereby to the demands from the society as such for well equipped candidates for the health sector. Both hospital and industry are giving very positive testimonials about the program and the candidates from it. A side result of the successful establishing of the BME program at AAU is that it has lead to an expansion of the tenured staff at the Department for Health Science and Technology. The department now counts 155 persons in its staff of which about 35 are tenured professors. This expansion has contributed to the decision to develop the new candidate education in Medicine with Industrial Specialization which started in 2006 and the department is also the main entrepreneur for the new Sports Science education initiated in 2007 at Aalborg University.

## REFERENCES

1. Kjærdsdam, F. and Enemark, S. (1994): The Aalborg Experiment, Aalborg University, [www.teknat.auc.dk/teknat\\_home/experiment/](http://www.teknat.auc.dk/teknat_home/experiment/)
2. Kolmos, A., Fink, F. K.; Krogh, L. (eds) (2004): The Aalborg PBL model: Progress, Diversity and Challenges; Aalborg University Press,
3. Nielsen, K. Dremstrup., Struijk, J. and Sinkjær T (2002): Five Years BME Curriculum With Problem Based And Project Organized Learning at Aalborg University; IFMBE Proceedings Vol; 12th NBC on Biom. Eng. and Med. Physics, p. 112-113
4. Nielsen, K. Dremstrup; Struijk, Johannes.(2005); BME education: the project organized and problem based learning model is the choice. Proc. IFMBE, Prague,. 4 s.
5. AAU-BME curriculum. Internet address: [www.hst.aau.dk/masterprogrammes.htm](http://www.hst.aau.dk/masterprogrammes.htm)
6. Department of Health Science and Technology at Aalborg University, internet address: [www.hst.aau.dk](http://www.hst.aau.dk)

Author: Kim Dremstrup  
 Institute: Department of Health Science and Technology,  
 Aalborg University  
 Street: Fredrik Bajersvej 7 D  
 City: Aalborg  
 Country: Denmark  
 Email: [kdn@hst.aau.dk](mailto:kdn@hst.aau.dk)

# Medical GRID and E-Learning in the Virtual Hospital

G. Grasczew<sup>1</sup>, T.A. Roelofs<sup>1</sup>, S. Rakowsky<sup>1</sup>, P.M. Schlag<sup>1</sup>

<sup>1</sup> Surgical Research Unit OP 2000, Robert-Roessle-Klinik and Max-Delbrueck-Center, Charité – University Medicine Berlin, Germany

**Abstract** — The development of virtual hospitals and digital medicine helps to bridge the digital divide between different regions of the world and enables equal access to high-level medical care. As data and computing resources in a virtual hospital are distributed over many sites the concept of the Grid should be integrated with other communication networks and platforms. A promising approach is the implementation of service-oriented architectures for an invisible grid, hiding complexity for both application developers and end-users. An example of a promising medical application of Grid technology is the real-time 3D-visualization and manipulation of patient data for individualized treatment planning. Global networks and the use of computers for educational purposes stimulate and support the development of virtual universities for e-learning. Especially real-time interactive applications can play an important role in tailored and personalised services. However, it takes more than just technology to move from pure e-learning towards the full expansion of ubiquitous access to educational services, anytime and anywhere (u-learning).

**Keywords** — Virtual Hospital, Health Grid Applications, Distance Education, Ubiquitous Learning (u-learning), Real-Time Interactivity

## I. INTRODUCTION

Virtual Hospitals (VH) aim to support the interconnection and interoperability of the various medical platforms and services of the organisations participating in a telemedical network, by integrating them into a consistent set of services. Thus, the development of VH and digital medicine helps to bridge the digital divide between different regions of the world and enables equal access to high-level medical care.

For the provision of global healthcare dedicated telemedicine and e-Health services are needed 24 hours per day, 7 days per week (24/7). These services should meet high standards for reliability and quality of service (QoS). Furthermore, open-source and open-standard solutions are essential for interoperability and integration of the various services. Also, gateways to other communication networks should be created.

The implementation of interactive remote control of medical devices will enhance tediagnosis. Consequently, the medical workflow and decision-making tree has to be re-evaluated and new management tools for global virtual

alliances have to be introduced. Mental, intellectual and educational e-services for citizens shall be created [1-3] (Fig. 3).

Pre-operative planning, intra-operative navigation and minimally-invasive surgery require a digital and virtual environment supporting the perception of the physician. To deal with such an amount of information multi-perception for multimedia performance in virtual reality environments (visualisation of virtual 3-D objects, full navigation, haptic simulation, etc.) are needed.

## II. MEDICAL GRID

Due to the geographically dispersed character of the Virtual Hospital, data and computing resources are distributed over many sites under different administrative domains. Therefore Grid-based infrastructures, architectures and services [4] become a useful tool for the successful deployment of medical applications and thus provide medical personnel with the required information, computation, and communication services [5]. Services like acquisition and processing of medical images, data storage, archiving and retrieval, as well as data mining being applied especially for evidence-based medicine are typical medical applications which profit strongly from the development and implementation of suitable medical Grid environments.

A promising approach is the implementation of service-oriented architectures for an invisible Grid, hiding

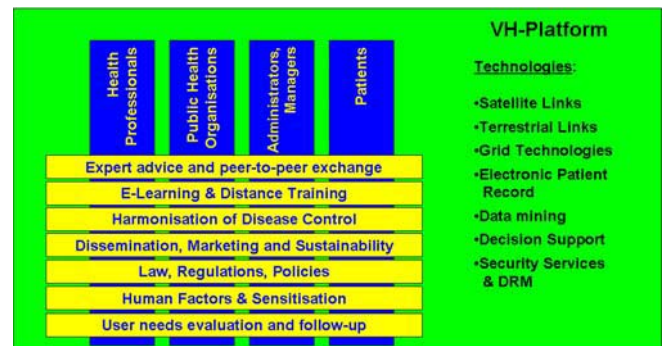


Fig. 1 Heterogeneous technologies with seamless transitions allow the users of the Virtual Hospital to access the services without knowledge of technological details

complexity for both application developers and end-users. While giving access to distributed services in a wide-area network of connected institutions a Grid-based system can integrate domain knowledge, powerful computing resources for analytical tasks and means of communication with partners and consultants in a trusted and secure system, tailored according to the users requirements in medico-clinical applications.

The main challenge in the domain of grid-based tools and applications is given by hiding the complexity of the underlying Grid infrastructure from the application developer by integrating higher level tools and services for grid application development.

The main reason for the lack of Grid-aware applications appears to be a gap between the Grid infrastructures and their developers / operators on the one side and the developers and end-users of Grid-based applications on the other side. To bridge this gap a user-driven approach needs to be implemented, which includes all stakeholders.

A Grid Tools Suite (GTS) needs to be developed that will facilitate and enhance the development of Grid-aware applications. The architecture of the GTS needs to be service-oriented and based on the needs of both application developers and end-users. Inclusion of already existing tools fulfilling the defined requirements, as well as the development of new tools and extensions of existing ones will guarantee building on previous achievements while not compromising on the strict requirements for architecture and functionalities.

Examples of medical applications of Grid technology are the real-time 3D-visualization and manipulation of patient data for individualized treatment planning and the creation of distributed intelligent databases of medical images. To enable fast 3D visualization and interactive inspection of CT, MRT and US patient data after semi-automatic segmentation and reconstruction Grid technology comes into consideration. Currently, using the existing View Sphere Rendering software about 5000 views on an imaginary sphere enclosing the data cube (CT, MRT) can be displayed as a result of off-line pre-calculation of the views [6]. As a result of these pre-calculation of the view sphere the user is able to rotate the data cube in real-time (50 frames per second on each channel) using different interaction devices such as joystick, mouse, keyboard, or voice control to inspect not only the original 2D slices but also recalculated slices for any new orientation of the data set, and to navigate through the data slices inside a region of interest (Fig. 2).

Using grid resources an on-line calculation of the view sphere would be possible thus enhancing operation planning facilities considerably. Also Grid services like the Grid Visualization Kernel (GVK) [7] can be used for 3D

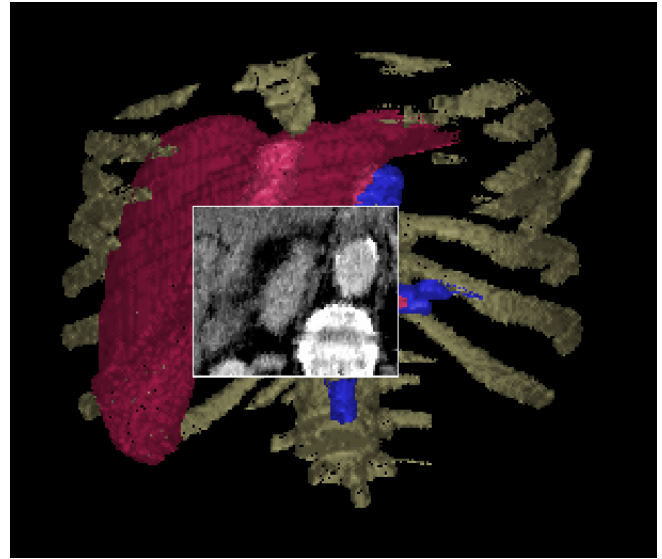


Fig. 2 3D visualisation and interactive inspection of reconstructed CT, MRT and US patient data

visualisation. The rendering of multiple images using different viewpoints is required. Taking into account the typically large size of medical datasets the rendering techniques have to be highly parallelized to exploit the performance of grid resources to the full extent. If multiple distributed grid resources are used for rendering, the input data has to be distributed onto the resources beforehand.

### III. E-LEARNING

Global networks like in the VH and the use of computers for educational purposes stimulate and support the development of virtual universities for e-learning. Especially real-time interactive applications like realized in the EMISPHER Virtual Medical University can play an important role in tailored and personalised services. The objectives of real-time education and training in medicine are live transmission directly from the operating theatre. By implementing interactive connections to the “point of action” and remote control of cameras to be viewed on the local monitors, live interaction with and participation in the remote event becomes possible [8-9].

The communication software WinVicos (Wavelet based interactive Video communication system) has specially been designed for a broad range of real-time interactive tele-applications. WinVicos is a high-end interactive video communication software, providing real-time transmission of video streams and still-images, based on IP-protocols. Due to a wavelet-based compression high-quality video



Fig. 3 Interactive multipoint e-Learning session: Instructors from Charité (Berlin), participants from ASU (Cairo), ANDS (Algiers), FMPC (Casablanca) and UCY (Nicosia)

transmission allowing remote medical diagnosis is possible even at moderate transmission bandwidth of 0,5-1,0 Mbit/s.

The EMISPHER project (Euro-Mediterranean Internet-Satellite Platform for Health, medical Education and Research) provides an integrated internet-satellite platform for the application of various telemedical services such as medical e-learning and real-time telemedicine. Since its deployment, the EMISPHER platform has hosted over 350 interactive tele-education sessions (Fig. 3). The EMISPHER network is thus very suited as a future basis for real-time tele-education applications.

Real-time telemedical applications contribute to improved quality of patient care and to accelerated qualification of medical doctors in their respective specialty. The main target audience are specialist doctors. A typical e-learning application is the education and training of young medical doctors by telementoring. By the realization of remote control of medical equipment a real telepresence is created allowing not only to see each other but to act as if one were locally present, thus enhancing telementoring by enabling interactive work of teacher and student.

Rather than putting emphasis only on the required technologies as means for e-learning, it will be necessary to focus also on the users and their needs and take this as primary driver for developments towards ubiquitous learning in the VH. Where the term e-learning merely reflects ICT-enabled methods of education, it bears the risk of putting the means (technology) in the focus rather than the goals (ubiquitous access to education). We therefore suggest using the term u-learning, thus focussing again more on the users and their needs, rather than the

technologies required for its realisation. In the following we address a number of factors that appear crucial for successful deployment of u-learning:

- *Integrated heterogeneous networks* with seamless transitions between the various segments (satellite, terrestrial, wireless, mobile, ad-hoc, etc.).
- *Transparent (or invisible) platform* technology layers: the user does not need to bother with technical details.
- *Tailored services* for the various segments of users (scholars, students, young professionals, senior professionals, etc.) and scenarios (first education, vocational training, CME, etc.).
- *Personalised avatars for Assisted Cognition*: artificial intelligence can support the communication between users and content providers and/or instructors.
- *Intelligent data mining tools*: e.g. standardised ontology, etc.
- Strategies for improved and wide-spread *technology acceptance*: E-literacy should be increased among all people, as it will be a prerequisite for continuous participation.
- Strategies for *collaboration in virtual communities*: the challenge is to create a feeling of teamwork, although the participants are geographically dispersed.
- *User-centric continuous evaluation*: it is important to address if the services indeed match the users' needs with special emphasis on the students' point of view.

#### IV. CONCLUSIONS

For successful deployment of the various medical and clinical services in the Virtual Hospital, the development and implementation of Health Grid services appears crucial. Life-long learning will soon be rule rather than exception, not only in the medical field. ICT enable new forms of distance learning and training. Especially its real-time interactivity makes the WinVicos system a valuable tool for continuous personalised learning and training, anytime and anywhere: ubiquitous access to learning (u-learning).

#### REFERENCES

1. Pande RU, Patel Y, Powers CJ, D'Ancona G, Karamanoukian HL (2003) The telecommunication revolution in the medical field: present applications and future perspective. *Curr. Surg.* 60: 636-640.
2. Dario C, Dunbar A, Feliciani F, et al. (2005) Opportunities and Challenges of eHealth and Telemedicine via Satellite. *Eur. J. Med. Res.* 10, Suppl I: 1-52.
3. Grasczew G, Roelofs TA, Rakowsky S, Schlag PM (2007) Virtual Hospitals and Homecare for ubiquitous Healthcare. *Journal of eHealth Technology and Application* 5, No. 3: 227-233.



4. Foster I, Kesselman C (Eds.) (1999) The Grid. Blueprint for a New Computing Infrastructure. Morgan Kaufmann Publishers.
5. Grasczew G, Roelofs TA, Rakowsky S, Schlag PM, Kaiser S, Albayrak S (2005) Telemedical applications and GRID technology. In: Advances in Grid Computing - EGC 2005: 1-5.
6. Bellaire G, Grasczew G, Engel-Murke F, Krauss M, Neumann P, Schlag PM (1997) Interactive telemedicine in surgery: Fast 3-D visualization of medical volume data. Min. Inv. Med. 8: 22-26.
7. Heinzlreiter P, Kranzlmüller D (2003) Visualization Services on the Grid – The Grid Visualization Kernel. Parallel Processing Letters 13, No. 2: 135-148..
8. Grasczew G, Roelofs TA, Rakowsky S, Schlag PM (2005) Überbrückung der digitalen Teilung in der Euro-Mediterranen Gesundheitsversorgung – das EMISPHER-Projekt. In: Telemedizinführer Deutschland, Ober-Mörlen, Ausgabe 2005: 231-236.
9. Grasczew G, Roelofs TA, Rakowsky S, Schlag PM (2007) From E-Learning Towards U-Learning: ICT-Enabled Ubiquitous Learning & Training. Proceedings of 10<sup>th</sup> IASTED International Conference on Computers and Advanced Technology in Education – CATE 2007: 141-146.

Author: Georgi Grasczew  
Institute: Max-Delbrueck-Centrum and Robert-Roessle-Klinik,  
Charite - University Medicine Berlin,  
Charité - Campus Berlin-Buch  
Street: Lindenberger Weg 80  
City: 13125 Berlin  
Country: Germany  
Email: [grasczew@mdc-berlin.de](mailto:grasczew@mdc-berlin.de)

# Luebeck's International BME Master's Program - Aim and Experiences

S. Klein<sup>1</sup>, T.M. Buzug<sup>2</sup> and B. Nestler<sup>1</sup>

<sup>1</sup>Luebeck University of Applied Sciences, Center of Biomedical Engineering, Luebeck, Germany

<sup>2</sup>University of Luebeck, Institute of Medical Engineering, Luebeck, Germany

*Abstract* — For more than 30 years Luebeck's two universities (University of Luebeck and Luebeck University of Applied Sciences) are cooperating in the Biomedical Engineering (BME) field. This cooperation leads to several teaching programs. One of these programs is an international Master's program "Biomedical Engineering" which is jointly organized by both universities, completely taught in English and enrolling students from all over the world. Program coursework is divided up into three semesters (90 ECTS Credits).

The paper describes the main structure and the experiences made during the development of the program. It reports the concept, the curriculum, and the results of the German accreditation.

*Keywords* — International BME program, Education, Master program, Biomedical Engineering

## I. AIM OF PROGRAM

Luebeck's Master's program "Biomedical Engineering" was introduced in 2002. Aim of the program is to qualify students with different technical background.

The master's examination forms the conclusion of the professional qualifying master's program in Biomedical Engineering. The master's examination is meant to determine whether the candidate has acquired additional advanced specialist knowledge after a first professional degree, has an overview of his or her subject and possesses the ability to apply scientific methods and knowledge in medical technology. On the basis of a passing grade in the master's examination the academic degree "Master of Science" (abbreviated: "M.Sc.") will be conferred.

## II. CONCEPT OF PROGRAM

Admissions requirements for this Master's program are a Bachelor's degree or a Diploma degree in one of the following areas:

- Electronics,
- Information Technology,
- Mechanical Engineering,
- Mechatronics,

- Physics or Physical Technology
- Process Engineering,
- Materials Technology, and
- Biomedical Engineering or equivalent.

First semester students will be enrolled individually in courses with the aim of achieving a common basis (Fig. 1).

Students with technical degrees listed above will be enrolled in introductory classes for basic medicine and medical technology in order to gain the necessary knowledge in these fields (Table 1).

Students with degrees in Medical Technology or similar will be enrolled in classes having technical subjects (e.g. signal processing, medical electronics, material sciences, photonic, and design methodology) as the main focus in order to intensify knowledge in these areas (Table 2).

Second semester students will be enrolled in courses for all participants where the common basis will be expanded. This includes practical application. Subjects taught are medical technology, product management and marketing, regulatory affairs, and clinical application of medical technology as a project (Table 3). In addition students have to choose technical electives (Table 4) as well as electives from the management field (Table 5).

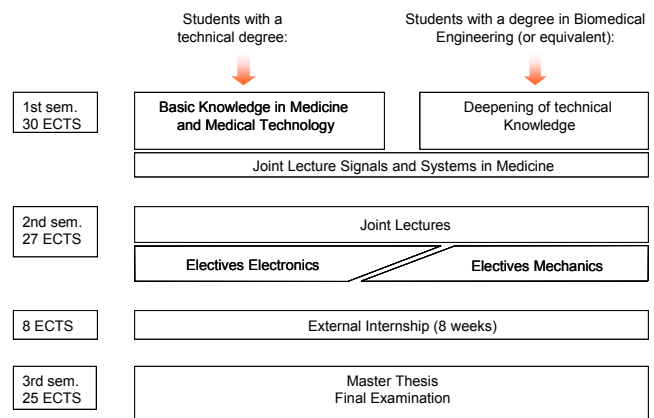


Fig. 1 Structure of program

Table 1: Required courses of 1<sup>st</sup> semester for students holding a technical degree (L: lecture, P: project, lab)

Courses	Hours per week		Credits
	L	P	
<b>Medicine</b>			<b>10</b>
Anatomy	2		
Hygiene and Sterilization	2		
Medical Microbiology		2	
Physiology	2		
Toxicology	2		
<b>Natural Sciences</b>			<b>5</b>
Biomechanics	2		
Biophysics	2		
<b>Medical Technology I</b>			<b>10</b>
Medical Technology	4		
Medical Technology – Laboratory		2	
<b>System Theory</b>			<b>5</b>
Signals and Systems in Medicine	4		
<b>Sum</b>	<b>20</b>	<b>4</b>	
<b>Total 1<sup>st</sup> Semester</b>	<b>24</b>		<b>30</b>

Table 2: Required courses of 1<sup>st</sup> semester for students holding a degree in Biomedical Engineering, Medical Technology or equivalent (L: lecture, P: project, lab)

Courses	Hours per week		Credit
	L	P	
<b>Signal Processing</b>			<b>5</b>
Signal Processing	2		
Signal Processing – Laboratory		2	
<b>Electronics and Optics</b>			<b>10</b>
Medical Electronics	2		
Medical Electronics Project		4	
Photonics I	2		
<b>Design Engineering</b>			<b>10</b>
Design Methodology	2		
Design Methodology – Project		2	
Material Science	4		
<b>System Theory</b>			<b>5</b>
Signals and Systems in Medicine	4		
<b>Sum</b>	<b>16</b>	<b>8</b>	
<b>Total 1<sup>st</sup> Semester</b>	<b>24</b>		<b>30</b>

Table 3: Required courses of 2<sup>nd</sup> semester for all students (L: lecture, P: project, lab)

Courses	Hours per week		Credits
	L	P	
<b>Medical Technology II</b>			<b>5</b>
Clinical Application of Medical Technology – Project		4	
Medical Technology – Selected Topics	2	2	
<b>Management</b>			<b>5</b>
Regulatory Affairs	2		
Elective from list II	2		
<b>Specialization in Electronics</b>			<b>17</b>
Design of Medical Electronic Devices		4	
Imaging and Image Processing	2		
Electives from list I		6	
<b>Specialization in Mechanics</b>			<b>17</b>
Biophysics – Laboratory		2	
Fluid Dynamics in Medical Technology	2		
Specialized Biomechanics	2		
Electives from list I		6	
<b>Total 2<sup>nd</sup> Semester</b>	<b>24</b>		<b>27</b>

Table 4: Technical elective courses of 2<sup>nd</sup> semester (L: lecture, P: project, lab)

Elective Courses	Hours per week		Credits
	L	P	
<b>List I of Electives</b>			
• Biophysics – Laboratory		2	
• Computational Neuroscience	2		
• Design of Medical Electronic Devices		4	
• Fluid Dynamics in Medical Technology	2		
• Human Biochemistry / Medical Biotechnology	2	2	
• Imaging and Image Processing	2		
• Neuroprosthetics	2		
• Microelectronic and Micromechanical Systems in Medical Technology	2		
• Photonic II and Laser Applications	2	2	
• Robotics – Algorithms and Medical Applications	2		
• Software Technology	2	2	
• Specialized Biomechanics		2	

Table 5: Management elective courses of 2<sup>nd</sup> semester (L: lecture, P: project, lab)

Elective Courses	Hours per week		Credits
	L	P	
<b>List II of Electives</b>			
• Health Technology Assessment	2		
• Innovation Management and Marketing	2		
• Quality Management in Healthcare	2		

After finishing the second semester the students have to go to an internship with a duration of at least eight weeks. They are not allowed to do this internship in their home-countries. German students have to go abroad, foreign students can stay in Germany or go to another country.

The third semester is reserved for preparing and writing the Master's thesis.

### III. EXPERIENCES

Usually about 120 applications per year lead to 50 admissions to the program and an average annual enrollment of 25 to 30 students. Up to now 159 students from 36 countries have been enrolled in the program, roughly 35 % from Germany (Fig. 2).

53 students finished the program until yet, most of them found a job within two months after the examination. Twelve of the students started a PhD project at various universities in Europe and overseas.

All lectures agree that teaching in mixed group with different cultural and technical is a great new experience. The program is jointly organized by the two universities. Jointly in this case means:

- Joint organizing committee
- Lectures held by lecturers from both universities
- Student's final certificate signed by presidents of both universities
- Joint web-site [www.mt-master.com](http://www.mt-master.com)
- Lectures and labs take place in a joint building

### IV. ACCREDITATION

The program is accredited at the German accreditation agency ASIIN, Duesseldorf, according to their standards as a research oriented program.

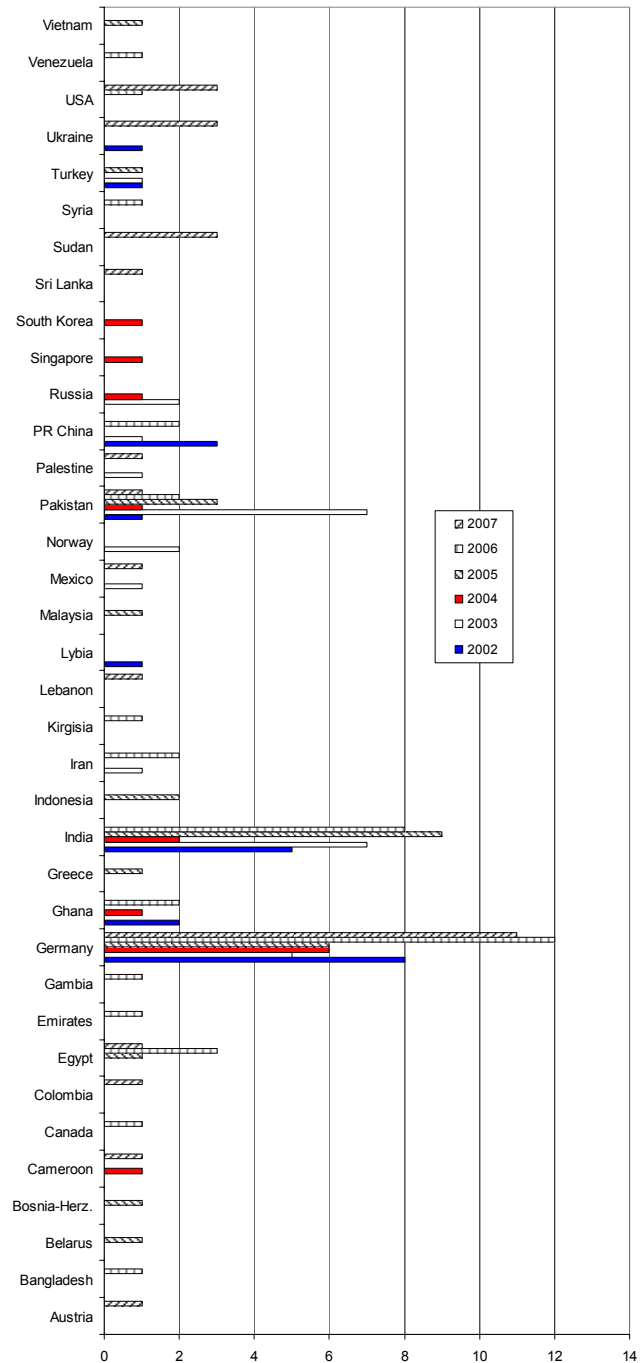


Fig. 2 Enrolment during the last six years

### V. CONCLUSIONS

The international BME program is a valuable contribution to the development of the two universities involved and

has been invited for national as well as international conferences for presentation [1], [2], [3].

The program offers an international accepted degree for students from all over the world. Students completing the program find jobs easily in German and international companies or research institutes.

#### ACKNOWLEDGMENT

The authors want to thank the German Academic Exchange Service (Deutscher Akademischer Austauschdienst - DAAD) and the federal government of Germany for funding the development of the program.

#### REFERENCES

1. Klein, St., Aach, T.: Biomedical Engineering in Lübeck: Konzept, Erfahrungen und Akkreditierung eines gemeinsamen Studiengangs. *Biomedizinische Technik* 49 (2004), pp. 938 - 939
2. Klein, St., Aach, T.: Luebeck's International Master Program Biomedical Engineering. 2nd Biomedical Engineering Educational Summit BEES II, The Whitaker Foundation, Washington, D.C., March 2005
3. Ryschka, M., Klein, St., Nestler, B.: Collaborative BME-Programs in Luebeck / Germany. International Medical Informatics and Biomedical Engineering Symposium IMIBE '06. Amman, Jordan, March 2006

Author: Stephan Klein  
 Institute: Luebeck University of Applied Sciences,  
 Center of Biomedical Engineering  
 Street: Moenkhofer Weg 239  
 City: Luebeck 23562  
 Country: Germany  
 Email: klein@fh-luebeck.de

# Developing Media Rich Virtual Learning Material for Biomedical Engineering Education

A. Kybartaitė, J. Malmivuo and J. Nousiainen

Ragnar Granit Institute, Tampere, Finland

**Abstract** — Learning materials for the European Virtual Campus for Biomedical Engineering (EVICAB) have been developed and are available in different formats, e.g., text based material delivered as HTML or PDF documents, animated material, electronic text book, audio and video based material. Video based material is a multimedia application with considerable promise for teaching and learning in the higher education. Video lectures have been produced and tested as a learning tool in EVICAB. The preliminary findings support further developments of the video based material for the Virtual Campus for Biomedical Engineering.

**Keywords** — Biomedical Engineering, e-Education, Video Lectures.

## I. INTRODUCTION

A critical goal of biomedical engineering education is the introduction of the students to some of the techniques necessary to apply engineering problem solving to living organisms and systems [1]. Educational programs in the field of biomedical engineering had their origins in the 1950s as several formalized training programs were created [2]. By 2005, more than 200 universities of applied science, polytechnic schools, academies and other institutions in Europe offered educational programs in biomedical engineering at all academic levels [3]. The survey conducted in 2006 revealed that about 9% of biomedical engineering related educational centers around the Europe already provide or plan to provide distance courses [4]. Distance teaching and learning (also electronic, virtual, Internet-based, web-based, computer-mediated or mobile) is seen as a future trend in the higher education [5].

As biomedical engineering is a relatively new field of study, not all universities, and especially newly established institutes in biomedical engineering are able to develop and provide a high quality up-to-date teaching and learning materials. Distant, open and free virtual learning environment could offer a possibility to access a high quality learning content for all students and make the teaching and learning not limited by time, place or pace. European Virtual Campus for Biomedical Engineering (EVICAB) is the solution for that.

EVICAB started in January, 2006 as the European Commission funded project with the aim to develop, build up and evaluate sustainable, dynamic solution for virtual mobility and e-learning in the field of biomedical engineering and medical physics [6].

Several different modalities have been used to develop the learning content for EVICAB: (1) text based material delivered as HTML or PDF documents; (2) hypertext material connected text, multimedia and exercises in a meaningful way; (3) animated material enriched text-oriented material by animations and made the content and appearance more interesting; (4) electronic textbook material followed specific textbook; (5) audio based material enhanced text transcription of the lectures; (6) video based material connected face-to-face classroom course with recorded lecturer speaking and presentation for illustration.

Video based material is a multimedia application with considerable promise for teaching and learning in the higher education [7]. The main areas where the video based material is especially effective are: (1) to grasp students' attention and motivate them to learn; (2) to provide highly realistic depiction of situation which students would not otherwise have the occasion to see e.g., medical procedure; (3) to watch again/ later recorded (videoed) live face-to-face lectures.

Our gathered experience when developing video lectures for biomedical engineering is presented in this paper.

## II. MATERIALS AND METHODS

### A. Theoretical approach: Modeling video lectures

"The aim of teaching is simple: it is to make student learning possible". While the aim is simple, the process is complex [8]. In order to make the virtual education more acceptable by lecturers and students we reviewed related learning theories (Table 1).

The reviewed learning theories support virtual education, e.g., by promoting more self reliance among students, following principle of knowledge construction, supporting different types and levels of learning, including multimedia and video based material in education.

Table 1 Connecting learning theories to virtual education

Theory/ Model	Key issue
Paivio's Dual Coding Theory (1986)	Postulates that both visual and verbal codes for representing information are used to organize incoming information into knowledge that can be acted upon, stored, and retrieved for subsequent use. [9], [10]
Severin's Cue Summation theory (1967)	States that learning is increased as the number of available stimuli is increased. The stimuli provided on different channels have to be relevant to each other or the distraction would cause a decrease rather than an increase in learning and retention. Deals specifically with learning and retention in a multimedia environment. [9]
Atkinson-Shiffrin Model (1968)	Proposes multi-store or multi-memory model for the structure of memory. It states human memory is a sequence of three stages: (1) sensory memory, (2) short-term memory, (3) long-term memory. [10]
Baddeley's Theory of Working	The model is composed of three main components; the central executive which acts as supervisory system and controls the flow of information from and to its slave systems: the phonological loop, visuo-spatial sketchpad, and episodic buffer. The slave systems are short-term storage systems dedicated to a content domain (i.e., verbal and visuo-spatial). [10]
Sweller's Cognitive Load Theory (1988)	Refers to the load on working memory during problem solving, thinking and reasoning (including perception, memory, language, etc). [9], [10]
Wittrock's Generative Learning Theory (1989)	Promotes less reliance on professor's lectures while simultaneously creating more self-reliance among students. [10]
Mayer's (SOI) theory of active learning	States that the promise of multimedia learning is that teachers can tap the power of visual and verbal forms of expression in the service of promoting student understanding.[10]
Constructivism	States that: (1) knowledge is constructed, not transmitted, (2) prior knowledge impacts the learning process, (3) initial understanding is local, not global, (4) building useful knowledge structures requires effortful and purposeful activity. [11]
Gagne's Information Processing theory	Stipulates that there are several different types or levels of learning. The significance of these classifications is that each different type requires different types of instruction. Gagne identifies five major categories of learning: verbal information, intellectual skills, cognitive strategies, motor skills and attitudes. Different internal and external conditions are necessary for each type of learning. [9], [10]

The application of video based material in education is not a new endeavor. A projects of combination of recorded lectures and accompanying presentations available via the WWW have been developed by several institutions, e.g., Tutored Video Instructions, eClass, eTeach, Webcast Berkeley, MIT Open Course Ware, Videolectures.NET, Free video lectures. Many more examples are available on

Table 2 Advantages of the video lectures

Allows grabbing students' attention and presenting information that is easy to absorb.
Provides high effect for students' motivation, training and instructions.
Helps to comprehend hard-to-understand concepts and engage in the learning process.
On-campus and off-campus learners can participate in the same learning program.
Provides flexibility for choosing learning place, pace and time.
Provides flexibility to use different equipments, gadgets for learning.
Provides possibility to adopt more flexible learning patterns.
Provides possibility to see recorded lectures given by eminent professor who would not be able to travel to a higher institution more than once.
Offers possibility to become self-sufficient learners.
Students may watch video lectures before attending workshop so that material contained in it might be explored in depth.
Students can better prepare for assessment.
Students can watch video over again until the skill has been mastered.
Students can stop, start and rewind the video to address their specific needs.
Students can watch video lectures to enrich their learning notes.
Allows students to catch up if they miss a face-to-face lecture.
Learning material can be accessed and transferred very fast.

Table 3 Disadvantages of the video lectures

Technical problems, e.g., computer access or Internet connection might be limited.
Quality issues.
Viewers are less forgiving of the lecturer's minor mistake and audience disruption when watching video lectures.
Re watching video lectures can become dull and repetitive learning process.
Students might see video lectures as the only source of knowledge, this could remove students' need to consult other sources, and hence reduce the opportunity to develop as individual learners.
Fast accessing of learning material might diminish the importance of constructing knowledge.
No direct interaction with lecturer, no possibility to ask direct questions.
Video lectures can have adverse effect for attendance.
Technology, e.g., software for producing video lectures is not yet mature.

the WWW. Based on these examples we defined advantages and disadvantages of the video lectures (Table 2 and 3).

In order to utilize the advantages and to find solutions for the disadvantages we implemented a practical model to develop video lectures.

### B. Practical approach: Model to develop video lectures

A video lecture is a combination of recorded live lecture, accompanying sound and synchronized presentation. It transmits information, encourages reflection, and promotes dialog. There are different approaches for producing video

lectures, e.g., videoing lecturer, capturing his speech and displaying all information in one frame; videoing lecturer and displaying presentation along site in a separate frame or recording lecturer’s voice and synchronizing with a presentation or graphical information, etc.

The process of developing video lectures has several steps: (1) research on the related technologies including software and hardware, (2) research on the lecture, its content, duration, presentation type, (3) test of the technologies in the real environment, (4) recording video lectures, (5) production of the video lectures including edition and synchronization of video, audio files and presentation, segmenting into easy to absorb parts, arranging table of content, (6) publishing via the Internet, web editing and web serving, (7) providing supporting information, e.g., computer or software requirements in order to access video lectures. The quality of video lectures depends on each step.

The step of production of video lectures for EVICAB was an experimental process. We started by using Synchronized Multimedia Integration Language (SMIL). SMIL code was provided by Hypermedia Laboratory in Tampere University of Technology. The benefit of the code was the possibility to change the lay-out, table of content and size of frames in the video lectures. These features are quite limited in commercial software. Despite that we faced the disadvantage: video lectures were viewable only with Real Player. As Flash Player is more and more used to deliver rich media content with video, graphs and animations we decided to use commercial software [12] and produce video lectures in the flash format. All video lectures were produced in the same way after experimenting and testing.

### III. RESULTS

#### A. Learning materials for EVICAB courses

EVICAB courses are composed of several elements and learning materials, e.g., textbook, e-book, quizzes, virtual lab works, assignments and video lectures. Five courses have been created which include video lectures. They are divided into three groups (Fig. 1). The levels of video lectures vary as introductory, middle or advanced. Bioelectromagnetism lectures can be presented as an example; they are supported by textbook, e-book, and quizzes for self-evaluation. Students can refer to the type of the learning material which is the most convenient for them.

The elements that make video lectures, i.e., audio, video recordings and presentations could be used as reusable learning objects (RO) by other instructors. A common bank for ROs could be created and assessable by permission of the authors.

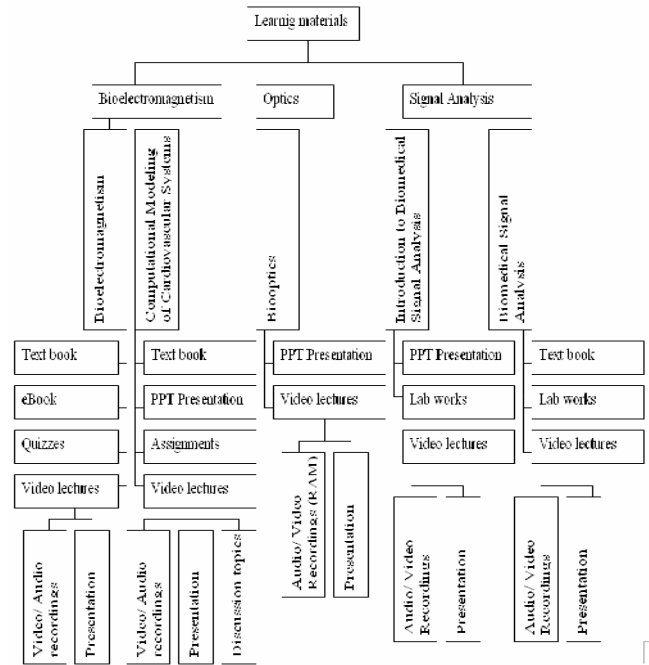


Fig. 1 Learning materials for EVICAB courses

#### B. Evaluation of the video lectures

The preliminary evaluation of video lectures was performed. It was important to know students’ opinions for further developments. The evaluation was based on the questionnaire form. Traditional five-point Likert scale was used to evaluate the usefulness, technical quality, and pedagogical value (Table 4). 18 students, who participated in Bioelectromagnetism course, Tampere University of Technology, 2007 autumn, provided their opinions. The course was available as traditional classroom activity or via virtual learning environment.

The evaluation also revealed that approximately half of the responded students spent most of their study time for attending traditional classroom activities and the other half preferred virtual learning activities, e.g., studying video

Table 4 Average evaluation of the video lectures (by the students)

Usefulness of the video lectures	4,29
Technical quality of the video lectures:	
• Audio quality	3,86
• Video quality	4,07
• Presentation	4
Pedagogical value	4,14

The used scale was from 1 to 5, where 1 meant satisfactory evaluation and 5 - excellent evaluation.



lectures, e-book, making virtual assignments. In addition, we inquired what students expected from the e-material? Most of all, students expected (1) animations that would enrich text-oriented learning material, (2) clear instruction in written format, and (3) learning material in video format. These expectations approved that students accept video lectures and encouraged for the further developments.

#### IV. DISCUSSION

We compared two learning environments in terms of the outcomes perceived by the students, i.e., results of the final exam of the students who participated in the traditional class activities and who studied video lectures with supporting materials via the virtual learning environment. The summated results showed that independent whether the students participated in the traditional class activities or used video lectures, learning outcomes were almost the same.

The combination of audio + video + presentation was well accepted by students in terms of usefulness, technical quality and pedagogical value (average evaluation was 4). The main reason, we see, why a low number of students used video lectures was the fact that students were not familiar with the video lectures. Still, more than half of the responded students (61%) preferred traditional classroom activity as the only learning method. Technical limitations could also discourage students to watch the video lectures, e.g., slow Internet connection or personal computer properties.

We noticed that more students become interested in e-learning activities, including video lectures. Thus future improvements are needed. They should focus on capturing, integration and access processes. In the video capture process, a system should be able to support generalized capture of the lecture materials without any extra instructor effort. The integration of video, audio and graphical presentation should be smarter; e.g., more semantic linking of the data. The access of video materials should support generalized replay, i.e., start, stop or rewind the video to address a specific need, rather than just showing the static result. Also the access interface could increase the value of video lectures, e.g., adding possibility for collaboration, interactive communication, discussion, links to the other related sources of information, subtitles in a native language, etc.

#### V. CONCLUSION

The idea behind video lectures is not to substitute a class activity or to eliminate the lecturer but to support and augment the teaching and learning process for biomedical engineering. Pedagogically based, virtual learning material taking advantages of developments in technology and appropriate learning theories suggests that students should be able to achieve higher learning outcomes.

#### ACKNOWLEDGMENT

The work has been supported by the eLearning Programme of European Commission.

#### REFERENCES

1. P.D. Schreuders, A. Johnson. A System Approach for Bioengineering. Intern. Journal of Engineering Education, 1999. 15(4): p.234-248.
2. P. Benkeser. Biomedical Engineering Education. Encyclopedia of Medical Devices and Instrumentation. 2006
3. Biomedea. Criteria for the Accreditation of Biomedical Engineering Programs in Europe, 2005
4. E.G. Salerud, H. Petersson, M.A. Ilias. European Biomedical Engineering/ Survey Report of Existing and Planned BME Distance Courses in Europe. EVICAB report, 2006
5. P. Pasternack, r. Bloch, C. Gellert, M. Hölscher, R. Kreckel, D. L. Ewin, I. Lischka, A. Schidberg. Current and Future Trends in Higher Education/ Summary.
6. EVICAB at [www.evicab.eu](http://www.evicab.eu)
7. J. Whatley, A. Ahmad. Using Video to Record Summary Lectures to Aid Student's Revision. Interdisciplinary Journal of Knowledge and Learning Objects, 2007, 3
8. S. Magennis, A. Farrell. Teaching and Learning Activities: Expanding the Repertoire to Support Student Learning. In Emerging Issues in the Practice of University Learning and Teaching, 2005 at: [www.aish.org/readings/2005-1/](http://www.aish.org/readings/2005-1/)
9. P. Kaur, H. Atan, S.F. Fong, R.M. Idrus, H. Dzakiria. The Combination of Different Modalities in the Web-Based Learning Environment: A Comparative Analysis of the Perceptual Instructional Outcomes. 2005, Proceedings of the Fifth IEEE International Conference on Advanced Learning Technologies.
10. R. Mayer. Multimedia Learning. 2001, Cambridge University Press.
11. Constructivism at: <http://srri.umass.edu/topics/constructivism>
12. Camtasia Studio at: <http://www.techsmith.com/camtasia.asp>

Author: Asta Kybartaitė  
 Institute: Ragnar Granit Institute/ Biomedical Engineering  
 Department, Tampere University of Techn.  
 Street: Korkeakoulunkatu 10  
 City: FI-33720 Tampere  
 Country: Finland  
 Email: [asta.kybartait@tut.fi](mailto:asta.kybartait@tut.fi)

# Development of the Biomedical Electronics Course for e-Learning

T. Parve<sup>1</sup>, R. Gordon<sup>1</sup> and M. Min<sup>1</sup>

<sup>1</sup> Department of Electronics, Tallinn University of Technology, Tallinn, Estonia

**Abstract** — The problems connected with development of the Master's course of Biomedical Electronics for e-Learning are presented in the paper. The history of development of the course is described, and the structure of the course is reviewed and analyzed. The current status and the scope of future development of the course are discussed.

**Keywords** — Biomedical electronics, e-learning course, Internet learning support.

## I. INTRODUCTION

Electronics is nearly obligatory part in nowadays biomedical devices. So, it is natural that all the specialists in the Biomedical Engineering (BME) field should have certain imagination about the electronics used in biomedical devices. From the other side, the electronics engineers who want to become professionally active in the field of BME should also have appropriate knowledge about the specifics of electronics.

To cover these needs, a course of Biomedical Electronics was launched by the Department of Electronics at Tallinn University of Technology (Tallinn UT) in the year 1993.

During the following 15 years the content of the course has been changed according to the development of the biomedical electronics subject in general.

The aim of teaching of the course has varied together with the basis of students learning it, and the number of students has varied too, being around 15 in average during these years.

In spite of the late launching, the content of the course was traditional, corresponding to the early meaning of medical electronics. The topics discussed were bio-signal amplifiers, bio-impedance, hearing aids, electrotherapy, etc. Similar classical treatment of the subject is met at several nearby technical and classical universities, e.g., at Tampere University of Technology (TUT), Kaunas University of Technology, Linköping University, etc.

## II. COURSE HISTORY AND STATUS

### A. Historical overview

In the beginning, the course was facultative for the 4-year diploma engineer students in electronics. Then, approximately 5 years later, it was re-oriented towards the students

studying according to the 4-year joint bachelor curriculum of Electronics and Biomedical Engineering.

The last version of the course, which is discussed in the paper, was launched 5 years ago. Now it is a 4-eurocredit course for the Master's degree students studying according to the 2-year curriculum (following 3-year Bachelor's studies).

As now the curriculum of electronics at Tallinn University of Technology belongs to the Faculty of Information Technology, the parts of the course dedicated to electronics design have been significantly compressed, approximately following the content of the chapter "Biomedical Electronics" in the 2006 *Wiley Encyclopedia of Biomedical Electronics*, 2006 [1], written by 2 authors of this paper and Dr. Rodney W. Salo from the USA.

And, vice versa, the parts of more wider interest were expanded. Some topics of general interest, like *bionics*, were even added to widen the scope.

During this transformation also one significant change was made – the exercises were excluded. But the practical laboratory works were still remained.

The next important stage started when the Biomedical Engineering Centre of Tallinn UT began to participate in the European Virtual Campus of Biomedical Engineering (the EViCaB) project in 2006-2007 [2]. The Biomedical Electronics was soon involved in the BME curriculum development as one possible course – a 4-credit course coded as IEM0070/BioEI.

Converting of the course into a virtual Internet version was initiated. Many concepts of course build-up needed reviewing. Support from the project leader prof. Jaakko Malmivuo (TUT) was noticeable in this process.

The EViCaB page of the course was opened in the Finnish Moodle server:

<http://www.moodle.fi/evicab/moodle/course/view.php?id=44>

Though the course is still not completed in its electronic form, there have already been a number of trials to apply from the side of international students interested in the course. Unfortunately these applicants were left not satisfied until the complete launch of the e-learning course.

In autumn 2007 a page of an e-learning course was launched also in the Moodle environment of Estonian e-University <http://www.e-ope.ee/>:

<http://www.e-ope.ee/course/view.php?id=808>

The course has open Internet pages at <http://www.elin.ttu.ee/mesel/Study/Subjects/0070BME/Index.htm>, which can be reached without restrictions.

The course is currently taught by the authors at Tallinn University of Technology, Faculty of Information Technology, Department of Electronics, Tallinn, Estonia. Annual number of students has been about 15, showing slight but permanent increase.

### B. Objectives of the courses

The course is aimed to give a wide spectrum of knowledge about the solutions of electronic units, systems and devices used in medical engineering practice and in biological research.

Necessary referring to corresponding biophysical knowledge is given together with explanation of possible bionic prostheses and technical analogies.

### C. Overview of the content of the course

At the current state the course of Biomedical Electronics has the following subsections:

- Introduction to the Biomedical Electronics
- Bioelectrical phenomena and signals, electrical properties of tissues.
- Electronic circuits for pick-up of the biopotentials.
- Electrodes and electronic bio-sensors and transducers.
- Electrical Bio-Impedance, measurement and diagnostical applications of it.
- Electronic means for medical monitoring, data processing, data presentation (displaying), and medical diagnostics.
- Bio-electronic stimulators, and electronic means in therapy.
- Electronic prosthetic appliances.
- Other electronics for the means of medical diagnostics and biometrics.
- Bionics.
- Special topics of medical electronics.

The last in this list is the most specific part of the course, consisting of a number of subtopics. The most significant ones of these are the following:

- Concepts of system design for biomedical applications.
- On-chip realization of medical electronic devices (Mixed system and System-on-Chip (SoC) solutions, ASIC, FPGA/PL);
- CMOS circuit design building blocks;
- Electro-magnetic compatibility (the EMC) and galvanic isolation of the biomedical electronic devices;
- Electrical power supply of biomedical electronic devices.

- Norms and standards, and other regulations related to electronic equipment.
- Accuracy (errors) and calibration, testing and technical diagnostics.

### D. Study books and other learning materials

Currently the following three study books are foreseen to be used:

- 1) R. B. Northrop. *Analysis and Application of Analog Electronic Circuits to Biomedical Instrumentation*. Boca Raton, Florida, USA: CRC Press, 2004 (The Biomedical Engineering Series).
- 2) J. D. Bronzino (ed.). *Biomedical Engineering Handbook*. CRC Press & IEEE Press, 1995.
- 3) M. Akay (ed.). *Wiley Encyclopedia of Biomedical Engineering*. John Wiley & Sons, Hoboken, New Jersey, USA, 2006. Vol. 1 - 6. (Incl. M.Min, R.W.Salo, T.Parve. Biomedical electronics. In Vol. 1, pp.500-514).

More bibliographic information is available on the course pages.

### E. Laboratory works of the course

Laboratory works are very traditional for the course as follows:

- Bioelectrical signals' pick-up.
- Electrical bio-impedance: measurement and applications.
- Electrotherapy.
- Hearing aids and audiology.
- Power supply and galvanic isolation.

The more detailed information about the laboratory works is available on the Internet pages of the course <http://www.elin.ttu.ee/mesel/Study/Subjects/0070BME/Laborat/index.htm>

All the laboratory works can be discussed as special cases of measurement of electrical parameters of circuits over the Internet. This is quite well applicable to the bioelectrical signal amplifiers, analogue filters, e.g. power line interference notch filters, antialiasing filters, etc.

We have the 10 year experience in making this kind of laboratory works available over the Internet in some other study courses (and, for example, we have also a temperature server running already for 10 years). But we are still not too enthusiastic in making all the labs available over the Internet. One can imagine the difficulties to perform it for the topics like the electromagnetic compatibility (EMC) or testing of electrical isolation.

As an exception, we have introduced a practical work in bioimpedance basics based on computer simulation. Two computer-simulation laboratory works have been designed that simulate bioimpedance on different scale factors.

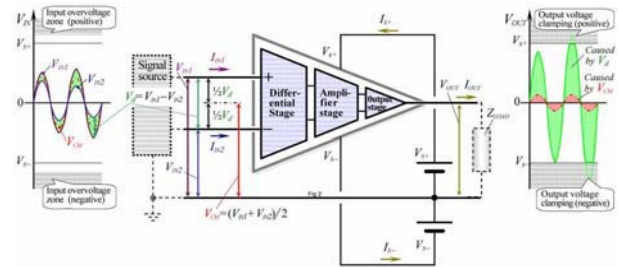
The first work is based on freeware software provided by A. Ivorra [3] by permission. It allows calculation of bioimpedance spectrum of tissues depending on cell size and shape, intracellular media, extra-cellular media and cell-membrane impedance properties and measurement electrode configuration. It allows students to observe changing bioimpedance and understand the physiological bases behind it.

The other computer-simulation work is visualisation of macroscopic impedance behaviour with electrodes on the body surface. This has been realized on Matlab-platform with modelling and simulation tools built in-house.

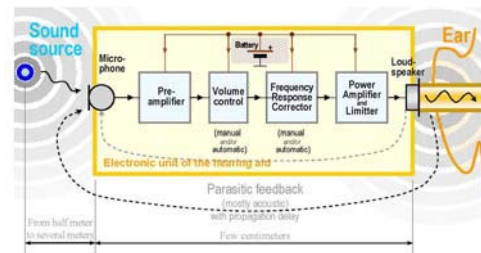
### III. THE COURSE

Development of the biomedical electronics is discussed mostly as it has taken place during the semiconductor era, which led to drastic changes in the electronics world. The manufacturing of the silicon transistor in 1954 ushered in the era of implantable electronics when Swedish engineer Rune Elmqvist designed and built the first implantable pacemaker in 1958, which was implanted by Swedish physician Åke Senning [1].

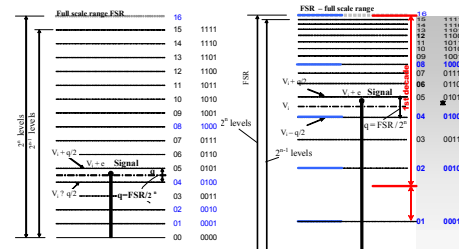
The main attention is paid to the later advancements, first of all to the contemporary solutions of the integrated circuits (ICs) and application specific ICs (ASICs). Nowadays this means mainly the insulated metal gate field effect transistor (MOSFET) technology in its complementary form of n- and p-channel FETs (CMOS) [1]. Now, at the beginning of the 21<sup>st</sup> century, the CMOS technology dominates as the same technology can be used for both analog and digital circuits. So, it is possible to design mixed signal analog/digital integrated microchips, particularly for low-voltage and super



a) signal level analysis and design (biosignal amplifier)

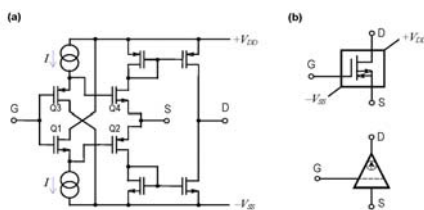


b) structural level design (an hearing aids)

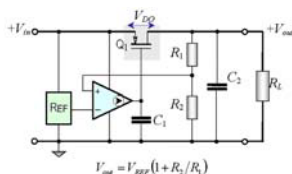


c) scaling and digitizing

Fig. 2 Examples illustrating the part of the course dedicated to the system design



a) integrated circuit design level (a transistor)



b) circuit design level (a controlled voltage source)

Fig. 1 Examples illustrating the part of the course dedicated to the circuit design

low-power biomedical electronics.

Some examples illustrating the part of the course dedicated to the circuit design are shown in Fig. 1.

Some other examples illustrating the part of the course dedicated to the system level design are shown in Fig. 2.

### IV. THE LEARNING FACILITIES

As the course was launched when the PCs have become into everyday use already, it have had some kind of presentation in electronic form from the very beginning. In the early 1990-s some material in textual form was available over the local faculty net.

In these times the simple ASCII text files were used with minor so called ASCII graphics. Also some other file types were used allowing some graphics, mostly in form of block

diagrams and very simple graphics, as for the frequency response characteristics.

The next stadium was concurrent with launching of the Internet server at the Department in 1997. The Internet site of the course was opened and the html-linked material was made available for the students. During the last 5 years the facilities in form of the Internet pages were widened step by step. Nowadays it covers the general matter of the course quite well. Nevertheless, there still exists the need in using of the study books.

Also the laboratory works still have been available only at the laboratory of the Department. As no principal restrictions exist, it is only a matter of time and resources to make them available over the Internet.

## V. THE LEARNING OUTCOMES

The student basis of the course has varied with time. First, it was only students of electronics of the faculty of Systems Engineering. Accordingly, the learning outcome was strongly oriented to circuits and systems engineering. Later, when the course was given to the students of electronics and biomedical engineering, general biomedical engineering orientation in the outcome was increased, and the demands in circuits and systems knowledge were lowered.

In fact, there has all the time been present certain duality in the course outcome in connection with the two main groups of students taking the course. One group has relatively strong level of knowledge in electronics and/or systems engineering. Another group of the students has some level of knowledge in biomedical engineering and in general also in physiology.

So the course has to fulfil the needs of two kinds of students with different basic knowledge in electronics, in biomedical engineering and in physiology and biophysics.

The students with relatively weak background in electronics and electrical and systems engineering have difficulties with the specific problems of electronics, and also with understanding of electrical properties of tissues and bioimpedance (e.g., with the electrical equivalents), and bioelectrical signals.

The students who have relatively strong background in electronics and systems engineering, in general do not have good imagination about the physiological processes and anatomy. They often also have difficulties with medical terminology, which has a multilingual basis and thus is quite troublesome, even error causing (e.g., AXON versus action, etc.). They also prefer model based approach to the description based one, very common in medical texts.

To overcome the latter problem, relatively big part of the course is dedicated to the physiology. And this is done in a

model based manner, as it is found to be useful for both groups of students.

But the problem remains in connection with the examination. To overcome this problem the master students of rather different specialisation than electronics have been allowed to write the special course work instead of passing the regular final examination. These works have been reviewed in a way, which is quite similar to the scientific paper reviewing, typically with 10 to 15 characteristics of the work being evaluated. Amongst these, actuality of the selected topic from the biomedical engineering point of view, and from the point of view of biomedical electronics are evaluated.

## VI. CONCLUSIONS

The Internet pages of the course in open form and in simple html format without hard formatting (via styles, etc.), linked via Moodle environment have shown themselves as a solution, suitable for using for all purposes, also for lecturing. This allows students to see the material in one and the same form, and simple formatting allows them to modify the material for better viewing or for printing (via scaling during printing).

Thus there is no need in various formats of learning materials (ppt, pdf, doc, etc.), which often cause quite big grumble among the students.

## ACKNOWLEDGMENT

The authors thank European Union Structural Funds in Estonia (project 1.0101.01-0480), and the EC (EViCAB project) for the support. The authors express their gratitude to Professor Jaakko Malmivuo, and to Dr. Rodney W. Salo personally.

## REFERENCES

1. Min M, Salo R W, Parve T (2006) Biomedical electronics. In: *Wiley Encyclopedia of Biomedical Engineering*, Metin Akay (editor-in-chief), John Wiley & Sons, Hoboken, NJ, USA, 2006, vol. 1, pp.500-514. ISBN-13:978-0-471-74037-7; ISBN-10:0-471-74037-3.
2. The European Virtual Campus for Biomedical Engineering (EviCaB) at <http://www.evicab.eu>
3. Ivorra A (2003) Bioimpedance monitoring for physicians: an overview. Review, Centre Nacional de Microelectronica, Biomedical Applications Group, 2003. URL: [http://www.cnm.es/mtrans/PDFs/Bioimpedance for physicians rev1.pdf](http://www.cnm.es/mtrans/PDFs/Bioimpedance%20for%20physicians%20rev1.pdf).

Author: Toomas Parve  
 Institute: Tallinn University of Technology  
 Street: Ehitajate Rd.  
 City: Tallinn  
 Country: Estonia  
 Email: [parveto@elin.ttu.ee](mailto:parveto@elin.ttu.ee)

# Cataract Surgery Simulator for Medical Education & Finite Element/3D Human Eye Model

J.F. Perez<sup>1</sup>, R. Barea<sup>1</sup>, L. Boquete<sup>1</sup>, M.A. Hidalgo<sup>2</sup>, M. Dapena<sup>3</sup>, G. Vilar<sup>1</sup>, I. Dapena<sup>3</sup>

<sup>1</sup> University of Alcalá/Department of Electronics, Alcalá de Henares, Spain

<sup>2</sup> University of Alcalá/Department of Physics, Alcalá de Henares, Spain

<sup>3</sup> University of Alcalá/Department of Medicine, Alcalá de Henares, Spain

**Abstract** — This work shows the results obtained in the development of a cataract surgery simulator for education and medical training. A Finite Element 3D human eye model has been developed with haptic feedback and the necessary surgical equipment to carry out the cataract surgery. The developed system provides the students and surgeons a tool for interactive learning that can be used for the anatomy study and physiology of the eye, diagnoses training or planning of ocular surgery.

**Keywords** — Virtual reality, Finite Elements, Haptic feedback, Surgical simulator, Phacoemulsification.

## I. INTRODUCTION

The Continuous Medical Education (CME) consists on an educational group activities that allow to maintain, to develop and to improve the basic medical knowledge and the necessary clinical practice for the professionals or people that provide services in the health sector. On the other hand, the surgical training consists of the knowledge acquisition supplemented with the practical observation during the surgery, and later on, the realization of surgical procedures under supervision. In a similar way, the surgeons also need training to improve their knowledge or to maintain these in procedures or non routine operations.

One of the areas in those virtual reality (VR) and Finite Elements models, has made more important taxes it is in the training and medical education. Those technologies combined with themselves allows the users to interact with three-dimensional environments (3D) and with on-line generated objects. This way, the surgical simulator that combine visual information (graphics 3D), tactile (feedback force), and physics responses (Finite Elements) can be a great tool for the training and medical education.

In the last years the necessity of surgical simulator is increasing considerably since it avoids has to train with "models of plastic", with "patient" or even with cadavers. Diverse applications have been developed in neurosurgery

[1], insertion of catheters [2], lumbar punction [3], acupuncture [4], cricotiroidostomia [5], surgery of cataract [6] [7] or even later capsulotomía [8], etc.

In this work the preliminary results are presented obtained in the casting of the human eye and in the development of a surgical simulator of the cataract surgery. Section II shows the cataract surgery procedure. In section III the system architecture is commented and section IV shows the results obtained with the software developed. Finally, section V and VI presents the finite elements research and conclusions.

## II. CATARACT SURGERY

The cataract is the transparency loss of the crystalline lens and it affects at 75% of the population older than 75 years old. The crystalline lens is a transparent lens located behind the pupil and that it is used to focus the objects clearly. Due to different circumstances, illnesses or more frequently due natural transparency and to become in an opaque lens. For a series of circumstances, illnesses or more frequently due to the step of the years, the crystalline lens can go losing its natural transparency and to become an opaque lens.

The treatment of the cataract is surgical fundamentally. The cataract surgical operation consists on the extraction of the crystalline lens, that is opaque and its substitution for an artificial lens that is placed in the same place that the original crystalline lens (intraocular lens), restoring the vision that had gotten lost as a consequence of the cataract. One of the most modern techniques to operate the cataract is the phacoemulsification. This procedure allows the extraction of the crystalline lens through an incision of only 3mm. The phacoemulsificator ("phaco") it usually uses an ultrasound probe or laser to fraction the crystalline one mechanically and then to aspire it. Finally a lens intraocular is implanted that replaces the crystalline lens. In most of the cases suture is not required the incision since it is the sufficiently small thing to be sealed by itself.

### III. SYSTEM ARCHITECTURE

#### A. Hardware

The developed system is based on an immersive system of virtual reality in 3D with tactile feedback - Reachin Display 2A [9]. This system has a typical PC monitor (TFT) that generates virtual images in 3D of the virtual organ patient, in this case, the human eye and its structures. The systems user, by means of a three-dimensional glass with shutter - CrystalEyes- perceives a three-dimensional image (Fig. 1).

The tactile sensation is perceived through a two Phantom Omni device [10] located inside the visual space. Therefore, a user working in this environment can feel and to see virtual objects. The information process is carried out in a computer with double nucleus at least 3 GHz, 2 GB of memory and a 3DLabs Wildcat graphics card. This system obtains a 20 Hz visual refresh and 1 KHz haptic refresh.

#### B. Software

The utilized software is the Reachin API. These API's allows carrying out a visual and tactile "rendering" in the hardware described previously. This way, models can be designed in 3D and later on to export them to the simulator.

The programming language is X3D and H3D for the virtual world models and Python to configure certain stocks. The H3D API libraries allow to add physical properties to the objects designed in X3D like stiffness, elasticity, texture, etc. It is also possible to design the instruments used in the surgical operation, this way, the pointer can adopt the form of the instrument used in each step of the process. Also we use any structure analysis software for the Finite Element analysis.



Fig. 1 System Architecture

### IV. RESULTS

#### A. Human Eye Model

To develop the cataract surgery simulator is necessary to have a model of the eye and the surgical. For it, we have acquired a commercial model "exchange3D" [11] and modified to obtain a definitive model with the most realistic as possible detail, shape, size, colour, texture, etc. (Fig. 2) Shows the program developed for training cataract surgery.

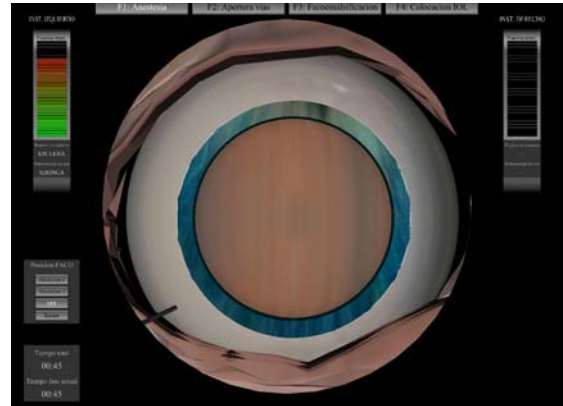


Fig. 2 Human Eye Model

The haptics attributes of each one structure that compose the ocular globe have been implemented by a finite elements study process and wide clinical experience. The necessary surgical instruments in the operation have been modeled by any commercial 3D design software (for example 3D Studio Max, Maya, etc.) For the instruments design (shape, size, texture and operation), has worked in collaboration the faculty of medicine of the University of Alcalá.

#### B. Incisions and Phacoemulsification

To carry out the cataract surgery, two small incisions are made in the edges of the cornea. The first one it is known as "main incision" (Fig. 3), its carried out by the Keratome, this incision is greater than the other one, and it will serve to introduce through it the Phacoemulsificator. On the other hand, the second incision is called "auxiliary incision" and it is used to introduce through it another surgical instruments, for example a cannula or another instrument into the Anterior chamber of the eye with the objective to help the surgeon. The above mentioned incisions are minimal and they do not provoke changes inside the IOP (Intraocular pressure) of the human eye.

Due to the action of the phacoemulsificator, see Figure 4, the crystalline structure it is destroyed in micro fragments

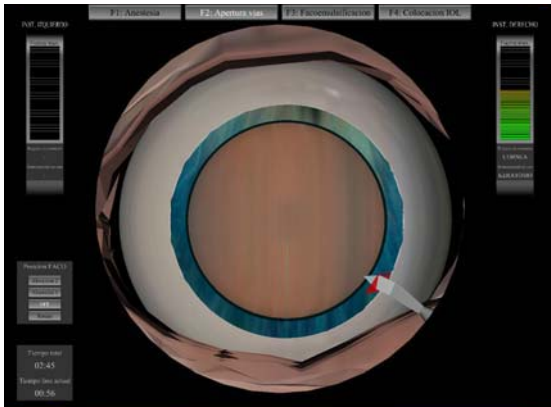


Fig. 3 Main Incision on the edge of cornea

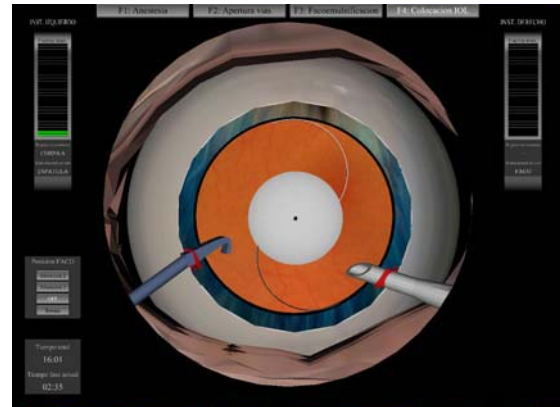


Fig. 5 IOL Allocation

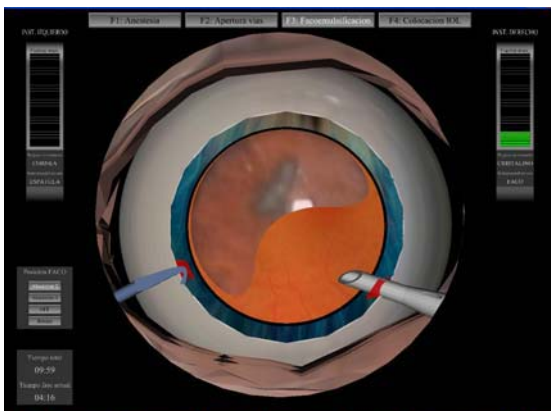


Fig. 4 Phacoemulsification Action

that the Phacoemulsificator absorbs later, leaving the Anterior chamber of the eye ready to implant the artificial lens (IOL). The above mentioned division in microstructures of the crystalline lens, allows to the surgeon simulates surgical skills as the erosion of the crystalline lens and the absorption of every dispersed fragment inside the Anterior chamber. H3D allows to us design deformable structures with Gaussians properties. We get these Gaussian characteristics to the crystalline surface, with the objective to simulate the erosion and the absorption of the lens. On the other hand, with these Gaussian properties is possible to graduate the erosion power of the phacoemulsificator, controlling this way the size of crystalline lens destroyed and absorbed by the Phacoemulsificator during the erosion procedure.

The surgeons use a surgical instruments seemed to a spatula to help to the destruction of lens and the absorption of the same one, which they allow to rotate the lens and to displace the fragments suspended in the liquid of the Anterior chamber. This allows a minimal incision in both sides of the cornea to be able to realize this operation. For it, we

have developed our operation providing the crystalline lens with rotational movements and inertia properties, which creates a real environment for the free displacement of the structures facilitating the surgical task.

Finally, once the Anterior chamber of the eye is empty thanks to the phacoemulsification, we can put on an artificial intraocular lens (IOL), ending this way with the procedure (Fig. 5).

## V. FINITE ELEMENTS RESEARCH

In parallel to design the virtual application, we are researching with models of finite elements that represent the Anterior chamber structures of the human eye. The above mentioned models are designed in CAD programs, those models can be exported and treated by finite elements programs, or if the structures are simples, to design them directly (Fig. 6).

This programs allows us to realize static and dynamics structural analisis on the distortions that suffers the eye on having applied to its courts or pressures, as well as to obtain response curves like for example: materials resistance, to see which might be the maximum pressure that would support the Anterior chamber of the eye without the membranes of separation between the Anterior and Posterior cavities of the eye were broken down. For the development of our finite elements model and his later study, we have taken the results as a base obtained by E. Uchio [12] and Neumann [13]. Thanks to this information, our finite elements model can estimate the maximum pressure that it is possible to apply in any point of the cornea. This information allows our simulator, thanks to the tactile feedback, to estimate the maximum pressure that the user can apply on any point of the virtual model without exceed the limits of rupture, and allow to develop this way a surgical training.



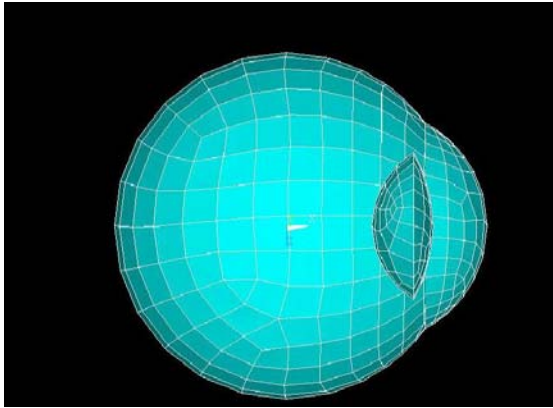


Fig. 6 Finite Elements Mesh Detail

## VI. CONCLUSIONS

The initial results presents a virtual simulator of the human eye allows carrying out the cataract surgery. The developed system provides the students and surgeons a tool of interactive learning that includes a precise representation of the anatomy and physiology of the human eye with a real behavior based on physics responses. It can be used for anatomy study, training and planning of the cataract surgery.

In these moments we are studying a generic caucasian human eye with a Finite Element 3D model and how to include this results on our Virtual Simulator with the objective to develop a Virtual Evaluator for the surgery, and in a near future try to include the possibility to record the virtual surgery by an expert ocular surgeon, and later in an automatic way, comparing the movements and skills of the expert with the virtual surgery of any user. All of these with a low cost hardware and software. On the other hand, use the Finite Elements analysis data response to provide our Virtual Simulator with surgical alarms to simulate and correct problems during the intervention, like for example: If the virtual surgeon applicates too much pressure during the phacoemulsification procedure, sporadic eye moves, IOP less, etc. It is also considered the possibility to adapt the realized program, to predict the effect of laser operations on the ocular system.

## ACKNOWLEDGMENT

The authors would like to express their gratitude to the Fundacion Medica Mutua Madrileña for their support

through the project “3D Virtual Eye Model with Haptics Feedback for Training and Medical Education in Ocular Surgery” (MMA-2006-002) and to the Comunidad de Madrid for their support through the GATARVISA Net (P-DPI-000235-0505).

## REFERENCES

1. Wanga, P. Beckera, A.A. Jonesa, I.A. Gloverb, A.T. Benfordb, S.D. Greenhalghb, C.M. and Vloeberghsc, M. (2006). A virtual reality surgery simulation of cutting and retraction in neurosurgery with force-feedback. *Computer methods and programs in biomedicine*, 11–18.
2. Zorcolo, A. Gobbetti, E. Zanetti, G. and Tuveri, M. (2000) “A volumetric virtual environment for catheter insertion simulation,” in Proc. EGVE’00 6th Eurographics Workshop on Virtual Environments, Amsterdam, Neatherlands.
3. Barea, R. Boquete, L. Valle, A. López, E. Dapena, M. A. Fraile, E. García Sancho, L. (2005) “Simulador de punción lumbar mediante realidad virtual con sensación táctil” *Actas del XXIII Congreso de la Sociedad Española de Ingeniería Biomédica CASEIB’05* (ISBN: 84-7402-325-4) Madrid, España.
4. Heng, P. Wong, T. Yang, R. Chui, Y. Xie, Y. M. Leung, K. and Leung, P. (2006). Intelligent Inferencing and Haptic Simulation for Chinese Acupuncture Learning and Training. *IEEE Transactions on Information Technology in Biomedicine*. Vol 10. January 2006.
5. Liu, A. Bhasin, Y. and Bowyer, M. (2005). A haptic-enabled simulator for cricothyroidotomy. *Medicine meets virtual reality*.
6. El-Far, N. R. Nourian, S. Zhou, J. Hamam, A. Shen, X. and Georganas, N. D. (2005). A Cataract Tele-Surgery Training Application in a Hapto-Visual Collaborative. *IEEE International Workshop on Haptic Audio Visual Environments and their Applications*. Ottawa, Ontario, Canada, October 2005.
7. Agus, M. Gobbetti, E. Pintore, G. Zanetti, G. Zorcolo, A. (2006). Real-time Cataract Surgery Simulation for Training. *Eurographics Italian Chapter Conference* (2006).
8. Webster, R. Sasanni, J. Senk, R. Zoppetti, G. (2004). Simulating the continuous curvilinear capsulorhexis procedure during cataract surgery. *International conference modelling and simulation*.
9. (Reachin, 2006). <http://www.reachin.se>. 20/01/2007.
10. (Reachin, 2007). <http://www.reachin.se>. 20/01/2007.
11. (Exchange3d, 2006). <http://www.exchange3d.com>. 20/01/2007.
12. E. Uchio, Shi. Ohno, Joju Kudoh, K. Aoki and Lech T. Kisielewicz (2007). Simulation model of an eyeball based on finite element analysis on a supercomputer. *Br. J. Ophthalmol.* 1999;83;1106-1111.
13. Neumann, P. F., Sadler, L. L. and Gieser, J. (1998) *Virtual Reality Vitrectomy Simulator*, MICCAI’98, LNCS 1496, pp. 910-917.

Author: Juan Francisco Perez

Rafael Barea

Institute: Department of Electronics. University of Alcalá

Street: 2885. Alcalá de Henares.

City: Madrid

Country: Spain

Email: [juanf.perez@depeca.uah.es](mailto:juanf.perez@depeca.uah.es)

[barea@depeca.uah.es](mailto:barea@depeca.uah.es)

# COMSOL Multiphysics in Undergraduate Education of Electromagnetic Field Biological Interactions

P. Togni<sup>1</sup>, M. Cifra<sup>1,2</sup> and T. Dřížd'al<sup>1</sup>

<sup>1</sup> Department of Electromagnetic Field, Czech Technical University, Prague, Czech Republic

<sup>2</sup> Institute of Photonics and Electronics of Academy of Sciences of the Czech Republic, Prague, Czech Republic

**Abstract** — In this paper we present a basic model created in COMSOL Multiphysics for undergraduate education purposes in courses dealing with biological effects of electromagnetic fields, electromagnetic fields in biological systems. COMSOL Multiphysics provides possibility to combine various physical processes described by differential equations to one simulation. Easy-to-do and attractive graphical post-processing of the calculated results in COMSOL Multiphysics are very useful for presentation in classroom and lecture what increases students' interest in the subject as well as their attention.

**Keywords** — COMSOL Multiphysics, undergraduate education, bioelectromagnetics, microwaves, hyperthermia

## INTRODUCTION

Application of simulation software based on various mathematical methods (FEM, FDTD, etc.) for modeling of various physical processes for research and education purposes has grown rapidly in recent years. Although researcher is able to solve various problems analytically or using various approximations, when the problem becomes too complex, he needs to use numerical calculations to obtain a solution. Nowadays, enough computer power is usually available for calculation of common problems. A substantial amount of the problems can be solved numerically when one, after understanding physical background of the problem, writes suitable script in programming language of his choice. However, in many cases this is too time consuming or demanding on programming skills. Thus, one reaches for one of the various simulation softwares, which are nowadays available commercially. It is reasonable considering that programming team containing number of software engineers are able to do more than a single researcher who needs to deal with many other tasks than programming of his tools. Software groups focus on specialized problems and as a team they can provide high valued product which saves the time of the researcher. Similar reasoning can be used in the field of undergraduate education.

Research and education interests of authors of this paper are industrial and biomedical applications of microwaves, effect of electromagnetic field on biological systems and

generation of electromagnetic field in biological systems. All topics include theoretical treatment of the problems, numerical and experimental verification of theoretical results. Parts of physics that needs to be covered range from electromagnetics, thermal physics – heat conduction, conduction and radiation, mechanics, stress and strain to chemistry and biophysics, prospectively. In order to provide interactive undergraduate education in these topics, one needs simulation software that fulfills several prerequisites. Software needs to be:

- user friendly and easily controllable
- able of multiphysical simulations
- able of easy-to-do and illustrative graphical visualization of results.

COMSOL Multiphysics<sup>®</sup> fulfills these prerequisites. It is finite element based unifying multiphysical simulation environment. The COMSOL Multiphysics<sup>®</sup> [4] (abbr. “COMSOL” in further text) simulation environment facilitates all steps in the modeling process - defining the geometry, specifying the physics, meshing, solving and then post-processing the results. Model set up is quick, thanks to a number of predefined modeling interfaces for applications ranging from fluid flow and heat transfer to structural mechanics and electromagnetic analyses. Material properties, source terms and boundary conditions can all be arbitrary functions of the dependent variables. Application-specific modules bring terminology, material libraries, solvers and elements, as well as visualization tools appropriately specialized to the application area. In addition to custom solutions, each of the add-on modules comes with a large number of ready-to-run and well-documented example models. Except the multiphysical core, COMSOL includes several modules which cover most fields of physics.

However, one is not limited by these modules. Problem can be described by partial differential equations (PDE) from scratch. PDEs can be also added to the existing module to make the model more precise in description. Although we can easily handle the physical problems using the modules, we do not lose contact with the physical description, since the PDE in actual form is visible whenever setting the subdomain, boundary or edge properties.

We focus in this paper on exemplary model of microwave applicator used in microwave hyperthermia. This model is easily constructed and shows advantages of COMSOL in multiphysical modeling in undergraduate education.

## MICROWAVE HYPERTHERMIA

Microwave induced hyperthermia represents an important tool in anti cancer treatments, both as an adjuvant of chemo and radiation therapies and as an ablative procedure, according to the type of applicator used. When the temperature of a part of the body is enhanced over 3 °C above its normal value, the cells start to be under thermal stress. Going above 41.5 °C this stress begins gradually to induce irreversible damages like cell apoptosis and necrosis, whose extent is inversely proportional to the ratio heat intensity over time. For this reason, commonly in clinical practice, the temperature in the tumour is enhanced in the range 41.5-45 °C for a period of about 30-60 minutes.

Microwaves can induce effective and quite homogeneous hyperthermia, associated to direct effects on cellular molecules and H<sub>2</sub>O.

Effective delivery of microwaves depends on precise characteristics of microwave applicators which must be able to focus the electromagnetic energy as much as possible in the cancer tissue in order not to damage the surrounding healthy tissue. In any case, temperature enhancement produced by microwave radiation induces blood perfusion changes [1] which increase heat conduction in healthy tissue producing a selective increase in tumour temperature providing an effective heat trap. In fact, when the temperature is enhanced, blood flow enhances as well, acting as a

cooler. Since the vascular system of tumours is generally irregular and incompletely developed, this cooling effect is thereby lower than in normal tissues. In these conditions, on equal electromagnetic energy exposure, the temperature inside the tumour will be maintained higher with cumulative effects [2].

Hyperthermia is newly back in the interest of both, clinical and research oncologists, because of its properties to directly produce permanent damages of the treated tumour and to elicit important immunological responses against cancer cells by changing their immunogenicity [3].

## MODEL

Microwave applicator suitable for hyperthermia needs to be properly designed in order to deliver electromagnetic energy into the tumor tissue with minimal irradiation of healthy tissue. This can be tuned by optimal radiation pattern of the applicator and water bolus which is used to cool down the surface of the tissue - skin. We will show exemplary design of the microwave patch applicator for frequency of 2.45 GHz. We will not treat underlying antenna theory, it can be found in standard antenna textbooks.

We will first draw the geometry of the problem. One of the advantages of COMSOL compared to other modeling software, even specialized on electromagnetics and radiofrequency modeling, is possibility to exploit axial symmetry of the problem. This enormously saves computer power and requirements on the memory by modeling in 2D instead of 3D. Geometry of the model is shown in the Fig. 1.

We create simple yet multiphysical model consisting of electromagnetic and heat transfer part. After drawing the model, one needs to define the physics of the model. This is done separately for electromagnetic and heat part, setting material properties of subdomain and boundary settings. Depending on the character of the boundary or the subdomain, corresponding equation describing the problem is displayed. If calculation in any subdomain is not desired, it can be excluded. Here, we are not interested in temperature of the water bolus. In praxis, water in the bolus is circulated and cooled to keep it at the same temperature. We approximated it in our model by setting the temperature of the water bolus-tissue boundary to constant 20 °C. Tissue is approximated to be homogenous in both electromagnetic and heat domain. Electromagnetic energy is transformed into the heat in the tissue since the tissue lossy. Coaxial cable is fed by 50 W via "Port" setting.

Bioheat equation is used for description of blood perfusion of the tissue. The coupling of the electromagnetic and heat path is done simply by including the external (spatial) heat source in bioheat equation (see Fig. 3). The external

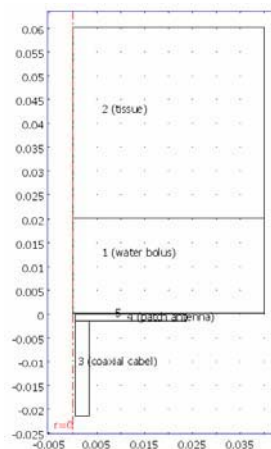


Fig. 1 Model drawn using axial symmetry, red line is symmetry axis. Dimensions are in meters. Subdomains labeled.

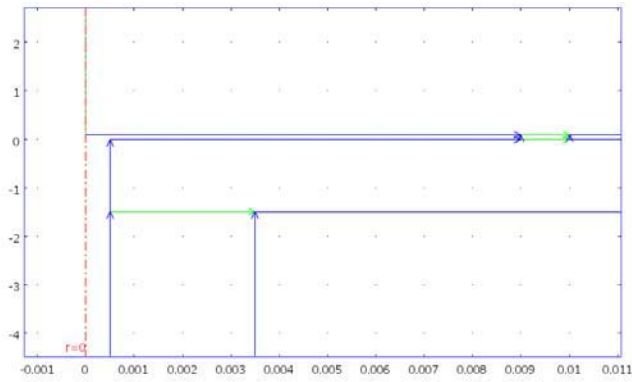


Fig. 2 Detail of the slot of the patch applicator. Dimensions of x and y axis are in meters and millimeters, respectively. Boundary mode displayed – blue lines represent perfectly conducting material (PEC), green lines are continuities.

heat is set to originate from the electromagnetic energy transformed into heat due to nonzero conductivity of the tissue. Coupling is done via variable Qav\_rfweh.

After the setting geometry and physics, we create a mesh which discretize the problem. Meshing can be done automatically. Additionally, various settings can be tuned manually or semi-automatically (e.g. mesh elements, element growth factor) to create a mesh which is reasonable fine for the given purpose and still not too large to be solvable with available PC.

Afterwards, we can start solving the problem. COMSOL has several solvers available to cope with various problems. Many solver settings can be changed manually. Firstly, we need to solve the electromagnetic part. It is independent from the heat part, since we assume that electric parameters

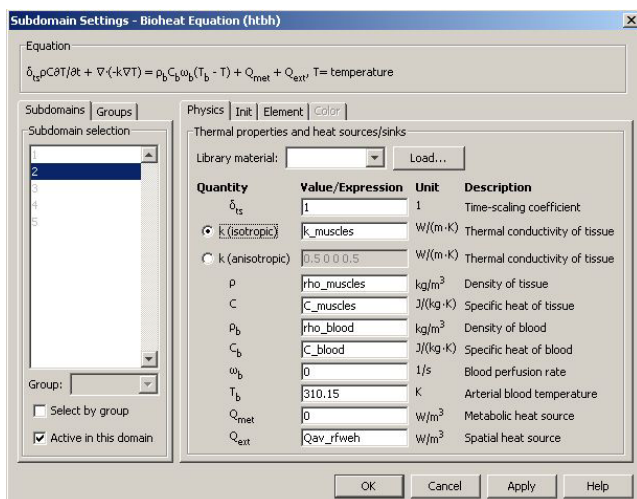


Fig. 3 Example of subdomain settings (subdomain 2 - tissue). Bioheat equation is a part of heat transfer module.

Table 1 Font sizes and styles

Description	Value
Thermal conductivity, muscle	0.56 [W/(m*K)]
Density, blood	1e3 [kg/m^3]
Specific heat, blood	3825 [J/(kg*K)]
Specific heat, muscle	3639 [J/(kg*K)]
Blood perfusion rate	3.6e-3 [1/s]
Blood temperature	37 [°C]
Relative permittivity, dielectric	4.3
Relative permittivity, catheter	77.6
Relative permittivity, muscle	53
Electric conductivity, muscle	1.73 [S/m]
Electric conductivity, water	1.26 [S/m]

of the tissue will not change with the temperature. With the automatic extra fine meshing (2 level above normal meshing) the mesh will consist of ca. 20 thousand elements, the solution of the electromagnetic and heat problem is done in 62 seconds (PC 3 GHz, Intel Pentium 4, L2 1MB, 1GB RAM).

Constants used for the material properties are in the Tab. 1

In some cases when the physical problems are inter-coupled, we need to solve for one single physical problem first, and then set it as initial conditions for the solution of multiphysical problem.

The solution is automatically plotted taking the default post-processing settings. The last step is to choose a proper quantity (or few of them) to be displayed. We show the calculated electric field and temperature distribution after 10 minutes of heating on the Fig. 4.

The immediate results show where the electrical power is focused. Most power is dissipated in water bolus. However,

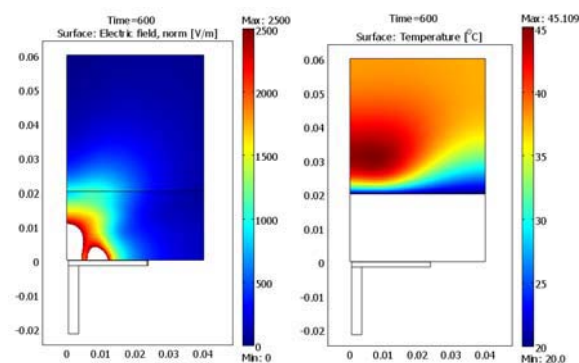


Fig. 4 left: Electric field distribution, white spaces are above displayed range (2500 V/m); right: Temperature distribution after 600 s of heating. All axes in meters

since circulation of water, here expressed by constant temperature of water bolus-tissue boundary, ensures the cooling of the tissue surface, the focused hotspot lies is under the surface of tissue.

## DISCUSSION & CONCLUSION

We have shown basic steps in modeling a microwave patch applicator for heating of tissue. The drawing of geometry of problem with setting of the physics can be done within several minutes, depending on the experience of the user. Automatic meshing followed by solving takes few minutes. Post-processing of the data and exporting of image is a matter of few minutes as well. If we want to produce a animated result, what can be done in our case (we calculated temperature evolution from 0 to 600 s) it may take several minutes, depending on the desired quality and frame rate of the movie. This is of great help not only in education but also in research presentation.

Regarding model shown in this paper, we could introduce relatively easily various enhancements to make it more corresponding to reality. We could simply introduce more layers of the tissue: several levels of skin, fat layer, even bone, if necessary. Further it would be reasonable to use other electrical and heat conduction properties for tumor tissue. Tumors have usually different structure and lower blood perfusion, depending on the type.

Computer aided design often includes optimization of various parameters. This can be done in COMSOL as well, either by using built in COMSOL scripting language or by exporting the model into MatLab m-file and running the model with various sweep parameters in cycle. Since MatLab is a standard engineering tool, easy export of a model into MatLab is very welcome.

COMSOL provides extensive manuals for every module and feature. There are also plenty of sample models available in model library. These models are freely editable and can serve as a base for inspiration and learning. For one from many see Fig. 5, which depicts specific absorption ratio (SAR) on human head caused by irradiation by patch antenna.

We would like to conclude that a COMSOL Multiphysics® fully fulfils the needs of educator and researcher providing him a tool which is not only easy to use (compared to other multiphysical tools) yet complex and universal but also capable to create attractive presentation of results.

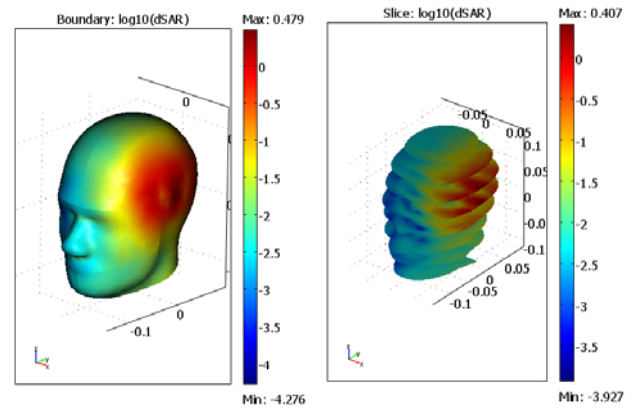


Fig. 5 left: SAR distribution on the boundary, right: SAR distribution on the slices. Axes in meters, SAR logarithmic

Regarding the undergraduate education, it will inevitably increase the interest of students by dragging them near to the research topics in visually appealing form.

## ACKNOWLEDGMENT

Authors would like to thank funding agency FRVS for support (g.n. 2300/2008), Grant Agency of the Czech Republic g.n. 102/08/H081, and last but not least to Humusoft, dealer of COMSOL Multiphysics in the Czech Republic.

## REFERENCES

1. Duran T. E., Rakesh K. J., Differential Response of Normal and Tumor Microcirculation to Hyperthermia, *Cancer Research* 44, 605-612, Feb. 1984
2. Vrba J., *Medical Applications of Microwaves (In Czech)*. CTU Press, Prague 2003.
3. Baronzio G., Gramaglia A., Fiorentini G., Hyperthermia and Immunity. A Brief Overview. *In Vivo*. 20(6A):p. 689-95, 2006
4. Internet website address: [www.comsol.com](http://www.comsol.com)

Corresponding author:

Author: Paolo Togni  
 Institute: Dept. of electromagnetic field, Czech Technical University  
 Street: Technická 2  
 City: Prague  
 Country: Czech Republic  
 Email: [tognip1@fel.cvut.cz](mailto:tognip1@fel.cvut.cz)

# Actual State of Medical Physics and Biomedical Engineering Education in Poland

M. Wasilewska-Radwanska<sup>1</sup> and T. Palko<sup>2</sup>

<sup>1</sup> AGH University of Science and Technology/Faculty of Physics and Applied Computer Science,  
Department of Medical Physics and Biophysics, Krakow, Poland

<sup>2</sup> Warsaw University of Technology/Faculty of Mechatronics, Institute of Precision and Biomedical Engineering, Warsaw, Poland

**Abstract** — The history and current state of medical physics and biomedical engineering education in Poland has been presented. In academic year 2007/2008 medical physics as specialization has been provided by 14 universities and biomedical engineering studies as a discipline by 6 universities of technology in Poland.

**Keywords** — medical physics, biomedical engineering, education.

## I. INTRODUCTION

In the paper we intend to present current state in education in Medical Physics (MP) and Biomedical Engineering (BME) in Poland. Education on medical physics and engineering has a long tradition in Poland [1] being linked to the history of the Radium Institute in Warsaw, which was established in 1934, following the initiative of Maria Sklodowska-Curie. In 1936 Prof. Cezary Pawlowski, one of the assistants and then collaborators of Madame Curie organized first courses on medical physics and biomedical engineering in the Physics Department of the Radium Institute.

In 1946 the first academic course of medical engineering started at the Faculty of Electrical Engineering of Warsaw University of Technology. In 1951 the specialization, called shortly "Electro-medicine" was created. Until 2006 Education in Biomedical Engineering was proposed as specialization in other fields of studies e.g. mechanics, automatics & robotics, electronics.

Education in Medical Physics in Poland [2] started in 1950 with the Technical Physics specialization at the Warsaw University of Technology created by Prof. Cezary Pawlowski and at the AGH University of Science and Technology (former University of Mining and Metallurgy) in Krakow by Prof. Marian Miesowicz. In 1974 Medical Physics program has been initiated at Warsaw University and in 1979 at the Jagellonian University In Krakow (undergraduate course in Experimental Physics). In 1990 Medical Physics and Dosimetry specialization has been established at the AGH University of Science and Technology in close cooperation with the Collegium Medicum (Faculty of Medicine) of the Jagellonian University in Krakow.

The paper was prepared using data collected from the information delivered to the candidates to the Higher Education Schools in academic year 2007/2008.

## II. EDUCATION IN MEDICAL PHYSICS

In academic year 2007/2008 Medical Physics education has been offered by 10 universities and 4 technical universities in Poland (Table 1).

Table 1 List of institutions which provide education in Medical Physics (MP) in Poland

Institutions	Faculty/ Department	Discip -line	Speciali- zation	BSc/MSc/PhD
Univ.of Gdansk (Gdansk)	Math., Physics and Computer Sc.	P*	BMP***	+ / + / +
Univ.of Silesia (Katowice)	Math., Phys. and Chem.	P	MP****	+ / + / +
Jagellonian Univ.(Krakow)	Phys., Astr. & Appl.CompSc	P	MP	+ / + / +
AGH Univ. of Sc &Techn. (Krakow)	Phys.& Appl. Comp. Sc.	TP**	MP&Do- simetry	+ / + / +
Un. of Lodz (Lodz)	Phys& Chem.	P	MP	+ / - / -
Techn.Univ.Lodz (Lodz)	TPhys., Comp Sc.& Appl.M.	P	MP	+ / - / -
Univ.of Opole (Opole)	Math., Phys & Chem.	P	MP	+ / - / -
Adam Mickiewicz Univ. (Poznan)	Physcis	P	MP	+ / + / +
Techn.Univ. (Rzeszow)	Math.& Appl. Physics	TP	PI*****	+ / - / -
Univ.of Szczecin (Szczecin)	Math.& Physics	P	MP	+ / + / -
Nicolaus Copernicus Univ. (Torun)	Phys., Astr& Informatics	P	MP and Comp. Appl.	+ / - / -
Warsaw Univ. (Warsaw)	Physics/Inst. of Exp.Phys.	P	MP	+ / + / +
Wroclaw Univ. of Techn. (Wroclaw)	Fund. Problems of Techn.	TP	Photo- nics	+ / + / +
Univ. of Wroclaw (Wroclaw)	Physics and Astr.	P	MP	+ / + / +

\*) P=Physics ; \*\*/TP=Technical Physics; \*\*\*) BMP= BioMedical Physics  
\*\*\*\*) MP=Medical Physics; \*\*\*\*\*)Physics and Informatics in Medicine

The specialization is in discipline of physics (experimental physics) or of technical physics, in general from the first year, except Warsaw University where it starts on the fourth year.

The curricula consist of lectures, problem classes, laboratory classes and seminars. Student exchange programs, such as ERASMUS, have been and are very successful in allowing Polish students in Medical Physics to study abroad.

The implementation of Directive 96/29 and Directive 97/43/EURATOM creates job opportunities for medical physicists, especially in Quality Control and Quality Assurance of X-Ray and nuclear medicine diagnostic equipment.

### III. EDUCATION IN BIOMEDICAL ENGINEERING

The development of medicine and sophisticated medical equipment caused the need for a new approach to the teaching of biomedical engineering in Poland. Therefore, a consortium of six technical universities was created, in order to elaborate the new program and to apply to the Ministry of Science and Higher Education to create a new educational direction called "Biomedical Engineering" (BME). The work was supported also by Committees of Polish Academy of Sciences. The application was prepared in June 2004 and accepted in June 2006. In Table 2 the list of institutions providing education in BME in academic year 2007/2008 has been presented.

The organization of the studies had to be consistent with the requirements of the so called Bologna Process which represents a commitment by forty-five European countries to undertake a series of reforms in order to achieve greater consistency and portability across their higher education systems, by harmonizing academic degree standards and quality assurance standards throughout Europe.

The curricula of BME education will prepare the graduates for the profession of designer of medical equipment or clinical engineer. The organization of the studies had to be consistent with the requirements of the so called Bologna Process which represents a commitment by forty-five European countries to undertake a series of reforms in order to achieve greater consistency and portability across their higher education systems, by harmonizing academic degree standards and quality assurance standards throughout Europe.

The curricula of BME education will prepare the graduates for the profession of designer of medical equipment or clinical engineer.

Table 2 List of institutions which provide education in Biomedical Engineering (BME) in Poland

Institutions	Faculty/ Department	Organisation (actual state)
AGH Univ. of Science and Technology (Krakow)	Electrical Eng., Automatics, Comp. Sc. & Electronics	Inter-Faculty School of Biomedical Engineering (BSc)
Gdansk Univ. of Technology (Gdansk)	Electronics, Telecommunications and Informatics	Specialisation: Medical and Ecological Electronics
Silesian Univ. of Technology (Gliwice)	Automatic Control, Electronics and Computer Science	Full-time studies (BSc)
Techn. Univ. Lodz (Lodz)	El., Electronic, Comp. & Control Eng.	(BSc) in English
Warsaw Univ. of Technology (Warsaw)	Mechatronics/ I. of Precision & Biomed. Engineering	Inter-Faculty full-time studies provided by the F. of Mechatronics and F. of Electronics and Information Technology (BSc)
Wroclaw Univ. of Technology (Wroclaw)	Fund. Problems of Technology	(BSc) (MSc) in English

### IV. CONCLUSIONS

Presently the main demand for medical physicists and biomedical engineers in Poland appears to be by hospitals (radiotherapy, radio-diagnostics and interventional radiology, nuclear medicine etc.) and by industry R & D.

Research in medical physics and biomedical engineering in Poland is partly supported by the Ministry of Science and Higher Education in form of grants and direct financing of universities. Some research activities are coordinated by the Polish Academy of Sciences, Department VI of Medical Sciences. Better research opportunities for students and graduates could be created through EU FP/6/7 instruments.

### REFERENCES

1. Palko T, Golnik N, Pawlicki G, Pawlowski Z (2002) Education on Biomedical Engineering at Warsaw University of Technology, Polish J Med & Eng 2002, 8(2): 121-127
2. Wasilewska-Radwanska M and Waligorski M (1995) The Curriculum of Medical Physics in Krakow in Medical Radiation Physics – a European Perspective, King's College London, Editors: Colin Roberts, Slavik D Tabakov, Cornelius Lewis, London 1995, pp.127-140

Author: Marta Wasilewska-Radwanska  
 Institute: AGH University of Science and Technology  
 Street: Al. Mickiewicza 30  
 City: 30-059 Krakow  
 Country: Poland,  
 Email: radwanska@novell.ftj.agh.edu.pl

# The Practice for Medical Physics and Engineering Students

A. Balodis<sup>1</sup>, V. Zemite<sup>1</sup>

<sup>1</sup>Riga Technical University, Riga, Latvia

*Abstract* — Medical engineering is formed up to unify two dynamic professions – engineering and medicine. The responsibility of medical engineering specialists is related with implementation in practice of medical equipment and instruments. Medical physics is inwrought with radiation therapy, nuclear medicine, diagnostic radiology and radiation protection in medicine. Biomedical engineers and medical physicists could design and produce equipment and systems, using of which could control physiological function of organisms.

Riga Technical University (RTU) today is the educational institution in Latvia, as well as Baltic States, that crams professional bachelor in medical physics, graduate “Engineer of physical technologies in medicine”. Professional bachelor studying program “Medical engineering and physics” is established in accordance with the laws for higher educational institutions.

According to State standard of second level professional higher education, the practice in volume of 26 credit points is anticipated. The content of practice is formed according to professional standard. The purpose of practice is to acquaint oneself with working conditions in real companies and organizations that is related to exploitation, maintenance or manufacturing of medical equipment. In consequence of practice the students are collecting and processing materials for bachelor thesis and engineer design project.

The four level systems for practice have been developed by RTU. At the first level of practice students are provided with initial practice to get the first skill on processing technologies and measurements. At the second level the students are directed to industry to acquire an experience on technologies development and machine design. After that the third level of practical training is clinical practice, when the students get the feel of working with equipment in radiological diagnostics and therapy. At the fifth level of practice the students master the knowledge and comprehensive skills at scientific work. Finally the students select the practical placements to develop their qualification projects.

*Keywords* — medical engineering, medical physics, education, system of practice.

## I. INTRODUCTION

Study programs in field of medical engineering and medical physics are comparatively young in Europe and in the World.

Medical engineering is formed up to unify two dynamic professions – engineering and medicine. The responsibility of medical engineering specialists is related with implemen-

tation in practice of medical equipment and instruments. Medical engineering contains several disciplines as:

- Biomechanics, that contains integrated static and flow studies of physiological systems;
- Biomaterials, that is related to development of bioimplantant materials design and manufacturing
- Physiological modeling, simulation and control, where the using of computer modeling have involved perception of correlation of physiological processes;
- Biosensors, that comprise fixation of biological processes and its transformation into electrical signals;
- Biomedical equipment that develops the measurements and observations of physiological processes involving to biosensors.
- The medical and biological analysis that contains determination, classification and analyzing of bioelectric signals;
- Rehabilitation engineering, that related to creation and evolving of therapeutical and rehabilitical equipment and procedures;
- Prostheses and artificial organs, those creation and development for substitution or restoration of body function;
- Medical informatics, that point is processing of data acquired from patient, interpretation of results and establishing of clinical diagnosis;
- Imaging in medicine what comprise imaging to graphic display of anatomical structures and physiological functions;
- Biotechnologies and tissue engineering to create and modify biological materials for medicinal purpose;
- Clinical engineering that contains design, installation and servicing of clinical equipment, instruments and systems.
- Medical micro – and nano technology etc.[1].

Medical physics is inwrought with radiation therapy, nuclear medicine, diagnostic radiology and radiation protection in medicine. Using a great many legislations of physics, medical physics explain biological effect of radiation to human body. From above-mentioned consequent the way of biomedical engineer is wide:

- Research in new materials for implanted artificial organs;
- Development of new diagnostic instruments for blood analysis;



- Computer modeling of the function of the human heart;
- Writing software for analysis of medical research data;
- Analysis of medical device hazards for safety and efficacy;
- Development of new diagnostic imaging systems;
- Design of telemetry systems for patient monitoring;
- Design of biomedical sensors for measurement of human physiologic systems variables;
- Development of expert systems for diagnosis of diseases;
- Design of closed-loop control systems for drug administration;
- Modeling of the physiologic systems of the human body;
- Design of instrumentation for sports medicine;
- Development of material to be used as replacement for human skin;
- Development of new dental materials;
- Design of communication aids for the handicapped etc.[1].

Biomedical engineers and medical physicists using several physical principles (electrical, mechanical and optical ect.) can deeply understand biological (human and animals) systems. These specialists can design and produce equipment and systems, the using of which can control physiological function of organisms. These equipments are unalienable components for diagnostic and treatment of diseases.

For those specialists specific education is indispensable. The large number of universities in Europe and outside organize education in medical engineering or medical physics, deeply specialized in one or two “small line” (specialty).

#### *A. Education for young specialists in medical engineering and physics in Latvia*

Riga Technical university (RTU) is the first university in Latvia and Baltic States, which initiates a study program in medical engineering and physics in order to obtain the second level professional higher education, what cover ground in two large fields: medical engineering and medical physics. Professional bachelor studying program “Medical engineering and physics” is established in accordance with Latvia State Standard of Second Level Professional Higher Education [2], The law for higher educational institutions, and the act of RTU Senate. Professional bachelor studying program “Medical engineering and physics” duration of study is provided 4,5 years with total volume 181 credit points. During one studying year, which is divided into 2 semesters, the total capacity is 40 credit points in the case of

full studying load. One KP corresponds to 16 contact hours in auditoria and laboratory.

Studying program “Medical engineering and physics” has been realized in RTU Faculty of Transport and Mechanical Engineering, Institute of Biomedical Engineering and Nanotechnologies, cooperation with Riga Stradins University, their academic personal. Theoretical basic course in medicine is provides by teaching staff from Riga Stradins University Departments of Normal physiology, Anatomy and histology

The purpose of program “Medical engineering and physics” is to provide fundamental and theoretical basics in the field, to make ready specialists with professional higher education, that manage realization of acquired knowledge in the field of medical engineering and physics.

After graduation the student can obtain the 5th level professional higher education - qualification –*Engineer of Medical Physical Technologies* and bachelor degree in *Medical physics*.

The program provides lectures, practical and laboratory studies, practice and in time of preparing bachelor thesis to get the feel theoretical, technical, economical, humanitarian and social subjects that correspond to the field of the medical engineering and physics.

The students at the time of studying obtain:

- theoretical knowledge in structure, physical and technical workings of medical equipment, machines and instruments, those manufacturing technology, utilization conditions and safety;
- practical skills working in medical institutions and companies – acquisition, installation, utilizing, regulation and quality leadership of medical engineer equipment,
- ability to use theoretical knowledge and skills in practical work using, projecting of technologies of medical engineering and physics;
- knowledge to perform public activity in Latvia and in interstate collaboration, understanding of professional ethic and implementation of project influence to environment and public.

Graduates will be motivated to continue education and systematical perfection of professional qualification.

## II. METHODS

According to RTU approved professional studying program and State standard of second level professional higher education, the practice in volume of 26 credit points is anticipated [2]. The content of practice is formed according to professional standard.

The purpose of practice is to acquaint oneself with working conditions in real companies and organizations that is related to exploitation, maintenance or manufacturing of medical equipment.

The principles of practices organizing for professional programs in Riga Technical University are established according to notice pro-rector RTU:

- The organization of practice manage practice manager of RTU departments;
- The contract for practice between companies providing the practice and institute of RTU is transacted. The responsibility and liability of the parties, the purpose, tasks, estimation arrangement of practice is reflected in contract.
- The practice is realized according to practice program making up the commission of studying program;
- The individual task of the practice is distributed for studios.

According to the decision of RTU Senate about evaluation of practice volume, in consequence the report of practice is writing, where the plan of practice with concrete tasks for each week is foreseen. Regular control of discharge of duties is indispensable. 1 week of practice is assessed with 1 credit point (KP).

The materials, obtained during the practice time, are used for elaboration of engineering project design and bachelor thesis.

### III. RESULTS

The main task is to developed the system of practice, where student could get acquainted with all facilities to work in field of medical engineering and medical physics - get acquainted: how design, produce and install the medical equipment, as well as responsibility of medical physicists at clinics and scientific work.

At the framework of European Union Foundation the project Nr. VPD1/ESF/PIAA/05/APK/3.2.6.3./0059/007 "The system of practical training of medical physicist" realization group in collaboration with employers and RTU academic staff four level system for practice have been developed by RTU: 1) Studying – basic skills yield practice, 2) Designing engineer-technologist practice, 3) Clinical practice and 4) Scientific practice.

At the 1 – 2 year the students have to proceed through first level of practice "Studying – basic skills yield practice"

where students get the first skills on processing technologies and measurements. This practice divide in two parts: mechanical and electronical /electrical. In mechanical practice the students obtain the practical skills to work with processing technologies of materials, such as grinding, milling, boring etc. In electronical /electrical practice the students study how produce the simple electrical/electronical equipment from scheme, preliminary design till equipment.

At the third course the students have to proceed through second level Designing engineer-technologist practice. This practice occur at companies where produce medical equipment. The students are directed to acquire an experience on technologies development and machine design. In companies students acquire with the rules, methods, projecting computer programs what used for design of medical equipment.

At the fourth year the students have to proceed through Clinical practice, what taking place in the great clinics, where improve in practice complicated medical technologies. The Clinical practice divided on two parts – 1) Diagnostic practice, work with diagnostic equipment such as computer tomography, magnetic resonance imaging technique ect. and 2) Radiotherapy practice, work with radiotherapeutical technologies and equipment.

At the forth and fifth year the students master the knowledge and comprehensive skills at scientific work. In this practice the students develop their qualification projects – bachelor work and engineer design project.

### IV. CONCLUSIONS

The four level systems for practice have been developed by RTU for students in medical engineering and medical physics.

### REFERENCES

1. The Biomedical Engineering handbook/ editor-in-chief Bronzino J.D. CRC Press, 1995, p.2862;
2. The Rules about State Standard of Second Level Professional Higher Education, The rules of Ministry of Latvia from 28 November, 2001.

Author: V.Zemite  
Institute: Riga Technical University  
Street: I. Kalku street  
City: Riga  
Country: Latvia  
Email: vzemite@latnet.lv

# Scientific Research, Telemedicine and Health Services: the “Burlo Garofolo” Hospital Web Portal

M. Bava<sup>1</sup>, A. Zambon<sup>1</sup>, L. Vecchi Brumatti<sup>1</sup>, R. Zangrando<sup>1</sup>, A. Accardo<sup>2</sup> and G. Tamburlini<sup>1</sup>

<sup>1</sup> Maternal-children Hospital “Burlo Garofolo”, Trieste, Italy

<sup>2</sup> Department of Electronics, DEEI, University of Trieste, Trieste, Italy

**Abstract** — The web portal designed at the “Burlo Garofolo”, the maternal-children hospital in Trieste (Italy), provides services to the users, the medical doctors involved in telemedicine and the researchers (medical doctors, biologists, psychologists, epidemiologists) both from university and hospital units. The platform has been completely developed and managed by an internal team of professionals and is housed in a dedicated hospital-based server. It is realized using the LAMP open-source technology, programming the CMS and the interface between forms and database using the php language.

**Keywords** — LAMP open source technology, web portal and databases, CMS.

## I. INTRODUCTION

In recent years many European hospitals offer health web services dedicated to the users and to medical professionals, generally contracting external web professionals for their implementation.

The web portal [1] of the Maternal-children Hospital “Burlo Garofolo”- Trieste, Italy - has been designed to offer services to the audience/users both to the medical doctors involved in telemedicine and to the researchers (medical doctors, biologists, psychologists, epidemiologists) both from university and hospital units.

From the home page is possible to reach all the services for the users, the telemedicine professionals and the researchers; the last two categories have an account controlled access to a Virtual Hospital Department page.

Currently the portal houses data gathering services for three research projects: a) a php form dedicated to a cohort study; b) a php form concerning children with gastroesophageal diseases; c) a web form for the study of atypical uterine polyps in women from several gynaecological departments of Italian hospitals.

Obstetrical ultrasonographers from the Friuli Venezia-Giulia’s Regional Hospitals and Health-Districts are provided with telemedicine services accessible using a required account by which they could ask a consult related to obstetric ultrasound images.

Appointments for specialty and private medical visits can be scheduled by compiling an on-line form.

Finally the platform administrators are provided with a modern CMS to create and manage the contents inside the pages of the hospital web site.

The platform has been developed and managed by an internal team of professionals and was realized using LAMP technology and is housed in a dedicated hospital server.

## II. DEVELOPMENT AND IMPLEMENTATION

In 2003 the “Burlo Garofolo’s” web portal committee decided to upgrade the static *html* web portal to a dynamic one. The purpose was to create a new platform to develop and to offer services to the researchers, the medical doctors and the public users. To accomplish these objectives the LAMP open source technology and the use of a new sophisticated hospital-hosted server were chosen. An internal technical group dedicated to the design, the implementation and the updating of the platform was formed.

The operating system used is Linux Debian 3.1 Stable [2], which was developed and maintained by the open source community and by a pool of Debian developers. The OS license is the GPL-GNU. Apache 2.0 [3] is the web server used for the portal; it was developed and sponsored by Apache Software Foundation both as source code and binary code. The database server is MySQL 4.1 [4] developed by MySQL AB, and PHP 4.4 is used as the server side scripting language.

The first step of the technical group was to replace the old static web site with a new one using the MySQL database and the PHP [5] engine to visualize the web pages. At this step the contents of the old web site were merely duplicated.

At the same time the group developed a new interface (the CMS) to update the web pages, instead of using the old-site Dreamweaver interface to modify the pages, and to upload the contents.

Other steps are described in the following sections and sub-sections.

### III. RESEARCH PROJECTS

The portal houses three databases for scientific data gathering related to three research projects: a) a cohort study; b) the IGARIS study concerning children with gastroesophageal reflux and early milk allergy; c) a study regarding atypical uterine polyps in women.

#### A. Cohort study

In February 2007 the I.R.C.C.S. “Burlo Garofolo”, with the co-operation of the University of Udine, started a cohort study to follow a population of mothers and children from the first months of the pregnancy, sampling biological, health and social information.

The longitudinal study is composed by five research projects: PHIME [6], VIVE, PAPP, OXI, Alimentazione.

The PHIME project (Public Health Impact of long-term, low-level mixed element exposure in susceptible population strata) studies a series of toxic elements – lead, mercury,

platinum, arsenic, etc... - and the susceptible populations include foetuses, children, women and elderly.

The VIVE project (Vertical Viruses in pregnant women) is a correlated study to the PHIME project, and investigates infectious and pathogenic factors that could impact on the neuropsychological outcomes described by PHIME.

The PAPP project studies the free HCG $\beta$  and the PAPP-A proteins and the blood flow of the intrauterine arteries in order to discover early foetal pathologies.

The OXI project studies the pathologies during pregnancy to enhance prevention and the early therapy.

The Alimentazione project studies the alimentation of the baby from breastfeeding to the normal alimentary diet.

According to the needs described above, the web site technical group developed a database and a related php form to allow the data entry of clinical and biological information. Every research group involved in the projects is allowed to edit or to view the database fields via the form, and the access to the web pages is protected by *https* protocol. The actual web form is shown in Fig. 1.

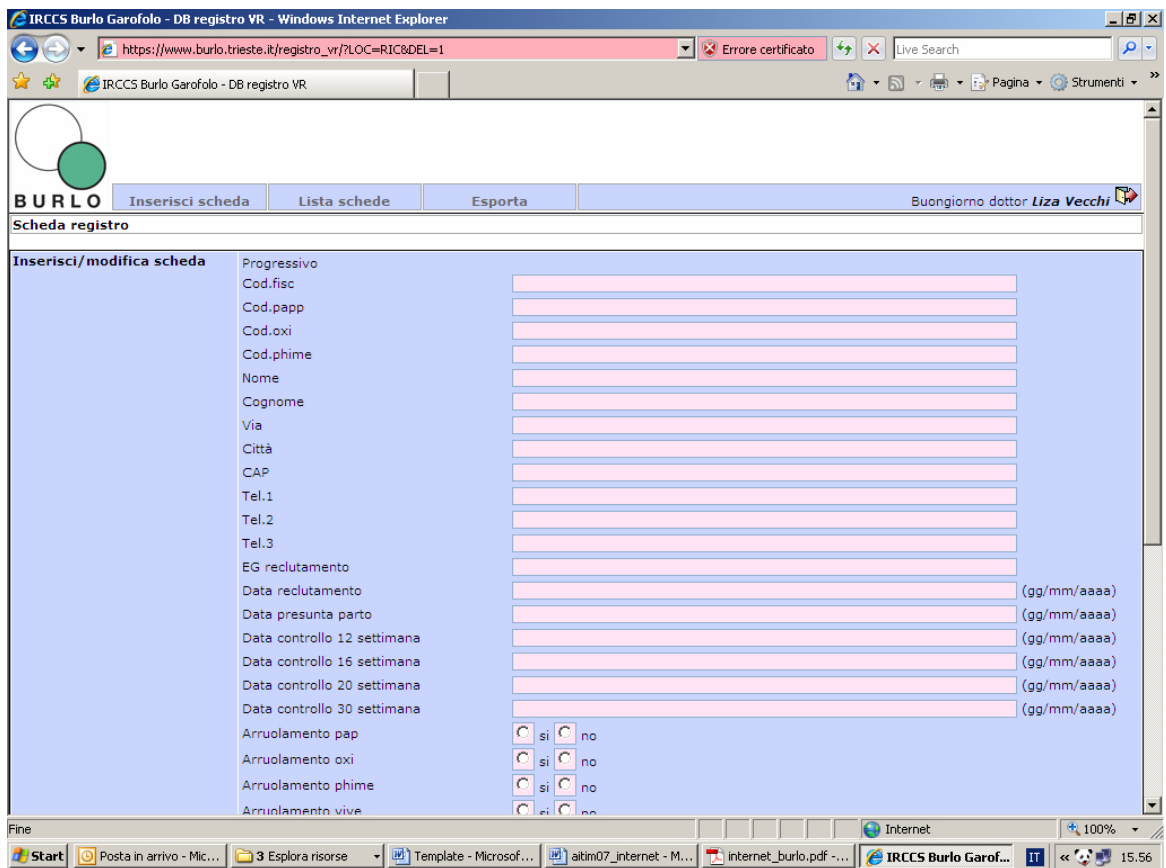


Fig. 1 Cohort study web form

*B. IGARIS project*

The IGARIS [7] (Iatrogenic Ghost Allergy and Reflux Infant Syndrome) project, addressed to the Friuli Venezia-Giulia pediatricians, analyzes the possibility of causing/sustaining food aversion by means of repeated medical interventions, especially imposing unjustified restricted diets and/or “over-diagnosing” gastro-esophageal reflux.

To record the IGARIS patients coming from the Friuli Venezia-Giulia region, and in the near future from other

Italian pediatric structures, a database and a related web form have been designed and implemented to monitor the clinical behavior of the involved pediatricians towards the problems of the affected babies. Two masks have been implemented for reporting the gastro-esophageal and the milk intolerance disorders. To access the forms it is necessary to be a pediatrician and to request the credentials from the Informative Service Unit at the I.R.C.C.S. “Burlo Garofolo”.

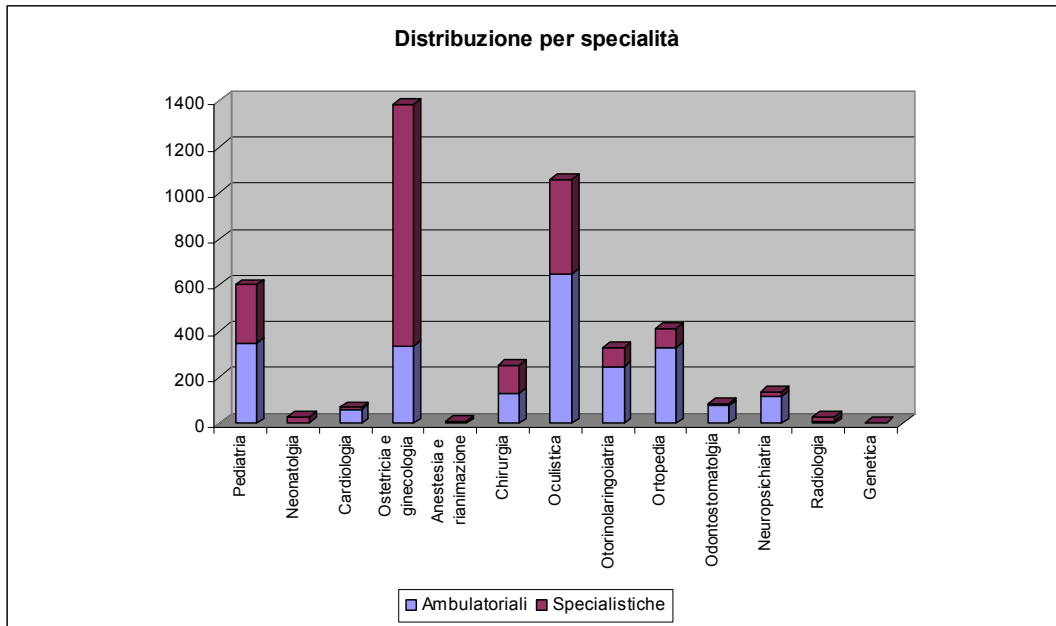


Fig. 2 Total appointments for specialties

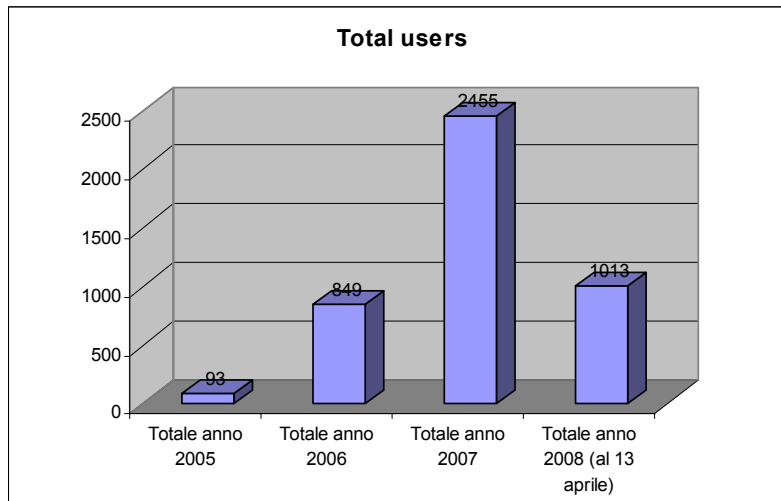


Fig. 3 Total users from the beginning of the service

### C. Multi-center study of atypical uterine polyps in women

This recent study started officially in April 2008 [8] and regards the conservative medical treatment of atypical uterine polyps in women monitored during five years, and eventually surgically operated.

A database has been developed to archive the patients' clinical data and to follow the patients from different and previously authorized Italian health centers.

## IV. TELEMEDICINE

In 2006 the creation of a Virtual Regional Department provided with telemedicine services such as radiological tele-consult and transmission of cardiologic diagrams was proposed.

In order to accomplish this aim and to expedite and secure the sending of ultrasound images and interpretation from the ultrasonographers to other specialists, the web site technical group realized a tele-consult system reachable through the web portal.

Using this system the obstetrical ultrasonographers from Regional Hospitals and Health-Districts are provided with telemedicine services accessible using a required account by which they could ask Burlo's specialists for a consult related to ultrasound images of foetal malformations.

Together with image acquisition the applicants fill in a web-form especially designed to support the diagnosis of a large variety of prenatal diseases regarding the digestive system, the central nervous system and the kidneys.

To improve the communication of relevant clinical information the specialists can start a thread, in which they communicate as in a private forum or in a blog.

## V. PUBLIC HEALTH SERVICES FOR THE USERS

One of the most advanced features of the old static web site was the possibility to make some specialist and outpatient appointments using a javascript form. This feature was very appreciated by the patients/clients (especially younger ones), and was decided to maintain and to improve it during the development of the actual web portal.

Thus, the appointment for specialist and private the reservation of specialistic and private medical visits is made possible by compiling the on-line server-side form. The system will then automatically generate and send a message to the hospital appointment office, that will confirm the request of the sender by e-mail.

In Figs. 2 and 3 some details regarding the quantification of the appointments registered until now using the platform are shown.

## VI. CMS AND ADMINISTRATORS' CONTROL PANEL

At the same time of the development of the public web portal and the services described above, a CMS was created for the management of the web pages and of the contents. The CMS, programmed in PHP, has been organized to replicate the web portal menus to facilitate the update process and administration.

It is possible to add or modify some menus of the first level (the horizontal bar) and of the second level (the vertical subjects) From the control panel interface. There is a third level (like all common CMS) to edit the various pages of the portal, and it is possible to edit all the lateral menus.

Adding more control of the functionality of all the databases by easily modifying the source code is even possible; it is possible to add and control other “satellite” sites residing in other directories (i.e. the I.R.C.C.S. “Burlo Garofolo” English web site or the “European School of maternal, neonatal, children, adolescent health”) and so on.

## VII. CONCLUSIONS AND FURTHER DEVELOPMENTS

Future developments pertain to the creation of a feed server system to collect relevant scientific publications from the subscribed e-journals, to the implementation of the new Web 2.0 technologies for the web site home page, in particular through the AJAX client-side programming language, and to the introduction of social networking tools such as personal web pages and dedicated blogs.

## REFERENCES

1. I.R.C.C.S. “Burlo Garofolo's” web portal at <http://www.burlo.trieste.it>
2. Debian at <http://www.debian.org>
3. Apache web server at <http://www.apache.org>
4. MySQL database at <http://www-it.mysql.com>
5. PHP at <http://www.php.net>
6. Phime at <http://www.phime.org>
7. Caniotto Z , Marchetti F, Barbi E, Ventura A (2006) Un bambino di due anni che rifiuta il cibo e vomita. *Medico & Bambino* Vol. 25 n° 5.
8. Isterectomianograzie at <http://www.isterectomianograzie.it>

Author: Michele Bava

Institute: Clinical engineering and medical informatics - I.R.C.C.S. “Burlo Garofolo”

Street: Via dell'Istria 65/1

City: Trieste

Country: Italy

Email: [bava@burlo.trieste.it](mailto:bava@burlo.trieste.it)

# A Neuro-Fuzzy Approach to the Classification of Fetal Cardiotocograms

R. Czabanski<sup>1</sup>, M. Jezewski<sup>1</sup>, J. Wrobel<sup>2</sup>, K. Horoba<sup>2</sup> and J. Jezewski<sup>2</sup>

<sup>1</sup> Institute of Electronics/Silesian University of Technology, Gliwice, Poland

<sup>2</sup> Biomedical Informatics Department/Institute of Medical Technology and Equipment, Zabrze, Poland

*Abstract* — **Cardiotocography (CTG) is a primary biophysical method of fetal monitoring. The assessment of the printed CTG traces is based on the visual analysis of patterns describing the variability of fetal heart rate signal. The correct interpretation of traces from a bedside monitor is rather difficult even for experienced clinicians, so computer-aided fetal monitoring systems have become very popular. At present effective techniques enabling automated conclusion generation based on cardiotocograms are still being searched. The presented work describes an application the Artificial Neural Network Based on Logical Interpretation of fuzzy if-then Rules (ANBLIR) to classification of the fetal state as being normal or abnormal. A set of quantitative parameters describing fetal cardiotocograms is the system input. To evaluate the quality of the classification we proposed the overall validity index as a function of various prognostic indices. The obtained results confirm the usability of the ANBLIR neuro-fuzzy system for records classification within computer-aided fetal surveillance systems.**

*Keywords* — fetal monitoring, signal classification, neuro-fuzzy systems.

## I. INTRODUCTION

Cardiotocography (CTG) is a biophysical method for monitoring of fetal condition during pregnancy and labour. It is based on analysis of fetal heart rate variability and its relationship to fetal movements and uterine contractions. However, visual analysis of printed cardiotocographic traces from a bedside monitor is relatively difficult. Therefore, computerized fetal monitoring systems based on CTG signal acquisition provide quantitative measures describing features of fetal heart rate records. Nevertheless, the interpretation made by clinicians remains still highly subjective and dependent on their individual experience. The repeatable and objective assessment of the fetal state is of particular importance, especially for high risk pregnancy, when thanks to early diagnosis, appropriate management can be carried out. Effective methods for diagnostic support are still an important topic of research. A promising approach seems to be the application of neuro-fuzzy systems. The Artificial Neural Network Based on Logical Interpretation of fuzzy if-then Rules (ANBLIR) is of our special interest.

ANBLIR is a computationally efficient fuzzy system with parameterized consequents based on conjunctive as well as logical interpretation of fuzzy rules. It connects advantages of neural networks (capability of learning and generalization) and fuzzy systems (ability of linguistic interpretation of learning results). ANBLIR was successfully applied to solve many practical problems [5]. In the proposed work, we try to classify the fetal state as being normal or abnormal, basing on quantitative parameters describing fetal cardiotocograms. The data used in our experiments was obtained from the database of the computerized fetal surveillance system MONAKO [6]. We investigated various learning algorithms of ANBLIR based on integration of the steepest descent method, the least squares algorithm, the deterministic annealing procedure and the epsilon-insensitive learning.

## II. RESEARCH MATERIAL

The computerized fetal monitoring system automatically estimates the fetal heart rate baseline, recognizes bradycardia and tachycardia, detects accelerations and decelerations of the fetal heart rate (FHR) signal, identifies uterine contractions as well as measures their detailed parameters [6]. It also evaluates the long- and short-term FHR variability and calculates a set of dedicated indices.

The research database comprised 685 traces (typically 30-60 minutes long) from 189 patients [7]. As input variables we used the set of 21 parameters describing CTG signals in time domain: statistical parameters concerning FHR (4 inputs), long-term variability (8 inputs), short-term variability (5 inputs), frequency measures of decelerations, accelerations, uterine contractions and fetal movements (4 inputs). The output of ANBLIR system was defined as two-state variable defining the so called fetal outcome (normal or abnormal). In obstetrics, it is assumed that validation of the fetal state diagnosed during the course of pregnancy, i.e. when the CTG traces are being recorded, can be made only retrospectively using data describing the newborn state and the history of the labour progress. Such retrospective verification is possible because the fetal state can not rapidly change during pregnancy. There are several attributes related to the fetal outcome. In our experiments we used the

four crucial parameters: neonatal birth weight, five minute Apgar score (visually assessed), umbilical artery pH and umbilical artery base excess (BE). Fetal outcome was defined as abnormal if at least the value of one attribute was outside the defined physiological range. According to our assumptions 251 records were classified as corresponding to abnormal fetal outcome.

### III. ANBLIR NEURO-FUZZY SYSTEM

The ANBLIR is a neuro-fuzzy system with parameterized consequents that generates inference results based on fuzzy if-then rules. Fuzzy sets of the antecedents have Gaussian membership function and the explicit connective “and” of predicates is represented by algebraic product  $t$ -norm. According to the assumptions made, the firing strength of the  $i$ -th rule is defined as [5]:

$$\forall_{i=1,2,\dots,I} F^{(i)} = \exp \left[ - \sum_{j=1}^t \frac{(x_{0j} - c_j^{(i)})^2}{2(s_j^{(i)})^2} \right], \quad (1)$$

where  $I$  is the number of rules,  $t$  is the number of system inputs,  $x_{0j}$  is the  $j$ -th element of the input vector  $\mathbf{x}_0 = [x_{01}, x_{02}, \dots, x_{0t}]^T$ ,  $c_j^{(i)}$  is the center of Gaussian membership function and  $s_j^{(i)}$  is its dispersion. Consequents of ANBLIR fuzzy rules have symmetric triangular membership functions. The triangle is defined with the set of two parameters: width of the triangle base  $w^{(i)}$  and center of gravity location  $y^{(i)}$  determined by linear combinations of fuzzy system inputs:

$$y^{(i)} = p_0^{(i)} + p_1^{(i)}x_{01} + \dots + p_t^{(i)}x_{0t} = \mathbf{p}^{(i)T} \mathbf{x}'_0, \quad (2)$$

where  $\mathbf{x}'_0 = [1, \mathbf{x}_0]^T$  is the extended input vector. The above dependency formulates so called parameterized (moving) consequent [5]. The neuro-fuzzy system with parameterized consequents allows both conjunctive and logical interpretations of fuzzy if-then rules [5]. In the next considerations we assume the conjunctive interpretation of fuzzy conditional statements using Mamdani’s fuzzy relation. Let us also assume a normalized arithmetic mean as an aggregation operator and modified indexed center of gravity [5] as a defuzzifier. Then, we can write the final crisp output value of the ANBLIR system in the following form:

$$y_0 = \frac{\sum_{i=1}^I w^{(i)} F^{(i)} (2 - F^{(i)})}{\sum_{j=1}^I w^{(j)} F^{(j)} (2 - F^{(j)})} y^{(i)} = \sum_{i=1}^I G^{(i)} y^{(i)}. \quad (3)$$

The unknown neuro-fuzzy system parameters (parameters of membership functions of fuzzy sets within if-then rules) can be estimated using learning algorithms of artificial neural networks. Several solutions of the ANBLIR learning problem were introduced in literature [5], [8], [2]-[4]. In this work, we investigate various learning algorithms of ANBLIR based on integration of the steepest descent method [5], the least squares algorithm [5], the deterministic annealing procedure [2] and the epsilon-insensitive learning [8], [3], [4].

For next considerations let us assume that we have  $N$  examples of the input vectors  $\mathbf{x}_0(n) \in \mathcal{X}'$  (quantitative description of the CTG records) and the same number of known output values  $t_0(n) \in \mathcal{Y}$  (fetal outcome) which formulate the training set.

The learning goal is the estimation of membership function parameters of antecedents as well as consequents  $\zeta = \{c_j^{(i)}, s_j^{(i)}, p_j^{(i)}, w^{(i)}\}$ . The number of rules  $I$  is also unknown. We assume that it is pre-set arbitrarily. The number of antecedents  $t$  is given directly by the size of the input training vector.

The original learning algorithm of ANBLIR combines the steepest descent and the least square methods [5]. To increase the ability to avoid many local minima that traps steepest descent algorithm, the deterministic annealing (DA) procedure [9] adapted for the purposes of learning the neuro-fuzzy system with parameterized consequents was employed [2]. The equation (3) defines the ANBLIR as a linear combination of  $I$  outputs  $y^{(i)}(\mathbf{x}_0)$  of local models, each represented by a single fuzzy rule. The randomness of the association between data samples and local models may be measured by Shannon entropy  $S$ . In the DA method the objective is the minimization of the squared-error cost  $E$  while simultaneously controlling the entropy level of a solution. The deterministic annealing optimization problem may be formulated as a minimization process of the Lagrangian  $L = E - TS$ , where  $T$  is the Lagrange multiplier.

The relation between the equation presented above and the annealing of solids leads to the interpretation of the quantity  $L$  as the Helmholtz free energy of physical system with energy  $E$ , entropy  $S$  and temperature  $T$  [9].

The DA algorithm involves a series of iterations while the entropy level is reduced gradually. The minimization of the Lagrangian is performed using a simulated annealing method framework. The algorithm starts at a high level of temperature  $T$  and tracks the solution for lowered values of  $T$ . The temperature parameter is reduced according to the so called annealing schedule function  $T \leftarrow qT$ , where  $q \in (0,1)$  is a pre-set parameter. At each level of temperature the Lagrangian is minimized using the steepest descent method.



In original ANBLIR learning method parameters of consequents  $\mathbf{p}^{(i)}$  were estimated using the least square (LS) method [5]. This solution speeds up the learning convergence. A novel method for estimating parameters of linear equations in rules consequents, so called  $\varepsilon$ -insensitive learning, was presented in [8]. The  $\varepsilon$ -insensitive learning improves the generalization ability of the ANBLIR in comparison to the LS algorithm [8], [3], [4]. The  $\varepsilon$  symbol represents the limiting value of tolerance to the imprecision. If the error value is less than  $\varepsilon$ , then the zero loss is obtained. Several approaches to solve the  $\varepsilon$ -insensitive learning problem were proposed in [8]. The  $\varepsilon$ -insensitive Learning by Solving a System of Linear Inequalities ( $\varepsilon$ LSSLI) is of our special interest due to its lowest computational complexity.

Integration of different optimization methods leads to the several variation of the learning algorithms of ANBLIR system. The parameters of fuzzy sets from antecedents and consequents of fuzzy rules can be adjusted separately: (i) premise parameters  $c_j^{(i)}$ ,  $s_j^{(i)}$  as well as triangle base widths  $w^{(i)}$  of fuzzy sets in consequents by means of the steepest descent or the deterministic annealing method, (ii) parameters of linear equations from consequents  $\mathbf{p}^{(i)}$  on the basis of the least squares procedure or the  $\varepsilon$ -insensitive learning.

For decreasing the computational time of the learning procedure the deterministic annealing method with "freezing" phase (DAF) may be also applied [3]. The "freezing" phase consists of the calculation of  $\mathbf{p}^{(i)}$  using  $\varepsilon$ LSSLI procedure after every decreasing step of temperature value while keeping  $c_j^{(i)}$ ,  $s_j^{(i)}$  and  $w^{(i)}$  constant. This solution leads to decrease of computational time of the DA based methods.

Another problem is the estimation of initial values of membership functions for antecedents. It may be solved by means of preliminary clustering of the input training data [5]. We used the fuzzy c-means (FCM) [1] for this task.

#### IV. CARDIOTOCOGRAMS CLASSIFICATION

We used five hybrid learning algorithms of the ANBLIR system: (i) the original training procedure which connects the steepest descent and the least squares methods (SDLS), (ii) a learning method that combines the deterministic annealing with the least squares algorithm (DALs) and (iii) its modified version, with the "freezing" phase (DAFLS), (iv) a hybrid method that integrates the deterministic annealing with the epsilon insensitive learning ( $\varepsilon$ DA) and (v) also its modification with the "freezing" phase ( $\varepsilon$ DAF). To assess the quality of the classification we used a set of prognostic

indices: Sensitivity ( $SE$ ), Specificity ( $SP$ ), Positive Predictive Value ( $PPV$ ) and Negative Predictive Value ( $NPV$ ). To make a comparison of the classification algorithms easier we calculated an overall index  $OI$  defined as  $OI = (2SE + NPV)(SP + PPV) / 60000$ . The influence of the sensitivity index on the  $OI$  value is doubled. It is due the fact that in clinical practice the false negative recognition of wellbeing may lead to the most serious consequents.

All experiments were conducted in the MATLAB7.0<sup>®</sup> environment. The learning process was carried out for the number of if-then rules changed from 2 to 10. The initial values of parameters of antecedents were calculated on the basis of FCM clustering results obtained for  $m = 2$ . The partition process was stopped if the maximum number of 500 iterations was achieved or when in sequential iterations the change of the criterion function was less than  $10^{-5}$ . The clustering procedure was repeated 25 times for different random realizations of the initial partition matrix. The results characterized by the minimal value of Xie-Beni validity index were chosen. For the deterministic annealing procedure the following parameters' values were applied: the initial step size  $\eta_{ini} = 0.01$ , the maximum number of iteration at given level of temperature  $k_{max} = 10$ ,  $T_{min} = 10^{-5}T_{max}$  and  $q = 0.95$ . There is no method for automatic estimation of initial temperature  $T_{max}$  for the deterministic annealing algorithm, so we changed its value in the range from  $10^{+5}$  to  $10^{-5}$  with step 0.1. For the epsilon insensitive learning we set: the initial value of the margin vector elements  $\mathbf{b}^{[1]} = 10^{-6}$  and the rate of the margin vector change  $\rho = 0.98$ . The  $\varepsilon$ LSSLI algorithm was stopped if  $\|\mathbf{b}^{[k+1]} - \mathbf{b}^{[k]}\| < 10^{-4}$ , or if the maximal number of iterations  $k_{max} = 1000$  was achieved. We changed values of the limiting tolerance to imprecision  $\varepsilon$  and the regularization parameter  $\tau$  from 0.01 to 0.1 with step 0.01. The algorithms were tested using 50 trials, with randomly mixed data contents in learning, validating and testing subsets. For all algorithms used, the best classification quality was obtained for the minimal number of if-then rules. The detailed results are shown in Table 1.

The best learning result  $OI = 0.64$  was obtained for DAFLS procedure, but also for  $\varepsilon$ DA and  $\varepsilon$ DAF we got almost the same quality of classification. For comparison,

Table 1 Values of the prognostic index  $OI$  for different learning procedures of the ANBLIR system

Learning procedure	Mean	SD	Max	Min
SDLS	0.60	0.03	0.69	0.54
DALS	0.63	0.03	0.72	0.55
DAFLS	0.64	0.03	0.71	0.57
$\varepsilon$ DA	0.64	0.04	0.71	0.54
$\varepsilon$ DAF	0.64	0.04	0.72	0.55

Table 2 Mean values of  $OI$  for different number of fuzzy rules  $I$ 

$I$	SDLS	DALS	DAFLS	$\epsilon$ DA	$\epsilon$ DAF
2	0.60	0.63	0.64	0.64	0.64
4	0.58	0.61	0.60	0.62	0.60
6	0.55	0.58	0.58	0.60	0.59
8	0.53	0.55	0.55	0.58	0.57
10	0.48	0.50	0.50	0.55	0.54

with the RBF neural network architecture presented in [7] we got  $OI = 0.57$ . The classification error for testing data decreased with increase of the number of fuzzy if-then rules. It is due to the overfitting effect of the training set. The  $OI$  values obtained for different number of rules are shown in Table 2.

Clearly, the learning procedure of ANBLIR based on  $\epsilon$ -insensitive learning demonstrates consistent improvement in generalization ability and the same a decrease of the classification error. Generally, the best quality of classification is achieved when  $\epsilon$ DA is employed. However, it should be noted, that the computational complexity of the  $\epsilon$ LSSL algorithm is approximately 3 times greater comparing to the LS method [8]. Also, the computational complexity of deterministic annealing method is approximately doubled in comparison to original ANBLIR learning algorithm. The most sensible compromise seems to be the application of the method which combines the deterministic annealing algorithm with „freezing” phase and  $\epsilon$ -insensitive learning. The  $\epsilon$ DAF algorithm leads to high quality of classification and provides learning results in reasonable time.

The most serious disadvantage of the deterministic annealing and  $\epsilon$ -insensitive learning based method is the necessity of the arbitrary selection of the learning parameters. As there is no automatic method for the selection of the learning parameters, the best method still remains the trial-and-error procedure.

## V. CONCLUSIONS

In the presented work, we investigated the ability of application of Artificial Neural Network Based on Logical Interpretation of fuzzy if-then Rules to classification of the fetal state based on evaluation of quantitative parameters describing fetal cardiotocograms. Five different learning algorithms of the neuro-fuzzy system, combining: the steepest descent method, least squares algorithm, deterministic annealing procedure and epsilon-insensitive learning were considered. The experiments show the usefulness of the neuro-fuzzy modeling with the ANBLIR system within computer-aided fetal surveillance systems and indicates the

learning procedure which integrates the deterministic annealing algorithm with „freezing” phase and  $\epsilon$ -insensitive learning as the most reasonable compromise between classification quality and the computational complexity. Also other deterministic annealing based learning methods led to satisfying results. However, the performance enhancement is achieved through an increase of the computational complexity of the learning procedures. Another problem is lack of the automatic method for the selection of learning parameters. Therefore, the optimal algorithm specification must be obtained through the trial-and-error procedure.

## ACKNOWLEDGMENT

This work was supported in part by the Ministry of Sciences and Higher Education resources in 2007-2009 under Research Project R1302802.

## REFERENCES

1. Bezdek J C (1981) Pattern recognition with fuzzy objective function algorithms. Plenum, New York
2. Czabanski R (2005) Neuro-fuzzy modeling based in a deterministic annealing approach. Int. J. Appl. Math. Comput. Sci. 15(4):561-576
3. Czabanski R (2006) Deterministic annealing integrated with  $\epsilon$ -insensitive learning in neuro-fuzzy systems. Proc. Of 8th Int. Con. ICAISC, Zakopane 2006:220-229
4. Czabanski R (2006) Extraction of fuzzy rules using deterministic annealing integrated with  $\epsilon$ -insensitive learning. Int. J. Appl. Math. Comput. Sci. 16(3):35-372
5. Czogała E, Leski J (1999) Fuzzy and neuro-fuzzy intelligent systems. Heidelberg: Physica-Verlag
6. Jezewski J, Wrobel J, Horoba K, Kupka T, Matonia A (2006) Centralized fetal monitoring system with hardware-based data flow control. Proc. Of III Int. Conf. MEDSIP, Glasgow 2006:51-54
7. Jezewski J, Wrobel J, Labaj P, Leski J, Henzel N, Horoba K, Jezewski J (2007) Some practical remarks on neural networks approach to fetal cardiotocograms classification. Proc. Of 29th Ann. Int. Conference of the IEEE/EMBS, Lyon 2007:5170-5173
8. Leski J (2003) Insensitive Learning Techniques for Approximate Reasoning Systems (Invited Paper). Int. J. of Computational Cognition 1:21-77
9. Rose K (1998) Deterministic annealing for clustering, compression, classification, regression and related optimization problems. Proc. IEEE 11:2210-2239

Author: Czabanski Robert  
 Institute: Silesian University of Technology, Institute of Electronics  
 Street: Akademicka 16  
 City: 44-100 Gliwice  
 Country: Poland  
 Email: robert.czabanski@polsl.pl

# Visions in Modeling of Cardiac Arrhythmogenic Diseases and their Therapies

O. Dössel, G. Seemann, D. Farina, D.U.J. Keller, R. Miri, F.M. Weber, D.L. Weiss

Institute of Biomedical Engineering, University of Karlsruhe, Karlsruhe, Germany

**Abstract** — After mathematical modeling of the healthy heart now modeling of diseases comes into the focus of research. Modeling of arrhythmias already shows a large degree of realism. This offers the chance of more detailed diagnosis and computer assisted therapy planning. Options for genetic diseases (channelopathies like Long-QT-syndrome), infarction and infarction-induced ventricular fibrillation, atrial fibrillation (AF) and cardiac resynchronization therapy are demonstrated.

**Keywords** — mathematical modeling of the heart, arrhythmias, channelopathies, atrial fibrillation, infarction, cardiac resynchronization therapy.

## I. INTRODUCTION

Computer models of the heart become more and more detailed and are able to describe healthy hearts very realistically [1,2,3,4]. Electrophysiology of individual cells can be described using mathematical models adapted to various cell types (endocardial, mid-myocardial, epicardial, atrial cells etc.). The bidomain model combines the cells to cell patches and even to the whole organ, but the simulations require long calculation times. Simplified models like e.g. monodomain models or cellular automata can deliver simulation results faster but with a reduced degree of accuracy. Forward calculations leading from the electrophysiological sources in the heart to the electric potential distributions on the surface of the body are carried out using techniques of numerical field calculation (e.g. Finite Difference or Finite Element Method) and deliver simulated Body Surface Potential Maps (BSPM) and in particular the Electrocardiogram (ECG) [5].

The next challenge is the modeling of various diseases of the heart. This paper will focus on arrhythmias. Modeling of genetic diseases (channelopathies like Long-QT- or Short-QT-syndrome) [6,7,8], infarction and infarction-induced ventricular fibrillation [9,10,11,12], atrial fibrillation (AF) [13,14,15,16] and cardiac resynchronization therapy [17] will be presented.

Modeling of arrhythmias can contribute in various ways to cardiology. The simulations can reveal the origin of arrhythmias (etiology), like the arrhythmogenic changes of the substrate, the potential triggers of fibrillation and the reasons for perpetuation. Computer models can demon-

strate, which kind of pathological processes can be discovered based on ECG and BSPM data and what kind of spatio-temporal patterns in the BSPM are characteristic for a disease, e.g. during AF or after infarction. It will be possible to check the consistency of a hypothesis about a disease with the measured data of a patient. Computer models can serve to improve regularization techniques to solve the inverse problem of ECG. They can finally assist cardiologists in optimizing therapeutical measures. RF-ablation strategies can be improved, delays during biventricular pacing (cardiac resynchronization therapy) can be adjusted, and pharmaceutical therapies that modify parameters of ion-channels can be optimized.

## II. ELECTROPHYSIOLOGICAL COMPUTER MODELS OF THE HEART

### A. Cellular Models

In recent years various mathematical models of electrophysiology of atrial and ventricular cells have been published [18,19,20]. Models for various different tissue classes of the heart are available like e.g. sinus node, terminal crest and pectinate muscle in the atria [21] and endo-, mid-, and epicardial cells in the ventricles [22]. They can describe the electrophysiological behavior properly even in unphysiological situations like e.g. tachycardia or hyperkalemia. The cell models are extended continuously as soon as new data on specific ion-channels are available from patch-clamp laboratories.

### B. Models of Tissue Patches

The electrophysiological behavior of patches of myocardial cells can be modeled mathematically using different approaches. The most extended model leading to the best results is the bidomain model [1, 2, 3, 4]. It takes into account all individual ion-channels and it employs two field equations for every time step: one for the intracellular domain and one for the extracellular domain. It considers different conductivity tensors for both domains, which is assumed to be essential for realistic description of cardiac tissue.

The monodomain model is a linear transformation of the field equations for the case that the intracellular and extra-

cellular conductivity tensors deviate only by a scalar factor. Now only one field equation has to be solved per time step leading to a significant reduction in calculation time.

The next possible simplification in order to speed up calculation times is the employment of simplified cell models like FitzHugh-Nagumo [23] or Fenton-Karma [24]. Not all individual ion-channels are taken into account, but only a few "symbolic" channels mixed together in order to just reproduce the action potential.

Finally cellular automaton models offer a very fast modeling of one heart beat in a few minutes [25]. The cellular automaton is using predefined action potentials and depolarization velocities. The predefined values can be calculated beforehand using specific cell models for the specific situation of the heart that is supposed to be investigated. They can thus deliver a reasonably good approximation of the real situation quite often but have to be employed with special care.

C. Modeling of Atria and Ventricles

For modeling complete atria or ventricles detailed geometrical knowledge about the patients heart is a prerequisite. General studies can be carried out using the Visible Man or Visible Female dataset. For a patient specific analysis 3D Magnetic Resonance or Computed Tomography data have to be acquired and segmented. Fiber direction can be included using simple or extended rules. Also the conduction system can be implemented using basic rules e.g. about the location of the AV-node and the tree of Purkinje fibers. A critical question is whether the temporal dynamics of the heart have to be taken into account explicitly. This would mean that 4D images have to be acquired for every patient, which is possible but very time consuming.

Computational load is obviously rising dramatically with the number of active nodes in the mesh. Parallel computing on a very large number of processors can be a solution to this problem.

III. MODELING OF DISEASES

A. Modeling of Channelopathias

A large community of research groups is focusing on the discovery and understanding of genetic diseases where single ion-channels playing a major role in cardiac electrophysiology are altered. Loss or gain of function may happen. This large interest is motivated by the fact, that in this example a clear chain can be outlined from genes to proteins, to cells, to tissue, to organ and to the behavior of the whole body. The various classes of Long-QT and Short-QT

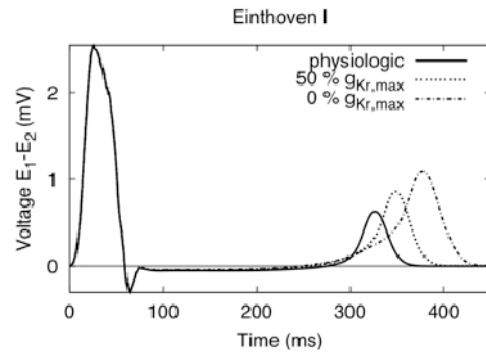


Fig. 1 ECG of the Visible Man with Long-QT 2 syndrome. The conductivity of the rapid potassium channel  $K_r$  was reduced by 50% or switched off.

syndrome can already be described quite well on cellular level. In some examples even the complete way from genes to ECG was calculated and the findings were consistent with measurements on patients [5].

Figure 1 shows the forward calculation resulting in an ECG of the Visible Man with Long-QT-2 syndrome [26].

B. Modeling of Infarction

Since myocardial infarction is one of the most important causes of death in industrialized countries the mathematical modeling of this disease also attracts a large community. In this article the focus is on the electrophysiological consequences. In case the patient has survived the first infarction a life threatening ventricular fibrillation may happen. Until now only simplified models of infarcted areas have been modeled to understand better the elevation (or depression) of the ST segment [10, 27].

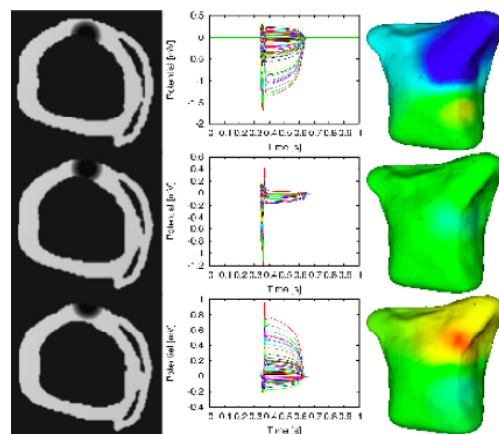


Fig. 2 Computer model of an infarction that was positioned into the heart of the patient to study the corresponding BSPM. Both ST segment elevation and depression can be observed.

Also attempts are made to find the exact location and extent of an infarction based on BSPM [9,10,12] (see 2007 Challenge of Computers in Cardiology). Basic understanding of the phenomena was achieved but many open questions remain.

Figure 2 shows the location of an infarction in the heart of a patient that was positioned by hand to study the corresponding BSPM. A cellular automaton was employed. The ST segment was elevated in the precordial leads as expected.

### C. Modeling of Atrial Fibrillation

Understanding of triggering and perpetuation of atrial fibrillation (AF) was significantly supported by computer modeling. It was shown, that only two ectopic beats - at the wrong location and time - can trigger sustained AF. A continuous change from atrial flutter to atrial fibrillation was observed. "Rotors" and "snakes", very similar to the patterns observed with catheter measurements, were also detected in computer models - sometimes even simultaneously [13].

## IV. MODELING THERAPEUTIC OPTIONS

### A. Modeling Ablation of Atrial Fibrillation

Millions of elderly people suffer from atrial fibrillation (AF). Often drugs are the therapy of choice but sometimes side effects are so severe, that ablation is envisaged. Success rate of AF ablation is only around 60%. A personalized planning of ablation could be the solution.

In a computer model of the heart various ablation lines can be defined using a user interface to mark points in a visualization of the patients left atrium [28,29,30]. First it can be tested whether an ongoing AF can be terminated. By testing with typical ectopic beats, e.g. in the pulmonaries, it can be observed whether the heart is now resistant against these triggers of AF. This way the success of an ablation strategy can be estimated beforehand.

Figure 3 shows the ablation strategy of Benussi [31] in a computer model of AF [32].

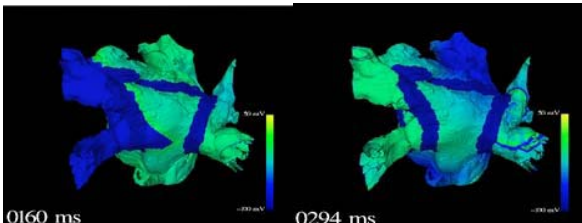


Fig. 3 AF Ablation strategy of Benussi et al. in a computer model [31].

### B. Modeling of Cardiac Resynchronization Therapy

Patients suffering from cardiomyopathy in conjunction with left bundle branch block (LBBB) can profit from a pacemaker with two electrodes. The timing and location of the stimulus of the two electrodes is optimized to achieve a better synchrony of the contraction of the two ventricles. Unfortunately many non-responders are observed that do not have any profit from the therapy. Patient specific optimization using computer models may lead to a higher success rate.

In principle the stroke volume of the heart has to be maximized [33]. Since modeling of the contraction of the heart is not as mature as needed yet, the optimization of the spread of depolarization may also help. Location and timing is optimized until the depolarization of the patient's heart resembles the physiological case as good as possible [17].

Figure 4 shows a depolarization pattern of a patient with cardiomyopathy and AV block with optimized pacing.

## V. CONCLUSIONS

Computer models of the heart contributed significantly to better understanding of physiology ("mathematical physiology"). Extending their scope to diseases the basic understanding of various pathologies is also improved significantly. First attempts are tried out today to adapt computer models of the diseased heart to individual patients. For the first time computer models of the heart can improve the in-depth diagnosis of a patient and contribute to an optimization of therapy. Thus they become an essential part of future software packages that assist the medical doctor in specific diagnosis and individualized therapy planning.

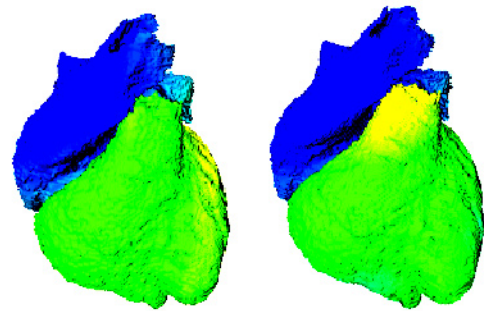


Fig. 4 Cardiac Resynchronization Therapy. Left: Physiological depolarization isochrones, right: depolarization with AV block and two optimized stimuli from a biventricular device [32].

## ACKNOWLEDGMENT

Matthias Reumann contributed significantly to the success of the research at the Institute of Biomedical Engineering. Frank Weber is supported by Philips Research Europe and Dima Farina is supported by Biosense Webster.

## REFERENCES

- Pullan A J, Buist M L, Cheng L K (2005) Mathematically modeling the electrical activity of the heart. From cell to body surface and back again. World Scientific Publishing, ISBN 981-256-373-3
- Sundnes J, Lines G T, Cai X et al. (2006) Computing the electrical activity in the heart. In Monographs in computational science and engineering 1. Ed. Barth T J, Griebel M. et al. Springer, ISBN 978-3-549-33432-3
- Computational Biology of the Heart*, Edited by Panfilov A V and Holden A V, 345, John Wiley & Sons, Chichester, 1997.
- Noble D (2002) Modeling the Heart: From genes to cell's to the whole organ. *Science* 295: 1678-1682
- Weiss D, Modeling of Heterogeneous Electrophysiology in the Human Heart with Respect to ECG Genesis. Proc. vol. 34, Computer in Cardiology, Durham, USA, 2007, pp 49-52
- Antzelevitch C, Oliva A (2006) Amplification of spatial dispersion of repolarization underlies sudden cardiac death associated with catecholaminergic polymorphic VT, long QT, short QT and Brugada syndromes. *J Intern Med* 259:48-58
- Seemann G, Sachse F B, Weiss D L et al. (2007) Modeling of IK1 mutations in human left ventricular myocytes and tissue. *Am J Physiol Heart Circ Physiol* 292(1):H549-H559
- Weiß D L, Seemann G, Sachse F B, Dössel O (2005) Modeling of the short QT syndrome in a heterogeneous model of the human ventricular wall. *Europace*, vol. 7, suppl 2: pp 105-117
- Li G, and He B. (2004) Non-invasive estimation of myocardial infarction by means of a heart-model based imaging approach: a simulation study. *Med Biol Eng Comput* 42(1):128-136
- Farina D and Dössel O (2007) Model-based approach to the localization of infarction. Proc. vol. 34, Comp. in Cardiol. Durham, USA, 2007, pp 173-176
- MacLeod R S, Shome S, Stinstra J et al. (2005) Mechanisms of ischemia-induced ST-segment changes. *J Electrocardiol* 38 (suppl. 4):8-13
- MacLachlan M C, Sundnes J, Lines G T (2005) Simulation of ST segment changes during subendocardial ischemia using a realistic 3-D cardiac geometry. *IEEE Trans. Biomed. Eng* 52:799-807
- Reumann M, Bohnert J, Osswald B et al. (2007) Multiple wavelets, rotors and snakes in atrial fibrillation – a computer simulation study. *J Electrocardiol* 40:328-334
- Vigmond E J, Ruckdeschel R, Trayanova N (2001) Reentry in a Morphologically Realistic Atrial Model. *J Cardiovasc Electrophysiol* 12:1046-1054
- Cherry E M, Xie F, Feliciano Z et al. (2001) Computer modeling of atrial fibrillation. *Cardiac Electrophysiology Review* 5:271-276
- Jacquemet V, Virag N, Kappenberger L (2005) Wavelength and vulnerability to atrial fibrillation: Insights from a computer model of human atria. *Europace*, vol. 7, (suppl 2):83-92
- Reumann M, Farina D, Miri R et al. (2007) Computer model for the optimization of AV and VV delay in cardiac resynchronization therapy. *Med Bio Eng Comput* 45:845-854
- Priebe L, Beuckelmann D J (1998) Simulation study of cellular electric properties in heart failure, *Circ Res* 82:1206-1223
- Tusscher ten K H W J, Noble D, Noble P J et al. (2004) A model for human ventricular tissue. *Am J Physiol* 286:H1573-H1598
- Courtemanche M, Ramirez R J and Nattel S (1998) Ionic mechanisms underlying human atrial action potential properties: Insights from a mathematical model. *Am J Physiol* 275(44):H301-H321
- Seemann G, Höper C, Sachse F B et al. (2006) Heterogeneous three-dimensional anatomical and electrophysiological model of human atria. *Phil Trans Roy Soc A* 364:1465-1481
- Seemann G, Sachse F B, Weiss D L et al. (2003) Quantitative reconstruction of cardiac electromechanics in human myocardium: regional heterogeneity. *J Cardiovasc Electrophysiol* 14:219-228
- FitzHugh R A (1961) Impulses and physiological states in theoretical models of nerve membrane. *Biophysical Journal* 1:445
- Fenton F, Karma A (1998) Vortex dynamics in three-dimensional continuous myocardium with fiber rotation: Filament instability and fibrillation. *Chaos* 8:20
- Werner C D, Sachse F B, Dössel O (2000) Electrical excitation propagation in the human heart. *International Journal of Bioelectromagnetism* 2(2)
- Keller D U J, Seemann G, Weiss DL et al. (2007) Computer based modeling of the congenital long-QT syndrome in the Visible Man torso: From genes to ECG. Proc. IEEE EMBC pp 1410-1413
- Van Oosterom A, Oostendorp T, ECGSim, www.ecgsim.com
- Reumann M, Bohnert J, Seemann G et al. (2007) Preventive ablation strategies in a biophysical model of atrial fibrillation based on realistic anatomical data. *IEEE Trans Biomed Eng In Press*
- Dang L, Virag N, Ihara Z et al. (2005) Evaluation of Ablation Patterns Using a Biophysical Model of Atrial Fibrillation. *Ann Biomed Eng* 33:465-474
- Rotter M, Dang L, Jacquemet V et al. (2007) Impact of varying ablation patterns in a simulation model of persistent atrial fibrillation. *Pacing Clin Electrophysiol* 30:314-321
- Benussi S, Pappone C, Nascimbene S et al. (2000) A simple way to treat chronic atrial fibrillation during mitral valve surgery: the epicardial radiofrequency approach. *Eur J Cardiothorac Surg* 17:527-529
- Reumann, M (2007) Computer assisted optimisation of non-pharmacological treatment of congestive heart failure and supraventricular arrhythmia. Karlsruhe Transactions on Biomedical Engineering, vol. 2, ISBN 978-3-86644-122-4
- Sermesant M, Delingette H, Ayache N (2006) An electromechanical model of the heart for image analysis and simulation. *IEEE Trans Med Imaging* 25:612-625

Author: Olaf Doessel  
 Institute: Institute of Biomedical Engineering, University of Karlsruhe  
 Street: Kaiserstr. 12  
 City: 76131 Karlsruhe  
 Country: Germany  
 Email: od@ibt.uni-karlsruhe.de

# Home Health Monitoring

Á. Jobbágy<sup>1</sup>, P. Csordás<sup>1</sup>, A. Mersich<sup>1</sup>, R. Magjarević<sup>2</sup>, I. Lacković<sup>2</sup>, J. Miheľ<sup>2</sup>

<sup>1</sup> Budapest University of Technology and Economics/Measurement and Information Systems, Budapest, Hungary

<sup>2</sup> University of Zagreb /Faculty of Electrical Engineering and Computing, Zagreb, Croatia

*Abstract* — Home health monitoring can help the national health care become more effective, cheaper for the society and guarantee better quality of life for individuals. Especially those living alone can get a user-friendly supervision. For elderly patients this technique guarantees a regular medical check including alerting of relevant health care service and/or in case of need, informing their relatives living apart. The aim of medical diagnostics is to obtain specific and sensitive diagnostic results at the earliest possible stage of illness with a minimally invasive procedure for the patient. This is often related to preventive diagnostic procedures performed at home, especially in the part of population at health risk, such as elderly people or children. Though many devices have been developed recently for home monitoring, there is still a need for development of specialized devices covering specific physiological parameters, as well as for improvement of performance of devices present at the market. In this paper, we focus on high blood pressure and pulmonary pathologies, which are both symptoms common among population with chronic diseases. Therefore, there is a need for continuous research of new and better measurement methods and development of intelligent instrumentation for home health monitoring of physiological parameters related to these symptoms. Our development includes non-invasive blood-pressure and respiration instrumentation for home health monitoring. Measuring blood-pressure is of vital importance in home health monitoring. The majority of blood-pressure meters available for home use on the market apply the oscillometric method. The accuracy of these devices is limited, especially when applied to patients with cardiovascular diseases. The method we developed assures better accuracy and even warns the tested persons if they are not in the resting status necessary for the measurement. The system for respiratory sound analysis we developed is based on Fast Fourier Transform computation and a robust algorithm for wheeze detection in the sound spectra. This system is intended for long-term monitoring and early stage assessment of asthma episodes, especially in children.

*Keywords* — home health monitoring, blood pressure, respiratory sounds

## I. INTRODUCTION

As the expected lifetime increases the problem of sustaining the good health of the society needs to be addressed. World life expectancy more than doubled over the past two centuries, from roughly 25 years to about 65 for men and 70

for women. It is estimated that life expectancy further increases. National health care systems should be accommodated; the prevalence rates of many diseases substantially change over age. In Japan, where the expected life time is longer than in other developed countries (78 year for men and 85 for women in 2002), sustaining of good health is promoted by home health monitoring [1]. The average medical expenditure per person is significantly higher for the elderly than for younger people. In Japan the increase in national medical expenditure by far exceeded the increase in GDP in the last decade of the XXth century. Home health monitoring accounts for an increasing share in Japan's medical expenditure. It is estimated that in the United States 20 – 30 % of patients receive inappropriate care [2]. Many diseases can be treated more effectively and at a lower cost if early signs are detected. The continuous monitoring requires appropriate instrumentation, including sensors and signal processing. However, the monitored person gets a better care only if the processed patient data are seen by medical experts in time.

In Hungary cardiovascular diseases are the leading cause of death, being responsible for about half of the deaths [3]. Furthermore, hypertension affects a high percentage of the population. It is estimated that 30 % of the Hungarian population has hypertension, over age 65 this ratio increases to approximately 65 %. Diagnosis in the early stage would make it possible to start medication and treatment to prevent the deterioration of the patients. The presently existing blood pressure meters either require trained operator or do not assure accurate measurement [4]. An easy-to-use and accurate device would help in early detection and home self-monitoring. This latter would mean an effective aid for the general practitioner to monitor the patient; giving a feedback for treatment and medication. Good solutions exist to transmit medical recordings of the patient to the doctor. Home telecare improves care and reduces cost [5]. Further advantage of such systems is that the medical expert and the patient do not have to be at the same place. A wearable device is described in [6] that permanently monitors physiological parameters.

Monitoring of respiratory sounds gives information on the condition of the airways. Wheezes are superimposed on normal respiratory sounds. Analysis of wheeze helps assess the actual state of a patient with airway disease.

## II. BLOOD-PRESSURE MONITORING

### A. Device for home use

Hypertension is called the “silent killer”, as it causes no easily detectable primer symptoms. When the secondary symptoms appear and the patient visits the doctor, organs might be severely and incurably damaged. Regular check-up of the population would be necessary. Devices applicable for self measurement [7] and providing the necessary accuracy would help involve people to care for their own health. Self measurement is advantageous also for patients already diagnosed to have hypertension. The majority of present day (semi)automatic blood pressure meters offered for home use apply the oscillometric technique. This method detects the mean pressure in the artery (MAP) and calculates only an estimate of the systolic and of the diastolic pressure. British and American standards for home blood pressure meters allow substantial deviation between the displayed values and the results measured by a trained operator manually [8], [9] [10]. Self blood pressure measurement might be complementary to 24-hour ambulatory blood pressure monitoring (ABPM). Usually oscillometric blood pressure meters give correct results for those with normal values and may give erroneous results for those with cardiovascular diseases. Furthermore, the state of the arteries can also be assessed during the measurement. This parameter is usually more important than the systolic and diastolic pressures. For the widespread application a device (HHM) has been developed. It can be used by persons at home without the aid of medical experts [11].

The results of daily measurements are stored in the device for two months so that the general practitioner gets detailed and objective information about the patient’s state between visits. Should the device detect an emergency situation or should the trend of the daily measurements show a possible deterioration of the patient’s state, the device is able to transmit a request for attention via mobile phone.

### B. Occlusion by the cuff influences the measurand

The inflation of the cuff has an effect on the circulatory system. The effect is individual. The arterial pressure in the radial artery was measured with a COLIN CBM7000 tonometer in parallel with slow inflation and deflation of the cuff around the upper arm. Results are shown for a senior (Fig. 1. a)) and a young (Fig. 1. b)) healthy subject.

The effect of the occlusion is rather different. The classical oscillometric method would result in a good estimate for the senior, and a distorted one for the young subject. For the young subject, at the time the cuff pressure is equal to the

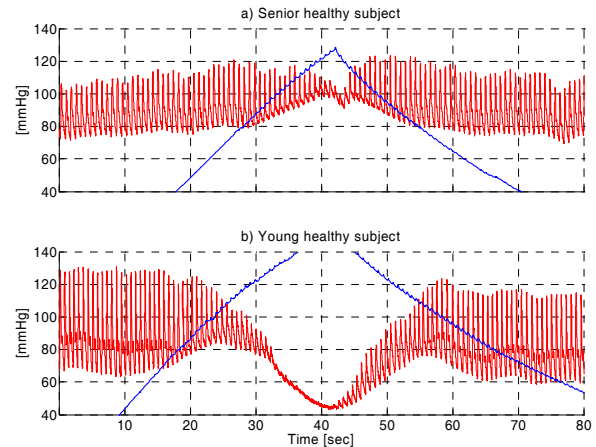


Fig. 1. Upper arm cuff (blue) and radial tonometer (red) pressure.

supposed systolic pressure, the actual pressure in the brachial artery is substantially smaller. This causes an error even if the pressure in the brachial artery at the beginning of cuff deflation differs from the one in the radial artery. Measuring during slow inflation gives better estimates.

### C. Improved oscillometric method

The oscillometric method is based on the assumption, that the tension of the vessel’s wall is minimal, if the transmural pressure ( $P_{tr}$ , the difference of external and internal pressure) is zero. Thus, the same pressure change causes the maximal volume (or diameter) change, if the pressure of the occluding cuff (CP) equals to the MAP.

Mathematically, this phenomenon can be described by the volume-pressure (V-P) diagram of the vessel, or by the compliance (C):

$$C = \frac{\Delta V}{\Delta P_{tr}} \quad C_{\max} = C \Big|_{P_{tr}=0, CP=MAP} \quad (1)$$

The V-P characteristic transforms the arterial pulse waves to oscillometric pulses (OP) that can be detected in cuff pressure. The maximal OP amplitude is measured ( $OPA_{MAP}$ ), and the systolic and diastolic values are related to the cuff pressures, where the OP amplitude above and below the MAP is  $k_{sys} \cdot OPA_{MAP}$  and  $k_{dia} \cdot OPA_{MAP}$ , respectively. The constants are determined based on statistical data [12].

In case of real measurements, even the detection of OP-s can be a challenge, even if the patient is at rest, and there are no extra “physiological noises” to deal with.

Fig. 2. shows a special record: our device (HHM) was used in parallel with an invasive blood pressure monitor



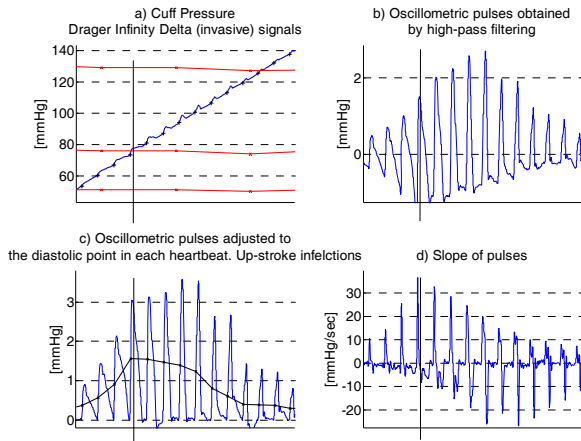


Fig. 2. Measuring the MAP with the improved oscillometric method. All subplots show variation in time.

(Dräger Infinity). The invasive sensor was in the femoral artery. Patients were lying in the bed. Subplot *a*) shows the cuff pressure (blue) and the diastolic, mean and systolic pressure (red). The beginning of each OP has been detected (black crosses). The oscillometric signal, obtained with high-pass filtering (0.5 Hz cutoff frequency) is drawn in subplot *b*). The oscillometric pulses can also be derived from the cuff pressure after detrending, see subplot *c*). This makes the determination of OP amplitudes more accurate. But even in this case, *the maximal amplitude cannot be related to MAP*. Taking the inflection point for each pulse up-stroke (subplot *c*), black) gives a better result. Examining the *derivative* of the adjusted pulses (which is strongly related to compliance) is even more effective (see subplot *d*). Based on our measurements, we claim that the maximum of the derivatives indicates the heartbeat, where the cuff pressure during deflation crosses the MAP.

Further, we claim, that the diastolic and systolic pressures can be determined by examining the shape of the OP-s, instead of using uncertain “magic constants” for the calculation. (And a more robust algorithm can be developed, if other parameters – e.g. pulse transit time from the heart to the fingertip – are also taken into consideration).

Because of the increasing external pressure during inflation, the closing of the artery is faster. By means of the peak amplitudes of the OP-s and their derivatives, the systolic pressure can be determined.

Assuming unvarying blood pressure pulses, the characteristic values could be measured accurately, if slow cuff-inflation were applied. But the blood pressure is continuously fluctuating and additionally, too slow inflation means more disturbance and inconvenience for the patient. Thus, choosing the optimal cuff pressure profile remains a challenge.

On the other hand, our measurements prove that if the oscillometric measurement is accurate enough, and additionally a photo-plethysmographic (PPG) signal is measured, the PPG can be calibrated, and used as a short-term continuous blood pressure signal. This makes the characterization of blood pressure fluctuation also possible.

### III. MONITORING OF RESPIRATORY SOUNDS

Acoustic signals generated by lungs are a source of information on the condition of the airways. Wheezes are continuous adventitious lung sounds that are superimposed on normal breathing sounds. They are common clinical signs of obstructive airway diseases and are particularly present during acute episodes of asthma as they often precede asthmatic attacks. Their waveform resembles that of a sinusoidal sound with a dominant frequency usually higher than 100 Hz and duration longer than 100 ms [13]. Due to increased incidence of asthma in children reported in the past few decades, respiratory sound diagnostics and monitoring improvement is of special interest and represents valuable and important research. Given the aforementioned reasons we decided to develop a method for continuous monitoring of respiratory sounds which can be used, among others, for detection of wheezes and can be implemented using relatively simple electronic circuits and a digital processing unit.

#### A. Device for home use

In order to enable continuous monitoring, we designed a portable device putting special emphasis on size, weight and power consumption minimization of the device. The device consists of three parts: an analog preprocessing block, a digital processing block and a communication block. The preprocessing measurement circuits enable amplification and filtering of respiratory sounds (measured either by a microphone or by an accelerometer). The digital processing block consists of an AD converter and a digital signal processor.

#### B. Wheeze detection algorithm

For wheeze detection, we adopted a method proposed by Shabtai-Musih et al. [14, 15] because of its simplicity of implementation in simpler processors like MCUs or FPGAs. The method itself is composed in three steps; first, the power spectra are calculated using the fast Fourier transform (FFT) and peaks in spectra are identified. In the second step, a scoring algorithm is implemented and the peaks are evaluated according to (seven) preset criteria. Each time

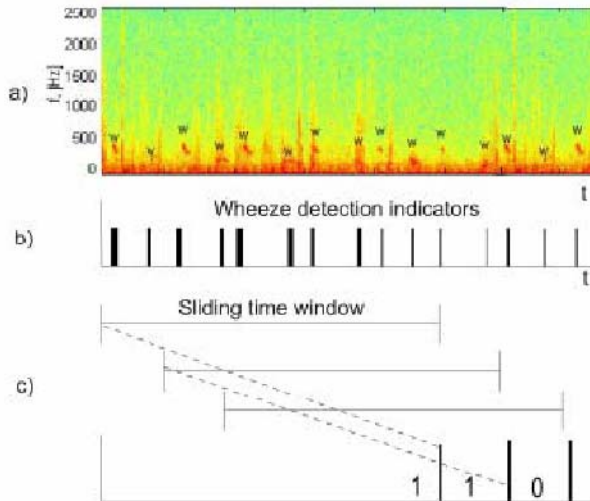


Fig. 3. a) Time frequency diagram of respiration sounds. Detected wheezes designated with "W". b) Sequence of wheeze detection indicators. c) Asthma attack detection using sliding time windows.

the criteria are met, the score is increased. If the final score is equal to or greater than 3, it indicates the presence of wheezes. Finally, the scoring result is transmitted to a health server for further decision-making based on incidence of detection in an application defined sliding time window. In future applications, decision-making will be enhanced with additional parameters extracted from physiological signals which will be introduced with different weight factors in order to increase positive predictivity and accuracy of the method.

#### IV. CONCLUSION

When national health care system decide to reimburse or equip patients living at home alone with home health monitoring systems, patients will get a better, more efficient health service. Furthermore, implementing such a system costs the society much less. Today's intensive ongoing research and development will in the near future produce more available solutions; health monitoring systems will cover greater numbers of different chronic diseases and will improve the quality of life and well being of all the age groups.

#### ACKNOWLEDGMENT

The research work is aided by the Hungarian-Croatian Intergovernmental S&T Cooperation Program.

#### REFERENCES

1. Togawa T: Home health monitoring J Med Dent Sci 1998; 45: 151-160.
2. Starfield B: Doctors are the third leading cause of death in the US causing 250,000 deaths every year. JAMA 2000, **284** (4) pp. 483-5.
3. <http://www.bel2.sote.hu/hipertonia/index.html>
4. NHBPEP/NHLBI/AHA Working Meeting on Blood Pressure Measurement. April 19, 2002. Natcher Conference Center, NIH, Bethesda, Maryland available at: <http://www.nhlbi.nih.gov/health/prof/heart/hbp/bpmeasu.pdf>
5. Celler BG, Lovell NH, Chan DKY: The potential impact of home telecare on clinical practice. MJA 1999; 171:518-521.
6. Anliker U, Ward JA, Lukowicz P, Tröster G, Dolveck F, Baer M, Keita F, Schenker EB, Catarsi F, Coluccini L, Belardinelli A, Shklar-ski D, Alon M, Hirt E, Schmid R, Vuskovic M: AMON: A Wearable Multiparameter Medical Monitoring and Alert System. IEEE Tr on Information Technology in Biomedicine, Vol. 8., No. 4. 2004. pp. 415-427.
7. O'Brien E: State of the market for devices for blood pressure measurement. Blood Pressure Monitoring 2001, 6:281-286
8. O'Brien E, Waeber B, Parati G, Staessen J, Myers MG on behalf of the European Society of Hypertension Working Group on Blood Pressure Monitoring. BMJ Vol. 322, 2001, pp 531-536.
9. O'Brien E : Blood pressure measurement is changing! Editorial. Heart, 2001(a) ; **85**: 3-5.
10. Asmar R, Zanchetti A, (on behalf of the Organizing Committee and participants): Guidelines for the use of self-blood pressure monitoring: a summary report of the first international consensus conference. Journal of Hypertension, 2000, **18**:493-508.
11. Jobbágy Á, Csordás P, Mersich A: Blood Pressure Measurement at Home. IFMBE Proceedings, Vol. 14. WC2006 Seoul, pp. 3319-3322.
12. Drzewiecki G, Hood R, Apple H: Theory of the oscillometric maximum and the systolic and diastolic detection ratios. Annals of Bio-medical Engineering, 1994, 22:88-96.
13. Sovijärvi ARA, Dalmasso F, Vanderschoot J, Malmberg LP, Righini G, Stoneman SAT. (2000) Definition of terms for applications of respiratory sounds. Eur Respir Rev **10**:597-610
14. Shabtai-Musih Y, Grotberg J, Gavriely N. (1992) Spectral content of forced expiratory wheezes during air, He, and SF6 breathing in normal humans. J Appl Physiol **72**:629-635
15. Alić, Ante; Lacković, Igor; Bilas, Vedran; Seršić, Damir; Magjarević, Ratko. A Novel Approach to Wheeze Detection. IFMBE Proceedings, Volume 14, World Congress on Med. Phys. & Biomed. Eng., Seoul, 2006. 857-860
16. Magjarevic, Ratko. Home Care Technologies for Ambient Assisted Living. IFMBE Proc. Vol. 16, 11<sup>th</sup> MEDICON 2007, Ljubljana, 2007, pp. 397-400.

Author: Ákos Jobbágy  
 Institute: Budapest University of Technology and Economics  
 Street: Magyar Tudósok krt. 2.  
 City: Budapest  
 Country: Hungary  
 Email: [jobbagy@mit.bme.hu](mailto:jobbagy@mit.bme.hu)

# Time Domain Signal Processing of Tibial Nerve Somatosensory Evoked Potentials During Anesthesia

A.S. Joutsen<sup>1</sup>, V. Jäntti<sup>2</sup> and H. Eskola<sup>1</sup>

<sup>1</sup>Department of Biomedical Engineering, Tampere University of Technology, Tampere, Finland

<sup>2</sup>Department of Neurophysiology, Tampere University Hospital, Tampere, Finland

**Abstract** — Somatosensory evoked potentials are used along with motor evoked potentials for ensuring patient safety during scoliosis surgery. The operating room is a difficult recording environment with electromagnetic noise overlapping the few  $\mu\text{V}$  signal that is used to assess the status of the somatosensory tract of the patient during the operation. In this paper we study three methods to improve the signal-to-noise ratio of the recorded samples. The widely used arithmetic mean is compared with median and trimmed mean methods.

Arithmetic mean smoothed the curves and median and trimmed mean preserved higher frequencies. The calculated signal-to-noise ratios using the three methods yielded similar values with some higher figures during suppression EEG epochs using median and trimmed mean. As a conclusion all methods gave results of our data, but none was significantly better than the others.

**Keywords** — Somatosensory evoked potentials, Signal-to-noise ratio, Ensemble averaging, Anaesthesia.

## I. INTRODUCTION

Somatosensory evoked potential examinations are at present routinely conducted in neurophysiology laboratories. They are also used in intra operative monitoring for securing the functionality of the somatosensory tract of the patient [1].

We have compared the signal-to-noise ratio (SNR) results of intraoperative monitoring (IOM) tibial somatosensory evoked potential (tSEP) data during different electroencephalography (EEG) phenomena, which contribute uniquely to the forming of the tSEP result. Ensemble averaging using arithmetic mean was used for improving the SNR of the results [2]. In this study we further explore the issue using different averaging methods for improving the SNR of tSEPs. Higher SNR yields results faster, which is important in ensuring the integrity of the somatosensory tract of the patient.

The methods we have used are all based on ensemble averaging but the usual arithmetic averaging process is replaced by median and trimmed mean processes. In cardiology median has been used in ambulatory ECG [3] and anaesthesia ECG [4] for transient filtering and in evoked potential studies for minimizing noise [5, 6]. The trimmed mean has been used also in ECG artifact detection [7] and

in event related potential studies [8]. Median is useful when there are sharp noise transients, but the combination of median and arithmetic mean, the trimmed mean, may improve the tSEP outcome by rejection of extreme values and preservation of data points.

## II. MATERIAL AND METHODS

For this study we have used the same set of patients as previously [2] to enable the comparison of the averaging methods. The 8 patients selected for this study were operated in Tampere University hospital during 2006 and 2007 for idiopathic scoliosis. The monitoring device was Endeavor Bravo intraoperative monitoring system (Viasys Healthcare, PA, USA). The acquired EEG was sampled at 8 kHz. The tSEP stimulation frequency was 3,1 Hz. After recording the EEG was moved to off-line analysis with Matlab (Mathworks, MA, USA), where it was band pass filtered with 30 to 200 Hz to reject high and low frequency noise not associated with tSEP. The EEG was visually scored using Somnologica Studio (Embla, Co, USA) to bursts, suppressions and spindles [9,10] and technical artifacts, which were omitted from the study. The EEG contained some 50 Hz mains artifact.

An optimal tSEP channel was calculated for each patient by selecting the EEG derivation yielding the highest tSEP responses [11]. Channels used were the derivations of standard 10-20 EEG locations [12], from which Fz-Cz or C3-C4

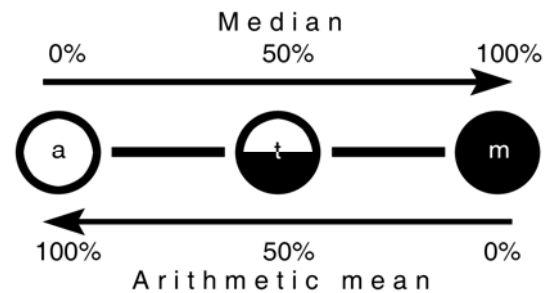


Fig. 1 Ensemble averaging of evoked potentials can be done using arithmetic mean (*a*), median (*m*) or a combination of the two called trimmed mean (*t*). In trimmed mean the ratio of arithmetic mean to median can be anything, but here we compare pure arithmetic mean, 50% trimmed mean and pure median.

was most frequently selected. The tSEP responses occurring during the three EEG epochs were separated to their respective datasets and ensemble averaging with a rejection criterion of 200  $\mu\text{V}$  peak-to-peak per single response was used to improve the SNR inside the sets.

Ensemble averaging is based on simple signal model in which the potential  $x_i$  of the  $i^{\text{th}}$  stimulus is assumed to be additively composed of a deterministic, evoked signal component  $s_i$  and a random noise  $n_i$  which is asynchronous to the stimulus

$$x_i = s_i + n_i \quad (1)$$

The noise is assumed to have zero mean and it is uncorrelated between measurements. Noise and signal need to be uncorrelated and signal needs to have constant waveform morphology [13].

The mean is calculated giving equal weigh factors of  $(1/N)$  to each sample in the set, where  $N$  is the total amount of samples (Eq 2).

$$\mu_{mean} = \sum_{i=1}^N \frac{1}{N} x_i \quad (2)$$

The trimmed mean (Eq 3) is a hybrid of both arithmetic mean and median, because after sorting the samples to ascending order equal amount of samples are removed from both high and low end. Arithmetic mean is thereafter calculated from the remaining samples. This is equal to giving a weight factor 0 to the samples outside the window  $p+1 \leq i \leq N-p$  where  $p=\alpha N$ ,  $\alpha=\{0..0,5\}$ , and a weigh factor  $1/(N-2p)$  inside the window [8,14]. In this study use an  $\alpha=0,25$  which removes 50% of the data points, 25% from the low and 25% from the high end. Equal amount of samples are removed from both ends to ensure that the remainder of the samples are located in the center of data. Arithmetic mean is calculated from the remaining samples.

$$\mu_{trimmed.mean} = \frac{1}{N - 2 \cdot (\alpha N)} \sum_{i=(\alpha N)+1}^{N-(\alpha N)} x_i \quad (3)$$

In median suppose that the data has the size of  $(2M+1)$ , where  $M$  is a positive integer, then the median is the value of the  $(M+1)^{\text{th}}$  ordered observation. In the case of even data size  $2M$  the median is defined as the value of the mean of the samples  $M$  and  $M+1$ . A weight of one is applied to the  $(M+1)^{\text{th}}$  sample in the case when the number of samples is odd and weights equal to  $1/2$  to both  $M^{\text{th}}$  and  $(M+1)^{\text{th}}$  samples when the number of samples is even [15].

The SNR of the averaged tSEPs from the sets were calculated using the method proposed in [16], where variances of the averaged signal and the noise estimate are divided giving the true SNR power ratio of the ensemble. This is used to compare the effectiveness of the methods.

### III. RESULTS

The results of the study are shown in Fig 2 and Table 1. In Fig 2 the ensemble averaged data with  $N=\{4,16,64, 256\}$  are shown using all the three methods: arithmetic mean, trimmed mean and median.  $N=256$  was chosen as an endpoint of the process because the tSEP response had already formed between 30 and 40 ms.

All methods are able to provide acceptable visual results of the tSEP response. Arithmetic mean smoothes the responses the more there are single responses in every result, whereas median is able to retain high frequency components

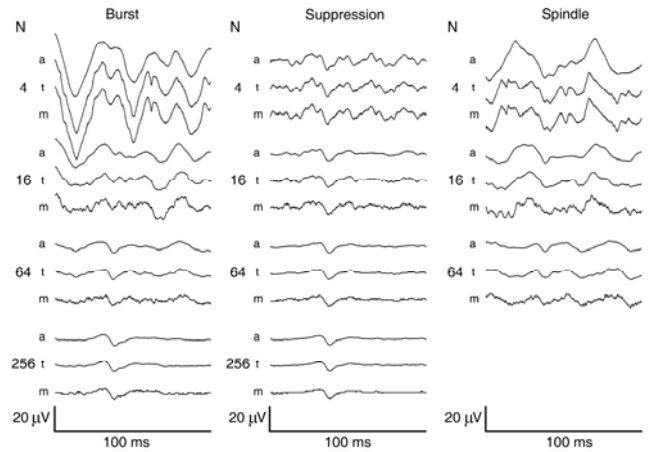


Fig. 2 The results of ensemble averaging of the data of an example patient with burst, suppression and spindle sets when  $N$  responses have been processed. For the sets three averaging techniques have been used: arithmetic mean (a), 50% trimmed mean (t) and median (m). The example patient had enough spindle responses only for  $N=64$ .

Table 1 The min and max SNRs of the patients using arithmetic mean (a), 50% trimmed mean (t) and median (m).

N	Method	Burst	Suppression	Spindle
4	a	0,46 - 6,90	0,54 - 3,57	0,61 - 3,18 (5)
4	t	0,49 - 7,06	0,43 - 3,75	0,54 - 3,53 (5)
4	m	0,49 - 7,06	0,43 - 3,75	0,54 - 3,53 (5)
16	a	0,57 - 3,45	1,15 - 7,80	0,89 - 1,40 (4)
16	t	0,24 - 3,50	1,45 - 7,35	0,90 - 1,35 (4)
16	m	0,29 - 3,84	1,40 - 8,63	0,96 - 1,76 (4)
64	a	0,37 - 9,53	1,77 - 63,30	0,41 - 3,49 (2)
64	t	0,31 - 9,32	2,45 - 62,58	0,48 - 3,54 (2)
64	m	0,35 - 9,28	3,39 - 62,70	0,54 - 4,09 (2)
256	a	1,32 - 32,86	5,44 - 398,08	
256	t	1,01 - 31,47	6,24 - 396,84	
256	m	1,25 - 34,18	9,80 - 403,29	

The amount of patients in burst and suppression set was 8. The amount of patients decrease in spindle column (shown in parenthesis) as  $N$  grows, because simultaneous spindles and tSEP responses were rare in this set of patients.

which can be seen as sharper peaks. Also arithmetic mean produces slightly lower amplitude for the response than median. Trimmed mean lies between the both methods in inspection of the response curve. From Table 1 it can be seen that the three methods produce similar SNR values through out the patients, except in the minimum values of suppressions with high N, where median and trimmed mean have the highest difference to arithmetic mean. Comparing the burst, suppression and spindle sets the tSEP responses during suppression yielded the significantly higher SNR values in  $N=\{16,64,256\}$  than during burst and spindles.

The maximum amplitude of the response lowers somewhat when N is high in all methods because of small amplitude and latency variations (jitter), in the single responses, s.

#### IV. CONCLUSIONS

We have compared three averaging methods for improving the SNR of anaesthesia tSEP responses recorded during scoliosis surgery. All the methods produced results, but arithmetic averaging smoothed the curves, where as median and trimmed mean preserved higher frequencies. This is visible as sharper peaks through out the example curves. In burst and suppression sets median and trimmed mean were promising but did not give any significant difference. Using an example with sharp transients could show the effectiveness of removing extreme values using median and trimmed mean.

Median suffers from quantization as N grows, because the recording equipment, Endeavor Bravo, uses 16 bits to store samples with a resolution of 1  $\mu$ V. In suppression when  $N=256$  there are only 9 voltage values representing the response, as the maximum amplitude is 9  $\mu$ V. This means that 4 bits are enough to encode the response. If the 16 bits could be used more effectively, it could improve at least the visual outcome of median and trimmed mean on of the tSEP with high N. The SNR calculation method used yielded quite similar values regardless of the averaging method; other SNR evaluation methods could be investigated. Further investigations are needed to find out more of these now studied methods in IOM tSEP use.

#### ACKNOWLEDGEMENT

This study was funded by the Finnish Ministry of Education through the International Graduate School in Biomedical Engineering and Medical Physics in the Tampere University of Technology. The use of the patient material was approved by the chief administrative medical officer of Tampere University Hospital (decision number R0853).

#### REFERENCES

1. Marc R. Nuwer, Edgar G. Dawson, Linda G. Carlson, Linda E. A. Kanim and John E. Sherman (1995) Somatosensory evoked potential spinal cord monitoring reduces neurologic deficits after scoliosis surgery: results of a large multicenter survey, *Electroencephalography and Clinical Neurophysiology/Evoked Potentials* 96:6-11.
2. Joutsen A, Puumala P, Lyytikäinen L-P, Pajulo O, Etelämäki A, Jurva J, Jäntti V, Eskola H (2008) Comparison of tibial nerve somatosensory evoked potential signal-to-noise ratios during anaesthesia, *IFMBE Proceedings, Nordic-Baltic Conference on Biomed. Eng. & Med. Phys.*, Riga, Latvia, 2008, pp.256-259
3. Taddei A, Costantino G, Silipo R, Emdin M, Marchesi C (1995) A System for the Detection of Ischemic Episodes in Ambulatory ECG. *Computers in Cardiology Computers in Cardiology*, Vienna, Austria 1995, pp.705-708
4. Loula P, Jäntti V, Yli-Hankala A (1997) Respiratory sinus arrhythmia during anaesthesia: assessment of respiration-related beat-to-beat heart rate variability analysis methods. *Int J Clin Monit Comput.* 14:241-9.
5. Fox LG, Dalebout SD (2002) Use of the median method to enhance detection of the mismatch negativity in the responses of individual listeners. *J Am Acad Audiol.* 13:83-92.
6. Özdamar Ö, Kalayci T (1999) Median averaging of auditory brain stem responses. *Ear Hear.* 20:253-64.
7. Greene BR, Boylan GB, Reilly RB, de Chazal P, Connolly S (2007) Combination of EEG and ECG for improved automatic neonatal seizure detection. *Clin Neurophysiol.* 118:1348-59
8. Leonowicz Z, Karvanen J, Shishkin S (2005) Trimmed estimator for robust averaging of event-related potentials. *J Neurosci Meth* 142:17-26
9. Huotari AM, Koskinen M, Suominen K, Alahuhta S, Remes R, Hartikainen KM, Jäntti V (2004) Evoked EEG patterns during burst suppression with propofol. *Br J Anaesth.* 92:18-24.
10. Jäntti V, Yli-Hankala A, Baer GA, Porkkala T (1993) Slow potentials of EEG burst suppression pattern during anaesthesia. *Acta Anaesthesiol Scand.* 37:121-3
11. MacDonald DB, Al Zayed Z, Stigsby B (2005) Tibial somatosensory evoked potential intraoperative monitoring: recommendations based on signal to noise ratio analysis of popliteal fossa, optimized P37, standard P37, and P31 potentials. *Clin Neurophysiol.* 116:1858-69
12. Klem G, Lüders H, Jasper H, Elger C (1999) The ten-twenty electrode system of the International Federation. *The International Federation of Clinical Neurophysiology Electroencephalogr Clin Neurophysiol Suppl.* 52:3-6.
13. Sörnmo L, Laguna P (2005) *Bioelectrical Signal Processing in Cardiac and Neurological Applications*, Academic Press, New York
14. Bednar J, Watt T (1984) Alpha-trimmed means and their relationship to median filters. *IEEE trans. on acoustics, speech, and signal processing* 32:145-153
15. Stuart A, Keith O (1994) *Kendall's advanced theory of statistics*. London, Edward Arnold
16. Schimmel H, Rapin I, Cohen MM (1974) Improving evoked response audiometry with special reference to the use of machine scoring. *Audiology*, 13:33-65

Author: Atte Joutsen

Institute: Department of Biomedical Engineering / Tampere University of Technology

Street: Biokatu 6, 4<sup>th</sup> floor

City: Tampere 33520

Country: Finland

Email: atte.joutsen@tut.fi

# Modelling Interrupter Measurements of Respiratory Resistance

J. Talts, J. Kivastik

Department of Physiology, University of Tartu, Tartu, Estonia

**Abstract** — The interrupter resistance ( $R_{\text{int}}$ ) technique for assessing respiratory mechanics requires minimal cooperation and can therefore be successfully performed in young children. The method involves a brief (100 ms) occlusion of the airflow during the tidal breathing while pressure measured at the airway opening equilibrates with alveolar pressure.  $R_{\text{int}}$  can be calculated when dividing the driving pressure by flow at the mouth immediately prior to occlusion.

The aim of our study was to develop an electrical circuit model capable of simulating the main changes observed in the pressure signal and to investigate the influence of model circuit elements on that signal.

We used a two compartment series model. Additionally, since the interrupter technique induces fast changes in air velocity, the inertial properties of the air column must be accounted for. This was done by inserting the inductance element into the model. The circuit consists of six elements, including the interrupter switch.

Using this model, it was possible to generate a variety of waveforms similar to pressure changes obtained from interrupter measurements with preschool children. Different calculation methods for  $R_{\text{int}}$  and oscillation amplitudes in various states of airway obstruction can be discussed from the modelling viewpoint. Furthermore, the influence of the construction of the interrupter device on the waveforms can be predicted.

**Keywords** — lung function, airway resistance, interrupter technique, modelling

## I. INTRODUCTION

The interrupter resistance ( $R_{\text{int}}$ ) technique is based upon the premise that when the airway is suddenly occluded during the tidal breathing, there is a pressure change at the mouth, which equals the resistive pressure drop across the airways. Resistance can be found by dividing this pressure difference by the preocclusion flow. Immediately after occlusion, there is a very rapid change in pressure, followed by damped pressure oscillations, and finally, there is a relatively slow rise in pressure.

$R_{\text{int}}$  measurement has been shown to be feasible for studying lung function in preschool children with mild bronchoconstriction. It has been stated that pressure equilibration between the alveoli and mouth can be incomplete in case of severe airway obstruction and therefore, the interrupter technique may underestimate airway resistance. For this reason its role in measuring increased resistance values,

such as during bronchoprovocation testing remains to be determined [1].

In addition to calculating just one  $R_{\text{int}}$  value, there have been attempts to pay more attention to the dynamic behavior of pressure equilibration between the mouth and alveoli seen as pressure oscillations. Analysis of those oscillations has been suggested to provide additional indices of change in airway mechanics [2-4]. In a previous study we calculated several different amplitude parameters and they all changed significantly after bronchoprovocation testing [5]. Unfortunately, it is difficult to compare results from different studies, because in addition to bronchial diameters the oscillations can also be influenced by several other factors, like the length of the mouthpiece up to the shutter and the lung volume [3]. All those factors could be accounted for when using a model of interrupter technique. The mechanical resistances, compliances and inertances of the respiratory system (and device) can be correlated with models consisting of electrical components that are analogous to the respiratory system's mechanical components.

The aim of our study was to develop an electrical circuit model capable of simulating the main changes observed in the pressure signal from the interrupter technique and to investigate the influence of model circuit elements on that signal.

## II. MATERIALS AND METHODS

### A. Modelling

The respiratory system with flow interrupter is modelled by the electrical circuit shown in Figure 1. This is a minimal configuration, capable of generating waveforms similar to those registered during airflow interruption.

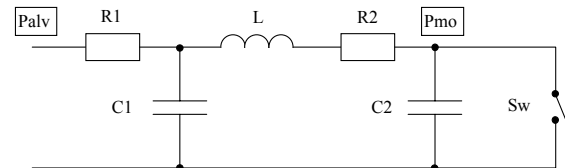


Fig. 1. Electrical model for interrupter measurements

The interrupter switch (Sw) is presented as a variable resistor with increasing resistance during interrupter closure, typically taking 5-10 ms. As a response to this the pressure curve shows a rapid rise, followed by damped pressure oscillations. These oscillations can be modeled by RLC circuit, where the element values determine the frequency and damping of oscillations [2]. Finally, there is a relatively slow rise in pressure curve, which cannot be described by the abovementioned RLC circuit alone, and hence, an additional RC section must be included. In essence, this is a two compartment series model.

All simulations were conducted in the MATLAB software environment. Mouth pressure ( $P_{mo}$ ) curves were generated by numerical integration. During the short time of interruption, the alveolar pressure ( $P_{alv}$ ) was considered to have a constant value of 500 Pa. First we fixed one set of element values as a baseline condition:  $R_1=500$  Pa·s /L,  $R_2=1000$  Pa·s /L,  $C_1=4 \cdot 10^{-5}$  L/Pa,  $C_2=5 \cdot 10^{-7}$  L/Pa and  $L=2$  Pa·s<sup>2</sup> /L. The resistance of the interrupter switch ( $R_{sw}$ ) during closing was modelled similar to [6],

$$R_{sw} = R_p + \frac{k}{1 - \sin\left(\frac{\pi}{2T} t\right)^2}, \quad (1)$$

where constant transducer resistance  $R_p=100$  Pa·s/L and valve dimension coefficient  $k= 6$  Pa·s·L<sup>-3</sup>. The closing time of the interrupter (T) for baseline was set to 5 ms.

In order to find out how the changes in different elements of the model influence the pressure transient, we changed the values for  $R_1$ ,  $R_2$  and  $C_2$  separately to 200, 125 and 200 % of their baseline value, respectively. Additionally, the closing time of the interrupter was doubled in one simulation.

### B. Comparison of simulations with actual data from children

As a second task, we fitted the pressure waveforms developed by the model to experimental interrupter curves from our previous measurements with preschool children.

Subjects were 44 healthy and symptomatic children aged 3-6 years who completed the methacholine challenge and were described in detail in a previous paper [7].  $R_{int}$  was assessed using a single MicroRint device (Micro Medical, UK). During normal and quiet breathing, up to 10 interruptions were made on the peak flow of the expiration. The valve of such a device closes within 10 ms and remains closed for 100 ms. Sampling frequency of the pressure signal was 2000 Hz.

We chose the curves from baseline and post-methacholine measurements, the latter representing the state of bronchoconstriction. The fitting was performed using the Levenberg-Marquardt algorithm.

## III. RESULTS

Using the model, we generated different waveforms according to specified conditions. The baseline conditions for simulation, described in the Methods section, are shown in Figures 2-4 with thin lines.

The increased airway resistance in the peripheral part of the respiratory system corresponds to a bigger value of  $R_1$ . This case, with  $R_1=1000$  Pa·s/L, is shown in Figure 2. The pressure rise after oscillations is slower, and it depends on the time factor  $R_1C_1$  how close the pressure at the end of the interruption reaches the theoretical steady state value.

The slightly enlarged value of  $R_2$  (the resistance of central airways and the device) caused damping of oscillations to a greater extent, as can be seen in Figure 3.

The influence of increased  $C_2$  (representing the volume close to the shutter, e.g. bigger mouthpiece, unsupported cheeks) is shown in Figure 4. The oscillation amplitudes and frequency were lower compared to those from the baseline curve.

The influence of increased interrupter closing time can be viewed in Figure 5. In addition to the time shift, the initial pressure rise was smaller.

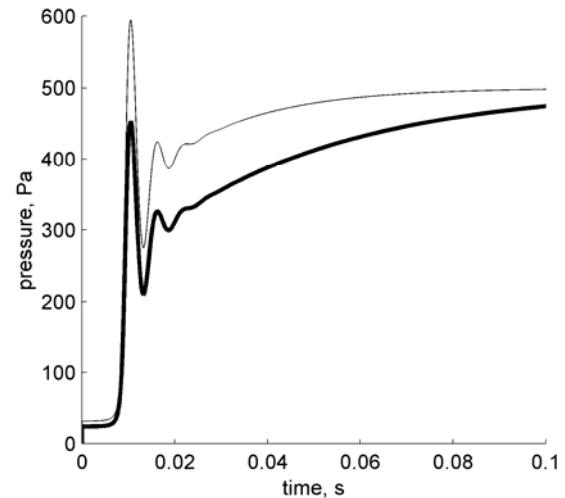


Fig.2. Simulated pressure waveforms for baseline conditions (thin) and for increased  $R_1$  (bold).

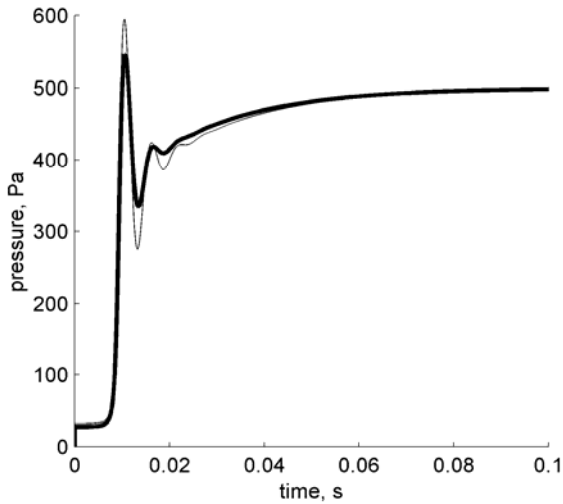


Fig.3. Simulated pressure waveforms for baseline conditions (thin) and for increased R2 (bold).

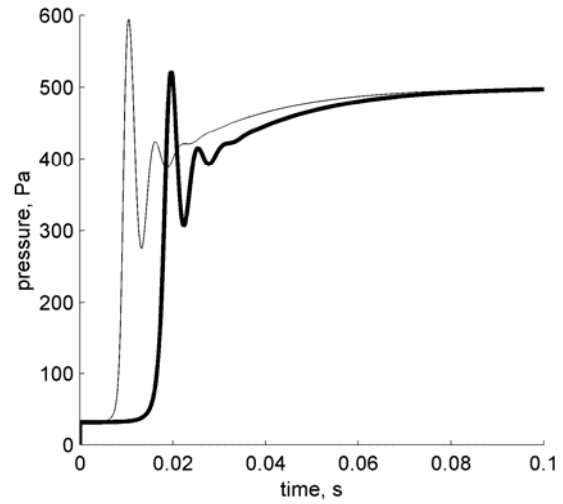


Fig.5. Simulated pressure waveforms for baseline conditions (thin) and for increased closing time (bold).

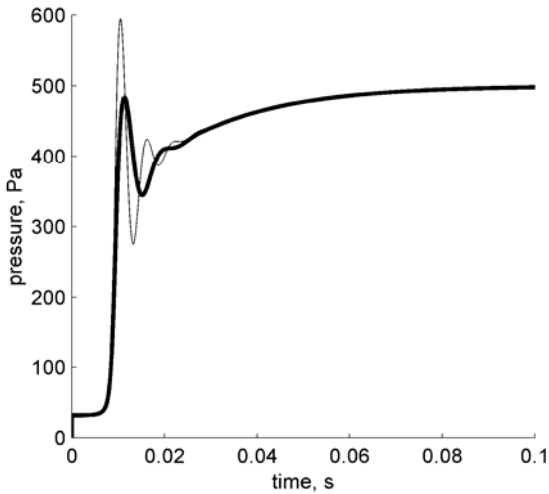


Fig.4. Simulated pressure waveforms for baseline conditions (thin) and for increased C2 (bold).

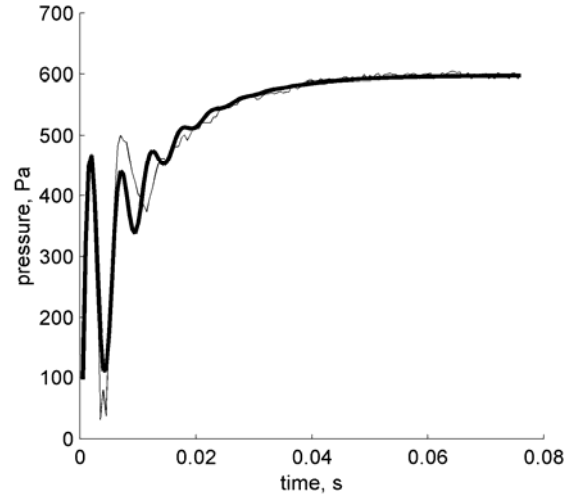


Fig.6. Measured pressure waveform from a child (thin) and a fitted curve generated by the model with linear elements (bold)

One example of our attempt to fit simulated pressure waveforms with actual data recorded from small children is shown in Figure 6. Typically, we found a remarkable fitting discrepancy during the oscillation process. This could be explained by the variable character of oscillations in measured waveforms, i.e. both the frequency and damping properties were changing in time. As a rule, the frequency was higher and the damping factor was lower at the beginning of oscillations.

#### IV. DISCUSSION

Different techniques for analyzing the mouth pressure curve after the flow interruption have been proposed and these have been compared to find a technique with the best combination of repeatability and sensitivity to change, e.g. in bronchodilatation testing [8]. However, there is still no consensus as to which of those would be preferred in describing changes in lung mechanics. The curves in obstructed children are considerably more concave with respect to the x-axis than in adults, and this can represent a difficulty when back-extrapolation is used. There is no clear



answer to the question about which changes in the respiratory system cause those differences in the pressure curve.

Modelling of the respiratory system is often used, starting from simple models including only total respiratory resistance and elastance and reaching much more sophisticated multiple compartment models. Many studies have concentrated on fitting respiratory impedance spectra with different models [9-10], but there are also some publications about modelling the interrupter technique. Jabłoński and coauthors have proposed a methodological transformation from the real physiological system, through its linear complex model (forward model) to the reduced metrological form (inverse model). Using those models they have assessed different algorithms of the post-interrupter data analysis [11] and also the influence of interrupter valve properties [6].

Our model was relatively simple, consisting of two sections, one of them oscillating quite rapidly and the other having a slower time constant. An assumption was made that during short interruption (100 ms), the alveolar pressure does not change substantially. This allowed simpler simulation and model identification. However, we think that those simplifications do not cause the fitting discrepancy during oscillations, but that this is mainly due to nonlinear effects, i.e. the fitting with linear elements cannot follow the variable character of oscillations in measured pressure curves.

## V. CONCLUSIONS

The modelling showed that the pressure oscillations and the later rise in pressure can be influenced by different parts of the airway/measuring system. Bronchoprovocation testing often causes changes in the phase of the slow rise of the pressure signal. This corresponds to the increase of R1 in the model. The oscillation amplitude depends on different factors, like the resistance and volume of the mouthpiece and central airways and the closing time of the shutter.

## ACKNOWLEDGMENT

This work was supported by Marie Curie Fellowship of the European Community programme "Improving Human Research Potential and the Socio-economic Knowledge Base" under contract number HPMF-CT-2002-01824 and Estonian Science Foundation Grant No 7322.

## REFERENCES

1. Beydon N, Davis SD, Lombardi E, et al. (2007) American Thoracic Society/European Respiratory Society Working Group on Infant and Young Children Pulmonary Function Testing. An official American Thoracic Society/European Respiratory Society statement: pulmonary function testing in preschool children. *Am J Respir Crit Care Med*. 175: 1304–1345.
2. Frey U, Schibler A, Kraemer R (1995) Pressure oscillations after flow interruption in relation to lung mechanics. *Respir Physiol* 102: 225–237.
3. Frey U, Kraemer R (1995) Interrelationship between postocclusion oscillatory pressure transients and standard lung function in healthy and asthmatic children. *Pediatr Pulmonol* 19: 379–388.
4. Bridge PD, Wertheim D, Jackson AC, McKenzie SA (2005) Pressure oscillation amplitude after interruption of tidal breathing as an index of change in airway mechanics in preschool children. *Pediatr Pulmonol* 40: 420–425.
5. Talts J, Kivastik J, Jagomägi K (2007) Amplitude analysis of pressure oscillations after interruption of tidal breathing in preschool children. *IEEE EMBS Proc, 29th Annual International Conference of the IEEE EMBS, Lyon, France, 2007*, pp 4239–4242.
6. Jabłoński I, Mrocza J (2007) Interrupter valve kinematics in the issues of parameter estimation of the respiratory system model. *Metrol & Meas Syst* 14: 339–350.
7. Kivastik J, Gibson AM, Primhak RA (2007) Methacholine challenge in pre-school children--which outcome measure? *Respir Med* 101: 2555–2560
8. Seddon P, Wertheim D, Bridge P, Bastian-Lee Y (2007) How should we estimate driving pressure to measure interrupter resistance in children? *Pediatr Pulmonol* 42:757–763.
9. Lutchen KR, Costa KD (1990) Physiological interpretations based on lumped element models fit to respiratory impedance data: use of forward-inverse modeling. *IEEE Trans Biomed Eng* 37: 1076–1086.
10. Nguyen TU, Diong B, Nazeran H, Goldman M (2007) A Study of IOS Data Using Two Mead-related Models of Respiratory Impedance. *IEEE EMBS Proc, 29th Annual International Conference of the IEEE EMBS, Lyon, France, 2007*, pp 1078–1081.
11. Jabłoński I, Mrocza J (2006) Computer-aided evaluation of a new interrupter algorithm in respiratory mechanics measurement. *Biocyb & Biomed Eng* 26: 33–47.

Author: Jaak Talts  
 Institute: Department of Physiology, University of Tartu  
 Street: Ravila Str 19  
 City: Tartu  
 Country: Estonia  
 Email: jaak.talts@ut.ee

# Coupling Axis-Length Profiles with Bezier Splines in Finite Element Head Models

K. Wendel, M. Osadebey and J. Malmivuo

Tampere University of Technology/Department of Biomedical Engineering, Tampere, Finland

**Abstract** — We built a realistically-shaped head volume conductor model using the finite element method (FEM). We lofted Bezier splines together to reduce the computational boundary complexity while preserving the geometrical structure. We based our spline reduction on coupling axis-length profile slopes of major and minor angular distances. We found that the optimal ratio of points per spline to the number of slices per tissue ranged from 1 to 1.5. We supported the structure reduction with an adaptive mesh, using quadratic-order tetrahedral basis elements with the highest resolution at the subdomain boundaries to maintain the geometric integrity.

**Keywords** — Profiles, Bezier splines, finite element models.

## I. INTRODUCTION

The complexity of models can make them intractable. Therefore, we should find ways to reduce the geometrical complexity while preserving the results. The finite difference method (FDM) is limited to merging or eliminating matrix rows, columns, and layers to reduce the number of elements in order to make the model more tractable. Since FDM is based on prism-shaped voxels (i.e. optimally cubic voxels), the geometry resolution is sacrificed, thus creating larger boundary-segment edges in a stair-stepped effect. When the resolution is high, these smaller stair-stepped edges simulate biological curves, but when the resolution is sacrificed, it does not [1].

Zhang and Molenbroek [2] lofted B-splines together to build their human head using approximately 200 splines and clearly indicated that they did not optimize the number of slices to build their model. Shyy and Fleury [3] used higher order basis elements with Bezier and B-splines. We built a spline-reduced head volume conductor model using the finite element method (FEM). We coupled axis-length profiles with slopes to minimize the profile energy of each Bezier curve [4]. We supported our frame-structure reduction with an adaptive mesh, using quadratic-order tetrahedral basis elements with the highest resolution at the subdomain boundaries [5, 6].

## II. MATERIALS AND METHODS

We provide the mathematical basis of Bezier splines in Section II A. Then we apply it to our model in Section II B.

### A. Bezier Splines

We constructed our realistically-shaped head volume conductor model by creating three dimensional (3-D) Bezier spline surfaces. We chose Bezier splines for their capability to realize biological shapes through a closed set of piecewise polynomial curves [4]. Each Bezier curve is described by the Bernstein basis function [3]

$$J_{ni}(t) = C_{ni}t^i(1-t)^{n-i} \quad (1)$$

where the binomial coefficient

$$C_{ni} = \frac{n!}{(i!(n-i)!)}, \quad (2)$$

which is determined by the degree of the polynomial  $n$  and the vertex  $i$ . The shape of the Bezier curves are regulated by control points  $P_i$  setting the position vector [3]

$$\vec{P}(t) = \sum_{i=0}^n P_i J_{ni}(t), \quad 0 < t < 1. \quad (3)$$

This definition of the Bezier splines through control points gives it the intrinsic geometry-preserving property.

### B. Finite Element Head Model

We started with a segmented head of the Visible Human Woman (VHW) measuring 640 by 530 by 670 pixels per dimension, having a 0.33 mm resolution per each axis unit. Ultimately, we constructed a four tissue model extending from the vertex down to the nasion with plans of extending it inferiorly in the future. We constrained our slice-selection criteria for each tissue beginning with the apical slice after the noise removal from the first few slices of the radial-angular distances, i.e. the length measured from the tissue centroid to the tissue boundary for each slice.

According to image analysis, we optimized our geometry based on the variation of the major and minor radial-angular axes of the transverse, coronal, and sagittal slice sections. From this analysis we selected which slices to use and how many splines per slice for each tissue. We used the radial-angular-axis lengths for the Bezier-spline control points. We began with a minimalist approach starting initially with a pair of slices. Meanwhile we added slices until the profile energy of the radial-angular axes was minimized past a threshold that eliminated side effects such as distortion,

warp or twisting between slices and surface spline curves. We set this threshold according to the slope of the profile to the number of slices.

We set our parametric compartments to conductivities of 0.45 S/m, 0.025 S/m, 1.79 S/m and 0.25 S/m for the scalp, skull, CSF and brain, respectively [7 – 9]. We tested our model by feeding a unit reciprocal current into our model according to the reciprocity theorem. Lastly, we mapped the spatial volumes of the model to verify the half sensitivity volume (HSV) [10] and the fifth sensitivity volume (FSV) [11].

### III. RESULTS

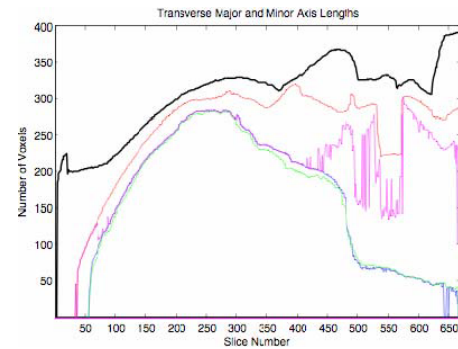
We analyzed the major and minor radial-angular axis lengths versus slice number for each type of cross section i.e. transverse, coronal and sagittal sets (Fig. 1). The outline of the forehead, nose, and lips can be identified from the transverse major axis length in Fig. 1a (thick black line). Underneath the nose the edge of the nasal and maxilla bones (Fig. 1a red line) sink below the cartilaginous nose [12]. Altogether these graphs of the major and minor profiles captured the changes in radial extrema. These profiles indicated the energy change per slice in the exterior-shape profile of each tissue.

The noise associated with the image analysis of the MRI slices correlates with the edges of each tissue detected or a complex tissue structure. The tissue-boundary noise was present in the first 2.5% of the measured radial-angular axis lengths as the measurements approached zero i.e. the first few slices of each set. The noise present in the transverse minor axis length of the skull (Fig. 1a light purple) correlates with the collection of several bones surrounding air cavities i.e. the nasal, maxilla, vomer, palatine bones [12].

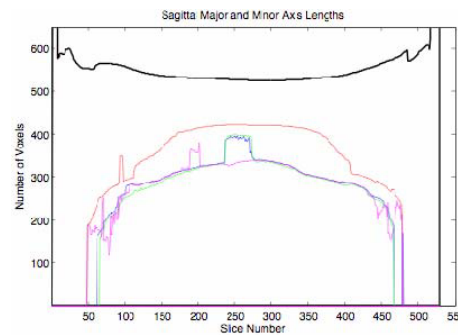
The exterior scalp, skull, cerebrospinal fluid (CSF), and brain required eight irregularly-spaced, splined slices as a minimum to preserve the geometrical integrity of the calvarium i.e. the natural curvature of the head (Fig. 2). We found that the optimal ratio of the number of Bezier splines to the number of slices per tissue approximately ranged from 1 to 1.5. We chose this range according to the slope ratio because it minimized the energy per Bezier curve, thereby eliminating twist and warp and minimizing distortion. These unwanted side effects were directly related to the number of control points i.e. radial angular axis lengths, included with each set of splines. When the ratio exceeded this range by one standard deviation, the lofted splines twisted, which distorted the actual surface geometry by adding unwanted concave curvature between the slices. Extreme aversion to this ratio yielded degenerated-triangular or tetrahedral mesh elements in the subsequent mesh phase.

Small, narrow, or high aspect ratio boundary features between tissues also caused poor mesh performance.

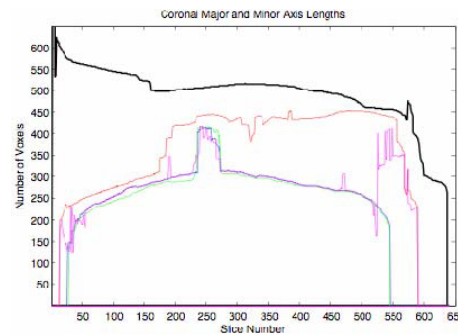
Our model yielded  $1 \pm 0.1\%$  HSV and  $0.08 + .004\%$  FSV for high-resolution electrode montages of 256 channels. The volumes increased to 3% and 0.35% for the HSV and FSV, respectively, of a 64-channel montage. The spatial volumes of the head models agreed with analytical spherical models and realistically shaped models [10, 11, 13].



(a) Transverse – Major & Minor Axis Lengths

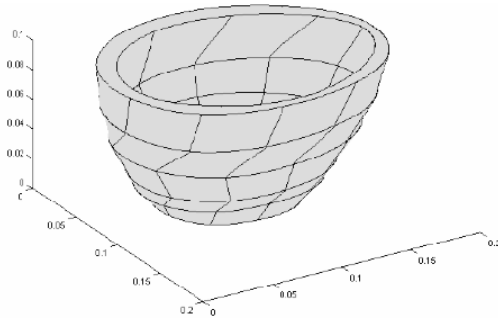


(b) Sagittal – Major & Minor Axis Lengths

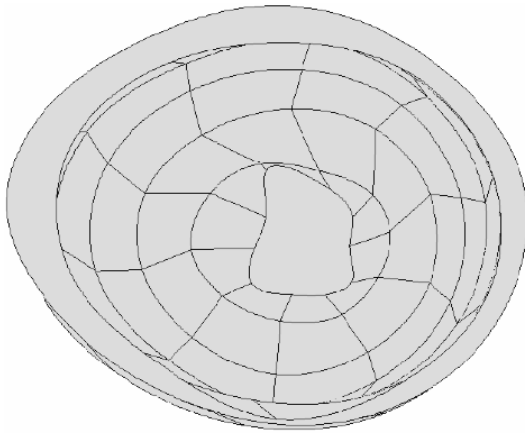


(c) Coronal – Major & Minor Axis Lengths

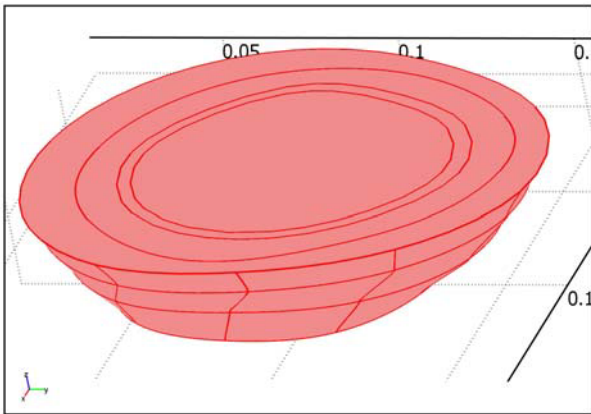
Fig. 1 The major axis-length profiles of the scalp/skin (thick black), skull (red), CSF (blue), and brain (green) and the minor axis-length profile of the skull (light purple). These axis lengths are measured from the tissue centroid per each slice in units of voxels.



(a) Scalp – Inferior view looking into the scalp/skin



(b) Skull – Superior view of the skull i.e. scalp removed



(c) All tissues – View looking into calvarium cut 4 cm from vertex

Fig. 2 (a) The geometrical frame of the scalp is a 3-D bowl shaped structure sitting inverted. (b) The top view of the skull is facing to the left. (c) The calvarium of all 4 tissues sits on the table as if it were removed.

#### IV. DISCUSSION

Splined volumes can preserve the geometrical integrity of the original object. When coupled with the slope of the cross-sectional radial-angular axis lengths, we can reduce the number of splines without compromising the geometry in order to reduce the computational geometric complexity. We chose closed quadratic splines to define the boundaries. Closed linear splines form polygons, whereas, the quadratic and cubic polynomials capture natural biological curvature [4].

The splines define the geometric boundaries i.e. the framework that defines the mesh boundaries. Even complex geometrical structures can be decomposed into simpler geometrical parts to take advantage of the Bezier splines [3]. Regardless of how closely each Bezier spline captures boundary images, the accuracy of the splines depends on the accuracy of the source data [2]; however, more spline curves must be added to capture finer localized details of interest such as sulci and gyri of the brain.

The model resolution can only be upheld if there is a high-resolution mesh at the boundary interfaces because the boundaries are the focus of the computational solutions. In our models we used adaptive meshes with highest resolution at the boundaries and reduced resolution within the subdomain interior to take advantage of the finite element (FE) basis function, the FE-solution interpolation over each element, and to reduce the model complexity [5, 6]. In agreement with Geneser et al. [6], we used a second degree basis function to more rapidly capture variation within the solution compared with the first degree. They found the second degree to be optimal for the geometry of biological nature and fitting to the solution of Maxwell’s equations.

An application of these axis-length distances can use the orthogonal radial-angular axis lengths to repair missing data or noise from one set of slices e.g. using the coronal and sagittal data to repair the transverse data. Furthermore, they can be used to alter the control points of a model for any desired localized deformations.

#### V. CONCLUSIONS

Splined volumes can preserve the geometrical integrity of the original object. When coupled with the slope of the cross-sectional axes, the number of splines can be optimized. Bezier splines can successfully reduce the model complexity while minimally altering the original geometry in order to preserve the solution of the model.

## ACKNOWLEDGMENT

We would like to thank Nathaniel G Narra and Markus Hannula for providing the segmentation of the Visible Human Woman dataset. This work was supported by the International Graduate School of Biomedical Engineering and Medical Physics, Finland.

## REFERENCES

1. Gordon R, Arola T, Wendel K, Ryyanen O, and Hyttinen J (2006) Accuracy of numerical methods in solving static and quasistatic electric fields. *Proc. Estonian Aca. Sci.; Eng., Min M, Ed.*, vol. 12/3-2. Tallinn, Estonia: Estonian Academy Publishers, Sept. 2006, pp 262 -283.
2. Zhang B and Molenbroek JFM (2004) Representation of a human head with bi-cubic B-splines technique based on the laser scanning technique in 3D surface anthropometry. *Applied Ergonomics*, vol. 35, pp 459 - 465, 29 March 2004.
3. Shyy YK and Fleury C (1987) Shape optimal design using high order elements. *MSC World Users Conference*, Universal City, California, USA, March 11-13, 1987.
4. Bookstein FL (1989) Principal Warps: Thin-Plate Splines and the Decomposition of Deformations. *IEEE Trans on Pattern Analysis and Machine Intelligence*, vol. 11, no. 6, pp 567 – 585, June 1989.
5. COMSOL Multiphysics: Command Reference, COMSOL Group, Ed. 3.3, 2006.
6. Geneser SE, Kirby RM, MacLeod RS (Accepted) Application of Stochastic Finite Element Methods to Study the Sensitivity of ECG Forward Modeling to Organ Conductivity. *IEEE TBME Accepted*.
7. Ferree T, Eriksen K, and Tucker D (2000) Regional head tissue conductivity estimation for improved EEG analysis. *IEEE TBME*, vol. 47, no. 12, pp 1584 - 1592, Dec. 2000.
8. Baumann S, Wozny D, Kelly S, Meno F (1997) The electrical conductivity of human cerebrospinal fluid at body temperature. *IEEE TBME*, vol. 44, no. 3, pp 220 - 223, March 1997.
9. Wendel K and Malmivuo J (2006) Correlation between live and post mortem skull conductivity measurements. *28<sup>th</sup> Annual Intl. Conf. of the IEEE Eng. in Medicine and Biology Society*, Aug. 2006.
10. Malmivuo J, Suihko V, Eskola H (1997) Sensitivity distributions of EEG and MEG measurements. *IEEE TBME*, vol. 44, no. 3, pp 196 - 208, March 1997.
11. Wendel K, Narra NG, Hannula M, Kauppinen P, and Malmivuo J (2008) The Influence of CSF on EEG Sensitivity Distributions of Multilayered Head Models. *IEEE TBME*, vol. 55, no. 4, pp 1454 - 1456, April 2008.
12. Netter FH (2006) *Atlas der Anatomie des Menschen*. Thieme, Stuttgart, 2006.
13. Ramon C, Schimpf PH, Haueisen J (2006) Influence of head models on EEG simulations and inverse source localizations. *BioMedical Engineering Online*, February 2006.

Author: Katrina Wendel  
 Institute: Tampere University of Technology/Dept. of Biomed. Eng.  
 Street: Korkeakoulunkatu 3, P.O. Box 692  
 City: FI-33101 Tampere  
 Country: Finland  
 Email: katrina.wendel@tut.fi

# Analysis of Bioelectrical Uterine Activity for Detection of Threatening Premature Labour

J. Zietek<sup>1</sup>, K. Horoba<sup>2</sup>, J. Jezewski<sup>2</sup>, A. Matonia<sup>2</sup>, J. Sikora<sup>1</sup> and T. Kupka<sup>2</sup>

<sup>1</sup> Medical University of Silesia/Department of Obstetrics and Gynecology, Katowice, Poland

<sup>2</sup> Institute of Medical Technology and Equipment/Department of Biomedical Informatics, Zabrze, Poland

**Abstract** — Premature birth is the leading cause of a neonatal death, so, it is extremely important to distinguish the pregnancy at risk of preterm threatening labour. The electrohysterography seems very promising as a method which enables noninvasive recording of readable bioelectrical signal of uterine muscle. The developed instrumentation enabled simultaneous recording of bioelectrical signals by means of electrodes attached to abdominal wall and mechanical activity of uterine muscle using fetal monitor. Material comprised 27 patients in physiological pregnancy (27 ÷ 40 week), and 21 patients (23 ÷ 36 week) with the symptoms of threatening premature labour. The obtained results showed that quantitative parameters of detected uterine contractions: amplitude and contraction area, obtained both for mechanical and electrical activity, were statistically significant ( $p < 0.05$ ) to distinguish the patients at risk of premature labour. However, their reliability is low because they strongly depend on individual patient features. We consider the parameters characteristic for electrohysterogram exclusively e.g. contraction power and its median frequency as more useful ( $p < 0.05$ ). Noninvasive electrohysterography ensures higher sensitivity and specificity for recognition of uterine contraction activity in comparison to classical mechanical method.

**Keywords** — electrohysterography, uterine activity, premature labour.

## I. INTRODUCTION

Premature birth is the leading cause of a neonatal death. Therefore, it is extremely important to distinguish the high-risk pregnancy group comprising pregnant women at risk of premature uterine contraction activity. As it has been confirmed in clinical practice, the classical external tocography is not sufficient for precise discrimination of patients at risk of premature labour. Thus, it seems very promising to introduce into clinical practice the electrohysterography (EHG), as a method which enables noninvasive recording of readable bioelectrical signal of uterine muscle [1, 2].

Contraction of the uterine muscle cell is a result of the flow of ion currents which causes in the cell surrounding a change of electromagnetic field called the bioelectrical activity. In the signal of potentials difference recorded between two points on maternal abdominal wall, the bioelectrical activity during uterine contractions is manifested by

the bursts of action potentials. They occur synchronously with the mechanical uterine activity. Current knowledge concerning electrical uterine activity confirms that the complete information on this kind of activity can be obtained from the signal analyzed in the frequency band of  $0 \div 5$  Hz. Slow wave component represents occurrence of bursts, which occur synchronously with the mechanical uterine contractions. Fast wave component (the useful frequency band is  $0.1 \div 3$  Hz) is supposed to comprise information on electrophysiological properties of the uterine muscle. The EHG signal can be modeled as an action potentials fast wave whose amplitude is modulated by the slow wave corresponding to the contractions frequency. Such model allows us for a detection of the uterine contractions in the electrohysterogram and performing their time domain analysis in similar way as for conventional tocogram. The additional spectral parameters can be obtained exclusively from the analysis of the EHG fast wave. This feature of the electrohysterography makes it very promising approach for evaluation of the risk of premature labour on the early stage of pregnancy. In this paper we described an attempt to estimate the efficiency of a set of parameters obtained from the EHG signal analysis for evaluation of a risk of premature labour.

## II. METHODOLOGY

### A. Signal acquisition

The research system for simultaneous recording of mechanical and electrical uterine activity is presented in Fig. 1. The computerized system for fetal monitoring MONAKO [3] was used as the channel for measurement of the mechanical activity, whereas the electrical activity was acquired by means of the system for acquisition and analysis of bioelectric signals KOMPOREL [4].

The HP 1351 fetal monitor (Hewlett-Packard, USA) equipped with strain gauge transducer was used as an input device in the fetal monitoring system. The monitor is connected to the computer through the interface unit, which accepts different types of signal output connection including digital serial link and analog output.

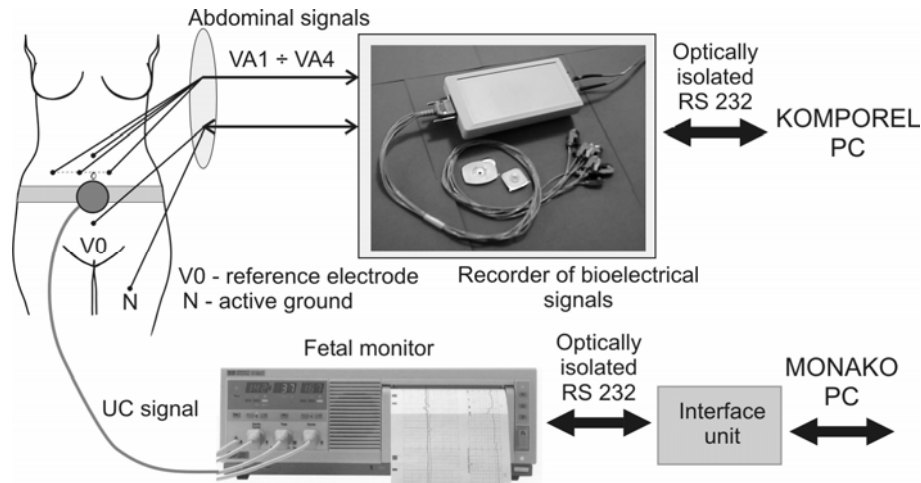


Fig. 1 System for simultaneous recording of mechanical and electrical uterine activity

Additionally, the interface unit assures the patient's safety complying with general international standards for medical equipment. Incoming signals of mechanical uterine activity (UC) are on-line analyzed and stored in the system database.

The system for acquisition and analysis of bioelectric signals being recorded on maternal abdomen surface consists of two separate parts: the microcontroller-based recorder of bioelectric signals and external computer. Recording circuit in a form of external, optically isolated module enables both the fetal ECG signal acquisition and electrical uterine activity by using the same signals being recorded on maternal abdomen surface. Entire circuit allows the amplification of recorded signals from the tens of microvolts up to a few volts level. Gain adjustment prevents the reaching of saturation state by the amplifiers in case of strong isoline drift. Moreover, the band-pass filters allow the change of lower cut-off frequency from 0.05 Hz to 1 Hz, thus also securing the circuit against too large low-frequency interferences. Selection of proper gain and cut-off frequency of filters can be done using virtual instrumentation screen at the beginning of monitoring taking into account the visual assessment of abdominal signals recorded. High cut-off frequency of filters is established at 150 Hz, hence at the sampling frequency of 500 Hz, the recorder circuit is fully protected against a possibility of aliasing occurrence.

Typical configuration of the abdominal electrodes comprises four electrodes placed around the navel and the reference electrode placed above the pubic symphysis. Additionally on the left leg, the common mode reference electrode is placed. Electrical activity of uterus is presented in all leads, however the strongest differential signal is obtained usually

in the channel which is formed by two electrodes placed in the vertical median axis of the abdomen.

### B. Material

Duration of one monitoring session was between 10 and 60 minutes (43 minutes on average), which allowed us to recognize from 15 to 25 contractions in each trace. Material was divided into two groups: Group I with 27 patients in physiological pregnancy between 27 and 40 gestation week, and Group II comprising 21 patients between 23 and 36 week with the symptoms of premature threatening labour.

### C. Signal analysis

In the fetal monitoring system the on-line analysis of UC signal relies on determination of quantitative parameters describing the detected uterine contractions: occurrence rate  $R_{UC}$ , duration  $D_{UC}$ , amplitude  $A_{UC}$  and area  $S_{UC}$  pattern. Detection relies on finding those segments in the UC signal whose amplitude exceeds the threshold level by 20 units for period longer than 30 seconds. The threshold level is obtained by adding the constant value of 10 units to the so called basal tone. The basal tone represents some resting strain exerted by the uterine muscle on the strain gauge transducer when contractions do not occur. The basal tone, which slowly changes during monitoring, is estimated basing on the analysis of UC values frequency distribution of the UC values [5].

In order to detect the contractions in electrohysterogram and to perform their classical time domain analysis, it is necessary first to extract the slow wave from acquired sig-

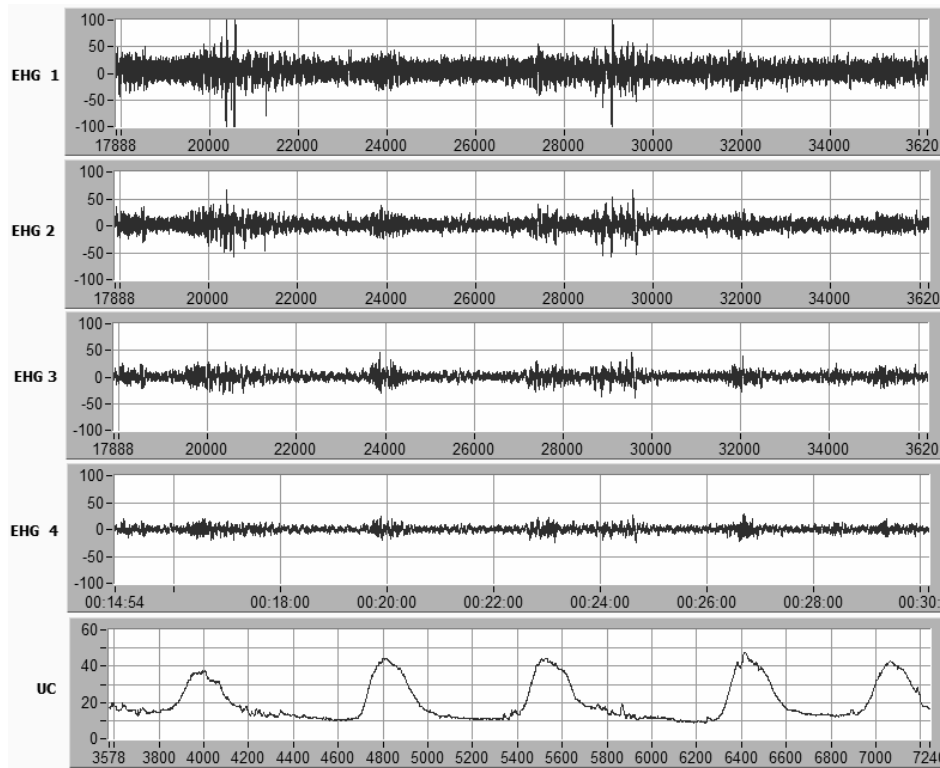


Fig. 2 Uterine electrical activity signals acquired from four abdominal leads, together with simultaneously recorded mechanical activity.

nal. The method of extraction of slow wave corresponding to UC signal is based on calculation of consecutive root-mean-square values in 60 s window stepped with 3 s. Unlike the mechanical activity signal, the amplitude of electrohysterogram strongly depends on a given patient. Therefore, the algorithm applied for contractions detection should to compensate the amplitude variation between electrohysterograms [5]. Contractions detected from EHG are described by the following quantitative parameters: occurrence rate  $R_{EHG}$ , duration  $D_{EHG}$ , amplitude  $A_{EHG}$  and area  $S_{EHG}$ .

After calculation of pattern timing parameters the segments with bursts of action potentials are selected from the raw EHG signal. They are used to determine parameters exclusive for electrical uterine activity: signal power  $P$ , median frequency  $F_{med}$ , maximum power frequency  $F_{max}$  and contraction intensity  $I$ .

### III. RESULTS

General descriptive statistics determined for quantitative parameters of contractions detected both in mechanical (UC) and electrical (slow wave component of EHG) signals

is presented in Table 1. As it can be seen, statistically significant differences were obtained between corresponding parameters in each group. In the Group I (women in physiological pregnancy) such conclusion concerns occurrence rates ( $R_{EHG}$  and  $R_{UC}$ ), durations ( $D_{EHG}$  and  $D_{UC}$ ), and finally areas of detected contractions ( $S_{EHG}$  and  $S_{UC}$ ). Whereas in the Group II (patients with symptoms of premature threatening labour) only occurrence rates ( $R_{EHG}$  and  $R_{UC}$ ) show significant differences. The obtained results confirm different characteristics of mechanical and electrical uterine activity. Additionally, in each group the contraction occurrence rate is higher for electrical activity, which suggests that the electrohysterography is indeed more sensitive method for uterine contractions detection.

In the next stage the significance of differences concerning contraction parameters between investigated groups was estimated. When analyzing the results presented in Table 2 it can be noticed that there are so called common contraction parameters (possible to be obtained from both electrical and mechanical uterine activity) which differ the groups. For the EHG analysis, they are  $A_{EHG}$  and  $S_{EHG}$  while for the UC analysis only  $A_{UC}$  (statistical significance  $< 0.05$ ). However the contraction amplitudes both from electrical and mechanical approaches are quite inaccurate measures,



Table 1 Descriptive statistics describing quantitative parameters of contractions in both groups

Parameter	Mean $\pm$ SD	Min	Max	
Group I				
R EHG [1/10 min]	3.2 $\pm$ 0.6	2.4	4.4	*
R UC [1/10 min]	1.9 $\pm$ 0.9	0.2	3.6	
D EHG [s]	88.6 $\pm$ 17.6	61.4	122.4	*
D UC [s]	78.2 $\pm$ 34.0	38.0	211.3	
A EHG [ $\mu$ V]	33.8 $\pm$ 53.6	3.8	285.4	
A UC [-]	18.8 $\pm$ 13.8	3.7	63.7	
S EHG	1815 $\pm$ 3011	186	16140	*
S UC	1095 $\pm$ 1305	87	6675	
Group II				
R EHG [1/10 min]	3.4 $\pm$ 0.9	2.0	6.3	
R UC [1/10 min]	2.4 $\pm$ 1.2	0.5	5.1	*
D EHG [s]	85.1 $\pm$ 20.5	48.4	129.2	
D UC [s]	84.6 $\pm$ 30.6	38.5	166.8	
A EHG [ $\mu$ V]	62.2 $\pm$ 75.3	2.3	320.8	
A UC [-]	31.7 $\pm$ 21.3	7.7	94.0	
S EHG	2841 $\pm$ 2809	200	10766	
S UC	1531 $\pm$ 1009	250	3813	

\* means statistical significance ( $p < 0.05$ )

Table 2 Statistical significance of the particular parameters differentiating the investigated groups

Parameter	Group I Mean $\pm$ SD	Group II Mean $\pm$ SD	I – II ( $p < 0.05$ )
UC			
R UC [1/10 min]	1.9 $\pm$ 0.1	2.4 $\pm$ 1.2	–
D UC [s]	78.2 $\pm$ 34.0	84.6 $\pm$ 30.6	–
A UC [-]	18.8 $\pm$ 13.8	31.7 $\pm$ 21.3	–
S UC	1095 $\pm$ 1305	1532 $\pm$ 1009	+
EHG			
R EHG [1/10 min]	3.2 $\pm$ 0.6	3.4 $\pm$ 1.0	–
D EHG [s]	88.6 $\pm$ 17.6	85.1 $\pm$ 20.5	–
A EHG [ $\mu$ V]	33.8 $\pm$ 53.6	62.2 $\pm$ 75.3	+
S EHG	1815 $\pm$ 3011	2841 $\pm$ 2809	+
I	17.5 $\pm$ 3.7	18.0 $\pm$ 4.5	–
P	1823 $\pm$ 5390	7492 $\pm$ 18098	+
F med [Hz]	0.30 $\pm$ 0.11	0.35 $\pm$ 0.10	+
F max [Hz]	0.25 $\pm$ 0.18	0.32 $\pm$ 0.29	–

+ means statistical significance ( $p < 0.05$ )

because they depends on the measurement conditions and a given patient. When applying the electrohysterography we can use exclusive parameters. Two of them: contraction power (P) and median frequency ( $F_{med}$ ) can be used to distinguish between groups of patients in physiological pregnancy and at risk of preterm threatening labour.

## IV. CONCLUSIONS

Identification of these pregnant women who are at risk of premature threatening labour leads to an enhanced perinatal surveillance which should allow for efficient tocolitic treatment and stimulation of fetal lungs growth. Therefore, there is still a need for development of novel, more accurate and commonly accessible methods for monitoring early symptoms of the premature increase of the uterine activity. Since the electrohysterography provides complete information on functioning of uterine muscle it may fulfill these requirements and play a leading role in modern perinatology. Our study has shown that the noninvasive electrohysterography ensures higher sensitivity and specificity for recognition of uterine contraction activity in comparison to manual palpation and classical mechanical method.

## ACKNOWLEDGMENT

This work was supported in part by the Ministry of Sciences and Higher Education resources in 2007-2009 under Research Project R1302802.

## REFERENCES

- Maner W L et al. (2003) Predicting term and preterm delivery with transabdominal uterine electromyography. *Obstet Gynecol* 101: 1254–1260
- Harrison A, Crowe J A, Hayes-Gill B R, van Wijngaarden W (1995) Use of the electrohysterogram for uterine contraction monitoring during labour, *Proc. 3rd Eur. Conf. on Eng. and Med.*, 1995, pp. 90.
- Jezewski J et al. (2006) Centralised fetal monitoring system with hardware-based data flow control, *Proc. of III Int. Conference MEDSIP, Glasgow, VII 2006*, pp. 51–54.
- Matonia A et al. (2005) Computer aided fetal monitoring system using noninvasive electrocardiogram, *IFMBE Proc. vol.9, 13th Nordic Baltic Conference Biomed. Eng. Med. Phys.*, Umea, Sweden, 2005, pp. 313–314.
- Jezewski J, Horoba K, Matonia A, Wróbel J (2005) Quantitative analysis of contraction patterns in electrical activity signal of pregnant uterus as an alternative to mechanical approach. *Physiol Meas* 26: 753–767

Author: Janusz Jezewski  
 Institute: Institute of Medical Technology and Equipment  
 Street: Roosevelt 118  
 City: Zabrze  
 Country: Poland  
 Email: jezewski@itam.zabrze.pl

# Comparison of DT-CWT Based Rotation Variant and Invariant Methods on Tissue Characterization

D.B. Aydogan<sup>1</sup>, M. Hannula<sup>1</sup>, T. Arola<sup>1</sup>, P. Dastidar<sup>2</sup> and J. Hyttinen<sup>1</sup>

<sup>1</sup> Tampere University of Technology/Department of Biomedical Engineering, Tampere, Finland

<sup>2</sup> Tampere University Hospital/Department of Radiology, Tampere, Finland

**Abstract** — The goal of this study is to compare the effect of rotation variance on dual-tree complex wavelet transform (DT-CWT) based tissue characterization methods. Rotation variant features are especially useful when estimating orientations of textures. On the other hand, since tissues can turn and orient themselves on different directions, in segmentation or classification problems, rotation invariance becomes important. The methods are tested on two texture compositions from the Brodatz texture database and two actual magnetic resonance (MR) images. Results show that, the classification performance is not significantly affected by using rotation variant or invariant methods. On the other hand, regarding segmentation, rotation invariant DT-CWT features performed slightly better compared to rotation variant features.

**Keywords** — texture analysis, tissue characterization, DT-CWT

## I. INTRODUCTION

Tissue characterization in biomedical image analysis has various applications such as detecting pathologies [1], segmenting anatomical regions [2] and tracking changes in tissues [3]. These applications are developed based on the extraction of texture features. Although, image textures do not have a strict mathematical definition, they can be regarded as visual patterns composed of entities or sub-patterns that have characteristic brightness or shape.

Directional properties of textures are commonly used to describe them. Extractions of directional components have been done using several signal processing methods. Among these; steerable wedge filters [4], rotated Gabor filters (GT) [5] and discrete wavelet transform (DWT) [6] are the most common approaches. GT has given considerably good results compared to DWT. The advantage of GT over DWT is that; it can be implemented for different scales which are strongly oriented at various directions. However GT is computationally expensive and costly to use compared with the DT-CWT.

The transform that has been used in this work is DT-CWT which is a recent wavelet method. DT-CWT aims to solve the drawbacks such as shift variance and poor directional selectivity associated with the commonly used DWT.

Consecutively, DT-CWT's approximate shift invariance property and high directional selectivity makes it an excellent candidate for texture analysis applications. Texture feature extraction based on DT-CWT has proven its success in several applications [7-10].

The high directional selectivity of DT-CWT is a desired property for texture analysis. If this property is used appropriately, it not only enables good characterization but also helps to estimate the orientations for directional textures. Most of the segmentation problems require the need of rotation invariant features since it is generally desired to categorize rotated samples of the same texture in the same group. A similar reasoning goes for classification of textures as well.

There are various ways of extracting texture features using DT-CWT. The very first studies were done by Hatipoglu, Mitra and Kingsbury in [11], which aimed to describe textures for image retrieval from large databases. Following this, Hill and Bull proposed a method to extract rotation invariant DT-CWT texture features in [12]. In this work, we compare these methods on four different images. Two of them are artificial texture compositions from Brodatz texture database [13] and the other two are actual MR images. For the segmentation problem, T2 weighted MR image of human brain and for the classification problem T1 weighted MR image of wrist is used.

With this work, we demonstrated the effect of using rotation variant and rotation invariant DT-CWT based texture feature extraction methods on segmentation and classification of tissues. Classification error is a widely used measure in the comparison of texture feature extraction methods. Taking the advantage of using Brodatz textures; which are common test images used in texture studies, the performance of the methods are also compared with other studies [14] and it is shown that both rotation variant and invariant

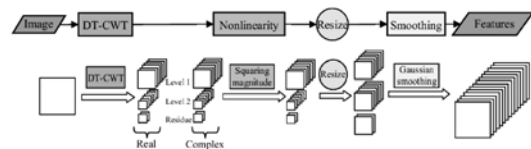


Fig. 1 DT-CWT based texture feature extraction (up to 2<sup>nd</sup> level)

DT-CWT methods are appropriate candidates for tissue characterization.

## II. MATERIALS AND METHODS

### A. Rotation variant DT-CWT features

The common approach of filter based texture analysis is the calculation of local energies by the application of nonlinearity followed by a smoothing function, Figure 1. Prior to this operation a filter is used to enhance characteristic features of textures. DWT based texture analysis inherently regards the problem of describing textures at coarser and finer scales due to multi-resolution analysis. Therefore it is capable of fetching texture similarities at different scales.

However, shifts in the input signal cause drastic changes in the DWT coefficients and DWT has limited directional selectivity for multi-dimensional data. To overcome these two restrictions, Kingsbury suggested designing an analytic wavelet transform [15]. This relatively recent wavelet transform is named the DT-CWT and it is proven to have approximate shift-invariance property. DT-CWT also has a higher directional selectivity compared to DWT; it can differentiate 6 different orientations on 2-D plane,  $\pm 15^\circ$ ,  $\pm 45^\circ$ ,  $\pm 75^\circ$ . High directional selectivity of DT-CWT is a desired property for texture analysis.

DT-CWT feature set for each pixel in the image is composed of 6 oriented features at a certain level of decomposition. These 6 features are denoted by  $f_\vartheta^L(x, y)$  for  $x = \{0, \dots, M-1\}$  and  $y = \{0, \dots, N-1\}$  ( $M, N$  being the dimensions of the image) defined for  $\vartheta = \{+15^\circ, +45^\circ, +75^\circ, -75^\circ, -45^\circ, -15^\circ\}$  and  $L$  being the level of DT-CWT decomposition.

2 more features are calculated using the residual images and they are denoted by  $f_{R1}^L(x, y)$  and  $f_{R2}^L(x, y)$ . The final feature set,  $f^L(x, y)$ , can be expressed in the following way:

$$f^L(x, y) = f_{R1}^L(x, y) \cup f_{R2}^L(x, y) \cup \bigcup_{p=1}^L f_\vartheta^p(x, y) \quad (1)$$

### B. Rotation invariant DT-CWT features

Rotation invariant texture features for a pixel at decomposition level  $L$  can be obtained by applying the discrete Fourier transform (DFT) on the oriented rotation variant feature set  $f_\vartheta^L(x, y)$  [12]. The magnitudes of the DFT coefficients are used as rotation invariant features.

In order to use DFT, the features in the set  $f_\vartheta^L(x, y)$  must be sorted. Let  $\tilde{f}^L[n]$  denote the sorted feature set which is in the following form:

$$\tilde{f}^L[n] = \{f_{+15}^L, f_{+45}^L, f_{+75}^L, f_{-75}^L, f_{-45}^L, f_{-15}^L\} \quad (2)$$

Applying DFT on  $\tilde{f}^L[n]$  yields:

$$F^L[k] = \sum_{j=0}^5 \tilde{f}^L[j] e^{\frac{-2\pi i k j}{6}} \quad (3)$$

$F^L[k]$  on equation (3) is defined for  $k = 0, 1, 2, 3, 4, 5$  however the phase information is not used for rotation invariant analysis, therefore after the magnitudes are calculated, the  $F^L[k]$  values for  $k = 4, 5$  are omitted. (Note that,  $|F^L[k]|$  is symmetric with respect to the third harmonic.) This scheme leaves behind 4 features for a particular decomposition level  $L$ , without the two residual images; for the second level decomposition total number of rotation invariant features is 8 and this number is 12 for third level.

### C. Test images

Tests are done on four different images. Two of them are artificial texture compositions from Brodatz texture database [1], Figure 2, and the other two are actual MR images, Figure 3. Brodatz texture compositions are used for both classification and segmentation tests. The ground truth for these images is also given in Figure 2. For the segmentation problem, T2 weighted MR image of human brain and for the classification problem T1 weighted MR image of wrist are used.

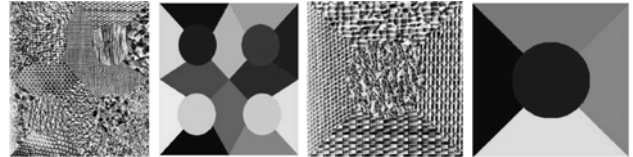


Fig. 2 Brodatz textures used in tests

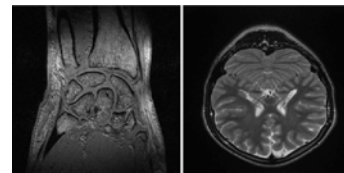


Fig. 3 T1 MRI of wrist and T2 MRI of brain

### III. RESULTS

#### A. Classification results

Given a certain region in an image, the supervised classification problem is assigning labels to each pixel a category that has already been described to the system. In this work the classifications are done based on a simple supervised method (*k*-means clustering). For the sake of fair comparison between rotation variant and invariant methods, training samples are chosen separately, instead of cropping them from the composed images. Same approach is followed for the training samples of the classification problem in the wrist image.

Texture features for classification are calculated based on the methods explained in the previous chapter. For each pixel, texture characteristic features are calculated up to DT-CWT level 2 and each pixel is classified according to their features' Mahalanobis distance to training data. A pixel is assigned the label of the training category which has the smallest distance.

Gaussian smoothing function is used throughout the tests with a constant standard deviation value of  $\sigma=8$ . A smoothing function with a window size of 27x27 is used for the Brodatz texture compositions. Classification results for Composition-1 and Composition-2 are shown in Figure 4.

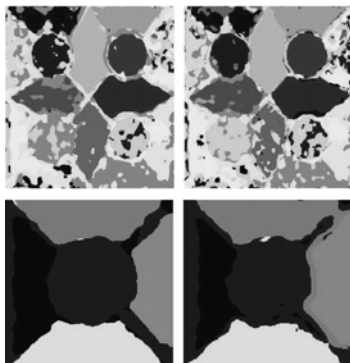


Fig. 4 Classification results for Composition-1 and Composition-2 based on rotation variant (left) and rotation invariant (right) features

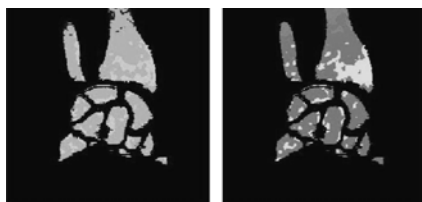


Fig. 5 Classification of bone in T1 MRI of wrist 2 based on rotation variant (left) and rotation invariant (right) features

Table 1 Classification errors

Classification errors	Rotation variant DT-CWT	Rotation invariant DT-CWT
Composition-1	39.99	37.52
Composition-2	18.46	21.94
Wrist image	23.79	28.23

For the wrist data, a smoothing function with a window size 13x13 is used. The results of the classification for are shown in Figure 5. The overall classification errors are given in Table 1.

#### B. Segmentation results

Conventional active contour based segmentation methods are mostly based on intensity levels or edges; which might both vary for textures. To address this issue, we used the information of texture similarity when segmenting regions. For this purpose, a modification has been done on Gradient Vector Flow (GVF) snakes.

Given an initial contour; in stead of using the original image to calculate an external field, a map of Mahalanobis distance is calculated; which gives a measure of texture similarity of the given region to the rest of the image. Tex-

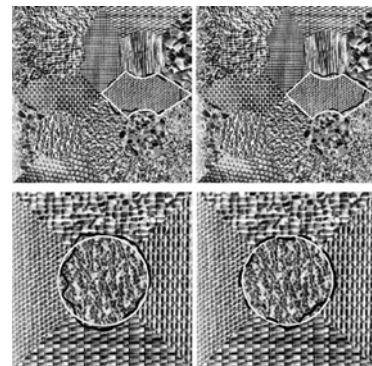


Fig. 6 Segmentation results for Composition-1 and Composition-2 based on rotation variant (left) and invariant (right) features

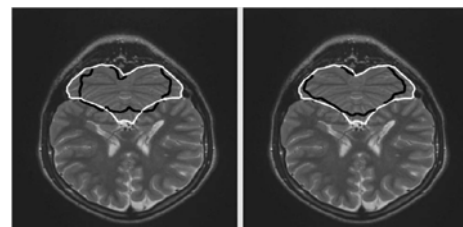


Fig. 7 Segmentation result for cerebellum seen in T2 MRI of brain based on rotation variant (left) and invariant (right) features

Table 2 Segmentation performances

Tanimoto ratio	Rotation variant DT-CWT	Rotation invariant DT-CWT
Composition-1	0.84	0.88
Composition-2	0.88	0.92
Brain image	0.75	0.81

ture features are calculated based on the methods given in the previous chapter. The shape of the smoothing function and the window size are also kept the same as the classification tests for the wrist.

In Figure 6 and 7, segmentation results are given for test images. White contours show the true segmentation, whereas darker lines are the calculated results.

The results of segmentation are compared using the Tanimoto ratio; corresponding values are given in Table 2.

#### IV. DISCUSSIONS

Filter based texture analysis is a common approach and studied well. Taking the advantage of testing DT-CWT based methods on Brodatz texture compositions, which are studied before in [14], performances can be compared with other methods as well, Table 3.

Table 3 Classification errors

Method	Composition-1	Composition-2
Laws filter	48.3	18.6
Ring/wedge filters	43.8	14.6
Dyadic Gabor filter banks	60.1	10.7
DCT	40.9	13.2
Wavelet frames	38.2	8.7
Rotation variant DT-CWT	39.9	18.4
Rotation invariant DT-CWT	37.5	21.9

It is clearly seen from the table that the classification of Composition-1 is rather hard compared to Composition-2 and the best performance for this test is obtain by using DT-CWT based rotation invariant method.

#### V. CONCLUSIONS

In this work, we compared rotation variant and rotation invariant DT-CWT texture features. Although there is not a clear winner for tissue classification and segmentation applications; rotation invariant features, overall, showed slightly better results.

#### REFERENCES

1. Mathias J, Tofts P, and Losseff N (1999) Texture analysis of spinal cord pathology in multiple sclerosis. *Magnetic Resonance in Medicine*, 42:929–935
2. Lu R and Shen Y (2006) Automatic ultrasound image segmentation by active contour model based on texture. *CICIC Proceedings of the First International Conference on Innovative Computing*, vol. 2, pp 689–692
3. Wang L, Tong L, Liu X, Li X (2005) Study on Normal Appearing White Matter of Multiple Sclerosis by Texture Analysis and Modeling with MRI. *IEEE Int. Conference on Information Acquisition June 27 - July 3, 2005, Hong Kong and Macau, China*, pp. 95-98
4. Coggins J. M, Jain A.K (1985) A Spatial Filtering Approach to Texture Analysis. *Pattern Recognition Letters*, 3:195–203
5. Jain A. K, Farrokhnia F (1991) Unsupervised Texture Segmentation Using Gabor Filters. *Pattern Recognition*, 24:1167-1186
6. Mallat S. G (1989) A Theory for Multiresolution Signal Decomposition: The Wavelet Representation. *IEEE Transactions on Pattern Analysis and Machine Intelligence*, 2:674-693
7. Rivaz P and Kingsbury N (1999) Complex wavelet features for fast texture image retrieval. *ICIP Proc. International Conference, Kobe*, vol 1, pp 109–113
8. Mumtaz A, Gilani S and Jameel T. (2006) A novel texture image retrieval system based on dual tree complex wavelet transform and support vector machines. *ICET International Conference, Peshawar*, pp 108–114
9. Sun J, Gu D, Zhang S, and Chen Y. (2004) Hidden markov bayesian texture segmentation using complex wavelet transform. *Vision, Image and Signal Processing, IEE Proceedings*, 151:215–223
10. Vasuki S and Ganesan L. (2005) Segmentation of color textured images using dual tree complex wavelet features and fuzzy clustering. *Computational Intelligence and Multimedia Applications, Sixth International Conference*, pp 309–314
11. Hatipoglu S, Mitra S. K, and Kingsbury N. (2000) Image texture description using complex wavelet transform. *International Conf. on Image Processing Proceedings, Vancouver*, vol. 2, pp 530–533
12. Hill P. R, Bull D. R and Canagarajah C. N. (2000) Rotationally invariant texture features using the DT-CWT *International Conf. on Image Processing Proceedings, Vancouver*, vol. 3, pp 901–904
13. Brodatz P. (1966) *Textures: A Photographic Album for Artists & Designers*. New York: Dover
14. Randen T and Husoy T. H. (1999) Filtering for texture classification: a comparative study. *IEEE Transactions on Pattern Analysis and Machine Intelligence*, 21:291–310
15. Selesnick I. W, Baraniuk R. G. and Kingsbury N. (2005) The dual-tree complex wavelet transform. *IEEE Signal Processing Magazine*, 22(6):123–151

Address of the corresponding author:

Author: Baran Aydogan  
 Institute: Department of Biomedical Engineering  
 Street: Finn-Medi 1 L 4, Biokatu 6  
 City: FI-33520 Tampere  
 Country: Finland  
 Email: baran.aydogan@tut.fi

# CdZnTe Pixel Detectors for Medical Imaging

A.A. Bulycheva, I.E. Tsirkunova and V.V. Gostilo

Bruker-Baltic, Riga, Latvia

**Abstract** — The paper analyzes results of several projects devoted to manufacturing of CdZnTe detectors for medical applications. The detectors were manufactured by standard technology developed at Bruker-Baltic for pixel detectors manufacturing. The dimensions of contacts pads for medical imaging is  $(50\div 300)\mu\text{m}$  and their quantity at such detectors may be up to thousand and more. It is obvious that contacts as such detectors should stand the machine assembly. The most advanced contacting method is a flip-chip technology applying an indium or polymer bumps. Current-voltage (I-V) characteristics of pixel detectors have been measured. Technologies provided at room temperatures for separate pixels in real switched-on state leakage currents 10-50 pA at detectors bias 500V. Interpixel resistivity on developed structures with gap 50-100  $\mu\text{m}$  was 40-300 GOhm at voltage 10 V. Spectrometric characteristics measurements at room temperature were made. At optimal temperatures we have obtained energy resolution (2-3)% and (14-15)% at energies 59.6 keV and 5.9 keV respectively.

**Keywords** — CdZnTe pixel detectors, room temperature semiconductor detectors.

## I. INTRODUCTION

Multidetector structures, created in one semiconductor crystal, like pixel arrays, have found wide application in imaging systems for X-ray medicine (digital mammography, dental, osteoporosis), astronomy and technical areas [1-2].

Semiconductor single crystals of CdZnTe (Cadmium Zinc Telluride) are important material for the development of X- and gamma-ray detectors as medical imaging devices. CdZnTe radiation detectors have the advantages of a large absorption coefficient, compact size and room temperature operation.

There are many examples of the use of CdZnTe detectors in medical imaging and diagnostics, ranging from simple x-rays carried out in a dentist's office to cardiac angiography, bone densitometry measurements, and the use of nuclear medicine to pinpoint areas of activity within the brain to help characterize conditions such as epilepsy. In addition, the medical imaging community is interested in developing large area CdZnTe detector arrays.

The main requirements to semiconductor CdZnTe crystals for detectors are high values of charge carriers transport characteristics (the product of mobility by life time), high specific resistance, as well as high level of crystals homogeneity, lack of impurities, crystal borders, twins.

Manufactured detectors should have high spectrometric characteristics, low level of leakage current to avoid additional noises and high stability of the available characteristics by time. The execution of these requirements depends on crystal quality, crystal processing and contacts manufacturing technology.

It is obvious that contacts at such pixel detectors should stand the machine assembly.

The given work is devoted the investigations of pixel CdZnTe detectors characteristics for medical applications.

## II. INITIAL CRYSTALS CHARACTERISTICS

For manufacturing of CdZnTe pixel detectors we use the crystals purchased from eV-Products ( $\mu\tau_e=5\times 10^{-3}\text{ cm}^2/\text{V}$ ,  $\rho=3\times 10^{10}\text{ }\Omega\text{cm}$ ) [3] and Yinnel Tech ( $\mu\tau_e=(3-5)\times 10^{-3}\text{ cm}^2/\text{V}$ ,  $\rho=(1-3)\times 10^{10}\text{ }\Omega\text{cm}$ ) [4]. Generally we carry out the input inspection of crystals also, inspecting  $\mu\tau(e)$  value, but mainly their uniformity and performance stability. Room temperature inspection test of CdZnTe crystals before making pixel detectors is our obligatory procedure carried out in order to determine the quality of the crystals and eliminate the possibility of poor results at the finish.

For this purpose we fabricate planar detector structures based on these crystals, which we use for performance testing. The electrodes to these crystals for the inspection test were deposited using the standard technology from a solution of hydrochloroaurate acid.

Current – voltage (I-V) characteristics have been used for stability evaluation. Crystals with linear I-V characteristics only were sampled for pixel detectors manufacture. As a rule, detectors with non-linear I-V characteristics were non-stable in time [5].

At the stage of input inspection of crystals we pay significant attention to the inspection of the homogeneity of the supplied crystals. In fact the homogeneity has a strong influence of the array characteristics from pad to pad. Generally, the applied CdZnTe crystals have inclusions, crystalline borders and twins that may considerably deteriorate pixel detectors characteristics, namely, results reproducibility from pad to pad. The life time value  $(\mu\tau)_e$  and mobility  $\mu_e$  were measured with a modified “time of flight” method using alpha-particles [6]. A part from that, the shape of alpha-spectra at low voltages ( $<100\text{V}$ ) was

examined, which gave us qualitative indication as to the homogeneity degree of the crystals.

After the inspection test planar solid contacts were removed from crystals to prepare them for making pixel contacts.

### III. THE TECHNOLOGICAL OPERATION

The simplified typical technological route of the fabrication of such arrays consists of the following technological operations:

- the cutting of crystals,
- the input inspection of defects and parameters of the material;
- the lapping and the polishing of the selected crystals;
- the chemical etching;
- the photolithography;
- the deposition of contact pads;
- the output control of detector crystal parameters;
- the assembly of the detectors;
- the measurement of final detectors performance.

At the crystals cutting there are a large number of defects distributed in depth on the boundary layer. The method and the quality of the cutting have great impact on the depth of this layer and concentration of the defects in it. For the cutting of CdZnTe crystals we apply wire sawing which, as it is stated [7], makes the damaged boundary layer of the smallest depth and provides the minimal quantity of the wastes of the expensive detector materials.

After cutting the semiconductors crystals are lapped and polished to delete the defects of the surface arising at the cutting. We have described this rather standard operation for CdZnTe in Refs. [5, 8]. Crystals can be processed either manually or automatically.

The chemical etching improves the crystal surface after lapped and polishing. In semiconductor surface treatments, the universal solutions of the bromine-ethanol system are used.

The multidetector structure can have hundreds and even thousands of pads. Such topology can be created only by the photolithography method. The main type of the photoresist which we have applied at the photolithography is the liquid photoresist, which allows to get the spatial resolution up to 0.5  $\mu\text{m}$ .

The detailed analysis of the various methods of the contacts creation for the detectors based on CdZnTe was presented in [6]. At the fabrication of the first multidetector arrays we have fabricated the pads by gold deposition from a chloraurate acid. However, this method makes the deposited gold film of 100-200  $\text{\AA}$  only. Such thin metal

layer brings certain technological limitations for the detector assembly technology because the detector could be easily damaged. At the present time the method of the vacuum deposition of the gold-nickel-gold films of thickness about 0.2  $\mu\text{m}$  is applied.

### IV. THE OUTPUT CONTROL OF DETECTOR CRYSTAL PARAMETERS

The output control of pixel detector parameters, such as pixel-pixe, pixel-steering grid, pixel-guard ring and pixel-cathode resistances, carries out on the non-destructive probe station of inspection. The typical characteristics of CdZnTe detectors are represented in Fig.1 and Fig. 2.

At present technology provides interpixel resistivity from 100GOhm till  $(1\div 10)\text{TOhm}$  at voltage 10 V on the developed structures with gap 50-100  $\mu\text{m}$ .

Technologies provided at room temperatures for separate pixels in real switched-on state leakage currents 10-50 pA at detectors bias 500V. The leakage current depends from pads dimensions and decreases with pads dimension increases.

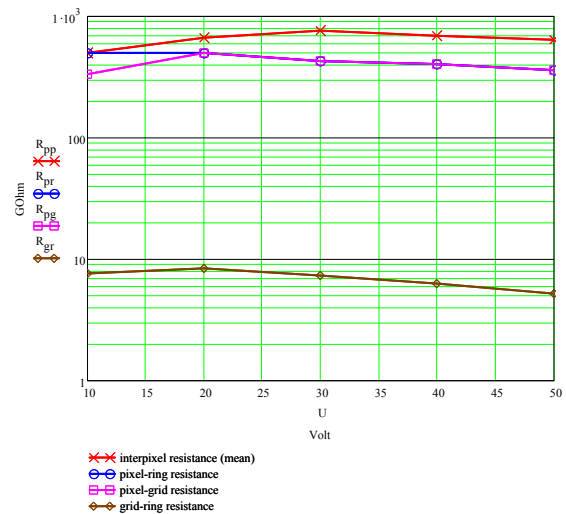


Fig. 1 Typical resistance-voltage dependence of CdZnTe detectors

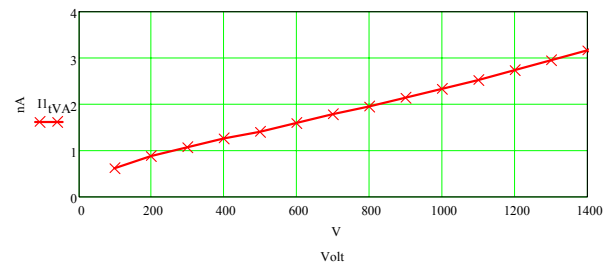


Fig. 2 The typical V-I dependence of CdZnTe detectors

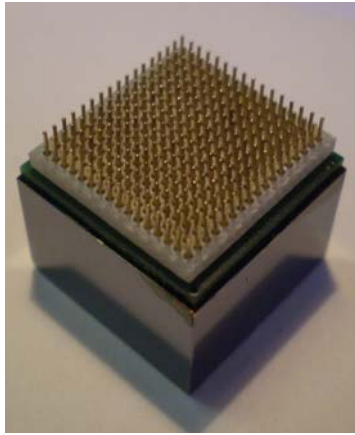


Fig.3 Assembled CdZnTe (32x32) pixels detector

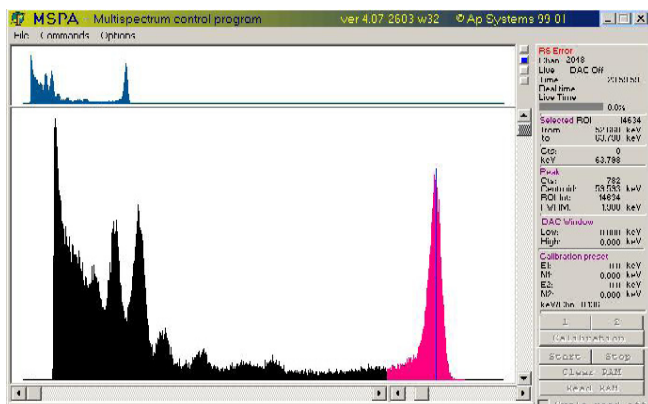


Fig. 4 Spectrum of Am-241 for single pixel of CdZnTe (32x32) pixels detector

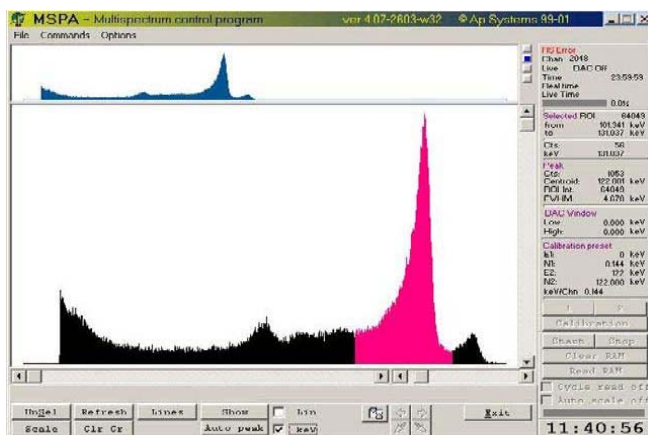


Fig. 5 Spectrum of Co-57 for single pixel of CdZnTe (32x32) pixels detector

## V. PRESSURE CONTACTS FOR PIXEL STRUCTURES

The first pixel detectors with the small number of pads we assembled using wire bonding of pads with gold wire [9].

At present when the number of pads on the detectors raised significantly the flip-chip technology is widely applied at the contact fabrication in segmented semiconductor elements, including layout for CdZnTe pixel detectors also [10-11]. At this technology electrical contact of detector pads and input of readout electronics is realized by indium or conductive glue bump bonds. Such technology has some undeniable advantages at the manufacturing of the detectors with great number of contact pads.

Due to high cost of the equipment specialized technological facilities only have such technology providing the assembling service for other companies. The CdZnTe (32x32) pixels detector fabricated by Bruker Baltic and assembled by Aguila Technologies [12] is present at the Fig.3.

## VI. SPECTROMETRIC

For the processing of signals from CdZnTe pixel detectors in medical imaging systems special multi channel ASICs are used. For testing of separate pixels spectrometric performance we connected them with the input of general charge sensitive preamplifier followed by spectrometric processor.

The typical energy resolutions for energies 60, 122 and 662 keV are 1.9 and 4.6 keV correspondingly.

Typical spectrums of Am-241 and Co-57 for CdZnTe pixel detector are presented on the Fig. 4 and Fig. 5.

## VII. CONCLUSIONS

All detectors were made by basic technology developed by Bruker-Baltic for pixels detectors. To achieve high interpixel resistance and spectrometric performance specially designed technological processes were used. For the interpixel resistance we obtained the value of about 100 GOhm till  $(1 \div 10)$  TOhm. All detectors based on the crystals grown by the eV-products and Yinnel Tech with various contact topologies has energy resolution 2-3% on energy 59.6 keV.

## REFERENCES

1. Arlt R, Brucher J, Gunnink R et al. (2001) Use of CdZnTe detectors in Hand-Held and portable isotope identifiers to detect illicit trafficking of nuclear material and radioactive sources, Proc. IEEE Nucl. Science Symp., Lyon, France, Conf. Rec., 2001, pp. 418-424
2. Hartley I, Arlt R (2003) Investigation of the peak shape parameter of CdZnTe detectors, Nucl. Instr. and Meth. A 485, 2001, pp. 498-502
3. www.evproducts.com



4. [www.yinnet.com](http://www.yinnet.com)
5. Stahle C, Shi Z, Hu K et al Proc. SPIE, vol. 3115, p.90
6. Gostilo V, Owens A, Bavdaz M et al (2001) 12<sup>th</sup> International workshop on room temperature semiconductor and X- and Gamma-ray detector, San Diego, USA, 2001, vol.1, pp.176-179
7. Zaporozhsky V, Lapshinov B (1988) Treatment of semiconductor materials, High school, Moskow
8. Owens A, Andersson H, Bavdaz M et al (2003) Development of compound semiconductors detectors for x- and gamma – rays spectroscopy, SPIE's 46<sup>th</sup> Annual Meeting, International Symposium on Optical Science and Technology, San-Diego, USA, 2001, p.244
9. Gostilo V., Ivanov V., Kostenko S et al (2001) Technological Aspects of Development of Pixel and Strip Detectors Based on CdTe and CdZnTe, Nucl. Instr. and Meth. A 460 (1), pp. 27-34
10. Barber H.B., Barret H.H., Augustine F.L. et al (1997) Journal of Electronic Materials, vol. 26, No. 6
11. Cuzin M., Glasser F., Marmet R., et al (1994) Proc. Of SPIE, vol. 2278, p.21
12. [www.aguilatech.com](http://www.aguilatech.com)

Author: A. Bulycheva  
Institute: Bruker-Baltic  
Street: Ganibu danbis 26  
City: Riga  
Country: Latvia  
Email: [czt@bruker-baltic.lv](mailto:czt@bruker-baltic.lv)

# The Analysis of Craniofacial Morphology in Posteroanterior View

K.-S. Cheng<sup>1,2</sup>, C.-H. Ou<sup>2</sup>, Y.-T. Chen<sup>3</sup>, J.-K. Liu<sup>4</sup> and C.-L. Kuo<sup>5</sup>

<sup>1</sup> Department of Information Engineering, Kun Shan University, Tainan Hsien, TAIWAN

<sup>2</sup> Institute of Biomedical Engineering, National Cheng Kung University, Tainan, TAIWAN

<sup>3</sup> Department of Electrical Engineering, Southern Taiwan University of Technology, Tainan Hsien, TAIWAN

<sup>4</sup> Department of Dentistry, National Cheng Kung University Hospital, Tainan, TAIWAN

<sup>5</sup> Department of Dentistry, Chi Mei Medical Center, Tainan Hsien, TAIWAN

**Abstract** — In this paper, a method for characterizing the morphological information of craniofacial structure using the tracings and cephalograms in posteroanterior view is proposed and the experimental results are analyzed. This is a retrospective study. In clinical practice of orthodontics, the cephalograms taken in lateral and posteroanterior views are often used. Here, the morphological analysis of craniofacial structure is characterized only in posteroanterior view. Firstly, the morphological feature parameters of cephalometric tracings are defined and extracted. Then, based on these parameters, the morphology of craniofacial structure in posteroanterior view is clustered using fuzzy c-means and ISODATA clustering method. In this study, the data sets of eighty tracings are investigated. From experimental results, the craniofacial structures are classified into six clusters. Each cluster has ten images, sixteen images, ten images, fifteen images, thirteen images, and sixteen images, respectively. The standard deviations for the landmark are all within 6 mm in each cluster. The morphological information can be further extended and used in cephalogram landmarking.

**Keywords** — Orthodontics, Morphological information, Craniofacial structure, Tracing.

## I. INTRODUCTION

Orthodontics is a field concerned with the study and treatment of malocclusions. During diagnosis and treatment, the morphological information plays an important role in clinical practice to orthodontists. The characterization of the morphology for craniofacial structure is a required step in cephalometric analysis. From the morphological information, any abnormal development of face such as the irregular arrangement of teeth, the disproportionate relationships of jaw, the sticking out of the mandible, and the cleft palate may be easily and precisely corrected [1].

Orthodontists usually obtain the morphological information of patients from cephalograms. The clinically available X-ray film for morphological analysis of craniofacial structure are in two views, that is the posteroanterior view (PA view) and the lateral view (LA view). Cephalometric tracing is a kind of manual measurement of craniofacial structure. It may reflect the morphological information from the

viewpoint of orthodontist. Thus, it is used for morphological analysis in this study. The tracing is a translucent paper made of acetate. After superimposing on the cephalogram, the feature curves and landmarks may be drawn and located manually.

Analysis of the cephalogram or tracing is based on a set of clinically useful feature points—landmarks. Cephalometry is a very important procedure to provide the measurement of craniofacial structure in orthodontics. It is a kind of measurement related to the geometric parameters defined by and related to the position of landmarks. In this study, the morphology of craniofacial structures of Chinese population in PA view is investigated. Afterwards, the characterized morphological information may then be applied to automate the cephalogram analysis.

## II. MATERIALS AND METHODS

In order to analyze the morphological information of craniofacial structure in PA view, the proposed method includes four parts. The first part is image acquisition. The tracings corresponding to the cephalograms that are drawn by orthodontists are scanned using the desk-top X-ray film scanner with the resolution of 150 dpi. This implies that 1 pixel is equal to 0.17 mm. The second part contains image processing for characterization of the morphological feature using a set of distances and angles. Based on these feature parameters, the morphologies of craniofacial structure are then clustered accordingly in the third part. The final part is system assessment. In this part, the spatial distribution of each landmark is statistically analyzed. The flow chart of the proposed image processing and morphological analysis is depicted in Fig. 1.

### A. Morphological feature extraction

How to characterize the morphological information with the useful and effective parameters is an important issue in this study. The outer contours with the tangent lines and the inner cavities of the eyes with the circles are the feature vectors proposed here. First of all, the feature vector for

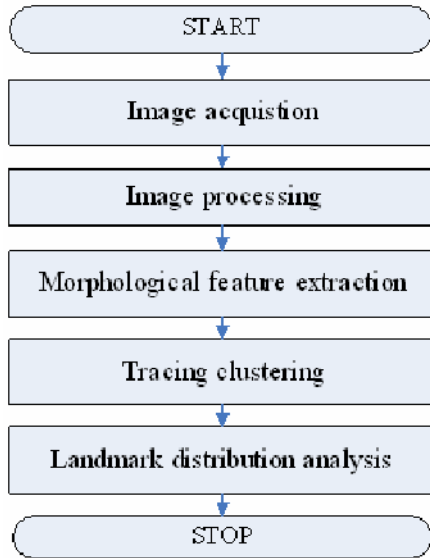


Fig. 1 Flow chart of proposed method

describing the craniofacial structure is extracted from each tracing. Firstly, the tracings are smoothed with the median filter to remove the noise. Then, the feature lines and circles are extracted easily.

Four lines and three circles are detected using Hough transform. The right and left orbits, and a largest circle tangential to the contours of mandible are fitted by circles. Then, the straight lines are fitted to the edge points detected for the hard tissues. There are three lines for the mandible, and one line passing through both the centers of right and left orbits. In addition, the angles for the intersecting points between two lines can be calculated using the inner product method.

As shown Fig. 2, the feature vector that combines the two angles for the contour lines of mandible, the one radius for the circle of mandible, and three distances from three centers of circle are obtained for each tracing. It is defined as (R, d1, d2, d3, Angle1, Angle2).

*B. Tracings clustering*

In this step, the fuzzy c-means (FCM) method is employed to cluster tracings based on the feature vector as described in the previous section. The FCM uses reciprocal distance to compute fuzzy weights[2], [3]. The basic idea of the application of FCM here is to represent the weights that minimize the total weighted mean-square error for each feature vector to its cluster centroid with a membership value between 0 and 1. The FCM update the center of cluster by using Eq. (1) and update the memberships of all feature vectors in all cluster by using Eq. (2)

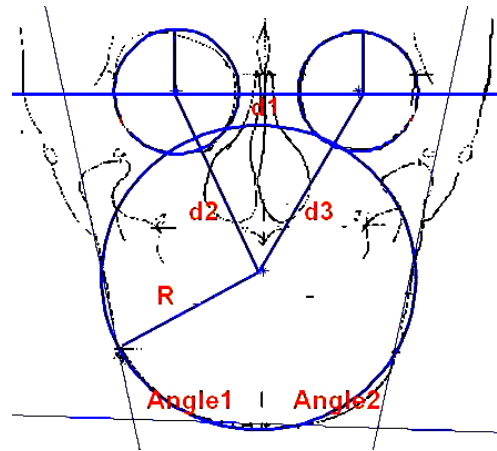


Fig. 2 Tracing and its feature parameters

$$V_i = \frac{\sum_{j=1}^N (u_{ij}^*)^m x_j}{\sum_{j=1}^N (u_{ij}^*)^m}, \text{ for } 1 \leq i \leq C \tag{1}$$

$$u_{ik}^* = \begin{cases} \frac{1}{\sum_{j=1}^C \left[ \frac{d_{ik}}{d_{jk}} \right]^{\frac{2}{m-1}}} & \text{if } I_k = \theta \\ 0 \forall i \in \tilde{I}_k & \text{if } I_k \neq \theta \\ \sum_{i \in I_k} u_{ik} = 1 & \text{if } I_k \neq \theta \end{cases} \tag{2}$$

The algorithm assigns a feature vector to a cluster according to the maximum weight of the feature vector over all clusters. For the FCM, the cluster number needs to be defined a priori. However, the cluster number of this data set is usually unknown in advance. Thus, a concept of ISODATA clustering method is combined in this study[4]. It allows the operation of cluster splitting and merging. When a cluster contains too many data number or has too large standard deviation of landmark distribution, it can be split. Likewise, a cluster contains a small data number, then it can be merged to other cluster.

*C. Landmark distribution analysis*

Once the tracings are classified, the spatial locations of the landmarks are statistically analyzed. In each cluster, all tracings are superimposed based on five landmarks (ZFL, ZFR, AgL, AgR, Me). The coordinate transform for the rotation and translation matrix between two tracings are

obtained using the Least-Square-Error (LSE) method proposed by [5], [6]. Afterwards, the standard deviation of the landmark distribution is computed and analyzed.

### III. EXPERIMENTAL RESULTS

#### A. Tracing analysis

In this study, a data set of eighty tracings in PA view for analysis is acquired from the Department of stomatology of National Cheng Kung University Hospital. The morphological feature parameters for eighty tracings are clustered using the fuzzy c-means clustering method with two prescribed constraints. They are the minimum data number (Nmin) in each cluster, and the maximum range (Rmax) of landmark distribution for the same cluster. Here, the initial cluster number is given as three, the Nmin is ten, and the Rmax is six mm. After processing, all the morphological feature parameters are classified into six clusters. Cluster 1 contains ten images, cluster 2 sixteen images, cluster 3 ten images, cluster 4 fifteen images, cluster 5 thirteen images, and cluster 6 sixteen images, respectively. All tracings in the same cluster are superimposed basing on five landmarks (ZFL, ZFR, AgL, AgR and Me) in a least squared error sense. Thus, a coordinate transformation matrix may be

obtained between any pair of tracings. Fig. 3 shows the superimposed results of tracings for all the clusters.

#### B. Landmark spatial distribution

The standard deviations of landmarks N, ANS, Me, ZFL, ZFR, JL, JR, AgL, and AgR are obtained from the tracings in each clusters as listed in Table 1. In this study, the circular range of landmark distribution is defined as 80% of standard deviation using Eq. (9). These ranges of landmarks are shown in Fig. 4 and the circular ranges of landmark distribution are listed in Table 2.

$$\text{Circular ranges} = M + 1.282 * S \tag{9}$$

where M denotes the means, and S the standard deviation.

Table 1 The standard deviations for the landmarks in each clusters

	cluster 1	cluster 2	cluster 3	cluster 4	cluster 5	cluster 6
N	1.7	4.4	4.4	2.6	3.0	3.0
ANS	1.8	2.8	3.6	2.8	3.1	2.9
Me	2.4	2.4	2.8	3.5	3.5	3.3
ZFL	5.0	3.7	5.6	3.3	4.3	3.4
ZFR	4.9	3.7	5.5	2.7	4.3	3.5
JL	2.8	3.3	3.9	2.5	3.7	3.0
JR	3.3	3.9	3.8	3.3	5.7	3.0
AgL	4.1	3.4	4.1	3.5	4.9	3.4
AgR	5.2	3.6	5.5	3.8	5.1	3.5

unit: mm

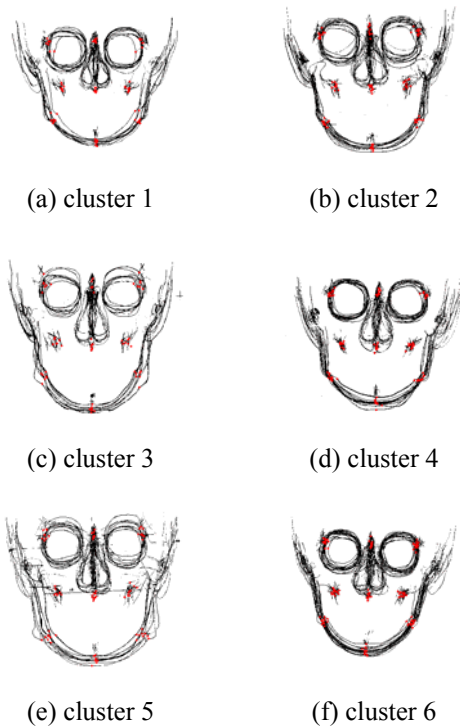


Fig. 3 The superimposed results of tracings

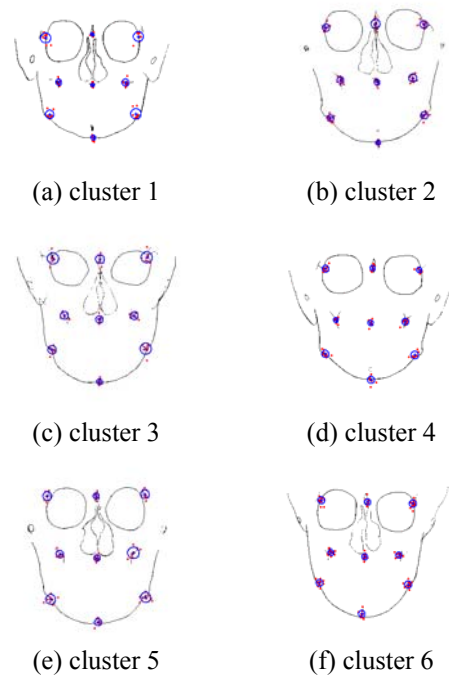


Fig. 4 The circular ranges of landmarks distribution

Table 2 The circular ranges of landmark distribution

	cluster 1	cluster 2	cluster 3	cluster 4	cluster 5	cluster 6
N	2.2	5.6	5.6	3.3	3.8	3.8
ANS	2.3	3.6	4.6	3.6	4.0	3.7
Me	3.0	3.1	3.6	4.5	4.5	4.2
ZFL	6.4	4.7	7.2	4.2	5.5	4.4
ZFR	6.3	4.7	7.1	3.5	5.5	4.5
JL	3.6	4.2	5.0	3.2	4.7	3.8
JR	4.2	5.0	4.9	4.2	7.3	3.8
AgL	5.3	4.3	5.2	4.5	6.3	4.4
AgR	6.7	4.6	7.0	4.9	6.5	4.5

unit: mm

#### IV. DISCUSSION AND CONCLUSION

In this study, the morphological information of the craniofacial structure in posteroanterior view from tracings clustering are obtained and analyzed. Firstly, the lines and circles based morphological features are extracted using Hough Transform. Then, the fuzzy c-means and ISODATA methods are applied to classify the tracings into six clusters. According to the clustering results, the standard deviations for the landmark distributions in each cluster are computed. From the experimental results, it is shown that the morphological information in PA view for a data set of eighty tracings is classified into six clusters. This data set does not include the normal subjects of Chinese craniofacial structure. The resulting clusters in tracings classification are heavily dependent on the sample number and six morphological feature parameters. In the future, it is needed to further investigate the better morphological feature parameters for representing the skull. Since the landmark distributions for each class are all within 6 mm, the proposed method may be good for the primary stage of cephalogram landmarking. From both the PA and LAT views of morpho-

logical information, an approach for 3D landmarking using the cone-beam dental CT may be feasible.

#### ACKNOWLEDGMENTS

This work is supported in part by the Minister of Economic Affairs, TAIWAN, ROC., under the Grant #96-EC-17-4-19-S1-053., and in part by the National Science Council, TAIWAN, ROC., under the Grant #NSC95-2221-E-006-218.

#### REFERENCES

1. A. Jacobson, *Radiographic Cephalometry: From Basics to 3-D imaging 2<sup>nd</sup> ed*, Chicago: Quintessence Publishing Co., 2006.
2. J. C. Bezdek, *Pattern Recognition with Fuzzy Objective Function Algorithms*, Plenum Press, 1981.
3. S. Theodoridis and K. Koutroumbas, *Pattern Recognition*. Academic Press, 2003.
4. G. H. Ball and D. hall, "ISODATA an iterative method of multivariate data analysis and pattern classification," *Proceedings of The IEEE International Communication Conference*, 1966.
5. K. S. Arun, T. S. Huang, and S. D. Blostein, "Least-square fitting of two 3-D point sets," *IEEE Trans. Patt. Ana. Mach. Intell.*, vol. 9, no. 5, pp. 698-700, 1987.
6. K.-S. Cheng, D.-S. Chen, W.-H. Tin, Y.-T. Chen, J.-K. Liu and C.-L. Kuo, "Morphological analysis of craniofacial structure," *Proc. IEEE Special Topic Conference on Information Technology Applications in Biomedicine*, Tokyo, JAPAN, Nov. 8-11, 2007.

Author: Kuo-Sheng Cheng  
 Institute: Institute of Biomedical Engineering,  
 National Cheng Kung University  
 Street: No.1, University Road  
 City: Tainan  
 Country: TAIWAN  
 Email: kscheng@mail.ncku.edu.tw

# VAMP – A Vision Based Sensor Network for Health Care Hygiene

P. Curran<sup>1</sup>, J. Buckley<sup>1</sup>, B. O’Flynn<sup>1</sup>, X. Li<sup>2</sup>, J. Zhou<sup>2</sup>, G. Lacey<sup>2</sup> and S.C. O’Mathuna<sup>1</sup>

<sup>1</sup> Microsystems Centre, Tyndall National Institute, Cork, Ireland

<sup>2</sup> Department of Computer Science, Trinity College Dublin, Dublin, Ireland

**Abstract** — Adequate hand-washing has been shown to be a critical activity in preventing the transmission of infections such as MRSA in health-care environments. Hand-washing guidelines published by various health-care related institutions recommend a technique incorporating six hand-washing poses that ensure all areas of the hands are thoroughly cleaned. In this paper, an embedded wireless vision system (VAMP) capable of accurately monitoring hand-washing quality is presented. The VAMP system hardware consists of a low resolution CMOS image sensor and FPGA processor which are integrated with a microcontroller and ZigBee standard wireless transceiver to create a wireless sensor network (WSN) based vision system that can be retargeted at a variety of health care applications. The device captures and processes images locally in real-time, determines if hand-washing procedures have been correctly undertaken and then passes the resulting high-level data over a low-bandwidth wireless link. The paper outlines the hardware and software mechanisms of the VAMP system and illustrates that it offers an easy to integrate sensor solution to adequately monitor and improve hand hygiene quality. Future work to develop a miniaturized, low cost system capable of being integrated into everyday products is also discussed.

**Keywords** — Hand-washing, Intelligent Vision System, FPGA, CMOS Image Sensor, Wireless Sensor Network.

## I. INTRODUCTION

According to the Health Service Executive (HSE) in Ireland and many other health-care institutions around the world, hand hygiene is the single most important intervention to prevent transmission of infection in health-care environments [1]. The cost of hospital acquired infections has been valued at €13 – 24 Billion in the EU [2] and \$5 Billion in the US [3] annually. It is internationally recognized that hands should be washed adequately before direct contact with patients and after any activity or contact that contaminates the hands [4]. It has also been shown that the technique used is the most important element of the hand-washing procedure to ensure hands are thoroughly cleaned [5]. Several hand hygiene guidelines published show that correct hand-washing should include six different poses [6] as depicted in Figure 1.

Advances in CMOS technology over the past 20 years have enabled designers to develop miniaturized, low power,

high resolution image sensors at a low cost. The ease at which CMOS sensors can be integrated with digital circuitry makes them a popular choice for use in the mobile phone camera and webcam markets. At the same time, the popularity of FPGA devices has seen a significant increase. This is due to their fast turnaround time, low start-up costs and ease of design. Increasing device densities have made large computational challenges feasible, allowing FPGAs to play a central processing role in system environments [7]. Unlike other sensing devices, image sensors generate large amounts of data due to the two-dimensional nature of their pixel array. Human analysis of raw image data can be ineffective for a wide variety of applications. By combining an image sensor with a processor, a high degree of intelligence can be added to a system. Local processing can be used to detect and track objects and extract high level information from their characteristics. Removing the need to transmit potentially irrelevant high density image data greatly reduces the bandwidth requirement of the system. The low bandwidth need of such a system makes it suitable to be integrated as part of a distributed wireless sensor network (WSN) where all system nodes connect with a single gateway node relaying relevant environmental events. WSNs are less intrusive than wired systems, simplifying the installation process of the system.

Depending on the image processing carried out; a vision based sensor network can be deployed to meet the requirements of a wide variety of application scenarios such as surveillance, environmental monitoring and smart meeting rooms [8]. In 2007, Hengstler et al. [9] developed a low power ARM7-based smart camera wireless node for applications in distributed intelligent surveillance. Vision algorithms to detect, track and acquire images of intruders in real-time were demonstrated. Over the last decade, several authors have addressed the issue of single hand gesture recognition [10] and in 2007 a PC based system for hand washing quality assessment based on six hand-



Fig. 1 Six poses from the hand-washing guidelines of the HPSC

washing poses was developed by Llorca et al. [11]. The system designed detects and tracks hand movements and classifies the motion carried out by performing the following steps:

- Skin Detection to locate hands
- Detection if hands are joined
- Region of interest (ROI) created around joined hands
- Analysis of hand motion within the ROI to produce a classification of the hand motion; e.g. Pose 1
- Classification of all motion to ensure adequate hand-washing has been achieved

In this paper an intelligent embedded vision system, VAMP comprising of a CMOS camera and FPGA processing node with Handle-C based algorithms is introduced as part of a distributed wireless sensor network with the aim of adequately monitoring hand-washing, based on image algorithms developed by Llorca [11].

This paper is organized as follows: Section 2 provides an overview of the VAMP system hardware and its architecture is discussed in detail. In Section 3 the software system comprising of the Handle-C based image processing algorithms is introduced. Section 4 details the integration and future deployment of the system. Finally, conclusions and future lines of research are presented in Section 5.

## II. HARDWARE SYSTEM ARCHITECTURE

The basic structure of the VAMP system node is shown in Figure 2. It can be broken into three main sections; CMOS image sensor, FPGA processor and micro-controller/Radio unit.

The CMOS image sensor chosen for the VAMP system is the OmniVision OV7649 Color CMOS CameraChip. The camera's low resolution (VGA/QVGA), adjustable sampling rate and sensor features meet all the specifications set by the PC based image algorithms. A dedicated CMOS camera interface PCB (see Figure 3) was designed to confirm compatibility with the image algorithms and to assist with image acquisition development. The camera sensor's low cost and efficient power consumption adds to its suitability for incorporation in a final user product.

When designing the first VAMP system prototype it was essential to choose an FPGA with high processing capability to meet the potentially high demands of a wide range of image algorithms. For this reason, the Xilinx Virtex-4 LX160 device was chosen. It offers high density, high performance logic architecture, advanced system clock management, integrated RAM and a large number of block I/Os with design potential in many application areas. Before the design of a VAMP specific system PCB, the Celoxica

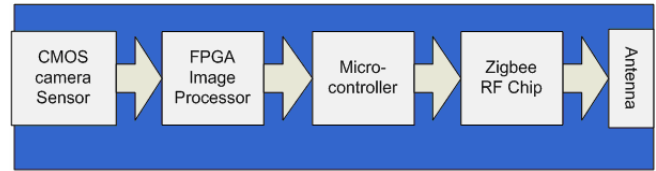


Fig. 2 VAMP system node block diagram

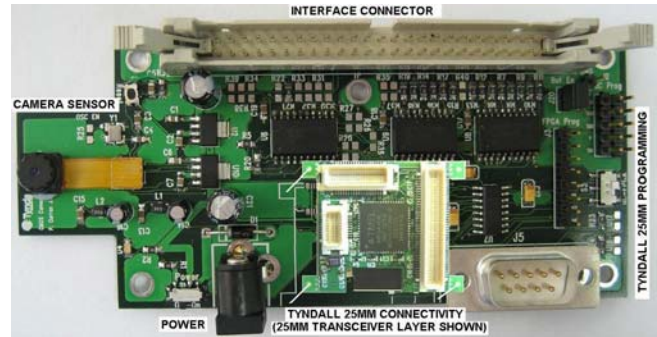


Fig. 3 CMOS camera interface PCB

RC340 Virtex-4 evaluation board was acquired. It combines the LX160 FPGA with a wide range of functionality giving users the ability to design Handle-C based system code. The RC340 was interfaced with the camera PCB, to assist in the development of the FPGA based image algorithms.

A low bandwidth, low power wireless transceiver is desirable for the VAMP system due to the minimal data bandwidth requirement of the system. ZigBee standard radios offer these features at a low cost. They also can easily be implemented on a microcontroller and support a number of different network topologies [12]. It was decided to use the Tyndall 25mm microcontroller/radio node layer developed in the Tyndall National Institute for the VAMP system network. The layer combines an Atmel ATmega128 microcontroller and an Ember EM2420 2.4GHz ZigBee standard RF transceiver. The Tyndall 25mm node is a modular based system which consists of a number of layers of different functionality that are stacked up on each other [13]. This unique design will allow for the addition of extra functionality to the VAMP system if required in the future.

The first system prototype combines the technologies summarized above with added functionality to produce an easy to use VAMP developmental platform. A detailed block diagram of the VAMP PCB architecture is shown in Figure 4. Included in the design is 72Mb of ZBT SRAM and 64Mb of non-volatile flash memory to meet any temporary frame buffering, image archival or algorithm needs of the system. Also included is 64Mb of configuration PROM memory for in-system programming when deployed in real-world environments. Other additions include a real

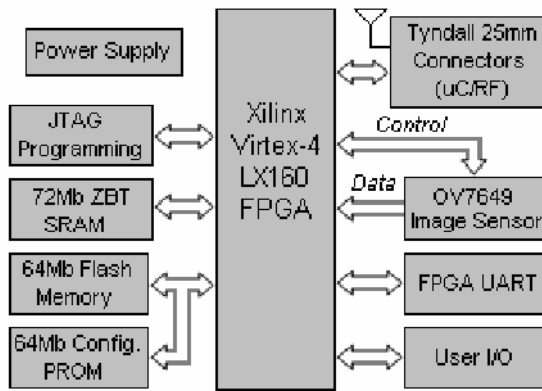


Fig. 4 Block diagram of the VAMP PCB architecture

time clock, UART communications and a high speed video DAC and VGA output port for system debugging. User interface functionality is included in the form of hand-washing pose display LEDs, an LCD screen and momentary push button contact switches.

The VAMP system PCB is currently in its manufacturing stage and once completed will have the functionality to host a wide variety of vision based applications that can be tested in real-world environments and can act as a stepping stone to a fully integrated miniaturized low cost product.

### III. SOFTWARE SYSTEM

The image processing carried out on the FPGA is the key element in the effective operation of the VAMP system. The algorithms developed for this system are based on PC based algorithms as discussed in Section I. These were originally designed in a C code environment. For the efficient development of the FPGA based code it was decided to use the Handle-C programming language. Handle-C is a hardware description language in which programs are written in a conventional sequential format but are compiled into hardware images for use on FPGAs. It is essentially a subset of the C programming language and includes many libraries to assist in the development of image processing algorithms.

The original PC based algorithms were based on a support vector machine (SVM) classifier. Although this produced a very accurate result, it would not have been feasible to implement on an FPGA due to the number of support vectors required. A Fisher LDA classifier was developed in C code to overcome this and when tested on a range of varying scenarios it was shown to be very effective with accuracies of up to 96%.

The PC based algorithms process images frame by frame with each frame made up of 24-bit RGB pixels from real-

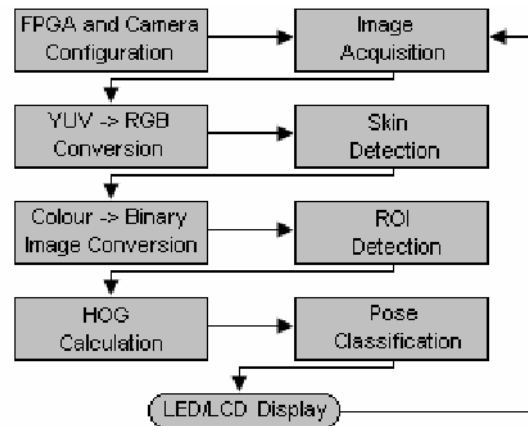


Fig. 5 Block diagram of the Handle-C algorithm operation

time video. The FPGA based system firstly captures the image data in a YUV format from the camera module, frame by frame. This image data is then up-sampled and converted to RGB before being processed further. A block diagram summarizing the operation of the image algorithms is shown in Figure 5.

Two main strategies had to be considered before porting the image algorithms to Handle-C; processing the image data row by row or frame by frame as carried out on the PC based algorithms. Processing row by row is more efficient as many parallel and pipeline programming techniques could be used to speed up the algorithm performance [14]. However, the complexity in converting the algorithm would require large amounts of debugging. Frame by frame processing would use more of the available FPGA resources but conversion and debugging time would be greatly reduced. Based on these findings, it was decided to develop the Handle-C code, processing image data frame by frame.

When porting the algorithm to Handle-C it was important to consider the programming constraints of the compiler as well as the architecture constraints of the FPGA. Complex mathematical equations are completed in one clock cycle in a C environment. To meet this specification in Handle-C, the compiler will build a large combinational circuit on the FPGA, which introduces path delays when implemented in practice. By breaking complex equations into a number of smaller pipelined calculation steps this issue can be overcome. Other considerations include the removal of float point data-types from the code as they are not supported by Handle-C and efficiently setting the bit length of variables and array sizes to limit the amount of FPGA logic cell resources used.

The algorithms are in the final stages of the porting process and once completed, will be customized for the VAMP system prototype and will be tested in a variety of real-world environments.



#### IV. SYSTEM INTEGRATION AND DEPLOYMENT

The VAMP system prototype will operate as if it were a final fully functional product. A user will make contact with the device via a system input (e.g. push button) and the unit will wake up and signal the user to begin hand-washing. As the user completes each pose in the hand-washing procedure, pose display LEDs will light. When hand-washing is adequately completed, an added LED will illuminate confirming this. If the user has failed to carry out adequate hand-washing in a pre-determined time a "hand-washing not completed" LED will light. At this point, all high-level hand-washing data compiled on the FPGA will be passed to the microcontroller and combined with user data. This will be transmitted over the ZigBee standard network to the single gateway node for storage. Multiple VAMP units can be used in a single network.

The VAMP PCB is the size of a standard A5 page. It will be packaged in a similar sized custom made unit allowing for easy installation and with the user push switches, status and pose display LEDs and the LCD screen mounted externally. The unit will be powered from the mains supply in the first prototype. When deployed in a real-world environment, the VAMP system unit will be mounted above a mirror with the camera faced down on the sink. Additional lighting will be added if required for the successful operation of the system. Multiple units will be tested in different health-care scenarios to confirm adequate operation of the VAMP system.

#### V. CONCLUSIONS AND FUTURE WORK

In this paper, a networked wireless vision system (VAMP) to monitor hand-washing quality was presented. The operation of the system is based on the detection of six hand-washing poses. VAMP is made up of a local system node and a gateway node and could be retargeted at a wide variety of applications. All processing is carried out locally and in real-time at the system node by Handle-C developed image algorithms stored on an FPGA. The resulting high-level hand-washing data is transmitted to the gateway node for record storage. The data could also be utilized for a wide variety of other fashions, such as providing records for use within Hazards Analysis and Critical Control Points (HACCP) controls. The system presented offers an easy to integrate, user friendly sensor solution to improve hand hygiene in health-care environments.

Future work can be split up into three sections. The first area that will be concentrated on will be optimizing the image algorithms to improve efficiency and reduce the amount of FPGA resources required by the system. User

interaction with the system will be improved by introducing an RF ID tagging system into VAMP to recognize users. This can be incorporated via the Tyndall 25mm connectors. Finally a miniaturized hardware system will then be designed capable of being integrated into everyday products, with emphasis on reduced manufacturing costs and power consumption.

#### ACKNOWLEDGMENTS

The support of the Informatics Commercialization initiative of Enterprise Ireland is gratefully acknowledged for its funding of the VAMP project, CFTD 06/216.

#### REFERENCES

1. SARI (2005) Guidelines for hand hygiene in Irish health care settings. HSE, Health Protection Surveillance Centre. ISBN-10:0-9540177-8-1
2. Suetens C (2005) What is the burden of health care associated infections in Europe? *Eur J Public Health* 15(1):36
3. Harrison P F, Lederberg J (1998) Antimicrobial Resistance: Issues and Options. The National Academies Press, USA. ISBN-10:0-309-06084-2
4. WHO (2002) Prevention of hospital-acquired infections, a practical guide, 2nd Edition. WHO/CDS/CSR/EPH/2002.12
5. Larson EL (1995) APIC guideline for handwashing and hand antisepsis in health care settings. *Am J Infect Control* 23(4):251-269
6. Royal College of Nursing (2005) Good practice in infection prevention and control – Guidance for nursing staff. RCN, London
7. Tessier R, Burlison W (2001) Reconfigurable computing for digital signal processing: A survey. *J VLSI Sig Proc* 28:7-27
8. Obraczka K et al. (2002) Managing the information flow in visual sensor networks. *WPMC Proc. vol. 3, Int. Symposium on Wirel. Pers. Multimedia Commun., Honolulu, Hawaii, 2002*, pp 1177-1181
9. Hengstler S, et al. (2007) MeseEye: A hybrid-resolution smart camera mote for applications in distributed intelligent surveillance. *IPSN Proc. International Conference on Inf. Proc. Sens. N., Cambridge, USA, 2007*, pp 360-369
10. Pavlovic V I et al. (1997) Visual interpretation of hand gestures for human-computer interaction: A review. *IEEE T Pattern Anal* 19(5):677-695
11. Llorca D F et al. (2007) A multi-class SVM classifier ensemble for automatic hand washing quality assessment. *BMVC Proc. Brit Mach Vision Conference, Warwick, UK, 2007*, Paper-223
12. ZigBee Alliance (2007) ZigBee Specification <http://www.zigbee.org>
13. O'Flynn B et al. (2005) The development of a novel miniaturized modular platform for wireless sensor networks. *IPSN Proc. International Symposium on Inf. Proc. Sens. N., Los Angeles, USA, 2005*, pp 370-375
14. Muthukumar V, Rao D V (2004) Image processing algorithms on reconfigurable architecture using Handle-C. *DSD Proc. Euromicro Symposium on Digit. Syst. Des., Rennes, France, 2004*, pp 218-226

Author: Padraig Curran  
 Institute: Tyndall National Institute  
 Street: Lee Maltings, Prospect Row  
 City: Cork  
 Country: Ireland  
 Email: padraig.curran@tyndall.ie

# An Augmented Reality Application for Minimally Invasive Surgery

L.T. De Paolis<sup>1,2</sup>, M. Pulimeno<sup>2</sup> and G. Aloisio<sup>1,2</sup>

<sup>1</sup> Department of Innovation Engineering, Salento University, Lecce, Italy

<sup>2</sup> SPACI Consortium, Italy

*Abstract*— **Augmented Reality (AR) technology can be used in minimally invasive surgery to provide direct visualisation, thus providing the advantage given by open surgery. It can be used to increase the physician's view by using and showing information gathered from patient medical images. The developed AR system can improve the performances of a surgeon involved in a minimally invasive surgery procedure and provide visual information, located in the correct position of the patient's body, not visible by means of normal senses. The virtual environment is built using the real patient's CT images of the abdominal area; information about shapes and dimensions of the human organs is obtained by means of segmentation and classification algorithms. The developed application is based on the AR Toolkit and it is possible to visualize all the organs in a given abdominal area or, using specific markers, only some of them. The system can be used in pre-operative planning of a laparoscopic surgical procedure in order to find both the right points to introduce the surgical instruments and the best path to reach the organ concerned in the surgical operation.**

*Keywords* — **Augmented Reality, Minimally Invasive Surgery, Image-guided Surgery.**

## I. INTRODUCTION

Recent technological developments have dramatically reduced the amount of unnecessary damage to the patient, by enabling the physician to visualize aspects of the patient's anatomy and physiology without disrupting the intervening tissues. In particular, imaging methods such as CT, MRI, and ultrasound scan make the safe guidance of instruments through the body possible without direct sight by the physician. In addition, optical technologies, such as laparoscopy, allow surgeons to perform entire procedures with only minimal damage to the patient.

The idea of Minimally Invasive Surgery (MIS) is to reduce the trauma for the patient by minimizing the incisions and the tissue retraction. Small incisions, called ports, are made on the chest and the surgery is performed through these ports. The surgical instruments are inserted through the ports using trocars and a camera is also inserted. Since the incision is kept as small as possible, the surgeon does not have direct vision and is thus guided by camera images. As a promising technique, the practice of MIS is becoming more and more widespread and is being adopted as an alternative to the classical procedure.

However, these new techniques come at a cost to the surgeon, whose view of the patient is not as clear and whose ability to manipulate the instruments is diminished in comparison with traditional open surgery. Laparoscopy suffers from a number of visual limitations such as a limited field of view for the surgeon, difficulties with hand-eye coordination and two-dimensional imagery with a lack of detailed information. In particular, the lack of depth in perception in laparoscopic surgery can place limits on delicate dissection or suturing.

Given that a great deal of the difficulties involved in MIS are related to perceptual disadvantages many research groups are now focusing on the development of surgical assistance systems, motivated by the benefits MIS can bring to patients.

Advances in technology are making it more and more possible to develop systems which can help doctors in general, and surgeons in particular, to perform their tasks in ways which are both faster and safer.

With the increasing trend towards filing all patient records and test results in electronic format, research into and practice of clinical medicine are undergoing several important changes. Appropriate visualisation tools and techniques are playing a vital role in providing health care professionals with the ability to get an overview as well as deeper insights into this vast multi-dimensional, multi-media information. The new medical image acquisition systems (CT, MR, PET and ultrasounds) allow access to detailed information regarding human organs and pathologies. The images need to be processed using specific segmentation and classification algorithms in order to distinguish the anatomical structures and to associate different chromatic scales to the organs.

Emerging Augmented Reality (AR) technology has the potential to bring the direct visualization advantage of open surgery back to minimally invasive surgery and can increase the physician's view of his surroundings with information gathered from patient medical images.

In contrast with Virtual Reality technology where a user is completely immersed inside a synthetic environment and cannot see the real world around him, AR technology, which consists of the addition of extra information to the real scene, allows the user to see virtual objects in addition to the real world. The user is under the impression that the virtual and real objects coexist in the same space.

For this reason Augmented Reality enhances the users' perception and improves their interaction with the real world because the virtual objects, displaying information that they cannot directly detect with their own senses, help them to perform real-world tasks better.

In medicine Augmented Reality technology makes it possible to overlay virtual medical images onto the patient, allowing surgeons to have a sort of "X-Ray" vision of the body and providing a view of the patient's anatomy. These types of information could be directly displayed on the patient's body or visualized on an AR surgical interface, showing exactly where to perform the operation.

A physician might also be able, for example, to see the exact location of a lesion on a patient's liver or where to drill a hole into the skull for brain surgery or where to perform a needle biopsy of a tiny tumour.

Augmented reality may be able to free surgeons from the technical limitations of their imaging and visualization equipment, thus recapturing the physical simplicity of open surgery.

Several research groups are exploring the use of the AR in surgery.

Azuma [1] presents a survey of AR and describes the characteristics of AR systems, registration and sensing errors with the efforts to overcome these.

Azuma et al. [2] present many AR applications that have been explored.

Bimber et al. [3] discuss Spatial Augmented Reality (SAR) concept, its advantages and limitations. They present real-time rendering techniques, details about hardware and software implementations, current areas of application and emerging technologies that might influence augmented reality technology in the future.

Furtado and Gersak [4] present some examples of how AR can be used to overcome the difficulties inherent to MIS in the specific case of cardiac surgery.

Devernay et al. [5] propose the use of an endoscopic AR system for robotically assisted minimally invasive cardiac surgery.

Fuchs et al. [6] present the design and a prototype implementation of a 3D visualization system to assist in laparoscopic surgical procedures.

Bichlmeier et al. [7] present a method for the use of AR for the convergence of improved perception of 3D medical imaging data in the context of the patient's anatomy, incorporating the physician's intuitive multi-sensory interaction and integrating direct manipulation with endoscopic instruments.

Sielhorst et al. [8] present a birth simulator for medical training with an augmented reality system.

Samset et al. [9] present tools for MIT by augmenting visual and sensorial feedback. These decision support tools are based on novel concepts in visualization, robotics and

haptics providing tailored solutions for a range of clinical applications.

## II. DEVELOPED APPLICATION

### *Technology used*

ARToolkit [10] is a software library for building Augmented Reality applications and uses square markers carrying a unique pattern that is a planar bitmap enclosed by a black border. Pattern recognition proceeds in two stages: recognition of the pattern boundaries and correlation of the interior pattern with the patterns stored in a database. These markers are observed by a single camera and the tracking software uses computer vision techniques to calculate the marker position and orientation from the captured image. Markers can be used as a tangible interfaces to handle virtual artefacts or as user interface elements.

Tracking is impeded whenever the marker to be tracked is not fully and clearly visible within the camera image; chances of full visibility can be improved by using several markers fixed to a rigid object. The offsets between the markers must be well-known and there must be some components in the application that calculates the final position of the object from the valid tracking input.

The accuracy of tracking depends on many parameters in the processing chain: the quality of the camera images, calibration of ARToolkit, size and visibility of the reference marker, the size of the marker to be tracked. If only one of these factors is not optimally set, the results of tracking may be inaccurate or even unusable.

### *Description of the Application*

Due to the transition in abdominal surgery from open procedures to minimally invasive laparoscopic interventions where visual feedback is only available through the laparoscope camera and direct palpation of organs is impossible, the availability of additional intra-operative feedback can be of great help to surgeons, especially in complex cases.

Besides the restricted view, an important issue in a laparoscopic procedure is the optimal planning of ports as well as enhanced visualization of hidden organs [11].

The aim of the AR system which has been developed is to improve the performances of surgeons involved in a minimally invasive surgery procedure; they are able to have visual information which is not visible by means of normal senses because virtual organs are inserted into the normal field of view. The AR system presents these objects located in the correct position of the body and in correct perspective depth, after an accurate acquisition of the organ geometry.

By superimposing 3D virtual models on the real patient view, the patient then becomes transparent.

In order to build a virtual environment from real patients' images, geometric models of the human organs have been reconstructed using patients' data acquired using a CT scanner. The acquired images relate to the abdominal area and have been processed in order to obtain three-dimensional reconstructions, to distinguish the anatomical structures and to associate different chromatic scales to the organs. The data processing procedure is based on the segmentation and classification phases carried out in order to obtain information about the size and the shape of the human organs. In particular, a "region growing algorithm" is used in the segmentation phase; whereas the classification phase is a user-driven process [12], [13].

An Augmented Reality system must display the resulting 3D imagery in the proper place with respect to the exterior anatomy of the patient. This is one of the most basic problems of the Augmented Reality applications [14]. In order to carry out the registration phase, real and virtual objects must be properly aligned in respect to each other; only in this way will the illusion that the two worlds coexist not be compromised.

This stage is very important because without accurate registration, Augmented Reality will not be accepted in many applications and, in particular, in surgery where the AR images help the doctor to take important decisions during the surgical procedure [15], [16]. If a system is not exact, it could be very dangerous for patients and irreparable damage could be caused, if the surgeon were to make a mistake.

In our application some fiducial points are used to carry out the registration phase and to have an accurate overlapping of the virtual organs on the real ones. CT images have been taken in conjunction with markers for AR that will be used in the registration phase. Special markers were attached to the patient's body before the patient was scanned in order to record all the marker positions. The virtual patient will be registered to the physical patient by registering the point sets. In addition, the patient must be placed in the same position on the operating table as in the CT image acquisition. At the moment the registration phase is carried out using a keyboard and a mouse.

The developed application is based on the ARToolkit and 6 markers, placed around the patient, make it possible to superimpose the virtual organs on the real scene. Other specific markers are used to choose if all organs of a abdominal area need to be visualized or only some of them.

Figure 1 shows the AR system during the visualization of all organs of the abdominal area; Figure 2 shows the visualization of only one specific organ using the appropriate marker of choice.

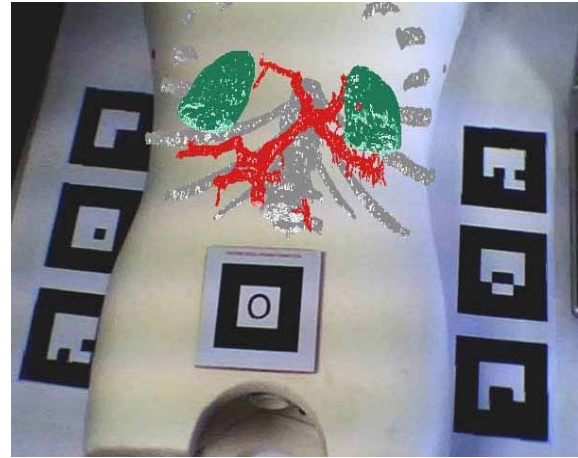


Fig. 1 Visualization of all the organs in the abdominal area

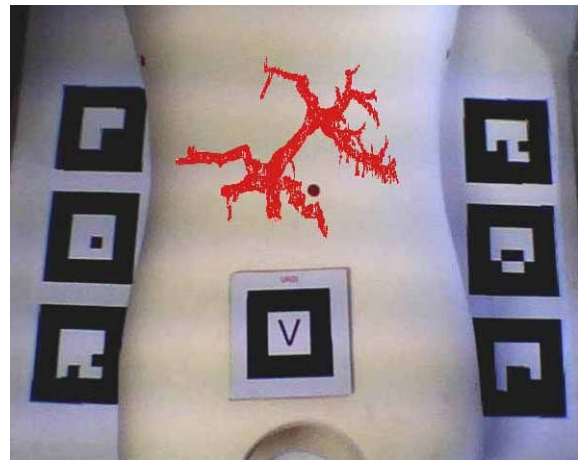


Fig. 2 Visualization of one specific organ

### III. CONCLUSIONS AND FUTURE WORK

The use of an Augmented Reality system in combination with surgery could be of great help, especially in minimally invasive procedures, because the surgeon has a sort of "X-Ray" vision of the patient's anatomy.

In the developed AR system the virtual environment is built using the real patient's CT images of the abdominal area; information about shapes and dimensions of the human organs is obtained by means of segmentation and classification algorithms.

The application is based on the ARToolkit and 6 markers are used to overlap the virtual organs onto the real scene; some specific markers are used to visualize all the organs in the abdominal area or only some of them.

At the moment, the development of the final system is still in progress, since some modifications to the first developed prototype are still being carried out. A study is being made of alternative positioning of the markers and a new set of CT images is being processed, relating to a wider abdominal area. In addition, to improve the performance of the system, optical tracking will be used and the registration phase will be carried out automatically.

The final system could be put to good use in pre-operative planning of a laparoscopic surgical procedure in order to choose the right points for introducing the surgical instruments, with the aim of improving accuracy in positioning the ports. In addition, this system could be used to find the best path to reach the organ concerned in the surgical operation.

### REFERENCES

1. Azuma R (1997) A Survey of Augmented Reality. *Presence: Teleoperators and Virtual Environments* 6:4 355–385
2. Azuma R, Baillot Y et al. (2001) Recent Advances in Augmented Reality, *IEEE Computer Graphics and Applications*, 21(6), 34–47
3. Bimber O, Raskar R (2006) Modern Approaches to Augmented Reality, *ACM Proc. International Conference on Computer Graphics and Interactive Techniques SIGGRAPH 2006*, Boston, Massachusetts, USA
4. Furtado H, Gersak B (2007) Minimally Invasive Surgery and Augmented Reality. *New Technology Frontiers in Minimally Invasive Therapies*, pp 195-201
5. Devernay F, Mourgues F et al. (2001) Towards Endoscopic Augmented Reality for Robotically Assisted Minimally Invasive Cardiac Surgery, *IEEE Proc. Int. Workshop on Medical Imaging and Augmented Reality*, pp. 16-20
6. Fuchs H, Livingston M et al. (1998) Augmented Reality Visualization for Laparoscopic Surgery, *Proc. First Int. Conference on Medical Image Computing and Computer-Assisted Intervention (MICCAI 1998)*, Lecture Notes In Computer Science, pp. 934-943
7. Bichlmeier C, Wimmer F et al. (2007) Contextual Anatomic Mimesis: Hybrid In-Situ Visualization Method for Improving Multi-Sensory Depth Perception in Medical Augmented Reality *IEEE Proc. Int. Symposium on Mixed and Augmented Reality*, Nara, Japan
8. Sielhorst T, Obst T et al. (2004) An Augmented Reality Delivery Simulator for Medical Training, *Proc. International Workshop on Augmented Environments for Medical Imaging – MICCAI*, pp 11-20
9. Samset E, Schmalstieg D et al. (2008) Augmented Reality in Surgical Procedures, *Proc. SPIE*, vol. 68.6
10. ARToolKit at <http://www.hitl.washington.edu/artoolkit/>
11. Feuerstein M, Mussack T et al. (2008) Intraoperative Laparoscope Augmentation for Port Placement and Resection Planning in Minimally Invasive Liver Resection, *IEEE Transactions on Medical Imaging*, 27:355-369
12. Gonzalez R, Woods R (2002) *Digital Image Processing - 2nd Edition*. Prentice Hall, New Jersey
13. Laugier C, D'Aulignac D et al. (2000) Modeling Human Tissues for Medical Simulators, *IEEE Proc. Int. Conf. on Intelligent Robots and Systems - IROS*, Japan
14. Malik S (2002) Robust Registration of Virtual Object for Real-Time Augmented Reality. Carleton University, Canada
15. Feuerstein M, Mussack T et al. (2007) Registration-Free Laparoscope Augmentation for Intra-Operative Liver Resection Planning, *SPIE Medical Imaging*, San Diego, California, USA
16. Feuerstein M, Wildhirt S et al. (2005) Automatic Patient Registration for Port Placement in Minimally Invasive Endoscopic Surgery, *Proc. 8th Int. Conf. Medical Image Computing and Computer-Assisted Intervention - MICCAI, Lecture Notes in Computer Science 3750*, Palm Springs, CA, USA, 2005, pp 287–294

Author: Lucio T. De Paolis  
 Institute: Dept. of Innovation Engineering - Salento University  
 Street: via Monteroni  
 City: 73100 Lecce  
 Country: Italy  
 Email: [lucio.depaolis@unile.it](mailto:lucio.depaolis@unile.it)

# Methods for Counting Cells Supported by Digital Image Processing

D. Dill<sup>1,2</sup>, A. Scholz<sup>1,2</sup>, M. Gül<sup>1,2</sup> and B. Wolf<sup>2</sup>

<sup>1</sup> Sensor GmbH, Munich, Germany

<sup>2</sup> Heinz Nixdorf-Lehrstuhl fuer Medizinische Elektronik, Technical University of Munich, Munich, Germany

**Abstract** — Multi-parametric cell-chip-systems for live monitoring living cells and tissue in the field of examination of effective substances and medical diagnostics are gaining more and more importance. Digital image processing offers support for the microscopic controlling of monitoring systems for living cells. Thanks to the enormously increased power and capacity of computers within the recent years, an automatic survey of proliferation in a not invasive manner and without any influence on the relevant experiment is possible.

On a molecular level cells are reacting very sensitive to changes in their environment, e.g. the contamination by toxic essences. Significant changes in the appearance of the cell culture will also be observed. The most evident indication, marking hostile conditions for living cells, is the decreased rate in growth of the cell culture. In addition the actual rate of cell propagation (splitting) might be used as a more accurate sign.

**Keywords** — digital image processing, cells, counting, noninvasive

## I. INTRODUCTION

Counting cells means high demand on digital image processing. On one hand cells of different origin are already very different from each other, on the other hand the same cells will appear different in transmission microscopy compared to microscopy with incident light. The efficiency of the image processing algorithms is also influenced by different conditions of light.

Currently, the cells are mainly counted external, e.g. by means of flow cytometry [1] and colouring with fluorescent dyes. This procedure often results in cell-death, or at least in an impact on their. Thanks to experience and wide background knowledge the human sight is able to analyse extremely difficult images and to extract important information. These properties are not actually transferable onto digital image processing. Nevertheless it is being attempted, but a universal software solution for fully automatic counting of diverse types of cells is practically not yet feasible.

This essay describes a procedure to count cells via digital image processing, without destroying the cell culture and without using fluorescent dyes. Furthermore, the conception of a data bank will be presented. This data bank contains individually tailored algorithms for a multiplicity of the most common cell lines to enable the counting of the

relevant cells. This data will be continually extended in order to achieve a maximum spectrum of cell lines in the data bank. The software will be reasonably priced and comfortable to use.

## II. MATERIALS AND METHODS

### A. Acquiring the image

The source material for this application consists of digitally captured images. As a minimum a resolution of 1200 by 1600 pixels (approximately 2 Megapixels) is required. By now this resolution is easily reached by standard consumer digital cameras. The pictures of the cells are taken in the usual procedure by either transmission-light microscopy or incident-light microscopy – both using visible light. (see Fig. 1.)

Carrier for the cell culture is a multiparametric glass-sensor-chip that provides an additional insight into the cells' vitality by measuring different electrical and electrochemical parameters of the cells and the culture medium via different especially designed electrode structures.

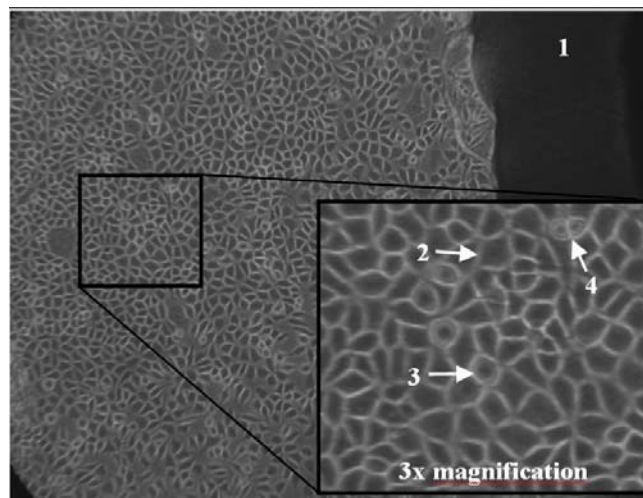


Fig. 1 Image of a cell culture grown on a multiparametric sensor chip with part of an electrode (1), normal cells (2), cytotoxic cells (3) and post-cytotoxic cells (4) at a resolution of 1200x1600 pixels. This image is taken via transmission-light microscopy

As shown in Fig. 1 the cell-culture-area of the glass-sensor-chip is completely and nearly homogeneously covered with cells. On the upper right corner of the image one can see a segment of an electrode structure (1). Electrodes are also covered with cells, but due to their metallic texture and therefore their opaqueness to light cells grown on electrode structures are invisible in transmission-light microscopy as it is the case here. The cells' boundaries stand out by a significant higher intensity than the electrode structure, the cell bodies and the culture medium. This enables the image processing algorithms to separate the cells.

Because of different shape and different intensity of the inner cell area normal cells (2) differ remarkably from cytotinetic cells (3) and post-cytocinetic cells (4). At this point the image processing algorithms join in.

### B. Processing the image

In the first step the source-image is resized to a resolution of 1200 by 1600 pixels. Because of being an optical photography the illumination of the pictures may vary in intra- and inter-picture dimensions. So the image is recalibrated to a homogeneous illumination and a normalized grayscale picture. This task is done by an implemented and especially tailored 'local-normalize'-algorithm [2]. Fig. 2 shows the result of the local-normalize algorithm.

Furthermore, non-usable parts of the image, e.g. the borders of the electrode-structures, have to be cut out to prevent falsifying the cell count result. Several morphological operations like erosion, dilation, opening and closing result a binary image (Fig. 3). This image contains white areas, which represent the segmented cells, and black areas, which represent the (uninteresting) rest. Counting the cells is simply done by counting closed white areas in the image. Also the position of the counted cells is stored.

In addition to the cell count algorithm another algorithm to detect cytotinetic and post-cytocinetic cells is implemented. As biological background, cytotinetic cells are in progress of being splitted into two identical cells. On that account the cytoplasm has to be reproduced and the cell appears in a more circular shape than the others. Also, post-cytocinetic cells appear more circular but smaller, and in addition doubly. Fig. 4 shows typical examples of both types of cells.

Detecting these cells is done by a template-matching algorithm. A template matching algorithm uses a predefined and optimized image - the template - with white, gray and black pixels. This template (Fig. 5) is moved line by line over the preprocessed binary image of the cell culture.

In case the white and black pixels of the template match with those on the binary image, a cytotinetic cell is found, counted and the position is stored. The gray pixels of the

template don't need to match. This allows a higher flexibility and a higher detection rate.

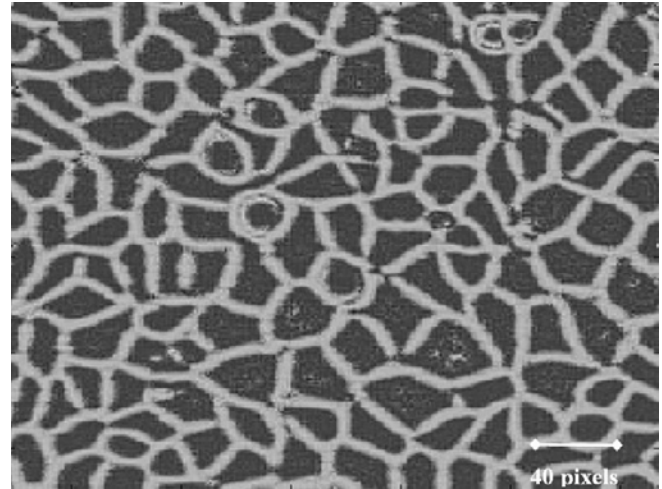


Fig. 2 Result of the 'local-normalize'-algorithm (3x magnification)

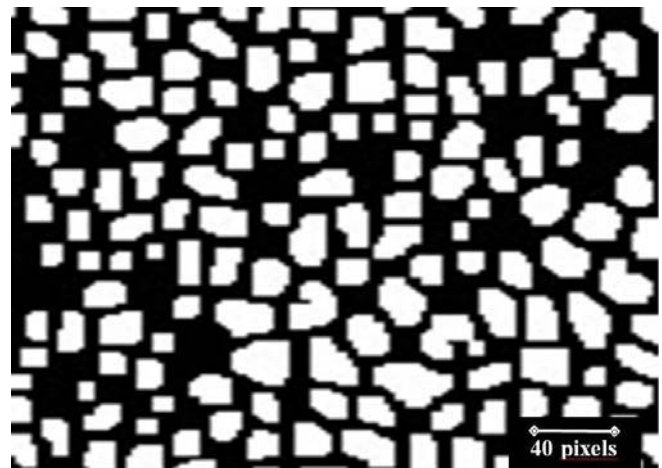


Fig. 3 binary image with the segmented cells (white)

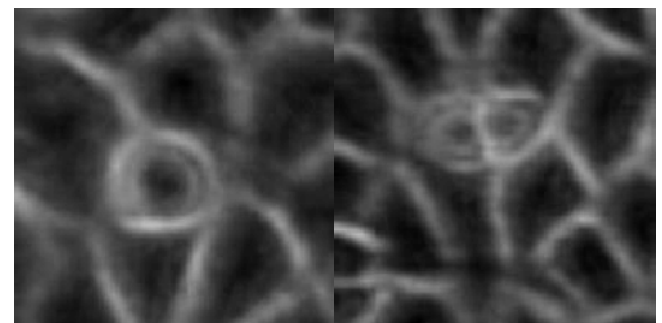


Fig. 4 cytotinetic cell (left) and post-cytocinetic cells (right)

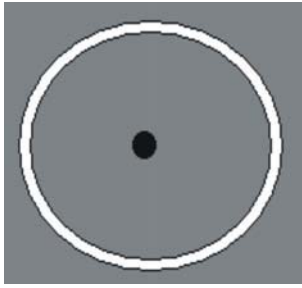


Fig. 5 template for detecting a cytotinetic cell

### III. RESULTS

The resulting image consists of the original (colored) image with three overlays: positions of the counted normal cells marked with a black (+), positions of the counted cytotinetic cells marked with a white (•) and the two different values of the counted cells in the upper right corner (Fig. 6). The values of the counted cells are also saved in a separate .txt-file to make it available for further processing. Fig. 7 shows a magnification of the resulting image.

In our tests the counting results for normal cells matched 90% with the results of manual counting. Processing time for both algorithms takes not more than ten seconds on a standard personal computer.

### IV. DISCUSSION

Detecting cytotinetic and post-cytotinetic cells is more difficult than detecting normal cells due to the fact that the cytokinesis is a step less progress and hence every state of a cytotinetic cell is present. The algorithm is tailored to a specific state, so not all cytotinetic cells are detected.

The algorithms used in this example are especially tailored to the parameters given. These parameters are cell-type, magnification and light source. They have to be known by the program in order to work properly.

### V. CONCLUSIONS

The Program works with static conditions but is, yet, not a universal solution. The knack is the creation of a database with algorithms especially adapted to the main variable parameters (cell-type, magnification, light source). The user's only task is to choose the cell type, the magnification that is written on the microscope and the light source used. After that cell counting works automatically.

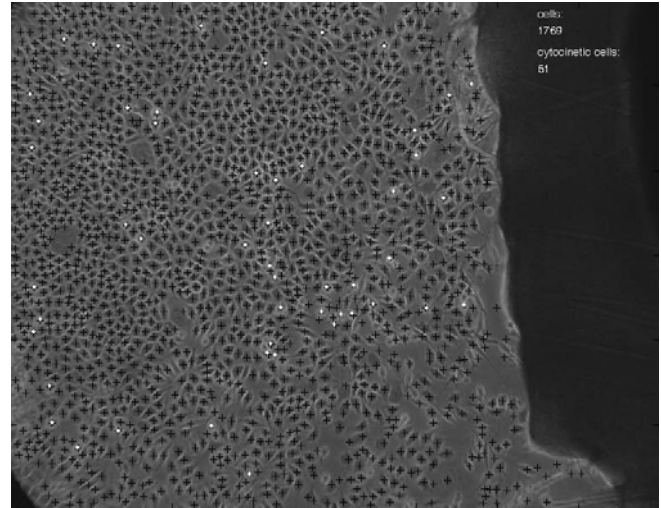


Fig. 6 result of the cell-count algorithms

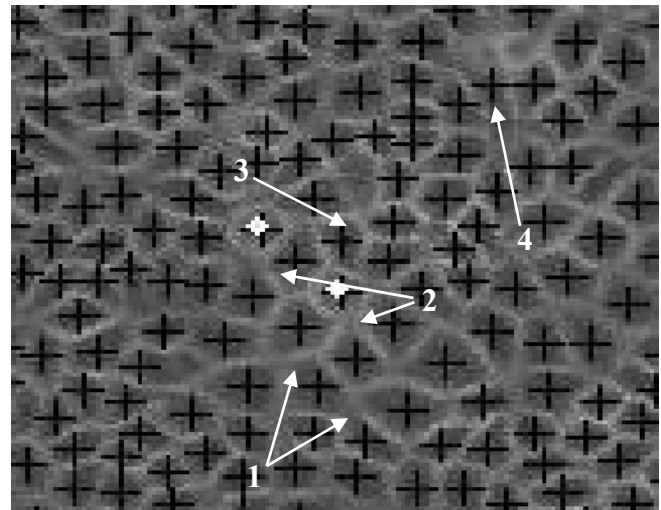


Fig. 7 magnification of the resulting image with detected normal cells (1, black +), detected cytotinetic cells (2, white •), not detected post-cytotinetic cells (3) and not detected normal cell (4)

The program will be able to count cells in single images as well as, automatically, in a series of images over a longer period of time. Statistics during and at the end of the periods show information about cell count, increase rate, cytotinetic cells and more.

Since not all cell types are needed for an experiment the program shall be distributable in a modular way. Users can choose which cell type data sets they want and can easily upgrade with more datasets. This makes the program much more comfortable, smaller and cheaper.



## REFERENCES

1. Eichmeier, Joseph: Medizinische Elektronik - Eine Einführung, Springer-Verlag 1997
2. Biomedical Imaging Group, EPFL Swiss Federal Institute of Technology, Lausanne, Switzerland, <http://bigwww.epfl.ch/demo/jlocalnormalization/> Contributed by Guanglei Xiong at Tsinghua University, Beijing, China.
3. Semmlow, John L.: Biosignal and Biomedical Image Processing - Matlab-Based Applications, Robert Wood Johnson Medical School, New Brunswick / Rutgers University, Piscataway, New Jersey, U.S.A, Marcel Dekker, Inc. 2004

Author: Dieter Dill, Dipl.-Ing  
Institute: Heinz Nixdorf-Lehrstuhl fuer Medizinische Elektronik  
Street: Theresienstrasse 90  
City: 80333 Munich  
Country: Germany  
Email: dill@tum.de

# Two Aspects of Calibrating a 3D Ultrasonic Computed–Tomography System

A. Filipík<sup>1</sup>, J. Jan<sup>1</sup>, I. Peterlík<sup>2</sup>, D. Hemzal<sup>3</sup>, R. Jiřík<sup>1</sup>

<sup>1</sup>Brno University of Technology, FEEC, Dept. of Biomedical Engineering, Brno, Czech Republic

<sup>2</sup>Masaryk University, Faculty of Informatics, Brno, Czech Republic

<sup>3</sup>Masaryk University, Faculty of Science, Brno, Czech Republic

**Abstract** — The paper concerns providing the auxiliary data for image reconstruction in ultrasonic computed tomography (USCT) by calibrating the measuring USCT system. Basically two aspects are considered: calibrating the individual transducers as to their transmitting and receiving properties concerns, and calibrating the geometry of the measuring system, i.e. providing the exact information on the individual transducer deviations from the expected precise positions (including the individual delays in signal processing that act similarly as to the image reconstruction concerns). We will concentrate primarily on the 3D generalization of the principle of individual transducer efficiency and directional characteristics calibration that appeared for 2D case in [3] and complement the information by overview on the other calibration aspects as well. The described methods, based on sc. empty measurements (no measuring phantoms needed) have been tested by both extensive simulations and by first practical applications utilising real measurement data. The tests proved the feasibility of the approach and its robustness under difficult circumstances – i.e. imprecise initial estimates of the calibrated quantities and presence of non-negligible noise in the measurements.

**Keywords** — Ultrasonic computed tomography, image reconstruction, computed calibration, ultrasonic transducers.

## I. INTRODUCTION

A USCT system is basically a cylindrical container equipped with a set of numerous (virtually up to the order of  $10^4$ ) ultrasonic (US) transducers in either 2D or 3D arrangement; the container is filled with water and the investigated tissue is submerged inside the container and surrounded by the transducers. The system provides a huge amount of A-scans – 1D signal sequences obtained by a sequence of many measurements: always a single transducer is transmitting and the others receiving the (scattered) US impulse; gradually all the transmitting transducers firing. In the concrete experimental 2D system (Fig.1), designed and developed in the Forschungszentrum Karlsruhe (Germany) [1], all the transducers take gradually the role of transmitters and receivers, while in the second-generation 3D system (Fig.2) these roles are separated [2]. The A-scan signals (Fig. 1b) are influenced (delayed and scattered) by the investigated tissue, i.e. by the spatial distribution of its

physical parameters determining its local acoustic impedance. The numerically reconstructed 2D or 3D image data based on the A-scans then describe these spatial distributions. The system being under development in the Forschungszentrum Karlsruhe (Germany) is primarily aimed at breast cancer diagnostics as an non-invasive addition or even alternative to X-ray based screening methods.

The exact knowledge of individual transducer properties as well as of their positions turns out to be crucial for a good quality of the reconstructed images. This contribution will briefly describe new approaches to determine both the transducer parameters and their positions based only on sc. empty measurements (*phantom-less calibration*) under precisely known physical conditions, e.g. water temperature determining the ultrasound velocity.

The calibration of individual transducer properties provides the directivity characteristic of transducers (common to all transducers due to their identical shape and material properties) and the individual efficiencies of each transducer as the transmitters or receivers. It is supposed that, thanks to duality principle, the efficiencies in both the transmitting and the receiving modes are identical (or at least mutually proportional). These characteristics may be obtained by solving an extensive linear equation system build of log-linearised received-signal equations in frequency domain, reflecting the unknown transmitting and receiving properties of the transducers, as will be shown in section II in a greater detail. First, the principle will be explained in 2D case followed by the detailed generalisation for the 3D case. This way, the directivity function, dependent on direction and frequency, is obtained besides a vector of the individual

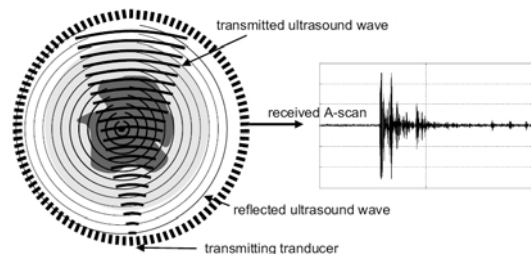


Fig. 1 a – Schematic geometry of the 2D USCT system built in Forschungszentrum Karlsruhe (FZK), b – a typical transducer response – an A-scan (from [1] with permit)

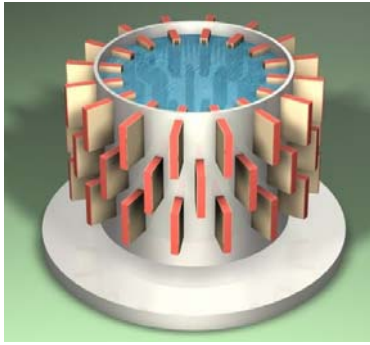


Fig. 2 Schematic geometry of the experimental 3D USCT system designed and built in the FZK Karlsruhe (Germany). The protrusions represent the transducer array systems (TASes) consisting each of eight combined groups of 1 transmitter and 4 receivers

transducer efficiencies. The results correspond very well to those few that could have been obtained by direct physical measurement (however, insufficiently scarce ones to replace or really support the practical calibration).

Geometrical calibration of the system, based entirely on the empty measurements, determines the exact individual positions of all the transducers as the initial estimates taken from the construction documentation modified by corrections computationally determined from a non-linear equation system utilising the empty measurements. No a-priori fixed spatial reference or use of a phantom are needed. The huge non-linear equation system is compiled using a similar approach as in GPS but without known reference positions. The calculations on simulated data proved the efficiency of the method in determining the positions with the desired high accuracy (up to a small fraction of the used ultrasound wavelength, i.e. a small fraction of a mm) that is by far not achievable by direct physical measurement that is also hardly feasible due to bad accessibility inside the system.

## II. CALIBRATING THE TRANSDUCER PROPERTIES

Initially, the assumptions on the transducer properties were simplified: they were supposed to be homogeneously omnidirectional (both in transmitting and receiving modes), i.e. with transmitting or receiving properties fully independent on the direction. This could have been expected, based on the small dimensions of the transducers (of only a small fraction of the used ultrasound wavelength). Also, the individual properties of the transducers were supposed fully equalised in the transducer set. However, when searching for sources of artefacts in the reconstructed images, it was suspected that the above assumptions might not be right; the respective verification (or correction) approach was obvi-

ously in determining the real properties experimentally and, when needed, in calibration of the differences.

To provide for complete generality, fully generic and individual directional characteristics (*radiation functions*)  $D(f, \nu, \varphi)$ , dependent on frequency and both directional angles are to be supposed. Determining these functions is the subject of the method presented in this section, based on measurements and consequently computed by solving the respective equation system. However, as it will be shown, the available equation system has fewer equations than unknowns in this most generic case; to rectify the situation, some reasonable limitations had to be introduced, concerning primarily some symmetry constraints on the radiation function shape and also uniformity of this shape (though not value equality) among transducers. Thanks to the limited power of ultrasound, linearity may be supposed.

The calibration is then based on a series of wide-band measurements with the USCT system tank filled only with water (so called “empty measurement”). First, the 2D approach for the system as on Fig.1 will be briefly described. Individual received signals on a particular path are influenced by the properties of the respective transmitter and receiver; when expressed in frequency domain, it can be modelled as

$$S_{e,r}(f) \cong R_e(f, \vartheta_{e \rightarrow r}) \cdot R_r(f, \vartheta_{e \leftarrow r}) \quad (1)$$

where  $S_{e,r}(f)$  is the amplitude spectrum of the received signal (using emitter  $e$  and receiver  $r$ ),  $R_e(f, \vartheta_{e \rightarrow r})$ ,  $R_r(f, \vartheta_{e \leftarrow r})$  are the radiation functions of the emitter and receiver, respectively,  $f$  frequency,  $\vartheta_{e \rightarrow r}$ ,  $\vartheta_{e \leftarrow r}$  are angles towards the receiver or emitter axis, respectively (Fig.3). When expressing the spectra discretely via DFT and taking each emitter – receiver – frequency combination, a system of equations can be constructed and log-linearised:

$$\log(S_{e,r}(f)) = \log(R_e(f, \vartheta_{e \rightarrow r})) + \log(R_r(f, \vartheta_{e \leftarrow r})), \forall e, r \quad (2)$$

Here, the components of the measured spectra  $S_{e,r}(f)$  are known; solving this system then provides the unknown parameters of the sensors. For  $N$  transducers with  $N-1$  possible emitting/receiving angles and  $M$  frequency coefficients,  $N \cdot (N-1) \cdot M$  equations can be built with the same number of unknown parameters. Thus, it is theoretically possible to solve for independent radiation functions individual for each of the used transducers.

However, given the properties of the used experimental systems, the measurements cannot provide a complete equation system and constraints must therefore be imposed on the solution, as follows. All transducers may be supposed to have similar radiation functions, thanks to equalized dimen-

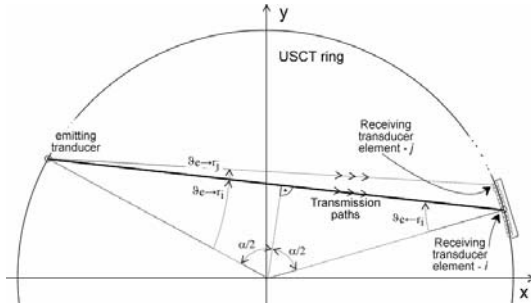


Fig. 3 Geometry of the 2D transducer arrangement (the 3D geometry is defined by straightforward generalisation) – adapted from [3]

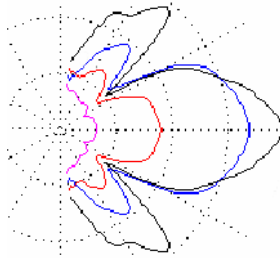


Fig. 4 Directional characteristics of the transducers for different frequencies determined via 2D computed calibration (profiles from the continuous 2D characteristic in the frequency – direction space, from [3])

sions and manufacturing; also the directivities in each direction on a path are identical,

$$D(f, \vartheta_{e \rightarrow r}) = D(f, \vartheta_{e \leftarrow r}) = D(f, \vartheta_{e \leftrightarrow r}) \quad (3)$$

The minor differences caused by material flaws and possibly fatigue may be reasonably represented by individual transmitting *efficiencies* or receiving *sensitivities*.

For a particular transducer, these are linearly dependent and may be considered equal. Thus the radiation function of any  $i$ -th transducer can be modelled as a product of a common 2D directivity function  $D(f, \vartheta)$  and an individual sensitivity  $s_i$  (or efficiency  $e_i$ ):

$$R_i(f, \vartheta) = s_i \cdot D(f, \vartheta). \quad (4)$$

Obviously, the considerations apply to 3D case equally as for 2D, as will be used later.

There might be still another problem: rank deficiency of the equation system (2) due to inseparability of individual factors in (1). This has to be eliminated by imposing other reasonable constraints, e.g. requiring unit product of all transducer efficiencies. This way, only relative values can be obtained, preserving the ratios in each transducer couple; this is sufficient for the image reconstruction (the absolute values are unnecessary).

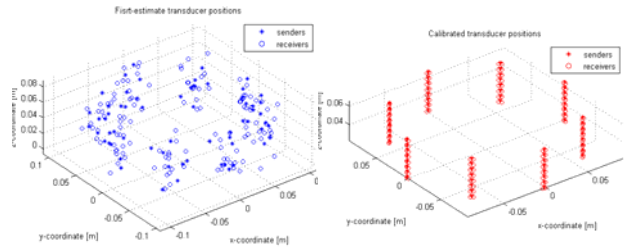


Fig. 4 Example of calibration result based on simulated data

Via these modifications, the system (2) becomes well solvable and provides reasonable estimates [3] of the transducer parameters (example on Fig. 4), which were partly qualitatively verified by direct ultrasonic measurement by a hydrophone or by wave equation based simulation.

This approach can be directly generalized to 3D problem, as arising in calibration of the newer USCT system. The differences to be taken into account are important: besides physical separation of the transmitters and receivers, the electrical signal initiating a transducer is a shaped pulse of a limited frequency content, which requires modification in the calibration model. The 3D transducer sensitivity calibration is thus built on a more detailed model than (1),

$$S_{out} = S_{in} \cdot T_{ee} \cdot R_e \cdot T_w \cdot R_r \cdot T_{re} \quad (5)$$

where  $S_{out} = S_{out}(i, j, k)$  is DFT spectrum of received signal,  $S_{in} = S_{in}(i, j, k)$  spectrum of the input pulse,  $T_{ee} = T_{ee}(i, k)$  transfer function of the  $i$ -th transmitter electronics,  $R_e = R_e(v_{i \rightarrow j}, \varphi_{i \rightarrow j}, i, k)$  transfer function of the transmitter in direction to  $j$ -th receiver),  $T_w = T_w(d_{i, j}, k)$  transfer function of the water path,  $R_r = R_r(v_{i \leftarrow j}, \varphi_{i \leftarrow j}, j, k)$  transfer function of the receiving  $j$ -th transducer in direction to transmitter,  $T_{re} = T_{re}(j, k)$  transfer function of the receiver electronics,  $k$  is the order of the DFT coefficient and  $v_{i \rightarrow j}$  or  $\varphi_{i \rightarrow j}$  are azimuthal/elevation angles of transmission while  $v_{i \leftarrow j}$  or  $\varphi_{i \leftarrow j}$  are similar angles at the receiver side. Besides taking into account the transition properties of electronics on both sides, the varying path lengths in the cylindrical geometry of the USCT was considered. Similarly as before, linear equation system is provided from (5) via logarithms.

As in 2D case, due to inseparability of terms like

$$T_e(i, v_{i \rightarrow j}, k) \cdot T_r(j, v_{i \leftarrow j}, k).$$

the system is incomplete and requires reduction of unknown count. It can be easily shown that, due to inherent symmetries, with a sufficient accuracy applies

$$D(v_{i \rightarrow j}, \varphi_{i \rightarrow j}, k) = D(v_{i \leftarrow j}, \varphi_{i \leftarrow j}, k) = D(v_{i \leftrightarrow j}, \varphi_{i \leftrightarrow j}, k),$$

and consequently, with a reasoning as in the 2D case,

$$R_e(v_{i \rightarrow j}, \varphi_{i \rightarrow j}, i, k) \equiv e(i) \cdot D(v_{i \leftrightarrow j}, \varphi_{i \leftrightarrow j}, k) -$$

$$R_r(v_{i \leftarrow j}, \varphi_{i \leftarrow j}, j, k) \equiv s(j) \cdot D(v_{i \leftrightarrow j}, \varphi_{i \leftrightarrow j}, k)$$

Again, due to inseparability of the transducer constants and transfer functions of the related electronics, we can only determine the combined (but sufficient) transfer functions,

$$T'_{ee}(i, k) \equiv T_{ee}(i, k) \cdot e(i), T'_{re}(j, k) \equiv T_{re}(j, k) \cdot s(j)$$

The transfer function of the water path is  $T'_w = e^{-\beta_w f d}$ , where  $\beta_w$  is the US attenuation coefficient of water, and the path length  $d$  is

$$d_{i,j} = |\vec{r}_e(i) - \vec{r}_r(j)| = \sqrt{(x_e - x_r)^2 + (y_e - y_r)^2 + (z_e - z_r)^2}$$

Summarizing, the resulting model of a path transfer reads

$$S_{out}(i, j, k) = S_{in} \cdot e^{-\beta_w f d} \cdot D^2(v_{i \leftrightarrow j}, k) \cdot T'_{ee}(i, k) \cdot T'_{re}(j, k) \quad (6)$$

for all  $i, j, k$ . As before, in this system (to be log-linearised similarly as in the 2D case), the measurements,  $d$ -s and  $\beta$  are the known quantities while samples of the common 3D directivity characteristic  $D$  and of the transfer functions  $T$  are the unknowns to be found. The system is presently considered for full-size implementation, to be tested with realistic measurement data.

### III. CALIBRATING GEOMETRY OF 3D USCT SYSTEM

The geometry calibration method [4] is based on “empty” direct-paths time-of-arrival ( $TOA_{s,r}$ ) measurements of the US impulses for a particular transmitter-receiver ( $s,r$ ) combination.. The approach is in principle similar to this of the GPS system but without a fixed spatial reference. The TOA is a function of positions of both transducers and of time-delays introduced at transducers by their electro-mechanical properties and related electronics. Thus

$$TOA_{s,r} = TOF_{s,r} + \tau_s + \tau_r + \varepsilon_{s,r} \quad (7)$$

where  $TOF_{s,r}$  is time-of-flight between transducers,  $\tau_s$  and  $\tau_r$  are the time delays, and  $\varepsilon$  is the measurement noise.

The Eq. (1) for all paths represents a system of nonlinear equations from which the exact path lengths can be computed thus enabling the geometrical calibration. The system is locally linearised in each iterative step:

$$\mathbf{J}_k \Delta \mathbf{x}_k = \mathbf{r}_k, \quad (8)$$

providing consecutive  $x$ -corrections based on residual vector  $\mathbf{r}$  dependent on measurements and system matrix  $\mathbf{J}$  reflecting the so far estimated geometry. New modification improves noise robustness by utilizing known partial geometrical relations among groups of transducers (TASes).

The new approach provides very precise results (in the range of a small fraction of the used US wave-length). A calibration example based on simulated data is on Fig. 5 showing the initial imprecise estimates of the transducer positions and the corrected final state of real positions in the USCT system.

## IV. CONCLUSIONS

Novel approaches were added to previously designed methodology of calibrating the USCT systems. The contribution concentrates on the generalization of the transducer-parameter calibration for the new three-dimensional USCT experimental system. Additions to geometry calibration in 3D system are briefly mentioned. Presently both principles are being implemented in a way complying with the requirements for calibration of the 3D USCT system under practical environment.

## V. ACKNOWLEDGEMENT

Valuable discussions with the group of N.V. Ruiter, Forschuns-zentrum Karlsruhe (Germany), and access to USCT data is highly acknowledged. The project is sponsored by the research centre DAR (no. 1M6798555601), partially also by the research frame FECC VUT (no. MSM 0021630513, both Ministry of Edu., Cz. Rep.) and also by the DAAD grant no. D12-CZ9/07-08.

## VI. REFERENCES

1. Stotzka, R., et al. (2004) A New 3D Ultrasound Computer Tomography Demonstration System, Forschungszentrum Karlsruhe, 2004
2. Ruiter, N.V., Schwarzenberg, G.F., Zapf, M., Liu, R., Stotzka, R., Gemmeke, H. (2006) 3D Ultrasound Computer Tomography: Results with a Clinical Breast Phantom, IEEE Symposium on Ultrasonics, 2006
3. Jirik R., Stotzka R., Tact, T. (2005): ‘Ultrasonic Attenuation Tomography Based on Log-Spectrum Analysis’, Proceedings of SPIE, Medical Imaging 2005. Volume: 5750, pp. 305-314
4. Filipik, A., Jan, J., Jirik, R., Ruiter, N., Stotzka, R. (2005) Transducer Calibration in Transmission Ultrasound Computed Tomography. Proc. EMBC conf. Pratur 2005
5. Filipik, A., Peterlík, I., Hemzal, D., Jan, J., Jirik, R., Kolar, R., Zapf, M., Ruiter, N., Gemmeke, H.: Calibrating an Ultrasonic Computed Tomography System Using a Time-of-Flight Based Positioning Algorithm. Proc. IEEE-EMBC 2007 conf., Lyon 2007

Author: Jiří Jan,  
Institute: Dept. of Biomedical Eng., FECC, Brno University  
of Technology,  
Street: Technická 4,  
City: 612 00 Brno,  
Country: Czech Republic  
Email: jan@fecc.vutbr.cz

# A Combined Bayesian Approach to Classifying Venous Flow during Contrast-Agent Injection using Doppler Ultrasound

M. Forfang<sup>1</sup>, L. Hoff<sup>1</sup>, N. Bérard-Andersen<sup>2</sup>, G.F. Olsen<sup>2</sup> and K. Brabrand<sup>3</sup>

<sup>1</sup> Faculty of Engineering, Vestfold University College, Norway

<sup>2</sup> Neorad AS, Oslo, Norway

<sup>3</sup> Rikshospitalet University Hospital, Oslo, Norway

*Abstract* — The administration of intravenous contrast media during CT examinations is routine, but carries with it a risk of extravasation. With a new Doppler ultrasound monitoring technique, we propose a method for automatic classification of injection flow states. The method combines a Bayesian network and a sparse kernel classifier. The network captures the dependencies between latent variables, observations and previous system states. The sparse kernel classifier is a Relevance Vector Machine that is well suited for spectral analysis and which provides a probabilistic estimate. We present preliminary results showing a challenging input signal variance and how the method applies to empirical data.

*Keywords* — classification, Bayesian, sparse kernel, relevance vector machine, Doppler, ultrasound, extravasation, accuracy, spectral analysis

## I. INTRODUCTION

X-ray contrast media is routinely used to enhance CT images. The media is typically administered using a remote controlled power injector. This ensures the flow is high, uniform and doesn't fragment easily. CT angiography and phased helical CT examinations may indicate such contrast media administration. The increase in contrast agent volume and speed carries with it the risk of extravasation. Extravasation might be due to vein rupture or that the injection needle fails to penetrate the vein. The injuries are normally minor, but more severe injuries like skin ulcerations, tissue necrosis and compartment syndrome are not uncommon. The reported frequency of injury ranges from less than 0.5% [2] to above 2% [1].

To reduce the incident rate, monitoring devices and detection technologies have been proposed [2][4]. Neorad [3] and the National Hospital of Norway is developing an ultrasound transducer with the same aim [5]. A key requirement is that the monitoring device minimizes risk, specifically that the incident detection accuracy is well above present detection rates.

Medical Doppler signals have been classified based on a time-frequency representation using Neural Networks [8] and Support Vector Machines [9]. Bayesian classifiers have been used to classify medical Doppler signals [11] and there

exists work on spectral analysis using an auto-regressive model with a Bayesian framework [12].

In this paper we propose an automated pattern classification method tailored for the particular contrast agent administration procedure. Firstly, we briefly describe the problem in terms of clinical procedure and the signals generated. Then we propose a method with a model. Finally we present some preliminary results and provide a brief conclusion.

## II. PROBLEM

3 continuous wave Doppler 4 MHz transducers are attached to the patient's arm, over the vein and proximal to the contrast cannula. The transducer array is attached perpendicularly to the vein direction, circumferentially around the arm. A saline injection is administered first and then after a pause, the contrast agent is administered. Finally another saline injection is administered. There is a synchronization signal available that specifies whether the injection of fluid has started or ended and whether the injection is saline or a contrast agent. The device characteristics, the agent types and administration are detailed in [5]. The quadrature demodulated signal is sampled at 25 kHz and high-pass filtered. The resulting power Doppler signal is short-time Fourier transformed with a 0.2 seconds Hanning window and a two window length overlap. This leaves us with a preprocessed 0.2 sec/2.5 Hz resolution time-frequency signal. Finally, the 50Hz band and its harmonics are removed.

With these inputs in mind, the challenge is to devise a statistically highly accurate, automatic extravasation classifier which can run in real time on a portable processing unit.

## III. METHOD

### A. Definitions

We define the inputs to the classifier to be

1. 3 x 2D preprocessed time-frequency samples
2. a synchronization signal tuple {(start, stop), (contrast, saline)}

The classification target is a state variable capturing whether the injected fluid is running normally through a vein, whether nothing seems to flow or whether an extravasation is occurring. We define

$$flowState = (\text{intravenous, no-flow, extravasated})$$

The patient examination goes through several distinct phases. For the classifier, important phases are a possible pre-check phase where a saline injection is administered, a possible saline injection before the contrast injection, the contrast injection itself and finally a possible saline injection after the contrast injection. We define

$$examinationPhase = (\text{saline-precheck, saline-preinjection, contrast-injection, saline-postinjection})$$

*B. General dependency model*

Firstly, we assume the flowState characteristically influences the received Doppler signal. We define a Temporal Feature (TF) to be some representation of the Doppler signal at time t. TF(t) then statistically depends on the flowState at time t.

We hypothesize that the chance for a particular flowState is dependent on the flowState at earlier times. For example, if it's not clear whether the flow is intravenous or extravasated during the saline-preinjection phase (e.g. the probabilities are roughly equal) then that might heighten the chance that the flowState is seen as extravasated during the contrast-injection phase. Thus, the probability of a flowState at time  $t_n$  depends on the flowState at time  $t_{n-1}$ .

Finally, since the task is pattern classification, we define an independent flowState probability estimate that stems from a classification model based on the Doppler signal. The flowState<sub>mod</sub> at time t depends on the flow state at time t.

In Figure 1 we show these dependencies in terms of a Bayesian network. The circles are statistical variables. The arrows denote a statistical dependency. Shaded circles are observed variables and white circles are latent variables.

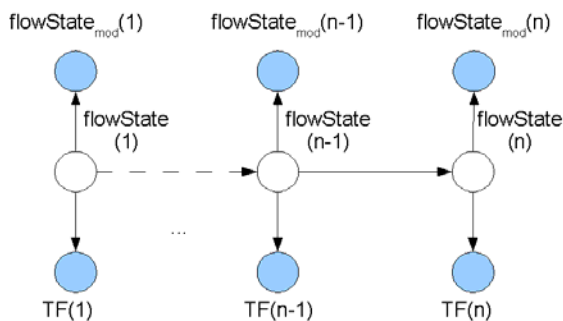


Figure 1: Dependency model

The “...” and the dotted arrow on the left illustrate a chain of dependencies from time 1 to time n-1.

Let **flowState** be a vector {flowState(1),... ,flowState(n)} and likewise for the vector **flowState<sub>mod</sub>** and **TF**. The joint probability for the sequence of flowStates, model estimated flowStates and temporal features is then  $p(\text{flowState, flowState}_{mod}, \text{TF}) =$

$$\prod_{n=1}^N p(\text{TF}(n) | \text{flowState}(n))$$

$$\prod_{n=1}^N p(\text{flowState}_{mod}(n) | \text{flowState}(n))$$

$$\prod_{n=1}^N p(\text{flowState}(n) | \text{flowState}(n-1))$$

Assuming the densities are Gaussian, an expectation-maximization algorithm may estimate the particular distributions given a set of observations, and the sum-product algorithm may be used to compute desired marginal distributions [10].

A normal Bayes risk estimator will be used to make class decisions, based on the marginal distribution  $p(\text{flowState}(n))$  and some reasonable loss function found in collaboration with our medical professional partners.

*C. Frequency domain classification*

Let's consider the independent flowState variable flowState<sub>mod</sub>.

The post-processed Doppler signal is rich in frequency content, and it is reasonable to attempt to classify the flowState based on a time-frequency representation of the signals. The Doppler baseband range is roughly 4 kHz. With the aforementioned 2.5 Hz resolution, we have some 1600 frequency coefficients per sample. We clearly need a classification approach which efficiently deals with high-dimensional data in real-time. Furthermore, it would be desirable if the classifier provides a confidence estimate, preferably as a probability that can directly serve as the  $p(\text{flowState}_{mod})$  estimate.

A sparse kernel machine seems to be a reasonable choice since they're capable of dealing efficiently with high-dimensional data and they're well suited for time-series [6]. Recently, a sparse kernel machine based on a Bayesian framework has been proposed [7], named the Relevance Vector Machine (RVM), where there now are available efficient implementations.

The RVM estimates a conditional distribution

$$p(\text{state} | x, w, \beta) = N(\text{state} | y(x), \beta^-)$$

where  $\mathbf{x}$  is the input vector,  $\mathbf{w}$  a parameter vector,  $N$  the normal distribution and  $\beta$  is the noise precision.  $y(\mathbf{x})$  is defined in terms of a set of basis functions that with the RVM formulation is constrained to the Support Vector Machine (SVM)-like form

$$y(x) = \sum_{n=1}^N w_n k(x, x_n) -$$

Here, in difference to SVMs, the kernel  $k$  doesn't need to be positive-definite.

On benchmark data the RVM has about equal accuracy as the SVM, training times are roughly an order higher, but there is no need to do explicit parameter optimization for RVM kernels. Classification of new data is significantly faster for RVMs than for SVMs [7].

#### IV. PRELIMINARY RESULTS

All figures depict samples from different patients. Figure 2 shows the spectrogram for one of the three transducer elements during the pre-check saline injection phase. The flowState is intravenous. The horizontal scale is in seconds and the vertical scale is Doppler frequency in Hertz. The injection starts at 16.5 seconds and ends at 18.5 seconds. Note the horizontal dark lines stemming from the 50 Hz and harmonics removal.

In this figure it is reasonably simple to discern a single time-slice of 0.2 seconds. The  $\text{flowState}_{\text{mod}}(n)$  RVM estimate is based on a single such time slice at time  $n$  and similarly  $\text{TF}(n)$  is a representation based on the same time slice. Other time slices in the saline and contrast injection phases maps onto other time ordinals in the dependency model.

In Figure 3 the injection starts at 333 seconds and ends at 353 seconds, immediately followed by a post-injection saline injection ending at 360 seconds. The flowState is still intravenous. For these samples the gain is 45 dB and the dynamic range 40 dB.

Figure 4 and 5 shows how the inter-patient signal variance may be quite large. In Figure 4 the injection starts at 75.5 seconds and lasts for 2 seconds. In Figure 5 the injection starts at 217 seconds and ends at 247, immediately followed by a post-injection saline injection ending at 257 seconds. The flowStates are intravenous. During the pre-check saline injection there is more noise and a less pronounced response than in Figure 2. During the contrast-injection the signal suffers from a marked response decay.

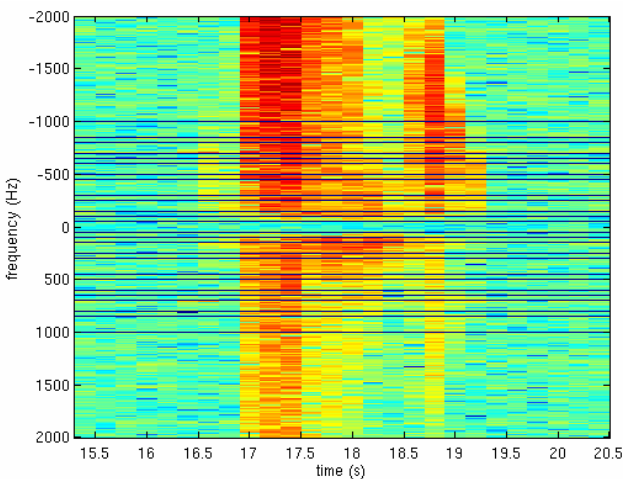


Figure 2: Pre-check saline injection spectrogram

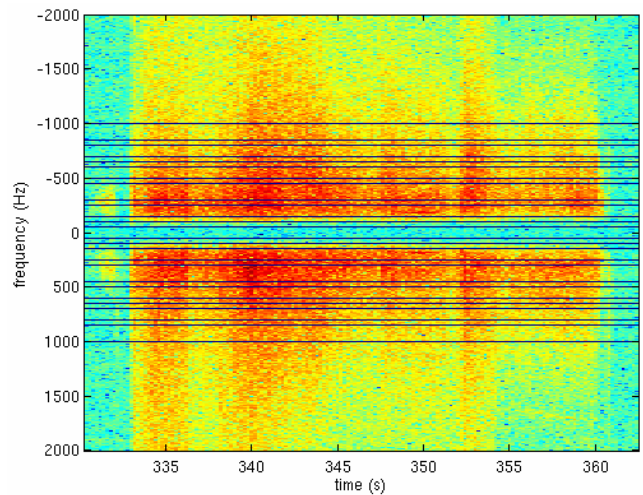


Figure 3: Contrast-agent injection spectrogram

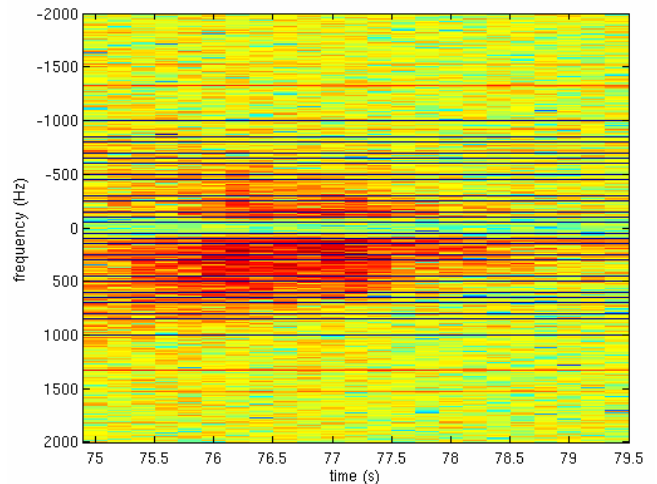


Figure 4: Pre-check saline injection spectrogram



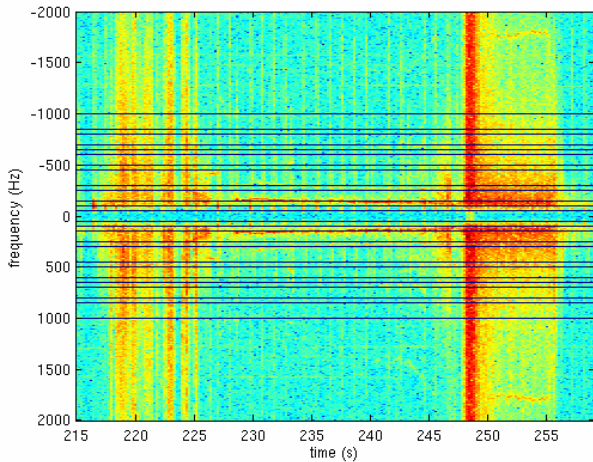


Figure 5: Contrast-agent injection spectrogram

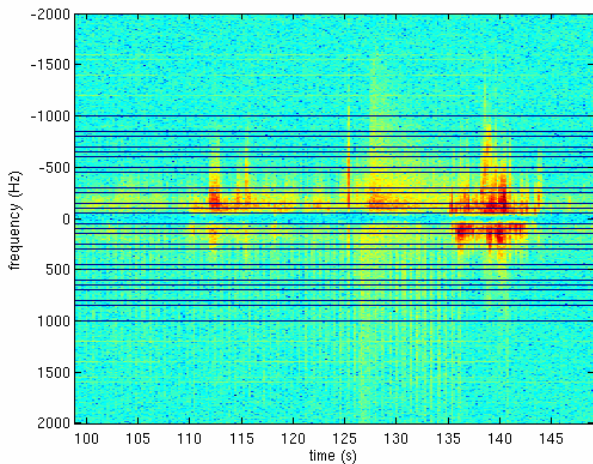


Figure 6: Contrast-agent injection spectrogram

Now consider Figure 6 where the contrast injection starts at 101 seconds and ends at 121, immediately followed by a post-injection saline injection ending at 131 seconds. Note the prolonged response after the end of injections. This sample is an extravasation incident and the flowState is extravasated.

## V. CONCLUSIONS

We've shown preliminary results illustrating some of the challenges in automatic injection state detection based on Doppler ultrasound. Furthermore we've presented a new method for pattern recognition tailored to the examination

procedure and illustrated how a particular statistical model may be instantiated based on the Doppler ultrasound data. Future work will focus on empirically evaluating the statistical accuracy of the proposed method.

There are several sources of additional information from the examinations that hasn't been taken into account. Examples are contrast agent types used, the volume administered, the flow rate, ultrasound gain and dynamic range settings. In case the empirical accuracy proves to be insufficient, one might extend the dependency model to include one or more of these sources.

The present dependency model makes distribution assumptions that may be too restrictive. If a wider range of distributions are to be considered, an investigation is needed on how marginals may be formed and distribution learning may be tractably achieved.

## REFERENCES

1. Birnbaum B. et al. "Extravasation detection accessory: Clinical evaluation in 500 patients.", *Radiology* 212:22, 431-438
2. Cohan RH, Ellis JH, Garner WL. "Extravasation of radiologic contrast material: recognition, prevention and treatment." *Radiology* 1996;199:697-701
3. www.neorad.no
4. "MEDRAD Introduces New Extravasation Detector Technology", <http://www.medrad.com/newsroom/display-press-release.html?PRid=205>
5. Hoff L. et al. "An ultrasound transducer to monitor CT contrast media injections", *forthcoming 2008*
6. Ruping S., "SVM Kernels for Time Series Analysis" in Klinkenberg et al., "LLWA 01 - Tagungsband der GI-Workshop-Woche Lernen - Lehren - Wissen - Adaptivität", pp. 43-50, Dortmund, Germany, 2001
7. Tipping, M. E., "Sparse Bayesian learning and the relevance vector machine". *Journal of Machine Learning Research* 1, 211-244. 2001
8. Guler I. and Ubeyli E., "A recurrent neural network classifier for Doppler ultrasound blood flow signals", *Pattern Recognition Letters*, Volume 27, Issue 13, 1 October 2006, Pages 1560-1571
9. Übeyli E., "Doppler ultrasound signals analysis using multiclass support vector machines with error correcting output codes.", *Expert Syst. Appl.* 33(3): 725-733 (2007)
10. Bishop C., "Pattern Recognition and Machine Learning", Springer 2006, ISBN 0-387-31073-8
11. Malek J., "Bayesian Classifier for Medical Data from Doppler Unit", *Acta Polytechnica*, Vol. 46, no. 4/2006
12. Herment A. et al., "Improved Characterization of Non-Stationary Flows Using a Regularized Spectral Analysis of Ultrasound Doppler Signals", *J. Phys. III France* 7 (1997) 2079-2102

Corr. author: Morten Forfang  
 Institute: Faculty of Eng., Vestfold University College  
 Street: Ravn. 197  
 City: Horten  
 Country: Norway  
 Email: mjpg@hive.no

# Optimization of fMRI Processing Parameters for Simultaneous Acquisition of EEG/fMRI in Focal Epilepsy

M. Forjaz Secca<sup>1,3</sup>, H.M. Fernandes<sup>1</sup>, J.R. Cabral<sup>1</sup> and A. Leal<sup>3,4</sup>

<sup>1</sup> Cefitec, Dep. of Physics, Universidade Nova de Lisboa, Portugal

<sup>2</sup> Ressonância Magnética de Caselas, Lisboa, Portugal

<sup>3</sup> Department of Neurophysiology, Hospital Júlio de Matos, Lisboa, Portugal

<sup>4</sup> Department of Pediatric Neurology, Hospital Dona Estefânia, Lisboa, Portugal

**Abstract** — In the context of focal epilepsy, the simultaneous combination of electroencephalography (EEG) and functional magnetic resonance imaging (fMRI) holds a great promise as a technique by which the hemodynamic correlates of interictal spikes detected on scalp EEG can be identified.

The fact that traditional EEG recordings have not been able to overcome the difficulty in correlating the ictal clinical symptoms to the onset in particular areas of the lobes, brings the need of mapping with more precision the epileptogenic cortical regions. On the other hand, fMRI suggested localizations more consistent with the ictal clinical manifestations detected.

This study was developed in order to improve the knowledge about the way parameters involved in the physical and mathematical data, produced by the EEG/fMRI technique processing, would influence the final results. The evaluation of the accuracy was made by comparing the BOLD results with: the high resolution EEG maps; the malformative lesions detected in the T1 weighted MR images; and the anatomical localizations of the diagnosed symptomatology of each studied patient. The optimization of the set of parameters used, will provide an important contribution to the diagnosis of epileptogenic foci, in patients included on an epilepsy surgery evaluation program.

The results obtained allowed us to conclude that: by associating the BOLD effect with interictal spikes, the epileptogenic areas are mapped to localizations different from those obtained by the EEG maps representing the electrical potential distribution across the scalp (EEG); there is an important and solid bond between the variation of particular parameters (manipulated during the fMRI data processing) and the optimization of the final results, from which smoothing, deleted volumes, HRF (used to convolve with the activation design), and the shape of the Gamma function can be certainly emphasized.

**Keywords** — fMRI, BOLD, EEG, Epilepsy.

## I. INTRODUCTION

The simultaneous acquisition of electroencephalography (EEG) and functional magnetic resonance imaging (fMRI) has been increasingly used in focal epilepsy to correlate the hemodynamic response to the interictal spikes detected on EEG. However EEG recordings have presented some difficulties in correlating the ictal clinical symptoms to the onset

in particular areas of the lobes, whereas fMRI suggested localizations more consistent with the ictal manifestations.

To further understand the differences between EEG and fMRI localizations it is important to study how the different parameters involved in the processing of physical and mathematical fMRI data can influence the final results in terms of consistency and proximity to the lesions observed.

In order to achieve that we analyzed two of our patients in detail, by varying some of the main fMRI processing parameters and compared the results with the EEG data and the lesion locations.

## II. MATERIALS AND METHODS

We studied two patients with a diagnosis of idiopathic OLE, submitting them to a 120-min EEG recording outside the scanner, with a cap of 64 AgCl electrodes. The position of each electrode was obtained using an electromagnetic digitizer PATRIOT. We used a sampling rate of 256 Hz, filters of 0.5–70 Hz. One week after this procedure, a session of functional MRI was performed while simultaneously recording the EEG (37 electrodes along the scalp and 2 located in the chest). Each patient demonstrated a single, topographically stable, paroxysm type. This was the main neurophysiological criteria for selection of patients for this study. Informed consent was obtained from the parents of the patients.

Source analysis of the EEG was done in spikes detected visually in recordings obtained outside the scanner for both patients. The EEG was high pass filtered at 3 Hz, and spikes with good signal to noise ratio were aligned by the peak amplitude to produce an average spike. The sources were obtained from instantaneous regional dipoles at the peak of averaged spikes, with a standard three layer Boundary Element Model (BEM) of volume conduction (conductances of 0.33, 0.0042, 0.33 S/m for scalp, bone and brain), provided in the Source2 software package (Neuroscan, El Paso, Mexico). Standard electrode positions were also used.

The EEG/fMRI consisted in the acquisition of blocks of 150 brain volumes for patient 1 and 140 brain volumes for patient 2, each one made of 34 EPI images (in plane resolu-

tion 3.75 mm and slice thickness of 7 mm, no spacing; FOV: 24 x 24 cm; matrix: 64 x 64; flip angle of 90°) obtained with a TE = 50ms, a TR = 2.275 s (patient 1) and TR = 2.475 s, (patient 2), corresponding to periods of 351 s and 357 s of continuous and simultaneous monitoring. 5 blocks were obtained per patient, providing 175v5 s of simultaneous monitoring for patient 1, and 1785 s for patient 2. A brain T1 weighted anatomic sequence (in plane resolution 0.94 mm and slice thickness of 1.3 mm) was obtained in the same session.

Images were acquired in a 1.5T GE CVi/NVi scanner, while the EEG was recorded through a set of AgCl electrodes connected to an amplifier located outside the scanner room through carbon fiber wires (MagLink, Neuroscan, El Paso, TX, U.S.A.). The cap did not produce detectable artifacts in the MRI sequences, so these could be processed without any special correction. The EEG was corrected for artifacts induced by the magnetic field and rapidly changing imaging gradients offline using commercial software (Scan

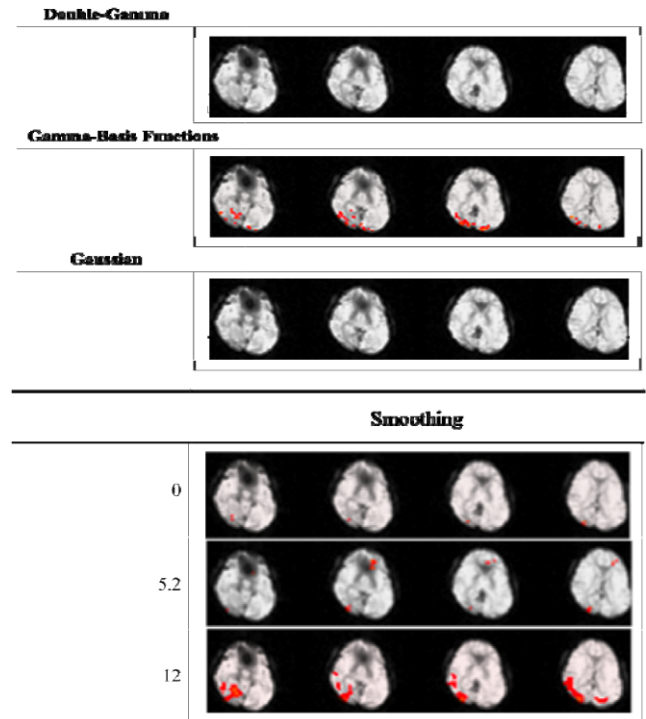
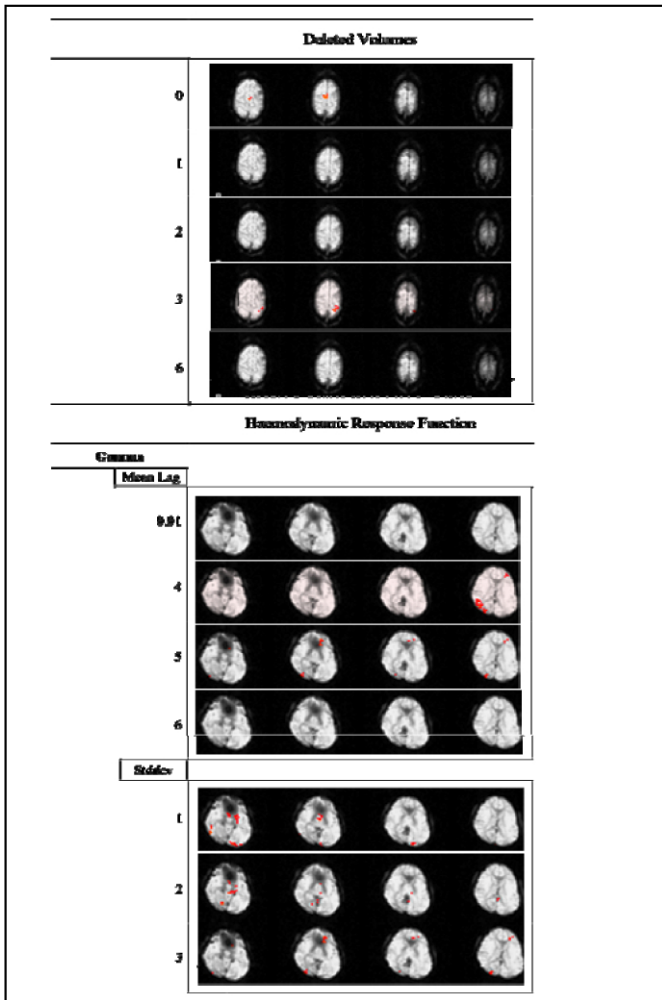


Fig. 1 Variation of some important parameters used in the fMRI data preprocessing. The left side of each brain slice image corresponds to the right side of the real brain.

4.3.2, Neuroscan). The time of occurrence of spikes was determined by visual inspection and used to classify the acquired image volumes, resulting in sequences of events of interest used to build an event-related paradigm.

The preprocessing and paradigm-related analysis of the fMRI was performed using the FSL software package [1]. In order to perform this study, a set of important parameters, involved in the fMRI data preprocessing, was initially selected. The tests presented along the study reveal the influence of each parameter in the accuracy of BOLD activation maps, and also its contribution to false positives. To model the haemodynamic function a standard Gamma function with derivatives was used [2] (with a FWHM of 3 s [3] and a mean lag of 5 s [4]). Four and twenty-four spikes were analyzed, respectively, for patients 1 and 2. The EPI sequences were corrected for movement and slice acquisition time and smoothed with a Gaussian kernel of FWHM 5.2 mm [5]. No initial volumes from the acquired fMRI sequence were deleted. A local autocorrelation correction was used and z statistic images generated. The correction for the multiple comparison problem was done using a cluster threshold with  $p = 0.05$ . [3]

Representation of dipoles on individual brain anatomy was performed by adjusting the fiducial points (nasion,

preauricular points,inion, and vertex) of the BEM model on the individual 3D T1 MRI.

### III. RESULTS

In order to improve the knowledge about how parameters involved in the fMRI data preprocessing influence the final results, we have performed several tests consisting in varying each parameter in a certain range, which included the group of values that had already been verified as scientifically reasonable.

The results of each test are represented by a sequence of 4 axial slices of the brain that includes the region of interest for each patient. The identification of this region was made by combining both information of the malformative lesion detected in the T1 weighted MR image, and the anatomical localization of the diagnosed symptomatology of each studied patient.

We have observed that each patient is a case on its own and should be studied individually. In this paper, in order to demonstrate the importance of these parameters and their individual variation we present the results of two of our patients.

For the “Deleted Volumes” test (patient 2), different BOLD activation maps were performed. The option of deleting the first 3 volumes of this sequence shows to be the best option, since the BOLD clusters detected are over the primary motor cortex area (Fig. 2, 3b), considerably near from the malformative lesion (Fig. 3a). These results are also consistent with the diagnosed symptomatology, since the patient has moved his right hand during the seizures.

In the study for the “Haemodynamic Response Function” (patient 1) parameter were included another two tests, in order to evaluate the influence of the Gamma function’s shape in the BOLD activation distribution map. The “Mean Lag” test showed that there was a restricted range of values (4 and 5) where it was possible to identify some BOLD clusters. The “Stddev” test for 1 s reveals a cluster located over the cortical left occipital region, in the same axial plan as the malformative lesion detected for this patient. For the rest of the haemodynamic response functions studied, only the set of Gamma-basis functions did show some BOLD clusters. Some of these clusters seem to be highly significant since they are near the expected area (Fig. 1, 2b).

The test for “Smoothing” (patient 2) reveals the great influence of this parameter in the production of accurate BOLD activation maps, since it is intimately related to the size of the clusters. However, its bad use may hide important clusters or even produce false positives.

The evaluation of the accuracy of the results that showed better correlation to the expected information, was made by

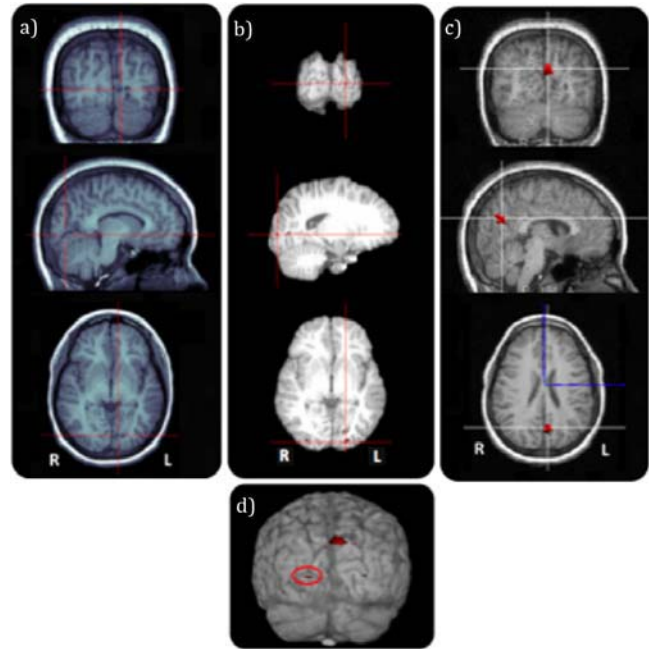


Fig. 2 Patient 1: (a) T1 weighted MR images identifying the malformative region; (b) BOLD fMRI images showing the cluster over the cortical left occipital region, near the malformative region; (c) Regional dipole model applied to calculate the electric source of the detected spike (EEG). (d) 3D fMRI BOLD activation map (rendering).

Table 1 Coordinates corresponding to the center of the detected malformative lesion, cluster BOLD and EEG source position for patient 1.

	Position		
	X (mm)	Y (mm)	Z (mm)
Lesion	128	62	64
Cluster BOLD	138	51	61
Regional Dipole (EEG)*	126	71	85

Table 2 Distances between the cluster BOLD, the lesion, and the regional dipole for patient 1.

	Lesion (mm)	Regional Dipole (mm)
Cluster BOLD	15.17	33.47
Regional Dipole	22.93	-

Table 3 Coordinates corresponding to the center of the detected malformative lesion, cluster BOLD and EEG source position for patient 1.

	Position		
	X (mm)	Y (mm)	Z (mm)
Lesion	140	89	104
Cluster BOLD	143	92	101
Regional Dipole (EEG)*	150	109	98

Table 4 Distances between the 3 types of results for patient 2.

	Lesion	Regional Dipole
Cluster	5.20	19.32
Regional Dipole	23.15	-

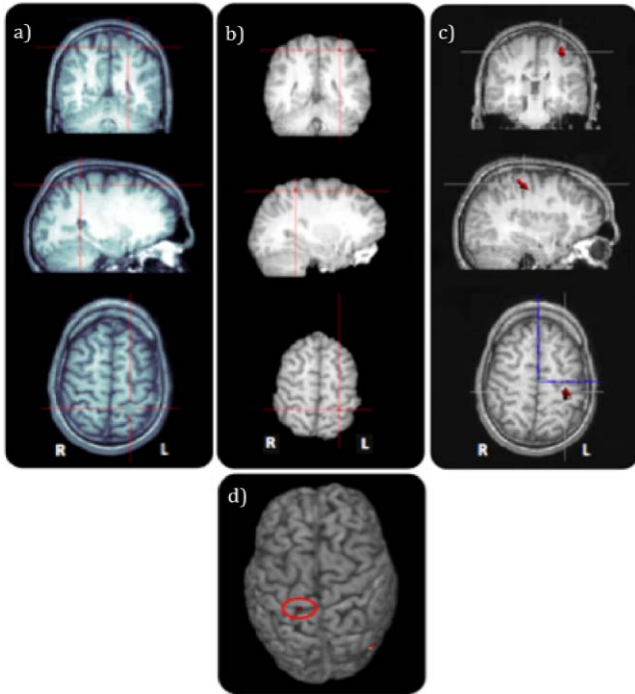


Fig.3. Patient 2: (a) T1 weighted MR images identifying the malformative region; (b) BOLD fMRI images showing the cluster over the primary motor cortex area, near the malformative region; (c) Regional dipole model applied to calculate the electric source of the detected spike (EEG). (d) 3D fMRI BOLD activation map (rendering).

comparing the BOLD results with: the Regional Dipole EEG maps (Fig. 2c, 3c); the malformative lesions detected (Fig. 2a, 3a) in the T1 weighted MR images; and the anatomical localizations of the diagnosed symptomatology of each studied patient. The correlation between the results (for the best set of parameters) has been analyzed through the measurement of the distances between the center of each focus for patient 1 and 2 (Table 2, 4).

The results reflect a very good correlation between the malformative lesion and the cluster BOLD (closest to the expected area) for each patient. For The Regional Dipole results presented a reliable GOF (0.959 and 0.953 for patient 1 and 2), and the estimated EEG sources are about 2.3

cm apart from the malformative lesion for both patients, showing also a good correlation between results.

#### IV. CONCLUSIONS

The results obtained allowed us to conclude that: by associating the BOLD effect with interictal spikes, the epileptogenic areas are mapped to localizations different from those obtained by regional dipole maps (EEG); there is an important and solid bond between the variation of particular parameters (manipulated during the fMRI data processing) and the optimization of the final results, from which smoothing, deleted volumes, HRF (used to convolve with the activation design), and the shape of the Gamma function can be certainly emphasized.

#### ACKNOWLEDGMENT

The work was supported by a grant for Research in Epilepsy from Tecnifar SA and by projects Topo3D (POSI/CPS/39758/2001) and EpilBI (POSC/EEA-CPS/60977/2004) from FCT.

#### REFERENCES

1. Smith S, Jenkinson M, Woolrich M, et al. Advances in functional and structural MR image analysis and implementation as FSL. *Neuroimage* 2004;23(suppl 1):208–19.
2. Huettel S, McKeown J, Song A, et al. Linking hemodynamic and electrophysiological measures of brain activity: evidence from functional MRI and intracranial field potentials. *Cereb Cortex* 2004;4:165–73.
3. Analysis Group, FMRIB, Oxford, UK. FSL. *FEAT - FMRI Expert Analysis Tool*. [Online] [Citação: 7 de Apr de 2007.] <http://fsl.fmrib.ox.ac.uk/fsl/feat5/>. IFMBE at <http://www.ifmbe.org>.
4. Kang, Joong Koo, et al. Using patient-specific hemodynamic response functions in combined. *NeuroImage*. 2003, Vol. Oct, 1162–1170.
5. Hawco, Colin S, et al. BOLD changes occur prior to epileptic spikes seen on scalp EEG. *NeuroImage*. May 1, 2007, Vol. 35(4), 1450–1458.

Author: Mario Forjaz Secca  
 Institute: Cefitec, Physics Department, Universidade Nova de Lisboa  
 Street: Quinta da Torre  
 City: 2829-516 Caparica  
 Country: Portugal  
 Email: mfs@fct.unl.pt

# Telemetric Personal Health Monitoring Systems for Asthma and Chronic Obstructive Pulmonary Disease

M. Guel<sup>1,2</sup>, A. Scholz<sup>1,2</sup>, D. Dill<sup>1,2</sup> and B. Wolf<sup>2</sup>

<sup>1</sup> Sendor GmbH, Munich, Germany

<sup>2</sup> Heinz Nixdorf-Lehrstuhl für Medizinische Elektronik, Technische Universität München, Munich, Germany

**Abstract** — In view of the worldwide increasing number of pulmonary diseases such as asthma bronchiale and COPD (Chronic Obstructive Pulmonary Disease) and the increasing scarcity of resources in health care systems it is necessary to find a treatment form, which supports and complements the conventional medical care and monitoring, without increasing time and personnel requirements. Such a system is realized by means of the Telemetric Personal Health Monitoring System (TPHM), which was developed by the Heinz-Nixdorf Lehrstuhl für Medizinische Elektronik. TPHM stands for a system, that embeds a wireless communication between physician and patient into a network, which consists of monitoring devices of vital functions and transmitter devices. In this case the monitoring device is a mobile aeroplethysmograph combined with an inhalation device.

**Keywords** — telemedicine, home monitoring, health monitoring, spirometry, pulmonary therapy

## I. INTRODUCTION

According to estimates of the World Health Organization WHO 300 million people suffered from asthma and 255,000 died of it in the year 2005. Asthma is the most common chronic disease among children. Asthma deaths will increase by almost 20% in the next 10 years, if urgent action is not taken [1].

Asthma bronchiale is a chronic inflammatory of the respiratory tracts. The obstruction of the airways is spontaneous and reversible by means of treatment. The causes for the disease are a spasm of the bronchial muscles, an inflammation and swelling of the bronchial mucosa and the increased secretion of mucus. The inflammation causes an increase of sensitivity of the respiratory tracts to many stimuli [2].

The main symptoms are sudden shortness of breath and coughing fits. The obstruction becomes apparent during the expiration, because the width of the respiratory tracts, caused by the secretion, is smaller than during the inspiration.

Asthma triggers are allergens, air pollutants such as exhaust gases or tobacco smoke, fog, cool air and medicines. Other triggers are a genetic disposition, physical exercise and psychological factors.

According to further estimates of the WHO (2007) 210 million people have COPD, heavy form of pulmonary disease, and 3 million people died of COPD in 2005. COPD will become the fourth leading cause of death worldwide by 2030.

The clear difference to the simple chronic bronchitis is the strong obstruction of the respiratory tracts. COPD is a slowly developing chronic disease, which is characterized by increasing irreversible damage and progressive obstruction of the airways. Symptoms are shortness of breath, persistent cough with sputum production.

COPD is caused by pollutants, which are inhaled during a longer period. These pollutants are particularly caused by tobacco smoke, air pollution, occupational treatment of organic and inorganic material, infection or genetics. If the pulmonary disease has progressed so far, that conventional therapy is not helpful anymore and the patient suffers from persistent shortness of breath, the lung transplantation followed by therapy is the last possibility of treatment.

## II. APPROACH

### A. Intention

If a pulmonary disease is detected by the physician during a simple lung functional test an aeroplethysmograph can help the patient for a better evaluation of his own state of health, therapy methods and progress of the therapy. Additionally, a better prognosis can be provided in this way. Mobile devices are used particularly for a fast examination of pulmonary functions in order to estimate the health status of the patient [3].

For therapy it is important to identify the trigger of the illness first. Allergic asthma can be treated well by a specific immunotherapy (Hyposensibilization). In case of the other forms of pulmonary disease it would be a great benefit to avoid the trigger of the disease to prevent the patient's state of health changing for the worse. Depending upon the severity level of the illness medicines which act anti-inflammatory, immunosuppressive or breath-way-extending have to be applied as well. These medicines are mostly applied by an inhaler.

In this case it is essential to monitor the effect of the therapy and medication to the patient's state of health.

This allows a henceforth optimal adjustment of medication and dosage. Much attention is given to the so called 'Home Monitoring', a modern form of care for chronically ill patients that considers the whole care chain including prevention, diagnosis, therapy and rehabilitation.

As core-element the technology of telemedicine is deployed. In combination with, by now, easy accessible and wide spread communication networks this technology allows the care of the patients' independent from their whereabouts. Thereby the patients have to measure their illness-specific parameters regularly whereas the acquired data is automatically forwarded to the physician in charge.

So the number of physician-patient contacts can be increased at lower costs per contact compared to ordinary home visits by the doctor [4]. The time and locally independent therapy of patients' matches the growing tend to mobility and the demand to reduce health care costs.

Due to permanent monitoring, changes concerning the illness pattern can be captured earlier and particularly aggravations detected in time and best possible absorbed.

Telemedical care in this case means the inclusion of a cellular phone as interface between the patient's measurement device and the physician's monitoring feasibility.

### B. Materials und Methods

Within the framework of the telemedicine-group at the Heinz Nixdorf-chair für Medizinische Elektronik a system has been developed that allows a better monitoring of representative human biological parameters (Fig. 1).

Especially developed diagnosis tools and 3<sup>rd</sup> party diagnosis tools have been upgraded with a self-designed transceiver module based on Bluetooth-technology and are now capable of telemetry.

Now data can be sent wireless from the measurement device to the cellular phone. Especially designed software for the phone has been developed to enable a smooth communication. The data could also be graphically displayed on the phone's display or be forwarded via the ordinary GSM-communication standard. The sent data is stored and processed in a data base and then delivered as email to the physician in charge.

Already at the beginning of 2004 a prototype of a Bluetooth-based aeroplethysmograph was developed at the Heinz-Nixdorf-Lehrstuhl für Medizinische Elektronik of the technical university of Munich (Fig. 2). The aeroplethysmograph already based on the principle of measuring differential pressure. For this application a Mitsumi Bluetooth chip as single-chip solution has been applied. Prob-

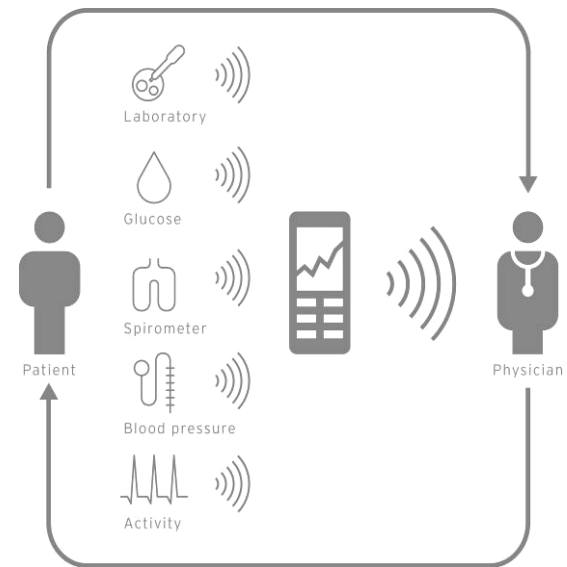


Fig. 1 components of the TPHM-system

lems occurred at the data transfer and, in addition, high data rates were not possible. Bad power management also appeared as a big disadvantage.

The second prototype followed in the middle of 2004. Again the principle of measuring differential pressure has been applied. But this time a microcontroller and a separate ALPS-Bluetooth-module were used. Problems with this version of prototype were the imprecise amplifier and sensor. Therefore the differential amplifier circuit has been reviewed but it turned out that the symmetrical structure of the circuit led to calibration problems.

The pulmonary diseases described at the beginning can easily be treated by inhalation of steam with water soluble medicaments or brines added. The medicament is directly brought to the airways and therefore acts in-situ. This avoids unwanted side effects, that might happen e.g. in the gastrointestinal tract during a treatment with pills

A good therapy support is given e.g. by the electrical inhalator OMRON Micro-AIR. At the end of 2004 as part of a project a device for the inhalator OMRON Micro-AIR has been developed that registers the on and off times of the inhalator and sends the data via Bluetooth to a mobile phone. Because of its very small dimensions this device can easily be applied everywhere. A water soluble medicament will be sputtered by ultrasound into most minute, respirable pieces.

Thanks to the increasing distribution of cellular phones in general and of those with integrated Bluetooth technology specifically additional acquisition of technology is not necessary in most cases. A basic feature at this juncture is the easy usability of mobile phones. Of course, the phone



Fig. 2 Telemetric Personal Health Monitoring System for monitoring of bodily functions [4]. In this case the system combines a newly developed aeropneumograph for measuring pulmonary functions with an inhaler for applying medicaments with integrated documentation of the applying times

has to be preconfigured, but for a successful data transfer it only has to be in Bluetooth range. No intervention by the patient is needed to send the measured data. The data transfer via email will be automatically activated after a successful measuring.

The regularly transmission of the pulmonary function parameters ensures an intensive connection of the patient to a centre that is specialized for this kind of disease. The health care by a physician will not be affected [5]. The system tends to create a more close collaboration and hence a better compliance of the patient.

### III. RESULTS AND DISCUSSIONS

With the use of the mobile phone as a relay device we faced different kinds of problems with the handling of the device.

Three premises have to be fulfilled so that the data can be transmitted successfully. Firstly software has to be installed on the mobile phone. Patients or physicians are generally not capable of that. Secondly the phone has to be able to establish a connection to the internet. This is usually preconfigured, but only valid for a specific SIM-card or country. At last the routing has to be defined (the address the email has to be sent to). The TPHM-System sends the messages via email. So an email-outgoing-server (SMTP), a target address and the type of encrypting in the mobile phone has to be defined.

In summary one can say that the configuration has to be done by a service technician.

As an alternative a Bluetooth modem for stationary home usage that can be easily connected to every telephone socket could be considered. One disadvantage would be that the patient cannot transmit his data at any time. The transfer would only happen, when the patient is at home. In most cases this would be sufficient. The handling is easy and can be done directly by the user. Only the routing has to be done by a technician. This has not to be done locally.

### IV. CONCLUSIONS

Depending on the application different forms of the TPHM-System have to be applied. One should consider how relevant a single measured value is and how dangerous a wrong measured value for the patient could be.

In case the applications' task is to analyse the data statistically and to document it a system should be chosen that sends the data once in a while. Systems like that can easily be realized with the help of a stationary TPHM-modem.

If it is necessary to intervene immediately according to the measured values, a mobile phone has to be applied. But, attention, the accessibility of the mobile phones is often not sufficient to ensure a data transfer. That means the application is in this case (no GSM-Service or battery empty) not capable of fulfilling its task.

### REFERENCES

1. Weltgesundheitsorganisation WHO; Asthma, COPD; <http://www.who.int/>; 2007
2. Gerd Herold; Innere Medizin; Eine vorlesungsorientierte Darstellung; Köln; 2002
3. Wolfgang T. Ulmer, Dietrich Nolte, Josef Lecheler; Die Lungenfunktion. Methodik und klinische Anwendung; Thieme Verlag; 2000
4. Wheeler T., Strategies for delivering tele-home-care provider profiles; *Telemed Today*; 1998 6(4), p. 37-40
5. A. Scholz, V. Lob, J. F. Clauss, J. M. Herrmann, B. Wolf; Einbindung von Sensorsystemen in das TPHM-System; *Biomedizinische Technik Band 49*, pp. 224-225, 9/2004
6. Michael Pfeifer, Bernhard Werner, Helgo Magnussen; *Telemedizinische Betreuung von Patienten mit chronischen Atemwegserkrankungen*; *Medizinische Klinik* 99; Februar 2004

Author: Murat Gül

Institute: Heinz Nixdorf-Lehrstuhl für Medizinische Elektronik

Street: Theresienstrasse 90

City: 80333 Muenchen

Country: Germany

Email: [guel@tum.de](mailto:guel@tum.de)



# Clinical Relevance of Preoperative CT-based Computer Aided 3D- Planning in Hepatobiliary, Pancreatic Surgery and Living Donor Liver Transplantation

J. Harms<sup>1</sup>, H.-M. Tautenhahn<sup>1</sup>, H. Bourquain<sup>2</sup>, T.H. Kahn<sup>3</sup>, H.-O. Peitgen<sup>2</sup>, J. Fangmann<sup>1</sup>, S. Jonas<sup>1</sup>

<sup>1</sup> University of Leipzig/Department of Visceral-, Transplantation-, Thoracic- and Vascular- Surgery, Leipzig, Germany

<sup>2</sup> MeVIS- Center for Medical Diagnostics and Visualization, Bremen, Germany

<sup>3</sup> University of Leipzig/Department of Diagnostic and Interventional Radiology, Leipzig, Germany

**Abstract** — Multiple imaging approaches are currently used for diagnosis and surgery planning of hepatobiliary tumors and living donor liver transplantations. Conventional imaging studies remain insufficient to demonstrate the individual anatomy. Refinements in CT technology with the introduction of «multidetector-row» CT scanners and implementation of mathematical methods on computerized digital data enabled CT based 3D- visualizations. This renders preoperative surgery planning more reliable and reproducible. Since the application in oncological liver surgery has been studied previously, our interest focussed on pancreatic- and biliary tract tumors including preoperative work-up in living donor liver transplantation. A total of 29 patients were assessed. CT based 3D- display provided accurate preoperative visualization and computerized risk analyses for safety margins of pancreatic- and biliary- tract tumors. In living related liver transplantation the 3D- procedure may help to recognize vascular variants and to define the splitting line. The results may have major impact on patient selection and in our opinion allow better planning of the appropriate surgical approach.

**Keywords** — 3D visualization, - computertomography, hepatobiliary cancer, - living donor liver transplantation, - computer assisted surgery, - image guided surgery

## I. INTRODUCTION

Hepatobiliary- and pancreatic surgery as well as liver transplantation have shown considerable developments, mainly due to improvements of surgical techniques, diagnostic imaging modalities and postoperative care. Recent developments of imaging techniques with the implementation of computer technologies have enabled a new quality of visualization consisting in 3D- representation to realize image guided and computer assisted surgery. These developments allow enhanced precision in preoperative planning and image guided surgery using intraoperative navigation tools. This is already practiced in neuro-, maxillo-facial and orthopaedic surgery.

3D- visualizations of visceral organs failed in the past because of technological limitations to create image data with minimal motion artifacts and lack of stable computerized image processing technologies. The introduction of «multidetector- row» helical CT, however, has offered the opportunity to

create digital data with minimal motion artifacts [1]. The application of a variety of dedicated and robust computerized image processing steps succeeded in visualizations, which enable precise localization and exact in- depth representation of tumors especially in surgery of liver cancers [2,3].

Because of limited availability of postmortal liver donors, the challenging technique of living related liver donor transplantation (LDLT) has gained increasing application worldwide. Especially this field reinforced the interest in computerized preoperative 3D- visualizations. Adult-to-adult LDLT is technically demanding. The liver has to be splitted into in a well preserved right lobe representing the graft and a remnant left liver lobe without any damage to the donor. To achieve these aims accurate anatomical and functional work- up for surgical planning is mandatory. The same holds true for planning of oncological resections in biliary- and pancreatic tumors. To analyze the clinical impact of computerized 3D- visualizations in hepatobiliary – pancreatic surgery and LDLT we performed a collaborative study with the IT- research institute MeVis, Bremen, Germany.

## II. MATERIAL AND METHODS

A total of 29 patients were assessed by CT based 3 D- visualization techniques. 12 patients were analysed for pancreatic-, 4 patients for biliary tract tumors and 13 patients for LDLT. CT scans were performed with a 4 slice «multi-row-detector» helical scanner machine (Siemens Volume Zoom<sup>®</sup>, Siemens Erlangen, Germany). For computer assisted 3D- visualisation data were transferred to the IT- Research Institute MeVis, Bremen, Germany. 3D- image processing of original CT- data included segmentation of specific anatomic and pathologic structures. For relevant vascular structures centre lines were calculated. A hierarchical mathematical model representing the vascular tree was created. This allowed calculation of individual vascular territories. Computerized “surgery planning” included virtual insertion of splitting lines in LDLT and safety margins in oncologic patients. Results were displayed either one by one or in arbitrary combinations in both, 3D- and overlaid to the original CT data [2,3].

### III. EXPERIMENTS AND RESULTS

#### A. Pancreatic Tumors

3D- visualization of pancreatic tumors succeeded in 11 of 12 cases. In a single case of cancer of the papilla of Vater with the tumor mass localized within the duodenum visualization was unsatisfactory. In 2 patients arterial variants of the common hepatic artery originating from the superior mesenteric artery could be displayed. Visualization of vascular structures in the vicinity of the tumor succeeded in all cases. Involvement of regional arteries by the tumor (A. gastroduodenalis n= 3, SMA n= 1, Celiac trunk n= 1, A. lienalis n=1) and/ or of the venous mesenterico- portal trunk (portal vein n= 1, confluens n= 2, SMV n= 1, V. lienalis n= 1) could be shown in 5 patients. On the basis of computerized surgery planning, resection of the tumor seemed likely in 9 cases. Operative procedures for cure were performed in 9 patients. Palliative surgery was carried out in 2 patients because of multivisceral tumor infiltration. In all patients the specific findings (tumor size, localization, vascular involvement) obtained by 3D- CT visualization could be reconfirmed intraoperatively. Because of non-resectability one patient was treated with palliative chemotherapy.

#### B. Biliary-Tract Tumors

3D- CT based visualizations demonstrated localization, extraluminal extend and involvement of adjacent vascular structures within the liver hilum and the hepatoduodenal ligament. Longitudinal ductal tumor extension could be demonstrated as well. ERC- and MRC- examination revealed biliary- tract tumors classified as Bismuth type IV in 1, Bismuth type I in 2 and tumor of the distal common hepatic duct in one case. 3D- CT based visualizations were discrepant in 2 cases. ERC- and MRC classified Bismuth type I tumors appeared as Bismuth type II/IIIa in 1 and as a tumor originating from the gall bladder in 1 case. Compared to conventional radiological methods, 3D- CT based visualizations seem to be more precise to determine the extend of tumor spread and vascular involvement. Thus 3D- CT based visualizations representing the advantage of a single non- invasive examination of biliary tumors may complement conventional diagnostic tools and may improve treatment planning.

#### C. Living Donor Liver Transplantation

3D- imaging studies were performed in 13 consecutive candidates evaluated for adult-to-adult living donor liver transplantation. Appropriate computerized 3D- visualizations of the arterial anatomy succeeded in 11/ 13 (84%) candidates. In the anatomy and the branching of the portal-

the hepatic veins could be visualized in all (13/13; 100%); clarification of the biliary tract anatomy succeeded in all of the 7 (7/7,100%) patients studied. Courses and branching points of the hepatic arteries, veins, bile ducts in relation to the intended splitting line could be displayed in a multidirectional view and in arbitrary combinations. Hepatic artery variants were detected in 5/13 (38.5%) patients. Display of the crucial segment IV artery succeeded in 11/13 (84.6%) patients. Both variants of the portal vein anatomy (n=2; 15.4%) were related to a trifurcation with early branching to the right liver lobe. Anatomic variants of hepatic vein ramification were observed in 6/13 (46.8%) patients. Computerized 3D-CT cholangiographic visualization provided precise mapping of the caliber, branching points, course and the relation to associated vascular structures. The course of the common and the hepatic bile ducts up to the to the 3<sup>rd</sup> order branches was clearly displayed. Variant bile duct anatomy with insulated drainage of the liver segment V into the cystic duct was detected in 1/7 patients. Adverse reactions related to the iodine content of biliary contrast agent used were absent in the observed patient set. In summary, our data indicate that 3D-CT based visualization facilitates diagnostic work-up with high accuracy. Multiple examinations especially with regard to invasive diagnostics may be avoided in future.

### IV. CONCLUSION

Research on computer assisted surgery has expanded rapidly allowing application for clinical procedures on routine basis. Two fields of engineering technologies are required to realize computer assisted surgery in visceral organs: (1) a surgical simulation system to realize planning according to the condition and anatomical feature of the patient, (2) an image fusion system which is applicable for visceral organ surgery and acts as an apparatus for image guided surgery. Application of computerized segmentation techniques on digital data derived from computer tomography facilitate 3D- geometrical and structural organ analyses. Computer simulations permit multiple viewing perspectives. Interactive insertion of resection lines ensures preoperative identification of "safety margins" and "areas of risk" in oncological patients and in living related liver donors. Results achieved are accurate and robust. Data may be used as a "virtual road map" during surgery.

Because of the inability of precise intraoperative registration image-fusion during visceral surgery render computer assisted surgery presently impossible. Physiologic organ shifting and soft organ composition with deformation during surgical manipulation are obstacles. The actual manual operating process is guided by fusion of visual and tactile

information. For image assistance and representation during surgery developments in the design of modern operating rooms with the operational availability of computer technologies offer an interim solution. Consequently computerized 3D- visualizations can be transferred and displayed on flat screen monitors near to the surgical field.

### A. Pancreatic Tumors

Imaging of pancreatic tumors shows considerable progress. About 35% of pancreatic tumors are demonstrated to be resectable with curative intent [4]. Assessment of resectability, in most cases remains unclear until surgical exploration. Conventional diagnostics often fail to provide accurate assessment of regional tumor infiltration. Further limitation is the inability to depict small hepatic and peritoneal metastases. Neither conventional CT techniques, nor MRI and angiography can rule out these problems. From the surgical point of view 3 issues have to be addressed clearly by the preoperative staging of pancreatic tumors: (1.) local resectability; (2.) lymph node metastases and (3.) distant metastases. Accuracy for these determinants can be established by CT- and MRI in 71% and 70% respectively [5]. Computerized CT based 3D- visualization techniques may allow improved precision of staging pancreatic tumors that includes: (1.) interactive visualization of the pancreatic tumor (2.) tumor size (3.) display of the vascular anatomy; i.e. variants which are essential for surgical dissection and lymphadenectomy; (4.) tumor involvement of vessels; (5.) preoperative computerized resection planning in order to ensure adequate "safety margins". The potential of CT based 3D- visualizations to detect metastatic lymph nodes remains to be shown on biological imaging studies such as PET-CT scanning. In summary, our preliminary experience suggests that 3D- modeling of CT data should be included in staging of pancreatic tumors in selected cases. Small peritoneal and hepatic metastases can not be visualized sufficiently. In such suspected cases laparoscopy is useful and favorable compared to diagnostic laparotomy.

### B. Biliary- Tract Tumors

Evaluation of biliary- tract tumors is an assessment of resectability, since resection is the only effective therapy. Resectability ranges between 10- 50% with 5-year survival rates of 20%. Preoperative staging must assess 4 critical issues: (1.) extend of tumor within the biliary tree, (2.) vascular invasion, (3.) hepatic lobar atrophy, (4.) metastatic disease [6]. Cholangiography (ERC) demonstrates the location of the tumor and the ductal extent of the disease. The procedure however carries a considerable risk. In addition MRC provides information regarding patency of hilar vas-

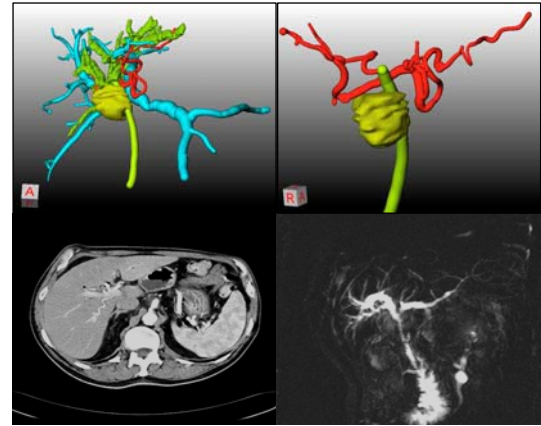


Fig.1 Computerized 3D visualization of a hilar biliary duct tumor, adjacent vascular structures the virtual oncological resection plane. Raw data with corresponding CT-scan and MR- cholangiography.

cular structures, presence of nodal and distant metastases and of lobar atrophy. There are a few limitations including cost, availability, operator dependence, patient tolerance and representation. In biliary- tract tumors experience with 3D- CT based visualizations is rare. CT based 3D- visualization meet above mentioned requirements. Quality and accuracy in the accomplished investigations in our opinion was superior to MRC. CT based 3D- visualizations provide improved tumor localization and a virtual view of vascular structures within the liver hilum and the hepatoduodenal ligament (Fig.1). 3D- mapping probably allows meticulous tumor dissection and effective protection of crucial vascular structures. In hilar bile duct tumors preoperative visualization of the course, the caliber and the branching of bile ducts will facilitate intraoperative identification for biliary reconstructive reconstruction. Application of the procedure is limited due to possible side effects of the contrast medium [7]. The procedure however may be indicated in cases of non-obstructed bile ducts (living donor liver candidates) or in patients with contraindications to PTC and MRC.

### C. Living Donor Liver Transplantation

3D- CT based visualizations achieved increasing acceptance in the work-up of in living donor liver transplantation especially in the Asian world. The complex anatomy of the liver with high incidence of vascular variants reinforces the necessity for accurate preoperative vascular imaging. Up to one-third of potential donors may not be eligible for the procedure because of unsuitable vascular anatomy [8]. CT based 3D- visualization is non- invasive. Our data presented suggest that the method has achieved a robust standard. The procedure gives essential and detailed information about: variants of the hepatic artery, origin of the artery to segment

IV, anatomy of portal and hepatic veins, variants of the biliary- tract. In addition the liver volume can be calculated. In our opinion the results of 3D- visualization of CT- based cholangiograms were as good as those by ERC and seem to be superior than MRC- scans. According to our experience preoperative interactive simulation of the splitting line in the donor liver is of major value because as it identifies “areas at risk”. These are margins along the splitting line of potential arterial devascularization or venous congestion (Fig.2). In conclusion, 3D- CT based visualization seems to be a valuable tool in order to perform this surgical procedure with high accuracy and to minimize potential risks to the donor and the graft.

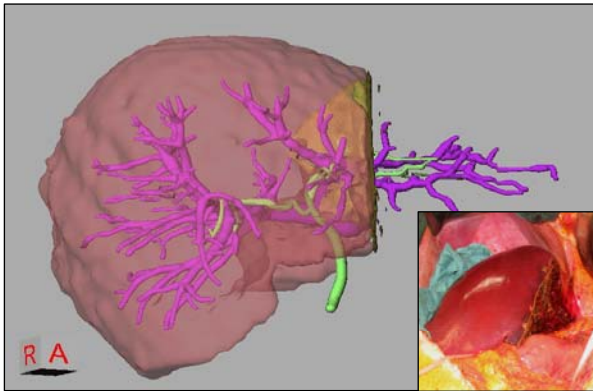


Fig.2 Simulation of the living donor remnant after virtual dissection of the left lobe lateral segment graft for a pediatric liver recipient. The splitting line follows the falciform ligament. Resultant areas of portal venous congestion are visualized.

## REFERENCES

1. Kamel, I.R., Kruksal, J.B., Pomfret, E. A.: Impact of multidetector CT on donor selection and surgical planning before living adult right lobe liver transplantation. *AJR* 176 (2001), pp.193- 200.
2. Bourquain, H., Schenk, A., Link, F.: HepaVision2-a software assistant for preoperative planning in living-related liver transplantation and oncologic liver surgery. In: CARS 2002; Computer-Assisted Radiology and Surgery. Proc of the 16<sup>th</sup> International Congress and Exhibition, Paris June 26-29;2002,(Eds: H.W. Lembke), Vol. 1, Leiden University Medical Center, 2002, pp. 341- 346.
3. Preim, B., Bourquain, H., Selle, D.: Resection proposals for oncologic liver surgery based on vascular territories. In: CARS 2002; Computer-Assisted Radiology and Surgery. Proc of the 16<sup>th</sup> International Congress and Exhibition, Paris June 26-29;2002, (Eds. H.W.Lembke), Vol.1, Leiden University Medical Center, 2002, pp. 353- 356
4. Baulieux, J., Delpero, J.R.: Surgical treatment of pancreatic cancer: curative resections. *Ann Chir.* 125 (2000), pp.609 - 611
5. Schwarz,M., Pauls,S., Sokiranski, R.: Is preoperative multidagnostic approach to predict surgical respectability of periampullary tumors still effective? *Am J Surg.*182 (2001), pp.243- 245
6. Blumgart, L.H., Fong, Y.: Biliary tumors. In: Surgery of the liver and biliary tract, (Eds: L.H. Blumgart, Y. Fong), Vol. 1, W.B. Saunders Co Ltd, GB, pp. 1021-1027.
7. Ott, D.J, Geland, D.W.: Complications of gastrointestinal radiologic procedures II. Complications related to biliary tract studies. *Gastrointest Radiol* 6(1981), pp.47 –52
8. Winter, T.C., Freeny, P.C., Nghiem, H.V.: Hepatic arterial anatomy in transplantation candidates: evaluation with three-dimensional CT arteriography. *Radiology* 195(1995), pp. 363-370.

Author: Jens Harms MD  
 Institute: University of Leipzig  
 Street: Liebigstraße 20  
 City: Leipzig  
 Country: Germany  
 Email: dr.jens.harms@gmx.de

# Assessing the Effects of Apneusis on Brain Functional Magnetic Resonance Imaging with Symbolic Dynamics

A.F.C. Infantosi<sup>1</sup>, F.C. Jandre<sup>1</sup> and C. Elefteriadis<sup>1</sup>

<sup>1</sup> Federal University of Rio de Janeiro, Biomedical Engineering Program, Rio de Janeiro, Brazil

**Abstract** — Symbolic dynamics was used to investigate the effect of breath-holding on brain functional Magnetic Resonance Imaging (fMRI). Data from 5 subjects, available as an open Internet database, were used. Three conditions were compared: resting (RS), breath-holding (BH) and sensorimotor-finger tapping (SM), the last two with on-off task period of 30 seconds. A symbolic dynamics parameter  $P(n)$ , equal to the proportion of brain voxels with positive derivatives at each scan in a run, was calculated from the blood oxygenation level dependent (BOLD) signal. The robustness of  $P(n)$  was assessed by comparing the results of the original data to those with preprocessed data, as well as with the data split into odd and even slices. Statistical analyses of  $P(n)$  in the frequency domain indicated global, periodic effects at the BH frequency in all 20 BH runs, in 3 out of the 20 RS runs and in 10 out of the 40 SM runs. The technique may be useful in the analysis of brain activity and vasoreactivity.

**Keywords** — fMRI, breath-holding, symbolic dynamics.

## I. INTRODUCTION

Functional magnetic resonance imaging (fMRI) relies mainly in the effects of changes in the balance between oxygen and deoxyhemoglobin in the blood that perfuses neural tissues to indirectly assess brain activity [1]. This balance is modified, among other factors, by changes in local blood flow, which in turn relates to neural activity [2].

Corrections are usually applied to compensate for motion, distortions in the main magnetic field and other artifacts [3], but there may be other confounders to this signal, since it conveys all the sources of changes in perfusion. One of such confounder is hypo- or hypercapnic vasoreactivity that may be caused by changes in lung ventilation [4]. Besides being a potential source of true image artifacts, for instance by changes in thorax susceptibility, lung ventilation may also affect local tissue perfusion.

Two main mechanisms may explain this effect: disturbances in hemodynamics (cardiac output, venous return, arterial pressure profile) and variations in blood gases [5,6,7]. The latter effect may be especially important in what concerns the partial pressure of  $\text{CO}_2$  ( $\text{PCO}_2$ ) in blood, and may be exploited intentionally as a means to study vasoreactivity[5].

This work aims at evaluating a new technique, the symbolic dynamics (SD), to study the global effects of respiration in fMRI, using coarse encoding of the blood oxygenation level dependent (BOLD) signals, obtained by weighting the image on  $T2^*$ .

## II. MATERIALS AND METHODS

### A. Experimental protocol

The data utilized is part of the First BIRN project database (<http://www.nbirn.net>) [8]. Five right-handed male subjects, ages 20 to 29, were scanned twice, in different days, on a 1.5 T Siemens scanner. For each day, 8 runs from 3 different tasks were analyzed: 2 resting state (RS), 2 breath-holding (BH) and 4 sensorimotor (SM).

In the BH task, the subjects held their breath at end-inspiration (apneusis) for 15 s, followed by 15 s of rest. This 30-s period was repeated 8 times for each run. In the sensorimotor task the subjects performed finger-tapping for 15 s according to a 3-Hz audio cue, alternating with a 15 s interval of rest; the sequence was performed 8 times for each run. In the resting task, subjects were told not to think of anything and just relax for the entire duration of the run.

In this study, fMRI volumes comprised 35 slices (each 4 mm thick) acquired in interleaved fashion, each one with 64x64 voxels in a 22 cm field of view; the repetition time (TR) was 3 s and echo time (TE) was 40 ms. Every run lasted about 4,5 min, resulting in 85 volumes scanned per run.

### B. Preprocessing

In the derivation of the SD parameter, the fMRI data was employed both with and without two typical preprocessing algorithms in fMRI studies: *slice-time correction* (STC), which synchronizes slices, and *motion correction* (MC), which corrects for head movements. In this work, either STC or both (STC+MC) were applied.

### C. Symbolic Dynamics

The methodology employed in this study is summarized in Figure 1. Firstly, a volume of interest VOI was derived for each run by setting:

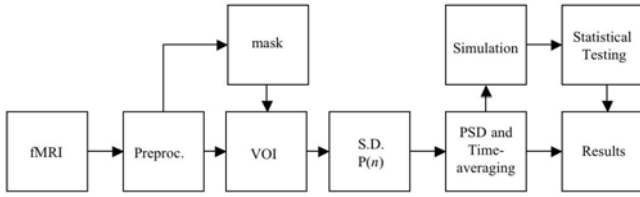


Figure 1: Block diagram of the methods. After fMRI preprocessing, the volume of interest is chosen with an intensity mask. The parameter  $P(n)$  is calculated, and analyzed in the time and frequency domains.

$$VOI(x, y, z, n) = V(x, y, z, n) \cdot M(x, y, z) \quad (1)$$

where  $V(x, y, z, n)$  is a voxel in the  $n$ -th scanned volume of the run and  $M(x, y, z)$  is a binary mask defined by:

$$M(x, y, z) = \begin{cases} 1 & \text{if } V_{mean}(x, y, z) > T_{mask} \\ 0 & \text{otherwise} \end{cases} \quad (2)$$

which depends on a intensity threshold  $T_{mask}$ , established based on the histogram of  $V_{mean}(x, y, z)$ , the time-average of all voxels' fMRI signals:

$$V_{mean}(x, y, z) = \frac{\sum_{n=1}^{85} V(x, y, z, n)}{85} \quad (3)$$

This way, the background image can be differentiated from tissue voxels. The forward difference of the time series of each voxel was calculated as:

$$D(x, y, z, n) = VOI(x, y, z, n) - VOI(x, y, z, n-1) \quad (4)$$

and a symbolic operator was used to transform the derivative series, according to its tendency (eq.5):

$$S(x, y, z, n) = \begin{cases} 1 & \text{if } D(x, y, z, n) > 0 \\ 0 & \text{otherwise} \end{cases} \quad (5)$$

Hence  $S(x, y, z, n)$  is a 4-D binary time series which indicates when the fMRI signal of each voxel is increasing or decreasing. For a single voxel,  $S(x, y, z, n)$  keeps track of the direction of its derivative, disregarding the amount of change. Then, a measure of global changes was obtained, based on the number of symbols "1" in  $S(x, y, z, n)$ , and a symbolic time series for a VOI was defined as:

$$P(n) = \frac{\sum_{xyz} S(x, y, z, n)}{\sum_{xyz} M(x, y, z)} \quad (6)$$

Such normalized parameter, which we referred to as "n-th positive proportion" ( $P(n)$ ), gives an insight of how synchronously the voxels within the brain are varying. If there is some hemodynamic or other physiological event affecting

a large fraction of the tissues within the mask, most voxels will likely change simultaneously, which would be reflected in  $P(n)$ . Only the last 80 points of  $P(n)$  for each run were kept in the present study, since the tasks had an adaptation time that spanned the first 5 scans.

#### D. Data Analysis: Time Domain

Initial exploratory analysis included calculating mean values and total power of all  $P(n)$  series. In order to examine its periodic behavior at the frequency of breath-holding ( $f_{bh} = 0.033$  Hz), the coherent average of  $P(n)$  series was performed by cutting them into 8 10-sample (30 s) intervals and finding the average of the 8 segments.

#### E. Data Analysis: Frequency Domain

For each series, the power spectral density (PSD) was estimated by the Welch's periodogram method, using 90-s intervals (30 samples) and a Hanning window without overlapping, after removing linear trends from the series. Also the mean PSD between sessions from the same subject was calculated. For each subject, the mean PSD for corresponding tasks was obtained, and the mean of the normalized PSDs between subjects was also computed (see Figure 2).

#### F. Data Analysis: Monte Carlo Simulation

A Monte Carlo simulation with 10.000 surrogates of  $P(n)$  tested the hypothesis of random contribution of power at  $f_{bh}$ . A c.d.f. derived from the histogram of the surrogates'  $PSD(f_{bh})$  provided the critical values at  $p = 0.05$  to test each series' power at this frequency.

In the time domain, an analogous simulation was run for each of the 10 samples of the time-averaged  $P(n)$ , for each session, testing its value against expected values from the 10.000 surrogates. Series with significant samples in a peak and valley of a cycle were considered significantly different (i.e. modulated at the period of time-averaging).

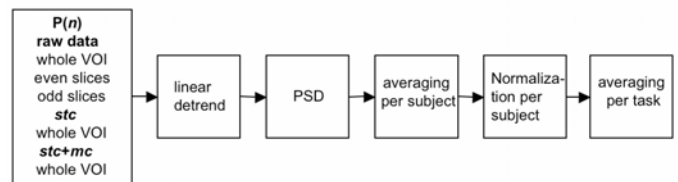


Figure 2: Analysis in the frequency domain. The PSD of  $P(n)$  is calculated after linear detrending. The power spectra from different sessions are averaged and normalized per subject, and then averaged again per task.

This results in one PSD per task for each combination of volume and preprocessing of the fMRI data.

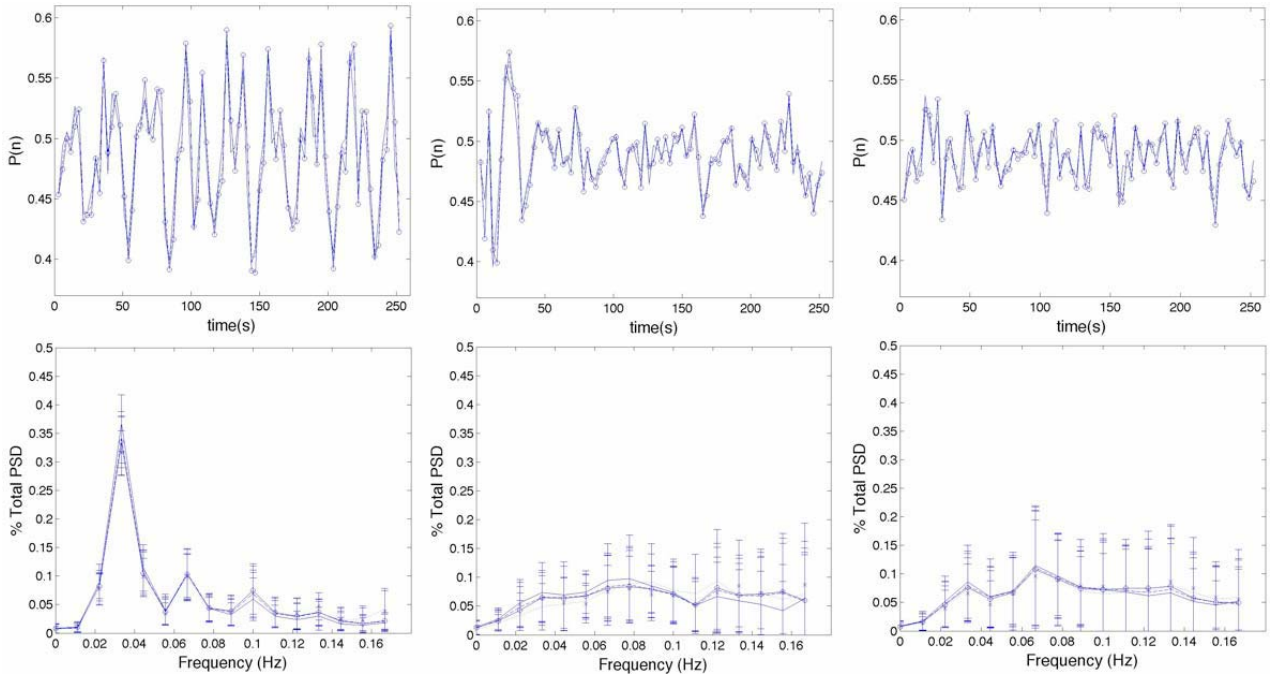


Figure 3. Top: examples of  $P(n)$  series from subject # 3. Bottom: Power Spectral Density plots of  $P(n)$  normalized by total power. Left: breath-holding task. Middle: resting task. Right: sensorimotor task. Raw data (continuous line),  $STC$  corrected data (---) and  $STC + MC$  corrected data (o). On the PSD plots only: odd slices (x) and even slices (:); vertical bars indicate one standard deviation. Note the 35% power contribution at breath-holding frequency.

G. Data Analysis: Spectral F Test

A Spectral F test (SFT) was used in order to compare the power at  $f_{bh}$  of the normalized mean PSDs per subject, between tasks [9]. The SFT compares the ratio of power at each frequency from two different power spectra with a critical value from Fisher’s F distribution, in order to test the hypothesis that the contributions are different. Mean normalized PSDs from breath-holding and resting tasks of each subject were compared.

III. RESULTS

Examples of  $P(n)$  series can be seen on top of Figure 3, for each of the three tasks: breath-holding, resting and sensorimotor, respectively. Each graph contains series of the same session before and after fMRI data preprocessing. The  $P(n)$  series in breath-holding tasks show well defined cycles, with varying amplitude ranging from 0.4 to 0.6, whereas in the other tasks there is more random behavior and smaller power.

The bottom graphs in Figure 3 show the estimates of the PSD for  $P(n)$  series of the five possible dvata types, separated by task. The bottom left graph represents the general behavior of breath-holding tasks’ PSD, with a distinguished peak at the task frequency of 0.033 Hz, and smaller peaks at its harmonics.

The PSDs of the resting tasks show distributed power and no visible peaks, while in the sensorimotor tasks there are small peaks, but with no concentration of energy compared to the rest of the power spectra.

Figure 3 shows no evident differences between the curves regarding the preprocessing. Likewise, the bottom graphs suggest there are no significant variations between power spectra obtained with half of the slices. The curves in Figure 4 from one subject represent the general results found for time-averaging and significant samples. The results of the spectral F test were significant for all five subjects ( $p < 0.01$ ), as the power at  $f_{bh}$  in breath-holding sessions was significantly greater than that in resting ones.

Monte Carlo simulations showed that all 20 breath-holding runs had significant peaks at  $f_{bh}$  ( $p = 0.05$ ) whereas only 3 resting runs exhibited such behavior (Table 1). How-

Table 1. Number of significant (S) and non-significant (NS) time- and frequency-domain runs as tested with the Monte Carlo methods. Frequency-domain results inside parentheses.

Task	runs	raw		STC		STC+MC	
		S	NS	S	NS	S	NS
<b>RS</b>	20	1(3)	19(17)	0(2)	20(18)	2(2)	18(18)
<b>SM</b>	40	2(10)	38(30)	5(6)	35(34)	5(6)	35(34)
<b>BH</b>	20	19(20)	1(0)	20(20)	0(0)	20(20)	0(0)

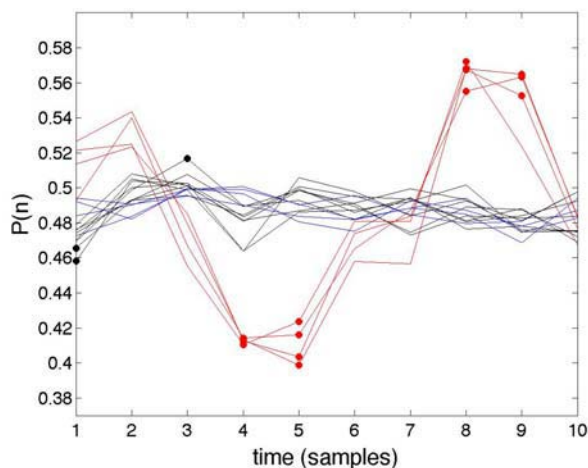


Figure 4. Time-averaging of  $P(n)$  series from subject #3, of the three tasks: breath-holding (red, large cycle), resting (blue) and sensorimotor (black, with 3 circles). The circles represent statistically significant (i.e. non-random) samples, compared to the Monte Carlo simulation with surrogates of  $P(n)$ .

ever, 10 out of the 40 sensorimotor runs also had significantly different peaks. Similar results were found in the time-domain Monte Carlo simulation.

#### IV. DISCUSSION

The parameter  $P(n)$  identified a global, periodic effect at the  $f_{bh}$  of 0.033 Hz in breath-holding tasks, modulated by the respiratory maneuver, as in other works [5,6]. The spectral peak at  $f_{bh}$  in the PSD of  $P(n)$  seems to reflect the breath-holding maneuver, given that the task period is of 30 s, which is not present in the RS task. Another evidence for the modulatory hypothesis is the presence of harmonics of  $f_{bh}$  in the PSD of the  $P(n)$  series of the BH tasks, which is also absent in other tasks'  $P(n)$  power spectra.

The five combinations of data types analyzed (whole volume, odd or even, with or without preprocessing) resulted in similar mean normalized PSDs, thus showing the robustness of  $P(n)$  as a global measure of change in the BOLD signal. This parameter extracted the same information before or after corrective algorithms (*STC* and *MC*) or with the odd or even halves of the slices. That may be a consequence of the global effect of respiration in the whole brain's vasoreactivity [10], so that a large proportion of voxels' fMRI signals vary in a coherent way. On the other hand, in the resting task there was no periodic variation in respiration, and hence the fMRI signal did not seem to be affected in the same way, showing no spectral peaks concentrating the energy of  $P(n)$ . The periodic behavior at some

sensorimotor runs could be attributed to external cueing at the task frequency. Besides, the chosen value of  $p$  is somewhat high, and may be excessively tolerant. Further study may be necessary to determine the value of  $p$  to give highest accuracy, sensitivity and specificity.

#### V. CONCLUSIONS

The symbolic dynamics parameter  $P(n)$  was capable of reflecting the global effect in breath-holding tasks, with or without fMRI data preprocessing, thus showing its robustness. This method can be applied in brain vasoreactivity research, and also in the investigation of global effects on the brain fMRI signal.

#### ACKNOWLEDGMENT

The authors thank Jessica Turner (BIRN project) and the CNPq and CAPES for the financial support.

#### REFERENCES

- Ogawa S, Lee TM *et al.* (1990) Brain magnetic resonance imaging with contrast dependent on blood oxygenation. *Proc Natl Acad Sci* 87(24):9868-9872
- Hoge RD, Atkinson J, Gill B *et al.* (1999) Investigation of BOLD Signal Dependence on Cerebral Blood Flow and Oxygen Consumption: The Deoxyhemoglobin Dilution Model. *Magn Reson Med* 42(5): 849-863
- Raj D, Paley DP *et al.* (2000) A model for susceptibility artifacts from respiration in functional echo-planar magnetic resonance imaging. *Physics in Med and Biol* 45:3809-3820
- Posse S, Olthoff U, Weckesser M *et al.* (1997) Regional Dynamic Signal Changes during Controlled Hyperventilation Assessed with Blood Oxygen Level-Dependent Functional MR Imaging. *AJNR Am J Neuroradiol* 18(9):1763-1770.
- Kastrup A., Li TQ, Glover GH *et al.* (1999) Cerebral blood flow-related signal changes during breath holding. *AJNR Am J Neuroradiol* 20 (7): 1233- 1238.
- Andrade KC, Pontes-Neto OM, Leite JP *et al.* (2006) Quantitative Aspects of Brain Perfusion Dynamic Induced by BOLD fMRI. *Arq Neuropsiquiatr* 64(4):895-898
- Jensen EW, Guillen P, Limn H *et al.* (2000) Symbolic Dynamics Applied to EEG Signal for Monitoring Anaesthetic Depth During Propofol Infusion. In: *Proc 22nd EMBS Conference*. Chicago, 2000.
- Project First BIRN. Dados de "Phase I". Site: <http://www.nbirn.net>
- Miranda de Sá AM, Cagy M *et al.* (2006) Spectral F-Test Power Evaluation in the EEG during Intermittent Photic Stimulation. *Arq Neuropsiquiatr* 64(2A): 228-232.
- Macey PM, Macey KE *et al.* (2004) A method for removal of global effects from fMRI time series. *Neuroimage* 22(1):360-366.

Author: Antonio Fernando Catelli Infantosi  
 Institute: Programa de Engenharia Biomédica - COPPE / UFRJ  
 Street: Av. Horácio Macedo, 2030 - Cidade Universitária  
 City: Rio de Janeiro  
 Country: Brazil  
 Email: [afci@peb.ufrj.br](mailto:afci@peb.ufrj.br)



# Breast Ultrasound Segmentation Using Morphologic Operators and a Gaussian Function Constraint

A.F.C. Infantosi<sup>1</sup>, L.M.S. Luz<sup>2</sup>, W.C.A. Pereira<sup>1</sup> and A.V. Alvarenga<sup>3</sup>

<sup>1</sup> Federal University of Rio de Janeiro, Biomedical Engineering Program, Rio de Janeiro, Brazil

<sup>2</sup> PETROBRAS TRANSPORTE S.A., Duque de Caxias, Brazil

<sup>3</sup> National Institute of Metrology, Standardization and Industrial Quality (INMETRO), Laboratory of Ultrasound, Duque de Caxias, Brazil

**Abstract**— This work proposes a hybrid segmentation method based on Morphological Operators and on a Gaussian function constraint to delimitate the search dominium, both used for tumor segmentation purposes. The Watershed operator was also used to find tumor contour. The proposed method was firstly evaluated using gear simulated images (eight and sixteen teeth with different width and height), a power speckle noise of 10% and a contrast ratio of 10:53 referred to the background. The hybrid method was also applied to 200 ultrasound (US) breast images. For assessing the segmentation performance, similarity parameters (overlap ratio,  $RS$ , normalized residual mean square value,  $nrv$ , and mean distance between contours,  $dmed$ ) based on the predefined shape or on the US tumor contour depicted by an expert as a gold standard. The segmented contour of the gear simulated images obtained with the hybrid method better preserves the original shape. This finding was evident for both gears, which is particularly important since the teeth mimic contour irregularities. For the US breast images, the proposed method keeps the tumor boundaries without aggregating improper structures, resulting in  $RS > 50\%$  for 91% of the images,  $nrv < 40\%$  for 70%, and  $dmed < 5$  pixels for 77% of the cases. These findings suggest that the hybrid method represents more realistically tumor contours, which is a vital diagnosis characteristic.

**Keywords**— Breast ultrasound images, morphologic operators, segmentation.

## I. INTRODUCTION

Malignant tumors generally infiltrate the surrounding tissue, resulting on an irregular or imprecise contour on the ultrasound image. Thus, the segmentation of such structures should be capable of identifying and preserving the morphological characteristics essential for the analysis.

Several works [1-3] have used the contour delineated by an experienced radiologist, even when computer-aided methods are proposed. However, operator-dependent procedures are highly susceptible to variations [4-6].

Despite the speckled nature of echograms, which makes image segmentation and object delineation a difficult task, various researchers [7-11] have developed segmentation procedures for supporting radiologists recognize abnormal

areas on US breast images as well as for their own computer-aided diagnosis (CAD) systems.

The present work proposes a hybrid segmentation method based on Morphological Operators [11] and on a Gaussian function constraint to delimitate the tumor search dominium [7], both used for tumor segmentation purposes.

## II. MATERIAL AND METHODS

### A. Database

In this study, using a 7.5-MHz linear array B-mode 40-mm ultrasound probe (Sonoline – Sienna ®Siemens) with axial and lateral resolutions of 0.45 mm and 0.49 mm, respectively, 200 breast tumor US images were acquired at the Cancer National Institute (Brazil - Rio de Janeiro). For each image, a rectangular ROI including the tumor and the area around it were determined by an experienced radiologist. Besides, the radiologist depicted all tumor contours and classified them as irregular (74) or regular (126).

### B. Existing segmentation Techniques

The technique proposed by [7], denoted here Hh, applies a 10 x 10 median filter to reduce speckle. The resulting image  $I_{med}$  is inverted and multiplied by a Gaussian constraint function placed at the manually defined tumor center. The variances in the lateral and height directions are estimated applying the Sobel edge detection filter to  $I_{med}$ . Different potential tumor margins are defined using a gray-level threshold procedure. The potential margin that maximizes the Average Radial Derivative (ARD) utility function is chosen as the tumor contour [7]:

$$ARD(k) = \frac{1}{N} \sum_{P \in T(k)} \nabla I(P) \cdot r(P) \quad (1)$$

where  $I$  is the processed image and  $r$  is the vector in the radial direction from the geometric center. The value  $k$ , where the maximum of ARD occurs, is the chosen gray-level to segment the tumor. The Hh segmentation tends to

yield “lesion-like” margins, outlining its general shape however it may miss details such as spiculation or high irregularity.

The technique described by [11], denoted here Aa, applies Morphologic Operators to the image and its histogram to reduce the gray-levels and to find the best threshold value to segment the tumor. Initially, the Opening by Reconstruction operator (with a square Structuring Element (SE) of 3 x 3 pixels) is applied to reduce speckle and increase contrast among distinct regions. Next the morphological Open operator (3-pixel line SE) is applied to the histogram of the reconstructed image to remove irrelevant peaks and the *Watershed* operator is then employed to determine histogram modal regions. The resulting detected regions are numerically labeled and sorted in ascending order to construct an image with a smaller number of gray-levels. Then, the Minima Imposition operator is used to enhance the tumor from the image background. The resulting image tends to present well-defined regions, and hence, well-defined histogram peaks, the first ones characterizing the tumor region. Then the gray-level corresponding to the maximum gradient of the histogram cumulative-area curve was used as a threshold value to obtain a binary image  $S_{Aa}$ .

The application of MO tends to preserve tumor contour details, which is a main feature to identify malignancy [1]. However, the inclusion of nearby areas having gray-levels similar to the tumor region is a drawback of this technique.

### C. Hybrid segmentation method

The proposed segmentation method uses MO to process the image and the segmentation obtained with Aa [11] and Hh [7] as markers to the *Watershed* operator. These markers help determine regions where the flooding can occur. The external *Watershed* marker is obtained by applying a morphological Dilatation to the segmentation provided by Hh and an internal *Watershed* marker is defined as the intersection between Aa and Hh segmentation results.

Before the *Watershed* operation, the original image is homogenized to avoid over-segmentation. With this aim, the image was filtered with an *Opening by Reconstruction*

followed by a *Closing by Reconstruction*, and to enhance the tumor boundary, a *morphological gradient* was applied to the filtered image (Fig. 1). Then the *Watershed* operator is applied to the resulting image, using the predefined internal and external markers, to obtain the final tumor contour.

### D. Simulated images

The hybrid method and the techniques proposed by [11] and [7] were first applied to simulated images for assessing their performances. Gear images (150 x 150 pixels) were simulated with eight (G8) and sixteen (G16) teeth (35-pixel radius), gray-level of 10 and 10% of multiplicative speckle noise. The image background has a gray-level of 53 with 40% of multiplicative speckle noise. The contrast between the gear and the background is obtained by the difference between their respective gray-levels as follows 10:53. The gray-level and speckle noise values were defined empirically.

The gears teeth have different height (4 to 7 pixels) and width (5 to 11 pixels) designed to assess the ability of the segmentation techniques in detecting contour irregularities.

### E. Segmentation procedures evaluation

The performance of the three methods (Hybrid, Hh, Aa) was assessed by calculating three parameters: overlap ratio ( $RS$ ) [7], normalized residual mean square value ( $nrv$ ) [11], and average distance between contours ( $dmed$ ) [12]. These parameters were determined between the segmented image by one of the methods ( $S_i$ ) and the simulated image, or the segmentation depicted by the radiologist ( $S_o$ ). Hence, the overlap ratio can be defined as [7]:

$$RS = \frac{Area(S_i \cap S_o)}{Area(S_i \cup S_o)} \quad (2)$$

where the symbols  $\cap$  and  $\cup$  mean the intersection and union areas, respectively. So when the areas have the same shape and size and are in the same position,  $RS$  is equal to unity.

The parameter  $nrv$  is defined as [11]:

$$nrv = \frac{Area(S_i \oplus S_o)}{Area(S_o)} \quad (3)$$

where  $\oplus$  represents an “exclusive-or” operation. Hence, if  $S_i$  and  $S_o$  are congruent,  $nrv = 0$ .

The third parameter is the average distance between contours ( $dmed$ )  $S_i$  and  $S_o$ , which is based on [12]:

$$d(t_j, M) = \min_i \|t_j - m_i\|, \forall t_j \in T \quad (4)$$

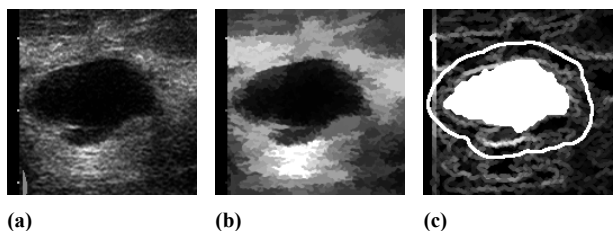


Fig. 1: Steps of the hybrid method: (a) original ROI, (b) processed ROI and (c) morphological gradient with superposed markers (white).

where  $T = [t_1, t_2, t_3, \dots, t_n]$  and  $M = [m_1, m_2, m_3, \dots, m_k]$  are the set of pixels from contours  $S_i$  and  $S_o$ , respectively, and  $\| - \|$  is the Euclidian distance between two pixels. Hence, the parameter  $dmed$  is estimated as the mean value of  $d(t_j, M)$ .

The parameters  $RS$ ,  $nrv$  and  $dmed$  were calculated as the average of 10 simulated images generated by varying one of the simulation variables, and keeping all the others fixed.

### III. RESULTS

#### A. Simulated images

The segmentation technique results for the G8 gear are in Fig. 2. The Aa technique is able to depict the eight teeth with different heights and widths. However, the contour adds small structures outside of the original contour (Fig. 2b). On the other hand, the Hh technique tends to smooth the teeth, while restricting the contour to the object boundary (Fig. 2c). The hybrid method preserves contour details, rejecting similar structures beyond the gear, and distinguishing the teeth in height and width (Fig. 2d).

Similar behavior is observed in the results for the G16 (Fig. 3). The hybrid method (Fig. 3d) and the technique Aa (Fig. 3b) are capable of identifying all sixteen teeth on the contour and teeth height and width variations as well. On the other hand, the technique Hh (Fig. 3c) fails to depict the irregularities represented by the smaller teeth. However, Hh and hybrid methods restrict the segmentation to the object region, while Aa tends to add regions next to the object.

The average values of  $RS$  (Table 1) indicate that the best performance is achieved by the hybrid method (96%), while

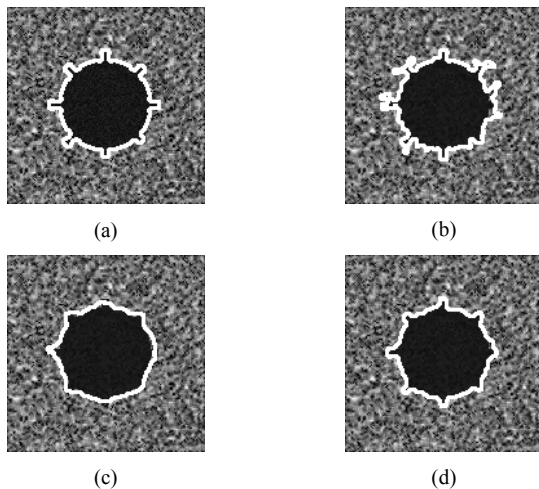


Fig. 2: Eight-tooth gear image simulated using 10:53 object-background contrast and speckle noise of 40% and 10% to background and teeth gear respectively. The (a) G8 image with its original contour (in white), and respective contours depicted by (b) Aa, (c) Hh and (d) the hybrid method.

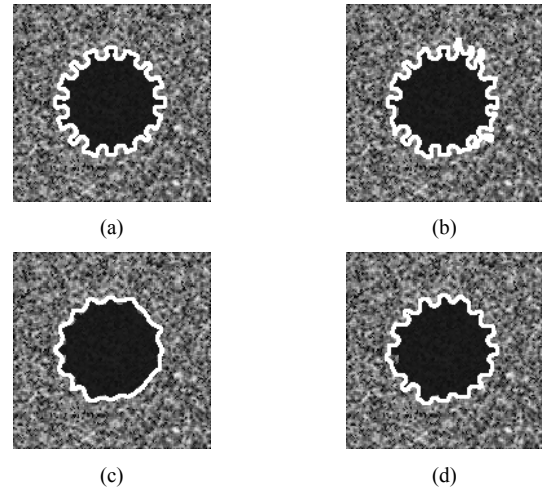


Fig. 3: Sixteen-tooth gear image simulated using 10:53 object-background contrast and speckle noise of 40% and 10% to background and teeth gear respectively. The (a) G16 image with its original contour (in white), and respective contours depicted by (b) Aa, (c) Hh and (d) the hybrid method.

Hh (90%) is the worst. Similarly, the average values of  $nrv$  (Table 2) suggests the hybrid method as the best (4.1%). Besides, Hh presents the worst performance (10.8%). Finally, the average values of  $dmed$  (Table 3) show clearly the hybrid method with the highest performance (0.6), while the worst was brought by Aa (1.9).

#### B. Breast US images

The three methods (hybrid, Aa and Hh) were applied to 200 breast US images and results assessed against a radiologist-defined contour. An example of the results for an irregular tumor is in Fig. 4. The technique Hh tends to smooth contour details (Fig. 4a), while Aa (Fig. 4b) and the hybrid (Fig. 4c) methods preserve irregularities. However, Aa (Fig. 4b) adds unwanted regions to the contour.

The hybrid method segmented 77% of the tumors with  $dmed < 5$  pixels, against 56% of Aa and 66% of Hh. Besides, 70% of tumors segmented using the proposed method resulted in a lower  $nrv$  ( $< 40\%$ ) compared to that of Aa

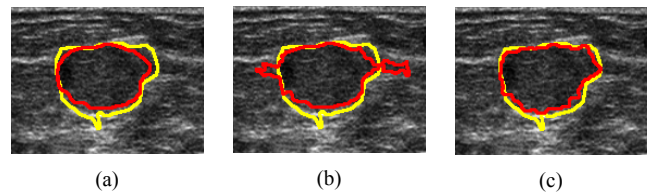


Fig. 4: Example of ROI presenting an irregular tumor depicted by the radiologist (yellow) and the contours obtained using (a) Hh, (b) Aa and (c) the hybrid method (all of them in red).

Table 1 Average values of *RS* (%)

Technique	Gear		Radius (pixels)	Speckle noise (%)	Contrast
	G8	G16	35	10	10:53
Aa	93.5	92.5	93.9	93.3	93.4
Hh	91.3	90.0	91.4	91.0	91.1
Hybrid	96.0	93.1	96.1	95.8	95.9

Table 2 Average values of *nrv* (%)

Technique	Gear		Radius (pixels)	Speckle noise (%)	Contrast
	G8	G16	35	10	10:53
Aa	6.9	8.2	6.5	7.2	7.0
Hh	9.3	10.8	9.3	9.6	9.5
Hybrid	4.2	7.4	4.1	4.3	4.3

Table 3 Average values of *dmed* (pixels)

Technique	Gear		Radius (pixels)	Speckle noise (%)	Contrast
	G8	G16	35	10	10:53
Aa	1.9	1.5	1.8	1.9	1.4
Hh	1.2	1.3	1.3	1.3	1.3
Hybrid	0.6	0.6	0.6	0.6	0.6

Table 4 P-values of the paired *t*-test ( $\alpha = 0.05$ )

Technique 1	Technique 2	<i>RS</i>	<i>nrv</i>	<i>dmed</i>
		H1: m1 < m2	H1: m1 > m2	H1: m1 > m2
Aa	Hh	p < 0,002	p < 0,0002	p < 0,001
Aa	Hybrid	p < 0,0001	p < 0,0001	p < 0,0001
Hh	Hybrid	p < 0,002	p < 0,008	p = 0,042

(57%) and Hh (61%), hence indicating more congruence. Considering  $RS > 50\%$ , the hybrid method also achieved a better performance (91%) than Aa (83%) and Hh (77%).

The best performance of the hybrid method was statistically evaluated by a paired *t*-test ( $\alpha = 0.05$ ), considering as alternative hypothesis (H1) that the average values m1 and m2 are not equal (for each parameter), as indicated in Table 4. The null hypothesis (H0) that the average values m1 and m2 are equal was rejected for all parameters.

#### IV. DISCUSSION AND CONCLUSION

The Aa technique was capable of segmenting tumors preserving details, which are essential for morphological analysis. This result suggests that MO's can adequately segment tumor irregularities. However, Aa technique can aggregate adjacent areas with gray-levels similar to the tumor region. The Gaussian constraint function in the Hh technique reduces the chance of merging those spurious structures; however, the median filter used in this technique smoothes the contour irregularities. The proposed hybrid method, on the

other hand, was capable to preserve the boundaries without including alien structures. The performance of this method was superior to Aa and Hh techniques for all studied parameters. Besides, the paired *t*-test indicated a significant difference among the segmentation techniques. These findings suggest that the hybrid method follows more realistically the tumor contour, which is a prime diagnosis feature.

#### ACKNOWLEDGMENT

To the Brazilian Sectorial Fund for Health (CT-Saúde, Ministry of Health) for financial support (MCT-CNPq/MS-SCTIE-DECIT/CT n° 06/2005 – The study of cancer diseases, project n° 401274/2005-5) and to the Brazilian Agencies CAPES/MEC.

#### REFERENCES

1. Chou Y, Tiu C, Hung G. et al. (2001) Stepwise logistic regression analysis of tumour contour features for breast ultrasound diagnosis. *Ultrasound Med. Biol.* 27:1493-1498
2. Chen C, Chou Y, Han K et al. (2003) Breast lesions on sonograms: computer-aided diagnosis with nearly setting-independent features and artificial neural networks. *Radiology* 206:504-514
3. Lefebvre F, Meunier M, Thibault F et al. (2000) Computerized ultrasound B-scan characterization of breast nodules. *Ultrasound Med. Biol.* 26:1421-1428
4. Skaane P (1999) Ultrasonography as adjunct to mammography in the evaluation of breast tumors. *Acta Radiologica Supplementum* 40:1-47
5. Huber S, Danes J, Zuna I et al (2000) Relevance of sonographic B-mode criteria and computer-aided ultrasonic tissue characterization in differential diagnosis of solid breast masses. *Ultrasound Med. Biol.* 26:1243-1252
6. Rahbar G, Sie A C, Hansen G C et al (1999) Benign versus malignant solid breast masses: US differentiation. *Radiology* 213:889-894
7. Horsh K, Giger M L, Venta L A et al. (2001) Automatic segmentation of breast lesions on ultrasound. *Medical Physics* 28:1652-1659
8. Huang Y and Chen D (2004) Watershed segmentation for breast tumor in 2-D sonography. *Ultrasound Med. Biol.* 30:625-632
9. Chang R F, Wu W J, Moon W K et al (2005) Automatic ultrasound segmentation and morphology based diagnosis of solid breast tumors", *Breast Research and Treatment* 89:179-185
10. Huang Y, Jiang Y, Chen D et al. (2007) Level set contouring for breast tumor in sonography. *Journal of Digital Imaging* 20:238-247.
11. Alvarenga A V, Infantosi A F C, Azevedo C M, Pereira W C A (2003) Application of morphological operators on the segmentation and contour detection of ultrasound breast images. *Brazilian Journal of Biomedical Engineering* 19:91-101
12. Chen C, Lu H H, Lin Y (2000) An early vision-based model for ultrasound image segmentation. *Ultrasound Med. Biol.* 26:273-285

Author: Antonio Fernando Catelli Infantosi  
 Institute: Federal Univ. of Rio de Janeiro, Biomedical Eng. Program  
 Street: Centre of Technology – Room H-327  
 City: Rio de Janeiro, ZIP 21949-970  
 Country: Brazil  
 Email: afci@peb.ufrj.br

# Image Analysis of DNA Repair and Apoptosis in Tumor Cells with Differing Sensitivity to DNA Damage

A. Ivanov<sup>1</sup>, M. Ivanova<sup>2</sup>, J. Erenpreisa<sup>3</sup>, S.V. Gloushen<sup>2</sup>, T. Freivalds<sup>4</sup> and M.S. Cragg<sup>5</sup>

<sup>1</sup>Paterson Institute of Cancer Research, Manchester, UK;

<sup>2</sup>Belarussian State University, Minsk, Belarussia;

<sup>3</sup>Latvian Biomedicine Centre, Riga, Latvia;

<sup>4</sup>Latvian Institute of Experimental and Clinical Medicine, Riga, Latvia;

<sup>5</sup>Tenovus Research Laboratory, Southampton University School of Medicine, Southampton, UK

**Abstract** — Homologous recombination of DNA double strand breaks was previously found to be protective against apoptosis in tumor cells lacking p53 function. Here, we studied the spatial and temporal relationship between the two processes in a pair of lymphoblastoid cell lines with wild-type or mutant p53 status. Clonogenic assays revealed that p53 mutant WI-L2-NS cells were ~ ten-fold more resistant to X-ray damage than p53 wild type TK6 cells and displayed 2-3 times lower levels of apoptosis 24 h after irradiation. The kinetics of DNA damage and repair after irradiation (5 Gy) were assessed by immunofluorescent staining for g-H2AX and Rad51, and DNA stained with DAPI. Using image analysis in the three (red/green/blue) fluorescence channels we found that repair foci were more prevalent in the p53 mutant radioresistant WI-L2-NS cells at many time points: 2.2 versus 1 per nucleus at 5 min, 3.2 versus 1.6 at 6 h, and 6.1 versus 3.6 at 72 h post-irradiation although the number of repair foci were equal at 24 h (8.8). Furthermore, the average size of foci in TK6 cells was smaller at all times post-irradiation ( $p < 0.001$ ). In contrast to the functional repair foci which were characterised by the co-localisation and high concentration of g-H2AX and Rad51, in pre-apoptotic cell nuclei, foci with greater quantities of g-H2AX relative to Rad51 were prevalent. The g-H2AX-predominant foci colocalized with little or no Rad51 and fused in a pattern typical of apoptotic chromatin. This pattern was seen more often in TK6 cells, where at 6 h the sum area occupied by g-H2AX was seven-fold higher than that of the Rad51 label. In contrast, WI-L2-NS cells displayed approximately equal areas of both components. These data suggest that formation of stable functional repair foci topologically protects the chromatin from relaxation and initiation of apoptotic fragmentation.

**Keywords** — tumors, DNA repair, apoptosis, image analysis.

## I. INTRODUCTION

Tumor cells lacking p53 function are selected during tumor progression and are resistant to therapy with DNA damaging agents. Homologous recombination (HR) of DNA double strand breaks (DSB) was previously found to be abnormally enhanced in p53 mutated tumor cells resulting in a reduction in tumor cell death through apoptosis [1,2]. Although it is

generally accepted that failed DNA repair leads to apoptosis, the spatial relationship between the two processes and its dependence on p53 status is unknown. In mammalian cells, the signaling cascade downstream of DNA damage phosphorylates histone H2AX (termed g-H2AX) at sites of DSB. In turn, g-H2AX plays a critical role in the organization of DNA repair foci by helping to recruit DNA repair factors involved in HR, such as the recombinase Rad51 [3]. g-H2AX forms at sites on the chromatin where DSB are present, including those sites where extensive apoptotic DNA fragmentation is occurring. Therefore, we applied immunofluorescent staining of g-H2AX and Rad51 and used image analysis to study the topological and kinetic relationships between HR and apoptosis, in a pair of linked human lymphoblastoid cell lines with wild-type (wt) or mutant (mut) p53 status.

## II. MATERIALS AND METHODS

Human lymphoblastoid cells lines TK6 and WI-L2-NS were obtained from the ATCC and grown in suspension in RPMI medium with 10% fetal calf serum. WI-L2-NS is a p53 mutated cell-line derived from the same source as the p53 wt TK6. Cells were irradiated using a Gulmay D3 225 X-ray source with a dose rate of 0.77 Gy/minute. Samples were analysed by flow cytometry and immunofluorescent staining for g-H2AX/ Rad51/DNA as detailed previously (Ivanov et al., 2003). Images were obtained by Axiocam (1300x1030) equipped with a calibrated Sony DXC 390P colour video camera. Image analysis was performed using Image Pro Plus 4.1 software (Media Cybernetics; REO 2001, Riga, Latvia). To discriminate DNA repair foci, the image was segmented using 180-255 empirically chosen intensity levels. Student's t- and non-parametric sign-test were used for statistical analysis of measurement results.

### III. RESULTS

**Clonogenic assay:** Clonogenic assays from three independent experiments showed that the p53 mut WI-L2-NS cells are approximately ten-fold more resistant to X-ray radiation than the related p53 wt TK6 cells.

**Kinetics of the cell cycle:** DNA flow cytometry revealed that 60% of irradiated TK6 cells and about 75% of WI-L2-NS cells have passed the first S-phase and arrived in the G2 arrest compartment at 24 h post 5 Gy irradiation (in control, G2-fraction comprised 22-26%, in the both tumours). Mitotic cycling restarted then, albeit at a low level, and returned to the normal level between day 5 to 7. Between d.2 to d.5, WI-L2-NS formed about 20% of polyploid cells (>4C), while TK6 produced almost none.

**Apoptosis:** The amount of apoptosis determined as the sub-G1 fraction by DNA flow cytometry at 24 h comprises 7% for WI-L2-NS and 15% for TK6. However later the difference increases further: at 72 h 65% of TK6 cells are in apoptosis, while only 25% of WI-L2-NS cells are apoptotic.

**Topological analysis of the DNA repair by HR:** Repair foci were observed in both cell-lines within 5 min post-damage. Notably, they were first assembled from diffuse forms of g-H2AX and Rad51 at the interface between the condensed chromatin and the interchromatin (nuclear matrix) space. Larger areas of g-H2AX and Rad51 were observed in WI-L2-NS 5 min after damage and the average number of repair foci per cell was 2.2 as compared with 1.0 for TK6 cells (Table 1).

Table 1. Kinetic analysis of g-H2AX and Rad51 components after irradiation determined by immunofluorescent staining and image analysis. Only foci containing both g-H2AX and Rad51 components were scored as repair foci.

Time after irradiation	5 min		6 h		24h		72h	
	TK6	WI-L2-NS	TK6	WI-L2-NS	TK6	WI-L2-NS	TK6	WI-L2-NS
Number of repair foci/cell	1.0	2.2	1.5	3.2	8.8	8.8	3.6	6.1
Average area of Rad51 foci (pxl)	38.4	45.1	51.0	56.8	52	53.6	43.9	49.3
Area occupied by Rad51/ cell	37.6	98.8	78.9	182.7	456	471	160	301
Area occupied by g-H2AX/cell	14.0	54.6	584	319.0	663	513	196	328

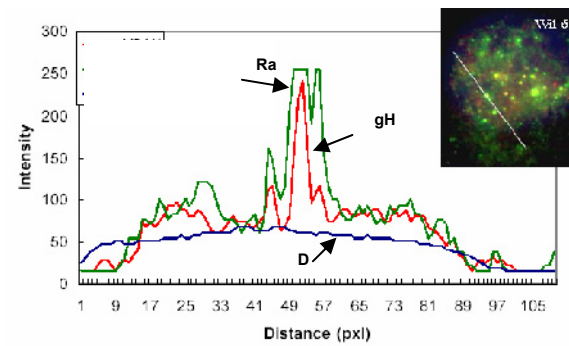


Fig.1. Segmentation of g-H2AX repair foci saturated with Rad51 in a WI-L2-NS cell, 6 h post-irradiation

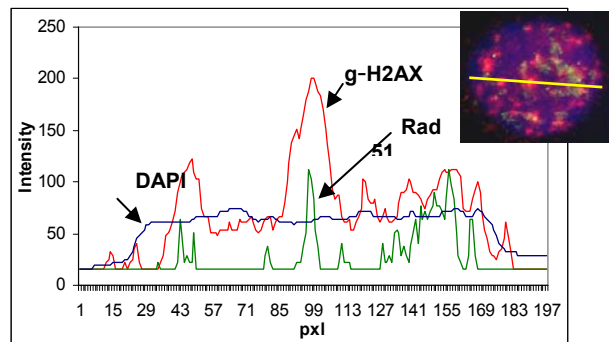


Fig.2. Segmentation through g-H2AX foci binding negligible amounts of Rad51 in a TK6 cell, 6 h post-irradiation

More effective formation of repair foci in WI-L2-NS was also observed at 6 h post-damage (3.2 versus 1.5 per nucleus) and notably, at this term the sum area occupied by g-H2AX in TK6 was seven-fold higher than the sum area of the Rad51 label, while this difference in WI-L2-NS cells was only 1.7 (Table 1).

The difference was also seen by one-line, three-colour (red, green, blue) scanning through the repair foci. In WI-L2-NS the highly colocalized concentration of g-H2AX/Rad51 sharply defined the functional repair foci (Fig.1).

In contrast, Rad51 was much less prevalent in the centre of large g-H2AX foci in many irradiated TK6 cells (Fig.2).

The g-H2AX-labelled foci, which were free of Rad51, tended to cluster and fuse forming the chromatin pattern typical of early apoptotic cells (Fig.3).

The discrepancy between the cell lines was diminished at 24 h, when similar amounts of cells were arrested in the G2 cell cycle compartment. At this time, both cell-lines showed similar levels of g-H2AX and Rad51 staining and the highest average number of repair foci per nucleus (8.8)

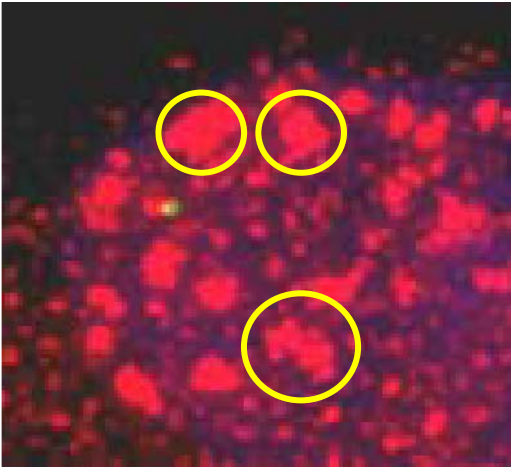


Fig.3. Clustering and fusion of multiple g-H2AX foci in a pre-apoptotic TK6 cell nucleus.

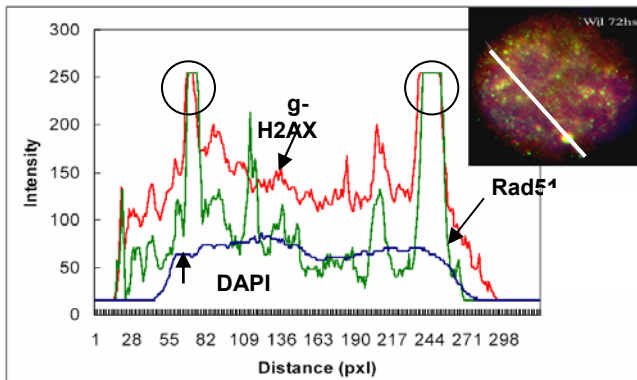


Fig.4. Giant repair foci segmented in a polyloid WI-L2-NS cell nucleus, 72 h post irradiation.

was apparent (Table 1). Some cell nuclei in both cell lines became free of both components (presumably having repaired the DSB). However, at 72 h, the difference in HR foci again showed the higher repair potential of the WI-L2-NS cells (6.1 versus 3.6 foci in TK6 cells). The average size of Rad51 foci in TK6 cells between 6-72 h was determined to be statistically smaller by the non-parametrical sign test ( $p < 0.001$ ). At 72 h, some of WI-L2-NS polyloid cells displayed giant repair foci of heterogenous size, with high concentration of the both components and increased local DAPI binding (Fig.4).

#### IV. DISCUSSION

Here we analysed the DNA damage response in two different lymphoblastoid cell lines derived from the same source which differ in their p53 status. After ionising irradiation, both cell lines formed HR repair foci containing

colocalized g-H2AX and Rad51. However, the p53 competent TK6 cells had a reduced ability to target Rad51 to g-H2AX-signaling foci coincident with the timing of the first (6h) and further (72h) S phases. Recombination in S-phase is assumed to be illegitimate as it favours mutation. Mutations arising as a result of enhanced recombination repair were found previously in WI-L2-NS cells as compared with TK6 [4]. More recently, a specific helicase Srs2 has been discovered which normally prevents uploading of Rad51 to the DNA replication processivity clamp [5]. Our data indirectly suggest that this mechanism may be p53-dependent, while phosphorylation of H2AX in the damage-signalling cascade may be independent of p53. The topological consequence of the restricted association of Rad51 with the g-H2AX foci was evidenced by their structural deterioration, multiplication of g-H2AX domains and decrease in DAPI binding. In contrast, the unrestricted binding of Rad51 to g-H2AX repair sites in p53 mut polyloid WI-L2-NS cells leads to the formation of enormous, well-shaped foci and notably – to the local increase of DAPI binding. DAPI is a DNA intercalating dye whose binding is dependent on both its DNA content and double-strandedness: DAPI does not bind single-stranded DNA. Therefore, our observations suggest that Rad51 may prevent relaxation of the DNA in the HR repair foci. Possibly, Rad51 filaments may penetrate into the sites of damage, locating single strand breaks (SSB) searching for the homology to ‘plug’ the breaks, thus favouring staining with DAPI. The relaxation of chromatin in the Rad51-depleted g-H2AX-foci was observed by us as the initiating step switching the chromatin from attempts of HR towards the initiation of apoptosis in the p53-competent TK6 cells. Excessive g-H2AX formation was shown to appear during apoptosis concurrently with the initial appearance of high molecular weight DNA fragments [6]. These high molecular weight DNA fragments observed during apoptosis are produced by topoisomerase II (Topo II). Paradoxically, Topo II has also recently been linked with preventing mutagenic DNA repair by illegitimate non-homologous recombination [7]. Therefore, currently the temporal regulation of this process is unclear – i.e. whether initial apoptosis started by Topo II is then interrupted by binding of Rad51 to SSB (shifting Topo II activity from DNA cleavage to religation) or the whether the DNA repair by HR fails, releasing Rad51 and thus allowing apoptosis to initiate (via Topo II). Regardless, it seems clear that protection from apoptosis by HR in p53-deficient tumor cells occurs in the chromatin providing these cells with genotoxic resistance and increased mutagenicity, thus promoting tumor progression.

## V. CONCLUSION

A restriction in binding of Rad51 recombinase to g-H2AX HR repair foci was observed in S-phase in p53 wt TK6 lymphoma cells, compared to the p53 mutated counterpart WI-L2-NS. The inability to stably bind Rad51 leads to a visible relaxation of the DNA resulting in the multiplication and fusion of g-H2AX domains in early apoptotic chromatin. These data indicate that prevention of apoptosis in p53-deficient tumor cells occurs through HR at the level of the chromatin.

## VI. ACKNOWLEDGMENT

Grant 05.1634 and 05.1634.1 of the Latvian Scientific Council supported this research in Riga, the exchange visit grant of the Royal Society of London and Cancer Research Foundation, in Southampton and Manchester, UK.

## VII. REFERENCES

1. Raderschall E, Bazarov A, Cao J et al (2002) Formation of higher-order nuclear Rad51 structures is functionally linked to p21 expression and protection from DNA damage-induced apoptosis. *J Cell Sci* 115:153-164
2. Ivanov A, Cragg MS, Erenpreisa J et al (2003) Endopolyploid cells produced after severe genotoxic damage have the potential to repair DNA double strand breaks. *J Cell Sci* 116: 4095-4106
3. Paull T, Rogakou EP, Yamazaki V, Kirchgessner CU et al (2000) A critical role for histone H2AX in recruitment of repair factors to nuclear foci after DNA damage *Curr Biol* 10:886-895
4. Xia F, Amundson SA, Nickoloff JA et al (1994) Different capacities for recombination in closely related human lymphoblastoid cell lines with different mutational responses to X-irradiation. *Mol Cell Biol* 14:5850-5857
5. Pfänder B, Moldovan GL, Sacher M et al (2005) SUMO-modified PCNA recruits Srs2 to prevent recombination during S phase. *Nature* 436:428-433
6. Rogakou EP, Nieves-Neira W, Boon C et al (2000) Initiation of DNA fragmentation during apoptosis induces phosphorylation of H2AX histone at serine 139. *J Biol Chem* 275:9390-9395
7. Umanskaya ON, Lebedeva SS, Gavrilov AA et al (2006) Inhibition of DNA topoisomerase II may trigger illegitimate recombination in living cells: experiments with a model system. *J Cell Biochem* 99:598-608

Author: Jekaterina Erenpreisa  
Institute: Latvian Biomedicine Centre  
Street: Ratsupites 1  
City: Riga  
Country: Latvia  
Email: [katrina@biomed.lu.lv](mailto:katrina@biomed.lu.lv)



# Parameterization of the Optic Nerve Disk in Eye Fundus Images

D. Jegelevicius<sup>1,2</sup>, D. Buteikiene<sup>3</sup>, V. Barzdziukas<sup>3</sup> and A. Paunksnis<sup>3</sup>

<sup>1</sup> Kaunas University of Technology/Biomedical Engineering Institute, Kaunas, Lithuania

<sup>2</sup> Kaunas University of Technology/Department of Signal processing, Kaunas, Lithuania

<sup>3</sup> Kaunas University of Medicine/Institute for Biomedical Research/Department of Ophthalmology, Kaunas, Lithuania

**Abstract** — Algorithms for interactive and automatic optic nerve disk parameterization are presented in this paper. Parameterization of the optic nerve disk is done by detection of the disk boundaries and calculation of parameters describing it. Automatic and interactive algorithms and user interface are designed and implemented in Matlab (The MathWorks, Inc.) programming environment. Interactive identification of the optic nerve disk boundaries was done by experienced ophthalmologist. Reference points interactively placed by physician on the nerve disk boundary then approximated by ellipse. Those boundaries were used as reference boundaries for the evaluation of automatic boundaries detection algorithm. Automatic algorithm is based on removing of vessels by segmentation and approximation and then using derivative image and verification algorithm to determine boundary location. Optic nerve disk boundary is then approximated by ellipse. Comparison of interactive and automatic algorithms shows that automatic algorithm worked well enough on more than 80% of images (in 300 images dataset).

**Keywords** — image processing, optic nerve disk, eye fundus, edge detection.

## I. INTRODUCTION

Ophthalmoscopic evaluation and tracking of changes of the eye fundus is important diagnostic method in ophthalmology. Photography of the eye fundus helps in documentation and follow-up of the eye fundus conditions and also other diseases. Evaluation of the eye fundus images is complicated because of variety of the anatomical structures and possible changes in case of eye diseases and requires good experience from the expert.

Main components of the eye fundus imaged by photography are optic nerve disk, fovea and blood vessels. The optic nerve disk (OND) is the exit site for all retinal nerve fibers. This is the part of the eye that carries visual information from the eye to the brain. OND lesions have a predilection for suppressing the eye function and cause the following clinical signs: reduction of visual acuity for distance and near, afferent pupillary conduction defect, dyschromatopsia (impairment of color vision), diminished light brightness and contrast sensitivity, visual field defects.

Description of the OND in clinical practice is done by experienced ophthalmologist. However it introduces large variability due to the human interpretation [1]. Development of automated, quantitative methods for OND analysis would be the right way for the decreasing of variability of interpretation results.

## II. METHODS

### A. Description of OND features

Optic nerve disk (see Fig. 1) is oval shaped, usually (but not always) bright spot in the eye fundus. OND is also entering point of retina vessels. In the centre of the optic nerve disk is the pit, called excavation – the normally occurring depression, also called physiological excavation or cup. The tissue between the outer edge of the cup and the outer margin of the disc is called neuroretinal rim.

Usually ophthalmologists estimate the parameters of the morphology of the optic nerve disc, excavation (cup) and neuroretinal rim visually. They estimate the following parameters: boundary distinctness; boundary shape; vertical and horizontal diameters of the optic disc; the area of the optic disc; vertical and horizontal diameters of the optic cup (excavation); area of the optic cup; area of the neuroretinal

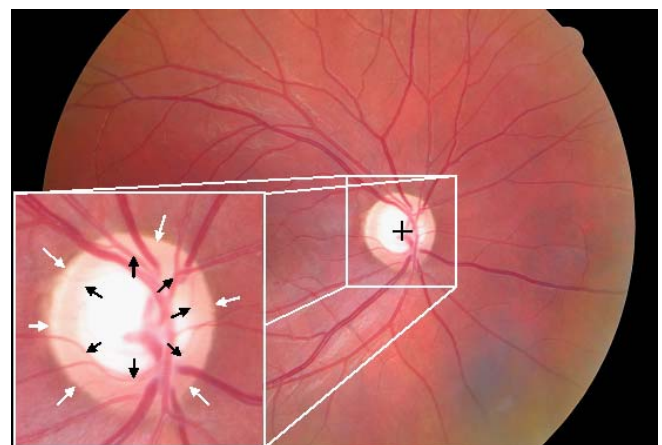


Fig. 1 Eye fundus image and optic nerve disk. White arrows point to the external OND boundary, black arrows point to the excavation boundary.

rim; four disc sectors of neuroretinal rim; the ratio between vertical diameters of the cup and disc; the ratio between horizontal diameters of the cup and disc; the color of the optic nerve disk.

OND appearance can be very various. Shape can vary from circular to extended oval. Disk boundary can be distinguished as steep contrast change, but can be also just noticeable by vessels winding or can be surrounded by bright oval due to peripapillar atrophy, congenital and myopic crescents (conus). Presence of vessels also complicates view and outline of the OND boundary. Excavation boundary is even more complicated and can be identified not in every image.

### B. Interactive OND boundaries detection and parameterization

Interactive optic nerve disk boundaries detection was realized by interactively placing several points on the boundary and then approximating them by ellipse. Detection of the OND boundaries was done by experienced ophthalmologist. We identified that ellipse describe well enough the shape of the OND boundaries. Also description by the ellipse is compact and it has good approximation of OND in “not clear situations”. As “not clear situation” we assume intervals of boundaries with vessels and not distinct OND boundary intervals. In such way placing of several points on distinct boundary we get OND estimation by ellipse.

Algorithm for interactive OND boundaries detection was as follows:

1. Point OND center
2. Crop area of OND

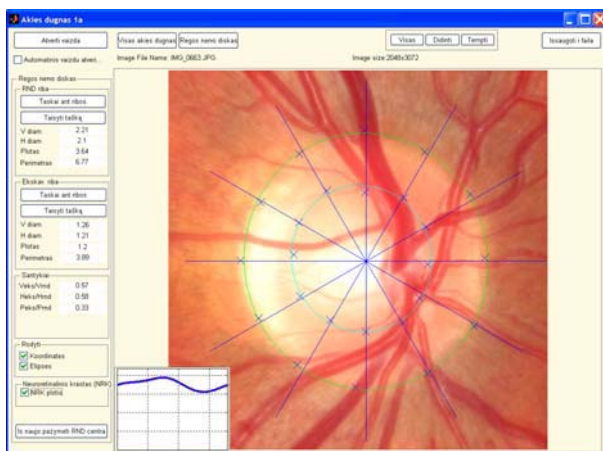


Fig. 2 Interactive OND parameterization tool

3. Place twelve points on OND external boundary
4. Approximate OND external boundary by ellipse
5. If approximated boundary satisfies, continue, if not – correct some points and go to step 4
6. If OND excavation boundary is distinguishable, place twelve points on this boundary
7. Approximate OND excavation boundary by ellipse
8. If approximated boundary satisfies, continue, if not – correct some points and go to step 7
9. If two boundaries exists, calculate neuroretinal rim width distribution

Algorithm was implemented in Matlab (2007a, The MathWorks, Inc.), compiled to stand alone executable program (see Fig. 2), installed in clinics and used by experienced ophthalmologists.

We calculated 14<sup>th</sup> numerical parameters using ellipses of external and excavation boundaries of OND. There were four groups of parameters: optic nerve disc, excavation, neuroretinal rim and ratios between these parameters. Parameters were used for ophthalmological data classification [1].

### C. Automatic OND boundary detection

Automatic methods for OND boundary detection are using different techniques: image pixel classification [2], graph search [3], active contour [4] or anatomical structure model based [5]. Our approach for boundary detection realizes graph search technique.

As a starting point of processing, OND centered and cropped images were used. Algorithm for automatic OND boundary detection was as follows:

1. Coimpare and choose red, green or intensity image for further processing:
  - a. calculate standard deviation of red, green and intensity images
  - b. choose image with maximum standard deviation
2. Make the mask of vessels:
  - a. Filter image by vessel adjusted steerable filters [6]
  - b. Convert filtered image to binary using Otsu threshold
  - c. Extend vessels mask by dilation
3. Eliminate vessels from OND image:
  - a. Interpolate OND image inward vessel mask
4. Transform OND image into polar coordinates in regard to image center
5. Search along transformed image for two biggest intensity gradient negative peaks and label them as candidate pixels for boundary

6. Remove candidate pixels that are on vessels using vessels mask
7. Group candidate pixels to candidate lines
8. Select candidate lines according to continuity
9. Transform candidate pixels into rectangular coordinates
10. Approximate candidate OND boundary lines by ellipse

Algorithm was implemented in Matlab (2007a, The MathWorks, Inc.) environment.

#### D. Evaluation of automatic OND detection

Evaluation of automatic OND boundary detection was done by comparing automatically outlined boundary (automatic detection, AD) with the boundary outlined interactively by experienced ophthalmologist (ground truth, GT). Some indices were calculated for comparison [7, 8]:

- overlap index

$$OI = \frac{areaGT \cap areaAD}{areaGT \cup areaAD} \quad (1)$$

- true positive fraction (sensitivity)

$$S^+ = \frac{areaGT \cap areaAD}{areaGT} \quad (2)$$

- true negative fraction (specificity)

$$S^- = \frac{areaGT - areaAD + areaGT \cap areaAD}{areaGT} \quad (3)$$

- similarity Kappa index

$$KI = \frac{areaGT \cap areaAD}{\frac{1}{2} \cdot (areaGT + areaAD)} \quad (4)$$

- accuracy:

$$A = \frac{areaGT - areaAD + 2 \cdot areaGT \cap areaAD}{2 \cdot areaGT} \quad (5)$$

### III. MATERIALS

Data set consisted of 300 eye fundus color photographs obtained using Canon C60UVi fundus camera in Department of Ophthalmology, Institute for Biomedical Research, Kaunas University of Medicine. Patients had diagnosis of: glaucoma, glaucoma with myopia, suspected glaucoma, hyperopia, myopia and normal refraction. Image size was 3072x2048 pixels and image compression format was JPEG. After interactively pointing OND center the

image was then cropped to 501x501 pixels keeping the optic disc in the center.

An experienced ophthalmologist marked optic nerve disk boundary by placing twelve points on it using previously described software. This boundary was then used as a reference for the evaluation of the automatic boundary recognition results.

### IV. EXPERIMENTS AND RESULTS

Automatic algorithm was applied on all data set images. Fig. 3 illustrates two successful cases of automatic OND boundary outlining. Table 1 presents indices for comparison of ground truth and automatic algorithm results.

Fig. 4 illustrates two typical not successful cases of boundary outlining. The first case failed due to the bright conus of OND that give much sharper image intensity variation in comparison with the true OND boundary,

$OI$	$S^+$	$S^-$	$KI$	$A$
80,5±10 %	95,7±10 %	80,1±15 %	88,8±7 %	87,9±7 %

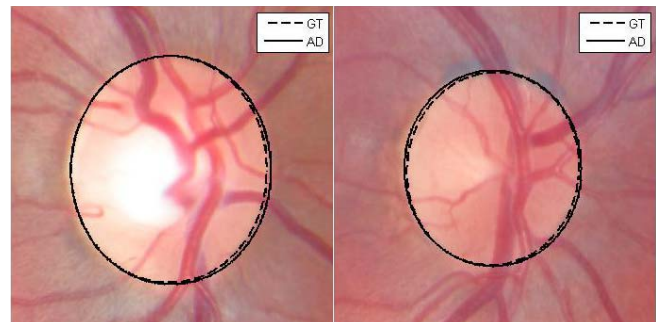


Fig. 3 Comparison of boundaries outlined by physician (GT) and automatic algorithm (AD): successful case.

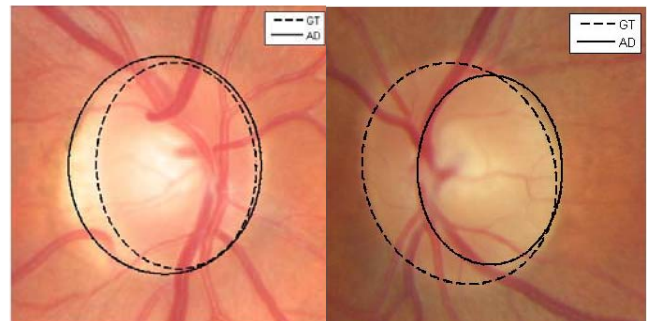


Fig. 4 Comparison of boundaries outlined by physician (GT) and automatic algorithm (AD): not successful case.

outlined by physician. The second case failed due to not successful vessel removal, leading to incorrect candidate pixels determination.

## V. DISCUSSION

Results show that automatic OND boundary outlining works good on images with expressed OND boundaries without pathologies. Boundaries with pathologies usually are overestimated, i.e. area of automatically outlined boundary cover area of true boundary. Analysis of this situation showed that positive peaks of intensity gradient could be used as boundary features. It is due to intensity transition from low to high in conus area of OND border versus to transition from high to low in usual case.

Better removing of vessels from OND image also could improve results. The main drawbacks in used method for vessel removing were filter design for the “mean” vessel and global threshold for vessel mask.

Outlining of excavation boundary is much more complicated due to mostly not expressed boundaries in eye fundus image.

Overall performance of proposed automatic algorithm for OND boundary outlining can be stated to be more than 80%.

## ACKNOWLEDGEMENT

The research was partly supported by the Lithuanian State Science and Studies Foundation project “Information technology tools of clinical decision support and citizens wellness for e.Health system”, No. B-07019.

## REFERENCES

1. Tielsch J M, Katz J, Quigley H A, Miller N R, and Sommer A (1988) Intraobserver and interobserver agreement in measurement of optic disc characteristics. *Ophthalmology* 95:350–356
2. Bernataviciene J, Dzemyda G, Kurasova O et al (2008) Rule induction for ophthalmological data classification. Proceedings of EURO Mini Conference on Continuous Optimization and Knowledge-Based Technologies, Neringa, Lithuania, 2008, in press
3. Merickel M B Jr, Abramoff M D, Sonka M, Wu X (2007) Segmentation of the optic nerve head combining pixel classification and graph search. Proc. of the SPIE Image Processing, Vol. 6512 DOI 10.1117/12.710588
4. Merickel M B Jr, Wu X, Sonka M and Abramoff M D (2006) Optimal segmentation of the optic nerve head from stereo retinal images. Proc. of SPIE Physiology and Function, Vol. 6143 DOI 10.1117/12.657923
5. Mendels F, Heneghan C and Thiran J P (1999) Identification of the Optic Disk Boundary in Retinal Images Using Active Contours. Proceedings of the Irish Machine Vision and Image Processing Conference, Dublin, Ireland, 1999, pp 103–115
6. Li H, Chutatape O (2003) A Model-Based Approach for Automated Feature Extraction in Fundus Images. Ninth IEEE International Conference on Computer Vision (ICCV'03), 2003, Vol. 1, pp 394–399
7. Freeman W T, Adelson E H (1991) The Design and Use of Steerable Filters. *IEEE Trans. Patt. Anal. and Machine Intell.*, Sept. 1991, Vol. 13, No. 9, pp. 891-906
8. Bueno G, Fisher M H, Burnham K, Mills J, Hass O C L (2001) Automatic segmentation of clinical structures for rtp: Evaluation of a morphological approach. *Medical Image Understanding and Analysis 2001*, Birmingham University, 2001, pp 73–76
9. Rangayyan R M (2002) *Biomedical Signal Analysis: A case-study approach*. IEEE Press/Wiley Inter-Science

Author: Darius Jegelevicius

Institute: Kaunas University of Technology/Department of Signal processing

Street: Studentu str. 50-344

City: Kaunas, LT-51368

Country: Lithuania

Email: [darius.jegelevicius@ktu.lt](mailto:darius.jegelevicius@ktu.lt)

# 3D Medical Image Visualization and Volume Estimation of Pathology Zones

K. Krechetova<sup>1</sup>, A. Glaz<sup>1</sup> and A. Platkajis<sup>2</sup>

<sup>1</sup>Institute of Computer Control, Automation and Computer Engineering, Riga Technical University, Riga, Latvia

<sup>2</sup>Institute of Radiology, Riga Stradins University, Riga, Latvia

**Abstract** — Medical image 3D visualization is one of the fundamental processes in medical diagnostics. Using the acquired 3D images it is possible to find the volume of pathology zone, which is the evidence of a specific disease. As a consequence, two problems emerge: visualization of 3D medical images and pathology zone extraction from acquired images.

Available imaging software in some cases provides the construction of 3D images based upon various medical data obtained by computer tomography, magnetic resonance imaging, scintigraphy, etc. But further processing of these images (image segmentation, pathology zone extraction) can result in loss of information during initial image reconstruction. Furthermore, existing medical imaging software does not provide the automatic extraction of regions of interest. As a consequence, often pathology zone volumes are calculated manually and that results in lack of precision.

In this work methods for solving these problems are proposed. This work describes an approach of 3D model reconstruction from medical images by using detailed initial information obtained for forming DICOM files. For extraction of pathology zones and volume estimation an automatic procedure of region calculation is proposed. The described methods can provide practical improvements to the reliability of medical diagnostics.

**Keywords** — Medical images, segmentation, visualization, volume estimation, pathology zone.

## I. INTRODUCTION

Medical images, acquired with computer tomography (CT) or magnetic resonance (MR), are widely used in medicine for patient diagnosis. One of the most important tasks of medical experts is pathology zone detection and its measurement. To successfully solve this task several problems have to be considered: image segmentation and further pathology zone extraction, estimation of diameter or volume of the zone. Standard medical software provides solution for these problems to some extent, but the results are not always satisfactory. The process of pathology zone extraction in some cases is very difficult and time consuming. Often the detection of pathology zone and its volume estimation is so complex, that the physicians prefer to measure only the pathology zone's maximum axial and coaxial diameters. Although it is clear, that precise volume estimation could offer great help to the physicians in patient diagnostics.

Also, the medical software is very specific, it is usually installed only on one work station that is linked to medical hardware and that is not always convenient.

To solve these problems, several algorithms for segmentation, volume measurement and 3D visualization are proposed in this work. The software is developed for medical images of a brain in DICOM format that are acquired with computer tomography and magnetic resonance.

## II. MEDICAL IMAGES

Illustrations used in this work are medical images of a brain, acquired with magnetic resonance and provided by the Institute of Radiology, Riga Stradinš University (using *General Electric GE Signa HDx 1,5T*). Figure 1 illustrates an example of such images.

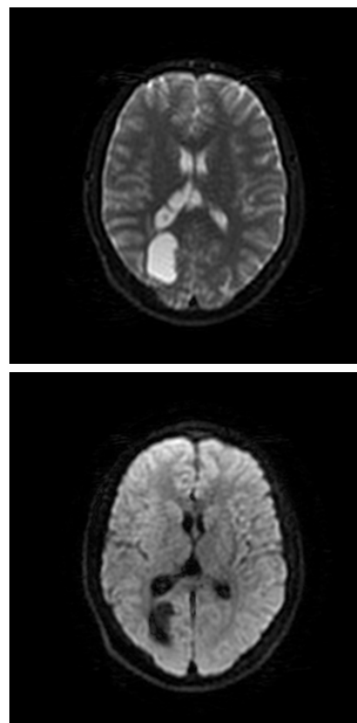


Fig. 1. Examples of medical image of a brain acquired with magnetic resonance

The initial images are in DICOM format [1]. Most modern ultrasound devices, X-ray photography systems and computer tomographs use DICOM image format (Digital Imaging and Communications in Medicine image) for storing images. DICOM is a universal data format which allows storing series of images as well as much additional information about these images. A single file contains both a header (which stores information about the patient's name, the type of scan, image dimensions, etc).

DICOM format allows storing the images in 16-bit palette, which is 65536 grayscale levels; this opens great possibilities for computer diagnosis, because additional data may be processed.

### III. SEGMENTATION

There are many known approaches to medical image segmentation [2], [3], [4]. However, these approaches are not without disadvantages (some require priority information input, like seed points, or histogram threshold levels, some cannot clearly extract the pathology zone). That is why in this work it is proposed to use a new semi-automatic segmentation method [5]. The method is based on several segmentation algorithm combinations (Fig.2).

The method combines one existing region-based segmentation algorithm for background extraction and two developed algorithms that are based on histogram threshold. Segmentation algorithms are combined with developed image enhancement algorithm that is based on image histogram enhancement and existing segmentation result post-processing algorithm. Figure 3 illustrates the result of the segmentation method on images of a brain acquired with magnetic resonance.

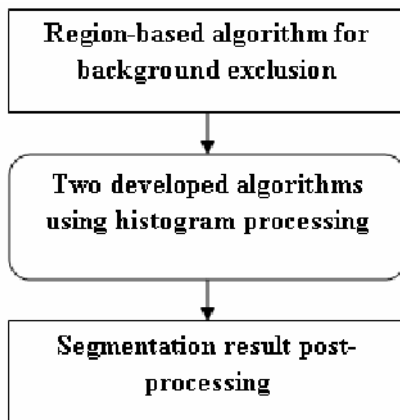


Fig. 2. Segmentation method

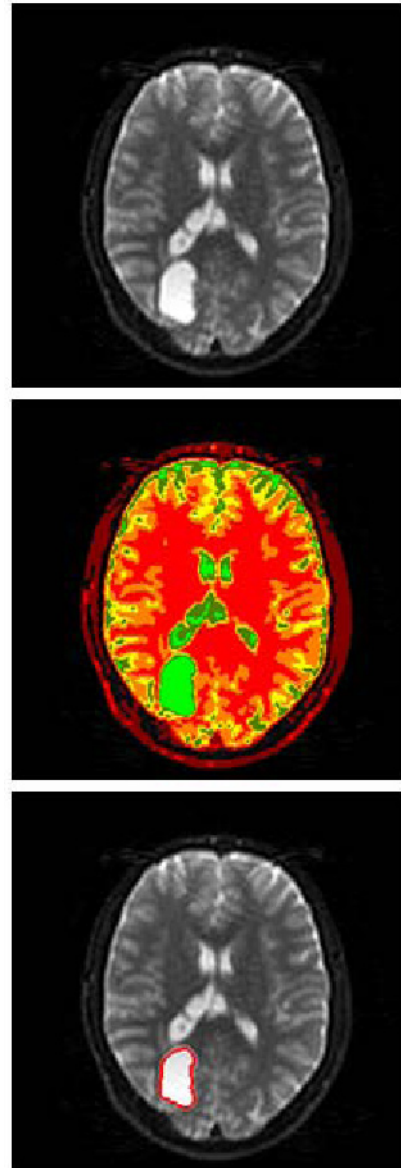


Fig. 3. Segmentation results. Top: initial image. Middle: segmented image. Bottom: extracted pathology zone

### IV. VISUALIZATION

For 3D visualization of medical objects an algorithm using standard OpenGL graphic library is proposed. The 3D model is based on contours acquired from segments on 2D medical image slices. The object can be extracted using histogram thresholds (for the whole brain) or the semi-automatic segmentation algorithm (for the pathology zone). Figure 4 illustrates the visualized objects.

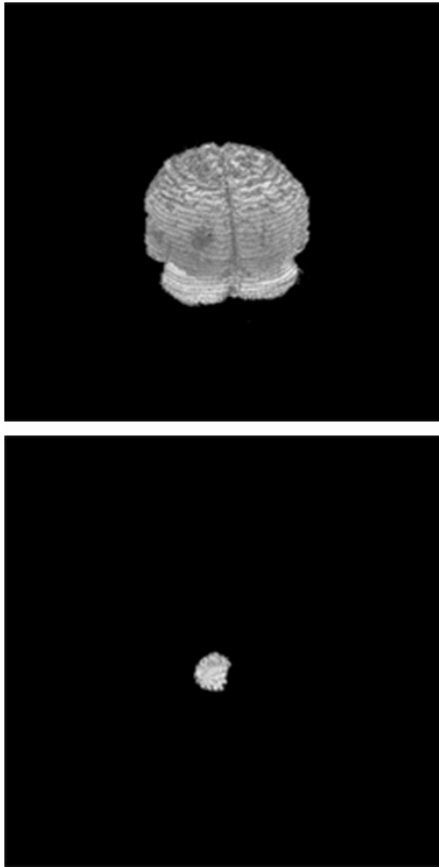


Fig. 4. 3D visualization. Top: visualization of brain using histogram thresholds. Bottom: visualization of segmented pathology zone

## V. VOLUME ESTIMATION

The proposed volume estimation method of pathology zone consists of the following.

First the area of diseased zone is measured on every slice. For this the number of points in each pixel has to be calculated. The additional information in DICOM file (image dimensions and distance between pixels) allows representation of the area in physical values ( $\text{mm}^2$ ).

Volume of the pathology zone is calculated according to the formula :

$$V = \sum_{i=1}^n v_i, \quad (1)$$

where

$n$  is the number of slices where pathology zone is detected;  $v_i$  is the volume of the zone between the segments of pathological slice and it is calculated according to the trape-

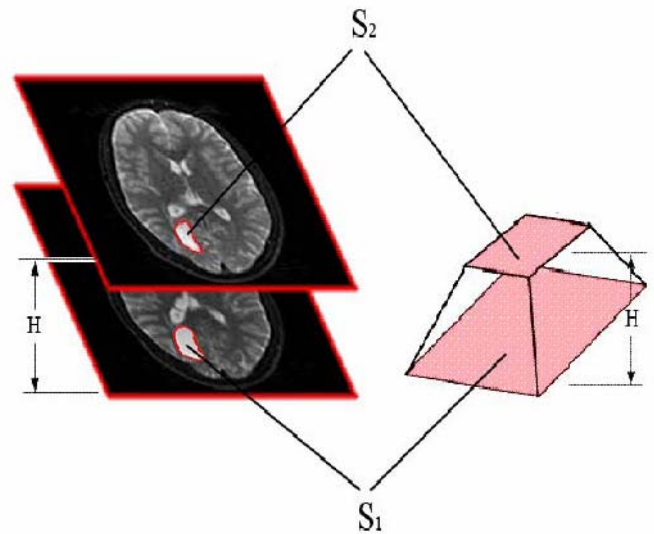


Fig. 5. Volume estimation for  $v_i$

zoid volume formula, meaning that the segments are approximated with rectangles:

$$v_i = \frac{1}{3} H (S_1 + \sqrt{S_1 S_2} + S_2), \quad (2)$$

where

$H$  is the distance between the 2D slices;

$S_1$  is the area of pathology zone in slice  $i$  ;

$S_2$  is the area of pathology zone in slice  $i + 1$  .

Figure 5 illustrates volume estimation for each  $v_i$ .

## VI. CONCLUSIONS

In this paper, several algorithms for medical image processing are proposed. The necessity for development of a new program is caused by disadvantages in existing medical software (for *General Electric GE Signa HDx 1,5T*):

- 1) difficulties in pathology zone extraction and volume estimation (available only for standard volumes: spheres, cubes);
- 2) difficulties using standard software in different work places – the analysis can only be performed on the computer linked to the medical hardware.

The developed program can be installed on any computer. That will allow the physicians to diagnose the medical images outside the hospitals. The program includes

semi-automatic segmentation algorithm that allows making the work of physicians less time consuming. The program also allows manual pathology zone correction.

#### REFERENCES

1. <http://medical.nema.org/Dicom/>
2. Dastidar P, Heinonen T, Vahvelainen T, Elovaara I, Eskola H (1999) Computerised volumetric analysis of lesions in multiple sclerosis using new semi-automatic segmentation software. *Med. Biol. Eng. Comput.*, vol. 37, 1999, pp 104-107
3. Jiang C, Jiang L, Zhang X, Gevantmakher M, Meinel C (2004) A New Practical Tool for 3D Medical Image Segmentation, Visualization and Measurement. *Proceedings of CCCT, 2004, Austin, USA*
4. Smitha S, Revathy K, Kesavadas C (2006) Segmentation and Volume Estimation of Brain tissues from MR Images. *IMECS, 2006*, pp 543-547
5. Krechetova K, Glaz A (2007) Development of a new segmentation method for medical images. *Biomed. Eng. conference proc., Kaunas, Lithuania, 2007*, pp 133-136

Author: Katrina Krechetova, PhD student  
Institute: Institute of Computer Control, Automation and Computer Engineering, Riga Technical University  
Street: Meza 1/3-304 (3<sup>rd</sup> floor)  
City: Riga  
Country: Latvia  
Email: [katrina.krecetova@rtu.lv](mailto:katrina.krecetova@rtu.lv)



# Biomedical Image Processing Based on Regression Models

A. Lorencs, I. Mednieks and J. Sinica-Sinavskis

Institute of Electronics and Computer Science, Riga, Latvia

**Abstract** — The problem of detecting specific objects or anomalies (OA) in tissue samples of living beings from their digital images is considered. Taking into account that pixel values in images (brightness levels) can be interpreted as sums of values related to physical objects and realizations of additive random variables, regression method (RM) for detection of OA was developed. It is based on mathematical approach of statistical analysis of regression models, coupled with hierarchic clustering method.

**Keywords** — pattern recognition, linear regression, biomedical image processing, computer-aided diagnostics, clustering.

## I. INTRODUCTION

Various formal methods have been developed for automated pattern recognition and classification. A wide spectrum of deterministic and statistic, analytic and structural (synthetic), training-based and conservative methods are described in [1,2,3].

Applicability of the particular method is largely determined by the form of information representing the category of real scenes to be analyzed. If this information is mainly of stochastic nature, classification rules must be based on statistics. However, it does not mean that the decision rules will be statistic; in all cases they will be formulated deterministically and, by chance, may lead to wrong decisions.

In this work we propose a pattern recognition method based on the assumption that scenes under consideration are represented by digital images formed from matrices  $A=(a_{ij})$  of rational numbers. At the same time it is assumed that acquisition of digital images can be influenced by random factors that introduce additive Gaussian noise with a definite variance. As a result, two images obtained from the same object in the same conditions may differ. Excellent description of analysis methods of such phenomena in the form appropriate for physicians is given in [4].

Regression method presented in this work is based on the same assumption that lays in the background of many pattern recognition methods except for so called statistical recognition of universal sets (see [3]). To apply the regression method, it is necessary that scenes of the analyzed category can be divided into the finite set of classes. This results in division of digital images into the same number of classes  $K_1, \dots, K_a$  so that  $K_s \cap K_t = \emptyset$  for all  $s \neq t$ . Of

course, there may not be a digital image of a scene related to none of the classes  $K_i$ .

Finally, it is assumed that sufficient number of images from each class is available for investigation. This condition is necessary to fulfill in order to form an efficient system of rules for classification of images to be used in practice.

Some ideas of the regression method are found in [5, 6].

Scientific publications [7,8] indicate that, in the field of medical diagnosis, assumptions formulated above can be fully satisfied. Digital mammograms and chest radiographs can be exploited for the development of automated diagnostic systems. Number of such projects is foreseen to increase in the future.

## II. IMAGE TRANSFORMATION WITH RM

Without limiting the generality of RM it may be assumed that digital images of all analyzed scenes are given with matrices of fixed size, i.e.  $A = A_{m,n}$ . Let us relate the image with the rectangle  $P$  in the first quadrant of the  $xoy$  plane extending  $n-1$  units on the  $x$  axis and  $m-1$  units on the  $y$  axis.

Let us assume that the continuous geometric surface exists, analytically described within the rectangle  $P$  by function  $z = z(x, y)$  with property  $z(i, j) \approx a_{ij}$ .

More precisely,  $a_{ij}$  is the sample taken from the universe represented by the random variable  $X_{ij} = z(i, j) + X$ , where  $X$  is a random variable with the mean value  $EX = 0$  and variance  $DX = \sigma^2$ . A well-grounded assumption is that  $\sigma^2$  is rather small and therefore  $z(i, j) \approx a_{ij}$ .

If we choose appropriate set of basis functions  $\{f_0(x, y), f_1(x, y), \dots, f_K(x, y)\}$  defined in rectangle  $P$  so that its elements form a linearly independent system of functions, then the unknown value  $z(x, y)$ ,  $(x, y) \in P$  may be expressed as a linear combination of functions  $f_k(x, y)$  with appropriate coefficients  $\theta'_k$ , i.e.  $z(x, y)$  can be well approximated by the expression

$$\sum_{k=0}^K \theta'_k f_k(x, y). \quad (1)$$

Unknown coefficients  $\theta'_k$  ensuring the „sufficiently good” approximation of  $z(x, y)$  can be estimated on the basis of the least squares method using the elements  $a_{ij}$  of

the matrix  $A_{m,n}$ . Such approach leads to the following algorithm for the calculation of estimated values  $\hat{\theta}_k$  of coefficients  $\theta'_k$ .

Let us define the matrix

$$F_{mn,K+1} = (f_{sk}), \tag{2}$$

where  $(f_{s0}, f_{s1}, \dots, f_{sK}) = (f_0(i, j), f_1(i, j), \dots, f_K(i, j))$  and  $s = in + j$ . If  $mn > K + 1$ , we will obtain the non-singular matrix

$$M = F^T F \tag{3}$$

with dimensions  $(K + 1) \times (K + 1)$ , where  $T$  denotes transpose operation.

As the matrix  $M$  is not singular, the inverse matrix  $M^{-1}$  exists. By enumeration of elements  $a_{ij}$  of matrix  $A_{m,n}$  in the same sequence as values of basis functions, we obtain the column vector of size  $m \times n$ :

$$a = (a_1, a_2, \dots, a_{mn})^T. \tag{4}$$

The sought estimate  $\hat{\theta}$  of the vector  $\theta'$  is calculated using to the following formula:

$$\hat{\theta} = M^{-1} F^T a. \tag{5}$$

As the digital image of the scene quite often is a matrix with rather large dimensions, practical implementation of the RM usually is based on fragmentation of  $A_{m,n}$  into submatrices of smaller size. When the fragmentation is applied, care should be taken to ensure that the size of the feature set of the scene does not exceed the size of the sub-matrix. Let us assume for now that the values of  $m$  and  $n$  are not large and can be practically used for implementation of the first stage of the regression method, i.e. estimation of vectors of regression coefficients  $\hat{\theta}$ . Using the sets of available digital images  $S_1, S_2, \dots, S_a$  related to classes  $K_1, K_2, \dots, K_a$  of scenes under investigation, we calculate the sets of vector estimates  $T_1, T_2, \dots, T_a$ . Obviously the cardinality of sets  $S_i$  and  $T_i$  is equal. It is preferable that the sets are sufficiently large.

### III. CLUSTERING OF THE VECTOR SETS OF REGRESSION COEFFICIENTS

The next stage of realization of the RM is clustering of the sets  $T_i$ . To perform this, it is necessary to choose the distance or similarity measure. Rather often the Euclidean metric is used, i.e. distance between two vectors  $\hat{\theta}_1$  and  $\hat{\theta}_2$  is defined as

$$d(\hat{\theta}_1, \hat{\theta}_2) = \sqrt{\sum_{k=0}^K (\hat{\theta}_{1,k} - \hat{\theta}_{2,k})^2}. \tag{6}$$

In some cases, Jordan's metric is applied, i.e. distance is calculated as

$$d(\hat{\theta}_1, \hat{\theta}_2) = \max_{k \in \{0, K\}} |\hat{\theta}_{1,k} - \hat{\theta}_{2,k}|. \tag{7}$$

More distance metrics are possible that meet the axioms of metric spaces, namely identity axiom, symmetry axiom and triangle axiom. On the basis of the chosen measure of distance, it is possible to define the similarity or closeness measure  $s(\hat{\theta}_1, \hat{\theta}_2)$  of two vectors, e.g.

$$s(\hat{\theta}_1, \hat{\theta}_2) = e^{-d(\hat{\theta}_1, \hat{\theta}_2)}. \tag{8}$$

Obviously, the inequality  $0 \leq s(\hat{\theta}_1, \hat{\theta}_2) \leq 1$  will hold.

Similarity measure  $s(\hat{\theta}_1, \hat{\theta}_2)$  may be defined also in a different way, independently of a distance measure. For example, it can be defined by the expression

$$s(\hat{\theta}_1, \hat{\theta}_2) = \frac{1}{2} \left( \frac{\sum_{k=0}^K \hat{\theta}_{1,k} \cdot \hat{\theta}_{2,k}}{\sqrt{\sum_{k=0}^K (\hat{\theta}_{1,k})^2} \cdot \sqrt{\sum_{k=0}^K (\hat{\theta}_{2,k})^2}} + 1 \right). \tag{9}$$

One of the most appropriate clustering methods, preferred also here, is the hierarchic clustering. Its implementation in any case is based on assumption that, initially, each element (vector) of each set  $T_i$  forms one cluster. To perform the following steps of clustering, it is necessary to define the distance measure between any two clusters. The similarity measure can be also used instead. The only difference (at least for traditional cases) will be that, in the case of using distance measure, the closest clusters will be merged, but in the case of using similarity measure, the most similar clusters will be merged.

Distance between any two clusters  $C_1$  and  $C_2$  is usually defined as

$$d(C_1, C_2) = \frac{1}{|C_1||C_2|} \sum_{x \in C_1, y \in C_2} d(x, y), \tag{10}$$

where  $|C|$  denotes the cardinal number.

If the  $\nu$ -th step of hierarchic clustering has produced clusters:  $C_{i,1}; C_{i,2}; \dots; C_{i,\nu_i}$ , then the  $(\nu + 1)$ -th step results in merging of two closest of them (according to the chosen distance measure). Researcher should choose the criterion for stopping the clustering process relevant for the particular classification task.

Potentially large cluster size may render their direct application impractical. Therefore the proposed approach recommends to replace the resulting clusters by their centers, i.e. vectors defined in a special way. The simplest case

is when the center  $\mathbf{x}_C$  of cluster  $C$  is defined by the expression

$$\mathbf{x}_C = \frac{1}{|C|} \sum_{\mathbf{x} \in C} \mathbf{x}. \quad (11)$$

For the following analysis cluster is represented by its center.

#### IV. CLASSIFICATION OF IMAGES

If the digital images of scenes under investigation are matrices of rather small dimensions, their fragmentation for forming classification rules is not necessary. If this is met, classification rule  $R(A_{m,n})$  is formed using the resulting set  $\{\mathbf{u}_{i,1}, \mathbf{u}_{i,2}, \dots, \mathbf{u}_{i,v_i}\}$  of cluster centers obtained from sets  $T_i$ , where  $\mathbf{u}_{i,j}$  is the center of resulting cluster  $C_{i,j}$ ;  $j = 1, 2, \dots, v_i$ ;  $v_i$  - number of resulting clusters formed from set  $T_i$ . We start then with transformation of image  $A_{m,n}$  into the estimate  $\hat{\theta}$  of the coefficient vector of the chosen regression model. After that, the distances of this vector to all cluster centers  $\mathbf{u}_{i,j}$  are calculated and minimum distance obtained as

$$d_i(\hat{\theta}) = \min_{j \in 1, v_i} d(\hat{\theta}, \mathbf{u}_{i,j}). \quad (12)$$

Rule  $R(A_{m,n})$  is defined as a functional, which takes the value  $q$  ( $q = 1, 2, \dots, a$ ) if and only if

$$\min_{i \in 1, a} d_i(\hat{\theta}) = d_q(\hat{\theta}). \quad (13)$$

Value  $q$  of the functional  $R(A_{m,n})$  is interpreted as a decision to relate the image  $A_{m,n}$  to the class  $K_q$ . Obviously, such decision may also prove wrong due to different reasons.

If the dimensions of images under investigation are too large, fragmentation of matrices  $A_{m,n}$  is performed first into matrices of sufficiently small and fixed dimensions. Sets  $T_i$  are then formed as sets of regression coefficient vector estimates. In this case, rules  $R$  defined above are applied to sub-matrices of full digital images. After that, a classification rule  $R^*$  for the entire images is formed, using the „voting” principle. If the majority of  $N$  fragments  $A_{m',n'}$  of the full image  $A_{m,n}$  were classified as related to class  $K_q$ , then the whole image is classified as related to class  $K_q$ . Such tradition “voting” in systems for medical diagnostics might be too trivial to provide effective classification; suitable solution could be based on application of weighing coefficients for the “votes” of each category. In the case of two

classes only, this leads to selection of the threshold  $\Delta$  such that  $R^*(A_{m,n}) = 1$  if and only if the number of fragments, for which the  $R^*(A_{m',n'}) = 1$ , exceeds  $\Delta$ .

Different modifications of rule  $R^*$  are possible. One of such modifications is exploited in the project where the method was approved, described below.

#### V. FINAL NOTES

The proposed RM of pattern recognition is not qualified as fully novel. The elements of the approach are found e.g. in [5,6,7]. Its first principles are given in publications [5,6] and even in a more generic form as in [7]. There are differences also related to mathematical correctness. In addition, the proposed method is tightly coupled with the set of clustering techniques. As a result, the proposed RM has the following degrees of freedom:

1. Selection of the appropriate system of basis functions
2. Selection of fragmentation size of the full digital image of the scene under investigation
3. Selection of metric for calculation of distance (resp. similarity measure) in the vector space of linear regression coefficients
4. Selection of metric for calculation of distance (resp. similarity) between the clusters
5. Selection of procedure for clustering of the set of coefficient vectors
6. Selection of classification rules of digital images
7. Selection of procedure of forming the cluster centers

Selection of pre-processing procedures of digital images is left outside the specifics of the RM. However, these can be of crucial importance to ensure the effectiveness of the RM.

The proposed method was developed and successfully used in European FP6 project MODULINSPEX for detection of small foreign objects in meat products by processing their X-ray images in real time mode. Initial digital images were transformed using the median filter. The set of basis functions contained 25 members; dimensions of the analyzed image fragments were  $25 \times 25$  pixels; distances between the vectors of regression coefficients were calculated using the Jordan’s metric. Hierarchic clustering method [9] was used for clustering of vectors of regression coefficients.

The solved task illustrated in Fig. 1. In Fig. 1a,b,c, a sample fragment containing foreign object is depicted; Fig. 1d shows the ‘normal’ fragment. 35 fragments containing foreign object and 75 ‘normal’ fragments were used for clustering resulting in 7 and 5 clusters correspondingly. 100 fragments from images of meat samples were processed then; they were classified by calculating distances to the

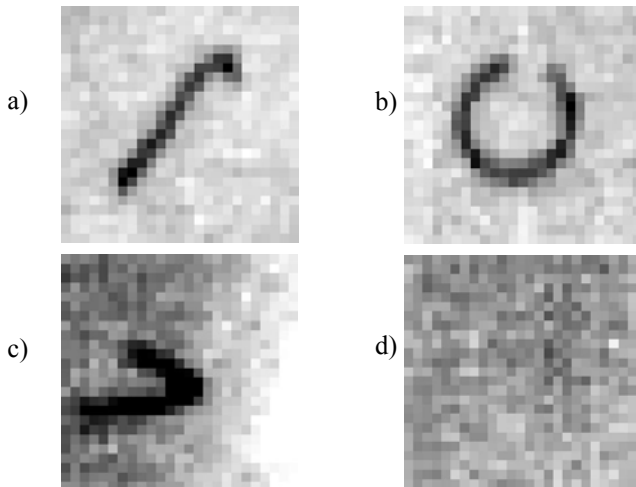


Fig. 1. a),b),c) - fragments with foreign object; d) "normal" fragment.

centers of these clusters. As a result, all fragments were classified properly as containing or not containing a foreign object.

The task solved within the MODULINSPEX project was not related to medical diagnostics or biological analysis. However, the mathematical approach is generic and exposes features that bring it close to problems faced in biomedical image processing. It is proposed for development of computer aided diagnostic systems (potential applications include but are not limited to mammography, radiography) based on processing of digital images regardless of the technology used to obtain them.

## REFERENCES

1. Tou J.T., Gonzales R.C. (1974) Pattern recognition principles. Addison-Wesley, London - Amsterdam
2. Fukunaga K. (1990) Introduction to Statistical Pattern Recognition (Second Edition). Academic Press, New York
3. Pratt W.K. (1991) Digital Image Processing. John Wiley & Sons, New York
4. Armitage P., Berry G., Matthews J.N.S. (2001) Statistical Methods in Medical Research. Wiley – Blackwell, New York
5. Lorencs A. (1984) Regression analysis and pattern recognition. In: Automation of analysis and recognition of images, Zinatne, vol.4, Riga, Latvia, 1984, pp 5-25 (in Russian)
6. Lorencs A. (1991) Statistical features of the integral method of standards, Proc. of University of Latvia. Mathematics, vol.562, Riga, Latvia, 1991, pp 53-64 (in Latvian)
7. Ohe Y., Shinohara N., Hara T., Fujita H., Endo T., Iwase T. (2004) Development of an automated detection system for microcalcifications on mammograms by using the higher-order autocorrelation features, SPIE Proc. vol. 5370, SPIE, Bellingham, WA, 2004, pp 1815-1822
8. Paola Campadelli, Elena Casiraghi, Giorgio Valentini (2005) Lung nodules detection and classification, IEEE Proc. vol. 1, ICIP, Genova, Italy, 2005, pp 1117-1120
9. Marques de Sá, J. P. (2001) Pattern recognition: concepts, methods and applications. Springer, Portugal

Author: Juris Sinica – Sinavskis  
 Institute: Institute of Electronics and Computer Science  
 Street: Dzerbenes 14  
 City: Riga  
 Country: Latvia  
 Email: jss@edi.lv

# Analysis of Outliers Effects in Voxel-Based Morphometry by means of Virtual Phantoms

F. Nocchi<sup>1</sup>, T. Franchin<sup>1,4</sup>, E. Genovese<sup>2</sup>, D. Longo<sup>3</sup>, G. Fariello<sup>3</sup> and V. Cannata<sup>2</sup>

<sup>1</sup>“Bambino Gesù” Children’s Hospital / Department of Clinical Engineering, Rome, Italy

<sup>2</sup>“Bambino Gesù” Children’s Hospital / Department of Medical Physics, Rome, Italy

<sup>3</sup>“Bambino Gesù” Children’s Hospital / Department of Paediatric Radiology, Rome, Italy

<sup>4</sup>Department of Bioengineering, Polytechnic of Milan, Milan, Italy

**Abstract** — Voxel-Based Morphometry (VBM) is a technique for analyzing inter-group neuroanatomic differences, frequently used to study a number of neurologic diseases. An important limit to the diffusion of VBM is related to the length of the recruiting process, due to the need of homogeneous and statistically significant samples. Therefore, quite often the need to search for statistically significant differences between small samples arises. The opportunity of analyzing small samples with VBM should be carefully considered. In each sample there could be one or more subjects with atypical local anatomic characteristics (outliers) that are not identifiable *a priori*, thus leading to erroneous inferences about the specific structural features correlated to the studied pathology. It follows the need to evaluate the limits within which including a certain number of outliers can be accepted when relying on small samples. The robustness of VBM performed within *SPM2* with respect to the inclusion of outliers was studied by implementing in *MatLab* sets of virtual phantoms with predetermined characteristics. A matrix of voxels cubes was superimposed on the preprocessed gray matter image of each scanned subject. Each cube has a uniform gray level, while its intensity distribution within each group is Gaussian with controlled group mean and variance. Variance and mean difference were chosen according to data from two ongoing clinical studies. The model implemented shows that applying VBM to small samples could lead to erroneous inferences. The minimum number of subjects should be evaluated according to specific variance and group mean difference values of the experimental samples. The implementation of virtual phantoms enabled the quantitative evaluation of outliers effects when performing VBM on small samples. This approach provides the clinicians with a support tool for evaluating the reliability of the results yielded by VBM analyses and for planning the recruiting process.

**Keywords** — VBM, outliers, phantoms, SPM, MRI.

## I. INTRODUCTION

During the last decade, the study of neuroanatomic differences between samples drawn from different populations has been developed by means of objective morphometric techniques, such as Voxel-Based Morphometry (VBM). VBM is a common method for processing Magnetic Resonance Imaging (MRI) data that allows a voxel-by-voxel

definition of altered structures of the brain, showing concentration or volume differences in cerebral tissues [1]. This method enables disclosing statistically significant local morphological differences between samples, while discounting macroscopic individual anatomic differences [2]. It can be used to study a number of pathological conditions (schizophrenia, anorexia-bulimia, epilepsy, Down’s syndrome, alexithymia, etc.) and to study healthy subjects [3].

An important limit to the diffusion of VBM is related to the need of homogeneous and statistically significant samples [4, 5]. This limit is especially relevant for paediatric applications, because recruiting sufficiently large pathological and control samples can be particularly time consuming. Hence, quite frequently the need to search for statistical significant differences between small samples arises. This could invalidate the statistical analysis and the resulting clinical assessment.

The opportunity of analyzing small samples with VBM should be carefully considered. This technique involves a normalization step, that is, the volumes representing single subjects are mapped onto the same stereotactic space by means of a low spatial frequency deformation field [2]. This way, large scale differences are removed and corresponding anatomic structures are overlapped. Subsequently, local differences are evaluated by means of a univariate statistical analysis. Thus, one can think of VBM as a processing technique that enables disclosing possible statistically significant morphological differences between populations, when recognizing individual alterations by means of other methods wouldn’t be possible. This means that in VBM analyses one cannot control the input to the statistical tests, so that in each sample there could be one or more subjects with structural abnormalities (outliers) that are not identifiable *a priori*. Even if the clinician can state that a given patient belongs to a certain pathological category, evaluating *a priori* if that particular subject shows a local concentration or volume variation of a cerebral tissue type could not be possible.

It follows the need to define the limits within which including a certain number of subjects with atypical anatomic characteristics in a sample can be accepted and the analysis

reliably answers the experimental question, that is, whether or not the pathology is correlated to specific structural features of the corresponding population. If the statistical analysis is carried out on relatively small samples, the occurrence of one or more subjects with atypical local anatomic characteristics can invalidate the analysis, thus leading to erroneous inferences about the anatomic characteristics correlated to the pathological population.

This study was carried out to assess to what extent inter-group differences highlighted from the statistical analysis of VBM preprocessed data can be considered reliable when relying on small samples. To attain this goal, tools for controlling the input to the statistical tests are needed. We implemented a model consisting in sets of virtual phantoms obtained by superimposing matrices of voxels cubes with predetermined characteristics (gray level distribution, mean and variance for each group) on the preprocessed gray matter images of real subjects. Group mean and variance value ranges were chosen according to the results yielded by the analysis of clinical data. The ultimate purpose of this study is giving the clinician the chance of making use of an advanced method such as VBM, while knowing the limits within which the results obtained can be considered reliable.

## II. MATERIALS AND METHODS

### A. Subjects.

Experimental data from two ongoing research projects at “Bambino Gesù” Children’s Hospital of Rome were used to obtain group mean and variance value ranges for the models. These studies (hereinafter referred to as “A” and “B”) pertain to two diseases with a clinical hypothesis of gray matter alteration. Twelve patients (eight males and four females, age  $15,99 \pm 2,18$ ) and twelve healthy control subjects (eight males and four females, age  $16,00 \pm 2,26$ ) were recruited for study “A”, while eighteen female patients (age  $15,76 \pm 1,95$ ) and eighteen female healthy control subjects (age  $15,64 \pm 2,24$ ) were recruited for study “B”.

### B. Structural MRI Scanning Protocol.

MRI was performed on a 1.5T Siemens Magnetom Vision scanner. A 3D structural MRI was acquired on each subject using a T1-weighted 3D MPRAGE sequence (TR=11.4 ms, TE=4.40 ms, slice thickness=1 mm, in-plane resolution of 1x1 mm, NEX=1, flip angle=15°, slice thickness =1.25 mm; voxel size: 0.97x0.97x1.25, acquisition matrix 200x256, field of view 250x250).

### C. Preprocessing of Structural Data.

Several variations in the implementation of the VBM preprocessing algorithm have been proposed in literature [6]. The most common implementation, however, is the optimized VBM. With respect to the standard approach, optimized VBM prevents abnormal cerebral regions from compromising the morphological analysis of other regions-of-interest as a consequence of the low spatial frequency deformation field applied while normalizing individual scans to a standard stereotactic space [1, 3]. This is obtained by using optimized normalization parameters for each kind of tissue, thus ensuring that highlighted statistically significant differences can be attributed to the kind of tissue being analyzed.

Individual structural images of each subject (for both studies, “A” and “B”) were then preprocessed in *SPM2* [Wellcome Department of Cognitive Neurology, London, UK; <http://www.fil.ion.ucl.ac.uk/spm/>] according to the following steps.

1. Registration of the individual images to a reference stereotactic space (*Montréal Neurological Institute* T1 template).
2. Segmentation of the normalized images in gray matter (GM), white matter (WM) and cerebrospinal fluid (CSF).
3. Spatial normalization of the original structural images in native space to the GM *a priori* probability map in the template stereotactic space.
4. Segmentation of the images obtained from the optimized normalization.
5. Smoothing of the segmented GM images with an 8 mm Gaussian kernel.

### D. Analysis of Preprocessed Data.

Preprocessed data were analyzed to obtain group mean and standard deviation of voxels gray levels over the whole brain for both studies, “A” and “B”. The same analysis was repeated for the most significant cluster, which was different for the two studies. Table 1 shows the voxels mean gray level, the standard deviation averaged over the whole brain and over the most significant cluster and the maximum standard deviation. For cluster analyses, mean and standard deviation were calculated over those voxels belonging both to the most significant cluster and to the main anatomical area of the cluster as defined according to an automatic anatomical labeling algorithm [7]. Only voxels with a probability  $\geq 10\%$  of being GM were included in the analysis. Results in Table 1 enabled specifying value ranges for variance and group mean difference in the model.

Table 1 Mean and standard deviation in patients and control groups (gray level of preprocessed GM concentration images).

		Study "A"		Study "B"	
		Control group	Patients group	Control group	Patients group
Whole Brain	Mean	93.2	92.4	92.8	82.5
	Mean difference		-0.8		-10.3
	Average Standard Deviation	14.9	16.7	14.8	15.5
	Maximum Standard Deviation	53.7	59.3	52.5	61.6
	Mean	97.3	120.9	117.7	100.0
Most Significant Cluster	Mean difference		23.6		-17.7
	Average Standard Deviation	9.6	9.3	9.9	14.8
	Maximum Standard Deviation	14.0	17.0	19.0	24.0

### E. Virtual Phantoms.

In order to obtain controlled data for evaluating the effects of outliers, we designed and implemented sets of digital phantoms in *Analyze 7.5* data format [[http://mayoresearch.mayo.edu/mayo/research/robb\\_lab/](http://mayoresearch.mayo.edu/mayo/research/robb_lab/)]. The virtual phantoms were created using *MatLab 7.0* code [<http://www.mathworks.com/products/matlab/>] and *MRICro 1.40* [<http://www.sph.sc.edu/comd/rorden/mricro.html>] software.

Groups with different numbers of subjects (7 to 20) were generated so that analyzing the effects of outliers for different sample dimensions was possible. For each set of phantoms, two identical groups of subjects were created. A 3D matrix of 4x4x4 voxels cubes was superimposed on the preprocessed GM image of each subject of the two groups. Each cube has a uniform gray level, while its intensity dis-

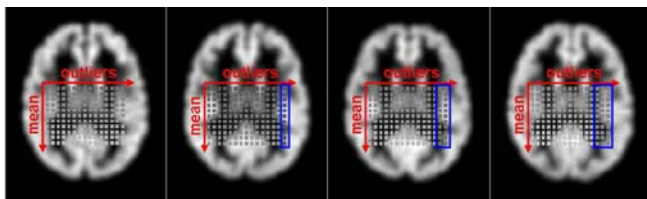


Fig. 1 Phantoms for evaluating the effects of outliers on the results of VBM analyses. Subjects of the first group show the following behavior. While the first subject (left) has the typical values of its own sample in all the cubes, the cubes of the last column of the second subject have the typical distribution of the ones of the second group, the third subject behaves in the same way for the last two columns, etc.

tribution within each group is Gaussian with controlled group mean and variance. The difference between group means varies along the anterior-posterior direction (Fig. 1) up to 50% of a predetermined gray level (100, in the range 0÷255), with 5% steps. The reference gray level was chosen according to the values in Table 1. The number of outliers (subjects of the first group with the same mean values as the ones in the second group) varies along the left-right direction. This way, simulating the effect of including in a group of pathological subjects one or more patients that do not show the typical morphological characteristics of the pathology was possible. Standard deviation varies along the foot-head direction and was set to 10, 15, 20, 25, 30 and 50 for both groups.

### III. RESULTS

For each set of phantoms, a statistical parametric analysis (one-tailed t-test) for comparing the two groups of subjects was performed within *SPM2*. Maps representing statistically significant results for each group mean difference and group variance values were obtained. The maps also enable assessing the effects of including outliers in a sample.

In Fig. 2 an example of the results yielded by the statistical analyses is shown. Fig. 3 represents the minimum statistically significant group mean difference as a function of the samples dimensions, for different numbers of outliers. According to the group mean and average standard deviation values in Table 1, results for standard deviation levels of 10 and 15 are represented.

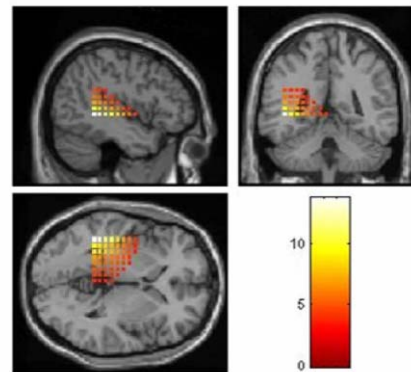


Fig. 2 Statistical parametric map obtained by comparing two groups of 15 subjects each, represented on the MNI single subject template (t-test without correction for multiple comparisons,  $p=0.001$ ,  $T=3.41$ ).

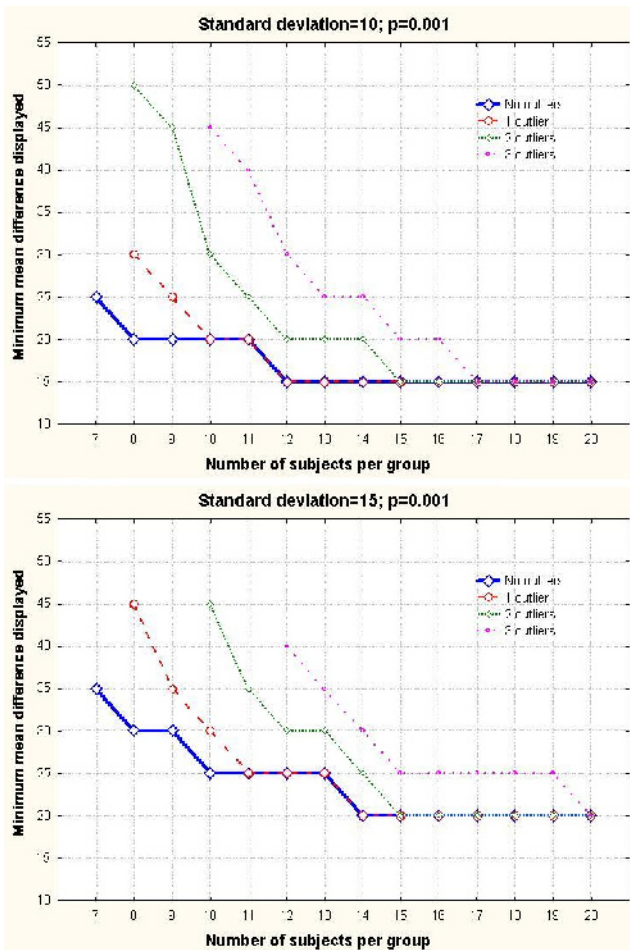


Fig. 3 Minimum statistically significant group mean difference as a function of the samples dimensions, for different numbers of outliers. Top: standard deviation=10. Bottom: standard deviation=15. According to the simulation results, with a standard deviation of 10, groups of 12 subjects are sufficient to account for up to 1 outlier when analyzing the most significant cluster in study “A”, while larger samples would be needed assuming that 2 or more outliers were included. 18 subjects per group are just sufficient for highlighting statistically significant differences in the most significant cluster in study “B”.

#### IV. DISCUSSION

Simulation results in Fig. 3 show that outliers may compromise the results of VBM analyses performed on small samples, thus leading to erroneous clinical inferences. As the number of subjects increases, the effect of outliers is less significant.

Results were compared to those obtained from the experimental data of studies “A” and “B”. The number of subjects for study “A” (12 subjects per group) is sufficient for reliably analyzing the GM concentration differences in the most significant cluster (group mean difference=23.6,

with standard deviation averaged over the cluster  $\leq 10$ , see Table 1), assuming that up to 1 outlier was included in the sample. According to values in Table 1, 18 subjects per group are just sufficient for highlighting statistically significant differences in the most significant cluster in study “B” and a larger sample would be desirable.

#### V. CONCLUSIONS

In this study a model for assessing the effects of including in VBM analyses subjects that do not have the typical anatomic characteristics of their group (outliers) is presented. Sets of digital phantoms were implemented to study these effects for different sample dimensions.

The results yielded by the simulations confirm that sample dimensions are a critical aspect to consider while designing a VBM study.

The present work is aimed at providing the clinician with a support tool for evaluating the conditions under which the clinical results yielded by VBM analyses can be considered acceptable and for driving the recruiting process. This is furthermore important in paediatric trials where this process is frequently particularly time consuming.

Further developments of the model are needed to take into account additional preprocessing and statistical analysis parameters.

#### REFERENCES

1. Good C. D., Johnsrude I. S. et al. (2001) A Voxel-Based Morphometric Study of Ageing in 465 Normal Adult Human Brains. *NeuroImage* 14: 21-36
2. Ashburner J., Friston K. J. (2000) Voxel-Based Morphometry – The Methods. *NeuroImage* 11: 805-821
3. Mechelli A., Price C. J. et al. (2005) Voxel-Based Morphometry of the Human Brain: Methods and Applications. *Current Medical Imaging Vol 1 n.1: 1-9*
4. Salmond C. H., Ashburner J. et al. (2002) Distributional Assumptions in Voxel-Based Morphometry. *NeuroImage* 17: 1027-1030
5. Thacker N.A. (2003) Tutorial: A Critical Analysis of Voxel Based Morphometry. *Imaging Science and Biomedical Engineering, University of Manchester. TiNA Memo No. 11*
6. Jenem M. L., Gunter J. L. et al. (2005) Comparison of Different Methodological Implementations of Voxel-Based Morphometry in Neurodegenerative Disease. *NeuroImage* 26: 600-608
7. Tzourio M., Landeau B. et al (2002) Automated Anatomical Labeling of Activations in SPM using a Macroscopic Anatomical Parcellation of the MNI MRI Single-Subject Brain. *NeuroImage Vol 15, N. 1: 273-289*

Author: Federico Nocchi  
 Institute: “Bambino Gesù” Children’s Hospital  
 Street: Piazza S. Onofrio, 4  
 City: Rome  
 Country: Italy  
 Email: federico.nocchi@opbg.net



# Stroke Monitor as a Device Improving Diagnostic Value of Computed Tomography in Hyperacute Stroke

A. Przelaskowski<sup>1</sup>, J. Walecki<sup>2</sup>, K. Sklinda<sup>3</sup> and G. Ostrek<sup>1</sup>

<sup>1</sup> Institute of Radioelectronics, Warsaw University of Technology, Warsaw, Poland

<sup>2</sup> Department of Radiology, Polish Academy of Sciences Medical Research Center, Warsaw, Poland

<sup>3</sup> Department of Radiology CMKP, CSK MSWiA, Warsaw, Poland

**Abstract** — Stroke Monitor as a computer-assisted support of ischemic stroke diagnosis was presented in this paper. Computer analysis, processing and image understanding was based on nonenhanced CT examinations acquired in hyperacute phase of stroke. The multiscale extraction of the subtlest signs of hypodensity in diagnostically important areas was designed to improve standard diagnosis procedure based on CT scan soft-copy review. Proposed method includes evidence-based description of ischemic conditions and changes, deskulling and segmenting of unusual areas, the analysis of hypodensity signs across scales and subbands with noise reduction and hypodensity extraction. Following visualization forms of empowered hypodensity symptoms localizes suggested ischemic areas in source brain image space. Increased visibility of cerebral ischemia for difficult-in-diagnosis cases was experimentally noticed and improved diagnostic value of CT was concluded.

**Keywords** — hyperacute stroke, CT, multiscale analysis, computer aided diagnosis.

## I. INTRODUCTION

Stroke is the third major reason of death after cardiac and oncologic diseases. Computed tomography (CT) plays a crucial role in the evaluation of stroke patients however it is not sufficient enough in the meaning of extraction of hypodense area corresponding with infarcted cerebral tissues in hyperacute stage. Many infarcts do not emerge on CT until hours after the onset of stroke. On the initial CT-scan, performed during the hyperacute phase of stroke, (0-6h) the hypodensity defined as any area in the brain with density lower than normal surrounding brain tissues does not have to be seen. Early indirect findings, like obscuration of gray/white matter differentiation and effacement of sulci, or "insular ribbon sign", may be noticed instead. Afterwards, it becomes possible to detect a slight hypodense area of infarction either in the cortices or the basal ganglia. The recent advent of thrombolytic therapy for hyperacute stroke treatment makes the earliest detection of areas of hypoattenuating ischemic parenchyma exceedingly important [1-4].

During the initial 3 h of ischemia, the intracellular increase in water and sodium contents is almost exclusively confined to the gray matter. Between 4 and 6 hours after

onset of ischemia the neurons begin to shrink, the synaptic gaps enlarge with expansion of astrocytic end feet, which lasts up to 24 h after ischemia. Infarcted region is characterized by loss of the borders between white and gray matter and focal swelling with effacement of the gyri. This swelling, due to intracellular cytotoxic edema, provokes decrease of tissues density in CT, which reaches maximal values between 24 and 48 h after infarction.

Furthermore, the attenuation coefficients of brain parenchyma vary, mainly due to the differing thickness of the cranial vault. Dense bone lowers the energy of the beam and thus, increases attenuation. M. Bendszus et al. [5] found inter-individual differences, i.e. bone artifacts, of up to 14 HU in brain parenchyma at comparable scan levels. The sufficient accuracy, stability and linearity of CT number and degradation of contrast resolution caused by noise, are the next problem. The CT number for water should ideally be zero, but the actual value changes because of variations in the stability of the detector system or x-ray source. Normally, these variations (i.e. standard deviation of the water value) are very small and most scanners should be able to stay within 2 HU of zero for water. The mean CT number measured over the central test ROI (region of interests) should be in the range of 4 HU, which is close to the possible changes within acute ischemic region.

Nevertheless, it is evident that the early changes with ischemia occur, but may vary within the limited range of HU scale depending on cerebral infarct case, discrepant patient characteristics, bone artifacts, non-optimum scanning and acquisition conditioning. The hypodense changes are slight, and ischemic area is not well outlined or contrasted (with low gradient, ill defined margins). Because of the limited human image perception, these subtle, noisy and relatively formed first ischemic signs can often be out of detection range. Typical preview window of width 80 HU gives maximum noticeable change of 1-2 grey shade within the first 4 h of ischemia.

The purpose of proposed computer assistance was to improve diagnostic value of emergency CT scans through increased visibility of hypodensity changes in hyperacute ischemic stroke cases. Suggested processing method was based on multiscale image data processing, denoising, le-

sion pattern identification and description, and final extraction optimized by visualization procedure.

## II. STROKE MONITOR

An intelligent data visualization method that extracts, strengthens, detects and communicates hypodensity as signature of ischemia to the observers was proposed. Stroke Monitor complements conventional CT scan view with highly specific to infarct cases display. Multiscale transformations were used to analyze image content basing on spatially distributed soft tissue properties over different scales and subbands. Hypodensity may be effectively identified through hierarchical local data processing, analysis, signal energy compaction and information ordering. Post-processing in space-scale domain is less susceptible to local perturbations, artifacts, and beneficial noise suppression and selective contrast enhancement is possible.

Initial two-stage segmentation of the regions susceptible to ischemic density changes was applied to eliminate false indications in diagnostically unusual areas. False positives have to be avoided, since treating ineligible patients with intravenous thrombolysis is associated with an unacceptable risk of hemorrhage and death. Low density (clearly not ischemic) areas were not intended to be empowered or extended by processing procedure masking or simulating ischemic hypodensity. Thus, brain tissue areas with low density were fulfilled with higher density tissue (certainly not ischemic) properties and processed for final visualization. The essential procedure of hypodensity extraction was based on multiscale data processing. Image wavelet decomposition with separated horizontal-vertical kernels, curvelets with 2D kernels (much better describing curvature of margins) [6] and mixed curvelet-wavelet transformations with adaptive thresholding of the coefficients distributed across scales and subbands were used.

Consequently, procedure of stroke-oriented computer assistance was based on brain tissue extraction in 3D multislice space, segmentation of diagnostic ROI as white and gray matter except sulci, prior ischemic scars etc., extension of the brain tissues for marginal and missing space after deskulling and segmenting of unusual areas, combined multiscale transformation with denoising and semantically defined features extraction in scale-space domain, visualization of processed CT scans in different, complementary forms – see Fig. 1.

### A. Basic algorithm

The successive steps are as follows:

#### 1. Segmentation of diagnostic ROIs

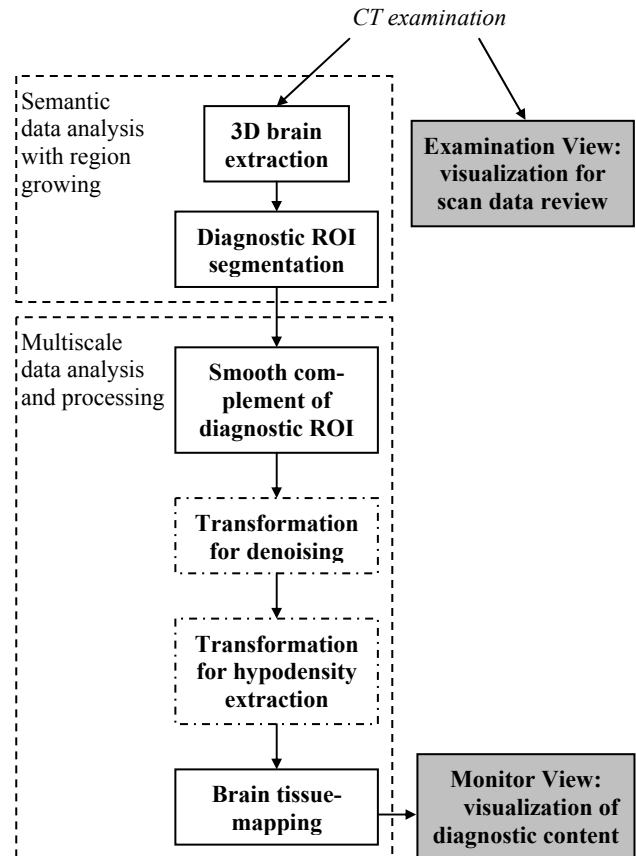


Fig. 1 Stroke Monitor algorithm – general view.

- a) the brain extraction to remove non-brain tissue from a CT volume (to deskull the brain in the image) through region growing, arranged in 3D space of successive slices, where the initial set of seeds were grown-up across successive slices to regular region of the brain tissue identified in CT acquisition expanse;
  - b) selection of the only tissue regions which are susceptible to ischemia called diagnostic ROIs; clear brain sulci, prior ischemic scars and other structures useless in acute stroke detection were discarded; designed method of mixed growing-thresholding was applied with weighted average filtering for noise reduction, detection of low density seeds based on adaptive thresholding, growing low density regions with adaptive membership function, adjusting of indicated areas to make them regular, smooth and big enough sized;
2. Hypodensity extraction
    - a) smooth complement of diagnostic ROIs with mean values of neighbor areas providing the continuity of density function and absence of any lower density fields;

- b) multiscale transformations according to different procedures:
- only curvelets (according to FDCT implementation [7]) with adaptive soft thresholding of curvelet coefficient modulus for subtle denoising and increasing the local mean data variability for perception improvement – PP monitor form,
  - curvelets followed by non-perfect orthogonal wavelets tspline2 (kernel defined by low pass analysis filter  $\tilde{h}=[1/4,2/4,1/4]$ ) for soft detector indications – DD monitor form,
  - two wavelets kernels: tspline2 followed by atrial (kernel defined by low pass analysis filter  $\tilde{h}=[0.01995, 0.04271, 0.05224, 0.29271, 0.56458, 0.29271, 0.05224, 0.04271, 0.01995]$ ) for definite perception improvement – SE monitor form;
  - wavelets tspline2 followed by curvelets for clear detector indications – DE monitor form;
- c) brain tissue mapping to source CT scans space and merging with background view of the scans; the brain areas processed in multiscale domain are reconstructed, adaptively converted to suitable presentation scales and respectively fitted to the source image with skull, scalp and surrounding tissue in the best view window;
3. Visualization of diagnostic image content
- a) display arrangement with contrast enhancement by adaptive histogram equalization of processed data in brain tissue area;
  - b) alternative and complementary view of image data processed according to 4 multiscale procedures; additionally, 3D view of segmented regions or structures may be used to assess brain morphology.

### III. EXPERIMENTS

Retrospective evaluation of 52 sets of examinations conducted in patients admitted with symptoms suggestive of stroke was undertaken by four radiologists unaware of the final clinical findings. All of the selected cases were considered as having no direct signs of hyperacute ischemia in the localization corresponding with clinical manifestation and follow-up studies (reported more exhaustively in [8]). At the first stage only the CTs performed at the admission were evaluated, after a month the same scans were evaluated again with additional use of wavelet-based Stroke Monitor (SE monitor form). Subtle tissue attenuation changes were investigated, denoised, extracted and visualized. Follow-up CT exam and/or clinical picture confirmed or excluded the

diagnosis. Sensitivity of 0.641 and specificity of 0.688 was gained for the wavelet-based stroke monitor aided diagnosis. However, for certain cases SE monitor occurred completely ineffective causing reduction of sensitivity from 0.58 to 0.5 and specificity – from 0.75 to 0.33.

Basing on the above results and concluded efficiency limitations additional post-processing based on complementary forms of visualization with curvelets and improved segmentation of stroke susceptible regions has been designed and performed later on for selected examinations regarded as difficult. A test set consisted of 6 CT exams of brain selected as extremely difficult in diagnosis basing on false decision of specialists and unusual role of Stroke Monitor in the experiments. For 3 clinically confirmed cases of acute stroke appearance the time between the onset of symptoms and the early CT examination was ranged from 1 to 5 hours. 3 other were clinically confirmed normal cases.

Preliminary subjective tests were performed to verify the efficiency of extended Stroke Monitor implementation. The valid presence and indicated position of asymmetric hypodense signs compared to the reference diagnosis (the location and size of the infarct) based on follow-up CT and MR scans were the performance criteria.

First of all, the clearness of Stroke Monitor indications for extremely difficult cases was tested. According to simple test rules monitor usefulness was verified even by non-specialists, biomedical engineers or medicine students with the aim of preliminary assessment of Stroke Monitor with different forms of visualization. 9 observers participated in the experiments (one radiologist, 4 medical students and 4 biomedical engineers or students).

The observer conviction of hypodensity extraction and any false suggestions dominantly affected responses in ischemic stroke detection procedure. Further enhancement of hypodensity based on improved Stroke Monitor in diagnostically difficult cases increased sensitivity and specificity of the diagnosis in comparison to basic SE form. Sensitivity for 6 difficult cases increased from 0.5 to 0.89, specificity – from 0.33 to 0.7 and predictive value positive – from 0.38 to 0.74. An example of different visualization forms were presented in Fig. 2.

According to observers opinions, extended to 4 forms Stroke Monitor improved the diagnosis for difficult cases because of distinct visibility of hypodense signs or generally ischemic susceptibility for test examinations. Improved perception of subtle tissue density distribution made image content assessment and interpretation more accurate. Soft and hard indications of detection forms increased significantly stroke detection efficiency.

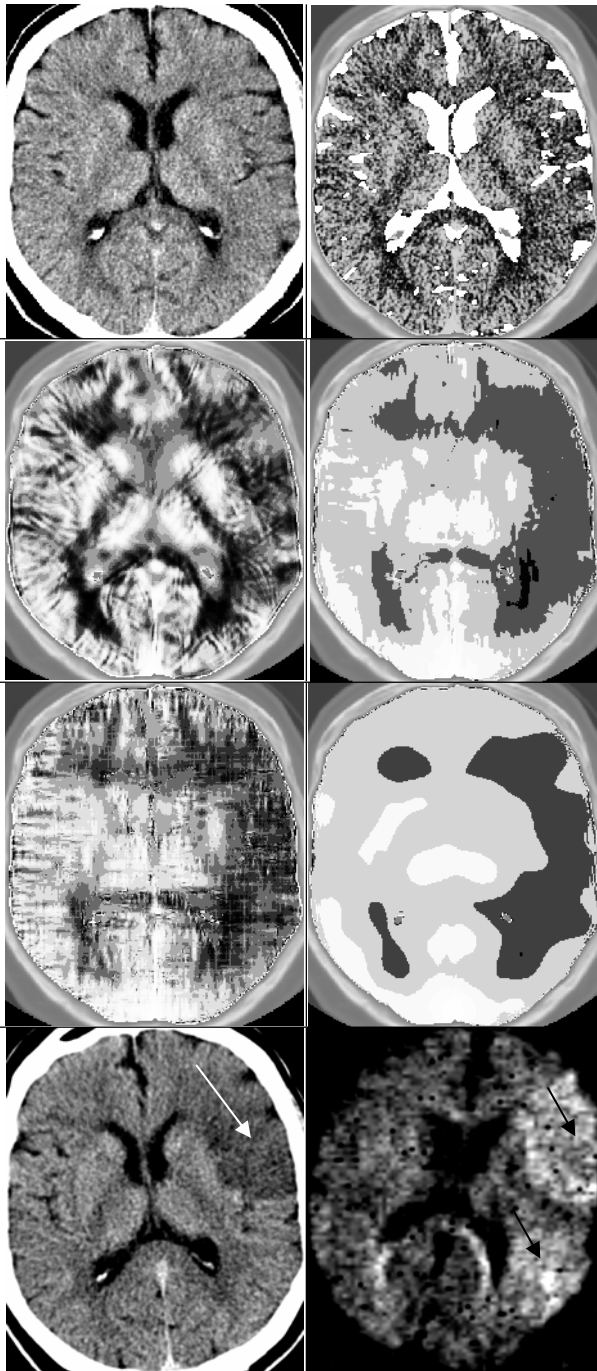


Fig. 2 The effects of computer assistance for stroke diagnosis improvement (top to bottom, left to right): view of CT scan, enhanced visibility of diagnostic ROI with segmented unusual areas (white), three visualization forms of Stroke Monitor – PP, DD, SE, DE, follow up CT and DWI with indicated visible ischemic changes.

#### IV. CONCLUSIONS

Combining the effects of standard CT scans review with Stroke Monitor assistance provided a better diagnosis of stroke. Presented consideration and test results indicated that hypodensity-oriented perception improvement with well-defined detection of ischemic areas may facilitate the interpretation of CT scans in hyperacute infarction.

Optimized multiscale extraction of ischemic changes with effective ROIS segmentation and different, complimentary forms of content visualization extends capabilities of computer assistance tools in a way that was useful for inexperienced observers, especially for difficult cases of ischemia.

In consequences, the reliable computer aided diagnosis with expressive display of distinct ischemic signs can considerably improve ischemic stroke diagnosis by increased objectivity, content perception improvement, clear observer conviction resulting in higher decision sensitivity and specificity. Increased usefulness of hyperacute CT examinations because of improved diagnostic value of visualized image content was concluded.

Further optimization of computer-based understanding of stroke presence in CT scans is required. Planned prospective studies will let evaluate the impact on further treatment of hyperacute stroke patients.

#### REFERENCES

1. von Kummer R (2005) The impact of CT on acute stroke treatment. In: P. Lyden (eds) *Thrombolytic Therapy for Stroke*. Humana Press, Totowa, New Jersey, USA
2. Tomura N, Uemura K et al (1988) Early CT finding in cerebral infarction. *Radiology* 168:463–467
3. Bozzao L, Bastianello S et al (1989) Correlation of angiographic and sequential CT findings in patients with evolving cerebral infarction. *AJNR Am J Neuroradiol* 10:1215--1222
4. von Kummer R, Allen KL et al. (1997) Acute stroke: usefulness of early CT findings before thrombolytic therapy. *Radiology* 205:327–333
5. Bendszus M, Urbach H, Meyer B, Schultheiss R, Solymosi L (1997) Improved CT diagnosis of acute middle cerebral artery territory infarcts with density-difference analysis. *Neuroradiology* 39(2):127–131
6. Candes EJ, Donoho D (1999) Curvelets – a surprisingly effective nonadaptive representation for objects with edges. In: L.L. Schumaker et al. (eds) *Curves and Surfaces*, Vanderbilt University Press, Nashville, TN
7. Candes EJ, Demanet L, Donoho D, Ying L (2005) Fast discrete curvelet transforms. *Multiscale Model Simul* 5:861–899
8. Przelaskowski A, Sklina K, Bargiel P, Walecki J, Biesiadko-Matuszewska M, Kazubek M (2007) Improved early stroke detection: wavelet-based perception enhancement of computerized tomography exams. *Comp Biol Med* 37:524–33

Author: Artur Przelaskowski

Institute: Institute of Radioelectronics, Warsaw University of Technology

Street: Nowowiejska 15/19

City: Warszawa

Country: Poland

Email: arturp@ire.pw.edu.pl

# Morphological and Brainstem Physiology Assessment of Patients with Congenital Craniocervical Anomalies

C.M. Rimkus<sup>1,2</sup>, A.V. Faria<sup>2</sup>, V.A. Zanardi<sup>2</sup>, V.M.F. Lima<sup>3</sup>, A. Cliquet Jr.<sup>1,4</sup>

<sup>1</sup> State University of Campinas, Department of Orthopaedics, Campinas-SP, Brazil

<sup>2</sup> State University of Campinas, Department of Radiology, Campinas-SP, Brazil

<sup>3</sup> General Gerency of Public Health Laboratory – ANVISA, São Paulo-SP, Brazil

<sup>4</sup> University of São Paulo, Department of Electrical Engineering, São Carlos-SP, Brazil

**Abstract** — The craniocervical junction (CCJ) comprehends the brainstem, proximal cervical spinal cord and cerebellar structures and is subjected to several congenital anomalies and anatomic variations. Although the morphological abnormalities are present at birth, many patients develop symptoms after third and fourth decades.

Magnetic Resonance Imaging (MRI) analyses were performed for 61 patients with these malformations towards discriminating the degree of compression, elevated signal in fluid sensitive sequences and presence of syringomyelia. The severity of skeletal disturbances correlated with the degree of neural tissue damage, with shorter base skull (represented by basilar hypoplasia) and greater basilar invagination (elevation of odontoid tip) correlating with compression and signals of tissue injury. The small posterior fossa correlated to a higher frequency of tonsillar invagination, and with higher incidence of syringomyelia.

Eight patients had brainstem auditory evoked potentials (BAEP) tests. 2 patients did not presented compression of neuro-axis; 2 showed compression and magnetic signal alteration, and 4 presented syringomyelia. One patient with compression and hyperintense signal in fluid sensitive sequences presented the greater delay in intervals I-III and I-V of auditory pathway. All patients with syringomyelia presented longer I-V interval, even after decompressive surgery. All patients with significant compromise to neural tissue showed asynchronous waves on binaural acquisition, with phase shift of wave V.

MRI is an important tool to assess the morphological abnormalities of craniocervical junction. The discrepancy between the duration of compressive injury and appearance of symptoms do not allow understand whether functional impairment is secondary to compressive state or to unknown neural tissue incipient malformations. BAEP analyses of these patients are not routinely done, and these previous data demonstrated that the image and functional correlation can lead to unrevealing features of morphophysiology of the craniocervical junction malformations.

**Keywords** — congenital malformation, magnetic resonance, evoked potential, spinal cord, brainstem.

## I. INTRODUCTION

A large spectrum of congenital anomalies and anatomic variations can affect the craniocervical junction, disturbing the interaction between bones of base skull and the first cervical vertebrae and thus can damage the central nervous system (CNS) structures such as brainstem, proximal spinal cord and cerebellar structures, as well as it can compromise the posterior encephalic vascularization [1].

The first postmortem studies, done by Chiari, in 1891, described a group of malformations that bears his name consisted by tonsillar ectopia with varying degrees of cerebellar caudal displacement through foramen magnum and narrowing of medullar tissue, followed or not by other CNS anomalies [2].

Symptoms are related to direct compression to neuro-axis, or indirectly by compression of vascular structures or by secondary syringomyelia. Frequently, patients show a pleomorphic and insidious presentation that vary as chronic headache, sensory and motor neural impairment with or without pyramidal liberation, gait disturbances, cerebellar ataxy, cranial nerve compromise (disphagia, trigeminal pain, auditory disturbances, etc) syncopes and vascular syndromes [1]. Many patients remain asymptomatic or with mild and unespecific symptomatology till adult age and this features can be associated to underdiagnosed cases with consequent higher level of unsuccessful treatment.

The progresses in medical imaging provided non invasive assessment to CNS and its skeleton. Computed tomography (CT) enables bone structures detailed analyses, but it do not define precisely the subarachnoid space, the intracranial and paraspinal soft tissues, which is better achieved with MRI [3]. Because of its multiplanar capabilities and advanced contrast differentiation MRI permits anatomic evaluation and correlation with signals of neural tissue injury, such as edema, gliose and demyelination as areas of increased signal intensity in fluid sensitive sequences [4], being the best way to detect syringomyelia.

Medical imaging gives a static picture of the patients, and as symptoms change with age, physiological condition may evolve. Important and well recognized cranial nerve nucleus

(V, VI, VII and VIII) lie in midbrain and pons, making this a critical area for these neural pathways [5]. Particularly, the VIII nerve function is easily assessed by electrophysiological tests. Evoked auditory electrical potentials get through peripheral nerve and cochlear nucleus to brainstem, excites the superior olivary nucleus and reaches the superior pons and inferior culliculi. Clinical and experimental studies have recorded five waves of electrical auditory potentials in brainstem, I and II reflecting the peripheral activity of VIII nerve, and III, IV and V waves representing the central brainstem conduction [6].

In this study, 61 MRI of patients with congenital CCJ anomalies were retrospectively analysed, aiming at describing the morphological particularities of these conditions. A percentage of these cases had brainstem auditory evoked potentials (BAEP) recorded, and a brief discussion of the patients physiological condition was also done.

## II. METHOD

### A. MRI data acquisition

Three radiologists retrospectively analyzed 61 patients (28 male; 35 female) aged between 11 and 81 years old, selected by presenting at least one of the following variations: clivus-canal angle below  $150^\circ$ , measured by the cross-section of Wackenheim line and the medullary canal, behind axis; basilar invagination, defined as violation of Chamberlain line for more than 7mm by the odontoid tip; tonsillar invagination, when cerebellar tonsils are displaced more than 5mm underneath the foramen magnum; presence of basioocciput hypoplasia (BOH), defined with clivus length less than 4.0cm, or presence of atlanto-occipital assimilation, observed as fusion of the atlas to occipital bone (Figure 1).

The image techniques varied slightly, but always included 2T MR sequences T1 spin echo for anatomic evaluation (time of echo (TE): 12 to 16ms); time of repetition (TR) 520 to 650ms and T2 fast spin echo was the chosen fluid sensitive sequence (TE: 126 to 128ms; TR: 3900 to 7300ms) multiplanar views. The slice thickness was within 3 to 6mm and reconstruction matrix varied from 256x256 to 320x252.

Patients were divided into: group 1(G1)- absence of neuro-axis compression; group 2(G2)- neuro-axis compression without signal alteration in T2; group 3(G3)- neuro-axis compression and increased signal in T2; group 4(G4)- syringomyelia.

### B. Brainstem auditory evoked potential (BAEP)

Eight patients, who are still under clinical treatment, and five controls had BAEP recorded. Bilateral data acquisition

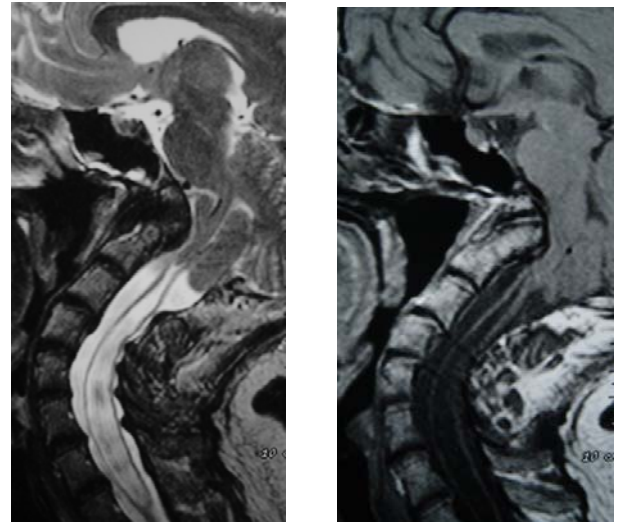


Fig. 1 Sagittal MRI at CCJ of patient with BOH with short clivus (arrow), tonsillar invagination (star) and secondary syringomyelia (expansion of medullary central canal filled with cerebral spinal fluid showing high signal in T2 (left) and low signal in T1(right).

Wackenheim line (dotted) and cervical canal (interrupted line) cross-section demonstrated reduced clivus-canal angle and odontoid violation of Chamberlain line (white line) demonstrating basilar invagination.

was performed for each patient and control. One patient had the right ear measurement excluded because of conductive auditory deficit secondary to a tympanoplasty as a sequelae of infectious otitis in infancy.

Surface active electrodes were placed bilaterally in the auricular lobe (A1: right; A2: left) referred to Cz (International system 10-20). Ground electrode was placed at Fz. Click stimuli were presented monoaurally at 60 to 65dB above the individual acoustic limiar with masking noise to contralateral ear 40 to 50dB below the stimulation intensity, and binaurally recorded simultaneously. At least two sequences of 1000 clicks at 10Hz rate were performed for each side. Additional 5Hz rate sequences were presented to patients aiming at a better evaluation of asynchronous waves observed during data acquisition. Low (10Hz) and high (3kHz) frequencies filters were applied.

Latencies (ms) of waves I, III and V were measured towards calculating intervals I-III, I-V and III-V.

The study was approved by the local ethics committee (CEP-UNICAMP, #073/2007).

Statistic analysis was done by *XLSTAT 2007.8.01*, for Windows. *T*-tests were applied and *p* value below 0.05 was considered significant.

III. RESULTS

A. Morphological description

Table 1 shows the mean of each morphological parameter for groups 1 to 4, and the percentage of tonsillar invagination. There is a progressive reduction of clivus-canal angle and clivus length, combined with higher degrees of odontoid violation of Chamberlein line paralleled to the severity of neural tissue damage.

Groups 2 to 4 are characterized by crescent compromise of neural tissue. They are similar by presenting significant violation of Chamberlein line, compared to group 1 ( $p < 0.05$ ). Although chronic compression can lead to neural tissue suffering, the signals of actual injury are present only in groups 3 and 4. Those subjects present significant shorter posterior fossa (represented by clivus length) when compared to groups 1 and 2 ( $p < 0.05$ ). Group 2 showed no significant difference of this parameter compared to group 1 ( $p > 0.05$ ).

The relationship between short posterior fossa and elevation of cervical spine was evident with the greatest degrees of basilar invagination in patients with BOH ( $p < 0.05$ ). The groups with increased signals of CNS injury also showed this relationship (Figure 2).

Table 1: Morphometric abnormalities for groups 1 to 4

Morphometric abnormality	G 1	G 2	G 3	G 4
Clivus-canal angle	145°	131.2°	115.1°	121.6°
Clivus length	3.51cm	3.14 cm	2.73 cm	2.27 cm
Basilar invagination	7 mm	12.3 mm	12.0 mm	13.3 mm
Tonsillar invagination	20.7%	63.6%	40%	81.8%

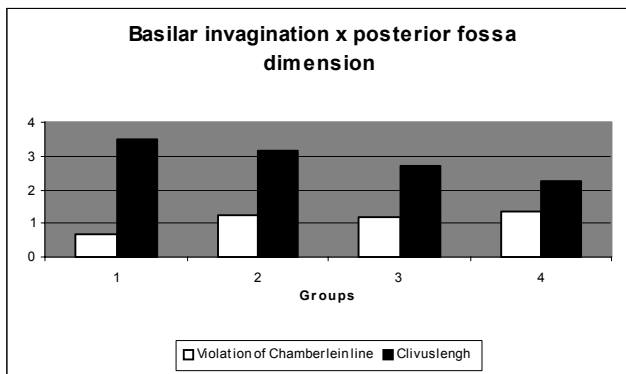


Fig. 2 Graphic demonstranting the relationship between the clivus reduction and odontoid violation of Chamberlein line.

Groups 3 and 4 show the most severe compromise of CNS, but they are not the same qualitatively. The most significant difference is that group 3 presented significant decrease of clivus-canal angle compared to groups 1 and 2 ( $p < 0.05$ ) and it was significant below group 4. Although the mean of the angles in group 4 was inferior than group 1, it was not statistically different compared with group 2 ( $p > 0.05$ ). Other discrepancy between group 3 and 4 was the incidence of tonsillar invagination, which is more frequent in group 4 (81.8%) than in group 3 (40%). These findings allow to hypothesize that elevated signal in neural tissue is more frequently correlated to anterior compression, while syringomyelia can be linked to posterior obstruction and possible compromise of the normal cerebral spinal fluid flow trough foramen magnum.

B. Electrophysiological analysis

Patients 1 and 2 are classified in group 1 and did not have surgical treatment indication. Patient 3 belong to group 3, but did not undergo to surgical procedure and persists with compression to neuro axis. Patient 4 is similar to patient 3 but was surgical decompressed before the BAEP analysis. Patients 5 to 8 presented syringomyelia and also had preview surgical decompression of CCJ.

The control latencies intervals I-III, I-V and III-V means were respectively 2.20ms (SD: 0.08), 4.26ms (SD: 0.20) and 1.92ms (SD: 0.11), and is similar to previous literature data [6,7]. Patients with no considerable compression to neuro-axis showed no significant differences in intervals I-III and I-V compared to control ( $p > 0.05$ ). The only difference for these patients appeared in interval III-V, increased in patient 1 ( $p < 0.05$ ).

The most considerable delay in interval I-III appeared in patient 3 ( $p < 0.05$ ) who presented persistent compression to neuro-axis. This subject also demonstrated prolonged intervals I-V and III-V ( $p < 0.05$ ). The same intervals measurements was normal in patient 4 ( $p > 0.05$ ), after surgical procedure.

Although patients 5 to 8 show no longer compression to neuro-axis after surgical procedure, the latencies and intervals did not achieve normal values. The interval I-V is significantly increased for patient 5, 6 and 8 ( $p < 0.05$ ) and interval III-V is increased for patients 6 and 8 ( $p < 0.05$ ).

Normally, when simultaneous records are made binaurally after monaurally stimulation, auditory evoked waves are almost synchronic in brainstem. In controls, the contralateral shift between waves V is about 0.21ms (SD: 0.09) (Figure 3). Patients 3 to 8 presented assynchronic waves, with significant longer shift between waves V ( $p < 0.05$ ) with 10Hz rate stimuli (Figure 4).

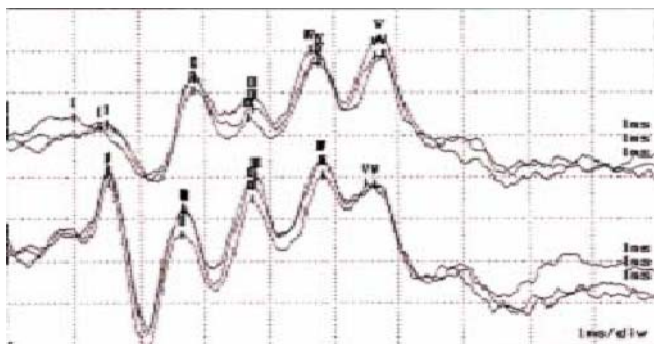


Fig. 3 Control BAEP. Inferior waves correspond to stimulated ear. No significant shift appear between superior contralateral acquisition.

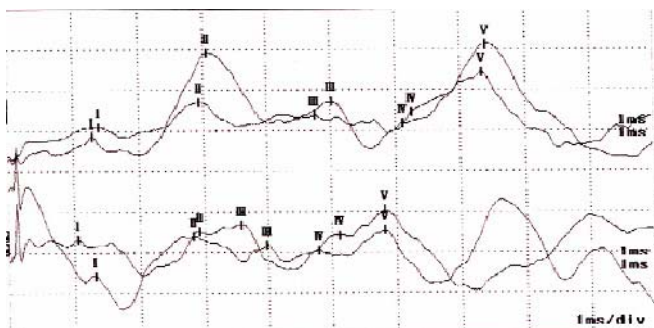


Fig. 4. Patient 8 BAEP. Right ear stimuli (inferior waves) show less defined and lower amplitude picks. Contralateral simultaneous acquisition (superior waves) demonstrate phase shift delay, especially for waves III to V.

#### IV. DISCUSSION

The atlanto-axial and atlanto-occipital joints have higher levels of mobility compared to the rest of vertebral spine allowing movements around three axes [8]. The stability of this region demands a complex and intact skeletal and ligamentar structure. The congenital bone malformations described in this study disfigure the anatomic relationships leading to chronic instability. It has been described in the literature the progressive aspect of basilar invagination probably secondary to increased “slippage” at the atlas over the axis [9].

Small posterior fossa frequently is related to cerebellar tonsils downshift with congenital narrowing of the liquoric space at the CCJ[10,11]. The consequent abnormal cerebral spinal fluid pressures and flux through the foramen magnum can be associated to fluid into spinal cord tissue and secondary syringomyelia.

The actual approach to CCJ congenital anomalies is based on medical imaging, especially MRI, providing detailed morphological visualization which correlates with signals of tissue damage. But conventional MRI gives a

static picture of the pathology and the progressive aspect of these anomalies demands a clinical and physiological follow up.

Brainstem evoked potentials tests provide an inexpensive and noninvasive approach to these patients and this study has demonstrated a good correlation to the severity of the compressive state and with some irreversible conditions (syringomyelia).

A combined biomedical instrumentation, with an evolutive physiological attention, can add evolutive approach to these conditions and maximize the value of anatomic evaluation with MRI, avoiding underdiagnosed cases and helping to achieve the best treatment strategy.

#### V. REFERENCES

1. Smoker WRK. Craniovertebral junction: Normal anatomy, craniometry and congenital anomalies. *Radiographics* 1994; 255-277.
2. Ball WS, Cronek R. Chiari I malformation: from Dr. Chiari to MR imaging. *Radiology* 1995; 195: 602-604.
3. Poe LB, Coleman LL, Mahmud F. Congenital central nervous system anomalies. *Radiographics* 1989; 9: 801-825.
4. Takahashi M, Yamashita Y, Sakamoto Y, Kojima R. Chronic cervical cord compression: clinical significance of increased signal intensity on MR imaging. *Radiology* 1989; 173: 219-224.
5. Mueler D. Brainstem conundrum: The Chiari I malformation. *Clinical Practice* 2001; 13: 154-159.
6. Blecker ML, Ford PD, Lindgren KN, Scheetz K, Tiburzzi MJ. Association of chronic and current measures of lead exposure with different components of brainstem evoked potentials. *Neurotoxicology* 2003; 24: 625-631.
7. Guilloto LMFF, Quintal VS, Costa MTZ. Brainstem auditory evoked response in normal term neonates. *Arq. Neuropsiquiatr* 2003; 61/4: 906-608.
8. Berlemann U, Läubli R, Moore RJ. Degeneration of the atlanto-axial joints: a histological study of nine cases. *Acta Orthop Scand* 2002; 73 (2): 130-133.
9. Goel A. Progressive basilar invagination after transoral odontoidectomy: treatment by atlanto-axial facet distraction and craniovertebral realignment. *Spine* 2005; 30 (18) 551-555.
10. Chen SC, Simon EM, Haselgrove JC, Bikaniuk LT, Sutton LN, Johnson MP, Shera DM, Zimmerman RA. Fetal posterior fossa volume: assessment with MR imaging. *Radiology* 2006; 283/3: 997-1003.
11. Wu YW, Chan KM, Barkovich AJ, Ferriero DM. Pediatric Chiari I malformations. *Neurology* 1999; 53: 1271.

Author: Carolina M Rimkus

Institute: State University of Campinas, Depto of Orthopaedics/ University Hospital

Street: (FCM-UNICAMP)

City: Campinas/ SP

Country: Brazil

Email: carolina.mr@uol.com.br



# Quality of the Computed Radiography Image Acquired with Decreased Doses

L. Bumbure<sup>1,2</sup>, Y. Dehtyar<sup>1</sup>, R. Falkan<sup>2</sup>, U. Jasper<sup>2</sup>

<sup>1</sup> Riga Technical University/BENI, Riga, Latvia

<sup>2</sup> Paul Stradins Clinical University Hospital/MTD, Riga, Latvia

**Abstract** — Decrease of radiation dose to patients and its management is important for modern radiographic imaging procedures. Computed radiography (CR) provides broader dynamic range and high potential for post-processing, lower radiation dose while maintaining usual image quality could be promoted. There is sufficiency of experiments, which finds clinical possibilities of patient dose reduced from usage of CR systems. However the experiments correlating radiation dose and x-ray image quality have not been found. Therefore the current research is directed to find ways to reduce patient dose keeping up the quality of x-ray image using CR system. The quality of image was evaluated as the contrast and lateral resolution. The Plexiglas phantom and test plate “ETR-1” were in use as the radiated objects. The x-ray machine “Bucky Diagnost” was employed to supply radiation flow. The digital images were provided both the Automatic Exposure Control (AEC) and manual modes. The voltage range from 40 to 90 kV was in use. The radiation dose was varied because of the mA·s control. The dose was estimated because of detected Air Kerma ( $\text{microGy}\cdot\text{m}^2$ ) by the DAP meter. The results demonstrated that the dose could be decreased on for 40-75% keeping the quality of image.

**Keywords** — Computed radiography (CR), CR systems, patient dose reducing.

## I. INTRODUCTION

Decrease of radiation dose to patients and its management is important for modern radiographic imaging procedures. Computed radiography (CR) provides broader dynamic range and high potential for post-processing, lower radiation dose while maintaining usual image quality could be promoted.

CR technology has been around since the early 1980s and has been widely accepted as a digital image acquisition process that produces images equivalent to conventional x-ray film-screen systems. CR is a process for capturing digital radiographic images. The phosphor plate captures and “stores” the x-rays. The image is “developed” in a CR reader instead of a film processor. The CR reader extracts the information stored in the plate and produces a digital image.

In our radiology departments, digital imaging is already in use. Since conventional film-based imaging is currently

being replaced by phosphor plate technology, a comparison between both technologies is made.

There is sufficiency of experiments, which finds clinical possibilities of patient dose reduced from usage of CR systems. However the experiments correlating radiation dose and x-ray image quality have not been found. Therefore the current research is directed to find ways to reduce patient’s dose keeping up the quality of x-ray image using CR system.

## II. MATERIALS AND METHODS

This examination was very important, because in our country are valid the National regulations, which describes necessity of patient’s dose decreasing in radiography (1).

The examination was performed in Diagnostic Radiology department of Paul Stradins clinical hospital.

*The x-ray machine:* The x-ray machine “Bucky Diagnost” was employed to supply radiation flow. The digital images were provided both the Automatic Exposure Control (AEC) and manual modes. The voltage range from 40 to 90 kV was in use.

*Radiated objects:* The Plexiglas phantom (40 mm) and test plate “ETR-1” (the set for radiological equipment’s quality checks) were in use as the radiated objects.

*Dose measuring:* The radiation dose was varied because of the mA\*s control.

The dose was estimated because of detected Air kerma ( $\text{microGy}\cdot\text{m}^2$ ) by the DAP meter.

Air kerma method is based on air kerma as conventional quantity that takes into account two-staged process of energy transfer from indirectly ionized particle to medium. Generally, this method, underestimates true value of absorbed dose, however air kerma is widely accepted and many national metrology organizations, including ours, developed air kerma primary standards.

*X-ray detector:* We used medium sensitivity “Kodak” phosphor plate as x-ray detector (the same phosphor plate for each exposure).

*Examination:* In first we needed to check what is the dose dependency of mA\*s. We took the different mA\*s values for exposure and measured dose by DAP meter. The results of measurements are shown in Fig. 1 and in the Table 1.

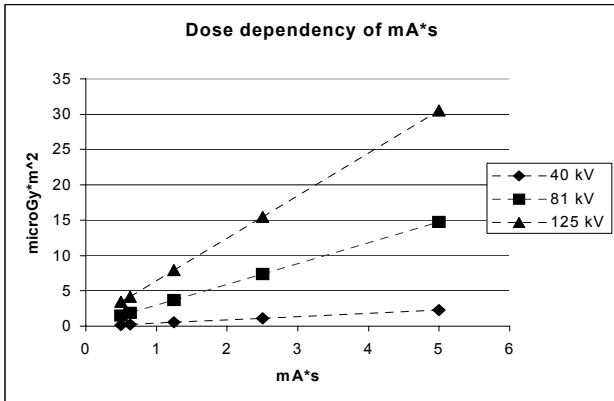


Fig. 1 Dose dependency of mA\*s

Table 1 Dose dependency on mA\*s

kV	mA*s	microGy*m <sup>2</sup>
40	0,5	0,16
40	0,63	0,23
40	1,25	0,52
40	2,5	1,11
40	5	2,29
81	0,5	1,46
81	0,63	1,85
81	1,25	3,69
81	2,5	7,38
81	5	14,72
125	0,5	3,42
125	0,63	4,18
125	1,25	7,95
125	2,5	15,43
125	5	30,55

It was clear that dose dependency of mA\*s was linear. Furthermore than larger was kV, than steeper was a curved line, which shows dose changes.

When the dose dependency of mA\*s was detected, we could start the examination.

The first examination’s part was done by using AEC mode, because in AEC mode the x-ray machine automatically finds optimally mA\*s for exposure to acquire good image quality.

We irradiated Plexiglas phantom with X-ray. The source-image-distance (SID) was the same for all exposures (115 cm). The field of x-ray collimation was 18 x 24 cm (the phantom’s size was the same). The kV range was from 40 to 90. The object placement’s diagram is shown in Fig. 2. All values of dose and mA\*s were documented.

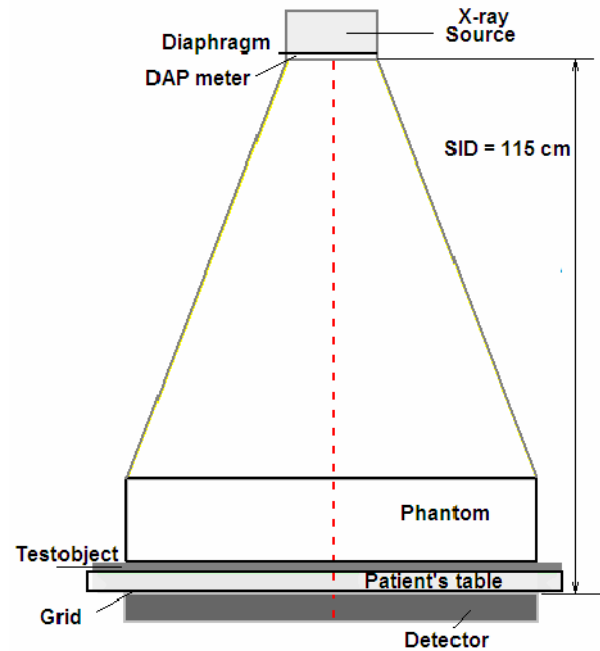


Fig. 2 Placement diagram

The second examination’s part was done by using manual mode with decreased (in comparison with AEC) mA\*s values. The mA\*s values were decreased step by step, that far, until image quality still good.

*Image processing:* We performed image processing, by using “Kodak Direct View CR 500” system. Then images were printed.

*Image quality:* The quality of image was evaluated as the contrast and lateral resolution.

For lateral resolution’s estimation the particular region on the test object’s image was used.

Image contrast (for each image separately) was calculated using optical density values, which were measured by sensitometer/densitometer “Duolight”.

### III. RESULTS

The results of lateral resolution’s comparison and some results of contrast’s comparison (between images, which was acquired in AEC mode and manual mode) are shown in this chapter. The lateral resolution’s comparison is shown in Fig. 3. The contrast’s comparison for different kV is shown in both Fig. 4 and 5. In this chapter in all figure’s legends A= AEC mode, but M = Manual mode.

As it is shown in fig.3, lateral resolution acquired in AEC mode and in manual mode are the same.

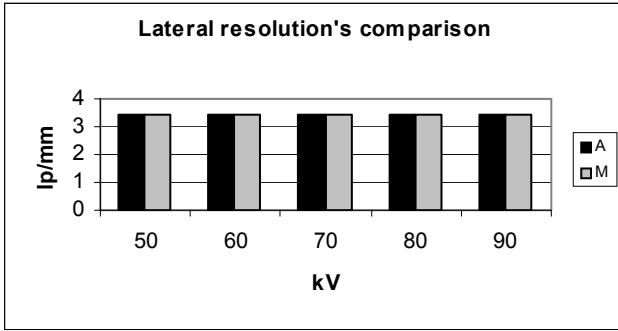


Fig. 3 Lateral resolution's comparison

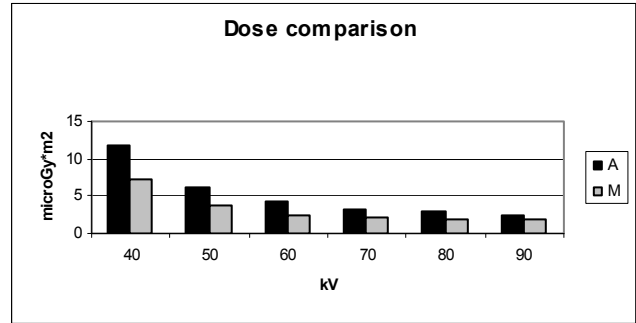


Fig. 6 Dose comparison

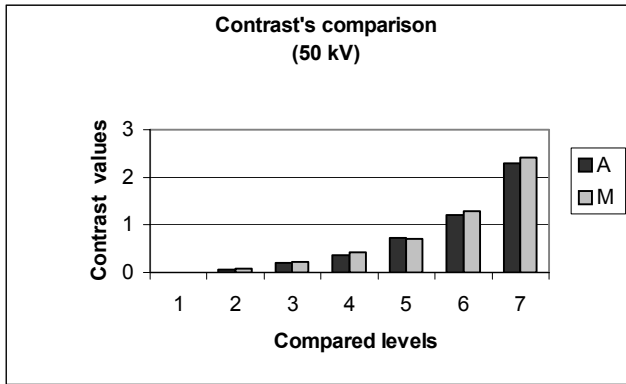


Fig. 4 Contrast's comparison (50 kV)

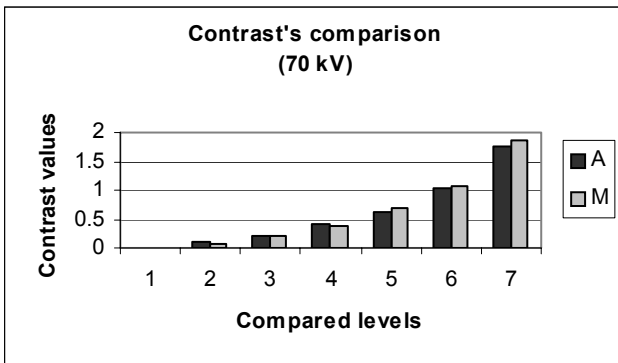


Fig. 5 Contrast's comparison (70 kV)

As it is shown in fig.4-5, contrast in AEC mode is even little worse than in manual mode.

The dose acquired in AEC mode and in manual mode also was compared. The dose comparison's results are shown in Table 2 (column "Relative dose") and in Fig. 6.

The decreased values of mA\*s, which were used in manual mode, are shown in Table 3. Used these values of mA\*s

Table 2 Dose in AEC mode

kV	mA*s	microGy*m <sup>2</sup>	Relative dose
40	23,7	11,8	161,42271
50	6,34	6,09	159,00783
60	2,79	4,2	175
70	1,59	3,33	158,57143
80	0,98	2,83	154,64481
90	0,59	2,46	140,57143

Table 3 Dose in manual mode with decreased mA\*s values

kV	mA*s	microGy*m <sup>2</sup>
40	16	7,31
50	4	3,83
60	1,6	2,4
70	1	2,1
80	0,63	1,83
90	0,5	1,75

in manual mode dose was reduced, but image quality was still good.

#### IV. CONCLUSIONS

As it is shown in Fig. 3 – 6, used manual mode, both contrast and lateral resolution are still good, but dose is reduced for 40 – 75%.

In our examination we found, that using phosphor plate it is possible to reduce patient's dose and keeping up image quality.

We wish to continue researches like this, because we wish to develop the new standards for radiography examinations using phosphor plate, which will allow us to reduce patient's dose more, keeping up image quality.

#### ACKNOWLEDGMENT

Special thanks to professors: Aldis Balodis, Alexey Katashev, Genady Sagalovich and doctor Vineta Zemite, Riga Technical University/BENI.

Author: Lada Bumbure  
Institute: Paul Stradins Clinical University Hospital / MTD,  
Street: Pilsonu stret 13  
City: Riga LV-1002  
Country: Latvia  
Email: havanagila@inbox.lv

#### REFERENCES

1. LR MK noteikumi Nr. 97 no 05.03.2002. „Noteikumi par aizsardzību pret jonizējošo starojumu medicīniskajā apstarošanā”.

# Evaluation of Acceptance Criteria for IMRT Plan Verification Based on Results of Film Dosimetry

K. Chelminski, W. Bulski, P. Kaminski, M. Kania, J. Rostkowska, A. Walewska and M. Zalewska

The Maria Sklodowska-Curie Memorial Cancer Center and Institute of Oncology, Department of Medical Physics, Warsaw, Poland

*Abstract* — The aim of this study was the evaluation of results of IMRT plans verification and derivation of criteria of acceptance for future verifications. The absolute film dosimetry for total planned dose distribution was evaluated. The acceptance criteria were derived for the gamma evaluation concept.

About 200 IMRT plans, mainly for head/neck and pelvic regions, were verified using the phantom. The plans were generated using Varian Eclipse treatment planning system. The verification plans were created using the CT images of the phantom. Kodak EDR2 films were placed in the phantom for the measurements of the dose distributions. Two methods of calculation of the gamma factor were compared: Depuydt and in-house developed (INH). The acceptance criteria were derived for the gamma evaluation concept.

In about 75% of evaluated plans the fraction of points for which gamma index value  $< 1$  was more than 95% for the calculation algorithm of gamma factor proposed by Depuydt. For the INH algorithm in about 60% of cases the fraction of passing points was more than 95%.

The acceptance criteria for IMRT plans verification based on the gamma concept must depend on the quality of equipment and materials used. Also the verification software and the calculation algorithm may influence on the results of verifications.

*Keywords* — gamma evaluation, film dosimetry, IMRT plan verification

## I. INTRODUCTION

Verification of the planned dose distribution became a very important question since the intensity modulated radiotherapy (IMRT) was introduced into clinical use. Highly modulated fluencies of the beams obtained in IMRT produce high gradients of the dose. High dose gradients appear often between critical structures and a target. In such cases not only the dose levels require verification but also spatial dose distributions must be checked.

Small geometrical shifts in the range of 1-3 mm between calculated and measured dose distributions give high differences of dose. Hence the gamma factor composed of spatial and dose components was proposed by Low et al. in 1998 [1] to describe differences between calculated and measured dose distributions. The first implementation of the gamma evaluation for IMRT plan verification was performed by Depuydt et al. 2002 [2].

## II. MATERIALS AND METHODS

### A. Treatment planning

Eclipse (Varian, USA) treatment planning system was used for planning 200 IMRT cases mainly for head/neck and pelvic regions. Field settings and numbers of monitor units of the plans were copied for the phantom CT images and the dose distribution were recalculated. The calculated dose distribution was exported for comparison with the measured one.

### B. Measurements and data processing

The CarPet phantom [3] (ESTRO Quasimodo project) was used for measurements. The anthropomorphic phantom consist of about 20 slabs 1 cm thick between which Kodak EDR2 films were sandwiched. The films in the phantom were irradiated using all fields of the plan for recording the total dose distribution. A calibration film was generated [4] using programmed dynamic multileaf collimator (dMLC) of Clinac 2300 C/D (Varian, USA) linear accelerator. The irradiated films and the calibration film as well as the non irradiated film were processed next day with Protec 45 Compact film processor. The processor is featured with automatic regeneration of developing and fixing solutions. After processing of few square meters of a film, a small amount of fresh developer and fixer is added to replace worn agents. The processor is routinely used for processing of check films. Thus, the temperature of chemical agents and the time of developing and fixing were set to optimal conditions for diagnostics films. The processor was filled with Agfa G138i developer and Agfa G334i fixer. After processing, the films were digitised using Vidar VXR-16 Dosimetry Pro scanner. Digital images were obtained with 16-bit depth greyscale and 72 dpi resolution.

### C. Verification

The digital images were converted into 2D dose maps with IMRTCompare software using the calibration film and the background image. The calibration curve based on the

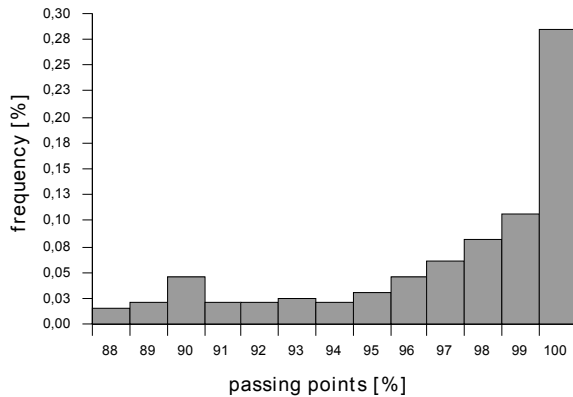


Fig. 1 Histogram of results of verifications for Depuydt implementation of the gamma evaluation. On the horizontal axis fraction of points passing gamma < 1 criterion.

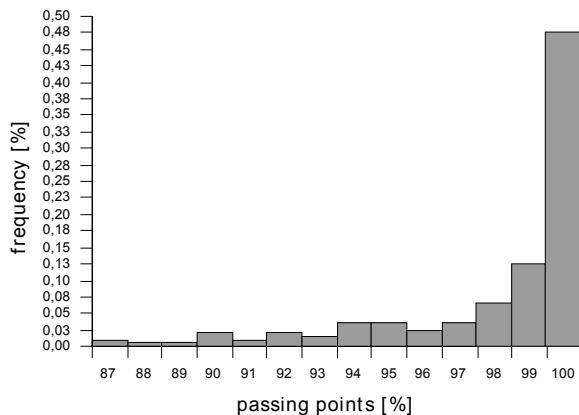


Fig. 2 Histogram of results of verifications for INH implementation of the gamma evaluation. On the horizontal axis fraction of points passing gamma < 1 criterion.

calibration and background films was created using FilmCal (PTW Freiburg) software and imported into IMRTCompare in-house developed verification system together with images of the films and the calculated dose distributions. The images converted into 2D dose maps were matched and compared in the system against the calculated dose distributions. In the software two methods of calculation of the gamma factor were implemented: Depuydt [2] and in-house developed (INH). For the gamma evaluation, 3 mm spatial parameter and 3 % of the planned dose in isocenter was set [1] for both implementations. The acceptance criteria were

derived for the rectangular region embedding the 80 % isodose. The fraction of points from rectangular region passing the gamma < 1 criteria was recorded for each plan.

### III. RESULTS

In 76 % of evaluated plans the fraction of points for which gamma index value < 1 was more than 95 % for the calculation algorithm of gamma factor proposed by Depuydt. For the INH algorithm in about 61 % of cases the fraction of passing points was more than 95 %. For acceptance criteria set as 90 % passing points, 86 % and 74 % plans would be accepted for the Depuydt and INH algorithms respectively.

### IV. CONCLUSIONS

The acceptance criteria for IMRT plans verification based on the gamma concept must depend on the quality of equipment and materials used. Also the verification software and the calculation algorithm used may influence the results of the verification. Thus, the series of verifications must be performed in order to eliminate the sources of systematic measurement or calculation errors by tuning the planning system or the measurement methodology. Then evaluation of the range of stochastic uncertainties must be included in the procedure of evaluation of the acceptance criteria.

### REFERENCES

1. Low D, Harms W, Mutic S, Purdy A (1998) A technique for the quantitative evaluation of dose distributions. *Med. Phys.* 25:656–661
2. Depuydt T, Van Esch A, Huyskens D (2002) A quantitative evaluation of IMRT dose distributions: refinement and clinical assessment of the gamma evaluation. *Radiother. Oncol.* 62:309–319
3. Bohsung J, Gillis S, Arrans R et al. (2005) IMRT treatment planning—A comparative inter-system and inter-centre planning exercise of the ESTRO QUASIMODO group. *Radiother. Oncol.* 76:354–361
4. Chełmiński K, Rostkowska J, Kania M, Bulski W, Gwiazdowska B (2005) Measurement of the sensitometric curves of Kodak EDR2 and X-Omat V films using Enhanced Dynamic Wedges and Dynamic Multileaf Collimators. *Rep Pract Oncol Radiother.* 10:293–300

Author: Wojciech Bulski  
 Institute: Zakład Fizyki Medycznej, Centrum Onkologii - Instytut im. M. Skł.-Curie  
 Street: ul. Roentgena 5  
 City: Warszawa 02-781  
 Country: Poland  
 Email: w.bulski@rth.coi.waw.pl

# Sensitivity of the Brain to Microwave Radiation

H. Hinrikus, M. Bachmann and J. Lass

Department of Biomedical Engineering, Technomedicum of the Tallinn University of Technology, Tallinn, Estonia

**Abstract** — This study is focused on evaluation of sensitivity of the brain to external microwave radiation. Up to this time all requirements and limitations established by national and international regulations and recommendations for safety of electromagnetic fields (EMF) are based on the quantitative data of EMF thermal effect. Analysis of different approaches for estimation of sensitivity of the brain were applied in this study: theoretical sensitivity of living cell to microwave radiation, hypothesis of the quasithermal effect, experimental data of microwave radiation effects on the brain, special experiments to avoid thermal effect, experiments at radiation power density lower and higher than thermal limit. As a result it was shown that statistically significant changes occurred in the EEG rhythms at microwave radiation power densities about 10 dB less than thermal limit. Clear dependence of the results on modulation frequency confirmed that the effect has nonthermal origin. The intensity of the effect is not linearly related to the applied field power density.

**Keywords** — EMF effect, cell model, safety limits, field effect, quasi-thermal effect

## I. INTRODUCTION

Effects of microwave radiation on the human brain have become of major interest with increasing applications of telecommunication devices [1]. Up to this time all regulations and limitations established by national and international authorities for safety of electromagnetic fields (EMF) are based on the quantitative data of the EMF thermal effect. Thermal heating is still the only commonly approved mechanism for microwave radiation effects. Despite many investigations, the difficulties in independent replication of the experimental results cause doubts in non-thermal effects and mechanisms behind the effects are still unclear. However, some experimental results showed effect of the microwave exposure on the brain at the microwave field power densities much less than the thermal limit [2, 3].

This study is focused on evaluation of sensitivity of the brain to external microwave radiation. Theoretical estimations of the sensitivity based on cellular model are taken into consideration. Results of experiments specially planned to reveal non-thermal field effects of modulated microwave radiation on the human electroencephalographic (EEG) rhythms are presented and discussed. Comparison of theoretical sensitivity and experimental results creates a bases

for estimation of real sensitivity of the human brain to microwave radiation.

## II. METHODS

### A. Theoretical estimation of sensitivity at cellular level

Theoretical estimation of sensitivity of the living tissue to external microwave radiation has been based on the simplified model of the cell. [4,5,6]. The model for estimation of the level of electrical noise on the cell membrane taking into account 1) only thermal noise [4] or 2) thermal and shot noise, and including the excess noise caused by conductance fluctuations due to stochastic opening and closing of ionic channels [5,6] was developed.

An electrical model of cell would be proposed as following: a number of current sources (ionic channels) are connected in parallel to the receiving system input (membrane) [5,6]. These sources are switching on and off stochastically and cause noise. The receiving system input has a capacity  $C$  and resistance  $R$  equal to the membrane capacity and resistance. These parameters determine the time constant of the system. The membrane resistance depends on number of open channels and can change million times [7]. The time constant of the cell as a receiving system varies also strongly.

The internal noise of receiver consists of thermal noise at membrane resistance and current noise caused by ionic current of channels. Two components of electrical noise, thermal and shot noise are fundamental and well described by a physical theory. The thermal noise due to random thermal fluctuations in electrical potential or voltage predicted is described by Nyquist formula. The shot noise due to fluctuations of number of current carriers is described by Schottky formula. The spectral density of noise power or fluctuations spectrum (SDPFS)  $S$  is selected as a parameter to be used for comparison of noise of different origin and estimation of threshold sensitivity of the cell. In calculations of noise for living cell we used typical numerical values for cell parameters: membrane resistance  $R = 1 \text{ M}\Omega$ , single channel current  $I = 1 \text{ pA}$  [8]. The SDPFS of current noise due to thermal fluctuations is  $S_T = 1.72 \times 10^{-26} \text{ A}^2/\text{Hz}$ . The SDPFS due to current carrier number fluctuations for single channel is  $S_I = 0.3 \times 10^{-30} \text{ A}^2/\text{Hz}$ . The noise caused by

current fluctuations in single channel was substantially less than the thermal noise. Nevertheless, the current carrier fluctuations take place in all of open channels. The total noise at cell's membrane is caused by all of these fluctuations. Let us assume that the ion's transfer processes in different channels are independent. In this case the SDPFS of the current noise when an average of  $10^4$  channels are conducting is  $S_{I\Sigma} = N \times S_I = 0.3 \times 10^{-26} \text{ A}^2/\text{Hz}$ . This level of current noise at cell's membrane corresponds to the model when all  $N$  channels are simultaneously open and the number of open channels is constant. Total noise power spectral density on the cell's membrane  $S_n = 2 \times 10^{-26} \text{ A}^2/\text{Hz}$ .

The sensitivity of the cell as an electromagnetic radiation receiver is determined by internal noise of the cell and its effective receiving area  $S_R$ . The size (radius) of the cell  $a$  is substantially less than the wavelength of the radiation, therefore the cell can be discussed as an elementary antenna. The effective receiving area of the cell as an antenna is equal to its geometric area. For a typical mammalian cell the radius is about of  $10 \mu\text{m}$  what is small indeed by comparison with microwave wavelength. The calculated value of sensitivity for typical parameters of cells is about of  $10^{-7}$ - $10^{-8} \text{ W/m}^2 \text{ Hz}$ . The minimum field to which a cell can respond is about of  $10^{-6}$  -  $10^{-7} \text{ V/m Hz}^{1/2}$ .

### *B. Theoretical estimation of sensitivity based on the field quasi-thermal effect*

The high frequency microwave field cannot cause any regular changes in the ions movement due to their small absorption cross-section (microwaves wavelength is much larger than cells dimension) as well as inertial properties and viscosity of the liquid medium [9]. However, the high frequency field can cause fluctuations and vibration of the charged particles and membranes. This phenomenon is similar to the effect caused by Brown motion, initiated by temperature, and results in the same effects – the mobility of the ions and fluctuations in membrane motions are increasing – but without rise in temperature [10,11]. The high frequency EM field and temperature have analogous effects on biological structures.

Such a quasi-thermal field interaction, caused by the low-level microwave exposure, does not lead to heating and to an increase in tissues' temperature. Anyway, the fluctuations, initiated by the high frequency EMF in ions movement and membranes, affect the gating variables and nerve cell properties as an increase in temperature does. Even a small difference in temperature (2 K) causes changes in transfer rate coefficients of the gating variables and Hodgkin-Huxley model needs correction of the rate constants with the factor 3.48 [12]. An increase about 1K in tempera-

ture has been reported to cause changes in mental ability and performance [13,14].

The energy levels, sufficient for quasithermal field effect, can be estimated by comparison of the thermal and EMF energies. The thermal energy, related to an increase in temperature  $T=1\text{K}$ , is  $kT = 1,38 \cdot 10^{-23} \text{ J}$ . The electrical equivalent to the thermal energy  $eV=kT= 1,38 \cdot 10^{-23} \text{ J}$  and voltage  $V= kT/e \approx 10^{-5} \text{ V}$ , where  $k$  is the Boltzman constant and  $e$  is the electron charge.

The electromagnetic disturbance of a thermal equilibrium in neurones (cells radius  $r \approx 10 \mu\text{m}$ ), equivalent to an increase in temperature 1 K, can be introduced by the electric field value of  $E= V/r \approx 1 \text{ V/m}$ , and the equivalent field power density  $S=0.0026 \text{ W/m}^2$ .

### *C. Experiment: selection of modulation frequencies*

Distinction of the temperature or the microwave field produced effects can be based on their time-frequency characteristics.

The heating of human tissues depends on: radiation power absorption rate (SAR), heat conduction, heat convection and blood perfusion rate inside the tissues. As shown by model analysis, the thermal response is governed by two time constants: one pertains to heat convection by blood flow, and is of the order of 20-30 min for physiologically normal perfusion rates; the second characterizes heat conduction and varies as the square of a distance that characterizes the spatial extent of the heating. Experimental investigations of the temperature distribution in human brain and other tissues confirm, that the thermal time constant is large, about hundred seconds [15].

The field effect depends on field strength inside the tissue and on its electric polarisation. The relaxation time for the field effects is much shorter, about of 0.001s for the most low-frequency alpha dispersion [16].

Application of the modulated microwave exposure would help to distinguish the thermal or non-thermal origin of the effect. Suitable type of modulation, as 100% amplitude modulation with duty cycle 50%, provides constant average power of radiation and leads to constant heating and temperature rise in the case of different modulation frequencies. If the period of modulating voltage  $T$  is selected much shorter than the thermal time constant, and longer than the relaxation time constant for field effect  $100\text{s} > T > 0.001\text{s}$ , such exposure produces different dependencies on modulation frequency in the cases of thermal and field effects. In this case heating, produced by the average power of radiation, and SAR do not depend on modulation frequency and the effect of thermal origin should be independent of modulation frequency. Any dependence on modulation frequency should be related to the phenomena different from average



heating. The modulation frequencies 7, 14 and 21 Hz were selected.

#### D. Experiment: subjects, exposure and recordings

The experiments were carried out on a group of healthy volunteers, 13 young persons (aged 21-30), 4 male and 9 female.

The applied microwave exposure (450 MHz, 1 W) was modulated at 7 Hz, 14 and 21 Hz. Ten cycles of the exposure (1 min off and 1 min on) at fixed modulation frequencies and sham exposure were applied. The measured field power density near the head was 0.16 mW/cm<sup>2</sup>. The specific absorption rate (SAR) was calculated using SEMCAD software. The calculated spatial peak SAR averaged over 1 g was 0.303 W/kg.

The changes in the electroencephalographic (EEG) signals were selected as a measure for evaluation of the effect of microwave radiation. Cadwell Easy II EEG measurement equipment was used for the EEG recordings. The EEG was recorded using 9 electrodes, which were placed on the subject's head according to the international 10-20-electrode position classification system. The channels for analysis were chosen to cover the entire head: frontal- FP1, FP2; temporal- T3, T4; parietal- P3, P4; occipital- O1, O2; and the reference electrode Cz. The EEG recordings were stored on a computer at 400 Hz sampling frequency.

The method of integration of differences was used for EEG analysis [17]. The relative differences of the average energies for segments with and without microwave exposure were calculated for every cycle. Integration of the differences over ten cycles of exposure was applied and characteristic measure  $S_n$  of for a subject  $n$  was calculated.

### III. RESULTS AND DISCUSSION

The calculated average relative changes in energy of different EEG rhythms with and without microwave radiation in percents – the parameter  $S_n$  averaged over 8 electrodes and 13 subjects – are presented in Fig. 1. The graphs illustrate the effect of the microwave radiation calculated in different EEG rhythms at 7 Hz, 14 Hz and 21 Hz modulation frequencies for the whole group. By comparison of the graphs for exposed and sham recordings one can conclude that microwave radiation modulated at frequencies 14 Hz causes remarkable increase in the EEG alpha and beta1 rhythms' energy. Modulated at 21 Hz microwave radiation enhanced alpha, beta1 and beta2 energy. Microwave exposure at the lowest modulation frequency 7 Hz does not produce any significant changes in the EEG rhythms energy.

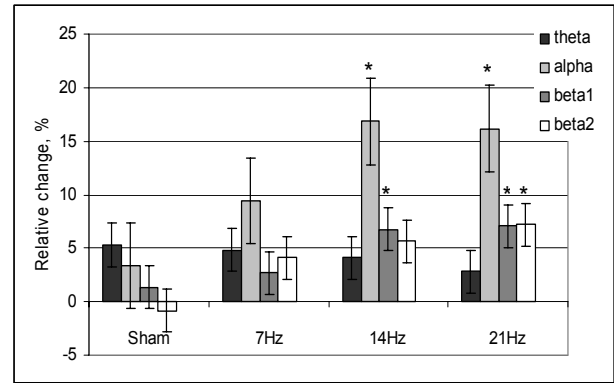


Fig. 1 The relative changes in the EEG rhythms energy of the recording segments with and without microwave radiation at different modulation frequencies for the whole group (n=13), significant marked \*.

The exposure at any modulation frequency does not affect theta rhythms.

Clear dependence of the microwave radiation effect on modulation frequency at permanent heating provided by exposure conditions confirms non-thermal origin of the effect. Calculated SAR value 0.3 W/kg was much lower than the thermal limit 2 W/kg. Significant changes in EEG and cerebral blood flow have been reported also by other researchers at SAR values 0.5-1 W/kg [18, 19]. Applied in this experiment field power density 1.6 W/m<sup>2</sup> was below the safety limits in ICNIRP recommendations and IEEE standards [20, 21].

Results of theoretical calculations of sensitivity to radiofrequency exposure, field power densities and SAR values at which the significant changes in physiological parameters during different experimental studies were reported as well as guidelines of the International Commission on Non-ionizing Radiation Protection and IEEE Standards are presented in Table 1. Alterations in physiological parameters caused by microwave exposure were experimentally detected at field power densities much higher than the calculated theoretical sensitivity. A reason is high natural variability of the parameters, for example EEG, and difficulties in detection of changes related to microwave exposure. Existing regulations are based on experimentally approved thermal effects and resulted in much higher values than the experimental data. It is important to underline that even short-term laboratory experiments do not provide information about long-term (years) effects of the microwave exposure. Therefore precautionary limits for EMF safety should have not higher but lower values than the field power density and SAR levels at which alterations in physiological parameters were approved in laboratory experiments.

Table 1 Values for theoretical sensitivity, experimental results and established regulations for EMF safety levels

Origin	Frequency (MHz)	Electric field (V/m)	Power density (W/m <sup>2</sup> )	SAR W/kg
Cellular model		10 <sup>-2</sup> - 10 <sup>-3</sup>	10 <sup>-4</sup>	
Quasi-thermal effect		1	0.0026	
Nerve cell damage, Salford et al., 2003	900		2.4	0.02
EEG, Hinrikus et al.	450		1.6	0.303
EEG and blood flow, Curcio et al. 2005	900			0.5
EEG and blood flow, Huber et al. 2002	900			1
ICNIRP guidelines 1997	10-400	28	2	
	400-2000	1,375 f <sup>0.5</sup>	f/200	
	2000-300 000	61	10	
	10 -10 000			2 (head)
IEEE Std C95.1-2005	100-400	27.5	2	
	400-2000		f/200	
	2000-100 000		10	
	100 000-300 000		(90f-7000)/200	

#### IV. CONCLUSIONS

The performed analysis shows clearly that even short-term laboratory experiments confirm evidence of significant changes in human brain physiology at field power densities and SAR values much lower than the health protection limits recommended in official regulations.

#### ACKNOWLEDGMENT

This study was supported by Estonian Science Foundation grant No 6632.

#### REFERENCES

- Valentini E, Curcio G, Moroni F, et al. (2007) Neurophysiological Effects of Mobile Phone Electromagnetic Fields on Humans: A Comprehensive Review. *Bioelectromagnetics* 28: 415-432
- Persson B, Salford L, Brun A (1997) Blood-brain barrier permeability in rats exposed to electromagnetic fields used in wireless communication. *Wireless Networks*, 3: 455-461
- Salford L, Brun A, Eberhardt J, et al. (2003) Nerve cell damage in mammalian brain after exposure to microwaves from GSM mobile phones. *Environmental Health Perspectives* 111: 881-883
- Weaver J, Astumian R (1990) The response of living cells to very weak electric fields: the thermal noise limit. *Science* 247:459-462
- Hinrikus H, Lass J, Riipulk J (1998) The Sensitivity of Living Tissue to Microwave Field. Proc. of the 20th Annual International Conference of the IEEE Engineering in Medicine and Biology Society, Hong Kong, 1998, vol. 20, pp. 3249 – 3252
- Hinrikus H, Bachmann M, Tomson R, Lass J (2005) Non-thermal effect of microwave radiation on human brain. *The Environmentalist* 25: 187-194
- Hinrikus H, Riipulk J (1999) Living Cell as a Receiver of Microwave Radiation. Proc. of the Estonian Academy of Sciences Engineering, 5: 260-269
- Hille B (1992) Ionic channels of excitable membranes Sinauer Associates, Massachusetts
- Adair R K (2002) Vibrational resonances in biological systems at microwave frequencies. *Biophysical Journal* 82: 1147-1152
- Hinrikus H, Lass J, Tuulik V. Interaction of low-level microwave radiation with nervous system – a quasi-thermal effect? (2004) Proc. of the Estonian Academy of Sciences, Engineering, 10: 82-94
- Hinrikus H, Bachmann M, Tomson R, Lass J (2005) Non-thermal effect of microwave radiation on human brain. *The Environmentalist* 25: 187-194
- Malmivuo J, Plonsey R (1995) *Bioelectromagnetism*. Oxford University Press, New York
- Adair ER, Mylacraine KS, Cobb BL (2001) Partial body exposure of human volunteers to 2450 MHz pulsed or CW field provokes similar thermoregulatory responses. *Bioelectromagnetics* 22: 246-259
- De Lorge JO, Ezell CS (1980) Observing responses of rats exposed to 1.28 and 5.62 GHz microwaves. *Bioelectromagnetics* 1:183-19
- Liu J, Zhou YX, Deng ZS. (2002) Sinusoidal heating method to noninvasively measure tissue perfusion. *IEEE Trans Biomed Eng.* 49:867-877
- Foster KR, Schwan HP (1996) Dielectric properties of tissues. *Handbook of Biological Effects of Electromagnetic Fields*, Ed. by C. Polk and E. Postow, CRC Press, Boca Raton, New York, London, Tokyo, 1996. pp. 25-102
- Hinrikus H, Bachmann M, Kalda J, Sakki M, Lass J, Tomson R (2007) Methods of electroencephalographic signal analysis for detection of small hidden changes. *Nonlinear Biomedical Physics* at <http://www.nonlinearbiomedphys.com/content/1/1/9>
- Huber R, Treyer V, Borbely AA, et al. (2002) Electromagnetic fields, such as those from mobile phones, alter regional cerebral blood flow and sleep and waking EEG. *Journal of Sleep Research* 11: 289–295
- Curcio G, Ferrara M, Moroni F et al. (2005) Is the brain influenced by a phone call? An EEG study of resting wakefulness. *Neuroscience Reserch* 53: 265–270
- Guidelines for limiting exposure to time-varying electric, magnetic, and electromagnetic fields (up to 300 GHz). International Commission on Non-ionizing Radiation Protection. *Health Physics*, 74:494-522, 1998
- IEEE Std C95.1™-2005. IEEE Standard for Safety Levels with Respect to Human Exposure to Radio Frequency Electromagnetic Fields, 3 kHz to 300 GHz. 2005.

Author: Hiie Hinrikus  
 Institute: Tallinn University of Technology  
 City: Tallinn  
 Country: Estonia  
 Email: hiie@cb.ttu.ee

# The Impact of the Anomalous Magnetic Field of the Earth on Demographic Indices (using Latvia as an example)

L. Kartunova<sup>1</sup>, V. Vetrennikov<sup>1</sup>

<sup>1</sup>“Urboekoloģija” Ltd., Riga, Latvia

**Abstract** — An analysis is given in the article of the impact of the anomalous magnetic field of the earth on the demographic indices of the population of the Latvian districts and parishes.

Magnetic anomalies in the Latvian territory are caused by the rocks and iron ore of the crystalline basement. The intensity of the anomalous magnetic field in Latvia varies from -2000 nT (in the area of Seda) to +10 000 nT (the Garsene anomaly).

Observations were carried out in 10 districts of Latvia. Using one of them as an example, it was demonstrated that the demographic indices change depending on the intensity of the anomalous magnetic field, and it was shown at which intensity values the population growth acquires negative values. Data of the birth rate, mortality and natural population growth of the Ogre District (Latvia) for the time period from 1989 to 1999 was used.

The results of the study of the distribution of the Latvian cities and towns in the anomalous field are presented.

**Keywords** — anomalous magnetic field of the earth, demographic indices change.

## I. ANOMALOUS MAGNETIC FIELD IN LATVIA

The magnetic field (hereinafter referred to as “MF”) in Latvia must be considered an integral part of the MF of the Earth in general – the Earth as a cosmic body. The MF of the Earth is divided into:

- the main MF, created by the sources situated inside the Earth (predominantly, in the liquid part of the Earth core);
- the external MF of the near-Earth space (the magnetosphere), created as a result of the interaction of the main MF with the flow of charged particles (the solar wind). That MF is the most dynamic; the variations of its intensity are associated with the solar activity phenomena.

The main MF creates 96-99% of the intensity of the general MF of the Earth. It magnetises the rocks of the Earth crust containing ferromagnetic minerals and creates anomalies, the intensity of which depends on the quantity of ferromagnetic materials in rocks.

The magnetic anomalies in the Latvian territory are created by rocks and iron ore in the crystalline basement. The spatial body of the anomalies forms the anomalous MF of an area. That field has an irregular configuration formed by an alternation of linear and mosaic, positive and negative anomalies. Their intensity varies considerably: from negative values, reaching a few hundred nT to several thousand nT with the positive sign.

The most intensive positive magnetic anomalies are situated in the areas of the occurrence of magnetic ore, while the most intensive negative magnetic anomalies are situated in the areas of the occurrence of migmatite-granite with a low content of ferromagnetic minerals.

The highest values of the intensity of the anomalous MF are observed in the central part of Latvia: the Garsene anomaly (+10000 nT) in the Jekabpils District, The Staicele anomaly (+8000nT) in the Limbazi District, the Anna anomaly (+7000 nT) in the Cesis District, the Birzgale anomaly (+6000 nT) in the Ogre District, the Inchukalns anomaly (approximately 5000 nT) in the Riga District [1, 2]. The Vidzeme Region is the most abundant in large positive anomalies, while they are quite scarce in the Kurzeme Region. The MF intensity in Riga, the capital of Latvia, varies from +300 nT to +1400 nT.

A simplified scheme of the anomalous MF in Latvia is shown in Fig. 1.1. It shows the field components, which influence the demographic indices of the population, i.e. the anomalies, the intensity of which exceeds 700 nT; local



Figure 1.1. Scheme of the anomalous MF in Latvia  
1 – positive MF; 2 – negative MF; 3 – zero line of MF; 4 – positive MF with the intensity > 700 nT; 5 – local anomalies containing ferromagnetic minerals.

magnetic zones of the iron ore nature; and the zero line, subdividing the positive and the negative values of MF.

## II. THE LOCATIONS OF THE EXISTING SETTLEMENTS IN THE ANOMALOUS MF OF LATVIA

All the living organisms are influenced by the MF of the Earth. In the scientific literature, dealing with the impact of MF organisms, many publications contain the results of the studies of the external MF, in particular, magnetic storms on organisms. The smallest number of studies deals with investigations of the impact of the main MF of the Earth on the living organisms, although their importance is evident.

The low frequencies of the MF of the Earth are close to the frequencies of MF in humans; due to that, complex biochemical processes, which take place in the human body, are very sensitive to the variations in the intensity of MF of the Earth. It is supported by the studies carried out by scientists in different countries: Y.A. Holodov, V.P. Kaznacheev, L.S. Kartunova, A.S. Golovatsky, M.P. Zhidkov, O.S. Tkachenko, M.A. Persinger, D.R. Russell and many others [3-7].

During the process of evolution, organisms have adapted to life in the anomalous MF of the Earth of certain intensity, choosing by intuition the territories near the MF zero line. Studies in Latvia, USA, Russia and other countries have demonstrated that 0 nT is the optimum intensity of MF for life, as well as the adjacent zone with the intensity varying within  $\pm 300 \div 500$  nT.

Practically all the historical settlements in Latvia, built as locations for long-term habitation, are associated with the zone of the zero line (like on a string) (see Table 2.1). The

system of settlements in the Dobele District of Latvia could serve as an example (Fig. 2.1) [5].

There are 54 cities/towns of the all-Latvian and district importance in Latvia. Out of those, 44 cities/towns are situated along the MF zero line or near it (in the zone with the field intensity of up to  $\pm 500$  nT).

The old towns, built as settlements, are situated along the zero line or near it. The former fortresses, which developed into towns later, are exceptions. E.g., the town of Izborsk (the Pechory District, Pskov Province, Russia (the intensity of MF from +500 nT to + 700 nT), Bauska (+700 nT), Limbazhi (- 700 nT), Ikshkile (+1000 nT) etc. Fortresses were constructed at highs, near tectonic faults, in the MF gradient zone. The settlements appearing near fortresses developed in the unfavourable MF zone involuntarily.

During the construction of new towns during the 20th and 21st centuries, such as Olaine ( $> 700$  nT), Seda (- 1000 nT), Strenchi (+ 2000 nT), Ogre (+ 2000 nT) etc., the factor of the impact of geophysical fields was ignored, because it was unknown.

At the moment, the old principles of distribution of settlements are lost, while the new knowledge exists on the theoretical level only and has not been incorporated into the legislation. Still, first attempts at the development of the norms of the permissible intensity of MF of the Earth were made.

An additional safety criterion was introduced in Sweden and some other countries as a recommendation, stating that, at the locations of night entertainment and gathering of children, the intensity of MF must not exceed 2000 nT [8].

First textbooks of applied geophysics for students of higher educational establishments were published [7, 8]. The textbooks set forth the task of achieving “the sustainable development of the human civilization”. That task cannot be achieved without taking the impact of physical fields, including MF of the Earth, into consideration [8].

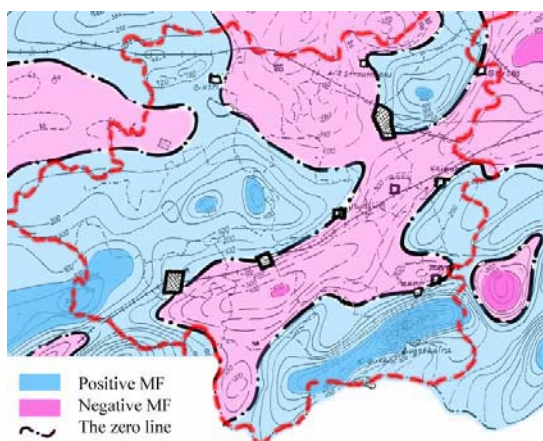


Figure 2.1. Distribution of settlements of the Dobele District in MF of the Earth.

## III. THE IMPACT OF THE ANOMALOUS MF IN LATVIA ON DEMOGRAPHIC INDICES OF THE POPULATION

The presence of the MF is a necessary condition for life. Still, it can develop successfully only within a certain range of the values of its intensity. Any considerable deviation from the values of that range could lead to the appearance of consequences, which negatively impact the organisms.

There is no hazard of an immediate death for humans. They continue to live, but systematic problems appear in the activity of the most important systems: the reproductive, nervous, endocrinous, cardiovascular and digestive ones. The organism reacts upon the conditions, which are

unsuitable for it, by pathological changes, which are a sort of “payment for life” under the conditions that differ from the normal ones [5, 6].

Outside the range of the MF intensity, which is optimum for life ( $\pm 500$  nT), the following phenomena are observed: a gradual increase in disease rate, which leads to the decrease in the birth rate and natural population growth, as well as an increase in the mortality rate. Besides, the normal sex structure of the newborn changes towards the prevalence of males, the character of the human behaviour changes etc.

The investigations of the authors of this article, carried out in ten Latvian districts and abroad, allowed to ascertain, which demographic indices of population are formed in the MF of different intensity. The data of the state demographic statistics and MF indices for different parishes were used in the investigations.

As a result, the general regularity, which is common for all the areas, was established:

Demographic indices improve when the MF intensity values become closer to zero.

Now we shall discuss that regularity in the graphic format, using the Ogre District as an example.

The Ogre District is situated in the central part of Latvia, to the southeast from Riga. It incorporates 16 parishes and 4 towns: Ikshkile, Ogre, Kegums and Lielvarde.

A map of the anomalous MF of the Ogre District is presented in Fig. 3.1. The MF has a complex differentiated configuration and demonstrates certain regularities. Those regularities are reflected in the objective existence of the natural interrelation of anomalies creating a certain type of MF.

The intensity of MF in the western part of the Ogre District is much higher than that in the eastern part of the district.

Calculations of the average indices of mortality, birth rate and population growth for the time period from 1989 to

Table 3.1. Average values of the indices of mortality, birth rate and natural population growth in parishes and towns of the Ogre District during 1989 - 1999, and average values of MF in those areas [6]

No.	Area	Average values, persons/1000 residents per year			Average MF intensity in the area, nT
		Birth rate	Mortality rate	Natural population growth	
1.	Birzgales	12.1	15.9	-3.8	1892
2.	Ikshkile	7.1	14.5	-7.4	1479
3.	Kegums	9.3	13.1	-3.7	1144
4.	Keipene	12.5	12.3	+0.3	276
5.	Krapes	15.1	11.9	+3.2	817
6.	Ledmane	10.8	13.9	-3.0	1499
7.	Lielvarde	10.9	11.9	-0.9	1715
8.	Lauberes	11.8	13.9	-2.1	653
9.	Mazozolu	13.4	15.1	-1.7	546
10.	Madlienas	13.9	15.4	-1.5	626
11.	Mengele	14.7	10.6	+4.0	668
12.	Ogre	9.3	11.3	-2.9	1298
13.	Ogresgala	9.9	13.2	-3.2	2375
14.	Rembates	11.7	14.5	-2.7	2304
15.	Suntazhu	12.8	14.8	-2.0	1298
16.	Taurupes	13.2	14.6	-1.3	998
17.	Jumpravas	9.0	13.2	-4.3	2255

1991 and the average values of intensity of MF for separate parishes are presented in Table 3.1.

The values of the indices of birth rate, mortality and natural population growth of the Ogre District in MF of different intensity are presented below (Figures 3.2, 3.3, 3.4).

Figure 3.2 demonstrates that the birth process is stable in the MF with the intensity of up to 1000 nT, then the deterioration of the indices and their dispersion are observed, being a proof of the instability of the process. The growth of the birth rate indices occurs parallel to the decrease in the intensity of MF.

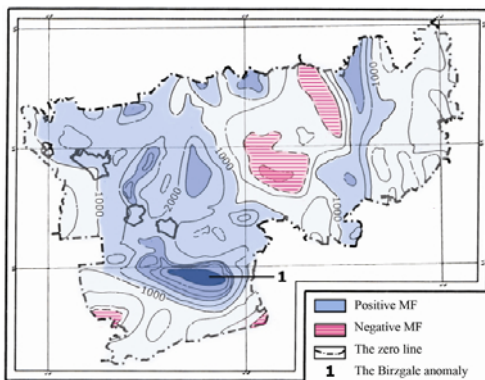


Figure 3.1. Scheme of anomalous MF in the Ogre District. [6]

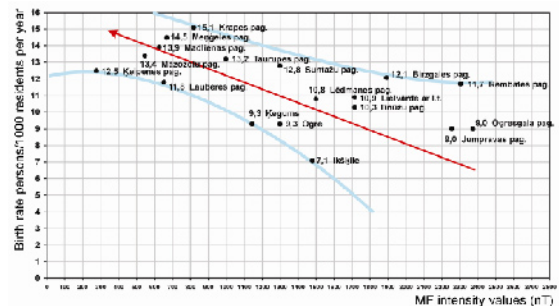


Figure 3.2. The area of values of average birth rate indices of the population of the Ogre District for the time period 1989 - 1999 in MF of different intensity. [6]

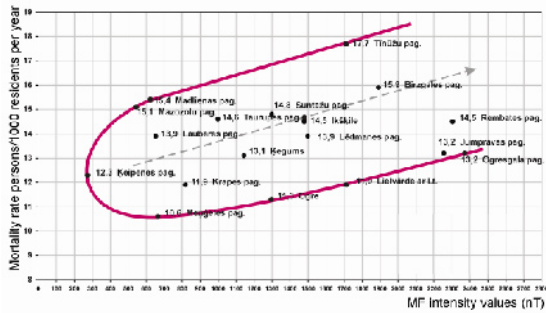


Figure 3.3. The area of values of average mortality rate indices of the population of the Ogre District for the time period 1989 - 1999 in MF of different intensity.

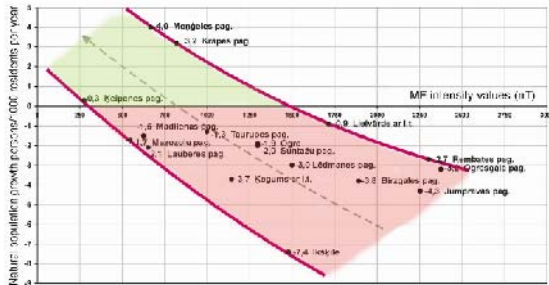


Figure 3.4. The area of values of natural population growth indices of the population of the Ogre District for the time period 1989 - 1999 in MF of different intensity. [6]

A similar regularity is observed in the variations in the mortality rate indices of the population of parishes: the closer the field intensity is to zero, the lower the mortality indices for the population of parishes of the eastern part of the Ogre District (Mengele, Krape, Keipene etc.).

Figure 3.4 shows the area of the indices of the natural population growth in parishes of the Ogre District in MF.

Positive values of natural population growth were observed only in the parishes where the average MF values do not exceed 750 nT. The trend of the graph demonstrates that the improvement of the indices occurs alongside with the decrease in MF intensity.

Similar results were obtained in other investigated areas as well, which allows to make the following conclusions:

The MF of the Earth considerably influences the values of the demographic indices of population. The intensity of

MF equal to 0 nT and that close to zero (from - 500 nT to + 500 nT) is optimal for the organism. The intensity value of ± 1000 nT could be recommended as the maximum permissible value for long-term residence of population.

The MF of the Earth in Latvia creates favourable conditions for the establishment of settlements in the zero nT zones, which is the most favourable for population.

The passing of legal acts incorporating the necessity of taking geophysical fields of the Earth into account would allow to improve the demographic situation in the country considerably and would contribute to stable development of settlements.

## REFERENCES

1. Ветренников В.В. Железисто-кремниевые формации докембрия и их прогнозная оценка. Рига, «Зинатне», 1991 г., 170 с.
2. Straume, J., Brangulis A., Prols J. u.c. Latvijas zemes dziļu resursi. – Rīga, 1997.g., 26-28 lpp., Valsts Ģeoloģiskais dienests.
3. Холодов Ю.А. Мозг в электромагнитных полях. – Наука, М, 1982 г.
4. Казначеев В.П., Непомнящих Г.И. Мысли о проблемах общей патологии на рубеже XXI века. – М., Препринт, 2000 г.
5. L.Kartunova, L.Fiļimoņenko, V.Gridins, J.Jankins, A.Reuta, Parskats par ZPD par temu: „Dobeles rajona teritorijas ģeoloģiskais zonejums”, 31/A-1011 (92) SL, Rīga, 288 lpp., 64 zīm., 42 tab., 154 lit. avoti, 19 piel., LVCZPI, 1993.g.
6. L.Kartunova, E.Aleksejevs, V.Abolkalns, A.Birgers, J.Jankins, V.Gridins, M.Laiviņš, V.Vetrenņikovs. Parskats par ZPD “Vides situācijas izpēte Ogres rajona, priekšlikumu izstrādāšana Ogres rajona sociālas un ekonomiskas attīstības virzieniem” – 2 gramatas: 309 lpp., 25 att., 31 tab., 13 graf., 1 diagr., 4 piel., 12 kartes. SIA “Urboekoloģija”, Rīga, 2001.g.
7. Богословский В.А., Жигалин А.Д., Хмельской В.К. Экологическая геофизика. – Изд-во Московского университета, 2000 г., 235 с.
8. Куклев Ю.И. Физическая экология. – Изд-во «Высшая школа», 2001 г., 351 с.

Author: Lyudmila Kartunova,  
 Vladimir Vetrennikov  
 Institute: “Urboekoloģija” Ltd.  
 Street: Kr. Valdemara 70-23  
 City: Riga  
 Country: Latvia  
 Email: urboekologija@gmail.com

# Development of the Positron Emission Tomography Center: Medical and Physical Aspects

A.V. Khmelev<sup>1</sup>, S.E. Evdonin<sup>2</sup>, V.A. Kostylev<sup>1</sup>, S.V. Shiryaev<sup>1</sup>, B.I. Dolgushin<sup>1</sup>

<sup>1</sup> N.N.Blokhin Russian Cancer Research Center RAMS / Department of Radionuclide Diagnostics, Moscow, Russia

<sup>2</sup> Institute of Medical Physics and Engineering, Moscow, Russia

**Abstract** — The study results of the PET facilities creation and design adaptation to the local conditions are analyzed. The PET Center development algorithm is proposed, detailed and implemented for oncology PET Center. Approach includes medical and physical studies, development of medical and technical requirements and conception as well as the initial data for the object projecting.

**Keywords** — positron emission tomography, PET-Center, development

## I. INTRODUCTION

The Positron emission tomography (PET) is relatively new technology of the preventive medicine which appeared in 1970-th. The PET is more often used in oncology (90%), neurology (5,5%) and cardiology (4,5%) [1, 2]. The PET-Center is created for realization of this technology, mainly used with [<sup>18</sup>F]-fluorodeoxyglucose (FDG), labeled by <sup>18</sup>F. It is intended for a cyclotron production of short lived radionuclide's, <sup>15</sup>O, <sup>13</sup>N, <sup>11</sup>C, <sup>18</sup>F, synthesis of the of the PET-radiopharmaceuticals (PET-RP) and expressed clinical use of the PET-RP [3, 4].

In Russia with approximately 150 million inhabitants there are only four clinical PET-Centers and four PET-departments (not having their own PET-RP production) in Moscow and St-Petersburg. 12 PET-scanners are applied in all. Today the actual task for Russia is a creation of big federal PET Centers capable to provide the multimode diagnostics of the population with high throughput in a numerous regions.

The assurance of economic efficiency of an expensive and complicated PET-Center and maintaining of radiation safety standards [5] should be provided by detailed development and careful planning of this object in the initial stage with the participation of qualified medical physicists, facility architect and vendor of PET equipment. The research approach to PET-Center creation [6-8], as an alternative to the simplest replication of the present PET-Centers, is especially important for the healthcare programs elaboration in Russia and, particularly, for PET introduction in its regions.

It is associated with the features of the country which population lives in large territory with the essentially different levels of the medical institutions equipment and staff support. At present in Russia a big PET-Centers are first requested [8] with the following parameters: the number of the combined PET and the computer tomographs (PET/CT) not less than 3, high throughout put, presence of the adjacent departments of the traditional diagnostic radiology as SPECT and/or MRI. Today there are no such PET-Centers in Russia. The detailed procedure of their development including the social, economic, medical, physical, technological, educational aspects and also problems does not exist [7-8]. Medical and physical aspects of the PET-Center development and the results of the development algorithm realization in practice are described in this paper.

## II. MATERIAL AND METHODS

The planning, exploitation, radiation safety, technical and manpower maintenance of the dedicated PET-Centers in Russia and abroad are studied. The results of the PET appliance in clinical practice and research have been investigated. The literature survey of the issues in creating and exploitation not introduced in Russia PET-Centers with combined PET/CT technology [2, 4, 5-9] has been analyzed.

The dedicated PET facilities (cyclotron-radiochemistry complex, PET-department and block of technical rooms and supplies) were planned referring to the GMP rules and GOST.

The radiation shielding of the personal from the patients with injected PET-RP has been calculated for the functional rooms of PET and adjacent SPECT departments referring to recommendations of AAPM TG 108 [10]. For such calculations the following factors affecting the amount of the shielding required for PET-department were used: the number of patient imaged, the amount of radiotracer administered per patient, the period of time that each patient remains in the PET-department, and the location of the facility and its general environs. The weekly dose  $D_{Tot}$  at a point  $d$  (m) from  $N_w$  patients with injected PET-RP during the uptake  $D_{wU}$  ( $\mu$ Sv) for time  $t_U$  (h) and from the patients

during PET-scanning  $D_{WS}(\mu\text{Sv})$  for time  $t_S$  are calculated respectively on formulas [11]:

$$D_{WU} = 0.092 \times N_W \times A_0 \times t_U \times R_{tU} / d^2$$

$$D_{WS} = 0.092 \times N_W \times A_0 \times F_U \times t_S \times R_{tS} / d^2$$

where  $F_U = \exp(-0.693t_U/110)$  is a administered activity  $A_0$  (MBq) decreasing for the uptake time,  $R$  – reduction factor [11]. Then the total weekly dose  $D_{Tot}$  at a differ rooms of PET-Department is determined. In accordance with federal code of regulation (NRB) the occupational effective dose limit for the personal of A and B class is 20 and 5 mSv/year and for the general public is 1 mSv/year. With apply of such dose limits and occupancy factor (T) the transmission factor B is calculated and then the concrete shielding thickness is estimated using table data [11].

Yearly/daily radionuclide's balance, PET-RP workflow and utilization, the patient and personal dose values were estimated.

Two decision strategies for selection of candidates for surgical cure of the most spread oncology disease non-small cell lung carcinoma (NSCLC) were compared with use of the clinical results [11]: CT along (strategy 1) and CT+PET (strategy 2). Sensitivity of the diagnostic procedures in so called decision trees [12] has been analyzed. The PET introduction additional cost (referring to Moscow region medical procedures prices) as well as the patient life expectancy change was calculated as result of the NSCLC restaging with PET use [11].

The output parameters of the developed PET-Center have been calculated in accordance with the social and epidemiology conditions of served territory and the technical and technological particulates of the PET-Center dedication.

### III. RESULTS

Proposed is the algorithm of the dedicated PET-Centers development which has been realized in practice for the planning of such objects in several Russia regions. This algorithm includes:

#### A. 1. The medical and physical investigations of the PET-Center creation and exploitation features

The subject of the study are the epidemiology conditions of served region and its needs in PET diagnostic, clinical and scientific tasks, types and cost-effectiveness of diagnostic exams, patients' workflow and radionuclide's balance, adaptation of technology to the real clinical conditions, sources of positron and gamma radiation in the PET-Center and radiation shielding of personal and precision equipment.

#### B. 2. The elaboration of medical and technical requirements for the PET-Center creation (in accordance with GMP and GOST)

The requirements to the PET facilities design planning, equipment parameters; staff qualification and quantity, equipment service, radiation shielding of the personnel, patients and environments, waste utilization, prophylactic and liquidation of radioactive contaminations are formulated.

#### C. 3. Development of the PET-Center conception

The conception includes the strategy and economic aspects of the PET-Center creation and exploitation, the planning of the functional rooms, workflows of the patients, personal and patients with injected RP, service realization, staff training, interlineal and interdepartmental interaction, FDG supply in other nearby clinics.

#### D. 4. Development of the PET equipment and technologies initial data's for the PET-Center projection

This work is performed with vendor of the equipment to provide the optimal planning of dedicated PET-Center. The initial data include technologies, technical parameters of equipment and its layout adapted to the local conditions as well as the parameters of the radiation sources in the PET-Center and radiation shielding calculation data. It includes also recommendations for organization of technical service, delivery of spare parts and personal training.

The proposed algorithm of the PET-Centers development has been realized in planning such object for oncology in one of Russia regions with nearly 3 000 000 inhabitants and yearly new cancer cases about 13 000. The results of parameters and characteristics development of such PET-Center are reported.

On Fig. 1 the schematic layout of the PET- and SPECT-departments functional rooms as well as the set of corresponding main equipment are shown. 3 PET/CT scanners and one gamma-camera are planned to provide the PET-Center throughout put of 8 000 patients/year and 6 000 patients/year respectively. The patient's injection quantities of PET-RP labeled by  $^{18}\text{F}$ ,  $^{11}\text{C}$  and  $^{13}\text{N}$  are related as 80:15:5. The workflows of the patients, patients with injected RP and personnel are pointed out on Fig.1.

In the Table 1 the calculated values of  $D_{WU}$ ,  $D_{WS}$ ,  $D_{Tot}$ , B and radiation shielding thickness are presented. The following parameters were used in these calculations:  $N_W=60$ ,  $t_U=1$  h,  $t_S=0.5$ h,  $A_0=555$  MBq,  $R_{tU}=0.83$ ,  $R_{tS}=0.91$ . The d values are determined form the schematic room's layout (Fig.1). The recommended thickness of the concrete radia-



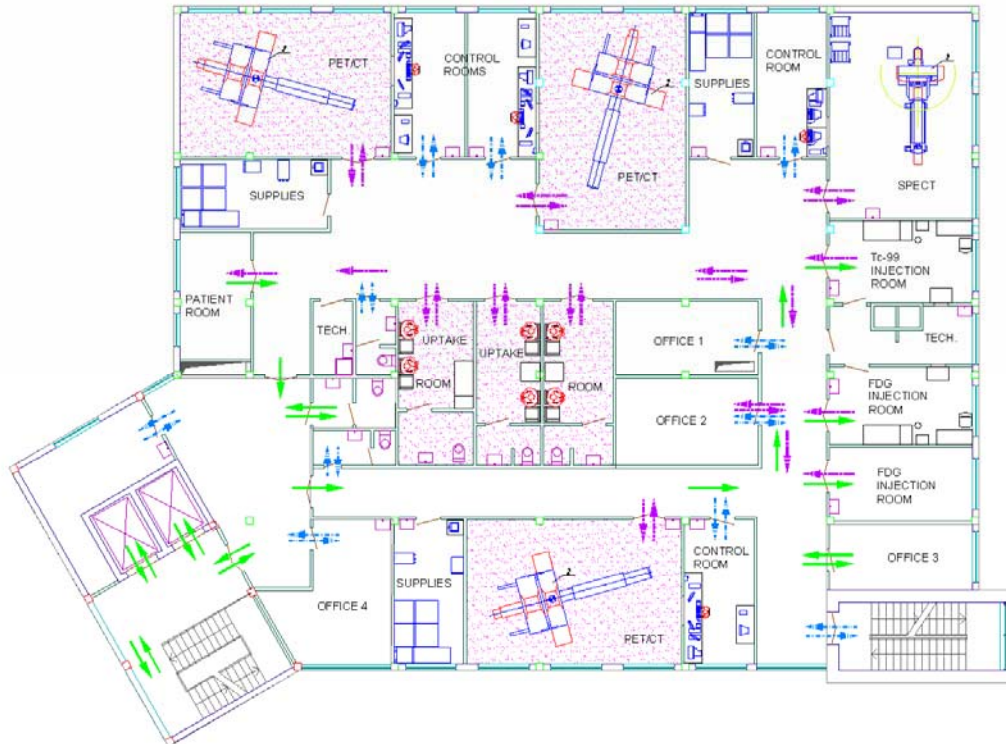


Fig. 1. Room layout of the PET-department in the PET-Center. The schematic is used for the calculations given in the Table 1. Workflow: solid arrow – non radioactive patients; dotted arrow – radioactive patients; dashed arrow - personal

tion shielding for the PET- and SPECT department rooms are in the range of 0-17 cm.

The cost increasing per patient of the NSCLC diagnostic and cure with the PET introduction for diagnostic of all patients (group of 79 people) was 80 Euro. The gain of life expectancy per patient was 0,327 year. Thus the PET examinations for the NSCLC management are a cost-effective and allow gaining the patient life at an annual cost of 250 Euro/life year saved/patient.

#### IV. DISCUSOIN

The pre-projecting performance executed according developed algorithm gives one opportunity to estimate degree of local conditions readiness for the PET-Center creation and PET technology installation, discover the medical, physical, technical and managing problems and solve them during scientific accompaniment of the project. The elaborators of Russian healthcare programs should pay attention to the document developed on this stage in order to stimulate active PET penetration in Russia since the availability of this method in the country is still limited.

The developed schematic layout of the PET-department functional rooms (Fig.1) as well as information on distances from potential sources in the uptake rooms and PET-scanner rooms to points of interest, along with the target weekly dose values, occupancy factors, radiation shielding thickness (Table 1), the PET-Center balance radionuclide calculations is required and used by architect company for this object planning and designing. The shielding requirements for the PET-department are different from those of SPECT –department. This is due to the high energy of the annihilation and positron radiation and the fact that the patients with injected PET-RP are the dangerous constant source of radiation in the PET-Centers with high through put.

The PET diagnostic accuracy and clinical effectiveness is high [11, 12]. It leads in the case of some oncology deceases (for example, NSCLC) to the cost-effective diagnostics and cure in spite of the high cost of the PET equipment and gain of the patient life expectancy.

According to the results of calculations had been done in this paper the recommended optimal ratio is one PET/CT scanner for 1 000 000 inhabitants.

Table 1 table specification Table 1. Dose, transmission and concrete shielding calculation data for a dedicated PET-department

	Uptake distance, m			Scanner distance, m			D <sub>WT</sub> , Zv x 10 <sup>6</sup>	T	D <sub>WU</sub> , μZv			D <sub>WS</sub> , μZv			D <sub>Tot</sub> Zv x 10 <sup>6</sup>	B	Concrete shield, cm
	16	18	20	8	18	20			10	8	8	15	3	2			
Gamma camera	16	18	20	8	18	20	100	1	10	8	8	15	3	2	46	>1	-
SPECT control room	12	14	16	5	17	18	100	1	18	13	10	38	3	3	85	>1	-
<sup>99m</sup> Tc-injection room	11	14	17	8	20	15	100	1	21	13	9	15	2	4	64	>1	-
FDG injection rooms	10	14	17	12	22	9	400	1	25	13	9	67	2	12	68	>1	-
PET control room 1,2	9	10	10	3	6	18	100	1	31	26	26	105	26	3	217	0.461	9
PET control room 3	7	9	12	3	15	22	100	1	52	31	18	105	4	2	212	0.471	9
Corridor 1	2.5	2.5	2.5	2.5	4	8	100	0.25	407	407	407	152	59	15	1447	0.275	13
Corridor 2	7	10	13	7	18	4	100	0.25	52	26	15	19	3	59	174	0.460	9
Corridor 3	2.5	2.5	2.5	2.5	10	15	100	0.25	407	407	407	152	95	4	1472	0.270	13
Patient room	7	11	13	4	14	12	100	1	52	21	15	59	5	7	159	0.629	4
Office 1	2.5	4	7	6	13	8	100	0.25	407	159	52	26	6	15	665	0.602	7
Office 2	2.5	4	7	4	8	16	100	1	407	159	52	59	15	4	696	0.144	17
Office 3	11	14	17	7	15	24	100	1	21	13	9	19	4	2	68	>1	-
Office 4	4	7	9	16	16	4	100	1	159	52	31	4	4	59	309	0.324	12
Hall	5	9	11	11	15	8	100	1	102	31	21	8	4	15	181	0.552	7

V. CONCLUSION

Development of the PET-Center is an important stage in its creation and has to be done in close cooperation with clinical medical physicists, architects and the PET equipment vendor specialists. Proposed PET-Center development algorithm and its detailed realization can be recommended for the use if there are no existing analogs or adaptation for local conditions and clinical tasks is needed.

REFERENCES

- Hichwa R D (1996) Production of PET radioisotopes and principles of PET imaging. J Nucl Med, vol. 1, Mosby-York Book, 1500 p.
- Khmelev A V, Shiryayev S V (2004) Positron emission tomography: physical and clinical aspects. Med Radiology and Radiation Protection, 5:52-82.
- Beyer G J (2000) How to set up a PET-Center. Int. Conf. on Current Status of Nucl. Med. and Radiopharmaceuticals. , II Congress of the Russian Society of Nucl. Med., Obninsk, Russia
- Shreve P (2005) Establishing a PET/CT practice, AJR, 184:146-151.
- Chuck A, Jacobs P, Logus J W et al (2005) Marginal cost of operating positron emission tomography center in a regulatory environment. Int. J Technol. Asses Helth Care, 21, pp 442-45.
- Faulkner D.B., Kearfott K.J., Manning R.J. Planning a clinical PET center. J. Nucl. Med. Technol., 1991, 19, p. 5-19.

- Janevik-Ivanovska E., Ristevska S.M., Lazarevik L. et al. Feasibility study for PET –The right choice for establishing PET in emerging counties. International conference on clinical PET and molecular nuclear medicine (IPET2007), Bangkok, 2007, c. 305-306.
- Khmelev A V, Shiryayev S V, Dolgushin B I et al (2007). PET-Center: scientific and technique aspects. High technology oncoradiology centers,, v.1, M., p. 26-34.
- Kearfott K.J., Carey J.E., Clemenshaw M.N., Faulkner D.B. Radiation protection design for a clinical positron emission tomography imaging using. Health Phys., 1992, 63, p. 581-589.
- Madsen M.T., Anderson J.A., Halama J.R. et al. AAPM Task group 108: PET and PET/CT shielding requirements. Med. Phys. 2006, 33, c.4-15.
- Gotsadze I D, Davydov M I, Polotskiy B E et al. (2007). Positron emission tomography in the management of non-small cell lung cancer. Journal of N N Blokhin Cancer Research Center RAMS 18:31-37
- Gambhir S S, Hoh C K, Phelps M E et al. (1996) Decision tree sensitivity analysis for cost-effectiveness of FDG-PET in the staging and management of non-small cell lung carcinoma J Nucl. Med 37: 1428-1436.

Author: Sergey E. Evdonin  
 Institute: Institute of Medical Physics and Engineering  
 Street: Kashirskoe Shosse 24  
 City: Moscow 115478  
 Country: Russia  
 Email: sergey.evdonin@mail.ru

# Modulated Microwave Effects on Visual Event-related Potentials during Oddball Task

K. Kruusing and J. Lass

Department of Biomedical Engineering, Technomedicum of the Tallinn University of Technology, Tallinn, Estonia

**Abstract** — The aim of this study was experimental investigation of the effects of low level modulated microwaves on human electroencephalographic (EEG) visual event-related potentials. Thirty healthy volunteers were exposed and sham exposed to electromagnetic field (EMF) (450 MHz, 0.16mW/cm<sup>2</sup>) modulated at 21Hz modulation frequency during visual oddball tasks. During the task the participants had to distinguish infrequent target stimuli from frequent standard stimuli. The task consisted of visually presented random ball shape stimuli, of which the 25% were target and 75% were standard stimuli. There were two tasks for a subject - EMF exposed task and sham exposed task. One task lasted 10 minutes, during the exposed task the EMF was switched on and off in one-minute intervals, so that the participants performed half of the task in exposed condition (EMF ON) and half of the task without the exposure (EMF OFF). The sham exposed task was identical to exposed task, except the EMF generator was switched off all the time. For analysis of the EEG event-related responses the channel Pz was used. The EEG responses of a task were grouped into four different categories taking into account the EMF exposure condition (ON, OFF) during the response and the response type (standard, target). The responses were averaged by categories. The EMF ON and OFF potentials were compared pair-wise. There were no statistically significant differences in responses in sham exposed tasks, neither in standard nor in target response components. In the exposed task the group mean N100 amplitude (measured from standard response) was  $-3,41 \pm 4,54 \mu\text{V}$  in EMF ON category and  $-2,50 \pm 4,71 \mu\text{V}$  in EMF OFF category, this difference was statistically highly significant ( $p < 0,00009$ ). Differences in another components' amplitudes, latencies and in RT between EMF ON and OFF conditions were not significant during exposed tasks. It was concluded that modulated microwave effect has stronger impact on sensory components of EEG visual event-related potentials compared to later stages of visual information processing.

**Keywords** — RF exposure, visual perception, psychological effects, evoked potentials

## I. INTRODUCTION

Modulated microwave effects on electroencephalographic (EEG) event-related potentials (ERP) has been the subject of extensive discussion during the last decade. Most researches in this field are done because of massive spreading of wireless communication devices and growing public

concern about probable health risk of the electromagnetic radiation emitted from the devices and networks.

In the study by Hamblin et al (2004) they examined the effects of electromagnetic fields emitted by GSM mobile phones on human EEG event-related potentials and performance during an auditory task with 12 subjects [1]. Participants of the study performed an auditory oddball task while they were exposed to electromagnetic field (EMF) of an active mobile phone during one session and sham exposed during another. Each condition lasted 1 h and the two sessions were done one week apart. For EEG ERP analysis they used phase-locked methods. The analysis showed that N100 amplitude and latency to non-targets were reduced when exposure and sham exposure conditions were compared. P300 latency to targets was delayed in the exposure condition and also the reaction time (RT) increase was observed in expose condition. The results suggested that mobile phone exposure may affect neural activity, however caution should be applied due to the small sample size. In the next ERP study by Hamblin et al (2006) they increased the sample size to 120 subjects and decreased the EMF exposure time to 30 minutes. The results of that study showed no significant difference between exposure conditions for any auditory or visual ERP component nor RT. As their previous positive findings were not replicated, it was concluded that there is currently no evidence that acute mobile phone exposure affects auditory N100 and P300 nor visual P100 and P300 amplitudes and latencies neither RT [2]. A study by Papageorgiu et al (2006) found that EMF emitted by mobile phone affect pre-attentive information processing reflected by P50 auditory evoked potential [3]. In the visual perception study by Rodina et al (2005) with face masking task it was shown that recognition of stimuli was better under the sham exposure conditions compared to exposed condition (450Mhz, modulation 7Hz) but the actual difference was only 5%. It was concluded that early stages of visual information processing are overwhelmingly robust and routine (and adaptively significant) activities, so that the low level 7 Hz modulated electromagnetic field effects exerted upon it are extremely weak [4]. In the visual perception study by Lass et al (2006) the EMF (450Mhz, modulation 40Hz) effects were examined with attention blink phenomenon that can be described as impairment of the identification of the second of two targets if it is presented less than about

500 ms after the first. The results showed that 40 Hz modulated EMF had no immediate effect on attentional blink characteristics of human visual perception [5]. The studies by Lass et al (2006) and Rodina et al (2005) have been different compared to mobile phone experiments described above in the extent that the electromagnetic field carrier had lower frequency (450MHz) and the modulation was simplified compared to a GSM standard. In these studies the simple on/off modulation was used where modulation frequencies were inside the EEG frequency band (7 or 40Hz).

The results of the described studies are quite different and contain contradictions when compared to each other. It is a clear indication to the fact that EMF effects on cognitive functions can not be easily detected and the interpretation of the results is extremely complicated. The reasons for that might be that the sensitivity to EMF is very different with different individuals and depends also very much on a physiological condition of a subject during the experiment. The aim of the current study was to experimentally investigate the effect of modulated microwave radiation in EEG ERP responses by method introduced by Polish (2004) and combine it with an original design of the EMF exposure setup [6]. The idea of exposure setup is to keep the experimental conditions for a subject as uniform as possible in order to minimize the fluctuations of the physiological condition and ERP responses by unknown factors. This goal is achieved by recording the reference and exposed responses in a mixed way during the same task and making the exposed and sham exposed tasks in the same day in short time.

## II. METHODS

### A. Subjects and Recording Conditions

30 adult subjects participated in the current study. The group of volunteers consisted of 12 male and 18 female subjects, aged between 19 and 36 years with a mean age of 25 years. All participants were healthy, without any known medical or psychiatric disorders, and had normal or corrected to normal visual acuity. All subjects gave their informed consent before the start of the experiment.

EEG activity was recorded at the Fz, Cz, and Pz electrode sites, referred to linked earlobes, using forehead ground, with impedances at 5 k $\Omega$  or less. Additional bipolar electrodes were placed at the outer canthus both eyes, also above and below the left eye to measure EOG activity. The data were recorded using a sampling rate of 500 Hz and bandpass filtered (0.05-40 Hz). All data were recorded using Compumedics Neuroscan (7850 Paseo Del Norte El Paso, TX 79912, USA) electrode cap, Syn Amps<sup>2</sup> amplifier and amplifier headbox.

### B. Exposure Conditions

Electromagnetic radiation of 450 MHz was generated by a signal generator (model SML02, Rhode & Swartz Munich, Germany). The radio frequency signal was 100% pulse-modulated using a modulator (SML-B3, Rhode & Swartz, Munich, Germany) at frequency of 21 Hz (duty cycle 50%). The signal from the generator was amplified by a power amplifier (model MSD-2597601, Dage Corporation, Stamford, CT, USA). The generator and the amplifier were carefully shielded. The output power of 1 W electromagnetic radiation was guided by a coaxial lead to the 13 cm quarter-wave antenna, (NMT450 RA3206, Allgon Mobile Communication AB, Stockholm, Sweden), located 10 cm from the skin on the left side of head. The spatial distribution of the power density of electromagnetic radiation was measured by a field strength meter (Fieldmeter C.A 43, Chauvin Arnoux, Paris, France). The measurements were done by the Central Physical Laboratory of the Estonian Health Protection Inspection. The calibration curves of the dependence of field power density on the distance from the radiating antenna were obtained from these measurements, performed under real experimental conditions. During the experiments a Digi Field C field strength meter (IC Engineering, Thousand Oaks, CA, USA) was used to monitor the stability of the electromagnetic radiation level. The average field power density of the modulated microwave at the skin on the left side of head was 0.16 mW/cm<sup>2</sup> as estimated from measured calibration curves. The specific absorption rate (SAR) was calculated using SEMCAD (Schmid & Partner Engineering AG, Zurich, Switzerland) software. The finite difference time domain (FDTD) computing method with specific anthropomorphic mannequin (SAM) specified in IEEE Standard 1528 was applied. The calculated spatial peak SAR averaged over 1 g was 0.303 W/kg, which is below the thermal level. In current study every subject performed two identical cognitive tasks, one of which was with exposure and the other was with sham exposure. One task lasted 10 minutes, during the exposed task the EMF was switched on and off in one-minute intervals, so that the participants performed half of the task with RF exposure (EMF ON) and half of the task as reference (EMF OFF). The sham exposed task was identical to EMF exposed task, except the EMF generator was switched off all the time.

### C. Visual Task Description

All subjects performed a visual oddball task, where they had to distinguish infrequent target stimuli from frequent standard stimuli by pressing the mouse button. The task consisted of randomly appearing ball-shaped stimuli, of

which 25 % were targets and 75 % were standards. The sequence of the stimuli was generated by the system Compumedics Neuroscan STIM<sup>2</sup> 4.0. There were two different sequences of stimuli (one for exposure task and another for sham task) and the order of the sequences was counterbalanced. The target stimulus was a blue circle with 2 cm diameter and standard stimulus a blue circle with 4 cm diameter [6]. Stimuli were presented in the middle of the black computer screen. The duration of every stimulus was 100 ms. The inter stimulus interval (ISI) was variable during the task in order to minimize habituation. ISI range was 1-2 seconds, mean 1,5 seconds. Altogether 400 stimuli were presented on the computer screen during one 10-minute task (Fig. 2), of which 100 were targets and 300 standards. The subjects were instructed to respond to the target as quickly as possible by pressing the left mouse button and to refrain from responding to standard stimuli.

#### D. Experimental Procedure

During the experiment, the room was dark and the participants were sitting in front of the 17" computer monitor with a viewing distance of approximately 80 cm. The monitor was calibrated at color temperature 6500K and luminance 200 cd/m<sup>2</sup>. The subjects were instructed to avoid movements and keep all eyes on the middle of the screen during tasks. During the pauses between the tasks the lights were put on and the subject was asked how he/she was feeling and whether he/she felt tired.

The experimental session started with a practice task (3min) and continued with two successive experimental tasks (10min both), one of which was exposure task and another sham task. There were 2 minutes resting time between the practise task and the first experimental task, and 10 minutes resting time between two experimental tasks. The whole session for a subject lasted 35 (3+2+10+10+10) minutes and was carried out on the same day, every subject had only one experimental session. EEG activity was recorded only during the experimental tasks. The order of experimental tasks (exposure versus sham) was counterbalanced as well as order of stimuli sequences. The subjects were blind to the exposure time and duration, the antenna was located near the right side of the head during all experimental tasks.

#### E. Data Processing

Eye moving artifacts were reduced, using Compumedics Neuroscan Edit 4.3.3 software. The method employs a regression analysis in combination with artifact averaging [7]. After that the signal was low pass filtered 30 Hz (48 dB octave/slope) and continuous EEG was offline epoched to

800 ms responses with a 200 ms prestimulus baseline. Every epoch was baseline corrected using prestimulus interval -200 to 0 ms. Epochs, where the voltage in VEOG or HEOG channels exceeded  $\pm 100$   $\mu$ V (in range -50 to 400 ms), were removed from the analysis. The epochs were grouped into four different categories taking into account the EMF condition (ON, OFF) and the response type (standard, target). The responses were averaged by categories. After the grouping and averaging process we had four different ERP responses for every experimental task for every subject (target EMF ON, standard EMF ON, target EMF OFF, standard EMF OFF). One averaged ERP standard signal contained approximately 150 epochs and target signal approximately 50 epochs. The reaction times (RT) for target recognition were also recorded, valid mouse clicks had to be between 100-800 ms from the stimulus onset. The components' amplitudes were measured relative to the mean of prestimulus baseline, with peak latency defined as the time point of the maximum positive (P) or negative (N) voltage within the latency window. Peak amplitudes and latencies were detected from Pz channel. Sensory evoked potentials (P100, N100, P200, N200) were measured from standard and P300 from target stimuli. Peaks' latency windows were defined as follows: P100(130-200ms), N100(170-230ms), P200(220-280ms), N200(250-350ms), P300(300-600ms). After software peak detection, waveforms were inspected manually to ensure that the peaks identified were genuine and proceeded each other in the correct order. Scalp distribution data from Fz and Cz channels were used for correct Pz peak detection. If the P300 wave had two peaks, the second peak was taken for the analysis. In addition to subjects averaged EEG ERP responses, grand mean responses over all the subjects were calculated.

#### F. Statistical Analysis

The zero hypothesis was that the EEG event-related potential component latencies, amplitudes and reaction times of the subjects to the target stimuli (RT) could not be different in EMF ON and EMF OFF conditions during the same task. The mean values of EMF ON and OFF response parameters were compared pair-wise by two tailed Students' t-test ( $p < 0.01$  considered to be significantly different). The exposed and sham tasks were analysed separately.

### III. RESULTS

The only parameter found significantly different when comparing the mean values of the parameters in the different EMF categories was N100 ( $p < 0,00009$ ) amplitude in the exposed task. In the exposed task the group mean N100

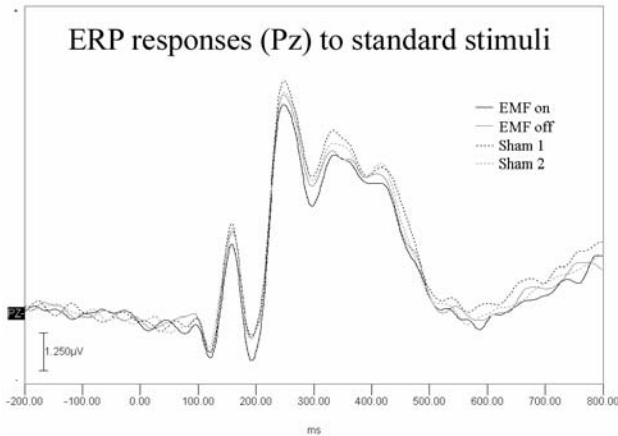


Fig. 1 EEG ERP grand mean for standard responses

amplitude (measured from standard response) was  $-3,41 \pm 4,54 \mu\text{V}$  in EMF ON category and  $-2,50 \pm 4,71 \mu\text{V}$  in EMF OFF category. In EMF ON category the N100 amplitude was  $1.1 \mu\text{V}$  (36%) lower compared to EMF OFF during the same task. The P100 amplitude was lower in EMF ON category ( $3,47 \pm 4,85 \mu\text{V}$ ) compared to EMF OFF category ( $4,01 \pm 4,55 \mu\text{V}$ ) but the significance was on borderline ( $p < 0,014$ ). No significant differences were found when sham task categories were compared.

This effect can also be observed on the grand mean response figure (Fig. 1) for standard stimuli, EMF ON grand mean has different amplitude at N100 compared to other three grand mean ERP responses on the same figure. Moreover, standard EMF ON grand mean response has noticeably lower amplitude compared to other standard responses from 150ms-300ms relative to stimulus onset.

In our experiment, mean RT in exposed tasks is somewhat shorter than in sham tasks. Respectively in milliseconds: 375 (EMF ON) and 374 (EMF OFF) versus 380 (sham 1) and 378 (sham 2). However within the same task the RT differences were not statistically significant.

#### IV. CONCLUSIONS

The results confirmed that EMF effects on visual cognitive processes are extremely weak and the detection of these effects is difficult. It was shown that modulated microwaves have rather strong impact on early (sensory) components of visual event related potentials (N100 amplitude) compared to later stages of visual information processing during the oddball task. No evidence was found that low-level 450MHz EMF modulated with 21Hz could alter EEG ERP response latencies or subject reaction times.

#### ACKNOWLEDGMENT

The study has been supported by Estonian Science Foundation grant No. 6173.

#### REFERENCES

1. Hamblin DL, Wood AW, Croft RJ et al. (2004) Examining the effects of electromagnetic fields emitted by GSM mobile phones on human event-related potentials and performance during an auditory task. *Clin Neurophysiol*, 115(1):171-178.
2. Hamblin DL, Croft RJ, Wood AW et al. (2006) The sensitivity of human event-related potentials and reaction time to mobile phone emitted electromagnetic fields. *Bioelectromagnetics*, 27(4): 265-273.
3. Papageorgiou CC, Nanou ED, Tsiafakis VG et al. (2006) Acute mobile phone effects on pre-attentive operation. *Neurosci Lett*, 397(1-2): 99-103.
4. Rodina A, Lass J, Riipulk J et al. (2005) Study of effects of low level microwave field by method of face masking. *Bioelectromagnetics*, 26(7): 571-577.
5. Lass J, Rodina A, Riipulk J, (2006) Are there modulated Electromagnetic Field Effects on Human Conscious Perception during Attentional Blink Test? *Conf Proc IEEE Eng Med Biol Soc*, 1:2924-2927.
6. Polich, J. (2004) Clinical application of the P300 event-related potential. *Phys Med Rehabil Clin*, 15(1): 133-161.
7. Semlitsch HV, Anderer P, Schuster P et al. (1986) A solution for reliable and valid reduction of ocular artifacts, applied to the P300 ERP. *Psychophysiology*, 23(6): 695-703.

Author: Kristjan Krusing  
 Institute: Department of Biomedical Engineering, Technomedicum of the Tallinn University of Technology  
 Street: 5 Ehitajate Rd  
 City: 19086 Tallinn  
 Country: Estonia  
 Email: kristjan.krusing@mail.ee

# Evaluation of the Independent Dose Calculation Algorithm

J. Laurikaitienė<sup>1,2</sup>, M. Laurikaitis<sup>1</sup>, D. Adlienė<sup>2</sup>, G.A. Adlys<sup>2</sup>, S. Raila<sup>2</sup>, F. Nordström<sup>3</sup>, S. Bäck<sup>3</sup>  
and S. Mattsson<sup>3</sup>

<sup>1</sup> Oncology Hospital of Kaunas Medical University Hospital, Kaunas, Lithuania

<sup>2</sup> Kaunas University of Technology, Physics Department, Kaunas, Lithuania

<sup>3</sup> Lund University, Malmö University Hospital, Department of Radiation Physics, Malmö, Sweden

**Abstract** — The results of the implementation of Radiotherapy Verification Program based on the application of the completely independent from TPS algorithm for dose calculations in checking of patient's treatment plans are presented in this paper. Algorithm includes calculation of the absorbed dose from photons scattered in the patient, calculation of the primary kerma transmission in the patient, calculation of the primary kerma variation in the air with collimator settings, and corrections for heterogeneities in the patient.

The results include checks of the dose plans of 90 patients performed in the clinical routine work.

It is shown, that the dose deviation between TPS and RVP is shifted towards positive side, indicating non normal distribution. Deviations vary in the interval from -4 % to +8%, with a median value of +2.97 % and standard deviation of 1.99.

After the installation of the verification program estimated findings in the dose plans, calculated using old 2D planning system, were serious enough to show the inefficiency of the old system and to stop its operation.

**Keywords** — Radiotherapy, Co-60 source, dose calculation, dose verification.

## I. INTRODUCTION

A number of oncological patients increase rapidly. Most of them have radiotherapy as a part of their treatment. Patients' treatment with high energy photons is very promising today. Therefore the requirements to deliver a prescribed dose to the certain target in modern radiotherapy are growing fast. Patient's treatment process is computerized, starting with the patient's data mapping and ending with the dose delivering to the patient. However errors can occur along the procedures chain. It is reported, that due to entering or replacing data occurring small mistakes can influence 15 % of treatments [1]. The prescribed dose errors larger than 5 %, may influence the clinical outcome of the treatment [2]. This might be prevented if treatment plans are checked before the first treatment. It is very important to notice, that the most of radiotherapy clinics are using different calculation algorithms for checking of dose plans, however the same input data are used for both: treatment planning system (TPS) and dose calculation algorithm. It is one

of the ways for the reduction of the errors in the dose plans. Nevertheless, the better way is to use independent calculation algorithms, which use the input data different from TPS algorithms for the dose calculations.

Despite of the fact, that the orthovoltage and cobalt units are going to be replaced by megavoltage linear accelerators, gamma therapy treatments are quite often used to treat patients in Lithuania. Summing up the situation – cobalt units are old and the planning systems that are used for this treatment planning are also very old. Due to these reasons possible errors may occur. To reduce the probability of possible errors, dose treatment plans should be checked before the treatment using different checking algorithm than the TPS algorithm is.

Completely independent from the TPS algorithm is presented in this work. Proposed algorithm includes calculation of the absorbed dose from photons scattered in the patient, calculation of the primary kerma transmission in the patient, calculation of the primary kerma variation in the air with collimator settings, and corrections for heterogeneities in the patient.

Radiotherapy Verification Program (RVP) was created and installed at one of the oncology hospitals of Lithuania for the testing of the algorithm in a clinical routine work, when Co-60 unit was used for the patient's treatment.

## II. MATERIALS AND METHODS

The absorbed dose  $D$  at the calculation point can be divided into its primary (subscript  $p$ ) and scatter (subscript  $s$ ) components. The total absorbed dose  $D$  can be written as:

$$D = D_p + D_s = \beta_p K_p + \beta_s K_s, \quad (1)$$

where  $K$  is kerma, and  $\beta$  is dose-to-kerma ratio.

Primary dose  $D_p$  is dose delivered from photons that have not interacted previously in the irradiated volume. Scatter dose  $D_s$  is dose delivered from photons that have interacted before at least once.

The scatter dose is nearly equal to scatter kerma [3], so we can consider that  $\beta_s = 1$ . In a case of clinical planning





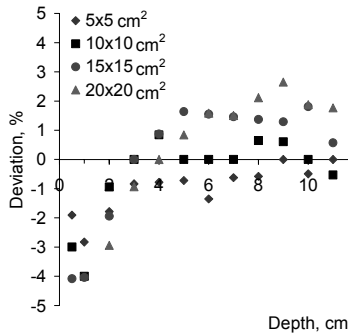


Fig. 2. Deviations between PDD and SPR as a function of the depth and the field size for Co-60 (SAD = 75 cm).

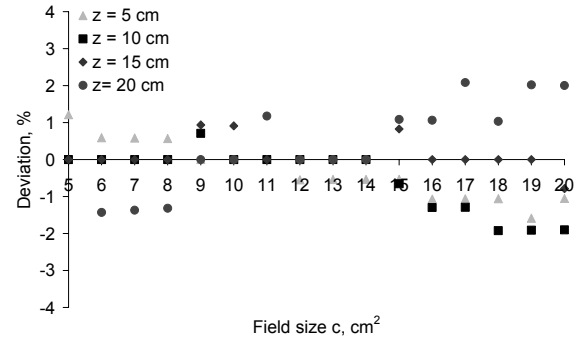


Fig. 4 Deviation between PDD and SPR as a function of the field size and the depth for Co-60 (SAD = 75 cm).

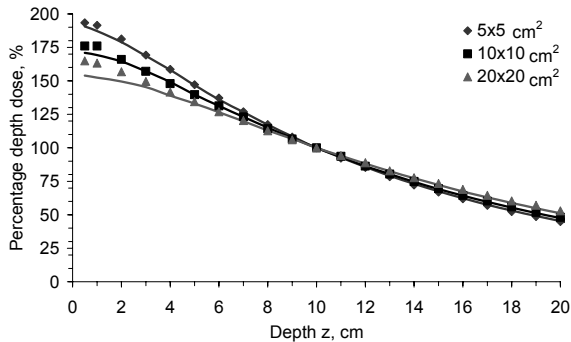


Fig. 3 Measured PDD (dots) and calculated using SPR method PDD (lines) as a function of field size (SSD = 75 cm). The PDDs are normalized at the 10 cm depth.

for Co-60 unit are shown in Fig. 2. The deviations are in 4 % range for the different depth  $z$  and field sizes. The largest deviations were observed in the large exposure fields for the case of small treatment depths. The deviations were found being about 2 % for the larger treatment depths. Medium treatment depths are dominant in the clinical practice and only for few localizations (breast, skin) the treatment depths are small.

Values of measured PDD were compared to those PDD values, which were obtained from the calculations using SPR method, and were used for the evaluation of the independent dose calculation method (Fig. 3). Normalization of the PDD curves at 10 cm depth, which corresponds to nearly all clinical cases, was performed prior to the evaluation.

The highest deviations for shallow depths and largest exposure fields were found. If we eliminate shallow depths, the disagreement between measured PDD and calculated PDD are from the range from 2.9 % to 1.3 %. (Mean disagreement – 0.3 %). Absorbed doses in the undersurface layer represent electrons generated in the exposed media. If

we would evaluate the electrons generated in the treatment head, it could be possible to evaluate doses in the shallow depths.

In real clinical practice most of patients are treated using source-axis distance (SAD) method. For this reason it was necessary to evaluate the time, which is needed for the delivery of the constant doses in the case of different field sizes under isocentric conditions, using independent calculation method (SPR). The evaluated time values were compared with a time, which was manually calculated from a simple formalism based on calculations of percentage depth dose (PDD) when delivery of doses was performed under the same treatment conditions as it was mentioned above. Dose deviations occurring due to the different time evaluation methods as a function of the field size and depth are shown in Fig. 4. It is to assume, that approximately all deviations lay within the interval of -2 % to +2 % for the different field sizes and different depths. It is good agreement of these two calculation methods. The largest deviation were found for the largest fields ( $> 17 \times 17 \text{ cm}^2$ ) and for the largest depths ( $z = 20 \text{ cm}$ ).

Due to rather small deviations ( $\pm 2 \%$ ) between the doses calculated by SPR and PDD methods at the isocentric conditions, the decision was made to implement the independent dose calculation program “Radiotherapy Verification Program” in the routine work for the checking of dose treatment plans. The deviation tolerances were increased to  $\pm 5 \%$ , to cover the deviation ( $\pm 3 \%$ ) of treatment planning system calculations and PDD manual calculations plus the deviation of ( $\pm 2 \%$ ) for the comparison of SPR and PDD methods. It was decided to perform manual checks of the dose plans using PDD calculation method, if calculations using SPR exceed 5 % tolerance. For the manual calculation the tolerance was decreased to  $\pm 3 \%$  and the requirement was set, that in the case, when the doses in the plan exceed manual calculation tolerance, the plan must be immediately recalculated.

### B. Practical application of the independent dose algorithm

The treatments for 87 patients were planned at the isocentric conditions by TPS and checked by RVP, using SPR method. 208 fields as total were checked. The investigation results were processed statistically. The distribution of the deviations obtained from the comparison of RVP and TPS is shown in Fig. 5. It was found, that the distribution of deviations is shifted towards a positive side of dose deviations. The deviations varied from -4 % to +8 %, with a mean deviation of 2.97 % and a standard deviation of 1.99 %. Results of the performed investigation are similar to those obtained from the investigation in which linear accelerator was used as a source of the patient's exposure. According to the data calculated for LINAC [8], the standard deviation was 2.05 %. It is to assume, that our deviation curve do not follow the form of normal distribution. The shift to the positive side of deviation could be due to the calculations, performed using the old 2D planning system. It was not possible to change the beam data in this system, while this data was programmed using the values, indicated in the old dose atlases of the Co-60 unit, that were derived long time ago. Comparison of measured PDD and calculated by dose planning system PDD showed a disagreement of about 3 %. After establishing of this fact, it was decided do not use the old dose planning system for the isocentric planning any more.

On the other hand, Fig. 5 indicates, that 12 % of plans are outside of RVP tolerance level. Almost all of these plans were recalculated due to the changes of physical depth to the radiological depth. Considering that 70 % of patient plans were calculated using this old treatment system, which was taken out of the operation, the number of the plans that are outside the tolerance level decreased to 4 %. The figure was approximately the same as for the LINAC,

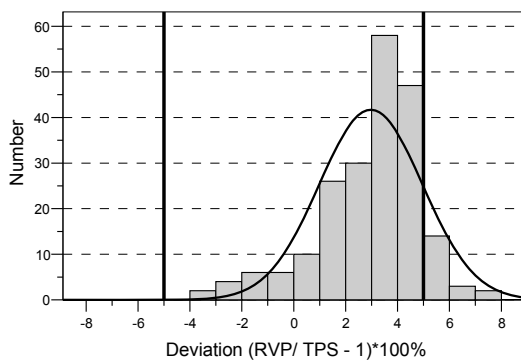


Fig. 5 The distribution of the deviation from comparison between RVP and TPS. The lines show values, that are outside of determined tolerance ( $\pm 5\%$ ).

where the number of the plans exceeding a tolerance level made 3.9 % [8].

## IV. CONCLUSIONS

Radiotherapy Verification Program which uses an independent calculation algorithm is a good and easy tool for the routine plan checking for gamma therapy treatment. Deviation between the doses calculated using PDD and SPR methods for the SSD treatment vary in the range of ( $\pm 2\%$ ) for the medium depths. Estimated deviation between measured PDD and calculated PDD using SPR was 3 %, as well as 2 % deviation was found between the doses calculated by PDD and SPR methods using SAD treatment method.

12 % of investigated dose plans exceeded the tolerance limits set for the independent checking with RVP, and needed manual recalculation using PDD method. This number was reduced to 4 % due to the decision to take this inefficient 2D planning system out of the operation.

## ACKNOWLEDGMENT

This work is supported by Lithuanian State Science and Studies Foundation.

## REFERENCES

- Valli M.C, Prina M, Bossi A et al. (1994) Evaluation of most frequent errors in daily compilation and use of a radiation treatment chart. *Radiother Oncol* 32:87-89
- International Commission on Radiation Units and Measurements (ICRU) (1999) Prescribing, recording and reporting photon beam therapy. ICRU Report no. 62
- Hannallah D, Zhu T C, Bjärnard B E (1996) Electron disequilibrium in high energy X-ray beams. *Med. Phys.* 23:1867-1871
- Bjärnard B E, Petti P L (1988) Description of the scatter component in photon-beam data. *Phys. Med. Biol.* 33:21-32
- Johnsson S A, Ceberg C P, Knöös T, Nilsson P (1999) Transmission measurements in air using the ESTRO mini-phantom. *Phys. Med. Biol.* 44:2445-2450
- International Atomic Energy Agency (2000) Absorbed dose determination in external beam radiotherapy. IAEA TRS No. 398
- Central axis depth dose data for use in radiotherapy. (1996) *Brit. J Radiol.*, Supplement 25
- Johnsson S, (2003) Development and Evaluation of an independent system for absorbed dose calculations in radiotherapy. Thesis for the degree of Doctor of Philosophy. Lund

Author: Jurgita Laurikaitienė  
 Institute: Oncology Hospital of Kaunas Medical University Hospital  
 Street: Volungių g. 16  
 City: Kaunas  
 Country: Lithuania  
 Email: jurgita.laurikaitiene@stud.ktu.lt

# Dosimetric Properties of Detectors for Quality Control of Intensity Modulated Radiotherapy

S. Plaude<sup>1</sup>, S. Popov<sup>1</sup>, A. Miller<sup>2</sup> and Y. Dekhtyar<sup>3</sup>

<sup>1</sup> Latvian Oncology Centre of Riga Eastern Clinical University Hospital, Riga, Latvia

<sup>2</sup> Vilnius University Oncology Institute, Vilnius, Lithuania

<sup>3</sup> Riga Technical University, Riga, Latvia

**Abstract** — Intensity Modulated Radiotherapy (IMRT) is extensively used for cancer patients treatment in modern Radiotherapy Clinics. Patient-related Quality Control (QC) is essential part of IMRT clinical implementation, as fluencies of Intensity Modulated (IM) fields has to be independently verified prior to delivery of the IMRT plan to the patient. In most cases, combination of ionometric and film dosimetry is in use for patient-related QC. The aim of this study was to evaluate volume-averaging effect of different ionization chambers used for ionometric dosimetry of the IMRT fields.

Examination of the response of three ionization chambers of different sensitive volumes was performed, using set of static and IM fields. Chambers were cross-calibrated in static field of size, sufficient to cover with homogeneous dose chamber with the largest sensitive volume. Dynamic IM fields with different dose gradients through chamber sensitive volume were designed. Fluencies of all IM test fields were verified by means of the film dosimetry. Measurements in the penumbra region of the static field were used to separate effects of dynamic dose delivery from the chamber averaging effect. Penumbra profile of the static field was acquired using all detectors under investigation.

Differences in the chambers response larger than 8% were found for measurements in high dose gradients both in penumbra of static field, and in gradient region of the dynamic IM field. Chamber of the largest volume had worst results in penumbra region of the static field and largest deviation from analytically reconstructed penumbra of IM fields.

**Keywords** — Intensity Modulated Radiotherapy, ionometric dosimetry, quality control.

## I. INTRODUCTION

Intensity Modulated Radiotherapy (IMRT) is a conformal radiotherapy technique. Using this technique it is possible to achieve a better dose conformity to the tumor volume and an increased sparing of normal tissues. IMRT is very complex technique and therefore it demands a high level of quality control both in the operation of the equipment and in the delivery of treatment to individual patients [1].

Ionization chambers are the preferred radiation detectors for measuring absorbed dose in IMRT fields. Absolute dose measurements using ionization chambers (ICs) is still the gold standard check for IMRT treatments [2]. Dose meas-

urements with ICs reflect the average dose value over their volumes [3]. Usually the beam central axis (CAX) is used for reference dose measurements, but that may cause large dose variations in IMRT fields. Consequently there will be reduced accuracy in the measurements.

A special interest is caused by penumbra and high dose gradient regions. Absolute patient related dosimetry in these regions can suffer from considerable high errors.

The aim of this work was to evaluate influence of spatial resolution of three different detectors widely used for relative dosimetry of the IMRT fields.

## II. MATERIALS AND METHODS

### A. Test field configuration

Static test field was designed (10 x 10 cm<sup>2</sup>). The point dose measurements were made at the CAX as well as at the ten points in the penumbra region of the field.

The dose in the same points was measured for the dynamic IM field. The dynamic IM test field was made so that in a middle part of the field (10 x 10 cm<sup>2</sup>) fluence was homogeneous but at each side there were regions with a high dose gradient like a penumbra region of the static field (Fig. 1).

In the IM test field, to get a dose profile like open static field, intensity was modulated using so called “sliding windows” technique (Fig. 2).

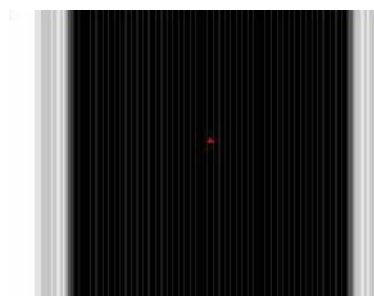


Fig. 1 Fluence of dynamic IM test field

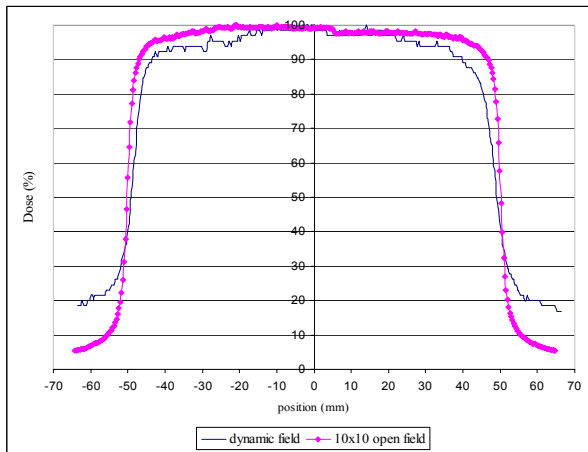


Fig. 2 Dose profiles of static and dynamic test fields acquired using film dosimetry

The farthest measurement point was located 55 mm from CAX. The penumbra region of both test fields was scanned with 1 mm step. All measurements were normalized to the CAX measurements in order to make a comparison between different detectors used in this study.

### B. In-phantom measurements

Measurements were made with linear accelerator (linac) Clinac 2100C/D (Varian Medical Systems, USA). This accelerator is a dual photon linac equipped with a multileaf collimator (MLC). The MLC has 40 opposed leaf pairs. Each MLC leaf is 6 cm thick made from wolfram with leaf transmission 1,5%-2% for 6MV photon energy. A width of each MLC leaf is 1 cm at the level of the isocenter.

Fields were irradiated with 6MV photon beam with dose rate 300 MU/min.

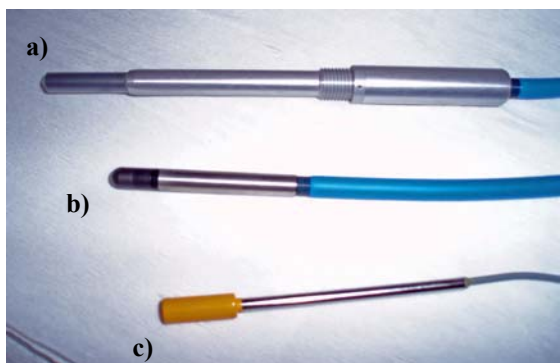


Fig. 3 Radiation detectors used for phantom measurements. a) "Farmer" type chamber; b) "Semiflex" ionization chamber and c) Scanditronix Wellöfer semiconductor p-type diode

Radiation beam incidence was perpendicular to the surface of a water phantom. The water phantom used in our measurements is Blue Phantom from Scanditronix Wellöfer. The Dose measurements were performed at a depth 5 cm and source-axis distance (SAD) 100 cm.

Three radiation detectors were used. PTW 30006 "Farmer" type chamber with its active volume 0,6 cm<sup>3</sup>; PTW 31002 "Semiflex" type IC 0,125 cm<sup>3</sup>; Scanditronix Wellöfer semiconductor p-type diode model PFD<sup>3G</sup> (Fig. 3). All of the detectors are of cylindrical geometry with diameter of active area 6,1 mm, 5,5 mm and 2,0 mm respectively [4].

ICs were positioned with their longitudinal axis parallel to the beam axis, while diode was positioned vertically. The diode used in this work was with inherent tungsten shielding.

### C. Film dosimetry

Dose profiles for static field as well as for dynamic field were acquired using film dosimetry. Films were irradiated in water equivalent phantom at a depth of 5 cm at the isocenter plane. Kodak<sup>®</sup> X-Omat films were used for the measurements.

Films were calibrated using method proposed by Childress et al. [5]. During measurements calibration film was exposed together with test films. The calibration field contains 9 dose levels (1,23 – 95,63 cGy). Areas with different dose levels were formed using dynamic MLC (dMLC) static sequence. Irradiated films were digitized using film scanner Vidar 16 VXR (Vidar Systems Corporation, USA) with resolution 75 dpi in 12 bit mode (point size 0,339 mm). Scanned films were stored in 12-bit TIFF format, for further processing using DoseLab 4.0 software [6]. Optical density image was converted to the dose image using calibration curve, acquired by means of calibration film.

## III. RESULTS AND DISCUSSION

Dose profiles, acquired in the 1 cm wide penumbra region of the static test field as well as IM dynamic field, are represented in Figure 4.

In the graph on the left (Fig. 4a), dose profiles for static test field are shown. As one can see, these dose profiles for static field represent a response of detectors in a penumbra region.

This graph also demonstrates that ICs with large volume have smeared signal in high dose gradients. More sensitive and thus more suitable for dose measurements in the penumbra region are semiconductor detectors and radiographic films.

From the dose measurements in the penumbra region of the static field one can also see, that the smallest detector is

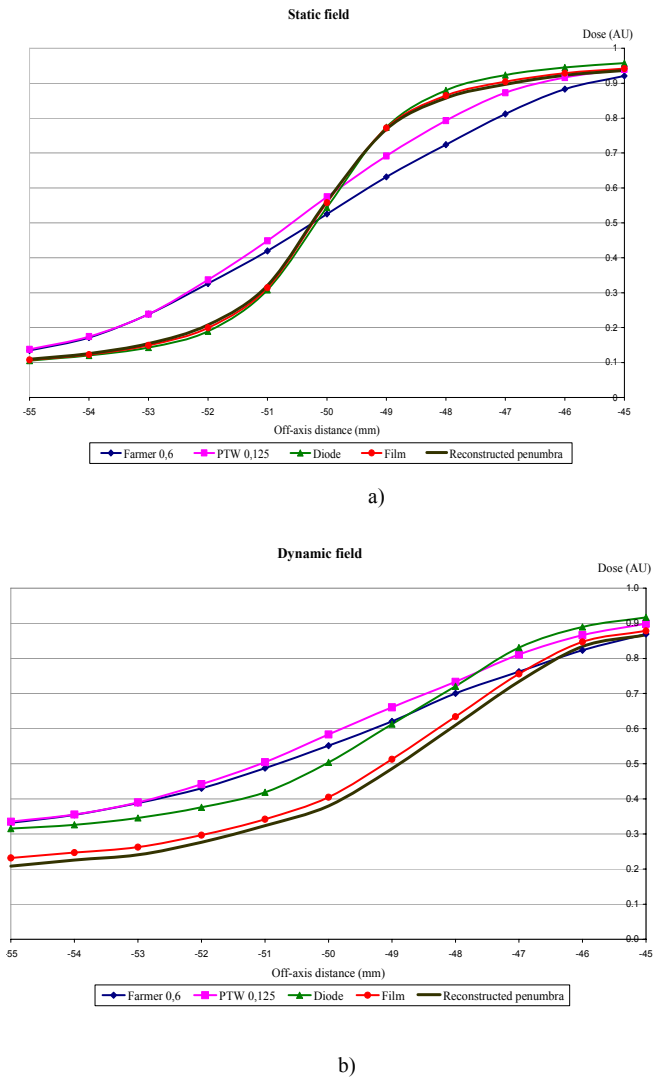


Fig. 4 Dose profiles in the penumbra region of a) static field and b) IM dynamic field acquired with different detectors.

more precise than both ICs. This graph shows that in uniform dose region, both low dose and high dose, all of the detectors, used in this study, have similar response.

Completely different situation is in the dynamic mode (Fig. 4b). Results show that only in a uniform and high dose region effect of spatial resolution of the detectors is lowest. In the high dose gradient and low dose region this effect is considerably high.

It is possible to extrapolate acquired data to a response of the detector with zero dimensions. In this way we can estimate deviation of each detector due to spatial resolution. In order to do this, the measurements results of all detectors at a single measured point were extrapolated with polynomial

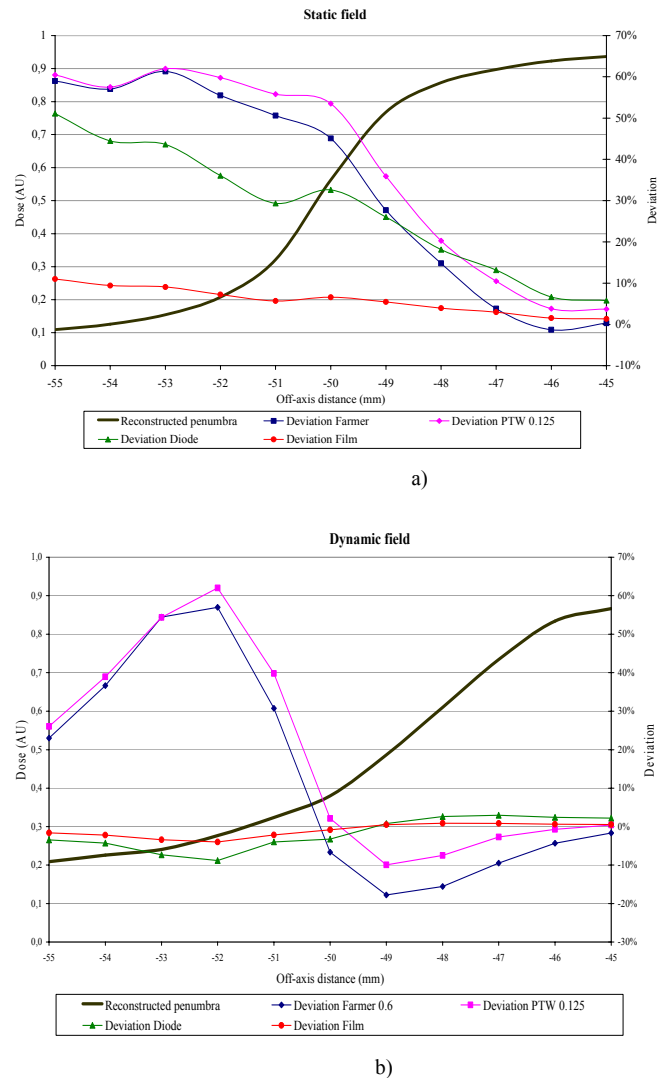


Fig. 5 Dose deviations from reconstructed penumbra for examined detectors for a) static field and b) dynamic field

regression to detector size with zero dimensions. Reconstructed penumbra represents results of polynomial regression analysis. Then, it is possible to calculate individual deviation for each detector under investigation (Table 1, Figure 5).

Figure 5 shows dose deviations from reconstructed penumbra for detectors under investigation for static field (Fig. 5a) and dynamic field (Fig. 5b). There is inconsistency in the response of detectors in areas with similar dose gradient in static and dynamic fields. On average Farmer type chamber shows greatest deviations from reconstructed penumbra. This can be partially explained by its large sensitive volume, which is in accordance to literature data [7, 8].

Table 1 Deviation from point detector

Off axis distance, mm	Static field			Dynamic field		
	Farmer 0,6	PTW 0,125	Diode	Farmer 0,6	PTW 0,125	Diode
-55,0	59%	60%	51%	23%	26%	-3%
-54,0	57%	58%	44%	37%	39%	-4%
-53,0	61%	62%	44%	54%	54%	-7%
-52,0	55%	60%	36%	57%	62%	-9%
-51,0	51%	56%	29%	31%	40%	-4%
-50,0	45%	54%	33%	-7%	2%	-3%
-49,0	28%	36%	26%	-18%	-10%	1%
-48,0	15%	20%	18%	-16%	-8%	3%
-47,0	4%	10%	13%	-9%	-3%	3%
-46,0	-1%	4%	7%	-4%	-1%	2%
-45,0	0%	4%	6%	-2%	0%	2%

Nevertheless one can see deviations of opposite sign in dynamic field as compared to static field for both ionization chambers.

#### IV. CONCLUSIONS

A correct modeling of the beam penumbra is especially important in IMRT because IM beam may have areas of high dose gradient anywhere in the field not only at the boundaries [9].

Farmer type IC is not suitable for IMRT field measurements due to its relatively large volume.

Both ICs have shown great difference of dose measurements in the region of high dose gradient. This can be partially explained by its large sensitive volume, but nevertheless there exist deviations of opposite sign in dynamic field as compared to static field for both ionization chambers. This fact could not be fully explained at present moment and requires additional investigation.

#### REFERENCES

1. Sanchez-Doblado F, Capote R, Rosello J V et al. (2005) Micro ionization chamber dosimetry in IMRT verification: Clinical implications of dosimetric errors in the PTV. *Radioth Oncol* 75:342–348
2. Metcalfe P, Kron T, Hoban P, (2007) *The physics of radiotherapy X-rays and electrons*. Medical Physics Publishing, 2007. p.705
3. Stasi M, Biaiotto B, Barboni G et al (2004) The behavior of several micro ionization chambers in small intensity modulated radiotherapy fields. *Med Phys* 31:2792-2795
4. Technical Data, PTW-Ionization Chambers, PTW-Freiburg
5. Childress N.L, Dong L, Rosen I.I, (2002) Rapid radiographic film calibration for IMRT verification using automated MLC fields. *Med Phys* 29:2384-2390
6. DoseLab software homepage, Internet, <http://www.doselab.com>
7. Low DA, Parikh P, Dempsey JF et al (2003) Ionization chamber volume averaging effects in dynamic intensity modulated radiotherapy beams. *Med Phys* 30:1706–1711
8. Khan F.M, (2003) *The physics of radiation therapy*. Lippincott Williams&Wilkins, 2003. 560 pp.
9. Escude L, Linero D, Molla M et al (2006) Quality assurance for radiotherapy in prostate cancer: point dose measurements in intensity modulated fields with large dose gradients. *Int J Radiat Oncol Biol Phys* 66:136-140

Author: Sandija Plaude  
 Institute: Latvian Oncology Centre of Riga Eastern Clinical University Hospital  
 Street: 4, Hopikrata str.  
 City: Riga  
 Country: Latvia  
 Email: sandija.plaude@aslimnica.lv

# Considering Dose Rate in Routine X-ray Examination by Thermoluminescent Dosimetry (TLD) in Radiology units of Mazandaran Hospitals

S.A. Rahimi<sup>1</sup>

<sup>1</sup> Mazandaran University of Medical Sciences, Department of Medical physics, Faculty of Member, Sari, IRAN

**Abstract** — Concerning the importance of radiography techniques for diagnosis of disease and considering daily application and emerging new techniques in radiography from one hand and potential misuse of radiation and exposure to patients and personnel from other, it seems necessary the measure the amount of received radiation in current radiography procedures. The aim of this research is to determine the surface dose to patients in chest and skull radiography procedures in the hospitals of Mazandaran medical science university and compare those to given standards for such examinations from national and international recommendations.

The study was based on the procedures, performed at six x-ray machines in six hospitals of the medical science university. Totally 120 patients with normal BMI, undergoing prescribed chest and skull examinations were involved. The exposure parameters, such as kVp – mAs product, film-screen combination and overall procedure setup at the all 6 x-ray machines were similar, thus provided unbiased evaluation of the surface dose. Surface dose was measured, using LiF thermoluminescent dosimeters (TLD). TLD after calibration was attached to the back and front skin surface of patients and after exposure TLD5 radiance was read with TLD reader.

The average surface dose, measured for patients undergoing examinations of posterior – anterior view for pectoral, profile view for chest and posterior – anterior or anterior – posterior view of skull and profile view of skull where 0.51 , 3.36 , 7.25 and 7.59 mGy, respectively. These figures exceed recommended standards.

To decrease patient surface dose, such measures, as periodic and continuous on – the – job education as well as supervision could increase technical and technological knowledge and rise awareness about radiation protection issues, thus improving the situation in hospitals.

**Keywords** — Radiography Standards, Radiography, Thermoluminescent Dosimetry, TLD.

## I. INTRODUCTION

Radiology is one of the important therapeutic and medical diagnosing ways that effective utilization of this technology was done along with definite and organized ways. Considering current protective situation and comparing it with valued standards (<sup>1</sup>ICRP, <sup>2</sup>NCRP, <sup>3</sup>NRPB) is a key

factor to ensuring and profitability of this technology (1). Radiography units are of basic and expensive units in every medical center. It could be said that investment in this part is more than all other parts. It is very expensive to protection proceeding against ionization ray, ionizing air ventilation and providing need full physical space for different radiography machines, particularly the biologic traces of the radiation are at the center focus of radiography personnel's, patients and their companions(2).

Statistics show that more than 80% of clientele to hospitals need to the kind of radiography (3). Disturbance in using trend of radiography machines result in giving unsuitable radiography report in one hand and in the other hand incorrect diagnosing and consequently the health of patients subject to danger (3), Additionally, about taking doses by patients, particularly in radiology units at the highest level of researching studies for their current importance and consider this in different aspects (4,5). Resultant radiation from diagnostic radiology machines could be have unnatural symptoms on radiology personnel's , particularly when they don't observe the security points and international commissions recommendations of protection against radiation (ICRP) and the problems regarding to machinery quality control in these units and result in destructive effects of radiations on personnel's and clientele(6). Precision measuring and continents and personnel's and comparing it with published information's and data by ICRP and Britain radiologic protection national board protocol (<sup>4</sup>DRL)

About the rate of taking dose in a year, taking dose in a year can significantly help about keeping health of radiography patients and personnel's and decreasing effects resultant of radiation(7). Iran in one of a few countries that didn't give perfect and specific information in this case and because of noncompliance of necessary considerations doesn't have data bank. Although these measure in some provinces, but complete information's were not presented about the measurements and the rate of taking dose, especially inpatients. There fore, it is not impossible to comparison of taking dose by patients to international standards in Iran.

So, lack of information and data bank show the importance of study about it. Result of measurements can affirm

<sup>1</sup> International Commission on Radiological Protection

<sup>2</sup> National Council on Radiation Protection

<sup>3</sup> National Radiological Protection Board

<sup>4</sup> Diagnostic Reference Level

the importance of complete protective considering against radiation to decreasing the destructive effects of radiations in radiology personnel's and patients.

Aim of this study is investigation of the taking dose rate in patient's skin in radiography techniques in chest and skull in Mazandaran medical science university hospitals to getting the necessary information about taking radiation and giving it to respective organizations

## II. MATERIAL AND METHODS

This is descriptive –sectioning study that considered six x-ray devices in six hospitals in Mazandaran medical science university (according to information they had the most clientele during 1385). the program in determining the reference dose was according to the national radiological protection board in Britain (DRL) 1992 (8). In this protocol was given complete information about selecting dosimeters of termluminescent , calibration of termluminescent dosimeters, the way of selecting patients, proposed radiography for their reference dose and analyzing way of data(8).

So, the numbers of sample considered 120 people according to national radiological protection board in dependability 95 percent. In every studied university were selected 20 patients with normal BMI (Body mass index)(20 – 25) and the age about 40 years – old (standard deviation  $\pm 10$  years). Because the severity of radiation that have an ideal effect on negative depends on the thickness and dimensions of body and these two factors are dependent of the patient weight, so, in this study the patients were selected both sex with the average weight of  $65 \pm 10$  kg and the ways of selecting patients according to their weight was done along with national radiological protection board instruction (8).

According to resulted information's in 1385, the most clientele to radiology units of Mazandaran medical science hospitals were tested by one of current techniques of radiography – experimentally such as posterior – anterior and lateral view of chest and skull. Five patients were tested to measuring the rate of surface dose in every foregoing technique. So, 20 patients in each hospital were selected for these four techniques.

It is noticeable that the composition situation, m as, kvp, kind of amplifier sheets, device daily work and the way of using x-ray device in these centers close in possible to independence of measuring surface dose to foregoing subjects.

To measure surface dose was done thermo luminance dosimeter. The kind of suitable dosimeter was Lif (TLD-100) because was equal with tissue in atomic number. And have many sensitivity and its dimensions is small (1\*3\*3 mm) and response of this dosimeter in low energy is bather than

the other. TLD's response to radiation depends to the different factors and it can change when a factor changes. So' TLD's chips and reader system should be calibrated. Calibration in this study was done in 3 steps and all the TLD chips were aniline before calibration (9).

For this purpose, we used two – steps aniline standard way. In first step, each TLD chip, which have a specific number, was set on a metal sheep according to its numeration and was left for an hour in 400 C0 and at the second step was closed the door of oven after reaching to 80 C0 and was leaved in this temperature for 24 hours

After that the oven was turned off and the TLD chips were cooled at the room temperature. According to two-step aniline standard way, cooling chips was done slowly in two steps.

At the third step, because similar TLD chips don't have a similar response against getting radiations, was determined ECC(Element correction coefficient) for each TLD chips. For this reason, the TLD's were leaved on a sheet in several close lines according to their numeration and were settled under radiation by the radiology device in radiology units.

The quantity of radiation in this step was not important and was attempted all TLD chips would at the center of radiation field with the minimum distance each other to preventing the effect of anode in the quantity of radiation. Then each TLD was read by TLD reader. We specified this with (Qi).

It was averaged for all Qi (Q1) and was calculated their standard deviation (SD). TLDs that their reading was deleted. And were averaged again and then the ECC of each crystal was calculated by formula (1).

$$ECC_i = Q/Q_i \quad (1)$$

According to the way of doing this study to measuring TLD. They were transmitted to radiography units after calibration. Dosimeter was installed on the back and the skin of patients and all TLDs were read by TLD reader after getting radiation and the results were received.

140 TLD chips were used in this study and 20 TLDs were kept beside the other as a witness of environment dose (field radiation) in a specific box and weren't settled under radiation. In each reading, the average of TLD chips reading as an environment field radiation declined from the installed TLD's reading on the back and skin of patients to preventing the effects of field radiation in final results of the surface dose in examined patients.

These results also showed the maximum getting dose were for the devices of hospitals in Imam Sajjad (Ramsar city) and Shohada (Noshahr city). In Table 2 have been shown the surface dose extents in patients for different maximum kilo voltage (70-105 kvp).



### III. CONCLUSIONS

The result of this study of determining the patients surface dose in radiology units of Mazandaran Medical Science University hospitals showed that getting surface dose by patients and also their substitute dose correspond with countries such as China and Tanzania that according to the earned information had the most clientele in last year (10,11,12). But the results were slightly higher there the extents in the United States, Greece, Nigeria and Bangladesh (12, 13). Averaged result of skin surface dose in these countries was 0.25 for chest posterior – interior view, 0.61 for lateral view of chest, 1.69 for interior – posterior and posterior in skull, and 1.14 for lateral view of skull. Comparison these rates to the results were shown in Table 2 we see that calculated skin surface dose in this study is slightly higher than these results, as the maximum getting dose by the patients in foregoing techniques respected the devices of Imam Sajjad (Ramsar city) and Shohada (Noshahr city) hospital. Of course, it should be said because the rates of skin surface dose are different according to the different maximum kilo voltage (KVP), these diversities may be consequence of using the different maximum kilo voltage. Because the x-ray generators which work more because of raising the number of radiographies in each day may increase the calculated surface dose, so the centers with the same volume work were considered to preventing the rais-

ing of surface dose in each day because of increasing clientele (14,15,16).

But comparison the result of this study with the determined standards by international organization showed that all calculated surface dose was higher than the authorized doses by Britain national radiological protection board (DRL) (8, 17, 18, 19).

Executing the quality control programs and the quality guarantee is necessary in every six month, because the excessive dose in patients will raise yearly accumulation dose and as a result will increase the risk of affecting to cancers and the problems consequence of radiation in population. According to ICRP recommendation, the maximum allowable dose should not be higher than 1(msv) to preventing possible emergence of accessing sickness (20, 21, 22).

Related to surface dose or getting dose by patients, several reports yearly were represented by NRPB, ICRP and NCRP.

Quality control and decreasing getting dose by patients is very important in most countries. The results showed to decreasing the surface dose in patients should execute periodic and continues on- the-job educations addition to improving radiography devices and also achieve to higher level of technical technological and protection knowledge with continues supervision and consideration to maintaining the health of radiography personnel's and patients.

Table 1 table specification

Hospital name	Posterior anterior view of chest	Lateral view of chest	Anterior posterior or posterior anterior view of skull	Lateral view of skull
Imam ali (amol)	0.33 ± 0.12	1.9 ± 0.12	3.19 ± 0.27	1.92 ± 0.57
Imam Khomeini (sari)	0.53 ± 0.13	1.61 ± 0.81	2.36 ± 0.68	1.69 ± 0.14
17 shahrivar (amol)	0.59 ± 0.45	1.25 ± 0.49	2.69 ± 0.37	1.75 ± 0.36
Imam reza Amol	0.72 ± 0.66	1.27 ± 0.63	3.57 ± 0.31	2.03 ± 0.17
Imam sajad Ramsar	0.75 ± 0.57	1.46 ± 0.28	3.85 ± 0.19	2.01 ± 0.47

Data: average ± standard deviation

Table 2 Surface skin patients in different radiography examinations from chest and skull view according to mGy for maximum kilo voltage (70 –105 kvp) with normal BMI and it's comparison to standard National Radiological Protection Board (DRL).

Type of radiography test	Surface dose Average ± standard deviation e	Maximum and minimum of surface dose	National Radiological Protection Board (DRL)
Anterior posterior view of chest	0.56 ± 0.35	0.19-1.32	0.15
Lateral view of chest	1.4 ± 0.47	0.80-2.34	0.75
Anterior posterior or posterior anterior view of skull	3.08 ± 0.44	1.68-4.04	2.3

### ACKNOWLEDGMENTS

I thanks to dear professor SHARAFI and Vice – Chancellor of Mazandaran Medical Science University who undertake this research expenses.

### REFERENCES

1. Muhogora WE, Nyanda AM, Kazema RR. Experiences with the European guidelines on quality criteria for radiographic images in Tanzania. *J Appl Clin Med Phys.* 2001;2(4):219-226.
2. Almen A, Tingberg A, Mathson S, et AL. Influence of different technique factors on image quality of lumbar spine radiographs as evaluated by establisher CEC image criteria. *Br J Radiol.* 2000;73(875):1192-1199.
3. Archer BR, Wagner LK. Protecting patients by training physicians in flouroscopy radiation management. *J Appl Clin Med Phys.* 2000.1(1):32-37.
4. Krutz C, Czapp W, Jrampe I, Leppke R, Klose KJ. X-Ray taken by radiologists influence on a continuous quality improvement process. *Rojo Fortschr Geb Rontgenstr Neuen Bildgeb Verfahr.* 2000; 172(4):391-396.
5. BruceI.Reiner. SCAR Radiologic technologist survey. 2000. <http://WWW.scarnet.org>.
6. Gogos KA, Yakoumakis EN, Tsalafoutos IA, Makri TK. Radiation dose consideration in common peadiatric X-ray examination. *Pediatr Radiol.* 2003;33(4):236-240.
7. Ember H. Radiation dosimetry. Cember H. Introduction to health physics. 1 Ed. New York: Pergamon Press; 1993. p. 135-76.
8. National protocol for patient dose measurements in diagnostic radiology. Prepared by dosimetry working party of the institute of physical sciences in medical publication 1992.
9. Benini A. Medical radiation exposure, IAEA regional workshop radiation and quality assurance in diagnostic radiology. Nicosia Cyprus. 1993; 14-25.
10. Benini A. Quality control measurements in diagnostic X –ray. IAEA Vienna. 1992; 100.
11. Benini S. Computer- assisted quality assurance for radiographic equipment. *Med phys.* 1980; 7(4):386-9.
12. Hourdakis CJ. A national survey: performance of medical x- ray systems in Greece. *Radiat protect Dosim.* 1999;81(3): 205-19.
13. United Nations scientific committee on the effects of atomic radiations Sources. Effects of ionizing radiation. New York: United Nations; 2000.30.
14. Declan R, Kyrio J. Radiation protection in interventional radiology. *Clin Radiol.* 2001; 56:99-106.
15. Faulkner k. Introduction to constancy check protocols in fluoroscopic systems. *Radiat prot Dosim.* 2001; 94(1-2):65-8.
16. Begum Z. Entrance surface, organ and effective dose for some of the patients undergoing different types of X-ray procedures in Bangladesh. *Radiat Prot Dosim.* 200 I; 95(3): 257-62.
17. Zhll XR. Entrance surface dose measurements for in vivo diode-dosimetry: comparison of correction factors for two types of commercial silicon diode detector. *J Appl Clin Med Phys.* 2000; 1(3): 100-7.
18. Li LB, Wang JP, Yu XR, et al. Medical radiation usage and exposures from medical X-ray diagnosis in shandong province of China. *Radiat Prot Dosim.* 2001; 93: 261-6.
19. Michel R, Perle Se. Effective dose equivalent estimates in diagnostic radiology with single dosimetry. *Health Phys.* 2002; 79: ] 7-19.
20. Ogunseyinde AO, Adeniran SA, abed RI, et al. Comparison of entrance surface doses of some X-ray examinations with CEC reference doses. *Radiat Prot Dosim.* 2002; 98: 231-4.
21. Papadimitriou 0, Perris A, Molfetas MG, et al. Patient dose, image quality and radiographic techniques for common X-ray examinations in two Greek hospitals and comparison with European guidelines. *Radiat Prot Dosim.* 2002; 95: 43-8.
22. Muhogora WE, Nyanda AM. The potential for reduction of radiation doses to patients undergoing some common X-ray examinations in Tanzania. *Radiat Prot Dosim.* 2002; 94: 381-4.
23. Rahimi S.A, Sarkar S, Abolhasani M.J, Salar S. Design of a computer software for calculation of required barrier against radiation at the diagnostic x-ray units. *Journal of Mazandaran University of Medical Sciences* 2005;15(47):90-97.
24. Rahimi S.A, Salar S. Study on the Performance of Recommended Standards in the Diagnostic Radiology Units of the Hospitals Affiliated to the Mazandaran University of Medical sciences. *Journal of Mazandaran University of Medical Sciences* 2006;15(49):65-72

Corresponding author address:

Author: Seyed Ali Rahimi  
 Institute: Faculty of Health  
 Mazandaran University of Medical Sciences  
 Street: Kilometer 18 KHAZARABAD Road  
 P.O.BOX 48175-1553  
 City: Sari  
 Country: Iran  
 Email: rahimi201@yahoo.com

# Cost-Effectiveness of the Positron Emission Tomography with [<sup>18</sup>F]-fluorodeoxyglucose for the Staging and Management of Lung Cancer in Russia

A.V. Khmelev<sup>1</sup>, S.V. Shiryaev<sup>1</sup>, B.I. Dolgushin<sup>1</sup>, I.D. Gotsadze<sup>1</sup>, I.P. Aslanidi<sup>2</sup>, O.V. Mukhortova<sup>2</sup>, S.E. Evdonin<sup>3</sup>

<sup>1</sup>N.N. Blokhin Russian Cancer Research Center RAMS/Department of Radionuclide Diagnostics, Moscow, Russia.

<sup>2</sup>A.N. Bakulev Scientific Center for Cardiovascular Surgery RAMS/Department of Nuclear Diagnostics, Moscow, Russia.

<sup>3</sup>Institute of Medical Physics and Engineering, Moscow, Russia.

**Abstract** — Two decision strategies for selection of candidates for non-small cell lung carcinoma surgical cure from the group of 79 patients were compared: one employing computer tomography (CT) along (strategy A) and one employing CT + positron emission tomography (strategy B). The B strategy in decision tree has showed higher cost and a gain of the patient life expectancy (LE). The estimated LE gain of B strategy versus A strategy is 0,327 year. The incremental cost-effectiveness ratio is 250 Euro/life year saved/patient.

**Keywords** — cost-effectiveness, lung cancer, positron-emission tomography.

The CE value of the PET for lung cancer had not been studied in Russian clinical centers. Results of the studies performed in other countries can not be used for the mentioned above purpose because of differences in healthcare systems, epidemiology, prevalence of disease and cost data.

The aim of this study is to compare the CE of the standard imaging technique with and without FDG PET in the staging and management of NSCLC from Russian healthcare perspectives. Another aim is to demonstrate the decision analysis using for quantitative estimation of the role of any diagnostic imaging technique in the management of disease.

## I. INTRODUCTION

At present lung cancer continues to be a major health problem worldwide. In Russia mortality rate from this disease is more than 60,000 (~20% of cancer mortality). The surgical resection is a standard treatment method of the non-small cell lung carcinoma (NSCLC) from patients with not established distant or extended lymph metastasis. Because of significant mortality and cost associated with this method it is important to select accurately the potential surgical candidates.

In many clinical cases the results of the computer tomography (CT) examinations are not determined for NSCLC staging and require using of the additional and more invasive diagnostics studies. Therefore apply CT only often is not enough for the management of patients. Last time the method of whole-body positron emission tomography (PET) with [<sup>18</sup>F]-fluorodeoxyglucose (FDG) is often used for diagnostics and staging of NSCLC [1, 2]. PET sensitivity and specificity is essentially higher as compared with CT [3-5]. Apart from PET is unique method for detection of distant metastasis which is unsuspected after conventional imaging.

Earlier the superior accuracy of the PET versus the CT for the staging of NSCLC and the cost-effectiveness (CE) of the PET with FDG (clinical effectiveness and cost effect) in the management of this disease was shown [7-10]. The clinical evidence regarding economic impact of PET introduction in Russia is currently absent though it would be actual for the new health programs and technologies development today.

## II. MATERIALS AND METHODS

The group of 79 patients with NSCLC established by histological analysis was included at present study. Two decision strategies for selection of candidates for surgical cure were compared: one employing CT only (strategy A) and one employing CT and PET (strategy B). The strategy A is a conventional procedure including NSCLC diagnostics (roentgenoscopy study and fibrobronchoscopy with morphology confirmation of disease), resectability assessment of the primary pulmonary nodule with undergoing of the chest CT examinations as well as excluding of the tumor process generalization (ultrasound (US) of abdominal cavity organs and neck-supraclavicular zones, skeletal scintigraphy (SG), brain CT). The patients with established CT-positive lymph node involvements were undergone for chemotherapy (ChT) or combined treatment (neoadjuvant chemotherapy+surgical cure). Patients with CT-negative results were undergone for surgical cure (SC) or combined cure (CC).

In B strategy all patients (including those with distant metastasis) underwent whole-body PET diagnostics with FDG. Patients with PET-positive results went on to have a transbronchial puncture biopsy (BP) with morphology examination to confirm that they are not a surgical candidates. Patients with PET-negative results were undergone for SC or CC. In result of the additional diagnostic exams and/or morphology verification of the nodule involvements

SC (or CC) and ChT were prescribed for a patients with false-positive and false-negative results respectively.

Quantitative modeling with using of so called decision trees had been performed for assessment of the clinical effectiveness and cost of A and B strategies apply for the NSCLC staging. We used decision-tree sensitivity analysis (described elsewhere [8-10]) based on current clinical data of N.N. Blokhin Russian Cancer Research Center [1] for a patients with pulmonary cancer (NSCLC, stages I-IV). The model disease prevalence (0.327 [9]) refers to the prevalence of surgically unresectable disease in the group of diagnosed patients with established NSCLC.

Decision models of the protocols established from quantitative decision analysis [8] and local practice [1] were structured with two outcomes (expected costs and life expectancy (LE)). Decision tree models were constructed with two competing strategies (CT + PET vs. CT along). The medical literature was surveyed to determine a mean and range for all variables of interest (prevalence, sensitivity, specificity, mortality, life expectancy).The identified data are listed in the Table 1. Applied costs of a diagnostics procedures and cure (EUR) are average for Moscow region.

Table 1 Baseline and range of variables used in the analysis

Variable	Baseline	Range	Reference
Prevalence	0.327	0.28-0.38	[9], [10]
CT			
Sensitivity	0.61	0.5-0.71	[3]
Specificity	0.79	0.66-0.89	[3]
Mortality	0.000025	0-0.0005	[9]
Cost (2 studies)	153		
PET			
Sensitivity	0.9	0.67-0.91	[3]
Specificity	0.91	0.82-0.96	[3]
Mortality	0	0	[9]
Cost	545		
Biopsy			
Sensitivity	1.000		[9]
Mortality	0.007		[9]
Cost (BP +US+SG)	161		
SC			
Mortality	0.03	0-0.2	[9]
Cost	3 150		
CC			
Mortality	0.03	0-0.2	[9]
Cost	3 690		
ChT			
Cost	475		
LE (years)			
SC, N1/N0, M0	4.5		[11]
SC, N2/N3, M0	1.8		[12]
SC N0-3, M1	0.5		[11]
ChT N2/N3, M0	1.8		[11]
ChT N0-3, M1	0.5		[11]

Expected costs and LE, as measured by life year saved (LYS) were estimated for each strategy. Then the incremental CE ratio (ICER) [5] was calculated to compare these two strategies and to determine the most effective one.

$$ICER = (Cost_A - Cost_B) / (LE_A - LE_B) \tag{1}$$

The ICER indicates the cost of one patient life year saved as a result of additional PET-diagnostics using, and it is expressed as a units of Euro per LYS.

### III. RESULTS

Effectiveness of the PET using for NSCLC diagnostics was determined on two aspects: changing of this disease management and ICER value acceptability. In the Table 2,3 the results of the NSCLC clinical management and staging obtained on two strategies are shown.

Figure 1 depicts a decision tree that directly compares A and B strategies. In this tree PET-positive and CT-positive refer to positive for metastasis. In B strategy all patients have CT imaging as well to insure proper anatomical information to the surgeon and diagnostic exams to exclude generalization of the tumor process.

Analysis of the tree showed the gain of expected cost of B strategy as compared with A strategy ~ on 2,5%. Corresponding costs of A and B strategies calculated using data of the Table 1-3 and Fig.1 were 3215 Euro and 3295 Euro respectively.

However the cost increasing entailed LE value gain. The estimated LE gain for B strategy as compared with A strategy is 0,327 year. The ICER value as calculated using (1) is about of 250 Euro/LYS/patient However the cost increasing entailed LE value gain. The estimated LE gain for B strategy as compared with A strategy is 0,327 year. The ICER value as calculated using (1) is about of 250 Euro/LYS/patient

Table. 2 Results of the disease staging and management on A strategy

Treatment modality	Stage of disease	Quantity of patients	%
ChT	M1	5	6.33
	N2/N3	11	13.92
SC	N1/N0, M0	29	36.71
CC	N2/N3	34	43.04

Table. 3 Results of the disease staging and management on B strategy

Treatment modality	Stage of disease	Quantity of patients	%
ChT	M1	9	11.39
	N2/N3	19	24.05
SC	N1/N0, M0	22	27.85
CC	N2/N3	29	36.71

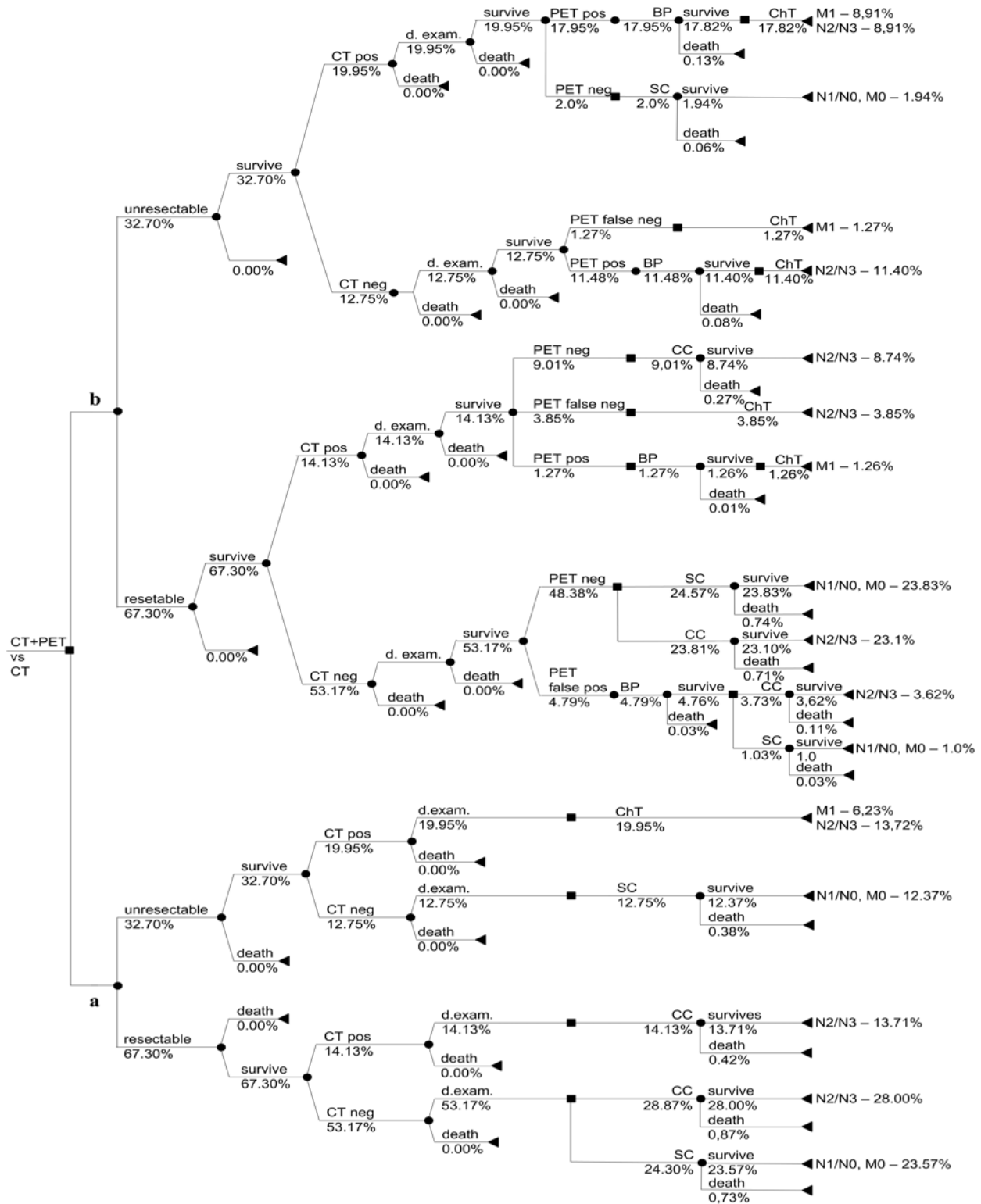


Fig. 1 Decision tree (a) of the algorithm with conventional (CT) staging (strategy A) and (b) of the algorithm with additional FDG-PET (strategy B). A squares represent a decision nodes, circles are change nodes and triangles are terminal nodes: neg.-negative, pos.-positive

Table. 4 Results of the stage and management changing after PET performance for the group of 79 patients

Strategy A		Strategy B		LE <sub>B</sub> - LE <sub>A</sub>
Q-ty	Stage / Planned management	Q-ty	Restaging / Corrected management	
5	N0 / SC	5	M1 / ChT	0,001
5	N1 / SC	5	N3 / ChT	0,003
2	N1 / SC	2	N3 / ChT	0,001
1	N2 / CC	1	M1 / ChT	0,000
1	N1 / SC	1	M1 / ChT	0,000
3	N1 / SC	3	N3 / CC	0,000
3	N0 / SC	3	N1 / SC	0
5	N2 / CC	5	N0 / SC	0,171
1	N2 / CC	1	N1 / SC	0,034
2	M1 / ChT	2	N1 / SC	0,101
1	M1 / ChT	1	N3 / ChT	0,016

IV. DISCUSSION

Compared with baseline strategy, the PET introduction changed clinical management from 37% of patients. The strategy B reduced the number of patients directed for SC and CC (for 7 and 5 people respectively) from the patient group in which PET scan had shown M1 or N2/N3 in mediastinal lymph nodes. At the same time the number of patients to whom was planned ChT was increased on 12 people (Table 2,3). The gain of LE for 0.327 LYS is the result of improved staging achieved mainly by the disease stage decreasing because of more high PET sensitivity and specificity as compared with CT (Table 1).

The calculated ICER value of 250 Euro/LYS indicates that the national healthcare system spent about 250 Euro for one patient LYS. Extra cost of 250 Euro for one life year saved is by far lower then internationally used threshold of about 50 000 Euro/LYS [7] and could be tolerated for economic situation in Russia.

Some quantitative differences of established in this paper parameters (LYS, ICER) from published earlier data can be explained by differ costs of medical procedures in Russia and in those countries where such studies were carried out or by differ stages limitations in involved groups of patients. Such groups included patients with benign and malignant tumors (415 Euro/LYS, 0,68 year [5]), with respectable tumors of I, II, IIIa stages (143 Euro/LYS, 0/014 year [7]), with tumors of I, II, IIIa, IIIb stages (1038 Euro/LYS, 0,607 year [10]), with respectable and unresectable tumors of I – IV stages (- 1455 Canadian dollars/LYS, 0,008 year [4]).

V. CONCLUSION

Strategy A is dominated by strategy B, which is more expensive, but also more effective. As a preliminary result, our analysis confirms that in Russia the introduction of the PET examinations for the NSCLC clinical management is a cost-effective and result in higher diagnostic accuracy and gaining of LE for 0,327 year at an annual cost of 250 Euro.

REFERENCES

- Gotsadze I D, Davydov M I, Polotskiy B E et al. (2007). Positron emission tomography in the management of non-small cell lung cancer. Journal of N N Blokhin Cancer Research Center RAMS 18:31-37
- Khmelev A V, Shiryaev S V (2004) Positron emission tomography: physical and clinical aspects. Medical radiology and radiation safety 5: 52-82.
- Gould M K, Kushner W G, Rydzak C E et al. (2003) Test performance of positron emission tomography and computed tomography for mediastinal staging in patients with non-small cell lung cancer: a meta-analysis. Ann Intern Med 139:879-900.
- Scott S J, Hollett P D, Mathews M. et al.(2004) Cost-effectiveness of positron emission tomography for non-small cell lung carcinoma in Canada. Med Sci Monit 10: MT73-80.
- Mansueto M, Grimaldi A, Torbica A et al.(2007) Cost-effectiveness analysis in the clinical management of patients with known or suspected lung cancer: [18F]-fluorodeoxyglucose PET and CT comparison. Q J Nucl Med Mol Imaging 51: 224-234.
- Valk P E, Pounds T R, Hopkins T M et al. (1995) Staging non-small cell lung cancer by whole body positron emission tomography imaging. Ann Thorac Surg 60: 1573-1581.
- Dietlein M, Weber K, Gandjour A et al. (2000) Cost-effectiveness of FDG PET for the management of potentially operable non-small cell lung cancer: priority for a PET-based strategy after nodal-negative CT-results. Eur J Nucl Med 27: 1598-1609.
- Guagiatti A, Grimaldi A, Rossetti C et al. (2004). Economic analysis of the use of the positron emission tomography for the work-up of solitary pulmonary nodules and for staging patients with non-small cell lung cancer in Italy Q J Nucl Med Mol Imaging 48:49-61.
- Gambhir S S, Hoh C K, Phelps M E et al. (1996) Decision tree sensitivity analysis for cost-effectiveness of FDG-PET in the staging and management of non-small cell lung carcinoma J Nucl. Med 37: 1428-1436.
- Kosuda S, Ichihara K, Watanabe M et al. (2000) Decision-tree sensitivity analysis for cost-effectiveness of chest 2-Fluoro-2-D- [18F]-fluorodeoxyglucose positron emission tomography in patients with pulmonary nodules (non-small cell lung carcinoma) in Japan. Chest 117: 346-353.
- Malenka D G, Colice J L, Beck G R (1991) Does the mediastinum of patients with non-small cell lung cancer require histologic staging? Am Rev Respir Dis 144:1134-1139.
- Seely J, Mayo J, Miller R et al. (1993) T1 lung cancer: prevalence of mediastinal nodal metastasis and diagnostic accuracy of CT. Radiology18:129-132.

Author: Alexander Khmelev, N.N. Blokhin  
 Institute: Cancer Research Center RAMS  
 City: Moscow  
 Country: Russia  
 E-mail: khmelev@amphr.ru

# Design of an Ultra-Near-Field System for Planar Coded Aperture Nuclear Medicine Imaging

D.M. Starfield<sup>1</sup>, D.M. Rubin<sup>1</sup> and T. Marwala<sup>1</sup>

<sup>1</sup> School of Electrical & Information Engineering, University of the Witwatersrand, Johannesburg, South Africa

*Abstract* — Collimators are typically used for the acquisition of nuclear medicine images. Coded apertures provide an alternative means of acquisition, and under specific conditions are associated with a signal-to-noise-ratio advantage. However, under the near-field conditions of nuclear medicine, the point spread function is no longer ideal, and near-field artifacts result. Our previous work has highlighted three potential advances, but in each case, application results in the loss of count statistics. An array of limited-field-of-view coded apertures reduces near-field artifacts, but decreases the number of counts of radioactivity that are acquired. A thin and highly transparent coded aperture allows for ease of manufacture, a potential increase in resolution, and a reduction of thickness artifacts. A greater number of counts must be acquired if the signal-to-noise-ratio is to be maintained. Coded aperture resolution can be enhanced without modification of either the open fraction of the material or the field-of-view of the system. The size of each element in the array is decreased, and the total number of elements in the coded aperture pattern is increased. However, a smaller pattern element collects fewer counts of radioactivity. The design of an ultra-near-field system is proposed, which increases counting efficiency, provided that gamma camera sensitivity is able to follow suit. The design is tested by means of a ray-tracing computer simulator, which utilizes a two-dimensional digital Shepp-Logan phantom as a distributed source. Simulation results are presented for the prior state-of-the-art, and for the proposed design, under both near-field and ultra-near-field geometries. Severe artifacts arise under ultra-near-field conditions. Nevertheless, results show that the proposed design leads to both artifact reduction and an enhancement of resolution, relative to the state-of-the-art and without adjustment of either dose or acquisition time.

*Keywords* — Nuclear medicine imaging, Coded apertures, Artifact reduction, Count statistics, Ultra-near-field system.

## I. INTRODUCTION

Collimators are typically used for the acquisition of nuclear medicine images [1]. Coded apertures provide an alternative means of acquisition, and under the far-field conditions of astrophysics [2] are associated with a signal-to-noise-ratio (SNR) advantage [3].

Under the near-field conditions of nuclear medicine the point spread function (PSF) is no longer ideal, and near-field artifacts result [4]. The SNR decreases further for distributed objects [3].

Our work has highlighted potential improvements, which allow for the reduction of both near-field and thickness artifacts, and allow for an optimal resolution to be achieved [5–7]. Application of these advances would, however, result in the loss of count statistics.

This paper proposes an ultra-near-field system design, in which the improvements can be implemented without cost to either dose or acquisition time.

## II. METHOD

### A. Background

A coded aperture has numerous pinholes, which increase the open fraction of the aperture without degradation of resolution. The pinholes multiplex the source, but are arranged so as to allow a unique reconstruction [8].

Coded aperture theory is defined for far-field two-dimensional (2D) noise-free data [2]. Provided that the autocorrelation function of the aperture pattern is a delta function, an ideal image PSF is achieved [8]. Perfect aperture properties, however, do not give an ideal PSF under ideal near-field conditions.

### B. Near-field artifacts

The mask anti-mask technique reduces near-field artifacts, by means of 90 ° rotation of the aperture [4], but ghosting remains [5]. Relative to the far-field scenario of astrophysics, incident gamma-rays are not parallel.

Geometric analysis shows that for a single point source, the maximum change in measured activity at the detector tends toward zero under far-field conditions [5]. The analysis also shows that at a given height above the detector, detector size can be used to manipulate the change in intensities [5]. That is, a limited field-of-view (FOV) controls the change in intensities, and can therefore limit near-field artifacts.

A radiation attenuation tube can enclose the coded aperture and can extend from the source to the detector. This quasi-collimator limits the FOV [5].

A matrix of identical limited-FOV coded apertures allows the FOV of the system to be maintained [5]. However,

the FOV of each individual coded aperture decreases, as do the number of counts of radioactivity that are acquired.

### C. Thickness artifacts

Thickness of the aperture material introduces collimation effects. The convolution model [8] associated with coded aperture imaging does not hold, and thickness artifacts result.

Thin coded apertures are advantageous. Apertures of micrometer range thickness exist [9, 10], but use is limited to photon energies at which the material thickness is opaque.

Thin and highly transparent aperture material attenuates a low percentage of incident gamma-rays, which decreases the contrast and increases the quantization of the acquisition [6]. The projected patterns become less recognizable and noise results.

If a pixel of the gamma camera has an appropriate bit-depth, and if a sufficient number of counts of radioactivity is acquired, high transparency need not be associated with significant quantization effects [6]. Phantom-based experimental results have indicated that the quality of a highly transparent aperture image can approach that of an opaque aperture image [6].

An aperture that is for example 10 times thinner, simplifies manufacture and allows for a 10 times improvement in aperture resolution, without an increase in collimation effects. Nevertheless, a greater number of counts of radioactivity must be acquired if the SNR is to be maintained.

### D. Optimal resolution

The partial volume effect arises if the measured activity due to a point source is distributed between pixels of the detector [1]. The total measured activity does not alter, but the peak is not correct. The solution requires the illumination of a 2 by 2 detector pixel area, such that at least one pixel is fully illuminated [8]. The peak of the measured activity is then correct.

Gamma camera pixel size limits image resolution, as it sets the smallest sample acquisition interval. Resolution is also limited by the requirements of the partial volume effect, and by the PSF of the detector.

The resolution of a coded aperture can be designed for optimal performance with a specific gamma camera, without modification of either the open fraction of the material or the FOV of the system [7]. A decrease in the size of all pattern elements is balanced by an increase in the total number of elements.

The illumination of a 1 by 1 detector pixel area sets a sample threshold, below which a greater number of pattern elements cannot be measured [7]. Any further enhancement

of resolution must reduce the open fraction of the aperture material. The partial volume effect aside, a coded aperture element that illuminates a 1 by 1, as opposed to a 2 by 2 detector pixel area, is then optimal.

Coded aperture simulation results have shown that the partial volume effect has little influence on the distributed sources that are frequently imaged in nuclear medicine [7]. Nevertheless, optimal resolution requires smaller pattern elements, which collect fewer counts of radioactivity.

### E. Ultra-near-field conditions

Each of the potential advances reduces count statistics. A greater number of counts of radioactivity must then be acquired if the SNR ratio is to be maintained. This can theoretically be achieved with an increase in dose, an increase in acquisition time, or with the use of a higher sensitivity system.

A practical solution is to position the source much closer to the camera in an ultra-near-field system design. Geometry increases the proportion of activity at the camera crystal, which enhances the counting efficiency of the system, provided that gamma camera sensitivity is able to follow suit.

Ultra-near-field conditions are expected to lead to the presence of severe artifacts. An array of thin and highly transparent limited-FOV coded apertures, however, has the potential to control both near-field and thickness artifacts.

### F. Design efficiency

An array of limited-FOV coded apertures that contains  $n$  individual apertures gives  $1/n$  the activity at the detector. That is, a specific point of the source illuminates only a single limited FOV.

Thin aperture material simplifies the construction of patterns that are not self-supporting. If the self-supporting pattern has an open fraction  $f_1$ , and the non-self-supporting pattern has an open fraction  $f_2$ , use of the latter increases activity at the detector by  $f_2/f_1$ .

A highly transparent aperture material of attenuation  $a_1$ , as opposed to an opaque material of attenuation  $a_2$ , must give  $a_2/a_1$  times the activity at the detector. However, this is only applicable to the closed fraction of the aperture pattern,  $1 - f_2$ .

Smaller pattern elements reduce the count statistics of the reconstructed image, but do not alter activity at the detector. A source positioned at a fraction  $1/r$  of the distance increases the activity at the detector by  $r^2$ .

Basic analysis of an ultra-near-field design that incorporates each of the independent theoretical advances then gives the increase in activity at the detector  $\Delta A$  as:



$$\Delta A = \frac{1}{n} \frac{f_2}{f_1} \frac{a_2}{a_1} (1 - f_2) r^2 \quad (1)$$

The potential increase in bit-depth  $\Delta b$  of the gamma camera acquisition is then:

$$\Delta b = \frac{\ln(\Delta A)}{\ln 2} \quad (2)$$

### G. Design specifications

As opposed to a single coded aperture, a 3 by 3 array of limited-FOV coded apertures allows for near-field artifact reduction [5]. Relative to a tungsten sheet of thickness 1 mm, 100  $\mu\text{m}$  thick tungsten foil allows for the reduction of thickness artifacts [6]. At the energy of Technetium-99m (140 keV), the former gives an opaque aperture with an attenuation of 97 %, while the latter gives a highly transparent aperture with an attenuation of 29 %.

The coded aperture pattern is based on the modified uniformly redundant array (MURA) [3], which has an open fraction of 50 %. By contrast, the no-two-holes-touching (NTHT) [3] self-supporting implementation attains an open fraction of only 12.5 %.

A 1 by 1, as opposed to a 2 by 2, detector pixel area projection does not alter the open fraction of the aperture material [7]. At one quarter the distance, use of equations 1 and 2 gives  $\Delta A = 11.89$ , or an additional 3.57 bits of data. That is, unless limited by the gamma camera, system sensitivity can be improved relative to the prior state-of-the-art.

### H. Testing

The concept is tested by means of a ray-tracing computer simulator. The model incorporates imaging geometry, thickness and transparency of the aperture material, and finite aperture hole widths.

Gamma camera digitization effects and the count statistics associated with radioactivity are included. Note that the sensitivity of the gamma camera is assumed to allow an increased count rate, and that the PSF of the gamma camera is modelled as ideal.

Simulation results are presented for the prior state-of-the-art, and for the proposed design, under both near-field and ultra-near-field geometries. Acquisition bit-depth is altered for each specific system, such that both the dose and the acquisition time remain constant.

## III. RESULTS

A 2D digital Shepp-Logan phantom [11] is utilized as a distributed source (Figure 1). The mask anti-mask technique, which requires 90° rotation of the aperture [4], was applied to all images.

A root-mean-square error (RMSE) measurement is used to quantify the results. It is computed over the full image, and represents the percentage by which a pixel of the source differs from the corresponding pixel of the phantom [12].

*Prior state-of-the-art:* Under near-field conditions the prior state-of-the-art, viz. a single self-supporting opaque coded aperture, is affected by both near-field and thickness artifacts (Figure 2).  $\Delta b$  increases by 4 relative to Figure 2 under ultra-near-field conditions, but there is a substantial increase in the RMSE measurement (Figure 3).

*Proposed design:* The radiation attenuation tubes are modelled so as to result in the absence of data in regions that correspond to tube walls. Results are presented without interpolation. Note that for this reason, computation of the RMSE measurement does not consider the absent data.

$\Delta b$  decreases by 0.5 relative to Figure 2 under near-field conditions, and the theoretical advances require increased count statistics (Figure 4). By comparison, ultra-near-field conditions increase  $\Delta b$  by 3.5 relative to Figure 2. Both the RMSE measurement and artifacts are reduced (Figure 5).

## IV. DISCUSSION

Ultra-near-field conditions substantially worsen artifacts with the prior state-of-the-art. The proposed design reduces the sensitivity of the system and decreases the SNR.

An ultra-near-field geometry coupled with the theoretical advances, however, not only reduces near-field and thickness artifacts but also enhances resolution – without degradation of the SNR, and without alteration of either dose or acquisition time. It is left for future work to verify the results by means of clinical phantom studies.



Fig. 1 2D digital Shepp-Logan phantom

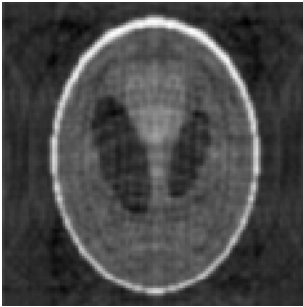


Fig. 2 Near-field prior state-of-the-art, RMSE of 50 %

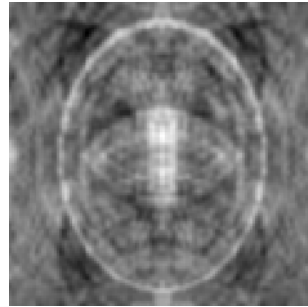


Fig. 3 Ultra-near-field prior state-of-the-art, RMSE of 97 %

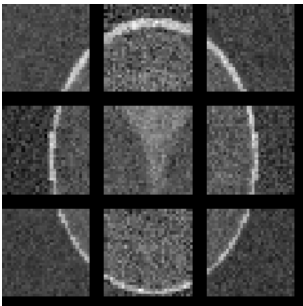


Fig. 4 Near-field proposed design, RMSE of 54 %

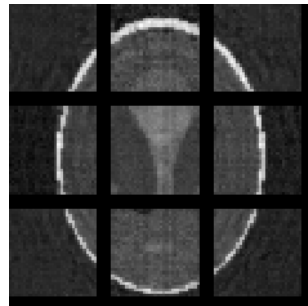


Fig. 5 Ultra-near-field proposed design, RMSE of 34 %

## V. CONCLUSIONS

Near-field and thickness artifacts are associated with the use of coded apertures in diagnostic nuclear medicine. Theoretical advances have the potential to reduce such artifacts, but decrease count statistics.

An ultra-near-field system design allows for an increase in the counting efficiency of the system, provided that gamma camera sensitivity is able to follow suit. However, with the prior state-of-the-art, severe artifacts arise under ultra-near-field conditions.

The proposed design is modelled as a 3 by 3 array of 100  $\mu\text{m}$  tungsten foil, 29 % attenuation limited-field-of-view coded apertures, which illuminate a 1 by 1 as opposed to a 2 by 2 detector pixel area.

The simulation results show that the improved efficiency associated with an ultra-near-field geometry can then be traded for both artifact reduction and an enhancement of resolution – relative to the prior state-of-the-art and without adjustment of either dose or acquisition time.

## REFERENCES

1. Cherry SR, Sorenson JA, Phelps ME (2003) *Physics in nuclear medicine* – 3rd ed. Saunders, Philadelphia
2. In 't Zand J (1996) Coded aperture imaging in high-energy astronomy. Laboratory for High Energy Astrophysics (LHEA) at [http://lheawww.gsfc.nasa.gov/docs/cai/coded\\_intr.html](http://lheawww.gsfc.nasa.gov/docs/cai/coded_intr.html). Last date of access: 30-03-2004
3. Accorsi R, Gasparini F, Lanza R (2001) A coded aperture for high-resolution nuclear medicine planar imaging with a conventional Anger camera: experimental results. *IEEE Transactions on Nuclear Science* 48(6):2411–2417
4. Accorsi R, Lanza R (2001) Near-field artifact reduction in planar coded aperture imaging. *Journal of Applied Optics* 40(26):4697–4705
5. Starfield DM, Rubin DM, Marwala T (2006) Near-field artifact reduction using realistic limited-field-of-view coded apertures in planar nuclear medicine imaging, *IFMBE Proc.* vol. 14, World Congress on Medical Physics and Biomedical Engineering, Seoul, South Korea, 2006, pp 1558–1561
6. Starfield DM, Rubin DM, Marwala T, Keddy RJ (2007) High-transparency coded apertures in planar nuclear medicine imaging: experimental results, *IEEE Nuclear Science Symposium Conference Record*, vol. 4, 2007, pp 3151–3154
7. Starfield DM, Rubin DM, Marwala T (2007) Sampling considerations and resolution enhancement in ideal planar coded aperture nuclear medicine imaging, *IFMBE Proc.* vol. 16, 11<sup>th</sup> Mediterranean Conference on Medical and Biological Engineering and Computing, Ljubljana, Slovenia, 2007, pp 806–809
8. Accorsi R (2001) Design of near-field coded aperture cameras for high-resolution medical and industrial gamma-ray imaging. PhD Thesis, Massachusetts Institute of Technology
9. Accorsi R (2004) A 15- $\mu\text{m}$  resolution imager for soft X-ray emitters, *IEEE Nuclear Science Symposium Conference Record*, vol. 5, 2004, pp 2975–2979
10. Accorsi R, Autiero M, Celentano L et al. (2004) Toward a Medipix2 coded aperture gamma microscope, *IEEE Nuclear Science Symposium Conference Record*, vol. 4, 2004, pp 2461–2464
11. Shepp LA, Logan BF (1974) The Fourier reconstruction of a head section. *IEEE Transactions on Nuclear Science* 21(3):21–43
12. Choi Y, Koo J-Y, Lee N-Y (2001) Image reconstruction using the wavelet transform for positron emission tomography. *IEEE Transactions on Medical Imaging* 20(11):1188–1193

Address of the corresponding author:

Author: D.M. Starfield  
 Institute: School of Electrical & Information Engineering  
 University of the Witwatersrand, Johannesburg  
 Street: Private Bag 3, WITS 2050  
 City: South Africa  
 Email: [d.starfield@ee.wits.ac.za](mailto:d.starfield@ee.wits.ac.za)

# Semiconductors and Biomedical Structures for Nanobiometric Applications

B.H. Bairamov<sup>1</sup>, V.V. Toporov<sup>1</sup>, F.B. Bayramov<sup>1,5</sup>, M. Vasudev<sup>2,3</sup>, M. Dutta<sup>2,4</sup>, M.A. Strosio<sup>2,3</sup>,  
and G. Irmer<sup>6</sup>

<sup>1</sup>Ioffe Physico-Technical Institute RAS, Department of Solid State Physics, St.Petersburg, 194021, Russia

<sup>2</sup>Department of Electrical and Computer Engineering, University of Illinois, Chicago, IL, 60607, USA

<sup>3</sup>Department of Bioengineering, University of Illinois, Chicago, IL, 60607, USA

<sup>4</sup>Department of Physics, University of Illinois, Chicago, IL, 60607, USA

<sup>5</sup>Petersburg Nuclear Physics Institute RAS, Gatchina, 188300, Russia

<sup>6</sup>Institute of Theoretical Physics, University of Mining and Technology, D-09596, Freiberg, Germany

**Abstract** — Nanoscale functionalization of semiconductor quantum dots with biomedical structures is promising for many applications and novel studies of intrinsic properties of both constituent systems. Results of our study of structural properties of the nanoscale functionalized colloidal semiconductor quantum dots such as CdS ZnS-capped CdSe, TiO<sub>2</sub> functionalized with biomolecules such as short peptides and cells will be presented. The use of semiconductor quantum dots as biotags has emphasized use of the semiconductor luminescence to determine the location where chemically functionalized semiconductor quantum dots bind to a biomedical sample. We study semiconductor quantum dots functionalized with peptides composed of the following amino acid chains: CGGGRGDS, CGGGRVDS, CGGIKVAV, and CGGGLDV, where R is arginine, D is aspartic acid, S is serine, V is valine, K is lysine and L is Levine. The RGDS, RVDS, IKAV, and LDV sequences have selective bonding affinities to specialized transmembrane cellular structures known as integrins of neurons and MDA-MB-435 cancer cells, respectively. We found that the quantum confinement and functionalizing in biomedical environments plays in altering and determining the electronic, optical, and vibrational properties of these nanostructures as well as demonstrated the effectiveness to use semiconductor quantum dots as integrin sensitive biotags.

**Keywords** — Nanoscale Functionalization, semiconductor quantum dots.

## I. INTRODUCTION

In recent years, the design, synthesis and applications of nanometer-scale particles have been the subject of intense fundamental and applied research. Current research activity involve development of novel, nanostructured materials specifically, semiconductor quantum dots with special emphasis on their size-dependent properties that determine a broad range of applications. Using self-organized colloidal chemical syntheses, such nanoparticles quantum dots, can be obtained with sub-nanometer precision having sizes from 1 to 10 nm. Due to the discrete structure of optical

transitions in semiconductor quantum dots structures, thermal depopulation of the lowest states that involved in the emitting processes is inhibited. Thus, semiconductor quantum dots are predicted to provide superior performance in sensor purposes. Especially applications of the semiconductor quantum dots functionalized with biomedical structures have been highlighted recently by a broad variety of applications [1-5] in the study of subcellular processes of fundamental importance in the biomedicine.

In this work, a set of key issues underlying the nanoscale functionalization of colloidal semiconductor quantum dots such as CdS, ZnS-capped CdSe, and TiO<sub>2</sub>, functionalized with biomolecules such as short peptides and cells by using inelastic laser light scattering and photoluminescence spectroscopy will be presented. Such functionalization of semiconductor quantum dots with biological structures is promising for many applications and novel investigations of intrinsic properties of both constituent systems though it is in an early stage of development. One intriguing application is the use of SQDs as biotags that has emphasized use of the semiconductor luminescence to determine the location where chemically functionalized SQDs bind to a biological sample. In the present study chemically prepared CdS SQDs are functionalized with different type of peptides. They were composed of the following amino acid chains: CGGGRGDS, CGGGRVDS, CGGIKVAV, and CGGGLDV.

Since protein hydration is known to be a key factor affecting protein energy balance, we also studied a role that water and other biological environments may play in stability, surface properties, dynamical and structural characteristics of these molecular systems.

As will be seen the cysteine (C) amino acid links to SQDs (in the case of CdS) via the thiol link, the GGG sequences of glycine (G) amino acid, provide a spacer in the amino acid chain. At the same time the RGDS, RVDS, IKAV, and LDV sequences have selective bonding affinities to specialized transmembrane cellular structures

known as integrins of neurons and MDA-MB-435 cancer cells, respectively.

Clearly, CGGGLDV and CGGGIKVAV functionalized CdS nanocrystals have potential applications in the study of cancer and the neuronal currents in neurons.

In addition to investigating RGDS and RVDS binding properties, this study investigates the interaction between colloidal CdS nanocrystals and the CGGGIKVAV and CGGGLDV peptides by measuring absorption, photoluminescence and vibrational inelastic laser light scattering spectra for these SQD-peptide complexes.

Particular emphasis is placed on determining the changes in the optical properties of the surface states as a result of being functionalized by the peptides.

We found the roles that the quantum confinement and functionalizing in biomedical environments plays in altering and determining the electronic, optical, and vibrational properties of these nanostructures as well as demonstrated the effectiveness to use SQD as integrin sensitive biotags.

These studies [1] emphasize the determination of the binding site rather than determination of how the interaction between the SQDs and the biological structure changes the electronic and optical properties of SQDs.

Recent efforts to study the interaction between SQDs and biological structures have investigated the binding of peptide-functionalized colloidal SQDs to transmembrane proteins in the bilipid membranes of cells [2]. In this study SQDs are bound to CGGGRGDS peptide through the thiol link between the cysteine (C) amino acid and the SQD.

## II. EXPERIMENTAL PROCEDURES

For our optical measurements the CdS SQDs were functionalized with peptides composed of the following amino acid chains: CGGGRGDS, CGGGRVDS, CGGGIKVAV, and CGGGLDV.

The investigated peptide-functionalized colloidal CdS nanocrystals were synthesized using techniques of colloidal chemistry [4].

Specifically a 5mM solution of CdCl<sub>2</sub> (36.6 mg of CdCl<sub>2</sub> in 40 mL of H<sub>2</sub>O) was titrated with mercaptoacetic acid until a pH of 2 was achieved. Concentrated NaOH was then added dropwise until a pH of 7 resulted.

Upon mixing this solution with a 5mM solution of Na<sub>2</sub>S·9H<sub>2</sub>O, a yellow colloidal suspension of CdS was formed. The functionalization of the colloidal CdS SQDs with peptides was accomplished by introducing 5 mg of CGGGRGDS in 2 mL of CdS suspension, 3 mg of CGGGRVDS in 2 mL of the CdS suspension, 2.4 mg of CGGGIKVAV in 5 mL of the CdS suspension, and 1.8 mg of CGGGLDV in 5 mL of the colloidal CdS suspension.

## III. RESULTS AND DISCUSSIONS

To determine whether the conjugation of peptides with semiconductor quantum dots has any effects on the optical properties, absorption spectra before and after attachment of peptides were measured. Based on these results, it appears that the attaching of peptide to the surface of the quantum dots does not affect the absorption properties of the dots significantly. The absorption spectrum in all cases shows well resolved features corresponding to inter-band optical transitions between quantized electron and hole states and the detected peaks can be assigned to transitions with significant oscillator strength. The observed absorption spectra of CdSe-ZnS quantum dots before and after conjugation with GGGGLDV peptide show the band at 545 nm is assigned to 1S(e)-1S<sub>3/2</sub>(h) transition, which is blue shifted with respect to bulk band gap of 1.751 eV.

In the absorption spectra of the CdS nanocrystal suspension with and without peptides for the cases of CGGGIKVAV and CGGGLDV, respectively, we found that there is a strong absorption peak in each of these spectra at about 440 nm. The band gap of bulk CdS at 10K is 2.58 eV (480.6 nm) and the band gap increases to ~ 2.8 eV (439.9 nm) for a CdS SQD dots as a result of the quantum confinement. By comparing the absorption edge with these scaling results, the diameter of the SQDs in the CdS suspension is estimated to be about 3 nm.

Since the electronic transitions of the QDs are strongly size dependent, the inhomogeneous broadening of the optical transitions is mainly due to similar but not identical particles in the sample - size and shape distribution. The typical steady-state photoluminescence spectrum of the CdSe/ZnS QDs-GGGC complex obtained at the room temperature (Fig. 1) shows highly symmetric an exciton emission Gaussian (red) band centered at 604.16 nm with the 26.83 nm full width at the half maximum. From the fit parameters the size distribution is estimated to be around 2%.

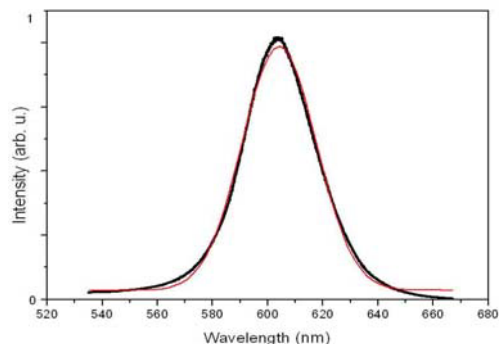


Fig. 1. Room temperature photoluminescence spectrum of CdSe-ZnS quantum dots functionalized with GGGC peptide.

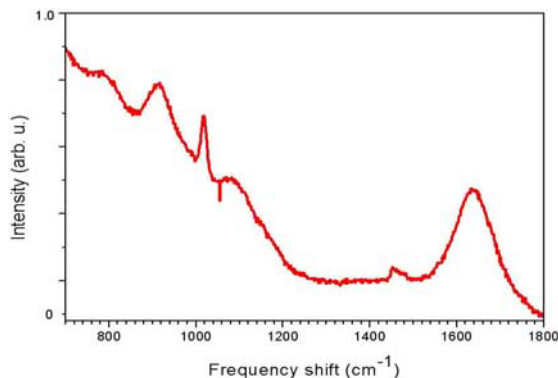


Fig. 2. Inelastic laser light (532 nm) scattering spectrum of CdSe-ZnS quantum dots functionalized with RGD peptide.

Fig. 2 shows the inelastic laser light (532 nm) scattering spectrum of the CdSe-ZnS quantum dots functionalized with RGD peptide demonstrating typical Raman lines.

Titanium is useful and a widely used material for biomedical applications in dentistry and restorative surgery due to his excellent mechanical properties. Titanium dioxide is not a direct bandgap semiconductor and its nanocomposites also possess the biologically and chemically unique property of a light – inducible nucleic acid endonuclease, which could provide a new means of using a photon-excited transitions for gene therapy.

The mechanism of peptide absorption on a surface of titanium dioxide is subject of ongoing studies. The surface of titanium dioxide quantum dots has a negative partial charge. The negative charge developed in a titanium-oxide nanoparticles is assumed to be due to partially bonded oxygen atoms (titanium-O<sup>-</sup>) at the nanoparticle surface [6]. The neutral hydroxyl group bonded at the nanoparticle surface (titanium-OH) also plays a very important role in the chemical equilibrium involving the positively and negatively charged nanoparticles and ions present in peptides can combine with the TiO<sub>2</sub> quantum dots.

Figure 3 demonstrates the typical inelastic laser light (532 nm) scattering spectrum of the TiO<sub>2</sub> quantum dots (lines at 158, 461 and 625 cm<sup>-1</sup>) suspended in high-purity water to form stable colloids and then slow evaporated at a constant temperature. Note that water adsorption at titanium dioxide quantum dots surfaces is a crucial process in many applications of this material.

We find that the spectrum is similar to that of the bulk anatase phase TiO<sub>2</sub> crystal with an exception of the observed blueshift of the frequency and increase of linewidth of the phonon lines. The observed spectral changes as well as high intensity and still narrow lines indicate on formation of the long-range order and high crystallinity of the TiO<sub>2</sub> nanocrystals. comparison to the

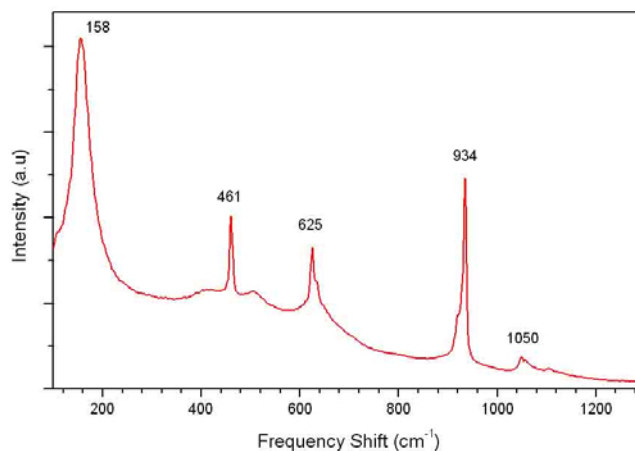


Fig. 3. Inelastic light scattering spectra of the TiO<sub>2</sub> nanocrystals suspended in high-purity water. The spectrum is obtained in a backscattering geometry using 532 nm excitation laser line.

bulk anatase and can be definitely prescribed to the E<sub>g</sub>. The most intense line at 158 cm<sup>-1</sup> exhibited approximately 15 cm<sup>-1</sup> blueshift in optical phonon confinement of the anatase phase of the TiO<sub>2</sub> quantum dots. The influence of the phonon confinement can be quantitatively estimated in terms of spatial correlation model [6]. This shows that the crystalline size of the TiO<sub>2</sub> quantum dots is approximately 4 nm. Theoretically calculated value of the confined phonon linewidth of 26 cm<sup>-1</sup> is smaller than the measured one of 32 cm<sup>-1</sup> indicating to the contribution of the non-stoichiometry effect. We note that the additional contribution to the observed broadening of the confined phonon line can be caused by interfacial vibrations as well [7].

To examine the role of peptide selectivity in the binding of quantum-dot-peptide (QDP) complexes to cells, the binding of CGGGRGDS-functionalized and CGGGRVDS-functionalized quantum dots to cancer cells the MDA-MB-435 cell line has been used and examined by direct observation under a fluorescence microscope to determine the presence or absence of quantum dots bound to the cells.

Figure 4 shows MDA-MB-435 cells as viewed with white light exposure. The general features of the cells are clearly visible. The image of this same group of CGGGRGDS-functionalized cells was then illuminated with 360-nm radiation and light was collected through a filter with a window in the 435-nm to 490-nm band.

As seen in the associated image in Fig. 5, the CGGGRDGS-based SQD-peptide complexes are bound to the MDA-MB-435. The binding is indicated by the collection of radiation near the 440-nm emission line of the lowest state of the CdS quantum dots with diameters of approximately 3 nm. On the other hand, similar images of cells exposed to CGGGRVDS-based QDP complex show

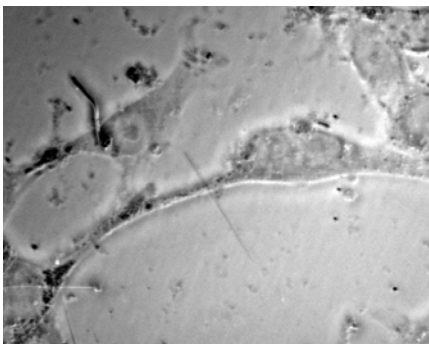


Fig. 4. Image of MDA-MB-435 cells under illumination by white light.

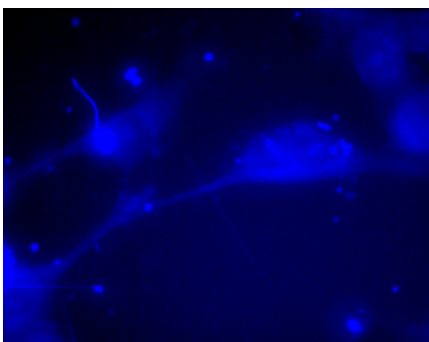


Fig. 5. Image of MDA-MB-435 cells functionalized with the CGGGRDGS-based SQD-peptide complexes.

no sign that the QDP bind to the cells. These results demonstrate peptide selectivity in the binding of QDP complexes to MDA-MB-435 cells. In addition, these finding demonstrate the utility of using peptides to link quantum dots the transmembrane proteins and to use quantum dots as integrin sensitive biotags.

#### IV. CONCLUSIONS

Our findings indicate that optical studies of semiconductor quantum dots in biological environments provide essential information on the interaction between quantum dots and their environments. We have identified amino acid sequences capable of interacting with biomaterials.

These results have demonstrated the integrin-selective binding of CdS QDP complexes to integrins of MDA-MB-435 cells. The demonstrated sensitivity of the optical spectra opens a new way to a wide range of studies of how integrated semiconductor quantum dots-biological

structures acquire modified properties as a result of their mutual interactions.

#### ACKNOWLEDGMENT

The work at the Ioffe institute is partially supported by the grant No.06-02-16304 of the Russian Foundation for Basic Research.

#### REFERENCES

1. Bairamov B H, Toporov V V, Bayramov F B, M Petukhov M, Glazunov E, Shchegolev A, B, Li Y, Ramadurai D, Shi P, Dutta M, and Stroschio M A. (2004) Inelastic Light Scattering Spectroscopy of Phonon Interaction with Multi-Component Plasma in Bulk & Quantum Dot Semiconductors Structures", *phys. stat. sol. (c)* **1**, 2773-2778.
2. Bairamov B H, Toporov V V, Bayramov F B, M Petukhov M, Glazunov (2004) Structural Properties & Dynamics of Low-Energy Collective Excitations of Water & lysozyme", *phys. stat. sol. (c)*, **1**, 3134-3137.
3. Bairamov B H, Toporov V V, Bayramov F B, M Petukhov M, Glazunov E, Shchegolev A, B, Li Y, Ramadurai D, Shi P, Dutta M, Stroschio M A, Irmer G (2006) Functionalization of II-VI Semiconductor Quantum Dots With Peptides and Integrins of Cancer Cells for Biophotonic Applications", B H Bairamov, et al, *Mol. J. Phys. Sciences*, **5**, 320-326 (2006).
4. Bairamov B H, Toporov V V, Bayramov F B, M Petukhov M, Glazunov Dutta M, Stroschio M A, Irmer G (2007) Selective Functionalization of Semiconductor Quantum Dots With Biomedical Structures", B H Bairamov, et al, *Molecular Genetics, Biophysics and Medicine To-day*, St. Petersburg, ed. V. A. Lanzov, PNPI, 2007, p. 405-414.
5. B. H. Bairamov, V. V. Toporov, and F. B. Bayramov, V. Lanzov, M. Petukhov, E. A. Glazunov, Y. Li, D. Ramadurai, and P. Shi, Mitra Dutta, M. A. Stroschio, and G. Irmer, Selective Functionalization of Semiconductor Quantum Dots With Short Peptides and Integrins of Cancer Cells for Biophotonic Applications, in: *Physics, Chemistry, and Applications of Nanostructures*, Proc. of International Conference "Nanomeeting-2007", World Scientific, 2007. p.511-515.
6. Qu F and Morais P. C. The pH Dependence of the Surface Charge Density in Oxide-Based Semiconductor Nanoparticles Immersed in Aqueous Solution (2001) *IEEE Transactions on Magnetics*, **37**, 2654.
7. Shen H, and Pollak F H, (1984) *Appl. Phys. Lett.* **45**, 692.
8. Zhang WF, He YL, Zhang M S, Yin Z, and Chen Q (2000) *J Phys. D: Appl. Phys.* **33**, 912.

The address of the corresponding author:

Author: F.B. Bayramov  
 Institute: Ioffe Physico-Technical Institute RAS  
 Department of Solid State Physics  
 Street: 26 Polytekhnicheskaya ul  
 City: St.Petersburg, 194021  
 Country: Russia  
 Email: Bairamov@mail.ioffe.ru

# Microcells Development and Endocytosis Ability Morphological and Quantitative Characterization in HeLa Cancer Cells

D. Bema<sup>1</sup>, T. Freivalds<sup>1</sup>, I. Buikis<sup>1</sup> and L. Harju<sup>1</sup>

<sup>1</sup>University of Latvia Institute of Experimental and Clinical Medicine, Riga, Latvia

**Abstract** — Determination of endocytotic ability of cancer cells could improve tumor treatment results. The aim of this study was to investigate morphological aspects of development in HeLa (*Henrietta Lacks cervical cancer cells*) microcells and to quantitatively estimate the endocytotic capability of these cells.

The HeLa cell line was maintained at 37 °C in DMEM medium 3-4 days. Cell samples were supravitaly stained with different markers (acridine orange, water soluble CdSe/ZnS nanoparticles, Indian ink, carmine red). Cell photographs were taken using a Leica DM6000B microscope connected to a DFC 490 digital camera. Microscope images were analyzed and measured with an IPP 5.0 image analysis program. Geometrical and photometrical measurements were obtained in order to distinguish particular cell classes in HeLa cell line subpopulations.

We found that different markers accumulate more in specific morphological states of cancer cells. An increased mean cell fluorescence intensity suggested greater endocytosis capability in early microcell development stages. We observed water soluble CdSe/ZnS nanoparticle accumulation and cell surface binding in all cell classes, but significant enhancement of fluorescence intensity was observed in microcells. Although we used different sizes of nanoparticles with different fluorescence emission spectra in our experiments, we acquired fluorescent emission spectra very similar to supravital staining with red and green nanoparticles, suggesting that nanoparticle spectral properties are determined by mutual binding with cell structures.

All supravital staining methods (Indian ink, carmine red, acridine orange (AO), red and green CdSe/ZnS nanoparticles) allowed determination of different endocytotic capabilities in various HeLa cancer cell classes. Measured fluorescence intensities and degrees of endocytosis are highly correlated, allowing characterization of endocytosis ability of different cancer cell classes.

**Keywords** — microcell, endocytosis, nanoparticles

## I. INTRODUCTION

Previous studies [1; 2] have demonstrated that cancer cells may undergo a process termed “sporosis” (figure 1) – a cancer cell’s self-renewal process in which mother cells can give rise to several microcells (in less than one percent of cases). Microcells are characterized by a round or oval form, scanty cytoplasm and homogenously and intensively

stained nuclei; they are metabolically very active and naturally resistant to anticancer agents. Microcells are transformed cells. They develop some stem cell-like properties (cell surface markers vimetin and CD68). Effective cancer stem cell marking in anti-cancer drug delivery could stop the development of cancer. Exploration of endocytosis in cancer cells could improve tumor treatment results. The aim of this study was to investigate HeLa (*Henrietta Lacks cervical cancer cells*) microcell development and to estimate the endocytotic capacity of these cells.

## II. METHODS

The HeLa cell line was maintained at 37 °C in DMEM medium for 3-4 days. Cancer cell samples were supravitaly stained with different markers: acridine orange (AO) (30 min.), Indian ink, carmine red and water soluble Cd/Se/ZnS Nanocrystalle nanoparticles (2 hours). Cells were fixed in acetone, dehydrated, clarified and mounted in specific medium (Canada balsam or fluoromount).

Microscopic photographs were taken using a DFC 490 digital camera. Images were analyzed and measured with an IPP 5.0 image analyzing program. Geometrical and photometrical measurements were obtained in order to distinguish particular cell classes in HeLa cell line subpopulations. Data about cells’ area, density and roundness were gathered. A confocal Leica TCS SP2 AOBs microscope was used to measure emission spectra.

Fluorescence intensity was measured in the green color channel in samples stained with AO and water soluble nanoparticles. The degree of endocytosis was calculated in

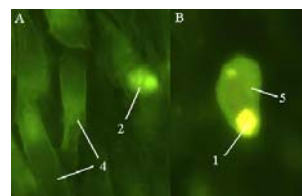


Fig. 1 – Cell classes in samples stained with red nanoparticles.  
1 – first microcell class; 2 – second microcell class;  
3 – third microcell class; 4 – matured cells; 5 – mother cells

all samples (stained with one dye) and gained using the formula:

$$EC = \frac{Ir - Ig}{Ir + Ig} \quad (1)$$

Where: EC – endocytosis capability; Ir – fluorescence intensity in red channel; Ig – fluorescence intensity in green channel.

**Sample staining with AO.** The HeLa cell population was divided into five classes. The first class of microcell development (figure 1.A) – small roundish or oval, light red cells in mother cells; second microcell class (figure 1.B) – small roundish cells, in which orange cytoplasm and a bright yellow nucleus can be distinguished; third microcell class (figure 1.C) – small cells with nucleus and cytoplasm, segregated from mother cells; fourth class – matured cell (figure 2.) – spindle like cells with green, stained cytoplasm, many nucleoli in nucleus; fifth class – mother cells – cells where microcell development could begin.

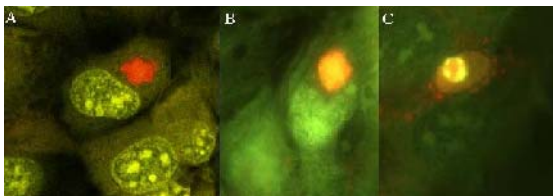


Fig.2 – Microcell classes in samples stained with AO

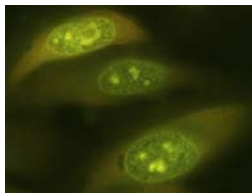


Fig. 3 – Fourth class – matured spindle like cells in samples supravitaly stained with AO

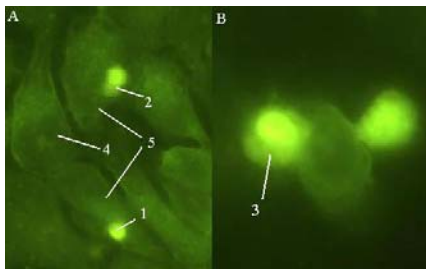


Fig. 4 – Cell classes in samples supravitaly stained with green nanoparticles. 1 – first microcell class; 2 – second microcell class; 3 – third microcell class; 4 – matured cells; 5 – mother cells;

**Sample staining with nanoparticles.** The HeLa cell population stained with green (figure 3) and red nanoparticles (figure 4) was also divided in 5 cell classes. In these pictures cell classes differed with fluorescence intensity (higher for microcells) and in size (microcells are smaller).

### III. RESULTS

#### A. Emission spectra measurements

Although red and green nanoparticles have different spectral ranges (as shown by the manufacturer – maximum of emission at 545 nm for green and 635nm for red nanoparticles – see figure 7), emission spectra in HeLa cancer cells measured in our laboratory does not show great differences in wavelength at spectra maximum between red and green nanoparticles (figure 5,6).

Microcells (stained with green nanoparticles), in comparison to mature cells, have a small displacement to longer wave length (figure 5.). This could be explained by nanoparticle interaction. Microcells show higher mean fluorescence intensity than mature cells (figure 6.).

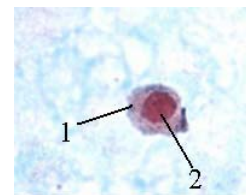


Fig. 5 – The 1<sup>st</sup> phase of microcellular development, accumulation of carmine red. 1- cytoplasm; 2 – nucleus; (obj. 40x)

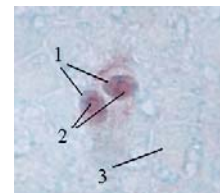


Fig. 6 – The 2<sup>nd</sup> phase of microcellular development, accumulation of carmine red. 1 – cytoplasm; 2 – nucleus; 3 –cell's necrotic detritus. (obj. 40x)

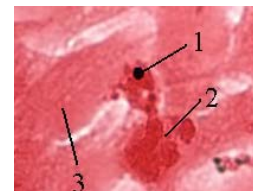


Fig. 7 – The 1<sup>st</sup> phase of microcellular development. 1 – first microcell class; 2 – residues of mother cell; 3 – matured cell



**B. Supravital staining**

Staining with carmine red. The ability of cancer cells to perform active phagocytosis is proved by sample staining with carmine red. In supravital staining microcells become clearly visible (fig.8,9). In background cells necrotic detritus can be seen (fig.9).

Supravital staining with Indian ink also marks microcells. At first Indian ink accumulates in the microcell's nucleus (fig.10), but later it forms a thin layer around the cytoplasm (fig.11).

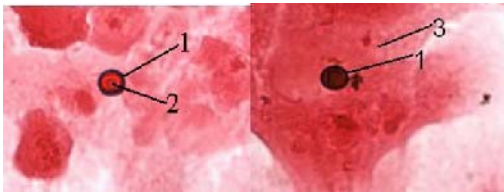


Fig. 8 – The 2<sup>nd</sup> phase of microcellular development. 1 – Indian ink layer inside cytoplasm; 2 – microcell's nucleus; 3 – mother cell

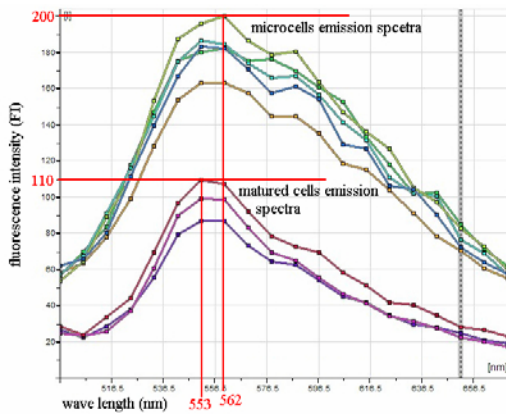


Fig. 9 – Emission spectra of green nanoparticles in HeLa cells

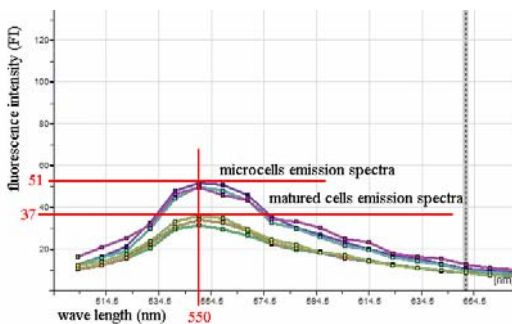


Fig. 10 – Emission spectra of red nanoparticles in HeLa cells

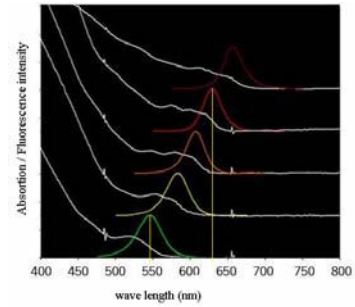


Fig. 11 – Emission spectra of nanoparticles of different sizes in water solution

**C. Fluorescence intensity**

We measured fluorescence intensity in the first three classes of microcells in samples stained with AO (fig. 12). Mean fluorescence intensity shows statistically significant difference in microcells and mature cells, according to Student's two-tailed t-test ( $p < 0.001$ ), but the difference between the first and second microcell classes is not statistically significant ( $p = 0.43$ ).

In samples stained with green nanoparticles the highest mean fluorescence intensity is in the 2-nd microcell class (Fig. 13). The difference of mean fluorescence intensity in all microcell classes is statistically significant compared to mature cells ( $p < 0.0001$ ), but there are no differences between 1st and 2nd classes ( $p = 0.21$ ). The third class population is very small, which can be explained by cell loss due to their poor ability to attach to cover slips. Cells of the 3rd class are mostly suspended in medium. In some cases 3rd class cells can be seen above the cell monolayer.

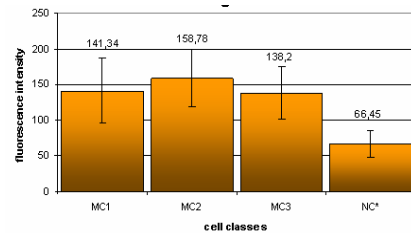


Fig. 12 – Fluorescence intensity staining with acridine orange

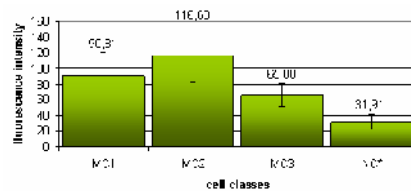


Fig. 13 – Fluorescence intensity staining with green nanoparticles

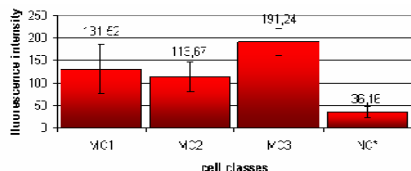


Fig. 14 – Fluorescence intensity staining with red nanoparticles

In supravital staining with red nanoparticles (Fig. 14.) statistically significant differences in fluorescence intensity can be observed in all microcell classes compared to mature cells ( $p < 0.0001$ ) and between 1st and 3rd classes ( $p = 0.018$ ). Maximal mean fluorescence intensity is in the 3rd class ( $191 \pm 29.84$ ) and the minimal intensity ( $31.91 \pm 9.42$ ) is in mature cells. In general, fluorescence intensity has similar changes as samples stained with green nanoparticles.

From our data, the influence of size difference between red and green nanoparticles on the endocytosis process is small.

**D. Endocytosis degree**

The degree of endocytosis is a parameter which is not dependent on fluorescence intensity, but is dependent on fluorescence emission spectra and on the concentration of AO in the cell. In this way, degree of endocytosis becomes cell class characterizing value. As a cell becomes more red, this number increases.

Acquired degree of endocytosis (table 1.) in all classes is highest in 1st microcell class ( $0.23 \pm 0.12$ ) but lowest in 3rd class ( $0.12 \pm 0.05$ ). A greater endocytosis degree in 1st class cells is suggested by the explicit red color and therefore increased accumulation of AO. This endocytosis mechanism could be developed for accelerated substance uptake, which is necessary for young cell growth. A smaller degree of endocytosis in the third microcell class indicates lowered microcell endocytosis ability after separation from the mother cell.

There are statistically significant ED differences in all three microcell classes ( $p < 0.001$ ) and between all microcell class compared to matured cells ( $p < 0.001$ ).

Table 1 Endocytosis degree value in cells stained with acridine orange

Cell classes	Endocytosis degree (whole cell)	Endocytosis degree (nucleus)	Endocytosis degree (cytoplasm)
1 <sup>st</sup> microcell class	$0.23 \pm 0.12$		
2 <sup>nd</sup> microcell class	$0.13 \pm 0.08$	$0.11 \pm 0.09$	$0.14 \pm 0.09$
3 <sup>rd</sup> microcell class	$0.09 \pm 0.04$	$0.07 \pm 0.06$	$0.10 \pm 0.04$
mature cells *	$0.12 \pm 0.05$	$0.14 \pm 0.06$	$0.11 \pm 0.05$

\* - statistically significant differences

Degree of endocytosis cannot be determined in HeLa cells stained with red or green nanoparticles because all sample staining is a uniform green color.

**IV. CONCLUSIONS**

All used supravital staining methods (acridine orange, red and green CdSe/ZnS nanoparticles, Indian ink, carmine red) allow the determination of differences in endocytosis ability in various HeLa cancer cell classes.

Measured mean fluorescence intensity and endocytosis degree are significant for characterizing the endocytosis ability of different cancer cell classes. Fluorescence intensity measurements can be used in samples stained with AO and nanoparticles, but endocytosis degree can be used only in samples stained with AO.

Different markers accumulate more in specific morphological states of cancer cells called microcells. High mean fluorescence intensity indicates more intense staining and higher endocytosis capability in early microcell development stages. Highest endocytosis degree and mean fluorescence intensity parameter is the greatest in early developmental microcells and the least for mature cells ( $p < 0.01$ ).

Although it is known that different sizes of nanoparticles have different fluorescence emission spectra, in our experiments red and green nanoparticles emission spectra become similar after supravital staining with water soluble CdSe/ZnS, suggesting that nanoparticle spectral properties are determined by mutual binding with cell structures.

**ACKNOWLEDGMENTS**

This study was supported by Latvia Science Council research grant Nr. 1114 and 1115.

**REFERENCES**

1. Buiķis I, Harju L, Freivalds T (1999) Origin of microcells in the human sarcoma cell line HT-1080. Analytical Cellular Pathology 18:73-85;
2. Buiķis I, Feivalds T, Harju L, Nikulshin S (2002) Sporosis: A Cytological Mechanism of Dedifferentiation of the Human Sarcoma Line HT-1080 Cells. Acta medica Lituanica. Supl.9:18-21;

Author: Dina Bēma  
 Institute: University of Latvia Institute of Experimental and Clinical Medicine  
 Street: O.Vaciesas 4  
 City: Riga  
 Country: Latvia  
 Email: dina\_bema@yahoo.com

# Atomic Force Microscopy Study of Yeast Cells Influenced by High Voltage Electrical Discharge

D. Borovikova<sup>1</sup>, S. Cifansky<sup>2</sup>, Y. Dekhtyar<sup>3</sup>, V. Fedotova<sup>3</sup>, V. Jakushevich<sup>2</sup>, A. Katashev<sup>3</sup>,  
A. Patmalnieks<sup>1</sup>, A. Rapoport<sup>1</sup>

<sup>1</sup> Microbiology Institute of the University of Latvia, Riga, Latvia

<sup>2</sup> Mechanical Institute of Riga Technical University, Riga, Latvia

<sup>3</sup> Biomedicine and Nanotechnologies Institute of Riga Technical University, Riga, Latvia

**Abstract** — Human cells are the eukaryotic ones. Simulation of wide-spectrum electromagnetic radiation influence on eukaryotic cells was performed with yeast which is usually used now in molecular biological and medical biological investigations as the ideal model of eukaryotic system. The aim of the research was to observe possible induced alterations of the cell morphology. Atomic force microscopy (AFM) and electron scanning microscopy (ESM) have been applied to image the surface of cells exposed to electromagnetic radiation.

Electromagnetic radiation was provided in a reactor tank due to high-voltage electrical discharge in water (HVD) [1]. The total accumulated discharge energy (E) density per cell solution volume was varied.

AFM images were obtained for the free cells placed on a polycrystalline corundum (polycor) substrate. Ten specimens fields contained around 100 cells each were explored.

HVD applied to the cells altered their surface morphology. Particularly, the surface became corrugated at  $E < 50$  J/ml. However higher levels of energy ( $> 50$  J/ml) could destroy part of the cells.

Microbiological experiments evidenced that yeast cells survived after treatment showed higher rate of the proliferation in the fresh nutrient medium comparing it with control cells which were not subjected to HVD treatment. Besides that new population of yeast which was received in our experiments using as the inoculum cells survived after HVD treatment were more resistant to another stress – dehydration-rehydration.

The reached results demonstrate that HVD could be applied to enhance proliferation rate of the culture as well as for the obtaining of more resistant population.

**Keywords** — Atomic force microscope, high-voltage electrical discharge, electromagnetic radiation, surface morphology, yeast cells.

## I. INTRODUCTION

Influence of wide-spectrum electromagnetic radiation on eukaryotic cells had recently become a subject of particular interest, since a human being, whose cells are the eukaryotic ones, might be exposed to combined types of radiation in various spheres of activity. Modern technologies allow simulation of wide-spectrum radiation in laboratory envi-

ronment thereby providing a possibility to perform studies of its influence on cells.

In this study we have investigated the wide-spectrum electromagnetic radiation influence on a yeast cell, as in molecular and medical biology it is considered to be an ideal model of eukaryotic system. The wide-spectrum radiation was simulated on an HVD device.

Resulting alterations caused in surface morphology of specimens can be examined in various ways. In our study we have chosen AFM as a major investigation method, considering it to be a powerful and prospective tool, and, in addition, ESM. To achieve more information about the physiologic effect of HVD treatment on cells we also performed microbiological tests.

## II. MATERIALS AND METHODS

### A. Preparation of yeast cells' samples

Water suspension of yeast cells was filled into the reactor tank of an HVD device. A control sample of the suspension was taken before an each experiment session. After applying the HVD on the suspension, a sample of treated cells was taken.

In order to prepare specimens for AFM measurements a drop of yeast suspension from each sample was applied on a separate polycor substrate and dried in air for 1 hour. In between AFM measurement sessions such samples prepared on polycor were stored in plates in a refrigerator. No additional methods of cells' immobilization were used to prepare the specimens for AFM measurements.

Additionally there were also prepared samples of suspensions for ESM measurements.

### B. HVD treatment

A home-built HVD device was used to treat yeast cells with electromagnetic radiation. The treatment was applied on the cells inside the reactor tank of the device in water environment. A total accumulated discharge energy density

Table 1 HVD energy densities

E, J/ml	E1, J/ml
0 (control)	0 (control)
1	1
10	10
50	50
50	75
50	83
100	100
100	149
100	167
150	224

per volume of the suspension (E1) and per volume of the reactor tank (E) were diversified. In order to achieve that, a volume of the reactor tank (V), a filled volume of the reactor tank (V1), a number of discharges (N), voltage per discharge (U) and capacitance per discharge (C) were varied. The resulting applied E and E1 are summarized in Table 1.

### C. Atomic force microscopy

Imaging of the cells was performed using AFM (Solver P47-PRO, NT-MDT) in semi-contact mode. Standard silicon probes for contact mode, type CSG10, with a typical spring constant of cantilevers of 0.1 N/m were used. We have chosen contact-type cantilevers due to their small spring constant that diminishes a risk to damage the cells when performing the surface scanning [2].

All measurements were carried out in air on dried specimens. Surface topography measurements were performed in several regions of each sample, imaging areas of various sizes from 5x5 up to 50x50  $\mu\text{m}$  in order to obtain an image either of a single cell or of a group of cells. To get more detailed information about the surface of samples we additionally registered changes in cantilever oscillation magnitude over the scanned area.

### D. Electron scanning microscopy

In this study ESM was used only as an additional imaging tool in order to compare with the results achieved by AFM, as preparation of samples for ESM itself induces changes in the cells under investigation. Samples for ESM were prepared in a routine procedure. Comparing to AFM there were obtained images of larger areas – starting from 10x8 and up to 200x150  $\mu\text{m}$ .

## III. RESULTS

Obtained AFM images of samples exposed to HVD were qualitatively compared to the corresponding control samples and, additionally, to ESM images. An AFM image of control sample is shown in Figure 1.

It was noted that relatively small energy densities (fewer than 50 J/ml) induced alterations in the surface morphology of yeast cells causing their corrugation comparing to the control sample, which shows smooth surface of the cells (see Figure 2).

Increasing the energy level over 50 J/ml partly destroyed the cells, as it is shown in Figure 3. It was not marked clearly on AFM images that increase in E1 at fixed E (see Table 1) would induce more damage to the cells, however microbiological tests evidenced that larger E1 induced overall slightly higher percentage of killed cells in the sample (from 6% of killed cells up to 10%).

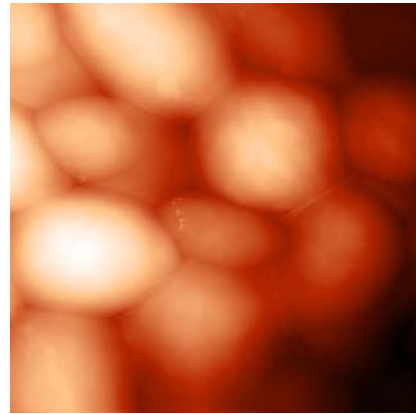
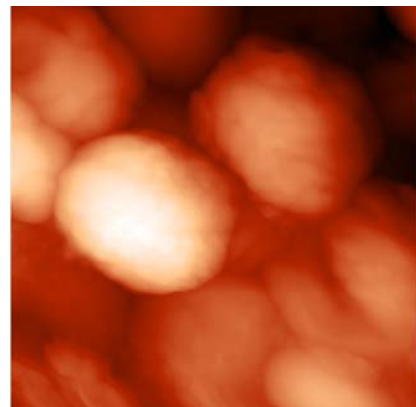
Fig. 1 AFM image of control yeast sample, image size 10x10  $\mu\text{m}$ Fig. 2 AFM image of yeast cells treated with HVD, image size 12x12  $\mu\text{m}$ ,  
E = 10 J/ml, E1 = 10 J/ml



Fig. 3 AFM image of yeast cells treated with HVD, image size 15x15  $\mu\text{m}$ ,  
E = 50 J/ml, E1 = 83 J/ml

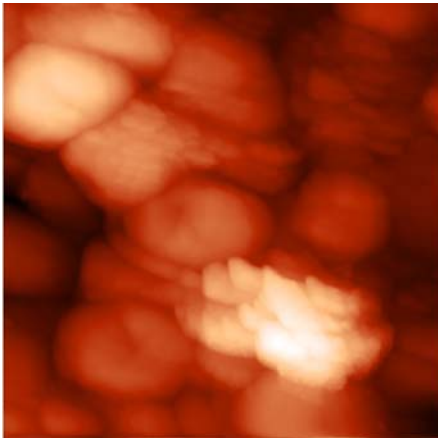


Fig. 4 AFM image of yeast cells treated with HVD, image size 12x12  $\mu\text{m}$ ,  
E = 150 J/ml, E1 = 224 J/ml

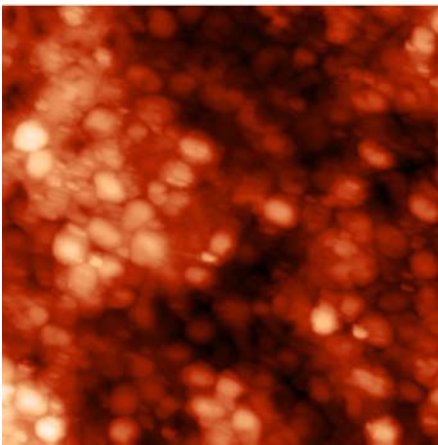


Fig. 5 AFM image of yeast cells treated with HVD, image size 50x50  $\mu\text{m}$ ,  
E = 100 J/ml, E1 = 149 J/ml

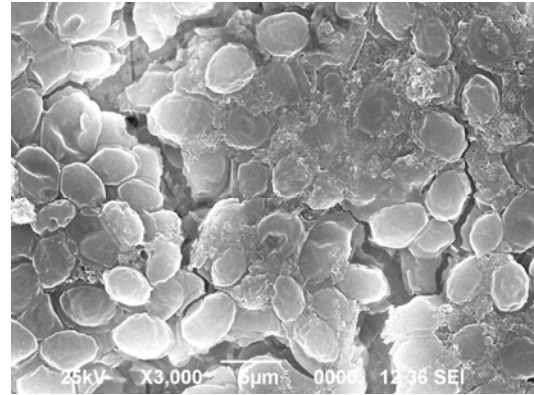


Fig. 6 ESM image of yeast cells treated with HVD, 1 cm = 5  $\mu\text{m}$ ,  
E = 150 J/ml, E1 = 224 J/ml

Applying even larger E values increased the damage caused to the cells (Figure 4) and destroyed more cells in the sample, which can be seen if observing a larger scan area, as shown in Figure 5. A sample of ESM image showing major destruction caused to yeast cells by the highest applied energy density can be seen on Figure 6.

As in previous case with E up to 50 J/ml, also in case of applying HVD with higher energy densities, increase in E1 at constant E (Table 1) did not result in changes visualized by AFM, but microbiological tests showed an increase in percentage of killed cells (from around 10% up to 20%).

Further microbiological experiments with the yeast cells survived after being exposed to HVD evidenced that those cells showed a higher rate of proliferation in the fresh nutrient medium if compared to the control cells.

The new population of cells received using as the inoculum yeast cells survived after the exposure to HVD was also more resistant to another stress dehydration-rehydration.

#### IV. DISCUSSION

The main objective of this work was to study possible alterations in the surface morphology of eukaryotic cells that might be induced by wide-spectrum electromagnetic radiation.

It was shown that HVD of smaller energy densities causes corrugation of cells' surface. Increasing the energy density induces partly destruction of the cells. That might be explained by a dramatic mechanical impact that yeast cells undergo in the reactor tank.

Qualitative analysis of the obtained images did not mark significant differences in the specimens exposed to varied E1 at constant E, however microbiological tests evidence larger percentage of killed cells in case of increasing E1 at constant E. It is a matter of further investigation. Using

AFM in such studies can be extended from only qualitative to quantitative evaluation of alterations induced in cells, if an appropriate calibration of the measuring tool is performed [3].

The higher rate of proliferation showed by the yeast cells survived after the HVD treatment comparing to the proliferation rate showed by the control group might be explained by assumption that HVD treatment kills weaker cells first, leaving only the strongest in the population, whilst the control group consists of all types of cells. This assumption might also explain another result of microbiological experiments – new population of cells received from the survived yeasts is more resistant comparing to the control population.

## V. CONCLUSIONS

Our study has evidenced that HVD treatment influences yeast cells inducing alterations in their surface morphology and in more severe treatment conditions partly destroying the specimens.

Microbiological tests performed within this study show that HVD treatment might be applied on cells in order to enhance the proliferation rate of the culture and to get a more resistant population.

AFM measurements proved to be a useful tool for qualitative evaluation of alterations induced in the surface morphology of the specimens, as they are easily performed and does not require a sophisticate sample preparation.

## REFERENCES

1. Цыфанский С.Л., Бересневич В.И., Окс А.Б. (1991) Нелинейные и параметрические колебания вибрационных машин технического назначения. Риж. техн. ун-т, Зинатне, Рига
2. NT-MDT company at <http://www.ntmdt.com>
3. Dublińska I., Targosz M., Strojny W. et al. (2006) Stiffness of normal and pathological erythrocytes studied by means of atomic force microscopy. *J. Biochem. Biophys. Methods* 66: 1–11

Author: Veronika Fedotova  
Institute: Riga Technical University  
Street: Kalku 1  
City: Riga  
Country: Latvia  
Email: [veronika.fedotova@latnet.lv](mailto:veronika.fedotova@latnet.lv)

# Dependence of DNA Electrotransfer into Cells *In vitro* on Cell Electroporation and DNA Electrophoresis

K. Čepurnienė, S. Šatkauskas

Department of Biology, Vytautas Magnus University, Lithuania

**Abstract** — Electroporation mostly refers to the technique of permeabilizing cell membranes by applying short and intense electric pulses across a cell, such that the barrier function of the membrane is temporally disturbed. This allows various molecules, including plasmid DNA to pass across the membrane and induce their biological effects. The mechanism of the translocation of plasmid DNA through the permeabilized membrane is different from simple diffusion and remains poorly understood. In this *in vitro* study we used two types of pulses, high voltage, short duration (HV) and low voltage short duration (LV) pulses to evaluate cell electrotransfection efficiency in dependence of cell permeabilization (HV pulse) and DNA electrophoresis (LV pulse). Our results showed that DNA electrotransfer was mainly dependent on permeabilizing HV pulse. Differently from *in vivo* studies, this study showed that contribution of LV pulse to DNA electrotransfer is negligible.

**Keywords** — electroporation, electropermeabilization, gene electrotransfer, gene therapy.

## I. INTRODUCTION

Viral vectors are considered to be the most efficient method for gene transfer. However, the use of these vectors is compromised because delivery of the viral vectors is associated with host inflammatory and immune responses. As a good alternative to viral vectors, nonviral methods can be used. Although in comparison to viral vectors, nonviral methods are currently less effective, new developments allow one to believe in the future of these methods. Basically nonviral methods can be divided into chemical or physical. Among physical methods most widespread is electroporation, a method based on the application of electric field pulses to cells. In comparison to viral and chemical vectors, DNA electrotransfer has proved as simple, cheap, non-toxic and safe method for transfer of foreign genes into cells and tissues. Indeed, so far the method has been applied to transfer plasmid DNA to various types of the cells and various tissues [3]. The transfer of the method into clinical trials is basically restricted by insufficient transfection efficiency. Various groups around the World are working to optimise the method. Despite a good progress is achieved the final optimisation is difficult since the mechanisms of gene

electrotransfer are still largely unknown. It is widely accepted that DNA transfer into the cells is possible only if cell permeabilization is achieved. However how DNA interacts with permeabilized membrane and what is the role of the DNA electrophoresis that takes place during delivery of the pulses is not well described [4, 5]. The hypothesis that efficiency of DNA electrotransfer is dependent on DNA electrophoresis originated from observations that longer pulses generally are more efficient [6]. Indeed, optimal conditions for DNA electrotransfer in murine muscles *in vivo* have been achieved using long 20 ms pulses [2]. To further characterise contribution of cell permeabilization and DNA electrophoresis two types of pulses, high voltage, short duration (HV) and low voltage short duration (LV) can be used [4, 7]. The experiment *in vivo* suggested that once cell permeabilization is achieved by HV pulse, DNA electrotransfer efficiency further depends of the electrophoretic LV pulse [1].

Taking in account these results in a preset work we decided to understand what role takes short duration, high voltage (HV) and longer duration, low voltage (LV) pulses in electrotransfection *in vitro*.

## II. MATERIALS AND METHODS

### A. Cell culture.

Chinese hamster ovary (CHO) cells were used. They were grown at 37°C and 5% CO<sub>2</sub> incubator. Cells were grown in DMEM medium with 10% fetal bovine serum, 1% L - glutamine, 1% 100 U/ml Streptomycin penicillin solutions.

### B. Application of electrical pulses to the cells.

HV and LV electric pulses were generated by custom made electroporator. This electroporator generates 1-9 square-wave electric pulses ranging from amplitude 0 to 1200 V in amplitude, 10 $\mu$ s - 2s in duration, and 0.5 - 100 Hz in frequency. The electrical parameters of the pulses during the experiments were controlled by digital oscilloscope. Electroporation chamber was build by using 2 parallel stainless steel plate electrodes (20 mm length, 8 mm width) 2mm apart.

For electroporation cells were washed and resuspended in a pulsing medium (10mM phosphate, 250 mM sucrose, 1mM  $MgCl_2$ ). 45  $\mu$ l of cell suspension and 5 $\mu$ l GFP (green fluorescent protein) plasmid were placed between the electrodes, voltage pulses were then applied. After 10 minutes of the incubation cells were plated in Petri dishes with 2 ml DMEM and incubated at 37°C for 24 h.

DNA electrotransfer efficiency was determined by evaluating the total and fluorescent number of the cells under fluorescence microscope. At each experiment conditions 6 photos have been taken. The cells were counted using Image tools program.

For cell viability evaluation 45  $\mu$ l of cell suspension and 5 $\mu$ l of NaCl (solution of sodium chloride) were placed between the electrodes and treated with defined electric pulses. For electroporation evaluation 45  $\mu$ l of cell suspension and 5 $\mu$ l of BLM (20nM) were placed between the electrodes, voltage pulses were then applied. After 10 minutes the cell suspension was diluted. About 200 cells were plated in 35 mm diameter Petri dishes with 2 ml DMEM and incubated at 37°C for 6 days. Six days later cells were fixed with 96% ethanol and engrained with gram violet crystal dyes. Comprised cells colonies were counted with binocular.

### III. RESULTS

The initial experiments were carried out to evaluate optimal HV (high voltage) pulse parameters that permeabilise nearly 100% of the CHO cells maintaining highest rate of viable cells. Permeabilization of the cells was detected by using nonpermeant cytotoxic drug bleomycin (20nM). The bleomycin has been proven to be a good permeabilization marker [8]. Indeed, bleomycin at 20 nm concentration has no effect on intact cells (data not shown), however kills those cells that undergone cell electroporation.

As we tried to limit DNA electrophoresis we have used one short 100  $\mu$ s duration pulse. The results showed that optimal conditions for CHO cell permeabilization were obtained at 1200 and 1400 V/cm (Fig. 1.). At 1200V/cm 88% of the cell were permeabilized, while 3% were killed., Therefore further experiment were performed with one 100  $\mu$ s duration and 1200 V/cm intensity HV pulse.

Similar experiment was performed to find out LV pulse parameters. We set up LV pulse duration to 100 ms and increased the voltage to the level that LV pulses just started to permeabilize the cells (Fig. 2).

Preliminary results showed that LV pulse up to 100 V/cm of pulse strength does not induce CHO cell permeabilization. At this voltage 100% of the cells

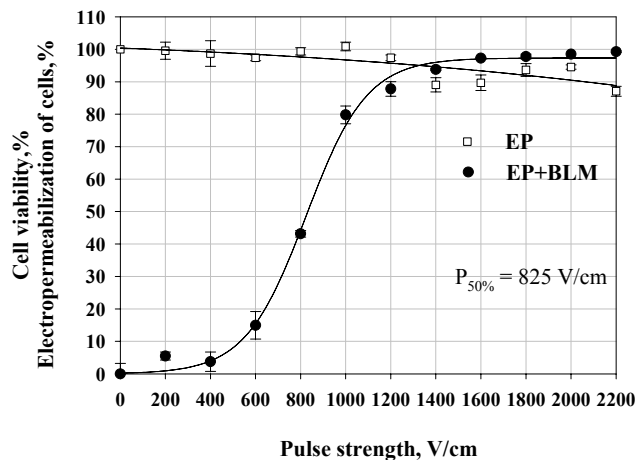


Fig. 1. Electroporation and viability of CHO cells using one 100  $\mu$ s duration HV pulse in dependence of pulse strength

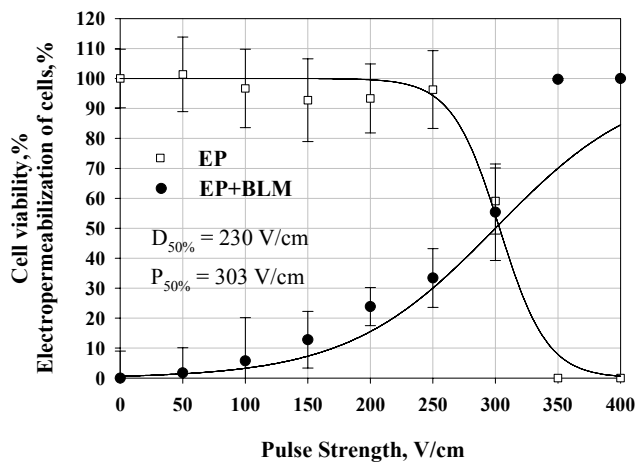


Fig. 2. Electroporation and viability of CHO cells using one 100 ms duration LV pulse in dependence of pulse strength

remained viable (Fig. 2). Further increase of the pulse strength resulted in net increase of the number of permeabilized cells. At LV pulse strength of 300 V/cm 34% of the cells were permeabilized while 32% were killed (Fig. 2). As we aimed to find out LV pulse conditions that do not permeabilize the cells, further experiment using HV and LV pulse combinations was performed at fixed 100 V/cm LV pulse strength.

In order to understand what is the role of HV pulse to the efficiency of DNA electrotransfer we used different number of HV pulses (1200 V/cm, 100  $\mu$ s). Electrotransfer experiments were performed using GFP plasmid. No transfected cells were detected in the absence of electric field (Fig.3). At one HV pulse 20 % of the cells were



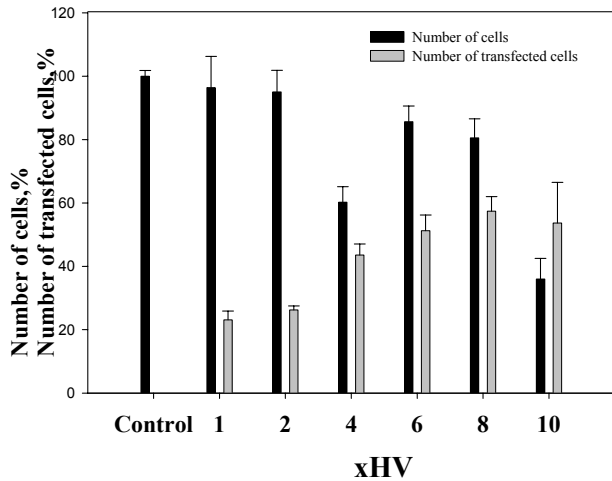


Fig. 3. Electrotransfection efficiency after applying various number of HV (1200 V/cm, 100 μs) pulses

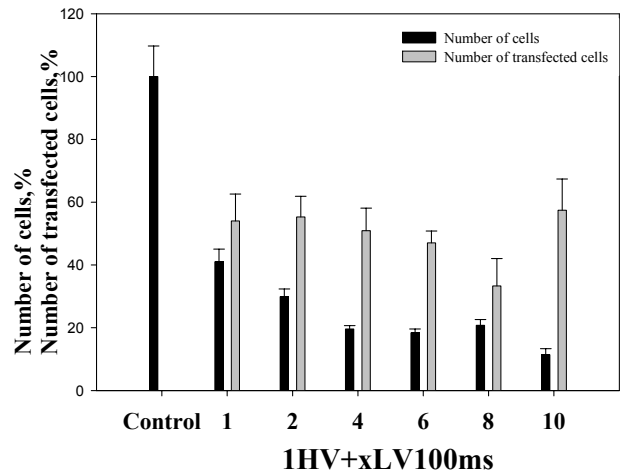


Fig. 5. Electrotransfection efficiency using combination of 1HV (1200V/cm, 100μs duration) and various 1LV pulses (100V/cm, 100ms duration) in dependence of LV pulse number

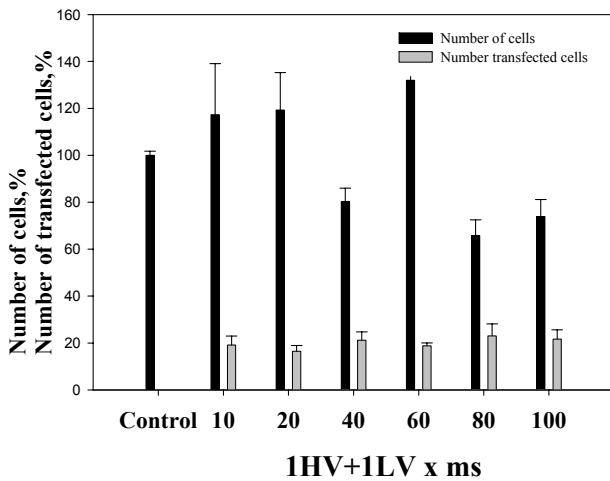


Fig. 4. Electrotransfection efficiency using combination of 1HV (1200 V/cm, 100 μs) and 1LV (100 V/cm) pulses in dependence of LV pulse duration.

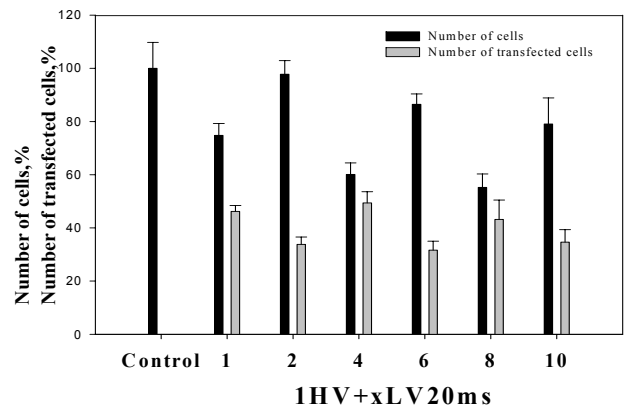


Fig. 6. Electrotransfection efficiency using combination of 1HV (1200V/cm, 100μs duration) and LV (100V/cm, 20ms duration) pulses in dependence of LV pulse number

transfected. Further increase in HV pulse number resulted in increase of the number of transfected cells.

Highest rate of transfected cells was obtained when 6 or 8 HV pulses were used. The transfection efficiency at these pulse conditions were 51% and 57% respectively. Although some cells at these conditions were killed, viability of the cells remained high and was 85% and 80% respectively. Using 10 HV pulses resulted in slight decrease of the number of transfected cells. However the number of viable cells at these conditions decreased to 40% (Fig. 3).

Efficient DNA electrotransfer *in vivo* can be achieved with combinations of HV and LV pulses. To evaluate the role of LV pulse for DNA electrotransfer efficiency we used

various HV and LV pulse combinations. First we have tried to evaluate DNA electrotransfer efficiency in dependence of LV pulse duration. We used HV at previously determined conditions - pulse strength of 1200 V/cm and pulse duration of 100μs. The strength of LV pulse was fixed to 100 V/cm (Fig.4).

At LV pulse duration of 10 ms a moderate number of transfected cells were obtained. However the number of the cells in this HV+LV pulse combination was very similar to the DNA electrotransfer efficiency obtained by HV pulse alone and was about 20% (Fig. 3). Interestingly, increase of LV pulse duration did not enhance efficiency of DNA electrotransfer (Fig.4).

We also determined DNA electrotransfer efficiency using HV and LV pulse combinations in dependence of the

number of LV pulses. Two LV pulse durations, 20 and 100 ms were tested (Figs 5 and 6).

The results showed that combination of 1HV (1200 V/cm, 100  $\mu$ s duration) pulse with different number of LV (100 V/cm, 20 and 100 ms duration) pulses did not increase of DNA electrotransfer efficiency. This was valid for both LV pulse durations tested (Figs. 5 and 6). Although comparing DNA electrotransfer efficiency obtained with 20 and 100 ms pulse duration one can see higher number of transfected cells at 100 ms LV pulse duration, no dependence on pulse duration was obtained (Fig. 4).

#### IV. DISCUSSION

In this study we setup our experiments to evaluate the roles of high-voltage, short-duration (HV) and low-voltage, long duration (LV) pulses for efficient DNA electrotransfer into cells in vitro. Consistently with others and our previous in vitro and in vivo results, this study confirmed that DNA electrotransfer is possible only if cell permeabilization is achieved [4, 6, 2, 7]. Cell treatment with only one LV pulse (100 V/cm pulse strength, 100 ms pulse duration), that do not permeabilize cells had no effect for DNA electrotransfer (data not shown). Contribution of LV pulse on overall DNA electrotransfer efficacy we tested by applying LV pulse 1 s following HV pulse. In in vivo study such type of experiments revealed that once cell is electroporated, DNA electrotransfer efficacy is governed by the parameters of LV pulse [1]. To further characterize how LV pulses facilitate DNA electrotransfer across the permeabilized membrane we setup this in vitro study. Contrary to in vivo studies, this work revealed that contribution of the LV pulses is negligible. Indeed, neither increase in LV pulse number, nor increase in LV pulse duration increased efficacy of DNA electrotransfer (Figs. 4-6). Although, various combinations of HV and LV pulses resulted in slightly variable electrotransfer efficacy, it did not differ significantly from the efficacy achieved with only HV pulse. How it happens that LV pulse in vivo facilitates DNA electrotransfer, but has no effect when applied to cell in suspension remains unclear. One possible explanation is possible taking into account cell stability differences when cells are arranged in tissue in vivo or in suspension in vitro.

Indeed, applying LV pulse following permeabilizing HV pulse, electrophoretic forces the LV pulse target same cell membrane sites as HV pulse. This allows one to assume that electrophoretic forces of LV pulse bring DNA to permeabilized sites of the membrane where translocation of the DNA across the membrane happens. In addition, electrophoretic forces directed to permeabilized sites of the membrane can itself facilitate translocation of the DNA into the cell. In in vitro case, cells are in suspension and can move freely. Therefore membrane sites facing the electrodes are constantly changing. So it is possible that after HV pulse cells orientation has changed and LV pulse targeted other place of the membrane, without induction of DNA electrophoresis and facilitated translocation of the DNA through the membrane. In the forthcoming experiments we are going to test this hypothesis by testing the roles of HV and LV pulses on cells grown in monolayer, where the cells are restricted from any rapid movements.

#### REFERENCES

1. Satkauskas S, et al. (2005) Electrophoretic component of electric pulses determines the efficacy of *in vivo* DNA electrotransfer. *Human Gene Ther J* 16:1194-1201
2. Mir L.M, et al. (1999) High efficiency gene transfer into skeletal muscle mediated by electric pulses. *PNAS* 96:4262-4267
3. Andre F and Mir L.M (2004) DNA electrotransfer: its principles updated reviews of its therapeutic applications. *Gene Ther.*0:1-10
4. Sukharev S.I et al. (1992) Electroporation and electrophoretic DNA transfer into cells. *Biophys J.* 63:1320-1327.
5. Liu F and Huang L. (2001) Improving plasmid DNA-mediated liver gene transfer by prolonging its retention in the hepatic vasculature. *J Gene Med.* 3:569-576.
6. Rols M.P and Teissie J. (1998) Electroporation of mammalian cells to macromolecules: control by pulse duration. *Biophys J.* 75:1415-1423.
7. Satkauskas S et al. (2002) Mechanisms of *in vivo* DNA electrotransfer: respective contributions of cell electroporation and DNA electrophoresis. *Mol Ther.* 5:133-140.
8. Kotnik T et al. (2000) *Biotechniques* 28(5):9 21-926.

Author: Karolina Cepurniene  
 Institute: Vytautas Magnus University  
 Street: Vileikos 8  
 City: Kaunas  
 Country: Lithuania  
 Email: K.Cepurniene@art.vdu.lt

# Measurement of Temperature Synchronized Yeast Cells kHz Electrical Oscillations

M. Cifra<sup>1,2</sup>, J. Pokorný<sup>2</sup>, F. Jelínek<sup>2</sup>, J. Hašek<sup>3</sup> and J. Šimša<sup>2</sup>

<sup>1</sup> Dept. of Electromagnetic Field, Czech Technical University, Prague, Czech Republic

<sup>2</sup> Institute of Photonics and Electronics, Academy of Sciences of the Czech Republic, Prague, Czech Republic

<sup>3</sup> Institute of Microbiology, Academy of Sciences of the Czech Republic, Prague, Czech Republic

**Abstract** — Electrical oscillations of the yeast cell membrane in the frequency range 0.4-1.6 kHz were measured. Synchronized cells in the M-phase generate greater power than the non-synchronized cells. The results correspond to Pohl's dielectrophoretic measurements and support Fröhlich's hypothesis of endogenous electromagnetic fields in living cells.

**Keywords** — bioelectromagnetism, microtubules, yeast cells, electric field

## I. INTRODUCTION

Biological systems generate electromagnetic field above thermal level. It was detected in the optical [1], infrared [2] and MHz [3, 4] bands of the spectrum. Estimated generation mechanism varies in dependence on the frequency of the field. Nanomechanical vibrations of the yeast cell membrane of the order of magnitude of 1 nm were detected in the region of 0.5 – 2 kHz by Atomic Force Microscope (AFM) [5]. The authors estimate the origin of these nanomechanical vibrations in the coordinated action of many proteins working in a concerted and cooperative manner and relate them to the metabolic activity of the cell. Levin et al. [6] observed nanoscale oscillations (at low frequencies of 0.2 – 30 Hz) of human erythrocytes membrane with point dark field microscopy and linked them to MgATP-dependent dynamic assembly of the sub-membrane skeleton. Spatial and time coherent properties of the erythrocyte membrane motions were described from the results of ms time and nm spatial resolution measurements with diffraction phase microscopy [7].

Fröhlich postulated electrical polar vibrations in biological systems giving rise to endogenous biological electromagnetic field [8-11]. The coherent vibrations are excited in systems with nonlinear coupling between elastic and polarization fields excited by metabolic energy supply.

The majority of proteins are electrically polar, for instance tubulin heterodimers. The static electric field is effectively screened by mobile ions under physiological conditions in a distance of a few nm. However, recently it was found that the strong electric field around the mitochondrial membrane may extend up to few  $\mu\text{m}$  into cytosol [12] and the authors conclude that cytosol cannot be considered to be a simple ionic solution but more likely a heterogeneous hydrogel.

Microtubules, a part of the cytoskeleton [13], are highly polar, deformable and dynamic structures. They resemble hollow tubes with inner and outer diameter of 17 nm and of 25 nm, respectively (Fig. 1a). Microtubule consists of 13 (or 14) protofilaments. The building subunits are tubulin heterodimers composed of  $\alpha$ -tubulin and  $\beta$ -tubulin (Fig. 1b). Heterodimers have high electrical dipole moment of over 1000 Debye ( $10^{-26}$  Cm) and are responsible for the high electrical polarity of microtubules. In the interphase, microtubules are radially organized with their minus ends embedded in a centrosome, which is located in the center of the cell near the cell nucleus. There are approximately 400 microtubules in a cell, depending on the organism and the cell type. In the interphase, microtubules can exist as dynamically stable with a turnover rate of about 18 hrs or dynamically unstable with a turnover rate of 5-10 mins. The unstable microtubules undergo dynamic growth (polymerization) and shrinkage (depolymerization), so-called “dynamic instability” (Fig. 1c.). In the M phase microtubules are subject to treadmilling, i.e. polymerize at the plus end and depolymerize at the minus end (chemical plus and minus).

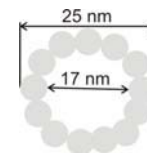


Fig. 1a. Cross section of a microtubule

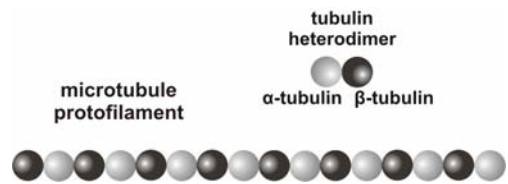


Fig. 1b. Structural subunits of microtubules: protofilaments composed of tubulin heterodimers

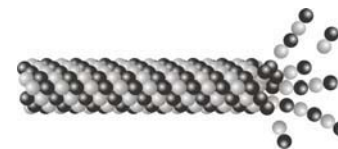


Fig. 1c. Detail of the plus end of a microtubule undergoing dynamic instability

Excitation of mechanical vibrations in microtubules (which are electrically polar) can give rise to electrical oscillations. Mechanical vibrations may be excited by:

- release of energy stored in a microtubule by hydrolysis of guanosine triphosphate (GTP) to guanosine diphosphate (GDP) [14]
- microtubule motor proteins (dyneins and kinesins) “crawling” along the microtubule [5, 15]
- wasted energy in the form of heat released from mitochondria during the production of ATP by oxidative phosphorylation in the citric acid cycle

Energy supply is a necessary condition for existence of the vibration states in the cytoskeleton. Extraordinary properties of microtubules (high shear deformability), layers of structured interstitial water in cytoplasm and high static electric fields created by surrounding mitochondria may participate in forming nonlinear conditions which comply with the Fröhlich’s requirements for coherent vibrations.

In this paper, we present a direct experimental proof of existence of yeast cell electrical activity in kHz region.

## II. MATERIALS & METHODS

### A. Yeast cells

Cold sensitive  $\beta$ -tubulin mutant *tub2-401* of yeast cells *Saccharomyces cerevisiae* (strain CUY67 Mata *tub2-401 ura3-52 ade2-101*) was used. Evolution of the cells in the cell cycle can be synchronized by cultivation at the restrictive temperature (14°C) when the microtubules cannot be formed. The mutant cells at the restrictive temperature continue in their pathway along the cell cycle up to the point before entering the M phase, which processes depend on the microtubules. Thus after certain time period all the mutant cells are stopped at the same point of the cell cycle. When the temperature is increased to the permissive temperature ( $\geq 25$  °C) microtubules are reassembled and the mitotic spindle is formed. Therefore, start of the M phase in the cells cultivated under the restrictive temperature is triggered by the temperature increase above 25 °C. Thus the cells are synchronized. Evolution of the M phase after the warm-up above the permissive temperature is described in detail in [4].

We measured synchronized and non-synchronized cells in suspension. The cells were suspended in the aqueous sucrose solution. After warming to the permissive temperature, the cells synchronously enter the M-phase.

### B. Measurement system

A schematic diagram of the measurement system is shown in the Fig. 2.

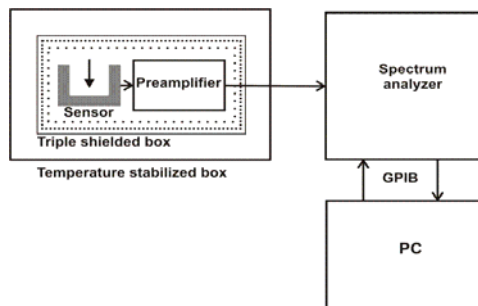


Fig. 2. Schematic depiction of the measurement system used

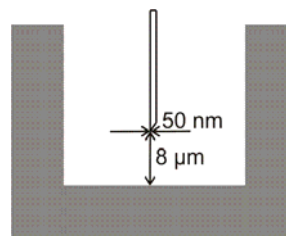


Fig. 3. Dimensions of the sensor used

The crucial parts are the sensor and the preamplifiers (Fig. 3), which are located in the temperature stabilized and triple shielded box (electrically and magnetically by mumetal box). The effectiveness of the screening was verified in [4]. The batteries for the power supply of the amplifier are located inside the screened box, too. At the bottom of a small cuvette there is an evaporated Pt layer forming one electrode. Detecting wire electrode cut at an angle to obtain a point end (about 50 nm) is at a distance of 8  $\mu\text{m}$  above the bottom of the cuvette. Dimension of 8  $\mu\text{m}$  corresponds approximately to the diameter of a yeast cell. After sedimentation cells form a double layer at the bottom of the cuvette. Signal from the sensor is amplified inside the screened box. The preamplifier is connected to the spectrum analyzer through a coaxial cable. Control of the spectrum analyzer is provided by a PC program via GPIB interface. Spectral analyzer Agilent E4448A has been used.

### C. Measurement protocol

Suspension with synchronized cells was cultivated at the temperature of 14°C. Suspension with non-synchronized cells was cultivated at the temperature of about 30°C. Before measurement the test tubes with the suspension were warmed in a water bath of 28°C for 3 minutes. Optical density (OD 600) of the suspension was 4.5 [4], which corresponds to concentration of about  $2 \times 10^8$  cells per milliliter. Afterwards, the cuvette was filled with the 60  $\mu\text{l}$  of suspension. Measurement started immediately after filling the cuvette. Cells sedimented at the

bottom of cuvette. Similar measurements of non-synchronized cells were performed, too.

#### D. Data processing

Measured data have been processed with specified scripts of Python programming language. Modules used: matplotlib, pylab, Numeric, SciPy.

### III. RESULTS

Measurements of the electrical activity of 25 synchronized cell suspensions and 25 non-synchronized cell suspensions have been carried out. Each measurement contained at least 400 double sweeps in the region 0.4 – 1.6 kHz (measured in two subbands of 0.6 kHz each) with resolution bandwidth 1 Hz. Each double sweep and transfer of data to PC took 6s. Measured power is of the order of magnitude of  $10^{-18}$  W.

Fig. 4 shows average power of synchronized and nonsynchronized cells. Two extreme cases in the measurements of synchronized cells, one of unexpectedly low power and one of unusually high power increased standard deviation (SD) by cca. 0.02 a.u. Each measurement was smoothed by moving average of 30 double sweeps wide windows to suppress the noise before taken for calculation of mean and SD.

Fig. 5 depicts 25 measurements of synchronized and nonsynchronized cells each. In some cases, the measured powers of synchronized cells are of similar level or lower than that of nonsynchronized cells. The cells are cultured and treated under the same experimental conditions and the measurements are carried out always under the same proto-

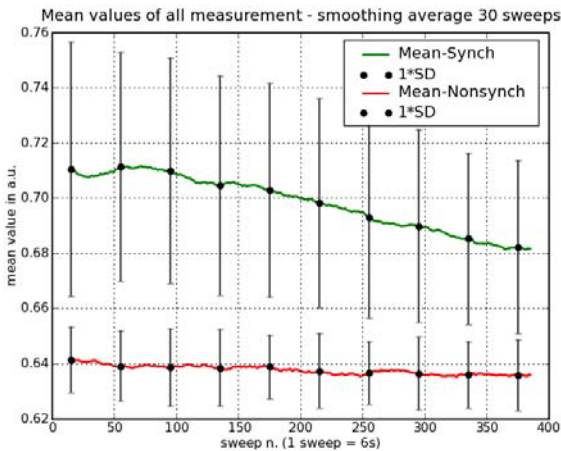


Fig. 4. Mean power of cellular electrical activity in a frequency band 0.4-1.6kHz, error bars – symmetric standard deviation

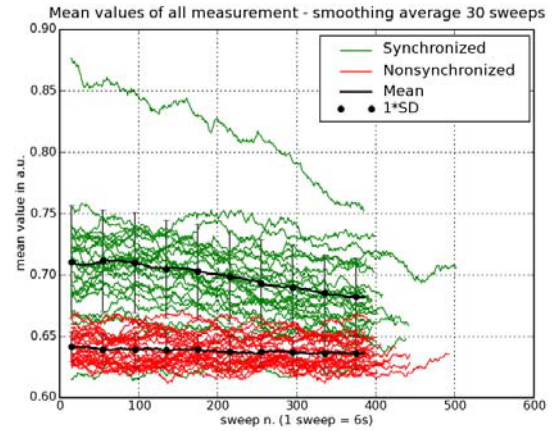


Fig. 5. 25 measurements of synchronized and nonsynchronized cells each

col. Biological variability probably plays a role here. When we evaluate the cells that come from the same inoculation, electrical activity of the synchronized cells is higher than that of nonsynchronized cells (data not shown).

### IV. DISCUSSION & CONCLUSION

Measurements described in this contribution show that the electrical activity of synchronized cells in the M-phase is greater than that of the nonsynchronized cells. It corresponds to the experimental findings of Pohl et al. [3] based on dielectrophoretic attraction of dielectric particles to yeast cells indicating that their electromagnetic activity is greatest in the M phase. However, in our measurements, lower electrical activity of nonsynchronized yeast cells may be also related to the energy depletion, since synchronized cells saved their energy when they are kept under restrictive temperature before measurement while nonsynchronized cells were normally active at the room temperature.

Electrical processes are important for cell activity. Cell cytoskeleton is a probable source of electrical polar vibrations. Endogenous biological electromagnetic field may play important role on temporal and spatial organization of structures and processes in living systems at least on cellular level. Effects on transfer of reaction components, of charge and mass particles were theoretically analyzed [16-18]. If one considers cell an electromagnetic resonator, the field distribution of various modes may play an important role in organization. Disturbed electromagnetic field can be related to pathological processes. One of the deepest disturbances in organization and regulation in multicellular systems is cancer. In cancer cell, regardless of their viral or other mutagenic origin, dysfunction of mitochondria and disintegration of the cytoskeleton are observed [19, 20].

Vibration states and generated electromagnetic field may be disturbed. The static electric field around mitochondria (and around microtubules too) is diminished, and the wasted energy efflux is cut off (the wasted energy may be used in microtubules in nonlinear processes). Restoration of mitochondrial function in cancer cells by treatment with dichloroacetate results in restoration of normal cell function or in apoptosis of aberrant cells [19].

#### ACKNOWLEDGMENT

This work is partially supported by Grant Agency of the Czech Republic, grant n. 102/08/H081.

#### REFERENCES

1. Belousov L., Popp F.A., Voiekov V., Van Wijk R., (2000) Biophotonics and coherent systems. Moscow University Press
2. Albrecht-Buehler G., Rudimentary Form of Cellular 'Vision'. (1992) Proc. Natl. Acad. Sci. USA 89:8288-8293.
3. Pohl H.A. (1980) Oscillating fields about growing cells. Int. J. Quant. Chem, Quant. Biol. Symp., 7: 411-431
4. Pokorný, J. Hašek, F. Jelínek, et al. (2001) Electromagnetic activity of yeast cells in the M phase, *Electro- and Magnetobiology*, 20:371-396
5. Pelling A.E., Sehati S., Gralla E.B. (2005) Time dependence of the frequency and amplitude of the local nanomechanical motion of yeast, *Nanomedicine: Nanotechnology, Biology, and Medicine* 1:178– 183
6. Levin A., Korenstein R. (1991) Membrane fluctuations in erythrocytes are linked to MgATP-dependent dynamic assembly of the membrane skeleton. *Biophys. J.*, 60:733-737
7. Popescu G., Park Y.-K., Dasari R.-R., et al., (2007) Coherence properties of red blood cell membrane motions, *Physical Review E*, 76: 031902
8. Fröhlich H., (1977) Long Range Coherence in Biological Systems. *Riv. del Nuovo Cimento* 7:399-418.
9. Fröhlich H. (1980) The Biological Effects of Microwaves and Related Questions. *Advances Electronics Electron Phys.* 53:85-152.
10. Fröhlich H. (1968) Bose Condensation of Strongly Excited Longitudinal Electric Modes, *Phys. Lett.* 26A:402-403.
11. Fröhlich H. (1968) Long-Range Coherence and Energy Storage in Biological Systems. *Int. J. Quant. Chem.* II, 641-649
12. Tyner K.M., Kopelman R., M.A. Philbert, (2007) "Nano-sized voltmeter" enables cellular-wide electric field mapping, *Biophys J*, 93:1163-1174
13. Alberts B. et al. (1994) *Molecular Biology of the Cell*, 3<sup>rd</sup> version, Garland Publishing
14. Caplow M., Ruhlen R.L., Shanks J. (1994) The Free Energy for Hydrolysis of a Microtubule-Bound Nucleotide Triphosphate Is Near Zero: All of the Free Energy for Hydrolysis Is Stored in the Microtubule Lattice. *J. Cell Biol.*, 127:779–788
15. Kawaguchi K., Ishiwata S., (2001) Thermal Activation of Single Kinesin Molecules With Temperature Pulse Microscopy, *Cell Motility and the Cytoskeleton*, 49: 41–47
16. Pokorný J. (2001) Endogenous Electromagnetic Forces in Living Cells: Implications for Transfer of Reaction Components. *Electro-Magnetobiology*, 20:59-73
17. Pokorný J., Hašek J., Jelínek F. (2005) Electromagnetic Field in Microtubules: Effects on Transfer of Mass Particles and Electrons. *Journal of Biological. Physics*, 31:501-514.
18. Pokorný J., Hašek J., Jelínek F. (2005) Endogenous Electric Field and Organization of Living Matter. *Electromagnetic Biology and Medicine*, 24:185-197.
19. Bonnet S., Archem S.L., Allalunis-Turner J., et al. (2007) A Mitochondria-K<sup>+</sup> Channel Axis Is Suppressed in Cancer and Its Normalization Promotes Apoptosis and Inhibits Cancer Growth, *Cancer Cell*, 11:37-51
20. Suresh S. (2007) Biomechanics and biophysics of cancer cells, *Acta Materialia*, 55:3989-4014

Address of the corresponding author:

Author: Michal Cifra  
 Institute: Dept. of Electromagnetic Field, Czech Technical University  
 Street: Technická 2  
 City: Prague 16027  
 Country: Czech Republic  
 Email: cifram1@fel.cvut.cz

# Self – Assembled System: Semiconductor and Virus Like Particles

Yu. Dekhtyar<sup>1</sup>, A. Kachanovska<sup>1</sup>, G. Mezinskis<sup>1</sup>, A. Patmalnieks<sup>2</sup>, P. Pumpens<sup>3</sup>, R. Renhofa<sup>3</sup>

<sup>1</sup>Biomedical engineering and nanotechnologies institute, Riga Technical University, Riga, Latvia

<sup>2</sup>Institute of Microbiology and Biotechnologies, University of Latvia

<sup>3</sup>Biomedical research and study centre, University of Latvia, Riga, Latvia

**Abstract** — Virus like nanoparticles (VLP) are in use to be absorbed by cells to cause biological effects. To increase a local concentration of VLP, nanoparticles-carriers bringing the latter to the target cell could be employed. N-type and p-type Si semiconductor nanoparticles, to control adhesion of VLP were applied. Optical absorbance spectra and electron microscopy evidenced that VLP became connected to Si nanoparticles. Moreover, a density of the adhered VLP depended on the type of both semiconductor and VLP.

**Keywords** — semiconductor nanoparticles, adhesion.

## I. INTRODUCTION

Modern treatment of humans has come to a scale of the targeted cell due to advantages by nanotechnologies that became "the manufacturing technology of the 21st century"[1].

Virus like particles (VLP) are in use for cell therapy because VLP recognize and easy penetrate via the cell's membrane. A typical diameter of VLP is around 25 nm. To do treatment more effective, a local (in a vicinity of the cell) concentration of VLP should be increased. To reach this, nanoparticles that perform the VLP carrier function could be in use.

Interaction between the particles is supplied by adhesive mechanisms, the latter having electrostatic nature. To influence this, an adjusted surface charge of the nanoparticles-carrier could be employed. From this point of view n- or p-type semiconductor, that surface is originally charged, could become as the carrier. This presentation is devoted to explore a possibility to use n-Si or P-Si to adhere VLP.

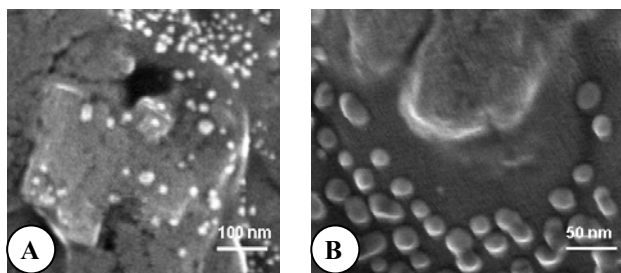


Fig.1. A) SEM image of VLP3 on p-Si particle, B) SEM image of VLP3 beside n-Si particle

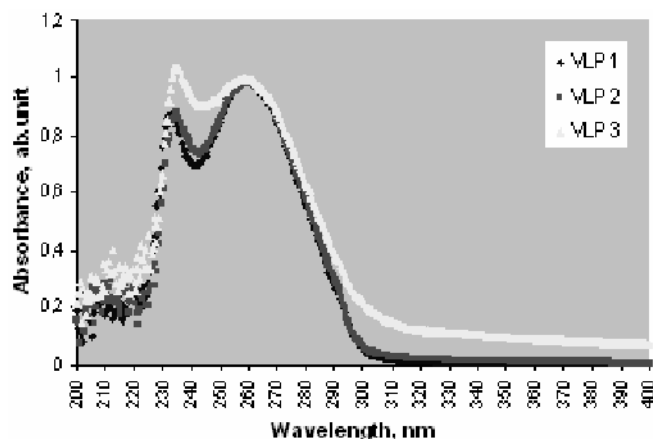


Fig. 2. The OA spectra of VLP

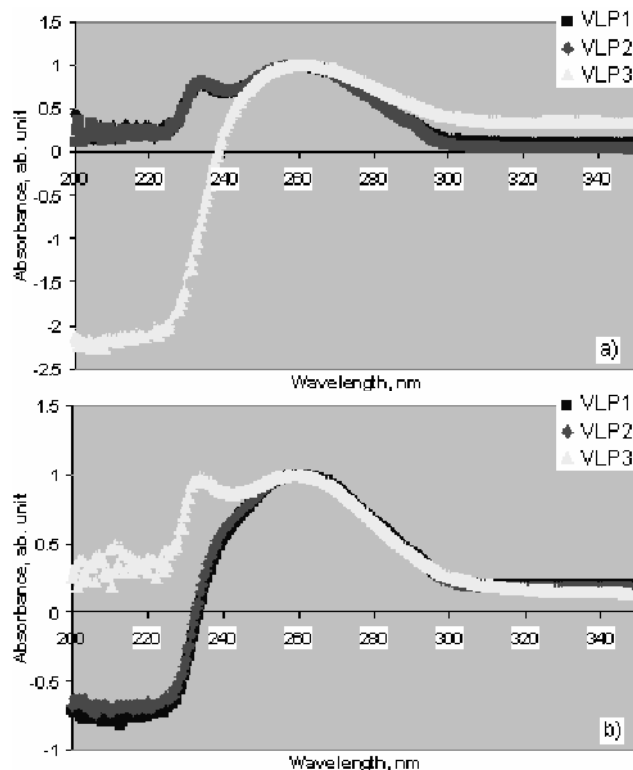


Fig. 3. OA spectra of the VLP mixture with p-Si (a) and n-Si (b)

## II. MATERIALS AND METHODS

The crystalline p-Si and n-Si having specific electrical resistance 1 and 2 Ohm-cm (for p-Si and n-Si, correspondingly) were in use to prepare nanoparticles. The latter were fabricated because of mechanical milling by the porcelain balls. As the result a typical size of the particles around 100 nm was achieved. The size and a shape of the nanoparticles were verified due to electron and atomic force microscopy. For this the scanning electron microscope (SEM) S4800 and atomic force machine (AFM) SOLVER-PRO47 were in use, correspondingly. Three types (VLP1, VLP2 and VLP3) of VLP were selected for the experiment.

The VLP were placed in a buffer solution and mixed with the semiconductor nanoparticles. The buffer was characterized with pH 7,8. Drops of the prepared solutions were dried and further analysed by the above electron microscope. Alongside optical attenuation (OA) of the solutions was measured. The Helios Gamma UV/VIS spectrophotometer with photometric accuracy  $\pm 0.005A @ 1A$  was in use.

## III. RESULTS AND DISCUSSION

SEM tests evidenced VLP were adhered on the Si nanoparticles. However, VLP3 demonstrated the highest capability for adhesion to p-Si in contrast with n-Si. Figure 1 demonstrates the example in this favour.

OA results are delivered in Figure 2, 3. All VLP types demonstrated the maximums of absorbance (ab. unit) at 235

and 260 nm. The Si particles in the buffer were characterized with the constant absorbance within the recorded wave length range. Mixture of VLP3 with p-Si did not have the maximum at 235 nm. However, the solution of VLP1 and VLP2 mixed n-Si did not have the same maximum. This means that the VLP1 and VLP2 were bonded to n-Si, in spite of VLP3 coupled with p-Si.

## IV. CONCLUSION

- VLP could be bonded to Si physically/chemically.
- VLP1 and VLP2 demonstrates coupling with n-Si, but VLP3 – with p-Si nanoparticles.
- Both p- and n- Si nanoparticles could be in use as the carries of eligible VLP.

## REFERENCES

1. LaVan DA, Lynn DM, Langer R. Moving smaller in drug discovery and delivery. *Nat Rev Drug Discov* 2002 Jan; 1(1):77-84.

Author: Anna Kachanovska  
Institute: Riga Technical University  
Street: Ezermalas 6  
City: Riga  
Country: Latvia  
Email: nibi@inbox.lv



# Quantum Chemical Simulation of Cytochrome P450 Catalyzed Oxidation and Carcinogenic potency of Benzene Derivatives

P.N. D'yachkov<sup>1</sup>, N.V. Kharchevnikova<sup>2</sup>, Z.I. Zholdakova<sup>2</sup>, N. Fjodorova<sup>3</sup>, M. Novich<sup>3</sup>  
and M. Vrachko<sup>3</sup>

<sup>1</sup> Kurnakov Institute of General and Inorganic Chemistry, Russian Academy of Sciences, Moscow, Russia

<sup>2</sup> Institutes of Human Ecology and Environmental Health, Russian Academy of Medical Sciences, Moscow, Russia

<sup>3</sup> National Institute of Chemistry, Ljubljana, Slovenia

**Abstract** — Using an oxenoid model and quantum chemical calculations, we have investigated a dependence of carcinogenic potency of the benzene derivatives  $C_6H_5-X$  on a nature of substituents X. According to the model, a P450 enzyme breaks the dioxygen molecule and generates the active atomic oxygen species (oxens) which readily react with substrates. We suggest that a stability of the intermediate  $OC_6H_6-X$  with one tetrahedrally coordinated C atom relative to the original molecule  $C_6H_5-X$  determines a rate of enzyme mediated substrate biotransformation. Using Molecular Orbitals Linear Combinations of Atomic Orbitals (MO LCAO) method and a Modified Neglect of Differential Overlap (MNDO) approach, we have calculated the total energies of molecules  $C_6H_6-X$  and those of arene oxides  $OC_6H_6-X$ . A difference  $\Delta E_{min}$  of these values determines an activation energy of oxidation reaction. We have shown that the compounds with the low  $\Delta E_{min}$  values are non-carcinogenic, and oxidation of benzene ring seems to be the detoxication reaction here. Benzene derivatives with high  $\Delta E_{min}$  values belong to carcinogenic compounds. The reason is a low rate of detoxication in this case.

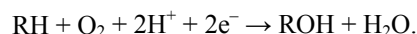
**Keywords** — quantum chemistry, carcinogenicity, benzenes, oxygen, P450.

## I. INTRODUCTION

Many chemical compounds require a biotransformation to exert the effects as the toxicants or tumor initiators [1-4]. Particularly, a concept of enzymatic activation of the pro-carcinogens to the proximate and ultimate carcinogens has strong basis both in *in vitro* and *in vivo* studies and in the quantum chemical calculations of structure-carcinogenic activity relationships of the polycyclic aromatic compounds [5,6], of their alkyl-, nitro-, and aminoderivatives [7 - 9], of the haloidalkanes, and haloidalkenes [10 - 11].

The oxidation catalyzed by a microsomal P450 monooxygenase system is a common mechanism of the foreign compounds biotransformation. Cytochrome P450 is a very large and diverse superfamily of hemoproteins found in all domains of life. The P450 enzymes take part in the detoxication, biodegradation, and bioactivation reactions of chemicals.

The most common reaction catalyzed by cytochrome P450 is a monooxygenase reaction, e.g. insertion of one atom of oxygen into an organic substrate (RH) while the other oxygen atom is reduced to water:



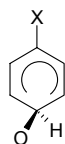
These enzymes have been identified from all lineages of life, including mammals, birds, fish, insects, worms, sea squirts, sea urchins, plants, fungi, slime molds, bacteria, and archaea. Human cytochromes P450 are primarily membrane-associated proteins, located either in the inner membrane of mitochondria or in the endoplasmic reticulum of cells. The cytochromes P450 metabolize thousands of endogenous and exogenous compounds. Most cytochromes P450 can metabolize multiple substrates, and many can catalyze multiple reactions, which accounts for their central importance in metabolizing the extremely large number of endogenous and exogenous molecules. In the liver, these substrates include drugs and toxic compounds as well as metabolic products such as bilirubin (a breakdown product of hemoglobin). Cytochrome P450 enzymes are present in many other tissues of the body including the mucosa of the gastrointestinal tract, and play important roles in hormone synthesis and breakdown (including estrogen and testosterone synthesis and metabolism), cholesterol synthesis, and vitamin D metabolism. Hepatic cytochromes P450 are the most widely studied of the P450 enzymes.

The benzene derivatives are known to be the typical substrates of the cytochrome P450 mediated hydroxylation. It is well known that a rate of oxidation, a yield of the hydroxylated products, as well as a toxicity of benzene derivatives  $C_6H_5-X$  depend strongly on a nature of substituent X.

In this paper, we study the dependences of carcinogenicity of the benzene derivatives on the basis of quantum chemical calculations using the so-called oxenoid model [12]. According to this model, the P450 enzyme breaks the dioxygen molecule and generates the active atomic oxygen species (oxens) [13]. The oxens readily react with substrates [12,13]. The relationships between the nature of substituents from one side and biological oxidation and acute toxicity of the benzene derivatives from another side as well as the

features of metabolism of di- and trichlorinated biphenyls by bacteria were studied using an oxenoid model in our recent paper [14].

We suggest that a stability of the intermediate  $\text{OC}_6\text{H}_5\text{-X}$



with one tetrahedrally coordinated carbon atom relative to the original molecule  $\text{C}_6\text{H}_5\text{-X}$  is a factor determining the rate of enzyme mediated substrate biotransformation. Using MO LCAO MNDO approach, we have calculated the total energies of molecules  $\text{C}_6\text{H}_5\text{-X}$  and arene oxides  $\text{OC}_6\text{H}_5\text{-X}$ . A difference between these values  $\Delta E$  determines approximately activation energy of oxidation reaction [12,14]. In our calculations of benzene derivatives  $\text{C}_6\text{H}_5\text{-X}$ , we have optimized the substituent geometries only. The structure of distorted benzene ring of the intermediates  $\text{OC}_6\text{H}_5\text{-X}$  was taken from paper [12]. The geometry of substituent X in intermediates  $\text{OC}_6\text{H}_5\text{-X}$  is suggested to be the same as in the original molecules  $\text{C}_6\text{H}_5\text{-X}$ .

## II. RESULTS OF CALCULATIONS

In Table 1, the calculated values of activation energies  $\Delta E_{\min} = \min\{\Delta E(\text{ortho}), \Delta E(\text{meta}), \Delta E(\text{para})\}$  for the addition of oxygen to the C atoms of monosubstituted benzenes are presented together with the experimental data on the carcinogenic potency of benzene derivatives  $\text{C}_6\text{H}_5\text{X}$  is presented. The activation energies  $\Delta E(\text{ortho})$ ,  $\Delta E(\text{meta})$ ,  $\Delta E(\text{para})$  correspond to oxidation of the ortho-, meta-, and para-positions. The  $\Delta E_{\min}$  value of benzene  $\text{C}_6\text{H}_6$  is taken as the energy reference point ( $\Delta E(\text{C}_6\text{H}_6) = 0$ ). The negative  $\Delta E_{\min}$  values point on the stabilization of the arene oxide derivative of the  $\text{C}_6\text{H}_5\text{X}$  molecule relative to that of the benzene. The positive  $\Delta E_{\min}$  values points on arene oxide destabilization. The carcinogenic potency of compounds is expressed using a numerical index  $\text{TD}_{50}$  (tumorigenic dose rate 50) in chronic-exposure animal experiments [15] for rats and mice. These values are taken from the Carcinogenic Potency Database (CPDB) – a unique and widely used international resource of the results of 6540 chronic, long-term animal cancer tests on 1547 chemicals [16]. In some cases, information from a Database Toxnet [17] was used too. The  $\text{TD}_{50}$  is the daily dose-rate in mg/kg/body weight/day which halves the probability of remaining tumorless to the end of the standard lifespan.

The  $\text{TD}_{50}$  provides a standardized quantitative measure that can be used for comparisons and analyses of many

Table 1. Activation energies  $\Delta E_{\min}$  for arene oxides formation and carcinogenic potency of benzene derivatives  $\text{C}_6\text{H}_5\text{X}$ . The letters o, m, and p indicate the oxidation positions of compound.

X	$\Delta E_{\min}$ eV	logTD <sub>50</sub> rats mg/kg bw/day		logTD <sub>50</sub> mice mg/kg bw/day	
		male	female	male	female
NHC <sub>2</sub> H <sub>5</sub>	-0.80 o	NP	NP	NP	NP
NH <sub>2</sub>	-0.78 o	-	-		
OH	-0.68 o	NP	NP	NP	NP
OCH <sub>2</sub> CH <sub>3</sub>	-0.48 p	NP	NP	NP	NP
OCH <sub>3</sub>	-0.39 p	NP	NP	NP	NP
OCOCH <sub>3</sub>	-0.38 p	NP	NP	NP	NP
NHCONHCH <sub>3</sub>	-0.37 p	NP	NP	NP	NP
NHCON(CH <sub>3</sub> ) <sub>2</sub>	-0.34 p	NP	NP	NP	NP
C <sub>6</sub> H <sub>5</sub>	-0.17 p			-	-
CH=CH <sub>2</sub>	-0.17 o	NP	1.37	2.32	2.32
F	-0.14 o	NP	NP	NP	NP
<i>i</i> -C <sub>3</sub> H <sub>7</sub>	-0.11 p	NP	NP	NP	NP
C <sub>3</sub> H <sub>7</sub>	-0.08 p	NP	NP	NP	NP
C <sub>2</sub> H <sub>5</sub>	-0.08 p	1.86	1.86	3.20	3.20
CH <sub>3</sub>	-0.07 p	3.49	3.49	-	-
COCH <sub>3</sub>	-0.07m	NP	NP	NP	NP
<i>i</i> -C <sub>4</sub> H <sub>9</sub>	-0.06 p	NP	NP	NP	NP
CH <sub>2</sub> OH	-0.03 p	-	-	-	-
H	0.00	2.23	2.23	1.89	1.89
CHO	0.02 m	-	-	3.17	3.17
COOH	0.04 m	-	-	-	-
Cl	0.10 m p	2.39	-	-	-
CCl <sub>3</sub>	0.10 m			-0.402	-0.402
NO <sub>2</sub>	0.20 m	1.41	1.41	2.47	2.47

issues in carcinogenesis. The range of  $\text{TD}_{50}$  values across chemicals that are rodent carcinogens is more than 100 million-fold. Since the tumor(s) of interest often does occur in control animals,  $\text{TD}_{50}$  is more precisely defined as: that dose-rate in mg/kg body wt/day which, if administered chronically for the standard lifespan of the species, will halve the probability of remaining tumorless throughout that period. A low value of  $\text{TD}_{50}$  indicates a potent carcinogen, whereas a high value indicates a weak one.

In the Table, minus signs point on negative experimental results in the CPDB database (absence of carcinogenic activity), NP implies the absence of carcinogenic activity according to Toxnet Database, blank – data are absent.

The calculated values  $\Delta E_{\min}$  vary between -0.80 and 0.20 eV. All the compounds in the Table 1 can be divided in two groups according to the values of the  $\Delta E_{\min}$ :

(i) Molecules with the  $\Delta E_{\min} < -0.17$  eV. The oxidation of carbon ring of these compounds is greatly activated rela-

tive to that of benzene and the phenols are expected to be formed readily. All these compounds are noncarcinogenic, and oxidation of benzene ring seems to be the detoxication reaction here;

(ii) Molecules with the  $-0.17 < \Delta E_{\min} < 0.20$  eV, the  $C_6H_6$  compound itself being in this group. Here, the oxidation of compounds is only slightly activated relative to that of benzene if the  $\Delta E_{\min} < 0$  or even deactivated if  $\Delta E_{\min} > 0$ . There are carcinogenic compounds in this group. The reason is a low rate of detoxication. Note, in a series of alkyl derivatives with  $X = CH_3, C_2H_5, C_3H_7, i-C_3H_7,$  and  $i-C_4H_9$ , only molecules with methyl and ethyl groups are carcinogenic probably because an enzymatic oxidation of a long alkyl chain is another detoxication mechanism.

#### ACKNOWLEDGMENT

The financial support of the European Union through CAESAR project (SSPI-022674) as well as of the Slovenian Ministry of Higher Education, Science and Technology (grant P1-017) is gratefully acknowledged.

#### REFERENCES

1. Miller EC, Miller JA (1981) Searches for ultimate chemical carcinogens and their reactions with cellular macromolecules *Cancer*, 47: 2327-2332.
2. McKinney JD (1996) Reactivity parameters in structure-activity relationship-based risk assessment of chemicals. *Environ Health Persp* 104: 810-816.
3. Guengerich FP (2001) Common and uncommon cytochrome P450 reactions related to metabolism and chemical toxicity. *Chem Res Toxicol*, 14: 612-649.
4. Loew GH, Poulsen M et al (1985) Computer assisted mechanistic structure-activity studies: application to diverse classes of chemical carcinogens. *Environ Health Perspec* 61:69-96.
5. Von Szentpaly SV (1984) Carcinogenesis by polycyclic aromatic hydrocarbons: a multilinear regression on new type PMO indices. *J Am Chem Soc*, 106, 6021.
6. Flesher J.W., Horn J., and Lehner A.F. Benzylic carbonium ions as ultimate carcinogens of polynuclear aromatic hydrocarbons (1996) *J Mol Struct (Theochem)*, 362, 29.
7. Rabinowitz J, Little S, and Brown K (2002) Why does 5-methylchrysene interact with DNA as both a planar and a nonplanar polycyclic aromatic hydrocarbon? Quantum mechanical studies. *Intern J Quant Chem*, 88: 99-106.
8. Hatch FT, Colvin M.E (1997) Quantitative structure-activity (QSAR) relationships of mutagenic aromatic and heterocyclic *Mutat. Res* 376: 87-96.
9. Benigni R, Passerini L (2002) Carcinogenicity of the aromatic amines: risk assessment *Mutat Res* 511: 191-206.
10. Lag M., Omichinski JG, Dybing E (1994) Mutagenic activity of halogenated propanes and propenes: effect of bromine and chlorine positioning. *Chem-Biol Interact* 93: 73-84.
11. Yin H., Anders M., Korzekwa K., Higgins L.A., Thummel K.E. (1995) Designing safer chemicals: predicting the rates of halogenated alkane metabolism *Proc Natl Acad Sci USA* 92: 11076-11080.
12. Korsekwa K, Trager W, Gouterman M, Spangler D, Loew GH (1985) Cytochrome P450 mediated aromatic oxidation: A theoretical study. *J Amer Chem Soc* 107: 4273-4279.
13. Pudzianowski AT, Loew GH (1983) Mechanistic studies of oxene reactions with organic substrates: reaction paths on MNDO enthalpy surfaces – models for cytochrome P450 oxidation. *Intern J Quantum Chem*, 23:1257-1268.
14. D'yachkov PN, Kharchevnikova NV, Dmitriev, AV, Kuznetsov A V, Poroikov VV (2007) Quantum chemical simulation of cytochrome P450 catalyzed aromatic oxidation: Metabolism, toxicity, and biodegradation of benzene derivatives *Int J Quant Chem* 107: 2454-2478.
15. Peto R., Pike MC, Bernstein L, Gold LS and Ames BN (1984). The TD50: A Proposed General Convention for the Numerical Description of the Carcinogenic Potency of Chemicals in Chronic-Exposure Animal Experiments *Environmental Health Perspectives* Vol. 58, p. 1-8
16. The Carcinogenic Potency Database (CPDB) at <http://potency.berkeley.edu/>
17. Database Toxnet at <http://toxnet.nlm.nih.gov>.

Corresponding author:

Author: D'yachkov PN  
 Institute: Kurnakov Institute of General and Inorganic Chemistry,  
 Russian Academy of Sciences  
 Street: Leninskii pr. 31  
 City: 119991 Moscow  
 Country: Russia  
 Email: [p\\_dyachkov@rambler.ru](mailto:p_dyachkov@rambler.ru)

# Evaluation of Highly-Water Soluble Drug Physical State in Biodegradable Microcapsules

D. Loca<sup>1</sup>, O. Pugovics<sup>2</sup> and L. Berzina-Cimdina<sup>1</sup>

<sup>1</sup> Riga Technical University/Riga Biomaterials Innovation and Development Centre, Pulka 3/3, Riga, Latvia

<sup>2</sup> Latvian Institute of Organic Synthesis, Aizkraukles 21, Riga, Latvia

**Abstract** — Microencapsulation of highly water soluble pharmaceuticals (solubility more than mg/ml) especially if high drug loading is required (more than 50%) is a big challenge. Biodegradable poly(lactic acid) (PLLA) as coating material and polyvinyl alcohol as surfactant were found suitable for this purpose. Active substance was microencapsulated using slightly modified water-in-oil-in-water technique which involves dissolving of the drug in water and polymer in methylene chloride and forming an emulsion in water using a surfactant. Procedure of microencapsulation was followed by filtration and drying of product obtained.

To evaluate the drug physical state in microcapsules powder X-Ray diffractometry (XRD), differential scanning calorimetry (DSC) and scanning electron microscopy (SEM) were used. Differential scanning calorimetry analysis confirmed absence of any drug-polymer interaction. At the same time decrease of glass transition temperature (T<sub>g</sub>) of microcapsules testify that molecularly dispersed drug is forming a true solution with a polymer. X-ray diffraction patterns showed the changes of polymer crystallinity during the encapsulation procedure as well as decrease of crystallinity of the drug. SEM investigations showed the morphology of obtained product and demonstrated the drug location inside the capsule.

**Keywords** — microencapsulation, drug delivery, differential scanning calorimetry. X-Ray diffractometry

## I. INTRODUCTION

Over the past 20 years researchers have focused their attention on biodegradable polymer microcapsules for drug delivery. One of the simplest methods to obtain microcapsules of biologically active agents is to physically mix or blend it with a polymer. In these systems it is suggested that the drug is not chemically attached to the polymer but it is simply encased within the polymer matrix. In this case drug remains in the biologically active form and can exert its effect upon the body as soon as it is released from the polymer matrix [1, 2].

Recently, synthetic biodegradable polymers have been studied for various applications including controlled release drug delivery systems. [3, 4, 5, 6]. Biodegradability, biocompatibility and non-toxicity are the main properties of homo- and co-polymers of poly(lactic acid) (PLLA) and

poly(glycolic acid) extensively used for preparation of controlled release drug carriers.

There are some variations of drug and polymer interaction that determine whether the product obtained forms microparticles, microspheres or microcapsules. Essentially formulation described as microparticle is comprised of a fairly homogenous mixture of polymer and active agent, whereas microcapsules have at least one discrete domain of active agent and sometimes more. Microspheres specifically refer to spherical microparticles [7, 8]. SEM can be used not only to investigate the morphology of microcapsules but also to determine whether product obtained refers to microcapsules, microparticles or microspheres [9].

By examining the thermal properties of microcapsule samples by DSC method, the presence or absence of a thermal event at the melting point temperature of the drug and polymer can be determined. It is often possible to determine whether molecularly dispersed drug is forming a true solution with a polymer by measuring the polymer glass transition temperature (T<sub>g</sub>). If drug interacts with a polymer to form a true solution it will plasticize the polymer and thereby lower the T<sub>g</sub>, whereas drug with no affinity toward the polymer will have no plasticizing effect and T<sub>g</sub> will remain unchanged [10, 11].

When a crystalline material is irradiated with X-rays, scattering patterns characteristic of the molecular arrangement within the crystal structure are produced. This technique is applied directly to microcapsules in order to detect the presence of crystalline drug and possible decrease in drug and polymer crystallinity [12].

## II. MATERIALS AND METHODS

### A. Materials used for microcapsule preparation

Poly(L-lactide) (Biomer L9000) (PLLA) with molecular weight of 200-300 kDa and polyvinyl alcohol (PVA) with molecular weight of 25 kDa and 98 mol % hydrolyzed was purchased from Polysciences (Warrington, USA). PLLA was used as polymer matrix and PVA was used as surfactant in process of microencapsulation. Active pharmaceutical ingredient used as model drug was a gift from JSC Grindex (Latvia). Methylene chloride was from Merck AG.

### B. Differential Scanning Calorimetry

The DSC analysis of pure drug, pure PLLA, blank capsules, mechanical mixture of blank capsules and active substance and drug loaded capsules was carried out using METTLER DSC-30 calorimeter to evaluate any possible drug-polymer interaction. Samples (5-9 mg) was accurately weighted and heated in sealed aluminum pans at a rate  $10^{\circ}\text{C}/\text{min}$  from  $0\dots 250^{\circ}\text{C}$  temperature range. Afterwards samples were rapidly ( $100^{\circ}\text{C}/\text{min}$ ) cooled down using liquid nitrogen and repeatedly heated within the temperature range of  $0\dots 250^{\circ}\text{C}$  for  $T_g$  measurements.

### C. Powder X-ray Diffractometry

XRD patterns were recorded on PANalytical X'Pert PRO diffractometer using Ni-filter and Cu radiation at 40 kV voltage and 30 mA current. The scanning step employed was  $0.017^{\circ}$  over the  $5\text{-}60^{\circ}$  diffraction angle range ( $2\theta$ ).

### D. Scanning Electron Microscopy

The surface morphology and drug physical state in microcapsules was examined using scanning electron microscopy (SEM Mira\LMU). Before observing each sample was coated with gold film using cold plasma sputtering technology.

## III. RESULTS AND DISCUSSION

During the process of microencapsulation the drug could be either dispersed or dissolved in polymer matrix or have no affinity to polymer. Also, any abrupt changes in the thermal behavior of either the drug or polymer may indicate the possible drug-polymer interaction. The thermal curves of pure components, blank microcapsules, physical mixture of drug and blank microcapsules and active component loaded microcapsules are presented in Figure 1.

There are two endotherms seen in the thermal curve of active component. We suggest that the first endotherm ( $T = 88.6^{\circ}\text{C}$ ) indicates the melting point, while the second one is due to the loss of chemically combined water.

Comparing the thermal curves of pure PLLA and blank microcapsules exothermic peak was observed for blank capsules. This peak refers to recrystallization of PLLA.

DSC curves of active component loaded microcapsules and physical mixture showed the significant differences. Peak at  $170^{\circ}\text{C}$  verify that thermodynamically compatible system is formed demonstrating the possibility of drug-polymer affinity.

The comparison of components  $T_g$  are summarized in Table 1.

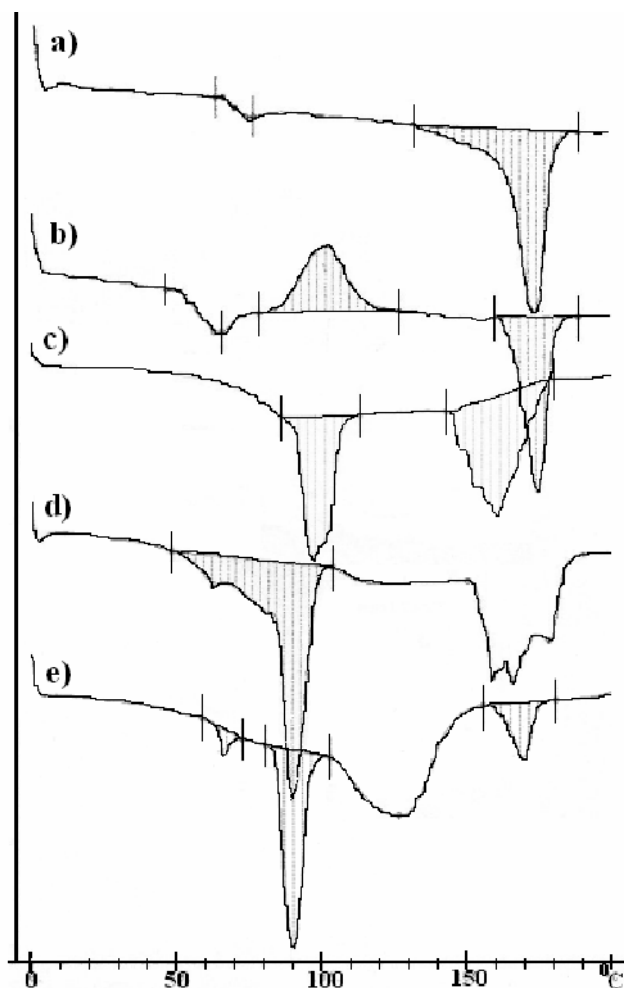


Fig. 1 DSC curves of: a) PLLA; b) blank microcapsules; c) active component d) physical mixture; e) drug loaded microcapsules

Table 1 Glass transition temperatures

Sample	$T_g$ , $^{\circ}\text{C}$
PLLA (pure polymer)	61.7
Physical mixture of blank microcapsules and active component	61.4
Drug loaded PLLA microcapsules	57.6

Results obtained showed the decrease of  $T_g$  for drug loaded microcapsules and it is the possible indication that plasticization of the PLLA by the active substance had occurred.

XRD was carried out to investigate the effect of microencapsulation process on crystallinity of the components involved in encapsulation process. The comparison of X-ray diffraction scans of PLLA and blank microcapsules are seen in Figure 2.

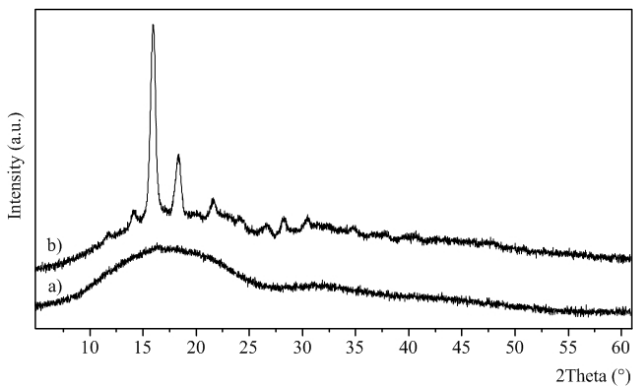


Fig. 2 XRD patterns of: a) PLLA; b) blank microcapsules

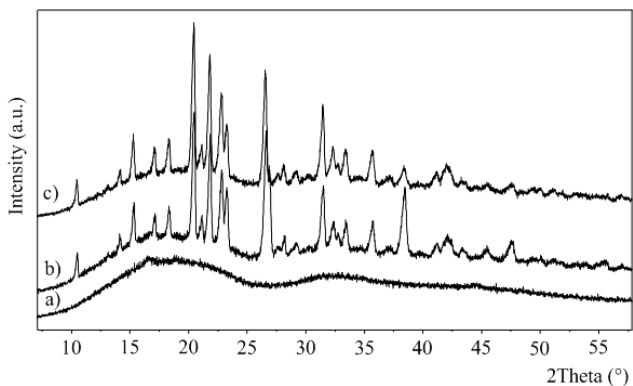


Fig. 3 XRD patterns of: a) blank microcapsules; b) physical mixture; c) drug loaded microcapsules

The blank microcapsules displayed no such peaks as crystalline PLLA, which suggested that the PLLA was presented only in the amorphous state. It was assumed that the solvent removal during the microencapsulation occurred too rapidly for the polymer to crystallize.

X-ray diffraction scans of the blank microcapsules, physical mixture of blank microcapsules and active substance and drug loaded microcapsules are seen in Figure 3.

The drug-PLLA system, in the form of microcapsules, indicated the presence of the crystalline drug and XRD scans were pretty similar to those of physical mixture. Since new peaks were not observed and they have not changed their positions it was suggested that during the crystallization process of drug from water solution, active substance specific crystalline lattice was formed.

SEM was used to evaluate the surface morphology and inner structure of the microcapsules obtained (see Figure 4).

As it is seen in microphotographs blank microcapsules are round preparations with hollow core surrounded by smooth and homogenous surface. Whereas, drug loaded microcapsules comprise of fairly homogenous mixture of

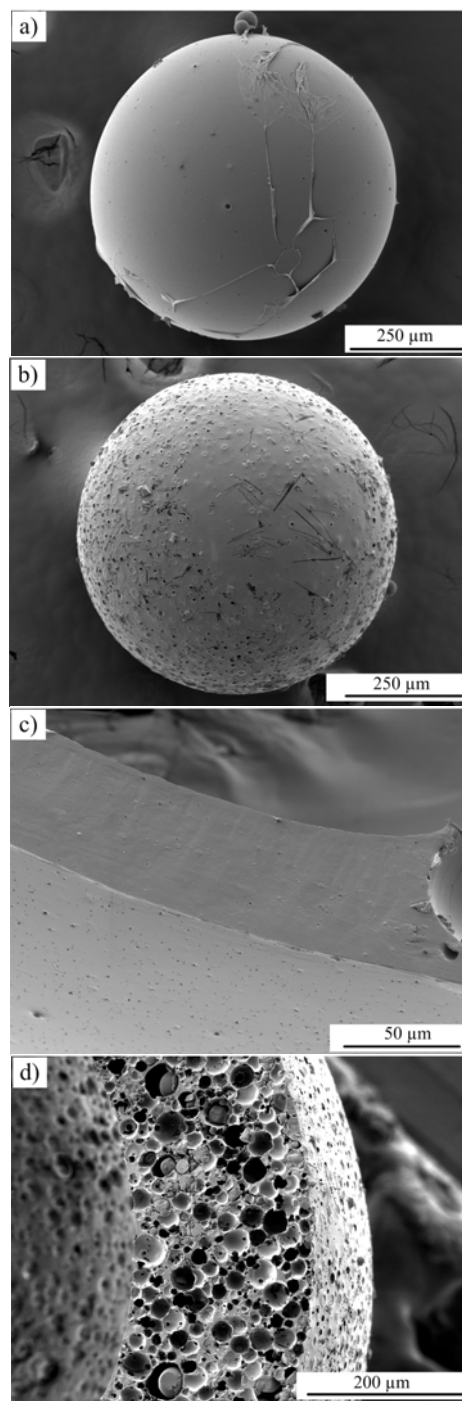


Fig. 4 SEM photographs of: a) blank microcapsule; b) drug loaded microcapsule; c) cross-section of blank microcapsule; d) cross-section of drug loaded microcapsule

both polymer and drug and have many discrete active substance loaded domains 2 - 45µm in diameter. The surface of

the drug loaded microcapsules significantly differs from the blank capsules, it is rough and porous. The size of pores covers the range of 0.2 - 10 $\mu$ m. During the SEM investigations some crystals of the active substance was also observed on the surface of the microcapsules.

#### IV. CONCLUSIONS

Drug physical state in microcapsules was investigated using powder X-Ray diffractometry, differential scanning calorimetry and scanning electron microscopy. Comparing XRD scans of drug loaded microcapsules and physical mixture it was found that new peaks have not appeared thus indicating no changes in crystalline structure. DSC results demonstrated that drug loaded microcapsules are not simple physical mixture of active substance and polymer but there exist certain drug-polymer interaction. Difference of morphology between drug loaded and blank microcapsules were examined via SEM. It was observed from microphotographs that both formulations obtained corresponds to microcapsules where blank capsules have hollow core surrounded by smooth and homogenous surface, while drug loaded microcapsules consist of discrete domains containing active substance.

#### ACKNOWLEDGMENT

This work has been partly supported by the European Social Fund within the National Programme "Support for the carrying out doctoral study programm's and post-doctoral researches" project "Support for the development of doctoral studies at Riga Technical University".

#### REFERENCES

1. Pistel K F, Kissel T. (2000) Effect of salt addition on the microencapsulation of proteins using w/o/w double emulsion technique. *J.Microencapsulation* 17:467-483
2. Chaw C S, Yang Y Y, Lim I J et al (2003) Water-soluble betamethasone-loaded poly(lactide-co-glycolide) hollow microparticles as a sustained release dosage form. *J.Microencapsulation* 20:349-359
3. Sato T, Kanke M, Schroeder H J et al. (1988) Porous biodegradable microspheres for controlled drug delivery. I. Assessment of processing conditions and solvent removal techniques. *Pharm. Res* 5:21-30
4. Chen X O, Yang Y Y, Wang L et al. (2001) Effects of inner water volume on the peculiar surface morphology of microspheres fabricated by double emulsion technique. *J.Microencapsulation* 18:637-649
5. Soppimath K S, Aminabhavi T M. (2002) Ethyl acetate as a dispersing solvent in the production of poly(dl-lactide-co-glycolide) microspheres: effect of process parameters and polymer type. *J.Microencapsulation* 19:281-292
6. Blanco M D, Sastre R L, Teijon C et al. (2006) Degradation behaviour of microspheres prepared by spray-drying poly(D,L-lactide) and poly(D,L-lactide-co-glycolide) polymers. *Int J Pharm* 326:139-147
7. Nihant N, Schugens C, Grandfils C et al. (1994) Polylactide microparticles prepared by double emulsion/evaporation technique. I. Effect of primary emulsion stability. *Pharm. Res.* 11:1479-1484
8. Brown M D (2003) Drug delivery systems in cancer therapy. Humana Press Inc., Totowa, NJ
9. Lamprecht A, Schefer U, Lehr C. (2000) Structural analysis of microparticles by confocal laser scanning microscopy. *AAPS Pharmsci* 6:article 17
10. Watts P J, Davies M C, Melia C D. Microencapsulation using emulsification/solvent evaporation: an overview of techniques and applications. (1990) *Crit Rev Ther Drug* 7:235-259
11. Tayade P T, Kale D R. (2004) encapsulation of water-insoluble drug by cross-linking technique: effect of process and formulation variables on encapsulation efficiency, particle size and in vitro dissolution rate. *AAPS Pharmsci* 6:article 12
12. O'Donnell P B, McGinity J W. (1997) Preparation of microspheres by the solvent evaporation technique. *Adv Drug deliver rev* 28:25-42

Author: Dagnija Loca  
 Institute: Riga Technical University, Riga Biomaterials innovation and development center  
 Street: Pulka3/3  
 City: Riga  
 Country: Latvia  
 Email: dagnija.loc@apollo.lv

# Time-dependent Model of Induced Transmembrane Voltage and Electroporation on Clusters of Cells

G. Pucihar, T. Kotnik and D. Miklavcic

University of Ljubljana, Faculty of Electrical Engineering, Ljubljana, Slovenia

**Abstract** — We present a realistic finite-elements numerical model of a cluster of cells in an electric field. The model enables the calculation of time-dependent changes of the induced transmembrane voltage (ITV) and simulation of electroporation. The model was used to investigate the influence of intracellular connections on the ITV and electroporation of cells, for the case of electrically connected and electrically insulated cells in a cluster. A different distribution of the ITV was observed for connected and insulated cells, resulting also in different course of electroporation - electrically connected cells were porated as one giant cell, while electrically insulated cells were porated individually. Experiments performed on the cluster from which the model was constructed demonstrated that cells in clusters electroporate individually, in agreement with simulations for insulated cells. Different behavior of cells in nonporating and porating fields was attributed to the opening and closing of intracellular connections. These data suggest that the effects of electric field exposure are more diverse for cells in tissues, where intracellular connections could play a role, than for cells in suspension.

**Keywords** — Finite Elements, Electropermeabilization, Transmembrane Potential, Propidium Iodide.

## I. INTRODUCTION

The distribution of the voltage induced on the membrane of a biological cell during the exposure of the cell to an external electric field (the induced transmembrane voltage – ITV) can be of interest in many theoretical and experimental settings, such as activation of voltage-dependent membrane channels and cell membrane electroporation [1, 2]. In the latter case, the distribution of the ITV is important because it determines the electroporated regions of the cell membrane and therefore the efficiency of electroporation [3]. In tissues, due to their complex structure (cells have irregular shapes, are mutually shielded, and have connections between them), numerical methods are often the only feasible approach in determination of the ITV. Many researchers base their studies on macroscopic models, in which bulk electric properties are assigned to each type of tissue in the model, disregarding the detailed cell structure [4]. The microscopic models of tissues, on the other hand, are usually built from several simple geometric objects, which are only rough approximations of the actual cells in tissues [5]. We recently presented a method

for constructing realistic models of irregularly shaped cells, as well as clusters of such cells, from their cross-section images [6, 7]. Compared to single cells, cell clusters represent a better model for studying the behavior of tissue during electroporation. Such models were already used for calculation of the ITV, but were limited to steady-state conditions [6, 7], and were as such unsuitable for modeling electroporation, which is a dynamic process.

Here, we present an extension of the steady-state finite-elements model that enables the computation of dynamic changes of ITV and electroporation on clusters of cells. Since the impact of the cell shape and shielding on ITV and electroporation was already thoroughly investigated [6, 8], we focused on the influence of intracellular connections, analyzing the two extreme cases of electrically connected and electrically insulated cells.

## II. MATERIALS AND METHODS

### A. Construction of the model

A detailed description of the model construction can be found in [6, 7]. Briefly, 3D models of cell clusters were constructed from a sequence of cross-section images of a cluster of Chinese hamster ovary cells attached to a cover glass. The cross-section images were acquired with a CCD camera (VisiCam 1280, Visitron, Germany) mounted on a fluorescence microscope (AxioVert 200, Zeiss, Germany). The cell contours were extracted from the images, combined into solid objects and imported into COMSOL (COMSOL 3.1, MA, USA) where the cluster model was generated (Fig. 1).

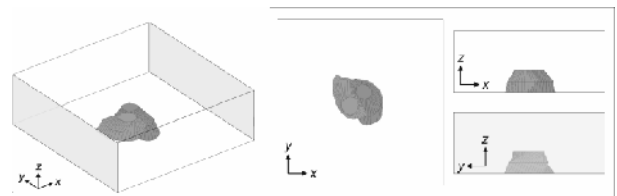


Fig. 1 Model of a cluster of two CHO cells. (A) The 3D geometry constructed from three parallel cross-sections. The box dimensions were  $84 \times 84 \times 27 \mu\text{m}$ . The grey faces are the electrodes, one set to 8.4 V and the other to the ground ( $U/d = 1000 \text{ V/cm}$ ). (B) Side views of the model.



Direct incorporation of a realistic cell membrane into the model is problematic. If the events inside the membrane are not of interest, it can be replaced by a surface to which a boundary condition is assigned [6]:

$$J(t) = (\lambda_m(\varphi_o - \varphi_i) + \varepsilon_m \partial(\varphi_o - \varphi_i) / \partial t) / d \quad (1)$$

where  $J$  is the current density,  $\lambda_m$  is the membrane electric conductivity,  $d$  is the membrane thickness,  $\varepsilon_m$  is the membrane dielectric permittivity, and  $\varphi_o$ ,  $\varphi_i$  are the electric potentials at the outer and inner surface of the membrane, respectively. As very small elements corresponding to the membrane are avoided, the mesh of finite elements is generated without difficulty [6].

### B. Model settings and calculations of the induced transmembrane voltage

The calculations were performed in COMSOL using the *electric currents, transient analysis* application mode. The conductivities of the cell interiors were set to 0.3 S/m and of the cell exterior to 0.14 S/m [6, 9]. The opposite vertical faces of the block were modeled as electrodes, one set to 8.4 V and the other to the ground, to obtain the same electric field of 1000 V/cm as in the experiments (see below). The remaining faces were modeled as insulating. The mesh of finite elements was generated and electric potential  $\varphi$  was calculated with COMSOL. The ITV on a cluster was then calculated as the difference between electric potentials inside and outside the outermost membranes of the cluster ( $ITV(t) = \varphi_i(t) - \varphi_o(t)$ ) and plotted as a function of the arc length. Cells in the cluster were modeled either as electrically connected or electrically insulated. This was done by assigning a conductivity to the contact surface between cells, which was in the first case by a factor of 1000 higher than the membrane conductivity, and in the second case equal to the membrane conductivity.

### C. Model of electroporation

Experiments show that during electroporation, the membrane conductivity in the electroporated regions increases by several orders of magnitude [3, 10]. Besides, electroporation occurs predominantly in the regions of the membrane where the  $|ITV|$  exceeds some threshold value [3]. Therefore, we modeled the course of electroporation by changing the membrane conductivity ( $\lambda_m$ ) in the regions of the membrane where  $|ITV|$  exceeded a threshold value (450 mV – unpublished data), and this included the membranes at the contact. We described the dependence of  $\lambda_m$  on ITV and on time  $t$  as:

$$\lambda_m(ITV, t) = \lambda_0 + A / \left[ 1 + \exp\left(\frac{ITV_c - |ITV|}{0.01}\right) \right] \quad (2)$$

$$A = a(1 - \exp(-t/\tau_1)) + b(1 - \exp(-t/\tau_2))$$

where  $\lambda_0$  is the conductivity of an intact (nonporated) membrane,  $ITV_c$  is the threshold ITV above which electroporation occurs,  $a$  and  $b$  are the increments of  $\lambda_m$  during electroporation, while  $\tau_1$  and  $\tau_2$  are the corresponding time constants of these increments. We applied  $\lambda_0 = 3 \times 10^7$  S/m [9],  $ITV_c = 450$  mV, and the values of  $a$ ,  $b$ ,  $\tau_1$ , and  $\tau_2$  were derived from the experimental data of Hibino [3]:  $2.9 \times 10^{-4}$  S/m,  $2.7 \times 10^{-4}$  S/m,  $1.6 \mu\text{s}$ , and  $238 \mu\text{s}$ , respectively. The changes in  $\lambda_m$  during the field exposure were modeled as irreversible. We should note that the functional dependence of  $\lambda_m$  given by Eq. 2, although in good agreement with some experimental data, does not have a physical background. If  $\lambda_m(ITV, t)$  is derived theoretically in the future, the formulation implemented in our current model can easily be replaced by this more accurate form.

### D. Monitoring the course of electroporation

Chinese hamster ovary cells (CHO) were grown on cover glasses in culture medium (HAM F-12, Sigma, USA). Prior to experiments, the culture medium was replaced by pulsing buffer containing  $100 \mu\text{M}$  membrane-impermeant fluorescent dye Propidium Iodide (PI, Sigma, USA) [6]. The fluorescence of the dye increased considerably after it entered the electroporated cells. A single 400 V,  $200 \mu\text{s}$  rectangular pulse was delivered to the electrodes, and fluorescence of the cluster was monitored in 100 ms time steps with the imaging system described in Section A.

## III. RESULTS AND DISCUSSION

### A. Time course of transmembrane voltage inducement and electroporation

The validity of calculating the ITV using the method applied here was verified in our previous studies by comparing the results to the ITV derived analytically for spherical and spheroidal cells, as well as to the ITV determined experimentally on irregularly shaped cells by a potentiometric dye [6].

In the first part of the study, the cells in the cluster were modeled as electrically connected, so the electric current between the cytoplasm of the cells in contact was not impeded by the membranes separating them. Changes in the membrane conductivity, which indicate electroporation, are presented in Fig. 2A and show a time dependent increase of conductivity in the regions where the ITV exceeded a threshold value. Because the two electrically connected

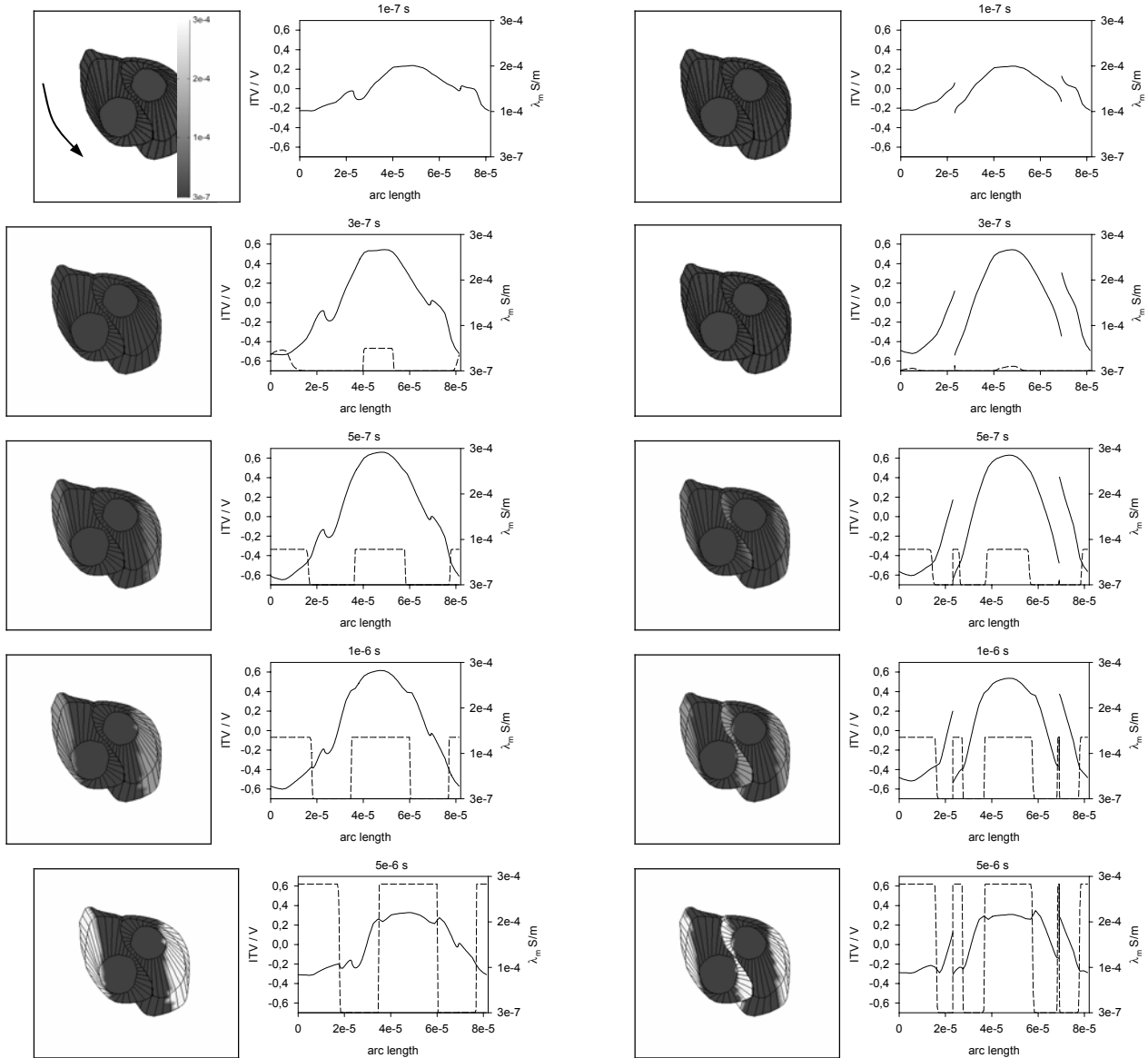


Fig. 2 *Left column: Electrically connected cells.* (A) Changes in membrane conductivity ( $\lambda_m$ ) shown for x-y plane of the model. The arrow marks the path along which the ITV and  $\lambda_m$  were sampled. The scale is in S/m. (B) ITV (solid) and  $\lambda_m$  (dashed) as a function of arc length. *Right column: Electrically insulated cells.* (C) Changes in membrane conductivity shown for x-y plane. (D) ITV (solid) and  $\lambda_m$  (dashed) as a function of arc length. Model settings:  $\lambda_o = 0.14$  S/m,  $\lambda_i = 0.3$  S/m,  $\lambda_m = 3 \times 10^{-7}$  S/m,  $\epsilon_m = 4.4 \times 10^{-11}$  As/Vm,  $\epsilon_o = \epsilon_i = 7.1 \times 10^{-10}$  As/Vm (values taken from [7, 9]),  $E = 1000$  V/cm,  $ITV_C = 450$  mV.

cells behaved as one giant cell, the maximal ITV was induced in the regions of the cluster facing the electrodes, and these parts also became porated first. A detailed spatial distribution of the ITV at the lowermost cross-section of the cluster is depicted in Fig. 2B with solid curves and shows a time-dependent increase of ITV up to the critical value of 450 mV (at  $3 \times 10^{-7}$  s), where electroporation occurred. At this point, the membrane conductivity started to increase

(Fig. 2B, dashed curves), deforming its spatial distribution (with respect to the situation before electroporation) and eventually bringing the increase of the ITV to a halt (at  $5 \times 10^{-6}$  s). Similar deformations of the ITV were observed by other authors in experiments performed on single cells [3].

In the second part of the study, the cells in the cluster were modeled as electrically insulated. As the contact

between two cells consists of two membranes, the threshold voltage for electroporation of this interface was set to twice the value of  $ITV_c$  (900 mV). Because insulated cells in the cluster behaved as individual cells, each cell in a cluster had a different intracellular electric potential ( $\phi_i$ ), which resulted in a disconnected distribution of the ITV along the outermost membranes of the cell cluster (Fig. 2D, solid curves). Such distribution of the ITV consequently provoked electroporation on both sides of each cell in a cluster (Fig. 2C and D, dashed curves), which is different from what was observed for connected cells.

The specific profile of the ITV depends both on the shape of individual cells in the cluster and the shape of the cluster itself. Therefore, in applications requiring a detailed determination of the course of the ITV on a cell membrane, realistic models of cells and clusters of such cells, such as the one presented here, are necessary.

### B. Monitoring electroporation

One of the advantages of the applied method of model construction [6] is that it allows a direct comparison of experiments with calculations. Therefore, the same cells that were modeled as described in Section IIIA were electroporated with a  $1 \times 400$  V, 200  $\mu$ s electric pulse in the presence of a fluorescent dye. An increase in fluorescence was observed on both sides of each cell in the cluster, implying that cells in the cluster electroporated individually (Fig. 3). These regions correspond to the calculated regions of increased membrane conductivity for electrically insulated cells (cf. Figs. 2C and 3A). On the other hand, measurements of the ITV performed on the same cluster but with a low, nonporating electric field showed that cells behaved as electrically connected, as reported previously [7]. The differences in the behavior of cells in clusters could perhaps be attributed to the changes in the properties of intracellular connections, which could occur during an exposure to a field of adequate strength or duration. This may be one of the explanations for the reported differences in electroporation of single cells and electroporation of cells in tissues.

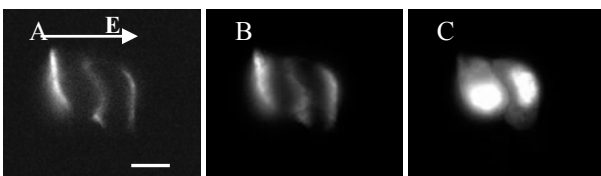


Fig. 3 Monitoring cell electroporation (A) 100 ms, (B) 1500 ms, (C) 3 min after pulse delivery. The cluster was exposed to  $1 \times 400$  V (1000 V/cm) 200  $\mu$ s rectangular pulse in the presence of Propidium Iodide. The bar in A corresponds to 10  $\mu$ m.

## IV. CONCLUSIONS

Our study shows that the conductivity of the contact surface between cells in a cluster can considerably affect the distribution of the ITV and consequently also electroporation. Namely, if cells are electrically connected, they are porated as one giant interconnected cell, while if cells are electrically insulated, they are porated individually. Calculated regions of increased membrane conductivity corresponded to the experimentally observed electroporated regions, but only if cells were modeled as electrically insulated. This is different from the observations in low, nonporating fields, where cells in clusters consistently behaved as electrically connected. The observed differences may be attributed to the changes in the intracellular connections during the exposure to electric fields. Although further research is necessary to confirm this hypothesis, the presented data suggest that the effects of electric field exposure is more diverse for cells in tissues, where intracellular connections could play a role, than for individual suspended cells.

## ACKNOWLEDGEMENTS

This work was supported by the Slovenian Research Agency (project No: Z2-9229 and program P2-0249).

## REFERENCES

1. Tsong T Y (1991) Electroporation of cell-membranes. *Biophys J* 60:297-306
2. Teissié J, Eynard N, Gabriel B et al. (1999) Electroporation of cell membranes. *Adv Drug Deliver Rev* 35:3-19
3. Hibino M, Itoh H, Kinoshita K (1993) Time courses of cell electroporation as revealed by submicrosecond imaging of transmembrane potential. *Biophys J* 64:1789-1800
4. Pavselj N, Bregar Z, Cukjati D et al. (2005) The course of tissue permeabilization studied on a mathematical model of a subcutaneous tumor in small animals. *IEEE T Biomed Eng* 52:1373-1381
5. Fear E C, Stuchly M A (1998) Modeling assemblies of biological cells exposed to electric fields. *IEEE T Biomed Eng* 45:1259-1271
6. Pucihar G, Kotnik T, Valic B et al. (2006) Numerical determination of transmembrane voltage induced on irregularly shaped cells. *Ann Biomed Eng* 34:642-652
7. Pucihar G, Kotnik T, Miklavcic D (2007) An experimental and numerical study of the induced transmembrane voltage and electroporation on clusters of irregularly shaped cells, *IFMBE Proc.* vol. 16, 11th MEDICON Conference, Ljubljana, Slovenia, 2007, pp 639-642
8. Valic B, Golzio M, Pavlin M et al. (2003) Effect of electric field induced transmembrane potential on spheroidal cells: theory and experiment. *Eur Biophys J* 32: 519-528
9. Kotnik T, Miklavcic D, Slivnik T (1998) Time course of transmembrane voltage induced by time-varying electric fields - a

- method for theoretical analysis and its application. Bioelectrochem Bioenerg 45:3-16
10. Kinoshita K, Tsong T Y (1979) Voltage-induced conductance in human-erythrocyte membranes. Biochim Biophys Acta 554:479-497

Author: Gorazd Pucihar  
Institute: University of Ljubljana, Faculty of Electrical Engineering  
Street: Trzaska 25  
City: Ljubljana  
Country: Slovenia  
Email: gorazd.pucihar@fe.uni-lj.si

# Mg<sup>2+</sup> and Ni<sup>2+</sup> ion Effects on Phase Transitions in AU and A2U under Conditions Close to Physiological Ones

V.A. Sorokin, E.L. Usenko and V.A. Valeev

B.I. Verkin Institute for Low Temperature Physics and Engineering, National Academy of Science of Ukraine,  
Dept. of Molecular Biophysics, Kharkov, Ukraine

**Abstract** — Dependences of heating-induced temperatures ( $T_m$ ) of conformational transitions in double-stranded (AU) and three-stranded (A2U) polynucleotides on Ni<sup>2+</sup> ion concentration were obtained for conditions close to physiological ones (0.1 M Na<sup>+</sup>, pH7). Both the diagrams display points in which the character of the conformational transition changes. In the case of AU two transitions 2→3 and 3→1 are observed instead of the transition 2→1. In the case of A2U sequential transitions 3→2 and 2→1 transitions substitutes for the 3→1 transition at [Ni<sup>2+</sup>] > 3·10<sup>-4</sup> M. Effective constants of Ni<sup>2+</sup> ion binding to AU and A2U as well as enthalpies of 2→3 and 3→2 transitions were estimated. The comparison of phase diagrams of AU complexes with Ni<sup>2+</sup> and Mg<sup>2+</sup> ions revealed that, unlike the last ions, Ni<sup>2+</sup> ones widen the region of the stable state of double-stranded AU and, accordingly, narrow the region of the three-stranded A2U existence. The thermodynamic nature of these differences has been established.

**Keywords** — polynucleotides, metal ions, conformational transitions.

## I. INTRODUCTION

Interest in studies on complexes of transition metal ions (TMI), oligo- and polynucleotides in different conformations is conditioned with ecological problems as well with a possibility of using polynucleotides for treating viral and oncological diseases [1]. TMI specific binding to heteroatoms of nucleic acid nitrogen bases induces mistakes in synthesis of polynucleotide sequences. As a result, normal functioning of genetic and regulator apparatus of cellular and subcellular organisms disorders. Specifically, this manifests itself in mutagenic and carcinogenic activities revealed for nickel salts [2].

## II. MATERIALS AND METHODS

Potassium salt of polyribouridylic (polyU) acid (Serva). Sodium salt of AU (Sigma Chemical Company). The NiCl<sub>2</sub>·6H<sub>2</sub>O salt (Reachim) was twice-recrystallized.

Three-stranded A2U was obtained after long (not lesser one month) keeping at 4 °C in buffer solution (0.001 M of sodium cacodylate, pH7; 0.099 M NaCl) of equimolar solution of AU and single-stranded polyU. In all measure-

ments the concentration of polynucleotides phosphorus in solution (P) made up (1±2)·10<sup>-5</sup> M. Ni<sup>2+</sup> ions ([Ni<sup>2+</sup>]) were introduced into solution just before measurements. The errors of P and [Ni<sup>2+</sup>] measurements did not exceed 0.5%.

Measurements were carried out by methods of differential UV spectroscopy (DUVS) and thermal denaturation, Specord UV VIS Spectrophotometer, Carl Zeiss Jena, being applied (Germany) [3].

## III. RESULTS

### A. DUVS

Ni<sup>2+</sup> and Mg<sup>2+</sup> ions induce no changes in A2U absorption spectra up to 0.001 M. This is conditioned by the fact that N7 and N1 atoms of poly A and N3 of two chains of poly U [4] (the above atoms being potentially able for binding) in the U-A-U triplet structure (Fig.1) are involved into the system of hydrogen bonds. This makes them being beyond the ion interaction. Ni<sup>2+</sup> and Mg<sup>2+</sup> ion do not change absorption spectra of AU and poly U too. In the case of AU this may be caused by small steric accessibility of adenine N7 in the rigid structure of AU double helix. With poly U this may be conditioned with weak Ni<sup>2+</sup> ion interaction with uracil [4]. The situation is different for poly A. At lower concentrations Mg<sup>2+</sup> and Ni<sup>2+</sup> ions induce the formation of helical chains in single-stranded polyA. At [Ni<sup>2+</sup>] > 0.001 M complexes are found out, in which Ni<sup>2+</sup> ions interact with N7 and N1 of polyA. The formation of such complexes leads to the destruction of helical chains of polyA.

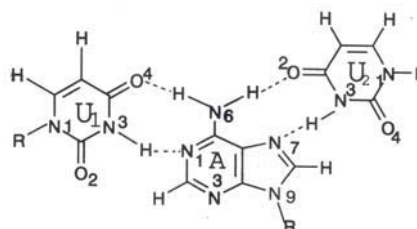


Fig. 1. Structure of triplex A2U formed by adenine and uracil [5]. (U<sub>1</sub>-A) and (A-U<sub>2</sub>) pairs are Watson-Crick and reverse Hoogsteen, respectively.

### B. Phase diagrams

**AU:** Diagrams of the conformational equilibrium for AU complexes with Ni<sup>2+</sup> and Mg<sup>2+</sup> ions include three regions corresponding to different conformational states of the polynucleotide (Fig. 2). In phase diagrams “critical” points (a and b) are observed, in which the conformational transition character changes for  $[Mt^{2+}] \geq [Mt^{2+}]_{cr}$ : two subsequent 2→3 and 3→1 transitions are observed instead of one single-staged 2→1 transition. Concentration dependences  $(T_m)_{21}$  and  $(T_m)_{31}$  (in the range of  $(0, 1 \div 4) \cdot 10^{-4}$  M) for both the ions coincide within 0.8°C. The main difference between phase diagrams of these metal complexes is  $(T_m)_{23}$  behavior: Mg<sup>2+</sup> ions lower this temperature while Ni<sup>2+</sup> ions increase it. Thus, unlike Mg<sup>2+</sup> ions widening the existence region of three-stranded A2U, Ni<sup>2+</sup> ions induce its narrowing, that widens the region of the stable state of double-stranded AU.

**A2U:** Dependences of  $(T_m)_{32}$  and  $(T_m)_{21}$  on Ni<sup>2+</sup> concentration cross in the point “c” corresponding to  $[Ni^{2+}]_{cr} \sim 3 \cdot 10^{-4}$  M and  $(T_m)_{cr} = 63.1^\circ\text{C}$  (Fig.3). Thus, at  $[Mt^{2+}] = [Mt^{2+}]_{cr}$  the values of thermostability of A2U and AU are identical and during heating of A2U only one transition takes place A2U→U+A+U (3→1 transition). We failed to obtain  $(T_m)_{31}$  dependence at  $[Ni^{2+}] > 3 \cdot 10^{-4}$  M because of light scattering that distorted the forms of melting curves.

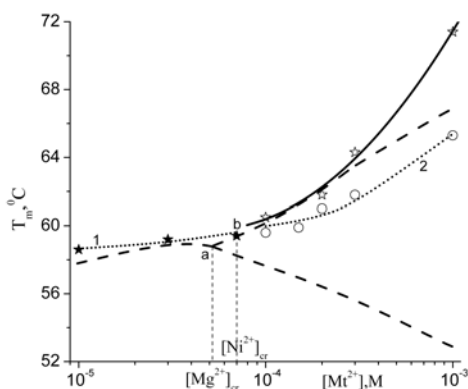


Fig.2. Phase diagram of Ni<sup>2+</sup> and Mg<sup>2+</sup> ion complexes with AU (0.1 M Na<sup>+</sup>, pH7).

Experimental  $T_m$  values for Ni<sup>2+</sup> ions are shown by ★ for  $(T_m)_{21}$ , ○ -  $(T_m)_{23}$ , ☆ for  $(T_m)_{31}$ . Solid line for 3→1 transition is obtained by the least squares method. Experimental dependences of  $T_m$  for 2→1 and 2→3 transitions coincide with the theoretical ones and are not shown. Shaped line is phase diagram of AU+ Mg<sup>2+</sup> complex [3]. Dotted lines 1 and 2 are dependences of conformational transition temperatures on Ni<sup>2+</sup> ion concentration, calculated by formulae (1), (2) and (4): 1- 2→1 transition; 2- 2→3 transition. “a” and “b” are “critical” points.

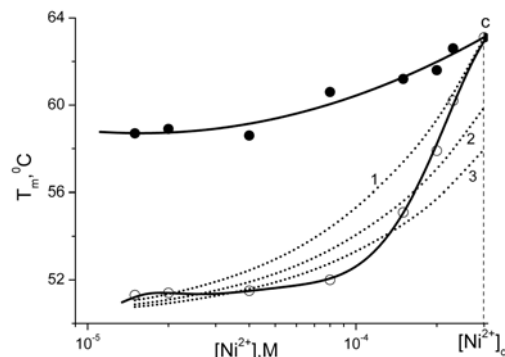


Fig.3. Phase diagram of A2U complex with Ni<sup>2+</sup> ions (0.1M Na<sup>+</sup>, pH7). Experimental  $T_m$  values are shown by signs: ○ -  $(T_m)_{32}$ ; ● -  $(T_m)_{21}$ . Solid line is obtained by the least squares method. Dotted lines 1-3 are concentration dependences of 3→2 transition temperatures, calculated by formulae (1) and (5): 1 -  $\Delta H=3$ ; 2 -  $\Delta H=4$ ; 3 -  $\Delta H=5$  kcal/mol-triplet. “c” is “critical” point.

### IV. DISCUSSION

It was shown by us earlier [3] that peculiarities of forms of phase diagrams for metal complexes of double- and three-stranded polynucleotides may be qualitatively (and sometimes quantitatively) explained by the equilibrium binding theory according to which the temperature of the transition from the conformation “a” to the conformation “b” ( $T_m)_{ab}$  [3] is:

$$(T_m)_{ab} = (T_m)_{ab} + (\delta T_m)_{ab} = (T_m)_{ab} + B \ln E + B \ln F \quad (1)$$

Here  $(\delta T_m)_{ab} = (T_m - T_{m0})_{ab}$  is a change in the temperature of Mt<sup>2+</sup> ion-induced transition of the polynucleotide, “a” and “b” are the initial and new polynucleotide conformations, respectively.  $B = \frac{RT_{m0} T_m}{\Delta H}$  where  $T_m$  is temperature of the transition of the half of polynucleotide links into a new conformation.  $T_{m0}$  is equal to  $T_m$  with  $[Mt^{2+}] = 0$  for 3→2 and 2→1 transitions and with  $[Mt^{2+}]_{cr}$  for 3→1 and 2→3 transitions,  $\Delta H$  is enthalpy of the conformational transition. It is supposed that, according to the principle of compensation of the ion charge [3], the complex stoichiometry (the number of ions per phosphate)  $n$  is equal to  $1/2$ .

For 2→1 transition

$$E_{21} = \frac{(1 + K_{AU} \cdot A_f)^{1/2}}{(1 + K_A \cdot A_f)^{1/2}}; \quad F_{21} = \frac{(1 + K_{AU} \cdot A_f)^{1/2}}{(1 + K_U \cdot A_f)^{1/2}} \quad (2)$$

3→1 transition

$$E_{31} = \frac{(1 + K_{A2U} \cdot A_f)^{1/3}}{(1 + K_A \cdot A_f)^{1/3}}; \quad F_{31} = \frac{(1 + K_{A2U} \cdot A_f)^{2/3}}{(1 + K_U \cdot A_f)^{2/3}} \quad (3)$$

2→3 transition

$$E_{23} = \frac{(1+K_{AU} \cdot A_f)^{1/2}}{(1+K_{A2U} \cdot A_f)^{1/2}}; \quad F_{23} = \frac{(1+K_{AU} \cdot A_f)^{1/2}}{(1+K_A \cdot A_f)^{1/2}} \quad (4)$$

3→2 transition

$$E_{32} = \frac{(1+K_{A2U} \cdot A_f)^{1/2}}{(1+K_{AU} \cdot A_f)^{1/2}}; \quad F_{32} = \frac{(1+K_{A2U} \cdot A_f)^{1/2}}{(1+K_U \cdot A_f)^{1/2}} \quad (5)$$

Here K are constants of the ion binding to polynucleotides,  $A_f$  is concentrations of free ions, assumed to be equal to  $[Mt^{2+}]$  as  $[Mt^{2+}] \gg P$ .

In principle, formulae (1)-(5) permit to determine constants of  $Ni^{2+}$  ion binding to different conformations of polynucleotides (these constants are practically unknown) from simultaneous analysis of phase diagrams for nickel complexes with AU and A2U.

Calculations by these formulae were performed for  $Mg^{2+}$  (only for 2→3 transition) and  $Ni^{2+}$  ions. In the first case only experimental K,  $T_{m0}$  and  $\Delta H$  values were used (Tables 1; 2). For the second case the following calculation scheme was applied:  $K_{AU}$  and  $K_{A2U}$  values were optimized, for which the difference between experimental and calculated  $T_m$  was not more than  $(0.5 \div 1)^\circ C$  in all the range of nickel concentrations for the corresponding conformational transition. In this case  $K_{A2U}$  was determined by  $(T_m)_{31}$  dependence on  $[Ni^{2+}]$  from AU phase diagram (Fig. 2), and  $K_{AU}$  was evaluated by the corresponding  $(T_m)_{21}$  dependence from A2U phase diagram (Fig. 3).

The optimal  $K_{A2U}$  value for  $Ni^{2+}$  ions is 30% higher than that found by us earlier for  $Mg^{2+}$  ions [3]. This difference is within the dispersion of experimental K values for metal ions with polynucleotides, revealed by different authors under comparable conditions [7]. Therefore, this result can be considered as supporting the electrostatic character of  $Ni^{2+}$  ion interaction with A2U.

Table 1 Constants of  $Mg^{2+}$  [3] and  $Ni^{2+}$  ion binding to polynucleotides (in  $M^{-1}$ ) at 0.1 M  $Na^+$

ion	$K_{A2U}$	$K_{AU}$	$K_A$	$K_U$
$Mg^{2+}$	1000	345	200	250
$Ni^{2+}$	1300 *	850 *		

When calculating  $K_{AU}$  and  $K_{A2U}$ , it was supposed that  $K_A$  and  $K_U$  for  $Ni^{2+}$  and  $Mg^{2+}$  ions are equal. \* - calculated by formulae (1)-(3).

Table 2 Initial temperatures ( $T_{m0}$ ) and enthalpies ( $\Delta H$ ) of conformational transitions in AU

Transition	2→1	3→1	2→3
$T_{m0}, K$	331.5		332.5±0.5
$\Delta H, kcal/mol$ [6]	8.2	12.7	4.2

The difference between  $K_{AU}$  for  $Ni^{2+}$  and  $Mg^{2+}$  ions ( $850 M^{-1}$  and  $345 M^{-1}$ , respectively) is essentially higher. Firstly, this may result from peculiarities of the Coulombic interaction of hydrated nickel and magnesium ions with phosphates of AU and, secondly, from the additional outer-spheric coordination of  $Ni^{2+}$  ions with N7 of AU, when they are connected with adenine N7 via water molecule. On the formation of hydrogen bonds by nitrogen-containing compounds shifts of absorption bands are small [8] and, therefore, can not be registered by DUVS.

Concentration dependences of  $(T_m)_{21}$  and  $(T_m)_{23}$  for AU were calculated.  $K_{A2U}$  and  $K_{AU}$  values obtained for  $Ni^{2+}$  ions were used. As Figure 2 shows, calculated and experimental dependences coincide practically.

The data obtained permit to ascertain the thermodynamic cause of qualitative different effects of  $Ni^{2+}$  and  $Mg^{2+}$  ions on 2→3 transition temperature. In this case the integral effect of its change is conditioned with the sum of opposite-signs members  $BlnE < 0$  as  $K_{AU} < K_{A2U}$  and  $BlnF > 0$  as  $K_{AU} > K_A$  (Table 1). Thus, differences in  $(T_m)_{23}$  behavior of AU in the presence of  $Mg^{2+}$  and  $Ni^{2+}$  ions are the result of  $|BlnE| > |BlnF|$  in the first case, whereas for  $Ni^{2+}$  ions the magnitude of the sum destabilizing constituent (1) is smaller than the stabilizing one (Table 3). Thus, the dominant factor of narrowing the region of the double-stranded conformation stable state (and of widening the region of the three-stranded conformation stable state, respectively) in the presence of  $Mg^{2+}$  ions is a higher difference between their affinity for A2U and AU than that for AU and polyA. Opposite relations for differences in constants of  $Ni^{2+}$  ion binding to corresponding polynucleotides result in an opposite influence on the equilibrium between three- and double-stranded helices (Fig. 2).

It is seen from Fig. 3 that it is impossible to describe all the concentration dependence  $(T_m)_{32}$  with one  $(\Delta H)_{32}$  value. Nevertheless, as Fig. 3 shows, its value has to be between 3 and 5 kcal/mol·triplet. These magnitudes narrow

Table 3 Experimental  $(\delta T_m)_{exp}$  and calculated  $(\delta T_m)_{theor}$  dependences of  $(\delta T_m)_{23}$  constituents ( $^\circ C$ ) for AU metal complexes, calculated by formulae (1) and (4) with  $\Delta H=4.2 kcal/mol$  [6]

$[Mt^{2+}], M$	BlnE	BlnF	$(\delta T_m)_{theor}$	$(\delta T_m)_{exp}$
$[Mg^{2+}]$				
$10^{-4}$	-1.8	0.4	-1.4	-1.8
$10^{-3}$	-10.9	3.1	-7.8	-6.2
$[Ni^{2+}]$				
$10^{-4}$	-1.1	1.7	0.6	0.2
$10^{-3}$	-6	12	6	5.9

significantly the interval of the uncertainty in  $(\Delta H)_{32}$  values. Experimental data by different authors reveal that dispersion of  $(\Delta H)_{32}$  values is in the range of 2-8 kcal/mol-triplet [9]. It is essential that effective  $K$  and  $\Delta H$  values obtained in the present work are self-correlated, though being calculated by the independent experimental data.

In spite of the fact that the results obtained are mainly of the fundamental character, in principle, they may be applied for solving problems connected with regulating the stability of polynucleotides multi-chained structures by metal ions.

## V. CONCLUSIONS

In phase diagrams of Ni<sup>2+</sup> and Mg<sup>2+</sup> ion complexes with AU and A2U "critical" points were revealed, in which the character of the conformational transition changes.

Mg<sup>2+</sup> and Ni<sup>2+</sup> ions have different effects on the temperature of 2→3 transition in AU: the first ions lower and second ones rise it. The thermodynamic cause of this effect is a difference in ratios of constants of the ion binding to polynucleotides being in different conformations.

It is shown that it is possible to evaluate parameters of the complex formation in polynucleotides with the use of phase diagrams, an uncertainty not exceeding the experimental one. For the first time, constants are obtained for nickel ion binding to AU and A2U.

The lower  $\Delta H_{32}$  value, as compared with  $\Delta H_{21}$ , is the permanent factor of the "critical" points appearance in A2U phase diagrams in the presence of metal ions.

## REFERENCES

1. Field A.K. (1999) Oligonucleotides as inhibitors of human immunodeficiency virus. *Curr.Opin. Mol. Ther.* 1:323-331
2. Sirover M.A., Loeb L.A. (1976) Infidelity of DNA synthesis in vitro: screening for potential metal mutagens or carcinogens. *Science* 194:1434-1436
3. Sorokin V.A., Valeev V.A., Gladchenko G.O. et al. (2003) Mg<sup>2+</sup> ion effect on the conformational equilibrium of polyU-polyA-polyU and polyA-polyU in aqueous solutions. *Int.J.Biol.Macromol.* 31:223-233
4. Aoki K. (1988) *Metalloproteins: Chemical properties and biological effects.* Elsevier, Amsterdam, Oxford, N.Y., Tokio
5. Andrushchenko V., Blagoi Yu., Van de Sande J.H., Wieser H. (2002) Poly(rA)-poly(rU) with Ni<sup>2+</sup> ions at different temperatures: infrared absorption and vibrational circular dichroism spectroscopy. *J.Biom.Struct.Dyn.* №5, 19: 889 – 906
6. Krakauer H., Sturtevant J.M. (1968) Heats of the helix – coil transition of the polyA – polyU complexes. *Biopolymers* 6: 491 – 512
7. Sorokin V.A., Valeev V.A., Gladchenko G.O. et al. (2002) Effect of Mg<sup>2+</sup> ions on the stability of polyA/polyU three-stranded helices in aqueous solutions. *Macromol.Biosci.* 2: 155-162
8. Higasi K., Baba H., Rembaum A. (1965) *Quantum Organic Chemistry.* Interscience Publishers A division of John Wiley & sons, New York
9. Plum G.E., Pilch D.S., Singleton S.C. Breslauer K.J. (1995) Nucleic acid hybridisation: triplex stability and energetic. *Annu. Rev. Biophys. Biomol. Struct.* 24: 319 – 350

Authors: Sorokin V.A., Usenko E. L., Valeev V.A.  
 Institute: B.I. Verkin Institute for Low Temperature Physics and Engineering, National Academy of Science of Ukraine  
 Street: 47 Lenin ave.  
 City: Kharkov  
 Country: Ukraine  
 Email: sorokin@ilt.kharkov.ua, usenko@ilt.kharkov.ua  
 valeev@ilt.kharkov.ua



# Studies of Mechanical Treatment on Surface Charge of Bioactive Composites

S. Szarska<sup>1</sup>, E. Szmidt<sup>1</sup>, A. Wójcik<sup>2</sup>

<sup>1</sup> Wrocław University of Technology, Institute of Physics, Wrocław, Poland

<sup>2</sup> University of Opole, Institute of Physics, Opole, Poland

**Abstract** — Composite materials containing a bioactive phase (sol-gel-derived bioglass) and a mechanical strength phase (aluminum oxide-porous corundum) are promising materials for repair of living tissues. The influence of mechanical treatment of composite structure containing sintered corundum and CaO-SiO<sub>2</sub>-P<sub>2</sub>O<sub>5</sub> glass system was examined by exoelectron emission and electrokinetic's potential method. The microstructure of the biocomposite material, its mechanical properties and the processing techniques used are all very strongly interrelated.. The charge layer generated on the surface of the composite biomaterials upon deformation and the type of the electrical charge in implants plays significant role in the generation and remodeling of a bone tissue.

**Keywords** — bioglass,  $\zeta$  potential, exoelectron emission

## I. INTRODUCTION

Facing a complex biological and sensitive system as the human body, the requirements of biomaterials for tissue engineering are manifold and extremely challenging. First, biocompatibility of the substrate materials is imperative; that is the material must not elicit an unresolved inflammatory response nor demonstrate immunogenicity or cytotoxicity. In addition, the mechanical properties of the composite materials must be sufficient and not collapse during handling and during the patient's normal activities [1]. Today, materials used for implants are natural or synthetic polymers, other important categories of materials are bioactive ceramics such as calcium phosphates and bioactive glasses or glass-ceramics. Bioactive glass and alumina (Al<sub>2</sub>O<sub>3</sub>) oxide are being combined in a variety of composite materials for tissue engineering. Currently, these composites are being developed with the aim to increase the mechanical implant stability and to improve tissue interaction.

The sol-gel process has extensive application for production of porous bioactive glasses and ceramics. This process involves the hydrolysis of silicon alkoxide in solution to form colloidal solution (sol) and the subsequent chemical polymerization of the silica units to form gel. The gel is heat treated to dry it and form a glass or ceramic structure at temperatures much lower than those used for classical method. If these materials have pores with diameters in excess of 100 $\mu$ m, bone ingrowths can occur, which anchors the bone to the material. In surface reactive materials (bioglasses), the

materials attach directly by chemical bonding with the bone. The mechanism of bone bonding to bioactive materials is depending to formation of hydroxyapatite layer (HA) of the materials after immersion in body fluid.

The main disadvantages of bioglasses are low tensile modulus.

The incorporation of particles into glass matrices forming composite materials is a common method used to increase the toughness of the brittle materials [2].

The composite materials constituents the alumina grains being the reinforcing agents (to improve mechanical performance) and a bioglass matrix we have investigated.

In the relevant literature we could find much information connected to the properties of ceramic composites materials such as biodegradation, biocompatibility and mechanical resistance [1-3]. Relatively little information exists concerning the electric charge which is created on the biocomposite surface layer caused by physiological solution or mechanical deformation [4].

The charge generated on the surface of the composite particles, dispersing in electrolytic solution, cause ions to attract from the water solution. This process results in the formation of an electric double layer in the glass- solution system, thus the electro-kinetic ( $\zeta$ ) potential is created. The creation and type of the electrical charge in implants plays significant role in the generation and remodeling of bone tissue [5].

One of the most sensitive methods of examining the surface properties is the stimulated electron emission method. Low energy electrons are emitted from the surface layer during different interactions causing stimulation of the surface. This method is very sensitive to different surface defects. Studying its kinetics, one can explore both the early stages of failure and the following relaxation of the material [6].

The occurrence of electron discharges in biogel sample is caused by accumulation of the surface charge and contamination of the surface. The studies on influence of external factors on the electric charge formation and its liberation are of great importance because in many cases the charge accumulation and further breakdowns leading to mechanical destruction of insulating material precede the irreversible changes. In the case all of these materials there is a simultaneous separation or recombination of charges that brings about a pulses fluctuation of emission current.

The problem of mechanism of stress generated surface charge upon mechanical deformation is not completely understood. Bioelectrical potentials have been hypothesized to be involved in generation, repair and remodeling of bone tissue. The phenomenon accompanying mechanical deformation and fracture of biomaterials, emission of energetic electrons, ions and neutral particles is called fractoemission [7].

## II. MATERIALS AND METHODS

### A. Matrix

In agreement with earlier investigation [8] biogel glasses with the nominal compositions was 36CaO, 60SiO<sub>2</sub>, 4 P<sub>2</sub>O<sub>5</sub> (mol%) were obtained.

The basic gel has been prepared from the mixture of: tetraethoxysilane TEOS - Si(OC<sub>2</sub>H<sub>5</sub>)<sub>4</sub>; calcium nitrate tetrahydrate Ca(NO<sub>3</sub>)<sub>2</sub> · 4H<sub>2</sub>O dissolved in distilled water; triethylphosphate OP(C<sub>2</sub>H<sub>5</sub>O)<sub>3</sub>, ethanol C<sub>2</sub>H<sub>5</sub>OH as organic solvent, 2N natrium acid HNO<sub>3</sub> as catalyst of the reaction of hydrolysis.

The basic composition of gel has been prepared from this mixture with addition of Ca(NO<sub>3</sub>)<sub>2</sub> · 4H<sub>2</sub>O and OP(C<sub>2</sub>H<sub>5</sub>O)<sub>3</sub> and distilled water. These hydrolyzed mixed about 2 hours.

Dried gels were subject to preliminary heat treatment at 60/90/120°C (in a drier) for three days, and then were heated in air at 2° C/min speed to 800° C and kept about 2 hour.

The samples are soaked in simulated body fluid (SBF), an aqueous solution that has approximately the same ion concentration and pH as human blood plasma [9]. After soaking in SBF for various periods of time, the specimen were removed from solution and dried in air.

### B. Reinforcement agents

Curent research is focused on composite materials made of bioglass coated or filled by submicrocrystalline sintered corundum particles. These particles are an aluminium oxide (α-Al<sub>2</sub>O<sub>3</sub>), which can be the implant core of ultradispersive structure received as a result of transforming aluminium oxide sole into gel and modified with magnesium oxide (MgO). This allows obtaining a specific structure of sinter containing short Al<sub>2</sub>O<sub>3</sub> needles, separated with MgAl<sub>2</sub>O<sub>4</sub> micro-threads. Technologies by particular producers differ in the manner of producing Al<sub>2</sub>O<sub>3</sub> sole and conditions of converting it into gel. At the moment the producers are: American company 3M – under the trade name Cubitron. Mechanochemical treatment (high energetic milling) leads

to changing the material structure. The milling process took place in ethanol. Cubitron was added to hydrolysate in 1:0,028 ratios. Hydrolysate containing submicrocrystalline sintered corundum grains, input granulation after 5, 10 and 15 hours of milling, was left in ambient conditions to be gelled, which occurred in a range of 7 to 14 days, depending on the quantity of water used [10].

The gel layer was coated on k9 glass substrate and then doped by cubitron was measured by exoelectron emission.

### C. ζ potential method

The ζ potential measurements were taken with equipment made by the Biophysics Laboratory Institute of Physics Wrocław University of Technology agree the W. Bialas project.

For investigation of ζ potential, the bioactive composite materials were powdered and soaked in a dilution of physiological solution (SBF), which is the perfect electrolyte.

Mechanochemical treatment (high energetic milling) leads to changing the material structure, dislocations and point defects, is favourable for chemical reactivity in microareas and has an influence on the growth of material specific surface area.

Pulverisette 6 planetary ball mill by Fritsch with a chamber and agate balls was used for mechanochemical treatment for bioglass (F) and cubitron doped bioglass samples. A small quantity of powder was taken from the mill chamber after a specified milling time (5, 10, 15 hours) to grains analyse. Analysis of size composition was made in Micromeritics Sedigraph 5.100 X-ray Analyzer with the use of 0,5 % solution of sodium pyrophosphate as sedimentation liquid and the Hilliard's method by optical microscope. The grain size after 10 hour milling was practically the same that 15 hour milling. The samples of basic (F) and cubitron [(F+5 cub; F+10 cub; F+15 cub) milling time, respectively] doped bioglass was sifted out in order to attain obtainment the same size of grains. The grains analyse of basic (F) and cubitron [(F+5 cub; F+10 cub; F+15 cub) milling time, respectively] doped bioglass in Fig. 1 is presented.

For the powdered composite samples we observed the maximum for 20-30 μm grains size. A small fraction of composite samples was achieved 150 μm value.

24-hour immersion in SBF resulted in formation of calcites as well as various types of calcium phosphate (Ca/P molar ratio ≤ 1). After 5-day immersion of samples in SBF, on the surface of biocomposites containing unmilled cubitron grain and after 10 hours of milling hydroxyapatite appeared, which was evidenced by the Ca/P molar ratio in selected points (1,5; 1,7). In the remaining samples most

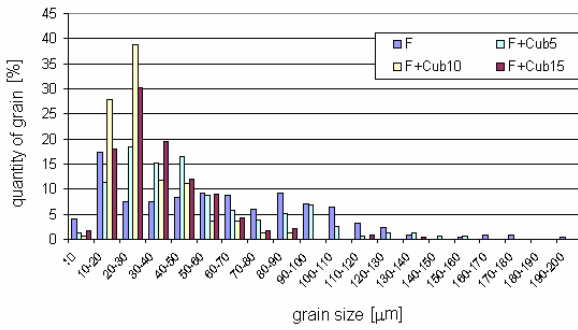


Fig. 1 Grain size analyze for 5/10/15 hour milling cubitron doped bioglasses

probably calcium phosphate crystallised on biocomposite surface. [10].

A charge appeared on the ceramic grain surfaces, dispersed in fluid systems, causing the attraction from water solution the ions of opposite sign, which lowers the effect of electric field agree the distance from these surfaces. A characteristic double electric layer is created, a consequence of which is the appearance of an electro-kinetic potential.

The  $\zeta$  potential results (Tab.1) indicated that the potential is smaller for the composite in comparison of component sample. Increase in the positive charge in all the various types of obtained composites.

Changes of the  $\zeta$  potential indicated on lowering of surface charge lead to hypotheses of proton desorptions, which is characteristic for porous gel composite structure. Maximum value of  $\zeta$  potential achieved for 5 hour milling of porous corundum. Prolongation of deformation process more than 10 hour didn't influence on the surface charge generation by milling process.

Tab.1  $\zeta$  potential results

Sample	$\zeta$ potential, [mV]	$\Delta \zeta$ [%]
<b>Cubitron 5</b>	4,09	8,1
<b>Cubitron 10</b>	3,34	14,9
<b>Cubitron 15</b>	3,48	7,2
<b>F</b>	3,20	11,2
<b>F+Cub5</b>	2,17	9,8
<b>F+Cub10</b>	1,54	16,6
<b>F+Cub15</b>	2,88	9,2

Tab.2  $\zeta$  potential results for doped 15 cubitron/bioglass composite immersed in SBF

Sample	$\zeta$ potential, [mV]
Cubitron 15	3,48
F+Cub15	2,88
F+Cub15 po SBF (7)	2,63
F+Cub15 po SBF (14)	2,06

It is possible that changes of surface charge caused by mechanical deformation may considerably enhance to healing or adverse reaction to the implant by the body.

The result (Table 2) of SBF interaction on 15 hour composite milling indicated that the growth of hydroxyapatite layer on the composite surface lowering the surface potential.

D. Exoelectron method

The OSEE current was registered by a secondary electron multiplier ( $10^{-18}$  A) in vacuum chamber with  $10^{-4}$  Pa. The electrons were focused with an electrostatic lens and registered with the electron multiplier. Measurements of fractoemission kinetics were carried out with an UV optical stimulation. This method has been described elsewhere [11].

By pushing the load applicator, the specimen is gradually deformed.

The area under the fractoemission curve represents the change of electron emission intensity versus time in proportion to the surface charge collected on the sample. Simultaneously this value is proportional to the quantity of the stresses on the glass surface.

Fig.2 presents the curve of fractoemission from bioglass reinforced by alumina.

This figure shows the time response of charge emission, and applied load upon fracture of sample. We observe a sharp, needle-like signal.

The results (average value of exoemission intensity) shown in fig.3 indicate, that in first stage of deformation increase the number of electron traps. We now consider, agree [4, 6] the following model explain this phenomenon. In time of beginning stage, the negative particles escaped from composites and charged the emitting surface positively, creating a positive electric potential. This, in turn, provided an additional barrier for positive charge. For

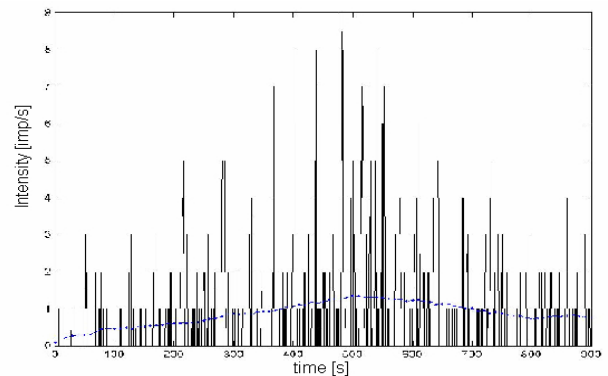


Fig. 2 Exoelectron emission curve of bioglass (F) under 9,6 [N] force deformation

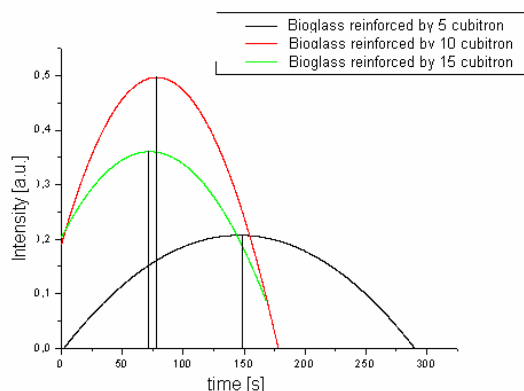


Fig. 3 Average value of exoelectron emission curve of [5/10/15] cubitron milling time F biocomposite under 4,6 [N] force deformation

longer time of milling process (10 and 15 hour) the time of charged positively of surface is shorter (Fig.3 10/15 milling time curves). But the intensity of these maximum (proportional to the quantity of the stresses on the glass surface) is more in comparison of the shorter time of milling (5 hour).

In the case of both the bioglasses and the biocomposites we found that disequilibrium layers formed that included either silica gel or areas with hydroxyapatite. We also found that both diffusion as well as relaxation processes took place in these layers. The emission should be due to the local electric field induced by the surface electric charges distributing on the fracture surface. That is, many dangling bonds and charged defect centers are created by bond breaking on the fracture zone; the mosaic charge distribution causes local electric field, and accelerates the unstable electrons emission. Upon fracture, ejection of oxygen atoms and ions and creation of oxygen vacancies are expected, and electrons released during fracture will be trapped to the oxygen vacancies, exoemission of electron is decaying

### III. CONCLUSIONS

1. Changing of surface potential could influence on the interactions between an implant and negative surface charge of bacteria. A charge appeared on the composite grain surfaces, which lowers the effect of electric field, compare

of the component biomaterials. Obtained results aim at the mechanism of surface potential interaction between biomaterials and the bacteria.

2. Mechanical surface interactions are always connected with electric reconstruction of the surface. In the case of biocomposite: bioglass and corundum, there is a simultaneous separation or recombination of charges that bring about a pulsed fluctuation of emission current. Fractoemission investigations indicate that the presence of reinforcement agents influence not only on the surface structure but it extended the time of release of electrons from the surface.

### REFERENCES

1. Rezwani K., Chen Q.Z., Blaker J.J., Boccaccini A. R. (2006) Biodegradable and bioactive porous polymer/inorganic composite scaffolds for bone tissue engineering, *Biomaterials* 27:3413–3431
2. Świąćki Z., Rosiek G., Wala D., (1999) Biokompozyty. *Prace Naukowe Instytutu Bud Politechniki Wrocławskiej*, 75: 187-196 (in polish)
3. Hench L.L., Jones J.J. (2005), CRC, Woodhead Publishing Limited, Cambridge
4. Szarska S., Kawaguchi Y. (2005) Exoelectron emission from bones and ceramic biomaterials. *Visnyk Lviv Univ* 38:370-377
5. Li P., Zhang F., (1990) The electrochemistry of a glass surface and its application to bioactive glass in solution, *J Non-Cryst Sol* 119:112-118
6. Dehtyar Yu., Kawaguchi Y., Arnautov A., (1997) Failure and relaxations of carbon fibre reinforced plastic tested by exoemission and luminescence methods. *Int J Adhesion and Adhesives* 17:75-78
7. Kawaguchi Y., (1995) Time-resolved fractoluminescence spectra of silica glass in a vacuum and nitrogen atmosphere. *Phys Rev B* 52:9224-9228
8. Pereira M.M., Clark A.E., Hench L.L., (1994) Calcium phosphate formation on sol-gel-derived bioactive glasses in vitro. *J Biomed Mater Res* 28: 693-698.
9. Kokubo T., (1990) Surface chemistry of bioactive glass ceramics. *J Non-Crystalline Solids* 120:138-151
10. Staniewicz-Brudnik B., Szarska S., Gamrat K., (2007) The influence of mechanochemical treatment of substrates on the bioglass composite structure. *J Mater Science* In press
11. Gralec P. (2005) Zmiana ładunku powierzchniowego w szklitych implantach kości pod wpływem deformacji, Master thesis, Wrocław Univ Technol Poland (in polish)

Author: Stanisława Szarska

Institute: Wrocław University of Technology, Institute of Physics

Street:

City: Wrocław

Country: Poland

Email: Stanisława.szarska@pwr.wroc.pl

## Author Index

- A**
- Aadamsoo, K. 331  
Accardo, A. 91, 95, 179, 315, 401, 442  
Adliene, D. 574  
Adlys, G.A. 574  
Alberto, M. 217  
Aldea, E. 8  
Aloisio, G. 489  
Alvarenga, A. 520  
Andersson-Engels, S. 363  
Anier, A. 183  
Antonov, E.N. 12  
Arabere, L. 45  
Arhipovich, V. 45  
Arola, T. 473  
Arshak, A. 225  
Arshak, K. 131, 225  
Artyukh, Y. 190  
Aslanidi, I.P. 586  
Atroshenko, S. 56  
Aydogan, B. 473
- B**
- Babarikins, D. 42  
Bachmann, M. 331, 335, 558  
Back, S. 574  
Bader, R. 30  
Bagratashvili, V.N. 12  
Bairamov, B.H. 594  
Bairamov, F.B. 594  
Bakker, de, J.M.T. 282  
Balodis, A. 439  
Barea, R. 429  
Barzdzukus, V. 528  
Bava, M. 401, 442  
Becker, B. 186  
Bema, D. 598  
Benyo, Z. 229  
Bérard-Andersen, N. 501  
Berzina-Cimdina, L. 48, 68, 72, 619  
Bezborodovs, N. 41  
Bifulco, P. 103, 303  
Bilinskis, I. 190  
Boquete, L. 429  
Borodajenko, N. 68  
Borovikova, D. 602  
Bossert, J. 16  
Bourquain, H. 512  
Brabrand, K. 501  
Brischwein, M. 353  
Britzina, N. 45  
Brumatti, L.V. 401, 442  
Buckley, J. 485  
Buikis, I. 598  
Bulski, W. 556  
Bulycheva, A.A. 477  
Bumbure, L. 552  
Busch, R. 238  
Buteikiene, D. 528  
Buzug, T.M. 417
- C**
- Cabral, J. 506  
Cannata', V. 540  
Caposi, A.M. 60  
Cattin, L. 315  
Cepurniene, K. 606  
Cerny, M. 194, 405  
Cesarelli, M. 103, 303  
Chang G.L. 135  
Chang, L.T. 135, 172  
Chelminski, K. 556  
Chen, Y.-T. 481  
Cheng, K.-S. 481  
Chernish, V.O. 294  
Cho, S. 150  
Cifansky, S. 602  
Cifra, M. 433, 610  
Cipijs A. 347  
Cliquet Jr., A. 548  
Comert, A. 198  
Cong, F. 202, 206  
Correia, C. 217  
Cragg, M. 524  
Csordás, P. 454  
Cunha, J. 278  
Cunha-Vaz J. 217  
Curran, P. 485  
Cusenza M. 91  
Czabanski, R. 446
- D**
- Damianic, C. 211  
Danielli, E. 401  
Dapena, Isabel 429  
Dapena, Miguel 429  
Dastidar, P. 473  
De Paolis, L.T. 489  
Dekhtyar, Yu. 23, 38, 45, 87, 357, 552, 578, 602, 614  
Demetrescu, I. 8, 26  
Dessel, van, P.F.H.M. 282  
Dicu, M.M. 8, 26  
Dill, D. 493, 509  
Dimopoulos, A. 213  
Djupsund, K. 286  
Doessel, O. 450  
Dolgushin, B.I. 566, 586  
Domingues, J. 217  
Dremstrup, K. 409  
Drizdal, T. 433  
Dubey, I. 397  
Dubey, L. 397  
Dukendjiev, E. 99, 139, 141  
Dutta, M. 594  
Dyachkov, P.N. 616  
Dzene, A. 80  
Dzyatkovskaya, N. 294
- E**
- Elberg, P. 409  
Elefteriadis, C. 516  
Elle, O.J. 221  
Erenpreisa, J. 524  
Erts, R. 386  
Eskola, H. 257, 458  
Etelämäki, A. 257  
Evdonin, S.E. 566, 586
- F**
- Fabbro, I. 314  
Falkan, R. 552  
Fan, H. 34  
Fangmann, J. 512  
Faria, A.V. 548  
Fariello, G. 540

Farina, D. 450  
 Fazekas, G. 127  
 Fedotova, V. 602  
 Fernandes, H. 505  
 Fernandes, J. 278  
 Filipenkova, V. 64  
 Filipik, A. 497  
 Finke, B. 30  
 Fjodorova, N. 616  
 Fleischer, L.A. 221  
 Fonda, M. 315  
 Fordos, G. 229  
 Forfang, M. 501  
 Fosse E. 221  
 Franchin, T. 540  
 Fratini, A. 103, 303  
 Freilibs, E. 361  
 Freivalds, T. 524, 598  
 Fricova, M. 107  
 Fridolin, I. 252, 323

## G

Gallo, J. 379, 390, 393  
 Gargiulo G.D. 103  
 Genovese, E. 540  
 Gibbon, G. 168  
 Gill, E. 225  
 Glaz, A. 532  
 Gleizes, A. 8, 26  
 Gloushen, S. 524  
 Goh, J. 34  
 Gordon, R. 425  
 Gostilo, V.V. 477  
 Gotsadze, I.D. 586  
 Goubergrits, L. 111  
 Grabovskis, A. 319  
 Graschew, G. 413  
 Grosz, Z. 127  
 Grothe, H. 353  
 Grube, J. 319  
 Grundl, D. 186  
 Guel, M. 493, 509

## H

Haidegger, T. 230  
 Haj-Hosseini, N. 363  
 Halvorsen, P.S. 221  
 Hannula, M. 115, 119, 234, 473  
 Harcos, P. 127  
 Harju, L. 598

Harms, J.H. 238, 512  
 Harvranek, V. 380  
 Hašek, J. 610  
 Havranek, V. 390, 393  
 Heblakova, E. 339  
 Hein, H.J. 87  
 Hemzal, D. 497  
 Henke, J. 238  
 Hidalgo, M.A. 429  
 Hildebrand, M. 175  
 Himanen, S.-L. 270  
 Hinkula, H. 234  
 Hinrikus, H. 331, 558  
 Hirvikoski A. 115, 119  
 Hlimonenko, I. 242  
 Hoff, L. 221, 501  
 Honkala, M. 198  
 Hoogendijk, M.G. 282  
 Horak, Z. 107  
 Horoba, K. 446, 469  
 Howdle, S.M. 12  
 Hrabovsky, M. 380, 390, 393  
 Huang, T.J. 135  
 Huotari, A.-M. 260  
 Huotari, M.J. 245  
 Huupponen, E. 270  
 Hyttinen, J. 327, 343, 473

## I

Ikaunieks, G. 366  
 Ilchmann, F. 186  
 Infantosi, A.F. 516, 520  
 Ionita D. 19  
 Iordachescu, D. 19, 60  
 Irmer, G. 594  
 Isorinne, M. 119  
 Ivanov, A. 524  
 Ivanova, M. 524  
 Iwabuchi, S. 264

## J

Jagomägi, K. 248  
 Jakaite, L. 123  
 Jakushevich, V. 602  
 Jan, J. 497  
 Jandre, F.C. 516  
 Jantti, V. 260, 257, 458  
 Janzen, N. 186  
 Jasper, U. 552  
 Jauhainen, J. 119, 234

Jegelevicius, D. 528  
 Jelínek, F. 610  
 Jerotskaja, J. 252, 469  
 Jezewski, J. 446  
 Jezewski, M. 446  
 Jirik, R. 497  
 Jobbágy, Á. 127, 454  
 Johansson, J. 371  
 Jonas, S. 512  
 Joutsen, A.S. 257, 458  
 Jurva, J. 257

## K

Kachanovska A. 615  
 Kahn, T.H. 512  
 Kaik, J. 183, 311  
 Kalnins, M. 80  
 Kalyakin, I. 202  
 Kaminski, P. 556  
 Kanczler, J.M. 12  
 Kaneswaran, K. 131  
 Kania, M. 556  
 Kapucu, F.E. 260  
 Karas, S. 339  
 Karlov, A.V. 38  
 Kartunova L. 562  
 Kasyanov, V. 76, 143, 154  
 Katashev, A. 356, 603  
 Katasheva, J. 357  
 Kawahara, K. 264  
 Kazanzides, P. 229  
 Keller, D. 450  
 Keller, T. 16  
 Kertzsch, U. 111  
 Kharchevnikova, N.V. 616  
 Khlusov, I.A. 38  
 Khmelev, A.V. 566, 586  
 Khosroshahi, M. 375, 383  
 Kim I.Y. 150  
 Kim S.I. 150  
 Kim, D.Y. 150  
 Kivastik J. 461  
 Klavinsh, A. 146  
 Klein, S. 210, 417  
 Klimanov, M.Yu. 294  
 Klonowski, W. 268  
 Kneppo, P. 339  
 Knets, I. 64  
 Konvickova, S. 107  
 Kopustinskis, A. 274  
 Korhonen, H. 286

Korostynska, O. 225  
 Kostylev, V. 566  
 Kotelnikovs, A. 299  
 Kotnik, T. 623  
 Kovacs, L. 229  
 Krechetova, K. 532  
 Krievina, G. 41  
 Krumin, M. 378  
 Krumina, Z. 278  
 Kruusing, K. 570  
 Krystufek, J. 107  
 Ku, J. 150  
 Kukulis, I. 319  
 Kulkas, A. 270  
 Kuo, C.-L. 481  
 Kupciunas, I. 274  
 Kupka, T. 469  
 Kustra, J. 278  
 Kybartaitė, A. 421

**L**

La Gatta, A. 104  
 Lacey, G. 485  
 Laciš, A. 76, 143  
 Laciš, I. 146, 299  
 Laciš, R. 154, 361  
 Lacković, I. 454  
 Laizans, J. 64  
 Lantto, V. 245  
 Lappalainen, R. 286  
 Lass, J. 311, 331, 335, 558, 570  
 Laurikaitiene, J. 574  
 Laurikaitis, M. 574  
 Leal, A. 505  
 Lee, C.T. 172  
 Lee, J.S. 172  
 Leice, A. 45  
 Leuchte, S. 175  
 Li, C.S. 135  
 Li, X. 485  
 Liefeyth, K. 30  
 Lima, V.M.F. 548  
 Lin, C.Y. 135  
 Linnenbank, A. 282  
 Lipping, T. 260  
 Liu, H. 34  
 Liu, J.-K. 481  
 Lo, H.C. 172  
 Lob, V. 186  
 Loca, D. 619  
 Locs, J. 48

Lok Toh, S. 34  
 Longo, D. 540  
 Lorencs, A. 536  
 Lucke, S. 30  
 Luethen, F. 30  
 Lukosevicius, A. 1  
 Luz, L. 520  
 Lyytikäinen, L.-P. 257  
 Lyytinen, H. 202, 206

**M**

Magjarević, R. 454  
 Makarenkova, G. 41  
 Malmivuo, J. 5, 350, 421, 465  
 Mandat, D. 380, 390, 393  
 Martinak, L. 194  
 Marwala, T. 160, 590  
 Mathey, M. 52  
 Matonia, A. 469  
 Matsuyama, D. 264  
 Mattsson, S. 574  
 Mednieks, I. 536  
 Meigas, K. 183, 242, 311  
 Mel'nik, Yu.I. 294  
 Mersich, A. 454  
 Menzinskis, G. 294  
 Mezzarobba, S. 179  
 Mihel, J. 454  
 Mihnovich, V. 139  
 Miklavcic, D. 307, 623  
 Miller, A. 578  
 Millevoi, M. 179  
 Min, M. 190, 425  
 Miri, R. 450  
 Mirmalek-Sani, S. 12  
 Monti, F. 91, 179  
 Mukhortova, O.V. 586  
 Muzik, J. 339  
 Myllymaa, K. 286  
 Myllymaa, S. 286

**N**

Nebe, J.B. 31  
 Nestler, B. 210, 417  
 Neumann, H.-G. 30  
 Nicholson, J. 52  
 Nielsen, K.R. 290  
 Nikolov, N. 294  
 Nikulsins, S. 41  
 Nocchi, F. 540

Nordstrom, F. 574  
 Nourbakhsh, M.S. 375, 383  
 Nousiainen J.J. 421  
 Novich, M. 616  
 Novikova, E. 56

**O**

O'Flynn, B. 486  
 Ogurcova, T. 141  
 Ohl, A. 30  
 Olsen, G.F. 501  
 O'Mathuna, C. 485  
 Oreffo, R.O. 12  
 Orel, V. 294  
 Orsini, A. 401  
 Osadebey, M. 465  
 Ostrek, G. 544  
 Ou, C.-H. 481  
 Ozolanta, I. 76, 143, 154, 357  
 Ozolins, V. 76, 143  
 Ozolinsh M. 367  
 Ozols, M. 386

**P**

Paeglis, R. 147, 298  
 Pajulo, O. 257  
 Palko, T. 437  
 Papakonstantinou, G. 213  
 Park, J. 150  
 Parve, T. 425  
 Pasquariello, G. 103, 303  
 Patmalnieks, A. 602, 294  
 Paturskis, J. 386  
 Paunksnis, A. 528  
 Pavars, J. 154  
 Pavlatos, C. 213  
 Pavšelj, N. 307  
 Peitgen, H.-O. 512  
 Penhaker, M. 194, 405  
 Pereira, W. 520  
 Perez, J.F. 429  
 Perhonen, M. 198  
 Perrone, I. 95  
 Peterec, D. 315  
 Peterlik, I. 497  
 Peterova, V. 107  
 Pilmane, M. 72  
 Pilt, K. 311  
 Plata, A. 68  
 Platkajis, A. 532

Plaude, S. 578  
 Pochmon, M. 380, 390, 393  
 Podniece, A. 299  
 Pokorný, J. 610  
 Polyaka, N. 23, 38  
 Popov, S. 578  
 Popov, V.K. 12  
 Postema, P.G. 282  
 Princi, T. 315  
 Prodana, M. 60  
 Przelaskowski, A. 544  
 Pucihar, G. 623  
 Pugovics, O. 619  
 Pulimeno, M. 489  
 Pumpens, P. 614  
 Puumala, P. 257  
 Puurtinen, M. 198, 343

**R**

Raamat, R. 248  
 Rangun, U. 248  
 Rahimi, S.A. 582  
 Raila, S. 574  
 Rakowsky, S. 413  
 Rapoport, A. 602  
 Rasmussen, A. 290  
 Renhafa, R. 614  
 Rimkus, C.M. 548  
 Ristaniemi, T. 202, 206  
 Roelofs, T.A. 413  
 Romano, M. 103, 303  
 Romanov, A.V. 294  
 Rosik, V. 339  
 Rosmann, M. 311  
 Rossler T. 380  
 Rossler, T. 390  
 Rossler, T. 393  
 Rostkowska, J. 556  
 Rosulek M. 194  
 Rozenberg, O. 156  
 Rubin, D. 160, 168, 590  
 Rubins, U. 319  
 Rupeks, L. 64  
 Russell, M. 160  
 Ryazanova, O. 397  
 Rychly, J. 30

**S**

Sakhaeimanesh, A.A. 165  
 Salma, I. 72

Salma, K. 68  
 Salms, G. 72  
 Sammons, R. 23  
 Saremi, S. 375, 383  
 Satkauskas, S. 606  
 Sato, R. 264  
 Schetinin, V. 123  
 Schlag, P.M. 413  
 Schlosser, M. 30  
 Schneider, A. 238  
 Scholz, A. 493, 509  
 Schroeder, K. 30  
 Secca, M.F. 505  
 Seemann, G. 450  
 Senatore, F. 168  
 Sevcencu, C. 290  
 Shcherbakov, A. 323  
 Shiryayev, S.V. 566, 586  
 Shoham, S. 378  
 Sikora, J. 469  
 Simon, P. 127  
 Sinica - Sinavskis, J. 536  
 Sinkkila, L. 327  
 Skagers, A. 72  
 Sklinda, K. 544  
 Smits, L. 76, 143  
 Smolanka, I. 294  
 Sokhan', S. 156  
 Sorokin, V. 628  
 Spigulis, J. 386  
 Spunde, A. 146  
 Starfield, D.M. 590  
 Stasko, J. 80  
 Stradins, P. 154  
 Strazdins, U. 361  
 Stroschio, M.A. 594  
 Struijk, J.J. 290  
 Stunda, A. 68  
 Suhhova, A. 331  
 Surana, V. 52  
 Svikis, I. 386  
 Szarska, E. 632  
 Szmidt, E. 632  
 Šimša, J. 610

**T**

Tabatabaee, F. 374, 382  
 Talts, J. 248, 461  
 Tamburlini, G. 442  
 Tan, H.L. 282  
 Tanila, H. 286

Tarasenko, S.O. 83  
 Tarticchio, D. 401  
 Tautenhahn, H.-M. 512  
 Tautenhahn, M. 238  
 Temitski, K. 242  
 Togni, P. 433  
 Toporov, V.V. 594  
 Tsai, K.H. 135, 172  
 Tsirkunova I.E. 477  
 Tupureina, V. 80  
 Tuulik, V. 335  
 Tysler, M. 339

**U**

Uhlin, F. 252  
 Ullmann, R. 175  
 Upton, C. 12  
 Usenko, E. 628

**V**

Vaisanen, J. 326, 342  
 Vaisanen, O. 327  
 Valdmanis, J. 347  
 Valeev, V. 628  
 Vasidev, M. 594  
 Veliks, V. 386  
 Vetra, J. 72  
 Vetrennikov, V. 562  
 Viigimaa, M. 242  
 Vilar, G. 429  
 Vilkausha, L. 146  
 Vitins, V. 64  
 Vöhma, Ü. 331  
 Voloshin, I. 397  
 Voznyy, V. 156  
 Vrachko, M. 616

**W**

Walecki, J. 545  
 Walewska, A. 556  
 Walschus, U. 30  
 Wårdell, K. 363, 371  
 Wasilewska-Radwanska M. 437  
 Weber, F. 450  
 Weiss, D. 450  
 Wellnhofer, E. 111  
 Weltmann, K.-D. 30  
 Wendel, K. 465  
 Wiest, J. 353



Wigdorowitz, B. 160  
Wójcik, A. 632  
Wolf, B. 186, 353, 493, 509  
Wong E.J.W. 34  
Wrobel, J. 446  
Wuetig, D. 210

**X**

Xu, X. 207

**Y**

Yeh, C.Y. 173

**Z**

Zalewska, M. 557  
Zambon, A. 442  
Zanardi, V.A. 548  
Zangrando, R. 401, 442

Zemite, V. 87, 439  
Zennaro, F. 401  
Zerbinati, A. 371  
Zholdakova, Z.I. 616  
Zhou, J. 485  
Zhurinsh, A. 48  
Zietek, J. 469  
Zinchenko, V.F. 83  
Zozulya, V. 397

# Subject Index

- 1**  
1-RM 116, 120
- 3**  
3D laser scan profilometry 390  
3D Topography 380  
3D visualization 512
- 5**  
5-aminolevulinic acid induced  
fluorescence 362
- A**  
absorbance 252  
AC component 311  
accelerometer 115, 119, 221  
acute rejection 238  
airway resistance 461  
Anaesthesia 257, 458  
analysis 141  
animal experiments 30  
animal model 290  
anomalous magnetic field 562  
anterior leaflet 154  
anti-microbial 52  
aortic stiffness 242  
apoptosis 72, 524  
arrhythmias 450  
arterial stiffness 319  
artery 274  
artifact reduction 590  
artificial heart valves 164  
artificial larynx 160  
artificial saliva 8  
assistive device, devices 131, 168  
asymmetry of electromagnetic fields  
294  
atherosclerosis 242  
atomic force microscope 602  
atrial fibrillation 450  
attribute Grammars 213  
augmentation Index 242  
augmented reality 489  
autologous pericardium 143  
automated 186  
automated detection 270  
automatic Speech Recognition 160
- B**  
ballistocardiogram 278  
Bayesian 501  
Bayesian model averaging 123  
beat-to-beat interval 270  
benzenes 616  
Bezier splines 465  
biocompatibility 19, 60, 64  
bioelectromagnetism 433, 610  
bioglass 632  
bioimpedance 190  
biomaterial, -s 48, 83  
biomechanical properties 76, 143  
biomedical electronics 425  
Biomedical engineering  
417, 421, 437  
biomedical image processing 536  
biomorphic 48  
biopotential 234  
biosensor 353  
bio-signal processing 319  
biotelemetry 194, 405  
bipolar 343  
bispectrum 260  
blood 225  
blood pressure 454  
blood-ocular barriers 217  
BME 409  
body surface mapping 282  
body surface potential mapping  
339  
bond strength 64  
bone 16  
bone cements 52  
bone marrow 38  
bone marrow multipotent  
mesenchymal stromal cells 41  
bone remodelling 357  
brain 371  
brainstem 548  
breast ultrasound images 520  
breath-holding 516  
Brugada syndrome 282
- C**  
Ca<sup>2+</sup> oscillation 264  
calcium apatites 83  
calcium phosphates 68  
calibration 115  
Canadian cardiovascular society  
angina class 361  
capacitive sensing 131  
carcinogenicity 616  
cardiac cycle 270  
cardiac myocytes 264  
cardio-vascular assessment 386  
carotid endarterectomy 91  
cartilage 16  
CdZnTe pixel detectors 477  
cell adhesion 19  
cell culture 30  
cell model 558  
cells 45, 186, 493  
cellular respiration 353  
cephalogram analysis 481  
cerebral 139  
channelopathies 450  
chemosensitivity 186  
Chordae tendineae 154  
classification 501  
Clinical engineering 234  
CLSM 16  
clustering 536  
CMOS Image Sensor 485  
CMS 442  
Co-60 source 574  
cobweb 56  
CoCr alloy 26  
coded apertures 590  
coherence 331  
colors 367  
computational fluid dynamics 111  
computed calibration 497  
computed radiography (CR) 552  
computer aided diagnosis 536, 544  
computer assisted surgery 512  
computer integrated surgery 229  
computer tomography, CT 512, 544  
COMSOL Multiphysics 433  
conformational transitions 628  
congenital heart defect 143

congenital malformation 548  
 congenital nystagmus 303  
 contact angle 8  
 contact surface measurement 390  
 contrast agent 501  
 coronary artery 111  
 coronary artery bypass graft surgery 361  
 coronary artery disease 361  
 coronary heart disease 242  
 correlations 378  
 cost-effectiveness 586  
 Cotyle ABG I 380  
 count statistics 590  
 counting 493  
 CR systems 552  
 craniofacial structure 481  
 cryopreservation 41  
 customisable platform 168

**D**

data acquisition 191, 218  
 decision tree 123  
 degradation 87  
 demographic indices change 562  
 dendritic integration 378  
 depression 331  
 deterministic chaos 268  
 development 566  
 devices 238  
 diabetes 217  
 diagnostic radiology 582  
 dialysis 252  
 dialysis adequacy 323  
 dialysis quality 323  
 DiaSens 323  
 differential oscillometric method 248  
 differential scanning calorimetry 619  
 diffuse reflectance spectroscopy 371  
 digital image processing 493  
 diode laser 383  
 direct matching 146  
 disabilities 168  
 disc displacement 107  
 dissolved oxygen 353  
 distance education 413  
 DNA repair 524  
 Doppler 501  
 dose calculation 574  
 dose verification 574  
 doubly stochastic Poisson 378

drug delivery 619  
 DT-CWT 473  
 dynamic time warping 278  
 dysgraphia 95

**E**

early detection of local ischemia 338  
 ECG 198, 213, 343  
 ectopic osteogenesis 38  
 edge detection 528  
 education 405, 409, 437, 439  
 education 417  
 e-education 421  
 EEG, electroencephalography 278, 350, 505  
 EEG analysis 331  
 EEG burst suppression 260  
 EEG monitoring 91  
 elasticity 274  
 e-learning course 425  
 electric field 610  
 electrical charge 23  
 electrochemical behavior 60  
 electrochemical stability 26  
 electrode 350  
 electrohysterography 469  
 electromagnetic field 347  
 electromagnetic radiation 602  
 electromagnetism 347  
 electropalatograph 160  
 electroporation 307, 606  
 EMD 206  
 EMF effect 558  
 EMG, electromyography 103, 179  
 endocytosis 598  
 ensemble averaging 257, 458  
 entrance dose 582  
 epicardial acceleration 221  
 epilepsy 290  
 equivalent dipole model 339  
 evaluation 274  
 evoked potential -s 548, 570  
 exoelectron emission 632  
 eye fundus 528  
 eye movement signal processing 303

**F**

fat 370  
 feature selection 123

feedback control 375  
 fetal monitoring 446  
 field effect 558  
 film dosimetry 556  
 finger tapping 127  
 finite element analysis 135  
 finite element method 64  
 finite element models 465  
 finite elements 307, 429, 623  
 fit 245  
 flow measuring 210  
 flow regulator 210  
 fluorescence 397  
 fluorescence spectroscopy 363  
 fMRI, functional magnetic resonance imaging 278, 505, 516  
 FOG 179  
 foot 141  
 foveation 303  
 FPGA 213, 485  
 fracture healing 357  
 Freezing in ON 179  
 gait analysis 175, 179  
 gait speed 175  
 gait training 150  
 gamma evaluation 556  
 gas-discharge plasma 30  
 gate 99  
 gels 80  
 gene electrotransfer 606  
 gene therapy 606  
 glioma resection 363  
 glutamate uncaging 378  
 glutaraldehyde 143  
 growth factors 72

**H**

hand-washing 486  
 handwriting 95  
 haptic feedback 429  
 head 465  
 head injury 135  
 Health Grid applications 413  
 health monitoring 509  
 heart motion 221  
 heart rate 234, 290  
 heart rate variability 315  
 higher order spectrum 260  
 high-voltage electrical discharge 602  
 Higuchi's fractal dimension 268  
 Hilbert transform 270

hip joint heads 156  
 histopathology 375  
 home (health) monitoring 454, 509  
 human bone 87  
 hydroxyapatite (ceramics) 23, 45,  
 68, 72  
 hyperacute stroke 544  
 z potential 632

**I**

ICA, 203  
 ICG 383  
 image analysis 524  
 image categorisation 299  
 image guided surgery 490, 512  
 image processing 528  
 image reconstruction 497  
 IMF 206  
 immobilization 23  
 impact 135  
 impedance 238  
 implantable pumps 210  
 implantation 64  
 implants 38  
 imprints 141  
 IMRT plan verification 556  
 inductotherapy 294  
 infant 76  
 infarction 450  
 Infra-red eye-tracking 146  
 infrared spectra 68  
 intelligent vision system 485  
 intensity modulated radiotherapy 578  
 intercalation 397  
 interface 16  
 International BME program 417  
 internet learning support 425  
 interrupter technique 461  
 intraocular light scattering 367  
 Intraoperative guide 363  
 inverse solution 339  
 ionometric dosimetry 578  
 ISO 9001:2000 quality standards 401  
 iViewX 146, 299

**J**

Joomla! CMS 401  
 joystick 131  
 karate 146  
 kinematic analysis 95

kinematics 107  
 knee 175  
 knee angle 150

**K**

Kt/V 322  
 lab on chip 353

**L**

LabView 379  
 LAMP open source technology 401,  
 442  
 laser sintering 12  
 laser soldering 375  
 late potentials 282  
 LDA technique 164  
 LDF 248  
 lead 343  
 LED current 311  
 leg-propulsion 172  
 life cell monitoring 353  
 ligament 34  
 linear regression 536  
 liver transplantation 238  
 living donor liver transplantation 512  
 local optimization 202  
 lognormal distributions 245  
 long-term culture 41  
 low-level effects 335  
 lung cancer 586  
 lung function 461

**M**

magnetic resonance 549  
 magnetic resonance imaging, MRI  
 107, 505, 540  
 master program 417  
 mathematical modeling of the heart  
 450  
 Matlab 380  
 MCMC 123  
 mean arterial pressure 248  
 Medical engineering 439  
 medical images 532  
 medical imaging 505  
 medical physics 437, 439  
 mesenchymal stem cells 34  
 metal ions 628  
 method 56, 274

Mg<sup>2+</sup> oscillation 264  
 mice 38  
 microcapsules 619  
 microcell 598  
 microelectrode array 286  
 microencapsulation 619  
 microfluidic 210  
 microscope method 393  
 microtubules 610  
 microwave radiation 331  
 microwaves, hyperthermia 433  
 minimally invasive surgery 489  
 mitral valve 154  
 MMN 206  
 mobile 198  
 MOCVD 8, 26  
 model 350  
 modelling 461  
 modulated microwaves 335  
 modulus of elasticity 154  
 morphologic operators 520  
 morphological information 481  
 motion 107  
 motion artifact 103  
 movement analysis 127  
 multimodal 278  
 multiscale analysis 544  
 muscle 371  
 muscle movement 103  
 nanoparticles 598, 614  
 nanoscale functionalization 594  
 navigation 131  
 nephrology 252  
 neural recording 286  
 neuro-fuzzy systems 446  
 neurosurgery 229  
 noninvasive 493  
 non-invasive blood pressure 248  
 non-invasive diagnostics 319  
 nonlinear Dynamics 268  
 non-Newtonian blood model 111  
 nuclear medicine imaging 590  
 numerical modeling 307

**O**

ocular fluorescence 218  
 online measurement 186  
 optic nerve disk 528  
 optical bio-sensing 386  
 optical dialysis monitoring 323  
 optical radiation 357

oral glucose tolerance test 315  
 orientation 343  
 orthodontics 481  
 orthosis 139  
 oscillation 164  
 osteoblasts 23  
 outliers 540  
 outside binding 397  
 oxygen 616  
 oxygen consumption 172

## P

P450 617  
 palsy 99  
 paralysis 139  
 Parkinson's disease 179  
 pathology zone 532  
 patient dose reducing 552  
 pattern recognition 536  
 PD current 311  
 PET-Center 566  
 pH 225  
 phacoemulsification 429  
 phantoms 540  
 phase-shifting profilometry 390  
 Pheophorbide-a 397  
 phosphate deposition 26  
 photolithography 286  
 photoplethysmography, PPG 245,  
 311, 319, 386  
 physical and chemical stressors 335  
 plasma polymer 30  
 platelets 45  
 pointing 127  
 polarity indeterminacy 202  
 poly(vinyl alcohol) 80  
 polyaniline 225  
 polyethylene wear measurement 393  
 polyimide 286  
 polymers 194  
 polynucleotides 397, 628  
 polytetrafluorethylene 76  
 porosity, roughness 19  
 positron emission tomography  
 566, 586  
 posterior leaflet 154  
 power density spectra 164  
 premature labour 469  
 probe efficiency 311  
 problem based learning 409  
 profiles 465

projection 202  
 propidium iodide 623  
 propofol anesthesia 260  
 protective 135  
 proteolytic degradation 143  
 psychological effects 570  
 pulmonary therapy 509  
 pulse wave velocity 245  
 pulsed laser modulation 363

## Q

quadratic phase coupling 260  
 quality control 578  
 quality level 56  
 quantum chemistry 616  
 quasi-thermal effect 558

## R

radio frequency ablation 370  
 radiographic techniques 393  
 radiotherapy 574  
 reactogenicity 72  
 reahbilitation 131  
 real-time interactivity 413  
 reciprocal 99, 139  
 red- white- blood 45  
 region of interest sensitivity ratio 327  
 rehabilitation 95, 150, 172  
 release 52  
 remote sampling 190  
 resistance 225  
 resonance 347  
 respiratory sounds 454  
 RF exposure 570  
 rhythmical oscillation 347  
 risk factors 242  
 robotic surgery 229  
 room temperature semiconductor  
 detectors 477  
 RR interval 290

## S

saccades 147  
 safety limits 558  
 saline melts 83  
 sapphire 156  
 SAR 206  
 scaffolds 12  
 scanning electronic microscopy 8

scanning profilometry 393  
 segmentation 520, 532  
 semiconductor 614  
 semiconductor quantum dots 594  
 sensitivity 350  
 sensitivity distribution 327  
 sensors 168, 194  
 shape memory alloy 56  
 shear stresses 164  
 shock loading 56  
 SiC 48  
 signal averaging 282  
 signal classification 446  
 signal-to-noise ratio 257, 327, 458  
 silk scaffold 34  
 skin 307  
 slit-lamp 217  
 smart textile 198  
 SoC 213  
 somatosensory evoked potentials  
 257, 458  
 spatio-temporal treatment 95  
 spectral analysis 91  
 spinal 139  
 spinal cord 548  
 spirometry 509  
 SPM 540  
 spontaneous beating 264  
 SRT 299  
 static and dynamic mode 383  
 stiff-knee 150  
 stroke 172  
 submaximal weight 119  
 surface analyses 60  
 surface modification 30  
 surface morphology 602  
 surface treatment 19, 60  
 surfacing 135  
 surgical simulator 429  
 symbolic dynamics 516  
 symbolis methods 268  
 synergy 99  
 synthesis 68, 83  
 system of practice 439

## T

telemedicine 510  
 telemetry 238  
 temporomandibular joint 107  
 tensile strength 383  
 textile electrode 198

texture analysis 473  
thermoluminescent dosimetry 582  
thick film 225  
thin film 286  
threshold current 183  
TiAlNb alloy 8  
time 87  
time-frequency 206  
TiNiNb, TiAlV and TiAlZr 60  
TiO<sub>2</sub> 26  
tissue characterization 473  
tissue engineering 12, 34  
tissue soldering 383  
titanium 19  
titanium alloy 156  
titanium plate 45  
TLD 582  
total endoprosthesis 390  
total hip arthroplasty 393  
total knee arthroplasty 175  
tracheal sound 270  
tracing 481  
transdifferentiation 41  
transesophageal pacing 183  
transmembrane potential 623  
transmitocardial laser  
  revascularization 361  
trauma care 123

treatment 99  
tumour 294, 524  
two-photon 378

## U

ubiquitous learning (u-learning) 413  
ultra violet 252  
ultra-near-field system 590  
ultrasonic computed tomography 497  
ultrasonic transducers 497  
ultrasound 274  
undergraduate education 433  
uterine activity 469

## V

vagus nerve stimulation 290  
validation 234  
vascular assessment 319  
vasotrac 248  
VBM 540  
vegetarians diets 315  
ventricular septal defect 76  
vibration treatment 103  
video lectures 421  
vigilance level 335  
Virtual Hospital 413

virtual reality 150, 429  
visual acuity 303, 367  
visual perception 570  
visualization 532  
VLP 614  
VOG 299  
volume estimation 532

## W

walking 142  
wall shear stress 111  
water absorption 80  
wearable 198  
web portal and databases 442  
wheelchair 172  
wireless communication 405  
wireless sensor network 485  
wood 48  
wound healing 375

## X

x-ray diffraction 69  
X-Ray diffractometry 619  
yeast cells 602, 610  
zero crossing 91  
zirconium ceramics 156